CODEN: JASMAN

The Journal of the Acoustical Society of America

ISSN: 0001-4966

Vol. 111, No. 2 February 2002

(Continued)

THE JOURNAL OF THE ACOUSTICAL SOCIETY OF AMERICA VOL. 111, NO. 2, FEBRUARY 2002

CONTENTS—*Continued from preceding page*

(Continued)

THE JOURNAL OF THE ACOUSTICAL SOCIETY OF AMERICA VOL. 111, NO. 2, FEBRUARY 2002

CONTENTS—*Continued from preceding page*

(Continued)

THE JOURNAL OF THE ACOUSTICAL SOCIETY OF AMERICA VOL. 111, NO. 2, FEBRUARY 2002

CONTENTS—*Continued from preceding page*

BIOACOUSTICS [80]

ERRATA

ACOUSTICAL NEWS—USA

Elaine Moran
Acoustical Society of America, Suite 1NO1, 2 Huntington Quadrangle, Melville, NY 11747-4502

Editor's Note: *Readers of this Journal are encouraged to submit news items on awards, appointments, and other activities about themselves or their colleagues. Deadline dates for news items and notices are 2 months prior to publication.*

New Fellows of the Acoustical Society of America

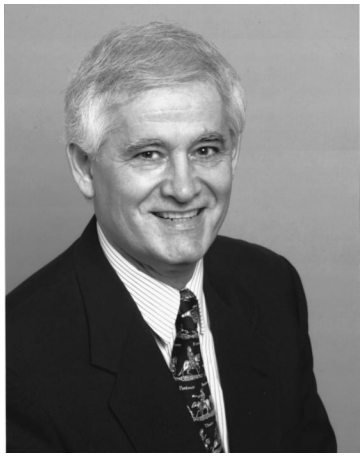

Anthony G. Galaitsis—For contributions to the control of machine noise and vibration.

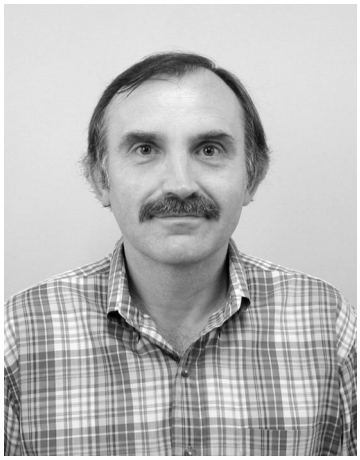

Anatoliy Ivakin—For contributions to the understanding of scattering of sound by the seafloor.

Jerry Lilly—For contributions to the dissemination of noise control knowledge.

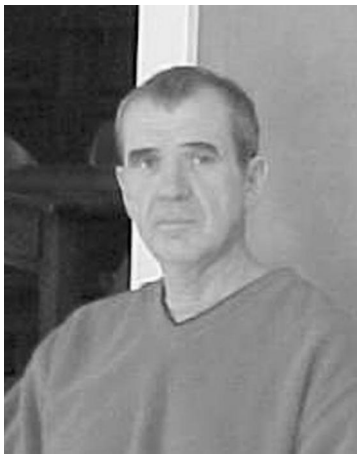

Chaslav Pavlovic—For contributions to objective measures of speech intelligibility, standards, and hearing aids.

 0001-4966/2002/111(2)/643/3/$19.00

Jeffery Jones selected recipient of the 2001 Stetson Scholarship

Jeffery A. Jones

ASA member Jeffery Jones was selected the recipient of the 2001 Raymond H. Stetson Scholarship in Phonetics and Speech Production. Mr. Jones is a graduate student in the Department of Psychology at Queen's University in Kingston, Ontario, Canada. He received a B.A. (Hons) from McMaster University and an M.A. from Queen's University. His current research includes issues related to the motor coordination of speech organs, studies on linguistic issues related to speech production, and control of the aerodynamics of speech production.

This scholarship, which was established in 1998, honors the memory of Professor Raymond H. Stetson, a pioneer investigator in phonetics and speech science. Its purpose is to facilitate the research efforts of promising graduate students and postgraduates. The Scholarship includes a $3000 stipend for one academic year. Past recipients have been Roger Steeve (1999) and Elizabeth K. Johnson (2000).

Applications for the award are due in March each year. For further information about the award please contact the Acoustical Society of America, Suite 1NO1, 2 Huntington Quadrangle, Melville, NY 11747-4502, Tel: 516-576-2360, Fax: 516-576-2377, E-mail: asa@aip.org. Application information can also be found on the ASA Home page at ⟨http://asa.aip.org/fellowships.html⟩.

Volunteers Review Patents of Acoustical Interest

The ''Reviews of Acoustical Patents'' section of the Journal is produced by a group of volunteers who read and review patents of relevance to their areas of expertise.

Each week, the United States Patent and Trademark Office releases approximately 3000 new patents covering a wide range of topics. These new releases are searched to find those patents which might be of interest to readers of the *Journal*. The topics currently being selected for possible review include the use of ultrasonics in medicine and industry, noise and vibration control in buildings, automobiles, and aircraft, underwater effects of sound, loudspeaker design, earphones, hearing aid design and ear protection, and speech transmission and processing.

Copies of the selected patents are purchased by the Acoustical Society and mailed to the reviewers, who study them and make the final decision as to whether the patent would merit being reviewed for publication. Currently, 14 reviewers volunteer their time to make these decisions and to write their reviews of the patents.

George L. Augspurger has been a JASA patent reviewer for more than 10 years. He is the principal consultant and president of Perception Incorporated, a consulting group in Los Angeles specializing in architectural acoustics and sound system design. George is a Fellow of the Audio Engineering Society and a member of the United States Institute of Theatre Technology. The company, Perception Inc., maintains membership in the National Council of Acoustical Consultants.

Robert B. Coleman has reviewed patents for the Acoustical Society for 6 years. He is a Principal Engineer in Applied Physics for BBN Technologies in Cambridge, Massachusetts.

Alireza Dibazar has only recently started writing patent reviews for the Acoustical Society. He is a student at the University of Southern California in Los Angeles, studying under Dr. Michael Arbib in the Department of Biomedical Engineering.

John Erdreich has been reviewing patents for JASA for at least 20 years. He is a principal in the firm Ostergaard Acoustical Associates in West Orange, New Jersey. John participates in the ASA technical committees on Noise, Architectural Acoustics, and Biomedical Ultrasound/Bioresponse to Vibration. He is a past chair of the Long Range Planning committee and has served on Medals and Awards, the Technical Council, Special Fellowships, numerous Standards working groups, ASACOS, and also served as president of the National Council of Acoustical Consultants.

Ibrahim Hallaj has been a patent reviewer for a little over 1 year. He is a Technology Specialist at Wolf, Greenfield & Sacks, P.C., a Boston law firm specializing in intellectual property law. Ibrahim is active in the ASA through its committees and meetings. He is a member of the Technical Committee on Biomedical Ultrasound/Bioresponse to Vibration and a past Technical Program Organizing Committee representative. Ibrahim has organized and chaired ASA meeting sessions and is a JASA author. He is also a member of IEEE, the American Bar Association, and the Boston Bar Association.

Hassan H. Namarvar started reviewing patents during the summer of 2001. He is employed by the University of Southern California in Los Angeles as a research assistant in the Department of Biomedical Engineering. Hassan is also a member of the student council of the Acoustical Society.

David Preves has been a patent reviewer for 2 years. He is self-employed as a technical consultant in the hearing aid industry and previously served as Vice President of Research and Development for Songbird Hearing in Cranbury, New Jersey. David is chair of the S3/WG48 working group on hearing aid measurements and is a fellow of the Acoustical Society.

Daniel Raichel started reviewing patents during the summer of 2001. He was an Adjunct Professor for the City University of New York's Graduate Center and worked with the School of Architecture, Urban Studies, and Landscape Design. He is now on the Auxiliary Faculty of Colorado State University in Fort Collins, Colorado. Daniel is a member of the College of Fellows Steering Committee and Acoustics Education Committee and organized and chaired a number of sessions in Noise, Bioacoustics, and Acoustics Education. He is a Fellow of the ASME International, Member of Audio Engineering Society and the American Physical Society.

Lloyd Rice has been reviewing speech-related patents for JASA since 1977, following in the footsteps of Homer Dudley. Since late 1999, he has edited the Patent Reviews section of the Journal, trying to carry on in the tradition of Dan Martin's prodigious efforts. In January 1999, Lloyd retired from Syvox, Incorporated, in Boulder, Colorado, where he worked for 10 years as a DSP programmer in speech recognition. Lloyd has been active in the Speech technical area of ASA since the 1970s. He is a member of IEEE and the Audio Engineering Society.

Carl J. Rosenberg has been reviewing patents for about 15 years. He is the president of and a principal in the ASA sustaining member company Acentech, Incorporated in Cambridge, Massachusetts. Carl is a member of the ASA Technical Committee on Architectural Acoustics.

Kevin Shepherd started reviewing patents for the Acoustical Society 4 years ago. He is the head of the Structural Acoustics Branch of NASA Langley Research Center in Hampton, Virginia. Kevin was the Chair of the ASA meeting held in Norfolk, Virginia in 1998 and will serve as a technical program chair for the 144th ASA Meeting in Cancun, Mexico.

William Thompson, Jr. has been a patent reviewer for about 11 years. He was recruited by the late Dan Martin at the ASA meeting held at Penn State in 1990. Bill is Professor Emeritus of Engineering Science at Penn State University and is on the ASA committee on Education. He previously served on the committee on Engineering Acoustics.

Eric E. Ungar has kept records of his patent reviewing since 1980, but believes that he started reviewing earlier than that. He is a Chief Engineering Scientist for Acentech Incorporated in Cambridge, Massachusetts, a title he has held since retiring in 1996 from BBN (formerly known as Bolt Beranek and Newman, Inc.), where he had the title of Chief Consulting Engineer.

Robert C. Waag reviews patents for JASA in the area of acoustical imaging as well as related areas such as measurements of scattering. He does not recall how many years he has been a patent reviewer, but says that Floyd Dunn recommended him as a reviewer during the time Dan Martin was working as Associate Editor for Patent Reviews. During spare moments at the joint ASA–ASJ meeting in Hawaii in 1978, Robert worked on reviews for a large accumulation of patents provided to him by Dan Martin. Robert is the Yates Professor of Engineering at the University of Rochester in Rochester, New York. He has also been a member of the ASA Physical

Acoustics Technical Committee on and off over the years.

When asked why they wanted to invest the time to review patents for JASA, each of the reviewers mentioned the opportunities for keeping in touch with recent technical developments in their field. This benefit was mentioned as being important for the reviewer as well as for the entire readership of the *Journal*. Some reviewers also mentioned the pleasure in seeing the names of their friends and associates appear as authors of an issued patent.

In addition, a reviewer offered specific thoughts on the nature of patents and their importance to our technically oriented society: ''Although not nearly a settled debate, I believe that responsible protection of intellectual property promotes invention and permits inventors to invest resources in the development of their ideas, which later result in benefits to society at large. It is unfortunate that many scientists possess superb technical talents but are unable to harness the economic value of their efforts to the same degree that other professionals do. By providing some service to the *Journal* I hope to use my experience to the benefit of other ASA members and to raise the awareness of intellectual property issues among ASA members.''

Besides the above-mentioned areas of technical interest, reviewers are being sought to cover several areas notably missing from the list. The most prominent gap is that of musical acoustics. Patents describing a wide variety of new musical instruments and music processing technology were reviewed by Dan Martin while he also served as the Editor-in-Chief and as Patent Reviews Associate Editor. Other areas of active interest as indicated by the number of papers presented at the ASA meetings and by the number of new patents issued include microelectronics devices, piezoelectric devices, surface wave technologies, and a variety of industrial vibration detection and application technologies.

LLOYD RICE

USA Meetings Calendar

Listed below is a summary of meetings related to acoustics to be held in the U.S. in the near future. The month/year notation refers to the issue in which a complete meeting announcement appeared.

2002

21–23 February	National Hearing Conservation Association Annual Conference, Dallas, TX [NHCA, 9101 E. Kenyon Ave., Ste. 3000, Denver, CO 80237; Tel.: 303-224-9022; Fax: 303-770-1812; E-mail: nhca@gwami.com; WWW: www.hearingconservation.org/index.html].
10–13 March	Annual Meeting of American Institute for Ultrasound in Medicine, Nashville, TN [American Institute for Ultrasound in Medicine, 14750 Sweitzer Lane, Suite 100, Laurel, MD 20707-5906; Tel.: 301-498-4100 or 800-638-5352; Fax: 301-498-4450; E-mail: conv_edu@aium.org; WWW: www.aium.org].
3–7 June	143rd Meeting of the Acoustical Society of America, Pittsburgh, PA [Acoustical Society of America, Suite 1NO1, 2 Huntington Quadrangle, Melville, NY 11747-4502; Tel.: 516-576-2360; Fax: 516-576-2377; E-mail: asa@aip.org; WWW: asa.aip.org].
19–21 August	INTER-NOISE 2002, Dearborn, MI [INTER-NOISE 02 Secretariat, The Ohio State University, Department of Mechanical Engineering, 206 West 18th Ave., Columbus, OH 43210-1107; E-mail: hp @internoise2002.org].
2–6 December	Joint Meeting: 144th Meeting of the Acoustical Society of America, 3rd Iberoamerican Congress of Acoustics and 9th Mexican Congress on Acoustics, Cancun, Mexico [Acoustical Society of America, Suite 1NO1, 2 Huntington Quadrangle, Melville, NY 11747-4502; Tel.: 516-576-2360; Fax: 516-576-2377; E-mail: asa@aip.org; WWW: asa.aip.org/cancun.html].

2003

28 April–2 May	145th Meeting of the Acoustical Society of America, Nashville, TN [Acoustical Society of America, Suite1NO1, 2 Huntington Quadrangle, Melville, NY 11747-4502; Tel.: 516-576-2360; Fax: 516-576-2377; E-mail: asa@aip.org; WWW: asa.aip.org].
10–14 November	146th Meeting of the Acoustical Society of America, Austin, TX [Acoustical Society of America, Suite 1NO1, 2 Huntington Quadrangle, Melville, NY 11747-4502; Tel.: 516-576-2360; Fax: 516-576-2377; E-mail: asa@aip.org; WWW: asa.aip.org].

2004

17–21 May	75th Anniversary Meeting (147th Meeting) of the Acoustical Society of America, New York, NY [Acoustical Society of America, Suite 1NO1, 2 Huntington Quadrangle, Melville, NY 11747-4502; Tel.: 516-576-2360; Fax: 516-576-2377; E-mail: asa@aip.org; WWW: asa.aip.org].

Cumulative Indexes to the *Journal of the Acoustical Society of America*

Ordering information: Orders must be paid by check or money order in U.S. funds drawn on a U.S. bank or by Mastercard, Visa, or American Express credit cards. Send orders to Circulation and Fulfillment Division, American Institute of Physics, Suite 1NO1, 2 Huntington Quadrangle, Melville, NY 11747-4502; Tel.: 516-576-2270. Non-U.S. orders add $11 per index.

Some indexes are out of print as noted below.

Volumes 1–10, 1929–1938: JASA and Contemporary Literature, 1937–1939. Classified by subject and indexed by author. Pp. 131. Price: ASA members $5; Nonmembers $10.

Volumes 11–20, 1939–1948: JASA, Contemporary Literature, and Patents. Classified by subject and indexed by author and inventor. Pp. 395. Out of Print.

Volumes 21–30, 1949–1958: JASA, Contemporary Literature, and Patents. Classified by subject and indexed by author and inventor. Pp. 952. Price: ASA members $20; Nonmembers $75.

Volumes 31–35, 1959–1963: JASA, Contemporary Literature, and Patents. Classified by subject and indexed by author and inventor. Pp. 1140. Price: ASA members $20; Nonmembers $90.

Volumes 36–44, 1964–1968: JASA and Patents. Classified by subject and indexed by author and inventor. Pp. 485. Out of Print.

Volumes 36–44, 1964–1968: Contemporary Literature. Classified by subject and indexed by author. Pp. 1060. Out of Print.

Volumes 45–54, 1969–1973: JASA and Patents. Classified by subject and indexed by author and inventor. Pp. 540. Price: $20 (paperbound); ASA members $25 (clothbound); Nonmembers $60 (clothbound).

Volumes 55–64, 1974–1978: JASA and Patents. Classified by subject and indexed by author and inventor. Pp. 816. Price: $20 (paperbound); ASA members $25 (clothbound); Nonmembers $60 (clothbound).

Volumes 65–74, 1979–1983: JASA and Patents. Classified by subject and indexed by author and inventor. Pp. 624. Price: ASA members $25 (paperbound); Nonmembers $75 (clothbound).

Volumes 75–84, 1984–1988: JASA and Patents. Classified by subject and indexed by author and inventor. Pp. 625. Price: ASA members $30 (paperbound); Nonmembers $80 (clothbound).

Volumes 85–94, 1989–1993: JASA and Patents. Classified by subject and indexed by author and inventor. Pp. 736. Price: ASA members $30 (paperbound); Nonmembers $80 (clothbound).

Volumes 95–104, 1994–1998: JASA and Patents. Classified by subject and indexed by author and inventor. Pp. 632. Price: ASA members $40 (paperbound); Nonmembers $90 (clothbound).

ACOUSTICAL NEWS—INTERNATIONAL

Walter G. Mayer
Physics Department, Georgetown University, Washington, DC 20057

Statistics—17th International Congress on Acoustics in Rome 2001

Statistics of the 17th International Congress on Acoustics which was held in Rome in September 2001 have now been released by the organizers.

The last column of the compilation below shows the number of registered participants from the various countries represented at the congress. The other columns show the number of participants at previous Congresses held in Paris (1983), Toronto (1986), Belgrade (1989), Beijing (1992), Trondheim (1995), and Seattle (1998). The table reflects the fact that there have been some political changes in the 18 years covered by these statistics.

Country	Paris	Toronto	Belgrade	Beijing	Trondheim	Seattle	Rome
Algeria	1	0	0	0	1	0	1
Argentina	3	5	0	0	0	0	5
Armenia				0	0	0	1
Australia	3	19	4	12	19	36	27
Austria	0	0	2	0	6	11	10
Belarus				0	0	0	2
Belgium	19	8	9	4	9	15	23
Brazil	1	4	1	3	3	12	18
Bulgaria	3	1	6	0	0	0	0
Canada	30	171	18	10	10	75	17
Chile	1	0	0	1	1	2	3
China	15	19	15	370	4	47	30
Colombia	0	0	0	0	0	1	0
Croatia				1	0	0	6
Cuba	1	0	0	0	0	0	0
Czech Republic					4	3	11
Czechoslovakia	6	1	7	0			
Denmark	36	23	19	9	28	17	25
Egypt	2	1	1	0	0	1	1
Estonia				0	4	2	3
Finland	5	2	4	2	10	7	14
France	350	98	67	35	63	95	99
Germany (FRG)	100	71	55	32	41	49	64
Germany (GDR)	2	1	3				
Greece	3	0	3	0	0	1	4
Hong Kong	2	0	0	2	0	4	0
Hungary	8	3	22	0	11	1	6
Iceland	0	0	0	0	0	0	1
India	10	7	8	3	3	9	12
Indonesia	0	0	0	1	0	0	2
Iran	2	0	1	2	0	0	0
Ireland	0	0	0	0	0	3	3
Israel	4	2	0	3	0	3	3
Italy	20	15	13	8	16	28	160
Japan	97	143	87	106	96	173	237
Korea	0	2	0	21	4	33	25
Kuwait	0	0	0	0	0	0	1
Lebanon	0	0	0	0	0	0	2
Lithuania				0	0	0	2
Malaysia	0	0	0	2	0	0	0
Mexico	0	0	0	0	0	8	2
Morocco	0	0	0	1	0	0	0
Netherlands	24	18	21	8	14	27	19
New Zealand	2	4	1	0	2	9	5
Nigeria	0	1	0	0	0	0	0
Norway	9	8	9	3	89	18	24
Peru	0	0	0	0	1	0	0
Poland	17	10	16	2	24	12	36
Portugal	4	1	1	1	3	0	9
Romania	3	0	1	0	1	0	6
Russia				8	13	27	32
Singapore	2	2	0	3	1	3	2

 0001-4966/2002/111(2)/647/3/$19.00

Slovakia					1	1	3
Slovenia				0	0	0	3
South Africa	3	8	1	1	0	3	0
Spain	18	16	4	2	7	13	25
Sweden	15	21	16	10	40	25	35
Switzerland	11	3	4	0	7	7	21
Syria	0	3	0	0	0	0	0
Thailand	0	0	0	1	0	0	0
Tunisia	0	0	0	0	0	0	2
Turkey	0	1	0	0	1	1	7
United Kingdom	75	46	27	20	35	77	55
Ukraine				0	0	2	1
Uruguay	0	0	0	0	0	0	2
USA	117	201	61	64	69	1066	176
USSR	17	12	31				
Uzbekistan				0	0	0	1
Venezuela	0	0	0	0	0	2	3
Yugoslavia	3	6	169	3	0	3	6
Total	1048	954	707	754	642	1932	1293
Accompanying persons	200	133	63	95	98	192	N/A

International Meetings Calendar

Below are announcements of meetings to be held abroad. Entries preceded by an * are new or updated listings with full contact addresses given in parentheses. *Month/year* listings following other entries refer to meeting announcements, with full contact addresses, which were published in previous issues of the *Journal*.

February 2002

21–24 **13th Interdisciplinary Phoniatrics Symposium**, Leipzig. (Fax: +49 341 972 1709; e-mail: fuchsm@medizin.uni-leipzig.de) *12/01*

March 2002

4–8 **German Acoustical Society Meeting (DAGA 2002)**, Bochum. (Web: www.ika.ruhr-uni-bochum.de) *10/00*

18–20 **Spring Meeting of the Acoustical Society of Japan**, Kanagawa. (Fax: +81 3 5256 1022; Web: http://wwwsoc.nacsis.ac.jp/asj/) *12/01*

25–27 **Institute of Acoustics Spring Conference**, Manchester. (Fax: +44 1727 850553; Web: http://www.ioa.org.uk) *12/01*

April 2002

8–11 **6th Congress of the French Acoustical Society, joint with the Belgian Acoustical Society**, Lille. (Web: www.isen.fr/cfa2002) *8/01*

22–24 **International Meeting on Acoustic Pollution in Cities**, Madrid. (Fax: +34 1 559 74 11; e-mail: dccimad8@viajeseci.es) *12/01*

May 2002

27–30 **Joint Meeting: Russian Acoustical Society and Conference on Ocean Acoustics**, Moscow. (Fax: +7 095 124 5983; Web: rav.sio.rssi.ru/Ixconf.html) *6/01*

28–31 ***6th International Conference on Applied Technologies of Hydroacoustics and Hydrophysics**, St. Petersburg, Russia. (46 Chkalovskii prospect, St. Petersburg 197376, Russia; Fax: +7 812 320 8052; e-mail: mfp@mail.wplus.net)

29–1 **Nonlinear Waves in Microstructured Solids (Euromech 436)**, Tallinn. (Fax: +371 645 1805; e-mail: je@ioc.ee) *10/01*

30–1 **2nd International Conference on Newborn Hearing Screening, Diagnosis, and Intervention**, Villa Erba/Como. (Fax: +1 303 764 8220; Web: http://www.biomed.polimi.it/nhs2002) *12/01*

June 2002

4–6 **6th International Symposium on Transport Noise and Vibration**, St. Petersburg. (Fax: +7 812 127 9323; Web: webcenter.ru/ ~eeaa/tn/eng/tn2002) *02/01*

10–14 **Acoustics in Fisheries and Aquatic Ecology**, Montpellier. (Web: www.ices.dk/symposia/) *12/00*

24–27 **6th European Conference on Underwater Acoustics**, Gdańsk. (Fax: +48 58 347 1535; Web: www.ecua2002.gda.pl/) *10/01*

24–28 **11th Symposium of the International Society for Acoustic Remote Sensing**, Rome. (Fax: +39 06 20660291; Web: ISARS2002.ifa.rm.cnr.it/) *10/01*

24–28 ***11th International Symposium on Nondestructive Characterization of Materials**, Berlin, Germany. (DGZfP, Max-Planck-Str. 6, 12489 Berlin, Germany; Fax: +49 30 678 07129; Web: www.cnde.com)

July 2002

2–7 **ClarinetFest 2002**, Stockholm. (e-mail: kkoons@pegasus.cc.ucf.edu) *10/01*

15–17 **International Symposium on Active Control of Sound & Vibration (Active 2002)**, Southampton. (Fax: +44 23 8059 3190; Web: http://www.isvr.soton.ac.uk/active2002) *10/01*

17–21 ***7th International Conference on Music Perception and Cognition (7th ICMPC)**, Sydney, Australia. (Fax: +61 2 9772 6736; Web: www.uws.edu.au/marcs/icmpc7)

19–21 ***Auditorium Acoustics: historical and contemporary design and performance**, London, UK. (M. Barron, Department of Architecture & Civil Engineering, University of Bath, Bath BA2 7AY, UK; Fax: +44 1225 826691; e-mail: m.barron@bath.ac.uk)

August 2002

19–23 **16th International Symposium on Nonlinear Acoustics (ISNA16)**, Moscow. (Fax: +7 095 126 8411; Web: acs366b.phys.msu.su/isna16/) *12/00*

26–28 **2nd Biot Conference on Poromechanics**, Grenoble. (Web: geo.hmg.inpg.fr/biot2001) *8/01*

26–28 **Joint Baltic-Nordic Acoustical Meeting 2002**, Lyngby. (Fax: +45 45 88 05 77; Web: www.dat.dtu.dk) *10/01*

September 2002

11–13 **10th International Meeting on Low Frequency Noise**

and Vibration, York. (Fax: +44 1277 223 453; Web: http:// www.lowfrequency2002.org.uk) *12/01*

16–18 *__International Conference on Noise and Vibration Engineering__, Leuven, Belgium. (Fax: +32 1632 2987; Web: www.isma.isaac.be)

16–21 **Forum Acusticum 2002 (Joint EAA-SEA-ASJ Meeting)**, Sevilla. (Fax: +34 91 411 7651; Web: www.cica.es/aliens/forum2002) *2/00*

26–28 **Autumn Meeting of the Acoustical Society of Japan**, Akita. (Fax: +81 3 5256 1022; Web: http:// wwwsoc.nacsis.ac.jp/asj/) *12/01*

November 2002

30–6 **Joint Meeting: 9th Mexican Congress on Acoustics, 144th Meeting of the Acoustical Society of America, and 3rd Iberoamerican Congress on Acoustics**, Cancún. (Web: asa.aip.org/cancun.html) *10/00*

December 2002

9–13 *__International Symposium on Musical Acoustics (ISMA Mexico City)__, Mexico City, Mexico. (E. Castro-Sierra, National School of Music, National Autonomous University of Mexico, Xicotencatl 126, 04100 Mexico, D. F., Mexico; Fax: +52 55 5601 3210; Web: http://www.unam.mx/enmusica/ismamexico.html)

March 2003

17–20 *__German Acoustical Society Meeting (DAGA2003)__, Aachen, Germany. (A. Sill, FB Physik-Akustik, Universität Oldenburg, 26111 Oldenburg, Germany; Fax: +49 441 798 3698; e-mail: dega@aku-physik.uni-oldenburg.de)

April 2003

7–9 **WESPAC8**, Melbourne, Australia. (Web: www.wespac8.com) *10/01*

June 2003

8–13 **XVIII International Evoked Response Audiometry Study Group Symposium**, Puerto de la Cruz. (Web: www.ierasg-2003.org) *8/01*

September 2003

1–4 **Eurospeech 2003**, Geneva. (Web: www.symporg.ch/eurospeech2003) *8/01*

April 2004

5–9 **18th International Congress on Acoustics (ICA2004)**, Kyoto. (Web: ica2004.or.jp) *4/01*

REVIEWS OF ACOUSTICAL PATENTS

Lloyd Rice
11222 Flatiron Drive, Lafayette, Colorado 80026

The purpose of these acoustical patent reviews is to provide enough information for a Journal reader to decide whether to seek more information from the patent itself. Any opinions expressed here are those of reviewers as individuals and are not legal opinions. Printed copies of United States Patents may be ordered at $3.00 each from the Commissioner of Patents and Trademarks, Washington, DC 20231. Patents are available via the Internet at http://www.uspto.gov.

Reviewers for this issue:

GEORGE L. AUGSPURGER, *Perception, Incorporated, Box 39536, Los Angeles, California 90039*
ALIREZA DIBAZAR, *Department of BioMed Engineering, University of Southern California, Los Angeles, California 90089*
DAVID PREVES, *4 Deerfield Drive, Princeton Junction, New Jersey 08550*
DANIEL R. RAICHEL, *2727 Moore Lane, Fort Collins, Colorado 80526*
CARL J. ROSENBERG, *Acentech, Incorporated, 33 Moulton Street, Cambridge, Massachusetts 02138*
KEVIN P. SHEPHERD, *Mail Stop 463, NASA Langley Research Center, Hampton, Virginia 23681*
WILLIAM THOMPSON, JR., *Pennsylvania State University, University Park, Pennsylvania 16802*
ERIC E. UNGAR, *Acentech, Incorporated, 33 Moulton Street, Cambridge, Massachusetts 02138*

6,259,653

43.25.Yw PORTABLE ENCAPSULATED UNDERWATER ULTRASONIC CLEANER

Billy Courson and John Shelburne, assignors to the United States of America as represented by the Secretary of the Navy
10 July 2001 (Class 367/141); filed 14 August 2000

A portable, diver-held and -operated device for cleaning underwater surfaces such as ships hulls is described. The contaminants could include marine growth as well as rust, scale, grease, dirt, etc. The device includes an electroacoustic transducer mounted within an open, bowl-shaped housing that has a compliant ring of material around its opening in order to fit tightly against the surface to be cleaned. The bowl is free-flooded with the ambient water prior to operation. The housing and its compliant seal provide sufficient transmission loss to prevent harmful levels of sound energy in the surrounding water. Power source, signal generator, amplifier, and impedance matching module are also housed in the wet side of the device, making it self-contained as well as portable.—WT

6,198,694

43.28.Tc METHOD AND DEVICE FOR PROJECTILE MEASUREMENTS

Olle Kröling and Håkan Appelgren, assignors to Håkan Appelgren
6 March 2001 (Class 367/127); filed in Sweden 29 March 1996

Probably the simplest form of small arms target practice is to shoot bottles off a fence. In this case it is easy to identify hits and misses. On a firing range, things are not that easy. Systems have been developed that use vibration sensors to detect the hit point of a bullet quickly and accurately. However, as this patent points out, sooner or later the sensors themselves will be hit. Acoustic noncontact detection is also known, but such prior art detects the shock wave produced by supersonic projectiles whereas not all bullets travel faster than sound. The invention overcomes these difficulties by analyzing signals from at least three acoustic sensors to compute the position, direction, and speed of a projectile in its flight toward a target.—GLA

6,178,141

43.28.Tc ACOUSTIC COUNTER-SNIPER SYSTEM

Gregory L. Duckworth *et al.*, assignors to GTE Internetworking, Incorporated
23 January 2001 (Class 367/127); filed 20 November 1996

One example of prior art processes signals from an array of microphones to detect the muzzle blast of a sniper's rifle and estimate its location. Other known systems analyze shock waves from supersonic bullets to estimate the bullet trajectory. This patent describes an improved, low cost system that utilizes a distributed array of acoustic sensors to detect a projectile's shock wave and muzzle blast, then processes this information to determine the projectile's trajectory and a line bearing to its origin. The system may be fixed, portable, or wearable. The patent is clearly written and includes detailed explanatory information.—GLA

6,272,073

43.30.Tg UNDERWATER LOCATION AND COMMUNICATION DEVICE

Gary L. Doucette, Burtonsville, Maryland and Matthew C. Rivotto, Lake in the Hills, Illinois
7 August 2001 (Class 367/131); filed 20 November 1998

A small, battery powered, ultrasonic transceiver is described that can measure distance, indicate relative direction, and, in general, maintain contact between two or more divers. One such unit is worn by each diver, either clipped to a belt or otherwise attached to the body via a Velcro strap. The device features a liquid crystal display and it can be set to indicate relative distance or direction and to provide a warning signal when the relative distance exceeds a preset limit.—WT

6,253,763

43.30.Yj MOUTHPIECE AND SPEAKER ASSEMBLIES FOR UNDERWATER SPEECH

O'Neal B. Pounders, Jr., Bossier City, Louisiana
3 July 2001 (Class 128/201.11); filed 8 February 1999

Two basic problems are encountered in speaking underwater, being able to breathe and coupling the speech sounds to the water. This device addresses the first ... sort of. A pair of flexible appendages attached to the snorkellike breathing device are intended to be held clamped between the teeth. In other words, speech is to be produced with lip and tongue movements but without jaw movement. This hinderence is well known by speech researchers as a ''bite block'' condition. Speech is possible, but distorted, at best. The discussion of the diaphragm which couples air vibrations to water vibrations suggests that suitable parameters were found by trial and error.—DLR

6,262,944

43.30.Yj SOLID FILL ACOUSTIC ARRAY

A. Douglas Meyer *et al.*, assignors to Litton Systems, Incorporated
17 July 2001 (Class 367/154); filed 22 February 1999

An underwater acoustic line array is realized as a sequence of fiber optic sensors **102** (only one is shown in this cross-sectional figure) wound on cylindrical mandrels that are axially spaced apart by buoyant solid fill material **106**, such as polyurethane filled with glass or metal micro-balloons, and covered with an acoustically transparent outer hose **110**. Support spacers **116** form water-filled cavities such as **112** in which the sensor elements are

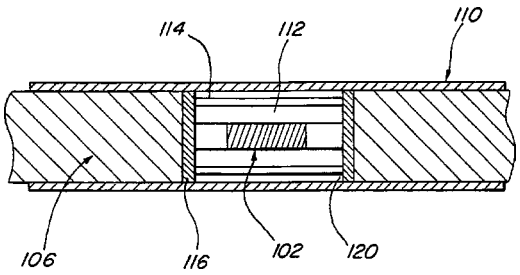

located. Item **114** is one of a set of axially extended strength members that support tensile loads applied to the structure. Because the sensing elements are electrically inert, which allows water to be used as the fill fluid, the device is claimed to be environmentally safer than oil-filled piezoelectric sensor arrays.—WT

6,185,152

43.38.Ar SPATIAL SOUND STEERING SYSTEM

Albert Shen, assignor to Intel Corporation
6 February 2001 (Class 367/118); filed 23 December 1998

The invention is a sound source locating system that mimics the pinnae functions of the human ear. Microphone **104** is surrounded by irregular ridges **214** and wells **216**. These produce interference notches in the acoustic

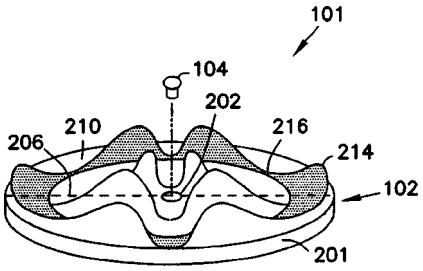

signal received by the microphone. The azimuth and elevation of the sound source can then be estimated by computerized acoustic spectrometry and used, for example, to aim a television camera. The patent document is purely conceptual and includes no hard data.—GLA

6,208,237

43.38.Dv ELECTRO-MECHANICAL AND ACOUSTIC TRANSDUCER FOR PORTABLE TERMINAL UNIT

Shuji Saiki *et al.*, assignors to Matsushita Electric Industrial Company Limited
27 March 2001 (Class 340/388.1); filed in Japan 29 November 1996

This transducer is intended for use in pagers, portable telephones, and the like. It aims to achieve economies by combining the functions of an ear-piece and a vibrator in a single unit. The transducer is configured much like any voice-coil unit, in that it has a diaphragm attached to a voice-coil, which is positioned in the circular gap of a magnetic circuit. However, in one patented configuration, the magnetic circuit assembly (which consists of a permanent magnet and of a ferromagnetic yoke and cover plate) is enclosed in a massive ring and supported from the transducer enclosure via flexible elements. The unit produces acoustic signals conventionally, but can generate relatively strong vibrations if the voice coil is driven at the resonance frequency of the system consisting of the mass of the magnetic circuit assembly and its flexible supports.—EEU

6,208,743

43.38.Dv ELECTRODYNAMIC ACOUSTIC TRANSDUCER WITH MAGNETIC GAP SEALING

Stefan Marten and Rainer Wiggers, assignors to Sennheiser Electronic GmbH & Company KG
27 March 2001 (Class 381/415); filed in Germany 21 March 1996

This patent describes a transducer, such as may be used for a hearing aid, in which the air gap between the voice coil and the magnet is sealed by a viscous fluid or ferrofluid. The purpose of this sealing is to reduce the acoustic short-circuiting that occurs via that gap and thus to improve the low-frequency performance of the transducer.—EEU

5,592,359

43.38.Fx TRANSDUCER

Harry W. Kompanek, assignor to Undersea Transducer Technology, Incorporated
7 January 1997 (Class 361/329); filed 13 July 1994

The device in question is used to vibrate oil-saturated sedimentation to separate the oil. It consists of two, essentially identical, metal-shrouded, slotted, piezoelectric cylinders. In this cross-sectional view, **16** and **30** are cylindrical metal shells and **20** and **32** are the piezoceramic cylinders. They

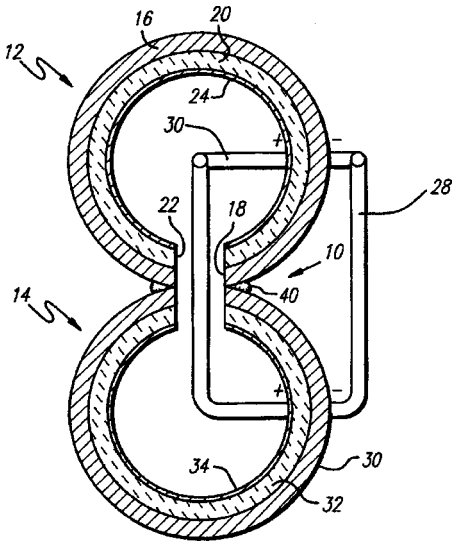

are aligned with their axes parallel and with their slots adjacently positioned. The shells **16** and **30** are bonded together at **40** where they about each other. Both ends of both cylinders are capped. Items **28** and **30** are electrical leads. The two cylinders are driven in phase with one another. The mutual bracing effect of one cylinder upon the other inhibits fracture of the ceramic at high drive levels.—WT

6,213,250

43.38.Fx TRANSDUCER FOR ACOUSTIC LOGGING

Laurence T. Wisniewski *et al.*, assignors to Dresser Industries, Incorporated
10 April 2001 (Class 181/104); filed 25 September 1998

This transducer is intended to be mounted in a downhole tool used in geological exploration. Such a tool incorporates a transmitter near one end and a receiver near its other end. The characteristics of the surrounding medium are determined from the distortion and/or delay of the received signal. The patent describes various transmitting and receiving transducers that act in only one direction perpendicular to their faces, with a cover providing shielding in the other direction. The transducer is decoupled from the tool's shell via rubber O-rings.—EEU

5,592,441

43.38.Hz HIGH-GAIN DIRECTIONAL TRANSDUCER ARRAY

Philip M. Kuhn, assignor to Martin Marietta Corporation
7 January 1997 (Class 367/153); filed 6 October 1995

A generally spherical shaped array is realized by locating transducers at the vertices of a ''Bucky Ball'' created by further subdivision of a regular icosahedron. The array contains a total of 42 transducers. By suitable choice of time delays, and operating over a range of frequencies such that the interelement spacing ranges between one-third and two-thirds of a wavelength, reasonably narrow beams are obtained in either the transmission or reception mode of operation.—WT

6,192,134

43.38.Hz SYSTEM AND METHOD FOR A MONOLITHIC DIRECTIONAL MICROPHONE ARRAY

Stanley A. White *et al.*, assignors to Conexant Systems, Incorporated
20 February 2001 (Class 381/92); filed 20 November 1997

Information from a number of local array processors is collected by a global processor to ''...track and/or locate a moving and changing source of acoustic signals or noise.'' A local unit contains a monolithic array of microphones, each connected to a preamplifier and A/D converter. Signals are then processed digitally and the information is transmitted to another detection unit or the base unit. Possible applications range from law enforcement surveillance to ''smart'' consumer electronic devices.—GLA

6,236,862

43.38.Hz CONTINUOUSLY ADAPTIVE DYNAMIC SIGNAL SEPARATION AND RECOVERY SYSTEM

Gamze Erten and Faihi M. Salam, assignors to Intersignal LLC
22 May 2001 (Class 455/501); filed 16 December 1996

This patent discloses a method for separating multiple source signals where the signals are mixed into multiple channels. The sources may be nonlinearly mixed into the various transmission channels, possibly with

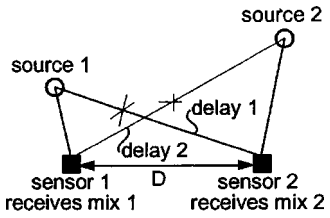

various amounts of delay. The received mixture channel outputs are processed by a differential equation system, allowing high-quality recovery of the original signal sources.—DLR

6,188,313

43.38.Ja DEVICE FOR GENERATING SOUND

Lars Stahl, assignor to Åm System AB
13 February 2001 (Class 340/384.73); filed in Sweden 22 July 1996

A conventional high-frequency horn driver includes a coupling chamber between its relatively large diaphragm and the smaller horn throat. A flextensional transducer utilizes mechanical leverage to produce large diaphragm excursions from a short-throw motor. Combining the two is a little like putting a telescope inside another telescope, but there may well be practical reasons for building such a device.—GLA

5,889,875

43.38.Ja ELECTROACOUSTICAL TRANSDUCING

Gerald F. Caron *et al.*, assignors to Bose Corporation
30 March 1999 (Class 381/338); filed 1 July 1994

A system is described for providing a sound field that is concentrated at the location of a single listener and which is also significantly lower in amplitude at positions outside of this region of concentration. With reference to the figure, which shows the system attached to the back of an office chair, **14** and **15** are small, baffled, moving coil loudspeakers positioned close to the ears of a person seated in the chair. The speakers are intended to cover

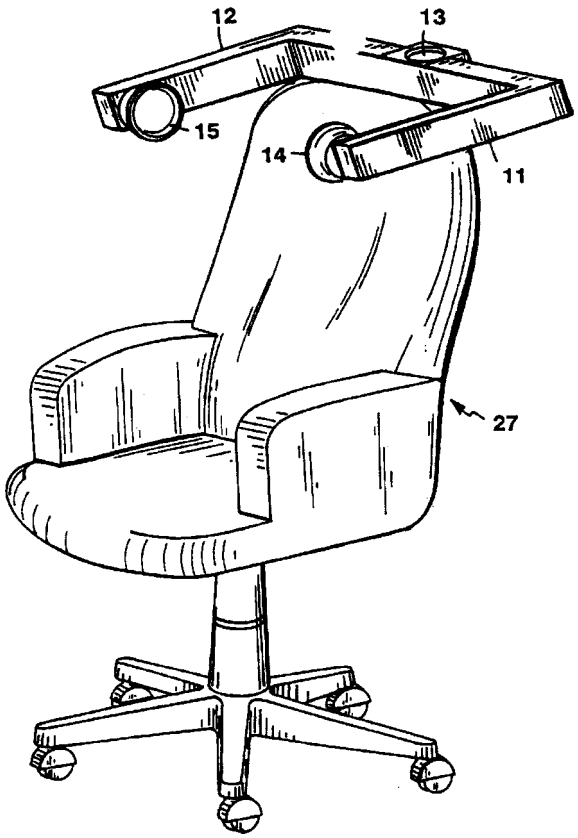

the frequency range from 300 Hz to 12 kHz. They are mounted at the ends of waveguides **11** and **12** which are excited by the single low-frequency driver **13**. The waveguide arms **11** and **12** are typically one-quarter of a wavelength long at 85 Hz and have useable response characteristics from 85 to 300 Hz. The signal leads from the source to the transducers, which would tend to tether the chair, are not shown.—WT

6,212,284

43.38.Ja SOUND REPRODUCTION DEVICE

Bernhard Puls, assignor to Harman Audio Electronic Systems GmbH
3 April 2001 (Class 381/345); filed in Germany 7 August 1997

The cavity formed between loudspeaker cone **15** and front plate **33** communicates to the outside world through a ring-shaped vent **34**, forming half of a sealed/vented bandpass system. The other half—sealed chamber **30** into which the assembly is mounted—is assumed to be larger than necessary so that the stiffness of the moving system is controlled primarily by the loudspeaker's mechanical suspension. Under these conditions, the device can be mounted in a sealed chamber of unknown volume, such as an automobile door, with predictable results. An earlier patent by Matthew Polk (not referenced) makes use of similar relationships for a residential in-wall bandpass system.—GLA

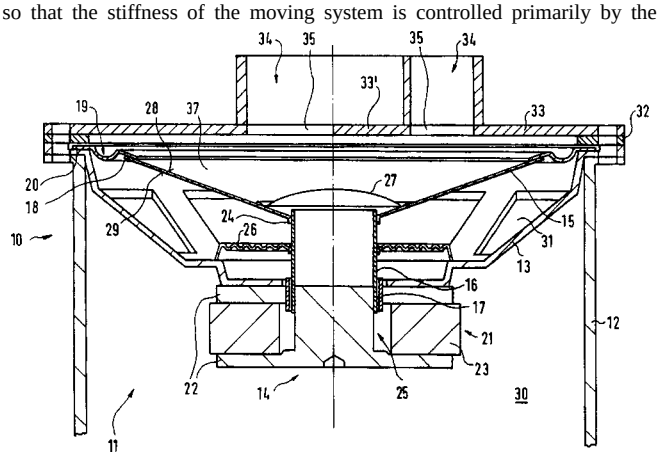

6,219,426

43.38.Ja CENTER POINT STEREO FIELD EXPANDER FOR AMPLIFIED MUSICAL INSTRUMENTS

Drew Daniels, North Hills and Richard Aspen Pittman, Sylmar, both of California
17 April 2001 (Class 381/307); filed 8 August 1996

Early adjustable-pattern microphones used a figure-8 (dipolar) element sitting above an omnidirectional (unipolar) element. With suitable connections this arrangement becomes the equivalent of back-to-back cardioid microphones and can be used for two-channel stereo pickup. If loudspeakers are substituted for the microphone elements, then a point source stereo reproducer is the result. The patent describes several embodiments of this basic scheme along with suitable electronic circuitry.—GLA

6,201,873

43.38.Lc LOUDSPEAKER-DEPENDENT AUDIO COMPRESSION

David Dal Farra, assignor to Nortel Networks Limited
13 March 2001 (Class 381/100); filed 8 June 1998

Television receivers, personal stereo systems, loudspeaking telephones, and answering machines all use small, inexpensive loudspeakers that overload easily. Today's integrated circuit technology makes it less expensive to add the electronic signal processing shown than to spend a few cents more for a better loudspeaker.—GLA

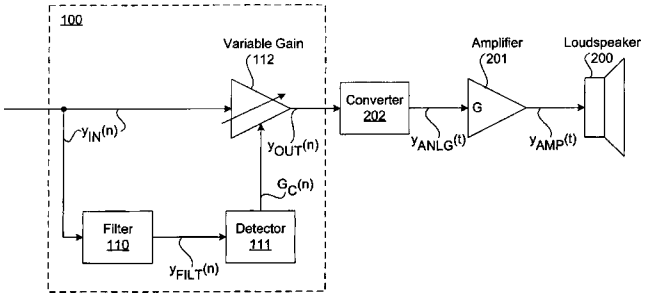

6,173,058

43.38.Si SOUND PROCESSING UNIT

Masashi Takada, assignor to Oki Electric Industry Company, Limited
9 January 2001 (Class 381/66); filed in Japan 18 February 1998

This sound processing unit is an all-in-one handset for use in very noisy environments. In addition to the usual microphone and speaker (receiver), a vibration pickup is included. This touches the ear of the user during conversations and functions as a bone conduction device. Signal

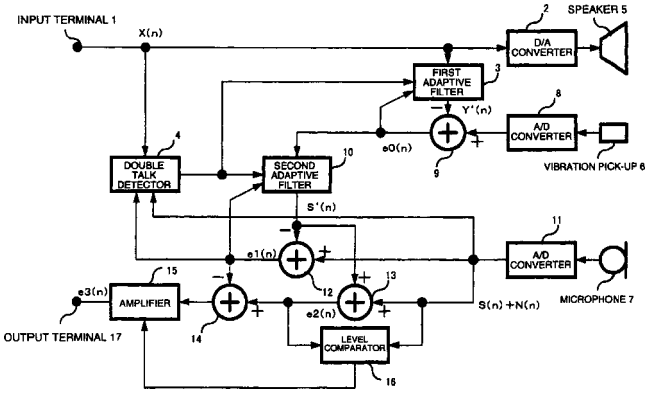

processing utilizes two adaptive digital filters plus a level comparator and voltage controlled amplifier. These operate dynamically to provide noise reduction, echo cancellation, and level matching during two-way conversations.—GLA

6,198,829

43.38.Tj PROCESS AND DEVICE FOR FOCUSING ACOUSTIC WAVES

Mathias Fink and Jacques Lewiner, assignors to Societe pour les Applications du Retournement Temporel
6 March 2001 (Class 381/71.12); filed in France 13 July 1995

Consider the all too familiar situation in a reverberant subway station or airline terminal where announcements are not intelligible unless the listener is within a few feet of a loudspeaker. At any other location, competing acoustic signals from distant loudspeakers and late room reflections mask the desired signal. By using a time reversal mirror (TRM) algorithm and independently processing the signals to all loudspeakers in a group, intelligibility and loudness can be concentrated in a specified listening area. Considerable memory and processing power are required, but the concept is clever and may be practical in certain acoustic environments.—GLA

6,178,247

43.38.Vk HEADPHONE APPARATUS

Kazuaki Ogita, assignor to Yugengaisha Ito Denkitekkousyo
23 January 2001 (Class 381/74); filed in Japan 17 July 1996

It has long been known that interaural crosstalk can be added to headphones to make them sound more like loudspeakers. More accurate out-of-head localization can be realized by also including simulated reflections from room surfaces. This patent goes one step further by taking into consideration sound reflected from the listener's shoulders.—GLA

6,195,434

43.38.Vk APPARATUS FOR CREATING 3D AUDIO IMAGING OVER HEADPHONES USING BINAURAL SYNTHESIS

Terry Cashion and Simon Williams, assignors to QSound Labs, Incorporated
27 February 2001 (Class 381/17); filed 25 September 1996

The inventor has previously patented a circuit that provides full front and rear panning for headphone stereo (United States Patent 5,371,799). This improved version allows multiple voices to be individually panned yet requires only a single set of standardized filters.—GLA

6,222,930

43.38.Vk METHOD OF REPRODUCING SOUND

Kenji Nakano *et al.*, assignors to Sony Corporation
24 April 2001 (Class 381/307); filed in Japan 6 February 1997

By exploiting the effects of interaural crosstalk and head-related transfer functions, virtual sound sources can be produced more or less convincingly almost anywhere. A number of existing patents describe methods for synthesizing multi-channel stereo from two front loudspeakers. On the other hand, suppose you have five loudspeakers, but they cannot be located exactly according to the 5:1 standard. More specifically, suppose that your surround speakers are in the rear of the room rather than at the recommended 110-degree angles. No problem. So long as you remain at the center point and face forward, Sony's virtual image orientation processor will subjectively relocate the offending speakers wherever you like.—GLA

6,208,590

43.38.Zp SAGNAC INTERFEROMETRIC SENSOR ARRAY FOR ACOUSTIC SENSING AND METHOD OF DETECTING ACOUSTIC SIGNALS

Byoung Yoon Kim *et al.*, assignors to Korea Advanced Institute of Science and Technology
27 March 2001 (Class 367/149); filed in the Republic of Korea 4 May 1999

Light from a source is split into two components that travel in opposite directions in a fiber-optic loop. Acoustic disturbances of the fibers are detected via observation of the phase differences in the two components. The present patent uses an array of such loops and associated delay lines for the simultaneous measurement of acoustic signals from multiple sources.—EEU

6,213,681

43.40.Tm SOIL COMPACTING DEVICE WITH ADJUSTABLE VIBRATION PROPERTIES

Georg Sick *et al.*, assignors to Wacker-Werke GmbH & Company, KG
10 April 2001 (Class 404/133.05); filed in Germany 23 July 1997

A mass, typically in the form of a skid, is set into vibration by means of one or more exciters. This mass rests on the soil to be compacted and supports a second mass via an arrangement of springs and dampers. The dampers employ electroviscous or magnetorheological fluids, permitting their damping action to be adjusted and permitting springs in series with the dampers in effect to be connected or disconnected so that the second mass vibrates at resonance. Use of a sensor and control system may allow not only automatic adjustment of the resonance frequency, but also pulsing of the damping to achieve desired motions.—EEU

6,216,817

43.40.Tm DAMPING STRUCTURAL SUBSTANCE AND A DAMPING COAT FORMING METHOD

Tatsumi Kannon *et al.*, assignors to Mitsubishi Jukogyo Kabushiki Kaisha
17 April 2001 (Class 181/296); filed in Japan 27 April 1995

According to this patent, the surface of a structure to be damped is coated with a mixture of molten photopolymerizable resin and a photopolymerization initiator. The coated surfaces are then subjected to irradiation, resulting in formation of a free-layer damping coating. This approach appears to be particularly suitable to complex structures.—EEU

6,220,367

43.40.Tm POWER TOOL AND VIBRATION ISOLATOR THEREFOR

Peter A. Masterson *et al.*, assignors to Chicago Pneumatic Tool Company; Lord Corporation
24 April 2001 (Class 173/162.2); filed 13 January 1998

This patent pertains to a hand-held pneumatic tool that incorporates a vibration isolator between the tool and its handle in order to protect the operator's hand. Compressed air is fed to the tool via an inlet in the handle. The isolator described in this design provides a seal between the tool and the handle and also permits adjustment of the handle's position relative to the tool.—EEU

6,220,563

43.40.Tm VIBRATION ISOLATION DEVICE AND METHOD

John Cunningham, Saratoga Springs, New York
24 April 2001 (Class 248/580); filed 15 June 1995

A bearing support is attached at the midpoint of an elastic member essentially in the form of a beam. The ends of this member are pin-supported and free to slide axially and this member is resilient enough so that it can bow substantially as the bearing load changes. This bowing makes the isolation system nonlinear, resulting in changes in the system's natural frequency with changes in the load. Various means are indicated for controlling the axial motion of the resilient element.—EEU

6,216,985

43.40.Yq RAILWAY HAZARD ACOUSTIC SENSING, LOCATING, AND ALARM SYSTEM

Robert Douglas Stephens, Port Coquitlam, British Columbia, Canada
17 April 2001 (Class 246/120); filed 13 August 1998

Signals from sensors attached to one of the rails of a railway are analyzed by a computer to ascertain the nature of the event causing the signals. An alarm is generated if a suspect condition is identified or if a high-energy signature is detected. The alarm may be transmitted via any communication link to the rail traffic control office and to the trains traveling toward the suspect track location. The system can also detect such problems as wheel flats and derailed cars.—EEU

6,223,601

43.40.Yq VIBRATION WAVE DETECTING METHOD AND VIBRATION WAVE DETECTOR

Muneo Harada and Naoki Ikeuchi, assignors to Sumitomo Metal Industries, Limited
1 May 2001 (Class 73/649); filed in Japan 22 May 1998

The vibration detector described in this patent is of the resonator array type. It consists of a number of cantilever beam elements, each having a different length and thus a different natural frequency, attached to a base element. A piezoresistor is installed on each beam element and these resistors are connected in parallel so as to provide an output corresponding to the sum of the vibrations of the beam elements. The resistors are placed at locations along the lengths of the beam elements so that the output signal from each element is set at a desired level.—EEU

6,250,422

43.50.Gf DUAL CROSS-FLOW MUFFLER

Gary D. Goplen *et al.*, assignors to Nelson Industries, Incorporated
26 June 2001 (Class 181/272); filed 14 December 1998

This muffler design, intended for use on a lawn tractor, is a continuation of United States Patent 6,076,632 for box-style or stamped mufflers.

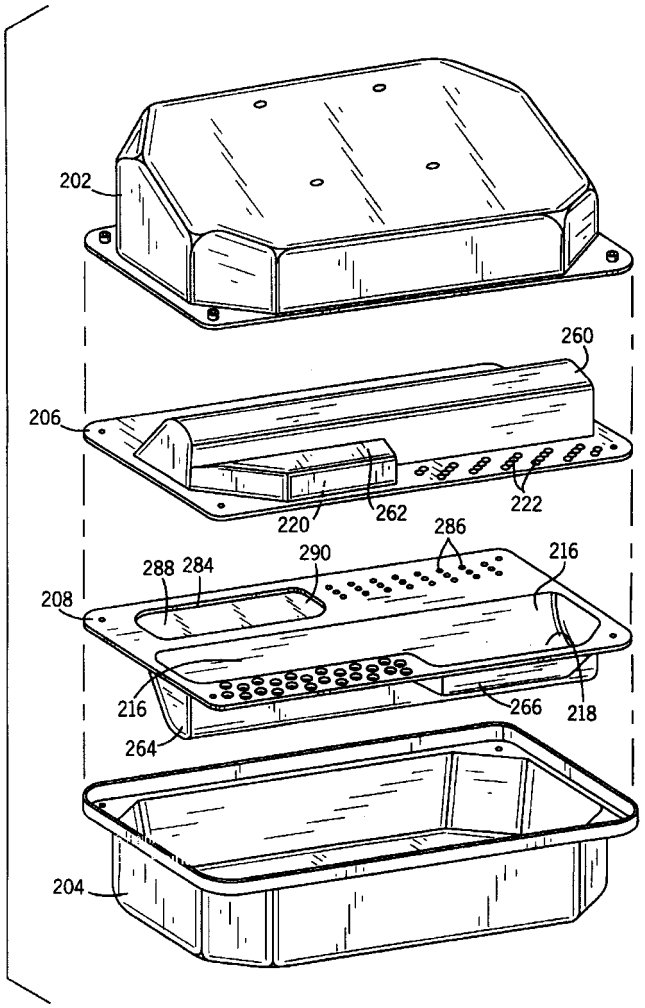

The cost-effective design cleverly creates multiple flow paths and exhaust chambers and also routes the hot gases to the large outer surface to enhance cooling, thus minimizing afterburning.—KPS

6,256,941

43.55.Ev PAD FOR PANEL

Shawn Yu *et al.*, assignors to Haworth, Incorporated
10 July 2001 (Class 52/144); filed 4 June 1999

This patent is for a space-dividing wall panel system (open-plan office furniture) that includes a tackable cover pad. The cover pad has an interior molded panel which is compressed about its edges, providing rigidity to the panel. There are rails attached to these edges which allow the panel to be mounted to the furniture frame.—CJR

6,266,936

43.55.Ti SOUND ATTENUATING AND THERMAL INSULATING WALL AND CEILING ASSEMBLY

Lawrence J. Gelin, assignor to Johns Manville International, Incorporated
31 July 2001 (Class 52/481.1); filed 24 June 1999

This device provides a resilient connection between framing members in a building system (studs, joists) and a surface material (gypsum wall

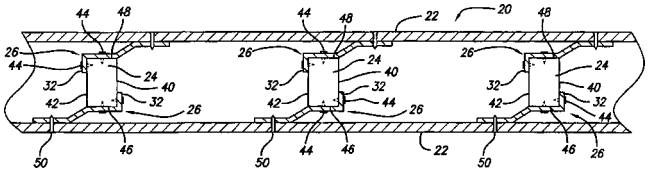

boards, for example). The device does this by means of an extended cantilevered portion that separates the boards from the structure. There are tabs that assure proper alignment during construction.—CJR

6,268,038

43.55.Ti ACOUSTICALLY RESISTIVE LAYER, PROCESS FOR PRODUCTION OF THIS LAYER AND ABSORBENT ACOUSTIC PANEL PROVIDED WITH AT LEAST ONE SUCH LAYER, AS WELL AS ITS PROCESS FOR PRODUCTION

Alain Porte *et al.*, assignors to Aerospatiale Societe Nationale Industrielle
31 July 2001 (Class 428/116); filed in France 13 August 1997

This patent shows how to take an acoustic damping cloth, place it on a mold, and wrap it with impregnated filaments in a variety of patterns. This might be useful for the nacelles of aircraft engines or gas turbines.—CJR

6,267,347

43.55.Vj ACOUSTIC MOUNT

Peter Anthony Ryan, Penrith and Geoff Grimish, Milperra, both of New South Wales, Australia
31 July 2001 (Class 248/562); filed 8 October 1999

This device is designed to isolate the transmission of low-frequency sound and vibration in building structures. It has a base, a resilient bushing,

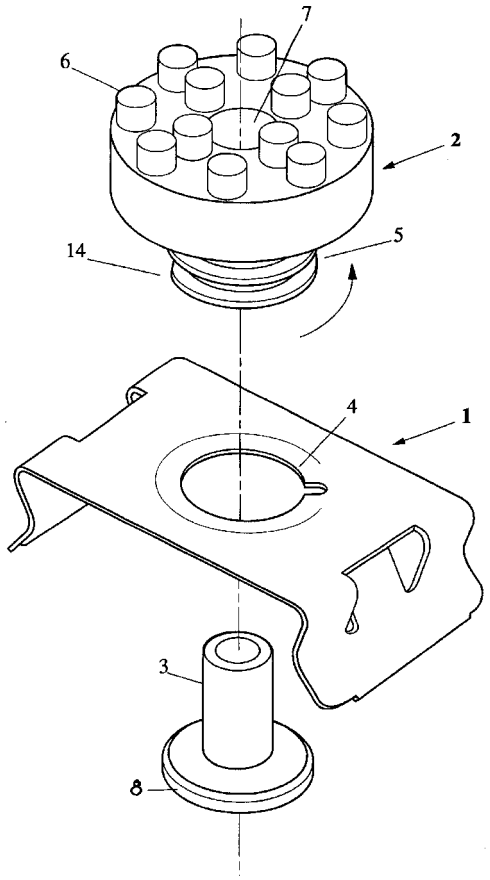

and an isolator section. The configuration of the device assures that any contact from one part of the structure to the other is made through the neoprene isolator in a simple, fool-proof manner.—CJR

6,256,959

43.55.Wk BUILDING PANEL WITH VIBRATION DAMPENING CORE

Michael J. Palmersten, assignor to KJMM, Incorporated
10 July 2001 (Class 52/588.1); filed 14 October 1999

This building panel has a skin on one side, a foam sheet (perhaps polystyrene) as its core, and a skin on the other side. The skins and core are bonded and interlocked to form a unified panel. If the panel is used on a building, it should reduce the radiated sound from the impact of rain or hail.—CJR

6,265,475

43.55.Wk HIGH DAMPING MATERIAL COMPOSITION

Wu Chifei *et al.*, assignors to Tokai Rubber Industries, Limited
24 July 2001 (Class 524/127); filed in Japan 30 July 1998

This high damping material combines a designated range of polymers and at least one damping agent selected from a group of phenol compounds. When combined, these make a homogeneous composition useful as a vibration damper, an acoustic insulating wall material for an acoustic room, a sound insulating partition for a construction structure, or a soundproofing wall for a vehicle. The patent describes the chemical and physical processes of the interaction between the polymer and the damping agent.—CJR

6,266,427

43.55.Wk DAMPED STRUCTURAL PANEL AND METHOD OF MAKING SAME

Gopal P. Mathur, assignor to McDonnell Douglas Corporation
24 July 2001 (Class 381/353); filed 19 June 1998

In this panel, a viscoelastic material is applied within a limited area adjacent to the panel edges based on the bending modes of the panel. The bending modes noted in the patent have subsonic bending waves along at least one axis, and require damping treatment based on the specific sound radiation properties of the panel. The viscoelastic material damps the sound radiation that is caused by the bending waves during use of the structural panel, such as its use as a body panel on an aircraft.—CJR

5,936,160

43.58.Dj METHOD AND APPARATUS FOR MEASURING SOUND VELOCITY IN LIQUID

Harri Salo, assignor to Janesko Oy
10 August 1999 (Class 73/597); filed in Finland 27 January 1997

A sound pulse is simultaneously transmitted from a single transmitter into both a liquid, whose sound velocity is to be determined, and into a reference material whose sound velocity is already known. The two transit times are measured with the same measurement device. Improved accuracy is the suggested advantage of this comparison measurement technique.—WT

6,246,322

43.58.Gn IMPULSE CHARACTERISTIC RESPONSIVE MISSING OBJECT LOCATOR OPERABLE IN NOISY ENVIRONMENTS

Timon Marc LeDain *et al.*, assignors to Headwaters Research & Development, Incorporated
12 June 2001 (Class 340/531); filed 26 December 1995

This fairly simple, analog sound analyzer is said to be able to distinguish hand claps from a variety of other impulsive or noise sources. In the intended use, the small device would be attached to easily lost items, such as car keys. Upon hearing a predetermined pattern of hand claps, the device emits a distinctive beeping sound.—DLR

6,263,074

43.60.Dh USER PROGRAMMABLE STATION SET BASS AND TREBLE CONTROL

Harry Tapley French *et al.*, assignors to Lucent Technologies, Incorporated
17 July 2001 (Class 379/389); filed 19 June 1998

This device, intended for use on telephone station sets, makes use of tones outside the voice range (above 3 kHz) to control bass and treble levels. A typical station set is configured so as to produce out-of-band tones, each tone representing an effect on the bass or treble in the vocal range. For example, a tone of 3.4 kHz may be associated with ''decrease bass,'' 3.6 kHz with ''increase bass,'' 3.8 kHz with ''decrease treble,'' and 4.0 kHz with ''increase treble.'' A central office line card is configured to include a tone detector in the receive signal path. Upon reception of these predefined tones, the tone detector transmits a tone signal to a programmable equalization filter deployed in the transmit signal path within the line card. Any well-known equalization filter may be used and is capable of increasing or decreasing bass or treble in response to the tone detector control signal.—DRR

6,208,944

43.60.Qv METHOD FOR DETERMINING AND DISPLAYING SPECTRA FOR VIBRATION SIGNALS

Dieter Franke *et al.*, assignors to Pruftechnik Dieter Busch AG
27 March 2001 (Class 702/56); filed in Germany 26 June 1997

The method described in this patent is intended to minimize the memory space needed for a spectral display unit. It recognizes the fact that resolution of vibration signals at different frequencies requires different bandwidths and thus employs different sampling rates for different frequency ranges.—EEU

6,249,766

43.60.Qv REAL-TIME DOWN-SAMPLING SYSTEM FOR DIGITAL AUDIO WAVEFORM DATA

Michael J. Wynblatt and Stuart Goose, assignors to Siemens Corporate Research, Incorporated
19 June 2001 (Class 704/503); filed 10 March 1998

This patent covers a method for fast, approximate conversion of the sampling rate of audio materials. New samples are generated at times in between existing samples with amplitudes given as a linear combination of the surrounding old samples. The method was described by Lagrange in the 18th century. In addition, the old and new sample rates are rounded off to the nearest kiloHertz.—DLR

6,249,704

43.66.Ts LOW VOLTAGE STIMULATION TO ELICIT STOCHASTIC RESPONSE PATTERNS THAT ENHANCE THE EFFECTIVENESS OF A COCHLEAR IMPLANT

Albert A. Maltan and William Vanbrooks Harrison, assignors to Advanced Bionics Corporation
19 June 2001 (Class 607/57); filed 11 August 1998

To make a cochlear stimulation device more effective, nonauditory information is applied through implanted electrodes that elicit stochastic response patterns to precondition or prepare the auditory nerve for the auditory information. If the nonauditory signal is of a low level having an amplitude just below or above the auditory threshold, neurons in the auditory nerve are said to be biased so that they are easily triggered by arrival of auditory stimuli.—DAP

6,251,138

43.66.Ts HEARING PROSTHESIS

Joseph B. Nadol, Jr. and Saumil N. Merchant, assignors to Massachusetts Eye & Ear Infirmary
26 June 2001 (Class 623/10); filed 28 July 1999

Persons with conductive hearing loss have reduced sound transmission capability due to abnormalities in the middle ear such as otitis media and Eustachian tube dysfunction. Rather than employing surgical intervention techniques that involve risk of tympanic membrane damage and postoperative hearing loss, a thin, synthetic gas-filled balloon comprising a pliant membrane of biocompatible material is surgically placed in the middle ear. The balloon contacts the tympanic membrane and has a low acoustic impedance so as to enhance sound vibration transfer through the ossicles to the inner ear.—DAP

6,254,526

43.66.Ts HEARING AID HAVING HARD MOUNTING PLATE AND SOFT BODY BONDED THERETO

Roger P. Juneau *et al.*, assignors to Softear Technologies, L.L.C.
3 July 2001 (Class 600/25); filed 18 December 1997

A method and material are described for the construction of soft but solid custom hearing aids ranging from full concha in-the-ear to completely in-the-canal styles. The electronic components of the hearing aid are embedded within a soft elastomer that replaces the traditional acrylic shell construction. This soft polymeric body, which is shaped to conform to the ear canal of the wearer, is bonded to a harder plate member. This invention is said to address problems of peripheral acoustic leakage, poor fit, and displacement that occurs with jaw motion of the hearing aid wearer.—DAP

6,256,395

43.66.Ts HEARING AID OUTPUT CLIPPING APPARATUS

John Laurence Melanson, assignor to GN ReSound as
3 July 2001 (Class 381/312); filed 30 January 1998

Clipping in hearing aids is caused by the signal swing exceeding the headroom provided in the amplifier and is typically accompanied by undesirable harmonic and intermodulation distortion. Normally the signal is clipped prior to interpolation and upsampling in the digital to analog converter, which results in a large amount of distortion. This patent describes a clipping system for a digital hearing aid which reduces distortion by assuring that any clipping will occur after the interpolation step.—DAP

6,246,751

43.72.Fx APPARATUS AND METHODS FOR USER IDENTIFICATION TO DENY ACCESS OR SERVICE TO UNAUTHORIZED USERS

Vladimir Bergl *et al.*, assignors to International Business Machines Corporation
12 June 2001 (Class 379/67.1); filed 11 August 1997

The technique described here allows a very specific type of cheating on telephone charges to be defeated. A voice dialing system set up for a limited group levies a charge for a normal call to a phone outside the system, but allows toll-free forwarding of calls to such outside phones. The cheater forwards his own number to the outside line, then calls himself from another phone in the system. The patented method uses a speaker identification system to detect when the caller's voice matches the voice of the called number, terminating the call if such a match is found.—DLR

6,253,179

43.72.Fx METHOD AND APPARATUS FOR MULTI-ENVIRONMENT SPEAKER VERIFICATION

Homayoon S. Beigi *et al.*, assignors to International Business Machines Corporation
26 June 2001 (Class 704/243); filed 29 January 1999

This speaker verification system uses several methods to update the speaker model database as new candidates are enrolled into the system. The initial set of speaker models is organized into a hierarchical tree based on analysis feature distances. The set is also grouped into cohort subsets based on pattern similarities. Finally, two different types of complementary models are generated based on feature distances or comparisons to other speakers not in a speaker's cohort set. Such complementary models help to identify imposters.—DLR

6,256,609

43.72.Gy METHOD AND APPARATUS FOR SPEAKER RECOGNITION USING LATTICE-LADDER FILTERS

Christopher I. Byrnes and Anders Lindquist, assignors to Washington University
3 July 2001 (Class 704/246); filed 9 May 1997

This lattice filter-based speech coding system is based on much of the lattice filter work done in the 1970s, but adds a method for analyzing both poles and zeros in the spectral representation. The pole/zero filter is referred to here as a lattice-ladder filter. The patent describes in detail how the lattice-ladder coefficients are obtained from the covariance matrix.—DLR

6,240,384

43.72.Ja SPEECH SYNTHESIS METHOD

Takehiko Kagoshima and Masami Akamine, assignors to Kabushiki Kaisha Toshiba
29 May 2001 (Class 704/220); filed in Japan 4 December 1995

This text-to-speech synthesis system contains tables of speech units, stored in a typical manner in the form of spectral parameters, but also has the ability to analyze an incoming speech signal, constructing new synthesis units dynamically. The patent describes a method called ''modulated clear speech'' in which the spectral shape is compensated for errors due to large shifts from the original fundamental frequency.—DLR

6,240,390

43.72.Ja MULTI-TASKING SPEECH SYNTHESIZER

Chaur-Wen Jih, assignor to Winbond Electronics Corporation
29 May 2001 (Class 704/267); filed in Taiwan, Province of China 18 May 1998

This speech playback device is identified as a synthesizer, but, in fact, does not allow any modification of the phoneme-sized speech segments, either in duration or fundamental frequency. The novel aspect of the device is a control structure which allows the output of prestored digital control bit streams interspersed with the speech data. Such bit streams may be used, for example, to select speech output channels, operate LED displays, or to drive other digital functions.—DLR

6,243,681

43.72.Ja MULTIPLE LANGUAGE SPEECH SYNTHESIZER

Yoshiki Guji and Koji Ohtsuki, assignors to Oki Electric Industry Company, Limited
5 June 2001 (Class 704/260); filed in Japan 19 April 1999

This multilingual speech synthesizer is actually a collection of single-language synthesis engines. Intended for operation in a network system, an initial guess of the text language is obtained from addresses or other information in the message header. The language guess is used to select one of the synthesis engines. However, the synthesis controller also checks the text sentence-by-sentence to verify the language choice and can switch to another language at any time.—DLR

6,246,983

43.72.Ja TEXT-TO-SPEECH E-MAIL READER WITH MULTI-MODAL REPLY PROCESSOR

Ranjun Zou *et al.*, assignors to Matsushita Electric Corporation of America
12 June 2001 (Class 704/260); filed 5 August 1998

This patent describes a system of speech recognition and synthesis processors and coding conventions to allow standard fixed or cellular phone units to use Internet e-mail systems as well as the standard telephone system. Procedures are described for voice entry of e-mail addresses, voice entry and editing of text materials, and voice control of all system functions. Incoming e-mail may be received in spoken form and a spoken reply may be generated.—DLR

6,250,928

43.72.Ja TALKING FACIAL DISPLAY METHOD AND APPARATUS

Tomaso A. Poggio and Antoine F. Ezzat, assignors to Massachusetts Institute of Technology
26 June 2001 (Class 434/185); filed 22 June 1998

This method of speech display provides both audio and facial images from an input text stream. Well-known text-to-phoneme methods are combined with the morphing of visemes to generate a facial image synchronized with the audio stream.—DLR

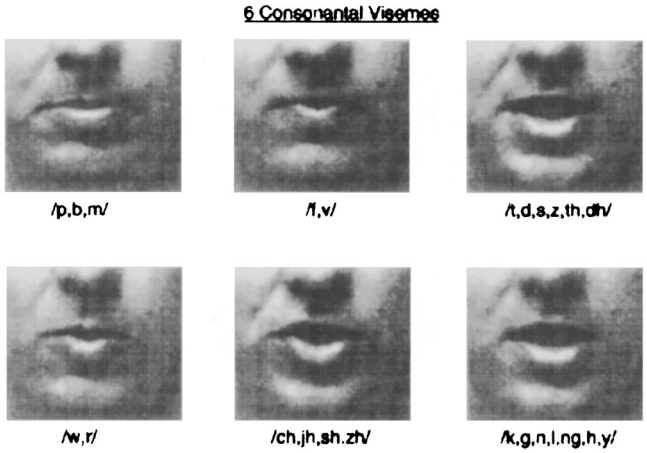

6,253,182

43.72.Ja METHOD AND APPARATUS FOR SPEECH SYNTHESIS WITH EFFICIENT SPECTRAL SMOOTHING

Alejandro Acero, assignor to Microsoft Corporation
26 June 2001 (Class 704/268); filed 24 November 1998

This speech synthesizer produces speech consisting of concatenated units which may range in length from phoneme to phrase segments. Each frame of an input speech unit is analyzed into voiced and unvoiced portions. For resynthesis, a new prosodic pattern is computed and the stored units are modified by independently altering the voiced and unvoiced portions.—DLR

6,236,968

43.72.Kb SLEEP PREVENTION DIALOG BASED CAR SYSTEM

Dimitri Kanevsky and Wlodek Wlodzimierz Zadrozny, assignors to International Business Machines Corporation
22 May 2001 (Class 704/275); filed 14 May 1998

This interesting application of speech recognition and synthesis systems provides conversation with a driver with the intention of keeping the driver awake beyond normal limits of stamina. In normal operation, the system maintains a dialog with the driver. The recognition system detects intoxication or fatigue. If it detects that the driver may be nodding off, it will voice a warning or change the topic of conversation. Failing in this, the system can also sound an alarm.—DLR

6,249,764

43.72.Kb SYSTEM AND METHOD FOR RETRIEVING AND PRESENTING SPEECH INFORMATION

Takahiko Kamae and Makoto Hirayama, assignors to Hewlett-Packard Company
19 June 2001 (Class 704/270.1); filed in Japan 27 February 1998

The ideas presented in this patent seem to be directed toward two different, but perhaps related, goals. Procedures for interacting with a speech interface include easier operation of a telephone services menu system and access to a speech database. A system of hyperlinks is described such that, similar to a text system with hypertext links, the presence of additional speech materials would be signaled by a hot spot indicator. The user could then optionally hear the extra material. Suggested hot spot indicators include a tone superimposed on the spoken material or, if available, activation of a light or buzzer.—DLR

6,263,306

43.72.Ne SPEECH PROCESSING TECHNIQUE FOR USE IN SPEECH RECOGNITION AND SPEECH CODING

Michael Sean Fee *et al.*, assignors to Lucent Technologies, Incorporated
17 July 2001 (Class 704/203); filed 26 February 1999

This patent relates to obtaining frequency-dependent features from the speech signal. The method provides an algorithm for front-end processing and pitch estimation. According to the patent, the product of Slepian functions and a segment of the time domain signal is calculated with the use of multiple tapers. A Fourier transform is applied to the resulting product to derive the multiple taper Fourier transform. The derivative of the resulting cepstrum is used for estimating pitch and can also be smoothed for use as a set of low-level features for a speech recognition front-end.—AAD

6,261,238

43.80.Ev PHONOPNEUMOGRAPH SYSTEM

Noam Gavriely, assignor to Karmel Medical Acoustic Technologies, Limited
17 July 2001 (Class 600/532); filed 4 October 1996

The patent concerns the analysis of respiratory sounds. This entails measuring the sounds and establishing their characteristics that correspond to specific types of respiratory conditions such as wheezing, pneumonia, snoring, tracheal malfunction, etc. A screening process can be positive (i.e., presence of a sound pattern characteristic of the particular breath sound) or

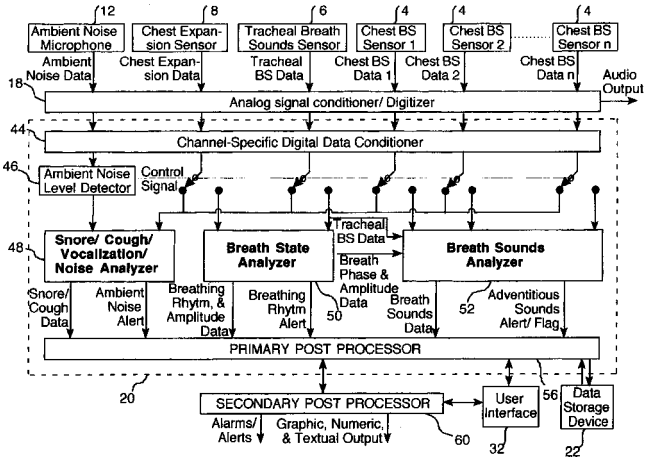

negative (i.e., the presence of a sound pattern that normally would not occur in a normal breath sound). The second step constitutes a verification process where a comparison is made between the breath sound features (spectral characteristics) and stored parameters to detect specific respiratory conditions.—DRR

6,264,616

43.80.Ev ACOUSTIC TUMOR DETECTION USING STACKED DERIVED-BAND ABR AMPLITUDE

Manuel Don, assignor to House Ear Institute
24 July 2001 (Class 600/559); filed 13 May 1998

This patent describes a variation of United States Patent 6,080,112 concerning the auditory brain response (ABR) method for detection of intracanalicular tumors, particularly small ones of less than 1 cm. The method involves recording of the patient's ABR to each of a plurality of auditory stimuli. The stimuli consist of 60 dB nHL clicks using high-pass noise masking procedures to isolate the cochlear response within specific frequency bands. The derived band ABRs are temporally shifted to align the peak amplitudes. The time-shifted responses are then summed to create the ''stacked'' ABR. This is compared to the mean stacked wave ABR amplitude for normal hearing individuals of the same gender as the patient. Patients having small intracanalicular tumors have significantly lower stacked wave ABR amplitudes than normal-hearing individuals without tumors.—DRR

6,270,466

43.80.Gx BRUXISM BIOFEEDBACK APPARATUS AND METHOD INCLUDING ACOUSTIC TRANSDUCER COUPLED CLOSELY TO USER'S HEAD BONES

Lee Weinstein *et al.*, assignors to BruxCare, Limited Liability Corporation
7 August 2001 (Class 600/590); filed 24 May 1996

Bruxism is generally defined as the nonfunctional clenching, grinding, gritting, gnashing, and/or clicking of teeth. The patent covers a method and apparatus for the treatment of bruxism through biofeedback. In one embodiment, the apparatus consists of electronics mounted in a lightweight headband that can be worn by a user during sleep or while awake. Electrodes

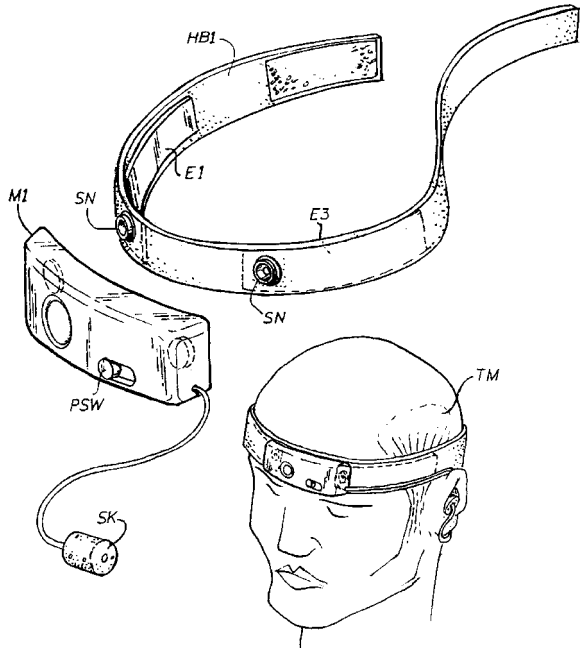

within the headband pick up surface EMG-voltage signals indicative of bruxism, and bio-feedback is sent to the user by a piezoelectric transducer in mechanical contact with the ear. One electrode of the piezoelectric transducer also serves as the reference sense electrode. Information detailing the timing, quantity, and duration of the bruxing events may be stored internally for later retrieval via display, computer interface, or voice synthesis interface.—DRR

6,263,877

43.80.Gx SNORE PREVENTION APPARATUS

Robert A. Gall, Waukesha, Wisconsin
24 July 2001 (Class 128/848); filed 13 November 1995

This appears to be one of those gadgets to be hawked on one of the late night TV programs. The snore prevention device consists of an oval plate that is to be positioned in the mouth of the user, between the teeth and the lips. An aperture in the middle of the oval plate allows for airflow into

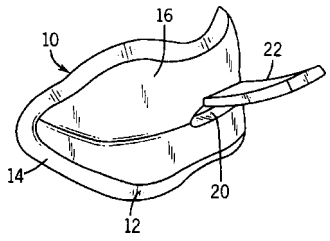

and out of the mouth. A tab extends from the oval plate just above the aperture through the lips to guide airflow into and out of the mouth when the lips are separated. The argument is made that reducing the airflow into the mouth lessens the vibration of the uvula, thus reducing the snoring sound. Comfort of use is rather questionable here.—DRR

6,264,608

43.80.Gx ACOUSTIC THERAPY APPARATUS COMPRISING A SOURCE OF THERAPEUTIC ACOUSTIC WAVES AND AN ULTRASOUND LOCATING MEANS

Ulrich Schätzle *et al.*, assignors to Siemens Aktiengesellschaft
24 July 2001 (Class 600/439); filed in Germany 2 April 1996

The device combines a source of therapeutic acoustic waves and an ultrasound locating system incorporating an ultrasonic transducer. The source and the ultrasound transducer combine to form an oblong applicator with a longitudinal axis for introducing signals into a patient's body. The source of the therapeutic waves is a linear array of piezoelectric elements. The ultrasonic locating system generates ultrasound images with respect to a plane that contains the longitudinal axis of the applicator. The interior of the applicator is filled with a liquid (such as light mineral oil) suitable as a propagation medium for ultrasound.—DRR

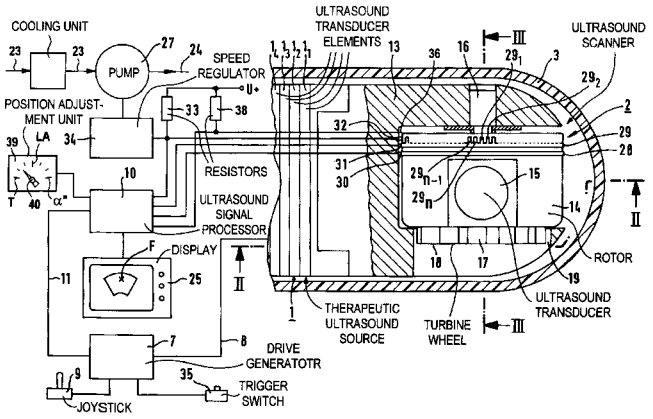

Relative loudness of low- and high-frequency bands of speech-shaped babble, including the influence of bandwidth and input level (L)

Gitte Keidser,[a] Richard Katsch, Harvey Dillon, and Frances Grant
The National Acoustic Laboratories, 126 Greville Street, Chatswood, NSW 2067, Australia

(Received 11 May 2001; revised 22 October 2001; accepted 19 November 2001)

In a balancing test, ten normal-hearing listeners adjusted filtered speech-shaped babble-noise to equally loud levels. On average, they selected about 10 dB less gain for bands below 1 kHz than for bands above and including 1 kHz. The findings applied to two bandwidths (octave and equivalent rectangular bandwidth) and two levels (65 and 85 dB SPL). The outcome suggests that hearing aid fitting procedures aiming to equalize loudness of speech bands should prescribe less low-frequency gain than procedures aiming to normalize loudness of speech bands. A significant interaction was found between bandwidth and input level for the high-frequency bands. © *2002 Acoustical Society of America.* [DOI: 10.1121/1.1436070]

PACS numbers: 43.66.Cb, 43.71.Bp, 43.66.Lj [MRL]

I. INTRODUCTION

Long-term power spectra of running speech produced with a normal vocal effort show that the low-frequency components of speech have more energy than the high-frequency components [e.g., the international long-term average speech spectrum, ILTASS, by Byrne *et al*. (1994)]. More specifically, the one-third octave root-mean-square (rms) level at 500 Hz is about 15 dB higher than the one-third octave rms level at 2000 Hz. Based on this picture, the assumption is often made that the low-frequency speech bands sound louder than the high-frequency speech bands. The assumption is supported by relating the one-third octave rms levels from 0.25 to 4 kHz of ILTASS to normal equal loudness contours measured for pure tones (ISO R 226, 1961). The result of this exercise suggests that normal-hearing listeners perceive the one-third octave speech bands below 1 kHz as being louder than the one-third octave speech bands at and above 1 kHz. The assumption is further supported by loudness measurements of ILTASS-shaped noise filtered in equivalent rectangular bandwidth (ERB) (Fig. 1 in Moore, 2000) using a loudness model developed by Moore and Glasberg (1997). However, the seemingly only published study on the relative loudness of speech bands, using a single-talker speech signal in the free-field as stimulus, suggests that normal-hearing listeners perceive the one-third octave speech bands from 0.5 kHz to at least 3.15 kHz as being equally loud (Holte and Margolis, 1987).

The assumption that low-frequency speech bands sound louder than high-frequency speech bands is made, for example, when developing prescriptive procedures for fitting hearing aids. Consequently, many prescriptive procedures, such as NAL-R (Byrne and Dillon, 1986), aim to present speech bands at an equally loud level to avoid a detrimental effect on speech intelligibility from upward spread of masking. To achieve this, the procedures prescribe relatively more gain in the high than in the low frequencies. The equal loudness of speech bands rationale is supported by empirical data of which some were measured under headphones (Byrne, 1986; Skinner, 1988). However, a recent investigation (Keidser *et al.*, 2000) found that the relative loudness of low- and high-frequency sounds may be affected by the type of receiver used, that is, whether the receiver is a loudspeaker, supra-aural headphones, or insert earphones. As part of that investigation, a balancing test was conducted to study the relative loudness of low- and high-frequency bands of speech-filtered babble-noise presented in the free field. The balancing test was completed using two bandwidths and two levels. As there is relatively little information available on this issue, the data are briefly reported here.

II. METHOD

A. Subjects

Ten subjects (five males and five females) who passed a screening test at 10 dB HL across the frequencies from 0.25 to 4 kHz on both ears were recruited.

B. Instrumentation

An eight-talker babble-noise (four male and four female talkers), prefiltered to match the one-third octave rms levels of ILTASS (Byrne *et al.*, 1994) in the sound field, was used as stimulus. This stimulus has all the characteristics of speech, but little or no intelligibility and less temporal intensity fluctuations. The babble-noise was played back from a digital audio recorder (SONY TCD-D10 PRO) and was bandpass filtered in real time using the Knowles' Experimental Processor for Acoustic Research (KEPAR). In KEPAR, octave bands and ERBs were implemented using Butterworth filters of 18th and 12th order, respectively. Both types of filter were created with the center frequencies of 0.25, 0.5, 1, 1.5, 2, 3, and 4 kHz. Two filters were running simultaneously in KEPAR and the processing from each filter was presented through each of two separate output channels. Each output was connected to a remotely controlled variable

[a]Electronic mail: gitte.keidser@nal.gov.au

attenuator. The output of each attenuator was taken to a selector box from which the filtered babble-noise was presented through an amplifier and a loudspeaker in the free field.

C. Procedure

In a large anechoic chamber the subject was seated about 2 m in front of a loudspeaker. By using a switch on the selector box the subject compared two bands of babble-noise. One band was always the 1.5-kHz band, which was used as reference. The subject's task was to adjust the level of a test band to match that of the reference using an unmarked knob attached to the remotely controlled attenuator and a bracketing method. At the beginning of each adjustment, the test band was always softer than the reference band. The subject could listen to each band for as long as desired and could switch between bands as many times as desired. Each subject completed four sessions, each testing one of two bandwidths (octave and ERB) and one of two levels (65 and 85 dB SPL). At the two levels the 1.5-kHz band was presented at the level corresponding to wideband ILTASS-shaped babble being presented at 65 and 85 dB SPL at the position of the subject's head. Five adjustments were completed for each level, bandwidth, and frequency (24 conditions). The four sessions were presented in a randomized order for each subject with the frequencies presented randomly within each session. The first adjustment for each condition was considered as a practice adjustment and was discarded in the following analyses.

III. RESULTS

Overall, the data were very consistent, both within and between subjects. For example, across 240 cases (24 test conditions$\times$10 subjects), the mean of the within-subject standard deviation values (SDs) of four selected attenuator levels was 2.6 dB (ranging from 0.2 to 7.6 dB). Further, across the twenty-four test conditions the mean of the between-subject SDs of the average selected attenuator levels was 4.4 dB (ranging from 2.0 to 6.6 dB).

For each bandwidth and each level, the average attenuator levels measured for each subject and each test frequency were subtracted from the attenuator level used for the 1.5-kHz band. The difference between the attenuator levels indicated the gain needed to make each speech band equally loud to the appropriate 1.5-kHz band. The gain levels relative to 1.5 kHz were used as observations in an analysis of variance using bandwidth, level, and frequency as repeated measures. The result of this analysis showed a highly significant interaction between the three factors ($p<0.004$). Figure 1 shows how the selected gain relative to 1.5 kHz varied with bandwidth, level, and frequency. Within each combination of bandwidth and level, the ovals show the frequency bands that were not significantly different from each other ($p \geqslant 0.05$) according to a *post hoc* analysis of means (Newman–Keuls). Generally, significantly less gain was required for the low (0.25 and 0.5 kHz) than for the mid and high (1, 2, 3, and 4 kHz) frequencies to make the test bands equally loud to the 1.5-kHz band ($p<0.05$).

IV. DISCUSSION

Ten normal-hearing subjects balanced the level of filtered ILTASS-shaped babble-noise to equal loudness. For two bandwidths (octave and ERB) and two input levels (wideband babble of 65 and 85 dB SPL), the subjects selected significantly less gain (about 10 dB) to make the bands of 0.25 and 0.5 kHz equal in loudness to the 1.5-kHz band than was needed to make the bands of 1, 2, 3, and 4 kHz equally loud to the 1.5-kHz band. This outcome is in agreement with the observations based on relating the one-third octave levels of ILTASS to the normal equal loudness contours for pure tones (ISO R 226, 1961) and a loudness model (Moore, 2000). However, the findings differ from those of Holte and Margolis (1987) who found no significant difference between levels selected for 0.5, 0.8, 1, 2, and 3.15 kHz, and a small difference in gain of 4 dB between 0.25 and 1 kHz.

There are several procedural differences among the four investigations, including method and test stimuli. It seems unlikely that differences in the psychometric method used to obtain the equal loudness curves [this study, ISO R 226 (1961) and Holte and Margolis (1987)] would affect one frequency region only. Further, differences in type of stimulus, test bandwidth, and temporal fluctuations seem unlikely to explain any discrepancy in relative levels between studies (Ricketts and Bentler, 1996; Moore *et al.*, 1999). Two factors, however, may account for the discrepancy between Holte and Margolis (1987) and the other observations. First, in this study and the ISO R 226 subjects balanced the level of two stimuli with the same bandwidth, whereas the subjects in Holte and Margolis' study balanced the level of unfiltered speech to that of filtered speech. If, in the latter case, the subjects matched the vocal effort of the filtered and unfiltered stimuli rather than the overall loudness, then this would bias the result in the direction that all bands were perceived equally loud. Second, this study and the investigations using the ISO R 226 equal loudness curves and the Moore and Glasberg loudness model were based on an ILTASS-shaped stimulus. Thus, these stimuli had a spectral shape different from the single-talker stimulus used in Holte

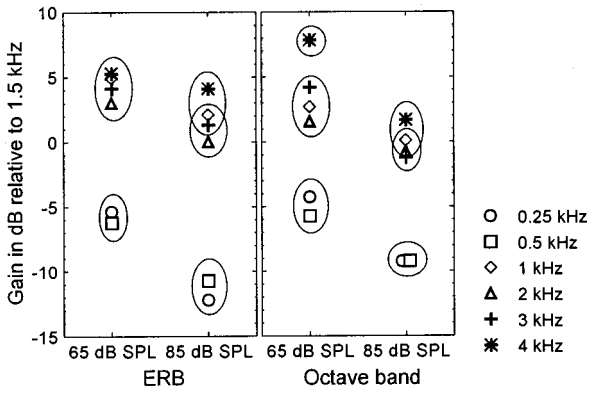

FIG. 1. The average gain levels relative to 1.5 kHz selected for each test frequency as a function of bandwidth and presentation level. Within each bandwidth and presentation level, the ovals group the frequencies for which the selected gain levels were not significantly different.

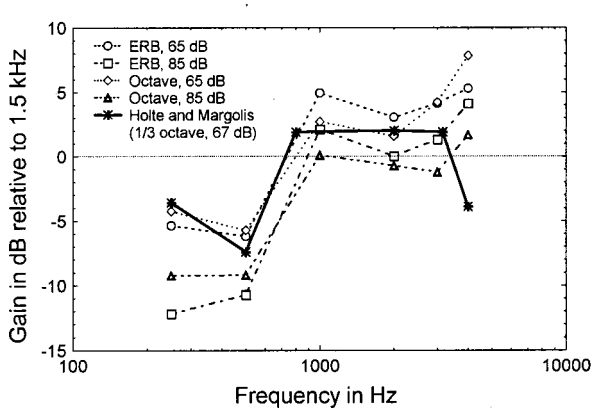

FIG. 2. The average gain levels measured relative to 1.5 kHz (this study) or 1 kHz (Holte and Margolis, 1987) as a function of frequencies. The levels from Holte and Margolis' study were adjusted for the difference between the one-third octave levels of their speech stimulus and ILTASS.

and Margolis (1987). Figure 2 shows how the data of Holte and Margolis would compare to the data from this study if (1) the levels presented in their Fig. 2 were converted to gain levels relative to the 1-kHz speech band, and (2) the differences in one-third octave speech levels used by Holte and Margolis and ILTASS were applied to the data. As seen in Fig. 2, the outcome of Holte and Margolis' study is then similar to the outcome of this study apart from at 4 kHz. The 4-kHz filtered stimulus is a difficult stimulus for the purpose of loudness judgments, as it has particularly strong variations of intensity (and therefore loudness) with time. This difficulty may have interacted in some unknown manner with the different reference stimuli used in the two experiments.

Overall, data show a prevalent support for the hypothesis that the low-frequency speech bands (<1 kHz) are louder than the high-frequency speech bands. Therefore, fitting procedures aiming to restore loudness of speech bands to normal must prescribe higher gain targets at 0.25 and 0.5 kHz than fitting procedures aiming to present speech bands at equally loud levels as demonstrated by Byrne *et al.* (2001).

This study found a significant interaction between bandwidth and input level. Particularly, the difference in selected gain levels among the two highest test bands varied across bandwidth and input level (Fig. 1). The higher test bands generally produced higher SDs than the lower test bands, which suggest that it was more difficult to judge the overall loudness of the high frequency bands, presumably because they sounded less familiar. Further, Fig. 1 suggests that for a given input level there is a trend for the relative loudness between low- and high-frequency speech bands to be smaller for the wider speech bands. It is also interesting to note that the subjects selected lower gain levels (relative to the 1.5-kHz reference band) when listening to the higher (85 dB SPL) than lower (65 dB SPL) input level. It is possible that these trends are the results of a combination of the following factors: (1) power summation within the broader bands, especially within the high-frequency bands where the speech spectrum displays a significant slope, (2) loudness summation, and (3) flattening of the equal loudness curves as the input level increases (ISO R 226, 1961). More systematic research is needed to understand relative loudness across frequencies of complex sounds.

V. CONCLUSION

When listening to filtered babble-noise that varied in one-third octave levels according to ILTASS, normal-hearing subjects judged the bands below 1 kHz to be significantly louder than the bands above and including 1 kHz. This observation applied to two different bandwidths (ERB and octave) and two different input levels (65 and 85 dB SPL). With respect to hearing aid fitting, the observations suggest that procedures aiming to equalize loudness of speech bands must produce less gain in the low frequencies than procedures aiming to normalize loudness of speech bands. Bandwidth and level showed a significant interaction among the high-frequency test bands, possibly because it is more difficult to judge loudness of these bands due to the unfamiliar sound.

ACKNOWLEDGMENTS

This work was partly supported by the Cooperative Research Center for Cochlear Implant and Hearing Aid Innovation. The authors would also like to thank Knowles for making their KEPAR system available for this project.

Byrne, D. (**1986**). "Effects of frequency response characteristics on speech discrimination and perceived intelligibility and pleasantness of speech for hearing-impaired listeners," J. Acoust. Soc. Am. **80**(2), 484–493.

Byrne, D., and Dillon, H. (**1986**). "The National Acoustic Laboratories' (NAL) new procedure for selecting the gain and frequency response of a hearing aid," Ear Hear. **7**(4), 257–265.

Byrne, D., Dillon, H., Katsch, R., Ching, T., and Keidser, G. (**2001**). "The NAL-NL1 procedure for fitting non-linear hearing aids: characteristics and comparisons with other procedures," J. Am. Acad. Audiol. **12**(1), 37–51.

Byrne, D., Dillon, H., Tran, K., Arlinger, S., Wilbraham, K., Cox, R., Hagerman, B., Hetu, R., Kei, J., Lui, C., Kiessling, J., Kotby, M. N., Nasser, N. H. A., El Kholy, W. A. H., Nakanishi, Y., Oyer, H., Powell, R., Stephens, D., Meredith, R., Sirimanna, T., Tavartkiladze, G., Frolenkov, G. I., Westerman, S., and Ludvigsen, C. (**1994**). "An international comparison of long-term average speech spectra," J. Acoust. Soc. Am. **96**(4), 2108–2120.

Holte, L., and Margolis, R. H. (**1987**). "The relative loudness of third-octave bands of speech," J. Acoust. Soc. Am. **81**(1), 186–190.

ISO R 226. (**1961**). "Normal Equal-loudness Contours for Pure Tones and Normal Threshold of Hearing under Free Field Listening Conditions" (International Organization for Standardization, Switzerland).

Keidser, G., Katsch, R., Dillon, H., and Grant, F. (**2000**). "Relative loudness perception of low and high frequency sounds in the open and occluded ear," J. Acoust. Soc. Am. **107**(6), 3351–3357.

Moore, B. C. J. (**2000**). "Use of a loudness model for hearing aid fitting. IV. Fitting hearing aids with multi-channel compression so as to restore 'normal' loudness for speech at different levels," Br. J. Audiol. **34**, 165–177.

Moore, B. C. J., and Glasberg, B. R. (**1997**). "A model of loudness perception applied to cochlear hearing loss," Aud. Neurosci. **3**, 289–311.

Moore, B. C. J., Vickers, D. A., Baer, T., and Launer, S. (**1999**). "Factors affecting the loudness of modulated sounds," J. Acoust. Soc. Am. **105**, 2757–2772.

Ricketts, T. A., and Bentler, R. A. (**1996**). "The effect of test signal type and bandwidth on the categorical scaling of loudness," J. Acoust. Soc. Am. **99**, 2281–2287.

Skinner, M. W. (**1988**). *Hearing Aid Evaluation* (Prentice–Hall, Englewood Cliffs, NJ), pp. 13–36.

Radiation impedance matrices for rectangular interfaces within rigid baffles: Calculation methodology and applications

Allan D. Pierce, Robin O. Cleveland, and Mario Zampolli[a)]
Department of Aerospace and Mechanical Engineering, Boston University, Boston, Massachusetts 02215

(Received 13 June 2001; revised 6 November 2001; accepted 6 November 2001)

The coupling of sound fields through a finite-sized aperture in a plane rigid baffle where the region (half-space) on one side is unbounded can be described by an integral equation which constitutes a boundary condition for the field on the other side of the aperture. Such a boundary condition, when the pressure and the normal velocity are expanded in basis functions defined over the aperture, can be recast into a matrix form relating the coefficients of the basis functions in the expansions, the principal feature being a matrix of fourfold (double-area) integrals analogous to those encountered in studies of radiation from flexible pistons in rigid baffles. A substantial analytical reduction to sums of single nonsingular integrals is derived for the elements of this radiation impedance matrix when the aperture is rectangular and the basis functions are expressible as a sum of products of exponential functions of the Cartesian coordinates of the aperture plane, with the exponential coefficients being arbitrary complex numbers. The validity of the result is substantiated by its reduction to previously published results for less general cases. Its utility is demonstrated with the example of diffraction by a square hole in a screen.
[DOI: 10.1121/1.1430684]

PACS numbers: 43.20.El, 43.20.Rz, 43.30.Jx [JGM]

I. INTRODUCTION

Many acoustical systems of topical interest involve interfaces, with an interface typically dividing two regions with distinct characteristics, although sometimes[1] interfaces are conceptually created to separate regions where different mathematical descriptions are used. Mathematical formulations involving interfaces typically lead to equations involving integrals over all or a portion of the interface. Derivations of such integral equations date back to Helmholtz,[2] Rayleigh,[3] Kirchhoff,[4] Kellogg,[5] and Maue.[6] A review and fresh derivations can be found in a monograph article by Pierce.[7] Modern acoustical literature makes extensive use of such integral equations, as is exemplified in recent papers by Koo, Ih, and Lee,[8] by Giordano and Koopmann,[9] by Ginsberg and McDaniel,[10] and by Cunefare and De Rosa.[11]

The present paper is concerned with when the interface is a plane surface (Fig. 1), for which only a finite portion is not rigid. On one side of the interface is a semi-infinite half-space, and on the other side is an acoustical system that need not be explicitly specified. The nonrigid portion of the plane is the active interface (here referred to simply as the aperture), and the examples that are treated in this paper are for when this aperture has a rectangular shape. However, the technique developed here could be applied to apertures of more general shape.

The principal mathematical entity that emerges during the development of the analysis within the paper is a fourfold integral of the general form

$$J_{\alpha,\beta}(k)=\int_A\int_{A'}\Phi_\alpha(x,y)\Psi_\beta(x',y')\frac{e^{ikR}}{R}dx'dy'\,dxdy, \tag{1}$$

where $R=[(x-x')^2+(y-y')^2]^{1/2}$ is distance between points on the aperture. Both of the area integrations extend over the area of the aperture. The functions $\Phi_\alpha(x,y)$ and $\Psi_\beta(x,y)$ are the αth and βth members of each of two sets of functions—each set having N members, with the number N possibly being ∞. The two sets can possibly be the same set. The article explains how matrices, where the (α,β)th element is proportional to $J_{\alpha,\beta}$, can arise in the analysis of individual problems within a wide class of acoustical problems, and it also discusses how the requisite fourfold integral can be evaluated.

The explicit evaluation of integrals of such a generic type has been discussed in many previous papers. The present authors have studied, for example, the work presented in papers by Snyder and Tanaka,[12] by Takahagi, Nakai, and Yamai,[13] by Li and Gibeling,[14] and by Leppington, Broadbent, and Heron.[15] Various numerical and analytical tricks are known and discussed in this literature for simplifying the numerical work of the integration for special cases of the aperture shape and for special forms of the functions $\Phi_\alpha(x,y)$ and $\Psi_\beta(x,y)$; the principal achievement in the current paper is the reduction of the integration to a finite sum of one-dimensional integrals, where the integration is over a finite region, where the integrand is finite, and where the real and imaginary parts of the integrand have a finite number of maxima and minima. This is also for a special case; in particular, the aperture must be of rectangular shape, and the functions $\Phi_\alpha(x,y)$ and $\Psi_\beta(x,y)$ must each be of the form of a finite sum of terms, each term of the form $e^{px}e^{qy}$, where the exponent coefficients (p and q) are (in general) complex numbers and differ from term to term. Such restrictions nevertheless allow the possibility for the $\Phi_\alpha(x,y)$ and $\Psi_\beta(x,y)$ to be functions that one would naturally use in the solution of many acoustic problems. (The reason for the restriction involving exponentials is so that one can exploit the property

[a)]Present address: SACLANT Undersea Research Centre, La Spezia, Italy.

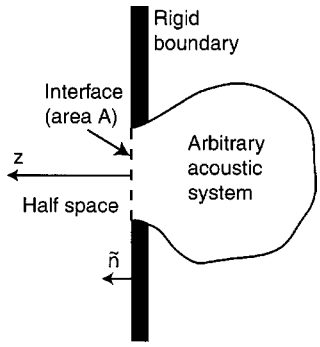

FIG. 1. Sketch of general situation for which the analysis of the present paper applies. An arbitrary acoustic system is coupled to a half-space through an interface of area A. The plane $[(x,y)$-plane$]$ of the interface except for the interface itself appears rigid to the medium on the other side ($z>0$) of the half-space.

$e^u e^v = e^{u+v}$ in the analytic simplification of the integrals.)

Apart from the discussion of the methodology of the evaluation of such integrals, the significance of the present paper is that it shows how many complex problems can be reduced to a manageable form in which the presence of half-spaces is replaced by a boundary condition, with the boundary condition expressed by a matrix relation, in which integrals of the form of that in Eq. (1) appear in the matrix elements. Prior literature making use of such integrals has for the most part been restricted to the classic case of radiation from a baffled diaphragm in various specified states of vibration. The recognition that analogous mathematical ideas apply to wider classes of problems deserves a systematic exposition.

II. INTEGRAL RELATIONSHIPS AND MATRICES

A. Integral relations on interfaces

The region of the interface plane that is not rigid is the aperture of area A. On the other side of the area A there may be virtually anything insofar as the present paper is concerned. There may, for example, be an elastic plate with a fluid cavity on the other side. As viewed from the half-space, the interface is such that the normal component of the fluid velocity is zero along the rigid portion, but over the bounded area portion, it is in general nonzero. Insofar as the rest of the universe is concerned (i.e., that on the other side of the interface) the half-space can be formally replaced by an interface boundary condition. A suitable derivation results when the field in the half-space is written as the sum of an incident wave, a reflected wave, and a wave radiated from the aperture. The pressure associated with the reflected wave is taken as of the same form as for the incident wave, except (in accord with the method of images) the argument z is replaced by its negative. The combination of the incident and reflected waves conforms to the rigid surface boundary condition everywhere on the surface $z=0$. This boundary condition does not apply, however, on the aperture, where the outward normal component (away from the surface, into the fluid, and back toward the source) of the fluid velocity has some possibly nonzero value of $v_{n,\mathrm{int}}(x,y)$. This velocity, although not necessarily known, can be regarded as the source of a wave that radiates from the aperture back into the half-space. The expression for this wave results from an analysis due to Rayleigh,[3] the result of which is most frequently used in the prediction of sound radiation from baffled pistons. For the case described here, the taking of the limit as $z \to 0$ results in the following integral equation,

$$p_{\mathrm{int}}(\mathbf{x}_S) = 2p_{\mathrm{inc}}(\mathbf{x}_S) + \mathcal{M}(\mathbf{x}_S, \{v_{n,\mathrm{int}}(\mathbf{x}_S)\}), \tag{2}$$

on the portion A of the surface, where $\mathbf{x}_S$ is a point on the surface, p_{inc} is the amplitude of the incident wave, p_{int} is the pressure at the interface, and where

$$\mathcal{M}(\mathbf{x}_S, \{v_{n,\mathrm{int}}\}) = -\frac{i\omega\rho}{2\pi} \int\int v_{n,\mathrm{int}}(x',y') \frac{e^{ikR}}{R} dx'\,dy'. \tag{3}$$

Here R is the distance that appears in Eq. (1).

[This integral relation is a special case of Eq. (427) in the 1993 tutorial article by Pierce,[7] as the term $\mathcal{L}_1\{\zeta, p_{\mathrm{tot}}\}$ that appears there is identically zero when the bounding surface is flat. The general equation appears, possibly for the first time, as Eq. (10) in the 1949 paper by Maue.[6] For planar surfaces, the equation dates in principle back to an 1897 paper by Rayleigh,[16] insofar as Rayleigh used integral equations in relation to the problem of diffraction of sound by an aperture in a thin rigid screen. Although one can identify various instances where analogous ideas appear in the literature, the first explicit appearance of a version of Eq. (2) that is applicable to diffraction by an aperture is apparently Eq. (2.15) in the second edition (1950, the relevant passage being written by Copson) of Baker and Copson's monograph.[17] Equation (2) that appears above follows directly from Copson's Eq. (2.13) when one sets $x_o = 0$.]

B. Integral relations as boundary conditions

A principal use for Eq. (2) is as a boundary condition for the portion of the overall acoustic system that lies on the other side of the aperture (i.e., that side that is not a half space). A nontrivial example is shown in Fig. 2. The mouth of the aperture is occupied by a cantilevered plate and this in turn is backed by a finite cavity with walls idealized as rigid. Because of the incident acoustic wave from the half-space side, both the backing cavity and the cantilevered plate are set into vibration. The partial differential equations of acoustics govern the fluid oscillations within the cavity, and the plate can be regarded as undergoing vibrations jointly forced by the pressure on the half-space side and by the pressure on the cavity side. The normal components of the fluid velocity on the two sides of the plate are equal and both are the same as the transverse velocity of the plate. The overall coupled vibration problem can be formulated with the integral relation (2) serving as the only requirement that relates the plate's transverse velocity to the pressure on its front side.

C. Matrix formulation of interface relationship

In the solution of specific problems, especially when the dimensions of the area A are less than a few wavelengths, the recasting of Eq. (2) into a matrix form provides a viable, although not necessarily exact, alternative. In the spirit of the

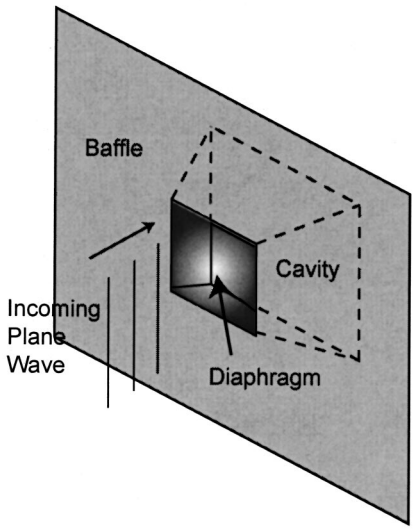

FIG. 2. Example of a problem to which the formulation in the paper applies. A plane wave is incident on a baffled cantilevered plate (displacements and slopes held to zero around the boundary), and the plate is backed by a cavity with rigid walls.

general Galerkin method, one chooses two sets of basis functions, $\{\Phi_\alpha(\mathbf{x}_S)\}$ and $\{\Psi_\beta(\mathbf{x}_S)\}$, each with N members, and assumes that sums of the form

$$p_{\text{int}}=\sum_\alpha p_\alpha\Phi_\alpha; \quad v_{n,\text{int}}=\sum_\beta v_\beta\Psi_\beta \tag{4}$$

for appropriate choices of the coefficients, p_α and v_β, give adequate representations for the corresponding functions for all points within the area A. These individual basis functions for either set are not necessarily taken as orthogonal and normalized, but they are taken as linearly independent. (There are various rational ways for choosing these basis functions, some involving variational formulations and a priori physical insight. They can be taken as complete sets of orthonormal functions, with $N=\infty$, so that no approximation is necessarily implied. The implied arbitrariness here is to allow extensive latitude in the actual choice, although the choices are restricted in the subsequent discussion regarding the evaluation of integrals.)

With the expansions taken as valid, Eqs. (4) can be substutited into Eq. (2), and multiplication by any one of the $\Phi_\alpha(x,y)$, followed by integration over the area A, yields the set of N algebraic equations:

$$\sum_{\alpha'} N_{\alpha,\alpha'}p_{\alpha'}=2F_\alpha-\frac{i\omega\rho}{2\pi}\sum_\beta J_{\alpha,\beta}v_\beta, \tag{5}$$

where the quantity $J_{\alpha,\beta}$ is the integral that appears in Eq. (1). The other quantities that appear are

$$N_{\alpha,\alpha'}=\int_A\Phi_\alpha\Phi_{\alpha'}dA; \quad F_\alpha=\int_A p_{\text{inc}}\Phi_\alpha dA. \tag{6}$$

Alternative recastings of the matrix relation (5) allow identification of what can be referred to as *radiation impedance* and *radiation admittance* matrices. In acoustical contexts the term impedance is used to refer to proportionality constants mapping velocity amplitudes to pressure amplitudes, while admittance is used to refer to proportionality constants mapping pressure amplitudes to velocity amplitudes. To identify the former, one multiplies both sides of (5) by the inverse of the (symmetric) matrix with elements $N_{\alpha,\alpha'}$, with the result

$$p_\alpha=2E_\alpha+\sum_\beta Z_{\alpha,\beta}v_\beta, \tag{7}$$

where E_α corresponds to the F_α term and

$$Z_{\alpha,\beta}=-\frac{i\omega\rho}{2\pi}\sum_{\alpha'}(N^{-1})_{\alpha,\alpha'}J_{\alpha',\beta}. \tag{8}$$

The latter is termed the *radiation impedance matrix* because

$$p_{\text{rad}}(\mathbf{x}_S)=\sum_\alpha\left\{\sum_\beta Z_{\alpha,\beta}v_\beta\right\}\Phi_\alpha(\mathbf{x}_S) \tag{9}$$

is to be regarded (although possibly only as an approximation because of the truncation to finite N) as the radiated portion of the acoustic pressure at the aperture. (The linear independence of the basis functions Φ_α guarantees that the requisite matrix inverse exists.)

The *radiation admittance matrix*, with elements $Y_{\beta,\alpha}$, is analogously identified as the inverse of the radiation impedance matrix, so that

$$\sum_\alpha Y_{\beta,\alpha}Z_{\alpha,\beta'}=\delta_{\beta,\beta'}; \quad \sum_\beta Z_{\alpha,\beta}Y_{\beta,\alpha'}=\delta_{\alpha,\alpha'}. \tag{10}$$

(The radiation impedance matrix is not necessarily symmetric; neither is the radiation admittance matrix. Nevertheless, right inverses are always the same as left inverses. The possibility that, with some choices of the two sets of basis functions, the radiation impedance matrix may not have an inverse is unlikely and is here disregarded.)

Pertinent results to be noted at this point are (*i*) that the boundary condition replacing the half-space can be expressed in terms of either the radiation impedance matrix or the radiation admittance matrix and (*ii*) evaluation of either of these matrices requires the evaluation of the integral in Eq. (1).

D. Fourier transform representation

In some of the applicable related literature, a recent example being a 1995 paper by Graham,[18] an alternate representation of the integral in Eq. (1) is used. Since the equivalence is not obvious and is typically not mentioned, a brief derivation is given here. A double Fourier transform of the kernel (Green's function evaluated at a point on the same plane as the source) that appears in the integral yields

$$\frac{e^{ikR}}{R}=-\frac{1}{2\pi i}\lim_{\epsilon\to 0}\int_{-\infty}^{\infty}\int_{-\infty}^{\infty}\frac{N(\epsilon,k_x,k_y)}{(k^2-k_x^2-k_y^2)^{1/2}}dk_x\,dk_y, \tag{11}$$

with the numerator in the integrand being

$$N(\epsilon,k_x,k_y)=e^{-\epsilon k_x^2}e^{ik_x(x-x')}e^{-\epsilon k_y^2}e^{ik_y(y-y')}. \tag{12}$$

The radical in the denominator is understood to have a phase of $\pi/2$ whenever $k_x^2+k_y^2$ is greater than k^2.

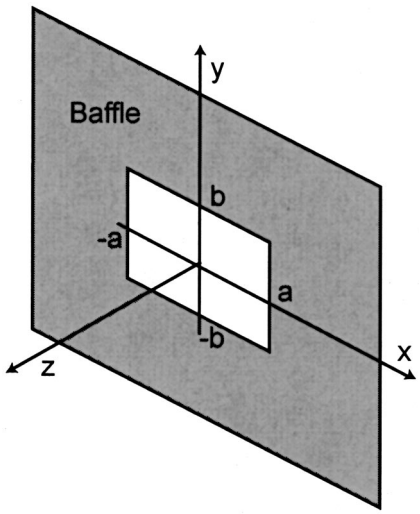

FIG. 3. Rectangular interface in a rigid baffle. The rectangle has dimensions $2a$ by $2b$, and the coordinate origin is in the center of the rectangle.

Insertion of the Fourier transform (11) into the quadruple integral (1), followed by an exchange of the order of integration, yields

$$J_{\alpha,\beta}=-\frac{1}{2\pi i}\int_{-\infty}^{\infty}\int_{-\infty}^{\infty}\frac{\hat{\Phi}_\alpha(k_x,k_y)\hat{\Psi}_\beta(-k_x,-k_y)}{(k^2-k_x^2-k_y^2)^{1/2}}\,dk_x\,dk_y, \tag{13}$$

where

$$\hat{\Phi}_\alpha(k_x,k_y)=\int\int \Phi_\alpha(x,y)e^{ik_x x}e^{ik_y y}\,dA \tag{14}$$

with the overcaret designating the Fourier transform of the corresponding function. Here the implied limit as $\epsilon\to 0$ has been taken; the principal reason for expressing Eq. (11) as a limit is to guarantee that the interchange of integration order is allowable.

One could be tempted into taking Eq. (13) as a starting point rather than Eq. (1), inasmuch as that, for the same circumstances as are taken further below, the two double Fourier transforms $\hat{\Phi}_\alpha(k_x,k_y)$ and $\hat{\Psi}_\beta(-k_x,-k_y)$ can be evaluated in closed form, so the initial fourfold integral is immediately reduced to a twofold integral. However, the integrations over k_x and k_y are between infinite limits and one still has a singular integrand with which to contend. Nevertheless, this representation is useful when one considers high-frequency limits and can exercise the option of using asymptotic methods. The interest here is with when the frequency is not large.

III. A FUNDAMENTAL INTEGRAL FOR RECTANGULAR APERTURES

A. Generic basis functions

The circumstances alluded to above where some analytical simplification of the integral (1) is achievable are when the aperture is rectangular. For definiteness, the aperture is here taken (Fig. 3) to extend from $x=-a$ to $x=a$, and from $y=-b$ to $y=b$, so that the area A is $4ab$. (In much of the prior literature, a and b denote the total rectangle dimensions, and they accordingly correspond to quantities that are twice as large as the present paper's a and b.)

Among possible basis functions $\Phi_\alpha(x,y)$ or $\Psi_\beta(x,y)$ that one might use for such a geometry are products of Warburton[19] functions, one factor depending on x/a and the other factor depending on y/b, with the even and odd Warburton functions appropriate to the x-coordinate being

$$w_{e,n}(x/a)=\frac{\cosh(\kappa_{e,n}x/a)}{\cosh(\kappa_{e,n})}-\frac{\cos(\kappa_{e,n}x/a)}{\cos(\kappa_{e,n})}, \tag{15}$$

$$w_{o,n}(x/a)=\frac{\sinh(\kappa_{o,n}x/a)}{\sinh(\kappa_{o,n})}-\frac{\sin(\kappa_{o,n}x/a)}{\sin(\kappa_{o,n})}, \tag{16}$$

where $\kappa_{e,n}$ and $\kappa_{o,n}$ are roots of

$$\tanh(\kappa_{e,n})=-\tan(\kappa_{e,n});\quad \tanh(\kappa_{o,n})=\tan(\kappa_{o,n}). \tag{17}$$

These functions satisfy the boundary conditions of being zero and of having zero slope at $x=\pm a$ and jointly constitute a complete set. (They occur naturally in the theory of beams that are cantilevered at both ends.) Use of products of Warburton functions would be a natural choice if the aperture were occupied by a cantilevered plate. (The terminology ''Warburton functions'' is not standard, but there is no other name associated with the functions listed above. Warburton was apparently the first to recognize their potential usefulness as basis functions in more general contexts.)

Alternative choices of basis functions would be products of trigonometric functions, e.g., $\cos(n\pi x/a)$, $\cos([n+(\frac{1}{2})]\pi x/a)$, $\sin(n\pi x/a)$, and $\sin([n+(\frac{1}{2})]\pi x/a)$. One could choose a complete set of basis functions of such a type where the sets of x- and y-dependent factors are themselves complete sets, and where every element in, say, the set of x-dependent factors satisfies the boundary condition of being zero at the two end-points ($x=\pm a$) or a complete set where every element satisfies the boundary condition of having zero derivative at the two end-points.

In all such considered cases, each basis function can be selected as a single product or as a sum of products of exponentials where a single term is a constant times a quantity of the generic form $e^{px/a}e^{qy/b}$. Here the quantities p and q, which differ from term to term, are constants, and can possibly be purely real, purely imaginary, or complex. Thus one has

$$\Phi_\alpha(x,y)=\sum_{\bar{n}} C_{\alpha,\bar{n}}e^{p_{\alpha,\bar{n}}x/a}e^{q_{\alpha,\bar{n}}y/b}, \tag{18}$$

$$\Psi_\beta(x,y)=\sum_{\bar{m}} D_{\beta,\bar{m}}e^{r_{\beta,\bar{m}}x/a}e^{s_{\alpha,\bar{m}}y/b}. \tag{19}$$

Here the sums should be regarded as sums over integers $\bar{n}$ and $\bar{m}$, respectively, with finite upper limits that depend on α and β, respectively. The quantities p and q depend on α and $\bar{n}$, while the quantities r and s depend on β and $\bar{m}$. The coefficients $C_{\alpha,\bar{n}}$ and $D_{\beta,\bar{m}}$ depend on the choice one has made for the basis functions, but are independent of position within the aperture. Note, for example, that any product and any sum of products of Warburton functions can be written in the form of Eqs. (18) and (19).

B. Definition of the fundamental integral

In the evaluation of the integrals that sum to yield the quantity in Eq. (1), a substantial notational simplicity results when one changes the integration variables to $\xi = x/a$ and $\eta = y/b$, thereby facilitating the definition $kR = \mathcal{R}$ with the identification

$$\mathcal{R}^2 = (ka)^2(\xi - \xi')^2 + (kb)^2(\eta - \eta')^2. \tag{20}$$

With such substitutions, the integral in (1) takes the form

$$J_{\alpha,\beta} = (ab)^{3/2} \sum_{n,m} C_{\alpha,\bar{n}} D_{\beta,\bar{m}} I_4(p,q,r,s,ka,kb), \tag{21}$$

where

$$I_4(p,q,r,s,ka,kb) = k(ab)^{1/2} \int_{-1}^{1}\int_{-1}^{1}\int_{-1}^{1}\int_{-1}^{1} \frac{e^{i\mathcal{R}}}{\mathcal{R}} P \, d\xi' \, d\eta' \, d\xi \, d\eta, \tag{22}$$

$$P = e^{p\xi} e^{q\eta} e^{r\xi'} e^{s\eta'}. \tag{23}$$

In the latter definition, for notational brevity, the subscripts on p, q, r, s have been suppressed. The subscript 4 on I_4 serves as a reminder that the integral, as originally posed, is a fourfold integral. The coefficient in front of the integral has been selected so that I_4 is (*i*) dimensionless, (*ii*) symmetric in interchange of p, r, ka with q, s, kb, (*iii*) unchanged if p and q are replaced by r and s, respectively, and (*iv*) finite, neither zero nor infinite, in the limit $k \to 0$, with a/b held fixed. The achievement here is that the evaluation of the generic integral (1) has been reduced to the evaluation of an integral with the specific form of Eq. (22), the value of which is completely specified by six numbers.

The notation introduced above has the inconvenient property that it is not readily amenable to one's taking the limit of $k = 0$, with the constraint that a/b be held constant. However, the analysis given below leads to a natural decomposition

$$I_4(p,q,r,s,ka,kb) = J_1(ka,p,r,q,s,a/b) + J_1(kb,q,s,p,r,b/a). \tag{24}$$

Neither of the two terms on the right individually exhibits the symmetry property "(*ii*)" above, but the sum does have this property by virtue of the way the argument lists are written. [Identification of the function J_1 (which is a single, rather than a fourfold, integral) appears further below in Eq. (37) and in Eq. (42).]

C. Tutorial derivation of the analytical reduction

The initial step for evaluation of the integral I_4 is the transformation

$$\int_{-1}^{1}\int_{-1}^{1} Q(\xi,\xi') \, d\xi' \, d\xi = \int_0^2 F(u) \, du, \tag{25}$$

where

$$F(u) = \int_{-1+u}^{1} Q(\xi,\xi-u) \, d\xi + \int_{-1}^{1-u} Q(\xi,\xi+u) \, d\xi. \tag{26}$$

[This is derived by first breaking the ξ' integration into integrals from -1 to ξ and from ξ to 1. In the first such integral, one sets $\xi' = \xi - u$; in the second, one sets $\xi' = \xi + u$. In each case the integration variable becomes u, with the integration limits becoming 0 and $1+\xi$ for the first integral, and becoming 0 and $1-\xi$ for the second integral. In each of the resulting double integrals over ξ and u, the order of integration is changed so that the ξ integration is done first, the u integration is done second. In the first double integral, the integration is over a triangle with vertices $(u=0,\ \xi=1)$, $(u=2,\ \xi=-1)$, and $(u=0,\ \xi=1)$, so the limits after the change of integration order become $-1+u$ and 1 for the ξ integration and 0 and 2 for the u integration. A similar interchange for the second double integral results in new integration limits of -1 and $1-u$ for the ξ integration and of 0 and 2 for the u integration.]

With an analogous transformation for the η and η' integrations, the integral I_4 becomes

$$I_4 = k(ab)^{1/2} \int_0^2 \int_0^2 \frac{e^{i\mathcal{R}}}{\mathcal{R}} A(u,p,r) A(v,q,s) \, du \, dv, \tag{27}$$

$$A(u,p,r) = B(u,p,r) + B(u,-p,-r) \tag{28}$$

$$B(u,p,r) = e^{-ru} \int_{-1+u}^{1} e^{[p+r]\xi} \, d\xi = \frac{1}{(p+r)} (e^{(p+r)} e^{-ru} - e^{-(p+r)} e^{pu}), \tag{29}$$

where now

$$\mathcal{R}^2 = (ka)^2 u^2 + (kb)^2 v^2. \tag{30}$$

[The result for the special case $p = -r$ follows directly (as discussed below) by setting $r = -p + \epsilon$ and then taking the limit as $\epsilon \to 0$, so it need not be considered separately. For typical choices of basis functions, this special case is likely.]

With the use of the splitting in Eq. (28), the integral I_4 breaks up into four terms, so one writes

$$\begin{aligned} I_4(p,q,r,s,ka,kb) &= \sum_{+,-} K_2(\pm(p,r),\pm(q,s),ka,kb) \\ &= K_2(p,r,q,s,ka,kb) + K_2(-p,-r,q,s,ka,kb) \\ &\quad + K_2(p,r,-q,-s,ka,kb) \\ &\quad + K_2(-p,-r,-q,-s,ka,kb), \end{aligned} \tag{31}$$

where

$$K_2(p,r,q,s,ka,kb) = k(ab)^{1/2} \int_0^2 \int_0^2 \frac{e^{i\mathcal{R}}}{\mathcal{R}} B(u,p,r) B(v,q,s) \, du \, dv. \tag{32}$$

Here the subscript 2 serves to remind one that the integral is a twofold integral. Note that the order of the exponent coefficients in the argument list of K_2 is different from that in the argument list of I_4. The reason is that the ensuing analysis tends to pair p with r and q with s. The summation convention implied by the notation in the first expression on the

right side of Eq. (31) is defined by the second expression. One sums over all four possible sign combinations, but with p and r having their signs changed simultaneously, and with q and s having their signs changed simultaneously.

To reduce the double integral in Eq. (32) to a sum of single integrals, it is sufficient to transform the integration to polar coordinates. Some simplification results if one divides the square in the (u, v)-plane into two right triangles, each having a common hypotenuse along the line proceeding at an angle of 45° from the origin to the point (2,2). In the lower triangle, one sets

$$u=\frac{1}{ka}\mathcal{R}\cos\phi; \quad v=\frac{1}{kb}\mathcal{R}\sin\phi, \tag{33}$$

so that the domain of integration is

$$0<\mathcal{R}<2ka/\cos\phi; \quad 0<\phi<\tan^{-1}(b/a). \tag{34}$$

Analogous relations hold for the upper triangle, only with a and b interchanged. In both cases the differential of integration transforms to

$$dudv\rightarrow\frac{1}{k^2ab}\mathcal{R}d\mathcal{R}d\phi. \tag{35}$$

One also recognizes that the two integrals have identical form, providing one interchanges p and r with q and s, and ka with kb. Thus one can set

$$K_2(p,r,q,s,ka,kb)=L_1(ka,p,r,q,s,a/b) + L_1(kb,q,s,p,r,b/a). \tag{36}$$

Here arguments ka and a/b, or kb and b/a, are used because they appear more naturally in the derived expressions for the L_1 and because the L_1 are not symmetric in the interchange of p, r, ka with q, s, kb. Use of such arguments also makes it easy to take a meaningful limit as $k\rightarrow 0$. This allows identification of the function J_1 that appears in Eq. (24), the identification being

$$J_1(ka,p,r,q,s,a/b)=\sum_{+,-}L_1(ka,\pm(p,r),\pm(q,s),a/b), \tag{37}$$

where the convention for doing the sum is the same as in Eq. (31).

Performance of the $\mathcal{R}$-integration involved in the evaluation of the L_1 function yields

$$L_1(ka,p,r,q,s,a/b)=2(a/b)^{1/2}\int_0^{\tan^{-1}(b/a)}\Lambda\sec\phi\,d\phi. \tag{38}$$

Here the factor Λ is recognized (but see comments further below) as

$$\Lambda(ka,p,r,q,s,a/b,\phi) = \frac{1}{(p+r)(q+s)}[e^{(p+r)}e^{(q+s)}F(ka,-r,-(a/b)s,\phi) - e^{(p+r)}e^{-(q+s)}F(ka,-r,(a/b)q,\phi) - e^{-(p+r)}e^{(q+s)}F(ka,p,-(a/b)s,\phi) + e^{-(p+r)}e^{-(q+s)}F(ka,p,(a/b)q,\phi)] \tag{39}$$

with

$$F(ka,p,(a/b)q,\phi)=\frac{e^{2D}-1}{2D}, \tag{40}$$

$$D(ka,p,(a/b)q,\phi)=ika\sec\phi+p+(a/b)q\tan\phi. \tag{41}$$

There is no convenient notational mnemonic for representing the sum of the four terms in Eq. (39), although a pattern is evident: the second term differs from the first in that $q\rightarrow -s$ and $s\rightarrow -q$; the third term differs from the first in that $r\rightarrow -p$ and $p\rightarrow -r$; and the fourth term differs from the first in that all of these sign changes and interchanges simultaneously take place.

Note that, with the result (38), the expression for the contributory term J_1 in Eq. (24) becomes

$$J_1(ka,p,r,q,s,a/b) = 2(a/b)^{1/2}\int_0^{\tan^{-1}(b/a)}\left(\sum\Lambda\right)\sec\phi\,d\phi, \tag{42}$$

where all the similar terms with the same integration limits have been expressed as a single integral over the sum of the integrands; in this particular instance, the integrand factor is

$$\left(\sum\Lambda\right)=\sum_{+,-}\Lambda(ka,\pm(p,r),\pm(q,s),a/b). \tag{43}$$

Here, again, the summation convention is the same as in Eq. (31).

Equation (38) is applicable regardless of the values of the arguments. However, the explicit form (39) for the integrand $\Lambda(ka,p,r,q,s,a/b)$ applies only if both $p+r$ and $q+s$ are nonzero. Special forms of $\Lambda(ka,p,r,q,s,a/b)$ that are valid when one or both of these quantities are zero are derived in the following section.

In summary, the integral I_4 is given by Eq. (24) with the quantities J_1 given by Eq. (37), or equivalently by Eq. (42), and by the associated definitions that define the integrand. In the statement given here, it is understood that the indicated arguments are all dummy arguments. Thus, for example, the result for $L_1(kb,q,s,-p,-r,b/a)$ is obtained with suitable substitutions for arguments in the stated expression for $L_1(ka,p,r,q,s,a/b)$.

Equations (24), (42), and (43) compose the principal result of the present paper. The achievement is that the original fourfold singular integral has been reduced to a sum of two nonsingular single integrals. Moreover, providing $p+r\neq 0$ and $q+s\neq 0$, each such integral is representable in turn as a weighted sum of integrals, each of the generic form

$$W(ka,p,q,a/b)=\int_0^{\tan^{-1}(b/a)}\frac{e^{2D}-1}{2D}\sec\phi\,d\phi, \tag{44}$$

$$D=ika\sec\phi+p+(a/b)q\tan\phi, \tag{45}$$

and each depending on four (rather than six) numerical constants. This can be rewritten in a variety of alternate ways, but a reduction of the overall integral W to an analytical expression does not appear to be possible. Nevertheless, its

direct numerical computation should present no difficulties. (Note that, in spite of the factor D in the denominator, the integrand is finite over the range of integration, regardless of the values of the four parameters. Three other generic integrals are needed to cover the special cases mentioned above—these are defined further below.)

D. Limiting cases

The above results strictly apply only if $p \neq -r$ and $q \neq -s$, but the special cases when one or both of the conditions $p=-r$ or $q=-s$ apply can be handled by taking limits. Thus, should the second and third arguments in the expression (39) for Λ be equal and opposite, one sets $r=-p+\epsilon$ and then takes the limit as $\epsilon \to 0$. Doing so yields

$$\begin{aligned}\Lambda(ka,p,-p,q,s,a/b,\phi) &= \frac{1}{(q+s)}\Bigg[2e^{(q+s)}F(ka,p,-(a/b)s,\phi) \\ &\quad + e^{(q+s)}\left\{\frac{\partial}{\partial r}F(ka,-r,-(a/b)s,\phi)\right\}_{r=-p} \\ &\quad - 2e^{-(q+s)}F(ka,p,(a/b)q,\phi) \\ &\quad - e^{-(q+s)}\left\{\frac{\partial}{\partial r}F(ka,-r,(a/b)q,\phi)\right\}_{r=-p}\Bigg], \end{aligned} \tag{46}$$

where it is presumed that the other pair of exponential coefficients is *not* equal and opposite. An analogous result, but one involving differentiation with respect to s, emerges should the fourth and fifth arguments be equal and opposite. If both pairs are equal and opposite, one takes an additional limit and a second derivative emerges in the result.

In all instances, the indicated first and second differentiations yield as factors the generic functions

$$\begin{aligned} G(ka,p,(a/b)q,\phi) &= \frac{\partial}{\partial D}\left\{\frac{e^{2D}-1}{2D}\right\} \\ &= \frac{1}{2D^2}(2De^{2D}-e^{2D}+1), \end{aligned} \tag{47}$$

$$\begin{aligned} H(ka,p,(a/b)q,\phi) &= \frac{\partial^2}{\partial D^2}\left\{\frac{e^{2D}-1}{2D}\right\} \\ &= \frac{1}{D^3}(2D^2e^{2D}-2De^{2D}+e^{2D}-1), \end{aligned} \tag{48}$$

where the function $D(ka,p,(a/b)q,\phi)$ is the same as is defined in Eq. (44). With this notation, Eq. (46) and its counterparts that result for other limiting cases are rewritten as

$$\begin{aligned}\Lambda(ka,p,-p,q,s,a/b,\phi) &= \frac{1}{(q+s)}[2e^{(q+s)}F(ka,p,-(a/b)s,\phi) \\ &\quad - e^{(q+s)}G(ka,p,-(a/b)s,\phi) \\ &\quad - 2e^{-(q+s)}F(ka,p,(a/b)q,\phi) \\ &\quad + e^{-(q+s)}G(ka,p,(a/b)q,\phi)], \end{aligned} \tag{49}$$

$$\begin{aligned}\Lambda(ka,p,r,q,-q,a/b,\phi) &= \frac{1}{(p+r)}[2e^{(p+r)}F(ka,-r,(a/b)q,\phi) \\ &\quad - (a/b)(\tan\phi)e^{(p+r)}G(ka,-r,(a/b)q,\phi) \\ &\quad - 2e^{-(p+r)}F(ka,p,(a/b)q,\phi) \\ &\quad + (a/b)(\tan\phi)e^{-(p+r)}G(ka,p,(a/b)q,\phi)], \end{aligned} \tag{50}$$

$$\begin{aligned}\Lambda(ka,p,-p,q,-q,(a/b)q,\phi) &= 4F(ka,p,(a/b)q,\phi)-2G(ka,p,(a/b)q,\phi) \\ &\quad - 2(a/b)(\tan\phi)[2G(ka,p,(a/b)q,\phi) \\ &\quad - H(ka,p,(a/b)q,\phi)]. \end{aligned} \tag{51}$$

With these latter three equations, one has the mathematical apparatus for the full use of Eqs. (42) and (43), regardless of the specific values for the exponent factors p, q, r, and s. One may note that the totality of such contingencies is expressible in terms of four generic four-parameter integrals. One of these is the $W(ka,p,q,a/b)$ that appears in Eq. (44). The other three are

$$X(ka,p,q,a/b) = \int_0^{\tan^{-1}(b/a)} [2F-G]\sec\phi\, d\phi \tag{52}$$

$$Y(ka,p,q,a/b) = \int_0^{\tan^{-1}(b/a)} G\tan\phi\sec\phi\, d\phi, \tag{53}$$

$$Z(ka,p,q,a/b) = \int_0^{\tan^{-1}(b/a)} [2G-H]\tan\phi\sec\phi\, d\phi. \tag{54}$$

Here, for brevity, the argument lists of the integrand factors $2F-G$, G, and H have been suppressed. In all cases, the list is the same as appears in the definition of the quantities F and D in Eqs. (40) and (41), as well as in Eqs. (47) and (48). As is emphasized above, the arguments in the list of these defined functions should be regarded as dummy arguments.

IV. REDUCTION TO SIMPLER CASE OF RADIATION FROM A RIGID RECTANGULAR PISTON

A. Expression for the mechanical impedance

The principal intent here is to establish credibility, for readers not having the motivation to trace through in detail the totality of the mathematical steps above, that the derived results are indeed correct. To this purpose the case is examined of the total radiation force (area integral of pressure) on a rigid piston vibrating in a rigid baffle. This is perhaps the simplest instance in which Eq. (1) is encountered, and it has been often discussed in the literature. The interest here is specifically with results reported by Swenson and Johnson,[20] Chetaev,[21] Stenzel,[22] Nomura and Aida,[23] Burnett and Soroka,[24,25] Stepanishen,[26] and Levine.[27]

The ratio of force to velocity is ordinarily termed a *mechanical impedance*, $Z_{\mathrm{mech,rad}}$. In terms of the quantities de-

rived in the previous section, and with the associated results incorporated, this mechanical impedance can be expressed so that

$$i\pi\frac{Z_{\text{mech,rad}}}{\rho cA}=\frac{k}{2A}\int\int\int\int\frac{e^{ikR}}{R}dx'\,dy'\,dx\,dy$$
$$=ka[2X(ka,0,0,a/b)-(a/b)Z(ka,0,0,a/b)]$$
$$+kb[2X(kb,0,0,b/a)-(b/a)Z(kb,0,0,b/a)]. \tag{55}$$

Here the integrals $X(ka,0,0,a/b)$ and $Z(ka,0,0,a/b)$ are as defined above by Eqs. (40), (41), (47), (48), (52), and (54). In this limiting case, however, when the second and third arguments are zero, the quantity D is simply $ika\sec\phi$. For notational convenience, these integrals are here reexpressed as

$$X(ka,0,0,a/b)=\int_0^{\tan^{-1}(b/a)}T_1(ika\sec\phi)\sec\phi\,d\phi \tag{56}$$

$$Z(ka,0,0,a/b)=\int_0^{\tan^{-1}(b/a)}T_2(ika\sec\phi)\tan\phi\sec\phi\,d\phi \tag{57}$$

with the identifications

$$T_1(D)=\frac{1}{2D^2}[e^{2D}-2D-1], \tag{58}$$

$$T_2(D)=\frac{1}{D^3}[De^{2D}-e^{2D}+D+1]. \tag{59}$$

In what follows, these expressions are used to show that the results of the present article are consistent with what has been given previously in the literature.

B. Swenson and Johnson's formula

A letter to the editor by Swenson and Johnson,[20] published in 1952, gives a highly abbreviated derivation (with only a brief suggestion of the methodology) of results for square and rectangular pistons and quotes (without any derivation) a result, here denoted as $I_{\overline{a},\overline{b}}$, for the quadruple integral that appears here in Eq. (55). (The quantities $\overline{a}$ and $\overline{b}$ are equal to the present paper's $2a$ and $2b$.)

Since the Swenson and Johnson formula is in the form of an expansion in powers of k, the comparison begins first with the development of power series for the T_1 and T_2 that appear in Eqs. (56) and (57), these being identified as

$$T_1(ika\sec\phi)=-i\sum_{n=1}^{\infty}\frac{(2i)^n}{(n+1)!}(ka)^{n-1}\sec^{n-1}\phi, \tag{60}$$

$$T_2(ika\sec\phi)=-2i\sum_{n=1}^{\infty}\frac{(2i)^n n}{(n+2)!}(ka)^{n-1}\sec^{n-1}\phi. \tag{61}$$

Insertion of these into Eqs. (56) and (57), followed by term-by-term integration, yields, after some additional mathematical steps,

$$I_{\overline{a},\overline{b}}=4(4ab)^{3/2}\sum_{m=0}^{\infty}(-1)^m(4k^2ab)^m$$
$$\times\left[\frac{A_m}{(2m+2)!}+ik(4ab)^{1/2}\frac{B_m}{(2m+3)!}\right], \tag{62}$$

where

$$A_m=(a/b)^{m+(1/2)}\int_0^{\tan^{-1}(b/a)}\sec^{2m+1}\phi\,d\phi$$
$$+(b/a)^{m+(1/2)}\int_0^{\tan^{-1}(a/b)}\sec^{2m+1}\phi\,d\phi$$
$$-\frac{1}{2m+3}[([a/b]+[b/a])^{m+(3/2)}-(a/b)^{m+(3/2)}$$
$$-(b/a)^{m+(3/2)}], \tag{63}$$

$$B_m=(a/b)^{m+1}\int_0^{\tan^{-1}(b/a)}\sec^{2m+2}\phi\,d\phi$$
$$+(b/a)^{m+1}\int_0^{\tan^{-1}(a/b)}\sec^{2m+2}\phi\,d\phi$$
$$-\frac{1}{2m+4}[([a/b]+[b/a])^{m+2}$$
$$-(a/b)^{m+2}-(b/a)^{m+2}]. \tag{64}$$

Apart from some minor cosmetic changes so as to make fuller use of dimensionless quantities, and the use of i instead of $-j$, the expressions above are the same as those given by Swenson and Johnson in their Eqs. (8)–(10). The precise correspondence is

$$\overline{A}_{2m}=(-1)^m(4ab)^{m+(3/2)}A_m, \tag{65}$$

$$\overline{B}_{2m}=(-1)^m(4ab)^{m+2}B_m, \tag{66}$$

in accord with Swenson and Johnson's result

$$I_{\overline{a},\overline{b}}=4\sum_{m=0}^{\infty}\frac{\overline{A}_{2m}k^{2m}}{(2m+2)!}+i4k\sum_{m=0}^{\infty}\frac{\overline{B}_{2m}k^{2m}}{(2m+3)!} \tag{67}$$

and with $\overline{a}=2a$, $\overline{b}=2b$. The overbars distinguish symbols used in their paper from those used in the present paper.

Swenson and Johnson's formulas were rewritten and used in numerical calculations in a 1971 paper by Sauter and Soroka.[28] As pointed out by Sauter and Soroka, all of the integrals over the powers of the secant can be evaluated in "closed" form. The values of the first four such integrals are relatively simple:

$$\int_0^{\tan^{-1}(b/a)}\sec\phi\,d\phi=\ln[(1+[b/a]^2)^{1/2}+b/a], \tag{68}$$

$$\int_0^{\tan^{-1}(b/a)}\sec^2\phi\,d\phi=b/a, \tag{69}$$

$$\int_0^{\tan^{-1}(b/a)} \sec^3\phi\, d\phi = \frac{b}{2a}[(1+[b/a]^2)^{1/2}+b/a] + \tfrac{1}{2}\ln[(1+[b/a]^2)^{1/2}+b/a], \tag{70}$$

$$\int_0^{\tan^{-1}(b/a)} \sec^4\phi\, d\phi = (b/a)+\tfrac{1}{3}(b/a)^3. \tag{71}$$

Expressions for integrals over higher-order powers of the secant can be derived by consistent use of the mathematical identities

$$(n-1)\sec^n\phi-(n-2)\sec^{n-2}\phi = \frac{d}{d\phi}(\tan\phi\sec^{n-2}\phi), \tag{72}$$

$$\frac{d}{d\phi}\tan\phi=\sec^2\phi; \quad \frac{d}{d\phi}\ln(\sec\phi+\tan\phi)=\sec\phi. \tag{73}$$

C. Entrained mass and low-frequency limit

Examination of the first two terms in the expansion in powers of the wave number k yields additional substantiation that the two derivations, that of the present paper and that of Swenson and Johnson,[20] in addition to agreeing with each other, are correct. One finds, in particular, that

$$A_0=(a/b)^{1/2}\ln[(1+[b/a]^2)^{1/2}+b/a]+(b/a)^{1/2} \times\ln[(1+[a/b]^2)^{1/2}+a/b]-\tfrac{1}{3}[([a/b]+[b/a])^{3/2} -(a/b)^{3/2}-(b/a)^{3/2}], \tag{74}$$

$$B_0=\tfrac{3}{2}, \tag{75}$$

so that in the limit of low frequencies, Eqs. (55) and (62) yield

$$Z_{\text{mech,rad}}\approx -i\omega M_{\text{ent}}+\frac{1}{2\pi}\rho cA^2k^2, \tag{76}$$

where

$$M_{\text{ent}}=\frac{A_o}{\pi}\rho A^{3/2} \tag{77}$$

is identified as the *entrained mass* (the apparent mass whose inertia produces the reactive part of the mechanical impedance).

The second term in Eq. (76) is the low-frequency radiation resistance and this is manifestly correct because, if one begins with Eq. (55) and expands the integrand factor $R^{-1}e^{ikR}$ in a power series, the corresponding term in the power series expansion of the double area integral is kA^2, where A is the area of the rectangle. What is reassuring is that the same result emerges also after a rather intricate limiting process from the more general result derived in the present paper.

In regard to the entrained mass, one notes that, for a square aperture, where $a/b=b/a=1$,

$$A_o=2\ln(1+\sqrt{2})-\tfrac{2}{3}[\sqrt{2}-1]=1.4866. \tag{78}$$

This yields an entrained mass for the square piston which may be compared with that for the circular piston,

$$M_{\text{ent}}=0.473\rho A^{3/2} \quad \text{(square)}, \tag{79}$$

$$M_{\text{ent}}=0.479\rho A^{3/2} \quad \text{(circular)}, \tag{80}$$

where the numerical coefficient in the former is the numerical value of A_o/π and the latter coefficient is the numerical value of $8/(3\pi^{3/2})$. The close agreement of the two numerical coefficients is striking and in accord with Rayleigh's prediction[29,30] that the entrained mass for an elliptical aperture (orifice) is very nearly the same as that of a circular aperture with the same area. From the standpoint of the present paper, the agreement is a striking confirmation that the analytical steps described here are correct.

D. Integral expressions of Chetaev and Levine

Chetaev[21] was the first to reduce the multiple integral describing the mechanical radiation impedance of a rigid piston to a sum of single integrals, although his integrals had higher transcendental functions, $Si(z)$ and $Ci(z)$, within the integrands. In subsequent years, various authors succeeded in finding clearer derivations and in reexpressing his result so that the integrands did not involve higher transcendental functions and so that the integrals would be more amenable to numerical evaluation. The version selected here for comparison with the present paper's result is that which appears as Eq. (13) of a 1983 paper by Levine.[27]

To derive Levine's equation from the present article's Eqs. (55)–(59), change the integration variable from ϕ to ζ, where, for the integrals, $X(ka,0,0,a/b)$ and $Z(ka,0,0,a/b)$, that appear in Eqs. (56) and (57), one sets $\sec\phi=\zeta$, so that

$$X(ka,0,0,a/b) = -\frac{1}{2(ka)^2}\int_1^{(1+[b/a]^2)^{1/2}} e^{2ika\zeta}\frac{d\zeta}{\zeta^2(\zeta^2-1)^{1/2}} + \frac{i}{ka}\int_1^{(1+[b/a]^2)^{1/2}}\frac{d\zeta}{\zeta(\zeta^2-1)^{1/2}} + \frac{1}{2(ka)^2}\int_1^{(1+[b/a]^2)^{1/2}}\frac{d\zeta}{\zeta^2(\zeta^2-1)^{1/2}}, \tag{81}$$

$$Z(ka,0,0,a/b) = \frac{i}{(ka)^3}\int_1^{(1+[b/a]^2)^{1/2}}\frac{d\zeta}{\zeta^3} - \frac{1}{(ka)^2}\int_1^{(1+[b/a]^2)^{1/2}}\frac{d\zeta}{\zeta^2} - \frac{i}{(ka)^3}\int_1^{(1+[b/a]^2)^{1/2}} e^{2ika\zeta}\frac{d\zeta}{\zeta^3} - \frac{1}{(ka)^2}\int_1^{(1+[b/a]^2)^{1/2}} e^{2ika\zeta}\frac{d\zeta}{\zeta^2}. \tag{82}$$

With the exception of the first term in Eq. (81), all of the integrals that appear in Eqs. (81) and (82) can either be directly performed or else combined, via integrations by parts, into expressions that are integrable. Thus, one derives

$$kaX(ka,0,0,a/b)+kbX(kb,0,0,b/a)$$
$$=i\pi/2+\frac{1}{2kab}[a^2+b^2]^{1/2}$$
$$-\frac{1}{2ka}\int_1^{(1+[b/a]^2)^{1/2}}\frac{e^{2ika\zeta}}{\zeta^2(\zeta^2-1)^{1/2}}d\zeta$$
$$-\frac{1}{2kb}\int_1^{(1+[a/b]^2)^{1/2}}\frac{e^{2ikb\zeta}}{\zeta^2(\zeta^2-1)^{1/2}}d\zeta, \tag{83}$$

$$(ka^2/b)Z(ka,0,0,a/b)+(kb^2/a)Z(kb,0,0,b/a)$$
$$=\frac{i}{2k^2ab}[e^{2ik[a^2+b^2]^{1/2}}-e^{2ika}-e^{2ikb}+1]$$
$$+\frac{1}{kba}[(a^2+b^2)^{1/2}-a-b]. \tag{84}$$

With the results in Eqs. (83) and (84), the expression in Eq. (55) consequentially yields

$$\frac{Z_{\text{mech,rad}}}{\rho cA}=1-\frac{i}{\pi abk}(a+b)-\frac{1}{2\pi abk^2}$$
$$+\frac{1}{2\pi abk^2}(e^{2ika}+e^{2ikb}-e^{2ik(a^2+b^2)^{1/2}})$$
$$+\frac{i}{\pi ka}\int_1^{(1+[b/a]^2)^{1/2}}\frac{e^{2ika\zeta}}{\zeta^2(\zeta^2-1)^{1/2}}d\zeta$$
$$+\frac{i}{\pi kb}\int_1^{(1+[a/b]^2)^{1/2}}\frac{e^{2ikb\zeta}}{\zeta^2(\zeta^2-1)^{1/2}}d\zeta, \tag{85}$$

which is identical to the result in Eq. (13) of the cited paper by Levine. His a and b are equal to the present paper's $2a$ and $2b$. [The presence of the factor $(\zeta^2-1)^{-1/2}$ in the integrands in the two integrals may seemingly belie the assertion that the present paper achieves a reduction to nonsingular integrals. However, the singularity above is illusory as it can be removed by rewriting this singular factor as $\zeta^{-1}(d/d\zeta)\times(\zeta^2-1)^{1/2}$ and then integrating by parts.]

V. DIFFRACTION BY A SQUARE APERTURE

A more stringent test of the algorithm described in the previous sections is provided by the example of the diffraction of sound by a square aperture (Fig. 4) in a rigid screen. This problem has been recently considered by Hongo and Serizawa[31] with the use of a relatively complicated procedure that is difficult to comprehend from the written paper. They do, however, present numerical results with which other results can be compared. The special case considered here is when the aperture is square and when the incident wave is at normal incidence. The restriction to normal incidence allows one to use only those basis functions that have the same symmetry as that of a square. Thus one can choose, for the basis functions that appear in Eq. (4), the following,

$$\Phi_\alpha(x,y)=\Psi_\alpha(x,y)$$
$$=\tfrac{1}{2}[\cos(n\pi x/a)\cos(m\pi y/a)$$
$$+\cos(n\pi y/a)\cos(m\pi x/a)], \tag{86}$$

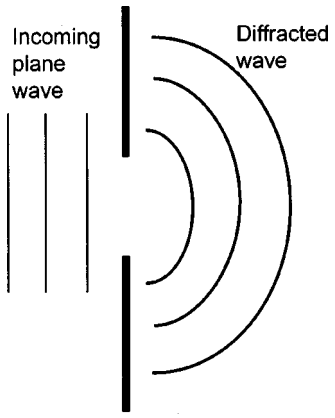

FIG. 4. Example of diffraction by a square aperture in a rigid screen. A plane wave at normal incidence impinges on a square orifice, and a diffracted wave emanates from the orifice on the other side of the screen.

where the integers $n(\alpha)$ and $m(\alpha)$ are to be regarded as functions of the integer α. An appropriate relationship that includes all possible basis functions of this type once and only once follows the pattern $n(1)=0$, $m(1)=0$; $n(2)=1$, $m(2)=0$; $n(3)=2$, $m(3)=0$; $n(4)=1$, $m(4)=1$; $n(5)=3$, $m(5)=0$; $n(6)=2$, $m(6)=1$; $n(7)=4$, $m(7)=0$; and $n(8)=3$, $m(8)=1$. The pattern of association is similar to the proof that one finds in some mathematics texts, as exemplified by the book by Courant and Robbins,[32] that the set of all pairs of integers is countable, or equivalently that the set of all rational numbers is countable, the original proof being due to Georg Cantor. Because the basis functions are symmetric in interchange of n and m, one can limit the set to just those when $n(\alpha)\geqslant m(\alpha)$, and progressively go down successive diagonals of a square of rows and columns, successive rows labeled by the values starting from 0 of the integer m, and successive columns labeled by the values starting from 0 of the integer n, so that $\alpha(0,0)=1$, $\alpha(1,0)=2$, $\alpha(2,0)=3$, $\alpha(1,1)=4$, $\alpha(3,0)=5$, etc., describes the inverse mapping from the pair (n,m) to $\alpha(n,m)$.

For the exponential expansions represented by either Eq. (18) or Eq. (19), the relevant constants, given the basis functions of Eq. (86), are identified such that $C_{\alpha,\bar{n}}=\frac{1}{8}$ for all $\bar{n}$, there being eight terms in the sum. The various pairs $(p_{\alpha,\bar{n}},q_{\alpha,\bar{n}})$ are the set (four in all) of the possible sign combinations of $(\pm in\pi/a,\pm im\pi/a)$ and the set (also four in all) of the possible sign combinations of $(\pm im\pi/a,\pm in\pi/a)$.

A convenient single number descriptor for the diffraction of the sound by the square aperture is the fraction of the incident power that is transmitted through the aperture. (Hongo and Serizawa refer to this quantity as the *transmission coefficient*.) If P_{inc} is the amplitude of the incident sound wave, then the incident time-averaged power is

$$[\text{Power}]_{\text{inc}}=\frac{1}{2}\frac{|P_{\text{inc}}|^2}{\rho c}A. \tag{87}$$

For the plane screen diffraction problem, the pressure associated with the diffracted wave at the aperture is

$$p_{\text{diffr}}(\mathbf{x}_S)=-\mathcal{M}(\mathbf{x}_S,\{v_{n,\text{int}}(\mathbf{x}_S)\}) \tag{88}$$

in accord with Rayleigh's result for the radiation from a vibrating portion of a plane and in accord with the definition that appears in Eq. (3). The minus sign on the right-hand side here is in accord with the previous definition of v_n as the component that points back toward the source. Since, along the interface, the continuity of pressure requires $p_{\text{diffr}}=p_{\text{int}}$, one concludes from Eqs. (2) and (88) that

$$p_{\text{diffr}}(\mathbf{x}_S)=p_{\text{inc}}(\mathbf{x}_S), \tag{89}$$

so the transmitted power is

$$[\text{Power}]_{\text{trans}}=-\frac{1}{2}\text{Re}\int\int v_{n,\text{int}}(x,y)p^*_{\text{inc}}\,dx\,dy$$

$$=-\frac{1}{2}\sum_{\beta}\ \text{Re}\left\{v_\beta\int\int p^*_{\text{inc}}\Psi_\beta\,dx\,dy\right\}, \tag{90}$$

where the quantities v_β are the solutions of the infinite set of equations

$$\sum_{\alpha'}(N^{-1})_{\alpha,\alpha'}\int\int p_{\text{inc}}\Phi_{\alpha'}\,dx\,dy=-\sum_{\beta}Z_{\alpha,\beta}v_\beta. \tag{91}$$

The selected basis functions are orthogonal and the incident pressure is uniform over the aperture, so the above relations reduce to

$$[\text{Power}]_{\text{trans}}=-\tfrac{1}{2}\text{Re}\{v_1P^*_{\text{inc}}A\}, \tag{92}$$

$$P_{\text{inc}}\delta_{\alpha,1}=-\sum_{\beta}Z_{\alpha,\beta}v_\beta. \tag{93}$$

The above relations, given the definition of the radiation admittance matrix in Eq. (10), reduce in turn to

$$[\text{Power}]_{\text{trans}}=\tfrac{1}{2}|P_{\text{inc}}|^2\text{Re}\{Y_{1,1}\}A, \tag{94}$$

where $Y_{1,1}$ is the corner element of the radiation admittance matrix. Thus, the fraction of the incident power that is transmitted is

$$\frac{[\text{Power}]_{\text{trans}}}{[\text{Power}]_{\text{inc}}}=\text{Re}\{Y_{1,1}\}\rho c. \tag{95}$$

The calculation of any element of the admittance matrix requires in principle that one invert a matrix (i.e., the radiation impedance matrix) with an infinite number of rows and columns. In practice, the computation of $Y_{1,1}$ is achieved by first defining $[Z_N]$ as the truncated impedance matrix, keeping only the square matrix formed from the first N rows and N columns. One defines $[Z_N]^{-1}$ as the inverse of this matrix. Then the appropriate identification of $Y_{1,1}$ is

$$Y_{1,1}=\lim_{N\to\infty}(\{[Z_N]^{-1}\}_{1,1}). \tag{96}$$

While one never takes such a limit with a computer, it can be inferred by simply plotting estimates resulting from successive values of N versus $1/N$ and extrapolating the plot to $1/N=0$.

Figure 5 shows plots of the fraction of the incident power that is transmitted through the aperture versus the dimensionless frequency parameter *ka*. One plot has been transcribed from the $q=1$ curve, q being b/a, of Fig. 6(a) (normal incidence) of the paper by Hongo and Serizawa;[31] the others result from the methodology of the current paper, as described above. The curves for $N=10$ and $N=66$ result from taking the approximate $Y_{1,1}$ as the (1, 1) element of the computed $[Z_N]^{-1}$ for the corresponding value of N. The fourth curve results from the extrapolation described by Eq. (96). The discrepancies are magnified somewhat by the choice of the vertical scale to a range fom 0.8 to 1.05. The most relevant observation from the standpoint of the present paper is that the curve based on the extrapolation agrees to within 0.5% with the curve taken from Hongo and Serizawa. At the time of this writing, it is not known which of the two curves is the more nearly correct, and there is no known third computation to adjudicate the discrepancy. What is here most important, however, is that the numerical results based on the paper's methodology depend on not just a single calculation of the integral in Eq. (1), but on each of N^2 elements, where N is up to 66, corresponding to $N^2=4056$. The fact that calculation of a continuous curve, each point depending on the calculation of so many fourfold integrals, is feasible testifies to the numerical speed-up achieved by the reduction of such integrals to a sum of integrations over a single variable. The good (even although not perfect) agreement with Hongo and Serizawa's results suggests furthermore that the mathematical analysis presented in earlier sections is indeed correct.

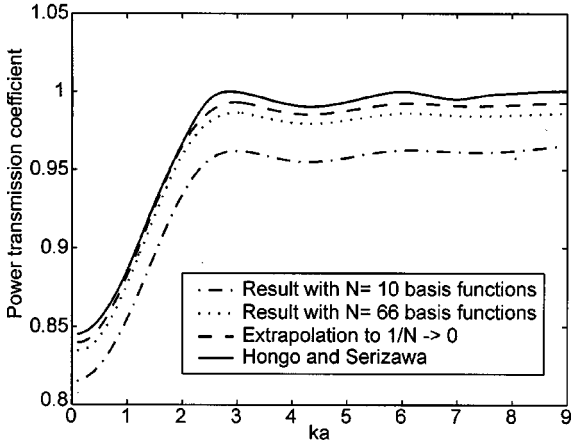

FIG. 5. Results of various approximate calculations for the power transmission coefficient versus frequency parameter *ka*. The case considered is that of a plane wave impinging at normal incidence on a square hole (dimensions $2a$ by $2a$) in a rigid screen. The solid curve is taken from a figure in a recent paper by Hongo and Serizawa (Ref. 31). The curves for $N=10$ and $N=66$ are based on estimates of the (1,1)-element of the radiation admittance matrix from the inverse of the truncated impedance matrix with N-rows and N-columns. The other curve results in the numerical extrapolation from finite N-approximations to when $1/N\to 0$. The power transmission coefficient is the fraction of the incident power on the hole that is transmitted to the diffracted wave on the other side of the screen.

[The seemingly slow convergence displayed by Fig. 5 of the curves for various N to the limiting case of $N\to\infty$ is a consequence of the somewhat simplistic choice of the basis functions Ψ_β represented by Eq. (86). It is known, from an analysis of the solution of Laplace's equation near a knife edge, that the normal velocity within the aperture must be singular at the edges, and that the singularity is an inverse square root singularity, so that, for example, $v_{\text{int},n}\sim 1/(a$

$-x)^{1/2}$ near $x=a$. The sum implied by the second of Eqs. (4) is accordingly not uniformly convergent, and rapid convergence of the computation represented by Eq. (96) is unlikely. An effort to speed-up this convergence by seeking a better set of basis functions that still conform to the constraint that each be expressible as a sum of products of exponentials, as in Eq. (19), was regarded as inappropriate for the present article. Other examples can be contemplated that illustrate the use of impedance matrix elements (with other choices of basis elements) for which either the matrix inversion is not necessary or for which more rapid convergence results, but the description of such examples will typically be longer.]

VI. CONCLUDING REMARKS

In practice, the principal results of this article, represented by the deduced equations in Sec. III, are relatively easy to program for numerical evaluation. The basic integrals, W, X, Y, Z, defined by Eqs. (44) and (52)–(54), are of the type that ordinarily presents negligible difficulties in numerical evaluation. One should be able to compute these integrals to any desired accuracy for zero to moderate values of ka. Numerical difficulties could arise for very large values of ka, $|p|$, or $|q|$, but in such cases asymptotic methods can be used. To limit the scope of the present paper, relevant asymptotic expressions are not given.

A possibly valid criticism of the overall methodology presented here is that the implied decompositions, as is exemplified, for example, by the sums in Eqs. (18) and (19), could lead to a moderately large (although certainly finite) number of terms. For specific cases, many of these terms can be analytically combined, and the number that one has to deal with could be drastically reduced. Here again, in the interest in restricting the scope of the article, examples dealing with such specific cases have been omitted. In practice, the computation of such a number of terms, even without analytical combinations, each only involving a single integration over one variable, will be quicker than evaluating a multiple integral, given a desired target of accuracy, especially if the target is not especially crude.

The applications that could make use of the formulation in Sec. II seem numerous, especially when one has in hand a convenient numerical method for calculating the individual elements of the radiation impedance matrix. We have previously studied the case of the radiation from a membrane at the mouth of a duct.[33] The listing and description of other applications that have occurred to the authors during the writing of this paper could be rather lengthy, but it is to be hoped that astute readers will perceive such applications and make use of the results of the present paper in some of their future research.

[1] J. B. Keller and D. Givoli, "Exact non-reflecting boundary conditions," J. Comput. Phys. **82**, 172–192 (1989).

[2] H. Helmholtz, "Theorie der Luftschwingungen in Röhren mit offenen Enden (Theory of air oscillations in tubes with open ends)," J. reine angew. Math. **57**, 1–72 (1859).

[3] J. W. S. Rayleigh, *Theory of Sound*, 2nd ed. (Macmillan, New York, 1894; reprinted by Dover, New York, 1945), Vol. 2, Secs. 277 and 278, pp. 104–109. (The indicated sections are the same as appeared in the first edition in 1877.)

[4] G. Kirchhoff, "Zur Theorie der Lichtstrahlen (Concerning the theory of light rays)," Ann. Phys. (Leipzig) **18**, 663–695 (1883).

[5] O. D. Kellogg, *Foundations of Potential Theory* (Springer, New York, 1929; reprinted by Dover, New York, 1954), pp. 160–172, 268–273.

[6] A.-W. Maue, "Zur Formulierung eines allgemeinen Beugungsproblems durch eine Integralgleichung (Concerning the formulation of a general diffraction problem by an integral equation)," Z. Phys. **126**, 601–618 (1949).

[7] A. D. Pierce, "Variational formulations in acoustic radiation and scattering," in *Physical Acoustics*, edited by A. D. Pierce and R. N. Thurston (Academic, New York, 1993), Vol. 12, pp. 195–371.

[8] B.-U. Koo, J.-G. Ih, and B.-C. Lee, "Acoustic shape sensitivity analysis using the boundary integral equation," J. Acoust. Soc. Am. **98**, 2851–2860 (1998).

[9] J. A. Giordano and G. H. Koopmann, "State-space boundary element-finite element coupling for fluid-structure interaction analysis," J. Acoust. Soc. Am. **98**, 363–372 (1995).

[10] J. H. Ginsberg and J. G. McDaniel, "An acoustic variational principle and component mode synthesis applied to the analysis of acoustic radiation from a concentrically stiffened plate," ASME J. Vibr. Acoust. **113**, 401–408 (1991).

[11] K. A. Cunefare and S. De Rosa, "An improved state-space method for coupled fluid-structure interaction analysis," J. Acoust. Soc. Am. **105**, 206–210 (1999).

[12] S. D. Snyder and N. Tanaka, "Calculating total acoustic power output using modal radiation efficiencies," J. Acoust. Soc. Am. **97**, 1702–1709 (1995).

[13] T. Takahagi, N. Nakai, and Y. Yamai, "Near field sound radiation from simply supported rectangular plates," J. Sound Vib. **185**, 455–471 (1995).

[14] W. L. Li, and H. J. Gibeling, "Determination of the mutual radiation resistances of a rectangular plate and their impact on the radiated acoustic power," J. Sound Vib. **229**, 1213–1233 (2000).

[15] F. G. Leppington, E. G. Broadbent, and K. H. Heron, "The acoustic radiation efficiency of rectangular panels," Proc. R. Soc. London, Ser. A **382**, 245–271 (1982).

[16] J. W. S. Rayleigh, "On the passage of waves through apertures in plane screens, and allied problems," Philos. Mag. **43**, 259–272 (1897).

[17] B. B. Baker and E. T. Copson, *The Mathematical Theory of Huygens' Principle*, 2nd ed. (Clarendon, Oxford, 1950; reprinted by Chelsea, New York, 1987), pp. 159–161.

[18] W. R. Graham, "High-frequency vibration and acoustic radiation of fluid-loaded plates," Philos. Trans. R. Soc. London, Ser. A **352**, 1–43 (1995).

[19] G. B. Warburton, "The vibration of rectangular plates," Proc. Inst. Mech. Eng. **168**, 371–384 (1954).

[20] G. W. Swenson, Jr. and W. E. Johnson, "Radiation impedance of a rigid square piston in an infinite baffle," J. Acoust. Soc. Am. **24**, 84 (1952).

[21] D. N. Chetaev, "The impedance of a rectangular piston vibrating in an opening in a flat baffle," (in Russian), Prikl. Mat. Mekh. **15**, 439–444 (1951).

[22] H. Stenzel, "Die akustische Strahlung der rechteckigen Kolbenmembrane (The acoustical radiation of a rectangular piston-membrane)," Acustica **2**, 263–281 (1952).

[23] Y. Nomura and Y. Aida, "On the radiation impedance of a rectangular plate with an infinitely large fixed baffle," Sci. Rep. Res. Inst. Tohuku Univ., Ser. B, **1**, 337–347 (1951).

[24] D. S. Burnett and W. W. Soroka, "Tables of rectangular piston radiation impedance functions, with application to sound transmission loss through deep apertures," J. Acoust. Soc. Am. **51**, 1618–1623 (1972).

[25] D. S. Burnett and W. W. Soroka, "An efficient numerical technique for evaluating large quantities of highly oscillatory integrals," J. Inst. Math. Appl. **10**, 325–332 (1972).

[26] P. R. Stepanishen, "The radiation impedance of a rectangular piston," J. Sound Vib. **55**, 275–288 (1977).

[27] H. Levine, "On the radiation impedance of a rectangular piston," J. Sound Vib. **89**, 447–455 (1983).

[28] A. Sauter, Jr., and W. W. Soroka, "Sound transmission through rectangular slots of finite depth between reverberant rooms," J. Acoust. Soc. Am. **47**, 5–11 (1970).

[29] J. W. S. Rayleigh, *Theory of Sound*, 2nd ed. (Macmillan, New York, 1894; reprinted by Dover, New York, 1945), Vol. 2, pp. 177–179. (The indicated passage is the same as appeared in the first edition in 1877.)

[30] C. L. Morfey, "Acoustic properties of openings at low frequencies," J. Sound Vib. **9**, 357–366 (1969).

[31] K. Hongo and H. Serizawa, "Diffraction of an acoustic plane wave by a

rectangular hole in an infinitely large rigid screen,'' J. Acoust. Soc. Am. **106**, 29–35 (1999).
[32] R. Courant and H. Robbins, *What is Mathematics?*, 4th ed. (Oxford U. P., Oxford, 1978), pp. 79–80.
[33] A. D. Pierce and R. O. Cleveland, ''Coupled-mode formulation of acoustic disturbances in ducts of variable cross-section with baffled ends,'' in *Proceedings of the ASME* [American Society of Mechanical Engineers, New York, 1998], NCA-Vol. 25, pp. 405–411.

Pole contribution to the field reflected by sand layers

Jean-François Allard, Michel Henry, and Julian Tizianel
Laboratoire d'Acoustique de l'Université du Maine, UMR CNRS 6613, Avenue Olivier Messiaen 72085, Le Mans Cedex 9, France

Jean Nicolas
Groupe d'Acoustique et Vibrations, Département Génie Mécanique, Université de Sherbrooke, Sherbrooke, Quebec J1K 2R1, Canada

Yasushi Miki
Takushoku University, 815-1 Tatemachi, Hachioji-shi, Tokyo 1938585, Japan

(Received 5 February 2001; revised 16 October 2001; accepted 22 October 2001)

Measurements of the reflection coefficient at oblique incidence and for inhomogeneous waves are presented for layers of sand having a large flow resistivity and different thicknesses. The dependence of the reflection coefficient on the angle of incidence is different for layers of small thickness and semi-infinite layers, due to the influence of a pole which is related to an ordinary guided wave in the first case, and the Zenneck wave in the second case. Simulations indicate that the amplitude of the Zenneck wave can be measured for small source receiver distances, allowing a simple evaluation *in situ* of the surface impedance. The same method can be used with the ordinary surface wave for thin layers. © *2002 Acoustical Society of America.* [DOI: 10.1121/1.1428283]

PACS numbers: 43.20.Fn, 43.60.−c [ANN]

I. INTRODUCTION

In a previous work,[1] for a layer of glass beads with a low flow resistivity, poles and zeros of the reflection coefficient in the sin θ plane, θ being the angle of incidence, and the related contributions to the reflected field, have been studied. A method of measuring the reflection coefficient around grazing incidence, worked out by Tamura,[2] was used, with recent models for sound propagation in air-saturated porous media. In the present study, a similar work is performed with a sand having a large flow resistivity. Layers of materials having a large flow resistivity can be replaced, at least at sufficiently low frequencies and in a limited domain of angles of incidence, by an impedance plane with a surface impedance independent on θ. Asymptotic equations obtained by Rudnick,[3] Chien and Soroka,[4] for large source–receiver distances, or equivalent formulations by Brekhovskikh and Godin[5] can be used in the context of the impedance plane approximation to calculate the amplitude of the spherical reflected field, and the contribution of the poles. They have been used in many papers devoted to long-range sound propagation over different types of grounds considered as porous media. A review of these works can be found in a work by Attenborough.[6] A simple modification of the impedance plane model has been suggested for the case of nonlocally reacting media by Li *et al.*[7] The contribution of the poles at small source–receiver distances has not been studied in these papers in spite of the previous works by Brekhovskikh[8] and Banos,[9] concerning electromagnetic waves, and also by Chien and Soroka[4] (see Sec. 5 2 1 of Ref. 4). In the present work, sound propagation is described with the model used previously for air-saturated glass beads,[10] which is briefly recalled in Sec. II. The macroscopic parameters are evaluated in a previous paper.[11] In Sec. III, comparisons are performed between measurements of the reflection coefficient close to grazing incidence and predictions where the nonlocally reacting behavior of the layer of sand is taken into account. The location of the poles of the reflection coefficient is studied in this last context. In Sec. IV, the previous results concerning the contribution of the poles at small numerical distances are recalled, and a simple expression for this contribution is given. In Sec. V, simulations are performed to test the possibility of *in situ* surface impedance evaluations from pressure measurements at grazing incidence and small source–receiver distances. It is shown that these pressure measurements correspond at small numerical distance to an evaluation of the amplitude of the contribution of the pole to the reflected field.

II. THE POROUS MEDIUM

A sand of high flow resistivity (Sand of Loire supplied by Société Baglione du Mans, carrière de Spay route d'Aulnays, 72700, Aulnays, France) has been used. Sound propagation in this material has been studied previously.[11] It has been shown that in the air-saturated sand the acoustic waves created by an aerial source propagate mainly in air, the granular frame being motionless. Contrary to the case of water-saturated sand,[12] the nonconsolidation has no consequences for sound propagation. Air in the porous medium is replaced by an equivalent fluid with an effective density ρ_1 and a bulk modulus χ_1. The model by Johnson *et al.*[13] is used to evaluate the effective density and the model by Lafarge[14] is used for the bulk modulus χ_1. The characteristic impedance Z_1 and the wave number k_1 in the air saturating the sand are given by $Z_1=(\rho_1\cdot\chi_1)^{1/2}$, and $k_1=\omega(\rho_1/\chi_1)^{1/2}$. After Brekhovskikh and Godin,[5] the symbols $m=\rho_1/\rho$ and $n=k_1/k$, where k is the wave number in air, are used. For all air-saturated porous media, $\mathrm{Im}(\rho_1)\to\infty$ when $\omega\to 0$, and ρ_1 tends to $\alpha_\infty\rho$ at high frequencies. The bulk

modulus χ_1 varies from the adiabatic value γP_o at high frequencies to the isothermal value P_o at low frequencies (P_o static atmospheric pressure, γ ratio of the specific heats). The refraction index n tends to $\sqrt{\alpha_\infty}$ when ω increases, and $|n| \to \infty$ when $\omega \to 0$. The square root of tortuosity generally lies in the interval [1, 1.5]. All porous media are locally reacting at sufficiently low frequencies and nonlocally reacting at sufficiently high frequencies (scattering is not taken into account). For porous grounds having a large flow resistivity, the domain where the media are locally reacting includes the whole audible frequency range, but for usual sound-absorbing porous media, n can be close to 1 at 1 kHz. The following set of parameters can be used,[11] porosity $\phi = 0.37$, viscous permeability $k_o = 1.42 \times 10^{-10}\,\mathrm{m}^2$ ($k_o = \eta/\sigma$, η viscosity, σ flow resistivity), thermal permeability $k_o' = 5 \times 10^{-10}\,\mathrm{m}^2$, tortuosity $\alpha_\infty = 1.7$, characteristic viscous and thermal dimension $\Lambda = 28\,\mu\mathrm{m}$, $\Lambda' = 80\,\mu\mathrm{m}$. With the time dependence $\exp(-i\omega t)$, the predicted quantities ρ_1, χ_1, k_1, m, and n at 500 Hz are $\rho_1 = 4.455 + i12.919\,\mathrm{kg/m}^3$, $\chi_1 = (102.37 - i5.1703) \times 10^3\,\mathrm{Pa}$, $k_1 = 31.936 + i24.003\,\mathrm{m}^{-1}$, and $n = 3.4786 + i2.61487$.

III. POLES OF REFLECTION COEFFICIENT-NON LOCALLY REACTING MEDIUM

The surface impedance of a layer of thickness l of sand is given by

$$Z_s = i \frac{Z_1}{\phi \cos\theta_1} \cot(k_1 l \cos\theta_1), \tag{1}$$

where θ_1 is the refraction angle, $n \sin\theta_1 = \sin\theta$. More precisely, the z axis, perpendicular to the porous layer, is directed opposite to the layer, in what follows, $k\cos\theta$ and $-k_1\cos\theta_1$ are the z wave number components of the reflected and the refracted wave, respectively. The reflection coefficient V is given by

$$V(\cos\theta) = \frac{Z_s - Z/\cos\theta}{Z_s + Z/\cos\theta}, \tag{2}$$

where Z is the characteristic impedance of air, and the poles θ_p of V are solutions of

$$\cos\theta_p = -\frac{Z}{Z_s(\cos\theta_p)}. \tag{3}$$

It can be shown[15,16] that a solution of Eqs. (1)–(3) exists for $|k_1 l| \ll 1$ and $|\cos\theta| \ll 1$. Then, $\cos^2\theta_1$ is close to $(1 - 1/n^2)$ and $Z_s(\cos\theta_p)$ close to $Z_s(\cos\pi/2)$. At the first-order approximation in $k_1 l$, $\sin\theta_p$ is given by

$$\sin\theta_p = 1 + (\phi k l)^2 \frac{(n^2-1)^2}{2m^2}. \tag{4}$$

A simple procedure can be used to determine the exact location of the pole. Experiments and simulations have been performed with a layer of small thickness, $l = 1.7$ cm, at 500 Hz. The predicted pole is located at $\sin\theta_p = 1.0028 + i1.577 \times 10^{-3}$, $\cos\theta_p = (-2.04 + i7.76) \times 10^{-2}$. Other poles exist, but they are far from the real $\sin\theta$ axis and their contribution to the reflected field can be neglected, the large imaginary part of the x wave number component leading to high attenuation.

The limits of $\sin\theta_p$ and $\cos\theta_p$ when $l \to \infty$ are

$$\sin\theta_p = \left[\left(\frac{m^2}{\phi^2} - n^2 \right) \Big/ \left(\frac{m^2}{\phi^2} - 1 \right) \right]^{1/2}, \tag{5}$$

$$\cos\theta_p = -\left[(n^2 - 1) \Big/ \left(\frac{m^2}{\phi^2} - 1 \right) \right]^{1/2}. \tag{6}$$

It may be shown that $\sin\theta_p$ given by Eq. (5) has a real part always smaller than 1.[16]

Experiments and simulations have been performed with a layer of large thickness, $l = 13$ cm, at 500 Hz. The predicted pole is located at $\sin\theta_p = 0.9971 + i6.259 \times 10^{-3}$ and $\cos\theta_p = (-9.874 + i6.321) \times 10^{-2}$, close to the values obtained from Eqs. (5)–(6). In this case, $\sin\theta_p$ is also close to 1 due to the large $|m|$ related at low frequencies to the high flow resistivity of the sand.

The location of the pole in both cases can be obtained with a good approximation by using

$$\cos\theta_p = -\frac{Z}{Z_s\left(\cos\frac{\pi}{2}\right)}, \tag{7}$$

θ_p being close to $\pi/2$ in Eq. (3).

Measurements are performed with the Tamura method.[2] A source creates an axisymmetric pressure field over the porous layer. The pressure field can be written

$$p(r,z) = \int_0^\infty k_r F(k_r) J_o(k_r r) \left(\exp(-ik_z z) + V\left(\frac{k_z}{k}\right) \times \exp(+ik_z z) \right) dk, \tag{8}$$

where r is the horizontal distance to the source and z the vertical distance to the reflecting surface, k_r and k_z the radial and z-wave number components, respectively ($k^2 = {k_r}^2 + {k_z}^2$), J_o the zero-order Bessel function, and $F(k_r)$ depends on the nature of the source. The reflection coefficient V is the same as for a plane wave with $\sin\theta = k_r/k$. The amplitudes of the incident and reflected components of the field for a couple (k_r, k_z) are obtained from a Hankel spatial transform of the field measured at two heights, z_1 and z_2, r varying from 0 to about 1 m. For $k_r > k$, $\sin\theta$ is larger than 1 and k_z imaginary. For $k_r < k$, $\sin\theta$ is smaller than 1 and k_z is real. The modulus of the reflection coefficient predicted from Eqs. (1)–(2) is compared at 500 Hz to measurements for $l = 1.7$ cm (Fig. 1) and $l = 13$ cm (Fig. 2). For $l = 1.7$ cm the pole is close to the real $\sin\theta$ axis and $\mathrm{Re}(\sin\theta) > 1$, and for $l = 13$ cm, the pole is at the left-hand side of $\mathrm{Re}(\sin\theta) = 1$. A sharp maximum due to the pole close to the real $\sin\theta$ axis appears for $l = 1.7$ cm at $\sin\theta = 1.003$. The measured maximum is smaller than the predicted one, probably due to small variations of the thickness of the layer. The related maximum is predicted at $\sin\theta = 1.0033$ on the real $\sin\theta$ axis. For $l = 13$ cm, there is a smaller maximum for $\sin\theta > 1$, and a sharper minimum for $\sin\theta < 1$. When the damping in the porous medium is very small, for sufficiently high frequencies, the minimum tends to zero at $\sin\theta = \mathrm{Re}(\sin\theta_p) < 1$ ($\sin\theta_p$ is

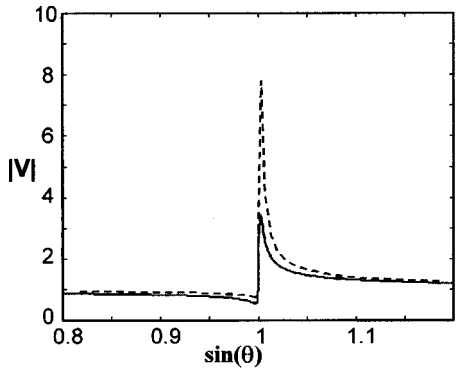

FIG. 1. Reflection coefficient measured ———, predicted by Eqs. (1)–(2) ---, for $f=500$ Hz, and $l=1.7$ cm.

almost real), θ_p is the Brewster angle of total refraction.[1]

As indicated in a previous paper,[1] strong analogies exist between the reflection of acoustic waves by porous layers and of T.M. (transverse magnetic) waves by dielectrics. For a thin grounded dielectric, the reflection coefficient has a pole with $\mathrm{Re}(\sin\theta_p)>1$, related to an ordinary surface wave.[17] For a semi-infinite dielectric or a conducting medium, $\mathrm{Re}(\sin\theta_p)<1$, and the pole is related to the Zenneck wave,[9] which exists only at small distances from the source. These analogies also exist for the acoustic surface waves studied by Daigle *et al.*[18] over a square lattice of cavities, as shown by Kelders *et al.*[19]

IV. CONTRIBUTION OF THE POLE TO THE SPHERICAL REFLECTED FIELD CLOSE TO GRAZING INCIDENCE

A monopole source S and a receiver P are located over a porous layer (see Fig. 3). Let z and z_o be the distance of the receiver and the source from the layer, respectively, r the distance between the receiver and the vertical axis where the source is located, R the distance from the source to the receiver, R_1 the distance from the image of the source S' to the receiver, and θ_o the angle of specular reflection. The direct field p_i created by the source is $p_i=\exp(ikR)/R$. Using the Sommerfeld integral, the reflected field can be written[5]

$$p_r=i\int_{-\infty}^{+\infty}\frac{\xi\,d\xi}{2\mu}V\left(\frac{\mu}{k}\right)H_0^{(1)}(\xi r)\exp(i\mu(z+z_o)), \tag{9}$$

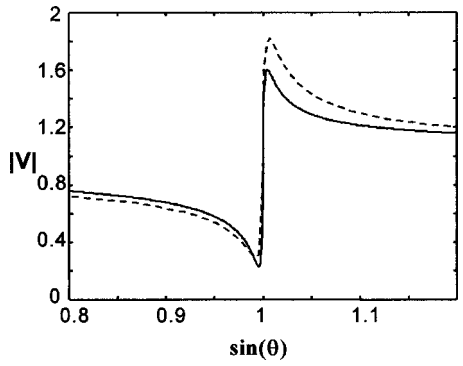

FIG. 2. Reflection coefficient measured ———, predicted by Eqs. (1)–(2) ---, for $f=500$ Hz, and thickness $l=13$ cm.

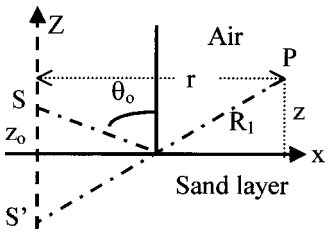

FIG. 3. The sound source S, the image S' of the source, and the receiver P.

where $\mu=\sqrt{k^2-\xi^2}$, $\mathrm{Im}(\mu)\geqslant 0$, and $H_o^{(1)}$ is the Hankel function of the first order. This integral is performed in the physical Riemann sheet of the complex $\sin\theta$ plane, on the real axis with V given by Eq. (2). In order to evaluate the contribution of the pole to p_r, the classical pole subtraction method valid for large kr and $\sin\theta_o$ and $\sin\theta_p$ close to 1, is used. At grazing incidence, for thick layers of sand, the effective density is sufficiently large at 500 Hz for $\sin\theta_p$ to be close to 1 and $\sin\theta_o$. For thin layers of large or small flow resistivity, $\sin\theta_p$ given by Eq. (4) can be close to 1 if kl is sufficiently small. Following Brekhovskikh and Godin,[5] the real $\sin\theta$ axis is replaced by a new path of integration, defined by $\cos(\theta-\theta_o)=1+is^2$, $-\infty<s<\infty$, including $\sin\theta_o$. The main contribution to p_r is obtained from the part of the path located around θ_o which is close to $\pi/2$ and θ_p. The surface impedance weakly varies in this domain around $Z_s(\cos\pi/2)$, because $\cos\theta_1$ in Eq. (1) is given by

$$\cos\theta_1=\left(1-\frac{1}{n^2}+\frac{\cos^2\theta}{n^2}\right)^{1/2}, \tag{10}$$

and $\cos^2\theta$ is negligible around $\theta=\pi/2$. From Eq. (7), Z_s can be replaced by $-Z/\cos\theta_p$, and the reflection coefficient around θ_o takes the simple form

$$V(\cos\theta)=\frac{\cos\theta+\cos\theta_p}{\cos\theta-\cos\theta_p}, \tag{11}$$

$\cos\theta_p$ being given by Eq. (7).

The reflected field p_r is given by Eq. (25) in the work by Chien and Soroka.[4] Using the same numerical distance u as in Ref. 5

$$u=\sqrt{2kR_1}\exp\left(\frac{3\pi i}{4}\right)\sin\left(\frac{\theta_p-\theta_o}{2}\right), \tag{12}$$

this equation can be rewritten

$$p_r=\frac{\exp(ikR_1)}{R_1}[1+(1-V(\cos\theta_o))\times(1+u\sqrt{\pi}\exp(u^2)\mathrm{erfc}(-u))]. \tag{13}$$

When θ_p and θ_o are close to $\pi/2$, at the first-order approximation in $\pi/2-\theta_p$ and $\pi/2-\theta_o$, u is given by

$$u=\sqrt{2kR_1}\exp\left(\frac{3\pi i}{4}\right)\frac{\cos\theta_o-\cos\theta_p}{2}. \tag{14}$$

Equations (11)–(14) are the same as those traditionally used for locally reacting surfaces. One difference is that $\cos\theta_p$ is defined by Eq. (7), where $Z_s(\cos\pi/2)$ replaces Z_s independent on θ for the locally reacting surface. For nonlocally thin layers Z_s can depend noticeably on the angle of incidence

and Eq. (7) can provide a correct evaluation of $\cos\theta_p$ when $|n|$ is close to 1. The second difference concerns Eq. (11), which gives for nonlocally reacting media a correct evaluation of the reflection coefficient only around $\theta=\pi/2$. These differences disappear when $|n|$ is sufficiently large.

Equation (13) can be rewritten

$$p_r=\frac{\exp(ikR_1)}{R_1}\left[1-\sqrt{2\pi kR_1}\exp\left(\frac{3\pi i}{4}\right)\times\cos\theta_p\exp(u^2)\mathrm{erfc}(-u)\right]. \quad (15)$$

The evaluation of $P(u)=\sqrt{\pi}\exp(u^2)\mathrm{erfc}(-u)$ can be performed from the well-known following expansions for small $|u|$:

$$P(u)=\sqrt{\pi}\exp(u^2)+2u\exp(u^2)\left[1-\frac{u^2}{3}+\cdots\right], \quad (16)$$

and large $|u|$

$$P(u)=(1+\mathrm{sgn}[\mathrm{Re}(u)])\sqrt{\pi}\exp(u^2)-1+\frac{1}{u}\left[\frac{1}{2u^2}-\frac{1.3}{(2u^2)^2}+\cdots\right]. \quad (17)$$

For large $|u|$ the surface wave is related to the term $2\sqrt{\pi}\exp(u^2)$ in Eq. (17), which can be present for thin layers around grazing incidence. The Zenneck wave, related to a semi-infinite layer, does not exist for large $|u|$ because $\mathrm{Re}(\sin\theta_p)<1$ leads to $\mathrm{Re}(u)<0$.

The amplitude S of the surface wave when $\mathrm{Re}(u)>1$, at large $|u|$, is given by

$$S=-2\frac{\exp(ikR_1)}{R_1}\sqrt{2\pi kR_1}\exp\left(\frac{3\pi i}{4}\right)\cos\theta_p\exp(u^2). \quad (18)$$

For small $|u|$, the term $\sqrt{\pi}\exp(u^2)$ in Eq. (16) provides the contribution $S/2$ for the Zenneck waves (or the surface wave) as indicated previously by Banos.[9] For $|u|\ll 1$, the Zenneck wave (or the surface wave) is the dominant term in the difference $p_r-\exp(ikR_1)/R_1$, with an amplitude $S/2$. The quantity $p_r-\exp(ikR_1)/R_1$ is the difference between the actual reflected pressure field and the field reflected by a rigid, impervious surface. It may be noticed that the evaluation of p_r in the model by Li *et al.*[7] is obtained by using, instead of Eq. (7), $\cos\theta_p=-Z/Z_s(\cos\theta)$. Both formulations provide similar evaluations around grazing incidence.

V. EVALUATION OF THE SURFACE IMPEDANCE FOR SMALL SOURCE–RECEIVER DISTANCES

An evaluation of $\cos\theta_p$, and the surface impedance Z_s at grazing incidence with Eq. (7) can be performed in the following way. The source and the receiver are located close to the reflecting surface. The reflected pressure p_r is measured; $\cos\theta_p$ is evaluated from Eq. (15)

$$\cos\theta_p=-\frac{[p_r-\exp(ikR_1)/R_1]R_1/\exp(ikR_1)}{\sqrt{2\pi kR_1}\exp(3\pi i/4)\exp(u^2)\mathrm{erfc}(-u)} \quad (19)$$

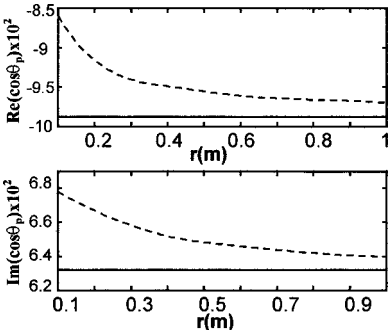

FIG. 4. Exact $\cos\theta_p$ ——— and evaluated $\cos\theta_p$ --- from Eq. (16) for a thick layer of sand ($l=13$ cm) as a function of the source–receiver distance r at 500 Hz ($z_o=z=0.5$ cm).

(the determination of the unknown amplitude of the source is not taken into account in this symbolic evaluation).

For $|u|\ll 1$ Eq. (19) can be simplified

$$\cos\theta_p=-\frac{[p_r-\exp(ikR_1)/R_1]R_1}{\sqrt{2\pi kR_1}\exp(ikR_1)\exp(3\pi i/4)}. \quad (20)$$

The quantity in the square brackets is the contribution $S/2$ of the pole, defined in the previous section. For *in situ* measurements on sound-absorbing materials, the source–receiver distance must be small to minimize the effect of the diffuse field and the finite lateral extent of the layers. As indicated previously, the pole subtraction method is an asymptotic evaluation of p_r valid at large kr. A simulation has been performed to test the limit of validity of Eq. (19) for small r. The pressure p_r in these equations is calculated without approximation from Eqs. (1), (2), and (9). The effect of the diffuse field and the finite lateral extent of the layer are not taken into account. A first approximation for $\cos\theta_p$ is obtained from Eq. (20), and is modified in an iterative process with Eq. (19). The geometry of the simulated experiment is defined by $z=z_o=0.5$ cm, and r varies from 10 cm to 1 m. The sound-absorbing material is the thick layer of sand, $l=13$ cm at 500 Hz. At $r=1$ m, $u=(-0.69+i2.6)\times10^{-1}$, the numerical distance is small in the whole r interval. The exact $\cos\theta_p$ is compared to the evaluated $\cos\theta_p$ in Fig. 4. The precision of the evaluation decreases at small r, but the order of magnitude of the estimation is good even at $r=0.1$ m, in spite of the small kr ($kr=4.6$). Measurements of Z_s at grazing incidence have been performed with this method for a thin layer of plastic foam.[20] Close results have been obtained with the Tamura method at $\theta=\pi/2$.

VI. CONCLUSION

Around grazing incidence at sufficiently low frequencies, a sand layer of large or small thickness behaves in first approximation as a locally reacting surface with an impedance large compared to the characteristic impedance of air. Simple models can be used to evaluate the contribution of the pole to the spherical reflected field at small numerical distances. This contribution is the Zenneck wave for thick layers and an ordinary surface wave for thin layers and is at small numerical distances close to the difference between the actual reflected pressure field and the field reflected by a

rigid impervious surface. Simulations show that *in situ* measurements of surface impedance at small source–receiver distance, based on an evaluation of this difference, is possible for sand layers. The method can also be used for thin layers of porous media having a smaller flow resistivity.

[1] J. F. Allard, M. Henry, J. Tizianel, L. Kelders, and W. Lauriks, ''Surface waves over bead layers,'' J. Acoust. Soc. Am. **105**, 3021–3025 (1999).

[2] B. Brouard, D. Lafarge, J. F. Allard, and M. Tamura, ''Measurement and prediction of the reflection coefficient of porous layers at oblique incidence and for inhomogeneous waves,'' J. Acoust. Soc. Am. **99**, 100–107 (1996).

[3] I. Rudnick, ''Propagation of an acoustic wave along a boundary,'' J. Acoust. Soc. Am. **19**, 348–356 (1947).

[4] C. F. Chien and W. W. Soroka, ''Sound propagation along an impedance plane,'' J. Sound Vib. **43**, 9–20 (1975).

[5] L. M. Brekhovskikh and O. A. Godin, *Acoustics of Layered Media II, Point Source and Bounded Beams*, Springer Series on Wave Phenomena (Springer, New York, 1992).

[6] K. Attenborough, ''Review of ground effects on outdoor sound propagation from continuous broadband sources,'' Appl. Acoust. **24**, 289–319 (1988).

[7] K. M. Li, T. Waters-Fuller, and K. Attenborough, ''Sound propagation from a point source over extended-reaction ground,'' J. Acoust. Soc. Am. **104**, 679–685 (1998).

[8] L. M. Brekhovskikh, *Waves in Layered Media* (Academic, New York, 1960).

[9] A. Banos, *Dipole Radiation in the Presence of a Conducting Half-Space* (Pergamon, Oxford, 1966).

[10] J. F. Allard, M. Henry, J. Tizianel, L. Kelders, and W. Lauriks, ''Sound propagation in air saturating random packings of beads,'' J. Acoust. Soc. Am. **104**, 2004–2007 (1998).

[11] J. Tizianel, J. F. Allard, C. Ayrault, B. Castagnède, M. Henry, A. Moussatov, and A. Gedeon, ''Transport parameters and propagation in air saturated sand,'' J. Appl. Phys. **86**, 5829–5834 (1999).

[12] N. P. Chotiros, ''Biot model of sound propagation in water-saturated sand,'' J. Acoust. Soc. Am. **97**, 199–214 (1995).

[13] D. L. Johnson, J. Koplik, and R. Dashen, ''Theory of dynamic permeability and tortuosity in fluid saturated porous media,'' J. Fluid Mech. **176**, 379–402 (1987).

[14] D. Lafarge, P. Lemarinier, J. F. Allard, and V. Tarnow, ''Dynamic compressibility of air in porous structures at audible frequencies,'' J. Acoust. Soc. Am. **102**, 1955–1963 (1997).

[15] W. Lauriks, L. Kelders, and J. F. Allard, ''Surface waves and leaky waves above a porous layer,'' Wave Motion **28**, 59–67 (1998).

[16] W. Lauriks, L. Kelders, and J. F. Allard, ''Poles and zeros of the plane wave reflection coefficient for porous surface,'' Acust. Acta Acust. **83**, 1045–1052 (1997).

[17] R. E. Collin, *Field Theory of Guided Waves* (McGraw-Hill, New York, 1960).

[18] G. A. Daigle, M. R. Stinson, and D. I. Havelock, ''Experiments on surface waves over a model impedance plane using acoustical pulses,'' J. Acoust. Soc. Am. **99**, 1993–2005 (1996).

[19] L. Kelders, J. F. Allard, and W. Lauriks, ''Ultrasonic surface waves above rectangular groove gratings,'' J. Acoust. Soc. Am. **103**, 2730–2733 (1998).

[20] J. F. Allard, M. Henry, V. Gareton, G. Jansens, and W. Lauriks, ''Impedance measurements around grazing incidence for nonlocally reacting thin porous layers,'' J. Acoust. Soc. Am. (submitted).

Frame-borne surface waves in air-saturated porous media

J. F. Allard, G. Jansens, G. Vermeir, and W. Lauriks[a)]
Laboratorium voor Akoestiek en Thermische Fysica, Katholieke Universiteit Leuven, Celestijnenlaan 200D, B-3001 Heverlee, Belgium

(Received 24 May 2001; revised 11 October 2001; accepted 17 October 2001)

A Rayleigh-type surface wave at an air–air saturated porous layer interface is predicted and detected experimentally in the audible frequency range. Applications of this surface wave for the metrology of sound-absorbing media are suggested. © *2002 Acoustical Society of America.*
[DOI: 10.1121/1.1427361]

PACS numbers: 43.20.Gp, 43.20.Jr, 43.20.Ye [ANN]

I. INTRODUCTION

Many systematic theoretical studies of the surface waves at fluid-filled saturated porous layer interfaces have been performed in the context of the Biot theory[1] from the early works of Deresiewicz[2] to the work by Feng and Johnson.[3] The prediction of the surface modes is more complicated than for elastic solids in contact with a fluid, due to the presence of three bulk waves, two compressional waves and a shear wave in the layer. Moreover, depending on the rigidity and the density of the frame, and the strength of the different fluid–frame coupling mechanisms, sound propagation in porous media presents very different aspects. The characterization of natural porous media saturated by water and petrol in a borehole with surface and bulk waves is an important topic for the oil industry. Many works have been performed with heavy fluids saturating sintered glass beads and synthetic or natural sandstones at ultrasonic frequencies. The state of the art in this domain is described in Ref. 4. The present work concerns usual sound-absorbing media saturated by air, at audible frequencies. The medium is in contact with air and there is no impervious screen set at the interface. For these media, the density of the porous frame is much greater than the density of air, and in the medium- and high-frequency range the shear wave and one of the compressional waves are very similar to the shear wave and the compressional wave that propagate in an elastic solid having the same density and the same rigidity.[5] These waves are the frame-borne waves that can easily be created by a mechanical excitation of the frame. They propagate simultaneously in air and in the frame. The other compressional wave propagates mainly in the air saturating the porous medium in the medium- and high-frequency range, the frame being too heavy to move noticeably under the effect of an aerial excitation. This wave is the airborne wave. Surface waves at an air–air saturated porous material interface for the case of a motionless frame have been studied previously.[6,7]

In the present work, the full Biot theory,[1] which takes into account the vibrations of the frame, is used to predict the reflection coefficient of a porous layer, and the related poles and surface waves. The losses due to the thermal exchanges and viscous interactions between air and frame and the intrinsic damping in the porous frame are taken into account. A Rayleigh-type surface wave is described theoretically and set in evidence experimentally, the frame being prompted by mechanical excitation. Similar waves created by aereal excitation have been predicted by Feng and Johnson[3] for lossless porous media.

The bulk waves in a porous medium are described in Appendix A in the context of the Biot theory.[1] The reflection coefficient of a poroelastic layer is predicted in Appendix B, and pressure and frame velocity at the surface of a porous layer subjected to a mechanical excitation in Appendix C. In Sec. III, the main properties of the Rayleigh-type surface wave are given, and in Sec. IV this wave is set in evidence experimentally for a polyurethane foam.

II. MAIN FEATURES OF BULK WAVES AND RAYLEIGH-TYPE SURFACE WAVE IN THE MEDIUM- AND HIGH AUDIBLE FREQUENCY RANGE

The general description of the three Biot bulk waves[1] is given in Appendix A. Simulations are performed with a material characterized by the parameters of Table I, having the same orders of magnitude as the usual sound-absorbing materials.[8,9] The three wave numbers, k_1 for the frame-borne compressional wave, k_2 for the airborne compressional wave, and k_3 for the frame-borne shear wave, calculated from Eqs. (A10)–(A11) at 2 kHz and the wave number in air k are equal to [the time dependence is $\exp(i\omega t)$] $k_1 = 118.9 - i24.1\ \mathrm{m}^{-1}$, $k_2 = 70.0 - i36.1\ \mathrm{m}^{-1}$, $k_3 = 230.6 - i24.0\ \mathrm{m}^{-1}$, $k = 36.9\ \mathrm{m}^{-1}$.

For an elastic solid with the same shear modulus N, Poisson coefficient ν and density ρ_s, the wave numbers for the compressional wave k_c and the shear wave k_s are: $k_c = 120.9 - i12\ \mathrm{m}^{-1}$, $k_s = 226 - i22.4\ \mathrm{m}^{-1}$ close to k_1 and k_3, respectively. The main difference is the larger loss angle for the frame-borne compressional wave, due to the viscous air–frame interaction in the porous medium. The reflection coefficient, for an incident plane wave under an angle of incidence θ [see Fig. 1(a)] is given by Eq. (B20). The poles of the reflection coefficient are solutions of Eq. (B21). We have only considered transmitted waves exponentially decreasing far away from the interface. When the shear wave is the slowest bulk wave, it has been pointed out by Feng and Johnson[3] that there is essentially one Rayleigh-type true sur-

a)Author to whom correspondence should be addressed. Walter Lauriks, LAB ATF, Department of Physics; electronic mail: Walter.Lauriks@fys.kuleuven.ac.be

TABLE I. Parameters for the porous medium used in the simulations.

Tortuosity α_∞	Flow resistivity Ns/m^4 σ	Porosity ϕ	Viscous dimension μm Λ	Thermal dimension μm Λ'	Frame density kg/m^3 ρ_s	Shear modulus Pa N	Poisson ratio ν
1.4	50 000	0.98	50	150	25	$(0.75+i0.15)10^5$	0.3

face mode. The other poles are not related to observable surface modes. For the material studied, at 2 kHz, two poles at different complex angles of incidence θ_p are related to the Rayleigh-type waves, such as $\cos\theta_p=0.705+i6.65$, $k\sin\theta_p=247.7-i25.7$, and $\cos\theta_p=-0.728-i6.68$, $k\sin\theta_p=249.1-i26.5$. With our convention, the wave number vector of the incident wave is $(k_x=k\sin\theta_p, k_z=k\cos\theta_p)$ and for the reflected wave $(k_x=k\sin\theta_p, k_z=-k\cos\theta_p)$. The second pole corresponds to an improper surface mode. The x-wave number component k_R for the Rayleigh mode at a free surface of the equivalent solid, obtained with the approximate evaluation[10]

$$k_R=k_s\frac{1+\nu}{0.87+1.12\nu}, \tag{1}$$

is equal to $k_R=243.7-i24.1$, close to k_x for both poles.

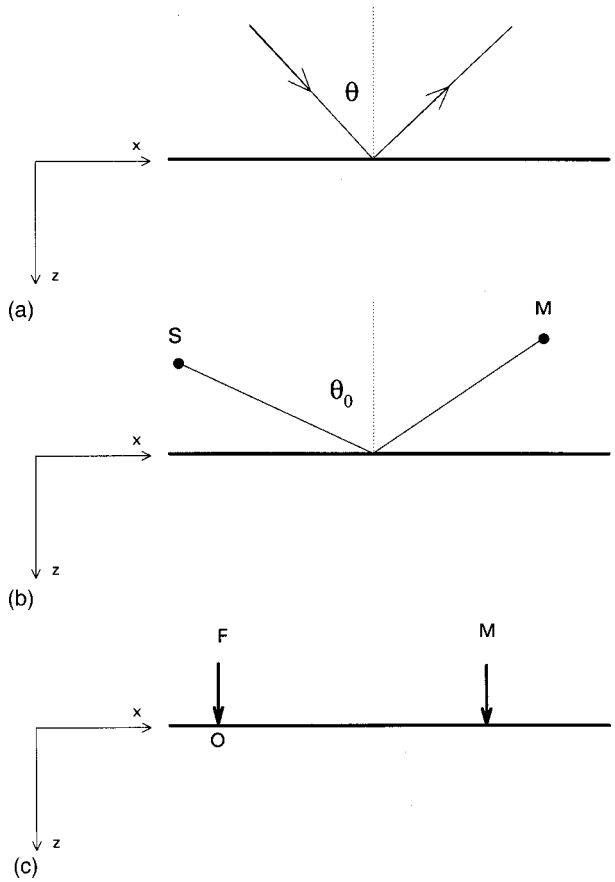

FIG. 1. (a) A plane wave under an angle of incidence θ and the reflected wave. (b) A point source in air at S and a receiver at M. (c) A point force at O, the vertical velocity of the frame v_z^s is measured at M.

III. GENERATION AND DETECTION OF THE SURFACE WAVE (MODELING)

For a monopole source in air [see Fig. 1(b)], the incident pressure field can be written[11]

$$p_i=ik\int_0^\infty\frac{\xi\,d\xi}{\mu}J_0(k\xi r)\exp(i\mu k|z-z_0|), \tag{2}$$

where r is the horizontal source–receiver distance, z_0 and z the distances from the reflecting surface to the source and the receiver, respectively, and the reflected field is given by[11]

$$p_r=ik\int_0^\infty\frac{\xi\,d\xi}{\mu}R(\xi)J_0(k\xi r)\exp(i\mu k(z+z_0)), \tag{3}$$

where $R(\xi)$ is the plane-wave reflection coefficient given by Eq. (B20) and $\mu=\sqrt{1-\xi^2}$, $\mathrm{Im}(\mu)>0$. Simulations show that, if the damping is removed, the surface wave can be detected in the reflected field generated by a line source or a point source.[3] If the losses are taken into account, for the material described in Table I in the medium- and high-frequency ranges, the amplitude of the surface wave is negligible. This is due to the frame-borne nature of the surface wave, which will be more easily created by a mechanical excitation of the frame than with aerial excitation. The prediction of pressure, air, and frame vertical velocity, created by a vertical periodic force acting on the frame at the surface of the porous layer with the same dependence on x, $\exp(-ikx\sin\theta)$, as the plane waves in Appendix B, is performed in Appendix C. It is shown that the same poles exist as for the reflection coefficient of plane acoustic waves. The vertical velcoity of the frame $v_z^s(0^+,x)$ can be written

$$v_z^s(0^+,x)=V_z^s(\sin\theta)\exp(-ikx\sin\theta), \tag{4}$$

V_z^s being given by Eq. (C11). Similarly, the vertical air velocity and the pressure in free air $v_z^f(0^-,x)$ and $p(0^-,x)$ can be written

$$v_z^f(0^-,x)=V_z^f(\sin\theta)\exp(-ikx\sin\theta), \tag{5}$$

$$p(0^-,x)=P(\sin\theta)\exp(-ikx\sin\theta), \tag{6}$$

V_z^f and P being given by Eqs. (C12) and (C13).

A vertical periodic point force $F\delta(x)\delta(y)$ can be replaced by a superposition of axisymmetric components[12]

$$F\delta(x)\delta(y)=\frac{Fk^2}{2\pi}\int_0^\infty J_0(k\xi r)\xi\,d\xi. \tag{7}$$

The related displacements and pressure are given by

$$v_z^s(0^+,r)=\frac{Fk^2}{2\pi}\int_0^\infty J_0(k\xi r)V_z^s(\xi)\xi\,d\xi, \tag{8}$$

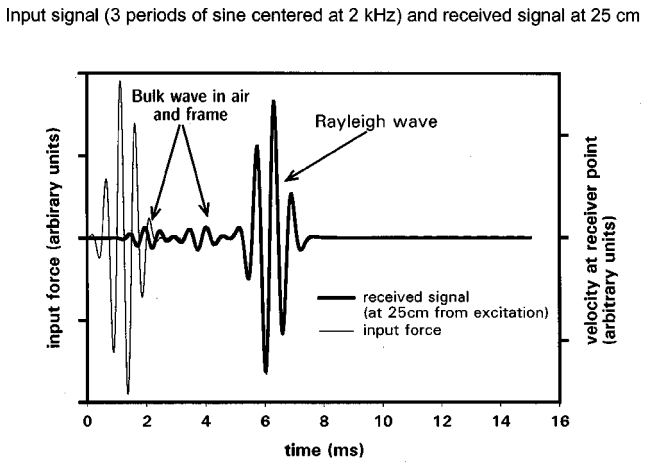

FIG. 2. The point force $F(t)$ and the resultant vertical velocity v_z^s of the frame at a distance of 25 cm (calculations).

$$v_z^f(0^-,r)=\frac{Fk^2}{2\pi}\int_0^\infty J_0(k\xi r)V_z^f(\xi)\xi\,d\xi, \tag{9}$$

$$p(0^-,r)=\frac{Fk^2}{2\pi}\int_0^\infty J_0(k\xi r)P(\xi)\xi\,d\xi. \tag{10}$$

The same transfer functions can be used for the plane and the axisymmetrical problem. This can be shown in the same way as for elastic solid[12] and elastic porous media with aerial excitation.[5] Moreover, it is indicated in Appendix C that the transfer functions V_z^s, V_z^f, and P have the same poles as the reflection coefficient R. Time representations can be obtained from Eqs. (8)–(10) with FFT. The calculated vertical velocity of the frame at 25 cm from the source, created by a burst of a vertical force $F(t)$ centered at 2 kHz, is shown in Fig. 2, in the time interval where it is noticeable. This signal is related to the Rayleigh-type surface wave. It is slightly different from $F(t)$, due to the increasing absorption in the high-frequency range. Similar calculations of the pressure and the air vertical velocity have been performed. The phase lag of air velocity compared to the pressure signal is close to $\pi/2$ and corresponds to the contribution of the pole in the physical Riemann sheet. Time-of-flight measurements are easily performed on this signal, which is not mixed with other noticeable contributions, and a rough estimation of damping is possible. The amplitude of the surface wave decreases in accordance with $1/\sqrt{r}\exp(r\,\mathrm{Im}(k_R))$ when r increases. Simulated measurements at $r=20$ cm and $r=30$ cm give $\mathrm{Im}(k_R)=-21\ \mathrm{m}^{-1}$. A more precise evaluation of $\mathrm{Im}\,k_R$ can be obtained with a continuous sine point source. At a distance $r>10$ cm, the velocity field is mainly due to the surface wave. Simulated measurements at $r=10$ cm and $r=30$ cm give $\mathrm{Im}\,k_R=-25\ \mathrm{m}^{-1}$.

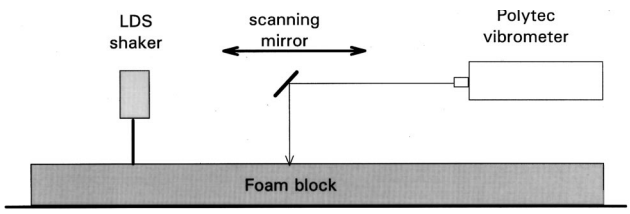

FIG. 3. The experimental setup.

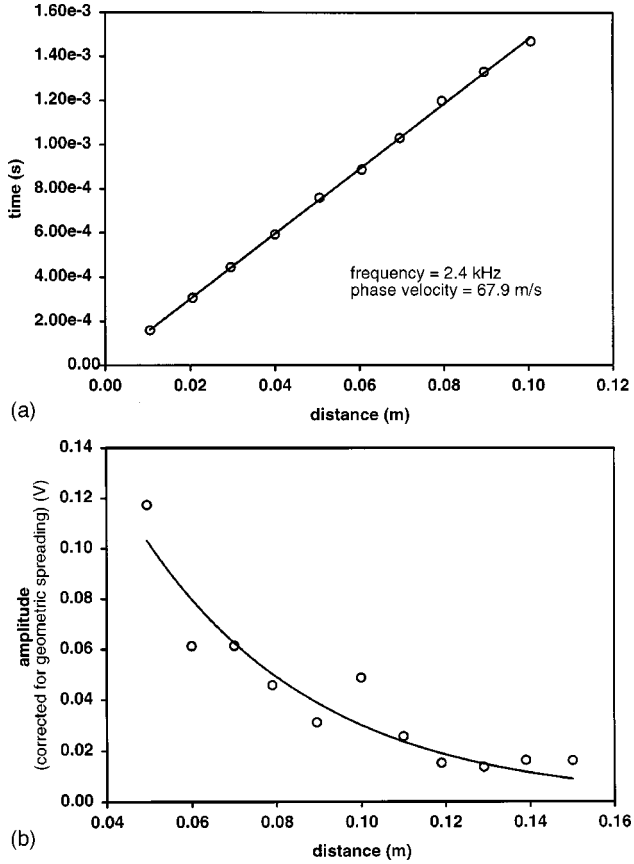

FIG. 4. Experimental results at 2.4 kHz. (a) Time of flight; (b) attenuation.

IV. EXPERIMENTAL RESULTS

The experimental setup is shown schematically in Fig. 3. A tone burst is fed to an LDS V 101 shaker, which generates surface waves on a thick slab (10 cm) of polyurethane foam. The amplitude and phase of the normal surface vibration is measured at several distances using a Polytec vibrometer and a scanning mirror. A small patch of retroreflecting tape is attached to the foam in order to obtain a good signal. A sine burst with 10 to 20 periods is used as excitation and the detected signal is cross correlated with the excitation in order to obtain the time of flight.

Measurements performed at 3 kHz indicate a wavelength for the Rayleigh wave close to 2 cm. The penetration depth of the Rayleigh wave is around 2 wavelengths and the layer can be considered as semi-infinite. This is confirmed by time-of-flight measurements at lower frequencies with a greater penetration, which give similar results for the velocity.

Measurements of the phase velocity and attenuation of the Rayleigh wave have been performed at 2.4 and 3 kHz. The results are shown in Figs. 4 and 5 and are summarized in Table II. These results are in agreement with data obtained on similar foams with different techniques.

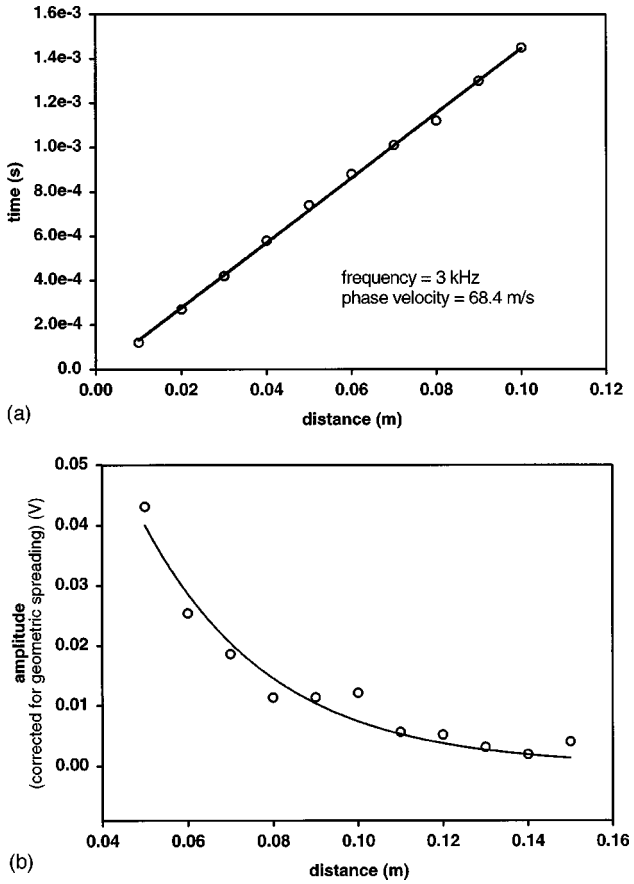

FIG. 5. Experimental results at 3 kHz. (a) Time of flight; (b) attenuation.

V. POSSIBLE APPLICATIONS OF THE RAYLEIGH-TYPE SURFACE WAVE FOR USUAL SOUND-ABSORBING POROUS LAYERS

Similar to the case of elastic solids, the phase velocity and attenuation of the Rayleigh wave allows the evaluation of elastic parameters of the substrate. Since the Rayleigh wave velocity is rather insensitive to the Poisson ratio and very insensitive to the other material parameters of Table I, measuring the phase velocity and attenuation of the Rayleigh wave provides a direct estimate of the real and imaginary part of the shear modulus at audible frequencies. This is important since at the present moment, the use of the full Biot model to predict the acoustic properties of sandwich panels and multilayered structures including porous media is limited by the absence of data concerning the dynamic rigidity of porous frames. The surface wave can also be used to detect and characterize a possible anisotropy in the interface plane.[13,14] The horizontal phase velocity of this wave is sufficiently small for precise measurements of this quantity to be performed with simple equipment. The surface wave can easily be generated and detected in the medium- and high audible frequency ranges. For the excitation, a low-cost lightweight shaker is sufficient. If only the phase velocity (or the real part of the shear modulus) is needed, a low-cost accelerometer is sufficient for the detection (we did successful tests using a Knowles-type BU-1771 accelerometer). Accurate attenuation measurements require a detection system that is less sensitive to the bonding with the sample such as a laser vibrometer.

As indicated in Sec. II, an equivalent elastic solid with the same shear modulus, Poisson ratio, and density as the porous foam will give a Rayleigh wave velocity close to that of the porous foam. This means that for practical purposes, Eq. (1) can be used for the extraction of the shear modulus instead of the full Biot model. First attempts to use this method are being performed.[15]

TABLE II. Experimental results.

Frequency (kHz)	Phase velocity (m/s)	Re (k_{Rayleigh}) m^{-1}	Im (k_{Rayleigh}) m^{-1}	Shear modulus[a] (N/m^2)
2.4	68.0±0.5	222±2	−24±3	$(1.55+i0.34)10^5$
3.0	68.0±0.5	277±2	−33±3	$(1.56+i0.38)10^5$

[a]Material density $\rho=30$ kg/m^3 and assuming a typical Poisson ratio of 0.3.

VI. CONCLUSION

A Rayleigh-type surface wave which propagates at the air–air saturated porous interface has been predicted and studied experimentally in the audible frequency range for an ordinary plastic foam. The frame for these materials has a bulk modulus of the same order of magnitude as air, but is much heavier. The wave is a frame-borne wave that can be generated from a mechanical solicitation of the foam but is related to a pole of the reflection coefficient of the porous layer. This wave is easily detected. Velocity measurements can provide information about the rigidity of the frame and the anisotropy of the material.

APPENDIX A: BULK WAVES IN AIR-SATURATED POROUS MEDIA

A description of sound propagation in air-saturated porous media, given in Ref. 5, is used in the present work.

Simplifications in the evaluation of the elastic parameters P, Q, and R can be performed for air-saturated porous media. Instead of the exact expressions, the following equations can be used:

$$P=\frac{4}{3}N+K_b+\frac{(1-\phi)^2}{\phi}K_f, \tag{A1}$$

$$Q=K_f(1-\phi), \tag{A2}$$

$$R=\phi K_f, \tag{A3}$$

where N and K_b are, respectively, the shear modulus and the bulk modulus of the frame in vacuum, K_f the incompressibility of air in the pores, and ϕ the porosity. The incompressibility of air in the pores depends on frequency due to the thermal exchanges with the frame. In the present work, K_f is given by

$$K_f=\frac{\gamma P_0}{\left\{\gamma-(\gamma-1)\left[1+\frac{8\eta}{i\Lambda'^2\,\mathrm{Pr}\,\omega\rho}\left(1+i\frac{\rho\omega\,\mathrm{Pr}\,\Lambda'^2}{16\eta}\right)^{1/2}\right]^{-1}\right\}}, \tag{A4}$$

where P_0 is the atmospheric (static) pressure, γ the ratio of the specific heats, η the viscosity, Pr the Prandtl number, ρ

the air density, and Λ' the thermal dimension. The inertial parameters $\tilde{\rho}_{11}$, $\tilde{\rho}_{12}$, and $\tilde{\rho}_{22}$ are given by

$$\tilde{\rho}_{11}=\rho_1+\rho_a-i\sigma\phi^2\frac{G(\omega)}{\omega}, \tag{A5}$$

$$\tilde{\rho}_{12}=-\rho_a+i\sigma\phi^2\frac{G(\omega)}{\omega}, \tag{A6}$$

$$\tilde{\rho}_{22}=\phi\rho+\rho_a-i\sigma\phi^2\frac{G(\omega)}{\omega}, \tag{A7}$$

where

$$\rho_a=\phi\rho(\alpha_\infty-1), \tag{A8}$$

$$G(\omega)=\left(1+\frac{4i\alpha_\infty^2\eta\rho\omega}{\sigma^2\Lambda^2\phi^2}\right)^{1/2}. \tag{A9}$$

In these equations, α_∞ is the tortuosity, σ the flow resistivity, and Λ the viscous characteristic dimension. The three wave numbers for the compressional waves (k_1 and k_2) and the shear wave (k_3) are given by

$$k_{1,2}^2=\frac{\omega^2}{2(PR-Q^2)}[P\tilde{\rho}_{22}+R\tilde{\rho}_{11}-2Q\tilde{\rho}_{12}\mp\sqrt{\Delta}], \tag{A10}$$

$$k_3^2=\frac{\omega^2}{N}\left(\frac{\tilde{\rho}_{11}\tilde{\rho}_{22}-\tilde{\rho}_{12}^2}{\tilde{\rho}_{22}}\right),$$

$$\Delta=(P\tilde{\rho}_{22}+R\tilde{\rho}_{11}-2Q\tilde{\rho}_{12})^2 -4(PR-Q^2)(\tilde{\rho}_{11}\tilde{\rho}_{22}-\tilde{\rho}_{12}^2). \tag{A11}$$

Each wave propagates simultaneously in air and in the frame. The ratios of the amplitudes of displacement of the air and the frame, μ_1, μ_2, and μ_3, are given by

$$\mu_i=\frac{Pk_i^2-\omega^2\tilde{\rho}_{11}}{\omega^2\tilde{\rho}_{12}-Qk_i^2}, \quad i=1,2, \tag{A12}$$

$$\mu_3=-\frac{\tilde{\rho}_{12}}{\tilde{\rho}_{22}}. \tag{A13}$$

APPENDIX B: REFLECTION COEFFICIENT OF A SEMI-INFINITE POROUS LAYER WITH OPEN PORES

The incidence plane is xoz. The wave number components of the incident pressure field are ($k_x=k\sin\theta, k_z=\sqrt{k^2-k_x^2}$), with θ the angle of incidence. Velocity potentials related to the three Biot waves are used. Let φ_1 and φ_2 be the potentials for the compressional waves, and $\varphi_3\,\boldsymbol{j}$ for the shear wave, $\boldsymbol{j}$ being the unit vector on the axis y perpendicular to the incidence plane [see Fig. 1(a)]. The velocity of the frame $\boldsymbol{v}^s$ and of the air inside the layer $\boldsymbol{v}^f$ are given by, respectively,

$$\boldsymbol{v}^s=\nabla\varphi_1+\nabla\varphi_2+\nabla\times\boldsymbol{j}\varphi_3, \tag{B1}$$

$$\boldsymbol{v}^f=\mu_1\nabla\varphi_1+\mu_2\nabla\varphi_2+\mu_3\nabla\times\boldsymbol{j}\varphi_3. \tag{B2}$$

Let α_1, α_2, and α_3 be the z wave number vector components for the three waves and $\beta=k\sin\theta$ the x component, related by $\alpha_i=(k_i^2-\beta^{23})^{1/2}$, $\mathrm{Im}(\alpha_i)>0$. Let σ_{ij}^s and u_{ij}^s be the stress and strain components for the frame and σ_{ij}^f, u_{ij}^f the stress and strain components for the air inside the porous medium, respectively. The stress–strain relationships are

$$\sigma_{ij}^s=(P-2N)u_{kk}^s\delta_{ij}+2Nu_{ij}^s+Qu_{kk}^f, \tag{B3}$$

$$\sigma_{ij}^f=-\phi p_f\delta_{ij}=(Qu_{kk}^s+Ru_{kk}^f)\,\delta_{ij}. \tag{B4}$$

(Implicit summation over repeated indices is assumed.) In Eq. (B4) p_f is the pressure inside the porous medium. At the interface, the boundary conditions at $z=0$ are

(i) the continuity of pressure

$$p_f(0^+)=p(0^-), \tag{B5}$$

where p is the pressure in free air.

(ii) the continuity of total stress

$$\phi\sigma_{zz}^f(0^+)+(1-\phi)\sigma_{zz}^s(0^+)=-p(0^-), \tag{B6}$$

$$\sigma_{xy}^s(0^+)=0. \tag{B7}$$

(iii) the conservation of fluid volume

$$(1-\phi)v_z^s(0^+)+\phi v_z^f(0^+)=v_z^f(0^-). \tag{B8}$$

In order to simplify the notations, the following symbols given in Table III are used. From Eqs. (B3)–(B4) and (B8), σ_{zz}^s, σ_{xy}^s, σ_{zz}^f, and $v_z^f(0^-)$ are given by

$$\sigma_{zz}^s=D\varphi_1+E\varphi_2+F\varphi_3, \tag{B9}$$

$$\sigma_{xy}^s=A\varphi_1+B\varphi_2+C\varphi_3, \tag{B10}$$

$$\sigma_{zz}^f=I\varphi_1+J\varphi_2, \tag{B11}$$

$$v_z^f(0^-)=-i\alpha_1(\phi\mu_1+1-\phi)\varphi_1(0^+) -i\alpha_2(\phi\mu_2+1-\phi)\varphi_2(0^+) -i\beta(\phi\mu_3+1-\phi)\varphi_3(0^+), \tag{B12}$$

and from Eqs. (B5)–(B7)

TABLE III. Symbols used in Appendices B and C.

$$A=\frac{2iN\beta\alpha_1}{\omega},$$

$$B=\frac{2iN\beta\alpha_2}{\omega},$$

$$C=\frac{iN}{\omega}(\beta^2-\alpha_3^2),$$

$$D=\frac{i}{\omega}(P+Q\mu_1)k_1^2-\frac{2iN\beta^2}{\omega},$$

$$E=\frac{i}{\omega}(P+Q\mu_2)k_2^2-\frac{2iN\beta^2}{\omega},$$

$$F=\frac{i}{\omega}2N\alpha_3,$$

$$G=D-\frac{FA}{C},$$

$$H=E-\frac{FB}{C},$$

$$I=\frac{i}{\omega}(Q+R\mu_1)k_1^2,$$

$$J=\frac{i}{\omega}(Q+R\mu_2)k_2^2.$$

$$\varphi_3(0^+) = -\frac{A}{C}\varphi_1(0^+) - \frac{B}{C}\varphi_2(0^+), \tag{B13}$$

$$I\varphi_1(0^+) + J\varphi_2(0^+) = -\phi p(0^-), \tag{B14}$$

$$G\varphi_1(0^+) + H\varphi_2(0^+) = -(1-\phi)p(0^-). \tag{B15}$$

From Eqs. (B14)–(B15), the potentials are given by

$$\varphi_1(0^+) = \frac{H\phi - J(1-\phi)}{GJ - HI}p, \tag{B16}$$

$$\varphi_2(0^+) = \frac{(1-\phi)I - \phi G}{GJ - HI}p. \tag{B17}$$

The surface impedance $Z_s = p(0^-)/v_z^f(0^-)$ is given by

$$Z_s = \frac{GJ - HI}{\Delta}, \tag{B18}$$

$$\Delta = \left[-i\alpha_1(1-\phi+\mu_1\phi) + i\beta\left(\mu_3\phi + (1-\phi)\frac{A}{C}\right)\right] \times [H\phi - J(1-\phi)] + \left[-i\alpha_2(1-\phi+\mu_2\phi) + i\beta\left(\mu_3\phi + (1-\phi)\frac{B}{C}\right)\right][(1-\phi)I - \phi G]. \tag{B19}$$

The reflection coefficient is given by

$$R(\beta) = \frac{Z_s(\beta) - Z/\cos\phi}{Z_s(\beta) + Z/\cos\theta}, \tag{B20}$$

where Z is the characteristic impedance of air, and the poles are solutions of

$$(GJ - HI)\cos\theta + Z\Delta = 0. \tag{B21}$$

APPENDIX C: VERTICAL PERIODIC POINT SOURCE ACTING ON A FRAME

The point source $F(t)$ can be replaced using the Bessel Hankel transform, by a distribution of axisymmetrical stresses acting on the frame

$$F\,\delta(x)\,\delta(y) = \frac{Fk^2}{2\pi}\int_0^\infty J_0(k\xi r)\,\xi\,d\xi. \tag{C1}$$

The frame vertical velocity field at $z=0$ created by a force distribution $J_0(k\xi r)$ acting on the frame can be written

$$v_z^s(k\xi r) = J_0(k\xi r)V_z^s(\xi). \tag{C2}$$

As for the reflection coefficient in Appendix B, the transfer function $V^s(\xi)$ is the same as for a ''plane'' excitation of the frame with $k_x = k\xi$. With a vertical force distribution $\exp(-ik\xi x)$, the vertical velocity field of the frame is $\exp(-ik\xi x)V^s(\xi)$. Equations (B9)–(B14) are always valid for this force distribution, and Eq. (B15) becomes

$$G\varphi_1(0^+) + H\varphi_2(0^+) = -(1-\phi)p(0^-) + \exp(-ik\xi x), \tag{C3}$$

which can be written with, $\exp(ik\sin\theta x)$ being removed, as

$$\left(G - \frac{1-\phi}{\phi}I\right)\varphi_1(0^+) + \left(H - \frac{1-\phi}{\phi}J\right)\varphi_2(0^+) = 1. \tag{C4}$$

The pressure $p(0^-)$ is related to a wave in free air with $\sin\phi = \xi$. The z wave number vector component is denoted as $-k\cos\theta$, like the reflected wave for an aerial plane excitation, and $p(0^-)/v(0^-) = -Z/\cos\theta$. In Eq. (B12), $v_z^f(0^-)$ can be replaced by $(I\varphi_1(0^+) + J\varphi_2(0^+))\cos\theta/\phi Z$, and Eq. (B12) can be written as

$$\left[-i\phi\left(\mu_1\alpha_1 - \mu_3\beta\frac{A}{C}\right) - i(1-\phi)\left(\alpha_1 - \beta\frac{A}{C}\right) - \frac{\cos\phi}{Z\phi}I\right] \times \varphi_1(0^+) + \left[-i\phi\left(\mu_2\alpha_2 - \mu_3\beta\frac{B}{C}\right) - i(1-\phi)\left(\alpha_2 - \beta\frac{B}{C}\right) - \frac{\cos\phi}{Z\phi}J\right]\varphi_2(0^+) = 0. \tag{C5}$$

Using the symbols AA, BB, and DD given by

$$AA = -i\phi\left(\mu_1\alpha_1 - \mu_3\beta\frac{A}{C}\right) - i(1-\phi)\left(\alpha_1 - \beta\frac{A}{C}\right) - \frac{\cos\theta}{Z\phi}I, \tag{C6}$$

$$BB = -i\phi\left(\mu_2\alpha_2 - \mu_3\beta\frac{B}{c}\right) - i(1-\phi)\left(\alpha_2 - \beta\frac{B}{C}\right) - \frac{\cos\theta}{Z\phi}J, \tag{C7}$$

$$DD = \left(G - \frac{1-\phi}{\phi}I\right)BB - \left(H - \frac{1-\phi}{\phi}J\right)AA, \tag{C8}$$

$\varphi_1(0^+)$ and $\varphi_2(0^+)$, solutions of the system of equations (C4)–(C5) are given by

$$\varphi_1(0^+) = \frac{BB}{DD}, \tag{C9}$$

$$\varphi_2(0^+) = -\frac{AA}{DD}, \tag{C10}$$

and $V_z^s(\xi)$ is given by

$$V_z^s(\xi) = -i\left(\alpha_1 - \beta\frac{A}{C}\right)\frac{BB}{DD} + i\left(\alpha_2 - \beta\frac{B}{C}\right)\frac{AA}{DD}. \tag{C11}$$

From Eqs. (B11)–(B12), V_z^f and P are given by, respectively,

$$V_z^f(\xi) = -i\alpha_1(\phi\mu_1 + 1 - \phi)\frac{BB}{DD} + i\alpha_2(\phi\mu_2 + 1 - \phi)\frac{AA}{DD}, \tag{C12}$$

$$P(\xi) = -\frac{I}{\phi}\frac{BB}{DD} + \frac{J}{\phi}\frac{AA}{DD}. \tag{C13}$$

It can easily be shown that DD has the same zeros as the denominator of R in Apppendix B; $V^s(\sin\theta)$ and $R(\sin\theta)$ have the same singularities.

[1] M. A. Biot, ''Theory of propagation of elastic waves in a fluid-saturated porous solid,'' J. Acoust. Soc. Am. **28**, 168–191 (1956).
[2] H. Deresiewicz, ''The effect of boundaries on wave propagation in a liquid-filled porous solid. IV. Surface waves in a half space,'' Bull. Seismol. Soc. Am. **52**, 627–638 (1962).
[3] S. Feng and D. L. Johnson, ''High-frequency acoustic properties of a fluid/porous solid interface. I. New surface mode. II. The 2D reflection Green's function,'' J. Acoust. Soc. Am. **74**, 906–924 (1983).
[4] K. Wisse, ''On frequency dependence of acoustic wave in porous cylinders,'' Ph.D. thesis, Delft University of Technology, The Netherlands, 1999.
[5] J. F. Allard, *Propagation of Sound in Porous Media: Modelling Sound Absorbing Materials* (Chapman & Hall, London, 1993).
[6] W. Lauriks, L. Kelders, and J. F. Allard, ''Surface waves and leaky waves above a porous layer,'' Wave Motion **28**, 59–67 (1998).
[7] J. F. Allard, M. Henry, J. Tizianel, L. Kelders, and W. Lauriks, ''Surface waves above bead layers,'' J. Acoust. Soc. Am. **105**, 3021–3025 (1999).
[8] Ph. Leclaire, L. Kelders, W. Lauriks, M. Melon, N. Brown, and B. Castagnede, ''Determination of the viscous and the thermal characteristic lengths of plastic foams by ultrasonic measurements in helium and air,'' J. Appl. Phys. **80**, 2009–2012 (1996).
[9] Ph. Leclaire, L. Kelders, W. Lauriks, C. Glorieux, and J. Thoen, ''Determination of the viscous characteristic length in air-filled porous materials by ultrasonic attenuation measurements,'' J. Acoust. Soc. Am. **99**, 1944–1948 (1996).
[10] I. A. Victorov, *Rayleigh and Lamb Waves* (Plenum, New York, 1967).
[11] L. M. Brekhovskikh and O. A. Godin, *Acoustics of Layered Media II Point Sources and Bounded Beams*, Springer Series on Wave Phenomena (Springer, New York, 1992).
[12] W. M. Ewing, W. S. Jardetzsky, and F. Press, *Elastic Waves in Layered Media*, McGraw-Hill Series in the Geological Science (McGraw-Hill, New York, 1957).
[13] L. J. Gibson and M. F. Ashby, *Cellular Solids, Structure and Properties* (Pergamon, Oxford, 1988).
[14] M. Melon, E. Mariez, C. Ayrault, and S. Sahraoui, ''Acoustical and mechanical characterization of anisotropic open-cell foams,'' J. Acoust. Soc. Am. **104**, 2622–2627 (1998).
[15] G. Jansens, W. Lauriks, J. F. Allard, and G. Vermeir, ''Measurement of the dynamic shear modulus on poroelastic foams,'' Proceedings of Inter-Noise, The Hague, The Netherlands, 27–30 August 2001.

The role of Biot slow waves in electroseismic wave phenomena

Steven R. Pride[a)]
Université de Rennes 1, Géosciences Rennes, Campus Beaulieu, Bât. 15, 35042 Rennes Cedex, France

Stéphane Garambois[b)]
IGP, Université de Pau et des Pays de l'Adour, 64000 Pau Cedex, France

(Received 11 July 2001; revised 18 September 2001; accepted 22 November 2001)

The electromagnetic fields that are generated as a spherical seismic wave (either *P* or *S*) traverses an interface separating two porous materials are numerically modeled both with and without the generation of Biot slow waves at the interface. In the case of an incident fast-*P* wave, the predicted electric-field amplitudes when slow waves are neglected can easily be off by as much as an order of magnitude. In the case of an incident *S* wave, the error is much smaller (typically on the order of 10% or less) because not much *S*-wave energy gets converted into slow waves. In neglecting the slow waves, only six plane waves (reflected and transmitted fast-*P*, *S*, and EM waves) are available with which to match the eight continuity conditions that hold at each interface. This overdetermined problem is solved by placing weights on the eight continuity conditions so that those conditions that are most important for obtaining the proper response are emphasized. It is demonstrated that when slow waves are neglected, it is best to also neglect the continuity of the Darcy flow and fluid pressure across an interface. The principal conclusion of this work is that to properly model the electromagnetic (EM) fields generated at an interface by an incident seismic wave, the full Biot theory that allows for generation of slow waves must be employed. [DOI: 10.1121/1.1436066]

PACS numbers: 43.20.Gp, 43.20.Bi, 43.30.Ky [JJM]

I. INTRODUCTION

Biot's (1956a, b, 1962a, b) theory of mechanical wave propagation in porous materials is the proper general framework for studying the effects of fluid movement into and out of each element of the porous material during the passage of a seismic wave (either *P* or *S*). The theory provides a set of differential equations for predicting the average displacement **u** of the grains in each element as well as the average ''fluid-filtration'' displacement **w** defined so that $\partial \mathbf{w}/\partial t$ corresponds to the Darcy filtration velocity in each element. By allowing for the dynamics controlling both the fluid and solid responses, the theory predicts the existence of two longitudinal modes, the so-called ''fast'' and ''slow'' *P* waves. For the problem of seismic wave propagation in the earth for which frequencies are generally below the kHz level, the slow-*P* wave is essentially a pure fluid-pressure diffusion through the pores of the material, while the fast-*P* wave is the compressional wave observed on seismograms.

As will be shown here, it is possible to completely eliminate slow waves from Biot's theory by requiring that the linear relation between $\nabla \cdot \mathbf{u}$ and $\nabla \cdot \mathbf{w}$ is everywhere that appropriate to fast-*P* waves. The price paid in neglecting slow waves is that the boundary conditions at isolated interfaces can never be exactly satisfied. Stated more generally, if slow waves are neglected, the response determined in heterogeneous porous continua can never be exact. However, since not much energy goes into slow-wave generation at isolated interfaces one may ask whether the error made in neglecting slow waves is significant.

One known situation in which the neglect of slow waves leads to a significant error (White *et al.*, 1975; Norris, 1993; Gurevich and Lopatnikov, 1995; Gelinsky and Shapiro, 1997; Gelinsky *et al.*, 1998; Pride *et al.*, 2002) is when the porous material possesses fine layering relative to the fast-*P* wavelength. Since many layers are being compressed (or expanded) simultaneously by the fast-*P* wave and since each layer will have, in general, a different fluid-pressure response, there is a fluid-pressure-diffusion or ''slow-wave-mediated'' equilibration process set up between adjacent layers that can attenuate significant amounts of energy, especially at low frequencies. An analogous situation is Johnson's (2001) treatment of the patchy saturation problem. In both cases, the full Biot theory is required to properly model the fluid-pressure equilibration induced within an averaging volume. The Biot theory in these cases describes the local physics and upon averaging yields a macroscopic theory of viscoelasticity.

A central purpose of the present article is to give an example of a situation in which the macroscopic response itself requires a direct macroscopic modeling of the slow waves. When either *P* or *S* waves traverse interfaces in a porous material they generate electromagnetic (EM) fields through an electrokinetic mechanism (Thompson and Gist, 1993; Pride, 1994; Pride and Haartsen, 1996; Haartsen and Pride; 1997; Garambois and Dietrich, 2001; Garambois and Dietrich, 2002). Such seismic-to-EM coupling is called ''electroseismic'' phenomena. In the present article, we numerically model the EM field generated when a spherical seismic wave is incident at an interface. We perform the

a)Electronic mail: spride@univ-rennes1.fr
b)Electronic mail: Stephane.Garambois@ujf-grenoble.fr; present address LIRIGM, Université Joseph Fourier, BP 53, 38041, Grenoble Cedex 9, France.

simulations both with and without slow waves and demonstrate the essential role played by slow waves in fixing the amplitudes of such seismic-to-EM converted wave fields. The conclusion is that one cannot properly model the converted EM fields without allowing for slow waves.

Interestingly, the first paper that provided a quantitative theory for seismic waves in porous materials (Frenkel, 1944) had as its goal the explanation of electroseismic phenomena; however, Frenkel's formulation only allowed for the coseismic E-fields (those contained within the support of the seismic wave) and did not allow for any converted E-fields generated, for example, as a seismic wave traverses an interface. A further historical curiosity is that in Biot's final article concerning his linear theory of porous-media acoustics (Biot, 1962b), he concludes with a discussion of the role of his theory in modeling electroseismic phenomena. What follows are the final three sentences of Biot's (1962b) article:

> *An interesting aspect of this* [electroseismic] *phenomena is the-relative importance assumed by the wave of the second kind* [the slow wave] *as compared to the wave of the first kind* [the fast wave]. *We have shown that the wave of the second kind is associated with a larger relative velocity of the fluid in the pores. This should have an important bearing on the electrokinetic effect.*

The present article quantitatively confirms Biot's prediction.

II. DEFINING ELECTROSEISMIC RESPONSE

The governing equations controlling the complete electroseismic response when an $e^{-i\omega t}$ time dependence is assumed have been determined by Pride (1994)

$$\nabla\cdot\boldsymbol{\tau}=-\omega^2\rho\mathbf{u}-\omega^2\rho_f\mathbf{w}, \tag{1}$$

$$\boldsymbol{\tau}=-p_c\mathbf{I}+G[\nabla\mathbf{u}+(\nabla\mathbf{u})^T-\tfrac{2}{3}\nabla\cdot\mathbf{u}\mathbf{I}] \tag{2}$$

$$-\begin{bmatrix}p_c\\ p_f\end{bmatrix}=\begin{bmatrix}K_G & C\\ C & M\end{bmatrix}\cdot\begin{bmatrix}\nabla\cdot\mathbf{u}\\ \nabla\cdot\mathbf{w}\end{bmatrix} \tag{3}$$

$$-i\omega\mathbf{w}=\frac{k(\omega)}{\eta}[-\nabla p_f+\omega^2\rho_f\mathbf{u}]+L\mathbf{E}, \tag{4}$$

$$\mathbf{J}=L[-\nabla p_f+\omega^2\rho_f\mathbf{u}]+\sigma\mathbf{E}, \tag{5}$$

$$\nabla\times\mathbf{E}=i\omega\mu\mathbf{H}, \tag{6}$$

$$\nabla\times\mathbf{H}=-i\omega\varepsilon\mathbf{E}+\mathbf{J}. \tag{7}$$

Here, $\mathbf{u}$ and $\mathbf{w}$ are the displacements defined in the Introduction, while p_f is the average fluid pressure in the pores of an averaging element. The remaining response fields p_c, $\boldsymbol{\tau}$, $\mathbf{E}$, $\mathbf{H}$, and $\mathbf{J}$ represent averages throughout both the fluid and solid phases of each averaging element and are, respectively, the bulk pressure, stress tensor, electric field, magnetic field, and electric-current density at each point in the porous continuum. Definition of the various coefficients is given by Pride (1994) and are modeled here in the Appendix. If the electrokinetic-coupling constant L is set to zero, these equations exactly separate into Biot's equations and Maxwell's equations. By integrating each of the above equations over a disk that straddles an initially uncharged interface, it is easy to establish [Pride and Haartsen (1996)] that the quantities

$$\mathbf{n}\cdot\boldsymbol{\tau},\ \ \mathbf{u},\ \ \mathbf{n}\cdot\mathbf{w},\ \ -p_f,\ \ \mathbf{n}\times\mathbf{E},\ \ \mathbf{n}\times\mathbf{H} \tag{8}$$

must all be continuous across an interface possessing a normal $\mathbf{n}$. Generalization to the case of an initially charged interface is given by Pride and Haartsen (1996).

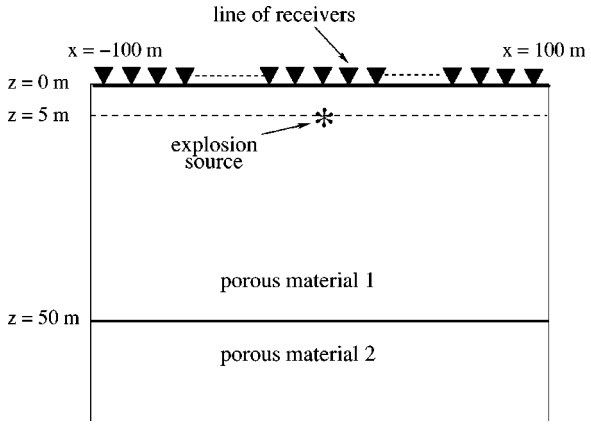

FIG. 1. The source, interface, and receiver locations used for all examples of this paper. There is no free surface at $z=0$ m.

Consider a spherical compressional wave propagating through a homogeneous porous material. A streaming electrical current $L(-\nabla p_f+\omega^2\rho_f\mathbf{u})$ is set up from regions of compression toward regions of dilation that results in an accumulation of charge of one sign in the peaks of the wave and of the opposite sign in the troughs. The $\mathbf{E}$ field associated with such half-wavelength scale charge separations then drives a conduction current $\sigma\mathbf{E}$ that exactly balances the streaming current so there is no net current inside the compressional wave. The charge density $\rho_e(\mathbf{r})$ within the support of the seismic wave is given by $\rho_e=\varepsilon\nabla\cdot\mathbf{E}$ so that from Eq. (5) we have $\rho_e=-(\varepsilon L/\sigma)\nabla\cdot(-\nabla p_f+\omega^2\rho_f\mathbf{u})$. Volume integrating $\nabla\cdot\mathbf{E}=\rho_e/\varepsilon$ over a Gaussian box that straddles the wavefront and completely contains the support of the seismic pulse, and using the fact that the volume integral of the charge density is zero (the wave separates charge but does not create charge) demonstrates that no electric fields are present outside the support of the compressional wave.

However, when the spherical wave is incident at an interface separating two different porous materials, the charge density distributed within the transmitted wave will be different, in general, than the charge density distributed in the combined incident and reflected pulses. This breaks the symmetry of the charge distribution that held before the spherical wave encountered the interface. There is thus created an effective charge separation (having a strong dipolar component) across the interface as the first Fresnel zone of the pulse traverses the interface. The electric fields generated by this dipole can be recorded at large distances from the interface.

These effects are now demonstrated numerically for the situation depicted in Fig. 1, in which a single plane interface is located at $z=50$ m and a point explosion source is located at $z=5$ m. Geophones and electrical and magnetic antennas are placed every 4 meters along a receiver line at $z=0$ m. Details of the numerical reflectivity algorithm that solves

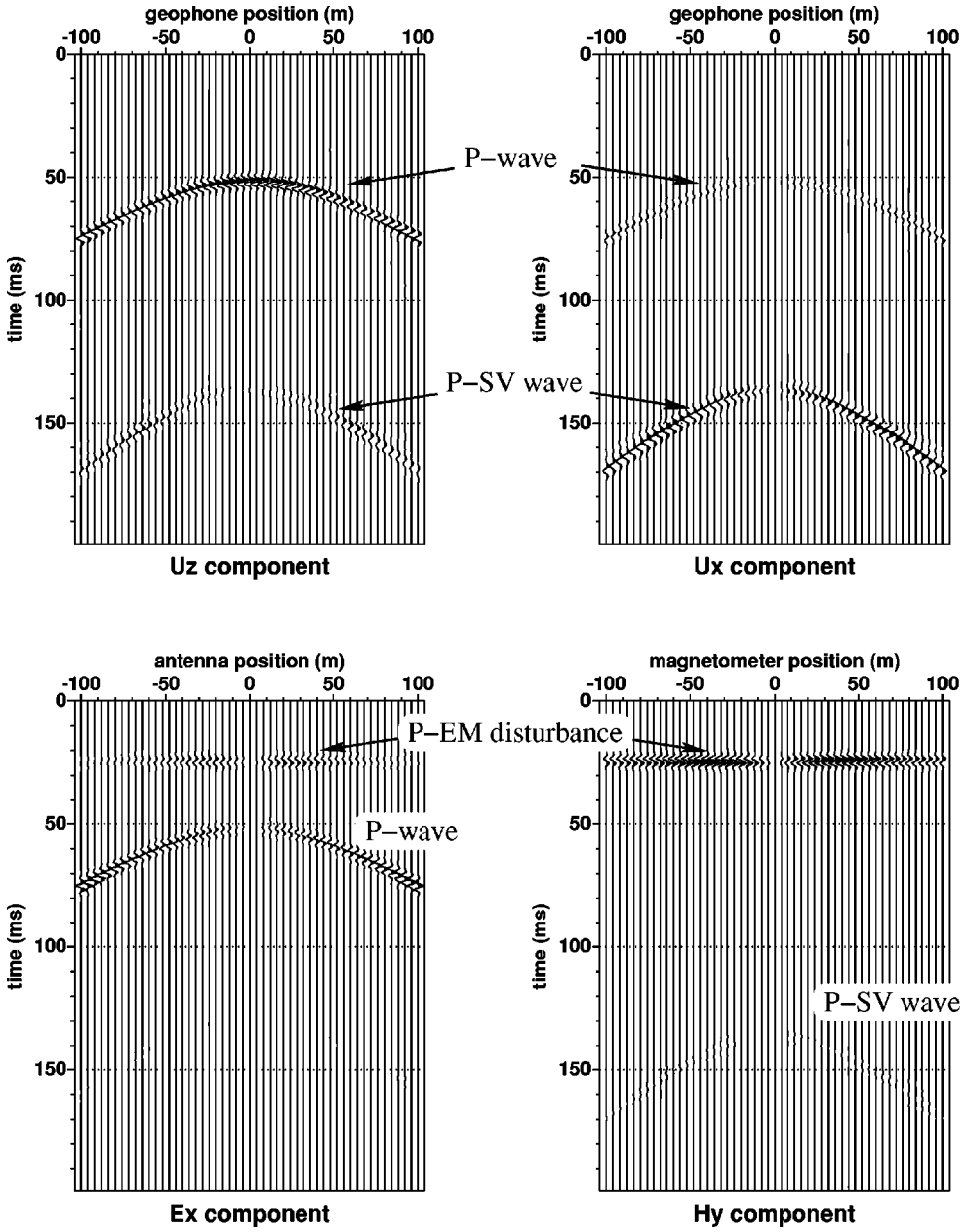

FIG. 2. An example of electroseismic response. The interface is located at a *P*-wave travel time of 21 ms. The no-moveout *P*-EM converted field generated as the *P* wave traverses the interface has been multiplied by 500 in both the electric and magnetic sections. The $P-SV$ conversion is just barely discernible on the magnetic section (the hyperbola at 132 ms).

Eqs. (1)–(7) while respecting the continuity conditions at each interface will be given later. The upper half-space is modeled as a sand while the lower half-space is modeled as a sandstone. Details of how we fix the material properties will also be given later.

In Fig. 2 are shown the displacements and electric and magnetic fields that are recorded along the line at $z=0$ m. We do not show the response of the direct *P* wave that travels in straight-line trajectory from the source to the receivers. At a time of $t=21$ ms, the *P* wave is incident at the interface and generates the symmetry-breaking charge separation discussed above. The associated electric and magnetic fields have essentially no moveout on the seismic time scale, as seen in the figure. For display purposes, such $P-$EM converted fields have been multiplied by a factor of 500 in both the electric and magnetic sections. At the interface, the *P* wave is reflected both into another *P* wave and an *S* wave. We observe the electric and magnetic fields contained within these reflected waves when they arrive at the antennas.

The no-moveout electric fields generated at the interface by the *P* wave are the fields of predominant interest in an electroseismic study. In the present example, these fields have an amplitude of about 10 μV/m along the receiver line at $z=0$ and are quite detectable in the field (e.g., Thompson and Gist, 1993). These converted EM fields are highly sensitive to the precise details of the fluid-pressure gradients in the immediate vicinity of the interface. The goal of this paper is to study the role played by Biot slow waves in fixing the amplitude of such no-moveout converted electric fields.

III. ELECTROSEIMSIC RESPONSE WITHOUT SLOW WAVES

A. Analytical considerations

If we place the transport equations for $-i\omega\mathbf{w}$ and $\mathbf{J}$ [Eqs. (4) and (5)] into their respective dynamical equations

[Eqs. (1) and (6)] and if we use Faraday's law in Ampère's law, we can write without approximation the two dynamical equations

$$\nabla\cdot\boldsymbol{\tau}-i\omega\frac{\rho_f k(\omega)}{\eta}\nabla p_f+\omega^2\rho\left(1-i\omega\frac{\rho_f^2 k(\omega)}{\rho\eta}\right)\mathbf{u}=-i\omega\rho_f L\mathbf{E} \tag{9}$$

$$-\nabla\times\nabla\times\mathbf{E}+\omega^2\varepsilon\left(1+\frac{i\sigma}{\omega\varepsilon}\right)\mathbf{E}=-i\omega\mu L(-\nabla p_f+\omega^2\rho_f\mathbf{u}) \tag{10}$$

that control the electroseismic response. The right-hand sides of these equations isolate the source terms responsible for cross coupling between the mechanical and electrical response.

Our approximation of neglecting slow-*P* waves amounts to writing a single additional relation

$$\nabla\cdot\mathbf{w}=\beta_L\nabla\cdot\mathbf{u}, \tag{11}$$

where an expression for β_L appropriate to fast-*P* waves will soon be derived. Note that the equivoluminal shear response also trivially satisfies this equation. The neglect of slow waves only affects the poroelastic constitutive laws, which are now given by

$$\boldsymbol{\tau}=(K_G+C\beta_L)\nabla\cdot\mathbf{u}\mathbf{I}+G[\nabla\mathbf{u}+(\nabla\mathbf{u})^T-\tfrac{2}{3}\nabla\cdot\mathbf{u}\mathbf{I}] \tag{12}$$

$$-p_f=(C+M\beta_L)\nabla\cdot\mathbf{u}. \tag{13}$$

Upon placing these ''slow-wave-free'' constitutive laws into the dynamical equations, we find that **u** and **E** are the only two independent fields to solve for. Simply by writing Eq. (11), **w** has been completely eliminated from the theory. Note, however, that **w** can still be determined from Eq. (4) if desired; i.e., our neglect of slow waves has not required that $\mathbf{w}=0$.

In the special case of a uniform porous material, the governing equations reduce to

$$[K_E(\omega)+G/3]\nabla\nabla\cdot\mathbf{u}+G\nabla^2\mathbf{u}+\omega^2\rho_E(\omega)\mathbf{u}=-i\omega\rho_f L\mathbf{E} \tag{14}$$

$$-\nabla\times\nabla\times\mathbf{E}+\omega^2\mu\varepsilon_E(\omega)\mathbf{E}=-i\omega\mu L[(C+M\beta_L)\nabla\nabla\cdot\mathbf{u}+\omega^2\rho_f\mathbf{u}]. \tag{15}$$

When $L=0$, these are the usual elastodynamic and electromagnetic wave equations in a material having effective properties given by

$$K_E(\omega)=(K_G+C\beta_L)\left[1+i\omega\frac{\rho_f k(\omega)}{\eta}\frac{C+M\beta_L}{K_G+C\beta_L}\right], \tag{16}$$

$$\rho_E(\omega)=\rho\left[1-i\omega\frac{\rho_f^2 k(\omega)}{\rho\eta}\right], \tag{17}$$

$$\varepsilon_E(\omega)=\varepsilon\left[1+\frac{i\sigma}{\varepsilon\omega}\right]. \tag{18}$$

Upon temporarily neglecting the electrokinetic coupling *L*, we obtain the complex compressional wave slowness s_p given by

$$s_p^2=\frac{\rho_E(\omega)}{K_E(\omega)+4G/3}. \tag{19}$$

The modification of this wave slowness due to the coupling coefficient *L* is, for all practical purposes, negligible [see Pride and Haartsen (1996) for both a discussion and exact expressions and numerical evaluations in the case where *L* is not neglected]. The coefficient β_L can be found by first taking the divergence of Eq. (1) to obtain

$$\nabla^2\left[\left(K_G+\frac{4G}{3}\right)\nabla\cdot\mathbf{u}+C\nabla\cdot\mathbf{w}\right]=-\omega^2\rho\nabla\cdot\mathbf{u}-\omega^2\rho_f\nabla\cdot\mathbf{w}. \tag{20}$$

For a plane *P* wave with spatial dependence $\exp(i\omega s_p\hat{\mathbf{k}}\cdot\mathbf{r})$ where $\hat{\mathbf{k}}$ is the propagation direction, we thus obtain

$$\beta_L\equiv\frac{\nabla\cdot\mathbf{w}}{\nabla\cdot\mathbf{u}}=-\frac{Hs_p^2(\omega)-\rho}{Cs_p^2(\omega)-\rho_f}, \tag{21}$$

where for convenience we have introduced Biot's *H* modulus defined as

$$H=K_G+4G/3. \tag{22}$$

Upon eliminating s_p^2 in Eq. (21) by introducing Eq. (19), we obtain the following quadratic equation for β_L:

$$a\beta_L^2+b\beta_L+c=0, \tag{23}$$

where the three coefficients are defined

$$a=C+i\omega\rho_f\frac{k}{\eta}M, \tag{24}$$

$$b=H+i\omega\rho_f\frac{k}{\eta}\left(2C+\frac{\rho}{\rho_f}M\right), \tag{25}$$

$$c=i\omega\rho_f\frac{k}{\eta}\left(H+\frac{\rho}{\rho_f}C\right). \tag{26}$$

The two roots correspond to the β_L for fast waves and slow waves. The fast-wave root of interest here is easily seen to be

$$\beta_L=-\frac{b}{2a}\left(1-\sqrt{1-\frac{4ac}{b^2}}\right). \tag{27}$$

For *P* waves in the seismic band of frequencies, we always have that $\omega\rho_f k/\eta\ll 1$, which allows us to write

$$\beta_L\to-i\omega\rho_f\frac{k}{\eta}\left(1+\frac{\rho}{\rho_f}\frac{C}{H}\right) \tag{28}$$

to leading order in the small dimensionless quantity $\omega\rho_f k/\eta$.

We have thus shown that our approximation of neglecting slow-*P* waves amounts to working with Eqs. (14) and (15) in each piecewise homogeneous portion of the porous material. The fast-*P* and *S* waves that are retained in this approximation have all the properties they usually have in Biot theory. But, by taking the β_L to be everywhere appropriate to fast-*P* waves, no slow waves can ever come into existence. The equation $\nabla\cdot\mathbf{w}=\beta_L\nabla\cdot\mathbf{u}$ is an additional constraint placed on the exact governing equations Eqs. (1)–(7) and in no way alters the requirement that all of the components in Eq. (8) should be continuous at an interface. There-

fore, the question of what continuity conditions to take at an interface when slow waves are neglected may not, at first sight, be entirely clear-cut.

However, in order that both P-SV and EM disturbances properly propagate across interfaces, we need to take the standard requirement that all of

$$\mathbf{u},\ \ \mathbf{n}\cdot\boldsymbol{\tau},\ \ \mathbf{n}\times\mathbf{E},\ \ \mathbf{n}\times\mathbf{H} \tag{29}$$

remain continuous when slow waves are neglected. This will be demonstrated numerically in the following subsection. Thus, when slow waves are neglected both p_f and $\mathbf{n}\cdot\mathbf{w}$ suffer jumps at interfaces.

Such an artificial jump in the fluid pressure at an interface created when slow waves are neglected has the effect of producing an effective electric dipole, as can be seen from the right-hand side of Eq. (10). Consider the extreme case of an interface in which only the permeability k changes with all other material properties held constant. In the exact treatment of the electroseismic response, the permeability contrast generates both transmitted and reflected slow waves. These slow waves alter the charge distribution that held in the spherically incident fast-P wave just prior to incidence and thus create an effective electric dipole (and higher-order multipoles) across the interface. The fast-P wave itself is not affected much by the permeability interface since never more than a few percent of the incident wave energy gets converted into slow waves (and typically much less). One might think, in this particular case, that the neglect of slow waves would lead to a large error in the predicted no-moveout electric field since it is the slow waves that have created the effective dipole.

However, as noted above, the jump in fluid pressure created when slow waves are neglected also produces an electric dipole. The fluid-pressure jump may be estimated from Eq. (13) using the fact that the permeability contrast has essentially no impact on the mechanical response of the fast-P and -S waves so that $\nabla\cdot\mathbf{u}$ remains essentially continuous at the interface (indeed, exactly continuous in the limit of very small frequencies). Upon using the β_L given by Eq. (28), we predict that the fluid pressure in the immediate vicinity of an interface located at $z=z_0$ is, in the low-frequency limit, distributed as

$$p_f(z)=i\omega\frac{\rho_f}{\eta}M\left(1+\frac{\rho}{\rho_f}\frac{C}{H}\right)\nabla\cdot\mathbf{u}[k_1+(k_2-k_1)H(z-z_0)], \tag{30}$$

where $H(z)$ is the Heaviside function, k_1 is the permeability of the overlying region, and k_2 that of the underlying region. We thus have that on the right-hand side of Eq. (10), there is an effective current dipole source $\mathbf{J}_e$ given by

$$\mathbf{J}_e=\omega^2\mu L\frac{\rho_f}{\eta}M\left(1+\frac{\rho}{\rho_f}\frac{C}{H}\right)\nabla\cdot\mathbf{u}(k_2-k_1)\,\delta(z-z_0)\hat{\mathbf{z}}. \tag{31}$$

We will see in a later numerical example that this effective electric dipole generated by the jump in fluid pressure when slow waves are neglected at a permeability contrast does a reasonable job at estimating the effects of the exact response involving slow waves. However, it will also be seen that when jumps in the elastic properties are also allowed for, the neglect of slow waves can lead to huge errors in the amplitudes of the predicted no-moveout electric fields.

B. Numerical considerations

We now show how to neglect slow waves in the numerical modeling. Both Haartsen and Pride (1997) and Garambois and Dietrich (2002) have given algorithms for determining the exact point-source electroseismic response for waves in stratified materials. These codes are based on Kennett's (1983) scheme for modeling seismic waves in layered media and begin by decomposing the wave fields into their plane-wave (or, more precisely, cylindrical-wave) components. The various decomposed plane-wave amplitudes are then determined by requiring that the continuity conditions that hold at each interface in the layer stack are exactly satisfied. Thus, proper modeling of how plane waves reflect and transmit at an isolated interface is a key part of the analysis. In the following subsection, we outline how to obtain the reflection and transmission coefficients when slow waves are neglected.

1. The response at a plane interface

Working in an (x,y,z) Cartesian system, consider that a fast-P plane wave in porous-material 1 is incident at a plane interface that separates material 1 from a second porous-material 2. If this interface is uncharged prior to the arrival of the P wave, we then have that [cf. Eq. (8)]

$$\underline{b}=[u_x,u_z,w_z,\tau_{xz},\tau_{zz},-p_f,H_y,E_x]^T \tag{32}$$

must be continuous across the interface (note that an underscore is used to denote an array while boldfaced symbols are used to denote vectorial and tensorial field quantities). Thus, at each interface we must satisfy the eight required equations $\underline{b}_1=\underline{b}_2$. To exactly allow for all eight of these conditions, one must allow for the creation of eight distinct waves which are the reflected and transmitted fast-P, slow-P, S, and EM responses. This is what Haartsen and Pride (1997) and Garambois and Dietrich (2002) have done. Without the slow waves we cannot exactly satisfy all eight continuity conditions, and our goal is to quantify the amount of error this causes in the predicted no-moveout electric fields.

The full 8×8 eigenvector matrix $\underline{\underline{D}}$ appropriate to the electroseismic problem (e.g., Haartsen and Pride, 1997) has the form

$$\underline{\underline{D}}=[\underline{b}^{u}_{pf},\underline{b}^{u}_{ps},\underline{b}^{u}_{s},\underline{b}^{u}_{em},\underline{b}^{d}_{pf},\underline{b}^{d}_{ps},\underline{b}^{d}_{s},\underline{b}^{d}_{em}], \tag{33}$$

where each column is the normalized plane-wave response of the stated wave type [e.g., $\underline{b}^{d}_{ps}$ is the response of a unit-amplitude downgoing slow-P wave where the physical components of $\underline{b}$ are those defined in Eq. (32)]. Analytical expressions for these various columns were initially worked out by Pride and Haartsen (1996) and are also given in Haartsen and Pride (1997). We now simply eliminate the two slow-wave columns and attempt to approximate the complete material response in each layer with only six wave types. In other words, with the definitions

$$\underline{\underline{D}}^{8\times6}=[\underline{b}^{u}_{pf},\underline{b}^{u}_{s},\underline{b}^{u}_{em},\underline{b}^{d}_{pf},\underline{b}^{d}_{s},\underline{b}^{d}_{em}], \tag{34}$$

$$\underline{w}=[w_{pf}^{u},w_{s}^{u},w_{em}^{u},w_{pf}^{d},w_{s}^{d},w_{em}^{d}]^{T}, \tag{35}$$

where the components of $\underline{w}$ are the (complex) amplitudes of the six wave types being allowed for in the approximation, we attempt to find the amplitudes $\underline{w}$ that best satisfy

$$\underline{\underline{D}}^{8\times 6}\cdot\underline{w}=\underline{b} \tag{36}$$

in each layer where $\underline{b}$ is the eight-component array defined in Eq. (32).

For the specific problem in which a unit-amplitude fast-*P* wave is incident from above at a plane interface, the eight continuity conditions $\underline{b}_1=\underline{b}_2$ are written

$$\begin{pmatrix}\underline{\underline{M}}_1^{u} & \underline{\underline{M}}_1^{d}\\ \underline{\underline{N}}_1^{u} & \underline{\underline{N}}_1^{d}\end{pmatrix}\cdot\begin{pmatrix}R_{pf}\\ R_{s}\\ R_{em}\\ 1\\ 0\\ 0\end{pmatrix}=\begin{pmatrix}\underline{\underline{M}}_2^{u} & \underline{\underline{M}}_2^{d}\\ \underline{\underline{N}}_2^{u} & \underline{\underline{N}}_2^{d}\end{pmatrix}\cdot\begin{pmatrix}0\\ 0\\ 0\\ T_{pf}\\ T_{s}\\ T_{em}\end{pmatrix}, \tag{37}$$

where the matrices $\underline{\underline{M}}^{u,d}$ and $\underline{\underline{N}}^{u,d}$ are the 4×3 partitions of the eigenvector matrix $\underline{\underline{D}}^{8\times 6}$. These equations can be rewritten as the overdetermined system

$$\underline{\underline{A}}\cdot\underline{x}=\underline{y}, \tag{38}$$

where $\underline{\underline{A}}$ is the 8×6 matrix

$$\underline{\underline{A}}=\begin{pmatrix}\underline{\underline{M}}_1^{u} & -\underline{\underline{M}}_2^{d}\\ \underline{\underline{N}}_1^{u} & -\underline{\underline{N}}_2^{d}\end{pmatrix}, \tag{39}$$

$\underline{x}$ contains the six unknown reflection and transmission coefficients of interest

$$\underline{x}=[R_{pf},R_{s},R_{em},T_{pf},T_{s},T_{em}]^{T}, \tag{40}$$

and $\underline{y}=-\underline{b}_{pf}^{d}$ is the negative of the response (eigenvector) of a unit-amplitude downgoing fast-*P* wave (the normalizations of the eigenvectors fix the physical interpretation of the reflection and transmission coefficients but otherwise play no role in obtaining the numerical results).

We solve for the reflection and transmission coefficients $\underline{x}$ by first placing weights p_i on each of the eight continuity conditions. These weights simply emphasize the importance given to satisfying any one condition. The only restriction on these weights is that no more than two of them can be zero so that the system never becomes underdetermined. Thus, following the usual least-squares argument, we determine $\underline{x}$ by minimizing the χ^2 error measure

$$\chi^2=\sum_{i=1}^{8}\sum_{j=1}^{6}[p_i(y_i-A_{ij}x_j)]^2. \tag{41}$$

As is well-known and simply demonstrated, the $\underline{x}$ that minimizes χ^2 is a solution of the following even (6×6) set of ''normal equations''

$$(\underline{\underline{A}}^{T}\cdot\underline{\underline{\Lambda}}\cdot\underline{\underline{A}})\cdot\underline{x}=(\underline{\underline{A}}^{T}\cdot\underline{\underline{\Lambda}})\cdot\underline{y}, \tag{42}$$

where the diagonal matrix $\underline{\underline{\Lambda}}$ has the weights p_i^2 along the diagonal and zeros elsewhere; i.e.,

$$\underline{\underline{\Lambda}}=\mathrm{diag}\{p_i^2\}. \tag{43}$$

In the subsection that follows, we numerically investigate the question of which two of the p_i are best set to zero; i.e., which of the continuity equations can be neglected without creating considerable error.

2. Defining the weighting scheme

Although we anticipate from our earlier analytical considerations that the best approximation is to neglect the continuity of w_z and p_f (i.e., $p_3=p_6=0$), we now numerically test this hypothesis.

A solution of the normal equations (42) for any given weighting of the eight continuity conditions determines the reflection and transmission coefficients at each isolated interface in a layer stack when no slow waves have been generated. The reflection and transmission coefficients at each interface are the fundamental material-property inputs for Kennett's (1983) reflectivity scheme. Garambois and Dietrich (2002) have generalized the reflectivity scheme to the electroseismic problem, and it is their code that is employed for the numerical simulations that follow and in the electroseismic response already shown in Fig. 2. Haartsen and Pride (1997) used the global-matrix approach, which is slightly different and will not be used here.

We again consider the simple geometry depicted in Fig. 1. Details of how to model a point-source explosion are given by Haartsen and Pride (1997) as well as by Garambois and Dietrich (2002). A Ricker wavelet with a center frequency of 200 Hz is chosen as the time signature of the source. Due to the rather large number of physical properties, we give a model in the Appendix that reduces the total number of free parameters down to just four: C (the salinity of the water in moles/liter), ϕ (the porosity), a (a dimensionless parameter defined in the Appendix that measures the degree of consolidation of the framework of grains), and k_0 (the dc permeability). This model is based on assuming the fluid is always water and the solid grains are always quartz. The properties of our two half-spaces are thus fixed by fixing these four parameters in each material.

Both in the present test and in the response of Fig. 2, we take the overlying material to be a sand characterized by $C_1=10^{-4}$ moles/liter, $\phi_1=0.35$, $a_1=100$, and $k_{01}=10^{-11}$ m^2. The underlying material is a sandstone characterized by $C_2=10^{-4}$ moles per liter, $\phi_2=0.20$, $a_2=10$, and $k_{02}=10^{-14}$ m^2. In Fig. 3, we give the amplitude of the reflected *P* wave when slow waves are neglected and when continuity of the pairs of components shown has been neglected at the interface. As anticipated, the exact result involving slow waves is indistinguishable from the case where slow waves are neglected and the continuity of w_z and p_f is neglected. Any other approximation of the exact continuity conditions leads to unacceptable error. In Fig. 4 the amplitude of the converted no-moveout electric field generated when the *P* wave traverses the interface is shown. Although, in the no-slow-wave approximation, neglecting the continuity of w_z and τ_{zz} provides a slightly better approximation than neglecting w_z and p_f, we have seen in Fig. 3 that it provides a much worse approximation of the reflected *P* wave.

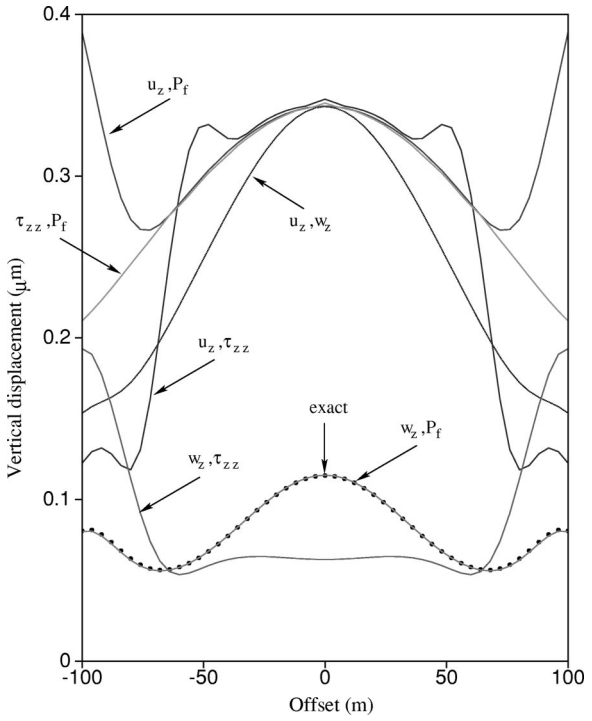

FIG. 3. The amplitude of the reflected P wave when slow waves are neglected and the continuity of the various shown displacement-stress components is neglected at the interface. The exact response with slow waves is shown both here and in all examples using dot symbols. This figure demonstrates that one must sacrifice the continuity of w_z and p_f when slow waves are neglected.

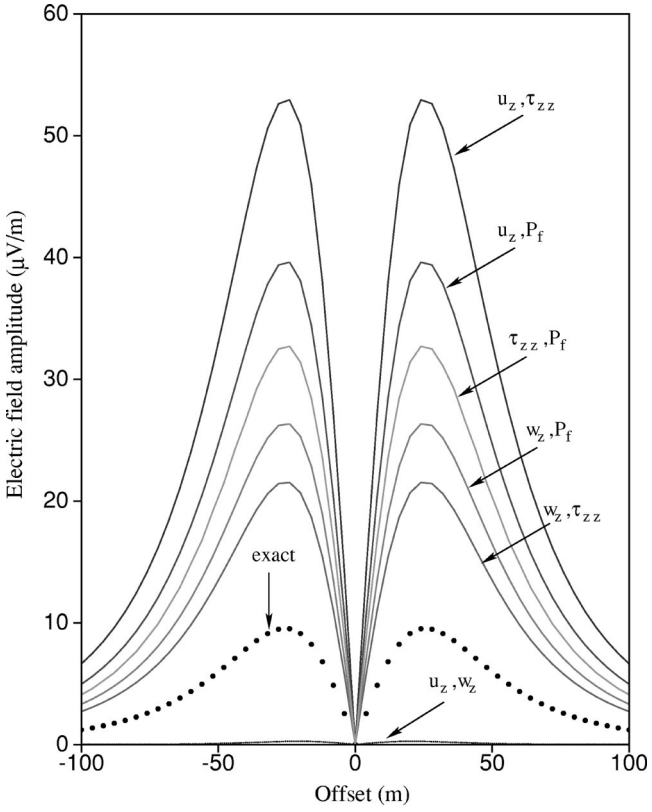

FIG. 4. The amplitude of the converted no-moveout electric field generated when the P wave is incident at the interface and recorded along the receiver line.

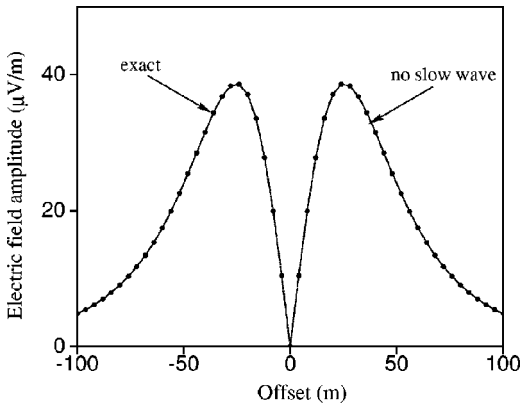

FIG. 5. The amplitude of the converted no-moveout electric field when the interface represents only a salinity jump.

The conclusion is that when slow waves are neglected, we must also neglect the continuity of w_z and p_f; neglect of any other combination leads to unacceptably large error. We also see that for a realistically modeled sand/sandstone interface, the neglect of slow waves has led to a converted electric-field amplitude that is almost three times too big. Proper modeling of the converted electric field in this case requires the explicit generation of slow waves. We now go on to consider other examples.

IV. NUMERICAL EXAMPLES

Five examples will be given here that serve to further illustrate the role of slow waves in the generation of the electroseismic converted field. For all of these examples, the modeling without slow waves has neglected the continuity of w_z and p_f at the interface.

A. Salinity contrast

We begin with a test example in which the contrast is only in the salinity. In this case, there is no way for the fast-P wave to change properties as it traverses the interface, and so no slow waves are generated. Accordingly, we expect no slow-wave effect in the electroseismic response. The material properties are taken everywhere to be those of a sand: $\phi=0.35$, $a=100$, and $k_0=10^{-11}$ m^2. The salinity contrast is defined by $C_1=10^{-4}$ moles/liter and $C_2=10^{-1}$ moles/liter.

In Fig. 5, we see indeed that the modeling both with and without slow waves leads to virtually identical results. We take this to be a positive numerical check of our modeling.

B. Permeability contrast

This was the case considered earlier in our analytical discussion. For the numerical example, we take the material to have everywhere the same properties of $C=10^{-4}$ moles/liter, $\phi=0.35$, $a=100$, but we now take the overlying material to have a permeability of $k_{01}=10^{-11}$ m^2 and the underlying material to have a permeability of $k_{02}=10^{-14}$ m^2.

In Fig. 6 the somewhat surprising result that the result without slow waves is almost as good as the result with

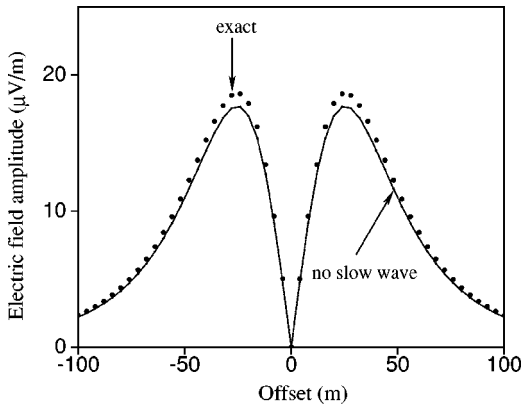

FIG. 6. The amplitude of the converted no-moveout electric field when the interface represents only a permeability jump.

slowwaves is seen. As discussed earlier, this is due to the artificial fluid-pressure jump in the modeling without slow waves acting as a current-dipole source in Ampère's law. However, this result is rather particular and requires that the jump in permeability not be accompanied by a jump in the elastic properties, a situation that never holds true in the earth.

C. Elastic-property contrast

In this example, we keep both the permeability and salinity constant everywhere, given by $k_0 = 10^{-11}$ m^2 and $C = 10^{-4}$ moles/liter. The jump is only in the elastic properties with $\phi_1 = 0.35$, $a_1 = 100$ and $\phi_2 = 0.20$, $a_2 = 10$. See Fig. 7.

We see that there is now a rather large error of about a factor of 7 in the predicted converted electric-field amplitude.

D. Sandstone 1/sandstone 2 interface

In this example, we attempt to model a typical interface that might be found at depth in a sedimentary basin. The overlying material is taken to be a well-consolidated sandstone having $\phi_1 = 0.10$, $a_1 = 5$, and $k_{01} = 10^{-15}$ m^2, while the underlying material is taken to be a much cleaner sandstone having $\phi_2 = 0.25$, $a_2 = 50$, and $k_{02} = 10^{-13}$ m^2. The same salinity $C = 10^{-2}$ moles/liter is present everywhere.

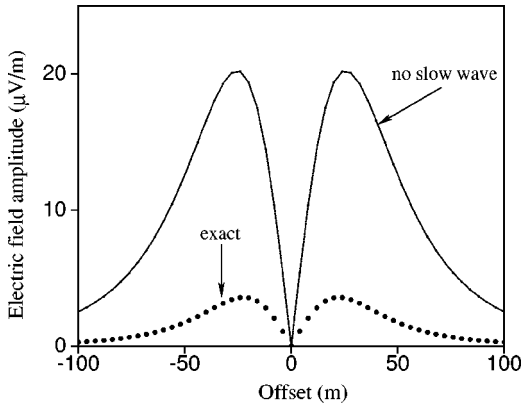

FIG. 7. The amplitude of the converted no-moveout electric field when the interface represents only a jump in elastic properties with permeability and salinity held constant.

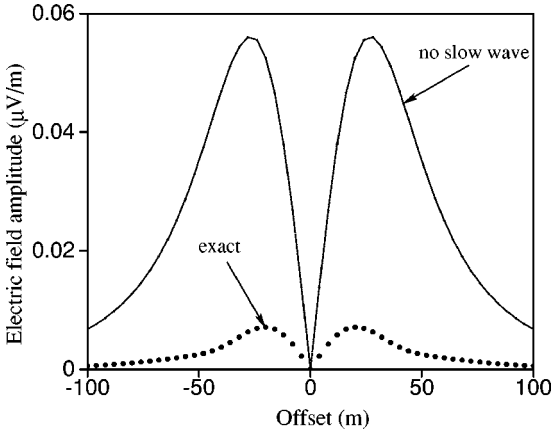

FIG. 8. The amplitude of the converted no-moveout electric field when the interface separates a well-consolidated sandstone from a relatively clean sandstone. This example is meant to represent a typical interface that might be found in a sedimentary basin.

In this case, the generation of both slow waves and the associated separation of charge is reduced compared to the previous examples due to both sides of the interface now having relatively stiff frameworks of grains. This is manifest in much smaller electric-field amplitudes. We again see in Fig. 8 that the full Biot theory is required in order to properly model the electroseismic response. The neglect of slow waves in this example has overestimated the converted electric field by more than a factor of 8. As compared to previous examples, the spatial distribution of the electric-field amplitudes with and without slow waves have different shapes. This is because the incident *P*-wave wavelength of roughly 17 m is much longer than in the previous examples and it now represents a significant fraction of the 45 m between the shot point and interface which changes the dimensions of the first Fresnel zone and the nature of the charge distribution relative to the antenna positions.

E. Incident shear wave

In this final example, a hammer source is now used that generates both compressional and shear waves. Our interest here is to study the EM conversion generated when the shear wave is incident at the interface. We consider the same sand/sandstone interface used in Figs. 2–4. With a shear wave incident at the interface, there is a discontinuity in the electrical-current sheets of the *S* waves. Such current sheets are entirely due to streaming current since there are no charge separations and, therefore, no electric fields inside a shear wave in a uniform material. The current-sheet discontinuity leads to charge separations across the interface and to converted no-moveout electric fields.

The slow waves converted from the incident shear wave act to further alter the amount of separated charge at the interface. However, in Fig. 9 we see that the effect is not very large. This is due to the fact that only a small amount of energy goes into slow waves when shear waves traverse an interface. In general, the seismic-EM converted wave fields are sensitive to the permeability contrast only through the generation of slow waves. Thus, the *S*–EM conversions are rather insensitive to the permeability contrast.

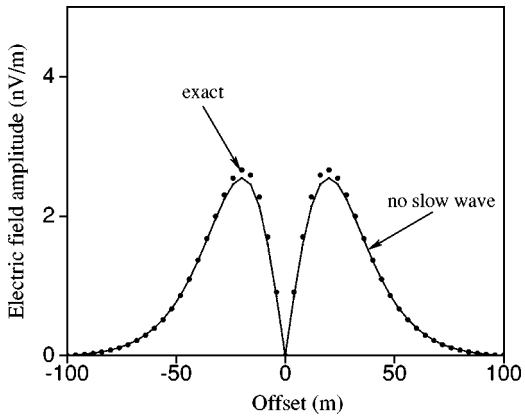

FIG. 9. The amplitude of the converted no-moveout electric field when the incident wave is a spherical shear wave coming from a shear-wave-generating "hammer" source again at $z=5$ m. The interface is the same sand/sandstone interface considered in Fig. 4.

V. CONCLUSIONS

We have numerically demonstrated that in order to properly model the generation of electric fields-when seismic waves traverse an interface, one must employ the full Biot theory in the modeling and take into account the generation of slow waves. This is the only way to properly model the details of the fluid-pressure gradients in the vicinity of the interface upon which the electrokinetically induced charge separations sensitively depend. The electroseismic problem may thus represent one of the most important applications of Biot's theory of porous media acoustics.

ACKNOWLEDGMENTS

S.R.P. would like to thank the Geophysics Department at Stanford University and the Stanford Rock Physics and Borehole Consortium (S.R.B.) for providing support during his sabbatical there. S.G. thanks TotalFinaElf for the support they have provided him. The comments of both reviewers are appreciated.

APPENDIX: THE ELECTROSEISMIC MATERIAL PROPERTIES

For the poroelastic moduli, we use the results of Biot and Willis (1957) that hold whenever the grains consist of a single isotropic mineral. These expressions can be written

$$K_G=\frac{K_D+[1-(1+\phi)K_D/K_s]K_f/\phi}{1+\Delta}, \tag{A1}$$

$$C=\frac{(1-K_D/K_s)K_f/\phi}{1+\Delta}, \tag{A2}$$

$$M=\frac{K_f/\phi}{1+\Delta}, \tag{A3}$$

where Δ is a small dimensionless parameter defined as

$$\Delta=\frac{1-\phi}{\phi}\frac{K_f}{K_s}\left(1-\frac{K_D}{(1-\phi)K_s}\right). \tag{A4}$$

Here, ϕ is the porosity, K_f is the fluid's bulk modulus, and K_s is the solid's bulk modulus. In the numerical examples, we will always take the fluid to be water ($K_f=2.2$ GPa) and the solid to be quartz ($K_s=36$ GPa). The drained bulk modulus K_D and shear modulus G of the framework of grains are assumed to obey simple effective-medium laws of the form [pore-inclusion-based effective-medium theories such as Korringa *et al.* (1979) predict drained moduli of this form]

$$K_D=K_s\frac{1-\phi}{1+a\phi}, \tag{A5}$$

$$G=G_s\frac{1-\phi}{1+b\phi}, \tag{A6}$$

where a and b will vary with lithology and G_s is taken to be the shear modulus of pure quartz 44 GPa. In the numerical simulations, we somewhat arbitrarily take $b=2a$ in order to eliminate a model parameter. Thus, using the above expressions, the poroelastic moduli K_G, C, M, and G are fixed by specifying the two dimensionless numbers ϕ and a. Depending on the assumed consolidation of the framework of grains, we can expect a to have a rather large range from roughly 3 for a highly consolidated sandstone to as much as 300 for an unconsolidated sand.

Other parameters to be fixed in the model are the transport coefficients k (fluid-flow permeability), σ (conductivity of the porous material) and L (the coupling coefficient). For the permeability we use the result of Johnson *et al.* (1987)

$$\frac{k(\omega)}{k_0}=\left[\sqrt{1-i\frac{\omega}{\omega_c}\frac{4}{n}}-i\frac{\omega}{\omega_c}\right]^{-1}, \tag{A7}$$

where k_0 is the dc permeability and the frequency ω_c corresponds to when viscous-boundary layers begin to form in the pores. Johnson's model predicts that

$$\omega_c=\frac{\eta}{\rho_f F k_0}, \tag{A8}$$

where η is the water viscosity 10^{-3} Pa s, ρ_f the water density 10^3 kg/m^3, and F the electrical formation factor. In this work, we assume Archie's (1942) law to hold

$$\frac{1}{F}=\phi^m, \tag{A9}$$

with a constant Archie exponent of $m=1.7$ for all materials. Depending on the permeability and porosity, one can expect that $\omega_c/2\pi>1$ kHz (and usually dramatically so for rocks) so our assumed source puts us in the lower-frequency range where no viscous-boundary layers have yet developed in the pores. Because of this, we make no great effort to model the pore-geometery terms contained within n. Johnson's model predicts that $n=\Lambda^2/(k_0F)$, where Λ is a weighted pore-volume to pore-surface ratio; however, we simply take $n=8$ for all materials.

The electrical conductivity of the porous material is

$$\sigma=\sigma_f/F, \tag{A10}$$

where F is again the formation factor given by Archie's law and σ_f is the conductivity of the water. We specify the water conductivity by fixing the molarity C (moles/liter) of NaCl in

the water and use the Einstein–Stokes estimate of the ionic mobilities to give the mks estimate

$$\sigma_f = \frac{e^2}{6\pi\eta}\left(\frac{1}{R_{\mathrm{Na}}}+\frac{1}{R_{\mathrm{Cl}}}\right)6.022\times 10^{26} C, \tag{A11}$$

where $R_{\mathrm{Na}}=1.83\times 10^{-10}$ m, $R_{\mathrm{Cl}}=1.20\times 10^{-10}$ m, and e is the fundamental charge.

The coupling coefficient L is given by

$$L=-\frac{\epsilon_0\kappa_f}{F\eta}\zeta, \tag{A12}$$

where ϵ_0 is the vacuum permittivity, $\kappa_f=80$ is the dielectric constant of water, and the ζ potential is a measure of the charge available for transport in the diffuse part of the electric double layer and is assumed to comply with the following empirical law that is roughly appropriate for quartz (this law holds strictly only for $p\mathrm{H}=7$ but gives the right general trend for the pH dependence):

$$\zeta(\text{in volts}) = (0.01+0.025\log_{10} C)\frac{(p\mathrm{H}-2)}{5}. \tag{A13}$$

In all examples we take $p\mathrm{H}=7$. Because the frequency of our source is such that $\sigma \gg \omega\epsilon$, we will not attempt to model precisely the rock's dielectric properties and will simply take $\varepsilon=\epsilon_0\kappa_f/F$ as our estimate of the rock permittivity. The magnetic permeability is taken to be that of vacuum $\mu=\mu_0$.

Thus, despite the rather large number of parameters involved, by assuming the fluid to be water and the grains to be quartz we have reduced the material properties down to just the following four free parameters: C (molarity), ϕ (porosity), a (frame compliance factor), and k_0 (dc permeability).

Archie, G. E. (**1942**). ''The electrical resistivity log as an aid in determining some reservoir characteristics,'' Trans. AIME **146**, 54–62.

Biot, M. A. (**1956a**). ''Theory of propagation of elastic waves in a fluid-saturated porous solid. I. Low-frequency range,'' J. Acoust. Soc. Am. **28**, 168–178.

Biot, M. A. (**1956b**). ''Theory of propagation of elastic waves in a fluid-saturated porous solid. II. Higher frequency range,'' J. Acoust. Soc. Am. **28**, 179–191.

Biot, M. A. (**1962a**). ''Mechanics of deformation and acoustic propagation in porous media,'' J. Appl. Phys. **33**, 1482–1498.

Biot, M. A. (**1962b**). ''Generalized theory of acoustic propagation in porous dissipative media,'' J. Acoust. Soc. Am. **34**, 1254–1264.

Biot, M. A., and Willis, D. G. (**1957**). ''The elastic coefficients of the theory of consolidation,'' J. Appl. Mech. **24**, 594–601.

Frenkel, J. (**1944**). ''On the theory of seismic and seismoelectric phenomena in a moist soil,'' J. Phys. (Soviet) **8**, 230–241.

Garambois, S., and Dietrich, M. (**2001**). ''Seismo-electric wave conversions in porous media: Field measurements and transfer function analysis,'' Geophysics **66**, 1417–1430.

Garambois, S., and Dietrich, M. (**2002**). ''Full-waveform numerical simulations of seismo-electromagnetic wave conversions in fluid-saturated stratified porous media,'' J. Geophys. Res. (in press).

Gelinsky, S., and Shapiro, S. A. (**1997**). ''Dynamic-equivalent medium approach for thinly layered saturated sediments,'' Geophys. J. Int. **128**, F1–F4.

Gelinsky, S., Shapiro, S. A., Müller, T., and Gurevich, B. (**1998**). ''Dynamic poroelasticity of thinly layered structures,'' Int. J. Solids Struct. **35**, 4739–4751.

Gurevich, B., and Lopatnikov, S. L. (**1995**). ''Velocity and attenuation of elastic waves in finely layered porous rocks,'' Geophys. J. Int. **121**, 933–947.

Haartsen, M. W., and Pride, S. R. (**1997**). ''Electroseismic waves from point sources in layered media,'' J. Geophys. Res. **102**, 24745–24769.

Johnson, D. L., Koplik, J., and Dashen, R. (**1987**). ''Theory of dynamic permeability and tortuosity in fluid-saturated porous media,'' J. Fluid Mech. **176**, 379–402.

Johnson, D. L. (**2001**). ''Theory of frequency dependent acoustics in patchy-saturated porous media,'' J. Acoust. Soc. Am. **110**, 682–694.

Kennett, B. L. N. (**1983**). *Seismic Wave Propagation in Stratified Media* (Cambridge University Press, Cambridge).

Korringa, J., Brown, R. J. S., Thompson, D. D., and Runge, R. J. (**1979**). ''Self-consistent imbedding and the ellipsoidal model for porous rocks,'' J. Geophys. Res. **84**, 5591–5598.

Norris, A. N. (**1993**). ''Low-frequency dispersion and attenuation in partially saturated rocks,'' J. Acoust. Soc. Am. **94**, 359–370.

Pride, S. R. (**1994**). ''Governing equations for the coupled electromagnetics and acoustics of porous media,'' Phys. Rev. B **50**, 15678–15696.

Pride, S. R., and Haartsen, M. W. (**1996**). ''Electroseismic wave properties,'' J. Acoust. Soc. Am. **100**, 1301–1315.

Pride, S. R., Tromeur, E., and Berryman, J. G. (**2002**). ''Biot slow-wave effects in stratified rocks,'' Geophysics **67**, 1–11.

Thompson, A., and Gist, G. (**1993**). ''Geophysical applications of electrokinetic conversion,'' The Leading Edge **12**, 1169–1173.

White, J. E., Mikhaylova, N. G., and Lyakhovitsky, F. M. (**1975**). ''Low-frequency seismic waves in fluid-saturated layered rocks,'' Izv., Acad. Sci., USSR, Phys. Solid Earth **11**, 654–659.

Measurement of the *B*/*A* nonlinearity parameter under high pressure: Application to water

F. Plantier, J. L. Daridon, and B. Lagourette
Laboratoire des Fluides Complexes, Faculté des Sciences et Techniques, BP 1155, 64013 Pau Cedex, France

(Received 9 February 2001; accepted for publication 6 November 2001)

An experimental apparatus was developed to measure, over a wide range of pressure, the acoustical nonlinear parameter *B/A* with an uncertainty of 2.2% in order to study the influence of pressure on the value of this parameter in liquids. The experimental technique rests on an improved thermodynamic method which uses a highly sensitive phase comparison technique to measure the change in speed of sound with pressure. The apparatus was then used to measure *B/A* in water within the pressure range from 0.1 to 50 MPa and at temperatures of between 303.15 and 373.15 K. The data obtained were compared with those in the literature which come from numerical derivation of speed of sound measurements. © *2002 Acoustical Society of America.* [DOI: 10.1121/1.1432978]

PACS numbers: 43.25.Ba [MFH]

I. INTRODUCTION

The nonlinear acoustic parameter *B/A*, also known as the Beyer parameter, is a physical property which can provide information on certain characteristics of the liquid state, such as internal pressure, intermolecular spacing, acoustic diffraction, all these characteristics are directly linked to the molecular structure of the fluids considered. This useful feature explains the fact that various experimental techniques (such as the phase comparison method,[1] or the finite amplitude method[2]) have been developed under atmospheric pressure with a view to achieving direct measurement of the *B/A* ratio, and that a substantial volume of work, both experimental and theoretical, has been devoted to it. In particular the behavior of *B/A* as a function of temperature has been studied in a number of investigations in extremely varied systems, and with objectives reflecting a very wide range of applications (biological, chemical, medical, acoustic, etc.).

Studies of the behavior of *B/A* as a function of pressure are much rarer and essentially involve numerical evaluations by derivation of ultrasound data, density and heat capacity at a given *P*, or estimations based on equations of state used to generate the necessary thermodynamic data. However, it is well known that properties deduced by successive numerical derivations are often subject to significant inaccuracies. The same holds for the use of equations of state in pure prediction. In the case of the *B/A* parameter, the accumulation of uncertainties affecting the contributive terms may reach substantial orders of magnitude. So, for a given family of organic substances (for example, the alkanes), evaluations carried out by different research teams[3,4] on the basis of distinct sources of information may yield diametrically opposed results. It is therefore essential to test the reliability of numerical methods by comparison with direct experimental determinations in order to validate these numerical techniques.

In this context we developed a system to measure *B/A* on the basis of a phase comparison method[5] able to function up to pressures of the order of 100 MPa. After recalling the main stages in the measurement of *B/A* by phase comparison, the first part of this article will describe in detail the characteristics of the measurement cell designed for this purpose. The second part will present values of *B/A* measured in the case of liquid water within a pressure interval of 0.1–50 MPa and at temperatures of between 303.15 and 373.15 K. Finally, the data obtained will be compared with those in the literature.

II. PHASE COMPARISON METHOD

The difference between instantaneous pressure P and hydrostatic pressure P_0 during the propagation of a plane acoustic wave can be developed, at values close to zero, in the form of a Taylor series expressed in terms of density $(\rho-\rho_0)$:

$$P=P_0+A\left(\frac{\rho-\rho_0}{\rho_0}\right)+\frac{B}{2}\left(\frac{\rho-\rho_0}{\rho_0}\right)^2+\frac{C}{6}\left(\frac{\rho-\rho_0}{\rho_0}\right)^3+\cdots \tag{1}$$

involving coefficients A, B, C defined by :

$$A=\rho_0\left(\frac{\partial P}{\partial \rho}\right)_S=\rho_0 c_0^2, \tag{2}$$

$$B=\rho_0^2\left(\frac{\partial^2 P}{\partial \rho^2}\right)_S=2\rho_0^2 c_0^3\left(\frac{\partial c}{\partial P}\right)_S, \tag{3}$$

$$C=\rho_0^3\left(\frac{\partial^3 P}{\partial \rho^3}\right)_S \tag{4}$$

in which c designates the infinitesimal speed of sound, subscript S referring to a constant entropy process to which the phenomenon of ultrasound propagation can be assimilated. Combination of the previous relationships yields the parameter *B/A* which can identify the nonlinear character of an acoustic propagation:

$$B/A=2\rho_0 c_0\left(\frac{\partial c}{\partial P}\right)_S. \tag{5}$$

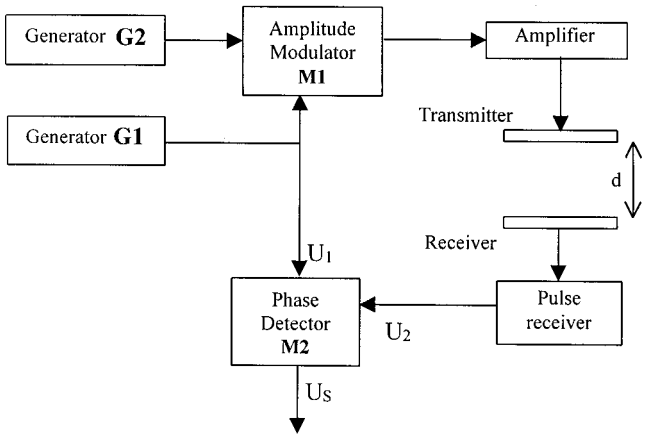

FIG. 1. Schematic representation of the phase comparison technique.

The experimental technique selected to measure this quantity under pressure is based on direct exploitation of relationship (5). Determination of *B/A* therefore depends on measurement of density, ultrasound velocity and its variation with pressure $(\Delta c/\Delta P)$. However, for the quantity $(\Delta c/\Delta P)$ to be assimilated to the derivative $(\partial c/\partial P)$ along an isentropic process it is essential to impose a rapid pressure change of small amplitude (of the order of 0.1 to 0.2 MPa during a time of 0.3 to 1 s) which generates a change in the velocity of approximately 0.2%. The conducto-convective characteristic times of the system, linked to the nature of the fluid and the geometry of the cell are incomparably higher (order of 1 hour) than the duration of the pressure variation.

To be able to measure such a change with sufficient accuracy it is preferable to measure the phase shift induced by pressure variation rather than to rely on direct measurement of ultrasound velocity. With this aim, a phase comparison method initially developed for use at atmospheric pressure was used.[6] The principle of this technique, presented schematically in Fig. 1, consists in measuring the phase shift generated by the acoustic wave passing through the liquid studied and in recording the variation of this phase shift when the fluid is subjected to a brief pressure change. A continuous wave signal U_1 delivered by the generator G1:

$$U_1 = A_1 \sin(\omega t) \tag{6}$$

with stabilized angular frequency ω, is applied at the input of the amplitude modulator M1. In this modulator, the wave is gated by the signal generator G2 in such a way as to generate a tone burst signal. This one is amplified and then applied to the transmission transducer. At the output of the receiver *R*, the signal U_2 has undergone a phase shift caused by the passage of the sound wave of speed c between the two transducers separated by a distance *d*:

$$U_2 = A_2 \sin\left[\omega\left(t - \frac{d}{c}\right) + \phi\right] \tag{7}$$

the constant term ϕ being added to account for phase changes taking place within the electronics and at the electric connection of the transducers. This signal U_2 is then multiplied by the reference signal U_1 in a double mixer M2 so as to produce a continuous output signal of amplitude U_S:

$$U_S = kA_1A_2 \sin\left(\omega\frac{d}{c} - \phi + \frac{\pi}{2}\right) \tag{8}$$

proportional to the amplitudes of signals U_1 and U_2 and also a sine function of the quantity $(\omega d/c - \phi + \pi/2)$. By tuning the frequency of the signal emitted by the generator, it is possible to achieve the following:

$$\omega\frac{d}{c} - \phi + \frac{\pi}{2} = n\pi + \delta, \tag{9}$$

where *n* is any integer and δ an infinitesimal. In the neighborhood of this condition, known as the ''null condition,'' the sine function involved in the relationship can be broken down into a limited power series of the first order and the signal U_s considered linearly dependent on the phase shift $\omega d/c$. Any variation in ultrasound velocity Δc caused by a change in the *P*, *T* conditions imposed on the fluid therefore leads to a variation in the output signal U_s given by:

$$\Delta U_S = kA_1A_2\omega\frac{d}{c^2}\Delta c \tag{10}$$

measurement of which can be used to calculate the nonlinearity coefficient:

$$\frac{B}{A} = -\frac{2\rho c^3}{\omega d}\frac{1}{kA_1A_2}\left(\frac{\Delta U_S}{\Delta P}\right)_S. \tag{11}$$

III. APPARATUS

The experimental apparatus is primarily composed of a high pressure measurement cell made up of a stainless steel autoclave cylinder in which a mobile piston can move in such a way as to transfer the pressure from the fluid studied and the compression oil. To ensure an effective seal between the sample and the compression oil and to avoid any pollution of the sample, two Viton segments are placed on the piston. The cylinder is closed, at the compression oil end, by a simple plug with an orifice through which compression oil can be introduced. The other end of the cell is closed by a plug in which three holes have been made for the electric connections to the transducers to pass through. The electrical connections under pressure were set up according to the method recommended by Bridgman.[7] A fourth hole was machined in the plug to allow the passage of a Pt 100 type 2 mm diameter heat probe housed in a metal finger to isolate it from the stresses of pressure. This plug also holds the acoustic probe, represented schematically in Fig. 2, made up of two piezoelectric transducers (of circular section, 12 mm diameter, QUARTZ and SILICE brand) whose resonating frequency is 5.0 MHz, one of them acting as a transmitter, the other as receiver. They are fixed parallel to the ends of a stainless steel cylindrical support (30 mm in length). This length represents an acceptable trade-off between shorter distances which would reduce the amount of sample required but would also reduce measuring accuracy and longer trajectories which would have the advantage of increasing the accuracy of the measurements but would at the same time increase the volume of liquid needed. The piezoelectric elements are held on their housing by a damper mechanism

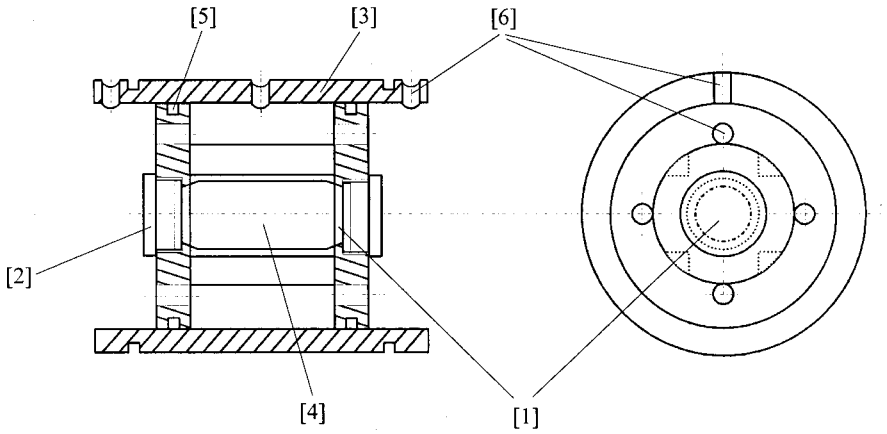

FIG. 2. Acoustic probe. (1) Transducers, (2) teflon plug, (3) buttress tube for the piston, (4) fluid volume, (5) viton segments, (6) hole for the circulation of fluid.

made up of a layer of epoxy resin mixed with aluminum powder in order to increase the effectiveness of transmission and reception and to improve the frequent response. The geometric characteristics chosen for this cell offer a useful internal volume of 0.66 liters and make it possible to carry out measurements at pressures up to 100 MPa over a temperature range of between 253.15 K and 423.15 K. This temperature range remains well within the operating limits of the transducers which impose a maximum operating temperature of the order of half the Curie temperature of the substance, i.e., 423.15 K. Apart from the measuring cell, the experimental apparatus includes various peripheral elements designed to ensure fluid flow regulation, controlled pressure changes and transmission, reception and processing of acoustic signals.

As the mass of the measurement cell is large, it has a large degree of thermal inertia which can cause temperature gradients. In order to ensure uniformity of the heat of the fluid, the cell is entirely immersed in a bath regulated by a HUBER brand polystat cc2 model with a heat instability of 0.02 K. Temperature of the bath is maintained homogenous using pulsed air jets. Moreover a cooling circuit is added to improve heat regulation in the vicinity of room temperature. The temperature is measured using a Pt 100 platinum probe (precision of 0.01 K) connected to an AOIP brand reference thermometer. With regard to the regulation and the geometry of the cell, there is any longitudinal gradient and axially temperature of the tested fluid is regulated by natural convection.

Pressure is applied and then maintained using a MAXIMATOR-brand pneumatic pump driven by an air manometer while a derivation circuit connected by a valve to the main circuit is introduced so as to be able to generate low intensity pressure variations. Pressure is measured at the output of the cell using an HBM-brand (Hottinger Baldwin Messtechnik) P3MB-100 MPa model manometer connected to a broad band amplifier (HBM AD5B40-01 model). Calibration of the probe is done using a pressure calibration weight balance BUDENBERG-brand with an accuracy in measuring pressure better than 0.02%.

The transmitter transducer is excited by pulse trains of duration 15 μs, of repetition rates of 2.2 kHz, the carrier frequency (of value 5.0 MHz, which is consistent with the minimum frequency of the piezoelectronic element) from an R&K Company brand, MIXCA model amplitude modulator (marked M1 in Fig. 1). This element is driven by two Hewlett-Packard HP33120A (G1 and G2) signal generators, amplified by a R&K Company brand, A300-10M type power amplifier. The receiving piezoelectric element is directly linked to a PANAMETRICS brand 5055 PRM model pulse receiver. In this piece of apparatus, the signal transmitted by the receiver transducer is amplified and then passed through a bandpass filter with a cutoff frequency of 1 MHz designed to reduce low-frequency noise. Finally, a second double R&K Company brand MIXCA model mixer (marked M2 on Fig. 1) was also introduced into the circuit to multiply the output signal of the PANAMETRICS with the reference signal from the generator G1. A frequency filter included in the mixer with a cut-off frequency of 300 kHz was included to eliminate the high- frequency component and the remaining harmonics of the carrier wave of the phase signal detected. A four-channel digital oscilloscope (GOULD brand, type 4094) is employed to visualize and verify the forms of the signals. Finally a PC type computer is used to process the pressure signal from the manometer directly, via an HP–IB interface and a 16 bit digitizing card (DATA TRANSLATION 3004).

Apart from the speed of sound and its derivative versus pressure, determination of the B/A coefficient requires measurement of the density of the sample. To do this we included in the experimental apparatus an ANTON PAAR (model DMA60) densitometer, which can only be used at atmospheric pressure. The principle of this device is to determine the period of oscillation of a U-shaped steel tube containing the sample after having set it into undamped vibration using an appropriate excitation system.

IV. MEASUREMENTS

As relationship (11) clearly shows, determination of the acoustic nonlinearity parameter using the phase comparison method involves measuring variation of the output signal U_s following a change in pressure, as well as variation of the speed of sound and of density after calibration of the response coefficient k of the mixer M2 and of the distance d between the piezoelectric elements.

A. Phase calibration

This procedure allows to measure the value of the coefficient kA_1A_2. In the phase calibration system, the phase difference between two signals whose frequency is 5 MHz generated by two Hewlett-Packard 33120A assemblies, is adjusted step by step, monitored on a digital oscilloscope (GOULD brand, type 4094) and read by a computer via a HP–IB interface. The phase signal proceeds from a phase detector (R&K Company brand MIXCA model mixer) linked to a low pass-filter with a cutoff frequency of 300 kHz. The output of this filter is given by

$$U_S = kA_1A_2 \sin\left(\phi_2 - \phi_1 + \frac{\pi}{2}\right), \tag{12}$$

where $\phi_2 - \phi_1$ is the phase difference between the two compared signals. The amplitudes of these signals are set at the same levels as in *B/A* measurement mode. In the neighborhood of the ''null condition'' the signal U_S can be considered linearly dependent on the phase difference $\phi_2 - \phi_1$. Then, a program of linear regression determine the constant coefficient kA_1A_2. Moreover, the effect of noise on these measurements is reduced by repeating 20 times the phase measurement and after the data are averaged.

B. Measurement of the term $\Delta U_s/\Delta P$

To measure the term $\Delta U_s/\Delta P$, a reduction in pressure of the order of 0.5 to 2 bar is applied to the fluid for 0.3–1 second by a hand operating of a valve. During this change, the signal emitted by the manometer as well as the signal from the mixer M2 are sampled at a rate of 2.2 kHz using the DT3004 data acquisition card. The points sampled (600 in all) are then smoothed to reduce the influence of noise. A linear regression method is then used to determine the gradient of $U_S(P)$ and thus calculate the term $(\Delta U_s/\Delta P)_S$ on the basis of the 600 points sampled.

C. Measurement of the speed of sound

The speed of sound is measured by direct chronometry, using a method developed by Daridon[8] to determine the speed of propagation of ultrasounds in petroleum fluids under pressure. This method consists in measuring the time taken by an acoustic wave to travel along a given trajectory in a fluid sample, in this case the distance *d* separating the two transducers. The PANAMETRICS (model 5055) pulse transmitter/receiver is used for this purpose. The memory oscilloscope in this case functions in delay mode and, by alignment of the leading edges of two continuous echoes of the signal, the time taken for the trajectory is directly recorded on the screen with a measurement error of ± 5 ns (maximum time resolution of the oscilloscope being 0.2 ns). For the ultrasound velocity determined in this way to be satisfactory the length of the passage *d* must be accurately established. As it is affected by the constraints of pressure and temperature, it is imperative to introduce terms designed to correct for these effects. This was done by introducing into distance *d* the following temperature and pressure dependency:

$$d(P,T) = d_0[1 + a(T - T_0)][1 + b(P - P_0)] \tag{13}$$

in which coefficients *a* and *b* are determined by measuring the speed of sound in various alkanes such as hexane, heptane or decane for which many ultrasound velocity data were given in the literature at atmospheric pressure and under pressure.

D. Measurement of density

Density is first measured at atmospheric pressure using the vibrating tube densitometer whose accuracy is 0.01%. It is then determined at higher pressures by integrating ultrasound velocity data according to the method proposed by Davis and Gordon[9] which is based on the equation linking isothermal compressibility with isentropic compressibility and thus ultrasound velocity:

$$\kappa_T = \kappa_S + \frac{T\alpha_P^2}{\rho C_P} = \frac{1}{\rho c^2} + \frac{T\alpha_P^2}{\rho C_P}. \tag{14}$$

Integration with respect to pressure of this relationship then leads to an expression which explicitly correlates density with ultrasound velocity in which C_P represents heat capacity and α_P isobaric thermal expansion:

$$\rho(P,T) - \rho(P_{\text{atmospheric}},T) = \int_{P\text{atmospheric}}^{P} 1/c^2 \, dP + T\int_{P\text{atmospheric}}^{P} (\alpha_P^2/C_P)dP. \tag{15}$$

To evaluate the first integral, which corresponds to the predominant contribution, the ultrasound velocity data are adjusted in the form of a rational function which is then integrated analytically. The second integral, which only represents a few percentage points of the first, is calculated iteratively according to a predictor–corrector-type algorithm proposed by Daridon *et al.*[10] which gives an uncertainty less than 0.1% over the entire field of investigation with *P*.

E. Discussion of errors

The inaccuracy in the determination of *B/A* stems from the addition of several causes of error concerning the successive determinations of density, frequency, distance, ultrasound velocity and, above all, the derivative $(\Delta c/\Delta P)_S$. The uncertainty regarding density (0.1%) leads to an identical contribution (0.1%) to *B/A*. The error on signal frequency is negligible and therefore has no impact on the accuracy of the *B/A* parameter. The term c^3/d, which is in fact equivalent to $d^2/\Delta t^3$ in which Δt represents the transit time of the acoustic wave within the medium, introduces an error of 0.1% on *B/A* according to the indications reported in the preceding paragraph. The phase amplitude kA_1A_2 is assumed to be constant in the procedure. However, when the pressure is modified, the amplitude of the two coherent signals sometimes fluctuates by about $\pm 1\%$. As the phase comparison technique is sensitive to amplitude, fluctuation of amplitude introduces uncertainty of similar significance, i.e., 1% on *B/A*. The other main source of error stems from uncertainty with respect to

TABLE I. Sound velocity values for water.

T (K) / P (MPa)	303.15	313.15	323.15	333.15	343.15	353.15	363.15	373.15
				u (ms^{-1})				
0.1	1509.4	1528.8	1542.9	1551.7	1555.4	1554.7		
5	1518.1	1537.6	1551.9	1560.9	1564.9	1564.5	1560.4	1553.5
10	1526.8	1546.5	1560.9	1570.1	1574.4	1574.3	1570.6	1564.1
15	1535.4	1555.2	1569.9	1579.3	1583.9	1584.1	1580.7	1574.6
20	1543.9	1563.9	1578.7	1588.4	1593.2	1593.6	1590.6	1584.8
30	1560.7	1581.0	1596.2	1606.2	1611.5	1612.5	1610.0	1605.0
40	1577.3	1597.9	1613.4	1623.8	1629.5	1631.0	1629.1	1624.7
50	1593.7	1614.6	1630.4	1641.1	1647.3	1649.3	1647.9	1644.1

the derivative $(\Delta U_s/\Delta P)_S$ which depends on the noise associated with pressure and phase measurements. However, the procedure adopted (with smoothing and adjustment by least squares method) reduces the noise effects and provides an uncertainty on the slope of $U_S(P)$ of only 1%. Assuming a random distribution of the above-mentioned uncertainties, the result is an overall inaccuracy of $\pm 1.5\%$. But three other sources of systematic errors on *B/A* must also be taken into account. The first of them, which is connected to the hypothesis of linearity of $U_S(\phi)$ leads to overestimation of *B/A* of approximately 0.5% with regard to the phase shift range of $\pm\pi/20$ rad. The second, which is a consequence of the temperature calibration, causes an uncertainty of approximately 0.2% on *B/A*. Finally, the last one, correlated to the quality of the weighing machine used to calibrate the pressure sensor, involves an error of 0.02% on the *B/A* parameter. In sum, the total error introduced as a result of adding together random and then systematic errors is consequently 2.2%.

V. EXPERIMENTAL RESULTS

As we have already indicated, the temperature and pressure domains covered by the experiment range from 303 to 373 K and from 0.1 to 50 MPa, respectively. The measurements are carried out by describing the isotherms: in other words, the temperature of the sample is adjusted to a given value and the properties are measured $(u, dc/dP, \ldots)$ for various successive pressures, the step, between two measurements being either 5 or 10 MPa. The direction in which each isotherm moves corresponds to that of increasing pressures. When the isotherm has been completely studied, the temperature value is changed and the entire process is reiterated. In all eight isothermal curves plotted in 10 K steps were defined. This operating method has the advantage of reducing considerably the time taken for the system to return to thermodynamic equilibrium within the sample.

The water used for these experiments is so-called superpure; in other words it has undergone various processes to be gradually cleansed of foreign ions. This treatment can be broken down successively into: passage of the fluid through a column of active charcoal followed by reverse osmosis; passage through another column of active charcoal, followed by filtering through two columns of mixed beds (made up of a set of cationic and anionic resins); finally passage through a cartridge containing active charcoal and mixed beds.

When the fluid emerges from this chain of purification, the electrical resistivity of the water reaches 18 Mohm cm and therefore corresponds to a degree of purity such that the concentration of foreign ions does not exceed 10^{-10} mole/liter.

The ultrasound velocity values, measured according to the method detailed above, are reported in Table I. Comparison with Wilson's data[11] yielded satisfactory results, the absolute average deviation being 0.02% and the maximum deviation 0.05%. In m/s, deviations are comprised between $+0.75$ and -0.46 m/s. On the basis of this initial data, the numerical procedure was used to obtain the density values presented in Table II. This set of values was compared with the values provided by Haar *et al.*[12] at the same pressure and temperature conditions. The absolute average deviation observed (AAD) was 0.002% while the maximum deviation was 0.005%; the discrepancies noted were between $+0.049$ and -0.0376 kg/m^3. With the phase comparison system, the behavior of the derivative $(dc/dp)_s$ was determined as a function of the $P-T$ conditions to which the fluid was subjected. Results for this quantity are indicated in Table III. For all these studies a temperature limit of 353.15 K was respected at atmospheric pressure to keep clear of the vapor

TABLE II. Density values for water.

T (K) / P (MPa)	303.15	313.15	323.15	333.15	343.15	353.15	363.15	373.15
				ρ (kg m^{-3})				
0.1	995.63	992.21	988.05	983.21	977.77	971.79		
5	997.80	994.35	990.17	985.34	979.92	973.97	967.55	960.73
10	1000.00	996.50	992.32	987.49	982.09	976.17	969.79	963.02
15	1002.17	998.64	994.44	989.61	984.23	978.34	972.00	965.28
20	1004.31	1000.75	996.53	991.71	986.34	980.48	974.19	967.51
30	1008.54	1004.91	1000.66	995.84	990.51	984.70	978.47	971.88
40	1012.68	1008.99	1004.71	999.89	994.57	988.82	982.66	976.14
50	1016.74	1012.99	1008.67	1003.85	998.56	992.84	986.74	980.30

TABLE III. $(\partial c/\partial P)_S$ values for water.

T (K) / P (MPa)	303.15	313.15	323.15	333.15	343.15	353.15	363.15	373.15
				$(\partial c/\partial P)_S$ ($\times 10^{-6}$ m^2 s kg^{-1})				
0.1	1.790	1.826	1.866	1.907	1.966	2.006		
5	1.802	1.828	1.874	1.908	1.969	1.993	1.997	2.027
10	1.818	1.823	1.866	1.916	1.951	1.988	1.989	1.995
15	1.810	1.822	1.867	1.907	1.946	1.965	1.988	1.990
20	1.809	1.815	1.846	1.898	1.941	1.965	1.975	1.976
30	1.788	1.794	1.828	1.860	1.901	1.939	1.933	1.949
40	1.794	1.789	1.808	1.854	1.885	1.904	1.924	1.936
50	1.796	1.785	1.803	1.833	1.863	1.881	1.882	1.889

state. Finally combination of these various thermodynamic properties can be used to determine the nonlinearity acoustic parameter *B/A*; values of this parameter for water are reported in Table IV. This last set of data was used to plot the curves in Figs. 3 and 4, illustrating the isothermal and isobaric behaviors, respectively, of *B/A*.

A few general trends can be deduced from these graphs. First, it appears that the nonlinearity parameter for water seems to be an increasing function of pressure at low temperature within the interval 0.1–50 MPa. At higher temperatures the influence of the pressure parameter is less marked (the variation is about 8% at $T=303.15$ K and decreases up to 0.7% at most at $T=373.15$ K) and curve seems to pass through a maximum. However, no conclusion can be drawn as the magnitude of the change is of the same order of the experimental accuracy (see Fig. 5). Despite the dispersion of the experimental points, linked with the overall uncertainty affecting determinations of *B/A* (i.e., approximately 2.2%), the nonlinearity parameter for water seems to be an increasing function of temperature at low temperature and a maximum seems also observed at higher ones for each pressure. Although this trend is found on every isobaric curve this observation can not be guarantee as the range of temperature investigated is limited to 373 K and the amplitude of the error is more important than the rate of variation (see Fig. 6).

It is possible to reflect graphically, in a way similar to the above, variations of the quantity $(dc/dp)_s$ as a function of P and T. This shows a tendency of the property to decrease with P, a tendency which is all the more marked as the temperature is lowered. This behavior, conversely to that observed for *B/A*, means that multiplication of $(dc/dp)_s$ by ρc^2 reverses the tendency connected with the effect of pressure. As regards the influence of temperature at fixed pressure, an increase of $(dc/dp)_s$ as a function of T is observed; the lower the pressure to which the fluid is subjected, the greater the influence.

VI. COMPARISON OF VALUES FOR *B/A* WITH THOSE IN THE LITERATURE

We confronted our experimental results for water (in the liquid state) with the data available in the literature, at atmospheric pressure[6,13,14] as well as over a wider range of pressure conditions: [0.1–50 MPa].[15]

As regards atmospheric pressure, the objective of the three authors cited above was to determine the influence of temperature alone, but using different approaches. Emery *et al.*[14] and Lu *et al.*[6] used a purely experimental method, the phase comparison method, while Beyer[13] adopted the classical thermodynamic method. This technique consists in measuring the speed of sound at different temperatures and pressures, so as to be able subsequently to deduce numerically the values of the derived terms $(\partial c/\partial P)_T$ and $(\partial c/\partial T)_P$ which are involved in the equivalent formulation of B/A:

$$B/A=2\rho c\left(\frac{\partial c}{\partial P}\right)_T+\frac{2\alpha Tc}{C_P}\left(\frac{\partial c}{\partial T}\right)_P. \tag{16}$$

Consequently, this is an approach which attempts to define all the quantities involved in the above expression on the basis of ultrasound velocity measurements and of a few additional thermodynamic properties (α and C_P). This widely used approach has a wide range of applications but its accuracy is reduced to 5%, at best, in the case of liquids. The evaluation of derived quantities, a source of major uncertainties, explains this situation.

TABLE IV. B/A values for water.

T (K) / P (MPa)	303.15	313.15	323.15	333.15	343.15	353.15	363.15	373.15
				B/A				
0.1	5.38±0.12	5.54±0.12	5.69±0.13	5.82±0.13	5.98±0.13	6.06±0.13	-	-
5	5.46±0.12	5.59±0.12	5.76±0.13	5.87±0.13	6.04±0.13	6.07±0.13	6.03±0.13	6.05±0.13
10	5.55±0.12	5.62±0.12	5.78±0.13	5.94±0.13	6.03±0.13	6.11±0.13	6.06±0.13	6.01±0.13
15	5.57±0.12	5.66±0.12	5.83±0.13	5.96±0.13	6.07±0.13	6.09±0.13	6.11±0.13	6.08±0.13
20	5.61±0.12	5.68±0.13	5.81±0.13	5.98±0.13	6.10±0.13	6.14±0.14	6.12±0.13	6.06±0.13
30	5.63±0.12	5.70±0.13	5.84±0.13	5.95±0.13	6.07±0.13	6.16±0.14	6.09±0.13	6.08±0.13
40	5.73±0.13	5.77±0.13	5.86±0.13	6.02±0.13	6.11±0.13	6.14±0.14	6.16±0.14	6.14±0.14
50	5.82±0.13	5.84±0.13	5.93±0.13	6.04±0.13	6.13±0.13	6.16±0.14	6.12±0.13	6.09±0.13

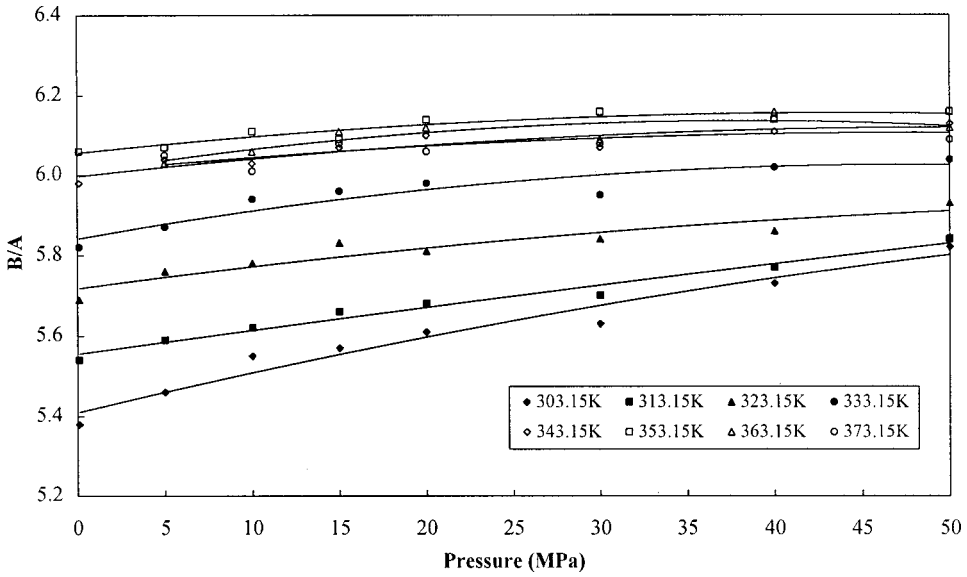

FIG. 3. B/A as a function of pressure at various temperatures.

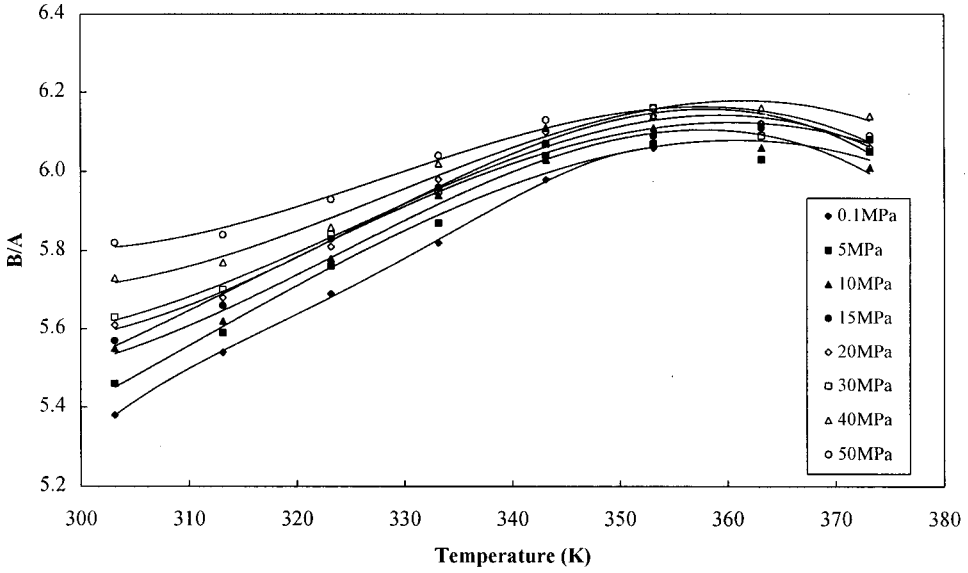

FIG. 4. B/A as a function of temperature at various pressures.

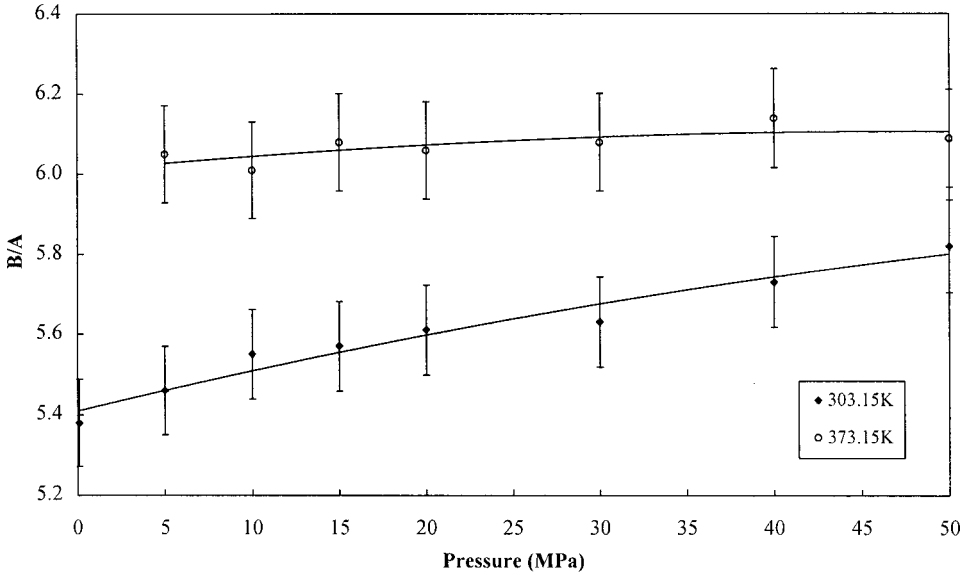

FIG. 5. Representation of the B/A uncertainty on isothermal curves.

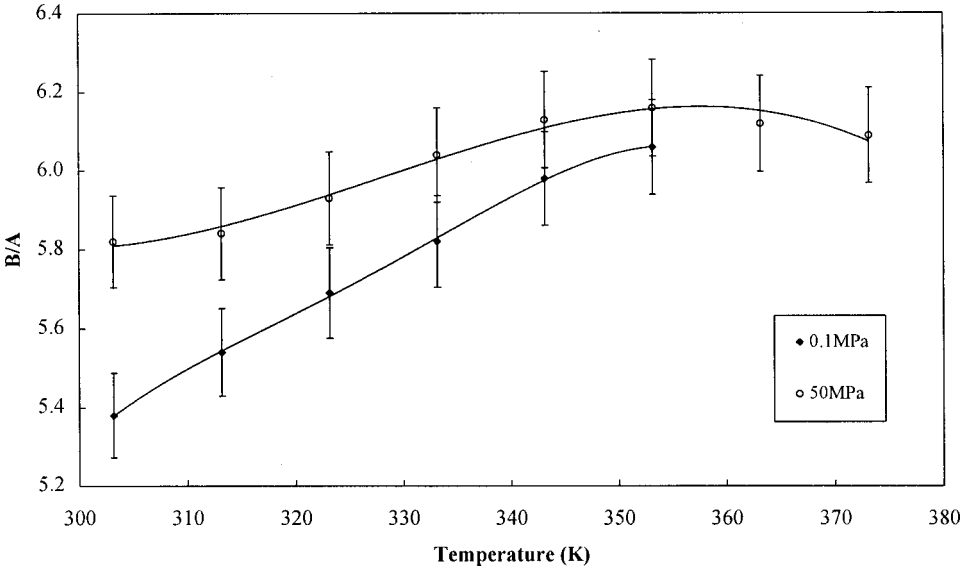

FIG. 6. Representation of the B/A uncertainty on isobaric curves.

Our values under pressure have been compared with those obtained from the work of Hagelberg *et al.*[15] dealing with the combined effects of temperature and pressure. However the increment adopted by these authors in their numerical procedure was large (in this particular case 50 MPa), and the only pressures common to both domains are 0.1 and 50 MPa. Table V below presents the results of the above authors (limited of course to the intervals 0.1–50 MPa and 303.15–353.15 K), our experimental results for B/A as well as the deviation (expressed in %) between these two data sets. It transpires that these different values are consistent to less than 3.5% in the case of atmospheric pressure and approximately 5% in the case in which the effect of pressure is taken into account. Overall these deviations proved satisfactory, taking account of the remarks already made regarding the respective inaccuracies of our measurement technique and of the classical thermodynamic approach.

VII. CONCLUSION

The measurements we made for water show only a small scale variation of B/A as a function of the variations imposed on the P, T parameters. In such a situation, it is clear that the accuracy of the determinations is a decisive factor in establishing the shape of the behavior of this property. In fact, a lack of accuracy could mask the phenomenon or even lead to a reversal of its evaluation, which clearly did happen with the classical thermodynamic method in certain cases, as we mentioned in our introduction.

Consequently, even if our apparatus, which was designed to investigate the effects of pressure, does not provide experimental data with less than 2% uncertainty, the gain in accuracy is nonetheless substantial with respect to the thermodynamic model. That is why the experimental contribution is absolutely essential and justifies the efforts made to develop the apparatus, all the more so as while data versus temperature are common in the literature, experimental information versus pressure is much less widely documented and even nonexistent in the case of the nonlinear acoustic parameter B/A. In the near future, these initial findings will be completed with experimental examination of the behavior under pressure of B/A in a variety of polar or nonpolar fluids such as different alcohols, alkanes, and other hydrocarbons.

TABLE V. Comparison of values for B/A with those in the literature.

		B/A		
T (K)	P (MPa)	Our values	Literature	AD (%)
303.15	0.1	5.38	5.32,[5] 5.2,[13] 5.23,[14] 5.21[15]	1.1 3.4 2.8 3.2
	50	5.82	5.63[15]	3.2
313.15	0.1	5.54	5.48,[5] 5.4,[13] 5.35,[14] 5.49[15]	1.1 2.5 3.4 0.9
	50	5.84	5.69[15]	2.6
323.15	0.1	5.69	5.65,[5] 5.57,[14] 5.55[15]	0.7 2.1 2.5
	50	5.93	5.69[15]	4.1
333.15	0.1	5.82	5.78,[5] 5.7,[13] 5.61[15]	0.7 2.1 3.6
	50	6.04	5.75[15]	4.8
343.15	0.1	5.98	6.06[5]	1.3
353.15	0.1	6.06	6.0,[13] 5.74[15]	1, 5.3
	50	6.16	5.84[15]	5.2

[1] C. Kammoun, J. Emery, and P. Alais, ''ULTRASONS—Mesure de faibles variations de la vitesse de propagation des ultrasons. Application à la détermination du paramètre de non-linéarité de l'eau distillée,'' C. R. Acad. Sci. Paris, Série B **281**, 465–467 (1975).
[2] L. Adler and E. A. Hiedemann, ''Determination of the nonlinearity parameter B/A for water and m-Xylene,'' J. Acoust. Soc. Am. **34**, 410–412 (1962).
[3] K. L. Narayana and K. M. Swamy, ''Acoustic nonlinear parameter (B/A) in *n*-pentane,'' Acustica **49**, 336–339 (1981).
[4] B. Hartmann and E. Balizer, ''Calculated B/A parameters for *n*-alkane liquids,'' J. Acoust. Soc. Am. **82**, 614–620 (1987).
[5] Z. Lu, Ph.D. dissertation, University of Pau, 1998.
[6] Z. Lu, J. L. Daridon, B. Lagourette, and S. Ye, ''Phase comparison method for measurement of the acoustic nonlinearity parameter B/A,'' Meas. Sci. Technol. **9**, 1699–1705 (1998).
[7] P. W. Bridgman, *The Physics of High Pressures* (G. Bells and Sons, London, 1949).
[8] J. L. Daridon, ''Mesure de la vitesse du son dans des fluides sous pression composés de constituants gazeux et liquides,'' Acustica **80**, 416–419 (1994).
[9] L. A. Davis and R. B. Gordon, ''Compression of mercury at high pressure,'' J. Chem. Phys. **46**, 2650–2660 (1967).
[10] J. L. Daridon and B. Lagourette, ''Mesure de la vitesse ultrasonore sous haute pression pour la caractérisation thermophysique d'un mélange ternaire,'' Acustica **82**, 32–38 (1996).
[11] W. D. Wilson, ''Speed of sound in distilled water as a function of temperature and pressure,'' J. Acoust. Soc. Am. **31**, 1067–1072 (1959).
[12] L. Haar, J. S. Gallagher, and G. S. Kell, *NBS/NRC Steam Tables* (Hemisphere, Washington, New York, 1984).
[13] R. T. Beyer, ''Parameter of nonlinearity in fluids,'' J. Acoust. Soc. Am. **32**, 719–721 (1960).
[14] J. Emery, S. Gasse, and C. Dugué, ''Coefficient de non-linéarité acoustique dans les mélanges eau-méthanol et eau-éthanol,'' J. Phys. (France) **11**, 231–234 (1979).
[15] M. P. Hagelberg, G. Holton, and S. Kao, ''Calculation of B/A for water from measurements of ultrasonic velocity versus temperature and pressure to 10000 kg/cm^2,'' J. Acoust. Soc. Am. **41**, 564–567 (1967).

Refracted arrival waves in a zone of silence from a finite thickness mixing layer

Takao Suzuki[a] and Sanjiva K. Lele
Department of Aeronautics and Astronautics, Stanford University, Stanford, California 94305-4035

(Received 5 July 2000; accepted for publication 3 October 2001)

Refracted arrival waves which propagate in the zone of silence of a finite thickness mixing layer are analyzed using geometrical acoustics in two dimensions. Here, two simplifying assumptions are made: (i) the mean flow field is transversely sheared, and (ii) the mean velocity and temperature profiles approach the free-stream conditions exponentially. Under these assumptions, ray trajectories are analytically solved, and a formula for acoustic pressure amplitude in the far field is derived in the high-frequency limit. This formula is compared with the existing theory based on a vortex sheet corresponding to the low-frequency limit. The analysis covers the dependence on the Mach number as well as on the temperature ratio. The results show that both limits have some qualitative similarities, but the amplitude in the zone of silence at high frequencies is proportional to $\omega^{-1/2}$, while that at low frequencies is proportional to $\omega^{-3/2}$, ω being the angular frequency of the source.
 [DOI: 10.1121/1.1428265]

PACS numbers: 43.28.Py, 43.28.Ra [MSH]

I. INTRODUCTION

Suppose an acoustic source is located in a slower medium, but adjacent to a faster medium. The slower or faster medium refers to the medium whose propagation speed is slower or faster than for the other (see Fig. 1). In such a case, there may exist a path arriving at the observer located in the slower medium which takes shorter time than direct waves; namely, once the ray arrives at the surface of the faster medium, propagates along it, and departs from it toward the observer. As the Fermat's principle indicates, under such a condition, actual waves propagate along this ray path, referred to as ''refracted arrival waves,[1–3]'' or sometimes as ''head waves,[4]'' or ''lateral waves,[5]'' etc.

The formula of refracted arrival waves can be derived using a contour integral when the interface between the two media can be treated as discontinuous. This case is considered to be a low-frequency limit in a sense that the acoustic wavelength is much longer than the thickness of the interface. However, when the acoustic wavelength becomes much shorter than the thickness of the interface, the low-frequency formula tends to underpredict the amplitude of refracted arrival waves. Instead, one should rather analyze these waves based on geometrical acoustics, namely, the high-frequency limit. Such distinction could be important in jet-noise problems (see Fig. 2) as described in this paper.

When a noise source is located right below or even inside a mixing layer, there exists a region in which direct waves from the source cannot reach, referred to as the ''zone of silence.'' Instead of direct waves, secondary waves occupy this region. In two dimensions, these waves are particularly expressed in the form of general plane waves. These waves are generated by disturbances of direct waves on the other side of the mixing layer. The formula of such waves was derived by Gottlieb[1] using a contour integral assuming a vortex sheet; however, the thickness of the mixing layer, in many realistic cases, can be equivalent to or longer than the acoustic wavelength of the sound radiated from jets.[6] In other words, the high-frequency sound in the zone of silence should not be estimated using a discontinuous interface model.

The purpose of this paper is to clarify the difference between the low- and high-frequency limits of refracted arrival waves from a transversely sheared mixing layer. By assuming that the thickness of the mixing layer is finite and the velocity and temperature profiles approach the uniform free-stream conditions exponentially, ray trajectories are asymptotically solved. Furthermore, a formula for pressure amplitude can be explicitly derived as a far-field asymptote using the Blokhintzev invariant[7] in the high-frequency limit. Unlike direct waves, refracted arrival waves cannot be derived using a stationary-phase-type method.[8] Note that at high frequencies, instability waves inherent in a mixing layer do not directly influence the noise radiation. In fact, dominant high-frequency noise sources exist relatively close to the jet exit in which the vortical disturbance level is relatively low.[9] Hence, the solution of refracted arrival waves from a finite thickness mixing layer should contain the basic mechanism of the high-frequency sound in the zone of silence for jet-noise problems. This study also indicates that the amplitude is fairly sensitive to the spreading rate of the mixing layer in reality.

The comparison between the low- and high-frequency limits demonstrates that as the frequency increases, the amplitude of refracted arrival waves tends to become larger than the prediction based on a vortex sheet. The key difference is that as the frequency varies, the low-frequency formula behaves as $\sim(\omega x)^{-3/2}$, while the high-frequency formula behaves as $\sim\omega^{-1/2}\alpha^{-1}x^{-3/2}$. (Here, ω denotes the angular frequency of the source, α denotes the exponential factor of either the velocity or temperature profile, which only de-

[a]Current address: Division of Engineering and Applied Science, California Institute of Technology, Pasadena, California 91125

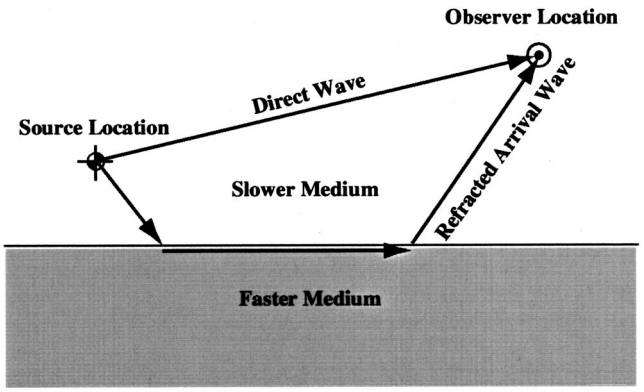

FIG. 1. Schematic of the paths of a refracted wave and a direct wave.

pends on the flow geometry, and x denotes the distance from the source in the flow direction.) In addition, the dependence on the Mach number and the temperature ratio as well as the source location is numerically investigated based on geometrical acoustics, and it is compared with the analytical expressions. It is observed that the analytical expression approximates the amplitude fairly well even if the source is located inside the mixing layer. Through this study, the sound radiation in the zone of silence at high frequencies can be understood in the context of jet-noise problems.

The outline of this paper is as follows: After the Introduction, the formulas of refracted arrival waves in the high-frequency limit are derived, and those in the low-frequency limit are also revisited. In Sec. III, numerical procedures of geometrical acoustics are described. Next, the analytical formulas and the numerical results are compared in Sec. IV; the conclusions are presented in Sec. V.

II. DERIVATION

Consider a two-dimensional, transversely sheared mixing layer. Take x to be the flow direction and y to be the vertical direction, and set M_- and a_- to be the free-stream Mach number and the speed of sound on the lower side, and M_+ and a_+ to be those on the upper side, respectively (see Fig. 3 for a schematic). In this paper, the subscript $-$ denotes the lower side, and $+$ the upper side. Assume that the Mach number and temperature profiles do not change in the x direction, and the mean pressure is constant everywhere (note that the effects of mixing layer spreading are discussed at the

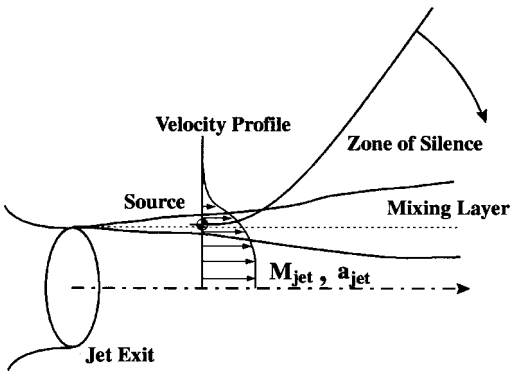

FIG. 2. Schematic of the noise from a jet.

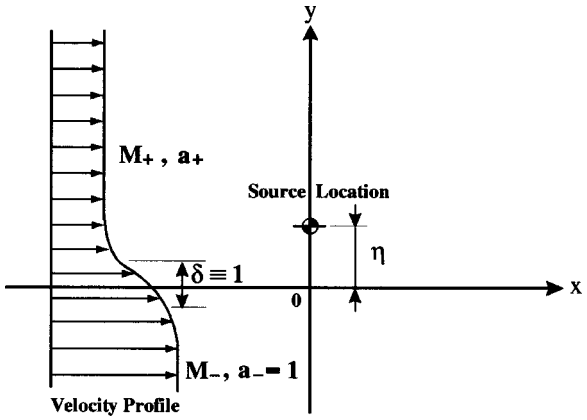

FIG. 3. Schematic of the coordinate system of a two-dimensional mixing layer.

end of Sec. IV). Set a monopole (single-frequency) source at $(x,y)=(0,\eta)$ without loss of generality. To solve acoustic fields in transversely sheared flows of this type, the third-order convective wave equation, called Lilley's equation,[10] is adequate. The homogeneous equation can be expressed as follows:

$$\frac{D}{Dt}\left[\frac{D^2\Pi}{Dt^2}-\frac{\partial}{\partial x_j}\left(a^2\frac{\partial\Pi}{\partial x_j}\right)\right]+2\frac{\partial u_k}{\partial x_j}\frac{\partial}{\partial x_k}\left(a^2\frac{\partial\Pi}{\partial x_j}\right)=0, \quad (1)$$

where $D/Dt=(\partial/\partial t)+u_1(\partial/\partial x_1)$ and $\Pi=\gamma^{-1}\log(p/p_\infty)$, p_∞ being the constant mean pressure, and γ the specific heat ratio. Furthermore, assume that (1) is nondimensionalized by taking the vorticity thickness δ to the length scale and the speed of sound at $y=-\infty$, a_-, to be the velocity scale; therefore, u_i denotes the local Mach number times the local speed of sound, and a^2 denotes the local temperature. Based on (1), the amplitude of diffracted waves in the zone of silence, referred to as ''refracted arrival waves,'' is analytically formulated in both low-and high-frequency limits in this section.

A. High-frequency limit (finite thickness model)

When the acoustic wavelength is much shorter than the characteristic length scale of the medium, in the present case the vorticity thickness, one can assume the high-frequency limit and apply geometrical acoustics.[4,7] Assume the acoustic pressure fluctuation to be the following form:

$$\Pi(t,\mathbf{x})=e^{-i\omega t}P(\mathbf{x})\exp[i\omega\phi(\mathbf{x})]. \quad (2)$$

Substitute (2) into (1), and asymptotically expand it with respect to ω. By taking the leading terms of ω, one can obtain the eikonal equation

$$(1-u_j\phi_j)^2-a^2\phi_j^2=0, \quad (3)$$

where $\phi_i\equiv\partial\phi/\partial x_i$, which corresponds to the local wavenumber vector. By using the method of characteristics,[4] one can reduce (3) to the following O.D.E. system:

$$\frac{dx_i}{dt}=\frac{a^2}{1-u_k\phi_k}\phi_i+u_i, \quad (4)$$

$$\frac{d\phi_i}{dt} = -\frac{\partial u_k}{\partial x_i}\phi_k - \frac{1-u_k\phi_k}{2a^2}\frac{\partial a^2}{\partial x_i}, \tag{5}$$

$$\frac{d\phi}{dt} = 1. \tag{6}$$

Notice that the phase ϕ has the same units (actually same scale) as time. Likewise, by taking the second-highest terms of ω, one can derive the first-order transport equation

$$2u_jP_j(1-u_k\phi_k) + 2a^2P_j\phi_j + \frac{2a^2P\phi_j\phi_k}{1-u_l\phi_l}\frac{\partial u_k}{\partial x_j} - P\left[3\left(u_ju_k\phi_{jk} + \phi_ju_k\frac{\partial u_j}{\partial x_k}\right) - a^2\phi_{jj}\right] + P\left[\phi_j\frac{\partial a^2}{\partial x_j} - \frac{\phi_j^2u_k}{1-u_l\phi_l}\frac{\partial a^2}{\partial x_k} - \frac{2a^2\phi_ju_k\phi_{jk}}{1-u_l\phi_l}\right] = 0. \tag{7}$$

Here, again $P_i \equiv \partial P/\partial x_i$. To simplify (7), use the following relation obtained by differentiating (3) by D/Dt:

$$2\left(u_ju_k\phi_{jk} + \phi_ju_k\frac{\partial u_j}{\partial x_k}\right) - \frac{2a^2\phi_j\phi_k}{1-u_l\phi_l}\frac{\partial u_k}{\partial x_j} - \left[\phi_j\frac{\partial a^2}{\partial x_j} - \frac{\phi_j^2u_k}{1-u_l\phi_l}\frac{\partial a^2}{\partial x_k} + \frac{2a^4\phi_j\phi_k\phi_{jk}}{(1-u_k\phi_k)^2}\right] = 0. \tag{8}$$

Substituting (8) into (7), using (4), and assuming the mean pressure is constant everywhere (hence, $(1/\rho)(D\rho/Dt) + (1/a^2)(Da^2/Dt) = 0$), (7) can be simplified as follows:

$$\frac{\partial}{\partial x_j}\left[\frac{P^2}{1-u_k\phi_k}\frac{dx_j}{dt}\right] = 0. \tag{9}$$

Hence, the quantity called the "Blokhintzev invariant"[7] is conserved along ray tubes

$$\frac{P^2S}{1-u_k\phi_k}\left|\frac{d\mathbf{x}}{dt}\right| = \text{Const.}, \tag{10}$$

where S denotes the cross section of the ray tube normal to the ray direction. In the denominator, the mean pressure, which is assumed to be constant, disappears compared with the general expression of the Blokhintzev invariant. This expression will be used later to calculate the amplitude of refracted arrival waves.

Now, when the mean velocity and temperature profiles are purely transversely sheared, the O.D.E. system (4)–(6) can be simplified: $d\phi_x/dt = 0$ in (5). In other words, ϕ_x is constant along the ray. Accordingly, they can be rewritten as follows:

$$\frac{dx}{dt} = \frac{a^2(y)}{1-M(y)\phi_x}\phi_x + M(y), \tag{11}$$

$$\frac{dy}{dt} = \frac{a^2(y)}{1-M(y)\phi_x}\phi_y, \tag{12}$$

$$\frac{d\phi_x}{dt} = 0, \tag{13}$$

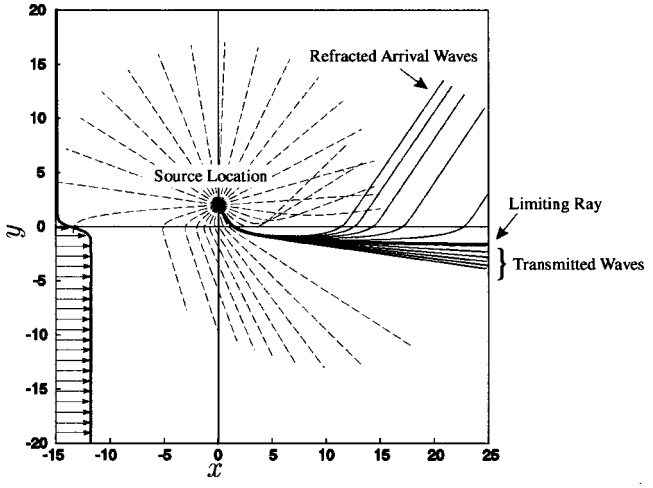

FIG. 4. Ray trajectories from a point source above a mixing layer. The source is located at $(x,y) = (0,2)$, the temperature is constant everywhere, and the velocity profile is given by $M(y) = 0.8[1-\tanh(2y)]/2$ shown on the left-hand side. The dashed lines are drawn every 3° in all directions, and the solid lines are drawn by the interval of 0.3° near the limiting ray.

$$\frac{d\phi_y}{dt} = -\frac{dM}{dy}\phi_x - \frac{1-M(y)\phi_x}{2a^2(y)}\frac{da^2}{dy}, \tag{14}$$

$$\frac{d\phi}{dt} = 1. \tag{15}$$

Again, $M(y)$ denotes the velocity profile (not the Mach number) whose reference speed is $a_- = a(-\infty)$.

For convenience, consider the case in which $\phi_x > 0$, and $d\phi_y/dt \geqslant 0$ along the ray in (14), such as rays propagating downstream above a hot jet. Among these rays, if the initial grazing angle θ is lower than a certain threshold value ($\theta < \theta^\star$, where $\theta^\star$ will be defined later), this ray propagates into the lower side and never appears on the upper side, called a "transmitted wave" in this paper (see Fig. 4). In contrast, if $\theta > \theta^\star$, this ray propagates on the upper side. In particular, when the rays whose grazing angles are only slightly higher than this threshold, they appear as refracted arrival waves departing from the mixing layer to the upper side at nearly the same angles. The ray whose initial grazing angle is exactly $\theta = \theta^\star$ is called a "limiting ray." As Fig. 4 shows, the turning points of the refracted arrival rays, at which the rays become parallel to the mixing layer, are fairly close to the lower free-stream region when the rays are propagating far downstream. Accordingly, these rays propagate horizontally just beneath the mixing layer for long distances. To solve these ray trajectories, assume that the velocity and temperature profiles approach the lower free-stream conditions exponentially. In other words, the velocity and the temperature profiles near the turning points can be approximated by

$$M(y) = M_- - \Delta M e^{\alpha_1 y}, \tag{16}$$

$$a^2(y) = 1 - \Delta a^2 e^{\alpha_2 y}, \tag{17}$$

as $y \to -\infty$, where $\alpha_1, \alpha_2 > 0$, and ΔM and Δa^2 are some constants determined from the flow field. In many real physical flows, α_1 and α_2 can be common near the free-stream

region (e.g., the Crocco–Busemann relation: $T \approx -u_1^2/C_p + C_1 u_1 + C_2$, where C_1 and C_2 are constants). Hence, set $\alpha_1 = \alpha_2 = \alpha$. If $\alpha_1 \neq \alpha_2$, just retain the term whose α is smaller. This model should cover realistic flows; however, if the profiles do not follow the formulas (16) and (17), extension of the present method is required, such as curve fitting. Nonetheless, the proportionality of the frequency and the distance from the source should show similar features as discussed at the end of this section. Substitute (16) and (17) into the O.D.E. system (11)–(15), and take the leading-order terms assuming $\Delta M e^{\alpha y}$ and $\Delta a^2 e^{\alpha y}$ to be small. Consequently, one can simplify them as follows:

$$\frac{dx}{dt} \approx \frac{1}{1 - M_- \phi_x} \phi_x + M_-, \tag{18}$$

$$\frac{dy}{dt} \approx \frac{1}{1 - M_- \phi_x} \phi_y, \tag{19}$$

$$\frac{d\phi_x}{dt} = 0, \tag{20}$$

$$\frac{d\phi_y}{dt} \approx \left[\phi_x \Delta M + \frac{(1 - M_- \phi_x)\Delta a^2}{2} \right] \alpha e^{\alpha y}, \tag{21}$$

$$\frac{d\phi}{dt} = 1. \tag{22}$$

Notice that at the leading order, dx/dt becomes constant from (18). Differentiating (19) with respect to t, and substituting (21) into it, yields

$$\frac{d^2 y}{dt^2} \approx \frac{1}{1 - M_- \phi_x} \frac{d\phi_y}{dt} \approx \left[\frac{\phi_x \Delta M}{1 - M_- \phi_x} + \frac{\Delta a^2}{2} \right] \alpha e^{\alpha y}$$

$$\equiv \alpha A e^{\alpha y}, \tag{23}$$

where $A \equiv \phi_x \Delta M/(1 - M_- \phi_x) + (\Delta a^2/2)$, which is constant and assumed to be non-negative along the ray. Redefining $z \equiv e^{\alpha y}$ and substituting it into (23), one can obtain the following O.D.E.:

$$z \frac{d^2 z}{dt^2} - \left(\frac{dz}{dt} \right)^2 - \alpha^2 A z^3 = 0. \tag{24}$$

To reduce (24) to an integrable form, convert the variables by setting $\psi_0 \equiv z$ and $\psi_1 \equiv \dot{z}$. After calculating $d\psi_1/d\psi_0$, (24) yields

$$\frac{d\dot{z}^2}{dz} = \frac{2\dot{z}^2}{z} + 2\alpha^2 A z^2. \tag{25}$$

From (25), the general solution can be obtained as

$$\dot{z}^2 = 2\alpha^2 A z^2 (z \pm \beta^2). \tag{26}$$

Here, β is an arbitrary constant (defined to be $\beta \in [0, \infty)$ here for convenience) always satisfying $z \pm \beta^2 \geqslant 0$. When one takes the plus sign in (26), it corresponds to a ray of a transmitted wave. In contrast, with the minus sign, $z = \beta^2$ at a certain point, corresponding to a ray of a refracted arrival wave. This point is actually the turning point, which can be expressed as

$$y^* = \frac{2}{\alpha} \log \beta. \tag{27}$$

In this paper, the superscript * denotes the quantity at the turning point. Note that if $\beta = 0$ in (26), it corresponds to the limiting ray.

First, to solve the ray trajectories of refracted arrival waves, take the minus sign in (26), convert the variable by setting $\sqrt{(z - \beta^2)} \equiv \beta \tan \vartheta$ $(0 \leqslant \vartheta < \pi/2)$, and integrate it. After some calculation, it yields

$$\vartheta = \pm \sqrt{\frac{\alpha^2 \beta^2 A}{2}} (t - t^*). \tag{28}$$

Here, t^* denotes the time when the ray passes through the turning point. Equation (28) indicates that the trajectory is symmetric about the turning point. Rewriting (18) and (28) in the physical domain, one can obtain the ray trajectory near the turning point as follows:

$$x - x^* \approx B(t - t^*), \tag{29}$$

$$y \approx \frac{2}{\alpha} \log \frac{\beta}{\cos[\sqrt{\alpha^2 \beta^2 A/2}(t - t^*)]}. \tag{30}$$

where $B = [M_- + (1 - M_-^2)\phi_x]/(1 - M_- \phi_x)$. Combining (29) and (30), it can be rewritten by

$$y \approx \frac{2}{\alpha} \log \frac{\beta}{\cos[\beta C (x - x^*)]}, \tag{31}$$

where $C = \sqrt{\alpha^2 A/2B^2}$. This equation will be used later to derive the amplitude of refracted arrival waves.

Second, a special solution, the limiting ray, can be obtained by setting $\beta = 0$ in (26). By directly integrating (26), one can obtain

$$y \approx \frac{2}{\alpha} \log \frac{1}{\sqrt{\alpha^2 A/2}(t - t_0)} \approx \frac{2}{\alpha} \log \frac{1}{C(x - x_0)}. \tag{32}$$

Here, x_0 denotes a certain reference point.

Finally, to solve the rays of transmitted waves, take the plus sign in (26), and set $z = \beta^2 \tan^2 \vartheta$ $(0 \leqslant \vartheta < \pi/2)$. After integrating the equation, one can obtain

$$y \approx \frac{1}{\alpha} \log \frac{\beta^2 (1 - \cos^2 \vartheta)}{\cos^2 \vartheta} \approx \frac{2}{\alpha} \log \frac{\beta}{\sinh[\beta C (x - x_0)]}. \tag{33}$$

Next, consider the trajectory of the turning points for refracted arrival waves propagating far downstream (see Fig. 5). The initial grazing angles of these rays are slightly higher than the angle of the limiting ray; hence, the locations where these rays enter the mixing layer are approximately the same. Here, these locations are called the ''incident points,'' denoted by x_{in} in this paper. On the other hand, due to the slight difference of the initial angles, the distances from the incident points to the turning points are quite different; accordingly, the locations at which the rays depart from the mixing layer are also different. These locations are called the ''departing points,'' denoted by x_{out}. Recalling the ray trajectories are symmetric about the turning points from (28), the

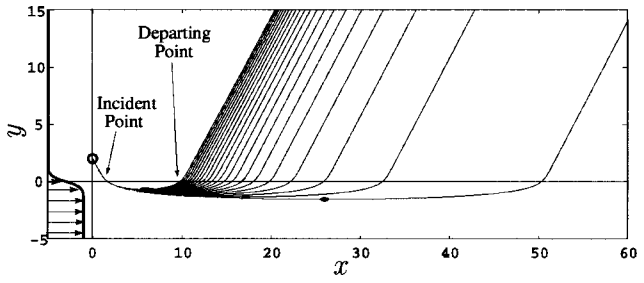

FIG. 5. Example of ray trajectories of refracted arrival waves. The velocity profile is depicted on the left-hand side ($M(y)=0.8[1-\tanh(2y)]/2$), and the temperature is constant everywhere. The source is located at $(x,y)=(0,2)$ (same as Fig. 4). The initial angles of the rays are $-56.25°$–$-55.25°$ with the interval of 0.05°. Solid dots denote the turning points.

distance from the incident point to the departing point is twice that to the turning point. Now, for the rays propagating far downstream, typically $|\alpha y^*|$ becomes a relatively large value; hence, $\beta=e^{\alpha y^*/2}$ tends to be a fairly small value. For example, when $\alpha y^*=-5$, $\beta=0.0821$. On the other hand, near the incident point, $y_{\rm in}\approx 0$; accordingly, $\beta/\cos[\beta C(x^*-x_{\rm in})]\approx 1$ from (31). Therefore, since $|\beta|\ll 1$, $|\cos[\beta C(x^*-x_{\rm in})]|\ll 1$ must be satisfied; namely

$$\beta C|x^*-x_{\rm in}|\approx\frac{\pi}{2}. \tag{34}$$

Hence, using (27) the trajectory of the turning point can be approximated by

$$y^*\approx\frac{2}{\alpha}\log\frac{\pi}{2C(x^*-x_{\rm in})}. \tag{35}$$

Now, the pressure amplitude of refracted arrival waves is derived using the Blokhintzev invariant (10). By calculating the departing points of adjacent rays, the amplitude can be approximately solved. First, using (35), calculate the turning points of adjacent rays. Knowing that C is a function of ϕ_x, differentiate (35) as follows:

$$\left[\frac{\alpha(x^*-x_{\rm in})}{2}dy^*+dx^*\right]e^{\alpha y^*/2}\approx-\frac{\pi}{2C^2}\frac{dC}{d\phi_x}d\phi_x. \tag{36}$$

On the other hand, the relation between y^* and ϕ_x can be obtained from the eikonal equation (3). Knowing that $\phi_y=0$ gives the turning point, differentiate (3) and simplify it as follows:

$$(1-M_-\phi_x)\alpha A e^{\alpha y^*}dy^*-Bd\phi_x=0. \tag{37}$$

Furthermore, from (3), ϕ_x for the limiting ray is given by

$$\phi_x^\star=\frac{1}{1+M_-}. \tag{38}$$

Here, the superscript $\star$ denotes the quantity of the limiting ray. Substituting (35) and (37) into (36) yields

$$\left[\frac{B}{2(1-M_-\phi_x^\star)A}+\frac{\pi^2}{4C^3}\frac{dC}{d\phi_x}(x^*-x_{\rm in})^{-2}\right]d\phi_x+\frac{\pi^2}{4C^2}(x^*-x_{\rm in})^{-3}dx^*\approx 0. \tag{39}$$

Here, the second term in [ ] becomes negligible far downstream (as $|x^*-x_{\rm in}|\to\infty$). Thus, the intensity is proportional to

$$I\sim\frac{d\phi_x}{dx^*}\approx-\frac{\pi^2(1-M_-\phi_x^\star)A}{2BC^2(x^*-x_{\rm in})^3}=-\frac{\pi^2}{\alpha^2}(x^*-x_{\rm in})^{-3}. \tag{40}$$

On the other hand, near the source the cross-section area can be calculated from the difference of the initial grazing angles. From (11) and (12), calculate the change of the ray path with respect to ϕ_x near the source

$$\frac{\partial}{\partial\phi_x}\left(\frac{dx}{dt}\right)_s=\frac{1}{\overline{n_s^2}}, \tag{41}$$

$$\frac{\partial}{\partial\phi_x}\left(\frac{dy}{dt}\right)_s=\frac{\phi_x}{\overline{n_s^2}\sqrt{\overline{n_s^2}-\phi_x^2}}, \tag{42}$$

where the quantities with the subscript s are evaluated at the source point, and $\overline{n}\equiv(1-M\phi_x)/a$. As seen later, $\overline{n}$ behaves as a refraction index. Now, to apply the ray tube theory using (10), it is convenient to calculate the following quantity:

$$\left|\frac{d\mathbf{x}/dt}{1-M(y)\phi_x}\frac{dS}{d\phi_x}\right|_s=\frac{\left|\left(\frac{dx}{dt},\frac{dy}{dt}\right)\times\left(\frac{\partial}{\partial\phi_x}\left(\frac{dx}{dt}\right),\frac{\partial}{\partial\phi_x}\left(\frac{dy}{dt}\right)\right)dt\right|_s}{1-M_s\phi_x}=\frac{dt}{a_s\overline{n_s^3}\sqrt{\overline{n_s^2}-\phi_x^2}}. \tag{43}$$

The distance from the source dr and the time dt is related as

$$\left(\frac{dr}{dt}\right)_s=\sqrt{\left(\frac{dx}{dt}\right)_s^2+\left(\frac{dy}{dt}\right)_s^2}=a_s\left[\left(1+\frac{M_s^2}{a_s^2}\right)+2\frac{M_s\phi_x}{a_s\overline{n_s}}\right]^{1/2}. \tag{44}$$

Likewise, calculate the same quantity at the departing point

$$\left|\frac{d\mathbf{x}/dt}{1-M(y)\phi_x}\frac{dS}{d\phi_x}\right|_{\rm out}=\frac{\left|\left(\frac{dx}{dt},\frac{dy}{dt}\right)_+\times\left(\frac{dx_{\rm out}}{d\phi_x},0\right)\right|}{1-M_+\phi_x}=\frac{\sqrt{\overline{n_+^\star}^2-\phi_x^{\star 2}}}{\overline{n_+^\star}^2}\frac{dx_{\rm out}}{d\phi_x}. \tag{45}$$

Here, (45) is evaluated in the uniform region right above the mixing layer. Remember that in the upper free-stream region, the rays are almost parallel, and refracted arrival waves propagate in the form of general plane waves.

Now, the solution close to a monopole source can be written as

$$\Pi_s(r)=\frac{1}{2\sqrt{2\pi}}\frac{\exp\left[i\left(\dfrac{-\dfrac{M_s}{a_s}\cos\theta+\sqrt{1-\dfrac{M_s^2}{a_s^2}\sin^2\theta}}{1-(M_s^2/a_s^2)}\dfrac{\omega r}{a_s}-\dfrac{3}{4}\pi\right)\right]}{\omega^{1/2}r^{1/2}a_s^{3/2}\left(1-\dfrac{M_s^2}{a_s^2}\sin^2\theta_s\right)^{1/4}},\tag{46}$$

where $x=r\cos\theta$ and $y=r\sin\theta$. In particular, the initial grazing angle for refracted arrival waves $\theta_s^\star$ is given by

$$\tan\theta_s^\star\equiv\frac{\left(\dfrac{dy}{dt}\right)_s}{\left(\dfrac{dx}{dt}\right)_s}=-\frac{\sqrt{\overline{n_s^\star}^2-\phi_x^{\star 2}}}{\left(1-\dfrac{M_s^2}{a_s^2}\right)\phi_x^\star+\dfrac{M_s}{a_s^2}},\tag{47}$$

where $\phi_x^\star$ is approximated by (38). The expression (46) can be obtained from (A11) (shown later) by assuming that the flow field near the source is uniform, and taking the limit of a far-field asymptote, $\omega r\to\infty$. Combining (40) and (43)–(46), the amplitude of refracted arrival waves from a finite thickness mixing layer is approximated by

$$\begin{aligned}|\Pi_+(\omega,x,y)|&\approx|\Pi_s(dr)|\frac{\sqrt{\left|\dfrac{d\mathbf{x}/dt}{1-M\phi_x^\star}\dfrac{dS}{d\phi_x}\right|_s}}{\sqrt{\left|\dfrac{d\mathbf{x}/dt}{1-M\phi_x^\star}\dfrac{dS}{d\phi_x}\right|_{\text{out}}}}\\&=\frac{\left|\dfrac{1}{2}\dfrac{d\phi_x}{dx^*}\right|^{1/2}\left(\dfrac{dt}{dr}\right)_s^{1/2}}{2\sqrt{2\pi}\omega^{1/2}a_s^{3/2}\left(1-\dfrac{M_s^2}{a_s^2}\sin^2\theta_s^\star\right)^{1/4}}\\&\quad\times\frac{\overline{n}_+}{a_s^{1/2}\overline{n_s^\star}^{3/2}\sqrt[4]{\overline{n_s^\star}^2-\phi_x^{\star 2}}\sqrt[4]{\overline{n_+^\star}^2-\phi_x^{\star 2}}}\\&=\frac{\sqrt{2\pi}}{2\omega^{1/2}\alpha}\frac{\overline{n}_+^\star}{a_s^2\overline{n_s^\star}^{3/2}\sqrt{|\sin\theta_s^\star|}\sqrt[4]{\overline{n_+^\star}^2-\phi_x^{\star 2}}}\\&\quad\times\frac{1}{\left[\left(1+\dfrac{M_s^2}{a_s^2}\right)+2\dfrac{M_s\phi_x^\star}{a_s\overline{n_s^\star}}\right]^{1/4}X^{3/2}},\end{aligned}\tag{48}$$

where $X\equiv x-(\sqrt{\overline{n_s^\star}^2-\phi_x^{\star 2}}/\phi_x^\star)y$. Here, since the ray trajectory is symmetric about the turning point, it is assumed that $2|x^*-x_{\text{in}}|=|x_{\text{out}}-x_{\text{in}}|$. Note when the source is at a large distance from the mixing layer ($\eta\gtrsim 1$), the correction for the distance from the source to the incident point needs to be included [see Eq. (59) shown later]. On the other hand, when the source approaches the lower free-stream region, e.g., $\eta\lesssim -1$, the corresponding incident points are no longer identical for the rays of refracted arrival waves, and the approximation fails. This expression (48) will be compared with the expressions based on a vortex sheet as well as the numerical results.

B. Low-frequency limit (vortex sheet model)

When the acoustic wavelength is much longer than the vorticity thickness, a vortex sheet can be used, which corresponds to the low frequency limit. Refracted arrival waves of this type have been reported in several studies.[1–3] In this section, the resultant formulas of refracted arrival waves in the low-frequency limit are shown in two cases (the source is located above and below the vortex sheet). For their derivation, please refer to the Appendix.

When the source is located above the mixing layer ($\eta>0$), the absolute value of pressure amplitude yields

$$|\Pi_+(\omega,x,y)|\approx\frac{1}{\sqrt{2\pi}\omega^{3/2}}\frac{\overline{n}_+^{\star 2}}{a_+^2\overline{n}_-^{\star 2}(\overline{n}_+^{\star 2}-\phi_x^{\star 2})X^{3/2}}.\tag{49}$$

Here the notation is the same as (48), and this expression is valid only in the zone of silence on the upper side. Likewise, when the source is located below the mixing layer ($\eta<0$)

$$|\Pi_+(\omega,x,y)|\approx\frac{1}{\sqrt{2\pi}\omega^{3/2}}\frac{\overline{n}_+^{\star 4}}{\overline{n}_-^{\star 4}(\overline{n}_+^{\star 2}-\phi_x^{\star 2})X^{3/2}}.\tag{50}$$

Note that the expression (50) gives larger amplitude than the expression (49), as shown later. Here, one can see that the decay rate of (49) or (50) for a vortex sheet and that of (48) for a finite thickness mixing layer are common ($X^{-3/2}=[x-\sqrt{(\overline{n}_+^{\star 2}-\phi_x^{\star 2})}y/\phi_x^\star]^{-3/2}$). However, their coefficients are different. It is important to notice that as the frequency varies, (49) and (50) are proportional to $\sim\omega^{-3/2}$, while (48) is proportional to $\sim\omega^{-1/2}$ with a fixed α. In other words, as the frequency increases with the flow geometry fixed, the amplitude is guaranteed to exceed the prediction based on the vortex sheet model. This proportionality is still valid for the finite thickness mixing layer with the velocity and temperature profiles other than $\sim e^{\alpha y}$. Remember that the ray trajectories are independent of the source frequency so long as the frequency is considered high enough; hence, the only part in which the frequency dependence appears is the amplitude expression near the source (46). These theoretical expressions (48), (49), and (50), are compared with the numerical results in Sec. IV later.

III. NUMERICAL SIMULATION

To compare the analytical formulas with more accurate solutions, pressure amplitude of refracted arrival waves is numerically solved based on geometrical acoustics. The procedures are to simply integrate the eikonal equation and to apply the ray-tube theory, which are described in this section.

To solve ray trajectories, the O.D.E. system of the eikonal equation, (11)–(15), was numerically integrated using the standard fourth-order Runge–Kutta scheme. The initial conditions are as follows:

$$x(0)=0, \tag{51}$$

$$y(0)=\eta, \tag{52}$$

$$\phi_x(0)=\frac{\cos\theta_i}{a_s+M_s\cos\theta_i}, \tag{53}$$

$$\phi_y(0)=\frac{\sin\theta_i}{a_s+M_s\cos\theta_i}, \tag{54}$$

$$\phi(0)=0, \tag{55}$$

where the initial grazing angle θ_s is given by $\tan\theta_s \equiv a_s\sin\theta_i/(M_s+a_s\cos\theta_i)$. For simplicity, the velocity profile was set to be

$$M(y)=\frac{M_-}{2}[1-\tanh(2y)] \qquad (M_->0). \tag{56}$$

This formula provides $M(y)\to M_- - M_- e^{4y}$ as $y\to-\infty$, which is consistent with (16) ($M_+=0.$, $\Delta M=M_-$, and $\alpha=4.$). In addition, this velocity profile yields the vorticity thickness of $\delta\equiv\Delta M/(dM/dy)_{\max}=1$. Similarly, the temperature profile was set to be

$$a^2(y)=\frac{1-a_+^2}{2}[1-\tanh(2y)]+a_+^2. \tag{57}$$

It also yields $a^2(y)\to 1-(1-a_+^2)e^{4y}$ as $y\to-\infty$. If $a_+^2<1$, the flow corresponds to a hot jet, while if $a_+^2>1$, it corresponds to a cold jet. [In this case, M_- must be reasonably large so that A is always non-negative. See Eq. (23).]

Once the ray trajectories were computed, the Blokhintzev invariant (10) was used to obtain pressure amplitude by calculating cross sections between adjacent rays. Defining (x_n, y_n) to be a certain grid point of the nth ray, the infinitesimal cross section of the nth ray was computed by the following midpoint rule:

$$dS_n \approx \frac{\left|(x_{n+1}-x_{n-1}, y_{n+1}-y_{n-1})\times\left(\frac{dx}{dt},\frac{dy}{dt}\right)_n\right|}{2\sqrt{\left(\frac{dx}{dt}\right)_n^2+\left(\frac{dy}{dt}\right)_n^2}}, \tag{58}$$

where dx/dt and dy/dt were given by (11) and (12), respectively. A total of 100 rays was issued with the interval of $\Delta\theta_i=0.005°$ from the angle of the limiting ray. The time step was taken to be $dt=0.025\,(\times\delta/a_-)$. The ratio of the infinitesimal cross section at the grid closest from the source to that at the grid right above $y=2$ (almost uniform flow) was used to calculate amplitude. In addition, the amplitude near the source point was calculated using (46), which is consistent with the analytic expression. Thus, pressure amplitude of refracted arrival waves was numerically calculated based on the ray-tube theory.

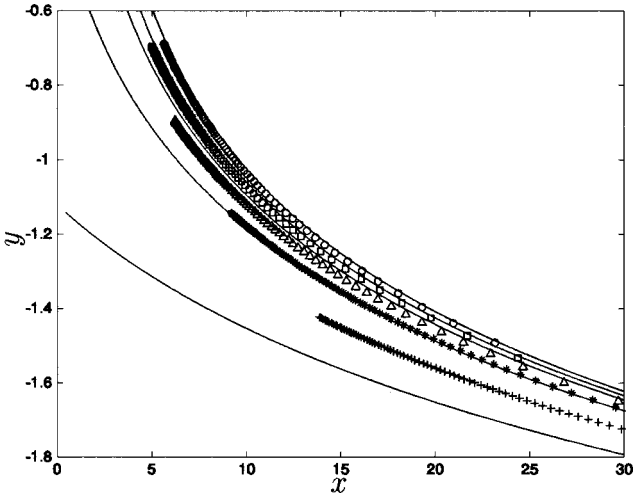

FIG. 6. Turning-point trajectories for different source locations. The lower free-stream velocity is $M_-=0.8$, and the temperature is constant everywhere. Symbols were computed by numerical integration: ○, $\eta=2$; □, $\eta=1$; △, $\eta=0$; *, $\eta=-0.5$; and +, $\eta=-1$. Lines were calculated using (35) corresponding to $\eta=2$, 1, 0, −0.5, and −1 from the top.

IV. RESULTS AND DISCUSSION

A. Turning point trajectory

First, to observe the accuracy of the analytical expression, turning-point trajectories were calculated using both analytical expression (35) and numerical integration (11)–(15), and the results are compared. Here, the incident locations in (35) were approximated by the following form:

$$x_{\text{in}}=-\frac{\eta}{\tan\theta_s^\star}, \tag{59}$$

where $\theta_s^\star\in[-\pi/2,0)$ is defined by (47).

Figure 6 represents the dependence of the turning-point trajectories on the source location. It shows that as the source location becomes lower (closer to the higher velocity side), the trajectories shift downward. When $\eta\geqslant-0.5$, the theoretical predictions agree with the numerical solutions fairly well. But, when the source location approaches the lower free-stream ($\eta=-1.$ case), the theoretical prediction deviates far lower than the numerical solution. Remember that the formula (35) assumes the incident points of the rays to be identical; hence, when the source approaches the lower free-stream region, this expression tends to fail. Nonetheless, the analytical expression approximates the ray trajectories fairly well when the source is above or close to the center line of the mixing layer.

Figure 7 represents the dependence of the ray trajectories on the lower free-stream velocity. (Although M_- actually yields the Mach number of the lower free-stream, the term ''free-stream velocity'' is used instead of ''free-stream Mach number'' to emphasize that $M(y)$ denotes the velocity normalized by a_- as opposed to the local Mach number.) This figure indicates that the analytical expression covers a

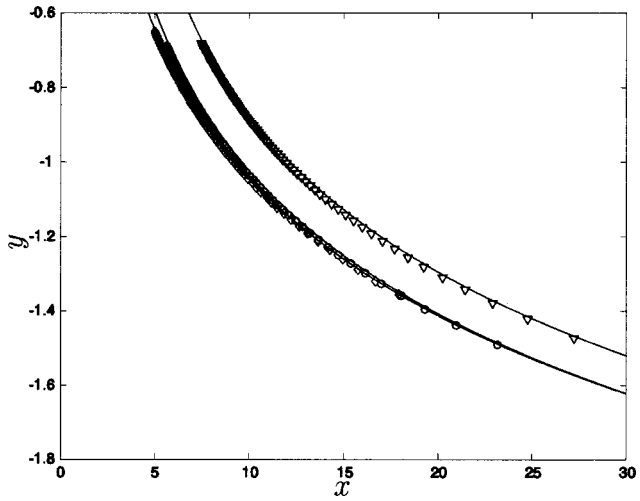

FIG. 7. Turning-point trajectories for different lower free-stream velocities. The source location is $\eta=2$, and the temperature is constant everywhere. Symbols were computed by numerical integration: ∇, $M_-=0.3$; $\bigcirc$, $M_-=0.8$; and $\diamond$, $M_-=1.5$. Lines were calculated using (35) corresponding to $M_-=0.3$, 0.8, and 1.5 from the top. Two cases ($M_-=0.8$ and 1.5) almost overlap.

wide velocity range. Thus, one can expect that the analytic expression provides a good approximation to the ray trajectories as long as the source is above or close to the center line of the mixing layer.

B. Pressure amplitude distribution

To validate the analytical expression for various lower free-stream velocities and source locations, pressure amplitude of refracted arrival waves was calculated using (48), and it is compared with the numerical integration using (10) and (11)–(15).

Figures 8(a)–(c) represent the amplitude profiles in the x direction for different lower free-stream velocities and source locations. As seen in Fig. 7, the theoretical predictions and the numerical results agree very well when the source is $\eta \geqslant -0.5$. Hence, one can expect that this expression can be used to estimate the noise generated inside the mixing layer and propagating in the zone of silence. Since the analytical formula (48) assumes a far-field asymptote, the theory and the numerical result agree better as X increases in all cases. Each figure shows that as the source approaches the lower free stream (η decreases), the amplitude increases; in particular, when the source is below $y=0$, the amplitude seems to be fairly sensitive to the source location. This series of figures also indicates that the noise from nearly the lower free stream tends to be strongly amplified as the velocity increases.

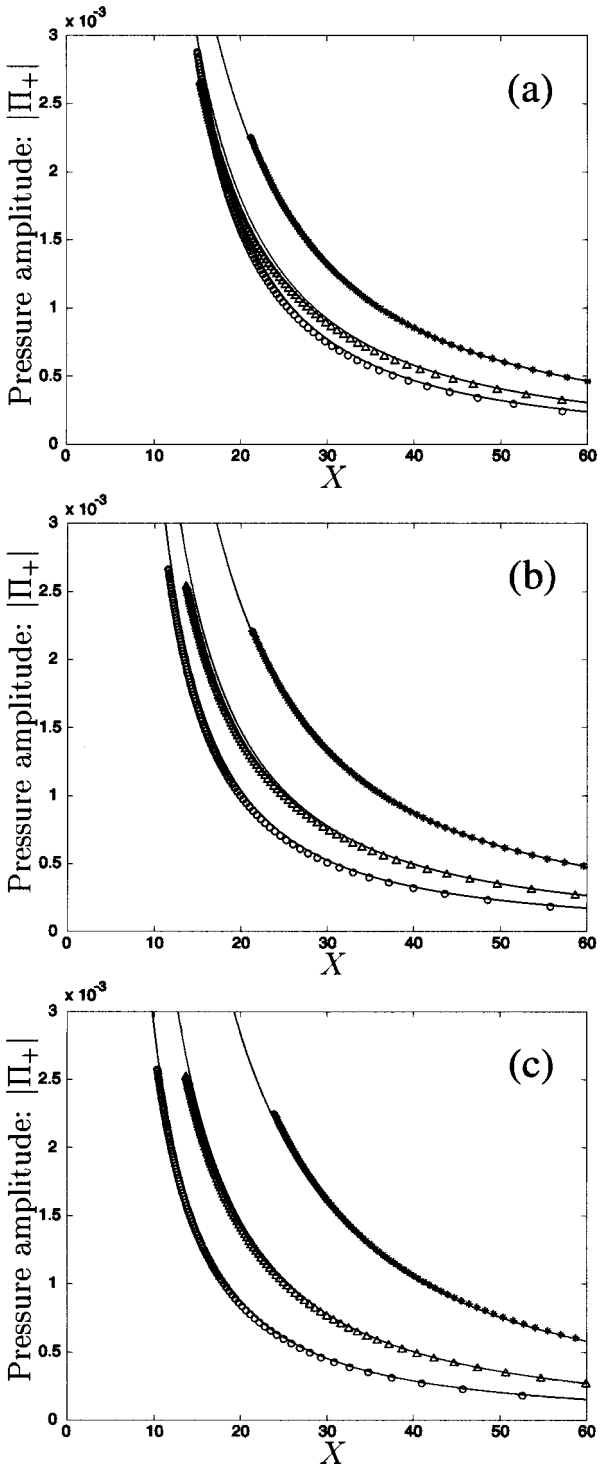

FIG. 8. Comparison of pressure amplitude between the finite thickness mixing layer model and the numerical integration. The amplitudes at $y=2$ are plotted. The lower free-stream velocity is (a) $M_-=0.3$; (b) $M_-=0.8$; and (c) $M_-=1.5$. The temperature is constant everywhere. Symbols were computed by numerical integration: $\bigcirc$, $\eta=2$; $\triangle$, $\eta=0$; and *, $\eta=-0.5$. Lines were calculated using (48) corresponding to $\eta=2, 0$, and 0.5 from the bottom.

C. Comparison between the finite thickness mixing layer model and the vortex sheet model

Next, two analytical models, the finite thickness mixing layer and the vortex sheet models, are compared. Remember that the finite thickness mixing layer model (48) corresponds to the high-frequency limit, while the vortex sheet models (49) and (50), correspond to the low-frequency limit. Figures 9(a)–(c) represent the comparison of these models at different lower free-stream velocities. Both models show that the amplitude increases as the source approaches the lower free stream. Moreover, all these cases show that as the frequency increases, the amplitude of the finite thickness model exceeds that of both vortex sheet models, as mentioned before.

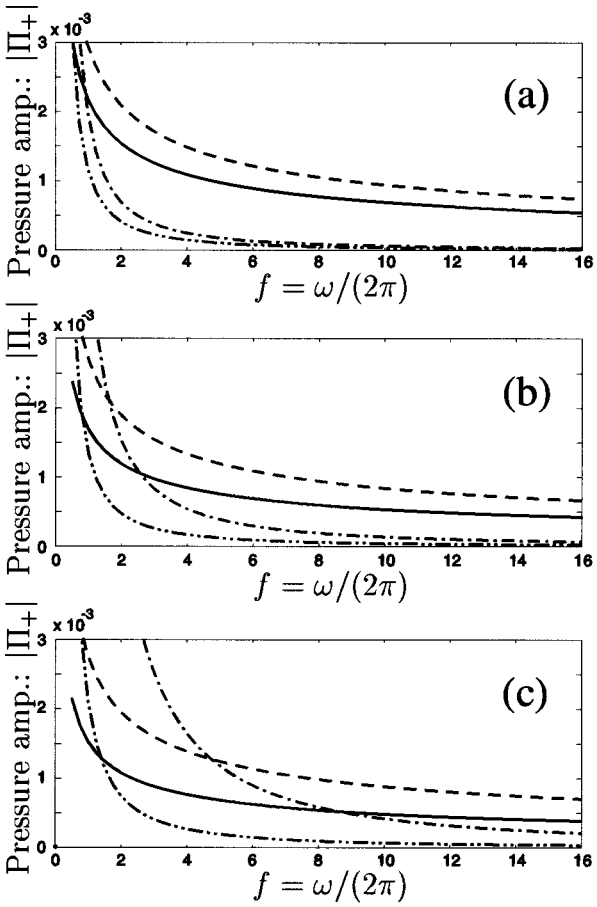

FIG. 9. Comparison between the finite thickness mixing layer model and the vortex sheet models in different lower free-stream velocities. The pressure amplitudes above the mixing layer are plotted. The lower free-stream velocity is (a) $M_-=0.3$; (b) $M_-=0.8$, and (c) $M_-=1.5$. The temperature is constant, and $X=20$. Lines represent as follows: ——, finite thickness model (48) with $\eta=2$; - - -, that with $\eta=0$; $-\cdots-$, vortex sheet model with the source above the mixing layer (49); and $-\cdot-$, the source below the mixing layer (50).

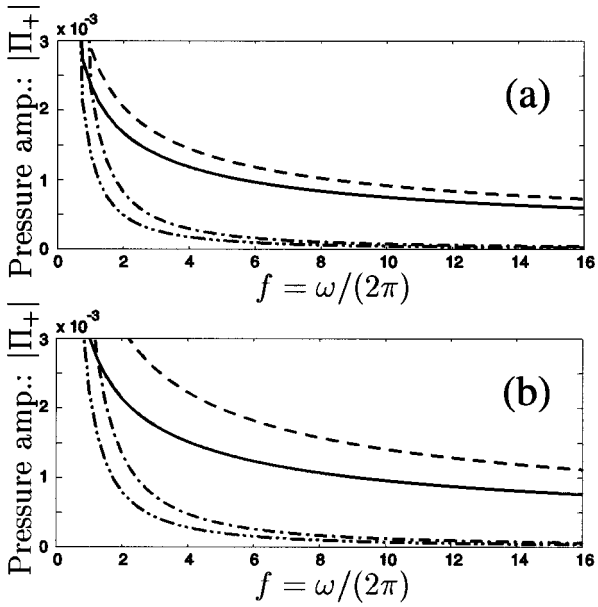

FIG. 10. Comparison between the finite thickness mixing layer model and the vortex sheet models in different speeds of sound. The speed of sound on the upper side is (a) $a_+=0.7$ and (b) $a_+=1.2$. The lower free-stream velocity is $M_-=0.3$. The rest of the conditions and notations are the same as Fig. 9.

This tendency is particularly striking in lower subsonic flows. Figure 9(a) clearly demonstrates that the vortex sheet model far underestimates the amplitude of refracted arrival waves in a wide range on the higher-frequency side. Remember that as the frequency increases, the finite thickness model decays as $\sim\omega^{-1/2}$, while the vortex sheet model as $\sim\omega^{-3/2}$.

Figures 10(a) and (b) show the comparison of these models at different speeds of sound. Here, (a) represents a hot jet and (b) a cold jet, and the constant temperature case corresponds to Fig. 9(a). They show that in the vortex sheet model, the temperature variation hardly affects the pressure amplitude. In contrast, in the finite thickness model, the amplitude strongly increases as the source approaches the lower free stream in cold jets; however, it barely changes in hot jets. Notice that due to the definition of the source term $(\hat{\Pi}''+[n_s^2-k^2]\hat{\Pi}\sim\delta(y-\eta)/a_s^2$, refers to (A1) shown in the Appendix), the amplitude may even decrease as the source approaches the core of hot jets though the distance between the adjacent rays become narrower. These tendencies will be summarized in the next figures.

Finally, to observe the dependence on the lower free-stream velocity and the speed of sound, the amplitude of refracted arrival waves was mapped onto the M_- and a_+ plane. Figures 11(a)–(c) represent the pressure amplitude contours calculated by the finite thickness model (48). The regions where contour lines are missing (the left top corner) indicate that refracted arrival waves do not or barely exist under such conditions: $\overline{n_s^\star}^2-\phi_x^{\star 2}$ approaches zero in (48). Hence, there are no rays which initially propagate downward and get refracted upward. This series of figures demonstrates the features observed in Figs. 8(a)–(c): As the source approaches the lower free stream, the amplitude tends to increase over the whole range; particularly, this tendency becomes striking when the source is below the center line of the mixing layer ($\eta\leqslant-0.5$). Figure 11 also reveals that the amplitude becomes more sensitive to the lower free-stream velocity as η decreases. They also show that as the jet becomes hotter (a_+ decreases), the amplitude increases in the supersonic range ($M_-\geqslant 1$) in all cases. On the other hand, in low subsonic flows the amplitude becomes fairly large when the jet becomes colder (a_+ increases). In this region, the critical angle $\theta_s^\star$ defined by (47) becomes considerably shallow so that wide angles of the rays are captured within the mixing layer, and the distinction between direct waves and refracted arrival waves becomes ambiguous.

For reference, Fig. 12 represents the amplitude contours calculated using the vortex sheet models for the source (a) above and (b) below the mixing layer, respectively. Note that the direct comparison of the magnitude between Figs. 11 and 12 may not be meaningful, since the amplitude ratio between them depends on the ratio of α/ω. Figures 11(b) and 12(a) as well as Figs. 11(c) and 12(b) show some qualitative similarities. However, when the source is below the mixing layer, the vortex sheet model indicates that the amplitude substantially increases as the velocity increases.

It is important to notice that the solution for refracted

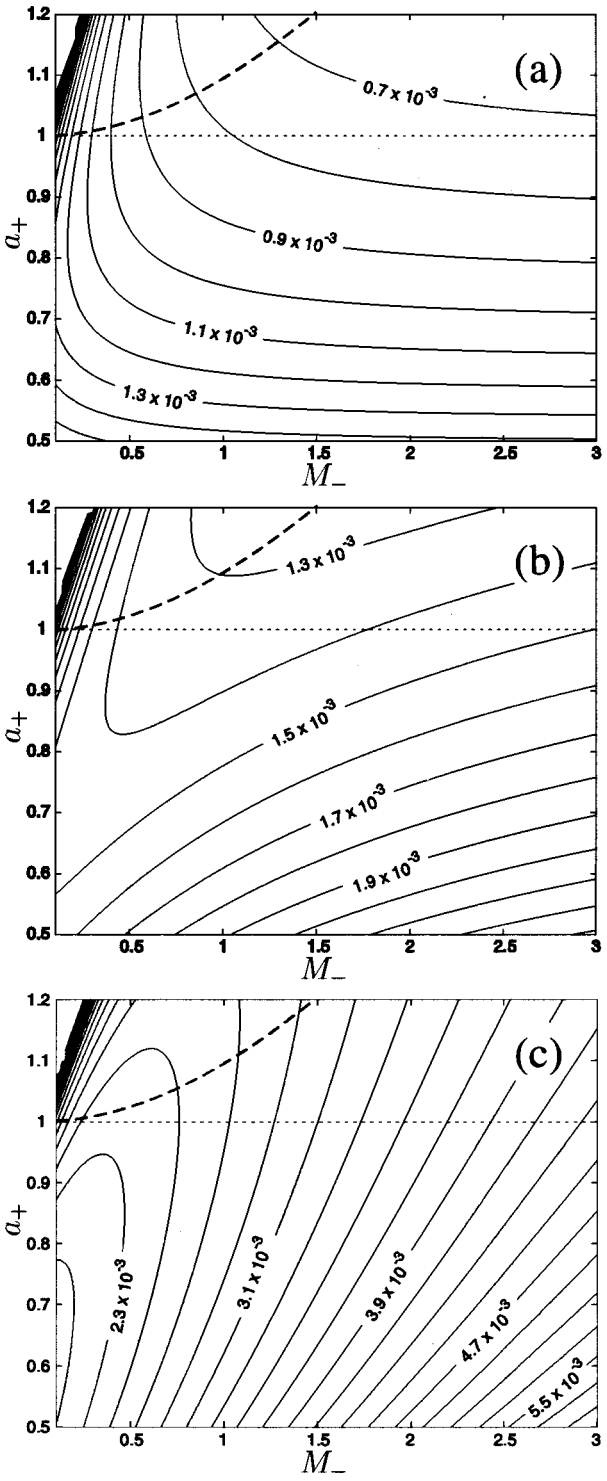

FIG. 11. Pressure amplitude contours in the plane of the lower free-stream velocity and the speed of sound based on the finite thickness mixing layer model. The pressure amplitudes of the finite thickness model (48) are shown. $\omega/2\pi=4$ and $X=20$. The source is set to be (a) $\eta=2$; (b) $\eta=0$; and (c) $\eta=-0.5$. The thicker dashed line denotes the isoenthalpy line.

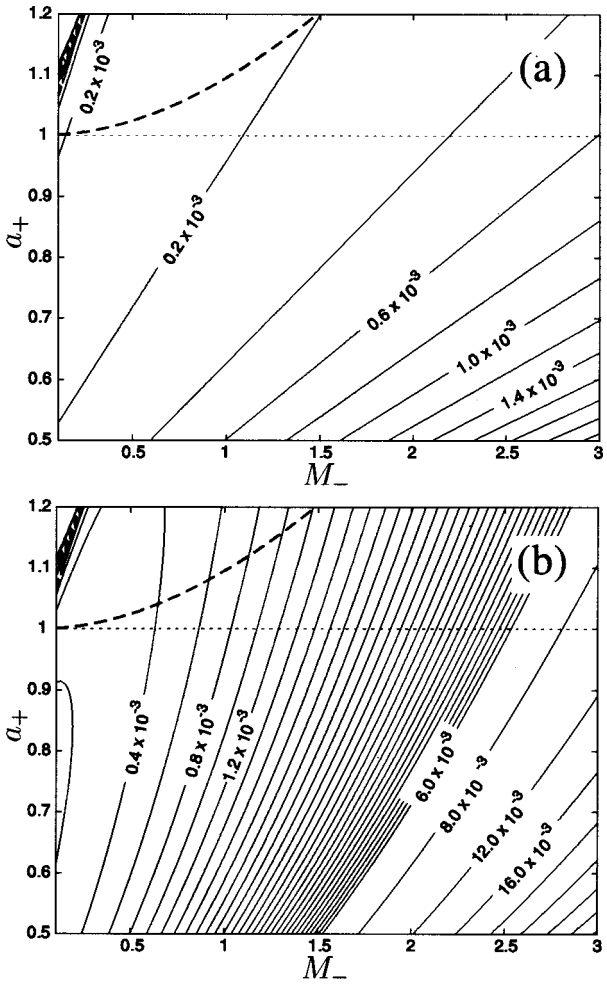

FIG. 12. Pressure amplitude contours in the plane of the lower free-stream velocity and the speed of sound based on the vortex sheet model. The conditions and notations are the same as Fig. 11. The source location is (a) above the mixing layer (49), and (b) below the mixing layer (50).

arrival waves belongs to the same family as Mach wave-type sound.[11] From a one-dimensional point of view, namely the linear analysis based on (A1), this family satisfies the boundary conditions of exponential decay toward the lower side (high speed) and oscillation toward the upper side (low speed), and changes its nature at the turning point. In this sense, refracted arrival waves from a finite thickness mixing layer have a similar feature of Mach waves studied in some previous works.[11–13] However, it is worthwhile to observe that supersonic phase velocity can be obtained not only by sources supersonically convected: Waves issued from an upstream source and refracted near the lower free stream have phase velocity of u_-+a_- (where u_- denotes the jet velocity); hence, they can propagate in the zone of silence although the intensity of refracted arrival waves tends to be fairly small, as Figs. 11 and 12 indicate.

It should also be emphasized that the present analysis is based on a parallel mixing layer. Of course, when the jet is spreading,[14] the turning points shift closer to the core; as a result, refracted arrival waves become ''more like direct waves'' and their amplitude is enhanced (refer to Ref. 15 for calculation in a more realistic flow geometry). Hence, the high-frequency sound in the zone of silence measured in experiments might be caused mainly by direct waves from the end of the potential core.[6] To estimate the mixing layer spreading effect on the sound radiation field, the pressure amplitude was numerically calculated at different spreading rates. The velocity profile was set to be

$$M(x,y)=\frac{M_-}{2}\left[1-\tanh\left(\frac{2y}{1+\delta' x}\right)\right], \tag{60}$$

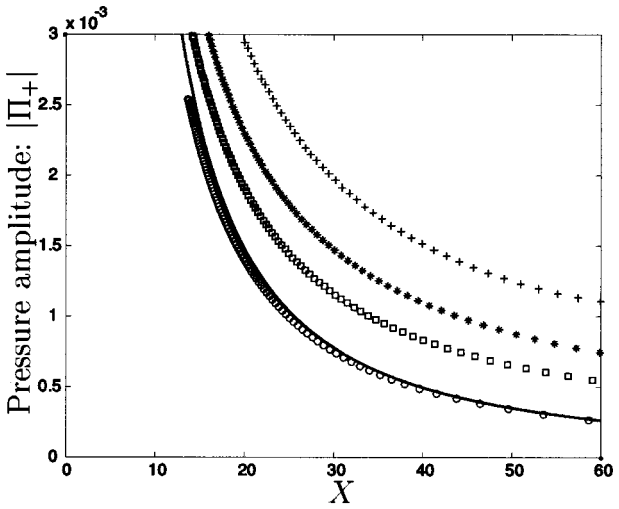

FIG. 13. Comparison of pressure amplitude profile of different spreading rates. The lower free-stream velocity is $M_{-}=0.8$, the source location is $\eta=0$, and the temperature is constant everywhere. Symbols were computed by numerical integration: ○, $\delta'=0$; □, $\delta'=0.05$; *, $\delta'=0.10$; and +, $\delta'=0.20$. A solid line was calculated using the finite thickness mixing layer model (48).

where the free-stream velocity was set to be $M_{-}=0.8$ and the temperature to be constant everywhere. Here, the source was placed at the origin. The results are plotted in Fig. 13 and compared with the parallel mixing layer model at high frequencies. Figure 13 clearly shows that even $\delta'=0.1$ of the spreading rate yields several times as large pressure amplitude as that in the parallel mixing layer case. Note that previous experimental and numerical studies (summarized in Ref. 16) have indicated that the spreading rate can be up to $\delta'\sim 0.2$ as the jet Mach number decreases. Therefore, to compare these theoretical expressions with actual experiments, one needs the information about the mean flow as well as rigorous source models and their distribution.

Furthermore, in terms of the frequency range, the most unstable mode of instability waves is likely to be somewhere in between the low- and high-frequency limits. The high-frequency formula derived here focuses on noise due to rather finer scale turbulence. As observed by experiments,[9] the high-frequency component of the jet noise is mainly generated near the nozzle lip, in which large-scale vortical disturbances have not yet significantly grown. In addition, a numerical study by Suzuki[17] shows that this high-frequency formula for refracted arrival waves is applicable when the ratio of the acoustic wavelength to the vorticity thickness becomes unity or less. Therefore, the analysis in this study is expected to be useful for noise generated near the jet exit. However, once instability waves have developed into large-scale vortical structures downstream, such as at the end of the potential core, the current analysis would no longer be valid. Other issues associated with jet noise, such as the multipole and moving sources, are also discussed in Ref. 17.

V. CONCLUSION

Through this study, refracted arrival waves propagating in the zone of silence are formulated in the high-frequency limit and compared with the formula in the low-frequency limit. These formulas show that the amplitude at high frequencies is proportional to $\omega^{-1/2}$, while that at low frequencies is proportional to $\omega^{-3/2}$, ω being the source angular frequency. This indicates that the existing low-frequency formula,[2,3] namely the vortex sheet model, tends to underestimate the sound-pressure level in the zone of silence as the frequency increases. It also implies that the previous high-frequency theory[8] ignoring refracted arrival waves does not correctly represent the sound radiation pattern in the zone of silence.

This high-frequency formula of refracted arrival waves has significant implications for the application to jet noise. In most previous studies, general plane-wave-type radiation has been considered only for supersonic jet flows (referred to as Mach waves). However, this study indicates that even in subsonic mixing layers, general plane-wave-type sound can theoretically propagate in the zone of silence. In particular, this formula is expected to be applicable to the high-frequency noise mainly generated near the nozzle lip of the jet exit. Therefore, it should be used to estimate the sound-pressure level in the zone of silence at high frequencies. However, at present the existence of such waves in real flows is uncertain, and as noted below, some extensions of the present theory are required for quantitative prediction.

For example, one may need to more rigorously analyze some additional effects of real flows: As the mixing layer spreads, more rays are trapped inside of it and the distinction between refracted arrival waves and direct waves becomes ambiguous. In fact, this study shows that a slight increase in the spreading rate of the mixing layer drastically enhances the amplitude of refracted arrival waves. Other examples which are not studied here are effects of unsteady flow disturbances, source models for turbulent mixing noise, and so on. Nonetheless, it is important to note this study demonstrates that sound radiation pattern in the zone of silence is fundamentally different from the region in which direct waves propagate and the amplitude of refracted arrival waves is different several times over between the low- and high-frequency limits.

ACKNOWLEDGMENTS

The authors would like to thank Professor Brian J. Cantwell and Professor Joseph B. Keller for many useful suggestions. We gratefully acknowledge the financial support by NASA Ames Research Center (Grant No. NAG 2-1373).

APPENDIX: Derivation for the low-frequency limit

To rederive the formulas of refracted arrival waves in the low-frequency limit, derivative matching[4] is used here. First, take a Fourier transform of (1) in time and the flow direction, and set a delta function at $y=\eta$,

$$\frac{\partial}{\partial y}\left(a^2\frac{\partial\hat{\Pi}}{\partial y}\right)+\frac{2k\dfrac{\partial M}{\partial y}}{\omega-kM}\left(a^2\frac{\partial\hat{\Pi}}{\partial y}\right)+[(\omega-kM)^2-a^2k^2]\hat{\Pi}=\delta(y-\eta), \tag{A1}$$

where

$$\hat{\Pi}(\omega,k,y)=\frac{1}{(2\pi)^2}\int_{-\infty}^{\infty}\int_{-\infty}^{\infty}\Pi(t,x,y)e^{i(\omega t-kx)}dt\,dx. \tag{A2}$$

When the wavelength is much longer than the vorticity thickness, the third term of (A1) becomes much smaller than the first two terms. Therefore, in the low-frequency limit (A1) can be approximated by

$$\frac{\partial}{\partial y}\left[\frac{a^2(y)}{(\omega-kM(y))^2}\frac{\partial\hat{\Pi}}{\partial y}\right]\approx\frac{\delta(y-\eta)}{(\omega-kM(y))^2}. \tag{A3}$$

Hence, the quantity $[a^2(y)/(\omega-kM(y))^2]\partial\hat{\Pi}/\partial y$ is constant across the vortex sheet. Subsequently, assuming $|\partial\hat{\Pi}/\partial y|$ is finite, it can be shown that $\hat{\Pi}$ is continuous across the vortex sheet. Although the pressure itself is continuous across the vortex sheet, the first derivative has a discontinuity. Thus, the jump conditions across the vortex sheet become

$$\hat{\Pi}_+(y=0_+)=\hat{\Pi}_-(y=0_-), \tag{A4}$$

$$\frac{1}{n_+^2}\frac{\partial\hat{\Pi}_+}{\partial y}\bigg|_{y=0_+}=\frac{1}{n_-^2}\frac{\partial\hat{\Pi}_-}{\partial y}\bigg|_{y=0_-}, \tag{A5}$$

where $n_\pm\equiv(\omega-kM_\pm)/a_\pm$, which is equivalent to $\omega\overline{n}_\pm$ [$\overline{n}$ is defined after (41) and (42)]. Likewise, k is equal to $\omega\phi_x$ used in the high-frequency limit.

To derive the formulas for refracted arrival waves, first put the source above the vortex sheet ($\eta>0$). In the transverse direction, incident and reflected waves propagate on the upper side, and transmitted waves on the lower side. Knowing that the second term of (A1) vanishes in the uniform flow region, the forms of the solution on the upper and lower sides can be expressed as follows:

$$\hat{\Pi}_+=\frac{e^{-i\sqrt{n_+^2-k^2}(y-\eta)}}{i2a_+^2\sqrt{n_+^2-k^2}}+\mathbf{C}_re^{i\sqrt{n_+^2-k^2}y}, \tag{A6}$$

$$\hat{\Pi}_-=\mathbf{C}_te^{-i\sqrt{n_-^2-k^2}y}. \tag{A7}$$

Here, $\mathbf{C}_r$ and $\mathbf{C}_t$ ($\in\mathbf{C}$) are the reflection and transmission coefficients, respectively. Note that the "resonance mode"[3,18] is not taken into account here for simplicity. Substituting (A6) and (A7) into (A4) and (A5), transmitted waves can be obtained as follows:

$$\hat{\Pi}_-=\frac{e^{i\sqrt{n_+^2-k^2}}\eta e^{-i\sqrt{n_-^2-k^2}y}}{ia_+^2n_+^2\left(\dfrac{\sqrt{n_+^2-k^2}}{n_+^2}+\dfrac{\sqrt{n_-^2-k^2}}{n_-^2}\right)}. \tag{A8}$$

By taking an inverse Fourier transform of (A8), the two-dimensional formula can be derived as

$$\Pi_-(\omega,r,\theta)=\frac{1}{2\pi i}\int_{-\infty}^{+\infty}\frac{e^{i\sqrt{n_+^2-k^2}}\eta e^{i(k\cos\theta-\sqrt{n_-^2-k^2}\sin\theta)r}}{a_+^2n_+^2\left(\dfrac{\sqrt{n_+^2-k^2}}{n_+^2}+\dfrac{\sqrt{n_-^2-k^2}}{n_-^2}\right)}dk. \tag{A9}$$

To evaluate (A9), assume $\eta\ll r$ and $r\gg1$, and use the stationary phase method. Defining the phase part to be $\varphi(k)\equiv k\cos\theta-\sqrt{(n_-^2-k^2)}\sin\theta$, $\varphi'(k)=0$ gives the stationary point, which becomes

$$k=\frac{\omega}{1-M_-^2}\left(-M_-+\frac{\cos\theta}{\sqrt{1-M_-^2\sin^2\theta}}\right). \tag{A10}$$

As a result, (A9) can be approximated in the far field as follows:

$$\Pi_-(\omega,r,\theta)\approx\frac{\omega^{1/2}}{\sqrt{2\pi}r^{3/2}}\frac{|r\sin\theta|}{(1-M_-^2\sin^2\theta)^{3/4}}\frac{e^{i\sqrt{n_+^2-k^2}}\eta e^{i[-M_-\cos\theta+\sqrt{1-M_-^2\sin^2\theta}/1-M_-^2]\,\omega r-(3/4)\pi)}}{a_+^2n_+^2\left(\dfrac{\sqrt{n_+^2-k^2}}{n_+^2}+\dfrac{\sqrt{n_-^2-k^2}}{n_-^2}\right)}, \tag{A11}$$

where k and $n_\pm$ are evaluated at the stationary point (A10). The solution for refracted arrival waves must match with (A11) across the mixing layer. To apply the derivative matching (A5), differentiate (A11) with respect to y and set $y=0$

$$\frac{\partial\Pi_-}{\partial y}\bigg|_{y=0}\approx\frac{-\omega^{1/2}e^{i\sqrt{n_+^2-k^2}}\eta}{\sqrt{2\pi}x^{3/2}}\frac{e^{i(kx-(3/4)\pi)}}{a_+^2\sqrt{n_+^2-k^2}}. \tag{A12}$$

Here, the stationary point is $k(\theta=0)=\omega/(1+M_-)$.

On the other hand, refracted arrival waves on the upper side should be expressed in the form of general plane waves; hence, they can be written by

$$\Pi_+(\omega,x,y)\approx\mathbf{A}_+\left(x-\frac{\sqrt{n_+^2-k^2}}{k}y\right)e^{i(kx+\sqrt{n_+^2-k^2}y)}. \tag{A13}$$

Similarly, differentiate (A13) with respect to y and evaluate at $y=0$ retaining the lowest order of x (namely, the $\mathbf{A}'_+$ term is eliminated)

$$\frac{\partial\Pi_+}{\partial y}\bigg|_{y=0}\approx i\sqrt{n_+^2-k^2}\mathbf{A}_+(x)e^{ikx}. \tag{A14}$$

Substituting (A12) and (A14) into (A5), it yields as follows:

$$\Pi_+(\omega,x,y)\approx \frac{\omega^{1/2}}{\sqrt{2\pi}}\frac{n_+^2}{a_+^2 n_-^2(n_+^2-k^2)} \times \frac{e^{i\sqrt{n_+^2-k^2}\,\eta}e^{i(kx+\sqrt{n_+^2-k^2}y-(\pi/4))}}{\left(x-\frac{\sqrt{n_+^2-k^2}}{k}y\right)^{3/2}}. \tag{A15}$$

One can obtain the same result by taking a contour integral of (A9). By using the same notation as (48), the absolute value of (A15) becomes (49).

Likewise, put the source below the vortex sheet ($\eta<0$), and follow the same procedure as described above. It is noticed that there exist incident waves and reflected waves on the lower side, but only the reflected waves contribute the derivative matching. Consequently, the absolute value of pressure amplitude for refracted arrival waves becomes (50) in this case.

[1] P. Gottlieb, "Sound source near a velocity discontinuity," J. Acoust. Soc. Am. **32**, 1117–1123 (1960).

[2] A. B. Friedland and A. D. Pierce, "Reflection of acoustic pulses from stable and instable interfaces between moving fluids," Phys. Fluids **12**(6), 1148–1159 (1969).

[3] M. S. Howe, "Transmission of an acoustic pulse through a plane vortex sheet," J. Fluid Mech. **43**(2), 353–367 (1970).

[4] J. B. Keller and R. M. Lewis, "Asymptotic methods for partial differential equations: The reduced wave equation and Maxwell's equations," in *Surveys in Applied Mathematics*, edited by J. B. Keller, D. W. McLaughlin, and G. C. Papanicolaou (Plenum, New York, 1995), Vol. 1, pp. 1–82.

[5] L. D. Landau and E. M. Lifshitz, *Fluid Mechanics*, Trans., 2nd ed. (Pergamon, New York, 1987), pp. 276–281.

[6] H. K. Tanna, "An experimental study of jet noise. I. Turbulent mixing noise," J. Sound Vib. **50**(3), 405–428 (1977).

[7] D. I. Blokhintzev, "Acoustics of a nonhomogeneous moving medium," Trans., NACA TM 1339 (1946).

[8] M. E. Goldstein, "High frequency sound emission from point multiple sources embedded in arbitrary transversely sheared mean flows," J. Sound Vib. **80**, 499–522 (1982).

[9] B. R. Dougherty, "Phased array beamforming for aeroacoustics," Lecture Notes in an AIAA Professional Development Short Course, 1999.

[10] G. M. Lilley, "On the noise from jets," AGARD, CP-13, 1–12 (1974).

[11] C. K. W. Tam and D. E. Burton, "Sound generated by instability waves of supersonic flows. I. Two-dimensional mixing layer," J. Fluid Mech. **138**, 249–271 (1984).

[12] J. E. Ffowcs Williams, "The noise from turbulence convected at high speed," Philos. Trans. R. Soc. London, Ser. A **255A**, 469–503 (1963).

[13] T. F. Balsa, "The far field of high frequency convected singularities in sheared flows, with an application to jet-noise prediction," J. Fluid Mech. **74**(2), 193–208 (1976).

[14] L. K. Schubert, "Numerical study of sound refraction by a jet flow. I. Ray acoustics," J. Acoust. Soc. Am. **51**, 439–446 (1972).

[15] C. K. W. Tam and L. Auriault, "Mean flow refraction effects on sound radiated from localized sources in a jet," J. Fluid Mech. **370**, 149–174 (1998).

[16] J. B. Freund and S. K. Lele, "Computer simulation and prediction of jet noise," to appear in High Speed Jet Flows, edited by G. Raman, D. K. McLaughlin, and P. J. Morris (Taylor & Francis, London, 2002).

[17] T. Suzuki, "Acoustic wave propagation in transversely sheared flows," Ph.D. dissertation, Stanford University, 2001.

[18] J. W. Miles, "On the reflection of sound at an interface of relative motion," J. Acoust. Soc. Am. **29**(2), 226–228 (1957).

A wide angle and high Mach number parabolic equation

Joseph F. Lingevitch, Michael D. Collins, Dalcio K. Dacol, and Douglas P. Drob
Naval Research Laboratory, Washington, DC 20375

Joel C. W. Rogers
Department of Mathematics, Polytechnic University, Brooklyn, New York 11201

William L. Siegmann
Rensselaer Polytechnic Institute, Troy, New York 12180

(Received 21 May 2001; revised 3 October 2001; accepted 9 October 2001)

Various parabolic equations for advected acoustic waves have been derived based on the assumptions of small Mach number and narrow propagation angles, which are of limited validity in atmospheric acoustics. A parabolic equation solution that does not require these assumptions is derived in the weak shear limit, which is appropriate for frequencies of about 0.1 Hz and above for atmospheric acoustics. When the variables are scaled appropriately in this limit, terms involving derivatives of the sound speed, density, and wind speed are small but can have significant cumulative effects. To obtain a solution that is valid at large distances from the source, it is necessary to account for linear terms in the first derivatives of these quantities [A. D. Pierce, J. Acoust. Soc. Am. **87**, 2292–2299 (1990)]. This approach is used to obtain a scalar wave equation for advected waves. Since this equation contains two depth operators that do not commute with each other, it does not readily factor into outgoing and incoming solutions. An approximate factorization is obtained that is correct to first order in the commutator of the depth operators. [DOI: 10.1121/1.1430683]

PACS numbers: 43.28.Py, 43.30.Dr [SAC-B]

I. INTRODUCTION

Parabolic equation techniques[1] provide an excellent combination of accuracy and efficiency for many wave propagation problems that are range dependent (i.e., the ambient properties have horizontal variations). Parabolic equations are often derived by factoring an operator in a wave equation, assuming that outgoing energy dominates backscattered energy, and approximating the square root of an operator. This approach is of limited use for advected acoustic waves. Various approximate parabolic equations[2–11] have been derived for this problem using the assumptions of low Mach number and narrow propagation angle, which are of limited validity for atmospheric acoustics problems. In this paper, we derive a parabolic equation solution that does not require these assumptions. This solution is based on the weak shear limit, which can also be regarded as the high-frequency limit and corresponds to about 0.1 Hz and above in atmospheric acoustics. When the variables are scaled appropriately in this limit, terms involving derivatives of the sound speed, density, and wind speed are small but can have significant cumulative effects. To obtain a solution that is valid at large distances from the source, it is necessary to account for linear terms in the first derivatives of these quantities.[12] These terms also need to be taken into account in the derivation of the parabolic equation. In Sec. II, we describe the problem and write the equations of motion. In Sec. III, we derive a scalar wave equation that is valid in the weak shear limit. In Sec. IV, we derive the parabolic equation solution and demonstrate its accuracy for an atmospheric acoustics problem.

II. ADVECTED ACOUSTIC WAVES

There exist various wave equations for advected acoustic waves that are based on different assumptions. For the cases considered in this paper, we assume that the ambient flow is independent of time, the vertical component of the flow can be neglected, and horizontal variations in the medium are much more gradual than vertical variations. We use the last of these assumptions to justify the neglect of range dependence during the derivations. The ambient properties are then allowed to depend on range in the parabolic equation solution. This standard approach for deriving parabolic equation solutions provides a high level of accuracy when combined with energy-conservation corrections.[13–15] We derive the wave equation in Cartesian coordinates, where x and y are the horizontal coordinates and z is the depth. The details of the derivation below generalize to cylindrical and spherical coordinate systems.

The velocity $\mathbf{u}=(u,v,w)$, pressure p, and density ρ satisfy the momentum equation, conservation of mass, and the equation of state[16]

$$\rho \frac{D\mathbf{u}}{Dt} = -\nabla p + \rho \mathbf{g}, \tag{1}$$

$$\frac{D\rho}{Dt} + \rho \nabla \cdot \mathbf{u} = 0, \tag{2}$$

$$\frac{Dp}{Dt} = c^2 \frac{D\rho}{Dt}, \tag{3}$$

where $D/Dt = \partial/\partial t + \mathbf{u}\cdot\nabla$, c is the speed of sound, and $\mathbf{g}$

$=(0,0,g)$ is the acceleration due to gravity. We consider a solution of the form

$$(\mathbf{u},p,\rho)\sim(\mathbf{u}_0,p_0,\rho_0)+(\mathbf{u}_1,p_1,\rho_1), \tag{4}$$

where the ambient state $(\mathbf{u}_0,p_0,\rho_0)$ is the solution in the absence of the perturbation $(\mathbf{u}_1,p_1,\rho_1)$. To obtain a linear equation for acoustic waves, we ignore the effect of gravity on the perturbation and retain linear terms in the perturbation. This assumption is valid if the forcing frequency is significantly larger than the buoyancy frequency of the ambient medium.

Substituting Eq. (4) into Eqs. (1), (2), and (3) and applying the assumptions, we obtain

$$D_t\mathbf{u}_1+w_1\frac{\partial\mathbf{u}_0}{\partial z}+\frac{1}{\rho_0}\nabla p_1=0, \tag{5}$$

$$\nabla\cdot\mathbf{u}_1+\frac{1}{c^2\rho_0}D_t p_1=0, \tag{6}$$

where $D_t=\partial/\partial t+\mathbf{u}_0\cdot\nabla$. Applying the divergence to Eq. (5), applying D_t to Eq. (6), and subtracting, we obtain

$$\nabla\cdot\left(\frac{1}{\rho_0}\nabla p_1\right)-\frac{1}{c^2\rho_0}D_t^2p_1+\nabla\cdot\left(D_t\mathbf{u}_1+w_1\frac{\partial\mathbf{u}_0}{\partial z}\right)-D_t\nabla\cdot\mathbf{u}_1=0. \tag{7}$$

Simplifying Eq. (7) and applying the assumptions, we obtain

$$\nabla\cdot\left(\frac{1}{\rho_0}\nabla p_1\right)-\frac{1}{c^2\rho_0}D_t^2p_1+2\frac{\partial\mathbf{u}_0}{\partial z}\cdot\nabla w_1=0. \tag{8}$$

From the z component of Eq. (5), we obtain

$$D_t w_1+\frac{1}{\rho_0}\frac{\partial p_1}{\partial z}=0. \tag{9}$$

Equations (8) and (9) are a coupled system for the dependent variables (w_1,p_1). For the case of negligible shear they reduce to a scalar equation for the pressure.

III. DERIVATION OF THE WAVE EQUATION

In this section, we derive a scalar wave equation in the weak shear limit. We account for terms that are linear in the first derivatives of the ambient properties but neglect higher-order terms. Reducing Eqs. (8) and (9) to two dimensions in the frequency domain, including a source term, and dropping subscripts, we obtain

$$(1-U^2)\frac{\partial^2p}{\partial x^2}+2ikU\frac{\partial p}{\partial x}+\rho\frac{\partial}{\partial z}\left(\frac{1}{\rho}\frac{\partial p}{\partial z}\right)+k^2p+2\rho\frac{\partial u}{\partial z}\frac{\partial w}{\partial x}=2i\delta(x)\delta(z-z_0), \tag{10}$$

$$i\omega w-u\frac{\partial w}{\partial x}=\frac{1}{\rho}\frac{\partial p}{\partial z}, \tag{11}$$

where $U=u/c$, the ambient horizontal flow velocity scaled by the sound speed. Taking the Fourier transform in x of Eqs. (10) and (11), we obtain

$$-(1-U^2)h^2\hat{p}-2khU\hat{p}+\rho\frac{\partial}{\partial z}\left(\frac{1}{\rho}\frac{\partial\hat{p}}{\partial z}\right)+k^2\hat{p}+2ih\rho\frac{\partial u}{\partial z}\hat{w}=2i\delta(z-z_0), \tag{12}$$

$$i\rho(\omega-uh)\hat{w}=\frac{\partial\hat{p}}{\partial z}, \tag{13}$$

where h is the horizontal wave number and $\hat{p}(h,z)$ is the wave-number spectrum. Using Eq. (13) to eliminate $\hat{w}$ from Eq. (12), we obtain

$$\frac{\partial^2\hat{p}}{\partial z^2}+\left(\frac{2h}{\omega-uh}\frac{\partial u}{\partial z}-\frac{1}{\rho}\frac{\partial\rho}{\partial z}\right)\frac{\partial\hat{p}}{\partial z}+(k^2-(1-U^2)h^2-2kUh)\hat{p}=2i\delta(z-z_0). \tag{14}$$

Inverting the Fourier transform, we obtain the spectral solution

$$p(x,z)=\frac{1}{2\pi}\int_{-\infty}^{\infty}\hat{p}(h,z)\exp(ihx)dh. \tag{15}$$

This solution is only valid for range-independent problems. The parabolic equation solution derived in Sec. IV can be applied to range-dependent problems.

Although the derivatives of ρ and u are small compared to gradients in pressure in the high-frequency limit, first-order terms involving $\partial\rho/\partial z$ and $\partial u/\partial z$ can have significant effects far from the source. Terms involving second-order factors such as $(\partial\rho/\partial z)^2$ and $\partial^2\rho/\partial z^2$ can be neglected for sufficiently high frequencies. To eliminate first-order terms, we introduce the change of variables $\hat{p}=\alpha\hat{\phi}$, where α is a function of ρ and u, and obtain

$$\frac{\partial\hat{p}}{\partial z}=\alpha\frac{\partial\hat{\phi}}{\partial z}+\frac{\partial\alpha}{\partial z}\hat{\phi}, \tag{16}$$

$$\frac{\partial^2\hat{p}}{\partial z^2}=\alpha\frac{\partial^2\hat{\phi}}{\partial z^2}+2\frac{\partial\alpha}{\partial z}\frac{\partial\hat{\phi}}{\partial z}+\frac{\partial^2\alpha}{\partial z^2}\hat{\phi}. \tag{17}$$

Selecting α so that the first-order terms vanish, we obtain

$$\frac{2}{\alpha}\frac{\partial\alpha}{\partial z}=\frac{1}{\rho}\frac{\partial\rho}{\partial z}-\frac{2h}{\omega-uh}\frac{\partial u}{\partial z}, \tag{18}$$

$$\alpha=\frac{(\omega-uh)\rho^{1/2}}{(\omega-\tilde{u}h)\tilde{\rho}^{1/2}}, \tag{19}$$

where the tildes indicate evaluation at $z=z_0$. In the time domain, this change of variables corresponds to $\tilde{\rho}^{1/2}\tilde{D}_t p=\rho^{1/2}D_t\phi$. A related change of variables was used in Ref. 12 to obtain a scalar wave equation. Substituting the new variable into Eq. (14) and neglecting second-order terms, we obtain

$$\frac{\partial^2\hat{\phi}}{\partial z^2}+(k^2-(1-U^2)h^2-2kUh)\hat{\phi}=2i\delta(z-z_0). \tag{20}$$

Inverting the Fourier transform, we obtain the advected acoustic wave equation

$$(1-U^2)\frac{\partial^2\phi}{\partial x^2}+2ikU\frac{\partial\phi}{\partial x}+\frac{\partial^2\phi}{\partial z^2}+k^2\phi=2i\delta(x)\delta(z-z_0). \tag{21}$$

IV. PARABOLIC EQUATION SOLUTION

Parabolic equations are often derived by factoring an operator. Since it is difficult to apply this approach to Eq. (21) when wind shear exists, we derive a parabolic equation solution from the spectral solution. Rearranging Eq. (21), we obtain

$$\left(\frac{\partial}{\partial x}+iM\right)^2\phi+L\phi=\frac{2i}{1-\tilde{U}^2}\,\delta(x)\,\delta(z-z_0), \tag{22}$$

$$L=\frac{1}{1-U^2}\,\frac{\partial^2}{\partial z^2}+\left(\frac{k}{1-U^2}\right)^2, \tag{23}$$

$$M=\frac{kU}{1-U^2}. \tag{24}$$

Taking the Fourier transform of Eq. (22), we obtain

$$L\hat{\phi}-(h+M)^2\hat{\phi}=\frac{2i}{1-\tilde{U}^2}\,\delta(z-z_0), \tag{25}$$

$$\phi(x,z)=\frac{i}{\pi(1-\tilde{U}^2)}\,S(x)\,\delta(z-z_0), \tag{26}$$

$$S(x)=\int_{-\infty}^{\infty}\frac{\exp(ihx)}{L-(h+M)^2}\,dh. \tag{27}$$

Since L and M do not commute in general, the denominator in Eq. (27) cannot be factored as a scalar. Expanding the denominator approximately, we obtain

$$\frac{2}{L-(h+M)^2}\sim\frac{1}{(L^{1/2}+h+M)(L^{1/2}-h-M)}+\frac{1}{(L^{1/2}-h-M)(L^{1/2}+h+M)}. \tag{28}$$

Both of the approximate factorizations of the denominator on the right side of Eq. (28) are correct to zeroth order in the commutator

$$[L^{1/2},M]=L^{1/2}M-ML^{1/2}. \tag{29}$$

Since the terms on the right side of Eq. (28) differ by the transformation $M\rightarrow -M$, their average is correct to first order in the commutator. To be consistent with the derivation of the wave equation in the high-frequency limit, we account for first-order commutators but neglect second-order commutators. Substituting Eq. (28) into Eq. (27), we obtain

$$S(x)=\tfrac{1}{2}S_+(x)+\tfrac{1}{2}S_-(x), \tag{30}$$

$$S_\pm(x)=\int_{-\infty}^{\infty}\frac{\exp(ihx)}{(L^{1/2}\pm(h+M))(L^{1/2}\mp(h+M))}\,dh. \tag{31}$$

To further simplify the integrand, we apply the identity

$$\frac{1}{L^{1/2}\pm(h+M)}+\frac{1}{L^{1/2}\mp(h+M)}=\frac{1}{(L^{1/2}\pm(h+M))(L^{1/2}\mp(h+M))}(L^{1/2}\pm M)+(L^{1/2}\mp M)\frac{1}{(L^{1/2}\pm(h+M))(L^{1/2}\mp(h+M))}, \tag{32}$$

which can be derived by replacing M with $(h+M)$ in the numerator factors, observing that the additional terms cancel, and applying the operator identity $(GH)^{-1}=H^{-1}G^{-1}$. Multiplying Eq. (32) by $\exp(ihx)$, integrating over h, applying the residue theorem for $x>0$, and comparing with Eq. (31), we obtain

$$S_\pm(x)(L^{1/2}\pm M)+(L^{1/2}\mp M)S_\pm(x)=-2\pi i\exp(ix(L^{1/2}-M)). \tag{33}$$

To simplify Eq. (33), we write $S_\pm(x)$ in the form

$$S_+(x)=\exp(ix(L^{1/2}-M))T_+, \tag{34}$$

$$S_-(x)=T_-\exp(ix(L^{1/2}-M)), \tag{35}$$

where the depth operators $T_\pm$ are to be determined. Substituting Eqs. (34) and (35) into Eq. (33), we obtain

$$T_\pm(L^{1/2}\pm M)+(L^{1/2}\mp M)T_\pm=-2\pi i. \tag{36}$$

When x is large, the commutator of $\exp(ix(L^{1/2}-M))$ and $T_\pm$ may be significant due to cumulative effects. We assume that the commutator of $T_\pm$ and $(L^{1/2}\pm M)$ is small in the high-frequency limit and apply the zeroth-order approximation

$$T_\pm\sim-\pi iL^{-1/2}. \tag{37}$$

From Eqs. (30), (34), (35), and (37), we obtain

$$S(x)\sim-\frac{\pi i}{2}\exp(ix(L^{1/2}-M))L^{-1/2}-\frac{\pi i}{2}L^{-1/2}\exp(ix(L^{1/2}-M)). \tag{38}$$

Applying the operator identity

$$G^2H+HG^2=2GHG+G[G,H]-[G,H]G=2GHG+[G,[G,H]], \tag{39}$$

to Eq. (38) and neglecting the second-order commutator, we obtain

$$S(x)\sim-\pi iL^{-1/4}\exp(ix(L^{1/2}-M))L^{-1/4}. \tag{40}$$

Substituting Eq. (40) into Eq. (26), we obtain

$$\phi(x,z)=\frac{1}{1-\tilde{U}^2}L^{-1/4}\exp(ix(L^{1/2}-M))L^{-1/4}\delta(z-z_0). \tag{41}$$

A parabolic equation solution can be obtained from Eq. (41) by defining the new dependent variable

$$\psi(x,z)=L^{1/4}\phi(x,z)=\frac{1}{1-\tilde{U}^2}\exp(ix(L^{1/2}-M))L^{-1/4}\delta(z-z_0). \tag{42}$$

Differentiating Eq. (42) with respect to x, we obtain the parabolic equation

$$\frac{\partial\psi}{\partial x}=i(L^{1/2}-M)\psi. \tag{43}$$

This equation can be implemented using the formal solution

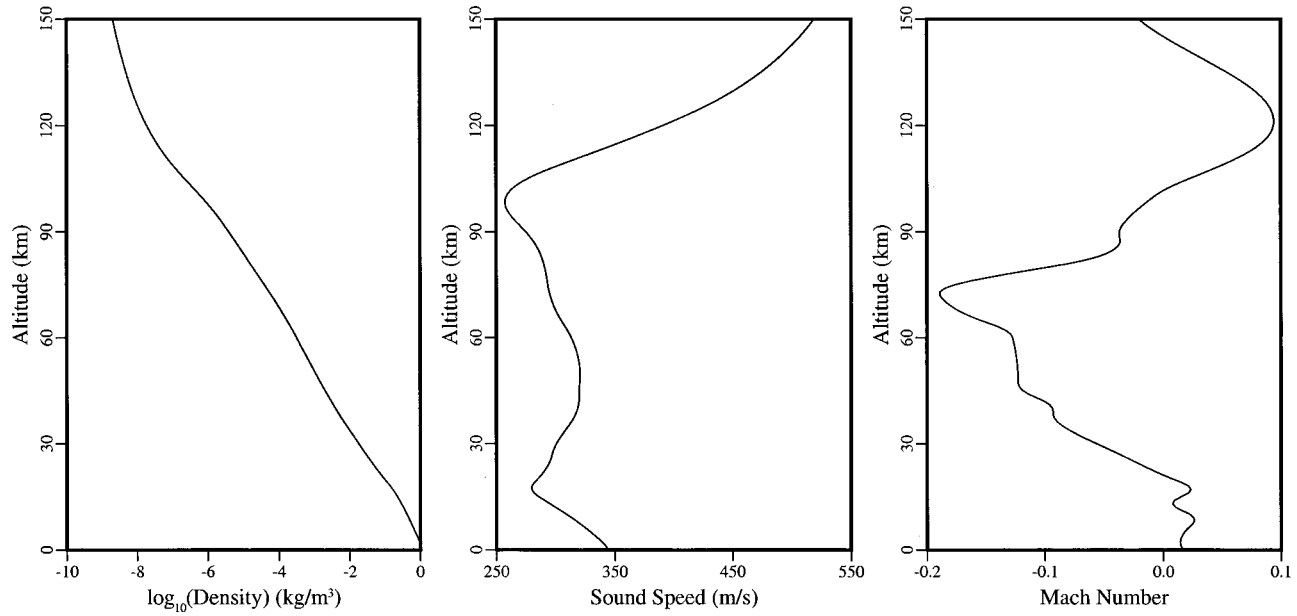

FIG. 1. Profiles for sound speed, density, and wind speed in the atmosphere, which are based on a combination of measurements and models (Refs. 18, 19).

$$\psi(x+\Delta x,z)=\exp(i\Delta x(L^{1/2}-M))\psi(x,z), \tag{44}$$

which follows from Eq. (42). Assuming that Δx is small and applying the splitting solution to Eq. (44), we obtain

$$\psi(x+\Delta x,z)=\exp(-i\Delta xM)\exp(i\Delta xL^{1/2})\psi(x,z). \tag{45}$$

This equation can be implemented by approximating $\exp(i\Delta xL^{1/2})$ with a rational function that is based on an expansion about the reference wave number k_0, as described in Ref. 17.

Before solving the parabolic equation, it is necessary to specify an initial condition. After solving the parabolic equation, it is necessary to apply a change of variables in order to obtain the acoustic pressure. For convenience, we incorporate part of the change of variables into the initial condition. Substituting the spectral solution for $\phi(x,z)$ in Eq. (41), we obtain

$$\psi(x,z)=\frac{1}{2\pi}L^{1/4}\int_{-\infty}^{\infty}\hat{\phi}(h,z)\exp(ihx)dh. \tag{46}$$

To account for the factor in the denominator in Eq. (19), we define the new dependent variable $\xi(x,z)$ by the equation

$$\tilde{\rho}^{1/2}\left(\omega+i\tilde{u}\frac{\partial}{\partial x}\right)\xi(x,z)=\psi(x,z). \tag{47}$$

Taking the Fourier transform of Eq. (47) and applying Eq. (46), we obtain

$$\xi(x,z)=\frac{1}{2\pi\tilde{\rho}^{1/2}}L^{1/4}\int_{-\infty}^{\infty}\frac{\hat{\phi}(h,z)\exp(ihx)}{\omega-\tilde{u}h}dh. \tag{48}$$

Since $\xi(x,z)$ satisfies Eq. (43), this variable can be marched in range using Eq. (45). An initial condition can be obtained by using Eqs. (20) and (48) to evaluate $\xi(x_0,z)$, where x_0 is comparable to a wavelength. Accounting for the

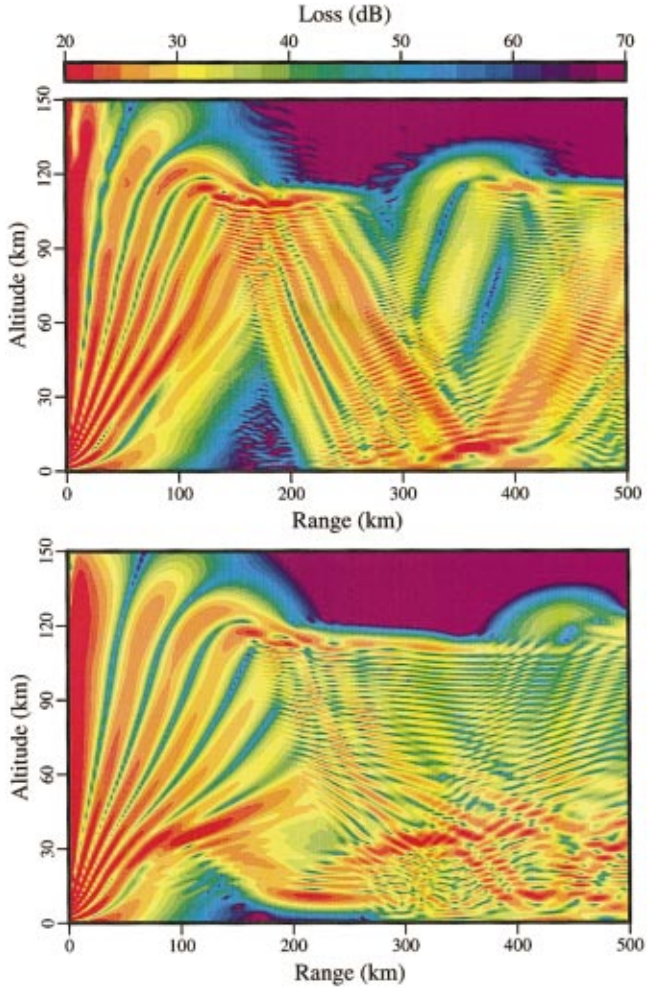

FIG. 2. Transmission loss obtained with the parabolic equation for a problem involving the profiles appearing in Fig. 1 and a 0.1-Hz source at $z=10$ km. The wind is accounted for in the solution appearing in the top frame and is neglected in the solution appearing in the bottom frame. The wind has a major effect on the acoustic field.

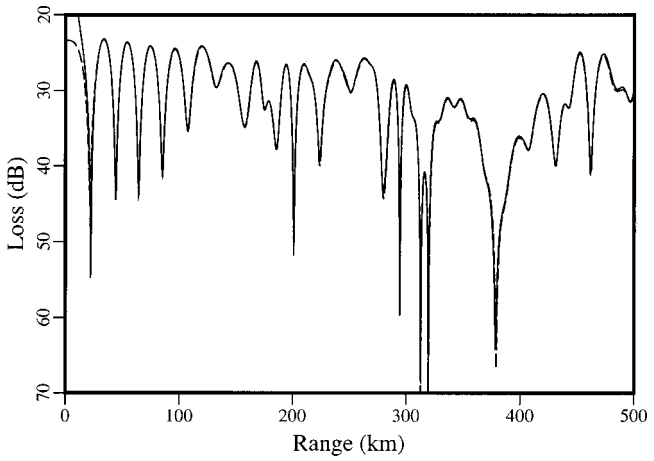

FIG. 3. Illustration of the accuracy of the parabolic equation solution. Transmission loss at $z=70$ km for a 0:1 Hz problem involving a source at $z=10$ km. The solid curve corresponds to the parabolic equation solution that accounts for commutators to leading order. The dashed curve corresponds to the exact spectral solution. The agreement is excellent away from short range, where energy propagates at very wide propagation angles.

factor in the numerator in Eq. (19) and including the factor of $L^{-1/4}$ that was removed in going from ϕ to ψ, we obtain

$$p=\rho^{1/2}\left(\omega+iu\frac{\partial}{\partial x}\right)L^{-1/4}\xi. \tag{49}$$

Using the parabolic equation to replace the range derivative, we obtain

$$p=\omega\rho^{1/2}L^{-1/4}\xi-u\rho^{1/2}L^{-1/4}(L^{1/2}-M)\xi. \tag{50}$$

We illustrate the parabolic equation solution for an example involving the atmospheric profiles appearing in Fig. 1, which are based on a combination of measurements and models.[18,19] This problem involves a 0.1-Hz source at $z=10$ km. To approximate the effects of attenuation in the upper atmosphere and prevent artificial reflections from the computational boundary at $z=200$ km, we replace ω with the complex frequency[20,21]

$$\tilde{\omega}=\omega+i\mu k_0^2\rho^{-1}, \tag{51}$$

where $\mu=1.5\times10^{-5}\,\mathrm{N\cdot s\cdot m^{-2}}$ is the viscosity. Due to the smallness of the density ratio at the air/water interface, we apply the rigid boundary condition $\partial p/\partial z=0$ at $z=0$. We implement Eq. (45) using a five-term rational approximation and take $k_0=\omega/c_0$, where $c_0=300$ m/s is the reference wave speed. The acoustic field appears in Fig. 2 for cases with and without wind, which causes large effects. The parabolic equation solution is compared with the spectral solution in Fig. 3. The solutions are in excellent agreement except at short range, where energy propagates at very wide angles (this error can be reduced by using additional terms in the rational approximation). We consider two erroneous solutions to illustrate the need to properly account for shear and commutators. Appearing in Fig. 4 is a spectral solution based on neglecting the shear term in Eq. (14) to obtain

$$\frac{\partial^2\hat{p}}{\partial z^2}-\frac{1}{\rho}\frac{\partial\rho}{\partial z}\frac{\partial\hat{p}}{\partial z}+(k^2-(1-U^2)h^2-2kUh)\hat{p}=2i\delta(z-z_0), \tag{52}$$

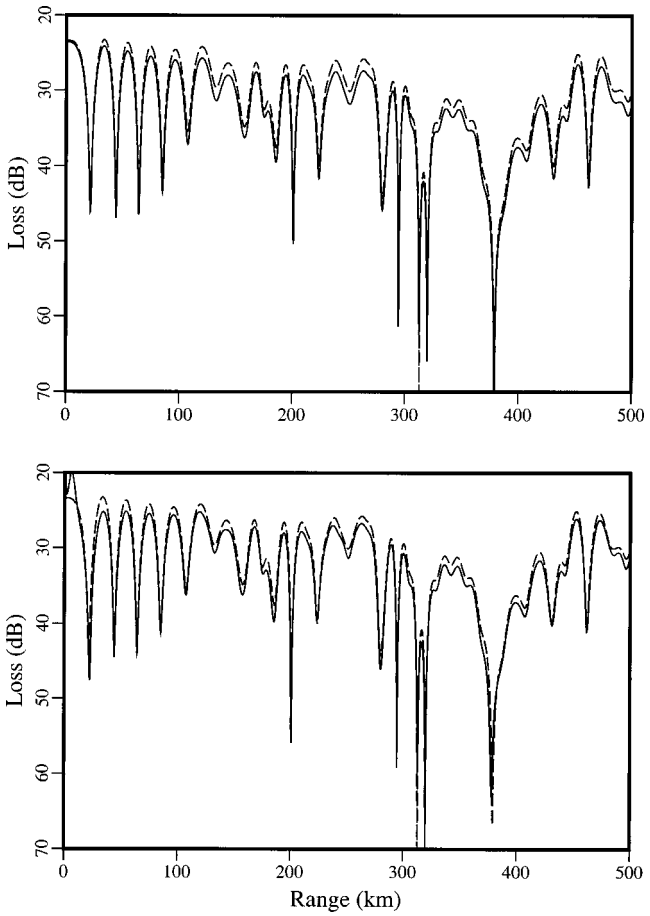

FIG. 4. Illustration of the need to properly account for shear and commutators. Transmission loss at $z=70$ km for a 0.1-Hz problem involving a source at $z=10$ km. The dashed curves correspond to the exact spectral solution. In the top frame, the solid curve corresponds to a spectral solution that neglects the shear term. In the bottom frame, the solid curve corresponds to a parabolic equation solution that neglects commutators.

and a parabolic equation solution based on neglecting commutators and factoring the denominator in Eq. (26) to obtain

$$S(x)=-\pi i\exp(ix(L^{1/2}-M))L^{-1/2}. \tag{53}$$

The result of neglecting the shear term and commutator is an amplitude shift in the parabolic equation solution relative to the exact spectral solution. The magnitude of the shift depends on the flow velocities at the source and receiver locations. In this example, the differences are a few decibels. For more extreme wind profiles, the difference would be greater. For weak shear cases (sufficiently high frequency) the shear terms can be neglected completely and an accurate solution obtained by a simplified parabolic equation.

V. CONCLUSION

We have derived a parabolic equation for advected acoustic waves that does not require low Mach number or narrow propagation angles. This solution was obtained in the weak shear or high-frequency limit, which is valid for frequencies as low as 0.1 Hz. We have demonstrated the accuracy of the parabolic equation solution for an atmospheric acoustics problem.

ACKNOWLEDGMENT

This work was supported by the Office of Naval Research.

[1] F. B. Jensen, W. A. Kuperman, M. B. Porter, and H. Schmidt, *Computational Ocean Acoustics* (American Institute of Physics, New York, 1994), pp. 343–412.
[2] M. K. Myers and G. L. McAninch, ''Parabolic approximation for sound propagation in the atmosphere,'' AIAA J. **16**, 836–842 (1978).
[3] J. S. Robertson, W. L. Siegmann, and M. J. Jacobson, ''Current and current shear effects in the parabolic approximation for underwater sound channels,'' J. Acoust. Soc. Am. **77**, 1768–1780 (1985).
[4] G. L. McAninch, ''Higher order parabolic approximations for sound propagation in stratified moving media,'' AIAA J. **24**, 253–260 (1986).
[5] G. L. McAninch, ''Reformulation of the parabolic approximation for waves in stratified moving media,'' AIAA J. **25**, 1547–1555 (1987).
[6] R. I. Brent, W. L. Siegmann, and M. J. Jacobson, ''Effects of uniform horizontal currents in the parabolic approximation,'' J. Acoust. Soc. Am. **82**, 545–558 (1987).
[7] J. S. Robertson, W. L. Siegmann, and M. J. Jacobson, ''Acoustical effects of ocean current shear structures in the parabolic approximation,'' J. Acoust. Soc. Am. **82**, 559–573 (1987).
[8] J. S. Robertson, W. L. Siegmann, and M. J. Jacobson, ''A treatment of three-dimensional underwater acoustic propagation through a steady shear flow,'' J. Acoust. Soc. Am. **86**, 1484–1489 (1989).
[9] O. A. Godin, ''Parabolic approximation in the acoustics of moving media,'' Sov. Phys. Acoust. **37**, 335–339 (1991).
[10] O. A. Godin and A. V. Kokhov, ''Small-angle parabolic approximation for a sound field in a moving medium,'' Sov. Phys. Acoust. **38**, 243–247 (1992).
[11] M. D. Collins, B. E. McDonald, W. A. Kuperman, and W. L. Siegmann, ''Jovian acoustics and Comet Shoemaker-Levy 9,'' J. Acoust. Soc. Am. **97**, 2147–2158 (1995).
[12] A. D. Pierce, ''Wave equation for sound in fluids with unsteady inhomogeneous flow,'' J. Acoust. Soc. Am. **87**, 2292–2299 (1990).
[13] M. B. Porter, F. B. Jensen, and C. M. Ferla, ''The problem of energy conservation in one-way models,'' J. Acoust. Soc. Am. **89**, 1058–1067 (1991).
[14] M. D. Collins and E. K. Westwood, ''A higher-order energy-conserving parabolic equation for range-dependent ocean depth, sound speed, and density,'' J. Acoust. Soc. Am. **89**, 1068–1075 (1991).
[15] M. D. Collins, ''An energy-conserving parabolic equation for elastic media,'' J. Acoust. Soc. Am. **94**, 975–982 (1993).
[16] A. E. Gill, *Ocean-Atmosphere Dynamics* (Academic, San Diego, 1982), pp. 128–130.
[17] M. D. Collins, ''A split-step Padé solution for parabolic equation method,'' J. Acoust. Soc. Am. **93**, 1736–1742 (1993).
[18] D. P. Drob and J. M. Picone, ''Statistical performance of measurements of the HWM-93 and MSISE-90 empirical atmospheric models and the relation to infrasonic CTBT monitoring,'' 22nd Annual DOD/DOE Seismic Research Symposium Proceedings: Planning for Verification and Compliance with the Comprehensive Nuclear Test Ban Treaty, Vol. III, pp. 161–169 (2000).
[19] M. Garcés, C. Potter, D. P. Drob, J. M. Picone, R. Hansen, and K. Lindquist, ''Characterization of predicted infrasonic phases of IS-59 Hawaii,'' 22nd Annual DOD/DOE Seismic Research Symposium Proceedings: Planning for Verification and Compliance with the Comprehensive Nuclear Test Ban Treaty, Vol. III, pp. 181–190 (2000).
[20] Reference 16, pp. 294–297.
[21] J. F. Lingevitch, M. D. Collins, and W. L. Siegmann, ''Parabolic equations for gravity and acousto-gravity waves,'' J. Acoust. Soc. Am. **105**, 3049–3056 (1999).

The connection between sound production and jet structure of the supersonic impinging jet[a)]

Brenda Henderson
Mechanical Engineering Department, Kettering University, Flint, Michigan 48504-4898

(Received 27 September 2001; accepted for publication 20 November 2001)

An experimental investigation into the sound-producing characteristics of moderately and highly underexpanded supersonic impinging jets exhausting from a round convergent nozzle is presented. The production of large plate tones by impingement on a square plate with a side dimension equal to 12 nozzle exit diameters is studied using random and phase-locked shadowgraph photography. Discrete frequency sound is produced in the near-wall region of the jet when a Mach disk occurs upstream of the standoff shock wave. Tones cease when the plate distance is approximately 2.2 free-jet cell lengths and the first and second shock waves are located in the free-jet positions. The production of impulsive sound appears to be associated with the collapse of the standoff shock wave during a portion of the oscillation cycle. Results from unsteady plate-pressure measurements indicate that plane-wave motion occurs in the impingement region and a secondary pressure maximum is observed on the plate adjacent to the flow region where sound appears to originate. © *2002 Acoustical Society of America.* [DOI: 10.1121/1.1436069]

PACS numbers: 43.28.Ra, 43.50.Nm [MSH]

I. INTRODUCTION

The impingement of a jet on a flat plate produces ground effects including surface erosion, nonuniform surface heat transfer, lift loss, and acoustic loading. Interest in this problem has spanned over 40 years because of its application to missile and rocket launching systems, lunar landing modules, thrust vectoring systems, and V/STOL aircraft. Many early studies, except for the acoustic study by Marsh (1961), focused predominantly on the flow structure of the supersonic impinging jet particularly in the impingement region and often for steady-flow conditions. Later work addressed unsteady characteristics of the supersonic impinging jet including tonal production characteristics. However, the connection between the production of intense discrete frequency sound and the oscillating flow structure is still not well understood. The complicated structure of the jet in the impingement and near-wall regions as well as the changes to the jet structure with overpressure, nozzle-to-plate spacing, and plate size has made it difficult to connect unsteady flow features with the production of sound. The purpose of the present study is to investigate the connection between the structure of the moderately and highly underexpanded supersonic jet impinging on large plates and the production of discrete frequency sound.

Marsh (1961) may have first reported the production of discrete frequency tones by the impingement of a jet on a normal flat plate. His investigation was the first of many subsonic impinging jet investigations focusing on acoustic radiation. Wagner (1971) developed an instability model later modified by Neuwerth (1974) which consisted of an upstream traveling wave within the jet and a downstream traveling pressure field resulting from flow instabilities initiated at the nozzle. Tam and Ahuja (1990) developed a theoretical model based on neutrally stable waves traveling upstream predominantly inside the jet. The model described some of the observed phenomena associated with impingement on a plate, although the plate was not accounted for in the analysis. Ho and Nosseir (1981) and Nosseir and Ho (1982) hypothesized that the discrete impinging tones were part of a feedback loop and were produced by the interaction of large coherent structures with the plate, results which were consistent with the earlier studies of Wagner (1971) and Neuwerth (1974). Preisser (1979) applied Curle's (1955) surface integral to analyze the production of discrete tones. The theoretical analysis of Powell (1988) for vanishingly small Mach numbers led to predicted directivity and an estimate of the magnitude of the sound pressure associated with viscous dissipation. Powell (1994) later modified this analysis to include an acoustic field produced by one type of lateral quadrupole randomly distributed in the plane of the plate. The studies of Didden and Ho (1985) documented the development of a primary and secondary vortex in the impingement region of a periodically forced jet, although the connection between this phenomenon and the production of tones was not investigated.

Both steady and unsteady supersonic impinging jet experiments have attracted attention from many researchers. The important parameters that appear to affect the flow structure are the nozzle pressure ratio (the ratio of the stagnation pressure to the ambient pressure), the nozzle-to-plate spacing, and the impinging plate size. Table I gives a summary of the operating conditions and some of the observed phenomena reported in experimental supersonic impinging jet studies.

Investigations into the steady-flow features of the supersonic impinging jet have focused mainly on the standoff shock-wave shape and location as well as the location of

[a)]Portions of this work were presented in "An experimental investigation into the sound producing characteristics of supersonic impinging jets," 7th AIAA/CEAS Aeroacoustics Conference, Maastricht, The Netherlands, Paper No. AIAA 2001-2145.

TABLE I. The operating conditions for supersonic impinging jet experiments. C=convergent, D=divergent, R=rectangular, n=nozzle exit pressure/ambient pressure, l=minimum nozzle dimension, and * indicates dimensions referenced to the nozzle exit diameter.

Authors	Nozzle	NPR[a] or n[b]	h/d	Plate size	Unstable	Recirculation	Shock motion
Marsh (1961)		1.34[a]	2–20	4d	X		
Morch (1964)	C	3.83[a]	0.5–2	0.33d–d	X		X
L. F. Henderson (1966)	CD	1[b]	1–3.5	4d		X	
Ginzburg *et al.* (1973)	CD	1.5–12[b]	1.4–3.4		X	X	
Gubanova *et al.* (1973)	CD	2.85[b]	1,2,3	Large	X	X	X
Donaldson, Snedeker (1971)	C	1.25,2.69,6.76[a]	<10	18.40d		X	
Nakatogawa *et al.* (1971)	Laval	1[b]	1–24	5d×5d	X		X
Gummer, Hunt (1971)*	CD	1[b]	0.4–0.53	19.7d×19.7d			
Neuwerth (1974)	C	1.12–3[a]	<6		X		
Semiletenko *et al.* (1974)	CD	1.5–4.0[b]	1.1–6.5	Large	X		X
Carling, Hunt (1974)*	CD	1[b]	0.5	15.7d×15.7d			
Golubkov *et al.* (1974)	CD	1–55[b]	1–12.5	1–8	X		
Gummer, Hunt (1974)*	CD,C	0, 5, 15[b]	0.5,1,1.5	19.7d×19.7d		X	
Ginzburg *et al.* (1975)	CD	1.2–36[b]	3–6.5	29.2d×37.5d	X	X	X
Glaznev (1977)	CD	2.7[b]	2.5–9	1.43	X		X
Glaznev *et al.* (1977)	CD	6.73[b]	3.5	7.50	X		
Kalghatgi, Hunt (1976)	CD	1[b]	0.5,0.7,5			X	
Back, Sarohia (1978)	C	1.75–8[a]	1,1.5	7.49d×7.49d	X		X
Lamont, Hunt (1980)	CD	1.2–2[b]	1–15	10d	X	X	
Krothapalli (1985)	R	2–5.8[a]	10–30$^+$	66.7l×66.7l	X		
Powell (1988)	C	2.7–4.74[a]	1.25–6	1d, 4d	X		X
Norum (1989)	RC	1.85–7.3[a]	2.5–20	88.4l	X		
Norum (1990)	C,RC,CD,RCD		0.56–17.8	Large	X		
Iwamoto (1990)	C	3, 4, 6[a]	0.5–4	16d			
Soderman (1990)			NASA Ames AV-8C Harrier Aircraft				
Henderson, Powell (1993)	C	2.02–4.74[a]	0.5–10	0.5d–38d	X		X
Wlezien, Ferraro (1990)	C,RC CD,RCD	3,3.5,4[a]	2.8–12.6	9.6d×9.6d	X		
Glaznev, Popov (1992)		3[b]	2.5	2.4d–6.2d	X		X
Messersmith (1995)	C,CD	2.5–6[a]	2–6	Large	X		
Henderson, Powell (1996, 1997)	C	2.02–4.74[a]	0.5–10	1d,2d,3d	X		X
Levin, Wardwell (1997)	C	1.5–6[a]	2–7	Large	X		
Krothapalli *et al.* (1999)	CD	1–1.35[b]	3–60	96d×96d	X	X	
Alvi, Iyer (1999)	1.5[b](CD) 2.5,3.7,5(C)[a]		1.6–8	39.4d×39.4d	X	X	

[a]NPR.
[b]n.

sonic lines in the flow. The early study of L. F. Henderson (1966) was devoted to developing a better understanding of the general flow features of jets impinging on plates at various inclinations to the jet axis. Unsteady conditions were also observed and Henderson noted that the oscillatory behavior appeared to be related to the Hartman whistle. Gummer and Hunt (1971) developed a detailed description of the impingement and near-wall regions of nominally uniform impinging jets. Carling and Hunt (1974) determined the radial extent of alternating expansion and compression regions (or shocks) that occur in the near-wall jet. The standoff shock-wave shape and location resulting from the impingement of a highly underexpanded jet is described by Pamadi (1982). Iwamoto (1990) documented the shape and location of the standoff shock wave as the nozzle-to-plate spacing increased and investigated the development of a recirculation zone in the impingement region for some operating condition.

The occurrence of a stagnation bubble in the impingement region of steady impinging jets is often reported and appears to be associated with a number of different flow features. Donaldson and Snedeker (1971) found that a stagnation region occurred for highly underexpanded supersonic impinging jets. Carling and Hunt (1974) attributed the occurrence of a stagnation bubble to experimental rig design or plate surface finish. Gummer and Hunt (1974) found little connection between the standoff shock structure and the occurrence of a stagnation region for nonuniform jets. The occurrence of a stagnation bubble at very small plate spacings in the study of Kalghatgi and Hunt (1976) appeared to be the result of weak shock waves originating from the nozzle and intersecting with the standoff shock wave. Their hypothesized mechanism was related to that proposed by Ginzburg *et al.* (1973) and Gubanova *et al.* (1973). Kalghatgi and Hunt (1976) also observed some unsteady operating conditions that were characterized by rapid plate pressure fluctuations and periodic changes in shock-wave shape. This phenomenon was presumed to be associated with bubbles being formed, then swept away. The numerical calculations of Kim and Chang (1994) and the experiments of Lamont and Hunt (1980) showed that the occurrence of a stagnation bubble is affected by the plate inclination. The occurrence of a stagnation bubble for very highly underexpanded impinging jets was documented in a numerical study performed by Kim and Chang (1992) and the experimental studies of Lamont and Hunt (1980).

The connection between unsteady behavior in the impinging jet flow structure and the occurrence of a stagnation zone in the impingement region was first proposed by Ginzburg *et al.* (1973). Unsteady behavior of the standoff shock wave was attributed to periodic fluid motion in the recirculation region near the plate. Behind the central portion of the standoff shock wave, the pressure is lower than in the peripheral regions of the jet where the fluid passes through a hanging shock and a reflected shock. This pressure differential leads to a recirculation zone in the central portion of the jet. Ginzburg *et al.* (1973) hypothesized that the recirculation region causes the central shock to move upstream until the pressure behind the central shock increases and the fluid accumulated in the recirculation region moves out into the mixing zone along the slip stream (tangential discontinuity). The operating conditions used in the unsteady flow experiments of Ginzburg *et al.* were numerically simulated by Hoo *et al.* (1980), although the numerical study was performed to obtain a steady-flow solution. Iwamoto and Deckker (1981) numerically investigated the early stages of the impingement process and found the motion of a toroidal vortex in the impingement region. The importance of the recirculation zone to the production of tones is still not well understood. Alvi and Iyer (1999) showed plate-pressure data that indicated the occurrence of a stagnation bubble for nozzle-to-plate spacings, where Henderson (2001) found no acoustic radiation.

One of the earliest instability studies for the unsteady supersonic impinging jet, that of Morch (1964), involved the development of a one-dimensional theory for the ''zero-depth'' Hartmann whistle (impingement of a supersonic jet on a small plate). In his experimental investigations, strong instability was associated with large standoff shock-wave oscillations and weak instability was associated with small standoff shock oscillations, a weak oscillating oblique shock near the plate periphery, and small pressure oscillations on the plate. Morch hypothesized that the inability to produce a strong resonant condition from a model based on plane waves traveling in the impingement region was due to the one-dimensional nature of the model, a deficiency he later addressed [see Morch (1973)] through an analysis using a composite jet. Kuo and Dowling (1996) allowed for entropy changes in the standoff region in addition to traveling plane waves and found good agreement between theory and frequency data taken by Powell (1988) for jets impinging on plates with diameters equal to the nozzle exit diameter (small plates).

The occurrence of unsteady shock motion in the impinging jet is often reported in the literature, but the important features of the motion appear to depend somewhat on the jet operating conditions. Ginzburg *et al.* (1973) found strong oscillations of the standoff shock wave when a recirculation zone occurred. Nakatogawa *et al.* (1971) investigated the case of an impinging jet with a nozzle reflector and found oscillations of the standoff shock wave when the standoff shock was located in a decelerating region of the jet. In the investigation of Golubkov *et al.* (1974), the flow was characterized by a fluctuating compression shock, fluctuating plate pressures, and strong acoustic radiation when a small plate affected the central compression shock in the jet. When the jet impinges on a large plate, Semiletenko *et al.* (1974) found oscillations of the shock waves in the jet upstream of the plate. Oscillations ceased when the nozzle-to-plate spacing became large enough so as to add a second compression shock ahead of the plate. Ginzburg *et al.* (1975) found strong and weak instabilities of the jet that were associated with large and small amplitude oscillations of the shock-wave structure, respectively. Strong instability first occurred when the plate pressures at the center of the plate became equal to that in the peripheral plate regions. As the plate spacing increased, flow reversal occurred in the standoff region. Glaznev *et al.* (1977) found a traveling wave in the impingement region that became planar as it approached the standoff shock. This finding is somewhat consistent with the unsteady plate pressure measurements made by Henderson (1993). Although Kalghatgi and Hunt (1976) focused on the steady impinging jet, unsteady conditions were observed and were characterized by periodic changes in the standoff shock-wave shape. Back and Sarohia (1978) found large oscillations in the plate pressure when large-amplitude shock oscillations occurred.

For the axisymmetric supersonic impinging jet, the sound-producing characteristics and related unsteady shock-wave structure in the jet are highly dependent on impingement plate size. Powell (1988) was perhaps the first to note the fundamental differences in the jet flow and the acoustic radiation for jets impinging on small plates and jets impinging on large plates. He hypothesized that, in the case of impingement on large plates, the tones were part of a feedback cycle similar to that of the edgetone or choked jet. In the case of impingement on small plates, the tones appeared to be related to the high harmonics of the Hartmann whistle, with large oscillations of the standoff shock being an important part of the sound production mechanism. Powell and Henderson (1990), Henderson and Powell (1993), and Henderson (1993) found that, at low pressures (nozzle pressure ratios less than, or equal to, 2.70), ''large plate'' type tones were produced for all plate sizes. For nozzle pressure ratios above 2.70, two classes of ''small plate'' tones, sometimes in addition to large plate tones, were produced for plate diameters less than, or equal to, the nozzle exit diameter. Glaznev and Popov (1992) looked at the effect of plate size and found that oscillations ceased when the plate diameter was less than the diameter of the Mach disk in the impinging jet.

Small plate impinging tones usually occur for plate diameters less than or equal to two nozzle diameters. The production of these tones is usually associated with shock-wave oscillations in the jet. Glaznev (1977) hypothesized that the production of discrete frequency sound was the result of an oscillating conical surface (the jet boundary) in the vicinity of the plate brought on by oscillations of the shock-wave system near the plate. Good agreement was obtained between measured sound-pressure levels and sound-pressure levels calculated by modeling the conical surface as an oscillating membrane. Henderson and Powell (1996, 1997) looked at both types of small plate tones and hypothesized that ''primary'' small plate tones are produced by periodic changes in the jet diameter resulting from large oscillations

of the shock wave upstream of the standoff shock wave. ''Secondary'' small plate tones resulted from the interaction of jet disturbances with the standoff shock wave and shock waves in the deflected flow. Although secondary small plate tones were part of a feedback loop to the nozzle, the fundamental frequencies of the primary small plate tones did not appear to be part of this type of feedback loop.

The production of tones resulting from impingement on large plates has been noted for moderately, highly, and very highly underexpanded supersonic jets exhausting onto plates of various sizes. The tonal characteristics are a strong function of nozzle-to-plate spacing and depend only moderately on nozzle-pressure ratio. Norum (1990) found that four different regions (based on nozzle-to-plate spacing) of tonal production exist with different frequency characteristics. Powell and Henderson (1990) and Henderson and Powell (1993) found that large plate tones are part of a feedback loop to the nozzle. Tones produced at small and moderate spacings originated in the impingement region while tones produced at ''very small'' spacings originated in the near-wall region and are possibly associated with the flow disturbances moving along the plate. The results from the study of Levin and Wardwell (1997) indicate that impinging jets with large flat surfaces placed behind the nozzle experience a dramatic decrease in suckdown (lift loss) when oscillations of the jet structure and tonal production cease.

Although the flow structure of the ideally expanded supersonic impinging jet is significantly different from that of the underexpanded jet, discrete impinging tones are produced in both cases. In the experiments of Krothapalli *et al.* (1999), strong discrete acoustic radiation resulted from the impingement of an ideally expanded jet but the tonal production could not have resulted from shock wave motion. They found only a weak shock cell structure in the jet and a standoff shock wave usually was not present. Acoustic radiation appeared to originate from the impingement region. However, an impingement shock occurred and was observed to oscillate in the numerical investigation of Childs *et al.* (1991). Wlezien and Ferraro (1990) compared the acoustic radiation from twin jets issuing from both ideally expanded jets and underexpanded jets and found that ideally expanded jets produce more intense acoustic radiation than underexpanded jets. Although acoustic measurements were not reported in the twin-jet experiments performed by Elavarasan *et al.* (2000), large lift loss changes were believed to be associated with flow–acoustic interactions.

Dispersion relations for rectangular and circular supersonic jets were developed by Sedel'nikov (1968). The intent of this original work was to describe the discrete frequency component associated with supersonic free jets. Tam and Norum (1990) derived the same relationship for the more limited case of a two-dimensional jet and identified a class of upstream propagating, neutrally stable waves and a downstream instability wave. They hypothesized that these waves formed the feedback acoustic waves and that the acoustic wave in the outer stationary fluid was an insignificant part of the process. Messersmith (1995) applied Powell's (1953) feedback model to the impingement tones and accounted for entrainment velocities in the external flow. His model did not account for phase differences between the impinging vortices and the sound produced at the plate or phase shifts between the acoustic wave and the jet disturbances created at the nozzle lip.

Impinging jet experiments on rectangular jets show impinging tones with wavefronts that appear to originate from the impingement region and choked jet tones with wavefronts emanating from around the end of the third shock cell [see Krothapalli (1985)]. Large-scale vortical motions are observed in the wall jet region for some operating conditions. Norum (1989) found that multiple discrete frequency tones occurred simultaneously and gave photographic evidence of simultaneous multiple-jet oscillation modes. Soderman (1990) conducted acoustic measurements on the NASA Ames AV-8C Harrier aircraft. He hypothesized that the lack of discrete frequency tones in the acoustic spectra was due to one of two factors: the large Reynolds numbers realized in full-scale models that are not obtained in small-scale laboratory tests or multiple-jet interactions that are often not studied in laboratory settings.

The sound production mechanism associated with the impingement of a moderately and highly underexpanded supersonic jet on a large flat plate is not well understood. Attempts to explain or model the production of discrete frequency tones are complicated by the complex nature of the flow structure. The jet contains unsteady disturbances that can be symmetrical, helical, or asymmetrical in nature. These disturbances interact with the jet shock waves, the standoff shock wave, and the compression and expansion regions in the near-wall jet. The interaction of the disturbances with the shock waves produces shock-wave distortion and, in some cases, large shock-wave oscillations. Large deflections of the jet boundary occur as the shock waves change position in the jet. In addition to this, the jet disturbances or vortices accelerate and decelerate as they approach the plate, then move out along the wall jet. All of these interactions can result in the production of acoustic radiation. To complicate the jet structure further, a stagnation bubble is sometimes present in the impingement region and may cause further oscillations of the shock wave as jet disturbances or traveling sound waves in the impingement region cause the stagnation bubble to collapse.

The current study investigates the connection between the flow structure and the production of discrete tones in the moderately and highly underexpanded supersonic impinging jet. Random and phase-locked shadowgraph photographs are coupled with far-field acoustic measurements to develop a better understanding of the oscillation cycle and the sound production mechanism.

II. STRUCTURE OF THE SUPERSONIC IMPINGING JET

The structure of the supersonic impinging jet is shown schematically in Fig. 1. The expansion waves at the nozzle lip reflect from the jet boundary as compression waves that merge to form the first shock wave. For lower nozzle-pressure ratios (NPR), the first shock wave has a conical shape [see Fig. 1(a)]. For higher NPR, a Mach disk cuts off the apex of the conical shock wave as shown in Fig. 1(b).

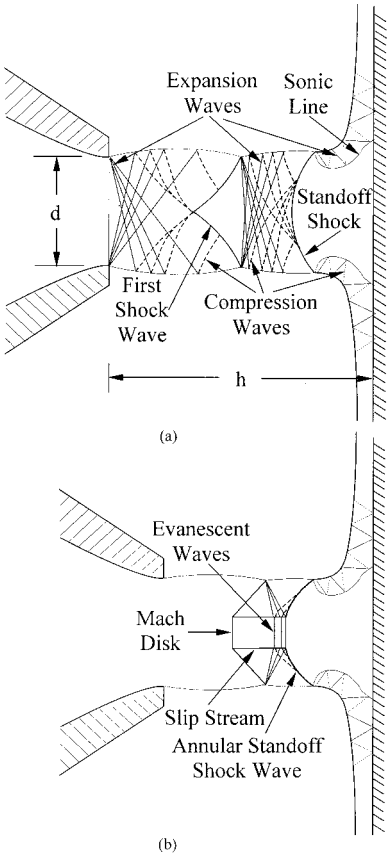

FIG. 1. The flow structure of the supersonic impinging jet.

Although Mach disks appear in free jets at NPR approximately equal to, or greater than, 3.8, Mach disks appear in impinging jets at lower pressures when the nozzle-to-plate distance is less than approximately $1\frac{1}{2}$-nozzle exit diameters. Because of this, the acoustic behavior and jet structure of impinging jets at moderate and high underexpansion are quite similar when the nozzle-to-plate distance is small (less than $1\frac{1}{2}$-nozzle exit diameters). The location and shape of the first shock wave in the impinging jet depend on NPR and nozzle-to-plate spacing, h/d, where h is the nozzle-to-plate distance and d is the nozzle exit diameter. The shock-wave locations for the impinging jet are discussed in Sec. IV(b).

Behind the first shock wave, an expansion fan occurs, bringing the pressure along the jet boundary to the ambient value. When the first shock wave has a conical shape, the entire flow behind the first shock wave is at supersonic speeds [see Fig. 1(a)] and the expansion waves extend across the entire jet. The expansion waves reflect as compression waves that merge to form the standoff shock wave. When a Mach disk occurs, the flow behind the first shock wave is divided by a slip stream into a subsonic region behind the Mach disk and a supersonic region behind the oblique section of the shock wave [see Fig. 1(b)]. The expansion waves reflect from the slip stream as compression waves and evanescent waves form in the subsonic region to balance the slight phase shift between the expansion waves and reflected compression waves. The evanescent waves cause the subsonic flow to slightly converge and accelerate. Mixing across the shear layer dividing the subsonic and supersonic regions also causes an increase in the flow velocity behind the Mach disk. The compression waves in the supersonic flow merge to form an annular standoff shock wave.

Behind the standoff shock wave, the flow is divided into a subsonic and a supersonic region by a sonic line. An expansion fan at the intersection of the standoff shock wave and the jet boundary maintains ambient pressure along the jet boundary. The expansion waves reflect as compression waves from the sonic line, and this successive pattern of expansion and compression continues until the plate is reached. When the wave pattern reaches the plate, the waves reflect in phase at the plate and out of phase at the wall-jet boundary. The successive pattern of compression and expansion in the wall jet can persist for many jet diameters depending on the jet NPR [see Carling and Hunt (1974)]. The exact shape and location of the standoff shock wave depends on NPR and nozzle-to-plate spacing.

The first cell length (Δ) is defined as the distance from the nozzle lip to the end of the first shock wave in the free jet. In the present investigations, Δ was determined from choked jet photographs taken prior to the impinging jet experiments.

III. EXPERIMENTAL APPARATUS

The experimental work was performed in the Acoustic Jet Flow facility at NASA Glenn Research Center. A detailed description of the apparatus may be found in Henderson (2001). Compressed air entered the rig, passed through a regulator and a 200-mm-diameter pipe equipped with acoustic treatment and flow straightening screens, then exhausted from a round convergent nozzle with a 25.4-mm exit diameter. In the present studies, the jet was operated at moderate and high underexpansion with NPR between 3.38 and 4.74. The flow exhausted onto a 305×305-mm plate oriented perpendicular to, and traversed along, the jet axis with nozzle-to-plate spacings between 2.54 and 12.7 cm.

Far-field acoustic measurements were made with a calibrated $\frac{1}{4}$-in. Bruel & Kjaer-type 4135 microphone directed toward the center of the plate. The signals were analyzed with an Ono Sokki-type CF-5200 spectrum analyzer.

The light source used for the schlieren and shadowgraph systems was a Photonics Analysis Pal Flash with a spark duration of approximately 1–2 μs. Collecting and focusing lenses were used to focus the light onto a small circular aperture located at the focal point of a 152-mm-diameter spherical mirror with a 152.4-cm focal length. The parallel light rays from the spherical mirror passed through the test section to a second 152-mm-diameter spherical mirror with a 152.4-cm focal length. A flat mirror was used to direct the light rays to a lens used to focus the image onto 35-mm film. For the schlieren photographs, the knife edge was oriented perpendicular to the jet axis. The light source for the phase-locked photographs was triggered by a pulse from a programmable Wavetek model 395 waveform generator that was triggered by a pulse from a Yokogawa-type DL708E digital oscilloscope at different positions in the oscillation cycle, but not the same cycle. The filtered signal from the far-field microphone was used as the reference signal for the oscillo-

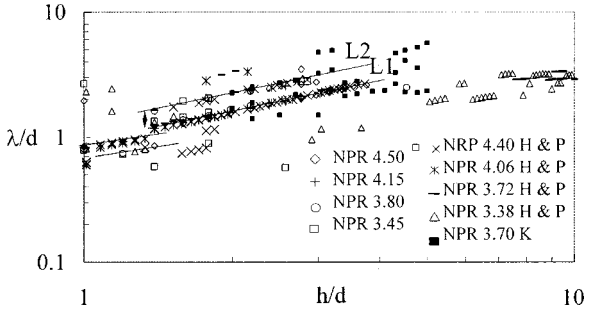

FIG. 2. Acosutic data from the present study, the studies of Henderson and Powell (1993) (H & P), and the studies of Krothapalli *et al.* (1999) (K).

scope. A photo-diode signal was recorded on the digital oscilloscope to determine the exact location in the oscillation cycle for each photograph.

IV. RESULTS

A. Acoustic measurements

Impingement tones are quite intense with amplitudes often exceeding the local broadband noise by more than 10 dB [see Henderson and Powell (1993)]. Multiple tones can occur and are often not harmonically related. In this section, only the data for the fundamental frequencies are presented and only for tones exceeding the local broadband noise by at least 5 dB.

The data from the present study, the studies of Henderson and Powell (1993), and the studies of Krothapalli *et al.* (1999), are shown in Fig. 2. The acoustic data from Krothapalli *et al.* were obtained for ideally expanded flow exhausting from a convergent–divergent nozzle with a lift gate (nozzle reflector), and the data from the studies of Henderson and Powell (1993) were obtained for an underexpanded jet exhausting from a convergent nozzle. Large impinging plates were used in all of the studies. Henderson and Powell (1993) identified the jet disturbances associated with the tones falling along the L1 line as symmetrical.

Although there are significant differences in the structure of the ideally expanded and underexpanded jets, the tonal characteristics of these jets are somewhat similar. Both types of jets produce impinging tones that display staging behavior. However, staging behavior is more common for the ideally expanded jet. The frequencies produced by both jets often fall along the L1 line for $1.5<h/d<3.5$, although multiple tones appear to be common for the ideally expanded jet.

The most notable difference in the tonal characteristics of the ideally expanded and underexpanded impinging jets is the occurrence of ''zones of silence'' for underexpanded flow that is not present for shock-free flows. The zones of silence where no discrete tones are produced are indicated in Fig. 3. The tones labeled primary tones have the largest amplitudes in the spectra, while secondary and tertiary tones have large, well-defined spectral peaks but their amplitudes are less than those of the primary tones. Although data for h/d greater than 5 were not taken in the present study, Henderson and Powell (1993) found that, as the nozzle pressure ratio increased beyond 3.38, limited tonal production occurred for h/d greater than 5. Tones that were produced for nozzle-to-plate spacings between 5 and 10 nozzle exit diameters may have been related to choked jet screech. The data in Fig. 3 show that the nozzle-to-plate locations where zones of silence occur depend on NPR and do not occur for spacings less than $h/d=4$ for higher pressures (NPR greater than or equal to 4.50). The data presented by Henderson and Powell also indicate that the zones of silence are affected by plate diameter. Krothapalli *et al.* (1999) found that tones occur continuously for spacings up to (and perhaps beyond) 10 nozzle diameters, indicating that the zones of silence are a phenomenon unique to the underexpanded jet. Since the jet and shock-wave structures are significantly different in these two cases, it appears that the production of impinging tones is affected by the shock-wave structure.

The data from Henderson and Powell (1993) closely overlap the data from the present study, indicating that impinging tones are reasonably independent of experimental apparatus and nozzle contour.

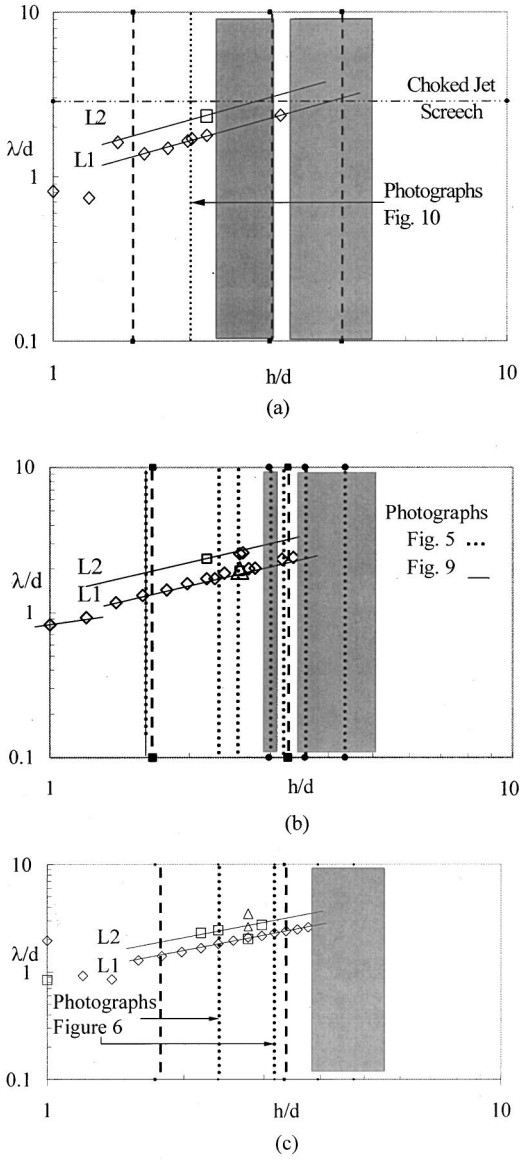

FIG. 3. The acoustic data for (a) NPR=3.80; (b) NPR=4.15; and (c) NPR=4.50. The primary, secondary, and tertiary tones are represented by ◇, □, and △, respectively. The free-jet cell endings are represented by - - and the zones of silence are shown by the shaded areas.

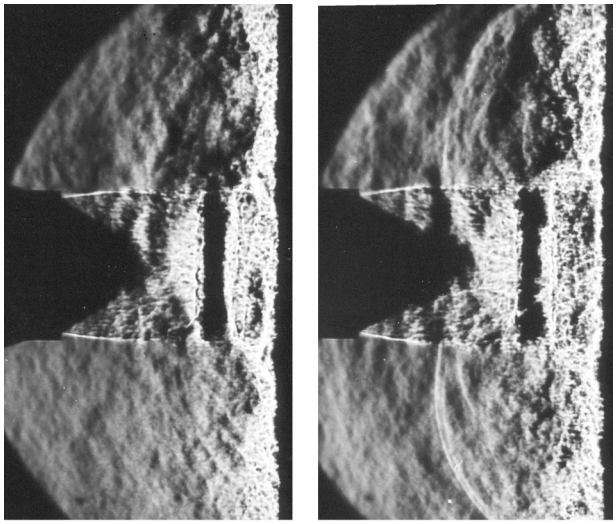

FIG. 4. Schlieren photographs taken at (a) NPR = 3.45 and $h/d = 1.7$ and (b) NPR = 4.15 and $h/d = 1.9$.

B. Random schlieren and shadowgraph photographs

The sound wavefronts associated with impinging tones can be impulsive or nonimpulsive and are centered on the near-wall region as shown in Fig. 4. Nonimpulsive waves are generally associated with smaller nozzle-to-plate (less than $h/d = 1.8$) spacings and lower pressures (NPR less than 4.15). Secondary wavefronts with much shorter wavelengths than the impinging tones are also observed to radiate from the shock waves in the jet for some operating conditions. The frequencies of the secondary waves are above the detection range of the microphones used in the experiments and are not the focus of this paper.

A series of random shadowgraph photographs taken at NPR equal to 4.15 and 4.50 is shown in Figs. 5 and 6. The values of h/d where these photographs were taken are indicated in Fig. 3. As shown in Fig. 5(a), when the nozzle-to-plate spacing is less than one free-jet cell length, the first shock wave is located near the nozzle. The oblique portion of the shock wave has an angle of approximately 65° and a large Mach disk lies in the central region of the jet. An annular standoff shock wave occurs in front of the plate and collapses during a portion of the oscillation cycle. As h/Δ increases to 1.38, the first shock wave moves downstream, the diameter of the Mach disk decreases, and impulsive sound waves are observed to radiated from the near-wall region [see Fig. 5(b)]. The angle of the oblique portion of the shock wave has decreased slightly to 57°. Waves are observed in the central region of the jet between the first shock wave and the standoff shock wave. Photographs taken at a slightly higher NPR and approximately the same free-jet cell location are shown in Fig. 6(a). In these photographs, the standoff annular shock wave collapses for a portion of the oscillation cycle.

When the plate is located at $h/\Delta = 1.57$ [see Fig. 5(c)], L2 tones are emitted by the jet. For this spacing, the first shock has moved downstream from its position in Fig. 5(b) and has an oblique angle of 49°. The diameter of the Mach disk is smaller than in Figs. 5(a) and (b), and a second shock wave begins to form and change shape dramatically throughout the oscillation cycle. The second shock at times develops an almost conical shape as occurs in the free jet and at other times, becomes more dome shaped. A third shock wave, an annular standoff shock wave, forms in front of the plate. Sound waves are observed to radiate from the near-wall region and higher frequency waves appear to radiate from the shock waves in the jet. Due to the symmetric nature of the oscillations, the tones falling along the L2 line appear to be associated with symmetrical jet disturbances, but the oscillation cycle may be quite different from that associated with the L1 tones.

The first zone of silence is reached for $h/\Delta = 1.78$ when the NPR is equal to 4.15. The photograph in Fig. 5(d) was taken at this location. The first shock wave is now located in the free-jet position. A stable dome-shaped second shock wave and an annular standoff shock wave reside close to the plate.

When the nozzle-to-plate spacing is increased slightly to $h/\Delta = 1.83$ and 1.90, L1 tones are produced and the jet structure once again begins to oscillate. As shown in Figs. 5(e) and 6(b), an oscillating second shock wave occurs downstream of the first shock wave and a third shock wave is periodically formed in front of the plate. During portions of the oscillation cycle, the third shock wave disappears.

Photographs taken for plate spacings greater than two free-jet cell lengths where no tones are produced are shown in Figs. 5(f) and (g). The second shock wave is located close to the free-jet location and has a conical shape as occurs in the free jet. A third stable shock wave appears in front of the plate.

The axial locations of the first and second shock waves for a range of nozzle-to-plate spacings and NPR are shown in Fig. 7. For the operating conditions where shock oscillations occurred, the average shock position was determined from available photographs. As shown in the figure, the shock locations depend highly on the plate location in the free-jet cell structure and only slightly on NPR. The first shock wave forms in the free-jet location for nozzle-to-plate distances greater than approximately 1.6 cell lengths. The second shock wave forms in the free-jet location for nozzle-to-plate distances greater than approximately 2.2 cell lengths.

Instability regions for a range of NPR and nozzle-to-plate spacings are shown in Fig. 8. When the nozzle-to-plate spacing is slightly greater than two free-jet cell lengths, tones are not produced and the second shock wave is in the free-jet location. As indicated in the figure, the first unstable zone ends for NPR less than 3.8 when the first shock develops a conical shape. A Mach disk forms for all nozzle-to-plate spacings at NPR greater than, or equal to, 3.8. Tones occurring at larger spacings and displaying staging behavior around the choked jet screech frequency have been omitted from the plot since these tones are likely related to choked jet screech.

C. Phase-locked shadowgraph studies

Phase-locked photographs are presented in Figs. 9 and 10. The beginning of the oscillation cycle has been arbitrarily

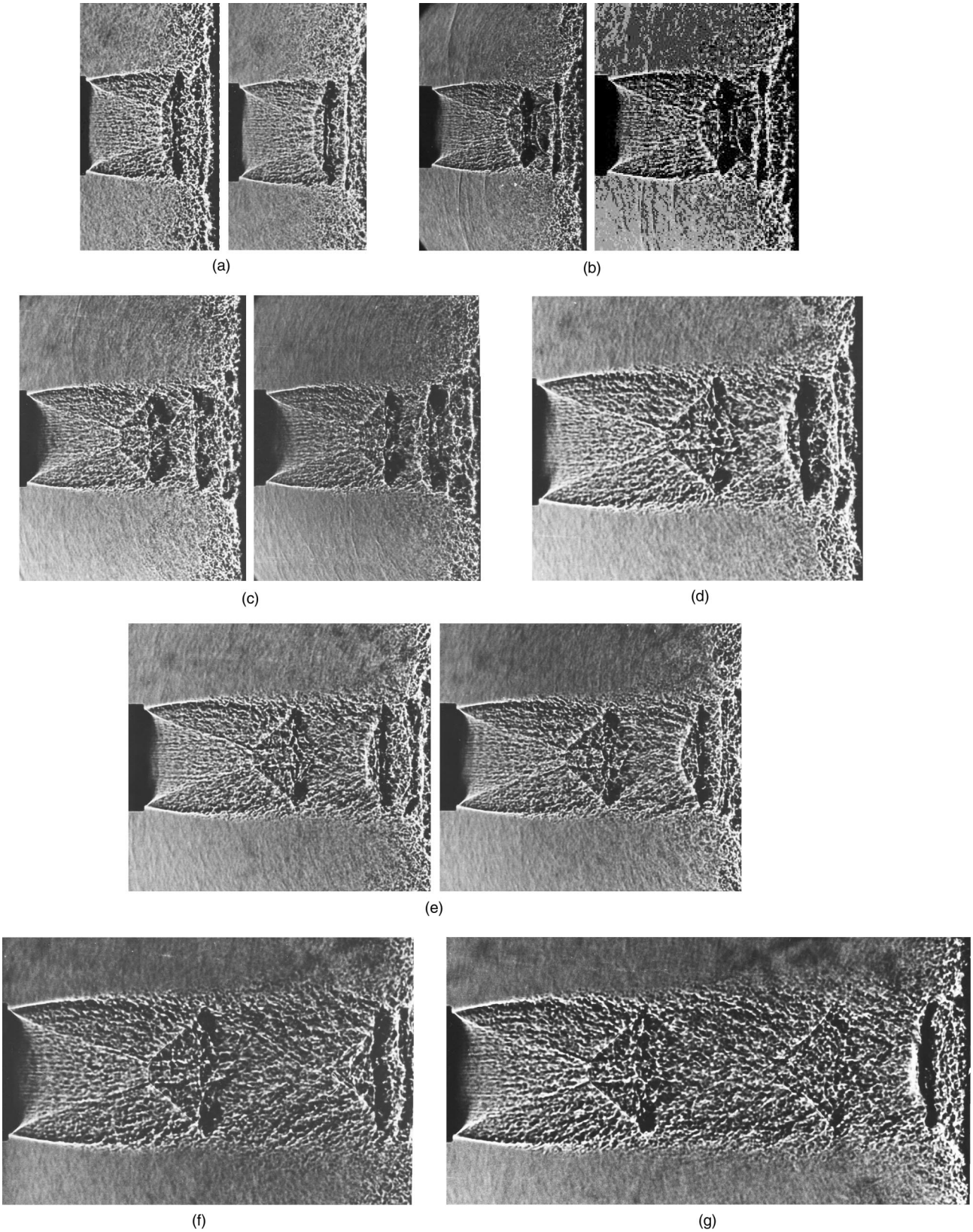

FIG. 5. Shadowgraph photographs taken at NPR = 4.15 and (a) $h/\Delta = 0.95$ (L1 tone); (b) $h/\Delta = 1.38$ (L1 tone); (c) $h/\Delta = 1.57$ (L2 tone); (d) $h/\Delta = 1.78$ (no tone); (e) $h/\Delta = 1.90$ (L1 tone); (f) $h/\Delta = 2.13$ (no tone); and (g) $h/\Delta = 2.60$ (no tone).

chosen to correspond with the photographs in Figs. 9(a) and 10(a). The time delay, t, between Figs. 9(a) and 10(a) and subsequent photographs is represented as a fraction of the period, T, in one cycle, although the photographs were taken in different cycles. For both operating conditions, the jet produced a single discrete frequency tone falling along the L1 in line in Fig. 2.

The photographs in Fig. 9 were taken at $h/\Delta = 0.96$ and

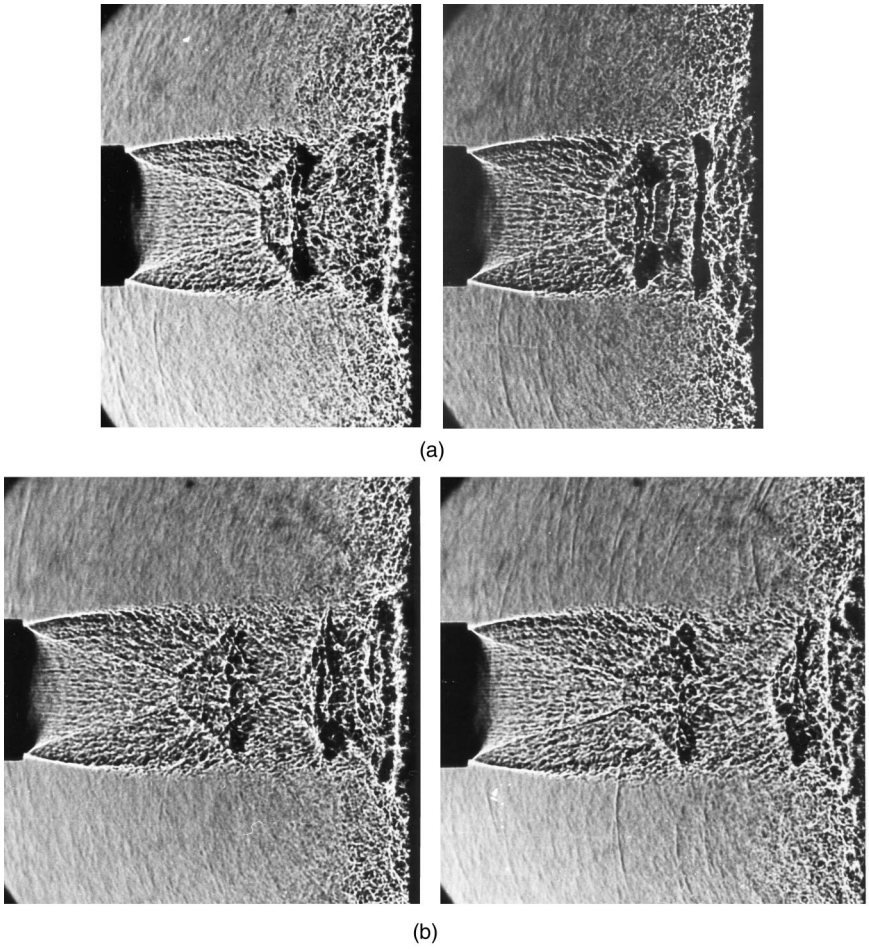

FIG. 6. Shadowgraph photographs taken at NPR=4.50 and (a) $h/\Delta = 0.95$ (L1 tone) and (b) $h/\Delta = 1.83$ (L1 tone).

NPR=4.15. As shown in Fig. 9(a), the first shock wave forms close to the nozzle exit and has an oblique angle of approximately 67°. A Mach disk with a large diameter forms along the central region of the jet. A very weak standoff shock can be seen in the outer regions of the jet near the plate. The slip stream dividing the inner subsonic flow behind the Mach disk and the supersonic flow behind the oblique shock wave appears to move outward with increasing distance from the nozzle. Due to the large oblique shock wave angle, the flow in the outer regions of the jet must be at low supersonic speeds. A sound wave is also evident in the stationary medium near the nozzle exit. As time progresses, the first shock wave moves slightly upstream, the radius of the first Mach disk increases slightly, and the standoff shock wave disappears as shown in Fig. 9(b). The location of the slip stream indicates that the majority of the flow downstream of the first shock wave is now subsonic and the flow transitions near the plate through a compression region rather than a shock wave. At $t/T = 0.41$ [see Fig. 9(c)], the oblique angle of the first shock wave decreases to 60° and a strong standoff shock wave appears. A region of strong second density gradient also appears in front of the plate and may be associated with a series of sound waves or a region of changing entropy as occurs in the model proposed by Kuo and Dowling (1996). A sound wave radiates from the near-wall region. Near the end of the oscillation cycle [see Fig. 9(d)], the region between the standoff shock wave and plate changes and the region of the strong second density gradient

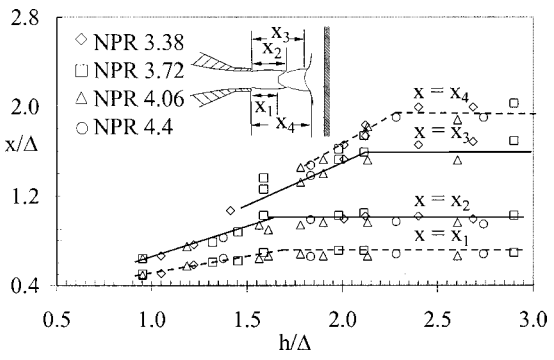

FIG. 7. The axial locations of the first and the second shock waves.

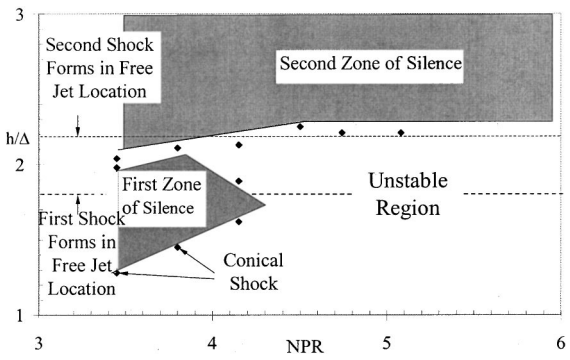

FIG. 8. The unstable regions of the impinging jet.

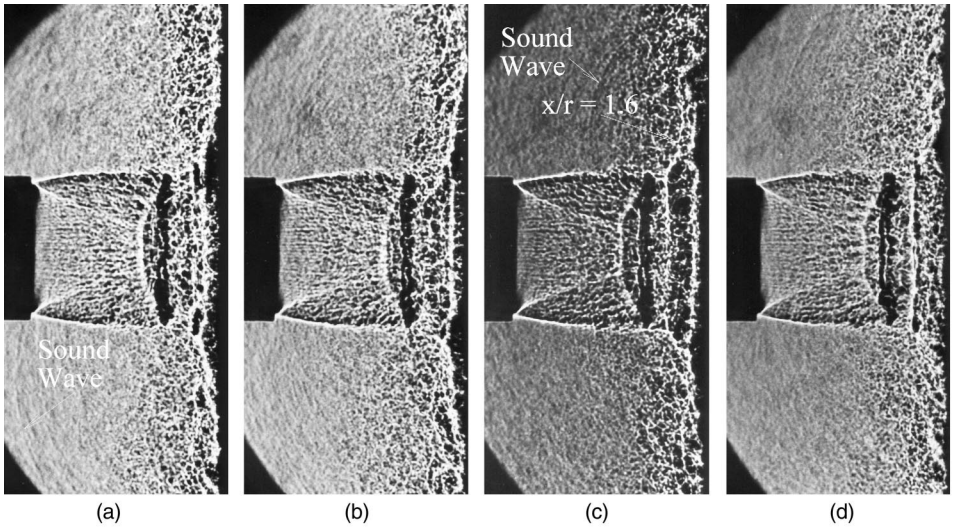

FIG. 9. Instantaneous phase-locked photographs taken at NPR=4.15 and $h/\Delta=0.96$ for (a) $t/T=0$; (b) $t/T=0.15$; (c) $t/T=0.41$; and (d) $t/T=0.72$.

observed in Fig. 9(c) disappears. The sound near the impingement region in Fig. 9(c) has now moved upstream. The point labeled $x/r=1.6$ in Fig. 9(c) will be discussed in Sec. IV(d).

Phase-locked photographs taken at a nozzle-pressure ratio of 3.80 and $h/\Delta=1.35$ are shown in Fig. 10. Near the beginning of the oscillation cycle [see Fig. 10(a)], the standoff shock wave is dome shaped and must be moving upstream so that the flow behind the first Mach disk is supersonic relative to a coordinate system fixed to the moving shock wave. In Figs. 10(b) and (c), the standoff shock wave moves downstream and must have an annular shape. A series of waves in the central region of the jet and jet disturbances near the first shock wave are observed in the photographs. In Fig. 10(d), the standoff shock wave is located close to the plate. Toward the end of the cycle, the standoff shock wave disappears, as shown in Figs. 10(e) and (f).

In the photographs of Fig. 10, the oblique angle of the first shock wave varies between 52° and 63°. The minimum oblique angle occurs at the beginning of the cycle when the second shock wave moves upstream. The maximum oblique angle occurs in Fig. 10(c), when the waves are observed in the central region of the jet.

An intense and impulsive sound wave radiating from the

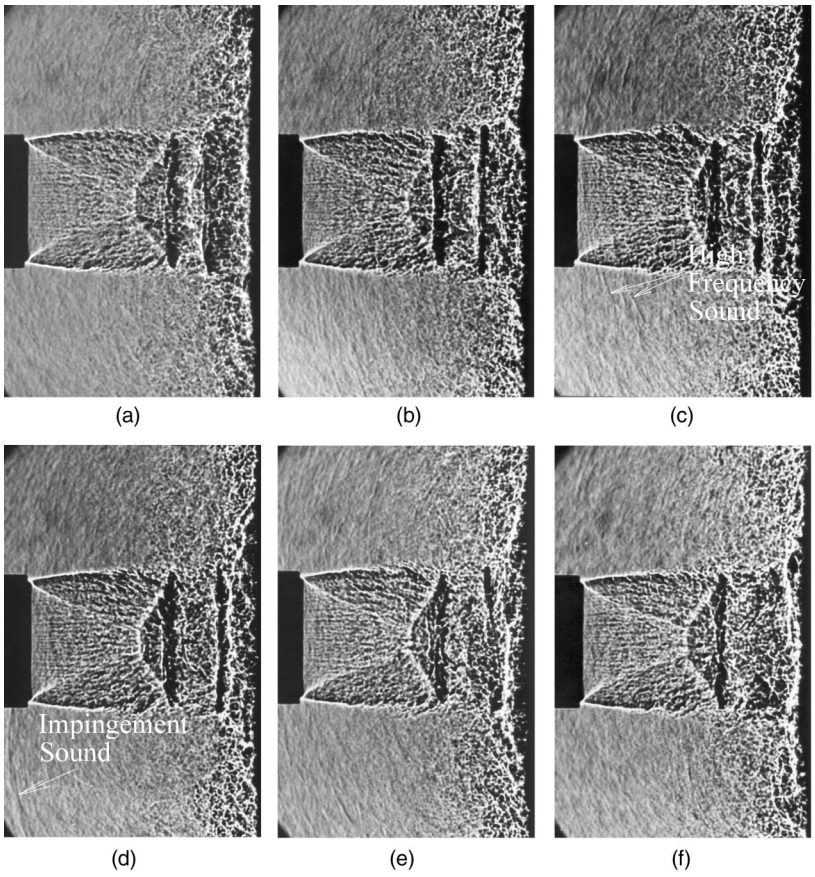

FIG. 10. Instantaneous phase-locked photographs taken at NPR=3.80 and $h/\Delta=1.35$ for (a) $t/T=0$; (b) $t/T=0.12$; (c) $t/T=0.28$; (d) $t/T=0.48$; (e) $t/T=0.60$, and (f) $t/T=0.78$.

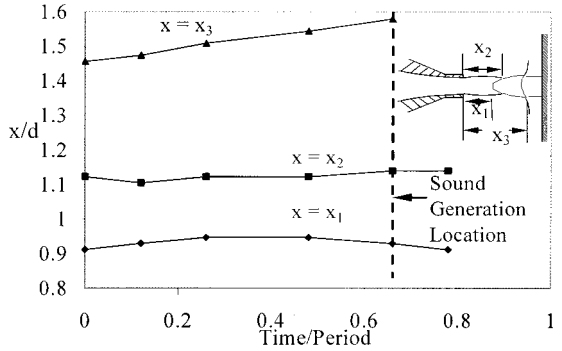

FIG. 11. Shock wave motion over one oscillation cycle for NPR = 3.80 and $h/\Delta = 1.35$.

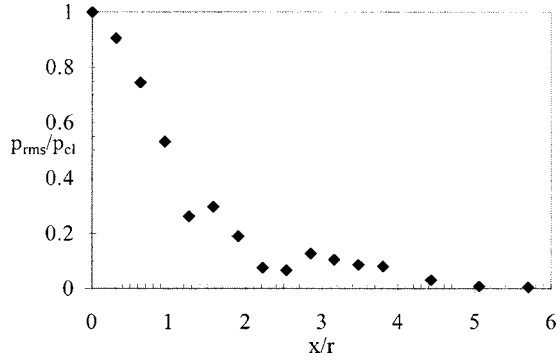

FIG. 12. Plate pressure amplitudes measured at the L1 tone frequency for NPR = 4.06 and $h/\Delta = 1.05$, where x is the distance from the plate center, r is the nozzle exit radius, p_{rms} is the root-mean-square pressure amplitude, and p_{cl} is the centerline pressure amplitude.

near-wall region is observed near the nozzle exit in Fig. 10(d), and high-frequency sound waves radiating from the first shock wave and the standoff shock wave are visible in Figs. 10(b), (c), and (e). The high-frequency sound is most likely produced by the interaction of the jet disturbances, visible in Fig. 10(c), with the first and standoff shock waves, while the low-frequency impingement tones appear to be associated with impulsive changes of the flow in the near-wall region.

Phase-locked photographs taken at nozzle-to-plate spacings less than $h/\Delta = 1.0$ and NPR equal to 3.80 indicate that, for lower pressures and small plate spacings, the sound waves appear less impulsive and the standoff shock wave does not always collapse during a portion of the oscillation cycle. However, the standoff shock wave appears to periodically weaken and the flow in the standoff and near-wall regions changes significantly throughout the cycle.

A plot of the shock wave motion over one cycle for NPR = 3.80 and $h/D = 1.35$ is shown in Fig. 11. The standoff shock wave moves downstream for approximately the first 70% of the cycle, then abruptly disappears. The first shock wave remains relatively stationary. As indicated in the figure, the sound appears to be emitted near the point in the oscillation cycle where the standoff shock wave disappears. This point was estimated by calculating the time required for the sound wave in Fig. 10(d) to propagate from the near-wall region to the nozzle exit in the surrounding media. The sudden change in the impingement flow structure is consistent with impulsive sound waves produced at a single time in the oscillation cycle.

D. Plate pressure measurements

Unsteady plate pressure measurements at different radial locations were taken by Henderson (1993) for operating conditions that correspond closely to those used in Fig. 9. A single peak appeared in the frequency spectra of the pressure data with a frequency equal to that of the emitted acoustic tone. The acoustic tone fell along the L1 line indicated in Fig. 2.

The amplitudes of the pressure fluctuations occurring at the L1 frequency are plotted in Fig. 12. The pressure at the plate center has been used for normalization. The pressure amplitude is higher in the impingement region, drops off rapidly at approximately 1.2 jet radii, and then increases to a secondary maximum near 1.6 jet radii. A higher amplitude is expected in the impingement region when plane waves move along the central region of the jet. The plate location corresponding to the secondary pressure maximum ($x/r = 1.6$) is indicated in Fig. 9(c). The sound source appears to be located in the flow adjacent to the wall at this radial location. The secondary pressure maximum may be the result of the motion of the expansion and compression regions in the near-wall jet as the standoff shock wave oscillates.

V. DISCUSSION

Large plate tones are often associated with impulsive wavefronts produced in the near-wall region. The sound appears to be produced when the standoff shock wave collapses for a portion of the oscillation cycle. Moderately and highly underexpanded jets usually produce impinging tones when a Mach disk occurs along the central region of the jet. Tones cease when a conical shock wave appears in the flow. Tones also cease when the first and second shock waves are in the free-jet location, but this is most likely due to the fact that the second shock wave is conical.

Large plate impinging tones are part of a feedback loop to the nozzle [see Henderson and Powell (1993)]. One-dimensional models that limit the resonance region to the impingement region do not produce a strong resonance condition [see Morch (1964)] unless entropy changes are considered [see Kuo and Dowling (1996)]. However, when a strong resonance condition is achieved, the predicted resonance frequencies match discrete frequencies produced by small impinging plates. Although plate pressure measurements indicate that plane-wave motion occurs in the impingement region, the flow instability for large plate impinging tones must be driven by downstream propagating disturbances created at the nozzle exit by acoustic waves.

When jet disturbances interact with the first shock wave, the shock wave distorts and measurable changes in the conical shock-wave angle and changes in the sonic line position behind the shock wave are observed. Sound waves are also emitted by the jet disturbance–shock wave interaction. As the sonic line distorts, the successive pattern of expansion and compression waves in the supersonic region of the jet distorts. A point in the cycle is reached where the compres-

sion waves reflected from the sonic line no longer merge into a standoff (often annular) shock wave, and the standoff shock wave collapses. Shadowgraph photographs indicate that, as the nozzle-to-plate distance increases, the flow instability appears to be enhanced by wave motion in the central subsonic region of the jet. This observation is consistent with plate pressure measurements. However, the relative importance of these waves in the flow instability process is still not well understood.

Periodic changes in the near-wall region are associated with changes in the impingement region. The successive pattern of expansion and compression regions in the near-wall flow (see Sec. II) distorts when the flow in the impingement region oscillates and the standoff shock wave collapses. As the expansion and compression regions periodically distort, the pressure gradients in the near-wall region change and the jet boundary oscillates. The occurrence of a secondary plate pressure peak occurring at the instability frequency is evidence of the oscillating pressure gradient in the near wall region. Carling and Hunt (1974) observed local separation for some operating conditions in their steady impinging jet experiments. Unsteady local separation may occur in the unsteady jet and enhance the oscillations of the jet boundary. The impulsive sound is most likely produced by the oscillating jet boundary in the near-wall region. The model proposed by Glaznev (1977) for small plate tones that consisted of an oscillating conical surface may perhaps have an application to large plate impinging tones.

Sound production ceases when a conical shock wave is formed because the conical shock-wave angles are relatively small and supersonic flow occurs across the entire flow downstream of the shock wave. Distortions of the shock wave upon interaction with the downstream propagating jet disturbances do not result in subsonic flow. The jet transitions to subsonic speeds upstream of the plate through a stable standoff shock wave, and the near-wall flow remains relatively steady.

A better understanding of the flow in the impingement and near-wall regions is necessary to fully understand the sound production mechanism. The connection between an oscillating stagnation bubble, plane-wave motion in the impingement region, local separation in the near-wall region, and the production of large plate impinging tones is not well understood and requires further investigation.

VI. CONCLUSIONS

Impinging tones produced by jets at moderate and high underexpansion originate from oscillations of the flow in the near-wall jet. Changes in the near-wall region of the jet are associated with the collapse of the standoff shock wave during a portion of the oscillation cycle. Tones are produced when a Mach disk occurs in the flow and cease when the first or second shock waves develop a conical shape. Tones cease for nozzle-to-plate spacings greater than approximately $h/\Delta = 2.2$, which is the first plate location where both the first and second shock waves have the same shape and location in the free and impinging jets. For plate locations greater than $h/\Delta = 2.2$, the second shock wave has a conical shape.

ACKNOWLEDGMENTS

This work was supported by NASA Glenn Research Center through the Summer Faculty Researcher program. I would like to thank James Brides and Kenneth Weiland of NASA Glenn Research Center and J. Panda of Modern Technologies Corporation for their assistance and support of this project.

Alvi, F. S., and Iyer, K. G. (**1999**). ''Mean and unsteady flowfield properties of supersonic impinging jets with lift plates,'' AIAA 99-1829.

Back, H. L., and Sarohia, V. (**1978**). ''Pressure pulsations on a flat plate normal to an underexpanded jet,'' AIAA J. **16**(6), 634–636.

Carling, J. C., and Hunt, B. L. (**1974**). ''The near wall jet of a normally impinging, uniform, axisymmetric, supersonic jet,'' J. Fluid Mech. **66**, 159–176.

Childs, R. E., Bower, W. W., and Chmielewski, G. E. (**1991**). ''Jet noise predictions from unsteady Navier–Stokes simulations,'' AIAA-91-0493.

Curle, N. (**1955**) ''The influence of solid boundaries upon aerodynamic sound,'' Proc. Ray. Soc. (London) **231A**, 505–514.

Didden, N., and Ho, C-M (**1985**). ''Unsteady separation in a boundary produced by an impinging jet,'' J. Fluid Mech. **160**, 235–256.

Donaldson, C. D., and Snedeker, R. S. (**1971**). ''A study of free jet impingement. I. Mean properties of free and impinging jets,'' J. Fluid Mech. **45**, 281–319.

Elavarasan, R., Venkatakrishnan, L., Krothapalli, A., and Lourenco, L. (**2000**). ''Supersonic twin impinging jets,'' AIAA 2000-0812.

Ginzburg, I. P., Semiletenko, B. G., Terpigor'ev, V. S., and Uskov, V. N. (**1973**). ''Some singularities of supersonic underexpanded jet interaction with a plane obstacle,'' Inzh.-Fiz. Zh. **19**(3), 412–417 [J. Eng. Phys. **19**, 1081–1084 (1970)].

Ginzburg, I. P., Semiletenko, V. N., and Uskov, V. N. (**1975**). ''Experimental study of underexpanded jets impinging normally on a plane baffle,'' Fluid Mech.-Sov. Res. **4**(3), 93–105.

Glaznev, V. N. (**1977**). ''Sound field of an underexpanded supersonic jet impinging on a barrier,'' Sov. Phys. Acoust. **23**, 142–145.

Glaznev, V. N., Demin, V. S., and Yakushev, A. M. (**1977**). ''Self-oscillations in an underexpanded jet flowing into a barrier,'' Fluid Dyn. **12**(6), 848–852.

Glaznev, V. N., and Popov, V. Y. (**1992**). ''Effects of the face dimensions of a flat barrier on the self-oscillations generated in the interaction with a supersonic underexpanded jet,'' trans. from Izv. Ross. Akad. Nauk, Mekh. Zhidk. Gaza **6**, 164–168.

Golubkov, A. G., Koz'menko, B. K., Ostapenko, V. A., and Solotchin, A. V. (**1974**). ''On the interaction of an underexpanded supersonic jet with a finite flat baffle,'' Fluid Mech.-Sov. Res. **3**, 96–102.

Gubanova, O. I., Lunev, V. V., and Plastinina, (**1973**). ''The central breakway zone with interaction between a supersonic underexpanded jet and a barrier,'' Izv. Akad. Nauk SSSR, Mekh. Zhidk. Gaza **2**, 135–138 [Fluid Dyn. **6**, 298–301 (1971)].

Gummer, J. H., and Hunt, B. L. (**1971**). ''The impingement of a uniform axisymmetric, supersonic jet on a perpendicular flat plate,'' Aeronaut. Q. **22**(4), 403–420.

Gummer, J. H., and Hunt, B. L. (**1974**). ''The impingement of non-uniform, axisymmetric supersonic jets on a perpendicular flat plate,'' Isr. J. Technol. **12**, 221–235.

Henderson, B. (**2001**). ''An experimental investigation into the sound producing characteristics of supersonic impinging jets,'' AIAA 2001–2145.

Henderson, B., and Powell, A. (**1993**). ''Experiments concerning tones produced by an axisymmetic choked jet impinging on a flat plate,'' J. Sound Vib. **168**(2), 307–326.

Henderson. B. (**1993**). ''Sound Source Mechanisms of the Axisymmetric Supersonic Impinging Jet,'' Ph.D. dissertation, University of Houston.

Henderson, B., and Powell, A. (**1996**). ''Sound-producing mechanisms of the axisymmetric choked jet impinging on small plates: The production of primary tones,'' J. Acoust. Soc. Am. **99**, 153–162.

Henderson, B., and Powell, A. (**1997**). ''The use of an array to explain the sound characteristics of secondary small plate tones produced by the impingement of an axisymmetric choked jet,'' J. Acoust. Soc. Am. **102**, 1454–1462.

Henderson, L. F. (**1966**). ''Experiments on the impingement of a supersonic jet on a flat plate,'' J. App. Math. Phys, **17**, 553–569.

Ho, C., and Nosseir, N. S. (**1981**). ''Dynamics of an impinging jet. I. The feedback phenomenon,'' J. Fluid Mech. **105**, 119–142.

Hoo, G. H., Moore, G. R., and Anderson, L. P. (**1980**). ''Supersonic impingement flow upon a flat plate,'' JANNAF 12th Plume Technology Meeting, CPIA Pub. 332, 205–226.
Iwamoto, J., (**1990**). ''Impingement of under-expanded jets on a flat plate,'' J. Fluids Eng. **112**, 179–184.
Iwamoto, J., and Deckker, B. E. L. (**1981**). ''Development of flow field when a symmetrical underexpanded sonic jet impinges on a flat plate,'' J. Fluid Mech. **113**, 299–313.
Kalghatgi, G. T., and Hunt, B. L. (**1976**). ''The occurrence of stagnation bubbles in supersonic jet impingement flows,'' Aeronaut. Q. **27**, 169–185.
Kim, K., and Chang, K. (**1992**). ''Axisymmetric jet impingement on a flat plate: Numerical simulation using a TVD scheme,'' Proceedings of the 18th International Symposium on Shock Waves.
Kim, K., and Chang, K. (**1994**). ''Three-dimensional structure of a supersonic jet impinging on an inclined plate,'' J. Spacecr. Rockets **31**, 778–782.
Krothapalli, A., (**1985**). ''Discrete tones generated by an impinging underexpanded rectangular jet,'' AIAA J. **23**, 1910–1915.
Krothapalli, A., Rajkuperan, E., Alvi, F., and Lourenco, L. (**1999**). ''Flow field noise characteristics of a supersonic impinging jet,'' J. Fluid Mech. **392**, 155–181.
Kuo, C., and Dowling, A. P. (**1996**). ''Oscillations of a moderately underexpanded choked jet impinging upon a flat plate,'' J. Fluid Mech. **315**, 267–291.
Lamont, P. J., and Hunt, B. L. (**1980**). ''The impingement of underexpanded, axisymmetric jets on perpendicular and inclined flat plates,'' J. Fluid Mech. **100**, 471–511.
Levin, D. B., and Wardwell, D. A. (**1997**). ''Single jet-induced effects on small-scale hover data in ground effect,'' J. Aircr. **34**, 400–407.
Marsh, A. (**1961**). ''Noise measurements around a subsonic air jet impinging on a plane, rigid surface,'' J. Acoust. Soc. Am. **33**, 1065–1066.
Messersmith, N. L. (**1995**). ''Aeroacoustics of supersonic and sonic impinging jets,'' 33rd Aerospace Sciences Meeting, Reno, NV, AIAA 95-0509.
Morch, K. A. (**1964**). ''A theory for the mode of operation of the Hartmann air jet generator,'' J. Fluid Mech. **20**, 141–159.
Morch, K. A. (**1973**). ''On the impingement of a composite jet,'' The Technical University of Denmark Report No. 47.
Nakatogawa, T., Hirata, M., and Kukita, Y. (**1971**). ''Disintegration of a supersonic jet impinging normally on a flat plate,'' J. Spacecr. Rockets **8**(4), 410–411.
Neuwerth, G. (**1974**). ''Acoustic feedback phenomena of the subsonic and hypersonic free jet impinging on a foreign body,'' NASA TT F-15, 719.
Norum, T. D. (**1989**). ''Supersonic rectangular jet impingement noise experiments,'' AIAA 12th Aeroacoustics Conference, San Antonio, TX, AIAA-89-1138.
Norum, T. D. (**1990**). ''Ground impingement of supersonic jets from nozzles with various exit geometries,'' AIAA 90-4015.
Nosseir, N. S., and Ho, C. (**1982**). ''Dynamics of an impinging jet. II. The noise generation,'' J. Fluid Mech. **116**, 379–391.
Pamadi, B. N. (**1982**). ''On the impingement of a supersonic jet on a normal flat surface,'' Aeronaut. Q. **33**, 199–218.
Powell, A. (**1988**). ''The sound-producing oscillations of round underexpanded jets impinging on normal plates,'' J. Acoust. Soc. Am. **83**, 515–533.
Powell, A. (**1994**). ''Nature of the sound sources in low-speed jet impingement-further considerations,'' J. Acoust. Soc. Am. **96**, 590–593.
Powell, A., and Henderson, B. (**1990**). ''On the tones of round underexpanded jets impinging on normal plates,'' AIAA-90-3985.
Preisser, J. S. (**1979**). ''Fluctuating surface pressure and acoustic radiation for subsonic normal jet impingement,'' NASA TP 1361.
Sedel'nikov, T. Kh. (**1968**). ''The discrete component of the frequency spectrum of the noise of a free supersonic jet,'' in *Physics of Aerodynamic Noise*, edited by A. V. Rimiskey-Korsakov (Nauka, Moscow, 1967), NASA TT F-538.
Semiletenko, B. G., Sobkolov, B. N., and Uskov, V. N. (**1974**). ''Features of unstable interaction between a supersonic jet and infinite baffle,'' Fluid Mech.-Sov. Res. **3**(1), 90–95.
Soderman, P. T. (**1990**). ''The prediction of STOVL noise-current semi-empirical methods and comparisons with jet noise data,'' SAE 901058.
Tam, C. K. W., and Ahuja, K. K. (**1990**). ''Theoretical model of discrete tone generation by impinging jets,'' J. Fluid Mech. **214**, 67–87.
Tam, C. K. W., and Norum, T. (**1990**). ''Impingement tones of large aspect ratio supersonic rectangular jets,'' AIAA-90-3984.
Wagner, F. R. (**1971**). ''The sound and flow field of an axially symmetric free jet upon impact on a wall,'' NASA TT F-13, 942.
Wlezien, R. W., and Feraro, P. J. (**1990**). ''Aeroacoustic environment of an advanced STOVL aircraft in hover,'' AIAA 90-4016.

Extraction of acoustic normal mode depth functions using vertical line array data

Tracianne B. Neilsen and Evan K. Westwood
Applied Research Laboratories, The University of Texas at Austin, P.O. Box 8029, Austin, Texas 78713-8029

(Received 24 January 2001; revised 27 August 2001; accepted 5 November 2001)

A method for extracting the normal modes of acoustic propagation in the shallow ocean from sound recorded on a vertical line array (VLA) of hydrophones as a source travels nearby is presented. The mode extraction is accomplished by performing a singular value decomposition (SVD) of individual frequency components of the signal's temporally averaged, spatial cross-spectral density matrix. The SVD produces a matrix containing a mutually orthogonal set of basis functions, which are proportional to the depth-dependent normal modes, and a diagonal matrix containing the singular values, which are proportional to the modal source excitations and mode eigenvalues. The conditions under which the method is expected to work are found to be (1) sufficient depth sampling of the propagating modes by the VLA receivers; (2) sufficient source–VLA range sampling, and (3) sufficient range interval traversed by the source. The mode extraction method is applied to data from the Area Characterization Test II, conducted in September 1993 in the Hudson Canyon Area off the New Jersey coast. Modes are successfully extracted from cw tones recorded while (1) the source traveled along a range-independent track with constant bathymetry and (2) the source traveled up-slope with gradual changes in bathymetry. In addition, modes are successfully extracted at multiple frequencies from ambient noise.
[DOI: 10.1121/1.1432982]

PACS numbers: 43.30.Bp, 43.30.Xm, 43.30.Wi [DLB]

I. INTRODUCTION

This paper investigates a method for determining the depth-dependent mode functions of underwater acoustic propagation using measurements on a vertical line array (VLA). The approach does not require any *a priori* information about the sound-speed profile in the water column or the geoacoustic profile of the bottom. The focus of this paper is on using a loud source of opportunity, such as a passing ship, to provide the data from which the mode functions are obtained.

Although we refer to the procedure just described as ''mode extraction,'' that term has also been used for the procedure of matching modeled mode shapes to measured data on a VLA to decompose the field into modal components (see, for example, Ref. 1). This method allows the different modal contributions to be identified and isolated, but it requires an estimate of the ocean's acoustic parameters to generate the modeled mode shapes. In contrast, the objective of the current method is to extract mode shapes from VLA data directly, with no *a priori* information.

The mode extraction technique explored here is similar to several other approaches that use an eigenvalue decomposition of a spatial cross-spectral density matrix **C** to obtain the depth-dependent mode functions. In Ref. 2, a dominant source at a fixed range is assumed, **C** is formed by averaging the outer products of measured pressure spectra over multiple-frequency bins in a narrow band, and a requirement related to the temporal separation of the modal pulse arrivals is derived. In Refs. 3 and 4, ambient noise from the ocean surface is assumed, and **C** is formed by averaging over time. In the present work, a dominant source traversing a significant range interval is assumed, **C** is formed by averaging over time, and a requirement related to the range interval is derived.[5] This approach was also used in Ref. 6.

The remainder of the paper is organized as follows. In Sec. II the required experimental setup, the theory of singular value decomposition (SVD), and its relationship to the expression for the pressure field as a sum over the depth-dependent normal modes are presented. The requirements for the SVD of the pressure field to yield reliable depth-dependent normal modes are examined, and the efficiency advantages of performing the SVD on the cross-spectral density matrix are then outlined. This is followed by a brief explanation of how the multiple-frequency and ambient-noise approaches are related to the current work.

Section III contains the results of mode extraction performed using experimental data taken in the Hudson Canyon area in September 1993.[7] Results are shown for mode extraction using data from a towed cw source. First, the results using data recorded along a range-independent source track are presented, followed by the results using data from a slightly range-dependent source track. Finally, the results of mode extraction using ambient noise recorded prior to the experiment are given. In the concluding section, Sec. IV, the mode extraction technique and results are summarized, and applications of the method are discussed.

II. THEORY: MODE EXTRACTION FROM VLA DATA

The experimental setup required for the mode extraction technique consists of a source moving outward in range in

the vicinity of a vertical line array (VLA) of N_Z hydrophones, as shown in Fig. 1(a). The sound pressure at each hydrophone is recorded over a time interval during which the source–receiver range is $r_1, r_2, \ldots, r_{N_R}$, where N_R is the total number of ranges. An equivalent experimental setup in a range-invariant environment consists of a stationary source in the vicinity of a moving VLA, as shown in Fig. 1(b). In both cases, the pressure time series is measured at each of the N_Z receiver depths and at each of the N_R source–receiver ranges. The frequency components of the time series are obtained by performing a fast Fourier transform (FFT). For an FFT integration time T_w, the frequency bin spacing is $\Delta f = 1/T_w$. For each frequency component or bin, the FFT yields an $N_Z \times N_R$ complex matrix $\mathbf{P}$

$$\mathbf{P}=\begin{bmatrix} p(z_1,r_1) & p(z_1,r_2) & \cdots & p(z_1,r_{N_R}) \\ p(z_2,r_1) & p(z_2,r_2) & \cdots & p(z_2,r_{N_R}) \\ \vdots & \vdots\ddots & & \vdots \\ p(z_{N_Z},r_1) & p(z_{N_Z},r_2) & \cdots & p(z_{N_Z},r_{N_R}) \end{bmatrix}. \quad (1)$$

The elements of $\mathbf{P}$ may be written according to normal-mode theory as

$$p_{ij} \equiv p(z_i,r_j) = \frac{\sqrt{2\pi}e^{i\pi/4}}{\rho(z_s)} \sum_{m=1}^{N_M} \overline{\phi}_n(z_s)\overline{\phi}_n(z_i) \frac{e^{ik_n r_j}}{\sqrt{k_n r_j}}, \quad (2)$$

where $\overline{\phi}_n(z)$ are the orthonormal, depth-dependent mode functions. For the trapped modes, it is a good approximation that

$$\int_0^H \frac{\overline{\phi}_n(z)\overline{\phi}_m(z)}{\rho(z)} dz = \delta_{nm}, \quad (3)$$

where H is the depth of the half-space.[8] The expression for $p(z_i,r_j)$ is used to demonstrate how a matrix operation called singular value decomposition (SVD) can yield the depth-dependent modes $\overline{\phi}_n(z)$. We first describe the general properties of the SVD and then explain how the SVD of the matrix $\mathbf{P}$ produces the depth-dependent modes.

A. Singular value decomposition

The SVD of an $N \times M$ complex matrix $\mathbf{A}$ is

$$\mathbf{A} = \mathbf{U}\mathbf{S}\mathbf{V}^{\dagger}, \quad (4)$$

where † indicates the conjugate transpose of the matrix, $\mathbf{S}$ is a real diagonal matrix with elements in order from largest to smallest down the diagonal, and the columns of both $\mathbf{U}$ and $\mathbf{V}$ satisfy the orthonormality condition

$$\sum_{i=1}^{N} U_{in}U_{im}^* = \sum_{i=1}^{M} V_{in}V_{im}^* = \delta_{nm}, \quad (5)$$

where * indicates complex conjugation. Since $\mathbf{S}$ is diagonal, each element of $\mathbf{A}$ may be written as

$$a_{ij} = \sum_{k=1}^{N} u_{ik}s_{kk}v_{kj}^*. \quad (6)$$

B. The connection between the SVD and the normal modes

Recognizing the similarity between the orthonormality conditions of the modes in Eq. (3) and the singular vectors in Eq. (5), we express the pressure matrix $\mathbf{P}$, defined by its elements in Eq. (2), as a product of matrices as in Eq. (4)

$$\mathbf{P} = e^{i\pi/4}\overline{\mathbf{\Phi}}\mathbf{\Lambda}\mathbf{R}, \quad (7)$$

where $\overline{\mathbf{\Phi}}$, $\mathbf{\Lambda}$, and $\mathbf{R}$ are given by

$$\overline{\mathbf{\Phi}} = \frac{1}{\sqrt{\rho(z_s)}}\begin{bmatrix} \overline{\phi}_1(z_1) & \overline{\phi}_2(z_1) & \cdots & \overline{\phi}_{N_M}(z_1) \\ \overline{\phi}_1(z_2) & \overline{\phi}_2(z_2) & \cdots & \overline{\phi}_{N_M}(z_2) \\ \vdots & \vdots & \ddots & \vdots \\ \overline{\phi}_1(z_{N_Z}) & \overline{\phi}_2(z_{N_Z}) & \cdots & \overline{\phi}_{N_M}(z_{N_Z}) \end{bmatrix}, \quad (8)$$

$$\mathbf{\Lambda} = \frac{\sqrt{2\pi N_R}}{\sqrt{\rho(z_s)}}\begin{bmatrix} \frac{1}{\sqrt{k_1}}\overline{\phi}_1(z_s) & 0 & \cdots & 0 \\ 0 & \frac{1}{\sqrt{k_2}}\overline{\phi}_2(z_s) & \cdots & 0 \\ \vdots & \vdots & \ddots & \vdots \\ 0 & 0 & \cdots & \frac{1}{\sqrt{k_{N_M}}}\overline{\phi}_{N_M}(z_s) \end{bmatrix}, \quad (9)$$

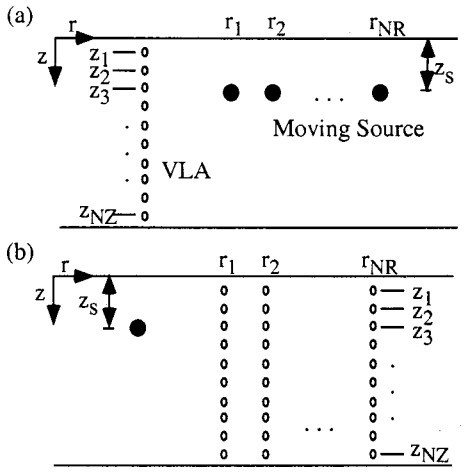

FIG. 1. Plot (a) shows a source (solid dots) moving in the vicinity of a vertical line array (VLA) of hydrophones (circles). The source depth is z_s, and the source to VLA ranges at successive times are r_j, with $j=1,...,N_R$. The hydrophones on the VLA are at depths z_i, with $i=1,...,N_Z$. Plot (b) illustrates an equivalent geometry in a range-invariant environment, namely a stationary source at depth z_s (solid dot) with a moving VLA. The VLA is shown at different times, corresponding to the source–receiver ranges r_j with $j=1,...,N_R$.

$$\mathbf{R}=\frac{1}{\sqrt{N_R}}\begin{bmatrix} \frac{e^{ik_1 r_1}}{\sqrt{r_1}} & \cdots & \frac{e^{ik_1 r_{N_R}}}{\sqrt{r_{N_R}}} \\ \frac{e^{ik_2 r_1}}{\sqrt{r_1}} & \cdots & \frac{e^{ik_2 r_{N_R}}}{\sqrt{r_{N_R}}} \\ \vdots & \ddots & \vdots \\ \frac{e^{ik_{N_M} r_1}}{\sqrt{r_1}} & \cdots & \frac{e^{ik_{N_M} r_{N_R}}}{\sqrt{r_{N_R}}} \end{bmatrix}, \tag{10}$$

where factors of $\sqrt{N_R}$ and $1/\sqrt{N_R}$ have been included in Eqs. (9) and (10), respectively, to reflect the size of the statistical ensemble.

We now examine the conditions under which the mode decomposition matrices $\overline{\mathbf{\Phi}}$, $\mathbf{\Lambda}$, and $\mathbf{R}$ correspond to the singular value decomposition matrices $\mathbf{U}$, $\mathbf{S}$, and $\mathbf{V}$. In order for $\overline{\mathbf{\Phi}}$ in Eq. (8) to correspond to $\mathbf{U}$ of Eq. (4), the orthonormality condition given in Eq. (5) must hold:

$$\sum_{i=1}^{N_Z} \overline{\Phi}_{in}\overline{\Phi}_{im}=\sum_{i=1}^{N_Z} \frac{\overline{\phi}_n(z_i)\overline{\phi}_m^*(z_i)}{\rho(z_s)} \stackrel{?}{=} \delta_{nm}, \tag{11}$$

where the notation $\stackrel{?}{=}$ indicates an approximate equality that has not yet been demonstrated.

The summation in Eq. (11) is a good approximation to the integral in Eq. (3) provided that (1) the mode functions are well sampled by the receivers in depth; (2) the density of the water is nearly constant; and (3) the possibly nonuniform depth sampling is accounted for by weighting each term of the summation in Eq. (11) by the average element spacing. Clearly, modes that have significant amplitudes in the bottom cannot be well sampled by a VLA in the water column. Therefore, the fields at short ranges, where bottom-penetrating modes are significant, should not be used to form $\mathbf{P}$ in Eq. (1).

The matrix $\mathbf{\Lambda}$ in Eq. (9) corresponds to the matrix $\mathbf{S}$ in Eq. (4) because it is diagonal and predominantly real. The latter condition holds because, especially for the modes that propagate to fairly long ranges, $\mathrm{Re}(k_n) \gg \mathrm{Im}(k_n)$ and $\mathrm{Re}(\overline{\phi}_n) \gg \mathrm{Im}(\overline{\phi}_n)$. Note that the diagonal elements of $\mathbf{\Lambda}$ are not necessarily in decreasing order but may be rearranged to be so as long as the corresponding columns of $\overline{\mathbf{\Phi}}$ and the rows of $\mathbf{R}$ are also rearranged. Because the values of $\mathbf{\Lambda}$ are proportional to the modal source excitation, the strongest propagating modes are found in the left-most columns of $\mathbf{U}$.

An important point regarding the matrix $\mathbf{S}$ is that if two or more of the singular values in $\mathbf{S}$ are nearly equal, the corresponding singular vectors in $\mathbf{U}$ are not uniquely determined,[9] and, as a result, the desired depth-dependent modes are linear combinations of the columns of $\mathbf{U}$. A good criterion for determining when extracted mode functions are not valid, developed by examining simulated data, is that those with adjacent singular values within 5%–10% of each other, when scaled by the largest singular value, *can* be degenerate, although many are well extracted.[10] Problems associated with close adjacent singular values are more likely to occur at higher frequencies because more modes are present in the waveguide, and hence there is a higher probability of two modes having close modal source excitations.

Finally, with regard to the third matrices of Eqs. (7) and (4), $\mathbf{R}$ of Eq. (10) must satisfy Eq. (5)

$$\sum_{j=1}^{N_R} R_{nj}R_{mj}^*=\sum_{j=1}^{N_R} \frac{e^{i(k_n-k_m^*)r_j}}{N_R r_j} \stackrel{?}{=} \delta_{nm}. \tag{12}$$

In order for all the columns of $\mathbf{P}$ to be weighted equally, the following amplitude normalization is performed:

$$\sum_{i=1}^{N_Z} p(z_i,r_j)p(z_i,r_j)^*=1. \tag{13}$$

As a result, the loss factors and the relative source amplitudes are effectively removed from the field $\mathbf{P}$. After the amplitude normalization, the orthonormality condition in Eq. (12) becomes

$$D_{nm}=\sum_{j=1}^{N_R} R_{nj}R_{mj}^*=\sum_{j=1}^{N_R} \frac{e^{i\,\mathrm{Re}(k_n-k_m)r_j}}{N_R} \stackrel{?}{=} \delta_{nm}. \tag{14}$$

The number of revolutions the elements of the sum D_{nm} complete in the complex plane is

$$n_{\mathrm{rot}}=\frac{\mathrm{Re}(k_n-k_m)\Delta r}{2\pi}, \tag{15}$$

where $\Delta r=r_{\max}-r_{\min}$ is the range interval. The dependence of $|D_{nm}|$ on n_{rot} is illustrated in Fig. 2. Details regarding the parameters used are given in the figure caption. It is clear from Fig. 2 that as n_{rot} increases, the exponential terms in the summation, for $n \neq m$, tend to cancel out, and the numerator of Eq. (14) is much less than the denominator N_R. Thus, when n_{rot} is large, the off-diagonal components of $\mathbf{RR}^\dagger$ are very small, and Eq. (14) holds approximately.

Guidelines have been developed, using simulated data, for selecting approximate source–VLA ranges that make Eq. (14) hold and thus optimize the performance of the mode

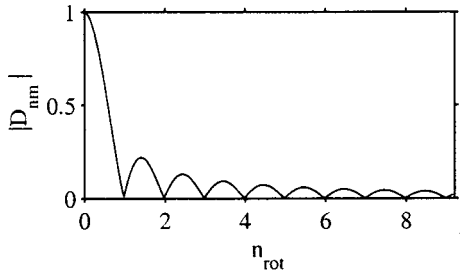

FIG. 2. Dependence of $|D_{nm}|$ from Eq. (14) on n_{rot} from Eq. (15). In constructing the plot, $r_{\min}$ was taken to be 6 km and $r_{\max}$ was varied from 6–14 km, causing n_{rot} to increase from 0 to 9.2. The value $\text{Re}(k_n - k_m) = 0.0072$ was taken to be the minimum eigenvalue separation for 200-Hz propagation in the ACT-II environment examined in Sec. III.

extraction technique. First, the range sampling dr should be sufficiently small that the field is sampled in range (or time) finely compared to the minimum interference distance, defined by the maximum difference in horizontal wave number

$$(dr) \ll (C_{nm})_{\min}, \tag{16}$$

where $C_{nm} = 2\pi/|k_m - k_n|$ is the modal cycle distance.

Second, the approximate range interval traversed by the source should be large compared to the maximum modal cycle distance

$$\Delta r \gg (C_{nm})_{\max}, \tag{17}$$

which means the elements of the sum in Eq. (14) complete a large number of revolutions in the complex plane. In shallow water, this condition is typically most difficult to achieve for neighboring low-order modes.

Third, the number of significant propagating modes should be relatively constant over the range interval. In shallow water, the trapped modes often have exponentially decaying tails in the bottom and are attenuated as they travel from the source to the receivers. When the number of significant modes changes within the range interval, the form of **P** no longer fits that of the SVD, and the mode extraction is less successful. A constant number of propagating modes is a frequency-dependent condition that is more stringent for higher frequencies. Thus, a large range extent Δr and a small range ratio $r_{\max}/r_{\min}$ is the ideal case because the same amount of relative modal attenuation occurs each time the range is doubled.

In summary, the optimum conditions for the SVD of **P** to result in a matrix **U** that corresponds to the depth-dependent mode functions are (1) the receivers must sample the propagating modes sufficiently well in depth; (2) the range extent Δr must be sufficiently large and sampled finely; and (3) the number of propagating modes over the range interval needs to be fairly constant. An additional requirement is that the signal-to-noise ratio needs to be positive. Since no information about the source, such as depth, exact range, or relative phase is needed, the mode extraction can be performed using a source of opportunity such as a passing ship.

Although the modes can be extracted by performing an SVD on the $N_Z \times N_R$ pressure matrix **P** at each frequency, the efficiency of the calculation can be improved, since typically, $N_Z \ll N_R$, by using the cross-spectral density matrix $\mathbf{C} = \mathbf{P}\mathbf{P}^\dagger$ instead. The cross-spectral density matrix at each frequency is a square $N_Z \times N_Z$ matrix that may be obtained by range averaging the outer products of the depth-dependent fields $\overline{p}(r_n)$

$$\mathbf{C} = \mathbf{P}\mathbf{P}^\dagger = \begin{bmatrix} \overline{p}(r_1) \\ \vdots \\ \overline{p}(r_{N_R}) \end{bmatrix} [\overline{p}(r_1), \ldots, \overline{p}(r_{N_R})] = \sum_{n=1}^{N_R} \overline{p}(r_n)\overline{p}^\dagger(r_n). \tag{18}$$

Using the matrix representation of **P** in Eq. (7), **C** can be expressed as a product of three matrices

$$\mathbf{C} = \mathbf{P}\mathbf{P}^\dagger = \overline{\mathbf{\Phi}}\mathbf{\Lambda}\mathbf{R}\mathbf{R}^\dagger\mathbf{\Lambda}^{\mathbf{T}}\overline{\mathbf{\Phi}}^\dagger \approx \overline{\mathbf{\Phi}}\mathbf{\Lambda}^2\overline{\mathbf{\Phi}}^\dagger, \tag{19}$$

where $\mathbf{R}\mathbf{R}^\dagger \approx \mathbf{1}$ when the conditions for orthonormality, discussed previously, are met. Therefore, the three matrices returned from an SVD of **C** can be identified as $\mathbf{U} = \mathbf{V} = \overline{\mathbf{\Phi}}$ and $\mathbf{S} = \mathbf{\Lambda}^2$. Note that **C** is Hermitian, and, therefore, an SVD of **C** produces identical **U** and **V** matrices. In addition, the number of VLA receivers N_Z must be at least as large as the number of propagating modes that contribute significantly to the field.

C. Additional configurations for mode extraction

The argument has been presented that a source traversing a sufficiently large range extent produces a pressure matrix **P** on a VLA that can be expressed as the product of three matrices that satisfy the same conditions as the matrices obtained from the singular value decomposition. Two other source–receiver configurations have been shown to lead to a pressure matrix that can be similarly decomposed. The requirement for successful mode extraction in each case is that the third matrix in a matrix representation of **P** [see Eq. (7)] be approximately orthonormal [$\mathbf{R}\mathbf{R}^\dagger \approx \mathbf{1}$]. When this condition holds, the spatial cross-spectral density matrix **C** reduces to the expression in Eq. (19), and the SVD of **C** yields the mode functions. Brief derivations of the two other approaches are given below.

1. Single range and multiple frequencies

In Ref. 2, the pressure field in a narrow frequency band B at a single source–VLA range r_o is used to construct an $N_Z \times N_F$ pressure matrix **P** versus depth and frequency bin. The elements of **P** are expressed, similar to Eq. (2), as

$$p_{ij} \equiv p(z_i, f_j) = \frac{\sqrt{2\pi}e^{i\pi/4}}{\rho(z_s)} \sum_{n=1}^{N_M} \overline{\phi}_n(z_s)\overline{\phi}_n(z_i) \frac{e^{ik_n(f_j)r_o}}{\sqrt{k_n(f_j)r_o}}, \tag{20}$$

where the mode functions $\overline{\phi}_n(z)$, which in reality depend weakly on frequency, are assumed constant over the bandwidth in order to perform the following decomposition. **P** can be expressed as the product of three matrices, as in Eq. (7)

$$\mathbf{P} = e^{i\pi/4}\overline{\mathbf{\Phi}}\mathbf{\Lambda}_{\mathbf{f}}\mathbf{F}, \tag{21}$$

where $\bar{\mathbf{\Phi}}$ is given by Eq. (8), $\mathbf{\Lambda_f}$ is a real, diagonal matrix, and the elements of $\mathbf{F}$ are

$$F_{nj}=\frac{e^{ik_n(f_j)r_o}}{\sqrt{N_F k_n(f_j)}}. \tag{22}$$

The orthonormality condition, $\mathbf{FF}^{\dagger}\approx\mathbf{1}$, equivalent to Eq. (14), is

$$\sum_{j=1}^{N_F} F_{nj}F_{mj}^{*}=\sum_{j=1}^{N_F}\frac{e^{i\,\mathrm{Re}[(k_n(f_j)-k_m(f_j)]r_o}}{N_F}\stackrel{?}{=}\delta_{nm}. \tag{23}$$

For this configuration n_{rot}, equivalent to Eq. (15), is given by

$$n_{\mathrm{rot}}=\frac{r_o}{2\pi}\{[k_n(f_{\max})-k_m(f_{\max})]-[k_n(f_{\min})-k_m(f_{\min})]\}, \tag{24}$$

where $f_{\min}$ and $f_{\max}$ are the minimum and maximum frequency of the band. As illustrated in Fig. 2, the matrix $\mathbf{F}$ is approximately orthonormal when n_{rot} is large. To obtain the physical condition that corresponds to large values of n_{rot}, both sides of Eq. (24) are divided by the bandwidth B

$$\frac{n_{\mathrm{rot}}}{B}=\frac{r_o}{2\pi}\left[\frac{k_n(f_{\max})-k_n(f_{\min})}{B}-\frac{k_m(f_{\max})-k_m(f_{\min})}{B}\right]. \tag{25}$$

For sufficiently small bandwidth, Eq. (25) reduces to

$$\frac{n_{\mathrm{rot}}}{B}=r_o\left[\frac{1}{v_n}-\frac{1}{v_m}\right], \tag{26}$$

where $v_n=2\pi df/dk_n$ is the modal group velocity. In terms of modal travel times, $\tau_n=r_o/v_n$, n_{rot} may be expressed as

$$n_{\mathrm{rot}}=B(\tau_n-\tau_m). \tag{27}$$

Since a pulse of bandwidth B has a nominal duration of $1/B$, Eq. (27) implies that $n_{\mathrm{rot}}>1$ when the modal arrivals are temporally resolved.

2. Uncorrelated sources

In Ref. 3, it is stated that a sheet of uncorrelated, uniformly distributed sources near the ocean surface also produces a pressure matrix that can be expressed as a product of three matrices similar to Eq. (7). For this ambient noise case, the elements of the pressure matrix are the same as those in Eq. (2) except the range r_j corresponds to the range from the VLA to source j (see Chap. 9, Sec. 2.4 of Ref. 11). Arguments equivalent to those already presented lead to the conclusion that if the uncorrelated sources are distributed finely enough over a sufficiently large range interval, then the matrix analogous to $\mathbf{R}$ in Eq. (10) satisfies $\mathbf{RR}^{\dagger}\approx\mathbf{1}$, and the SVD of $\mathbf{P}$ yields the depth-dependent modes.

There are inherent advantages and limitations to using either ambient noise sources or a traveling source of opportunity for the mode extraction. One apparent advantage of using ambient noise is that $\mathbf{P}$ may be constructed using a relatively short time period, during which the sound-speed profile is likely to be constant. When using a traveling source, $\mathbf{P}$ must be constructed using a time period that is sufficiently large for the source to traverse the required range extent, during which the sound-speed profile could fluctuate. On the other hand, a possible limiting factor in using ambient noise for the mode extraction is that the sources are likely to be distributed at all ranges. The presence of the short-range sources can lead to difficulty in the mode extraction, as described above, because the number of propagating modes may vary significantly. The shorter ranges can be more easily excluded when using a traveling source.

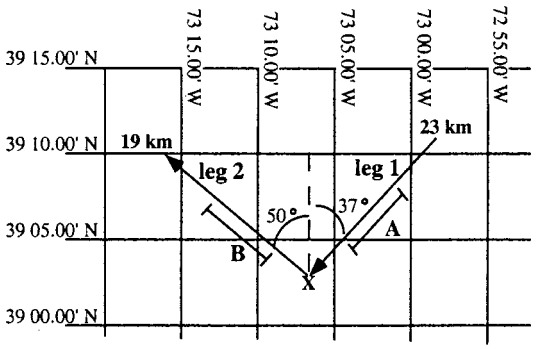

FIG. 3. Diagram of the first two legs of the ACT-II TL2 run. The X indicates the location of the VLA. The segments A and B indicate the range intervals used in Figs. 5–11.

III. APPLICATION OF THE MODE EXTRACTION METHOD TO THE ACT-II DATA

The mode extraction method is now applied to experimental data. In this section, the Area Characterization Test II (ACT-II) and the data sets used for mode extraction are described. Examples of modes extracted from the data at the frequencies of a towed cw source while the ship traveled along (1) a constant-bathymetry (range-independent) track and (2) an up-slope (range-dependent) track are given. Results of mode extraction using ambient noise recorded on the VLA are also presented.

A. Source–receiver geometry

The ACT-II experiment was conducted in September 1993 in the Hudson Canyon area of the New Jersey Shelf. Mode extraction is performed using data obtained during run TL2 at a location called the AMCOR site, named after the nearby AMCOR 6010 borehole.[12–14] An illustration of the first two legs of run TL2 is given in Fig. 3. Leg 1 lies along a region of basically constant bathymetry; leg 2 lies upslope.

The VLA, indicated by the X in Fig. 3, consists of 20 vertical elements, 19 of which were connected to the SEACAL recording system. The interelement spacing and relative distance of each element from the ocean bottom are shown in Fig. 4. The water depth is approximately 73 m. The receivers are concentrated in the lower half of the water column, where the spacing is 1.905 m. The receiver spacing near the top of the water column is 7.62 m. The sparseness of the receivers in the upper part of the water column is not optimal for the mode extraction technique.

Data from the first two source tracks of run TL2 are used for mode extraction: (1) a range-independent leg (constant bathymetry) during which the ship traveled from a source–

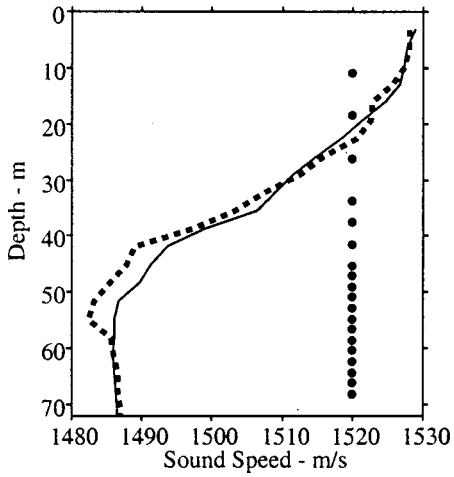

FIG. 4. The ACT-II VLA receivers (circles) and two of the sound-speed profiles obtained from XBTs. The solid line was measured at 0330 Z and the dashed line at 0212 Z, day 261.

VLA range of 22 km towards the array with a true bearing angle of 37 deg and a minimum source–VLA range of 1 km; and (2) a range-dependent leg (up-slope) during which the ship traveled out to a maximum source–VLA distance of 18 km with a true bearing of 310 deg. A J15-3 source projector emitted cw tones that were pulsed cyclically (see Ref. 7, Sec. 5.0) and was towed at a depth of 36 m.

B. The ocean environment

During the ACT-II experiment many sound-speed profiles were measured using conductivity–temperature–density casts (CTDs) and expendable bathy-thermograms (XBTs). Examples of the measured profiles are shown in Fig. 4; a more complete set may be found in Ref. 15.

Descriptions of the ocean bottom in the Hudson Canyon area are available from other experiments that have been performed in the area.[16] A borehole known as AMCOR 6010 was drilled in 1976,[12] and seismic surveying was performed in the area.[17,18] Geoacoustic profile values for the first 50 m of the ocean bottom from Ref. 15, with attenuation factors from Ref. 16, are listed in Table I.

C. Modes extracted from a range-independent track

Modes extracted using data from the middle of leg 1 of run TL2 are now presented. The results of mode extraction at 100, 150, and 200 Hz using data recorded from 0315 to 0420 Z, with $T_w = 0.63$ s, corresponding to approximate source–

TABLE I. Table of the sediment properties from Refs. 14, 15, and 17.

Depth (m)	c_p (m/s)	c_s (m/s)	ρ (g/cm^3)	α_p (dB/λ)	α_s (dB/λ)
5	1560	138	1.86	0.08	1.04
10	1610	182	1.96	0.13	0.82
20	1740	260	2.09	0.22	1.23
30	1830	326	2.17	0.18	0.82
40	1760	310	2.09	0.09	1.09
50	1710	299	2.03	0.16	1.06

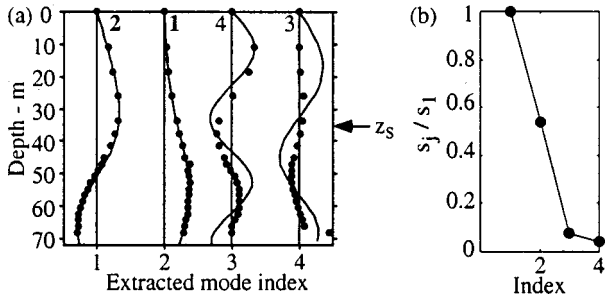

FIG. 5. (a) Extracted modes (dots) and predicted modes (lines) and (b) the corresponding scaled singular values obtained using the 100-Hz tone data recorded from 0315 to 0420 Z on day 261, leg 1 of run TL2, during which the ship traveled from ranges of approximately 14 to 6 km. The numbers at the top of part (a) are the modeled mode numbers.

VLA ranges of 14 to 6 km are shown in Figs. 5–7. This range interval is labeled section A in Fig. 3 and is sufficiently large to satisfy the range requirement as illustrated in Fig. 2. In part (a) of Figs. 5–7, the extracted modes at the VLA depths are indicated by the dots. The lines are the mode functions obtained from the ORCA normal mode model using measured sound-speed profiles, a nominal water depth of 73 m, and the historical bottom geoacoustic profile given in Ref. 17. The total number of modes shown in Figs. 5–7 equals the total number of modes found by the model at each frequency. The modes are generally well extracted. Discrepancies between extracted and modeled modes are expected and may be caused by either poor mode extraction or by inaccurate model inputs. The order of the extracted modes agrees well with the reported source depth of 36 m, since the mode function amplitudes at z_s decrease as the extracted mode index, which corresponds to the SVD column number, increases. For example, at 150 Hz in Fig. 6(a), a source depth closer to 50 m would lead to the extraction of modes 1 and 3 in the first two columns of **U** instead of modes 2 and 4. Part (b) of Figs. 5–7 contains the scaled singular values. The singular values are shown to illustrate that extracted modes with close singular values can be degenerate even though many are well extracted. An example of degenerate modes is modes 3 and 4 at 100 Hz in Fig. 5(a). The corresponding difference in scaled singular values is 0.03 or 3% of the largest singular value.

The mode extraction technique works best at lower frequencies when the number of propagating modes is relatively small. However, to test the limits of the method and develop additional criteria, the results of mode extraction at 300, 400, and 500 Hz are shown in Figs. 8–10. To obtain the

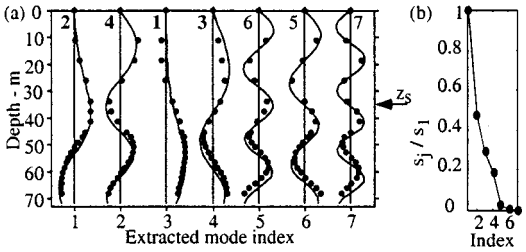

FIG. 6. Mode extraction results for the tone at 150 Hz. The format is the same as in Fig. 5.

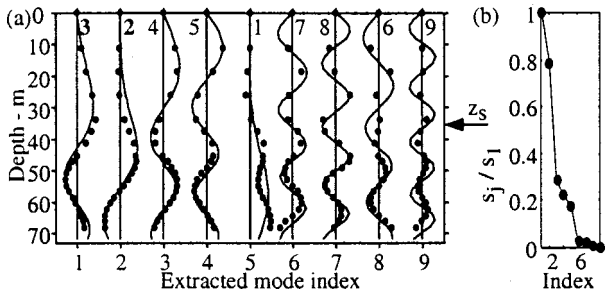

FIG. 7. Mode extraction results for the tone at 200 Hz. The format is the same as in Fig. 5.

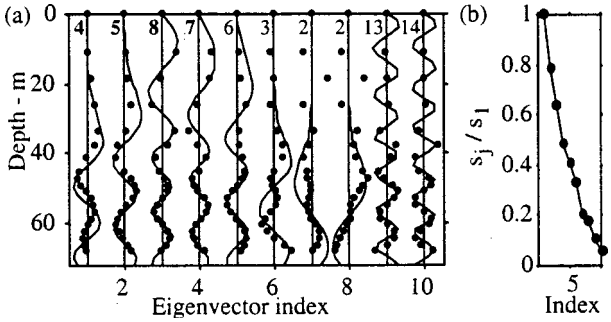

FIG. 9. Mode extraction results for the tone at 400 Hz. The format is the same as in Fig. 5.

best results at the higher frequencies, a larger coherent integration time, $T_w = 1.26$ s, is used to take advantage of the longer pulse duration and thus increase the SNR. Many of the low-order modes are well extracted, but, unfortunately, the high-order modes are not well sampled by the VLA in the upper part of the water column. The order of the well-extracted modes again agrees well with the source depth of 36 m. It is evident from part (b) of Figs. 8–10 that the probability that extracted modes are degenerate because of close singular values increases with frequency. If an approximate water depth is known, the degenerate modes can be identified as those that bear no resemblance to the modeled mode shapes (see, for example, extracted modes 7 and 8 at 400 Hz in Fig. 9).

In summary, mode extraction from a range-independent leg of the ACT-II experiment is quite successful and exhibits characteristics consistent with our theoretical development: the modes are extracted better at the lower frequencies; the higher-order modes cannot be well extracted unless they are well sampled in depth; and the source depth primarily determines the order of the extracted modes.

D. Modes extracted from a range-dependent track

Although the mode extraction technique was developed for a range-independent environment in Sec. II, we now show that the mode extraction also works for a mildly range-dependent environment. Using the adiabatic approximation, which assumes that the modes do not couple in a weakly range-dependent environment, the expression for the spectral components of the pressure field at a depth z and range r from a source as a sum over normal modes [see Eq. (2)] becomes

$$p(z,r) = \frac{\sqrt{2\pi}e^{i\pi/4}}{\rho(z_s)} \sum_{n=1}^{\infty} \overline{\phi}_n(z_s,r_s)\overline{\phi}_n(z,r) \frac{e^{i\int_0^r k_n(r')dr'}}{\sqrt{\int_0^r k_n(r')dr'}}. \tag{28}$$

During leg 2 of run TL2, the ship traveled away from the VLA along an up-slope track. The change in water depth was approximately 12 m over 18 km. The results of mode extraction at the low frequencies using data taken from the middle of leg 2 are shown in Fig. 11. Specifically, data recorded from 0620 to 0740 Z, which correspond to approximate ranges of 6 to 15 km and are shown as section B in Fig. 3, are used. The modes are extracted well. Note that the order of the extracted modes in part (a) of Figs. 5–7 is different than the order in Fig. 11. In particular, mode 1, which has larger amplitude at lower depths, appears earlier in the columns of **U** at all three frequencies in Fig. 11, indicating a deeper effective source depth. The deeper effective source depth is reasonable because the mode shapes elongate as they travel down-slope from the ship to the VLA. In Ref. 19, a deeper effective source depth caused by adiabatic mode propagation is referred to as a "mirage." Thus, the mode extraction technique does work for a range-dependent environment as long as the changes in range occur slowly enough or far enough from the VLA for the mode shapes to adapt to the environment at the VLA.

E. Modes extracted from ambient noise

Modes extracted using data recorded on the VLA from 0200 to 0210 Z, day 261 are now shown. During this time, the ship was at least 22 km from the VLA and the source for

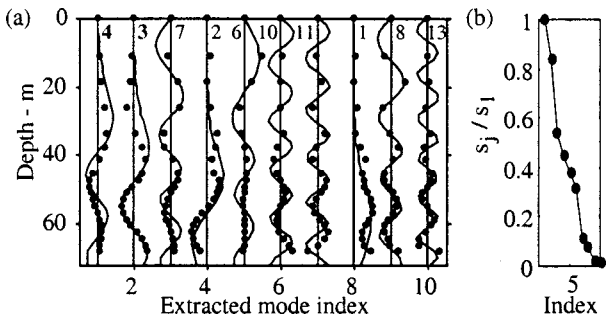

FIG. 8. Mode extraction results for the tone at 300 Hz. The format is the same as in Fig. 5.

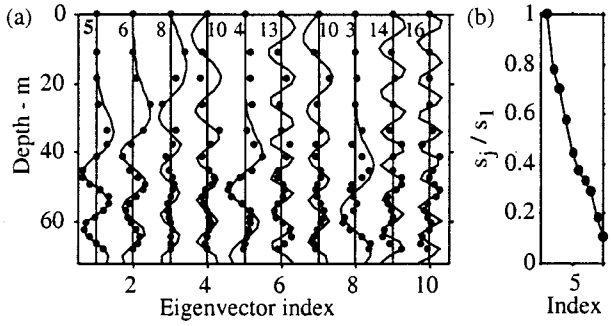

FIG. 10. Mode extraction results for the tone at 500 Hz. The format is the same as in Fig. 5.

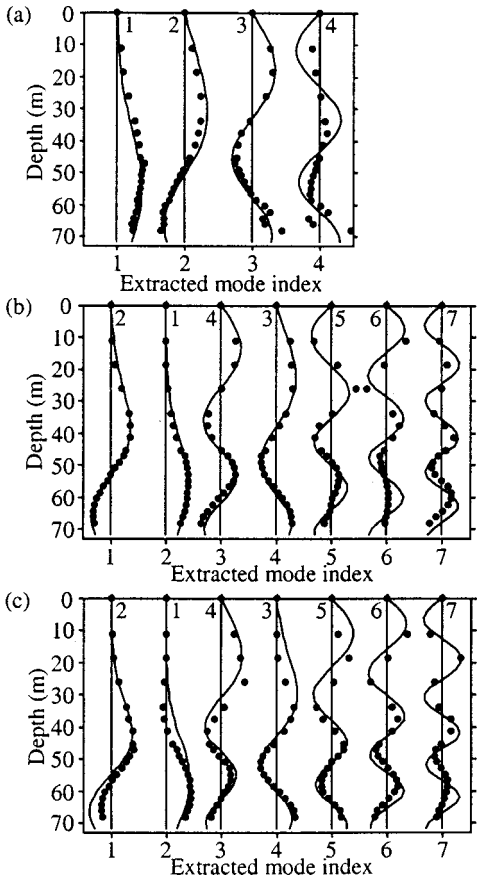

FIG. 11. Modes extracted at 100 Hz (a); 150 Hz (b); and 200 Hz (c) from data recorded from 0620 to 0740 Z on day 261 during range-dependent leg 2 of run TL2. The approximate range interval is 6 to 15 km.

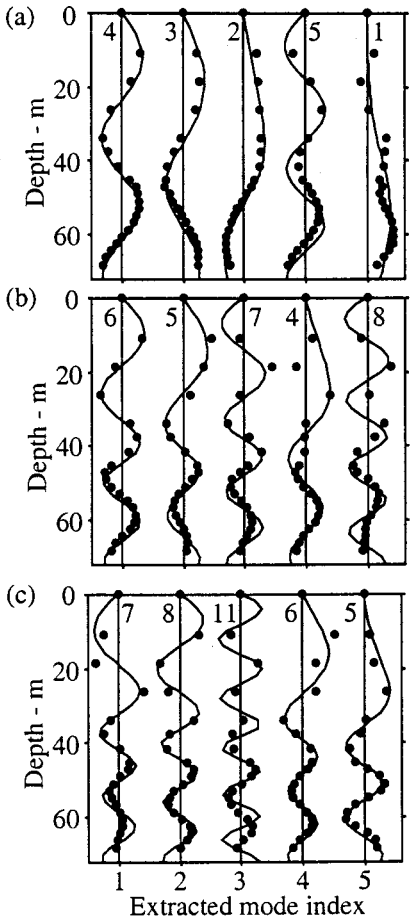

FIG. 12. Modes extracted from ambient noise recorded prior to the experiment at (a) 120 Hz; (b) 250 Hz; and (c) 350 Hz.

the cw tones was not yet on. The signal processing is performed using a coherent integration time of $T_w = 0.16$ s and a 50% overlap. The frequency bin size corresponding to this integration time is 6.4 Hz; thus, the data are averaged over a 6.4-Hz frequency band during the Fourier transform. This resulted in 7420 time samples over the 10-min time interval that was used to form the cross-spectral density matrix.

Figure 12 shows the first five modes extracted from the resulting cross-spectral density matrix at (a) 120 Hz; (b) 250 Hz; and (c) 350 Hz. Many of the extracted modes have excellent correlation with the modes modeled using the sound-speed profile from an XBT measurement taken at 0212 Z.

The order of the extracted modes gives an approximate value for the effective source depth of the ambient noise. The primary extracted modes all have larger amplitudes at depths of less than 10 m than the modes that appear in subsequent columns of **U**. Thus, the effective source depth for the ambient noise implied from the mode extraction is less than 10 m. A shallow source depth for the ambient noise is logical because the sound recorded during the time interval 0200 to 0210 Z was most likely associated with surface noise.

IV. SUMMARY

In this paper we have presented an approach for extracting mode functions from data measured on a vertical line array and applied the method successfully to experimental data. The mode extraction technique is predicted to work well if the VLA samples the water column well and if either a single source covers a sufficient range extent or a large number of uncorrelated sources produce the field, as in the case of ambient noise from the ocean surface. In the single-source case, the acoustic source need not be controlled: its depth, the phase of its tonals, and its precise track do not need to be known. Also, the ocean environment need not be known.

The mode extraction technique was applied to the ACT-II data set. Despite the relative sparseness of the array near the top of the water column, depth-dependent normal modes were successfully extracted using data acquired in both range-independent and slightly range-dependent environments. Modes were also successfully extracted from ambient noise.

Depth-dependent modes obtained using this mode extraction technique may be used as inputs for additional data analysis. For example, in Ref. 20, the data-extracted modes may be used in environmental inversions to obtain properties of the upper sediment layer. In Ref. 6, depth-dependent mode functions and horizontal wave numbers are calculated using a VLA that partially spans the water column, and the resulting data-derived modes and wave numbers are used in matched-field processing.

ACKNOWLEDGMENTS

This research was sponsored by the Office of Naval Research. We thank the authors of Refs. 4 and 6 for providing preprints of their work, and the reviewers for their helpful comments.

[1] C. T. Tindle, K. M. Guthrie, G. E. J. Bold, M. D. Johns, D. Jones, K. O. Dixon, and T. G. Birdsall, ''Measurements of the frequency dependence of normal modes,'' J. Acoust. Soc. Am. **64**, 1178–1185 (1978).

[2] S. N. Wolf, D. K. Cooper, and B. J. Orchard, ''Environmentally adaptive signal processing in shallow water,'' in *Oceans '93, Engineering in Harmony with Ocean Proceedings* (IEEE, Piscataway, NJ, 1993), Vol. 1 of 3.

[3] P. Hursky, W. S. Hodgkiss, and W. A. Kuperman, ''Extracting modal structure from vertical array ambient noise data in shallow water,'' J. Acoust. Soc. Am. **98**, 2971 (1995).

[4] G. B. Smith, '''Through the sensor' environmental estimation,'' J. Acoust. Soc. Am. **101**, 3046 (1997).

[5] T. B. Neilsen, and E. K. Westwood, ''Mode function extraction from a VLA using singular value decomposition,'' J. Acoust. Soc. Am. **101**, 3025 (1997).

[6] P. Hursky, W. S. Hodgkiss, and W. A. Kuperman, ''Matched field processing with data-derived modes,'' J. Acoust. Soc. Am. **109**, 1355–1366 (2000).

[7] J. Kwon, O. Marcia, and C. Brundick, ''ACT-II reconstruction data base,'' BBN Systems and Technologies, Arlington, VA, BBN Tech. Memo W1208, May 1994.

[8] E. K. Westwood, C. T. Tindle, and N. R. Chapman, ''A normal mode model for acousto-elastic environments,'' J. Acoust. Soc. Am. **100**, 3631–3645 (1996). The general orthonormality condition satisfied by the mode functions is given in Eq. (12) therein.

[9] W. H. Press, A. Teukolsky, W. T. Vetterling, and B. P. Flannery, *Numerical Recipes in* FORTRAN: *The Art of Scientific Computing* (Cambridge University Press, Cambridge, 1992).

[10] Although Ref. 9 states that the singular vectors are degenerate when the singular values are *exactly* equal, we have found, using simulated data with ideal range and depth sampling, that the singular values only need to be *relatively* close to one another for the extracted modes to be invalid.

[11] F. B. Jensen, W. A. Kuperman, M. B. Porter, and H. Schmidt, *Computational Ocean Acoustics* (AIP, New York, 1994).

[12] J. C. Hathaway, C. W. Poag, P. C. Valentine, R. E. Miller, D. M. Schultz, F. T. Manhiem, F. A. Kohout, M. H. Bothner, and D. A. Sangrey, ''U.S. geological core drilling on the Atlantic shelf,'' Science **94**, 515–527 (1976).

[13] T. Yamamoto, M. V. Trevorrow, M. Badiey, and A. Turgut, ''Seabed porosity and shear modulus inversion using surface gravity (wave) water-induced seabed motion,'' Geophys. J. Int. **98(1)**, 173–178 (1989).

[14] M. V. Trevorrow and T. Yamamoto, ''Summary of marine sedimentary shear modulus and acoustic speed profile results using a gravity wave inversion technique,'' J. Acoust. Soc. Am. **90**, 441–455 (1991).

[15] D. P. Knobles, E. K. Westwood, and J. E. LeMond, ''Modal time-series structure in a shallow-water environment,'' IEEE J. Ocean. Eng. **23**, 188–202 (1998).

[16] W. M. Carey, J. D. Doutt, R. B. Evans, and L. M. Dillman, ''Shallow-water sound transmission measurements on the New Jersey continental shelf,'' IEEE J. Ocean. Eng. **20**, 321–336 (1995).

[17] T. A. Davies, J. A. Austin, M. B. Lagoe, and J. D. Milliman, ''Late quaternary sedimentation off New Jersey: New results using 3D seismic profiles and cores,'' Mar. Geol. **108**, 323–343 (1992).

[18] R. D. Stoll, G. M. Bryan, R. Mithal, and R. Flood, ''Field experiments to study seafloor seismoacoustic response,'' J. Acoust. Soc. Am. **89**, 2232–2240 (1991).

[19] G. L. D'Spain, J. J. Murray, W. S. Hodgkiss, N. O. Booth, and P. W. Schey, ''Mirages in shallow-water matched-field processing,'' J. Acoust. Soc. Am. **105**, 3245–3265 (1999).

[20] T. B. Neilsen and E. K. Westwood (unpublished).

Study of a novel range-dependent propagation effect with application to the axial injection of signals from the Kaneohe source

Frederick D. Tappert
Division of Applied Marine Physics, University of Miami, RSMAS, Miami, Florida 33149

John L. Spiesberger
Department of Earth and Environmental Science, University of Pennsylvania, Philadelphia, Pennsylvania 19104-6316

Michael A. Wolfson
Applied Physics Laboratory, College of Ocean and Fishery Sciences, University of Washington, Seattle, Washington 98105-6698

(Received 9 February 1998; revised 6 August 2001; accepted 30 October 2001)

A novel range-dependent propagation effect occurs when a source is placed on the seafloor in shallow water with a downward refracting sound speed profile, and sound waves propagate down a slope into deep water. Under these conditions, small grazing-angle sound waves slide along the bottom downward and outward from the source until they reach the depth of the sound channel axis in deep water, where they are detached from the sloping bottom and continue to propagate outward near the sound channel axis. This ''mudslide'' effect is one of a few robust and predictable acoustic propagation effects that occur in range-dependent ocean environments. As a consequence of this effect, a bottom mounted source in shallow water can inject a significant amount of acoustic energy into the axis of the deep ocean sound channel that can then propagate to very long ranges. Numerical simulations with a full-wave range-dependent acoustic model show that the Kaneohe experiment had the appropriate source, bathymetry, and sound speed profiles that allows this effect to operate efficiently. This supports the interpretation that some of the near-axial acoustic signals, received near the coast of California from the bottom mounted source located in shallow water in Kaneohe Bay, Oahu, Hawaii, were injected into the sound channel of the deep Pacific Ocean by this mechanism. Numerical simulations suggest that the mudslide effect is robust. [DOI: 10.1121/1.1432983]

PACS numbers: 43.30.Dr, 43.30.Hw, 43.30.Qd [DLB]

I. INTRODUCTION

Sound propagation in range-dependent ocean environments has long been recognized to be a difficult modeling and prediction problem. Normal modes are in general coupled in complicated ways that defy simple physical explanation, and rays may be converted from one type to another and often back again in an exceedingly complex manner.

The recent discovery of ray chaos in underwater acoustics, and its associated finite frequency manifestations, has re-emphasized the distinction between range-independent and range-dependent propagation, since a necessary condition for chaos is range dependence of the environment. For range-independent propagation, variables separate, the ray equations are completely integrable, and in principle the solution of the acoustic wave equation can be explicitly written down at any range and then analyzed in detail. In outline, at least, the physics of range-independent propagation is fully understood, numerically computed solutions are stable and robust, and no surprising new physical effects are expected. In contrast, for range-dependent propagation there exist numerical models that march the solution in range out from the source (or from the receiver when reciprocity is invoked), and almost every new application reveals new phenomena unique to the particular range-dependent environment where propagation is modeled.[1,2]

Although it is unlikely that the complete set of phenomena that occur in range-dependent sound propagation will ever be classified and fully understood, it is worthwhile to look for a subset of range-dependent propagation phenomena that are robust and at least qualitatively predictable. Several examples come to mind: the cross-frontal propagation effect, the bathymetric blockage effect, and the slope enhancement effect.[1–3] One purpose of this article is to add to this list a novel range-dependent propagation effect that we call the ''mudslide'' effect.

A second purpose of this article is to further understand the acoustic propagation effects associated with signals received at ranges of about 4000 km from the source located in Kaneohe Bay, Oahu, Hawaii.[4–6] A fundamental question is how can acoustic signals be efficiently injected into the axis of the deep ocean sound channel from a bottom mounted source located in shallow water? The mudslide effect described below offers one plausible answer to this question. In fact, this is what Spiesberger and Tappert[6] showed must be happening although the specific mechanism was not identified.

The mudslide effect is explained in Sec. II in terms of the basic physics of sound propagation in range-dependent oceanic wave guides. Section III contains numerical simulations with the UMPE acoustic model of the mudslide effect in the context of the Kaneohe source. Finally, the results are discussed in Section IV.

II. MUDSLIDE EFFECT

This novel range-dependent propagation effect occurs when a source is placed on the seafloor in shallow water with a downward refracting sound speed profile, and sound waves propagate down a slope into deep water. As a rule, sound speed profiles in shallow water are downward refracting at nonpolar latitudes, so this assumption is not a major restriction. Since bottom losses would significantly attenuate the signal, the source should not be placed too far shoreward from deep water.

Under these conditions, small grazing-angle sound waves slide along the bottom downward and outward from the source until they reach the sound channel axis in deep water, where they detach from the sloping bottom and continue to propagate outward near the sound channel axis. The reason for this behavior is that the minimum sound speed in the water column in shallow water is at the bottom. Since the seafloor is a good reflector of small grazing-angle waves, and those that penetrate are refracted upward by sediment gradients of sound speed, these small angle waves are trapped in a wave guide that follows the down-sloping bathymetry toward deeper water. Waves that have steeper grazing angles are more strongly attenuated by bottom losses, and are not guided downward by this sound speed minimum.

As the nearly bottom-grazing sound waves descend the slope, the sound speed gradient $g=dc/dz$ decreases in magnitude until it vanishes when the axis of the deep ocean sound channel is reached. At and near this depth, the sound waves no longer feel the sound speed gradient and they detach from the bottom and propagate freely near the sound channel axis without being further influenced by bottom interactions.

The term mudslide effect is used to describe this range-dependent acoustic propagation effect. The name is derived from a pictorial analogy (not physical) with undersea mudslides, or turbidity currents, whereby water containing suspended sediments flows down slopes beneath the less dense ambient seawater until a depth of neutral buoyancy is reached where the sediment-laden water moves off horizontally into the deep ocean. Turbidity currents are important in marine geology, and survey articles describing the associated hydrodynamic phenomena have recently appeared.[7,8] Observations of the resulting marine deposits, called turbidites, have been reported by Tucholke,[9,10] who observed them in the abyssal plains of the Atlantic Ocean, several thousand kilometers from their presumed place of origin.

The above physical description of the underwater acoustic mudslide effect indicates that it is robust and qualitatively predictable in real ocean environments. This effect is expected to have wide applicability in ocean acoustics. However, quantitatively accurate predictions of sound pressure levels, depth spreads around the axis, multipath time spreads, etc., require a high-fidelity, range-dependent acoustic model and accurate environmental input data.

The above physical description can be partly substantiated by the following idealized ray theoretic analysis based on the first-order parabolic approximation and specular reflections from the sloping bottom. The usual convention calls for the depth z to increase downward, and a positive grazing angle θ to be downgoing. Let us assume that the sound speed gradient in the shallow water is constant and downward refracting, $dc/dz=g=\text{const}$ with $g<0$, and that the water depth has constant slope, $z_b=z_0+sr$ with $s>0$. If the launch angle of a ray is $\theta_0<s$ and the ray starts at the seafloor at $r=0$ and $z=z_0$, then it can be shown that the maximum height of the ray above the bottom is constant and given by

$$h=\frac{c_0}{2|g|}(s-\theta_0)^2. \tag{1}$$

Physically, this result means that the rays follow the slope downward into deeper water. For example, if $g=-0.1\ \mathrm{s}^{-1}$, $s=0.1$, and a ray is launched horizontally, then $h=75$ m and this ray remains within 75 m of the bottom as it proceeds outward and downward. Other realistic values of g, s, and θ_0 give comparable values of h. A similar calculation yields the travel time of an RBR (refracted-bottom-reflected)^3 ray after N reflections from the bottom as

$$t=\frac{r}{c_0}-\frac{N}{3|g|}(s-\theta_0)^3. \tag{2}$$

Since $N\approx(|g|r/2c_0)/(s-\theta_0)$, it follows that the travel time to range r is approximately

$$t\approx\frac{r}{c_0}\left[1-\frac{1}{6}(s-\theta_0)^2\right]. \tag{3}$$

This shows that the multipath travel time spread of small grazing-angle rays ($|s-\theta_0|\ll 1$) is quite small during the downslope portion of the mudslide effect. The mudslide effect is not qualitatively altered by the inclusion of diffraction or by invoking the parabolic approximation.

The robustness of the mudslide effect requires analysis of more general environmental conditions: variable sound speed gradients, variable bottom slopes, bottom losses, bottom roughness, and surface reflections. This is best done with a numerical acoustic model. In the next section, a real ocean acoustic problem is modeled and robustness is established. Figure 1, that is more fully discussed in the next section, gives a dramatic illustration of the mudslide effect and shows that sound waves appear to flow down a slope in a manner that resembles an undersea mudslide.

Similar plots appeared earlier in model studies of sound propagation in the Straits of Florida.[11,12] Modeled sound propagated downwards hugging the bottom slope of the Florida Terrace eastwards into deeper water. The significance for tomography, which was the purpose of those studies, was that this sound went deeper than the core of the Gulf Stream. The generality of the mudslide effect was not described by those researchers.

The slope enhancement effect[13] has recently been thoroughly explored in a master article by Dosso and

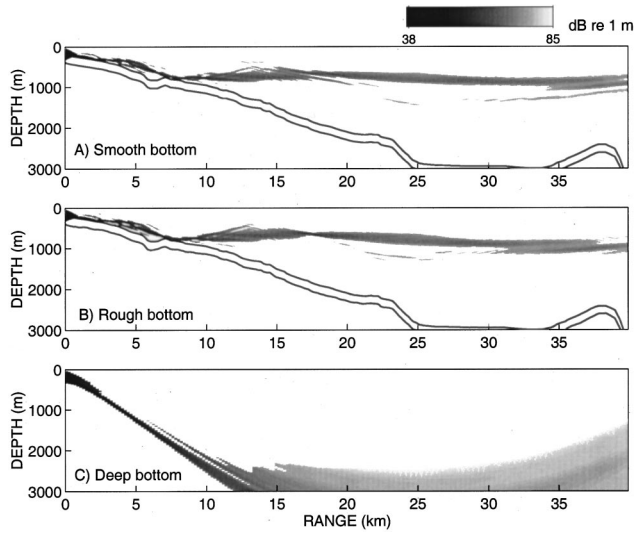

FIG. 1. The mudslide effect. (A) Downward propagating sound inclined near 5 degrees in about a one-degree beam width is modeled from the depth of the Kaneohe source into the ocean along smooth water/sediment and sediment/basement interfaces. Only the top 6 dB of sound pressure levels are shown at each range step to emphasize the location of the loudest sound. The top and bottom lines show the water/sediment and sediment/basement interfaces. (B) Same as (A) except the standard deviation of the water/sediment and sediment/basement interfaces are 2 and 8 m, respectively. (C) Same as (A) except the bottom is moved to 5000 m. No energy is trapped near 800 m depth without the mudslide effect arising from the sound speed gradients near the water/sediment interface.

Chapman,[14] which includes experimental data and a full-wave PE modeling effort that yields excellent agreement with the data. The slope enhancement effect differs from the mudslide effect in two important ways. First, in the slope enhancement effect the source is near the sea surface and is horizontally located where the depth of the minimum of sound speed intersects the bathymetric slope. In the mudslide effect, the source is mounted on the bottom and is in shallower water. Second, in the slope enhancement effect the downward refracting sound speed profile in shallow water plays no significant role, whereas it is essential to the mudslide effect. Thus, although both of these effects inject significant amounts of energy from a source into the axis of the deep water sound channel, the mechanisms of injection are distinctly different with the mudslide effect allowing the source to be far removed from the point where the axis of the sound channel intersects the slope.

III. KANEOHE SOURCE

The University of Miami Parabolic Equation (UMPE) acoustic model[15] is used to perform numerical simulations of propagation from the Kaneohe source.[4] This full-wave UMPE model uses the efficient Split-Step Fourier (SSF) algorithm[16] to march the acoustic field outward from the source, and the efficient Fourier synthesis technique to obtain pulse response functions in the time domain.[17] The propagator used in this study is the recently developed wide-angle c_0-insensitive parabolic approximation[18] that is fully second order accurate.[19] Convergence of the UMPE model has been tested for the cases presented below by refining the meshes in depth and range. The range mesh is 25.0 m and the depth mesh is 7.8 m.

The Kaneohe source,[4–6] that was active in the years 1983–1989, was located at 21.512 35°N latitude and 202.228 48°E longitude. Acoustic signals from this source, received at megameter ranges, were used to investigate possible global warming.[4] Since the source was bottom-mounted in shallow water at about 180 m depth and had only about 180 dB source level, it was not initially obvious that signals could be transmitted to megameter ranges with enough power to be detectable. However, this proved to be possible.[4,5]

The center frequency of the omnidirectional source was 133 Hz, and the bandwidth was 16 Hz. The geodesic on the ellipsoidal Earth from the source to the northern California receiver, whose location was indicated in Ref. 6, has a bearing at the source of 48.826° with respect to true North. Along this geodesic track, high resolution bathymetry near Hawaii was extracted from a detailed nautical chart compiled with Sea Beam[20] data and was then slightly smoothed. This deterministic bathymetry is shown in the upper two panels of Fig. 1. The same bathymetry was used in Ref. 6. Sound speed profiles along the same geodesic were obtained from the Levitus[21] springtime data base using Del Grosso's sound speed formula as described in Ref. 6. The sound channel axis is at a depth of about 800 m (Fig. 3) within 100 km of the source.

In the numerical Fourier synthesis from frequency space to time, a Hann window (raised cosine) having bandwidth of 33 Hz is used in frequency space to generate the source function.[18] This gives an effective bandwidth of 16 Hz, corresponding to a transmitted pulse length of about 60 ms.[5,6]

The techniques for modeling the geoacoustic bottom interactions are described in Ref. 22. The thickness of the sediment layer out to 100 km from the Kaneohe source is assumed to have the constant value of 200 m. The ratio of the compressional wave speed at the top of the sediment layer to the sound speed (range-dependent) at the bottom of the water column is 1.02, and the sound speed gradient within the penetrable sediment layer is $g = 1.0\ \mathrm{s}^{-1}$. The density ratio of the sediment to water is 1.7, and the attenuation is 0.02 dB/km Hz. The semi-infinite basement layer is modeled as a fluid with enhanced attenuation to account for shear wave conversion losses. The constant properties of the basement are modeled as in Ref. 23: sound speed ratio is 2.0; density ratio is 2.5; and the attenuation is 0.5 dB/km Hz. Bottom and basement roughness is modeled as described in Ref. 22. The horizontal correlation length of the power-law spectrum is 2000 m (unless noted otherwise), the rms displacement of the water-sediment interface is 2.0 m, and the rms displacement of the sediment-basement interface is 8.0 m. Modeling is also done with the roughness turned off, and is labeled ''smooth bottom'' in this case.

Three traditional PE field plots[1,2] displaying the CW transmission loss (in units of dB re 1 m) at center frequency 133 Hz out to the range of 40 km are shown in Fig. 1. In order to clearly show the mudslide effect from the Kaneohe source, the omnidirectionality of that source is replaced with

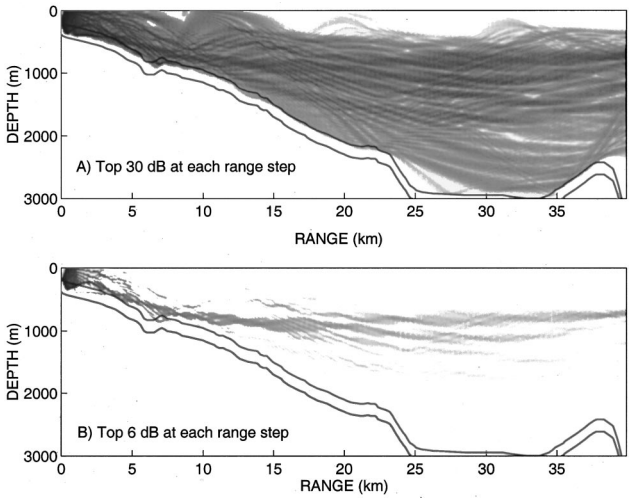

FIG. 2. Same as Fig. 1(A) except for an omnidirectional source. Panel (A) shows the top 30 dB of transmission loss at each range step. Panel (B) shows the top 6 dB of transmission loss at each range step.

an acoustic beam inclined downwards at 5 degrees in a 1 degree beam width. It is more difficult to see the mudslide effect if the acoustic model has an omnidirectional source (Fig. 2), because sound emitted from the real Kaneohe source also reflects from the surface and bottom slope of Oahu before becoming trapped in the acoustic wave guide in the deep ocean.[6] Referring then to panel (A) in Fig. 1, some of the acoustic field propagates out from the Kaneohe source along a smooth bottom. Panel (B) shows the same process with a rough bottom. Both field plots dramatically illustrate the mudslide effect. Sound ''slides'' down the slope to the range of about 7 km and then propagates in deep water near the depth at which the sound speed is a minimum, i.e., 800 m (Fig. 3). Although the influence of bottom and sub-bottom roughness changes the details of the acoustic field, the mudslide effect is seen to be robust. There is no acoustic energy trapped near the depth of minimum sound speed when the source is placed at the same depth in deep water [Fig. 1(C)]. Panel (B) is computed for a horizontal roughness length of 2000 m. Very similar results are obtained with a horizontal

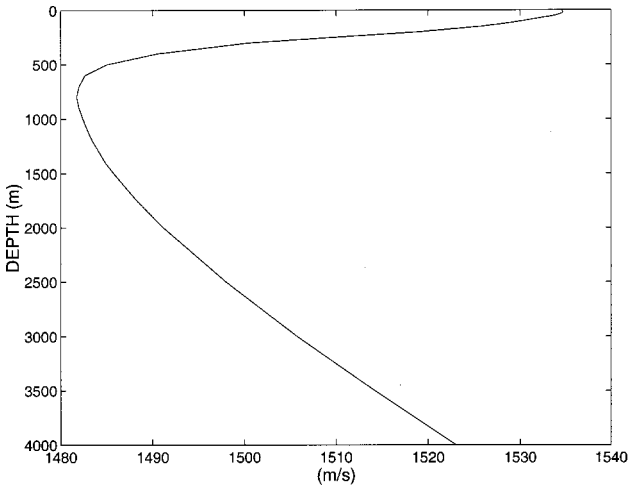

FIG. 3. The average speed of sound versus depth near the Kaneohe source from Spring (Ref. 21). The depth at which the speed is minimum is 800 m.

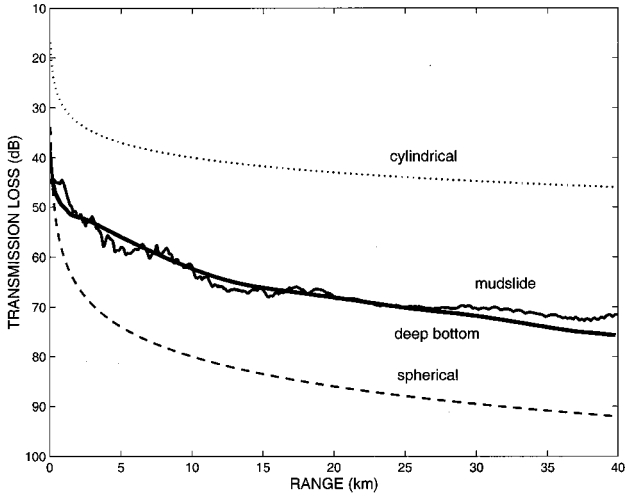

FIG. 4. The minimum transmission loss at each range step for panels (A) and (C) of Fig. 1. For reference, spherical and cylindrical losses are indicated. These losses are defined to be 10 $\log_{10}(R^2)$ and 10 $\log_{10}(R)$, respectively, where R is the distance from the source in meters. Note that the transmission loss from the mudslide effect is within a few decibels of that from sound which propagates into deep water.

roughness length of 200 m, so the mudslide effect is robust for these shorter undulations of the bottom too (not shown).

The amount of energy transmitted by the mudslide effect to the depth of minimum sound speed is within a few decibels of that obtained by placing the same source in deep water where the sound does not interact with a bathymetric slope (Fig. 4). These results are obtained from identical sources that beam energy downwards at 5 degrees in a 1 degree beam width as shown in panels (A) and (C) of Fig. 1. Thus the mudslide effect efficiently injects a large amount of acoustic power into near-axial waves that can then propagate to very long ranges, as observed by Spiesberger *et al.*[5,6] Once the sound waves are injected into the sound channel, they hardly interact further with the surface or bottom; the only significant loss mechanism thereafter is cylindrical spreading and a small amount of loss due to seawater absorption.

As opposed to the single frequency runs discussed above, a narrow band of frequencies over 16 Hz are modeled with the same full wave model to mimic the frequencies emitted from the Kaneohe source. It is possible to then examine the temporal aspects of modeled signals from this source using an inverse Fourier transform.

The time interval between the last and first arriving paths at distances of about 40 and 105 km is small (Fig. 5). At a distance of 40 km, the energy arrives within about 0.06 s. This is the same as the resolution of the transmitted pulse, i.e., 1/(16 Hz) which is 0.06 s. Thus, despite the complicated bottom interactions that occur during the mudslide process, the multipath time spread is actually quite small, just as predicted by the simplified analysis leading to Eq. (3). Some of the energy near 800 m depth comes from the mudslide effect and it arrives before the energy at other depths. This arrival order is opposite to that found for propagation in deep water in the northeast Pacific Ocean where the energy near the depth of minimum sound speed arrives last. The mudslide effect appears to contribute to the small time spread of paths

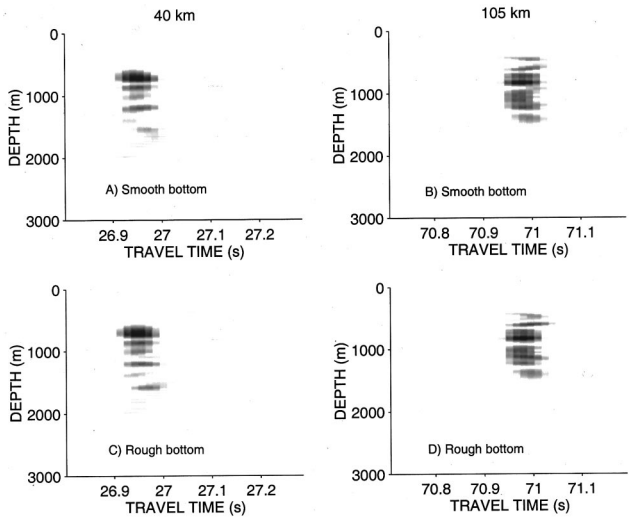

FIG. 5. Simulated time fronts from the Kaneohe source at distances of 40 and 105 km using smooth and rough water/sediment and sediment/basement interfaces. Note that the travel times at about 800 m depth correspond to the energy from the mudslide effect, and it arrives before the steeper inclined energy. Without a mudslide effect, the steeper energy arrives first in the northeast Pacific Ocean. The top 16 dB of energy is shown at each range with loudest as black. For the ''rough'' cases, the rms values of the water/sediment and sediment/basement interfaces are 2 and 8 m, respectively. The correlation distance is 200 m for these roughness values. The rms values of the roughness are zero for the ''smooth'' cases. Results are computed for an acoustic center frequency of 133 Hz and a bandwidth of 16 Hz.

at the receiver at 3709 km distance.[6] As the time fronts propagate out to the receiver at 3709 km, the energy near 800 m near the source is eventually overtaken by the energy from rays at steeper angles. At the receiver, the more steeply inclined energy (rays) arrives first.[6] Bottom and sub-bottom roughness has little influence at 40 and 105 km, and thus the mudslide effect is again seen to be robust (Fig. 5).

IV. DISCUSSION

The mudslide effect occurs naturally in the ocean in the vicinity of continental slopes, and is conjectured to be of general significance in underwater acoustics. It is one of a few robust and predictable acoustic propagation effects that occur in range-dependent ocean environments.

Numerical simulations of the mudslide effect have been performed using the University of Miami PE (UMPE) model. Using the real ocean environment near Kaneohe Bay, Oahu, Hawaii, it has been shown that the mudslide effect facilitates the injection of acoustic signals from a bottom-mounted source in shallow water into the deep water sound channel. These signals can then propagate to very long ranges with relatively small losses. Although the version of UMPE used in this work is two dimensional with no azimuthal coupling, it is believed that fully three-dimensional broadband model predictions would not differ significantly from those presented here.

There are different kinds of environmental situations that are not modeled here. For example, sometimes the water's sound speed at the bottom is greater than the sound speed at the top of the sediment layer. Then there is usually a minimum of sound speed near the top of the sediment layer, and the mudslide effect should occur for the same reasons it occurs in the cases modeled in this article. Because the attenuation coefficient for shear waves is so much greater than that for compressional waves near 133 Hz,[24] it appears that compressional waves, modeled here, should be the dominant process by which sound propagates in this experiment. This may not be so at much lower frequencies.[25]

The transition from shallow-water propagation to deep-water propagation is known to be a difficult modeling problem, as is the reciprocal problem (deep to shallow). It is hoped that the numerical modeling results presented here will contribute to an improved understanding of this important problem.

There appears to be two mechanisms by which the Kaneohe source injected energy near the depth of minimum speed in the Pacific Ocean. One is the mudslide effect. The other is due to rays bouncing from the surface and steep slope of Oahu.[6,23] Some of this reflected energy leaves the Oahu slope at a flat angle at the depth of minimum speed. It is not known what the relative contributions of these two effects may be, but this study indicates that the mudslide effect is significant in that experiment.

One conclusion of this study is that it is not necessary to place a bottom-mounted source at a distance from the shore that is near the point where the axis of the sound channel intersects the slope in order to couple the signals efficiently into the sound channel. Utilization of the mudslide effect accomplishes the same goal, and is more economical with sources cabled to shore because those cables are shorter. This observation, based on numerical simulations and experimental data from the Kaneohe source, has application to long-range ocean acoustic tomography, underwater noise, and possibly the so-called ''T-phase'' associated with sounds detected from underwater seismic events.[25] Direct experimental verification of the mudslide effect is needed.

ACKNOWLEDGMENTS

This research was managed by the Defense Advanced Research Projects Agency, Grant No. MDA972-93-1-0004, supported by the Strategic Environmental Research Development Program, and was also supported by the Office of Naval Research, Contract No. N00014-00-C-0317, Code 321OA. We thank Dr. Roger Lhermitte for numerous helpful suggestions that improved the clarity of exposition. N. R. Chapman kindly suggested the mudslide effect may play a role in forming the T-phase.

[1] F. D. Tappert, ''Selected applications of the parabolic-equation method in underwater acoustics,'' in *International Workshop on Low-Frequency Propagation and Noise*, Woods Hole, Massachusetts, 14–19 October 1974 (Department of the Navy, Washington, DC, 1977), Vol. 1, pp. 155–194.

[2] F. D. Tappert, ''The parabolic approximation method,'' in *Wave Propagation and Underwater Acoustics*, Lecture Notes in Physics, Vol. 70, edited by J. B. Keller and J. S. Papadakis (Springer-Verlag, New York, 1977), pp. 224–287.

[3] R. J. Urick, *Principles of Underwater Sound*, 3rd ed. (McGraw-Hill, New York, 1983).

[4] J. L. Spiesberger and K. Metzger, ''Basin-scale ocean monitoring with acoustic thermometers,'' Oceanography **5**, 92–98 (1992).

[5] J. L. Spiesberger, K. Metzger, and J. A. Furgerson, ''Listening for climatic temperature change in the northeast Pacific: 1983–1989,'' J. Acoust. Soc. Am. **92**, 384–396 (1992).

[6] J. L. Spiesberger and F. D. Tappert, ''Kaneohe acoustic thermometer fur-

ther validated with rays over 3700 km and the demise of the idea of axially trapped energy,'' J. Acoust. Soc. Am. **99**, 173–184 (1996).
[7] G. V. Middleton, ''Sediment deposition from turbidity currents,'' Annu. Rev. Earth Planet Sci. **21**, 89–114 (1993).
[8] D. A. Edwards, *Turbidity Currents: Dynamics, Deposits and Reversals*, Lecture Notes in Earth Sciences, Vol. 44 (Springer-Verlag, Berlin, 1993).
[9] B. E. Tucholke, ''Acoustic environment of the Hatteras and Nares Abyssal Plains, western North Atlantic Ocean, determined from velocities and physical properties of sediment cores,'' J. Acoust. Soc. Am. **68**, 1376–1390 (1980).
[10] B. E. Tucholke, ''Submarine geology,'' in *The Marine Environment of the U.S. Atlantic Slope and Rise*, edited by J. D. Milliman and W. R. Wright (Jones and Bartlett, Boston and Woods Hole, MA, 1987), pp. 56–113.
[11] D. R. Palmer, L. M. Lawson, D. A. Seem, and Y.-H. Daneshzadeh, ''Ray path identification and acoustic tomography in the Straits of Florida,'' J. Geophys. Res. **90**, 4977–4989 (1985).
[12] L. Nghim-Phu and H. A. DeFerrari, ''Numerical modeling of acoustic tomography in the Straits of Florida: Sensitivity to bathymetry,'' J. Acoust. Soc. Am. **81**, 1385–1398 (1987).
[13] J. Northrop, M. S. Loughridge, and E. W. Werner, ''Effect of near-source bottom conditions on long-range sound propagation in the ocean,'' J. Geophys. Res. **73**, 3905–3908 (1968).
[14] S. E. Dosso and N. R. Chapman, ''Measurement and modeling of downslope propagation loss over a continental slope,'' J. Acoust. Soc. Am. **81**, 258–268 (1987).
[15] K. B. Smith and F. D. Tappert, ''UMPE: The University of Miami Parabolic Equation Model, Version 1.3,'' MPL Technical Memorandum 432, 1993.
[16] F. D. Tappert, M. A. Wolfson, and K. B. Smith (unpublished).
[17] L. Nghiem-Phu and F. D. Tappert, ''Modeling of reciprocity in the time domain using the parabolic equation method,'' J. Acoust. Soc. Am. **78**, 164–171 (1985).
[18] E. D. Tappert, J. L. Spiesberger, and L. Boden, ''New full-wave approximation for ocean acoustic travel time predictions,'' J. Acoust. Soc. Am. **97**, 2771–2782 (1995).
[19] F. D. Tappert and M. G. Brown, ''Asymptotic phase errors in parabolic approximations to the one-way Helmholtz equation,'' J. Acoust. Soc. Am. **99**, 1405–1413 (1996).
[20] V. Renard and J. P. Allenon, ''Sea Beam, multi-beam echo-sounding in 'Jean Charcot': Description, evaluation and first results,'' Int. Hydrogr. Rev. **56**, 35–67 (1979).
[21] S. Levitus, ''Climatological atlas of the world ocean,'' in NOAA Prof. Pap. 13, U.S. Government Printing Office, Washington, DC, 1982.
[22] F. D. Tappert and L. Nghiem-Phu, ''Modeling of pulse response functions of bottom interacting sound using the parabolic equation method,'' in *Ocean Seismo-Acoustics*, edited by T. Akal and J. M. Berkson (Plenum, New York, 1986), pp. 129–137.
[23] M. A. Wolfson and J. L. Spiesberger, ''Full wave simulation of the forward scattering of sound in a structured ocean: A comparison with observations,'' J. Acoust. Soc. Am. **106**, 1293–1306 (1999).
[24] E. L. Hamilton, ''Geoacoustic modeling of the sea floor,'' J. Acoust. Soc. Am. **68**, 1313–1340 (1980).
[25] C. D. de Groat-Hedlin and J. A. Orcutt, ''Excitation of *T*-phases by seafloor scattering,'' J. Acoust. Soc. Am. **109**, 1944–1954 (2001).

Hydrodynamic acoustic absorption at the fluid/solid transition of suspensions

R. Esquivel-Sirvent[a)]
Instituto de Física, UNAM, Apdo. Postal. 20-364, Mexico D.F. 01000, Mexico

D. H. Green
Department of Geological Sciences, Condensed Matter and Surface Science Program, Ohio University, Athens, Ohio 45701

(Received 29 May 2001; revised 8 October 2001; accepted 7 November 2001)

A theoretical calculation of the excess acoustic attenuation due to hydrodynamic interactions in colloidal suspensions, when the suspended particles are spheres or plates, is presented. Our model is based on the fluid flow shearing between suspended particles during the passage of a longitudinal acoustic wave. To incorporate the many-body effects of the system, the nearest-neighbor distribution function for finite-size particles is introduced. The results of the modeling are compared to available experimental results. The main features of the experimental curves (e.g., attenuation maxima as a function of concentration and an increase in attenuation with frequency) are reproduced and it is shown that the attenuation due to hydrodynamic effects is a significant contribution to wave damping in high-concentration suspensions. © *2002 Acoustical Society of America.* [DOI: 10.1121/1.1432985]

PACS numbers: 43.30.Ft, 43.30.Ma [DLB]

I. INTRODUCTION

Suspended matter can play important roles in geochemical, biological, and physical systems of aquatic environments.[1] Because of their high specific surface areas and associated cation exchange capacity, suspended solids (clays and organic matter, in particular) play an important role in the transport and eventual deposition of cations.[2,3] Suspensions are also important to aquatic biology, as in the examples of suspended organic material leading to anoxia and fishkills and of biogenetic suspensions of carbonate and opal in the ocean.[4] Suspension concentrations as high as 38% by volume have been observed in rivers and elevated concentrations can be found in estuarine and coastal settings as well.[1] From a sedimentological standpoint, accurate characterization of suspensions is essential to understanding the sediment budgets of rivers and, on a broader scale, continents. Furthermore, since suspended materials include nondissolved contaminants in rivers, the ability to quantify the suspended load of rivers is also important to investigations of contamination in rivers, lakes, estuaries, and oceans.

Standard methods of measuring concentrations in the field rely on point-sampling using probes lowered into the water column. These include filtration, optical, and radiometric techniques, see, e.g., Refs. 5–7. Pointwise sampling can be highly accurate but has limited efficiency in monitoring large areas. Furthermore, optical sensors are designed for dilute suspensions (typically $<20\%$) due to the severe attenuation of light at high concentrations. For concentrated suspensions, less attenuated acoustic waves can be effective probes provided that a detailed understanding of acoustic wave propagation in these media can be achieved. Substantial progress has been made in the understanding of acoustic scattering by suspensions. The scattering of wave energy off of suspended particles is strongly frequency dependent and dominates acoustic attenuation at wavelengths up to the particle size, see, e.g., Refs. 8 and 9. At longer wavelengths, however, viscous losses generally exceed those due to scattering.[10,11] As viscous loss mechanisms are inherently mechanical as opposed to geometrical, viscous attenuation is a potential indicator of suspension rheology. We have previously suggested a link between viscous losses and the Atterberg limits of geomechanics.[12] In this paper, we will be primarily concerned with this long-wavelength (i.e., Rayleigh) regime.

Theoretical treatment of suspension acoustics range from simple averaging schemes to sophisticated effective medium methods. Wood[13] presented a velocity formula based on volume fraction weighted constituent compressibilities that gives an adequate description of overall velocity/concentration behavior but tends to underestimate velocity at high concentrations.[14,12] Urick[15] examined viscous attenuation of sound due to individual particles oscillating within a viscous fluid. He derived a result predicting an attenuation coefficient proportional to the solid volume concentration. Interparticle effects were considered by McCann,[16] who examined the inhibition of clay particle motion due to Coulomb forces. His results show a decrease in the amount of attenuation predicted by Urick's single-particle theory. They also show a maximum in the attenuation as a function of concentration.

The Biot[17,18] theory of porous media has been applied to suspensions by Hovem[19] and Ogushwitz.[20] In these applications, the moduli and permeability of the medium ''frame'' must be estimated for the case of fluid-based suspension as does a structure factor used in Biot theory to account for pore-space tortuosity in fluid-saturated porous solids. These ''Biot'' models show that viscous effects can control wave

a)Electronic mail: raul@fenix.ifisicacu.unam.mx

attenuation in high-concentration suspensions and that viscous losses can show a maximum with respect to concentration. Their practical application is hampered somewhat by the need to determine some of the model parameters empirically as adjustable constants or through other approximate methods.

Berryman[21,22] derived expressions for compressional wave velocity and attenuation for two-phase media in which one phase exists as ellipsoidal or spherical inclusions. Using a self-consistent method for determining effective moduli, a ''rigidity threshold'' is predicted at a specific concentration. This threshold is characterized by an abrupt change in velocity and a sharp peak in wave absorption as a function of concentration.

Observations of suspension acoustics in the laboratory have shown that attenuation increases linearly with concentration at low concentrations (<20%).[15,23,24] Marion and Nur[25] reported a sharp increase in compressional wave velocity at 61% concentration and attributed this to a substantial change in system rigidity. A complex frequency dependence of acoustic attenuation has been reported by Greenwood *et al.*[26] for kaolinite/water suspensions near 40% concentration. Recently, we reported measurements of acoustic absorption maxima and velocity extrema near 40% concentration in suspensions of silica or kaolinite in water or oil.[27,12] These effects were qualitatively attributed to hydrodynamic shearing of fluid in the narrow interparticle gaps at high concentrations. In the present paper, we put this model on a quantitative footing by deriving an expression for the intrinsic attenuation (Q^{-1}) due to interparticle fluid flow in a suspension. This model assumes a concentration-dependent distribution of interparticle gaps and replicates the absorption maxima seen previously.

II. ACOUSTIC ATTENUATION DUE TO HYDRODYNAMIC INTERACTIONS

In a suspension made of solid particles embedded in a viscous fluid matrix, hydrodynamic interactions are due to the relative motion of adjacent solid particles in the viscous fluid and the shearing fluid flow between them. The driving mechanism considered here is the passage of an acoustic wave. Consider two particles separated by a distance h_0. During acoustic loading the separation will vary as $h = \Delta h \cos(\omega t)$, where ω is the frequency of the loading. The irrecoverable energy needed to change the gap between the particles during periodic loading is lost from the wave and causes an acoustic attenuation. The gap, therefore presents an effective stiffness

$$k^* = -\frac{\Delta F}{\Delta h}, \tag{1}$$

where ΔF is the loading force. The resulting attenuation Q^{-1} (defined as the fraction of wave energy lost per cycle) is obtained from

$$Q^{-1} = \frac{\mathrm{Im}(k^*)}{\mathrm{Real}(k^*)}, \tag{2}$$

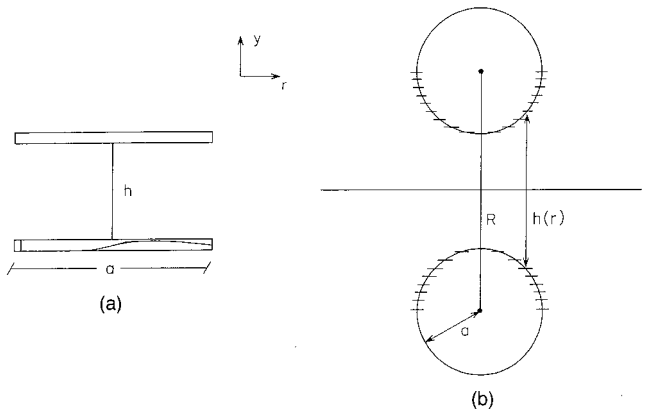

FIG. 1. Geometry and coordinate system for modeling the two-body hydrodynamic interactions due to (a) plates and (b) spheres. For the case of spheres the subdivisions made on the surface to calculate the attenuation are also shown.

where Im and Real refer to the imaginary part and the real parts, respectively. The particular form of the effective stiffness depends on, among other things, the geometry of the particles, the separation between them, and the properties of the fluid (viscosity and compressibility). In this work we calculate the effective stiffness for plate-shaped and spherical particles.

A. Attenuation due to plates

First we consider the attenuation of a pair of parallel circular plates of mean radius a, and negligible thickness. The plates are immersed in a fluid of viscosity η, density ρ, bulk modulus K_w, and at rest are separated by a distance h_0.

The complex stiffness k^* is derived from the Navier–Stokes equations in cylindrical coordinates assuming there is no contact between the particles, subject to the boundary condition that the velocity of the fluid should be zero at the surface of the plates. The coordinate system is shown in Fig. 1.

The y axis is taken perpendicular to the plates and the r axis lies in the $y=0$ plane midway between them. For our problem we assume azimuthal symmetry. The governing equations for the fluid motion as obtained by Murphy *et al.*[28] are

$$\frac{\partial^2 p}{\partial r^2} + \frac{1}{r}\frac{\partial p}{\partial r} + \frac{h_0}{K_w}(\omega^2 L_0 - i\omega D_0)p = -(\omega^2 L_0 - i\omega D_0)\Delta h, \tag{3}$$

where $L_0 = 2\rho/h_0$ is an inertial term and $D_0 = 12\eta/h_0^3$ is the viscous resistance. The right-hand side of Eq. (3) describes the dynamics of the separation between the plates, and can be recognized as a damped harmonic oscillator in the frequency domain. The left-hand side of Eq. (3) describes the pressure field via a zero-order Bessel equation whose convergent solution is of $cJ_0(\kappa r)$, where the $J_i(\kappa r)$ will denote the Bessel functions of the first kind of order i, c is an arbitrary constant to be determined, and $\kappa^2 = (h_0/K_w)(\omega^2 L_0 - i\omega D_0)$. The solution of Eq. (3) is

$$p(r,t) = p_0 + cJ_0(\kappa r) - \frac{K_w}{h_0}\Delta h, \tag{4}$$

where p_0 is the pressure field at $r \to \infty$. Due to the finite fluid compressibility, as the plate gap changes, so also does the volume of gap liquid (i.e., the fluid is squirted). Thus, a condition that must be satisfied by the pressure field is

$$p(r=a)-p(r=0)=\frac{\pi a^2 \Delta h}{V_0}K_w, \tag{5}$$

V_0 being the initial volume of liquid between the plates. Equation (5) is the thermodynamic definition of bulk modulus. It is a constraint since the energy needed to close the gap between the particles depends on compressibility of the fluid. The use of this condition yields the value of the constant c in Eq. (4):

$$c=\frac{\pi a^2 K_w}{V_0}\frac{\Delta h}{J_0(\kappa a)-1}. \tag{6}$$

The force needed to change the gap can now be calculated as

$$\Delta F=2\pi\int_0^a (p(r,t)-p_0)r\,dr, \tag{7}$$

and using this in Eq. (1), the effective stiffness is

$$k^*=\frac{3\pi}{2}\frac{K_w}{\kappa}\frac{J_1(\kappa a)}{J_0(\kappa a)-1}+\frac{\pi K_w a^2}{h_0}. \tag{8}$$

The acoustic attenuation is obtained from Eq. (2). Since we assumed that the plates are aligned, our model predicts the maximum possible attenuation due to fluid shearing.

B. Attenuation due to spheres

The hydrodynamic attenuation mechanism also operates between particles other than plates. We consider two identical spheres that oscillate during loading along the line joining their centers. The spheres have equal radius a and their centers are separated by a distance R. As shown in Fig. 1 we consider again cylindrical coordinates. In terms of the radial coordinate r, the gap between the spheres is given by

$$h(r)=R-2(a^2-r^2)^{1/2}. \tag{9}$$

To use the results developed in Sec. II A, we assume that the spheres can be divided into annular surface elements of mean size ϵ (with $\epsilon \to 0$), separated by a distance $h(r)$ (see Fig. 1). Applying the formalism for parallel plates to each one of these elements is now straightforward, by regarding h as no longer constant but a function of r as given in Eq. (9). Therefore, for a pair of parallel annular elements on the surface of the spheres, the pressure satisfies Eq. (3) and is given by

$$p(r,t)=p_0-\Delta h\frac{K_w}{h(r)}+cJ_0(\kappa(r)r). \tag{10}$$

Again, the constant c is determined using the condition on the fluid compressibility (5), for an annular region of minimum radius r' and maximum radius $r'+\epsilon$. In this case $h(r') \sim h(r'+\epsilon)$ and the value of c is

$$c=\frac{K_w \pi a^2}{V_0}\frac{\Delta h}{J_0(\kappa(r'+\epsilon)(r'+\epsilon)-J_0(\kappa(r')r'}, \tag{11}$$

where the initial fluid volume between the spheres is $V_0=\pi a^2(R-4a/3)$.

Notice that c is constant for a particular value of r'. The force during loading and thus the effective stiffness can be calculated as before using Eqs. (7) and (1). Taking into account the functional dependence of $\kappa(r)$ with the radial coordinate r, the effective stiffness is

$$k^*=\lim_{\epsilon \to 0}\frac{2\pi\int_0^a p(r',t)r'\,dr'}{\Delta h}. \tag{12}$$

III. MANY-BODY INTERACTIONS

Thus far the attenuation due to the hydrodynamic interaction of a single particle pair has been considered. The attenuation is a function of the separation of the particles, as was shown in Sec. II. In a many-body system, such as a suspension, to take into account the attenuation due to all possible nearest-neighbor pairs it is necessary to perform an average weighted by a nearest-neighbor distribution function $H(\xi)$. This distribution function gives the probability density of finding a nearest neighbor at a distance ξ from the center of a reference particle at a given concentration. The coordinate ξ represents the separation between the centers of two particles. For example, in the case of a suspension of hard spheres of radius a the mean separation between particles is

$$\lambda=a\int_1^\infty H(\bar{\xi})d\bar{\xi}, \tag{13}$$

where $\bar{\xi}$ is the normalized distance ξ/a. In a similar way we can define the average attenuation as

$$\langle Q^{-1}\rangle=\int_1^\infty H(\bar{\xi})Q^{-1}\,d\bar{\xi}, \tag{14}$$

where the attenuation in the integrand is that of only a pair of particles as described in the previous sections.

The pair distribution function $H(\xi)$ for finite-size objects was developed by Torquato.[29–31] This distribution not only takes into account the finite size of the suspended particles but also considers the change in functional dependence of $H(\xi)$ on volume concentration ϕ above the random close packing of spheres, whose value has been estimated at $\phi_c \sim 0.49$.[32] Notice that the random close packing occurs at a lower concentration than the close packing ($\phi \sim 0.74$) for spheres.[33] Summarizing Torquato's results, the nearest-neighbor distribution function for finite-size spheres is

$$H(\bar{\xi})=24\phi(a_0\bar{\xi}^2+a_1\bar{\xi}+a_2)\exp(-\phi[8a_0(\bar{\xi}^3-1)+12a_1(\bar{\xi}^2-1)+24a_2(\bar{\xi}-1)]). \tag{15}$$

The coefficients a_0, a_1, and a_2 depend only on the volume filling fractions as

$$a_0=\frac{1+\phi+\phi^2-\phi^3}{(1-\phi)^3},$$

$$a_1=\frac{\phi(3\phi^2-4\phi-3)}{2(1-\phi)^3}, \tag{16}$$

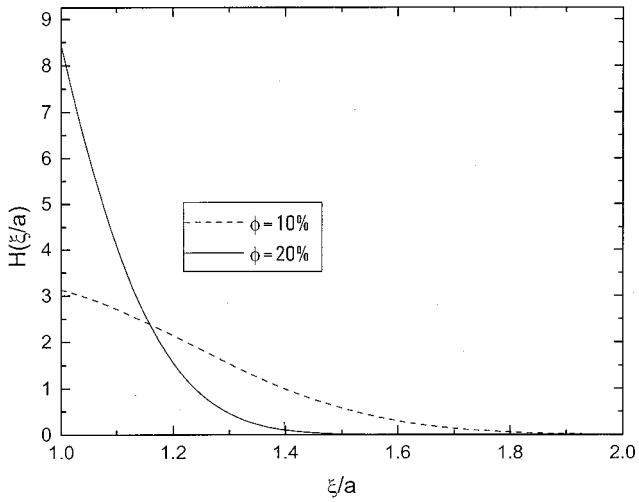

FIG. 2. Nearest-neighbor distribution function for spherical particles plotted as a function of the distance from a reference particle, for two different solid volume concentrations of the suspended particles (Ref. 30). As the concentration increases, the probability of finding a near-neighbor increases.

$$a_2 = \frac{\phi^2(2-\phi)}{2(1-\phi)^3}.$$

For filling fractions above the random close packing, interparticle contacts start dominating the attenuation process and our model must be modified. In Fig. 2, $H(\bar{\xi})$ is shown for two different solid volume concentrations. As expected, increasing the volume concentration reduces the probability of finding a nearest neighbor at large distances from a reference sphere.

IV. RESULTS

To test our model, we compare it with experimental results obtained previously.[27,12] The comparison is made for glass beads in water or oil and kaolinite clay in water. The glass beads are spherical in shape and have a diameter of 1 μm, while the kaolinite particles are plate shaped with a diameter also of ~ 1 μm. In the reported experiments the attenuation coefficient α and the velocity v were measured separately. To make a direct comparison with the model presented here, we constructed $Q^{-1} = \alpha v / 2\pi f$, where f is the transducer frequency. At each concentration, the experimental data are compared with the attenuation predicted by Eq. (14). It should be remarked that our model represents only the attenuation due to hydrodynamic interactions, and that a comparison with the experimental data yields information on the relative importance of this effect with other attenuation mechanisms.

The comparison between experimental results and our modeling [Eq. (8)] for the kaolinite–water suspension, is presented in Fig. 3 for three different frequencies (3, 5, and 7 MHz). We observe that the theoretical curves (solid and dashed lines) follow the general trend of the experimental data, have the correct frequency dependence, and show maxima at about 36%. The maxima in the experimental data are at a concentration near 41%. At the concentration where the maxima occur, both theory and experiment show attenuation increasing with frequency. The model predicts a higher

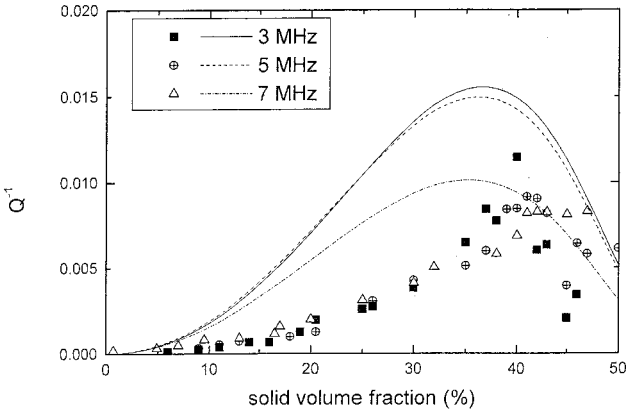

FIG. 3. Comparison between theory [Eq. (8)] and experiment for a suspension made of water and kaolinite plates as a function of concentration for three different frequencies. The theoretical curves show the same qualitative behavior as the experiment.

attenuation than what is observed in the experiments since the model assumes parallel plates at all times. At high concentrations the energy needed to squirt fluid from a pair of particles separated by a distance h, is assumed here to be the same as a pair separated the same distance but a lower concentrations. The only influence of concentration in the modeling enters through the pair distribution function. Although not considered by the model increasing the concentration also changes the ''reservoir'' surrounding each particle pair and which can accommodate the ''squirting'' fluid.

Similarly, Fig. 4 shows the experimental and theoretical attenuation for the glass beads–water suspension as a function of filling fraction at two frequencies. In this case we compare the experimental data with the theory for spherical particles. Again there is good agreement with the experimental data up to a concentration of $\sim$50%, after which interparticle contacts may begin to take place and our model is no longer applicable. The maxima in the experimental data are at a concentration of $\sim$42% and the corresponding maxima in the theoretical curves occur at 36%. The value of the

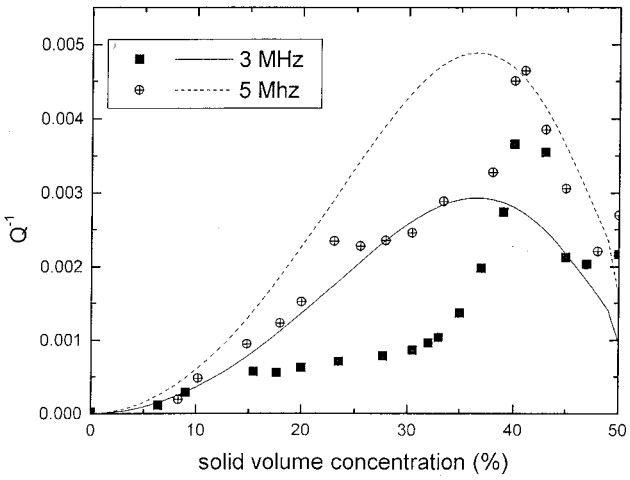

FIG. 4. Experimental and theoretical curves for a suspension made of glass beads in water. The agreement is indicative of the preponderance of the fluid-flow shearing attenuation mechanism. As in Fig. 3 a maximum in the attenuation is present in all cases.

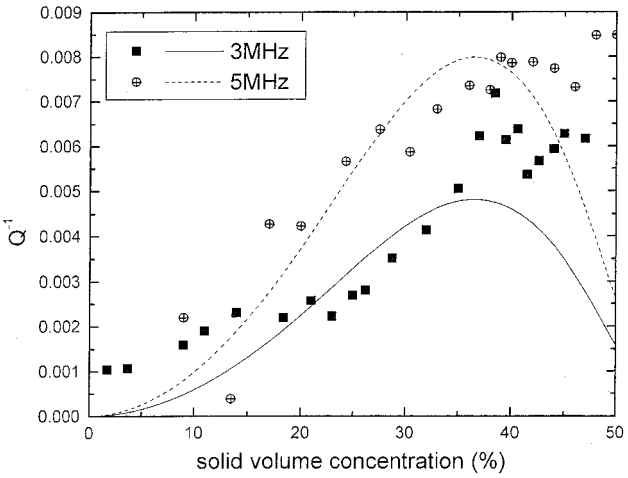

FIG. 5. Results for a suspension made of glass beads and LPS-1, light oil. The theoretical curves are multiplied by a factor of 10. The maxima of both frequencies is present, however the difference in the attenuation between the model and the experimental data shows other attenuation mechanisms such as those due to a viscoelastic behavior of the system during the acoustic loading.

attenuation we obtain is correct within an order of magnitude of that observed.

Finally we consider a suspension made of light-oil and glass beads. The oil (LPS-1) has a viscosity of .021 poise and a relative density of 0.8. The results are presented in Fig. 5. In this case the position of the maxima are closer to ~36%, and the overall behavior of the experimental and theoretical curves is similar. At low concentrations the experimental values are higher than those predicted by our model. The difference is that the intrinsic acoustic attenuation of the fluid is much larger for oil than for water. Other mechanisms (e.g., scattering, intrinsic fluid absorption) can become significant as conditions change (frequency, particle sizes, fluid viscosity), since the hydrodynamic mechanism is linear, then contributions from such other linear processes may be combined to evaluate the total attenuation of the system.

As described here, the interparticle flow mechanism operates only between noncontacting particles. Neglecting fluid shearing around contacting particles is justified by the greater oscillation of the unconstrained noncontacting particles. As the concentration becomes large, however, most particle pairs will be in contact and the contributions from them (currently set to zero) should be accounted for using an elastic deforming particle model. Future work will combine such a model with the noncontacting model developed here to predict the attenuation at all concentrations from suspensions to sediments.

The use of the pair-distribution function avoids reliance on a mean separation. This is particularly advantageous since the attenuation per pair becomes quit large as the separation becomes small (but not zero). Torquato's distributions were obtained from numerical random-packing experiments. This is adequate for low-to-intermediate concentration suspensions, but may not be appropriate to describe the geometry of precipitated sediments. Extension of the suspension model described here will require a particle distribution function appropriate for sediments.

V. CONCLUSIONS

In this paper we calculated the role that hydrodynamic interactions play in the acoustic attenuation of suspensions. The interaction is mediated by the shearing fluid flow between noncontacting particles during the passage of an acoustic wave. To take into account the many-body interactions that take place during loading, we introduced the nearest-neighbor distribution function to calculate the average attenuation. The attenuation was calculated for two different particle shapes: plates and spheres. The model we present considers the ideal situation of perfectly parallel and edge-aligned plates or spheres that oscillate only along the line joining their centers. Thus, our model predicts the maximum possible value for attenuation due to a shearing flow mechanism.

The theoretical results were compared with available experimental data. In all cases under consideration there is good agreement. In particular, the model predicts the maxima in attenuation observed in the experiments. These results show the relative importance of hydrodynamic interactions in the acoustic attenuation up to the random packing concentration, after which other mechanisms have to come into play (e.g., Hertzian contacts between the particles).

Given the good order of magnitude agreement between theory and experiment, we can also conclude that the hydrodynamic interactions are short-ranged and nearest-neighbor statistics are sufficient to calculate the effect. Future work should include viscoelastic and orientational dependent interactions among the suspended particles, and should account for losses between contacting particles.

ACKNOWLEDGMENTS

This work was partially supported by Fondo R. J. Zevada and CONACyT J27710-T.

APPENDIX A

In this section we briefly describe the experimental setup for measuring the acoustic properties of the suspensions previously reported in Refs. 27 and 12.

The velocity and acoustic attenuation of longitudinal waves was measured using the pulse-echo technique. A quartz transducer of a given central frequency was excited using a Matec BR-815 repetion, period and pulse width generator. After propagating through the suspension the signal was received by a second frequency-matched transducer and fed into the Matec MBS-8000 pulse-echo phase detection system. The frequencies used in experiment were 3, 5, and 8 MHz. The sample was placed in a temperature controlled test cell. The transducers are mounted on rods and are immerse in the sample, and the separation between them was varied using a precision micrometer, allowing for relative acoustic measurements. The resulting data points are the average of several runs at different transducer separations. The liquid matrix of the suspensions was doubly distilled water orlow viscosity lubricant oil (LPS-1). The viscosity of the oil (.021 poise at 25 °C) was measured using a Brookfield LVTD viscometer. The solids used in the measurements were kaolinite and glass beads. Kaolinite is a layered alumino-silicate clay

that forms hexagonal plate-shaped particles. The average diameter is $\sim 1\ \mu$m as determined by scanning electron microscope pictures. The glass beads (SiO_2) were supplied by Alfa Aesar Co. and their mean diameter was also $\sim 1\ \mu$m. Calibration runs for acoustic velocity and absorption were made using doubly distilled water at different temperatures. The errors involved in the measurements are of the order of 0.7% for velocity and about 6% for attenuation. All the measurements were corrected for diffraction effects.[34]

[1] D. Eisma, *Suspended Matter in the Aquatic Environment* (Springer, Berlin, 1993).
[2] U. Forstner and G. T. W. Wittmann, *Metal Pollution in the Aquatic Environment* (Springer, Berlin, 1979).
[3] T. C. Loder and P. S. Liss, ''Control by organic coatings of the surface charge of estuarine suspended particles,'' Limnol. Oceanogr. **30**, 418–421 (1985).
[4] D. Lal, ''The oceanic microcosm of particles,'' Science **198**, 997–1009 (1977).
[5] J. M. Martin, M. Meybeck, and M. Heuzel, ''A study of the dynamics of suspended matter by means of natural radiactive tracers, an application to the Gironde estuary,'' Sedimentology **14**, 27–37 (1970).
[6] J. K. B. Bishop and J. M. Edmond, ''A new, large volume *in situ* filtration system for sampling oceanic particulate matter,'' J. Mar. Res. **34**, 181–198 (1976).
[7] R. W. Sternberg, ''Instrumentation for estuarine research,'' J. Geophys. Res., [Atmos.] **94**, 14.289–14.301 (1989).
[8] A. E. Hay and D. G. Mercer, ''On the theory of sound scattering and viscous absorption in aqueous suspensions at medium and short wavelengths,'' J. Acoust. Soc. Am. **78**, 1761–1771 (1985).
[9] A. S. Schaafsma and A. E. Hay, ''Attenuation in suspensions of irregularly shaped sediment particles: A two-parameter equivalent spherical scatterer model,'' J. Acoust. Soc. Am. **102**, 1485–1502 (1997).
[10] M. C. Davis, ''Attenuation of sound in highly concentrated suspensions and emulsions,'' J. Acoust. Soc. Am. **65**, 387–390 (1979).
[11] A. E. Hay, ''On the remote acoustic detection of suspended sediment at long wavelengths,'' J. Geophys. Res., [Atmos.] **88**, 7525–7542 (1983).
[12] D. H. Green and R. Esquivel-Sirvent, ''Acoustic behavior at the fluid-solid transition of kaolinite suspensions,'' Geophysics **64**, 88–92 (1999).
[13] A. B. Wood, *A Textbook of Sound* (Bell, Chicago, 1930).
[14] Z. Wang and A. Nur, ''Elastic wave velocities in porous media: A theoretical recipe,'' in Seismic and Acoustic Velocities in Reservoir Rocks Vol. 2 Theoretical and Model Studies, edited by Z. Wang and A. Nur, Society of Exploration Geophysics (Tulsa, 1992).
[15] R. J. Urick, ''The absorption of sound in suspensions of irregular particles,'' J. Acoust. Soc. Am. **20**, 283–289 (1948).
[16] C. McCann, ''Compressional wave attenuation in concentrated clay suspensions,'' Acustica **22**, 352–356 (1969).
[17] M. A. Biot, ''Theory of propagation of elastic waves in a fluid-saturated porous solid. I. Low-frequency range,'' J. Acoust. Soc. Am. **28**, 168–178 (1956).
[18] M. A. Biot, ''Theory of propagation of elastic waves in a fluid-saturated porous solid. II. Higher-frequency range,'' J. Acoust. Soc. Am. **28**, 179–191 (1956).
[19] J. M. Hovem, ''Viscous attenuation of sound in suspensions and high-porosity marine sediments,'' J. Acoust. Soc. Am. **67**, 1559–1563 (1980).
[20] P. R. Ogushwitz, ''Applicability of the Biot theory. II. Suspensions,'' J. Acoust. Soc. Am. **77**, 441–452 (1985).
[21] J. G. Berryman, ''Long wavelength propagation in composite elastic media. I. Spherical inclusions,'' J. Acoust. Soc. Am. **68**, 1809–1819 (1980).
[22] J. G. Berryman, ''Long wavelength propagation in composite elastic media. II. Ellipsoidal inclusions,'' J. Acoust. Soc. Am. **68**, 1820–1831 (1980).
[23] L. D. Hampton, ''Acoustic properties of sediments,'' J. Acoust. Soc. Am. **24**, 882–890 (1967).
[24] J. E. Blue and E. G. McLeroy, ''Attenuation of sound in suspensions and gels,'' J. Acoust. Soc. Am. **44**, 1145–1148 (1968).
[25] D. Marion and A. Nur, ''Percolation of electrical and elastic properties of granular materials at the transition from a suspension to a loose packing,'' Physica A **157**, 575–579 (1989).
[26] M. S. Greenwood, J. L. Mai, and M. S. Good, ''Attenuation measurements of ultrasound in a kaolin-water slurry: A linear dependence upon frequency,'' J. Acoust. Soc. Am. **94**, 908–916 (1993).
[27] R. Esquivel-Sirvent, D. H. Green, and S. S. Yun, ''Critical mechanical behavior in the fluid/solid transition of suspensions,'' Appl. Phys. Lett. **67**, 3087–3089 (1995).
[28] W. F. Murphy, K. W. Winkler, and R. L. Kleinberg, ''Acoustic relaxation in sedimentary rocks: Dependence on grain contacts and fluid saturation,'' Geophysics **51**, 757–766 (1986).
[29] S. Torquato, ''Nearest-neighbor distribution functions and mean separation for impenetrable particles in one to three dimensions,'' Phys. Rev. A **46**, R2988–R2991 (1992).
[30] S. Torquato, ''Nearest-neighbor statistics for packings of hard spheres and disks,'' Phys. Rev. E **51**, 3170–3182 (1995).
[31] S. Torquato, ''Mean nearest-neighbor-distance in random packings of hard *D*-dimensional spheres,'' Phys. Rev. Lett. **74**, 2156–2159 (1995).
[32] S. Torquato and B. S. Lee, ''Computer simulations of nearest neighbor distribution functions and related quantities for hard-sphere systems,'' Physica A **167**, 361–368 (1990).
[33] J. R. Christman, *Fundamentals of Solid State Physics* (Wiley, New York, 1988).
[34] G. C. Benson and O. Kiyohara, ''Table of Integral Functions Describing Diffraction Effects in Ultrasonic Field of a Circular Piston Source,'' Depository of Unpublished Data, National Research Council Canada (Depository No. 559).

Acoustic propagation through anisotropic internal wave fields: Transmission loss, cross-range coherence, and horizontal refraction

Roger Oba and Steven Finette
Acoustics Division, Naval Research Lab, Washington, D.C. 20375

(Received 12 March 2001; revised 20 August 2001; accepted 7 November 2001)

Results of a computer simulation study are presented for acoustic propagation in a shallow water, anisotropic ocean environment. The water column is characterized by random volume fluctuations in the sound speed field that are induced by internal gravity waves, and this variability is superimposed on a dominant summer thermocline. Both the internal wave field and resulting sound speed perturbations are represented in three-dimensional (3D) space and evolve in time. The isopycnal displacements consist of two components: a spatially diffuse, horizontally isotropic component and a spatially localized contribution from an undular bore (i.e., a solitary wave packet or solibore) that exhibits horizontal (azimuthal) anisotropy. An acoustic field is propagated through this waveguide using a 3D parabolic equation code based on differential operators representing wide-angle coverage in elevation and narrow-angle coverage in azimuth. Transmission loss is evaluated both for fixed time snapshots of the environment and as a function of time over an ordered set of snapshots which represent the time-evolving sound speed distribution. Horizontal acoustic coherence, also known as transverse or cross-range coherence, is estimated for horizontally separated points in the direction normal to the source–receiver orientation. Both transmission loss and spatial coherence are computed at acoustic frequencies 200 and 400 Hz for ranges extending to 10 km, a cross-range of 1 km, and a water depth of 68 m. Azimuthal filtering of the propagated field occurs for this environment, with the strongest variations appearing when propagation is parallel to the solitary wave depressions of the thermocline. A large anisotropic degradation in horizontal coherence occurs under the same conditions. Horizontal refraction of the acoustic wave front is responsible for the degradation, as demonstrated by an energy gradient analysis of in-plane and out-of-plane energy transfer. The solitary wave packet is interpreted as a nonstationary oceanographic waveguide within the water column, preferentially funneling acoustic energy between the thermocline depressions.
[DOI: 10.1121/1.1434943]

PACS numbers: 43.30.Ft, 43.30.Re [DLB]

I. INTRODUCTION

While the sound speed fluctuations in shallow water waveguides are typically less than one percent of the mean speed, their influence on the amplitude and phase of an acoustic field propagating through the region is significant over relatively short ranges.[1–10] When an acoustic wave propagates in such an environment, the fluctuations induce space-dependent phase shifts in the acoustic field that can accumulate over range and lead to both amplitude fluctuations and a loss of spatial coherence. Our interest in this behavior stems from two points related to sonar performance. One is that signal detection is a function of the signal-to-noise ratio and is affected by transmission loss variability caused by random sound speed perturbations. The other is related to the fact that phase decorrelation across a horizontal aperture is responsible for a decrease in coherence length. Phase decorrelation of the pressure field, induced by oceanographic variability, represents a physical process leading to degraded performance for phase sensitive array processing schemes such as classical beamforming and matched field processing.

Computer simulation offers a practical method for systematic assessment of transmission loss and coherence degradation in complex ocean environments. This approach is applied here, where the transmission loss and horizontal spatial coherence are estimated for frequencies of 200 and 400 Hz as a function of range, cross-range, depth, and azimuth in a shallow water, continental shelf environment under summer conditions. The azimuthal dependence is associated with horizontal anisotropy of the ocean environment and is discussed below. Sound speed fluctuations considered in this paper are induced by an internal gravity wave field that perturbs the thermocline, leading to a space–time varying sound speed distribution throughout the waveguide. Some recent theoretical efforts have considered the effect of internal wave induced phase decorrelation on horizontal arrays in both deep and shallow water environments under a variety of modeling assumptions.[11–13] Our analysis differs from those of previous studies in that we employ a data-constrained internal wave model that includes a horizontally anisotropic component, and apply 3D acoustic modeling techniques to estimate transmission loss and spatial coherence in this environment. This methodology allows one to study more realistic oceanographic environments without the rather restric-

tive set of assumptions necessary in the development of analytical models.

Spatial coherence in continental shelf environments is affected by the presence of intermittent oceanographic features that exhibit horizontal anisotropy. Such features arise naturally from tidal forcing in regions with strong bathymetric gradients. For example, an internal tide can be generated from tidal forcing of stratified water through a shelf-break environment. As the tide propagates from the deep ocean onto the shallower water of the continental shelf, the phase speed decreases and the tide amplitude increases. The resulting interplay between nonlinearity and dispersion (from the fluid dynamic equations of motion) often causes the leading edge of the internal tide to become unstable. Energy is then transferred from low to high spatial frequencies through the emergence of an undular bore or solitary wave packet having a length of several kilometers. These packets are common in such environments.[14] They travel at speeds of roughly 0.5–1.0 m per second, exhibiting both azimuthal anisotropy and temporal nonstationarity. In contrast, a linear internal wave field is also present; this spatially diffuse field is described here by a stationary, isotropic component. The presence of an anisotropic component indicates that 3D acoustic modeling, rather than a set of $N\times 2$D calculations, may be needed to properly account for cross-range variation in the acoustic field. An additional complication is that the internal wave field must be described in four dimensions $(\mathbf{x},t)=(x,y,z,t)$ in order to account for the underlying non-stationary sound speed dynamics and its resulting influence on acoustic propagation.

This paper presents evidence that acoustic field structure can be significantly affected in an environment supporting oceanographic features that break azimuthal symmetry. Such structure might not be predicted from $N\times 2$D acoustic field calculations since those computations ignore horizontal refraction and may produce misleading transmission loss and horizontal coherence estimates for these environments. Horizontal refraction is associated with an azimuthal transfer of energy and is usually ignored in underwater acoustics computations. While it can be linked, for example, with strong bathymetric variation or mesoscale eddies, a major result of this study is that solitary wave packets can be the source of significant acoustic effects attributable to horizontal refraction in a typical continental shelf environment. A note on the terminology is appropriate here. Generally speaking, both refraction and diffraction can contribute to the azimuthal redirection of acoustic energy caused by the acoustic field interaction with the internal wave field. For the environments considered here, our results indicate that significant energy focusing/defocusing effects and coherence degradation are dominated by horizontal refraction rather than diffraction. For this reason we refer to azimuthal energy transfer in terms of horizontal refraction.

In Sec. II we briefly review the internal wave model used in our acoustic calculations and describe the 3D acoustic simulation approach. Section III gives the results of numerical experiments that estimate transmission loss and cross-range coherence under several conditions, as well as results of an energy gradient analysis that demonstrates the presence of horizontal refraction. The summary and conclusions are presented in Sec. IV.

II. SIMULATION APPROACH

An overview of the numerical methods used to compute the acoustic field results is presented in this section. We first briefly consider the oceanographic model describing the sound speed distribution induced by internal gravity waves; details of this approach are given in Ref. 2. This summary is followed by a discussion of the acoustic propagation model and its implementation.

A. Space–time sound speed distribution

The isopycnal displacements $\eta(x,y,z,t)$ caused by internal waves are assumed to be a sum of two contributions. One of these terms, $\eta_D(x,y,z,t)$, is represented by a superposition of plane waves propagating in different horizontal (x, y) directions. Energy is distributed among the plane wave amplitudes by sampling an isotropic internal wave energy spectral density $F(k_x,k_y,j)$, where (k_x,k_y) are the magnitudes of the spatial wave number components of a horizontal wave vector $\mathbf{k}_h$ and j is an internal wave mode number. A small amplitude assumption is implicitly assumed here, reflecting the underlying linear internal wave dynamics associated with this contribution. Knowledge of the buoyancy frequency allows the depth dependence (z) of the displacement to be computed by solving a linear eigenvalue problem for the eigenmodes $W(k_h,j,z)$, where $k_h=|\mathbf{k}_h|$. A dispersion relation $\omega(k_h,j)$ relates the space and time varying components of the motion and the resulting expression for η_D is given by

$$\eta_D(x,y,z,t)=\sum_j \left[\int_{k_x}\int_{k_y} F(k_x,k_y,j)W(k_h,j,z) \times e^{i[k_x x+k_y y-\omega(k_h,j)t]}\,dk_x\,dk_y \right]. \tag{1}$$

The linear superposition given in Eq. (1) is distributed throughout the environment and is sometimes referred to as the diffuse background field. This component supports sound speed perturbations within a wave number range $\{0.0014, 0.122\}$ m^{-1} and maximum (mode one) phase speeds of approximately 0.5 m/s.

The second term contributing to the isopycnal displacement describes an undular bore or solitary wave packet propagating in the x-direction, and it is associated with ''large'' amplitude, nonlinear fluid motion. The general form of this term is written as

$$\eta_S(x,z,t)=\sum_j \eta_j W(k_h,j,z)A_j(x,t), \tag{2}$$

where η_j represents the amplitude of the solitary wave displacement for mode j. The space–time evolution of the packet, $A_j(x,t)$, is determined by a solution of a Korteweg–deVries (KdV) equation in terms of Jacobi elliptic functions,[2,15] multiplied by a relaxation term that smoothly returns the depressed thermocline back to its equilibrium position after the packet has passed through the region. It is

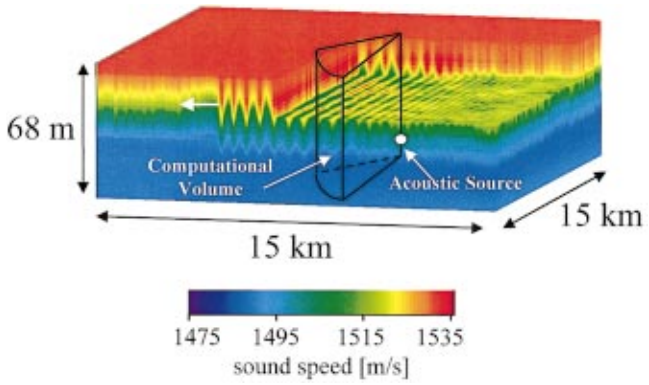

FIG. 1. Environmental snapshot of the total sound speed field, with a propagation wedge superimposed.

assumed that the packet has a planar wave front and is traveling in the x direction. This solution represents first-order nonlinearity (via the KdV equation) in the form of a spatially localized, large amplitude waveform. The nonlinearity and dispersion parameters of the KdV equation determine the packet speed and spreading behavior; they are computed from depth integrals over the eigenmodes. These parameters, as well as other internal wave quantities such as the energy spectral density, dispersion relation, mode structure, phase speed, etc. have been estimated from a continental shelf data set obtained during the SWARM experiment.[2,16] On the continental shelf, the first internal wave mode tends to dominate the field so that the sums over modes in Eqs. (1) and (2) may be neglected for the environment considered here with only the $j=1$ term retained.

The total isopycnal displacement, $\eta_D+\eta_S$, is mapped into the sound speed perturbation $\delta c(x,y,z,t)$ at each depth by integrating, between z and $z+\eta$, a function of buoyancy frequency, mean sound speed and a ratio of temperature and salinity depth gradients.[2] The resulting perturbation is then added to the mean sound speed profile $\overline{c}(x,z)$ describing the quiescent sound speed structure. Note that the mean profile is not estimated from data for the cross-range (y) direction, but is assumed to be independent of cross-range for this study. An example of the total sound speed field $c(x,y,z,t)=\overline{c}(x,z)+\delta c(x,y,z,t)$ is illustrated at a fixed instant of time in Fig. 1. The summer thermocline structure is evident in the left-hand side of the sound speed volume; the ''fuzzy'' stratification is due to the spatially diffuse isopycnal component described above. The undular bore is shown as a set of wavelike depressions of the thermocline and the wave packet, propagating to the left at a speed of about 0.7–0.8 m/s, has been extended in the y-direction (out of the page) to model a plane wave. A section of the volume has been cut out so that the interior region may be seen. The full widths of the larger depressions at half maximum are approximately 250–300 m with peak-to-peak distances of about 500 m. The relative sound speed perturbations are bounded as $[\delta c/\overline{c}]_{\max}\sim 10^{-2}$. Relaxation of the thermocline back to its unperturbed position after the packet has passed through the region is not evident in the picture, since this phase of the packet has just entered the displayed volume at the right side.

Superimposed on the sound speed volume in Fig. 1 is an acoustic point source placed on the z-axis of a cylindrical wedge volume which defines the computational domain for acoustic field simulation. The acoustic field is propagated in a wedge oriented at some angle with respect to the wave number vector of the solitary wave packet. Details of the acoustic propagation model are given in the next section.

Finally, the bottom parameters are constant in range and selected from a somewhat hard, sandy bottom in the 70 m bathymetry of the SWARM propagation path. For this range independent bathymetry, a sound speed of 1700 m/s is chosen for the water/sediment interface and linearly increased to 1750 at 100 m depth (38 m into sediment). The bottom sound speed structure is not illustrated in this figure. Sediment density is set to be twice that of the water density. An artificial absorbing boundary is used at the bottom of the 38 m sediment layer.

B. Three-dimensional acoustic simulation model

The acoustic propagation model is based on the 3D parabolic approximation to the Helmholtz equation implemented in the computer code FOR3D.[17] This code implements a finite difference solution scheme, using discretized differential operators to represent wide-angle propagation in elevation and narrow-angle azimuthal coupling. The parabolic pseudo-differential equation is specified in cylindrical coordinates by

$$\frac{\partial u}{\partial r}=-(ik_0+ik_0\sqrt{1+Z+Y})u, \tag{3}$$

where $u(r,\phi,z)$ is the forward propagating pressure field and k_0 represents a nominal acoustic wave number. The depth, range, and azimuthal variations are given by the operators $Z=(n^2-1)+k_0^{-2}\rho\,\partial/\partial z(\rho^{-1}\,\partial/\partial z)$ and $Y=(rk_0)^{-2}\,\partial^2/\partial^2\phi$ with density specified by $\rho=\rho(z)$ and index of refraction $n=n(r,\phi,z)=c_0/c(r,\phi,z)$. Equation (3) is implemented by a rational approximation in implicit form that is second order in z and second order in ϕ, which allows azimuthal interaction to be computed relatively quickly.

C. Modifications and implementation

Three coordinate systems are used in this study. One of these frames is the Cartesian system describing the internal wave field discussed in the previous section. The origin is located at the upper left-hand corner of the sound speed volume shown in Fig. 1 and illustrated schematically in Fig. 2. The undular bore propagates from large x toward $x=0$ in both figures. It is depicted in Fig. 2 by parallel dotted lines on the upper surface which represent the plane wave crests of the bore, with sub-surface depressions illustrated as oscillating curves. The second frame of reference is cylindrical and used for acoustic calculations. Consider a cylindrical coordinate system (r,ϕ,z) whose z-axis is located at $(x_0,y_0,z=0)$ with respect to the origin of the Cartesian frame. An acoustic point source is positioned on this z-axis at $(r=0,\phi=0,z=z_0)$. The depth variable is identical in both systems and a coordinate mapping between the two frames is defined by $(x,y)=(r\cos\phi+x_0,r\sin\phi+y_0)$. In order to explore the path dependence of acoustic propagation relative to the anisotropic component of the internal wave field, ϕ_0 will be

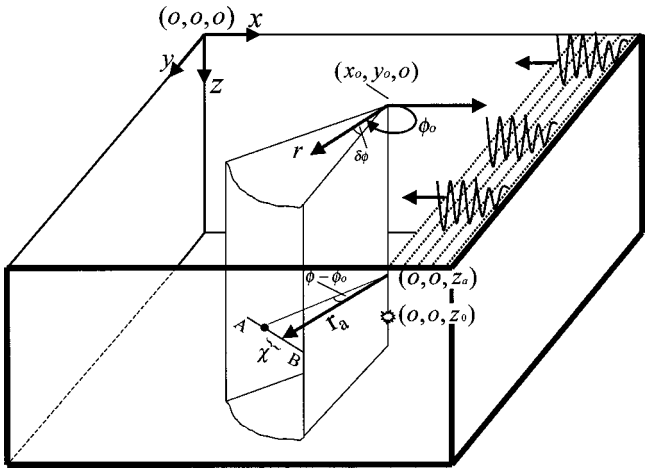

FIG. 2. Schematic diagram of the environment, illustrating the coordinate systems used in the simulations.

used to denote a central reference angle for propagation. Note that $\phi_0 = 0°$ lies in the direction parallel to the x-axis and that this direction is anti-parallel to the propagation vector of the internal wave packet. The acoustic field is computed throughout the water column and sediment for a set of range values such that $r_{\min} \leqslant r \leqslant r_{\max}$ and within a cylindrical wedge defined by $\phi_0 - \delta\phi < \phi < \phi_0 + \delta\phi$ with $\delta\phi = 15°$. Neumann-type boundary conditions are applied at the sidewalls; but sidewall boundary artifacts, such as spurious oscillatory field structure, are minimized by padding the 30° propagation wedge with an additional $\pm 5°$ at the boundaries located at $\phi_0 \pm \delta\phi$. Additionally, bottom attenuation is raised in the padding region near the sidewall. Wider azimuthal coverage is obtained by combining results from separate computations over adjacent wedges for different ''look'' directions ϕ_0, e.g., a 120° azimuthal sector is assembled from four 30° sectors, and the TL agreement at the sector boundaries is within about 0.1 dB.

Transmission loss (TL) as a function of (r, ϕ, z) is computed on this cylindrical grid with cylindrical spreading removed. A third reference system is used in the computation of horizontal coherence, estimated along straight lines (e.g., *AB* in Fig. 2) normal to the radial propagation vector $\mathbf{r}(r, \phi_0)$ at a given depth z_a. Horizontal line segment *AB* is positioned at a distance $|\mathbf{r}_a| = r_a$ from the z-axis and bisected by the radial vector; the position of a field point on *AB* is specified by $\chi = r_a \tan(\phi - \phi_0)$ for a line segment whose center is located at (r_a, ϕ_0, z_a). The position of the line segment for fixed ϕ_0 is then determined by a choice of (r_a, z_a). Correlating the complex pressure field $u(r, \phi, z)$ along the line *AB* with its value at $\chi = 0$ for each environmental snapshot, temporally averaging over snapshots and normalizing the result to unity yields the horizontal coherence function C_{ϕ_0} for a given central reference angle ϕ_0:

$$C_{\phi_0}(r_a, z_a, \chi) = \frac{|\langle u(r_a, z_a, 0) u^*(r_a, z_a, \chi)\rangle|}{\sqrt{\langle |u(r_a, z_a, 0)|^2\rangle \langle |u(r_a, z_a, \chi)|^2\rangle}}. \quad (4)$$

Cross-range coherence is a three-dimensional function parametrized by ϕ_0. The angle brackets represent the time average over environmental snapshots. The anisotropy of the sound speed field means that the propagation is a function of absolute location and orientation in the environment; the pressure field is neither translationally or rotationally invariant. Thus the usual definition of coherence in terms of relative spatial separations is inappropriate. Though not explicitly noted in Eq. (4), coherence is also a function of the duration over which environmental averaging is performed. This dependence on integration time is due to the nonstationary nature of the sound speed field induced by the solitary wave packet if it is present in the propagation wedge. Because of the implicit dependence of Eq. (4) on the time interval of the averaging window, we note that this expression does not represent a statistically consistent estimator of horizontal coherence for nonstationary environments. It would not be appropriate, for example, to use Eq. (4) to estimate phase-sensitive quantities related array performance (signal gain, etc.) under those conditions. However, by limiting our interest to relative changes in horizontal coherence, computed and compared by averaging over time windows of equal length, this expression can serve as a useful measure of such variations. In this regard, our use of the term ''coherence length'' in the following sections should be interpreted within this context. Results for both large and small durations are presented in the next section.

We have indicated that anisotropic internal wave fields may introduce significant azimuthal transfer of energy. Acoustic field calculations performed through a set of 2D range/depth planes (a.k.a. $N \times 2$D computations) for different azimuthal directions allow for variations in sound speed within range/depth planes but ignore horizontal refraction of energy between adjacent planes. The 3D calculations presented here include such azimuthal coupling, if present, and can be used to assess the relative importance of horizontal refraction in complex oceanographic environments. A rather simple means of estimating the amount of azimuthal energy transfer is outlined here and used to interpret transmission loss and coherence results. Define a depth-averaged energy density E:

$$E = E(r, \phi) \equiv c_0^{-2} H^{-1} \int_0^H |u|^2 \rho^{-1}\, dz, \quad (5)$$

where H is the total depth of water column and sediment, and c_0 is a nominal reference sound speed. The depth-averaged or mean TL, TL_z, is

$$TL_z = 10 \log E, \quad (6)$$

where E has units of energy per area. If we consider the azimuthally independent case of 2D parabolic propagation in r and z, the total energy at any fixed range can only have contributions from smaller ranges and the range gradient of this integral should obey

$$\partial E / \partial r \leqslant 0. \quad (7)$$

The proof of this inequality is given in the Appendix. Dividing Eq. (7) by E and multiplying by $10/\ln 10$, one obtains a logarithmic derivative γ, where

$$\gamma = \frac{\partial TL_z}{\partial r} = \frac{10}{\ln 10 E} \frac{\partial E}{\partial r} \leqslant 0. \quad (8)$$

This expression has units of dB/km, and can be interpreted as a measure of the range gradient of the depth-averaged transmission loss. It will be referred to as the TL gradient. Note that transmission loss must be averaged over both the water column and sediment to obtain results given by Eqs. (7)–(8). Also note that this inequality necessarily holds in the absence of azimuthal coupling and γ is of fixed sign only for propagation in two dimensions. When $\gamma<0$ there is a loss of energy along the radial direction. The additional degree of freedom present in 3D propagation implies that the inequality need not hold along a radial since horizontally refracted energy can enter from other range-depth planes. The 3D analysis in the Appendix shows that if γ is positive, there must be energy transferred into a range-depth plane from other azimuthal directions. The degree to which the TL gradient satisfies $\gamma>0$ is a rough estimate of the out-of (vertical)-plane refraction. When $\gamma>0$, the TL gradient measures energy transferred into the region. If $\gamma<0$, energy is lost from the region. In addition, when γ is sufficiently negative compared to the typical maximum attenuation loss, negative γ will indicate energy loss due to horizontal refraction.

Grid spacing is chosen to provide for the largest space sampling that permitted consistent numerical results, defined as a small change in pressure amplitude ($<0.1\%$) over a 2 km path for a 200 Hz signal, and selection of vertical, range, and azimuthal gridding are adjusted in that order. In high amplitude regions for ranges up to 10 km at 400 Hz, the amplitudes are within 1 dB and the phases are within 10 deg. Additionally, the azimuthal grid spacing is limited by the horizontal aperture spacing of 1.25 m at 10 km. The azimuthal spacing of $\Delta\phi\leqslant 1.25\times 10^{-4}$ radians is significantly smaller than required.

As indicated above, the sound speed data is provided on a rectangular grid within a volume 15 km square and 68 m deep. Interpolation of the environment is necessary since FOR3D required sound speed in cylindrical coordinates. This is accomplished via a preprocessing routine so that only relevant information from the environment is stored. Finally, since the pressure on linear segments at constant depth are desired, a final conversion of the acoustic field data back into Cartesian coordinates is performed. A routine for converting the acoustic results in cylindrical coordinates to the output Cartesian coordinates creates the proper format for plotting coherence as well as transmission loss and the TL gradient. While some computations were initially performed on a Cray, most numerical experiments are performed on a Compaq dual processor Alpha.

The internal wave spectrum is sampled using Monte Carlo techniques to provide a realization of the spatially diffuse contribution.[2] The total field evolved in either 1 or 3 min time steps over a 3–5 h period, yielding 100–180 environmental snapshots. These snapshots represent one time-evolved realization of the sound speed distribution. As a check on the robustness of the approach, another realization was considered but it did not qualitatively affect the results presented in the next section. The individual snapshots provide a means for trivial parallelization of the acoustic field calculations via simultaneous execution over snapshots. Practical processing constraints limit the range to 10 km for a maximum frequency of 400 Hz and preclude averaging over multiple realizations of the environment. Results for 200 and 400 Hz are considered below.

III. NUMERICAL RESULTS

This section presents some results of acoustic calculations for transmission loss, cross-range coherence, and azimuthal coupling of the field by horizontal refraction. Several environmental scenarios are considered in order to highlight certain acoustic effects. All scenarios contain the time-invariant profile $\overline{c}(x,z)$ as the baseline environment and are abbreviated in the text as follows: TI—time invariant field; DB—diffuse background internal wave field; DBSW—diffuse background field plus solitary wave packet; and SW—solitary wave packet. Unless otherwise noted, the source depth is fixed at $z_a=30$ m corresponding to a depth just below the thermocline. Transmission loss is considered first and illustrated in terms of range-azimuth and depth-azimuth slices of the TL volumes. Spatial coherence is then presented as a function of range, depth, and cross-range for several azimuthal directions using a long integration time for averaging over snapshots. Results for short-time windowed data are then considered in order to illustrate the effect of environmental nonstationarity on the coherence lengths. Some of these results can be explained in terms of horizontal refraction of energy between range-depth planes. Plots of the TL gradient are presented to facilitate interpretation of field calculations in terms of horizontal refraction of energy.

We note here that it is difficult to assess the relative importance of adiabaticity and mode coupling on the total field structure without performing a modal decomposition of the three-dimensional field. While such an analysis is beyond the scope of this paper, some guidance can be obtained from both recent work[1,2,4–6] and a TL gradient analysis in order to gain some insight into the spatial structure of the acoustic field. A few comments along these lines are made in this section.

A. Transmission loss

Transmission loss examples for several environments are presented below for frequencies of 200 and 400 Hz. For all cases, loss is displayed for a propagation wedge opening of 120° with ranges spanning 2.5–10.0 km from the source. Range/azimuth and depth/azimuth slices of the 3D transmission loss volumes are illustrated. Transmission loss is presented for a single environmental snapshot, while the time dependence of the loss is discussed latter in conjunction with nonstationary coherence results. Cylindrical spreading has been removed in all plots.

1. Case TI (time invariant)

This baseline case illustrates the underlying spatial structure of the transmission loss at 200 Hz in the absence of internal wave perturbations. The upper, pie shaped wedge in Fig. 3 represents transmission loss for a range/azimuth slice taken at depth 35 m while the lower surface corresponds to a depth/azimuth slice obtained at a range of 10 km from the source. Note that the loss is azimuthally symmetric about $\phi=0$ although the full symmetry in $\phi=\pm 90°$ is not shown

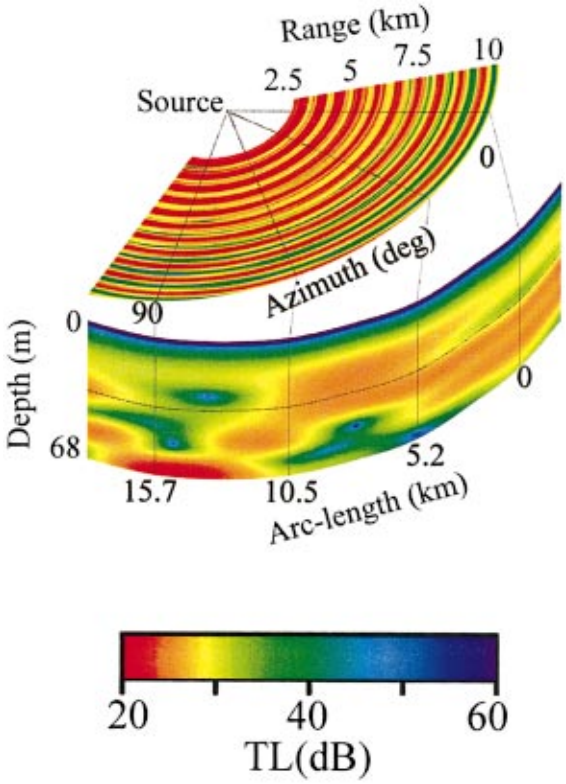

FIG. 3. Transmission loss at 200 Hz for the baseline case TI. A range/azimuth slice chosen at $z=35$ m and a depth/azimuth slice at $r=10$ km are shown. The propagation wedge aperture is 120°.

here. The range/azimuth slice shows a quasi-periodic loss structure as a function of range, with some azimuthal dependence due to the mild spatial variation of the time-invariant thermocline. The radial field oscillations are due to modal interference, with the beat pattern exhibiting weak azimuthal dependence caused by weak angular variations in the horizontal acoustic wave numbers. It should be noted that choosing a different depth for a range/azimuth slice would reflect a different modal phasing and result in a modification of the interference pattern. The modal structure at 10 km is illustrated in the depth/azimuth slice which indicates a uniform modal structure for $-15° \leqslant \phi \leqslant 15°$. Beyond this sector, the depth-dependent variations reflect a change in the azimuthal distribution of modal energy at this range.

2. Case DB (diffuse background)

Here we consider the case where spatially diffuse internal wave perturbations are present in the environment. An example of transmission loss at 200 Hz is shown in Fig. 4(a). The loss in the range/azimuth slice differs from the previous case in that a weak azimuthal modulation of the modal interference pattern is now present throughout the slice. This angular dependence varies over several degrees, and is observed as smaller scale striations in the peaks of the modal interference patterns. Some of this variation appears to be aligned in range along constant azimuth. The structure is more clearly illustrated by a depth-averaged transmission loss plot, as shown in Fig. 5(a) where TL_z is given in Eq. (6). Note that the range periodicity is partially smoothed out because the averaging is over depth-dependent interference patterns whose maxima and minima are not aligned throughout the water column. Additional computations indicate that for a given azimuth direction the loss tends to be consistently lower or higher than in case TI throughout the radial propagation path.

The radial nature of the pattern in Fig. 5(a) is related to the fact that the ratio of the acoustic wavelength λ to a characteristic spatial scale L of the internal wave field is much less than unity ($\lambda/L \ll 1$), corresponding to primarily forward (i.e., radial) propagation. It should be noted that both adiabatic propagation and mode coupling could play a role in determining the overall spatial dependence of the transmission loss. An interpretation of transmission loss in terms of adiabatic propagation or mode coupling depends, to some extent, on the particular criterion used to determine the dividing line between adiabatic invariance for two modes *i, j*, and coupling between those modes. Roughly speaking, the criteria depend on the depth-weighted overlap between the modes in question, the range gradient of the sound speed variation and a length scale determined by the acoustic modal interference length. Adiabatic propagation is more likely to dominate in situations where the sound speed gradient is weak over the modal interference length. The relatively weak range gradients associated with the background internal wave field tend to satisfy this requirement because the background spectrum emphasizes lower spatial frequencies. On the other hand, solitary wave energy is confined to higher spatial frequencies and dominates the background contribution at those frequencies. Therefore, acoustic propagation through solitary waves is more likely to cause mode coupling than the background internal wave field. Mode coupling has been demonstrated for two-dimensional propagation[1,2,5,6] normal to the wave crests, though the situation here is more complicated because the anisotropy of the wave packet is included in the computations. In this case, one might expect adiabaticity when propagation is nearly parallel to the wave crests of a solitary wave packet because of the weak sound speed gradients along those azimuthal directions, though mode coupling can occur at other propagation angles.

The TL gradient plot corresponding to Fig. 5(a) is given in Fig. 5(b). Note that γ is negative throughout the propagation region and that the modal interference pattern, associated with the bottom loss, is only weakly dependent on azimuth and range. This pattern indicates that phase and amplitude relationships among the modes show little variation, consistent with adiabatic propagation. The acoustic field propagates in range-depth planes, independent of azimuth, a result confirmed by comparing $N \times 2\mathrm{D}$ calculations of γ (not shown) with the result in Fig. 5(b).

3. Case SW (solitary wave)

This case describes transmission loss in an environment containing the solitary wave packet. Referring again to Fig. 2, the packet propagates with its wave crests (i.e., the horizontal location of maximal vertical displacement of the isopycnal or thermocline) aligned along the $\phi = 90°$ azimuth. Two examples using a frequency of 200 Hz are given in Figs. 4(b), (c) for environmental snapshots separated in time by 79

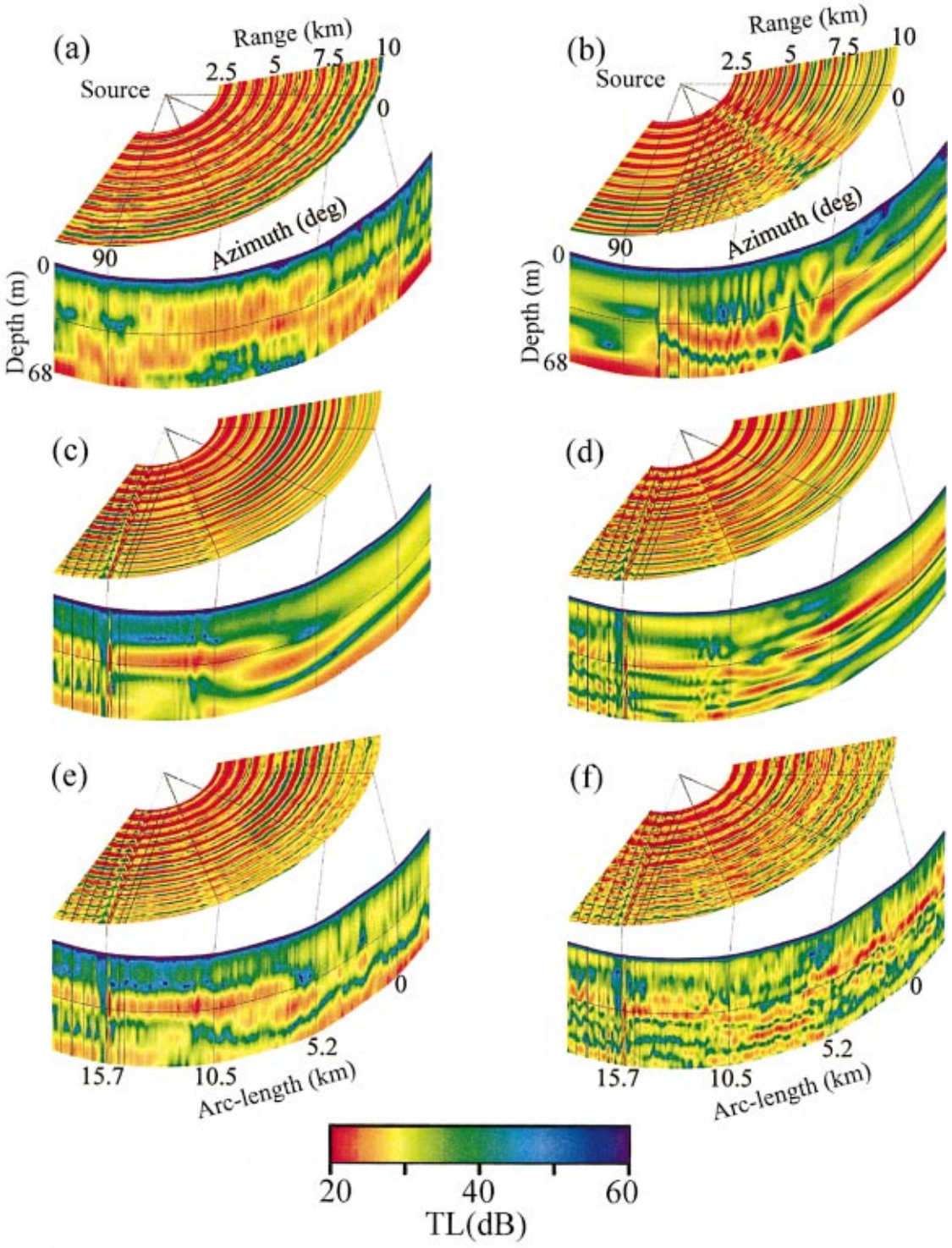

FIG. 4. Transmission loss plots: (a) 200 Hz for case DB, (b) 200 Hz for case SW at $t=-36$ min, (c) 200 Hz for case SW at $t=42$ min, (d) 400 Hz for case SW at $t=42$ min, (e) 200 Hz for case DBSW at $t=42$ min, (f) 400 Hz for case DBSW at $t=42$ min. Note that the parallel black lines between 2.5 and 10 Km denote positions of the major thermocline depressions.

min. For reference, a time origin $t=0$ is defined to be the time at which the first depression is centered along the $\phi=90°$ azimuth. The examples in Figs. 4(b), (c) then occur at $t=-36$ min and $t=42$ min, respectively. The light black parallel lines superimposed on the range/azimuth plots represent the locations of the larger depressions, and correspond to regions where the higher sound speed layers intrude into the lower sound speed layers.

The shape of the undular bore and its orientation relative to the radial direction of acoustic propagation are important factors in determining the transmission loss pattern. First consider propagation within $-15°<\phi<15°$ for the packet location corresponding to $t=-36$ min in Fig. 4(b). Compared to the same region shown in Fig. 3 for case TI, there is a significant change in both magnitude of the signal and phase of the modal interference pattern, with an overall in-

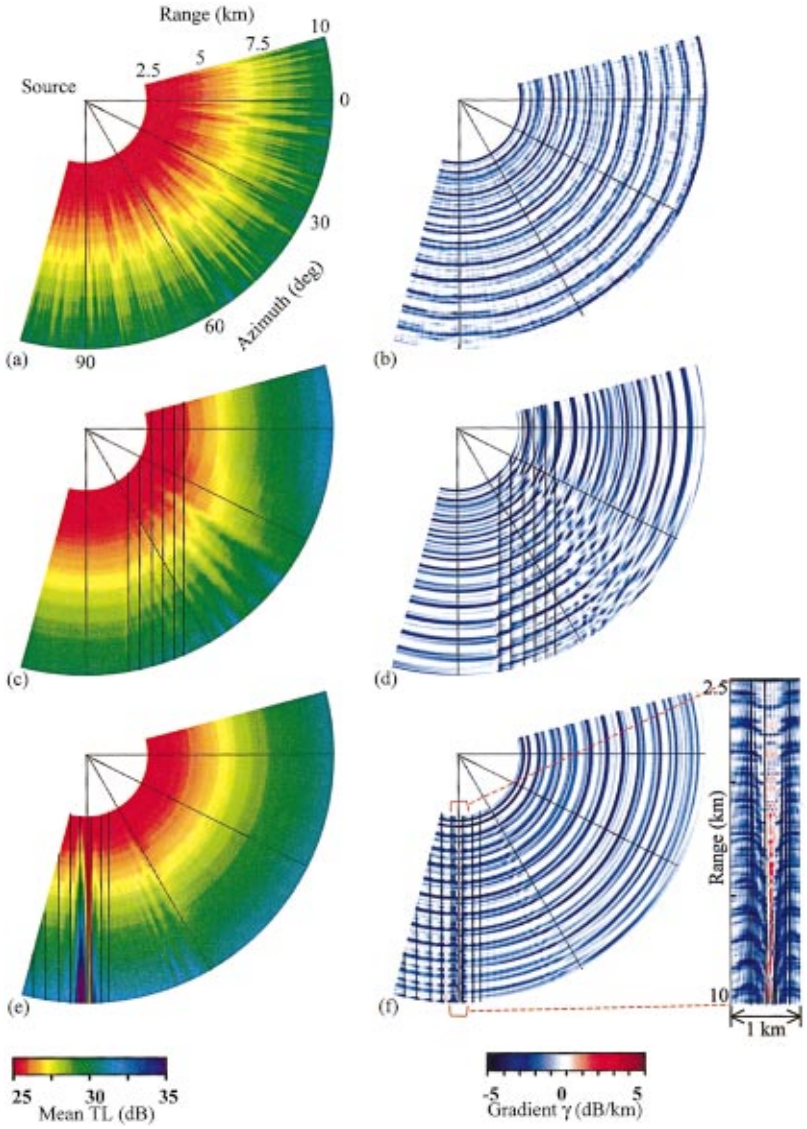

FIG. 5. Depth averaged transmission loss at 200 Hz for (a) case DB, (c) case SW at $t=-36$ min, (e) case SW at $t=42$ min. Corresponding transmission loss gradient plots are shown in (b), (d), and (f) with the indicated region of (f) magnified at the right.

crease in transmission loss in this environment. The enhanced loss and associated variation in the interference pattern is likely due to (in-plane) range-dependent acoustic mode coupling caused by the solitary wave packet.[1,2,5,6] The coupling is quite sensitive to the packet's shape and range from the acoustic source. Figures 5(c), (d) are depth averaged TL and γ plots for this case. The depth-averaged loss shows negligible azimuthal variation in this angular sector. Since $\gamma<0$ in that sector, this suggests that azimuthal coupling is minimal; this result was confirmed by comparison with $N\times 2$D computations.

For angles $15°\leqslant\phi\leqslant 70°$ there is an azimuthal dependence qualitatively similar to, but more structured than that shown in Figs. 4(a) and 5(a). Several two-dimensional modeling efforts that addressed acoustic-internal wave scattering in simpler environments[5,6,7,18] concluded that significant energy transfer occurred when the modal wavenumber difference k_p-k_q between two acoustic modes p,q was an integer multiple of a horizontal wave number associated with a strong spectral contribution $F(k_h=k_p-k_q)$ from the internal wave field. This resonance coupling condition is more complicated in our environment for several reasons. The packet is a spatially localized, finite bandwidth entity which evolves and undergoes dispersion so that the spectral shape and bandwidth are functions of the packet's absolute location relative to its source generating region. In addition, the acoustic propagation is azimuthally dependent and an effective wave number $k_h\cos\phi$ is required for evaluation of the modal resonance condition.[4,8] Since the acoustic field senses different projected wave number components as a function of azimuth, the resonance condition selectively increases or decreases the modal coupling coefficients in an azimuthally dependent manner. The angular variation in transmission loss shown in Fig. 4(b) is assumed to be caused by this resonance effect, although a modal decomposition of the field is needed to confirm this interpretation. A similar conclusion was recently inferred, however, from a modal analysis and $N\times 2$D calculations for a 2D model environment including a solitary wave packet.[4] The TL gradient plot in Fig. 5(d), corresponding to the SW case at $t=-36$ min, shows that in-plane propagation is dominant for $\phi\leqslant 70°$. For $70°\leqslant\phi\leqslant 80°$, $\gamma>0$ just to the left of the leading thermocline depression and indicates horizontal refraction of energy is occurring near the leading edge of the packet. The result also

implies that for $\phi \leqslant 70°$, $N \times 2\mathrm{D}$ calculations are sufficient to describe the propagation, a result consistent with a recent theoretical prediction obtained from a ray-mode based argument.[5] Similar comments apply to the SW case at $t = 42$ min, illustrated in Fig. 4(c) for transmission loss and in Figs. 5(e), (f) for TL_z and γ, respectively. The leading edge of the packet has now propagated approximately 3.4 km and several thermocline depressions have passed by the source location. Note that a strong enhanced transmission path has emerged at $\phi \approx 90°$. This path corresponds to propagation parallel to the wave crests, and the enhanced transmission is accompanied by a range-dependent increase in loss for adjacent propagation directions. For $\phi > 90°$ a depth-dependent, periodic oscillation in transmission loss is observed in Fig. 4(c). The distribution of energy associated with propagation parallel to the wave crests suggests acoustic ducting into the lower sound speed regions between the depressions. Energy is trapped between adjacent thermocline depressions because the slightly higher sound speed regions defining the depressions act as oceanographic waveguide boundaries within which there exists a slightly lower sound speed distribution. The TL gradient near $\phi \approx 90°$ in Fig. 5(f) and its accompanying magnified view show that $\gamma > 0$ between the neighboring thermocline depressions, consistent with the interpretation of energy being horizontally refracted into these regions. This interpretation is discussed in more detail in Sec. III C where the effect of time dependence is considered. For comparison, an example of transmission loss at 400 Hz is given in Fig. 4(d) and shows qualitatively similar results for selective transmission along the wave crests.

For the SW case at $t = 42$ min the $N \times 2\mathrm{D}$ case incorrectly implies that, along any radial, the depth summed energy will decrease by at least the cylindrical spreading rate. The calculations here show that the internal wave packets cause energy to be redirected from the radial direction, and may in fact be ducted into the lower sound speed regions between the depressions with the following two consequences: (1) The dominant propagation direction is then parallel to internal wave packet crests and troughs (2) Energy initially propagates radially outward from the origin in all azimuthal angles. As linearly aligned wave packet depressions cross azimuthal bearings, energy is redirected from these radials and is focused to propagate in the ducting region. Thus the energy level may actually increase in the duct.

4. Case DBSW (diffuse background plus solitary wave packet)

Simulation of transmission loss in this case included both internal wave components and results are shown in Figs. 4(e), (f) at $t = 42$ min for both 200 Hz and 400 Hz, respectively. Both examples reflect properties of the field illustrated for cases DB and SW. While there is azimuthal modulation of the loss due to the addition of the diffuse component to the internal wave field, it is important to note that the enhanced transmission path occurring in case SW near $\phi \approx 90°$ is still present. The robustness of this feature is evident from a comparison of the range/azimuth slices in Figs. 4(c), (d) and the pair in Figs. 4(e), (f). A closer examination of the region around $\phi \approx 90°$ (not illustrated) for cases SW and DBSW at 200 Hz shows that the transmission loss is 2–4 dB higher in case DBSW than in case SW. The spatially diffuse contribution apparently represents a small perturbation on loss in this region. At other azimuths, however, the effects of the packet are more difficult to distinguish from those caused by the diffuse internal wave field. At 400 Hz, the sensitivity of the acoustic field to the sound speed perturbations is greater than at 200 Hz. In particular, at 400 Hz, horizontal refraction from internal wave depressions can occur not only between adjacent internal wave troughs as shown for 200 Hz, but also occurs to a diminished degree in neighboring ducting regions. Thus, at 400 Hz, a shadow region at $\phi \approx 90°$ will have focusing regions on either side.

A case with a shallow source at a depth of 5 m (not shown here) exhibited a higher transmission loss gradient of approximately 4 dB/km away from the strongly ducted region. In the focusing region, the loss was about 5 dB higher than for the deep source case, but the focusing appeared sharper with respect to the higher loss regions. Since surface ship noise is commonly modeled by a source at 5 m depth, this means that shipping noise contributions could be smaller than otherwise expected in this environment, especially compared to deeper sources of interest.

B. Horizontal coherence

The transmission loss results discussed in the previous section indicate that anisotropic internal wave fields operate like spatial filters on the acoustic waves. Horizontal refraction of energy was seen to introduce ducted transmission between thermocline depressions for propagation near $\phi \approx 90°$. This latter effect is considered here in the context of cross-range coherence. Measurements of horizontal coherence in deep and shallow water have been summarized recently;[19] however, the simulation ranges and nonstationary environments considered here differ substantially from those in Ref. 19 so that a comparison will not be attempted.

For several azimuthal directions horizontal line segments of one kilometer length are specified, spanning the water column depth of 68 m. They are located at ranges of 2.5 km to 10 km from the acoustic source placed at a depth of 30 m. Considered first is a long time average using 100 snapshots, each separated by three minute increments for a total averaging time of 5 h. This integration time smooths out nonstationary effects associated with the time-evolving internal wave field. In the following sub-section, short-term averaging (one minute updates over 36 min sliding windows) is applied to high-light the effect of temporal variability. Note that if the sound speed field is time invariant, Eq. (4) implies $|C| = 1$. Horizontal coherence for the long time averages are presented below as coherence volumes that are functions of range, cross-range, and depth for high values $|C| \geqslant 0.8$. The central reference angles for propagation, ϕ_0, serve as parameters; they are shown in plan view as inserts in the figures with the shaded region covering the propagation domain. For short-term averaging (Sec. III C), snapshots of depth-averaged coherence, sound speed, and transmission loss are presented along with a TL gradient plot.

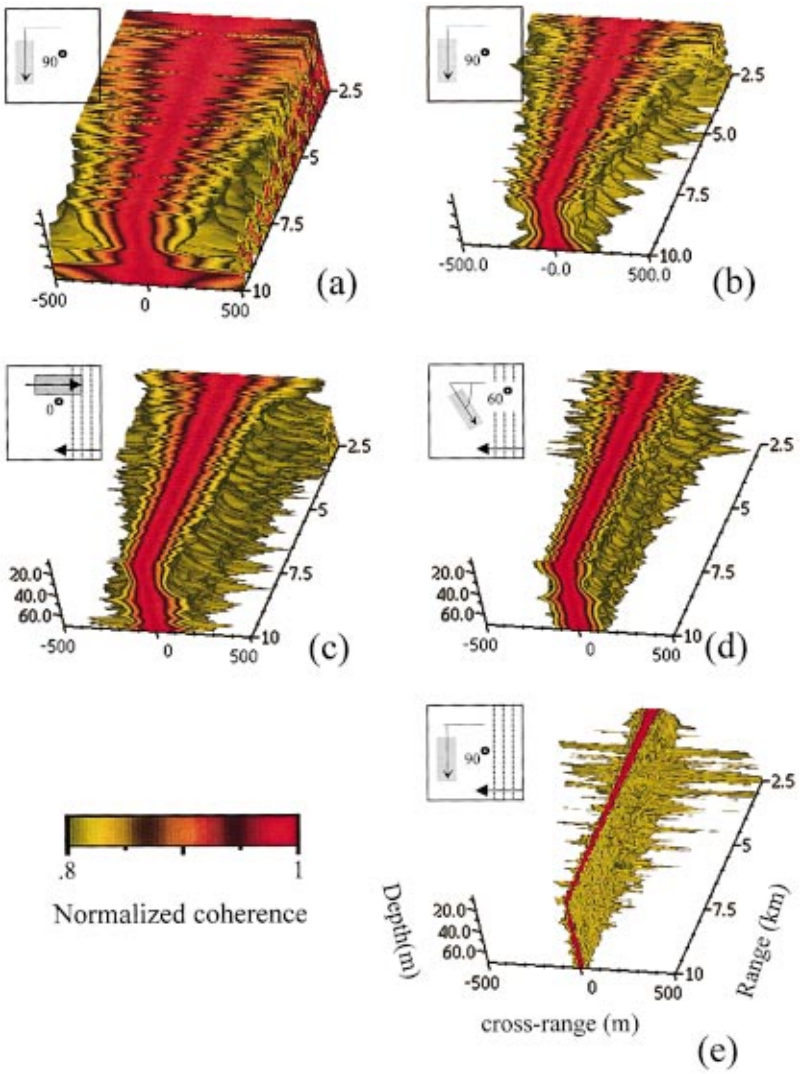

FIG. 6. Horizontal coherence volumes for long integration time (5 h): (a) at 200 Hz for case DB, (b) at 400 Hz for case DB, (c)–(e) at 400 Hz for case DBSW with central reference angles of 0°, 60°, 90°. The inserts are plane views with shaded areas denoting the propagation region; parallel dotted lines, if present, indicate direction of packet propagation.

1. Case DB

Long time averages for horizontal coherence estimated at 200 and 400 Hz are shown in Figs. 6(a), (b), respectively. The environment includes the spatially diffuse component so that the choice of central reference angle is arbitrary; for concreteness, the line segments for this case are chosen to be oriented normal to $\phi_0 = 90°$ although no wave packet is present here. Constructive and destructive phasor addition is reflected in the scalloped variation of the coherence in the range and cross-range directions. It is noted that the coherence remains quite high throughout most of the water column though a range-dependent falloff is visible in the upper to mid-water region in Fig. 6(a) and throughout depth in Fig. 6(b). Differences in the modal distribution of energy between the acoustic fields at 200 and 400 Hz are probably responsible for the depth dependent variation of the coherence and the overall cross-range decrease in coherence for the 400 Hz case relative to that at 200 Hz. While the depth variation indicates that cross-range coherence will be higher in the lower third of the water column at 200 Hz, this result is not a general feature shared by other environments. The presence of additional modes at 400 Hz tends to smooth out the depth variations. The larger coherence near the bottom can be attributed in part to the downward refracting profile inducing larger field amplitudes in regions less prone to the phase variations that are caused by the thermocline variability.

The range-dependent degradation occurs in the other cases as well, and represents a common characteristic of waves propagating in random media. Case DB represents one time evolving realization of a random medium, in that the initial spatial distribution of δc was chosen by Monte Carlo sampling of an internal wave spectrum. As a coherent wave front propagates away from its source region, the wave encounters local sound speed perturbations that cause phase retardation or advancement. The accumulation of these phase changes leads to phase degradation and a consequent loss of spatial coherence. At long ranges (beyond those considered here), the field becomes incoherent as memory of the original wave front is lost. For both frequencies, the coherence is only weakly affected by azimuthal variation and results for this reference angle are representative of those obtained for others. The absence of strong azimuthal variation is expected, since the spatially diffuse component of the internal wave field is a function of $|\mathbf{k}_h|$. The mild range/cross-range dependence of the sound speed profile also has negligible effect.

If we take the coherence length as the cross-range distance along the aperture (normalized by wavelength λ) over

which $|C| \geqslant 0.8$ then, at both frequencies, coherence lengths exceed 100λ and indicate that the spatially diffuse component has not introduced a significant phase degradation over this propagation range.

2. Cases SW and DBSW

Before the packet enters the propagation wedge, the sound speed field in the wedge for case SW corresponds to the one in case TI. After the packet enters the propagation region, a strong azimuthal dependence is observed for the cross-range coherence, particularly noticeable through a large drop in coherence length near $\phi_0 = 90°$. Rather than illustrate this situation (SW) separately from the two-component DBSW case, the results are discussed with respect to case DBSW only since the horizontal coherence estimates are quite similar in both and the latter environment illustrates the robustness of the coherence degradation. Examples are given for acoustic coherence at 400 Hz in Figs. 6(c)–(e) for central reference angles of $\phi_0 = 0°$, 60°, 90°, respectively. These results are computed from environmental snapshots for $t = -183$ to $t = 117$ min. While not shown here, the horizontal coherence volumes for central reference angles in the range $15° < \phi_0 < 80°$ are quite similar to that illustrated for $\phi_0 = 60°$.

At $\phi_0 = 0$ [Fig. 6(c)], cross-range coherence is comparable with that in case DB [Fig. 6(b)], though there is a larger transverse coherence length (≈160λ vs ≈110λ) near the bottom. The solitary wave packet tends to dominate the effects of environmental variability on cross-range coherence for most azimuthal angles ⩾15°. For $15° \leqslant \phi \leqslant 80°$, there is a noticeable drop in coherence length from ≈160λ to ≈60λ. For a central reference angle of $\phi_0 = 90°$, an even larger degradation occurs, with coherence lengths falling to <20λ throughout the propagation volume for ranges greater than a few kilometers. This sharp drop results from propagation along the crests and can be traced to a redistribution of energy across the line segments caused by horizontal refraction of energy from neighboring range-depth planes. Refraction is seen in the TL gradient plots shown in Figs. 5(d), (f) and more clearly illustrated in a magnified view of this region for shorter integration times, discussed below.

C. Time dependence of horizontal coherence

While useful in illustrating the general dependence of horizontal coherence on azimuth over fairly large geophysical timescales, the long integration time estimates given in Fig. 6 effectively smooth out nonstationary effects which occur over shorter timescales. These long term averages are formed over much longer periods than typical integration times for sonar array processing. This situation is partially rectified below, where a 36 min time window is used to compute the cross-range coherence and highlight nonstationary effects. For example, a solitary wave speed ~0.5 m/s would allow 2–3 depressions of a wave packet to pass by an aperature of length ~1080 m. This situation corresponds approximately to a 7 m/s towed aperture looking over ~2–3 min, during which time it transits 840–1260 m. Such a time period corresponds to a more reasonable array processing timescale.

The undular bore introduces a nonstationary component in both the transmission loss and cross-range coherence. This temporal variability is examined here for case DBSW with field computations made at 400 Hz. Attention is focused on a section of the propagation wedge with reference angle $\phi_0 = 90°$, corresponding to the region where horizontal refraction is strongest. Examples are presented for a rectangular patch 1 km in cross-range with range values between 2.5 and 10 km.

Results illustrating nonstationary effects are presented in Fig. 7. Recall that the time origin $t = 0$ min was defined to be the time that the first thermocline depression is centered along the $\phi = 90°$ azimuth. The depth-averaged sound speed environment is depicted in Fig. 7(a) at times $t = \{-12, -1, 14, 18, 27\}$ min representing environmental conditions when the packet is initially located exterior to this patch and periods when several packet depressions enter and propagate throughout the region. At $t = -12$ min only the spatially diffuse contribution is present, while at $t = -1$ min the leading thermocline depression has entered the area propagating from right to left. Subsequent snapshots show additional thermocline depressions moving across the rectangular region. Evaluating Eq. (6) for these environmental snapshots, the depth-averaged TL are given in Fig. 7(b). At time $t = -12$ min the combination of the (time-invariant) thermocline and sound speed perturbations induced by the diffuse internal wave component are responsible for a more or less uniform loss distribution in the transverse direction, with weak cross-range variability of 1–2 dB. However, when the depressions are within the propagation region, focusing and defocusing of the acoustic field are evident. Note that at $t = -1$ min, there is a significant energy concentration to the left of the packet's leading edge. The snapshot at $t = 14$ min shows another high energy event focusing between two internal wave packet depressions. Finally, at $t = 18$ min, a deep shadow zone appears and is centered on the second isopycnal depression. Energy is transferred from high sound speed regions to low sound speed regions for all times where the solitary wave packet is present. Azimuthal scattering away from the depressions results in enhanced loss of ~5 dB within those regions relative to the loss at $t = -12$ min, when the solitary wave packet is absent. Focusing leads to 8–10 dB lower mean loss relative to that occurring when the packet is not present.

The behavior discussed above is due to horizontal refraction of energy from neighboring areas, as seen in the corresponding γ plots of Fig. 7(c). At $t = -12$ min the out-of-plane refraction is negligible ($\gamma < 0.4$ dB/km), a result seen at all azimuths in Fig. 5(b) for 200 Hz. The result is nearly identical to that obtained through $N \times 2$D calculations (not illustrated). A significant feature is the banding structure of the TL gradient. The bands represent regions of higher loss; the range dependence of the loss is related to modal interference with the bands closely aligned to regions of high field amplitude in or near the sediment layer. The loss can be attributed to bottom penetration (see the Appendix). Larger

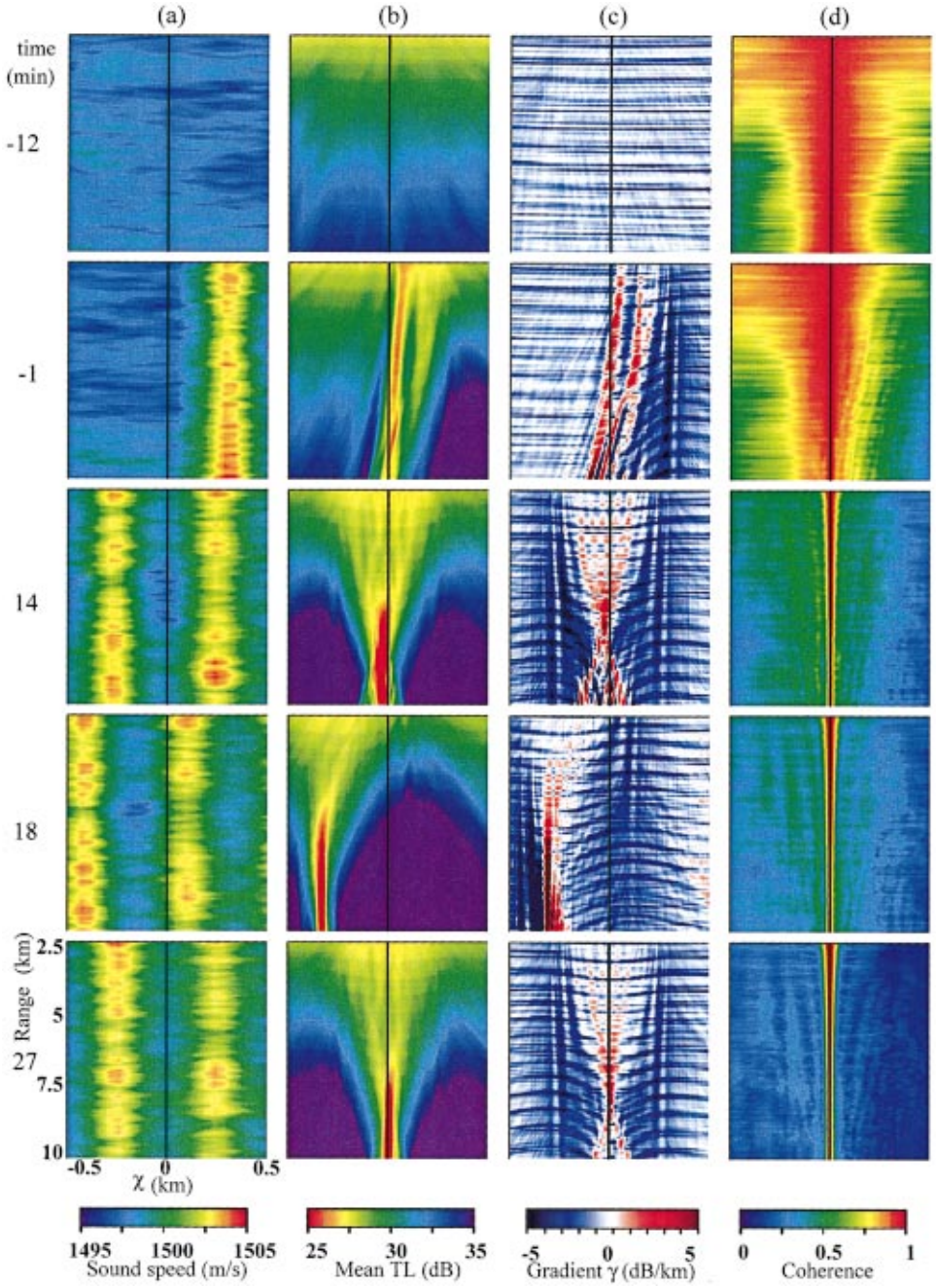

FIG. 7. Nonstationary behavior of depth averaged acoustic quantities presented over a 36 min time window (a) sound speed distribution, (b) corresponding transmission loss for the environments in (a), (c) corresponding transmission loss gradient for the environments in (a), (d) cross-range coherence computed for a 30 min moving average. The environments in (a) correspond to that in the last time snapshot included in the moving averages.

values of γ occur in Fig. 7(c) at all times when the packet is in the propagation domain and they mark locations where energy is azimuthally transferred to adjacent areas of relatively lower sound speed (positive gradient). The latter regions correspond to the areas between the thermocline depressions. A complex cross-range beat pattern is evident in the refracted component of the TL gradient, suggesting the presence of several azimuthally interacting modes. In effect, the oceanographic environment forms a set of parallel, rough boundary waveguides through which acoustic energy can be ducted. The roughness is due to the diffuse component which contributes some random variability in range and depth to the otherwise smooth isopycnal depressions.

Depth-averaged horizontal coherence for values of $|C|$ between $[0, 1]$ is illustrated in Fig. 7(d) and is computed over a ''sliding'' ensemble of 36 1 min time steps. The window includes the 35 min period occurring just prior to each of the environmental snapshots in Fig. 7(a), plus the contribution of the field computed from that particular snapshot. Therefore, the sound speed plot represents the most recent environmental snapshot included in the coherence estimate. Horizontal coherence is highest for the diffuse perturbation environment existing prior to the introduction of the packet and this observation is consistent with the long integration time predictions illustrated in Fig. 6. At $t=-1$ min, there is a significant asymmetric drop in coherence on the right side of the region since coherence is computed with respect to the region's center points (denoted by the black vertical line in the plots) and the refracted, (rapidly time-varying) energy is primarily found on the right half of the region. For later times, the degradation of coherence has continued across the area with the lowest cross-range coherence in the time window occur-

ring by $t=27$ min. A significant drop in coherence length from $\approx 80\lambda$ to $\approx 15\lambda$ occurs over a period as short as 10–15 mins.

IV. SUMMARY AND CONCLUSIONS

This paper describes results of 3D numerical experiments involving the propagation of acoustic wave fields through a dynamic, 3D oceanographic environment in a shallow water waveguide. The environment consists of sound speed perturbations superimposed on a dominant summer thermocline, the latter having mild range dependence. The perturbations include horizontally isotropic and azimuthally dependent contributions, the former from a spatially diffuse internal wave field and the latter from an undular bore or solitary wave packet. A parabolic equation code is used to compute transmission loss and horizontal coherence as a function of range, depth, cross-range, azimuth, and time for frequencies of 200 and 400 Hz. Time is treated as a parameter and the frozen ocean assumption is invoked for acoustic transmission through each environmental snapshot.

A solitary wave packet represents a dynamic oceanographic feature that breaks horizontal symmetry in the water column, resulting in anisotropic correlation lengths for the sound speed field. The simulations reveal that the space–time structure of an acoustic field can be significantly altered in this type of oceanographic environment for certain propagation conditions. Such structure cannot be fully predicted on the basis of $N\times 2$D calculations because those computations ignore azimuthal coupling and can produce misleading estimates of both transmission loss and horizontal coherence in these environments.

Transmission loss was computed for several environments in which one or both internal wave components were present. When a solitary wave packet is present in the transmission path, results indicate that $N\times 2$D calculations provide sufficient accuracy for acoustic modeling of transmission loss, provided that the azimuthal angles are less than about 70°. This result is consistent with a recent prediction obtained under simpler environmental conditions.[5] For larger azimuthal angles, a 3D acoustic computation is needed in order to include horizontal refraction effects. The horizontally anisotropic component of the internal wave field induces selective transmission paths, most dominant in the direction $\phi\approx 90°$, where acoustic propagation is approximately aligned with the wave crests of the solitary wave packet. Horizontal refraction of energy is responsible for strong transmission loss variations and coherence degradation for angles $\phi\geqslant 70°$. These variations are maximal near $\phi=90°$, when propagation is along the wave crests and energy is ducted into the region between thermocline depressions. When propagating through solitary wave packets, mode coupling within range/depth planes is most likely responsible for transmission loss variability over angles $\phi\leqslant 70°$. Adiabatic propagation is argued to be dominant for angles $\phi\geqslant 70°$ in the presence of solitary waves and for arbitrary angles in cases where only the spatially diffuse internal wave field is present.

Numerical experiments that estimate transmission loss and horizontal spatial coherence suggest that signal detection rates and phase sensitive array processing may be significantly affected in such an oceanographic environment for selective array orientations relative to the anisotropic component of the internal wave field. Both enhanced and degraded detection may occur under these circumstances, while the horizontally refracted energy can introduce significant beam wander and beam splitting in this environment. These nonstationary beamforming effects have been simulated recently.[20]

Several features may modify the above results in a real ocean environment. Bathymetric variability has not been taken into account here, and may contribute to focusing/defocusing and horizontal refraction under certain conditions. In addition, bathymetric variation directly influences mode structure and horizontal wave number. Curvature of the solitary wave packet may cause leakage of acoustic energy out of this natural oceanographic duct, much like a bend in an optical fiber can radiate electromagnetic energy. In this study, the diffuse component added an element of random variability to the acoustic field structure, but did not affect the major conclusions. However, the relative strengths of the internal wave components determine the influence of the anisotropic packet on acoustic propagation as a function of azimuth, and a stronger isotropic contribution could mask the packet's horizontal refractive effect that is responsible for focusing and coherence degradation.

At the time this manuscript was completed, an analytic model describing acoustic propagation through a simple anisotropic solitary wave packet appeared in the literature.[21] The theory supports our conclusions concerning time-dependent focusing/de-focusing of the acoustic field due to horizontal refraction for planar solitary wave fronts, and extends these results to wave fronts possessing mild radii of curvature ($\sim 10^4$ m).

ACKNOWLEDGMENTS

This work was supported by funds from the Office of Naval Research. A grant of HPC time was obtained from Corps of Engineers Water Experiment Station and Aeronautical Systems Center. The authors wish to thank Dr. Stephen Wolf for several useful discussions and a careful reading of the manuscript. The insightful comments of the reviewers were very much appreciated.

APPENDIX: TRANSMISSION LOSS GRADIENT AND HORIZONTAL REFRACTION

This Appendix considers the transmission of energy along a range/depth slice and its generalization to azimuthal energy transfer within the framework of a parabolic approximation. Functions related to an energy or transmission loss gradient are described for both 2D and 3D propagation. The sign of these quantities is an indicator of those regions of the propagation wedge that can be treated as purely 2D and described by $N\times 2$D computations, and regions where azimuthal energy coupling between range/depth planes occurs and a 3D treatment is necessary. For simplicity, we treat only

the case presented in the paper—a flat bottom waveguide with uniform density in range and azimuth. The 2D analysis is considered first.

Let u, c_0, and ρ represent pressure, a reference sound speed, and density, respectively. Define $E=E(r,\phi)$ to be the integral of an energy density over all depths for a fixed range and azimuth:

$$E(r,\phi)=\int_0^H u^2\rho^{-1}c_0^{-2}\,dz. \tag{A1}$$

This integral has units of energy per unit area, where H is the constant total depth (water+bottom, which may be extended to ∞). The integrand is an energy density for the Helmholtz equation that is analogous to the energy density for the time dependent wave equation (see Ref. 22, p. 333). Indeed, the energy density for the wave equation is obtained by using the variable sound speed in the medium instead of a reference speed c_0 as in this paper. The approach below requires an L_2 function space on the interval $0\leqslant z\leqslant H$. In this space, the L_2 norm of a function $f(z)$ is defined by $\|f(z)\|_2=\sqrt{\int f^2(z)w\,dz}$ where w is a weighting factor. With a weighting factor $\rho^{-1}c_0^{-2}$, the norm for $u(z)$, will be $\|u\|^2=E$.

Conservation of energy implies that for two dimensional parabolic propagation in r and z, energy can only be transferred from smaller ranges to larger ranges so that one has the inequality

$$\partial E/\partial r\leqslant 0. \tag{A2}$$

The equal sign holds for strict energy conservation, i.e., zero net energy flux through a vertical interface, and the inequality holds for an attenuating medium. This inequality, with the assumptions made below, is identical to a recently derived energy flux relation.[23] Approximation by a forward finite difference approximation changes the inequality to

$$\Delta E/\Delta r=\frac{\|u(r+\Delta r)\|^2-\|u(r)\|^2}{\Delta r}\leqslant 0. \tag{A3}$$

In the computer model implementation FOR3D, the propagator [Eq. (3)] is expressed by a pseudo-differential operator[17] based on the differential operators $Y=(rk_0)^{-2}\,\partial^2/\partial^2\phi$ and $Z=(n^2-1)+k_0^{-2}\rho\,\partial/\partial z(\rho^{-1}\,\partial/\partial z)$. The operator approximation used to propagate the field u from r to $r+\Delta r$ with piecewise range-constant sound speed is[17]

$$u(r+\Delta r)=e^{-ik_0\Delta r}MLu(r). \tag{A4}$$

The approximate range propagation operators L, M are expressed as

$$M=(1+p^*Z)^{-1}(1+pZ), \tag{A5}$$

and $L=(1+ik_0\Delta rY/4)^{-1}(1-ik_0\Delta rY/4)$, where a scalar p is given by $p=1/4(1+ik_0\Delta r)$. In the two-dimensional case, the propagation is azimuthally independent with $Y\equiv 0$, so that $L=1$.

With these definitions, the inequality given by Eq. (A3) becomes

$$\|u(r+\Delta r)\|^2-\|u(r)\|^2=\|Mu(r)\|^2-\|u(r)\|^2\leqslant 0 \tag{A6}$$

after multiplication by Δr; difference of squares factorization of Eq. (A6) allows one to conclude that

$$\|Mu(r)\|-\|u(r)\|\leqslant 0. \tag{A7}$$

If the operator norm $\|M\|\leqslant 1$, then the definition of operator norm states

$$\|Mu(r)\|\leqslant\|M\|\|u(r)\|\leqslant\|u(r)\| \tag{A8}$$

and inequality (A6) follows. The last inequality mathematically captures the spirit of energy conservation and attenuation of the field for the 2D case. Spectral methods are now applied to prove that $\|M\|\leqslant 1$ and, therefore, show that Eq. (A2) is satisfied.

The easiest way to proceed is to use the usual eigenfunction decomposition. Then an integral transform can be defined that allows simple algebraic representations of differential operators. Simple algebraic inequalities in the transformed space prove the operator norm is less than or equal to unity in the nontransformed case. Several assumptions must be satisfied to allow eigenmode decompositions when the index of refraction $n=c_0/c$ is generalized to complex values (to model attenuation); the existence proof uses perturbations of an appropriate real index of refraction case.[24] Take $\mathrm{Im}(c)\leqslant 0$ and $\mathrm{Re}(c)>0$; straightforward algebra shows $\mathrm{Im}(n^2)\geqslant 0$. If, in addition, one requires that $\mathrm{Im}(n^2)$ is relatively small [smaller than the minimum eigenvalue spacing of the corresponding ''unperturbed'' operator using the real index of refraction $\mathrm{Re}(n^2)$], there exist eigenvalues λ_j and eigenfunctions $\psi_j(z)$ such that $\lambda_j\psi_j(z)=Z\psi_j(z)$, and the $\psi_j(z)$ satisfy the usual orthonormality conditions. It also follows[25] that $\mathrm{Im}(\lambda_j)\geqslant\min(\mathrm{Im}(n^2))\geqslant 0$. In this case the usual modal decomposition may be accomplished by

$$\tilde{u}_j=\int_0^H\rho^{-1}c_0^{-2}u(z)\psi_j(z)dz. \tag{A9}$$

This defines an integral transform $u(z)\Rightarrow\tilde{u}_j$. The symbol $\Rightarrow$ indicates the integral transformation in Eq. (A9) which has the special spectral property $Zu\Rightarrow\lambda_j\tilde{u}_j$. Use of linearity gives $(1+pZ)u\Rightarrow(1+p\lambda_j)\tilde{u}_j$. If we introduce an inverse operator C of $(1+p^*Z)$ with $(1+p^*Z)Cu=u$, the transformed operator $\tilde{C}$ satisfies $(1+p^*\lambda_j)\tilde{C}\tilde{u}_j=\tilde{u}_j$, so that $\tilde{C}=(1+p^*\lambda)^{-1}$. Thus for $M=C(1+pZ)$, the transformed operator is $\tilde{M}=(1+p^*\lambda)^{-1}(1+p\lambda)$, a simple multiplicative operation. Elementary complex algebra shows $|\tilde{M}|\leqslant 1$, if $\mathrm{Im}(\lambda)\geqslant 0$. One now defines $\tilde{\mathbf{u}}=[\tilde{u}_1,\tilde{u}_2,\tilde{u}_3,\ldots]^T$, which is a vector in the L_2 of square summable sequences. With the usual norm on this space, the integral transform satisfies $\|\tilde{\mathbf{v}}\|=\|v\|$ for any appropriate $v(z)$ and its integral transform $\tilde{\mathbf{v}}$ in L_2. One concludes that $|\tilde{M}\tilde{\mathbf{u}}|\leqslant|\tilde{M}||\tilde{\mathbf{u}}|\leqslant|\tilde{\mathbf{u}}|$, and in turn $\|Mu\|=\|\tilde{M}\tilde{\mathbf{u}}\|\leqslant\|\tilde{\mathbf{u}}\|=\|u\|$ which is exactly Eq. (A7). Thus, the algorithm implemented in FOR3D obeys the relation Eq. (A2). Alternatively, note that if one instead uses the exact range step operator $M=e^{ik_0\Delta r\sqrt{1+Z}}$, then Eq. (A7) is again satisfied since $|\tilde{M}|\leqslant 1$ if $\mathrm{Im}(\lambda)\geqslant 0$ in this case as well. Therefore, the inequality expressed in Eq. (A2) is satisfied in the exact range step, 2D case.

For 3D propagation, the sign of the energy gradient can be positive since energy can flow into or out of a range/depth

plane. If this range gradient becomes positive, the propagation cannot be purely 2D and there must be an energy flux in the azimuthal direction (i.e., horizontal refraction of energy). Note, however, that if the energy gradient is negative or zero, this does not imply the absence of horizontal refraction. For example, the energy gradient may be negative due to refraction effects being masked by excess attenuation loss. For propagation described by Eq. (A4), the operator M contributes energy conservation and attenuation, and so any increase of E on a fixed radial caused by horizontal refraction must be due to the operator L.

If one integrates E over azimuth, an energy flux theorem for three-dimensional propagation similar to that obtained above can be derived using the operator $\sqrt{1+Z+Y}$ given in Eq. (3). However, such a result is not useful for tracking local azimuthal energy flux since the angular dependence is averaged out. A general quantification of L for fixed azimuth is not easily achieved using spectral arguments. We consider instead a less rigorous, but physically motivated analysis of a related 3D parabolic equation.

Without resorting to spectral methods, a physical approach is outlined below in order to demonstrate how a 3D parabolic equation permits cross-azimuth energy transfer. The result will be related to the energy gradient inequality expressed by Eq. (A2). Consider the following 3D parabolic equation:[26]

$$\frac{\partial u}{\partial r}=\frac{ik_0}{2}\left[(n^2-1)+k_0^{-2}\left\{\rho\frac{\partial}{\partial z}\left(\frac{1}{\rho}\frac{\partial}{\partial z}\right)+r^{-2}\frac{\partial^2}{\partial\phi^2}\right\}\right]u. \tag{A10}$$

This equation differs from the operator approximations of FOR3D in that Eq. (A10) uses a polynomial approximation to the square root, rather than the rational function approximation incorporated by FOR3D.

Differentiating Eq. (A1) with respect to range, one obtains

$$\frac{\partial E}{\partial r}=\int_0^H u^*\frac{\partial u}{\partial r}\rho^{-1}c_0^{-2}\,dz+\int_0^H\frac{\partial u^*}{\partial r}u\rho^{-1}c_0^{-2}\,dz - \int_0^H u^*u\frac{\partial\rho}{\partial r}\rho^{-1}c_0^{-2}\,dz. \tag{A11}$$

For range-independent density, the final term vanishes so that $(\partial E/\partial r)=I_1+I_2$, where the first integral is

$$I_1=\int_0^H u^*\frac{\partial u}{\partial r}\rho^{-1}c_0^{-2}\,dz$$

and the second satisfies $I_2=I_1^*$. Substitution of Eq. (A10) gives

$$I_1=\int_0^H\frac{ik_0u^*}{2c_0^2\rho}\left[(n^2-1)+\rho k_0^{-2}\frac{\partial}{\partial z}\left(\rho^{-1}\frac{\partial}{\partial z}\right)\right]u\,dz + \int_0^H\frac{iu^*}{2c_0^2k_0\rho r^2}\frac{\partial^2}{\partial\phi^2}u\,dz. \tag{A12}$$

Consider first only the z-derivative terms, obtained by neglecting azimuthal dependence ($(\partial^2/\partial\phi^2)u=0$). Integration by parts allows Eq. (A12) to be written in the form

$$c_0^2I_1=\frac{ik_0}{2}\int_0^H(n^2-1)\rho^{-1}|u|^2\,dz - \frac{i}{2k_0}\int_0^H\rho^{-1}\frac{\partial}{\partial z}u^*\frac{\partial}{\partial z}u\,dz, \tag{A13}$$

where impedance conditions at density jumps have been imposed. Addition of I_1 and I_2 yields the expression

$$c_0^2(I_1+I_2)=-\frac{ik_0}{2}\int_0^H\rho^{-1}|u|^2[(n^2-1)-(n^{*2}-1)]dz, \tag{A14}$$

where the second term of Eq. (A13) cancels its conjugate in I_2. The transmission loss or energy gradient for the case of no azimuthal variation can then be expressed as

$$\frac{\partial E}{\partial r}=-k_0c_0^{-2}\int_b^H\rho^{-1}|u|^2\,\mathrm{Im}(n^2)dz\leqslant 0. \tag{A15}$$

This is a two-dimensional result and implies that the decrease in E is due to attenuation in the sediment. The range of integration is limited to the sediment by the following reasoning. The integral determining the range derivative is broken into two parts: define

$$\left[\frac{\partial E}{\partial r}\right]_W=-k_0c_0^{-2}\int_0^b\rho^{-1}|u|^2\,\mathrm{Im}(n^2)dz$$

to be the integral over the water column and $[\partial E/\partial r]_S$ to be the integral over the sediment where $b\leqslant z\leqslant H$. If the water is lossless, as assumed by FOR3D, then $\mathrm{Im}(n^2)=0$ implies that $[\partial E/\partial r]_W=0$. Thus $(\partial E/\partial r)=[\partial E/\partial r]_S$, and one concludes that the gradient is determined entirely by the sediment attenuation integral given by Eq. (A15). The relation given by Eq. (A15) reconfirms the proof of inequality (A2) for the 2D version of Eq. (A10).

When azimuthal dependence is present, one must include in Eq. (A13) the ϕ derivative term neglected from Eq. (A12). Inclusion of this term leads to the result

$$\frac{\partial E}{\partial r}=\frac{-k_0}{c_0^2}\int_b^H\rho^{-1}|u|^2\,\mathrm{Im}(n^2)dz - \frac{1}{c_0^2k_0r^2}\int_0^H\mathrm{Im}\left(u^*\frac{\partial^2}{\partial\phi^2}u\right)\frac{dz}{\rho}. \tag{A16}$$

Let J represent the second integral in Eq. (A16); this integral represents the azimuthal contribution to the energy gradient due to horizontal refraction. Now define $\langle J\rangle$ as the average of the azimuthal contribution over a small angle $\delta\phi$:

$$\langle J\rangle=\frac{1}{\delta\phi}\int_\phi^{\phi+\delta\phi}J\,d\phi.$$

Changing the order of integration and integrating by parts over ϕ give

$$\langle J\rangle=\frac{1}{\delta\phi c_0^2k_0r^2}\int_0^H\mathrm{Im}\left(-u^*\frac{\partial}{\partial\phi}u\Big|_\phi^{\phi+\delta\phi} + \int_\phi^{\phi+\delta\phi}\frac{\partial}{\partial\phi}u^*\frac{\partial}{\partial\phi}u\,d\phi\right)\frac{dz}{\rho}. \tag{A17}$$

If the density is azimuthally invariant, then the velocity in the tangential direction, V_ϕ, is given by $V_\phi = i(\omega r \rho)^{-1}(\partial/\partial\phi)u$ and one may rewrite Eq. (A17) as

$$\langle J \rangle = \frac{1}{\delta\phi\omega\rho c_0^2 k_0 r^2} \int_0^H \mathrm{Im}\left(-iu^* V_\phi \Big|_{\phi}^{\phi+\delta\phi} + \int_\phi^{\phi+\delta\phi} (\omega\rho)^{-2} |V_\phi|^2 d\phi \right) \frac{dz}{\rho}. \quad \text{(A18)}$$

The second term in the integrand is real and has the form of kinetic energy density. Only the first term remains, and one recovers J as $\delta\phi \to 0$

$$J = \frac{1}{\omega c_0^2 k_0 r^2} \int_0^H \rho^{-1} \lim_{\delta\phi\to 0} \frac{\mathrm{Re}[-u^* V_\phi]_\phi^{\phi+\delta\phi}}{\delta\phi} dz. \quad \text{(A19)}$$

This result can be viewed as the rate of work done at the side interfaces of this infinitesimal vertical volume on the neighboring elements in the ϕ direction. Thus Eq. (A19) measures energy flux tangentially to and from the volume.

[1] D. Tielbuerger, S. Finette, and S. Wolf, "Acoustic propagation through an internal wave field in a shallow water waveguide," J. Acoust. Soc. Am. **101**, 789–808 (1997).

[2] S. Finette, M. H. Orr, A. Turgut, J. Apel, M. Badiey, C. S. Chiu, R. H. Headrick, J. N. Kemp, J. F. Lynch, A. E. Newhall, K. von der Heydt, B. Pasewark, S. N. Wolf, and D. Tielbuerger, "Acoustic field variability induced by time-evolving internal wave fields," J. Acoust. Soc. Am. **108**, 957–972 (2000).

[3] J. Lynch, G. Jin, RF. Pawlowicz, D. Ray, A. J. Plueddemann, C. S. Chiu, J. H. Miller, R. H. Bourke, A. Rost Parsons, and R. Muench, "Acoustic travel-time perturbations due to shallow water internal waves and internal tides in the Barents sea polar front: Theory and experiment," J. Acoust. Soc. Am. **99**, 803–821 (1996).

[4] D. Rubenstein, "Observations of cnoidal internal waves and their effect on acoustic propagation in shallow water," IEEE J. Ocean. Eng. **24**, 346–357 (1999).

[5] J. C. Preisig and T. F. Duda, "Coupled acoustic mode propagation through continental-shelf internal solitary waves," IEEE J. Ocean. Eng. **22**, 256–269 (1997).

[6] T. F. Duda and J. C. Preisig, "A modeling study of acoustic propagation through moving shallow water solitary wave packets," IEEE J. Ocean. Eng. **24**, 16–32 (1999).

[7] J. Zhou, X. Z. Zhang, and P. H. Rogers, "Resonant interaction of sound wave with internal solitons in the coastal zone," J. Acoust. Soc. Am. **90**, 2042–2054 (1991).

[8] B. G. Katsnel'son and S. A. Pereselkov, "Resonance effects in sound scattering by internal wave packets in a shallow sea," Acoust. Phys. **44**, 786–792 (1998).

[9] K. V. Konyaev, D. E. Leikin, K. D. Sabinin, Yu I. Tuzhilkin, and V. R. D'yachenko, "Correlations between internal solitons and amplitude variations of a sound signal on a fixed path," Acoust. Phys. **44**, 476–485 (1998).

[10] A. N. Rutenko, "Experimental study of the effect of internal waves on the frequency interference structure of the sound field in shallow sea," Acoust. Phys. **46**, 252–258 (2000).

[11] F. S. Henyey, D. Rouseff, J. M. Grahocinski, S. A. Reynolds, K. L. Williams, and T. E. Ewart, "Effects of internal waves and turbulence on a horizontal aperture sonar," IEEE J. Ocean. Eng. **22**, 270–280 (1997).

[12] E. Gorodetskaya, A. Malekhanov, A. Sazontov, and N. Vdovicheva, "Deep water acoustic coherence at long ranges: Theoretical predictions and effects on large array signal processing," IEEE J. Ocean. Eng. **24**, 156–171 (1999).

[13] B. J. Uscinski and D. Reeve, "The effect of ocean inhomogeneities on array output," J. Acoust. Soc. Am. **87**, 2527–2534 (1990).

[14] J. R. Apel, L. A. Ostrovsky, and Y. A. Stepanyants, "Internal solitons in the ocean," Johns Hopkins University Applied Physics Laboratory, Laurel, MD, Report MERCJRA0695 (1995).

[15] J. R. Apel, S. Finette, M. H. Orr, and J. F. Lynch, "The 'dnoidal' model for internal tides and solitons on the continental shelf," J. Geophys. Res. (submitted).

[16] J. R. Apel, M. Badiey, C. S. Chiu, S. Finette, R. Headrick, J. Kemp, J. F. Lynch, A. Newhall, M. H. Orr, B. H. Pasewark, D. Tielbuerger, A. Turgut, K. von der Heydt, and S. Wolf, "An overview of the 1995 SWARM shallow-water internal wave acoustic scattering experiment," IEEE J. Ocean. Eng. **22**, 465–500 (1997).

[17] D. Lee and M. H. Schultz, *Numerical Ocean Acoustic Propagation in Three Dimensions* (World Scientific, Singapore, 1995).

[18] L. Dozier and F. Tappert, "Statistics of normal mode amplitudes in a random ocean: I. Theory," J. Acoust. Soc. Am. **63**, 353–365 (1978).

[19] W. M. Carey, "The determination of signal coherence length based on signal coherence and gain measurements in deep and shallow water," J. Acoust. Soc. Am. **104**, 831–837 (1998).

[20] S. Finette and R. Oba, "Beamforming through an anisotropic, time varying internal wave field," J. Acoust. Soc. Am. **108**, 2544 (2000).

[21] B. G. Katsnel'son and S. A. Pereselkov, "Low-frequency horizontal acoustic refraction caused by internal wave solitons in a shallow sea," Acoust. Phys. **46**, 684–691 (2000).

[22] L. M. Brekhovskikh and O. A. Godin, *Acoustics of Layered Media II* (Springer Verlag, Berlin, 1992).

[23] M. D. Collins, H. Schmidt, and W. Siegmann, "An energy-conserving spectral solution," J. Acoust. Soc. Am. **107**, 1964–1966 (2000).

[24] R. B. Evans, "The continuation of the normal mode solution of the underwater acoustic wave equation," Wave Motion **20**, 13–20 (1994).

[25] R. B. Evans, "Existence of generalized eigenfunctions and multiple eigenvalues in underwater acoustics," J. Acoust. Soc. Am. **92**, 2024–2029 (1992).

[26] J. S. Perkins and R. N. Baer, "An approximation to the three-dimensional parabolic equation method for acoustic propagation," J. Acoust. Soc. Am. **72**, 515–522 (1982).

Velocity dispersion in water-saturated granular sediment

Robert D. Stoll
Lamont-Doherty Earth Observatory of Columbia University, Palisades, New York 10964

(Received 25 September 2000; revised 11 June 2001; accepted 6 November 2001)

Recent experiments in the Gulf of Mexico have yielded a wealth of information on the environmental conditions and geoacoustic response of a uniform sand stratum immediately beneath the seafloor. A comparison of *p*-wave velocities measured at low (125 Hz) and high (11–50 kHz) frequencies in this layer indicates that there is a significant amount of velocity dispersion that occurs in the interval between these extremes. This narrow-band dispersion, which is not consistent with the often-used assumption of a nearly constant-Q model, is in accordance with the predictions of the Biot theory. It results from viscous damping in the fluid as it moves relative to the skeletal frame. Other recent field data that support this conclusion are presented. © *2002 Acoustical Society of America.* [DOI: 10.1121/1.1432981]

PACS numbers: 43.30.Ma, 43.20.Mv [DLB]

I. INTRODUCTION

In the fall of 1999 a series of field experiments named ''SAX99'' (for Sediment Acoustics Experiments—1999), was carried out in the Gulf of Mexico near Fort Walton Beach, Florida, While the bulk of the acoustics experiments in this program were high-frequency studies aimed at determining scattering and seafloor penetration at low grazing angles, a few of the experiments were designed to investigate the lower frequency response of the sand strata immediately beneath the bottom, wherein most of the higher frequency work was carried out. Results of some of this lower-frequency work, obtained by a team from Lamont-Doherty Earth Observatory of Columbia University (LDEO), are given in this paper. The main objectives were to define a baseline model valid over a somewhat wider frequency range than that covered by the main high-frequency experiments and to see if velocity dispersion, as predicted by the Biot theory, would play an important role in the interpretation of these experiments.

II. BASIC CONSIDERATIONS

Ever since the Biot theory for porous media[1,2] has been applied to problems in sediment acoustics,[3–6] there have been questions about the nonlinear variation of attenuation and the marked velocity dispersion that is predicted, particularly in the coarser granular sediments such as sand. Part of the reason for these questions is that the attenuation predicted in conjunction with this dispersive behavior does not match the time-honored assumption that there will be a linear variation with frequency over the full range of interest in ocean acoustics. The intrinsic attenuation predicted by the Biot theory, as applied by Stoll and others,[3–6] is the result of two kinds of energy dissipation that are occurring simultaneously in a water-saturated sediment—frictional losses at grain-to-grain contacts and viscous losses in the pore–water as it moves relative to the skeletal frame. The relative dominance of these two mechanisms and the relatively narrow frequency range wherein significant velocity dispersion occurs depend on the fluid mobility (permeability) and associated parameters.

Many of the traditional models for granular sediments assume that attenuation varies uniformly with frequency and therefore that there is very little velocity dispersion over the entire frequency range of interest. This is partly due to the fact that several widely used plots of attenuation versus frequency that cover a wide range of frequency and sediment types have lumped together data for all different kinds of sediment and from many different kinds of experiment without separating intrinsic from overall attenuation. The result is a band of data points that suggests an overall attenuation varying linearly or nearly linearly with frequency[7,8] over a wide range. Since the points plotted in these compilations are subjective interpretations of the results from many different kinds of experiment, individual values must be carefully examined to see if they are applicable to a particular application.

As an example, two points labeled ''sand,'' one at 250 Hz and one at 1 kHz in Fig. 12 of Ref. 8 are each based on a single value of attenuation given in units of dB/wavelength based on tests of a normal-mode propagation model. The original data are in the form of transmission loss curves in the frequency range from 50 Hz to 6.4 kHz, resulting from explosive sources deployed in the water column. In these experiments the authors explicitly assumed *a priori* that the attenuation was linear in frequency and very little environmental data were available to allow a careful evaluation of the sediment through which propagation was occurring. Hence, these points are inappropriate for studies of intrinsic attenuation and velocity if one is seeking to accurately define the frequency dependence for different classes of sediment such as sand. In fact, if the source data for the above figure are carefully examined, it can be seen that there are no data below a frequency of about 4 or 5 kHz that are useful for studying intrinsic attenuation in uniform sand.

In the present case, the focus is on velocity dispersion and intrinsic attenuation that occurs in the frequency range of about 50 Hz to 10 kHz, wherein the Biot theory predicts that the effects of fluid motion relative to the skeletal frame will be most pronounced in a typical, uncemented sand near the seafloor (e.g., a beach sand with little overburden pressure).

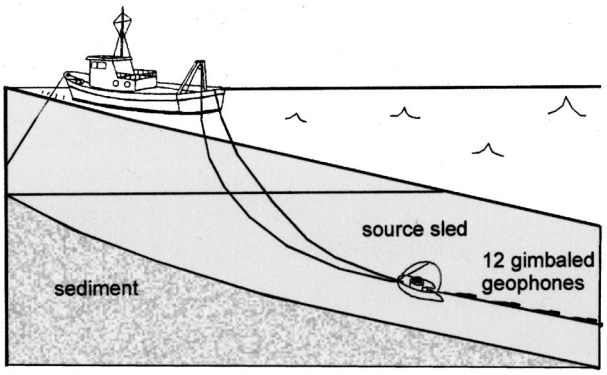

FIG. 1. Experimental setup.

Under these circumstances, shear-wave velocities will be quite low and an extremely small amount of energy will be converted into waves of the ''second kind'' at a water–sediment boundary or other interface. Hence, we concentrate on *p* waves of the ''first kind'' (the so-called ''fast wave'') which behave in a manner similar to the traditional elastic compressional wave except for subtle, frequency-dependent effects on velocity and reflection/transmission coefficients. In particular, the classical ''critical angle'' is no longer entirely meaningful in that there is no longer total reflection and an evanescent wave in the usual sense.[9] Fortunately, there are some recent experimental data in this frequency range that may be used to compare with the predictions of the theory. These data will be discussed in a later section.

The experiments described in this paper were designed to obtain low-frequency measurements of *p*-wave velocity in a homogeneous sand sediment located in the first meter or so below the seafloor in that part of the sediment column where high-frequency measurements and detailed environmental data are available from the SAX99 experiments. In addition, measurements of shear-wave velocity and attenuation were made as a basis for defining a baseline geoacoustic model valid over a wide range of frequencies. Another objective was to see whether any velocity dispersion, such as that predicted by the Biot theory, could be documented and compared with reliable velocity and intrinsic attenuation measurements made by other investigators, both as a part of the SAX99 program and elsewhere.

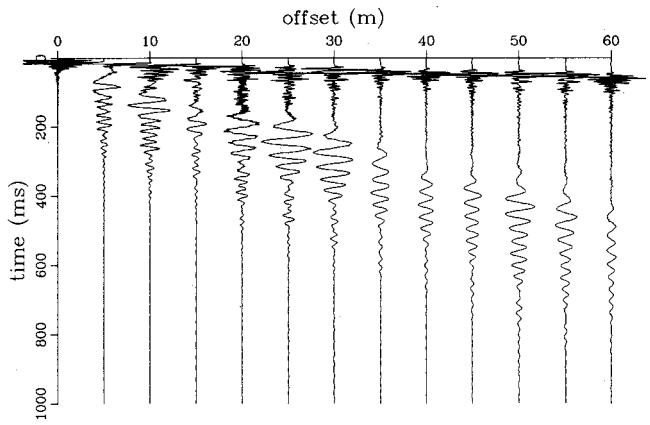

FIG. 2. Travel-time curves normalized to maximum amplitude.

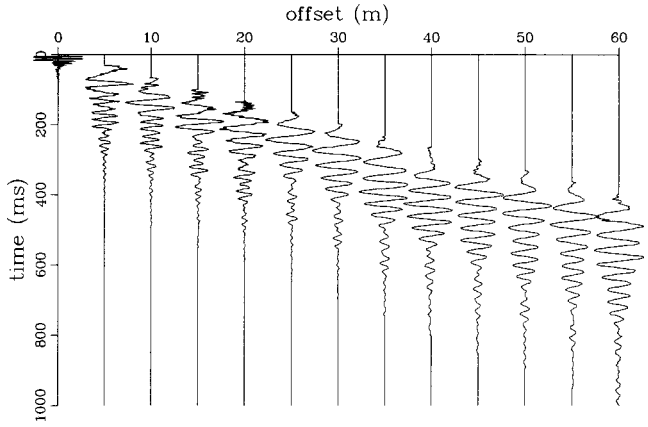

FIG. 3. Windowed portion of travel-time curves centered around Scholte wave and normalized to maximum amplitude.

III. EXPERIMENTS

In the experiments carried out by the Lamont-Doherty team, an impulsive source and a linear array of 12 gimbaled, vertical geophones were deployed on the seafloor in a manner similar to that described by Stoll *et al.*[10] with the exception that the array of phones was situated as closely as possible to the source in order to optimize the study of very shallow diving *p* waves. The source was an 11-shot gun that utilizes 22-caliber blank cartridges discharged into a helmet-shaped chamber that is mounted on a self-righting sled. The string of geophones is attached to the sled by a bridle in such a way that the array is dragged behind the sled in a straight line when it is moved forward along a straight path. A hydrophone attached to the sled acted as a shot phone to record the instant of firing. The 12 channels of data and the hydrophone channel were connected to a multichannel amplifier/filter unit and a 12-bit A/D converter. The digital data are stored on the hard disk of a personal computer. The experimental setup is shown in Fig. 1.

Two types of experiment were performed. The first type, designed to provide an accurate record of the first arrivals of *p*-wave energy, utilized a sampling rate of 5 kHz to provide a temporal resolution of 200 μs for each data point. The second type utilized a sampling rate of 1 kHz and a longer total recording time in order to record the propagation of the Scholte wave over the full length of the 12-phone array. A record of the second type is shown in Fig. 2, with the amplitude normalized to the maximum amplitude for each trace. Both the first arrival of *p*-wave energy and the progression of the dispersive Scholte wave are evident in this figure. When the data is windowed to exclude the first arrivals and direct water waves, the Scholte wave arrivals are isolated, as shown in Fig. 3. Here again the data have been normalized to the maximum amplitude within the window.

All of the high- and low-frequency experiments were performed in the Gulf of Mexico in an area just off of Fort Walton Beach, Florida in about 20 m of water. During the course of the SAX99 experiments, extensive environmental studies were made to determine grain-size distribution, porosity, permeability, and a number of other variables.[11,12] In general, the top 1 or 2 m of the sediment column was composed of a coarse to medium sand containing numerous

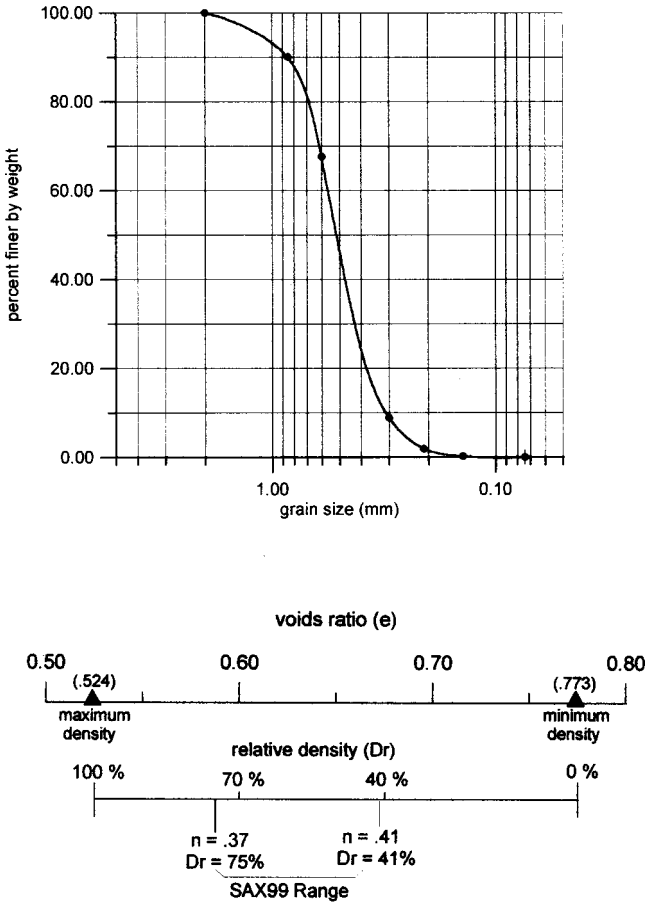

FIG. 4. Voids ratio—relative density diagram.

small shell fragments. A typical grain-size curve from a grab sample taken in the area near the first deployment of the LDEO bottom array is shown in Fig. 4, along with information about the maximum and minimum density of the sediment. Maximum and minimum density are geotechnical terms that describe the densest and loosest dry unit weight that would normally be expected in a naturally occurring sediment; each different gradation of sand exhibits its own unique pair of values. The maximum density is determined by compacting the dry sediment into a cylindrical container of known volume using a vibrating compactor and the minimum density is determined by gently placing the dry sediment into the container using a long-nosed funnel. Relative density, D_r, is then defined as

$$D_r = \frac{e_l - e_n}{e_l - e_d} \times 100\%,$$

where $e_l = 0.773$ and $e_d = 0.524$ are the voids ratio at the minimum and maximum density, respectively, and e_n is the voids ratio at some natural density of interest. Voids ratio is defined as the ratio of the volume of the voids to the volume of the solids. The porosity n is related to the voids ratio by the relationship $n = e/(1+e)$. The porosity measured by various investigators participating in the SAX99 experiments varied from 0.37 to 0.41, which corresponds to relative densities ranging from 41% to 75% as shown in the figure. An accurate value of the *in situ* porosity is probably the most important of the primitive parameters needed when estimating sediment velocity and attenuation, since it plays a role in determining overburden pressure, total density, and the moduli of the skeletal frame.[13] However, accurate determination of *in situ* sand porosity has been a problem that has plagued geotechnical engineers for many years. Any vibration or shearing deformation of an unconfined, saturated sand can cause a significant change in the relative density and therefore the sediment geoacoustic properties. Hence, the shearing and displacement caused by any sampling operations and the transportation of a sample from the sea bottom to the laboratory, even if carefully done, will usually have an influence on the density measured in the lab. For this reason it is usually wise to consider a range of values when modeling the effects of porosity.

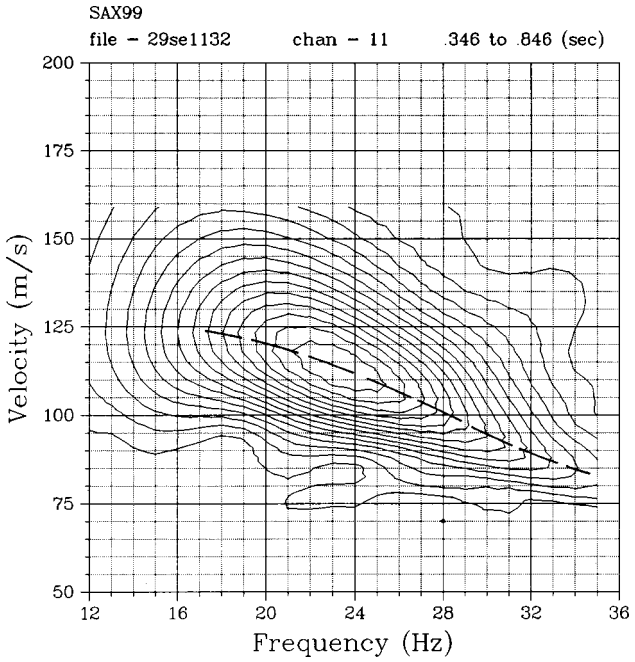

FIG. 5. Results of multiple filter analysis to determine group velocity dispersion.

IV. DATA ANALYSIS

A. Scholte wave dispersion curves

Dispersive Scholte waves, such as the one shown in Fig. 3, may be analyzed in a number of different ways. For example, when the windowed travel-time curve for channel 11 shown in Fig. 3 is transformed into the frequency domain and subjected to a series of narrow-band Gaussian filters and a Hilbert transform, the result after transformation back to the time domain is a Gabor diagram of the type shown in Fig. 5. By tracing out the maxima of this diagram (i.e., following the "ridge crest") a group velocity dispersion curve is determined. Details of this kind of analysis have been given by Stoll *et al.*[14] and a number of other authors.[15]

A second approach to the determination of dispersion curves, in this case the phase velocity dispersion, is to perform a cross correlation between adjacent traces and then use the phase of the result at each frequency and the known spacing between traces to determine phase velocity versus frequency (i.e., the phase of the cross spectrum at each fre-

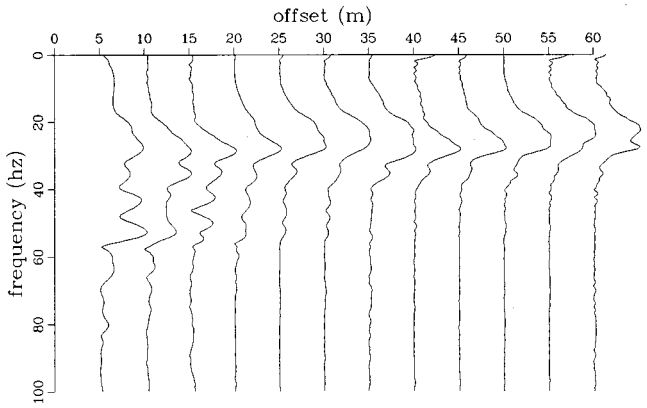

FIG. 6. Fourier frequency spectra for windowed curves showing frequency content of Scholte waves. Curves are normalized to maxima.

quency is equal to the difference in phase between the two traces at that frequency).[14] Other methods for determining phase velocity dispersion include cross multiplication of traces, the method of sums and differences, and slant stacking of the data.[15]

In order to measure the attenuation of the Scholte wave and estimate the attenuation of shear waves that may propagate through the strata which are excited by the surface wave, each trace of the windowed data shown in Fig. 3 was transformed to the frequency domain with the result shown in Fig. 6. Before this transformation the amplitude of each trace was corrected for amplifier gain and the effect of radial spreading. For clarity each trace is normalized to its maximum amplitude.

B. Inverse modeling to obtain shear-wave velocity

A constrained, least-squares inversion used in conjunction with singular value decomposition was utilized to derive a sediment model from the dispersion curves discussed above. The inversion is based on a forward modeling algorithm, which utilizes a modified version of the Thompson–Haskell matrix method[16,17] for integrating the equations of motion for a stack of horizontal, homogeneous layers to find dispersion of the interface waves propagating along the water–sediment interface. Because this process is nonlinear, an iterative process is used to solve for shear-wave velocity and attenuation of the layers that result in a dispersion curve that matches the experimental curve. Figures 7 and 8 show shear-wave velocity as a function of depth for models derived on the basis of both group- and phase velocity dispersion. Figure 7 shows a model based on eight layers derived on the basis of the group velocity dispersion curve for channel 11 of the data shown in Fig. 3. The Gabor diagram for this case, from which the dotted group velocity dispersion was derived, is the one shown in Fig. 5. The cross symbols show the group velocity dispersion for the assumed model after 30 iterations and the asterisks the corresponding phase velocity dispersion curve.

Since the model shown in Fig. 7 is based on the characteristics of a single trace at a range of 55 m from the source, it represents the average conditions over this entire distance. As a result local variations in the sediment velocity profile,

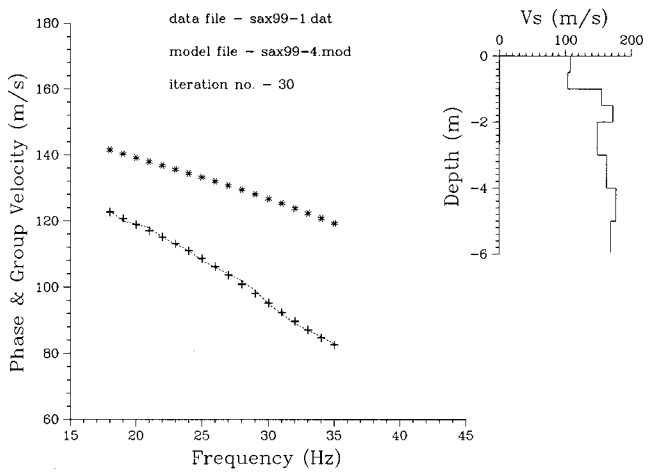

FIG. 7. Shear-wave velocity versus depth obtained by matching group velocity dispersion of horizontally layered model to experimentally determined dispersion. The corresponding phase velocity dispersion is also shown.

which are typical in most shelf sediments,[14] may not be fully apparent. Moreover, the rather smooth, bulbous shape of the contours in the Gabor diagram, Fig. 5, makes it difficult to pick the most representative position for the group velocity dispersion curve at the lower frequencies. Since the dispersion at these lower frequencies tends to control the details of the velocity–depth model in the deeper strata, this portion of the model may be somewhat different than that derived by other techniques such as the two-station method described below.

Figure 8 is based on a phase velocity dispersion curve derived by averaging the dispersion between adjacent channels from 5 to 12 (25- to 60-m range) in Fig. 3. Data from channels near the source (1 through 4) were not included in the analysis to avoid any contaminating effects from direct and refracted *p*-wave arrivals. The solid line is the smoothed result of this averaging, and the cross and asterisk symbols are the group and phase velocity curves, respectively, for the model that evolved after 30 iterations. The phase velocity

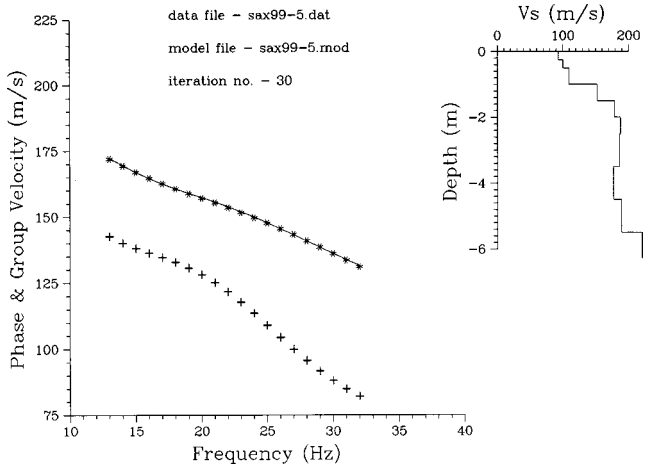

FIG. 8. Shear-wave velocity versus depth obtained by matching phase velocity dispersion of horizontally layered model to experimentally determined dispersion. Experimental dispersion curve is the result of averaging the dispersion between adjacent channels 5 to 12. Dispersion for each channel pair determined by cross correlation.

dispersion between adjacent channels was obtained by cross correlation as discussed above. More layers were included in this analysis in order to increase the resolution near the seafloor.

Both of the models shown in Figs. 7 and 8 suggest an upper layer about 1 m thick, wherein the maximum shear-wave velocity reaches about 100 m/s. Beneath this layer is a somewhat stiffer stratum where the maximum velocity approaches about 200 m/s, with some differences between the two models as discussed above. Possible reasons for the slower upper layer include bioturbation and/or reworking due to wave action.

In order to estimate shear-wave attenuation, the amplitude spectra shown in Fig. 6 were used to estimate the attenuation of the Scholte wave at several different frequencies. These data was then used to invert for the shear-wave attenuation in the upper and lower strata using the same Jacobian matrix used to invert for the shear-wave velocities. The details of this procedure are given in Stoll *et al.*[18] Using this procedure the attenuation in the upper layer was estimated to be 0.47 dB/m and in the lower stratum 0.19 dB/m at 25 Hz.

C. *p*-wave velocity from refraction analysis

As mentioned above, *p*-wave velocity was determined based on an analysis of diving waves (surface-to-surface refracted waves) utilizing shots with a 5-kHz sampling rate. The success of this method is due largely to the unique source used in our experiments wherein energy from an impulsive source is focused into the seabed by a helmet mounted on a self-righting sled and precisely spaced geophones were deployed as closely as possible to the source. Using the stored digital data, each channel was scanned to determine the time of first arrival and a polynomial travel-time curve was derived from a least-squares fit to these points. For most shots it was found that the data for the first channel, located at a range of 5 m from the source, were contaminated with high-frequency noise caused by the wire bridle that was used to secure the geophone cable to the sled. For this reason only channels 2 through 12 were used to determine the curve of first arrivals. An amplified and clipped portion of the travel-time curves for one shot is shown in Fig. 9. The broken line is a plot of the polynomial obtained by a least-squares fit to the first arrivals and, as can be seen from the figure, it is an excellent fit to the data. It is slightly concave towards the range axis, indicating that the first arrivals correspond to shallow diving waves caused by the gradual increase of *p*-wave velocity with depth.

Using the slope at each range of the curve of first arrivals, the *p*-wave velocity as a function of depth was determined using the classical Weichert–Herglotz–Bateman (WHB) integral.[19] The results of the integration and the trajectories corresponding to each range are shown in Fig. 10. The *p*-wave velocity at the lowest point of each trajectory, marked by a small circular symbol, is equal to the slope of the travel-time curve at the point where the trajectory intersects the surface. The second-order polynomial fitted to the first arrivals has no physical significance and was used only to insure a consistent set of slopes at the various ranges.

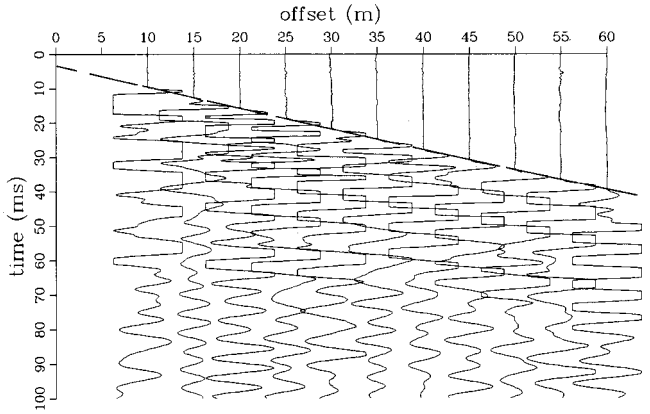

FIG. 9. Amplified, expanded, and clipped portion of travel-time curves showing first arrivals. Broken line is a plot of polynomial obtained by least-squares fit to first arrivals. It is slightly concave towards the range axis, indicating that first arrivals correspond to shallow diving waves.

Other reasonable functions that are good fits to the data will produce similar results with slightly different velocity–depth curves from the integration.

An important feature of the current experimental configuration is the position of the geophone array relative to the source. As can be seen from Fig. 10, the deepest penetration of the diving *p* waves is about 5 m, corresponding to a receiver range of 60 m. Hence, all of the phones are receiving data from shallower paths that are in the zone of interest in the current experiment.

In using surface-to-surface refracted ray paths to determine a *p*-wave model, some of the same problems encountered in the analysis of the Scholte interface waves must be considered. Use of the WHB integral implies a horizontally homogeneous medium with the *p*-wave velocity continuously increasing with depth. Since our array is spread out over a range of 60 m, there are undoubtedly some lateral variations in sediment properties and geophone coupling with the seabed that affect the travel-time curves. Without the use of a reasonable smoothing curve such as the one employed herein, the results can be quite erratic. Moreover, in view of the least-squares fit that is utilized to define the

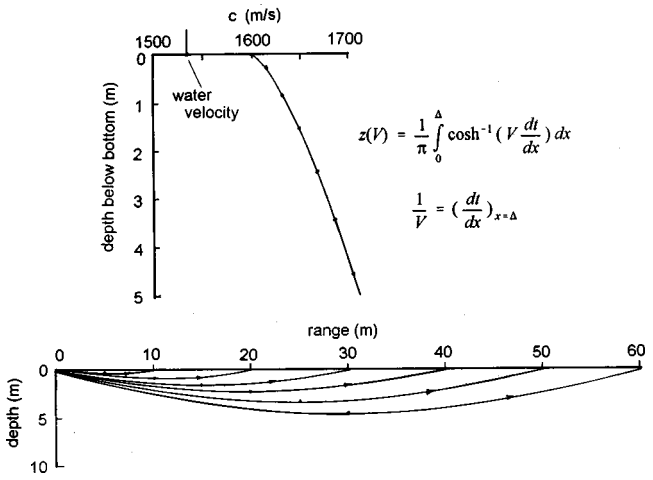

FIG. 10. Plot of *p*-wave velocity versus depth obtained by Herglotz–Bateman–Weichert analysis of first arrivals and wave trajectories corresponding to different ranges.

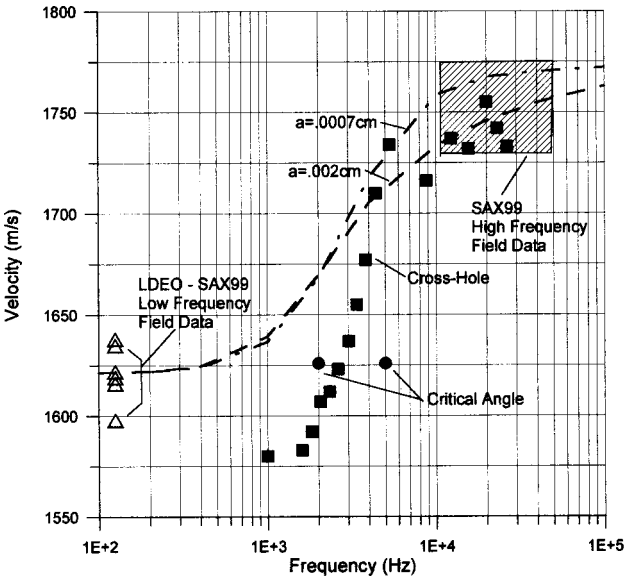

FIG. 11. Measured *p*-wave velocity in homogeneous, unconsolidated sands and velocity dispersion curves based on the Biot theory. Input parameters are given in Table I. Solid squares labeled ''cross hole'' are based on data from Ref. 20 and solid circles labeled ''critical angle'' from Ref. 21.

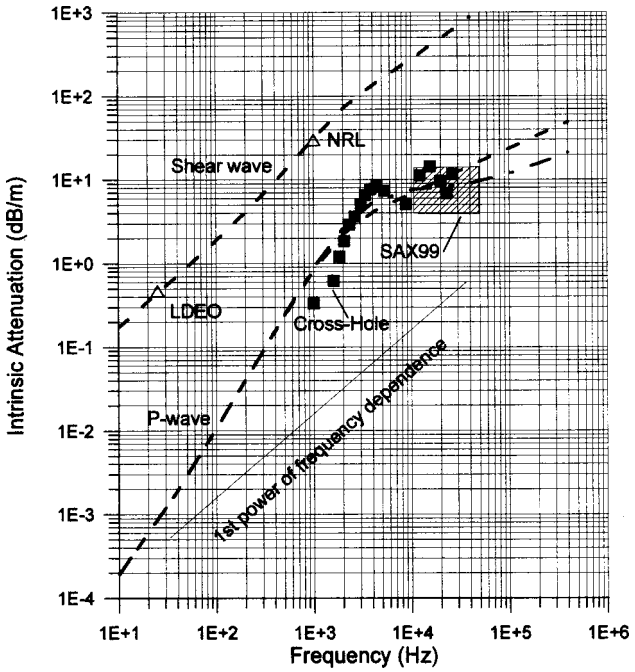

FIG. 12. Intrinsic attenuation in homogeneous, unconsolidated sand. Measured *p*- and *s*-wave values and predictions of Biot theory using the same parameters as for Fig. 11.

curve of first arrivals, it was felt that a sampling rate higher than the 5 kHz chosen for the *p*-wave experiments would do little to improve the final model. Fortunately, the SAX99 site was carefully chosen in an effort to minimize both vertical and lateral inhomogeneity in the top few meters of the seabed. As a result, the analysis described above has resulted in a model that is quite reasonable.

A frequency spectrum of that part of the signal that contains the first arrival of the diving *p* waves and vestiges of the direct water arrival shows significant energy in the range of 50 to 200 Hz with a peak at around 125 Hz. The results of a number of *p*-wave velocity determinations have been plotted at this frequency in Fig. 11 and labeled ''SAX99 low-frequency field data.'' These points are based on the slope of the travel-time curve at a range of 10 m from the source which corresponds to the *p*-wave velocity in the upper 30 cm or so of the sand stratum. Since the *p*-wave velocity in the water at the seafloor was about 1535 m/s, the signals from the diving *p* waves, which are only slightly faster, are modulated by the water wave after a very short time interval. Hence, it is virtually impossible to extract a reliable estimate of attenuation for the diving waves. The cross-hatched area between 11 kHz and 50 kHz labeled ''SAX99'' shows the range of *in situ* velocities measured in the high-frequency range using probes[11] and buried hydrophone arrays.[12,20]

In addition to the results just described, Fig. 11 contains some new data from other investigators that were obtained from experiments in homogeneous, unconsolidated sands. This data includes the results of *in situ* cross-hole studies by Turgut and Yamamoto[21] and field studies by Maguer *et al.*,[22] wherein the measured critical angle is used to infer *p*-wave velocity in the sediment. In the cross-hole studies the authors were able to measure both *p*-wave velocity and attenuation in the frequency range from 1 to 35 kHz. This remarkable set of data clearly illustrates the velocity dispersion and the corresponding nonlinear variation of attenuation that occurs in a typical sand sediment. Their measured velocities ranged from a low of about 1580 m/s at 1 kHz to about 1755 m/s at about 20 kHz. Since both velocity and attenuation were measured, the authors were able to integrate their attenuation data to obtain a theoretical estimate of the corresponding velocity using the Kramers–Kronig relationships. A comparison of this estimate with measured velocities provided an excellent check on the consistency of their data. The cross-hole attenuation measurements corresponding to the velocity measurements in Fig. 11 are shown in Fig. 12, along with other data that include the SAX99 shear-wave attenuation measurements.

In the critical angle studies,[22] the authors showed that a velocity of 1626 m/s corresponding to measured critical angles in the frequency range (2–5 kHz) was significantly less than the velocity of 1720 m/s measured in cores at 200 kHz, again suggesting that there is significant velocity dispersion of the type predicted by the Biot theory.

The data shown in Fig. 11 clearly indicate that there is a significant amount of nonlinear velocity dispersion that occurs when going from the low- to high-frequency regime. Not as clear is how this dispersion occurs as a function of frequency. The robust data set from the cross-hole experiments suggests a very steep dispersion curve, with the transition from low to high velocity occurring in about one decade of frequency. On the other hand, the much more limited data from the critical angle study were analyzed on the basis of a Biot model that suggested a transition occurring over a somewhat wider frequency range. In the next section, the parameters controlling the velocity dispersion in this transition range are more thoroughly discussed and some preliminary predictions of the Biot theory are presented.

V. CHOOSING A BASE-LINE MODEL

In the basic Biot theory, it is largely three parameters that control the fluid motion that results in the nonlinear dispersion that is so important in the coarser granular sediments. These are the permeability, k, the pore-size parameter, a, and the structure parameter α which defines the necessary amount of ''added mass.'' Moreover, these three parameters (as well as others in the Biot theory) are inter-related so that care must be taken in any parametric studies to insure that the chosen values are physically meaningful. A very brief summary of the Biot model is given in the Appendix for reference.

To reiterate, the interest in the current study is to evaluate the Biot parameters appropriate to p-wave propagation in unconsolidated sand located in the first 1 or 2 m below the seafloor. Hence, the overburden pressure will play a minor role in determining the velocity which should approach a value close to that given by the Wood equation at low frequencies. The Wood equation, which is a limiting case of the Biot equations for vanishingly small shear and frame moduli, has the form

$$c = \sqrt{\frac{K_g K_w / (nK_g + (1-n)K_w)}{\rho}},$$

where c is p-wave velocity, K_g and K_w are the bulk moduli of the grains and the water, respectively, n is porosity, and ρ is the total density, given by

$$\rho = n\rho_w + (1-n)\rho_g,$$

where ρ_w and ρ_g are the densities of the water and the grains, respectively.

In the full Biot theory the difference between the velocity at very low frequency and very high frequency is controlled mainly by the structure factor, whereas the rate at which one moves from one extreme to the other as a function of frequency depends on the pore-size parameter, a. This parameter plays the role of a scaling factor and its value depends on both the size and shape of the interstitial channels. As suggested by Biot, a should be chosen such that the dispersion and attenuation curves fit the experimental data. Finally, the permeability determines the critical frequency at which the maximum viscous attenuation occurs. As sediment grain size decreases, permeability also decreases and the characteristic frequency takes on higher and higher values. For typical clean sands of interest in the current study, this frequency falls in the range between several hundred Hz and several kHz.

Two sample velocity dispersion curves calculated with the Biot equations are shown in Fig. 11. The various parameters used to generate these curves are given in Table I. The values of bulk and shear moduli of the frame are based on a shear-wave velocity of about 100 m/s in the top meter of sediment and a Poisson's ratio of 0.2. Other environmental parameters such as permeability and porosity were chosen to fall within the range of values measured in the SAX99 experiments. In making these choices it was necessary to take into account several aspects of the particular field environment at Fort Walton beach to avoid inconsistencies between measured geoacoustic response and the predictions of the theory. For example, the presence of a large population of bacteria in the interstices of the near-bottom sediment suggested that the overall apparent compressibility of the pore water may be somewhat different than that of pure water containing no organic contaminants. For this reason the fluid bulk modulus of the interstitial water, K_f, was chosen to be somewhat different than the value that would result in a velocity of 1536 m/s, which is the velocity that would be inferred for uncontaminated bottom water based strictly on temperature and salinity. The value for modeling was chosen to produce a p-wave velocity at low frequencies that matched our field measurements using the Wood equation (or the full Biot equations which reduce to the Wood equation at low frequency). An alternative way to account for the effect of the bacteria might be to alter the bulk modulus of the sand grains assuming that the organic material exists as a coating on the grains.

TABLE I. Input parameters for preliminary Biot model.

Physical property	Symbol (units)	Value
Density of grains	ρ_r (kg/m^3)	2.65×10^3
Density of fluid	ρ_f (kg/m^3)	1.026×10^3
Bulk modulus of grains	K_r (N/m^2)	3.6×10^{10}
Bulk modulus of fluid	K_f (N/m^2)	2.27×10^9
Bulk modulus of frame	K_b (N/m^2)	2.63×10^7
Shear modulus of frame	G_b (N/m^2)	1.98×10^7
Porosity	n	0.4
Permeability	k (m^2)	2.0×10^{-11}
Structure parameter	α	1.15
Log decrement of frame	δ	0.2
Pore-size parameter	a (cm)	0.002 and 0.0007

The two dispersion curves in Fig. 11 show the effect of changing the pore-size parameter, a from 0.0007 to 0.002 cm with other parameters held constant. As mentioned previously, the low- and high-frequency results from the SAX99 experiments as well as the cross-hole and critical angle experiments are also shown. It is clear from this figure that the preliminary Biot models chosen for this illustration predict velocity dispersion that approaches the experimental results at high and low frequencies; however, without more experimental results in the intermediate range, the ''best'' value for a is not fully defined. Other values of parameters such as permeability and structure factor appropriate for the sediment being studied produce similar curves shifted somewhat in frequency and velocity span. Thus, it is possible to fit a wide variety of experimental results that corresponds to the almost-infinite variety of sediments found in nature.

Figure 12 shows the p- and s-wave attenuation corresponding to the two dispersion curves of Fig. 11, as well as the range of p-wave values measured in the SAX99 high-frequency experiments. Also shown are the p-wave attenuations measured in the cross-hole experiments and shear-wave attenuation measured by the LDEO team at 25 Hz and the NRL team at 1 kHz.[11] Here again, it is clear that there is a complete lack of experimental data for p-wave attenuation at frequencies below 1 kHz. Finally, one of the most interesting aspects of this figure is the fact that an extrapolation down in frequency assuming that the attenuation varies linearly with

frequency (see the guideline labeled ''first power of frequency dependence'') results in a considerable mismatch with the lower-frequency values predicted by the Biot model.

VI. SUMMARY AND CONCLUSIONS

A comparison of *p*-wave velocities measured at high (11–50 kHz) and low (50–200 Hz) frequencies in a uniform sand stratum just below the seafloor indicates that there is a significant amount of velocity dispersion occurring in the frequency interval between these extremes. Moreover, recent experimental data at frequencies within this interval involving both direct cross-hole measurements and measurements of the critical angle substantiate this conclusion. This kind of pronounced dispersion occurring at a critical frequency in the intermediate frequency range is predicted by the Biot theory and is attributable to pore fluid motion relative to the skeletal frame of the sediment. In addition to the observed velocity dispersion, the theory predicts that intrinsic attenuation will be a nonlinear function of frequency because of the combination of viscous losses due to fluid motion relative to the frame and frictional losses occurring at the intergranular contacts.

In view of the above, it is clear that the often-used assumption of a constant or nearly constant Q which leads to attenuation that varies essentially linearly with frequency and velocities that are nearly constant is not appropriate when modeling the seismoacoustic response of uniform coarse sediments such as sand when they are fully saturated. Moreover, the results presented herein show that the traditional method of cataloguing attenuation of a sediment by a single value valid at 1 kHz is likely to lead to misleading results when extrapolating over a significant frequency range on the basis of a linear variation with frequency.

A review of the available experimental data for velocity in the relatively low-frequency range (e.g., see Figs. 11 and 12) shows that more experimental work needs to be done in order to fully define the response at these frequencies and to offer guidance in the choice of model parameters.

ACKNOWLEDGMENT

The work described in this paper was supported by the Office of Naval Research, Code No. 321OA.

APPENDIX:

In the Biot theory, the equations of motion for compressional waves have solutions when the following characteristic equation is satisfied:

$$\begin{vmatrix} \overline{H}l^2-\rho\omega^2 & \rho_f\omega^2-\overline{C}l^2 \\ \overline{C}l^2-\rho_f\omega^2 & m\omega^2-\overline{M}l^2-i\omega F\eta/k \end{vmatrix}=0.$$

The two complex roots of this equation are of the form $l=l_r+il_i$, giving the attenuation l_i and the phase velocity ω/l_r for the first and second kind of dilatational waves. η is fluid viscosity, k is permeability, and m is an apparent mass defined as $m=\alpha\rho_f/n$, where n is porosity, ρ_f is fluid mass density, and α is the so-called structure factor. $F=F(\kappa)$ is a complex correction factor derived by Biot to account for the deviation from Poiseuille flow at higher frequencies. The argument κ has the form

$$\kappa=a(\omega\rho_f/\eta)^{1/2},$$

where a is the pore-size parameter. The operators $\overline{H}$, $\overline{C}$, and $\overline{M}$ are given by

$$\overline{H}=\frac{(K_r-\overline{K}_b)^2}{D-\overline{K}_b}+\overline{K}_b+4\overline{\mu}/3,$$

$$\overline{C}=\frac{K_r(K_r-\overline{K}_b)}{D-\overline{K}_b},\quad \overline{M}=\frac{K_r^2}{D-\overline{K}_b},$$

where

$$D=K_r(1+n(K_r/\overline{K}_f-1)).$$

K_r is the bulk modulus of the individual sediment grains, K_b is the bulk modulus of the assemblage of particles comprising the frame measured in a drained test, and $\overline{\mu}$ is the shear modulus of the frame in a water environment. The overbars indicate complex functions of frequency, ω. The above expressions for the moduli are strictly true only when the volumetric strain of the pore volume is the same as the volumetric strain of the frame (i.e., constant porosity-see Stoll[5], pp. 9–10).

There have been several recent papers[23,24] that offer approximations to the full Biot theory which avoid the necessity of evaluating $F(\kappa)$ and solving the fourth-order equation given above. These approximations are particularly useful when making the preliminary choice of parameters for a given sediment.

[1] M. A. Biot, ''Mechanics of deformation and acoustic propagation in porous dissipative media,'' J. Appl. Phys. **33**, 1982–1498 (1962).

[2] M. A. Biot, ''Generalized theory of acoustic propagation in porous dissipative media,'' J. Acoust. Soc. Am. **34**, 1254–1264 (1962).

[3] R. D. Stoll and G. M. Bryan, ''Wave attenuation in saturated sediments,'' J. Acoust. Soc. Am. **47**, 1440–1447 (1970).

[4] R. D. Stoll, ''Acoustic waves in saturated sediments,'' in *Physics of Sound in Marine Sediments*, edited by L. Hampton (Plenum, New York, 1974), pp. 19–39.

[5] R. D. Stoll, *Sediment Acoustics* (Springer, Berlin, 1989).

[6] R. D. Stoll and E. O. Bautista, ''Using the Biot theory to establish a baseline geoacoustic model for seafloor sediments,'' Cont. Shelf Res. **18**, 39–1857 (1998).

[7] E. L. Hamilton, ''Compressional wave attenuation in marine sediments,'' Geophysics **37**, 620–646 (1972).

[8] E. L. Hamilton, ''Acoustic properties of sediments,'' in *Acoustics and the Ocean Bottom*, edited by A. Lara-Asaen, C. anz Guerraz, and C. Carbo-Fite [Consejo Superio de Invesigaciones Cientficas (CSIC), Madrid (1987)].

[9] R. D. Stoll and T. K. Kan, ''Reflection of acoustic waves at a water–sediment interface,'' J. Acoust. Soc. Am. **70**, 149–156 (1981).

[10] R. D. Stoll, E. O. Bautista, and R. Flood, ''New tools for studying seafloor geotechnical and geoacoustic properties,'' J. Acoust. Soc. Am. **96**, 2937–2944 (1994).

[11] M. D. Richardson, K. B. Briggs, L. D. Bibee, P. A. Jumars, W. B. Sawyer, D. B. Albert, R. H. Bennett, T. K. Burger, M. J. Buckingham, N. P. Chotiros, P. H. Dahl, N. T. DeWitt, P. Fleicher, R. Flood, C. F. Greenlaw, D. V. Holliday, M. H. Hulbert, M. P. Hutnak, P. D. Jackson, J. S. Jaffe, H. P. Johnson, D. L. Lavoie, A. P. Lyons, C. S. Martens, D. E. McGehee, K. D. Moore, T. H. Orsi, J. N. Piper, R. I. Ray, A. H. Reed, R. F. L. Self, J. L. Schmidt, S. G. Shock, F. Simonet, R. D. Stoll, D. Tang, D. E. Thistle, E. I. Thorsos, D. J. Walter, and R. A. Wheatcroft, ''Overview of SAX99: Environmental considerations,'' IEEE J. Ocean. Eng. **26**, 26–53 (2001).

[12] E. I. Thorsos, K. L. Williams, N. P. Chotiros, J. T. Christoff, K. W. Commander, C. F. Greenlaw, D. V. Holliday, D. R. Jackson, J. L. Lopes, D. E. McGehee, J. E. Piper, M. D. Richardson, and D. Tang, ''An overview of SAX99: Acoustics measurements,'' IEEE J. Ocean. Eng. **26**, 4–25 (2001).
[13] G. M. Bryan and R. D. Stoll, ''The dynamic shear modulus of marine sediments,'' J. Acoust. Soc. Am. **83**, 2159–2164 (1988).
[14] R. D. Stoll, G. M. Bryan, and E. O. Bautista, ''Measuring lateral variability of sediment geoacoustic properties,'' J. Acoust. Soc. Am. **96**, 427–438 (1994).
[15] A. Dziewonski, S. Block, and M. Landisman, ''A technique for analysis of transient seismic signals,'' Bull. Seismol. Soc. Am. **59**, 427–444 (1969).
[16] S. Bloch and A. L. Hales, ''New techniques for determination of surface wave phase velocities,'' Bull. Seismol. Soc. Am. **58**, 1021–1034 (1968).
[17] H. Takeuchi and M. Saito, ''Seismic surface waves,'' in *Methods in Computational Physics, Vol. 11, Seismology: Surface Waves and Earth Oscillations* (Academic, New York, 1972), pp. 217–295.
[18] R. D. Stoll, G. M. Bryan, R. Mithal, and R. Flood, ''Field experiments to study seafloor seismoacoustic response,'' J. Acoust. Soc. Am. **89**, 2232–2240 (1991).
[19] F. S. Grant and G. F. West, *Interpretation Theory in Applied Geophysics* (McGraw-Hill, New York, 1965).
[20] Personal communication from Kevin Williams, University of Washington, Applied Physics Lab.
[21] A. Turgut and T. Yamamoto, ''Measurements of acoustic wave velocities and attenuation in marine sediments,'' J. Acoust. Soc. Am. **87**, 2376–2383 (1990).
[22] A. Maguer, E. Bovio, W. L. J. Fox, and H. Schmidt, ''*In situ* estimation of sediment sound speed and critical angle,'' J. Acoust. Soc. Am. **108**, 987–996 (2000).
[23] M. Badiey, A. H-D. Cheng, and Y. Mu, ''From geology to geoacoustics—Evaluation of Biot–Stoll sound speed and attenuation for shallow water acoustics,'' J. Acoust. Soc. Am. **103**, 309–320 (1998).
[24] A. Turgut, ''Approximate expressions for viscous attenuation in marine sediments: Relating Biot's 'critical' and 'peak' frequencies,'' J. Acoust. Soc. Am. **108**, 513–518 (2000).

Seabed classification from acoustic profiling data using the similarity index

Han-Joon Kim, Jae-Kyeong Chang, Hyeong-Tae Jou, Gun-Tae Park, and Bong-Chool Suk
Korea Ocean R & D Institute, Ansan, P.O. Box 29, 425-600, Korea

Ki Young Kim
Department of Geophysics, Kangwon National University, 200-701, Korea

(Received 22 January 2001; revised 19 October 2001; accepted 13 November 2001)

We introduce the similarity index (SI) for the classification of the sea floor from acoustic profiling data. The essential part of our approach is the singular value decomposition of the data to extract a signal coherent trace-to-trace using the Karhunen–Loeve transform. SI is defined as the percentage of the energy of the coherent part contained in the bottom return signals. Important aspects of SI are that it is easily computed and that it represents the textural roughness of the sea floor as a function of grain size, hardness, and a degree of sediment sorting. In a real data example, we classified a section of the sea floor off Cheju Island south of the Korean Peninsula and compared the result with the sedimentology defined from direct sediment sampling and side scan sonar records. The comparison shows that SI can efficiently discriminate the bottom properties by delineating sediment-type boundaries and transition zones in more detail. Therefore, we propose that SI is an effective parameter for geoacoustic modeling. © *2002 Acoustical Society of America.* [DOI: 10.1121/1.1433812]

PACS numbers: 43.30.Ma, 43.30.Gv [DLB]

I. INTRODUCTION

High-resolution profiling systems are used to reveal geological structure of the sea floor composed of various types of sediments and rocks. A great deal of work has been performed to quantitatively determine or discriminate physical properties of the sea floor from profiling data. These studies encompass a wide spectrum of data processing. Earlier studies used monochromatic sonar data for the direct measurement of a pressure reflection coefficient of the sea floor.[1] Milligan *et al.*[2] introduced a statistical approach using the Karhunen–Loeve (KL) transform. Instead of measuring the reflection coefficient, they utilized the entire acoustic echo signal from the sea floor. They classified the sea floor in a certain area according to the textural difference resulting from the cluster analysis of a whole set of data. With the development of a wideband chirp sonar, more quantitative approaches were introduced to estimate parameters of surficial sediments such as reflection and attenuation coefficients.[3–5] The wide frequency band nature of the chirp sonar was also utilized to recognize the statistical properties of the bottom type based on time-frequency analysis.[6]

In this paper, we present the similarity index (SI) as a new acoustic measure for sea floor classification. Our method is similar to that of Milligan *et al.*[2] in that both are based on the KL transform. However, the computation of SI does not require the whole set of data like their cluster analysis does; instead, it is computed from several consecutive return traces. Further, SI, although computed statistically, is a physical parameter that appears to represent the variation of the sea floor in terms of surface texture and sediment type. Our discussions are illustrated with a real data example that includes a verification by dense sediment sampling and side scan sonar records.

II. THE SIMILARITY INDEX (SI) FROM THE KL TRANSFORM

The KL transform produces a set of uncorrelated (orthogonal) principal components from the data set, thus has been widely applied to seismic data analysis and digital image enhancement.[7–9] Although there are many ways to implement the KL transform, the singular value decomposition (SVD) approach of Freire and Ulrych[10] is a straightforward way.

Let $\mathbf{X}$ be an acoustic profiling data matrix which contains M traces each with N data points, i.e.,

$$X=\{x_{ij}\}, \quad i=1,2,\ldots,M; \quad j=1,2,\ldots,N. \tag{1}$$

The SVD of $\mathbf{X}$ is given by

$$X=\sum_{i=1}^{r} \sigma_i u_i v_i^T, \tag{2}$$

where superscript T indicates transpose, r is the rank of $\mathbf{X}$, u_i is the ith eigenvector of $\mathbf{XX^T}$, v_i is the ith eigenvector of $\mathbf{X^TX}$, and σ_i is the ith singular value of $\mathbf{X}$. The singular values σ_i are the positive square roots of the eigenvalues of the covariance matrices $\mathbf{XX^T}$ or $\mathbf{X^TX}$ (Lanczos[11]). In Eq. (2) the factor $u_i v_i^T$ is an $(M\times N)$ matrix of unit norm which is called the ith eigenimage of $\mathbf{X}$. Since the singular values are always ordered in decreasing magnitude, the greatest contributions in the representation of $\mathbf{X}$ are contained in the first eigenimages.

If the data are considered to be composed of traces which show a high degree of trace-to-trace correlation, $\mathbf{X}$

 0001-4966/2002/111(2)/794/6/$19.00

may be reconstructed from only the first few eigenimages. Reconstruction using the first few singular values is called the principal component reconstruction. Whereas, reconstruction using the remaining singular values is called the misfit reconstruction.

Freire and Ulrych[10] showed that the percentage of energy contained in a reconstructed image is given by E, where

$$E=\frac{\Sigma_{i=p}^{q}\sigma_i^2}{\Sigma_{i=p}^{r}\sigma_i^2}, \quad 1\leqslant p\leqslant q\leqslant r. \tag{3}$$

The choice of p and q depends on the relative magnitudes of the singular values, which are a function of the input data.

The acoustic return from the sea floor is the sum of both reflected and scattered signals. In general, acoustic profiling data are gathered continuously in the form of signal traces at a very short interval. When the sea floor is flat over a short distance, we regard it appropriate that the sea floor condition varies negligibly, and consequently reflections are coherent. Whereas, the incoherent part of the data is assumed to arise from various inhomogeneities on a variety of scales at the sea floor and in its surficial volume that are reflective of roughness and degree of sediment sorting. There is a strong correlation between grain size and sorting;[12] finer grained sediments are well sorted; in contrast, coarser grained sediments tend to be poorly sorted not only because they are hardly uniform in size but also because abundant intergranular pores accommodate smaller particles such as silt and fine sand. Coarse sediments will also increase the textural roughness of the sea floor. Therefore, coarse sediments increase inhomogeneities internal and external. These inhomogeneities are small compared with the wavelength of a pulse generated from acoustic profiling devices, giving rise to scattering.

Milligan *et al.*[2] showed that in their experiment the largest characteristic root of the covariance matrix accounted for 97% of the observed variance. This means that almost all of pure reflectivity of the bottom can be reconstructed from the first principal component. Although the analysis of Milligan *et al.* required all the acoustic return signals collected in the survey area, the same principle can be applied to a much smaller data set. If a coherent signal in adjoining traces refers to an event which is similar horizontally in a trace-to-trace sense, it is contained in the first eigenimage. We thus take q as 1 in Eq. (3) to measure the coherence of a few consecutive return pulses. The resultant quantity is referred to as the similarity index (SI):

$$\mathrm{SI}=\frac{\sigma_1^2}{\Sigma_{i=p}^{r}\sigma_i^2}. \tag{4}$$

From Eq. (4) it is easily conceived that SI ranges from 0 to 1 for various seabed conditions and increases in accordance with homogeneity and softness of the bottom. On the contrary, textural inhomogeneity and large roughness will result in a decreased SI value.

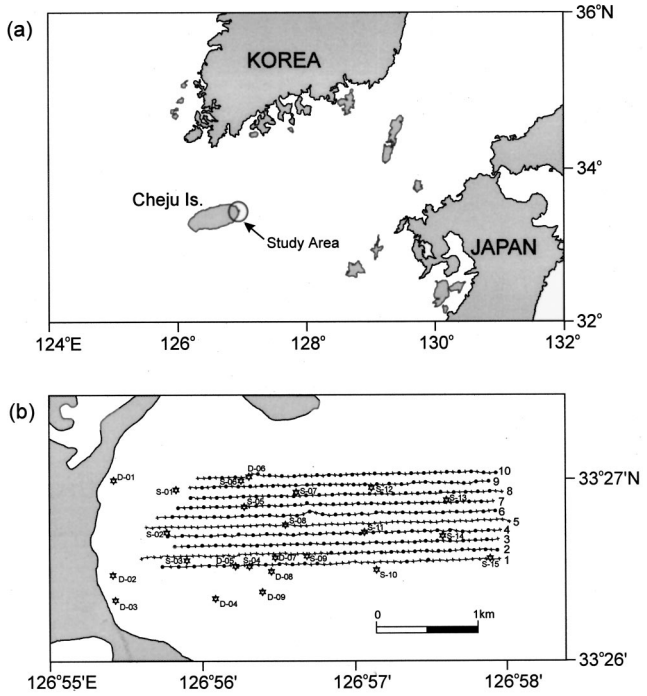

FIG. 1. (a) Location map of the study area. (b) Locations of chirp sonar profiles off the east coast of Cheju Island with positions of sediment sampling using a grab and by divers.

For some discrimination methods of the sea floor using acoustic profiling data, it is necessary to correct for amplifier gains and spreading losses. This is especially true when a pressure reflection coefficient of the bottom is directly measured. Even the statistical grouping method of Milligan *et al.*[2] needed such correction to obtain mean acoustic reflection. The KL transform dictates that if $\mathbf{X}$ consists of M traces equal to within a scale factor, $\mathbf{X}$ can be perfectly reconstructed by the first eigenimage $\sigma_1 u_1 v_1^T$. Therefore, SI is independent of ping-to-ping amplitude variation induced by extraneous factors such as amplifier gains and spreading losses.

III. EXPERIMENT AND RESULT

A. Data collection

A high-resolution profiling survey was carried out off the east coast of Cheju Island south of the Korean Peninsula (Fig. 1). The chirp sonar system (model: Data Sonics CAP 6000W) was set up and calibrated to transmit a 20 ms pulse ranging in frequency from 1 to 10 kHz at a repetition rate of 250 ms. Since the ship's speed was kept at 5 knots, this repetition rate corresponds to 0.64 m distance. The survey area was covered by 10 east–west lines at an interval of 100 m each about 3.5 km long (Fig. 1). Along with chirp profiles, side scan sonar records were collected to obtain the sea floor image of the survey area. For ground truth, surficial sediments were sampled at 23 points using a grab and by divers. These sediment samples were analyzed for grain size and sediment type (Table I).

The water depth in the survey area increases monotonously seawards from 6 to 92 m. Figure 2 is the sea floor features map of the survey area synthesized from sediment

TABLE I. The results of bottom sediment analysis (S=grab, D=Diving).

Sample No.	Sediment texture (%)				Type	Mean grain size (Φ)
	Gravel	Sand	Silt	Clay		
S-01		99.94	0.06		*S*	2.12
S-02		99.92	0.08		*S*	2.43
S-03		99.88	0.12		*S*	2.06
S-04	2.16	97.63	0.21		(*g*)*S*	2.31
S-05	0.27	99.57	0.16		(*g*)*S*	1.93
S-06		99.78	0.22		*S*	2.18
S-07		99.82	0.18		*S*	2.17
S-08		99.78	0.22		*S*	2.27
S-09		99.50	0.50		*S*	2.35
S-10	0.19	99.67	0.14		(*g*)*S*	1.46
S-11		99.89	0.11		*S*	2.16
S-12	52.77	46.77	0.46		*sG*	−0.98
S-14	36.20	35.08	8.23	20.47	*msG*	2.39
S-15	7.90	47.67	15.09	29.36	*gmS*	4.68
D-02	0.08	99.75	0.17		(*g*)*S*	2.29
D-03		99.90	0.10		*S*	2.44
D-04		99.86	0.14		*S*	2.19
D-05		99.95	0.05		*S*	2.22
D-06		99.95	0.05		*S*	1.97
D-07		99.93	0.07		*S*	2.01
D-08		99.83	0.17		*S*	2.43
D-09		99.95	0.05		*S*	2.34

Mean grain size: Φ scale=$-\log_2$ (mean grain diameter in mm). Sediment type: *S* (sand), (*g*)*S* (gravely sand), *sG* (sandy gravel), *msG* (mud–sand–gravel), *gmS* (gravel–mud–sand).

analysis results and side scan records. Sediments in the study area are mainly clastic, varying from sands, gravelly muddy sands, to muddy sands accordingly as the seabed deepens to the east. The northeastern and southwestern parts are characterized by outcrops of volcanic rocks. In particular, the rocks in the southwest are composed of consolidated (or lithified) volcanic ash deposited in the quaternary and termed the Shinyang-ri formation. Thus the sea bottom of the survey area is distinctively divided into five regions comprising (volcanic) sedimentary rock, sand, gravelly muddy sand, muddy sand, and volcanic rock.

B. Experimental result

The chirp sonar system transmits the chirp pulse that is a linearly frequency-modulated signal [Fig. 3(a)] between 1 and 10 kHz [Fig. 3(b)]. Because the recorded trace contains both the transmitted pulse and the bottom signal [Fig. 3(c)], the bottom signal portion of 20 ms consisting of 1000 samples was selected and matched filtered using the simulated pulse of transmission [Fig. 3(d)]. As a result, pulse

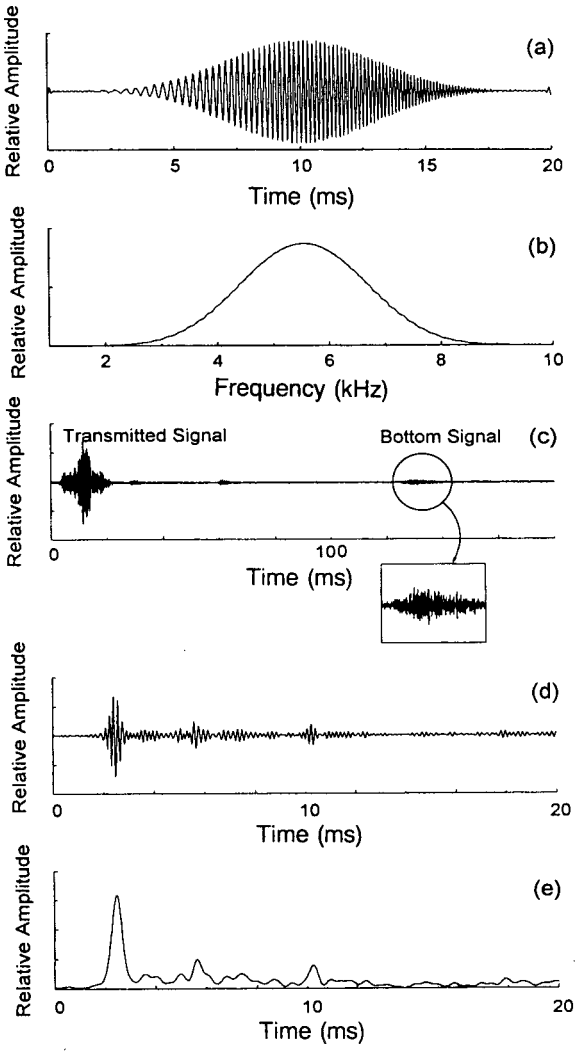

FIG. 3. (a) The transmitted chirp signal and (b) its amplitude spectrum. (c) A single chirp sonar trace. (d) The portion of the bottom return in (c) after matched filtering and (e) its envelope.

compression is achieved and a signal gain over background noise is enhanced. For display on the graphic record section the compressed signal is represented by its envelope [Fig. 3(e)].

To demonstrate the discrimination of the sea floor using SI, we illustrate a simple example. Figures 4(a), (b), and (c) represent 10 consecutive return signal traces after matched filtering from three different bottom types (panel 1): rock, inhomogeneous sand, and muddy sand, respectively. Inhomogeneous sand refers to a mixture of sediments consisting

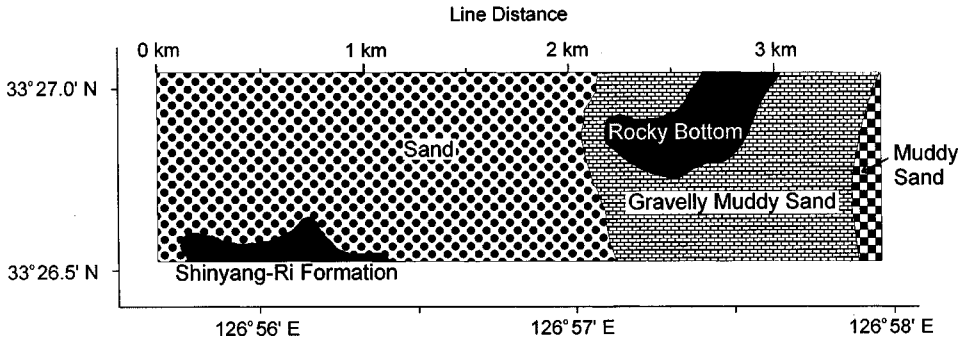

FIG. 2. The sea floor features map synthesized from sediment sample analysis and side scan sonar records.

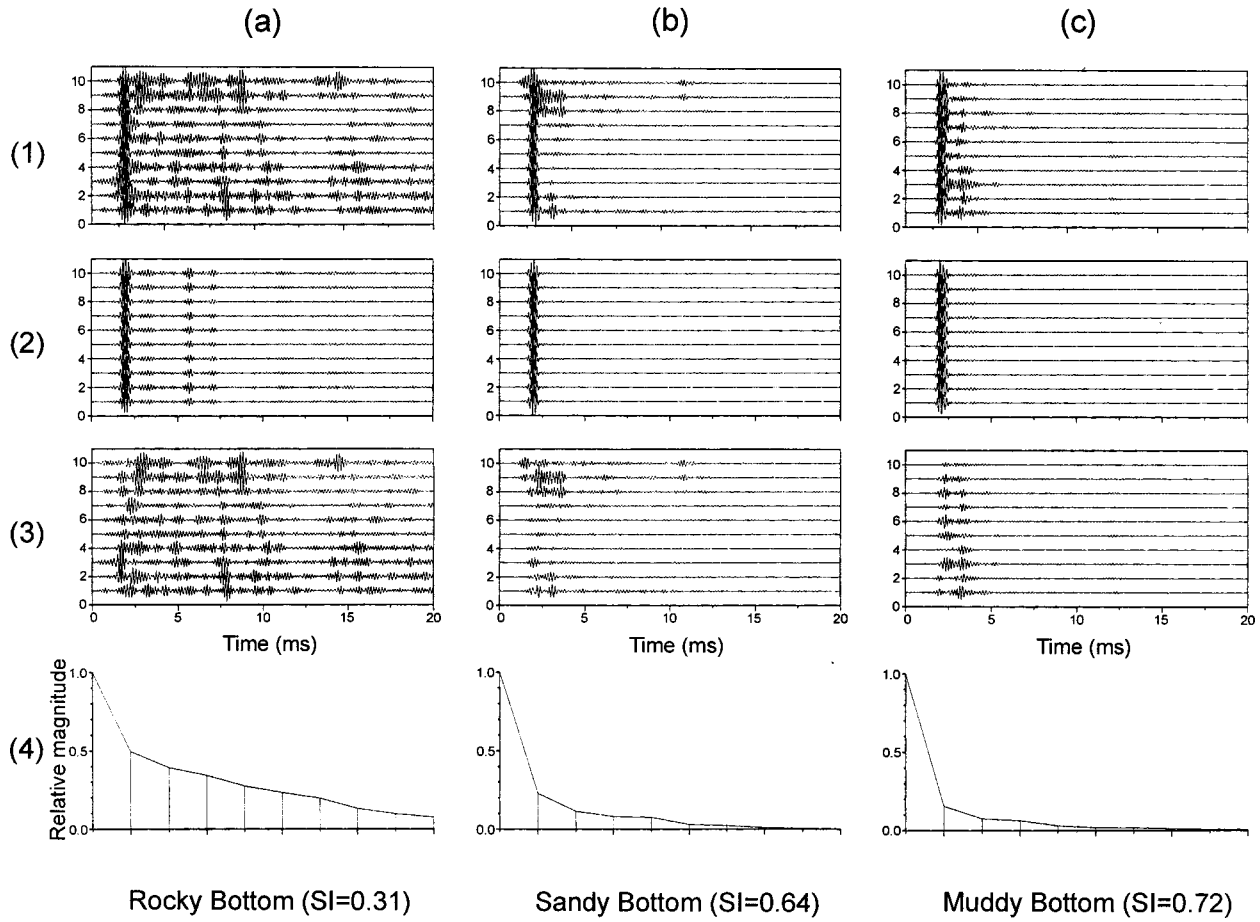

FIG. 4. Ten consecutive bottom returns from (a) rocky, (b) sandy, and (c) muddy sandy bottoms. From top to lowest panels are shown return traces (1) after time alignment, (2) principal component, (3) misfit reconstruction, and (4) plot of the relative magnitude of the eigenvalues associated with the data in panel (1).

of sand and smaller portions of gravel and silt (e.g., S-15 in Table I). The profiling traces were shifted so that the bottom return signals are aligned. The principal component and misfit reconstructions of aligned traces are shown in panel 2 and panel 3, respectively. The lowermost panel shows the variation of the relative magnitudes of the eigenvalues. In this particular case, Fig. 4 shows that the coherent signal for muddy sand is explained mostly by the first eigenimage [Fig. 4(c)], and for inhomogeneous sand the relative magnitude of the second eigenvalue slightly increases [Fig. 4(b)]. In contrast, for the rocky bottom, the magnitudes of the remaining eigenvalues are significant [Fig. 4(a)]. Quantitatively, SI is less than 0.4 for the rocky bottom, 0.5–0.7 for sand and higher than 0.7 for muddy sand. Because the bottom returns were aligned, SI does not contain the effect of irregular topography significantly. Therefore, SI is a useful parameter to distinguish the bottom type as a function of grain size, hardness, and degree of sorting which aggregately define the bottom sediment facies. A simplifying but feasible assumption is that the change in bottom geology is negligible over a distance interval of less than 6 m that corresponds to 10 consecutive traces. Consequently, adjacent traces do not differ drastically from each other. This observation allows SI to be computed from the KL transform of several consecutively recorded bottom returns.

Figure 5 shows the variation of SI values along the even numbered lines. The individual SI value was computed from

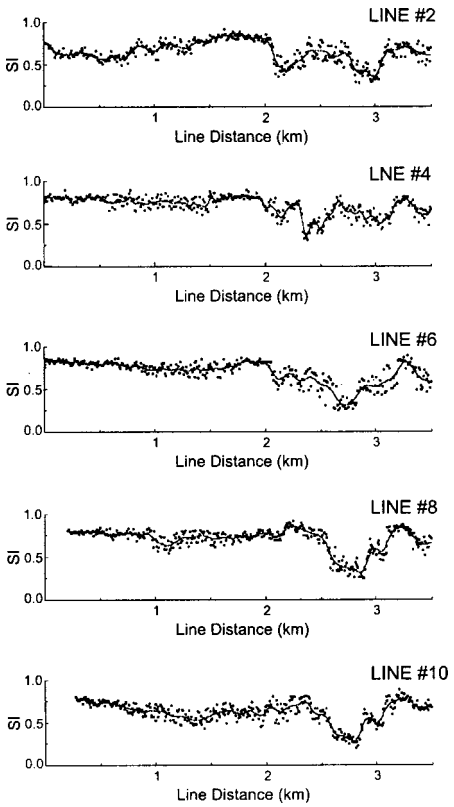

FIG. 5. The computed similarity index (SI) along even-numbered lines. For each line a piecewise smooth curve was fitted to SI values.

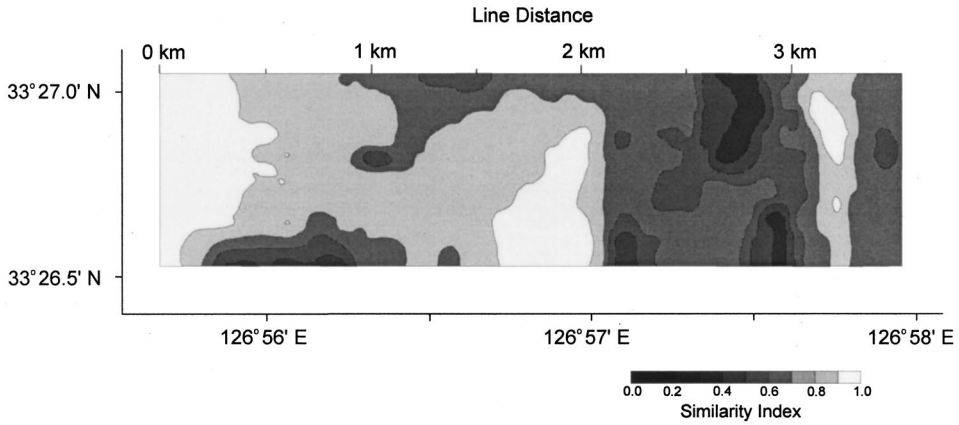

FIG. 6. The sea floor image map constructed from SI values.

a window consisting of 10 consecutive traces as in the previous example in a moving average fashion, then projected onto the survey track at the location of the central position of the window. In this example we plotted every tenth SI value. We fit a piecewise continuous curve to SI values using an average interval of five points that slided over the survey lines. However, some SI values show a small degree of deviation from the fitted curve. This deviation can probably be attributed to a local inhomogeneity and might have been exaggerated by the loss of continuity because every tenth SI value was plotted.

Figure 6 is the sea floor image of the survey area which was obtained by interpolating all the SI values using the bicubic spline scheme. A comparison of Figs. 2 and 6 shows a remarkable agreement on the discrimination of bottom types and enables certain general statements on the sedimentology of the survey area. The inner area contiguous to the shore except for the Shinyang-ri sedimentary rock outcrop is covered with homogeneous fine sand [Fig. 7(a)], showing high SI values of about 0.8. The lowest SI values of less than 0.4 are observed at the rocky bottom in the northeast between 2.6–2.8 km range. Figure 7(b) is the chirp sonar profile that shows the rock outcrop in this area characterized by internal scatters and stretching of bottom returns. The area surrounding the rocky bottom is associated with SI values of 0.4 to 0.6, which seems to define the transition zone from the relatively homogeneous sandy bottom to the rugged rocky bottom. In some parts adjacent to the rock outcrop, the bottom is covered with semi-consolidated material that is interpreted as relict sediments exposed after the removal of overlying fine grained sediments during the low sea level stand. In the southeastern part between 2.8 and 3.0 km distance, is located a north–south elongated belt of SI values much lower than the average. Sediment analysis indicates that the

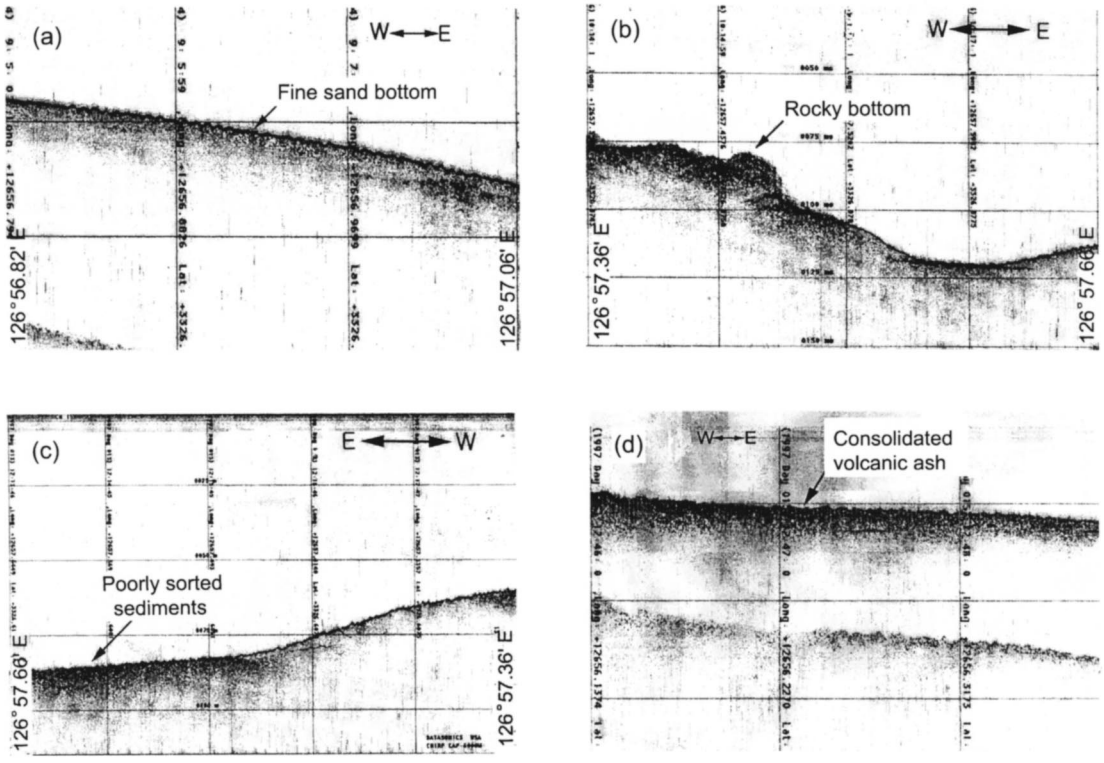

FIG. 7. Chirp sonar profiles for the sea floor composed of (a) fine sands, (b) rocks, (c) poorly sorted sediments, and (d) consolidated sediments.

bottom here is composed of a poorly sorted mixture of gravel, sand, and silt (S-14 in Table I), resulting in enhanced textural inhomogeneity which, in turn, made SI values comparable to those for the rocky bottom. The representative chirp sonar profile of this area [Fig. 7(c)] shows internal chaotic facies that are distinguished from the adjacent homogeneous sand bottom [Fig. 7(a)]. The Shinyang-ri formation in the southwest composed of consolidated volcanic ash is also characterized by low SI values of 0.4–0.6 whose pertinent profile [Fig. 7(d)] is suggestive of textural irregularity.

The previous discussions showed that SI can discriminate the different bottom sediment types and the sediment/rock boundary. Moreover, the clear definition of transition zones is expected to provide valuable information on the facies changes. The excellent internal consistency observed in the regions of the same sediment type indicates the reliability of SI as a robust acoustic parameter.

IV. CONCLUSIONS

In this paper, we have presented the similarity index (SI) as an acoustic measure to classify the sea floor. Since the singular value decomposition of adjoining acoustic profiling traces suffices for the computation of SI, this approach offers the advantage that the proposed processing scheme is extremely easy to implement. We have found by application to real data that (1) SI correlates well with the bottom sediment facies that is controlled by grain size, hardness, and degree of sorting, (2) SI, ranging from 0 to 1, increases in accordance with the homogeneity and softness of the bottom, and (3) sediment sampling and side scan sonar records verify the effective discrimination of the sea floor using SI. Further, the delineation of detailed facies boundaries and transition zones is achieved by the proposed method in this paper. These features suggest that SI can be a useful parameter for geoacoustic modeling that remotely discriminates the sea floor from acoustic data. Finally, although we have shown the real data example using the wideband chirp sonar, we would like to mention that SI is also effectively computed for monochromatic sonar profiling data and that real-time classification of the sea floor is possible because SI can be computed once a few consecutive profiling traces are acquired.

ACKNOWLEDGMENT

This research was supported by KORDI (Korea Ocean R & D Inst.) under grant PE01-817-02. Dr. D. J. Min (KORDI) kindly performed seismic modeling for a point diffractor, that provided significant insight into scattering. We dedicate this work to one of the authors, the late J.-K. Chang.

[1] S. H. Danbom, Ph.D. thesis, University of Connecticut, 1975.
[2] S. D. Milligan, L. R. LeBlanc, and F. H. Middleton, ''Statistical grouping of acoustic reflection profiles,'' J. Acoust. Soc. Am. **64**, 795–807 (1978).
[3] L. R. LeBlanc, L. Mayer, M. Rufino, S. G. Schock, and J. King, ''Marine sediment classification using the chirp sonar,'' J. Acoust. Soc. Am. **91**, 107–115 (1992).
[4] L. R. LeBlanc, S. Panda, and G. Schock, ''Sonar attenuation modeling for classification of marine sediments,'' J. Acoust. Soc. Am. **91**, 116–126 (1992).
[5] S. G. Schock, L. R. LeBlanc, and L. A. Mayer, ''Chirp subbottom profiler for quantitative sediment analysis,'' Geophysics **54**, 445–450 (1989).
[6] N. Andrieux, P. Delachartre, D. Vray, and G. Gimenez, ''Lake-bottom recognition using a wideband sonar system and time-frequency analysis,'' J. Acoust. Soc. Am. **98**, 552–559 (1995).
[7] H. C. Andrews and C. L. Patterson, ''Singular value decomposition and digital image processing,'' IEEE Trans. Acoust., Speech, Signal Process. **24**, 26–53 (1976).
[8] K. Mallick and Y. V. S. Murthy, ''Pattern of Landsat MSS data over Zawar lead-zinc mines, Rajasthan, India,'' First Break **2**, 16–21 (1984).
[9] I. F. Jones and S. Levy, ''Signal-to-noise ratio enhancement in multichannel seismic data via the Karhunen-Loeve transformation,'' Geophys. Prospect. **35**, 12–32 (1987).
[10] S. L. M. Freire and T. Ulrych, ''Application of singular value decomposition to vertical seismic profiling,'' Geophysics **53**, 778–785 (1988).
[11] C. Lanczos, *Linear Differential Operators* (Van Nostrand, New York, 1961).
[12] J. Gidman, W. J. Schweller, C. W. Grant, and A. A. Reed, ''Reservoir character of deep marine sandstones, Inglewood Field, Los Angeles Basin,'' in *Marine Clastic Reservoirs*, edited by E. G. Rhodes and T. F. Moslow (Springer-Verlag, New York, 1993), pp. 231–261.

A phase regulated back wave propagation technique for geoacoustic inversion

Reza M. Dizaji
Electrical and Computer Engineering Department, P.O. Box 3055, University of Victoria, Victoria, British Columbia V8W 3P6, Canada

N. Ross Chapman
Electrical and Computer Engineering Department and School of Earth and Ocean Sciences, P.O. Box 3055, University of Victoria, Victoria, British Columbia V8W 3P6, Canada

R. Lynn Kirlin
Electrical and Computer Engineering Department, P.O. Box 3055, University of Victoria, Victoria, British Columbia V8W 3P6, Canada

(Received 20 November 2000; revised 15 August 2001; accepted 30 October 2001)

An inversion method based on the concept of back wave propagation (BWP) is described in this paper for estimation of geoacoustic parameters from acoustic field data. A phase-regulation technique is introduced to increase the sensitivity of the method for geoacoustic model parameters having low sensitivity. The case of data consisting of signal plus additive noise is also addressed. It is shown theoretically that the sensitivity can be increased by a factor α using the phase regulation procedure, and that the spatial resolution of signal energy that is concentrated by BWP at the known source position is increased when α increases. This result suggests an effective criterion for use in the inversion, based on the spatial distribution of signal energy around the true source location. The basis for the criterion is the spatial variance of the back-propagated pressure field in a window around the known source location. A multistep search process is proposed to avoid using a complicated multidimensional search process. Inversion results from both simulations and experimental data are given. The real data were taken from the Pacific Shelf experiment carried out in shallow water off the West Coast of Vancouver Island in the Northeast Pacific Ocean. [DOI: 10.1121/1.1430691]

PACS numbers: 43.30.Nb, 43.30.Wi [DLB]

I. INTRODUCTION

In underwater acoustics there has been an intensive research effort over the past 20 years to develop model based signal processing methods for use in advanced sonar design. One of the techniques, known as matched field processing (MFP), has gained widespread use. MFP was described in the underwater acoustics literature initially as a generalized beam forming method for source localization with an array of sensors.[1–3] More recently, MFP has been applied as an inversion method to estimate either the source location or the environmental parameters of the ocean wave guide from measurements of the acoustic field.[4–7] The approach is to maximize or minimize an objective function that compares the measured acoustic pressure field with a modeled field (replica) that is calculated for a specific geoacoustic parametrization. Well-known processors such as the Bartlett, matched mode, minimum variance, and multiple constraints processors have been applied to data obtained using multisensor arrays.[8] The technique has been remarkably successful, and there is now an extensive literature on simulation and benchmarking exercises[9] and applications with experimental data in shallow water.[7]

An alternative picture of matched field processing is provided by the concept of back wave propagation (BWP). A method for source localization based on back propagation of acoustic fields calculated by the parabolic equation (PE) was originally suggested by Tappert *et al.* in 1985.[10] However, since then the technique has received relatively little attention in MFP, although Collins *et al.*[11] and Thomson *et al.*[12] have shown the use of BWP for source localization in range dependent environments. The recent time-reversal experiments in underwater acoustics are based on the same concept.[13] Back wave propagation is based on the reciprocity and superposition properties of the ocean wave guide which ensure that the measured pressure fields can be considered as sources for an array of transmitters. In practical terms, the conjugate of the measured field at the receiving array is weighted by the range and then back propagated from the array. If the geometry of the transmitting array is the same as the experimental geometry for the receiving array, then it can be shown[10] that only for the true ocean environmental parameters does the back-propagated wave field converge to the location of the source. Figure 1 shows a simple model of the forward and backward propagation geometry.

For geoacoustic inversions using conventional MFP methods it is well known that there can be weak sensitivity of the pressure field measurements to environmental parameters such as shear speed, shear attenuation, and density. In this paper we develop an inversion method based on BWP for estimating geoacoustic parameters in a shallow water wave guide. We introduce a post processing, phase regulation technique to improve the performance of the method for

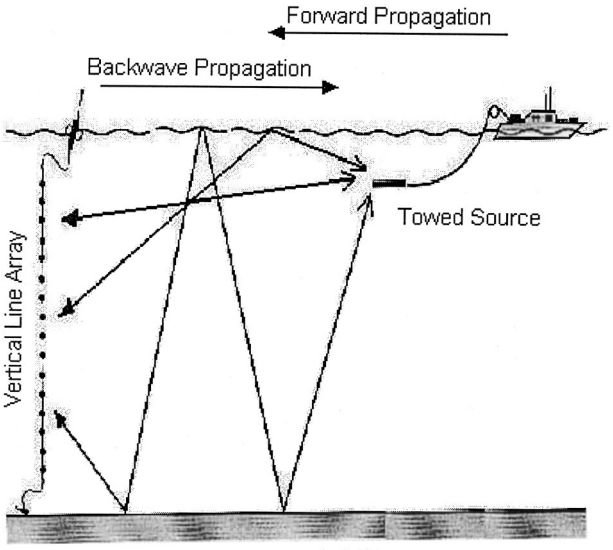

FIG. 1. Schematic diagram of the experimental geometry at the PACIFIC SHELF site, sketching the forward and back-propagated waves.

estimating parameters with low sensitivities. In this procedure we vary a sensitivity factor α that enhances the phase changes due to model and environmental mismatch. By appropriately choosing values of α we can estimate environmental parameters to a required accuracy. For convenience, we assume that the experimental source geometry is known. In practice, however, we are limited in choosing arbitrarily high values for α because of experimental noise in the data. The theory of this concept is presented in Sec. II, and in Sec. III we discuss the effects of noise on the sensitivity value and source location estimation.

In Sec. IV we introduce a criterion for estimating the best match between the measured field and the replica generated by the geoacoustic model parameters. The criterion minimizes the spatial variance of the back-propagated signal energy in the vicinity of the source location.

A significant disadvantage of MF inversion methods is the use of computationally intensive search methods to navigate the multidimensional model parameter space. To overcome this difficulty, we implement a multistage search process, based on appropriate choices of the sensitivity factors and environmental parameters, that approximates a multidimensional searching process with a series of search processes of reduced dimension.[9,14–16] The approximation is achieved by classifying the environmental parameters into three sets of high, medium, and low sensitivity, and then choosing an appropriate value of α for each set. This procedure is discussed in Sec. V.

Inversion results from simulations and experimental data are given in Sec. VI. The data were taken from the Pacific Shelf experiment[17] carried out in shallow water off the West Coast of Vancouver Island in the Northeast Pacific Ocean.

II. PHASE REGULATED BACK WAVE PROPAGATION

The BWP concept assumes that the fields received at an array of N sensors can be used as sources. The pressure field used as the source in the back-propagation step is the conjugate of the measured field, $P_f^*(r_a,z_k)$, $k=1,...,N$, that was transmitted from the experimental source and received at the array. Here r_a is the array range, z_k is the depth of the kth sensor and* denotes the complex conjugate. The back-propagated field, $P_b(r,z)$, at location (r,z) for a range-independent environment can be expressed using normal modes by[18]

$$P_b(r,z,\gamma)=\sum_{k=1}^{N}\frac{P_f^*(r_a,z_k,\gamma)}{4\rho(z_k)}\sum_{m=1}^{M}\Psi_m(z_k)\Psi_m(z)\times H_0^{(1)}(k_m r), \tag{1}$$

where $\gamma=[\gamma_1,\gamma_2,...,\gamma_q]$ is a vector that contains both the environmental and the source parameters, $\rho(z)$ is the depth dependent density function, $H_0^{(1)}$ is a Hankel function (type 1, order 0), and $\Psi_m(z)$ and k_m are the eigenfunction and the eigenvalue of the mth mode, respectively. Let us define the function $R_k(r,z,\gamma)$ as the pressure signal measured at a point (r,z) weighted by the square root of the range,

$$R_k(r,z,\gamma)=\frac{ir^{1/2}P_f^*(r_c,z_k,\gamma)}{4\rho(z_k)}\sum_{m=1}^{M}\Psi_m(z_k)\Psi_m(z)\times H_0^{(1)}(k_m r). \tag{2}$$

Using (2) and (1) we can express a range-weighted back-propagated field as

$$P_b(r,z,\gamma)=\sum_{k=1}^{N}|R_k(r,z,\gamma)|e^{i\phi_k(r,z,\gamma)}. \tag{3}$$

Although the phase $\phi_k(r,z,\gamma)$ of $R_k(r,z,\gamma)$ is very complicated, inspection of (2) shows that it becomes zero at the source location because the phase of the normal mode sum is exactly opposite to the phase of $P_f^*(r_a,z_k)$. As the back-propagated field point moves away from the source location, the phase is no longer zero and $P_b(r,z)$ will be smaller since the terms in (2) no longer combine in phase. Thus, the maximum values of $P_b(r,z,\gamma)$ occur whenever the phase $\phi_k(r,z,\gamma)\approx 0$; $k=1,...,N$.

To evaluate how the pressure signal changes with changes in the parameters, we introduce the *sensitivity vector*,

$$S=[S_1,S_2,...,S_q], \tag{4}$$

where

$$S_i=\left|\frac{\partial P_b(r,z,\gamma)}{\partial\gamma_i}\right|,\quad i=1,...,q. \tag{5}$$

Substituting (3) into (5), we obtain

$$S_i=\left|\sum_{k=1}^{N}\left(\frac{\partial|R_k(r,z,\gamma)|}{\partial\gamma_i}e^{i\phi_k(r,z,\gamma)}+i\frac{\partial\phi_k(r,z,\gamma)}{\partial\gamma_i}|R_k(r,z,\gamma)|e^{i\phi_k(r,z,\gamma)}\right)\right|. \tag{6}$$

In geoacoustic inversion it is well known that the changes in the signal pressure relative to changes in some particular environmental parameters are small. In order to overcome this problem we introduce a phase enhanced technique wherein we amplify the phase changes arising from

environmental mismatch by a *sensitivity factor* α. By multiplying the phase function $\phi_k(r,z,\gamma)$ in (3) by α we obtain

$$P_b^{\alpha}(r,z,\gamma)=\sum_{k=1}^{N}|R_k(r,z,\gamma)|e^{i\alpha\phi_k(r,z,\gamma)}. \tag{7}$$

For this new expression we calculate the sensitivity

$$S_i^{\alpha}=\left|\sum_{k=1}^{N}\left(\frac{\partial|R_k(r,z,\gamma)|}{\partial\gamma_i}e^{i\alpha\phi_k(r,z,\gamma)} + i\alpha\frac{\partial\phi_k(r,z,\gamma)}{\partial\gamma_i}|R_k(r,z,\gamma)|e^{i\alpha\phi_k(r,z,\gamma)}\right)\right|. \tag{8}$$

In the case of low sensitivity to an environmental parameter, the expressions in (6) and (8) are close to zero. We can approximate them by

$$S_i\approx\left|\sum_{k=1}^{N}\left(i\frac{\partial\phi_k(r,z,\gamma)}{\partial\gamma_i}|R_k(r,z,\gamma)|e^{i\phi_k(r,z,\gamma)}\right)\right| \tag{9}$$

and

$$S_i^{\alpha}\approx\left|\sum_{k=1}^{N}\left(i\alpha\frac{\partial\phi_k(r,z,\gamma)}{\partial\gamma_i}|R_k(r,z,\gamma)|e^{i\alpha\phi_k(r,z,\gamma)}\right)\right|. \tag{10}$$

In the BWP technique the geoacoustic model parameter mismatch can be evaluated by assessing the spatial resolution of the back-propagated signal that is focused near the source. These regions of strong focus refer to the places where $\phi_k(r,z,\gamma)\approx 0;\ k=1,...,N$. At these points S_i and S_i^{α} take the form

$$S_i\approx\left|\sum_{k=1}^{N}\left(i\frac{\partial\phi_k(r,z,\gamma)}{\partial\gamma_i}|R_k(r,z,\gamma)|\right)\right| \tag{11}$$

and

$$S_i^{\alpha}\approx|\alpha|\left|\sum_{k=1}^{N}\left(i\frac{\partial\phi_k(r,z,\gamma)}{\partial\gamma_i}|R_k(r,z,\gamma)|\right)\right|=|\alpha|S_i. \tag{12}$$

Referring to (3) and (7), the back-propagated field will still be zero at the true source location if the phase terms are multiplied by α, since the phases $\phi_k(r,z,\gamma)$ are all zero at that point. However, as the field point moves away from the source location, the terms in (7) will get out of phase more rapidly and the peak occurring at the source will become narrower. Thus, the sensitivity of the back-propagated field to a particular parameter is increased by the sensitivity factor α. In principle by appropriately choosing α we can estimate environmental parameters to a required resolution. The effect of noise in limiting the value of α is considered in Sec. III.

Applying the phase factor also changes the spatial resolution of the focused energy points; i.e., it concentrates the back-propagated signal that is focused near the source. We can show this by calculating the derivative of $P_b^{\alpha}(r,z,\gamma)$ with respect to the displacement vector $\mathbf{u}=(r,z)$ at the focused energy points:

$$\frac{\partial P_b^{\alpha}(\mathbf{u},\gamma)}{\partial\mathbf{u}}=\sum_{k=1}^{N}\left(\frac{\partial|R_k(\mathbf{u},\gamma)|}{\partial\mathbf{u}}e^{i\alpha\phi_k(\mathbf{u},\gamma)} + i\alpha\frac{\partial\phi_k(\mathbf{u},\gamma)}{\partial\mathbf{u}}|R_k(\mathbf{u},\gamma)|e^{i\alpha\phi_k(\mathbf{u},\gamma)}\right). \tag{13}$$

Since the changes in the signal pressure with respect to changes in location are small relative to the effect of the changes in phase, Eq. (13) can be rewritten as

$$\frac{\partial P_b^{\alpha}(\mathbf{u},\gamma)}{\partial\mathbf{u}}\approx\alpha\sum_{k=1}^{N}\left(i\frac{\partial\phi_k(\mathbf{u},\gamma)}{\partial\mathbf{u}}|R_k(\mathbf{u},\gamma)|e^{i\alpha\phi_k(\mathbf{u},\gamma)}\right). \tag{14}$$

At focused points $[\phi_k(r,z,\gamma)\approx 0;k=1,...,N]$ we obtain

$$\frac{\partial P_b^{\alpha}(\mathbf{u},\gamma)}{\partial\mathbf{u}}\approx\alpha\sum_{k=1}^{N}\left(i\frac{\partial\phi_k(\mathbf{u},\gamma)}{\partial\mathbf{u}}|R_k(\mathbf{u},\gamma)|\right) \approx\alpha\frac{\partial P_b(\mathbf{u},\gamma)}{\partial\vec{\mathbf{u}}}. \tag{15}$$

III. NOISE EFFECTS

Because of background noise, we are limited in choosing arbitrarily high values for α. Let us assume that the noise effect appears in the form of an additive random phase with a uniform distribution having a depth dependent mean equal to $\phi_{k,0}$ and variance d_k. The total field in the presence of noise is then

$$P_f^n(r_a,z_k,\gamma)=P_f(r_a,z_k,\gamma)e^{i\phi_{k,n}}. \tag{16}$$

If we substitute (16) into (3) and use the fact that $E\{e^{i\phi_{k,n}}\}=2[\sin(d_k)/d_k]e^{i\phi_{0,k}}$, we can write the back-propagated field as

$$E\{P_b(r,z,\gamma)\}=\sum_{k=1}^{N}|R_k(r,z,\gamma)|e^{i\phi_k(r,z,\gamma)}E\{e^{i\phi_{k,n}}\} =2\sum_{k=1}^{N}|R_k(r,z,\gamma)|\frac{\sin(d_k)}{d_k}e^{i\phi_{0,k}}e^{i\phi_k(r,z,\gamma)}. \tag{17}$$

The maximum value of $E\{P_b(r,z,\gamma)\}$ now occurs whenever

$$\phi_k(r,z,\gamma)+\gamma_{0,k}\approx 0;\quad k=1,...,N. \tag{18}$$

The meaning of (18) is that noise causes a distortion in the phase function that results in a bias in the source location estimation. When incorporating the phase factor α we have

$$E\{P_b^{\alpha}(r,z,\gamma)\} =2\sum_{k=1}^{N}|R_k(r,z,\gamma)|\frac{\sin(\alpha d_k)}{\alpha d_k}e^{i\alpha\phi_{k,0}}e^{i\alpha\phi_k(r,z,\gamma)}. \tag{19}$$

The sensitivity factor α does not have a significant effect on the source localization estimate since the zeros of Eq. (18) are not affected by α.

Following the procedure used to obtain Eq. (17), the sensitivity function in the presence of noise becomes ($\alpha=1$)

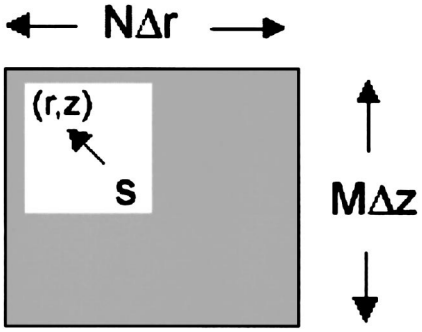

FIG. 2. Diagram of the reduced $N\Delta r \times M\Delta z$ search window around the source location S, within which the focal function is evaluated.

$$S_i \approx 2\left|\sum_{k=1}^{N}\left(i\frac{\partial\phi_k(r,z,\gamma)}{\partial\gamma_i}\frac{\sin(d_k)}{d_k}|R_k(r,z,\gamma)|\right)\right|, \quad (20)$$

assuming that $\phi_{k,0}$ is small enough that the bias imposed on the source location is negligible. Equation (20) indicates that the phase variation due to the background noise has considerable effect on the sensitivity function. The sensitivity nulls occur for $d_k = n\pi$, $n =$ integer for all k. For $\alpha \neq 1$, Eqs. (12) and (19) show that the phase regulated sensitivity for $\phi_{k,0}$ small is

$$S_i^{\alpha} \approx 2\alpha\left|\sum_{k=1}^{N}\left(i\frac{\partial\phi_k(r,z,\gamma)}{\partial\gamma_i}\frac{\sin(\alpha d_k)}{\alpha d_k}|R_k(r,z,\gamma)|\right)\right|. \quad (21)$$

From Eq. (21) we see that for the α-enhanced phase the sensitivity amplification is modified by the phase variation due to the noise. For very small phase variance d_k we have $\sin(\alpha d_k)/\alpha d_k \approx 1$ and obtain the same results as for the noiseless case.

IV. THE BWP FOCAL FUNCTION

The essence of the BWP technique is the convergence of back-propagated waves at the true source location if the environmental model parameters are exactly matched to the true environment. However, if there is mismatch in the model parameters, there will be instead a distribution of the back-propagated field around the source position. This fact leads us to consider the distribution of the back-propagated field near the source as a criterion to determine the best set of model parameters. A measure of the field distribution is obtained by calculating the field spatial variance with respect to the true source location in a window around the source (see Fig. 2). Its value is minimized when most of the signal energy concentrates at the source point, i.e., for the best match between the estimated geoacoustic model parameters and the true environment.

Let us define

$$f(r,z), \quad |r-r_0| \leqslant \frac{N\Delta r}{2}, \quad |z-z_0| \leqslant \frac{M\Delta z}{2}$$

as the back-propagated energy in an $N\Delta r \times M\Delta z$ spatial window around the true source location, (r_0, z_0), where $\|f\| = 1$ and $\|\cdot\|_F^{\beta}$ denotes the Frobenius norm. The best match criterion minimizes the spatial variance of the back-propagated field strength with respect to the true source location. If we denote

$$f(r,z) = \frac{|P_b^{\alpha}(r,z,\gamma)|^{\beta}}{\|P_b^{\alpha}(r,z,\gamma)\|_F^{\beta}}$$

as the distance probability density function, the criterion can be interpreted (with $\beta = 2$) as the mean square distance of the normalized field strength from the true source location

$$\mathrm{BWP}_{\mathrm{criterion}} = \frac{1}{MN}\sum_{m=-M/2}^{M/2}\sum_{n=-N/2}^{N/2} d^2(r_n, z_m) f(r_n, z_m), \quad (22)$$

where

$$d(r_n, z_m) = \sqrt{(r_n - r_0)^2 + (z_m - z_0)^2}.$$

We refer to the above criterion as the BWP focal function.

V. AN EFFICIENT MULTISTEP SEARCH PROCEDURE

A direct way to find the best estimates of D unknown environmental parameters is to use a D-dimensional grid search among possible parameter values. Since this search is generally computationally expensive, we can reduce the D-dimensional search space to a series of T successive d-dimensional search space ($D = Td$ where $T < D$) by exploiting the fact that the pressure field has different sensitivity with respect to different parameters.[9,14–16] For example, the pressure field is most sensitive to the water depth even for small sensitivity factors while for a small sensitivity factor α, the field is only weakly sensitive to changes with respect to other environmental parameters such as shear wave speed and density changes. A block diagram of the search procedure is shown in Fig. 3.

In summary we first estimate the most sensitive parameter(s) such as water depth. In the next step we search among potential values of medium sensitivity parameters such as compressional speed using a greater value of α. For this value of α the sensitivity to the remaining less sensitive parameters such as density remains low. At the last step we increase the sensitivity factor to a higher value to adjust the parameters with the lowest sensitivity. At each step in the inversion process we use the estimated values for the more sensitive parameters that were determined from the previous steps. This example gives a three-step technique. We can increase the number of steps by more precisely categorizing the environmental parameters.

VI. BWP INVERSION OF SIMULATED AND EXPERIMENTAL DATA

In the first part of this section we present results of an inversion of simulated data for a 45 Hz continuous wave (CW) source at a depth of 30 m and a range of 5.6 km from a 16-element vertical line array. The array hydrophones are equispaced 15 m apart from a depth of 90 m in the water column. This geometry simulated the source and receiver configuration from the Pacific Shelf experiment.[17] In the second part, we apply the BWP inversion to the experimental data. For both inversions, the back-propagated fields were calculated using the normal mode code ORCA.[19] This ap-

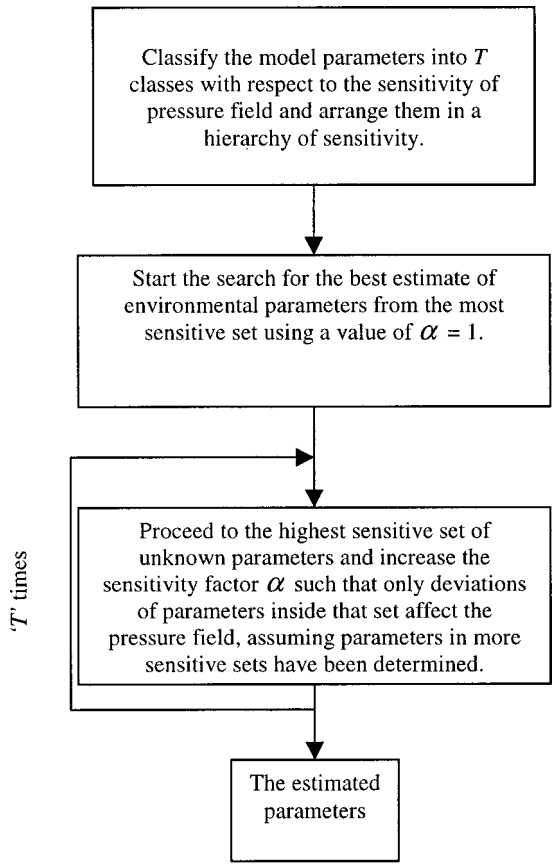

FIG. 3. A block diagram of the multistep search process.

proach is appropriate for the data that were selected from a portion of the experimental track where the environment was range independent.

A multilayer geoacoustic model is used to simulate the nominal environment at the experimental site. The model parameters include the compressional and shear wave speeds and attenuations and the density in each layer. The compressional speed is linear with depth in the first sediment layer, as shown in Fig. 4. The values of all the other parameters are constant within the layers. The water sound speed profile was measured in the experiment. We estimate values for three of the model parameters including the water depth, the compressional speed at the base of the first sediment layer, and the density of the sediment layer. From parameter sensitivity studies carried out previously,[20] these three parameters are essentially uncorrelated and can be classed in terms of high, medium, and weak sensitivity to the acoustic field. All the other parameters were set at the nominal values for the environment at the site. The search bounds for the estimated parameters and the values of the other fixed parameters were obtained from previous inversions at the site using other data from the experiment,[21,22] or from the literature.[23] In particular, the sea floor sound speed was estimated at 1550 m/s from waveform inversion of shot data,[21], and the thickness of the first sediment layer was estimated at about 150 m from an inversion of head wave data.[22] The nominal values for the model parameters and the search bounds for the estimated parameters are listed in Table I.

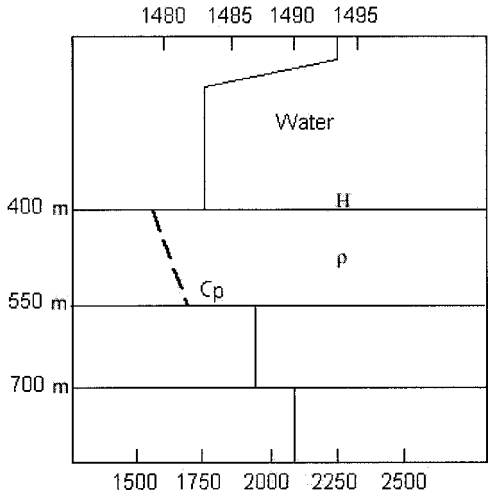

FIG. 4. The multilayer geoacoustic model showing the nominal values of the compressional wave sound speed profiles for the Pacific Shelf experimental site. The sound speeds are in m/s; the values at the top of the figure refer to the water layer, and the values at the bottom refer to all the sediment layers. The estimated parameters are indicated as H, water depth, C_p, sound speed at bottom of first sediment layer, and ρ, the sediment density.

A. Simulation results

Following the procedure described in Sec. V, we first estimate the water depth using $\alpha=1$, and then search among potential values of compressional speed, using a value of $\alpha=2$. For this value of α the sensitivity to density remains low. In the last step we increase the sensitivity factor to $\alpha=4$ to estimate the density. This three-step technique is efficient computationally and effective in providing realistic estimates.

We start the procedure by defining a search window around the source location from ranges between 4.5 km and 6.5 km and depths between 1 m and 100 m. The search over water depth values between 350 m and 440 m with a resolution of 5 m is shown in Fig. 5. The sharpest focus of the main peak is obtained for the true value of 395 m, as indicated by the minimum in the normalized BWP focal function

TABLE I. Geoacoustic model parameters.

Geoacoustic parameter	Nominal value	Lower bound	Upper bound
Water depth (m)	395	350	440
First sediment layer			
Thickness (m)	150		
Compressional speed (m/s)			
at top	1550		
at bottom	1692	1680	1720
Shear speed (m/s)	125–350		
Density (g/cm^3)	1.5	1.15	2.1
Second sediment layer			
Thickness (m)	150		
Compressional speed (m/s)	1900		
Shear speed (m/s)	400		
Density (g/cm^3)	1.8		
Basement			
Compressional speed (m/s)	2070		
Shear speed (m/s)	600		
Density (g/cm^3)	2.1		

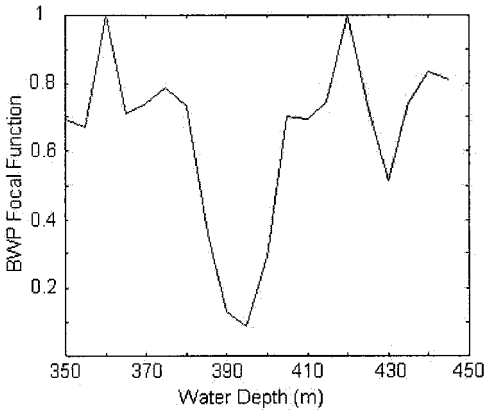

FIG. 5. The focal function plotted for different water depth values between 350 m and 440 m with resolution 5 m ($\alpha=1$).

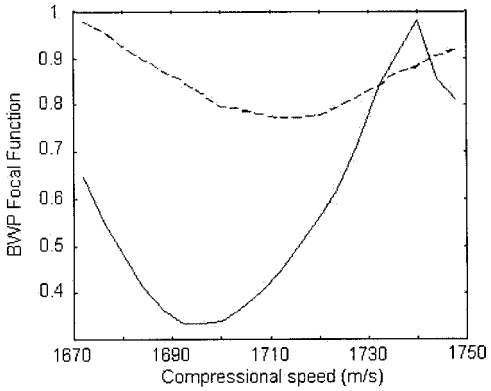

FIG. 7. The focal function plotted for compressional speed values between 1680 m/s and 1715 m/s with 2 m/s resolution for $\alpha=2$ (solid) and $\alpha=1$ (dashed).

data. The corresponding 45 Hz ambiguity surface calculated using the estimated water depth is shown in Fig. 6.

In the next step, we search the compressional speed from 1680 m/s to 1715 m/s with 2 m/s resolution, using $\alpha=2$ and setting the water depth at 395 m. The normalized BWP focal function for this value of α has a minimum value at 1692 m/s, and is plotted in the solid curve in Fig. 7. The result for $\alpha=1$ is also shown in the figure by the dashed line. This curve shows relatively small change with respect to changes in the compressional speed, and illustrates the expected behavior of the sequential search procedure. The corresponding ambiguity surface for $\alpha=2$ and the estimated values of water depth and sediment sound speed is shown in Fig. 8.

In the final step we change the density value from 1.15 g/cm^3 to 2.1 g/cm^3 with 0.05 g/cm^3 resolution using $\alpha=4$ and the estimated values for the first two parameters. The normalized BWP focal function shows a minimum value at 1.5 g/cm^3. This result (solid line) is shown in Fig. 9, where we also have shown BWP focal functions for $\alpha=2$ (dashed–dotted line) and $\alpha=1$ (dotted line). The minima in the latter two curves are much less distinct than that for $\alpha=1$. The BWP ambiguity surface obtained with $\alpha=4$ and the estimated values for the water depth, compressional speed and density is shown in Fig. 10. Compared to the ambiguity surface for $\alpha=1$ in Fig. 6, the back-propagated field is highly concentrated around the true source location for the greater value of α.

B. Experimental results

In this section we apply the phase regulated BWP to Pacific Shelf data, and present results of the inversion of data from a 45 Hz continuous wave (CW) source that was towed at a depth of 25 m along an arc at a range of 5.6 km from the array.[17] The source and receiver positions were recorded by GPS (global position system), which had an error of ~100 m. The signal-to-noise ratio (SNR) for the 45 Hz tone was about 20 dB, so we expect that relatively large values of α can be used. The geoacoustic model for the site is shown in Fig. 4. We follow the same procedure as in the inversion of

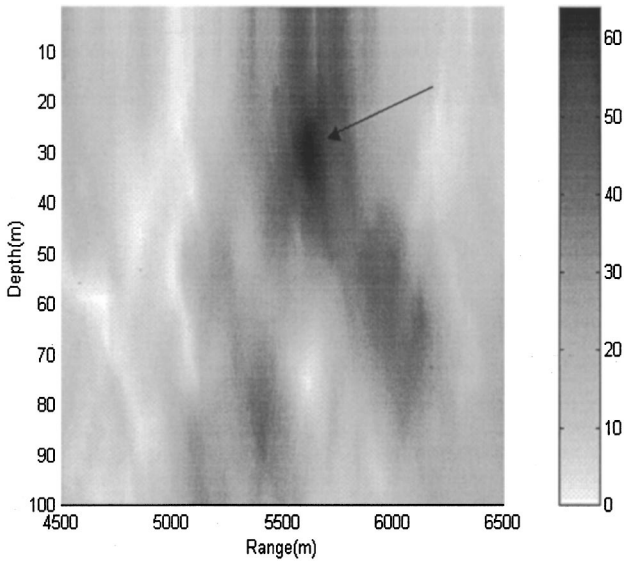

FIG. 6. The 45 Hz ambiguity surface for the reduced search window around the source location obtained using the estimated value of the water depth with $\alpha=1$. The arrow shows the true source location.

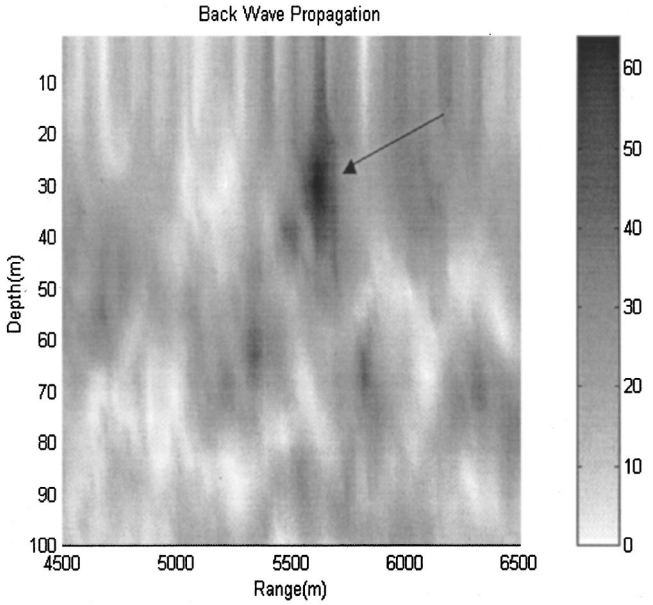

FIG. 8. The 45 Hz ambiguity surface for the reduced search window around the source location using $\alpha=2$ and the estimated values of water depth and compressional speed.

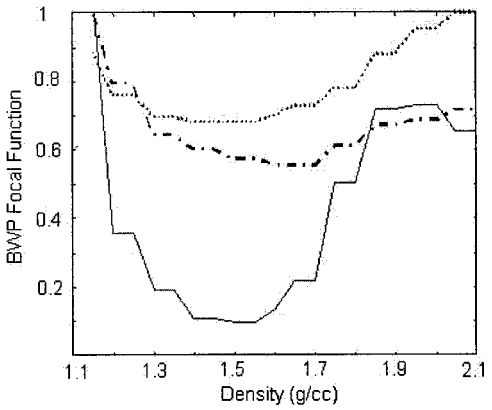

FIG. 9. The focal function using $\alpha=4$ (solid), $\alpha=1$ (dotted), and $\alpha=2$ (dashed–dotted) for density values from 1.15 g/cm^3 to 2.1 g/cm^3 with 0.05 g/cm^3 resolution.

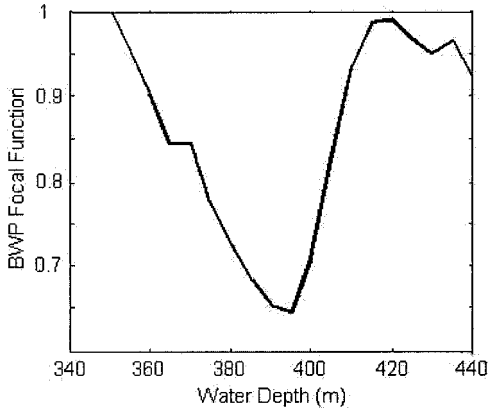

FIG. 11. The focal function plotted for water depth values between 350 m and 440 m with 5 m resolution ($\alpha=1$).

the simulated data to estimate the same three environmental parameters including water depth, compressional speed at the base of the first sediment layer and the density of the sediment layer.

We start the inversion by searching over water depth values between 350 m and 440 m with a resolution of 5 m, and setting the other two parameters at the midpoints of their respective search ranges. The sharpest focus of the main peak is obtained for a depth of 395 m, as indicated by the minimum in the normalized BWP focal function curve shown in Fig. 11. The minimum point is higher than the corresponding minimum point value for the simulation (see Fig. 5) due to mismatch between model and environmental parameters for the experimental site. The ambiguity surface for the experimental data is shown in Fig. 12. Next, the compressional speed is varied from 1680 m/s to 1710 m/s with 2 m/s resolution, using $\alpha=2$ and the estimated value for the water depth. The normalized BWP focal function shows a minimum value at 1692 m/s. The curves are shown in Fig. 13 for $\alpha=2$ (solid line) and $\alpha=1$ (dotted line). The corresponding ambiguity surface for $\alpha=2$ shows a much sharper focus around the source (Fig. 14). In the last step, we change the density value from 1.35 g/cm^3 to 1.9 g/cm^3 with 0.05 g/cm^3 resolution using $\alpha=4$ and the estimated values for the water depth and compressional speed. The normalized BWP focal function shows a minimum value at 1.5 g/cm^3. The curves for $\alpha=4$ (solid line), $\alpha=2$ (dashed line), and $\alpha=1$ (dotted line) are compared in Fig. 15. In all the inversions with the experimental data the focal function values at the minimum points (Figs. 11, 13, and 15) are greater than those for the corresponding inversions using the synthetic data (Figs. 5, 7, and 9). This is likely due to mismatch in the other parameters that define the geoacoustic model for the site. The values for those other parameters were fixed at the nominal values in Table I. However, the inversion is able to find distinct minima for the three unknown parameters, regardless of the residual mismatch. The ambiguity surface for $\alpha=4$ shown in Fig. 16 has a sharp focus at 5600 m and a depth of about 20 m, consistent with the experimental geometry. Although

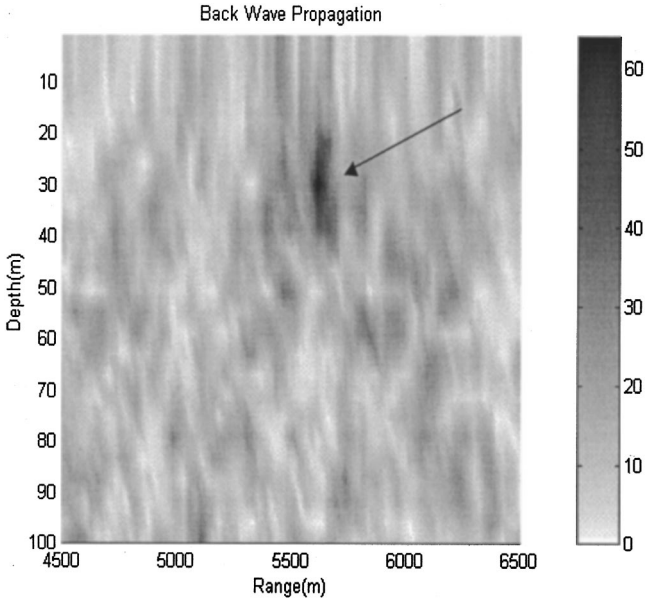

FIG. 10. The 45 Hz ambiguity surface for the reduced search window around the source using $\alpha=4$ and the estimated values of water depth, compressional speed and density.

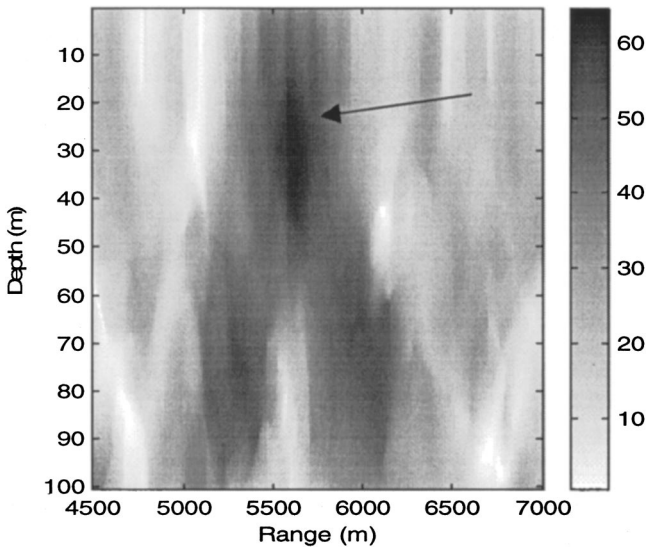

FIG. 12. The 45 Hz ambiguity surface displayed for a reduced search window around the expected source position, calculated using $\alpha=1$ and the estimated value of the water depth (395 m). The arrow shows the experimental source location.

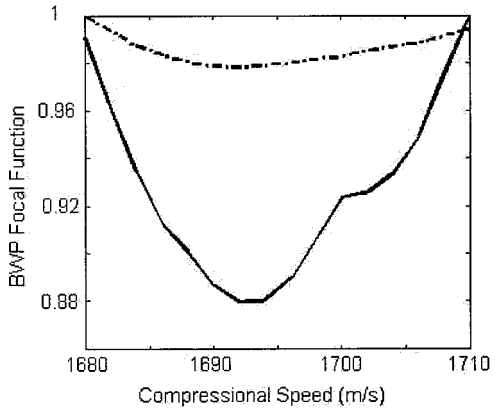

FIG. 13. The focal function plotted for compressional speed values between 1680 m/s and 1710 m/s with 2 m/s resolution for $\alpha=2$ (solid) and $\alpha=1$ (dotted).

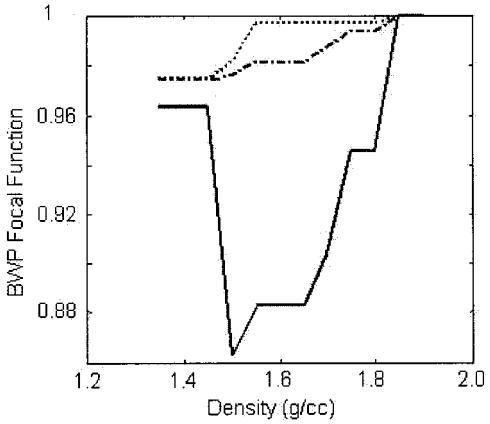

FIG. 15. The focal function plotted for density values from 1.35 g/cm^3 to 1.9 g/cm^3 with 0.05 g/cm^3 resolution for $\alpha=4$ (solid), $\alpha=1$ (dotted), and $\alpha=2$ (dashed–dotted).

there are many sidelobes, the focus is very sharp compared to that for $\alpha=1$.

The estimated value for the water depth agrees closely with the measured bathymetry of ~400 m from the experiment. The estimate for the compressional speed can be compared to the value estimated from an inversion of head wave data from an experiment with explosive charges at the same site. The head wave inversion estimated a sound speed of 1710 m/s for a layer about 100 m below the sea floor.[22] This value is very close to the estimate from the BWP inversion. The density estimate is consistent with expected values for the medium to fine grain sand sediment at the site.[23]

VII. CONCLUSIONS

We have presented an inversion method based on the back wave propagation concept for estimation of geoacoustic model parameters. The phase regulated BWP technique was introduced that allows the advantage of adapting to the environmental conditions through the variation of the sensitivity factor, α, which enhances the phase changes due to model and environmental mismatch. The value of α that can be used is limited by the signal-to-noise ratio in the experiment.

We also introduced a criterion to determine the best estimate of the model parameters based on the focus of back-propagated waves at the source location. In order to reduce the multidimensional search space to more manageable searches of smaller dimension we have proposed a multistep inversion process that is effective for uncorrelated or weakly correlated parameters. We first adjust the most sensitive parameters such as water depth, then search among potential values of medium sensitive parameters such as compressional speed using a higher value of α, and at the last step increase the sensitivity factor again to adjust the least sensitive parameters. The inversion method has been demonstrated in a simulation, and then applied to estimate geoacoustic model parameters from experimental data obtained in shallow water. Values consistent with known ground truth were estimated for three model parameters: water depth, compressional speed at the base of the first sediment layer and the density of the sediment layer. The results show that

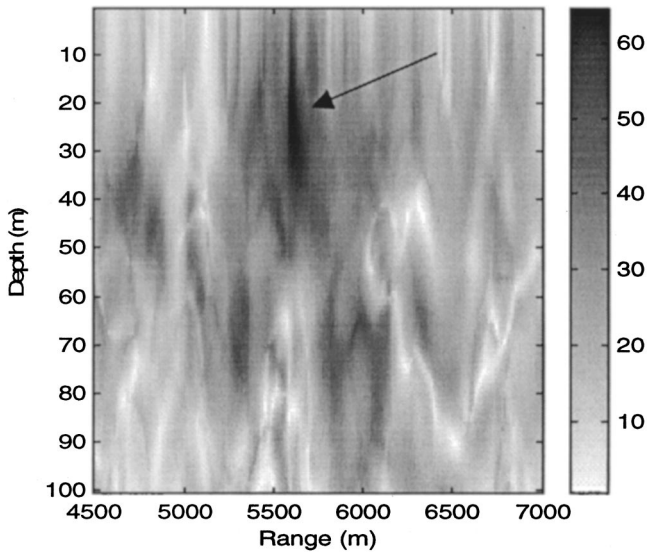

FIG. 14. The 45 Hz ambiguity surface using $\alpha=2$ with the estimated values of water depth (395 m) and compressional speed (1692 m/s).

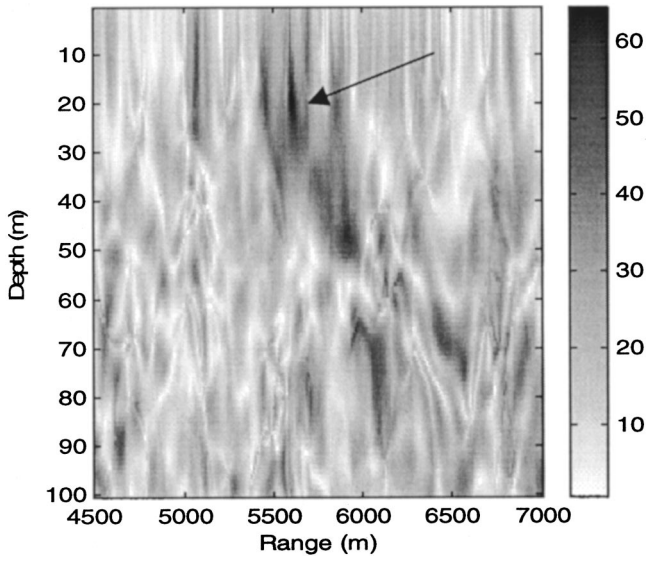

FIG. 16. The 45 Hz ambiguity surface using $\alpha=4$ with the estimated values of water depth (395 m), compressional speed (1692 m/s), and density (1.5 g/cm^3).

the BWP is successful for estimating geoacoustic parameters with different sensitivities.

ACKNOWLEDGMENTS

This research was sponsored by a partnership program between the Department of National Defense (Canada), the Natural Sciences and Engineering Research Council (NSERC), and MacDonald Dettwiler and Associates.

[1] H. P. Bucker, ''Use of calculated sound fields and matched field detection to locate sound sources in shallow water,'' J. Acoust. Soc. Am. **59**, 368–373 (1976).
[2] R. G. Fizell, ''Application of high-resolution processing to range and depth estimation using ambiguity function methods,'' J. Acoust. Soc. Am. **82**, 606–613 (1987).
[3] A. B. Baggeroer, W. A. Kuperman, and H. Schmidt, ''Matched field processing: Source localization in correlated noise as an optimum parameter estimation problems,'' J. Acoust. Soc. Am. **83**, 571–587 (1988).
[4] M. D. Collins, W. A. Kuperman, and H. Schmidt, ''Nonlinear inversion for ocean bottom properties,'' J. Acoust. Soc. Am. **92**, 2770–2883 (1992).
[5] C. E. Lindsay and N. R. Chapman, ''Matched field inversion for geoacoustic model parameters using adaptive simulated annealing,'' IEEE J. Ocean. Eng. **18**, 224–231 (1993).
[6] P. Gerstoft, ''Inversion of seismo-acoustic data using genetic algorithms and a posteriori probability distributions,'' J. Acoust. Soc. Am. **95**, 770–782 (1994).
[7] ''Inversion techniques and the variability of sound propagation in shallow water,'' edited by J. H. Wilson, S. Rajan, and J. M. Null, IEEE J. Ocean. Eng. **21**, 321–323 (1996).
[8] A. Tolstoy, *Matched Field Processing in Underwater Acoustics* (World Scientific, Singapore, 1993).
[9] A. Tolstoy, N. R. Chapman, and G. H. Brooke, ''Benchmarking geoacoustic inversion methods,'' J. Comput. Acoust. **6**, 1–28 (1998).
[10] F. D. Tappert, L. Nghiem-Phu, and S. C. Daubin, ''Source localization by using the PE method,'' J. Acoust. Soc. Am. Suppl. 1 **78**, S30 (1985).
[11] M. D. Collins and W. A. Kuperman, ''Focalization: environmental focusing and source localization,'' J. Acoust. Soc. Am. **90**, 1410–1422 (1991).
[12] D. J. Thomson, G. R. Ebbeson, and B. H. Maranda, ''A matched-field backpropagation algorithm for source localization,'' MTS/IEEE *Oceans 97*, Proceedings Vol. 1, pp. 602–607, 1997.
[13] W. A. Kuperman, W. S. Hodgkiss, H. C. Song, T. Akal, C. Ferla, and D. R. Jackson, ''Phase conjugation in the ocean: Experimental demonstration of an acoustic time-reversal mirror,'' J. Acoust. Soc. Am. **103**, 25–40 (1998).
[14] D. P. Knobles, R. A. Koch, E. K. Westwood, and T. Udagawa, ''The inversion of ocean waveguide parameters using a nonlinear least squares approach,'' J. Comput. Acoust. **6**, 83–98 (1998).
[15] Y. Stephan, X. Demoulin, and O. Sarzeaud, ''Direct neural approaches for geoacoustic inversion,'' J. Comput. Acoust. **6**, 151–166 (1998).
[16] M. I. Taroudakis and M. G. Markaki, ''Bottom geoacoustic inversion by matched field processing-a sensitivity study,'' Inverse Probl. **16**, 1679–1692 (2000).
[17] J. M. Ozard, M. L. Yeremy, N. R. Chapman, and M. J. Wilmut, ''Matched field processing in a range-dependent shallow water environment in the Northeast Pacific Ocean,'' IEEE J. Ocean. Eng. **21**, 377–383 (1996).
[18] F. B. Jensen, W. A. Kuperman, M. B. Porter, and H. Schmidt, *Computational Ocean Acoustics* (AIP, New York, 1994).
[19] E. K. Westwood, C. T. Tindle, and N. R. Chapman, ''A normal mode model for acoustoelastic ocean environments,'' J. Acoust. Soc. Am. **100**, 3631–3645 (1996).
[20] R. M. Dizaji, Ph.D. thesis, University of Victoria, 2000.
[21] N. R. Chapman and D. E. Hannay, ''Broadband matched field inversion for estimation of geoacoustic properties,'' in *Shallow Water Acoustics*, edited by R. Zhang and J. Zhou (China Ocean Press, Beijing, 1997), pp. 145–150.
[22] O. A. Godin, N. R. Chapman, M. C. A. Laidlaw, and D. E. Hannay, ''Head wave data inversion for geoacoustic parameters of the ocean bottom off Vancouver Island,'' J. Acoust. Soc. Am. **106**, 2540–2551 (1999).
[23] E. L. Hamilton, ''Geoacoustic modeling of the sea floor,'' J. Acoust. Soc. Am. **68**, 1313–1340 (1980).

Modeling of high-frequency propagation in inhomogeneous background random media

Reuven Mazar[a)]
Department of Electrical and Computer Engineering, Ben Gurion University of the Negev, P.O. Box 653, Beer Sheva 84105, Israel

(Received 4 August 2000; revised 27 September 2001; accepted 30 October 2001)

When a high-frequency electromagnetic wave propagates in a complicated scattering environment, the contribution at the observer is usually composed of a number of field species arriving along different ray trajectories. In order to describe each contribution separately the parabolic extension along an isolated ray trajectory in an inhomogeneous background medium was performed. This leads to the parabolic wave equation along a deterministic ray trajectory in a randomly perturbed medium with the possibility of presenting the solution of the high-frequency field and the higher-order coherence functions in the functional path-integral form. It is shown that uncertainty considerations play an important role in relating the path-integral solutions to the approximate asymptotic solutions. The solutions for the high-frequency propagators derived in this work preserve the random information accumulated along the propagation path and therefore can be applied to the analysis of double-passage effects where the correlation between the forward–backward propagating fields has to be accounted for. This results in double-passage algorithms, which have been applied to analyze the resolution of two point scatterers. Under strong scattering conditions, the backscattering effects cannot be neglected and the ray trajectories cannot be treated separately. The final part is devoted to the generalized parabolic extension method applied to the scalar Helmholtz's equation, and possible approximations for obtaining numerically manageable solutions in the presence of random media. [DOI: 10.1121/1.1430692]

PACS numbers: 43.30.Re, 43.30.Ft, 43.30.Cq, 43.20.Bi [DLB]

I. INTRODUCTION

Acoustic waves represent the main tool in the remote sensing and location of distant objects in the ocean and for the design of underwater communication channels. A great number of analytical and numerical methods have been developed to describe sound propagation in deterministic structures existing in a spatially varying ocean medium.[1–4] In the high-frequency limit when the propagation takes place along some preferred propagation direction the propagating field can be expressed as a product of a slowly varying wave amplitude and a rapidly varying term that accounts for the main phase variation. It was shown that the propagation of the wave amplitude could be approximately described by a parabolic wave equation.[5,6]

The need to account for the stochastic effects in inhomogeneous propagation environments stimulated the development of techniques based on the transport of statistical moments (the so-called coherence functions) of the field.[7] On the basis of the parabolic extension it was shown that the coherence functions and their spectral transforms could be transported along paraxial trajectories in a weakly stratified medium.[8–12] Direct asymptotic analysis of the moment equations resulted in the development of sophisticated analytical methods, among them the multiscale expansion procedure, which enabled approximate analytical solutions for the average coherence measures to be found.[10–16] In principle, the field statistics can be determined if one knows all its statistical moments. Therefore the most desirable result would be an explicit solution for the random field from which the expressions for the statistical moments can be constructed. Formally such a solution is available and follows from the similarity between the equation for the parabolic wave amplitude and the Schrodinger's equation describing the movement of a quantum particle. Such a similarity allows the solution for the randomly scattered wave to be presented in the form of a Feynman path integral.[17,18] The application of path integrals to wave propagation in random media was first suggested in several works.[19–25] Using the path-integral solutions, the expressions for the statistical field measures have been constructed in the homogeneous background case, and their asymptotic evaluations lead to correct expressions for the correlation characteristics.[24–27] The path-integral approach has been applied to sound transmission,[28–31] and has stimulated the development of efficient numerical methods based on marching algorithms.[32,33]

The above-described results cannot be applied, however, in situations when propagation takes place in a strongly refractive medium in the presence of multiple scattering events. In the high-frequency limit the propagation in such types of media is intuitively related to the geometrical ray trajectories representing the paths of energy flux transfer. The localization concept around these ray trajectories, and the reflection, refraction, and (or) diffraction of the local plane-wave fields by boundaries, inhomogeneities, and (or) scattering centers has been combined through the geometrical theory of diffraction (GTD)[34,35] into one of the most effec-

a)Electronic mail: mazar@ee.bgu.ac.il

tive means for analyzing high-frequency wave phenomena in complex deterministic environments.

Attempts to perform more realistic modeling of acoustic wave propagation, required to account for the effect of random fluctuations characteristic of the ocean environments, lead to the stochastic extension of the deterministic GTD and resulted in the formulation of the stochastic geometrical theory of diffraction (SGTD).[36–41] Similarly to the deterministic case, the field at the observer according to the SGTD is also composed of multiple field species arriving along different ray trajectories resulting from multiple refraction and/or after encountering scattering at boundaries and scattering centers. The advantage of the SGTD is that it accounts also for the random phase and amplitude variations occurring in each ray event.

As in the deterministic case, the main concern of the SGTD is the construction of the propagators responsible for the transport of the high-frequency fields and their statistical measures along geometrical rays of the deterministic background medium from source distributions at the initial plane (actual or virtual) to some observation plane. It is desirable to have a solution which contains, in an explicit form, information about the random refractive index variation along the propagation path. The advantage of this approach is evident since it enables the averaging procedure to be easily applied for the construction of expressions for the spatial and spectral correlation characteristics with no need to solve complicated partial differential equations. According to the spirit of the SGTD, derivations of the relevant equations is based on a parabolic extension along a strongly refracting ray in the background medium developed initially for the deterministic problems[42–45] and later extended to propagation in inhomogeneous background random media.[46,36] To solve the equations for the statistical measures propagating in an inhomogeneous background random medium the multiscale asymptotic method was applied.[40,41] This technique involves the extraction of ''slow'' and ''fast'' variables and a sequence of spectral transforms. The resulting solutions are expressed as spectral integrals, which contain the necessary spectral information to eliminate the divergence in the transitional zones and correctly represent the statistical characteristics of the propagating field. The spectral parameters in these integrals are related to the ray slopes, thereby defining the important ray trajectories contributing to the field at the observer. As was mentioned above in the case of a paraxial straight-ray propagation, the solution can be presented in the form of a Feynman path integral that accounts for the contribution of multiple trajectories. Approximate solutions can be interpreted as partial approximations of the functional solutions. It would also be important, therefore, to possess a solution in a functional path-integral form for the high-frequency field along strongly refracted ray trajectories in the inhomogeneous background media. Such a solution could be helpful in establishing a connection with available asymptotic and heuristic solutions similarly to what was done along a straight propagation direction. Also it would be useful in constructing efficient numerical marching algorithms along curved ray trajectories.

The present work consists of three parts. The first one represented by Secs. II–IV deals with the derivation of the path-integral solutions and their relation with the approximate asymptotic results. In Sec. II, the derivation of the parabolic wave equation describing propagation in a large-scale random medium is presented. In Sec. III the parabolic equation is reduced to a simplified form in order to employ the path integral formulation of the problem and present the parabolic equation Green's function written as a path-integral solution along a curved ray in the inhomogeneous background medium. The next step is reducing the path-integral solutions to approximate solutions. For this purpose in Sec. IV the two-point random product of the field is introduced with consequent definition of its spectral transforms known as the Wigner distribution and the ambiguity function. By constructing the continual integral solutions of these measures and applying the uncertainty considerations in the mixed phase space—configuration space domain, the connection between these solutions and the asymptotic multiscale solutions has been established.

Section V is devoted to the application of the random propagators to the analysis of double-passage resolution. As a result of the mutual coherence of forward–backward propagating events new effects arise originating from the double passage of waves through the same random inhomogeneities. These effects have been predicted theoretically[47,48] and also observed experimentally.[49,50] The fact that the solutions considered in this work preserve the random information accumulated along the propagating path makes them suitable for the double-passage analysis. The main result of the double-passage problem is an anomalous intensity distribution of backscattered radiation expressed by a local intensity enhancement effect.[51–53] Such an anomaly raises a question about the possibility of resolving several scattering centers and imaging under double-passage conditions. The possibility of resolving the scattering centers under double-passage conditions is also being considered.

The problems described in Secs. II–IV have been analyzed in the limits of the parabolic approximation, which assumes a weak variability of the medium and neglect of backscattering effects. The final part of the paper deals with the situations for which some of the above assumptions are not fulfilled. In Sec. VI the analysis based on the method originally proposed by Fock for the integration of quantum mechanical equations is presented. In wave propagation theory this method has been used earlier,[54–58] while we applied this method in our previous works[59–61] for the analysis of backscattering and localization effects in the perturbation regime. In Sec. VI, the problem is formulated and possible solution methods, which are also suitable for the strong scattering conditions while taking account of backscattering, are considered.

II. PARABOLIC WAVE EQUATION IN THE RAY COORDINATES

The starting point is the time-harmonic wave equation for the scalar wave field $U(\mathbf{R})$:

$$\nabla^2 U(\mathbf{R}) + k^2 N^2(\mathbf{R}) U(\mathbf{R}) = 0 \tag{1}$$

in which the location is measured by the radius vector $\mathbf{R}=\{x,y,z\}$, and the reference wave number k is related to the radiation frequency ω and the reference wavelength λ, via the relation $k=\omega/c_0=2\pi/\lambda$. The refractive index

$$N(\mathbf{R})=n(\mathbf{R})+\tilde{n}(\mathbf{R}) \tag{2}$$

is composed of the deterministic part $n(\mathbf{R})$ describing the background variation, on which are superimposed random fluctuations described by the function $\tilde{n}(\mathbf{R})$, so that

$$n(\mathbf{R})=\langle N(\mathbf{R})\rangle, \tag{3}$$

where the angular braces denote ensemble average. It is assumed that the refractive index variations are large scale, and that the characteristic scales l_b characterizing the deterministic background variation and the l_s characterizing the correlation properties of the medium satisfy the relation $l_b \gg l_s \gg \lambda$. Under these high-frequency conditions, the main propagation takes place along the deterministic background ray trajectories determined by a set of parametric equations:

$$\frac{d}{d\sigma}\left[n(\mathbf{R})\frac{d\mathbf{R}(\sigma)}{d\sigma}\right]=\nabla n(\mathbf{R}), \tag{4}$$

where σ is the range coordinate representing the distance along the background ray. Considering propagation along a chosen ray it is convenient to introduce a ray-centered coordinate system $\mathbf{R}=\{\mathbf{r},\sigma\}$.[36–46] Here σ is the above-defined range coordinate along the reference ray, and $\mathbf{r}$ measures the transverse location in the plane normal to that ray at σ. Next, the parabolic extension is performed by presenting the field as a product of slowly varying amplitude and the term, which accounts for the dominant phase accumulation along the reference ray

$$U(\mathbf{r},\sigma)=u(\mathbf{r},\sigma)\exp\left\{ik\int_{\sigma_0}^{\sigma}d\zeta\, n_0(\zeta)\right\}. \tag{5}$$

Here

$$n_0(\sigma)=n(0,\sigma). \tag{6}$$

is the deterministic (background) part of the refractive index at the range coordinate σ measured along the reference ray. Substituting (5) into the wave equation (1) and neglecting the ''slow'' range derivatives of the second order, leads to the parabolic ray-centered wave equation for the wave function $u(\mathbf{r},\sigma)$:[36–46]

$$2ikn_0(\sigma)\frac{\partial u}{\partial\sigma}+h^2(\mathbf{r},\sigma)\nabla_r^2 u+\mathbf{b}(\sigma)\cdot\nabla_{\mathbf{r}}u + k^2[f_b(\mathbf{r},\sigma)+f_s(\mathbf{r},\sigma)]u=0. \tag{7}$$

Here the operators $\nabla_{\mathbf{r}}$ and ∇_r^2 are expressed in the transverse ray coordinates $\mathbf{r}=\{\xi,\eta\}$. Furthermore, the vector function

$$\mathbf{b}(\sigma)=[\nabla_{\mathbf{r}}n(\mathbf{r},\sigma)]_{\mathbf{r}=0} \tag{8}$$

is related to the curvature and torsion of the reference ray, and

$$h(\mathbf{r},\sigma)=1+\mathbf{r}\cdot\mathbf{b}(\sigma) \tag{9}$$

is the metric coefficient. The following functions have also been defined:

$$f_b(\mathbf{r},\sigma)=h^2(\mathbf{r},\sigma)n^2(\mathbf{r},\sigma)-n_0^2(\sigma) + ik^{-1}\left[\frac{\partial n_0(\sigma)}{\partial\sigma}-\frac{n_0(\sigma)}{h(\mathbf{r},\sigma)}\frac{\partial h(\mathbf{r},\sigma)}{\partial\sigma}\right], \tag{10}$$

describing the effect of the background, and

$$f_s(\mathbf{r},\sigma)=h^2(\mathbf{r},\sigma)[2n(\mathbf{r},\sigma)\tilde{n}(\mathbf{r},\sigma)+\tilde{n}^2(\mathbf{r},\sigma)], \tag{11}$$

describing the scattering by the random refractive index fluctuations.

III. PATH-INTEGRAL SOLUTION FOR THE PARABOLIC-RAY EQUATION

In most of the practically important situations, Eq. (6) can be essentially simplified.[41–46] For high-frequency propagation the propagating field is localized near the reference ray. If the radius of curvature of the reference ray represented by the inverse modulus of the function $\mathbf{b}(\sigma)$ is sufficiently large, the metric coefficient can be set equal to unity: $h(\mathbf{r},\sigma)=1$. In a homogeneous medium in the absence of scattering, the transverse region contributing to the field at the observer is of the order of the first Fresnel's radius $r_F=\sqrt{\lambda L/2}=\sqrt{\pi L/k}$, where L is the propagation range along the reference ray. It was shown[27] that for the sound channel in the ocean the Fresnel's radius is always smaller than that in the homogeneous medium. If the radius of curvature is of the order l, the ratio between the first Fresnel radius and the ray curvature is $\sqrt{\pi L/l}/\sqrt{kl}$, which defines the order of the second term in the metric coefficient (9). This ratio can be used for specifying the propagation ranges for which the second term in the metric coefficient can be neglected. In the presence of scattering there appears an additional scale—the coherence radius of the field r_c which defines the transverse field region contributions from which, at the observer, add coherently. In the case of weak scattering $r_c > r_F$, the validity of setting $h(\mathbf{r},\sigma)=1$ remains the same as in the absence of scattering. With increase of the scattering strength, the coherence radius decreases very sharply and the ratio between the relevant transverse coherent region and the radius of curvature of the ray decreases. Apart from the decrease of the field coherence the scattering causes spread of the propagating radiation, the angular magnitude of which is of the order $1/(kr_c)$. The relevant transverse region contributing to the field at the observer is therefore $L/(kr_c)$, and its ratio to the ray curvature is $1/(kr_c)(L/l)$. Both of the above-defined parameters increase with range. However, since the multiple field contributions add incoherently at the observer, the scattering diminishes the phase and curvature effect and the metric coefficient, without great error, can be set equal to unity.

If the random part of the refractive index is much smaller than the background part, $|\tilde{n}| \ll n_0$, the scattering function (11) can be approximated by the first term. Then, in terms of the Green's function, Eq. (6) reduces to

$$\frac{\partial g(\mathbf{r},\sigma|\mathbf{r}_0,\sigma_0)}{\partial \sigma} - \frac{ik}{2n_0(\sigma)} \nabla_r^2 g(\mathbf{r},\sigma|\mathbf{r}_0,\sigma_0) - \frac{ik}{2n_0(\sigma)} \mathbf{b}(\sigma)\cdot \nabla_{\mathbf{r}} g(\mathbf{r},\sigma|\mathbf{r}_0,\sigma_0) = ik\mu(\mathbf{r},\sigma) g(\mathbf{r},\sigma|\mathbf{r}_0,\sigma_0) + \frac{1}{n_0(\sigma)} \frac{\partial n_0(\sigma)}{\partial \sigma} g(\mathbf{r},\sigma|\mathbf{r}_0,\sigma_0), \tag{12a}$$

$$g(\mathbf{r},\sigma_0|\mathbf{r}_0,\sigma_0) = \delta(\mathbf{r}-\mathbf{r}_0) \tag{12b}$$

where function $\mu(\mathbf{r},\sigma)$ is defined as a sum of two functions

$$\mu(\mathbf{r},\sigma) = \mu_b(\mathbf{r},\sigma) + \mu_s(\mathbf{r},\sigma), \tag{13}$$

one of which is related to the deterministic part

$$\mu_b(\mathbf{r},\sigma) = \frac{n^2(\mathbf{r},\sigma) - n_0^2(\sigma)}{2n_0(\sigma)}, \tag{14a}$$

and the second to the fluctuating part:

$$\mu_s(\mathbf{r},\sigma) = \frac{n(\mathbf{r},\sigma)\tilde{n}(\mathbf{r},\sigma)}{n_0(\sigma)}. \tag{14b}$$

For an arbitrary source distribution the solution is obtained via the propagation relation:

$$u(\mathbf{r},\sigma) = \int_{-\infty}^{\infty} \int d^2 r_0\, u(\mathbf{r}_0,\sigma_0) g(\mathbf{r},\sigma|\mathbf{r}_0,\sigma_0). \tag{15}$$

The solution of Eq. (12a) can be presented in a functional path-integral form which in the velocity representation is given by[24–26]

$$g(\mathbf{r},\sigma|\mathbf{r}_0,\sigma_0) = \left[\frac{n_0(\sigma)}{n_0(\sigma_0)}\right] \times \int\int D\mathbf{v}\, \delta\left[\mathbf{r}-\mathbf{r}_0 - \int_{\sigma_0}^{\sigma} \frac{d\zeta}{n_0(\zeta)} \mathbf{v}(\zeta)\right] \times \exp\left\{\frac{ik}{2}\int_{\sigma_0}^{\sigma} \frac{d\zeta}{n_0(\zeta)} \mathbf{v}(\zeta)\cdot[\mathbf{v}(\zeta)-\mathbf{b}(\zeta)]\right\} \times \exp\left\{ik\int_{\sigma_0}^{\sigma} d\zeta\, \mu\left[\mathbf{r} - \int_{\zeta}^{\sigma} \frac{dt}{n_0(t)} \mathbf{v}(t),\zeta\right]\right\}, \tag{16a}$$

$$\int\int D\mathbf{v}(\zeta) \exp\left\{\frac{ik}{2}\int_{\sigma_0}^{\sigma} \frac{d\zeta}{n_0(\zeta)} \nu^2(\zeta)\right\} = 1. \tag{16b}$$

This functional solution is expressed as a contribution of multiple ray trajectories connecting the source and observation points. By analogy with quantum mechanics, multiple trajectory formalism contains the uncertainty principle according to which the exact trajectory and its slope can be identified within certain limits. Replacing these multiple trajectories by straight rays violates this principle which results in incorrect results for the intensity correlation measures.

IV. APPROXIMATE SOLUTIONS

One of the ways to keep some sort of uncertainty can be achieved by considering a higher dimensional space, for example, by defining a paired field measure called the two-point function (TPF):

$$\Gamma(\mathbf{p},\mathbf{s},\sigma) = u\left(\mathbf{p}+\frac{\mathbf{s}}{2},\sigma\right) u^*\left(\mathbf{p}-\frac{\mathbf{s}}{2},\sigma\right), \tag{17}$$

where $\mathbf{p}$ and $\mathbf{s}$ are transverse sum and difference coordinates

$$\mathbf{p} = \frac{\mathbf{r}_1+\mathbf{r}_2}{2}, \quad \mathbf{s} = \mathbf{r}_1 - \mathbf{r}_2. \tag{18}$$

The propagation relation for the TPF $\Gamma(\mathbf{p},\mathbf{s},\sigma)$ is given by

$$\Gamma(\mathbf{p},\mathbf{s},\sigma) = \int_{-\infty}^{\infty} \cdots \int d^2 p_0\, d^2 s_0\, \Gamma(\mathbf{p}_0,\mathbf{s}_0,\sigma_0) \times g_2(\mathbf{p},\mathbf{s},\sigma|\mathbf{p}_0,\mathbf{s}_0,\sigma_0), \tag{19}$$

where the propagator $g_2(\mathbf{p},\mathbf{s},\sigma|\mathbf{p}_0,\mathbf{s}_0,\sigma_0)$ relating the values of $\Gamma(\mathbf{p},\mathbf{s},\sigma)$ at the source plane σ_0 and the observation planes σ can be expressed as a product of the propagators in (16) in which the configurational coordinates are replaced by $\mathbf{r}_1 = \mathbf{p} + (\mathbf{s}/2)$, $\mathbf{r}_2 = \mathbf{p} - (\mathbf{s}/2)$. The result after changing the integration variables is

$$g_2(\mathbf{p},\mathbf{s},\sigma|\mathbf{p}_0,\mathbf{s}_0,\sigma_0) = \left[\frac{n_0(\sigma)}{n_0(\sigma_0)}\right]^2 \int\int D\mathbf{v}(\zeta) D\mathbf{w}(\zeta)\, \delta\left\{\mathbf{p}-\mathbf{p}_0 + \frac{\mathbf{s}-\mathbf{s}_0}{2} - \int_{\sigma_0}^{\sigma} \frac{d\zeta}{n_0(\zeta)}\left[\mathbf{v}(\zeta)+\frac{\mathbf{w}(\zeta)}{2}\right]\right\} \times \delta\left\{\mathbf{p}-\mathbf{p}_0 - \frac{\mathbf{s}-\mathbf{s}_0}{2} - \int_{\sigma_0}^{\sigma} \frac{d\zeta}{n_0(\zeta)}\left[\mathbf{v}(\zeta)-\frac{\mathbf{w}(\zeta)}{2}\right]\right\} \exp\left\{ik\int_{\sigma_0}^{\sigma} \frac{d\zeta}{n_0(\zeta)} \mathbf{v}(\zeta)\cdot[\mathbf{w}(\zeta)-\mathbf{b}(\zeta)]\right\} \times \exp\left\{ik\int_{\sigma_0}^{\sigma} d\zeta\, \mu\left[\mathbf{p}+\frac{\mathbf{s}}{2} - \int_{\zeta}^{\sigma} \frac{dt}{n_0(t)}\left[\mathbf{v}(t)+\frac{\mathbf{w}(t)}{2}\right]\right] - \mu\left[\mathbf{p}-\frac{\mathbf{s}}{2} - \int_{\zeta}^{\sigma} \frac{dt}{n_0(t)}\left[\mathbf{v}(t)-\frac{\mathbf{w}(t)}{2}\right]\right]\right\}. \tag{20}$$

The next step is the transfer to the mixed configurational-spectral spaces. It is achieved by defining the Fourier transform of the TPF in the **s** coordinate, called the Wigner function,

$$W(\mathbf{p},\boldsymbol{\rho},\sigma)=\int_{-\infty}^{\infty}\cdots\int d^2s\,\Gamma(\mathbf{p},\mathbf{s},\sigma)\exp(-ik\boldsymbol{\rho}\cdot\mathbf{s}), \quad (21)$$

and the Fourier transform in the **p** coordinate, called the ambiguity function

$$A(\boldsymbol{\eta},\mathbf{s},\sigma)=\int_{-\infty}^{\infty}\cdots\int d^2s\,\Gamma(\mathbf{p},\mathbf{s},\sigma)\exp(-ik\boldsymbol{\eta}\cdot\mathbf{p}). \quad (22)$$

In principle one of these functions can be specified at the source plane creating the distribution of the other one at the observation plane according to the following propagation relations:

$$A(\boldsymbol{\eta},\mathbf{s},\sigma)=\int_{-\infty}^{\infty}\cdots\int dp_0{}^2\,d^2\rho_0 \times W(\mathbf{p}_0,\boldsymbol{\rho}_0,\sigma_0)\tilde{g}_2^{+}(\boldsymbol{\eta},\mathbf{s},\sigma|\mathbf{p}_0,\boldsymbol{\rho}_0,\sigma_0) \quad (23)$$

and

$$W(\mathbf{p},\rho,\sigma)=\int_{-\infty}^{\infty}\cdots\int d\,\eta_0{}^2\,d^2s_0\,A(\boldsymbol{\eta}_0,\mathbf{s}_0,\sigma_0) \times\tilde{g}_2^{-}(\mathbf{p},\boldsymbol{\rho},\sigma|\,\boldsymbol{\eta}_0,\mathbf{s}_0,\sigma_0), \quad (24)$$

where the propagators $\tilde{g}_2^{+}$ and $\tilde{g}_2^{-}$ are defined as

$$\tilde{g}_2^{+}(\boldsymbol{\eta},\mathbf{s},\sigma|\mathbf{p}_0,\boldsymbol{\rho}_0,\sigma_0)=\left(\frac{k}{2\pi}\right)^2\int_{-\infty}^{\infty}\cdots\int dp^2\,d^2s_0 \times g_2(\mathbf{p},\mathbf{s},\sigma|\mathbf{p}_0,\boldsymbol{\rho}_0,\sigma_0) \times\exp[ik(\boldsymbol{\rho}_0\cdot\mathbf{s}_0-\boldsymbol{\eta}\cdot\mathbf{p})] \quad (25)$$

and

$$\tilde{g}_2^{-}(\mathbf{p},\rho,\sigma|\,\eta_0,\mathbf{s}_0,\sigma_0)=\left(\frac{k}{2\pi}\right)^2\int_{-\infty}^{\infty}\cdots\int dp_0^2\,d^2s \times g_2(\mathbf{p},\mathbf{s},\sigma|\mathbf{p}_0,\rho_0,\sigma_0) \times\exp[ik(\boldsymbol{\eta}_0\cdot\mathbf{p}_0-\boldsymbol{\rho}\cdot\mathbf{s})]. \quad (26)$$

Substituting the explicit expression of the propagator g_2 from (20) into (25) and (26), gives the explicit form of the propagators $\tilde{g}_2^{+}$ and $\tilde{g}_2^{-}$:

$$\begin{aligned}\tilde{g}_2^{+}(\boldsymbol{\eta},\mathbf{s},\sigma|\mathbf{p}_0,\boldsymbol{\rho}_0,\sigma_0)=&\left(\frac{k}{2\pi}\right)^2\left[\frac{n_0(\sigma)}{n_0(\sigma_0)}\right]^2\int\int D\mathbf{v}(\zeta)D\mathbf{w}(\zeta)\exp\left\{ik\int_{\sigma_0}^{\sigma}\frac{d\zeta}{n_0(\zeta)}\mathbf{v}(\zeta)\cdot[\mathbf{w}(\zeta)-\mathbf{b}(\zeta)]\right\}\\ &\times\exp\left\{-ik\boldsymbol{\eta}\cdot\left[\mathbf{p}_0+\int_{\sigma_0}^{\sigma}\frac{d\zeta}{n_0(\zeta)}\mathbf{v}(\zeta)\right]\right\}\exp\left\{ik\boldsymbol{\rho}_0\cdot\left[\mathbf{s}-\int_{\sigma_0}^{\sigma}\frac{d\zeta}{n_0(\zeta)}\mathbf{w}(\zeta)\right]\right\}\\ &\times\exp\left\{ik\int_{\sigma_0}^{\sigma}d\zeta\,\mu\left[\mathbf{p}_0+\int_{\sigma_0}^{\zeta}\frac{dt}{n_0(t)}\mathbf{v}(t)+\frac{s}{2}-\frac{1}{2}\int_{\zeta}^{\sigma}\frac{dt}{n_0(t)}\mathbf{w}(t)\right]\right.\\ &\left.-\mu\left[\mathbf{p}_0+\int_{\sigma_0}^{\zeta}\frac{dt}{n_0(t)}\mathbf{v}(t)-\frac{s}{2}+\frac{1}{2}\int_{\zeta}^{\sigma}\frac{dt}{n_0(t)}\mathbf{w}(t)\right],\end{aligned} \quad (27)$$

and

$$\begin{aligned}\tilde{g}_2^{-}(\mathbf{p},\boldsymbol{\rho},\sigma|\,\boldsymbol{\eta}_0,\mathbf{s}_0,\sigma_0)=&\left(\frac{k}{2\pi}\right)^2\left[\frac{n_0(\sigma)}{n_0(\sigma_0)}\right]^2\int\int D\mathbf{v}(\zeta)D\mathbf{w}(\zeta)\exp\left\{ik\int_{\sigma_0}^{\sigma}\frac{d\zeta}{n_0(\zeta)}\mathbf{v}(\zeta)\cdot[\mathbf{w}(\zeta)-\mathbf{b}(\zeta)]\right\}\\ &\times\exp\left\{-ik\boldsymbol{\eta}_0\cdot\left[\mathbf{p}-\int_{\sigma_0}^{\sigma}\frac{d\zeta}{n_0(\zeta)}\mathbf{v}(\zeta)\right]\right\}\exp\left\{ik\boldsymbol{\rho}\cdot\left[\mathbf{s}_0+\int_{\sigma_0}^{\sigma}\frac{d\zeta}{n_0(\zeta)}\mathbf{w}(\zeta)\right]\right\}\\ &\times\exp\left\{ik\int_{\sigma_0}^{\sigma}d\zeta\,\mu\left[\mathbf{p}-\int_{\zeta}^{\sigma}\frac{dt}{n_0(t)}\mathbf{v}(t)+\frac{\mathbf{s}}{2}+\frac{1}{2}\int_{\sigma_0}^{\zeta}\frac{dt}{n_0(t)}\mathbf{w}(t)\right]\right.\\ &\left.-\mu\left[\mathbf{p}-\int_{\zeta}^{\sigma}\frac{dt}{n_0(t)}\mathbf{v}(t)-\frac{\mathbf{s}}{2}-\frac{1}{2}\int_{\sigma_0}^{\zeta}\frac{dt}{n_0(t)}\mathbf{w}(t)\right].\end{aligned} \quad (28)$$

The integrals over the range coordinate in the integrands of (27) and (28) represent integrations over all the possible slopes $\mathbf{v}(\zeta)$ and $\mathbf{w}(\zeta)$. In constructing approximate solutions the purpose is to take into account only certain rays having the most important contribution to the field at the observer. Defining such trajectories in the deterministic background medium is equivalent to the stationary phase approximation. These deterministic ray trajectories are solutions of the ray-tracing equations which in the ray-centered coordinates are presented by the following set:

$$\frac{d\mathbf{p}}{d\sigma}=\frac{\boldsymbol{\rho}}{n_0(\sigma)}, \quad (29a)$$

$$\frac{d\boldsymbol{\rho}}{d\sigma}=\boldsymbol{\nabla}_{\mathbf{p}}\mu_b(\mathbf{p},\sigma), \tag{29b}$$

$$\frac{d\mathbf{s}}{d\sigma}=\frac{\boldsymbol{\eta}}{n_0(\sigma)}, \tag{29c}$$

$$\frac{d\boldsymbol{\eta}}{d\sigma}=\boldsymbol{\nabla}_{\mathbf{p}}[\boldsymbol{\nabla}_{\mathbf{p}}\mu_b(\mathbf{p},\sigma)\cdot\mathbf{s}]. \tag{29d}$$

Equations (29) are solved subject to the boundary conditions, which define the initial location and slope either at the source plane or at the observation plane. Taking into account only the trajectories having the slopes $\mathbf{v}(\zeta=\sigma)=\boldsymbol{\rho}$ and $\mathbf{w}(\zeta=\sigma)=\boldsymbol{\eta}$, respectively, leads to the formulation equivalent to the phase approximation of the extended Huygens–Kirchoff methods (PAHKM).[63] The PAHKM solution which can be derived from the path-integral solution has a limited applicability region especially for the construction of the higher order statistical moments which, as proposed in the present work, is a result of violation of the uncertainty principle.

By analogy with quantum mechanics the multiple trajectory formalism contains the uncertainty principle, according to which the exact trajectory and its slope can be determined only within certain limits. The uncertainty is a result of the finite wavelength of the propagating radiation and is revealed because of diffraction when the propagating wave interacts with medium inhomogeneities. When the refractive index of the medium contains a random part superimposed on the inhomogeneous background an additional uncertainty is introduced because of the extended number of random rays connecting the source and the observer. Accounting for these uncertainty relations is essential in constructing the approximate propagators and consequent manageable algorithms for the statistical characteristics of the propagating field. The ray uncertainty in the propagators (27) and (28) is accounted for by considering different configurational–spectral spaces in the source and observation planes. Only the deterministic trajectories emanating from the source with the initial slope $\mathbf{v}(\zeta=\sigma_0)=\boldsymbol{\rho}_0$ and arriving at the observation plane with slope difference $\mathbf{w}(\zeta=\sigma)=\boldsymbol{\eta}$ in (23) and (25), and the trajectories emanating from the source plane with slope differences $\mathbf{w}(\zeta=\sigma_0)=\boldsymbol{\eta}_0$, and arriving at the observer with the slope $\mathbf{v}(\zeta=\sigma)=\boldsymbol{\rho}$ in (24) and (26) have been taken into account. It has to be emphasized, however, that even when the deterministic background rays replace the continual trajectories, there is an uncertainty in identifying the rays emanating from the source and those approaching the observer. Replacing in Eqs. (27) and (28) the spectral variables $\boldsymbol{\rho}(\zeta)/n_0(\zeta)$ and $\boldsymbol{\eta}(\zeta)/n_0(\zeta)$ by the derivatives according to the ray-tracing equations (29), and performing the ζ and t-integrations, leads to the following propagators:

$$\overrightarrow{g_2^+}(\boldsymbol{\eta},\mathbf{s},\sigma|\mathbf{p}_0,\boldsymbol{\rho}_0,\sigma_0)=\left(\frac{k}{2\pi}\right)^2\left[\frac{n_0(\sigma)}{n_0(\sigma_0)}\right]^2\exp\{ik[\boldsymbol{\rho}(\sigma)\cdot\mathbf{s}-\boldsymbol{\eta}\cdot\mathbf{p}(\sigma)]\}\exp\left\{-k\int_{\sigma_0}^{\sigma}\frac{d\zeta}{n_0(\zeta)}\boldsymbol{\rho}(\zeta)\cdot\mathbf{b}(\zeta)\right\}$$
$$\times\exp\left\{ik\int_{\sigma_0}^{\sigma}d\zeta\left(\mu\left[\mathbf{p}(\zeta)+\frac{\mathbf{s}(\zeta)}{2},\zeta\right]-\mu\left[\mathbf{p}(\zeta)-\frac{\mathbf{s}(\zeta)}{2},\zeta\right]\right)\right\}\exp\left\{-ik\int_{\sigma_0}^{\sigma}d\zeta\,\boldsymbol{\nabla}_{\mathbf{p}}\mu[\mathbf{p}(\zeta),\zeta]\cdot\mathbf{s}(\zeta)\right\} \tag{30}$$

and

$$\overleftarrow{g_2^-}(\mathbf{p},\boldsymbol{\rho},\sigma|\boldsymbol{\eta}_0,\mathbf{s}_0,\sigma_0)=\left(\frac{k}{2\pi}\right)^2\left[\frac{n_0(\sigma)}{n_0(\sigma_0)}\right]^2\exp\{ik[\boldsymbol{\rho}\cdot\mathbf{s}(\sigma)-\boldsymbol{\eta}(\sigma)\cdot\mathbf{p}]\}\exp\left\{-k\int_{\sigma_0}^{\sigma}\frac{d\zeta}{n_0(\zeta)}\boldsymbol{\rho}(\zeta)\cdot\mathbf{b}(\zeta)\right\}$$
$$\times\exp\left\{ik\int_{\sigma_0}^{\sigma}d\zeta\left(\mu\left[\mathbf{p}(\zeta)+\frac{\mathbf{s}(\zeta)}{2},\zeta\right]-\mu\left[\mathbf{p}(\zeta)-\frac{\mathbf{s}(\zeta)}{2},\zeta\right]\right)\right\}\exp\left\{-ik\int_{\sigma_0}^{\sigma}d\zeta\,\boldsymbol{\nabla}_{\mathbf{p}}\mu[\mathbf{p}(\zeta),\zeta]\cdot\mathbf{s}(\zeta)\right\}. \tag{31}$$

The physical interpretation of the propagators (30) and (31) is evident. For example in (30), the transverse separation $\mathbf{s}$ between two rays having the slope differences $\boldsymbol{\eta}$ at the observation plane σ can be created by two rays emerging from the source with the center of mass coordinate $\mathbf{p}_0$ and the average slope $\boldsymbol{\rho}_0$.

Retransforming the spectral dependencies, results in the configuration space propagators

$$g_2^+(\mathbf{p},\mathbf{s}\sigma|\mathbf{p}_0,\mathbf{s}_0,\sigma_0)=\left(\frac{k}{2\pi}\right)^2\left[\frac{n_0(\sigma)}{n_0(\sigma_0)}\right]^2\int_{-\infty}^{\infty}\cdots\int d^2\rho_0\,d^2\eta\exp\left\{-k\int_{\sigma_0}^{\sigma}\frac{d\zeta}{n_0(\zeta)}\boldsymbol{\rho}(\zeta)\cdot\mathbf{b}(\zeta)\right\}$$
$$\times\exp\{ik\boldsymbol{\eta}\cdot[\mathbf{p}-\mathbf{p}(\sigma)]\}\exp\{ik[\boldsymbol{\rho}(\sigma)\cdot\mathbf{s}-\boldsymbol{\rho}_0\cdot\mathbf{s}_0]\}$$
$$\times\exp\left\{ik\int_{\sigma_0}^{\sigma}d\zeta\left(\mu\left[\mathbf{p}(\zeta)+\frac{\mathbf{s}(\zeta)}{2},\zeta\right]-\mu\left[\mathbf{p}(\zeta)-\frac{\mathbf{s}(\zeta)}{2},\zeta\right]\right)\right\}\exp\left\{-ik\int_{\sigma_0}^{\sigma}d\zeta\,\boldsymbol{\nabla}_{\mathbf{p}}\mu[\mathbf{p}(\zeta),\zeta]\cdot\mathbf{s}(\zeta)\right\}, \tag{32}$$

and

$$g_2^-(\mathbf{p},\mathbf{s},\sigma|\mathbf{p}_0,\mathbf{s}_0,\sigma_0)=\left(\frac{k}{2\pi}\right)^2\left[\frac{n_0(\sigma)}{n_0(\sigma_0)}\right]^2\int_{-\infty}^{\infty}\cdots\int d^2\rho\, d^2\eta_0\exp\left\{-k\int_{\sigma_0}^{\sigma}\frac{d\zeta}{n_0(\zeta)}\boldsymbol{\rho}(\zeta)\cdot\mathbf{b}(\zeta)\right\}$$
$$\times\exp\{ik[\boldsymbol{\eta}(\sigma)\cdot\mathbf{p}-\boldsymbol{\eta}_0\cdot\mathbf{p}_0]\}\exp\{ik\boldsymbol{\rho}\cdot[\mathbf{s}-\mathbf{s}(\sigma)]\}\exp\left\{ik\int_{\sigma_0}^{\sigma}d\zeta\left(\mu\left[\mathbf{p}(\zeta)+\frac{\mathbf{s}(\zeta)}{2},\zeta\right]\right.\right.$$
$$\left.\left.-\mu\left[\mathbf{p}(\zeta)-\frac{\mathbf{s}(\zeta)}{2},\zeta\right]\right)\right\}\exp\left\{-ik\int_{\sigma_0}^{\sigma}d\zeta\,\boldsymbol{\nabla}_{\mathbf{p}}\mu[\mathbf{p}(\zeta),\zeta]\cdot\mathbf{s}(\zeta)\right\}. \tag{33}$$

The expressions in (32) and (33) coincide with the main order solutions obtained by the two-scale expansion method.[37,40] Thus, by showing how the multiscale expansion result can be obtained from the functional integral solution we revealed the physical meaning of the multiscale solutions. The propagators derived by the multiscale expansion procedure in principle relate quantities defined in different configuration-spectral domains what allows to account for the uncertainty introduced into the wave propagation phenomena by random refractive index fluctuations. Once the propagation relations between such mixed spaces are formulated explicitly, the propagators relating the configuration spaces both at the source and observation planes can be easily obtained by application of the spectral transforms to the mixed propagators. Because of these spectral transformations, the multiscale result cannot be factorized into separate field solutions. As can be seen from Eqs. (32) and (33), the multiscale expansion approach allows to considerably reduce the integration volume and present expressions for the propagation characteristics in a form of finite-dimensional integrals that include only a limited range of continual trajectories taken into account in the path-integral solutions, and consequently lead to the numerically manageable algorithms for the statistical field measures.

In absence of scattering expanding the $\mu_b(\cdot)$ functions in Eqs. (32) and (33) into power series, and keeping the terms up to the third order allows the integrations to be performed. The result is the Airy-type distribution characteristic to the intensity at the simple caustic.[36,37,40] Retaining the additional terms in the expansion is responsible for the intensity corrections in the caustics of the higher order.

In the case of a homogeneous background medium the solutions in (32) and (33) become

$$g_2^+(\mathbf{p},\mathbf{s}\sigma|\mathbf{p},\mathbf{s}\sigma_0)=\left(\frac{k}{2\pi}\right)^2\int_{-\infty}^{\infty}\cdots\int d^2\rho_0\, d^2\eta\exp\{ik\boldsymbol{\eta}\cdot[\mathbf{p}-\mathbf{p}_0-\boldsymbol{\rho}(\sigma-\sigma_0)]\}\exp[ik\boldsymbol{\rho}_0\cdot(\mathbf{s}-\mathbf{s}_0)]$$
$$\times\exp\left\{ik\int_{\sigma_0}^{\sigma}d\zeta\left(\tilde{n}\left[\mathbf{p}_0+\boldsymbol{\rho}_0(\zeta-\sigma_0)+\frac{\mathbf{s}}{2}+\frac{\boldsymbol{\eta}(\zeta-\sigma)}{2},\zeta\right]-\tilde{n}\left[\mathbf{p}_0+\boldsymbol{\rho}_0(\zeta-\sigma_0)-\frac{\mathbf{s}}{2}-\frac{\boldsymbol{\eta}(\zeta-\sigma)}{2},\zeta\right]\right)\right\}, \tag{34}$$

and

$$g_2^-(\mathbf{p},\mathbf{s},\sigma|\mathbf{p},\mathbf{s},\sigma_0)=\left(\frac{k}{2\pi}\right)^2\int_{-\infty}^{\infty}\cdots\int d^2\rho\, d^2\eta_0\exp\{ik\boldsymbol{\eta}_0\cdot[\mathbf{p}-\mathbf{p}_0-\boldsymbol{\rho}(\sigma-\sigma_0)]\}\exp[ik\boldsymbol{\rho}\cdot(\mathbf{s}-\mathbf{s}_0)]$$
$$\times\exp\left\{ik\int_{\sigma_0}^{\sigma}d\zeta\left(\tilde{n}\left[\mathbf{p}+\boldsymbol{\rho}(\zeta-\sigma_0)+\frac{\mathbf{s}_0}{2}+\frac{\boldsymbol{\eta}_0(\zeta-\sigma)}{2},\zeta\right]-\tilde{n}\left[\mathbf{p}+\boldsymbol{\rho}(\zeta-\sigma_0)-\frac{\mathbf{s}_0}{2}-\frac{\boldsymbol{\eta}_0(\zeta-\sigma)}{2},\zeta\right]\right)\right\}. \tag{35}$$

The propagators in Eqs. (34) and (35) have been used for constructing the field and intensity correlation characteristics in a statistically homogeneous random medium.[40] Also they have been tested for the point source–point scatter configuration which serves as a canonical double-passage problem. Consequently they have been successfully applied to double-passage analysis[41,52,53] in random media.

V. APPLICATION TO THE ANALYSIS OF DOUBLE-PASSAGE RESOLUTION EFFECTS

The high-frequency propagators constructed in this work contain information about the random refractive index variation along the propagation path. The confirmation of their performance in one-directional propagation problems together with the ability to account for forward–backward correlation, supports their application to the analysis of double-passage effects. One of the consequences of the forward–backward correlation is the intensity enhancement effect observed in various areas of physics.[47–53]

Let the TPRF $\Gamma(\mathbf{r}_{i1},\mathbf{r}_{i2},\sigma)$ propagates along the reference ray in the backward direction from σ to σ_0 ($\sigma>\sigma_0$). Its propagation is governed by the propagation relation (19) with the complex-conjugate propagator in Eq. (30), and at the range plane σ_0 creates the field pattern $u(\mathbf{r}_0,\sigma)$, which is reflected with the local reflection coefficient $K(\mathbf{r}_0)$ and then propagates in the forward direction. The reflected field is observed at the range plane σ and creates there the following distribution for the TPRF:

$$r_{\mathrm{ref}}(\mathbf{p},\mathbf{s},\sigma)=\int_{-\infty}^{\infty}\cdots\int d^m p_0\, d^m s_0\, d^m p_1\, d^m s_1 \times K\left(\mathbf{p}_0+\frac{\mathbf{s}_0}{2}\right)K^*\left(\mathbf{p}_0-\frac{\mathbf{s}_0}{2}\right) \times g_2(\mathbf{p}_1,\mathbf{s}_1,\sigma|\mathbf{p}_0,\mathbf{s}_0,\sigma_0) \times g_2(\mathbf{p},\mathbf{s},\sigma|\mathbf{p}_0,\mathbf{s}_0,\sigma_0)\Gamma(\mathbf{p}_1,\mathbf{s}_1,\sigma). \quad (36)$$

The average intensity distribution observed at the source plane σ_0 is obtained by applying ensemble averaging to (36) and setting $\mathbf{p}=\mathbf{r},\ \mathbf{s}=0$:

$$\langle I(\mathbf{r},\sigma_0,\sigma)\rangle=\int_{-\infty}^{\infty}\cdots\int d^m p_0\, d^m s_0\, d^m p_1\, d^m s_1 \times K\left(\mathbf{p}_0+\frac{\mathbf{s}_0}{2}\right)K^*\left(\mathbf{p}_0-\frac{\mathbf{s}_0}{2}\right) \times\langle g_2(\mathbf{p}_1,\mathbf{s}_1,\sigma|\mathbf{p}_0,\mathbf{s}_0,\sigma_0) g_2(\mathbf{p},\mathbf{s},\sigma|\mathbf{p}_0,\mathbf{s}_0,\sigma_0)\rangle\Gamma(\mathbf{p}_1,\mathbf{s}_1,\sigma), \quad (37)$$

where the angular brackets denote ensemble average.

The averaging procedure on the product of the propagators in (37) can be performed by assuming that the refractive index fluctuations represent a Gaussian random field. Also as applicable in the random propagation problems, these fluctuations are assumed to be delta correlated along the main propagation direction, and can be presented by the following correlation function:

$$B_n(\mathbf{r}_1-\mathbf{r}_2,\sigma_1-\sigma_2)=\langle\tilde{n}(\mathbf{r}_1,\sigma_1)\tilde{n}(\mathbf{r}_2,\sigma_2)\rangle =A_n(\mathbf{r}_1-\mathbf{r}_2,\sigma_1)\,\delta(\sigma_1-\sigma_2). \quad (38)$$

Here, the function $A_n\ (\mathbf{r}_1-\mathbf{r}_2,\sigma_1)$ describes correlation in the transverse plane σ_1. The averaging procedure is described in a number of works,[39,40,52] and the result for the propagator (32) is given by the following expression:

$$\langle g_2(\mathbf{p}_1,\mathbf{s}_1,\sigma|\mathbf{p}_0,\mathbf{s}_0,\sigma_0)g_2(\mathbf{p}_2,\mathbf{s}_2,\sigma|\mathbf{p}_0,\mathbf{s}_0,\sigma_0)\rangle$$
$$=\left(\frac{k}{2\pi}\right)^4\left[\frac{n_0(\sigma)}{n_0(\sigma_0)}\right]^4\int_{-\infty}^{\infty}\cdots\int d^2\rho_1\, d^2\eta_{10}\, d^2\rho_2\, d^2\eta_{20}\exp\{ik\boldsymbol{\eta}_1\cdot[\mathbf{p}_1-\mathbf{p}_1(\sigma)]\}$$
$$\times\exp\{ik\boldsymbol{\eta}_2\cdot[\mathbf{p}_2-\mathbf{p}_2(\sigma)]\}\exp\{ik[\boldsymbol{\rho}_1(\sigma)\cdot\mathbf{s}_1-\boldsymbol{\rho}_{10}\cdot\mathbf{s}_{10}]\}\exp\{ik[\boldsymbol{\rho}_2(\sigma)\cdot\mathbf{s}_2-\boldsymbol{\rho}_{20}\cdot\mathbf{s}_{20}]\}$$
$$\times\exp\left\{ik\int_{\sigma_0}^{\sigma}d\zeta\left(\mu_b\left[\mathbf{p}_1(\zeta)+\frac{\mathbf{s}_1(\zeta)}{2},\zeta\right]-\mu_b\left[\mathbf{p}_1(\zeta)-\frac{\mathbf{s}_1(\zeta)}{2},\zeta\right]\right)\right\}$$
$$\times\exp\left\{ik\int_{\sigma_0}^{\sigma}d\zeta\left(\mu_b\left[\mathbf{p}_2(\zeta)+\frac{\mathbf{s}_2(\zeta)}{2},\zeta\right]-\mu_b\left[\mathbf{p}_2(\zeta)-\frac{\mathbf{s}_2(\zeta)}{2},\zeta\right]\right)\right\}$$
$$\times\exp\left\{-ik\int_{\sigma_0}^{\sigma}d\zeta[\nabla_{\mathbf{p}_1},\mu_b[\mathbf{p}_1(\zeta),\zeta]\cdot\mathbf{s}_1(\zeta)+\nabla_{\mathbf{p}_2}\mu_b[\mathbf{p}_2(\zeta),\zeta]\cdot\mathbf{s}_2(\zeta)]\right\}\exp\left\{-\frac{1}{2}k^2\int_0^{\Delta\sigma}\frac{d\zeta}{n_0^2(\zeta)}F_{bs}(\mathbf{s}_0,\mathbf{s}_s,\boldsymbol{\rho},\boldsymbol{\eta},\zeta)\right\}, \quad (39a)$$

with the scattering function

$$F_{bs}(\mathbf{s}_0,\mathbf{s}_1,\mathbf{s}_2,\boldsymbol{\rho},\boldsymbol{\eta},\zeta)=\frac{1}{n_0^2(\zeta)}\left\{\left(n^2\left[\mathbf{p}(\zeta)+\frac{\mathbf{s}_1(\zeta)}{2},\zeta\right]+\eta^2\left[\mathbf{p}_1(\zeta)-\frac{\mathbf{s}_1(\zeta)}{2},\zeta\right]\right)A_n(0,\zeta)\right\}$$
$$+\left(n^2\left[\mathbf{p}_2(\zeta)+\frac{\mathbf{s}_2(\zeta)}{2},\zeta\right]+n^2\left[\mathbf{p}_2(\zeta)-\frac{\mathbf{s}_2(\zeta)}{2},\zeta\right]\right)A_n(0,\zeta)-2n\left[\mathbf{p}_1(\zeta)+\frac{\mathbf{s}_1(\zeta)}{2},\zeta\right]n$$
$$\times\left[\mathbf{p}_1(\zeta)-\frac{\mathbf{s}_1(\zeta)}{2},\zeta\right]A_n[\mathbf{s}_1(\zeta),\zeta]-2n\left[\mathbf{p}_2(\zeta)+\frac{\mathbf{s}_2(\zeta)}{2},\zeta\right]n\left[\mathbf{p}_2(\zeta)-\frac{\mathbf{s}_2(\zeta)}{2},\zeta\right]A_n[\mathbf{s}_2(\zeta),\zeta]$$
$$-2n\left[\mathbf{p}_1(\zeta)+\frac{\mathbf{s}_1(\zeta)}{2},\zeta\right]n\left[\mathbf{p}_2(\zeta)-\frac{\mathbf{s}_2(\zeta)}{2},\zeta\right]A_n\left[\mathbf{p}_1(\zeta)-\mathbf{p}_2(\zeta)+\frac{\mathbf{s}_1(\zeta)+\mathbf{s}_2(\zeta)}{2},\zeta\right]$$
$$-2n\left[\mathbf{p}_1(\zeta)-\frac{\mathbf{s}_1(\zeta)}{2},\zeta\right]n\left[\mathbf{p}_2(\zeta)+\frac{\mathbf{s}_2(\zeta)}{2},\zeta\right]A_n\left[\mathbf{p}_1(\zeta)-\mathbf{p}_2(\zeta)-\frac{\mathbf{s}_1(\zeta)+\mathbf{s}_2(\zeta)}{2},\zeta\right]$$
$$+2n\left[\mathbf{p}(\zeta)+\frac{\mathbf{s}_1(\zeta)}{2},\zeta\right]n\left[\mathbf{p}_2(\zeta)+\frac{\mathbf{s}_2(\zeta)}{2},\zeta\right]A_n\left[\mathbf{p}_1(\zeta)-\mathbf{p}_2(\zeta)+\frac{\mathbf{s}_1(\zeta)-\mathbf{s}_2(\zeta)}{2},\zeta\right]$$
$$\times\left\{+2n\left[\mathbf{p}(\zeta)-\frac{\mathbf{s}_1(\zeta)}{2},\zeta\right]n\left[\mathbf{p}_2(\zeta)-\frac{\mathbf{s}_2(\zeta)}{2},\zeta\right]A_n\left[\mathbf{p}_1(\zeta)-\mathbf{p}_2(\zeta)-\frac{\mathbf{s}_1(\zeta)-\mathbf{s}_2(\zeta)}{2},\zeta\right]\right\}. \quad (39b)$$

The expression in (39a) contains a fourfold integral over the spectral variables $\boldsymbol{\rho}_1$, $\boldsymbol{\eta}_{10}$, $\boldsymbol{\rho}_2$, and $\boldsymbol{\eta}_{20}$ which appear in the functions $p_1(\zeta)$, $s_1(\zeta)$, $p_2(\zeta)$, $s_2(\zeta)$ and $\rho_1(\sigma)$, $\rho_2(\sigma)$. Its computation in a general inhomogeneous background case represents a difficult task. However it can be considerably simplified in the case of a statistically isotropic homogeneous random medium. The average product of the propagators in Eq. (39a) then reduces to

$$\langle g_2(\mathbf{p}_1,\mathbf{s}_1,\sigma|\mathbf{p}_0,\mathbf{s}_0,\sigma_0)g_2(\mathbf{p}_2,\mathbf{s}_2,\sigma|\mathbf{p}_0,\mathbf{s}_0,\sigma_0)\rangle$$
$$=\left(\frac{k}{2\pi\Delta\sigma}\right)^{2m}\int_{-\infty}^{\infty}\cdots\int d^m\rho\, d^m\eta\exp[ik\boldsymbol{\eta}\cdot(\mathbf{p}_1-\mathbf{p}_2)]\exp\left[\frac{ik}{2}\boldsymbol{\rho}\cdot(\mathbf{s}-\mathbf{s}_2)\right]\exp(-ik\boldsymbol{\eta}\cdot\boldsymbol{\rho}\Delta\sigma)$$
$$\times\exp\left\{\frac{ik}{2}\mathbf{p}_0\cdot(2\mathbf{s}_0-\mathbf{s}-\mathbf{s}_2)\right\}\exp\left\{\frac{ik}{2\Delta\sigma}(\mathbf{p}_1-\mathbf{p}_2)\cdot(\mathbf{s}_1+\mathbf{s}_2-2\mathbf{s}_0)\right\}\exp\left\{-k^2\int_0^{\Delta\sigma}d\zeta\, F_s(\mathbf{s}_0,\mathbf{s}_s,\boldsymbol{\rho},\boldsymbol{\eta},\zeta)\right\}, \tag{40a}$$

with the function F_s defined as

$$F_s(\mathbf{s}_0,\mathbf{s}_1,\mathbf{s}_2,\boldsymbol{\rho},\boldsymbol{\eta},\zeta)=2A_n(0)-A_n\left[\mathbf{s}_1+\frac{2\mathbf{s}_0-\mathbf{s}_1-\mathbf{s}_2}{2}(1-\zeta/\Delta\sigma)+\boldsymbol{\eta}(\zeta-\Delta\sigma)\right]$$
$$-A_n\left[\mathbf{s}_2+\frac{2\mathbf{s}_0-\mathbf{s}_1-\mathbf{s}_2}{2}(1-\zeta/\Delta\sigma)-\boldsymbol{\eta}(\zeta-\Delta\sigma)\right]-A_n\left[\boldsymbol{\rho}\zeta+\frac{\mathbf{s}_1+\mathbf{s}_2}{2}+\frac{2\mathbf{s}_0-\mathbf{s}_1-\mathbf{s}_2}{2}(1-\zeta/\Delta\sigma)\right]$$
$$-A_n\left[\boldsymbol{\rho}\zeta-\frac{\mathbf{s}_1+\mathbf{s}_2}{2}-\frac{2\mathbf{s}_0-\mathbf{s}_1-\mathbf{s}_2}{2}(1-\zeta/\Delta\sigma)\right]+A_n\left[\boldsymbol{\rho}\zeta+\frac{\mathbf{s}_1-\mathbf{s}_2}{2}+\boldsymbol{\eta}(1-\zeta/\Delta\sigma)\right]$$
$$+A_n\left[\boldsymbol{\rho}\zeta-\frac{\mathbf{s}_1-\mathbf{s}_2}{2}-(1-\zeta/\delta\sigma)\right]. \tag{40b}$$

The transverse correlation function is described then by the range independent function $A_n(\mathbf{r})$.

To exemplify the double-passage problem, the possibility of resolving two two-dimensional line scatterers illuminated by a plane wave is considered. Such a configuration occurs when an incident wave is backscattered by two parallel wedges as exhibited in Fig. 1. The backscattered intensity distribution observed at the source plane can be presented as a sum of noncoherent and coherent portions:

$$I(r,\Delta\sigma,a)=I_{nc}(r,\Delta\sigma,a)+I_c(r,\Delta\sigma,a). \tag{41}$$

With range the phase coherence in presence of random refractive index fluctuations decreases very rapidly. Beyond this point the analysis is performed by considering only the noncoherent contribution obtained by using the following boundary condition in (37):

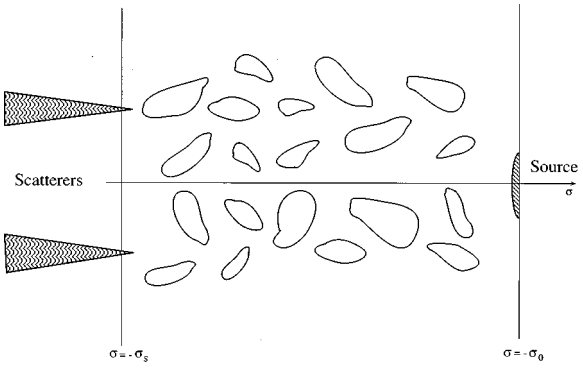

FIG. 1. Double-passage configuration for two point scatterers.

$$K\left(p_0+\frac{s_0}{2}\right)K^*\left(p_0+\frac{s_0}{2}\right)$$
$$=[\kappa_1\delta(p_0-a)+\kappa_2\delta(p_0+a)]\delta(s_0), \tag{42}$$

where κ_1 and κ_2 are the scattering amplitudes and are given by the corresponding GTD wedge diffraction coefficients.[34,35,37] For simplicity, these amplitudes are chosen to be equal: $\kappa_1=\kappa_2=\chi$. This leads to the following expression for the incoherent intensity distribution:

$$I_{nc}(r,\Delta\sigma,a)=\left(\frac{k}{2\pi}\right)^2\frac{4\chi}{\Delta\sigma}\int_0^{\infty}d\rho\int_{-\infty}^{\infty}d\eta$$
$$\times\cos\left(\frac{k\eta\rho}{\Delta\sigma}\right)\cos\left(\frac{k\eta r}{\Delta\sigma}\right)\cos\left(\frac{k\eta a}{\Delta\sigma}\right)$$
$$\times\exp\left[-\frac{1}{2}k^2\Delta\sigma\int_0^1 dt\, f_1(\rho,\eta,t)\right] \tag{43}$$

with the scattering functions being

$$f_1(\rho,\eta,t)=2A_n(0)-A_n(\eta)-A_n[\eta(1-t)]$$
$$-A_n\left(\rho t+\frac{\eta t}{2}\right)-A_n\left(\rho t-\frac{\eta t}{2}\right)$$
$$+A_n\left[\rho t+\frac{\eta(2-t)}{2}\right]+A_n\left[\rho t-\frac{\eta(2-t)}{2}\right]. \tag{44}$$

To investigate that image pattern a random medium characterized by a Gaussian correlation function

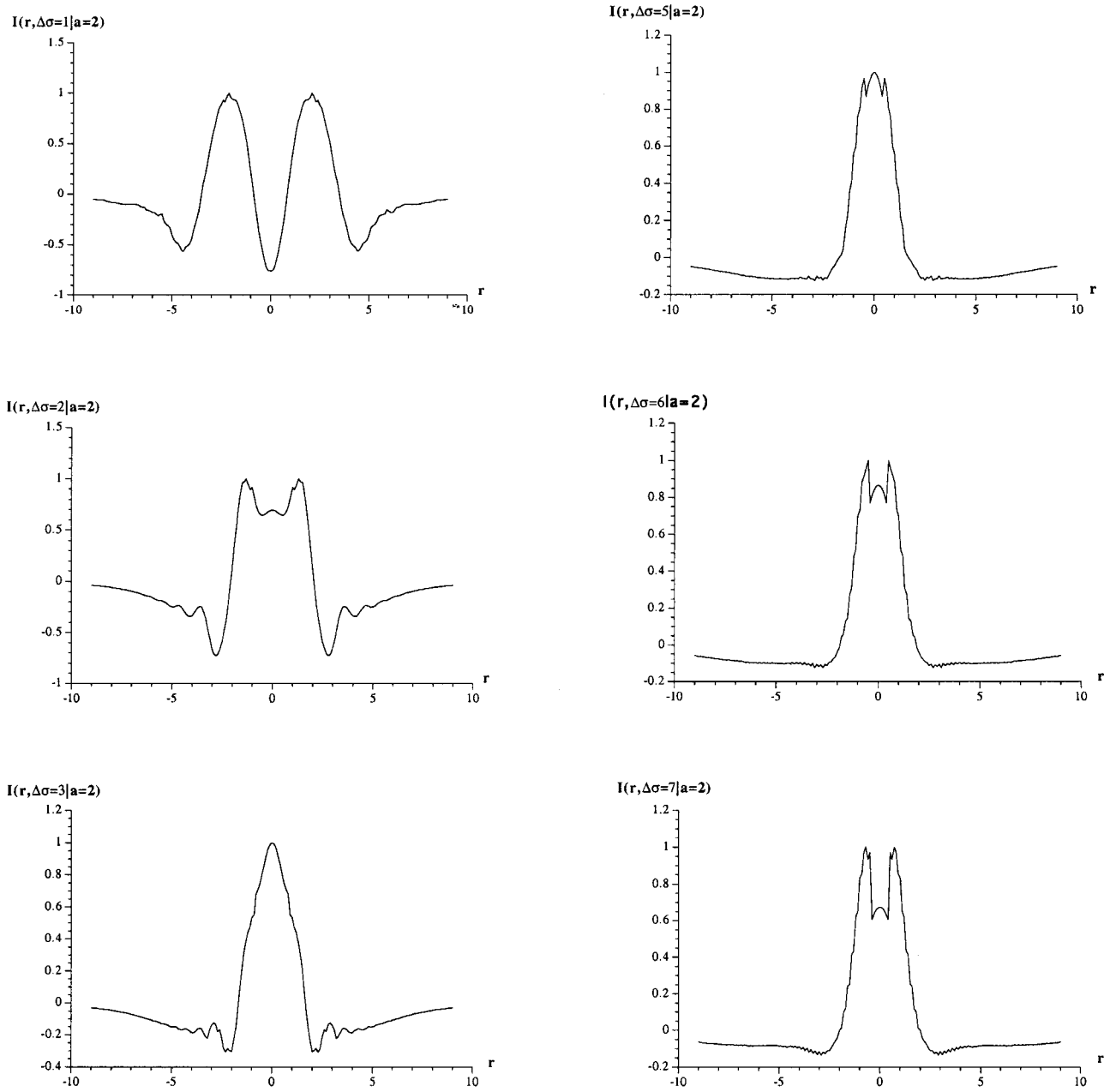

FIG. 2. Intensity distribution in the transverse plane at the observer for different normalized source–object separation ranges $\Delta\sigma{:}a=2$. Gaussian spectrum.

$$A_n(r)=A_n(0)\overline{A}_n\left(\frac{r}{l_n}\right) \tag{45}$$

is chosen, and the calculations are performed by introducing scaled coordinates

$$r=l_n\overline{r},\quad a=l_n\overline{a},\quad \sigma=kl_n^2\overline{\sigma}, \tag{46}$$

and the scattering parameter

$$\gamma=k^3A_n(0)l_n^2. \tag{47}$$

In Figs. 2(a)–(d) and 3(a)–(d) the normalized transverse backscattered intensity distribution measured above the constant intensity level (dc level measured without taking into account the noncorrelated backscattering effects) is presented as a function of the normalized transverse coordinate $\overline{r}=r/F$ for different values of the normalized distance between the scatterers $\overline{a}=a/l_n$. The scattering parameter was chosen $\gamma=1$.

For the separation $\overline{a}=2$ initially the two scatterers can be resolved up to the range $\Delta\overline{\sigma}=3$. After this range there is an intensity enhancement in the double-passage intensity distribution, but the scatterers cannot be resolved. At the range $\Delta\overline{\sigma}=5$, the resolving ability appears again in a form of a hollow in the double-passage intensity distribution. Its depth increases with the range. Decreasing the scatterer separation to $\overline{a}=1$ leads to disappearance of the double-passage resolution until the range $\Delta\overline{\sigma}=4$. However the hollow in the double-passage image distribution for this separation appears again at the range $\Delta\overline{\sigma}=5$ and its depth increases with range. Similar behavior is found for higher values of $\overline{a}$.

The appearance of a hollow in the double-passage picture exhibits a new, though weak, superresolution effect.

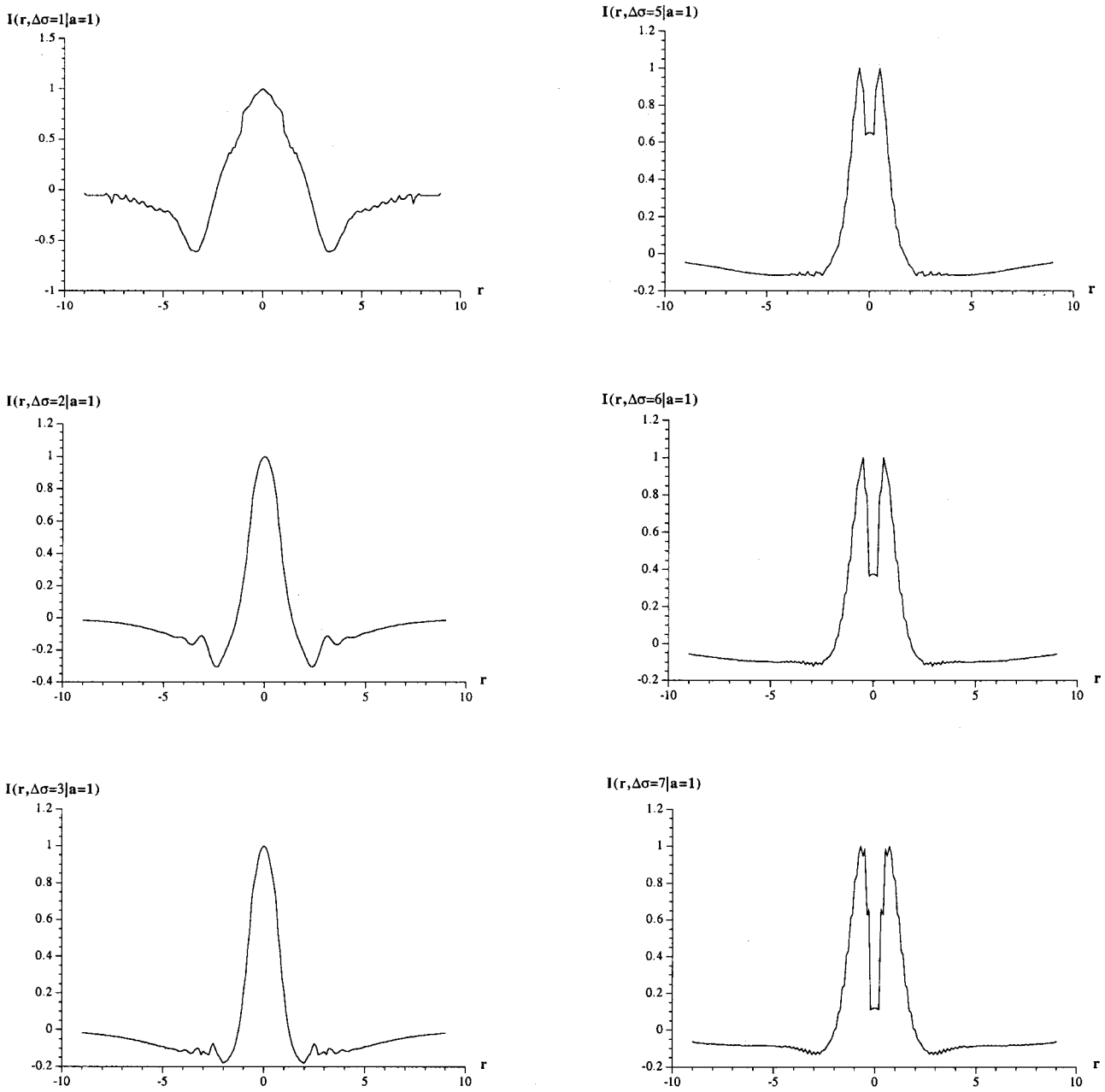

FIG. 3. Intensity distribution in the transverse plane at the observer for different normalized source–object separation ranges $\Delta\sigma{:}a=1$. Gaussian spectrum.

VI. PARABOLIC EQUATION METHOD FOR THE EXTENDED MEDIUM

In this section a more general case, when the parabolic ray extension cannot be performed is being considered. To solve this problem the approach originally proposed by Fock for the integration of quantum-mechanical equations is applied in a number of works related to deterministic and stochastic wave propagation and scattering problems.[54–62]

We start with the Helmholtz equation (1) formulating it for Green's function

$$\nabla^2 G(\mathbf{R}|\mathbf{R}_0)+k^2[\,\nu^2(\mathbf{R})+1\,]G(\mathbf{R}|\mathbf{R}_0)=-\,\delta(\mathbf{R}-\mathbf{R}_0), \tag{48}$$

where $G(\mathbf{R}|\mathbf{R}_0)$ is the free-space Green's function, and the function $(\mathbf{R})$ is defined as

$$\nu(\mathbf{R})=N^2(\mathbf{R})-1. \tag{49}$$

Now let us consider an auxiliary problem for a function $g(\mathbf{R},\tau|\mathbf{R}_0,\tau_0)$ satisfying the generalized parabolic equation

$$2ik\,\frac{\partial g(\mathbf{R},\tau|\mathbf{R}_0,\tau_0)}{\partial\tau}+\nabla^2 g(\mathbf{R},\tau|\mathbf{R}_0,\tau_0)$$

$$+k^2\nu(\mathbf{R})g(\mathbf{R},\tau|\mathbf{R}_0,\tau_0)=0,\quad \tau>\tau_0, \tag{50a}$$

with the initial condition

$$g(\mathbf{R},\tau_0|\mathbf{R}_0,\tau_0)=\delta(\mathbf{R}-\mathbf{R}_0). \tag{50b}$$

The function $g(\mathbf{R},\tau|\mathbf{R}_0,\tau_0)$ is also supposed to satisfy the radiation condition. It can be shown[57–59] that the solutions of (36) and (37) are related by the integral transform

$$G(\mathbf{R}|\mathbf{R}_0)=\frac{i}{2k}\int_0^\infty d\tau\exp\left[\frac{ik}{2}(\tau-\tau_0)\right]g(\mathbf{R},\tau|\mathbf{R}_0,\tau_0). \tag{51}$$

We note that the generalized parabolic equation (50a) has a higher dimension than the classical one. For a homogeneous medium $[n(\mathbf{R})=1]$, the solution of (50a) is

$$g(\mathbf{R},\tau|\mathbf{R}_0,\tau_0)=\left[\frac{k}{2\pi i(\tau-\tau_0)}\right]^{3/2}\exp\left[\frac{ik(\mathbf{R}-\mathbf{R}_0)^2}{2(\tau-\tau_0)}\right]. \tag{52}$$

Substituting (52) into (51) and taking into account the Hankel function representation, gives the required expression for the free-space Green's function.

Since Eq. (50a) is of a parabolic type, its solution can be presented in a continual integral form

$$g(\mathbf{R},\tau|\mathbf{R}_0,\tau_0)=\int D\mathbf{V}\,\delta\left[\mathbf{R}-\mathbf{R}_0-\int_0^\tau d\zeta\,\mathbf{V}(\zeta)\right]\times\exp\left\{\frac{ik}{2}\int_{\tau_0}^{\tau}d\zeta\,\mathbf{V}^2(\zeta)\right\}\times\exp\left\{ik\int_{\tau_0}^{\tau}d\zeta\,\nu\left[\mathbf{R}-\int_\zeta^\tau dt\,\mathbf{V}(t)\right]\right\}, \tag{53a}$$

$$\int D\mathbf{V}(\zeta)\exp\left\{\frac{ik}{2}\int_{\tau_0}^{\tau}d\zeta\,\mathbf{V}^2(\zeta)\right\}=1. \tag{53b}$$

The generalized two-point random function propagator (GTPRF) can also be defined as a product of propagators in (53a). We note that this product has to be taken at different range-like coordinates τ_1 and τ_2. Taking $\tau_0=0$, and introducing the sum and difference coordinates

$$\mathbf{P}=\frac{\mathbf{R}_1+\mathbf{R}_2}{2},\quad \mathbf{S}=\mathbf{R}_1-\mathbf{R}_2, \tag{54}$$

$$\tau=\frac{\tau_1+\tau_2}{2},\quad \zeta=\tau_1-\tau_2. \tag{55}$$

The propagator g_2 can be expressed as a product of propagators g,

$$g_2\left(\mathbf{P},\mathbf{S},\tau+\frac{\zeta}{2},\tau-\frac{\zeta}{2}\middle|\mathbf{P}_0,\mathbf{S}_0,0,0\right)=g\left(\mathbf{P}+\frac{\mathbf{S}}{2},\tau+\frac{\zeta}{2}\middle|\mathbf{P}_0+\frac{\mathbf{S}_0}{2},0\right)g^*\times\left(\mathbf{P}-\frac{\mathbf{S}}{2},\tau-\frac{\zeta}{2}\middle|\mathbf{P}_0-\frac{\mathbf{S}_0}{2},0\right). \tag{56}$$

Reducing the approximate solutions from (55) is not straightforward. Therefore the following procedure is proposed. The generalized parabolic equation (50a) can be written in the coordinates $\mathbf{R}_1$, τ_1 and a complex-conjugate one written in the coordinates $\mathbf{R}_2$, τ_2. Taking their sum and difference leads to the following equations governing propagation of the two-point propagator g_2:

$$\frac{\partial g_2}{\partial\tau_1}+\frac{\partial g_2}{\partial\tau_2}=\frac{i}{2k}(\boldsymbol{\nabla}_1^2-\boldsymbol{\nabla}_2^2)g_2+\frac{ik}{2}[\nu(\mathbf{R}_1)-\nu(\mathbf{R}_2)]g_2=0, \tag{57}$$

$$\frac{\partial g_2}{\partial\tau_1}-\frac{\partial g_2}{\partial\tau_2}=\frac{i}{2k}(\boldsymbol{\nabla}_1^2+\boldsymbol{\nabla}_2^2)g_2+\frac{ik}{2}[\nu(\mathbf{R}_1)+\nu(\mathbf{R}_2)]g_2=0, \tag{58}$$

Or, in the sum and difference coordinates defined in Eqs. (54) and (55), Eqs. (57) and (58) take the following form:

$$\frac{\partial g_2}{\partial\tau}=\frac{i}{k}(\boldsymbol{\nabla}_\mathbf{P}\cdot\boldsymbol{\nabla}_\mathbf{S})g_2+\frac{ik}{2}\left[\nu\left(\mathbf{P}+\frac{\mathbf{S}}{2}\right)-\nu\left(\mathbf{P}-\frac{\mathbf{S}}{2}\right)\right]g_2, \tag{59}$$

$$\frac{\partial g_2}{\partial\zeta}=\frac{i}{k}\left(\frac{1}{4}\boldsymbol{\nabla}_p^2+\boldsymbol{\nabla}_S^2\right)g_2+\frac{ik}{2}\left[\nu\left(\mathbf{P}+\frac{\mathbf{S}}{2}\right)+\nu\left(\mathbf{P}-\frac{\mathbf{S}}{2}\right)\right]g_2, \tag{60}$$

where the coordinate ζ in (59) and coordinate τ in (60) appear as parameters only. For weak scattering conditions, we applied the perturbation solutions of the generalized parabolic equation to the analysis of the backscattering and localization effects.[59–61] Here we will discuss some possible solutions, which can be applied for strong scattering. Equation (59) can be solved for $\zeta=0$, and this solution can be used as an initial condition for (60). The solution of (59) can be written in a similar form to (34) and/or (35) of the regular parabolic equation. As for Eq. (60) a good approximation for its solution can be to take a solution presented in a Huygens–Kirchoff form. Another possibility is to apply to (60) the reference wave method which is presently being developed.[63,64] A detailed analysis of these problems is beyond the scope of this paper and will be presented in future works.

VII. SUMMARY

In this paper, the acoustic waves described by a scalar Helmholtz's equation have been considered. By extracting the term that accounts for the main phase variation, the Helmholtz equation has been reduced to a parabolic wave equation describing the high-frequency propagation along a properly chosen reference ray in an inhomogeneous background random medium. The parabolic formulation enabled the solutions for the high-frequency ray propagators of the random field and its paired measures to be presented in the path-integral form. Using these path-integral solutions it has been shown that uncertainty considerations play an important role in choosing the most essential ray trajectories for the construction of the approximate propagators and computations of the statistical propagation characteristics. In order to account for the uncertainty in the high-frequency propagation there was a need to choose a proper pair of coordinates related to the spatial location and to the slope of geometrical ray trajectories. The above quantities can be introduced into the propagation process analytically only by considering a higher dimensional space which allows a transfer to mixed configurational-phase space quantities. As a starting point a paired field measure called the two-point function (TPF) and its spectral transforms known as Wigner and ambiguity functions have been defined. Constructing the path-integral solutions for the above defined measures and applying the spec-

tral transformations lead to the path-integral expressions also for the propagators relating the quantities in the mixed configuration-spectral domains. Formulation of the propagation relations between different configuration-spectral spaces allows to account for the uncertainty introduced into the propagation phenomena by the random refractive index fluctuations and to obtain both physically and quantitatively correct results while retaining a limited range of the trajectories in the path-integral solutions. For example, replacing the multiple trajectories by straight ray trajectories in the expressions derived leads to solutions equal to those obtained by the two-scale expansion method. In addition, considering the mixed spaces allowed revealing the physical meaning of the results derived by the multiscale asymptotic expansions and constructing them directly from the path-integral constructions.

As for every approximate result there is a question of comparison with the experimental data and determining its validity region. First let us take the case of propagation in a medium with absence of scattering. Here, as was shown previously, the multiscale solutions result in correct intensity distributions both in the paraxial case[10] and near a strongly refracted ray[36,37,41] and are equal to those obtained by the methods of uniform asymptotics. Scattering in the presence of random inhomogeneities has been extensively studied in the case of a homogeneous background random medium.[11–16,26,27] The results derived for the average field and the second order coherence measures of the field are shown to be in good agreement with the experimental data. Moreover, the intensity correlation measures constructed from the multiscale expansion solutions correctly represent the behavior in a turbulent medium. This gives confidence that the statistical field moments will also properly describe the correlation properties of the propagating high-frequency field around curved ray trajectories in the inhomogeneous background random medium when the ray curvatures are much larger than the characteristic random fluctuations scales.

The fact that the solutions for the high-frequency propagators preserve the random information along the propagation path makes them suitable for the analysis of double-passage effects. The point source—point scatterer configuration here serves as a canonical double-passage problem. The performance of the propagators derived in this work in this canonical situation, both in weak and strong scattering regimes, gave encouragement to present a scheme in which the filtering properties of an optical system were applied to resolve the backscattering enhancement effects and to extract the information about the spatial structure of distant objects. The resulting algorithm was applied to the two-point scatterers object. In addition to the ability to resolve these point scatterers in the weak scattering case, the results exhibit a weak super resolution effect. Investigations of these effects and their application to resolving objects of arbitrary shape for different source-object configurations will be addressed in future works.

Finally, there are arbitrary situations that do not allow the performance of the direct parabolic extension as described in Sec. II and require the analysis of the full Helmholtz's equation. For this case the approach originally proposed by Fock for the integration of quantum-mechanical equations was suggested. This general formulation allows the reduction of the elliptic propagation model at the level of the Helmholtz's equation to the parabolic type of problem. In the final part of this work the possible approximation methods for obtaining specific solutions of such types of problems are presented, leaving the analysis of the effects for future work. It is important to mention that there are alternative approaches to scattering problems, which take, into account radiation backscatter and two-way propagation.[65,66] Although these approaches may be more rigorous from the mathematical point of view, the solutions proposed in this work have several advantages because they contain the refractive index of the medium in an explicit form. This essentially simplifies the averaging procedure and the construction of the various statistical measures.

ACKNOWLEDGMENT

This research was supported by The Israel Science Foundation founded by the Israel Academy of Sciences and Humanities.

[1] L. B. Felsen and N. Marcuvitz, *Radiation and Scattering of Waves* (Prentice Hall, New Jersey, 1973).
[2] L. M. Brekhovskikh, *Waves in Layered Media* (Academic, New York, 1976).
[3] L. M. Brekhovskikh and Yu. Lysanov, *Fundamentals of Ocean Acoustics* (Springer, New York, 1982).
[4] *Wave Propagation and Underwater Acoustics*, edited by J. B. Keller and J. S. Papadakis (Springer, New York, 1977).
[5] M. A. Leontovich and V. A. Fock, "Solution of propagation of electromagnetic waves along the Earth's surface by the method of parabolic equations," J. Phys. (Moscow) **10**, 13–23 (1946).
[6] F. Tappert, "The parabolic equation method," in *Wave Propagation and Underwater Acoustics*, edited by J. B. Keller and J. S. Papadakis (Springer, New York, 1977), pp. 224–287.
[7] M. J. Beran, "Coherence equations governing propagation through random media," Radio Sci. **10**, 15–21 (1975).
[8] J. J. McCoy and M. J. Beran, "Propagation of beamed signals through inhomogeneous media: A diffraction theory," J. Acoust. Soc. Am. **59**, 1142–1149 (1976).
[9] M. J. Beran and A. M. Whitman, "Scattering of a finite beam in a random medium with a nonhomogeneous background," J. Math. Phys. **16**, 214–217 (1975).
[10] S. Frankenthal, M. J. Beran, and A. M. Whitman, "Caustic corrections using coherence theory," J. Acoust. Soc. Am. **71**, 348–358 (1982).
[11] M. J. Beran, A. M. Whitman, and S. Frankenthal, "Scattering calculations using the characteristic rays of the coherence function," J. Acoust. Soc. Am. **71**, 1124–1130 (1982).
[12] R. Mazar and M. J. Beran, "Intensity in stratified random media," J. Acoust. Soc. Am. **75**, 1748–1759 (1984).
[13] C. Macaskill, "An improved solution to the fourth moment equation for intensity fluctuations," Proc. R. Soc. London, Ser. A **386**, 461–474 (1983).
[14] S. Frankenthal, A. M. Whitman, and M. J. Beran, "Two-scale solutions for the intensity fluctuations in strong scattering," J. Opt. Soc. Am. A **1**, 585–597 (1984).
[15] A. M. Whitman and M. J. Beran, "Two-scale solution for atmospheric scintillation," J. Opt. Soc. Am. A **2**, 2133–2143 (1985).
[16] R. Mazar, J. Gozani, and M. Tur, "Two-scale solution for the intensity fluctuations of two-frequency wave propagation in a random medium," J. Opt. Soc. Am. A **2**, 2152–2160 (1985).
[17] R. P. Feynmann and A. R. Hibbs, *Quantum Mechanics and Path Integrals* (McGraw-Hill, New York, 1965).
[18] L. S. Schulman, *Techniques and Applications of Path Integration* (Wiley, New York, 1981).
[19] V. I. Klyatskin and V. I. Tatarskii, "The parabolic equation approximation

for propagation of waves in a medium with random inhomogeneities,'' Sov. Phys. JETP **31**, 335–339 (1970).
[20] J. E. Molyneux, ''Propagation of the *N*-th order coherence function in a random medium. General solutions and asymptotic behavior,'' J. Opt. Soc. Am. **61**, 369 (1971).
[21] P.-L. Chow, ''Applications of function space integrals to problems in wave propagation in random media,'' J. Math. Phys. **13**, 1224–1236 (1972).
[22] P.-L. Chow, ''On the exact and approximate solutions of a random parabolic equation,'' SIAM (Soc. Ind. Appl. Math.) J. Appl. Math. **27**, 376–397 (1974).
[23] P.-L. Chow, ''A functional phase-integral method and applications to the laser beam propagation in random media,'' J. Stat. Phys. **12**, 93–109 (1975).
[24] V. U. Zavorotny, V. I. Klyatskin, and V. I. Tatarskii, ''Strong fluctuations of the intensity of electromagnetic waves in randomly inhomogeneous media,'' Sov. Phys. JETP **46**, 252–260 (1978).
[25] R. Dashen, ''Path integrals for waves in random media,'' J. Math. Phys. **20**, 894–920 (1979).
[26] V. I. Tatarskii and V. U. Zavorotnyi, ''Strong fluctuations in light propagation in randomly inhomogeneous media,'' in *Progress in Optics*, edited by E. Wolf (North-Holland, Amsterdam, 1980), Vol. XVIII, pp. 205–256.
[27] M. I. Charnotskii, J. Gozani, V. I. Tatarskii, and V. U. Zavorotny, ''Wave propagation theories in random media based on the path-integral approach,'' in *Progress in Optics*, edited by E. Wolf (Elsevier, Amsterdam, 1993), Vol. XXXII, pp. 203–266.
[28] S. M. Flatte, R. Dashen, W. H. Munk, K. M. Watson, and F. Zachariasen, *Sound Transmission through a Fluctuating Ocean* (Cambridge University Press, London, 1980).
[29] S. M. Flatte, D. R. Bernstein, and R. Dashen, ''Intensity moments by path integral techniques for wave propagation through random media, with application to sound in the ocean,'' Phys. Fluids **26**, 1701–1713 (1983).
[30] R. Dashen, S. M. Flatte, and S. A. Reynolds, ''Path-integral treatment of acoustic mutual coherence functions for rays in sound channel,'' J. Acoust. Soc. Am. **77**, 1716–1722 (1985).
[31] B. J. Uscinski, C. Macaskill, and M. Spivak, ''Path integral for wave intensity fluctuations in random media,'' J. Sound Vib. **106**, 509–528 (1986).
[32] M. Levy, *Parabolic Equation Methods for Electromagnetic Wave Propagation* (IEE, London, 2000).
[33] F. B. Jensen, W. A. Kuperman, M. B. Porter, and H. Schmidt, *Computational Ocean Acoustics*, AIP series in Modern Acoustics and Signal Processing (AIP, New York, 1994).
[34] J. B. Keller, ''A geometrical theory of diffraction,'' in *Calculus of Variations and its Applications* (McGraw-Hill, New York, 1958), Vol. 8, pp. 27–52.
[35] *Geometric Theory of Diffraction*, edited by R. C. Hansen (IEEE, New York, 1981).
[36] R. Mazar and L. B. Felsen, ''High-frequency coherence functions propagated along ray paths in the inhomogeneous background of a weakly random medium: I—Formulation and Evaluation of the Second Moment,'' J. Acoust. Soc. Am. **81**, 925–937 (1987); ''II-Higher Moments,'' *ibid.* **82**, 593–600 (1987).
[37] R. Mazar and L. B. Felsen, ''Stochastic geometrical theory of diffraction,'' J. Acoust. Soc. Am. **86**, 2292–2308 (1989).
[38] R. Mazar and L. B. Felsen, ''Edge diffraction of high-frequency coherence functions in a random medium,'' Opt. Lett. **12**, 4–6 (1987).
[39] R. Mazar and L. B. Felsen, ''Stochastic geometrical diffraction theory in a random medium with inhomogeneous background,'' Opt. Lett. **12**, 301–303 (1987).
[40] R. Mazar, ''High-frequency propagators for diffraction and backscattering in random media,'' J. Opt. Soc. Am. A **7**, 34–46 (1990).
[41] R. Mazar and A. Bronshtein, ''Multiscale solutions for the high-frequency propagators in an inhomogeneous background random medium,'' J. Acoust. Soc. Am. **91**, 802–812 (1992).
[42] V. A. Babich and N. J. Kirpichnikova, *Boundary Layer Method in Diffraction Problems* (translated from Russian) (Springer, Berlin, 1980).
[43] V. M. Babich and V. S. Buldyrev, *Asymptotic Methods in Short Wave Diffraction Problems* (translated from Russian) (Springer, Berlin, 1989).
[44] V. M. Babich and M. M. Popov, ''Propagation of concentrated sound beams in a three-dimensional inhomogeneous medium,'' Sov. Phys. Acoust. **27**, 459–462 (1982).
[45] V. Cerveny, M. M. Popov, and I. Psencik, ''Computation of wave fields in inhomogeneous media–Gaussian beam approach,'' Geophys. J. R. Astron. Soc. **70**, 109–128 (1982).
[46] R. J. Hill, ''A stochastic parabolic wave equation and field-moment equations for random media having spatial variation of mean refractive index,'' J. Acoust. Soc. Am. **77**, 1742–1753 (1985).
[47] A. G. Vinogradov, Yu. A. Kravtsov, and V. I. Tatarskii, ''Amplification effect of backscattering by bodies placed in a medium with random inhomogeneities,'' Radiophys. Quantum Electron. **16**, 818–823 (1973).
[48] Y. A. Kravtsov and A. I. Saichev, ''Effects of double passage of waves in randomly inhomogeneous media,'' Sov. Phys. Usp. **25**, 494–508 (1982).
[49] A. S. Gurvich and S. S. Kashkarov, ''Amplification of scattering in a turbulent medium,'' Radiophys. Quantum Electron. **20**, 794–796 (1977).
[50] S. S. Kashkarov, ''Amplification of the mean intensity of backscattering in a turbulent atmosphere,'' Radiophys. Quantum Electron. **26**, 36–40 (1983).
[51] V. A. Banakh and V. L. Mironov, *Locational Propagation of Laser Radiation in Turbulent Atmosphere* (translated from Russian) (Artech House, New York, 1988).
[52] R. Mazar and A. Bronshtein, ''Double passage analysis in random media,'' Waves Random Media **1**, 341–362 (1991).
[53] R. Mazar and A. Bronshtein, ''Enhancement of backscattered intensity in a random medium,'' Opt. Lett. **16**, 1304–1306 (1991).
[54] U. Frisch, ''Wave propagation in random media,'' in *Probabilistic Methods in Applied Mathematics*, edited by A. T. Bharucha-Reid (Academic, New York, 1968), Vol. 1, pp. 75–198.
[55] V. S. Buslaev, ''Continuum integrals and the asymptotic behavior of the solutions of parabolic equations as $t \to 0$. Applications to diffraction,'' in *Topics in Mathematical Physics, Vol. 2. Spectral Theory and Problems in Diffraction* (Translated from Russian) edited by M. Sh. Birman (Consultants Bureau, New York, 1968), pp. 67–86.
[56] S. W. Lee, ''Path integrals for solving some electromagnetic edge diffraction problems,'' J. Math. Phys. **19**, 1414–1422 (1978).
[57] D. R. Palmer, ''A path-integral approach to the parabolic approximation. I,'' J. Acoust. Soc. Am. **66**, 862–871 (1979).
[58] L. Fishman and J. J. McCoy, ''Derivation and application of extended parabolic wave theories. II. Path integral representations,'' J. Math. Phys. **25**, 297–308 (1984).
[59] G. Samelsohn and R. Mazar, ''Path-integral analysis of scalar wave propagation in multiple-scattering random media,'' Phys. Rev. E **54**, 5697–5706 (1996).
[60] G. Samelsohn and R. Mazar, ''Asymptotic analysis of classical wave localization in multiple-scattering random media,'' Phys. Rev. E **56**, 6095–6103 (1997).
[61] G. Samelsohn, S. A. Gredeskul, and R. Mazar, ''Resonances and localization of classical waves in random systems with correlation disorder,'' Phys. Rev. E **60**, 6081–6090 (1999).
[62] V. P. Aksenov and V. L. Mironov, ''Phase approximation of the Huygens-Kirchhoff method in problems of reflection of optical waves in the turbulent atmosphere,'' J. Opt. Soc. Am. **69**, 1609–1619 (1979).
[63] R. Mazar and A. Bronshtein, ''High-frequency beam propagation in complex random structures,'' Proc. SPIE **3609**, 111–120 (1999).
[64] R. Mazar and A. Bronshtein, ''Reference-wave solutions with applications to the analysis of frequency correlation in random media,'' Proc. SPIE **4167**, 138–146 (2000).
[65] L. Fishman, ''Uniform high-frequency approximations of the square root Helmholtz operator symbol,'' Wave Motion **26**, 127–161 (1997).
[66] L. Fishman and J. J. McCoy, ''Factorization and path integration of the Helmholtz equation: numerical algorithms,'' J. Acoust. Soc. Am. **81**, 1355–1376 (1987).

Broadband time-reversing array retrofocusing in noisy environments

Karim G. Sabra, Sunny R. Khosla, and David R. Dowling[a)]
Department of Mechanical Engineering, University of Michigan, Ann Arbor, Michigan 48109-2121

(Received 30 January 2001; revised 5 July 2001; accepted 6 November 2001)

Acoustic time reversal is a promising technique for spatial and temporal focusing of sound in unknown environments. Acoustic time reversal can be implemented with an array of transducers that listens to a remote sound source and then transmits a time-reversed version of what was heard. In a noisy environment, the performance of such a time-reversing array (TRA) will be degraded because the array will receive and transmit noise, and the intended signal may be masked by ambient noise at the retrofocus location. This article presents formal results for the signal-to-noise ratio at the intended focus (SNR_f) for TRAs that receive and send finite-duration broadband signals in noisy environments. When the noise is homogeneous and uncorrelated, and a broadcast power limitation sets the TRA's electronic amplification, the formal results can be simplified to an algebraic formula that includes the characteristics of the signal, the remote source, the TRA, and the noisy environment. Here, SNR_f is found to be proportional to the product of the signal bandwidth and the duration of the signal pulse after propagation through the environment. Using parabolic-equation propagation simulations, the formal results for SNR_f are illustrated for a shallow water environment at source-array ranges of 1 to 40 km and bandwidths from several tens of Hz to more than 500 Hz for a signal center frequency of 500 Hz. Shallow-water TRA noise rejection is predicted to be superior to that possible in free space because TRAs successfully exploit multipath-propagation.
 [DOI: 10.1121/1.1432984]

PACS numbers: 43.30.Vh, 43.30.Yj, 43.60.Cg, 43.30.Nb [DLB]

I. INTRODUCTION

Active acoustic time reversal is the process of recording the signal from a remote source, and then replaying the signal in a time-reversed fashion to retro-direct the replayed sound back to the remote source to form a retrofocus. This process, and various other active and passive extensions of it, have led to exciting possibilities for technical advancements in several areas of acoustic research. Recent work in underwater acoustics (Dowling, 1994; Kuperman *et al.*, 1998; Song *et al.*, 1998; Khosla and Dowling, 1998; Song *et al.*, 1999; Hodgkiss *et al.*, 1999; Roux and Fink, 2000; Dungan and Dowling, 2000; Jackson *et al.*, 2000; Edelmann *et al.*, 2000; Khosla and Dowling, 2001) suggests that time-reversing arrays (TRAs) can be used for robust beamforming and underwater communication in unknown environments. In addition, acoustic time reversal is now being developed and deployed for an ever-expanding realm of intriguing imaging and nondestructive-evaluation techniques involving fluid and solid media (Chakroun *et al.*, 1995; Draeger *et al.*, 1998; Tanter *et al.*, 1998; Draeger and Fink, 1999; Draeger *et al.*, 1999; Rose *et al.*, 1999; Roux *et al.*, 1999a; Yonak and Dowling, 1999; Manneville *et al.*, 1999; Ohno *et al.*, 1999; Roux *et al.*, 1999b; Yamamoto *et al.*, 1999; Derode *et al.*, 2000). Popular accounts of acoustic time reversal are given by Fink (1997, 1999). Early ultrasound TRA work is presented in Fink *et al.* (1989).

The performance of TRAs—as determined by the size, longevity, and field amplitude of the array's retrofucus—is limited by lack of reciprocity and absorption in acoustic propagation between the source and the array, by insufficient array aperture, and by noise in the acoustic environment. Although all of these topics have been the subject of previous investigations, only one (Khosla and Dowling, 2001) has emphasized how noise affects acoustic time reversal. However, the results presented therein were limited to narrowband signals. This article extends their work to finite duration broadband signal pulses, propagating in a generic shallow water environment. Experimental retrofocus size and duration results for broadband ultrasonic signals propagating in a hard-bottom laboratory sound channel are provided in Roux and Fink (2000). Oceanic experimental retrofocus size and longevity results are presented in Kuperman *et al.* (1998) and Hodgkiss *et al.* (1999). A thorough noise analysis of Bartlett matched field processing, the intellectual twin on acoustic time reversal, is given in Baggeroer *et al.* (1988).

Noise influences TRA performance twice because the array both listens and transmits. While the TRA is listening, noise can corrupt the received signal from the remote source. Thus, when the array generates its time-reversed transmission, it unintentionally broadcasts the noise it heard along with the signal. Hence, at the intended retrofocus location, there are two noise components: the array-broadcast noise and the ambient noise. The analysis presented herein predicts the signal-to-noise ratio in the vicinity of the original source, SNR_f, at the expected time of the retrofocus. The results are developed from the basic formulation of acoustic time rever-

a)Author to whom correspondence should be addressed. Electronic mail: drd@engin.umich.edu

sal provided in Jackson and Dowling (1991) with a random noise fluctuation added to the array's reception from the remote source and to the acoustic field at the intended retrofocus location.

The purpose of this article is to provide quantitative parametric predictions of how noise influences TRA retrofocusing performance for realistic broadband signals propagating in complex environments. Such predictions are essential for preliminary design of practical TRA systems for underwater communication or active sonar. The new analytical results presented here quantitatively predict how broadband TRA retrofocusing benefits from multipath propagation. Many previous TRA investigations have demonstrated a variety of fascinating ways through which TRAs exploit multipath propagation when the signal-to-noise ratio of the array's reception is high. The main result presented in this article provides a quantitative means of assessing the likely noise rejection performance of acoustic time reversal in noisy environments before a TRA system is built or deployed.

The remainder of this article is divided into four sections. In the next section, the formal results are presented for time-dependent TRA-produced sound fields and signal-to-noise ratios for arbitrary finite-duration signals and correlated noise fields. The formal signal-to-noise ratio results are evaluated in Sec. III for homogeneous noise that is uncorrelated between the elements of the TRA and between the array and the remote source location when a broadcast power constraint sets the electronic amplification of the array. Although it is approximate, the final algebraic expression presented in this section is important because it can be used to predict TRA performance based only on system-design-level parameters for the signal characteristics, the remote source's broadcast, the array's reception and transmission, the acoustic environment, and the noise levels at the source and the array. Section IV provides illustrations of the results from Secs. II and III for TRA retrofocus temporal compression, and signal-to-noise ratios based on Gaussian-windowed sinusoidal signal pulses propagating in a shallow water environment. Results from signals having both large and small relative bandwidths are presented, and comparisons are made to equivalent free-space results. The final section summarizes this work and presents the conclusions drawn from it.

II. GENERAL FORMULATION

The basic operating cycle for a TRA involves sound traveling from a remote source through an acoustic environment to the TRA where it is recorded. For active time reversal, this recorded sound is then transmitted from the same array after time inversion (i.e., first-in becomes last-out). When the environment is sufficiently benign and the array has sufficient aperture, this TRA-transmitted sound retraverses the environment and retrofocuses at the location of the original source. For passive time reversal (Dowling, 1994) the recorded sound can be correlated with previous receptions for sound channel equalization, or played back into a computer simulation of the environment to localize the source via Bartlett matched-field processing (Baggeroer *et al.*, 1988). The original source may be cooperating with the TRA, as in an underwater communications situation, or the source may be trying to evade acoustic illumination by the TRA. In all scenarios, the time-reversal process is robust when the environment is reciprocal, the array is large, acoustic absorption is weak, and the received signal-to-noise ratio is high.

The formal theory of time-reversing or phase-conjugate arrays is presented in Jackson and Dowling (1991). The following development for broadband signals and noise parallels the narrow-band effort in Khosla and Dowling (2001) but extends it to arbitrary finite duration broadband signals. The formal results provided here address the size, duration, and signal-to-noise ratio of a TRA's retrofocus in a reciprocal environment. The possible effects of nonreciprocal ocean propagation have been covered by previous efforts (Dowling and Jackson, 1992; Dowling, 1993, 1994; Khosla and Dowling, 1998; Dungan and Dowling, 2000). Subsequent sections of this article provide specific predictions of transverse focal size and retrofocus signal-to-noise ratio.

Consider a real deterministic finite-duration broadband signal having shape $s(t)$ with Fourier transform $S(\omega)$ defined by

$$S(\omega)=\frac{1}{2\pi}\int_{-\infty}^{+\infty}s(t)e^{i\omega t}\,dt, \tag{1}$$

with bandwidth, $B=(\omega_2-\omega_1)/2\pi$ (in Hz), defined as the smallest range of positive frequencies where 99% of the signals's energy is concentrated: i.e., ω_1 and ω_2 are determined from

$$\int_{\omega_1}^{\omega_2}|S(\omega)|^2\,d\omega=0.99\int_{0}^{+\infty}|S(\omega)|^2\,d\omega. \tag{2}$$

Similarly, the 99% signal duration, $T_s=t_2-t_1$, can be defined as the smallest time interval that contains 99% of the signal energy:

$$\int_{t_1}^{t_2}s^2(t)\,dt=0.99\int_{-\infty}^{+\infty}s^2(t)\,dt. \tag{3}$$

If $s(t)$ is broadcast by the original source located at $\mathbf{r}_s$, the signal $w(\mathbf{r},t)$ recorded by the TRA elements located at $\mathbf{r}_i$ is given by

$$w(\mathbf{r}_i,t)=\int_{-\infty}^{+\infty}M_s g(\mathbf{r}_i,t;\mathbf{r}_s,t_s)s(t_s)\,dt_s, \tag{4}$$

where M_s is the root-mean-square amplitude of the source transmission (M_s has units of pressure times length), and $g(\mathbf{r}_f,t_f;\mathbf{r}_0,t_0)$ is the time-dependent Green's function linking spatial-temporal coordinates $(\mathbf{r}_0,t_0)$ with $(\mathbf{r}_f,t_f)$.

Throughout this article, the signal shape $s(t)$ is a normalized dimensionless function,

$$\frac{1}{T_s}\int_{-\infty}^{+\infty}s^2(t)\,dt=1. \tag{5}$$

Thus, the source level, SL_s, for the initial source transmission which has a duration T_s can be defined from M_s alone:

$$\mathrm{SL}_s(\text{in dB})=20\log_{10}\{M_s/P_{\mathrm{ref}}(1m)\}, \tag{6}$$

where $P_{\text{ref}}=1\ \mu$Pa, the usual reference pressure for underwater sound.

Using these definitions and following Jackson and Dowling (1991), the array is formulated as a set of N monopole transducers ($i=1,N$) that both receive and transmit. Thus, the time-dependent pressure, P, at a field point $\mathbf{r}_f$ that includes the TRA's transmission, the noise field at the array location n_r, and the noise field at the retrofocus location n_f, is given by

$$P(\mathbf{r}_f,t)=P_{\text{signal}}(\mathbf{r}_f,t)+n_{\text{total}}(\mathbf{r}_f,t)$$
$$=\sum_{i=1}^{N}\int_{-\infty}^{+\infty}g(\mathbf{r}_f,t;\mathbf{r}_i,t')A[w(\mathbf{r}_i,T_c-t')+n_r(\mathbf{r}_i,T_c-t')]\,dt'+n_f(\mathbf{r}_f,t), \tag{7a}$$

where

$$P_{\text{signal}}(\mathbf{r}_f,t)=\sum_{i=1}^{N}\int_{-\infty}^{+\infty}g(\mathbf{r}_f,t;\mathbf{r}_i,t')Aw(\mathbf{r}_i,T_c-t')\,dt', \tag{7b}$$

$$n_{\text{total}}(\mathbf{r}_f,t)=P(\mathbf{r}_f,t)-\langle P(\mathbf{r}_f,t)\rangle$$
$$=\sum_{i=1}^{N}\int_{-\infty}^{+\infty}g(\mathbf{r}_f,t;\mathbf{r}_i,t')An_r(\mathbf{r}_i,T_c-t')\,dt'+n_f(\mathbf{r}_f,t), \tag{7c}$$

the angle brackets denote an ensemble average, $\langle n_r(\mathbf{r},t)\rangle=\langle n_f(\mathbf{r},t)\rangle=0$, A is the electrical amplification between the array's reception and its time-reversed broadcast (A has units of source strength divided by pressure, i.e., length), and T_c is the requisite time delay for causality. In practice, the value of A may be determined *in situ* by the TRA system operator but it will always be limited by the broadcast capabilities of the TRA's transducers. Results based on one strategy for setting A are presented in Sec. IV. Possible advantages and concerns raised by the use of dipole sources and receivers in (6) are discussed in Jackson and Dowling (1991). The location, size, and duration of the TRA's intended retrofocus can be predicted from (7b) provided g, A, s, the array configuration, and the source location $\mathbf{r}_s$ are known.

In order to evaluate the performance of a TRA in a noisy environment, two signal-to-noise ratios must be defined. The first, SNR_r, is the array-averaged signal-to-noise ratio for a single element of the array for reception of the original source broadcast:

$$\text{SNR}_r=\sum_{i=1}^{N}\int_{t_0}^{t_f}w^2(\mathbf{r}_i,t)dt\Big/\sum_{i=1}^{N}\int_{t_0}^{t_f}\langle n_r^2(\mathbf{r}_i,t)\rangle\,dt, \tag{8}$$

where $T_r=t_f-t_0$, the received signal duration, is defined as the smallest time interval that contains 99% of the received signal energy. This definition is appropriate for shallow water environments where the signal is primarily concentrated in a small time window that lacks temporal gaps without signal energy. However, in deep ocean environments, signal dispersion may be completely different because arrival time differences between propagation paths may be much larger than the signal duration T_s. Thus, a deep-water signal received by the array may be composed of several short-duration bursts separated by relatively long temporal gaps without signal energy. In such a deep-water situation, T_r might be defined in terms of a sum over a set of smallest time intervals—one for each propagation path—that together contain 99% of the received signal energy. In both shallow and deep water, T_r may be much greater than the broadcast signal duration T_s. The relative strengths of the source broadcast and the noise at the TRA are specified by SNR_r. It is the main independent parameter of this analysis.

The second signal-to-noise ratio specifies the relative strengths of signal and noise in the retrofocus region of the TRA. Here, the signal component will be similar to $s(T_c-t)$ if the array is working well. Thus, a matched-filtering operation on $P(\mathbf{r}_f,t)$ with a time-inverted replica of the original signal, i.e.,

$$C(\mathbf{r}_f,\gamma)=\int_{-\infty}^{+\infty}s(\gamma-t)P(\mathbf{r}_f,t)\,dt, \tag{9}$$

should be the optimum receiver for the signal in a noisy retrofocus region. Hence, the maximum retrofocus signal-to-noise, $\text{SNR}_f(\mathbf{r}_f)$, can be defined based on (9) at the time-shift for maximum signal correlation, $\gamma=T_c$,

$$\text{SNR}_f(\mathbf{r}_f)=\frac{[\langle C(\mathbf{r}_f,T_c)\rangle]^2}{\langle C(\mathbf{r}_f,T_c)^2\rangle-[\langle C(\mathbf{r}_f,T_c)\rangle]^2}$$
$$=\frac{[\int_{-\infty}^{+\infty}s(T_c-t)P_{\text{signal}}(\mathbf{r}_f,t)\,dt]^2}{\langle[\int_{-\infty}^{+\infty}s(T_c-t)n_{\text{total}}(\mathbf{r}_f,t)\,dt]^2\rangle}. \tag{10}$$

The second equality in (10) follows from (7b), (7c), the fact that $\langle n_r(\mathbf{r},t)\rangle=\langle n_f(\mathbf{r},t)\rangle=0$, and the linearity of the matched filtering operation (9). Here, SNR_f is the main performance measure in determining how well a TRA rejects broadband noise at its retrofocus.

All of the equations presented above are fully general for deterministic finite duration signals and spatially correlated random noise fields. The main TRA performance results are contained in (7) and (10). The purpose of the next section is to evaluate the relationship between SNR_r and SNR_f for a simple noise field when a broadcast power constraint sets the array's electronic amplification factor.

III. RESULTS FOR HOMOGENEOUS UNCORRELATED BANDPASS NOISE

Since the general expressions for SNR_r and SNR_f include both noise fields characteristics, a noise model must be selected to produce specific performance predictions. Here, the simplest possible noise model is chosen: a stationary homogeneous flat-spectrum band-limited zero-mean random field that is uncorrelated between array elements and between the source and array locations. Although this noise field is idealized, it allows simplification of the general formulas to mere algebraic expressions and should provide gauge performance results for actual TRA systems.

Oceanic noise is an area of continuing investigation and considerable information is available from classic sources (Urick, 1983, 1986). Modern modeling approaches for oceanic noise are discussed in Jensen *et al.* (1994). Recent coast

measurements and more references are provided by Dean *et al.* (2000). The main difference between a realistic oceanic noise field and the idealized one used here is the spatial correlation within the realistic field. When there are significant noise field correlations between the transducers of the array, the signal-to-noise ratio predictions made in this section [Eqs. (12) and (19)] will be optimistic. Hence, the results obtained herein provide an upper bound for TRA noise rejection performance.

The idealized noise model is a direct extension of that developed in Proakis (1995). Since both the signal and noise would be subjected to the same filtering in any actual TRA application, the noise bandwidth is assumed to coincide with the signal bandwidth B defined by (1), and, for simplicity, the bandpass filtering is assumed to be ideal (unity bandpass response with complete spectral rejection outside the passband). Under these circumstances, the autocorrelation function of the idealized noise field is

$$\langle n(\mathbf{r}_i,t)n(\mathbf{r}_j,t')\rangle=\sigma_n^2\delta_{ij}\frac{\sin(\pi B(t-t'))}{\pi B(t-t')}\times\cos(2\pi f_c(t-t')), \tag{11}$$

where σ_n^2 is the variance of the idealized noise field, δ_{ij} is the Kronecker delta function, and $2\pi f_c=(\omega_2+\omega_1)/2$ is the center frequency of the signal band. In the following development, the variance of the noise field at the TRA (σ_r^2) and its retrofocus (σ_f^2) are taken to be different.

The noise model (11) allows the denominator in (8) to be evaluated so that SNR_r becomes

$$\mathrm{SNR}_r=\sum_{i=1}^{N}\int_{t_0}^{t_f}w^2(\mathbf{r}_i,t)\,dt\Big/NT_r\sigma_r^2. \tag{12}$$

Use of (11) to simplify the denominator term in (10) is more involved; the final form is

$$\left\langle\left[\int_{-\infty}^{+\infty}s(T_c-t)n_{\mathrm{total}}(\mathbf{r}_f,t)\,dt\right]^2\right\rangle \approx\frac{A^2\sigma_r^2}{2B}\sum_{i=1}^{N}\int_{t_0}^{t_f}\left[\int_{-\infty}^{+\infty}g(\mathbf{r}_f,t;\mathbf{r}_i,t')s(t')\,dt'\right]^2dt+\frac{\sigma_f^2}{2B}\int_{-\infty}^{+\infty}[s(t)]^2\,dt, \tag{13}$$

where the approximate relationship (with n representing n_r or n_f),

$$\int_{-\infty}^{+\infty}s(t')\langle n(\mathbf{r}_i,t)n(\mathbf{r}_i,t')\rangle\,dt'\approx\frac{\sigma_n^2}{2B}s(t), \tag{14}$$

has been used to obtain (13). The approximation (14) is common in analyzing bandpass noise and signals (Ziomek, 1995) and is based on the fact that one can neglect, as an engineering approximation, the portion of the signal spectrum that lies outside of the 99%-signal-energy bandwidth B. Given the extent of noise-field idealization in (11), neglect of 1% of the signal energy is comparatively inconsequential.

To achieve a final simplified form for SNR_f, the numerator of (10) is best evaluated at the intended retrofocus location, $\mathbf{r}_f=\mathbf{r}_s$,

$$\left[\int_{-\infty}^{+\infty}s(T_c-t)P_{\mathrm{signal}}(\mathbf{r}_s,t)\,dt\right]^2=A^2M_s^2\left[\sum_{i=1}^{N}\int_{-\infty}^{+\infty}\left(\int_{-\infty}^{+\infty}g(\mathbf{r}_s,t;\mathbf{r}_i,t')s(t')\,dt'\right)^2dt\right]^2. \tag{15}$$

Combining (8), (10), (12), (13), and (15) produces a nearly final form:

$$\mathrm{SNR}_f(\mathbf{r}_s)=\left[1+\frac{(\int_{-\infty}^{+\infty}[s(t)]^2\,dt)\cdot\sigma_f^2/\sigma_r^2}{A^2\Sigma_{i=1}^{N}\int_{-\infty}^{+\infty}(\int_{-\infty}^{+\infty}g(\mathbf{r}_s,t;\mathbf{r}_i,t')s(t')\,dt')^2\,dt}\right]^{-1}\times2B\cdot\frac{T_r}{0.99}\cdot N\cdot\mathrm{SNR}_r. \tag{16}$$

This equation shows the parametric dependencies of SNR_f, and highlights one of the main advantages of TRA systems: SNR_f increases with increasing received-signal time-bandwidth product, BT_r. Thus, when a multipath environment causes significant temporal spreading of the original source broadcast, a TRA can take advantage of this spreading to improve SNR_f and reject noise.

Further simplification of (16) is possible, once a formula or strategy for setting the array's electronic amplification A is defined. For example, an A that limits the array-averaged power per element to Π_e can be developed from (7) and (11) if the elements of the array are assumed to radiate independently:

$$A^2=\frac{\rho c\Pi_e/4\pi}{(M_s^2/NT_r)\Sigma_{i=1}^{N}\int_{-\infty}^{+\infty}(\int_{-\infty}^{+\infty}g(\mathbf{r}_s,t;\mathbf{r}_i,t')s(t')\,dt')^2dt+\sigma_r^2}=\frac{\rho c\Pi_e}{4\pi\sigma_r^2(1+\mathrm{SNR}_r)}. \tag{17}$$

Here ρ and c are the average water density and speed of sound at the array element locations. The average broadcast power of an array element, Π_e, is related to the source level (in dB) of the TRA's transmitting elements by

$$\mathrm{SL}_e=10\log_{10}\{\rho c\Pi_e/4\pi P_{\mathrm{ref}}^2(1m)^2\}. \tag{18}$$

The two denominator terms in (17) represent the mean-square signal and noise pressures recorded at the array during the listening interval T_r. If (5), (8), and (17) are used to evaluate (16), an algebraic form for the retrofocus signal-to-noise ratio is obtained:

$$\mathrm{SNR}_f(\mathbf{r}_s)=2B\cdot T_r\cdot N\cdot\mathrm{SNR}_r\Big/\left[1+\frac{\Pi_sT_s}{N\Pi_eT_r}\left(\frac{1+\mathrm{SNR}_r}{\mathrm{SNR}_r}\right)\cdot\frac{\sigma_f^2}{\sigma_r^2}\right], \tag{19}$$

where $\Pi_s=4\pi M_s^2/\rho c$ is the power output of the original source, $\mathrm{NL}_r=20\log_{10}\{\sigma_r/P_{\mathrm{ref}}\}$ is the noise level at the TRA, $\mathrm{NL}_f=20\log_{10}\{\sigma_f/P_{\mathrm{ref}}\}$ is the noise level at the retrofocus,

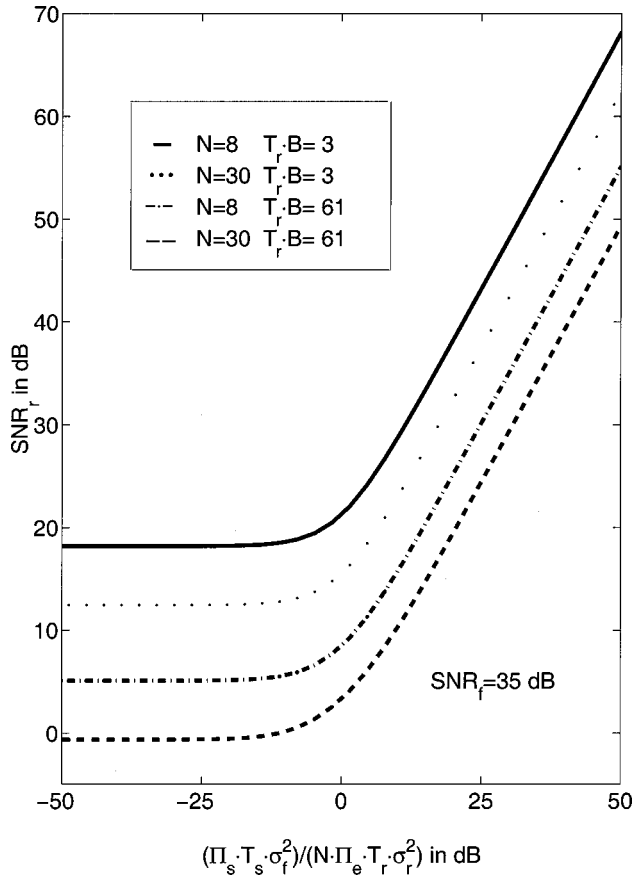

FIG. 1. Curves predicted by (19) for $\mathrm{SNR}_f = 35$ dB vs. SNR_r and the source/array broadcast energy ratio, $\Pi_s T_s / N \Pi_e T_e$ times the noise field variance ratio σ_f^2/σ_r^2. More array elements (larger N) and greater received-signal time-bandwidth products $T_r B$ allow TRAs to operate effectively at lower SNR_r.

$\Pi_s / \Pi_e = 10^{[(SL_s - SL_e)/10]}$, and the various factors of 0.99 arising from the definitions of T_s, B, and T_r have all been set to unity.

This final result, (19), includes all of the parameters that influence TRA retrofocusing and is the main contribution of this article. Although (19) has been developed for idealized noise fields and an assumed strategy for setting the array's amplification factor, it provides a simple parametric relationship involving the characteristics of the signal, the original source, the array, the noise, and the environment. It can be used for parameter studies that determine performance curves of SNR_f vs. SNR_r without recourse to propagation calculations provided reliable estimates for T_r are available. Relationships like (19) are critical for the preliminary design of practical TRA-based sonar systems that operate in noisy environments, and for comparison of predicted TRA-system performance to that possible from other competing technologies, like inverse filtering (Nelson *et al.*, 1992; Tanter *et al.*, 2000). The previous narrow-band results of Khosla and Dowling (2001) for SNR_f can be recovered from (19) by setting $\sigma_f^2/\sigma_r^2 = 1$, and taking the constrained limit $B \to 0$ and $T_r \to \infty$ with $2BT_r = 1$ and $T_s/T_r \to 1$.

Figure 1 illustrates the type of parametric predictions that can be made with (19). It shows contours of $\mathrm{SNR}_f = 35$ dB for TRA element numbers of $N = 8$ and 30 for received-signal time-bandwidth products of $T_r B = 3$ and 61 when SNR_r is varied from -5 to $+70$ dB (vertical axis) and source broadcast energy, $\Pi_s T_s$, divided by average TRA transmitted energy, $N \Pi_e T_e$, multiplied by the ratio of the noise variances (horizontal axis) in dB is varied from -50 to $+50$ dB. Thus, relatively quiet sources (loud arrays) or low noise levels at the retrofocus location (high noise level at the TRA location) occur toward the left in Fig. 1 while loud sources (quiet arrays) or relatively high noise level at the retrofocus location (low noise level at the TRA location) occur toward the right in Fig. 1. The main feature shown in Fig. 1 is that more elements and larger received time-bandwidth products are predicted to allow a broadband TRA to retrofocus successfully at lower received signal-to-noise ratios regardless of the broadcast capabilities of the array or the source. In addition, the character of the 35 dB-SNR_f curves allows a system designer to assess the importance of a TRA's broadcast capabilities. For instance, assume that $\sigma_f^2/\sigma_r^2 \approx 1$. Then in the quiet source regime ($\Pi_s T_s / N \Pi_e T_r \ll 1$), the 35 dB-$\mathrm{SNR}_f$ curves are horizontal which implies that any increase in TRA broadcast capability will go unutilized. On the other hand, in the strong source regime ($\Pi_s T_s / N \Pi_e T_r \gg 1$), the 35 dB-$\mathrm{SNR}_f$ curves have a positive slope which implies any increase in TRA broadcast capability will allow the TRA to produce the same SNR_f at a lower SNR_r. Thus, an array-power SNR_f-performance tradeoff places optimum TRA operations near $\Pi_s T_s / N \Pi_e T_r \approx 1$, when $\sigma_f^2/\sigma_r^2 \approx 1$

The next section illustrates the use of the formulas presented in this and in the previous section for vertical linear TRAs.

IV. ILLUSTRATIONS OF PREDICTED TRA PERFORMANCE

The TRA performance parameters presented here are the extent of pulse compression at the original source location, and the predicted retrofocus signal-to-noise ratio as a function of source-array range. Computational results for a shallow water sound channel environment are provided and compared to equivalent free space results. In both environments, the array is linear and vertical, and the original source is at a (horizontal) range R from the array. The free space results are based on the usual analytical Green's function (see Pierce, 1989), while the sound channel results are based on propagation calculations using the wide-angle parabolic-equation code RAM (Collins, 1993, 1994, 1998). Here, time-domain signals were generated by a Fourier superposition of single-frequency results.

The geometry and parameters for the computational sound channel are shown in Fig. 2. The channel has a downward refracting sound speed profile, a depth $D = 65$ m, and a two-layer bottom. The range coordinate, r, runs in the horizontal direction, and the depth coordinate, z, has its origin at the water surface and increases downward. The depth-dependent speed of sound (c), bottom layer densities (ρ), and bottom attenuation coefficients (α) are all specified on Fig. 2. The array was centered in the sound channel and had 20 elements with 3-m spacing.

The signals used here were Gaussian-windowed sine waves,

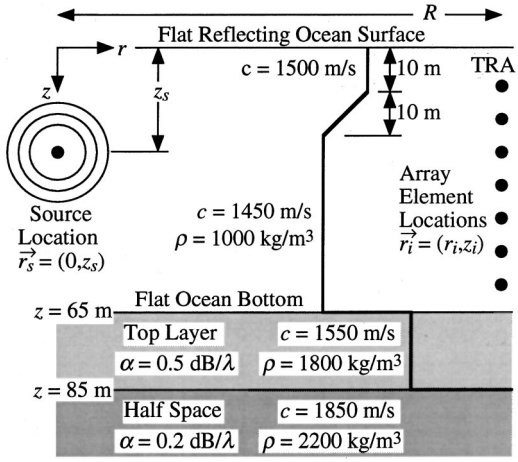

FIG. 2. Computational shallow water sound channel. Here, density is ρ, the attenuation coefficient is α (with λ = wavelength), and the sound speed, indicated by the heavier black line, is c.

$$s(t) = S_0 \exp\{-t^2/\tau^2\} \sin(2\pi f_c t), \tag{20}$$

where S_0 is a normalization constant chosen to satisfy (5), τ sets the duration of the pulse, and f_c is the center frequency of the pulse. For the present study, $f_c = 500$ Hz.

The period or time window for Fourier synthesis of the pulses described by (20) was 0.256 s, leading to a frequency spacing between Fourier components of 3.91 Hz. These values were chosen so that the sound-channel-spread signal was still clearly contained in a single time window for source-array ranges of 300 m to 40 km. The number of frequencies used by the computations was chosen so that the bandwidth B of the signal was fully covered, and typically numbered between 100 and 300, depending on the choice of τ and f_c in (20).

For the RAM computations, eight Padé terms were used. The range step was at most one wavelength and the depth step at most $\frac{1}{30}$ of a wavelength for each frequency component of the signal. These choices are somewhat smaller than the range and depth steps typically used with RAM. They are based on a trade-off between computational accuracy and efficiency and ensure reciprocity for both amplitude and phase in the computed pressure fields. Furthermore, the relatively short range step is appropriate here to properly resolve the details of the retrofocus region. The computational basement was set to 400 m, and within the last few wavelengths of this basement the attenuation coefficient was ramped up to 10 dB per wavelength to prevent artificial reflections from the bottom edge of the computational domain.

A sample of the computed results for a broadband noise-free signal based on (7b) are presented in Figs. 3 and 4. For these illustrations $f_c = 500$ Hz, $\tau = 5/(2\pi f_c)$, $z_s = 25$ m, and $N = 20$ which lead to $B = 516$ Hz (i.e., $B/f_c \approx 1$), $T_s = 4.0$ ms, and $T_r = 120$ ms. Specific predictions based on a full evaluation of (12) and (19) for free space and the shallow water sound channel of Fig. 2 are presented in Fig. 5.

Figure 3 depicts (a) the original pulse, (b) the pulse after propagation from the source to the array at a depth of 25 m, (c) the pulse energy and recording time T_r, and (d) the retrofocused pulse at the source location after back propagation

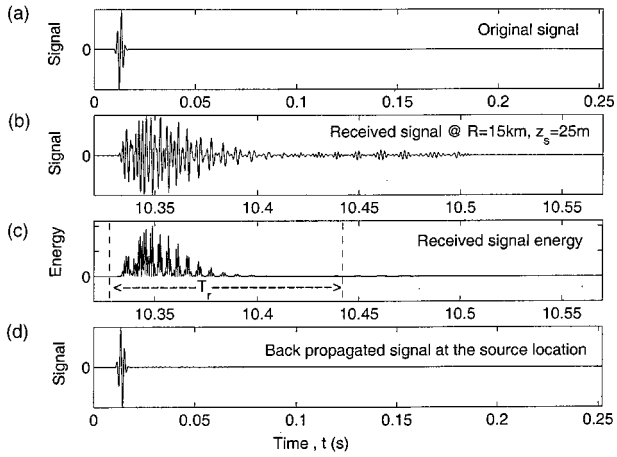

FIG. 3. Simulated signal pulse shapes for $f_c = 500$ Hz, $\tau = 5/(2\pi f_c)$, $R = 15$ km, and $z_s = 25$ m at various points within the operating cycle of a time-reversing array having $N = 20$ elements: (a) original pulse with $T_s = 4.0$ ms, (b) pulse after propagation from the source to the array, (c) pulse energy versus time at the array with $T_r = 120$ ms, and (d) recompressed pulse produced at the original source location after back propagation. All horizontal axes present the entire time window of a simulation although the origins of the various axes have been shifted to ease comparisons.

from the array for $R = 15$ km. All the horizontal time axes on Fig. 3 have the same duration (one time window) but they have been shifted so that the various signals are easily compared. As expected, the original pulse undergoes considerable temporal spreading after propagation from the source to the array, but the signal is successfully recompressed during back propagation. In fact, the correlation between the time-reversed original pulse and the simulated retrofocused signal is greater than 99% for 300 m$\leqslant R \leqslant$30 km in the computational sound channel. Thus, as expected from prior experimental measurements having a smaller signal bandwidth (Kuperman *et al.*, 1998; Hodgkiss *et al.*, 1999), TRA pulse compression approaches the ideal limit in the absence of noise and sound channel dynamics.

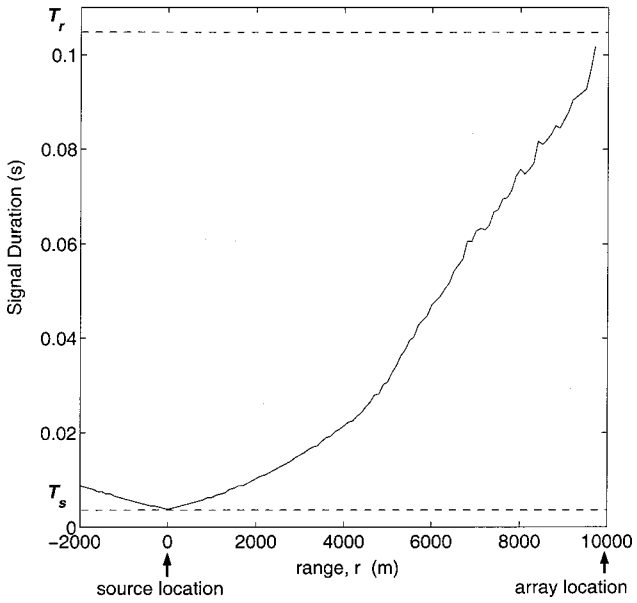

FIG. 4. Pulse duration versus range for the signal pulse of Fig. 3.

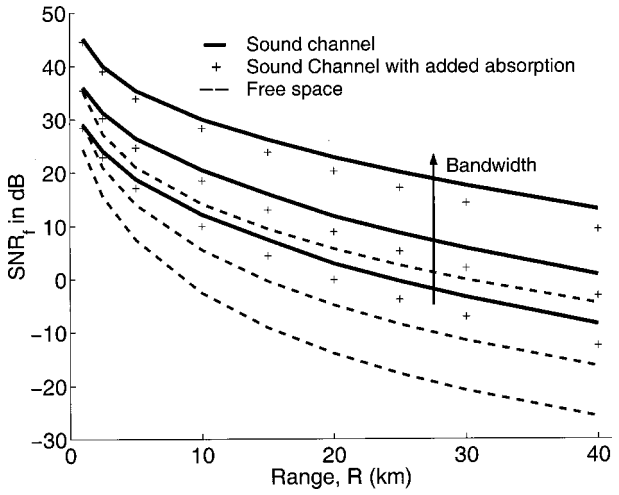

FIG. 5. Specific predictions of the range dependence of SNR_f in the computational sound channel and in free space based on (12), (19), and (20) for $B=516$, 129, and 43.0 Hz with $f_c=500$ Hz, $SL_s=120$ dB, $SL_e=100$ dB, and $NL_f=NL_r=60$ dB. The solid curves are for the sound channel. The dashed curves are for free space. The arrows show the direction of increasing bandwidth for the two types of curves. The + symbols denote the position that the sound channel curves shift down to when the absorption coefficient in the first layer of the computational bottom is increased from 0.5 to 0.75 dB per wavelength.

Figure 4 shows the duration of the TRA-broadcast signal at a depth of 25 m as a function of range when $R=10$ km for the pulse illustrated in Fig. 3. The original and received signal durations, T_s and T_r, are marked near the bottom and top of the vertical axis in Fig. 4. As in Fig. 2 the array is on the right and the source on the left in Fig. 4. Here, pulse recompression is seen to take place gradually with range; the pulse duration is only double its minimum value approximately 1.5 km up- or down-range of the source location.

When the signals shown in Figs. 2–4 are immersed in noise, their strength relative to the noise becomes important. To illustrate this, Fig. 5 provides specific predictions of SNR_f vs R based on (12), (19), and (20) for $B=516$ Hz $[\tau=5/(2\pi f_c)]$, 129 Hz $[\tau=20/(2\pi f_c)]$, and 43.0 Hz $[\tau=60/(2\pi f_c)]$ with $f_c=500$ Hz, $SL_s=120$ dB, $SL_e=100$ dB, and a $NL_f=NL_r=60$ dB. In current TRA experiments, the source amplitude is higher than the TRA amplitude because time reversal takes advantage of constructive interference from each array element to increase the retrofocused signal energy. This is parametrically confirmed by the fact that the relevant ratio in Fig. 1 is $\Pi_s T_s/N\Pi_e T_r$ when the noise fields have equal variances. Here, either the propagation simulations—leading to the solid curves in Fig. 5—or the analytical free-space Green's function—leading to the dashed curves in Fig. 5—were used to evaluate the numerator of (12). The highest curves of each type are for the shortest pulse and the lowest curve of each type are for the longest pulse. Comparing any two curves for the same signal clearly shows that SNR_f is higher and TRA noise-rejection performance is better in the sound channel. The separation of any two same-signal curves in Fig. 5 is primarily produced by the increased received-signal time-bandwidth product resulting from multipath propagation in the sound channel. Table I lists T_rB and T_sB for the three signals shapes used to create

TABLE I. Predicted sound-channel received-signal time-bandwidth products, T_rB.

	Signal bandwidth, B (Hz)			
Source-array Range, R (km)	$B=$	516	129	43.0
	$T_sB=$	1.96	2.13	2.12
1	$T_rB=$	23.3	6.51	3.09
5		41.0	10.5	4.23
10		54.3	14.4	5.61
15		61.7	17.1	6.42
20		42.5	10.4	4.35
25		44.2	12.1	4.73
30		46.8	13.5	5.19
40		50.7	12.2	4.84

Fig. 5. Most of the approximately 15-dB SNR_f advantage of the sound channel can be attributed to T_rB in the sound channel greatly exceeding T_sB, the time-bandwidth product for all the free space results. Additionally, Fig. 5 illustrates how the higher bandwidth signals lead to greater SNR_f in both environments. And finally, the + symbols in Fig. 5 show where the sound channel curves just above them shift to when the absorption coefficient in the first layer of the computational bottom model is increased from 0.5 to 0.75 dB per wavelength. In all cases, increased absorption losses lower SNR_f, a finding that matches the previous narrowband result (Khosla and Dowling, 2001).

V. SUMMARY AND CONCLUSIONS

This article presents formal mathematical results for the signal-to-noise ratio at the retrofocus of a time-reversing array operating in a noisy environment with broadband signals. The formal results are simplified for the case of homogeneous uncorrelated bandpass noise fields, and illustrated through broadband simulations of TRA performance in shallow water. The simulated sound channel results are compared to equivalent free space TRA performance predictions.

The work presented here supports three main conclusions. First, the evaluation of the retrofocus signal-to-noise ratio, SNR_f, for homogeneous uncorrelated noise represents an important simplification of the formal results because it is an algebraic relationship between all of the system-level parameters necessary for preliminary design of TRA-based sonar systems. Most (if not all) recent TRA research has been done with high signal-to-noise ratios, thus this article is intended for assessment of future applications of time reversal where quiet sources, quiet arrays, abundant shipping activity, breaking wind waves, or long ranges cause signal-to-noise limitations to be important. Furthermore, because the noise model used to produce the main algebraic relationship is highly idealized, the final formula (19) should accurately represent best-case TRA performance in a noisy environment and thereby provide a performance gauge for actual TRA systems operating in correlated noise environments. In fact, natural variability in both oceanic noise levels and propagation losses produce significant uncertainty in SNR_r which, through (19), is likely to mask any inaccuracy in the predictions of SNR_f originating from the idealized noise model. Thus, the idealized-noise predictions of (19) may actually be

as good as any that could be obtained from the exact formal result (10) because noise model deficiencies may be hidden by oceanic propagation and noise-field variability. Second, because time-reversing arrays exploit multipath propagation, they are well suited to beamforming in unknown underwater sound channels where pulse spreading is ubiquitous. This conclusion is based on the appearance of the received-signal time-bandwidth product in (19) instead of the broadcast-signal time-bandwidth product. Third, the parametric variations seen in the broadband signal calculations reported here follow the expectations set by prior oceanic experiments and narrow-band calculations.

ACKNOWLEDGMENTS

The research was sponsored by the Ocean Acoustics Program of the Office of Naval Research under Grant No. N00014-96-1-0040. The authors also wish to recognize the contributions of the reviewers to correcting and improving the original manuscript.

Baggeroer, A. B., Kuperman, W. A., and Schmidt, H. (**1988**). ''Matched field processing: Source localization in correlated noise as an optimum parameter estimation problem,'' J. Acoust. Soc. Am. **83**, 571–587.

Chakroun, N., Fink, M., and Wu, F. (**1995**). ''Time reversal processing in ultrasonic nondestructive testing,'' IEEE Trans. Ultrason. Ferroelectr. Freq. Control **42**, 1087–1098.

Collins, M. D. (**1993**). ''A split-step Padé solution for parabolic equation method,'' J. Acoust. Soc. Am. **93**, 1736–1742.

Collins, M. D. (**1994**). ''Generalization of the split-step Padé solution,'' J. Acoust. Soc. Am. **96**, 382–385.

Collins, M. D. (**1998**). ''New and improved parabolic equation models,'' J. Acoust. Soc. Am. **104**(3), 1808(A).

Dean, G. B. (**2000**). ''Long time-base observations of surf noise,'' J. Acoust. Soc. Am. **107**, 758–770.

Derode, A., Tourin, A., and Fink, M. (**2000**). ''Limits of time-reversal focusing through multiple scattering: Long-range correlation,'' J. Acoust. Soc. Am. **107**, 2987–2998.

Draeger, C., and Fink, M. (**1999**). ''One channel time-reversal in chaotic cavities: Theoretical limits,'' J. Acoust. Soc. Am. **105**, 611–617.

Draeger, C., Aime, J.-C., and Fink, M. (**1999**). ''One channel time-reversal in chaotic cavities: Experimental results,'' J. Acoust. Soc. Am. **105**, 618–625.

Draeger, C., Cassereau, D., and Fink, M. (**1998**). ''Theory of the time-reversal process in solids,'' J. Acoust. Soc. Am. **102**, 1289–1295.

Dowling, D. R. (**1993**). ''Phase-conjugate array focusing in a moving medium,'' J. Acoust. Soc. Am. **94**, 1716–1718.

Dowling, D. R. (**1994**). ''Acoustic pulse compression using passive phase-conjugate processing,'' J. Acoust. Soc. Am. **95**, 1450–1458.

Dowling, D. R., and Jackson, D. R. (**1992**). ''Narrow-band performance of acoustic phase-conjugate arrays in dynamic random media,'' J. Acoust. Soc. Am. **91**, 3257–3277.

Dungan, M. R., and Dowling, D. R. (**2000**). ''Computed narrowband time-reversing array retrofocusing in a dynamic shallow ocean,'' J. Acoust. Soc. Am. **107**, 3101–3112.

Edelmann, G., Akal, T., Hodgkiss, W. S., Kim, S., Kuperman, W. A., and Song, H. C. (**2000**). ''Self-equalization communications using a time-reversal mirror,'' J. Acoust. Soc. Am. **108**(5), 2607(A).

Fink, M. (**1997**). ''Time-Reversed Acoustics,'' Phys. Today **50**(3), 34–40.

Fink, M. (**1999**). ''Time-Reversed Acoustics,'' Sci. Am. **281**(5), 91–97.

Fink, M., Prada, C., Wu, F., and Cassereau, D. (**1989**). ''Self focusing in inhomogeneous media with time reversal mirrors,'' Proc. IEEE Ultrason. Symp., pp. 681–686.

Hodgkiss, W. S., Song, H. C., Kuperman, W. A., Akal, T., Ferla, C., and Jackson, D. R. (**1999**). ''A long-range and variable focus phase-conjugation experiment in shallow water,'' J. Acoust. Soc. Am. **105**, 1597–1604.

Jackson, D. R., and Dowling, D. R. (**1991**). ''Phase-conjugation in underwater acoustics,'' J. Acoust. Soc. Am. **89**, 171–181.

Jackson, D. R., Rouseff, D., Fox, W. L. J., Jones, C. D., Ritecy, J. A., and Dowling, D. R. (**2000**). ''Underwater communication by passive phase conjugation: Theory and experiment,'' J. Acoust. Soc. Am. **108**, 2607.

Jensen, F. B., Kuperman, W. A., Porter, M. B., and Schmidt, H. (**1994**). *Computational Ocean Acoustics* (AIP, New York), p. 41 and Chap. 9.

Khosla, S. R., and Dowling, D. R. (**1998**). ''Time-reversing array retrofocusing in simple dynamic underwater environments,'' J. Acoust. Soc. Am. **104**, 3339–3350.

Khosla, S. R., and Dowling, D. R. (**2001**). ''Time-reversing array retrofocusing in noisy environments,'' J. Acoust. Soc. Am. **109**, 538.

Kuperman, W. A., Hodgkiss, W. S., Song, H. C., Akal, T., Ferla, C., and Jackson, D. R. (**1998**). ''Phase-conjugation in the ocean: experimental demonstration of an acoustic time reversal mirror,'' J. Acoust. Soc. Am. **103**, 25–40.

Manneville, S., Robres, J. H., Maurel, A., Petitjeans, P., and Fink, M. (**1999**). ''Vortex dynamics investigation using an acoustic technique,'' Phys. Fluids **11**, 3380–3389.

Nelson, P. A., Hareo, H., and Elliot, S. J. (**1992**). ''Adaptive inverse filters for stereophonic sound reproduction,'' IEEE Trans. Signal Process. **40**, 1621–1632.

Ohno, M., Yamamoto, K., Kokubo, A., Sakai, K., and Takagi, K. (**1999**). ''Acoustic phase conjugation by nonlinear piezoelectricity. I. Principle and basic experiments,'' J. Acoust. Soc. Am. **106**, 1330–1338.

Pierce, A. D. (**1989**). *Acoustics* (ASA and AIP, New York), pp. 163–165.

Proakis, J. G. (**1995**). *Digital Communications* (McGraw–Hill, New York), pp. 159–163.

Rose, J. H., Bilgen, M., Roux, P., and Fink, M. (**1999**). ''Time-reversal mirrors and rough surfaces: Theory,'' J. Acoust. Soc. Am. **106**, 716–723.

Roux, P., De Rosny, J., Fink, M., and Rose, J. H. (**1999a**). ''Time-reversal mirrors and rough surfaces: Experiment,'' J. Acoust. Soc. Am. **106**, 724–732.

Roux, P., Derode, A., Peyre, A., Tourin, A., and Fink, M. (**1999b**). ''Acoustic imaging through a multiple scattering medium using a time-reversal mirror,'' J. Acoust. Soc. Am. **107**, L7–L12.

Roux, P., and Fink, M. (**2000**). ''Time reversal in a waveguide: Study of the temporal and spatial focusing,'' J. Acoust. Soc. Am. **107**, 2418–2429.

Song, H. C., Kuperman, W. A., and Hodgkiss, W. S. (**1998**). ''A time-reversal mirror with variable range focusing,'' J. Acoust. Soc. Am. **103**, 3234–3240.

Song, H. C., Kuperman, W. A., Hodgkiss, W. S., Akal, T., and Ferla, C. (**1999**). ''Iterative time reversal in the ocean,'' J. Acoust. Soc. Am. **105**, 3176–3184.

Tanter, M., Thomas, J.-L., and Fink, M. (**1998**). ''Focusing and steering through absorbing and aberrating layers: Application to ultrasonic propagation through the skull,'' J. Acoust. Soc. Am. **103**, 2403–2410.

Tanter, M., Thomas, J.-L., and Fink, M. (**2000**). ''Time reversal and the inverse filter,'' J. Acoust. Soc. Am. **108**, 223–234.

Urick, R. J. (**1983**). *Principles of Underwater Sound* (McGraw–Hill, New York), Chap. 7.

Urick, R. J. (**1986**). *Ambient Noise in the Sea* (Peninsula, Los Altos, CA).

Yamamoto, K., Ohno, M., Kokubo, A., Sakai, K., and Takagi, K. (**1999**). ''Acoustic phase conjugation by nonlinear piezoelectricity II. Visualization and application to imaging systems,'' J. Acoust. Soc. Am. **106**, 1339–1345.

Yönak, S. H., and Dowling, D. R. (**1999**). ''Photoacoustic detection and localization of small gas leaks,'' J. Acoust. Soc. Am. **105**, 2685–2694.

Ziomek, L. J. (**1995**). *Fundamentals of Acoustic Field Theory and Space-Time Signal Processing* (CRC, Boca Raton, FL), pp. 619–621.

Numerical investigations of flow and energy fields near a thermoacoustic couple

Haruko Ishikawa and David J. Mee
Department of Mechanical Engineering, The University of Queensland, St. Lucia, Queensland 4072, Australia

(Received 19 January 2001; revised 9 September 2001; accepted 23 October 2001)

The flow field and the energy transport near thermoacoustic couples are simulated using a 2D full Navier–Stokes solver. The thermoacoustic couple plate is maintained at a constant temperature; plate lengths, which are ''short'' and ''long'' compared with the particle displacement lengths of the acoustic standing waves, are tested. Also investigated are the effects of plate spacing and the amplitude of the standing wave. Results are examined in the form of energy vectors, particle paths, and overall entropy generation rates. These show that a net heat-pumping effect appears only near the edges of thermoacoustic couple plates, within about a particle displacement distance from the ends. A heat-pumping effect can be seen even on the shortest plates tested when the plate spacing exceeds the thermal penetration depth. It is observed that energy dissipation near the plate increases quadratically as the plate spacing is reduced. The results also indicate that there may be a larger scale vortical motion outside the plates which disappears as the plate spacing is reduced. [DOI: 10.1121/1.1430687]

PACS numbers: 43.35.Ud [SGK]

I. INTRODUCTION

Thermoacoustic engines are devices which make use of thermoacoustic phenomena and function as heat pumps or prime movers. They can provide cooling or heating using environmentally benign gases. Despite recent developments in thermoacoustic engines (Swift, 1999), there are many areas requiring further investigation in order to better predict their performance and guide future designs of thermoacoustic engines. Particularly lacking is overall research into heat exchangers in thermoacoustic engines, for which there are no established design methodologies.

Analytical models of thermoacoustic devices have been developed for the calculation of time-averaged energy fluxes for devices operating at low pressure amplitudes (Swift, 1988). However, these models do not account for entrance effects at the ends of regenerators and heat exchangers. The main differences between regenerators and heat exchangers are that regenerator plates are normally at least ten times as long as heat exchanger plates and have a temperature gradient along their length. Heat exchanger plates are usually considered to be isothermal and short enough that plate end effects should prevail over their length.

The motivation for the current work is to understand the energy transfer mechanisms at heat exchangers in thermoacoustic devices. However, in order to model the heat exchanger section only, boundary conditions reproducing the energy and flow fields developed due to the interaction between the regenerator and the heat exchanger must be applied at the edge of the domain. Suitable information to apply at such a boundary is currently not available.

Therefore, the current work deals with the simpler case of a thermoacoustic couple. The thermoacoustic couple retains most of the physical processes that occur in heat exchangers but is more tractable numerically. The thermoacoustic couple was originally proposed and tested by Wheatley *et al.* (1983) in order to clearly demonstrate the thermoacoustic phenomenon. The thermoacoustic couple is a stack of a few short plates in a resonator and is designed so that the stack can be placed at any position within the standing wave.

Several works have addressed the numerical simulation of thermoacoustic devices, but most have concentrated on the regenerators [Worlikar and Knio (1996); Watanabe *et al.* (1997); Yuan *et al.* (1997)]. In addition, although nonlinearity is incorporated into their models, various simplifications to the governing equations have been made.

The work of Cao *et al.* (1996) is the only one that simulates isothermal plates in a standing wave using the full 2D Navier–Stokes equations. However, only one plate length (which corresponds to the length of typical regenerator plates) was tested and the simulation became unstable for small plate spacings.

An analytical model for heat exchanger plates near a stack is presented by Mozurkewich (1998a). Worlikar and Knio (1999) included heat exchanger plates in their simulation. They considered a single plate but imposed isothermal conditions at either edge to represent hot and cold heat exchangers. In order to simplify the governing equations, assumptions such as low Mach number and constant viscosity and thermal conductivity were made. Their simulations indicate that there is heat pumping action on heat exchanger plates that are as short as the particle displacement length and that the efficiency of a thermoacoustic engine is optimum when the heat exchanger plates are approximately that length. However, the effect of plate spacing was not tested in their work.

II. DOMAIN AND OPERATING CONDITIONS

Figure 1(a) is a slice (in the $x-y$ plane) of a thermoacoustic couple. The extent of the simulation domain is indi-

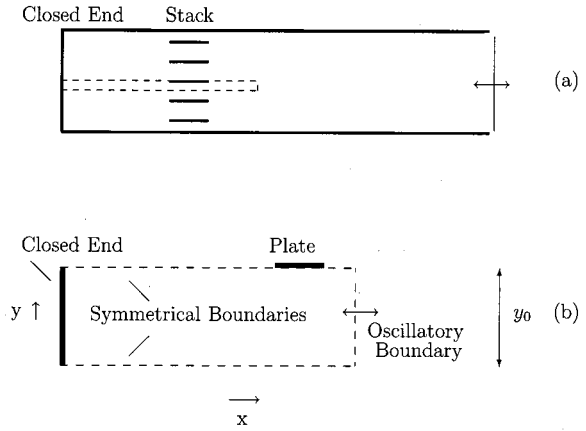

FIG. 1. (a) Thermoacoustic couple in a resonator. (b) The computational domain.

cated by the dotted lines and is enlarged in Fig. 1(b). The simulation model is an isothermal plate subject to a standing wave in a helium-filled resonator. The plate thickness is not modeled. y_0 is the plate half-spacing. Throughout this paper the right-hand end of the plate in Fig. 1(b) is referred to as the outer edge and the left end is referred to as the inner edge.

The mean temperature, T_m, is 300 K, the mean pressure, p_m, is 10 kPa, the frequency, f, is 100 Hz, and the outer edge of the plate is located one-eighth of the wavelength, 126 cm, from the closed end of the resonator. The oscillatory boundary conditions are specified 0.0085λ from the outer edge of the plate where λ is the wavelength. These operating conditions were chosen to replicate the test cases of Cao *et al.* (1996). The mean pressure used by Cao *et al.* (1996) is approximately one-tenth of atmospheric pressure (assuming T_m and f to be 300 K and 100 Hz, respectively). This is two orders of magnitude smaller than that commonly used for existing operating thermoacoustic devices. Parametric studies for operating conditions closer to those of existing thermoacoustic devices were done by Ishikawa (2000). The characteristics of the flow and energy fields for the various plate geometries were similar to those tested at the operating conditions of Cao *et al.* despite the fact that the Reynolds numbers differed by two orders of magnitude.

Table I presents conditions for the present test cases. L is the plate length. $\delta_{km}(=\sqrt{2k/\omega})$ is the thermal penetration depth where k is the thermal diffusivity and ω is the angular frequency. δ_{km} is 0.24 cm when evaluated at T_m and p_m.

Turbulence is neglected for all test cases because the critical Reynolds number, $\mathrm{Re}=2u_1/\sqrt{(\nu\omega)}$, as defined by Merkli and Thomann (1975), was always below 400.

Mach numbers, M, are evaluated at the mean temperature and are based on the velocity amplitude at the velocity antinode of the standing wave. P_A/p_m is the drive ratio, which is the ratio of pressure amplitude at the pressure antinode of the standing wave, P_A, and the mean pressure. Δx and Δy are the grid sizes in the x and y directions. The particle displacement length, $2u_1/\omega$ (where u_1 is the first-order x-component velocity amplitude) evaluated at the plate outer edge, is 2.3 cm when the Mach number is 0.01.

The sizes of the spatial and temporal grids used are close to those of Cao *et al.* (1996). Grid independency was confirmed by comparing the energy flux at the plate surface for grids of various sizes in Ishikawa (2000). As shown in Sec. VII, the results the current work agree with those of Cao *et al.* which, in turn agree with the analytical calculations of Mozurkewich (1998b).

TABLE I. Thermoacoustic couple test cases. The test gas is helium, $\gamma=5/3$, Pr=0.68, $p_m=1.0$ kPa. $2u_1/\omega=2.3$ cm, $\delta_{km}=0.24$ cm.

Run	L	δ_{km}/y_0	M	$P_A/p_m[\%]$	$\Delta x/\lambda$	$\Delta y/\delta_{km}$
1	$22u_1/\omega$	0.3	0.03	5.1	$2.5E-4$	$8.3E-2$
2	$22u_1/\omega$	0.6	0.03	5.1	$2.5E-4$	$4.2E-2$
3	$22u_1/\omega$	1.0	0.03	5.1	$2.5E-4$	$4.2E-2$
4	$22u_1/\omega$	1.2	0.03	5.1	$2.5E-4$	$4.2E-2$
5	$22u_1/\omega$	1.6	0.03	5.1	$2.5E-4$	$4.2E-2$
6	$22u_1/\omega$	1.8	0.03	5.1	$2.5E-4$	$4.2E-2$
7	$22u_1/\omega$	0.3	0.01	1.7	$2.5E-4$	$8.3E-2$
8	$22u_1/\omega$	0.3	0.02	3.4	$2.5E-4$	$8.3E-2$
9	$22u_1/\omega$	0.3	0.04	6.8	$2.5E-4$	$8.3E-2$
10	$22u_1/\omega$	0.3	0.05	8.5	$2.5E-4$	$8.3E-2$
11	$2u_1/\omega$	0.3	0.01	1.7	$8.2E-5$	$8.3E-2$
12	$2u_1/\omega$	2.0	0.01	1.7	$8.2E-5$	$4.2E-2$
13	$2u_1/\omega$	3.0	0.01	1.7	$8.2E-5$	$2.8E-2$
14	u_1/ω	0.3	0.01	1.7	$8.2E-5$	$8.3E-2$
15	u_1/ω	2.0	0.01	1.7	$8.2E-5$	$4.2E-2$
16	u_1/ω	3.0	0.01	1.7	$8.2E-5$	$2.8E-2$

III. NUMERICAL METHOD

The continuity, momentum, and energy equations for a 2D compressible ideal gas at low Mach number are solved in the current simulations. The commercial code PHOENICS, developed by CHAM Ltd., which solves the governing equations using a finite volume method (Spalding, 1991), was used for the present simulations. Schemes used to discretize the governing equations in PHOENICS give second-order accuracy in space and first-order accuracy in time. In order to couple the momentum and continuity equations, PHOENICS uses the SIMPLEST (SIMPLE ShorTend) algorithm suggested by Spalding (1980), which is a variant of the SIMPLE (semi-implicit method for pressure-linked equations) method (Patankar and Spalding, 1972).

In the current work, convergence of the simulation was determined by monitoring the change in each variable after each iteration and also by looking at the energy balance of the simulation domain. Simulations were considered to have reached steady state when the changes in all quantities were less than 0.1% of their fluctuating amplitudes from one cycle to the next. At this stage, the difference between the cycle-averaged heat flux through the plate and the energy flux through the oscillatory boundary was less than 5% of the maximum fluctuating energy flux in the domain. Larger energy imbalances are attributed to the fact that the energy flux and heat flux are second-order quantities which are derived from differences between two first-order quantities. Limitations of the code (such as single precision in calculations) restricted the overall accuracy that could be achieved in the second-order quantities.

In order to close the equation set, auxiliary equations for thermodynamic properties, transport properties, and bound-

ary conditions are required. In the current work, the gas used for the simulations is helium. The equation of state for an ideal gas is used to calculate the density. PHOENICS solves the energy equation in terms of enthalpy assuming a calorically perfect gas. The transport properties required in the current model are the viscosity and the thermal conductivity of the gas. For simplicity, a power-law model is used for the variation of viscosity with temperature

$$\mu = \mu' \left(\frac{T}{T'} \right)^s, \tag{1}$$

where s is a constant, and μ' is the dynamic viscosity at the reference temperature T'. The constant s used for the current work is 0.647, which is appropriate for temperatures between 15 and 460 K (Chapman and Cowling, 1970). In the current work, T' was chosen as the initial mean temperature of the whole simulation domain.

The kinematic viscosity is calculated by dividing Eq. (1) by the temperature-dependent density of the gas. The Prandtl number is assumed to be constant over the temperature range of the simulations. This, along with the assumption of constant specific heats, leads to the variation of thermal conductivity with temperature having the same form as Eq. (1) with the same exponent.

IV. INITIAL AND BOUNDARY CONDITIONS

At the start of the simulations all variables throughout the simulation domain were set at their mean values as follows:

$$\left.\begin{aligned} u &= 0 \\ v &= 0 \\ T &= T_m \end{aligned}\right\} \quad \text{at } t=0 \quad \text{at all } x\text{- and } y\text{-cells}, \tag{2}$$

where u and v are the x- and y-components of the velocity vector and T_m is the mean temperature of the gas.

The conditions imposed on each boundary [except for the oscillatory boundary of Fig. 1(b), hereafter referred to as BC_{os}], are as follows:

$$\left.\begin{aligned} u &= 0 \\ v &= 0 \\ \frac{dT}{dx} &= 0 \end{aligned}\right\} \quad \text{Closed end}, \tag{3}$$

$$\left.\begin{aligned} v &= 0 \\ \frac{dT}{dy} &= 0 \end{aligned}\right\} \quad \text{Symmetrical boundary}, \tag{4}$$

$$\left.\begin{aligned} u &= 0 \\ v &= 0 \\ T &= T_m \end{aligned}\right\} \quad \text{Plate}. \tag{5}$$

Special considerations were required at the oscillatory boundary, BC_{os}. In the current work, thermoacoustic couples were simulated by applying standing-wave conditions at the open end of the simulation domain [BC_{os} of Fig. 1(b)]. It is apparent that the flow field near the plate is strongly y dependent, and it would not be appropriate to use standing-wave conditions if the oscillatory boundary was placed very near the plate. In order to take account of the plate end effect, Cao *et al.* (1996) varied the temporal phase shift between the pressure and the velocity from that of a standing wave at oscillatory boundaries on either side of the plates. Their simulation domain is similar to the current work except that it does not extend to the tube wall; instead, it encompasses just the region near the plate. In the current work, one end of the simulation domain is chosen as the closed end of the tube. At the other end, an oscillatory boundary condition (an ideal standing-wave condition) is specified far enough away from the plate that moving the boundary further away did not significantly affect the simulation results presented in this paper.

Since a constant temperature is specified at the plate, a rise in the mean temperature of the gas in the simulation domain, due to viscous dissipation, will cause heat to flow out of the domain through the plate. In order to maintain an energy balance for the simulation domain, any heat entering (or leaving) the plate must be balanced by an energy flux through the oscillatory boundary. The values of p, u, and T at BC_{os} are set to be those of a standing wave. However, gradients in properties are not fixed here and energy flux can pass through the oscillatory boundary because of these gradients. The oscillatory boundary is further discussed in Sec. VII.

The pressure, the velocity, and the temperature at BC_{os} are as follows:

$$p = p_m + \mathrm{Re}\{p_1 e^{i\omega t}\}, \tag{6}$$

$$u = \mathrm{Re}\{u_1 e^{i\omega t}\}, \tag{7}$$

$$T = T_m + \mathrm{Re}\{T_1 e^{i\omega t}\}, \tag{8}$$

where Re{ } signifies the real part and p_1, u_1, and T_1 are the first-order complex amplitudes of pressure, x component of velocity and temperature, respectively, fluctuating about their mean values. p_1, u_1, and T_1 for an ideal standing wave are

$$p_1 = P_A \cos(kx), \quad u_1 = i \frac{-P_A}{\rho_m a} \sin(kx), \tag{9}$$

and

$$T_1 = p_1 / \rho_m c_p,$$

where a is the sound speed, k is the wave number, ρ_m is the mean density, and c_p is the specific heat at a constant pressure.

V. VISUALIZATION OF THE ENERGY AND FLOW FIELDS

In order to visualize the direction of heat flux, temperature contours generally are sufficient for steady heat transfer problems but they are not suitable when convection is involved. For the latter case, the energy density flux (as displayed by Cao *et al.*, 1996) is useful for visualizing energy transfer. The x- and y-components of energy flux density can be written as

$$\dot{e}_x = \rho u \left(\frac{1}{2} v^2 + h \right) - K \frac{\partial T}{\partial x} - (u \sigma_{xx} + v \sigma_{yx}), \tag{10}$$

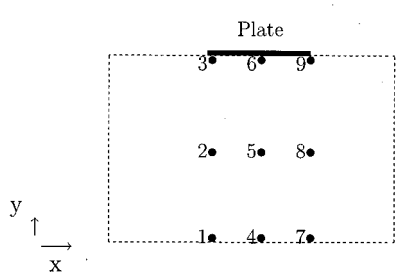

FIG. 2. Starting positions for nine particles in the simulation domain.

where v is the total velocity, h is the enthalpy, σ_{ij} signifies components of the viscous stress tensor, K is the thermal conductivity, and

$$\dot{e}_y = \rho v\left(\frac{1}{2}v^2 + h\right) - K\frac{\partial T}{\partial y} - (u\sigma_{xy} + v\sigma_{yy}), \tag{11}$$

where

$$\sigma_{xx} = \mu\frac{2}{3}\left[2\frac{\partial u}{\partial x} - \frac{\partial v}{\partial y}\right], \quad \sigma_{yy} = \mu\frac{2}{3}\left[2\frac{\partial v}{\partial y} - \frac{\partial u}{\partial x}\right],$$
$$\sigma_{xy} = \mu\left[\frac{\partial u}{\partial y} + \frac{\partial v}{\partial x}\right] = \sigma_{yx}. \tag{12}$$

While energy vectors are useful for visualizing the energy field, particle traces are useful for visualizing the flow field. The movements of gas parcels were traced over several cycles. The initial locations of nine particles are shown in Fig. 2. The initial x locations are at each end and at the middle of the plate. The initial y locations are one cell above the plate surface, at a quarter of the interplate spacing, and near the middle of the interspacing.

The locations of the particles after a short time increment Δt are calculated by multiplying velocities (in both x- and y directions) at the initial particle location by the time-step size Δt. Then, velocities at the new locations are used to calculate the particle locations at time, $2\times\Delta t$. This process is repeated every time step until the end of the cycle. Particles are traced for a maximum of three consecutive cycles after the simulations are considered to have reached steady state.

In order to estimate the sensitivity of the particle traces to time-step size, particle tracks were calculated for two different time-step sizes $\Delta t = 0.28\%$ and 0.21% of the duration of a cycle. The differences between locations at the start and end of a cycle for the two different time-step sizes were less than 0.1% of the half-plate spacing y_0.

VI. CALCULATION OF ENERGY DISSIPATION

As described by Landau (1959), energy dissipation in the simulation domain can be calculated from

$$\dot{e}_{\text{diss}} = -T_0\dot{s}_{\text{gen}}, \tag{13}$$

where $\dot{s}_{\text{gen}}$ is the entropy generation rate per unit volume, and T_0 is the temperature that the system would have if it were in thermodynamic equilibrium at that entropy. The entropy generation rate per unit volume in an ideal gas with viscosity for a two-dimensional system in Cartesian coordinates is

$$\dot{s}_{\text{gen}} = \frac{K}{T^2}\left[\left(\frac{\partial T}{\partial x}\right)^2 + \left(\frac{\partial T}{\partial y}\right)^2\right] + \frac{\mu}{T}\left\{-\frac{2}{3}\left(\frac{\partial u}{\partial x} + \frac{\partial v}{\partial y}\right)^2 + 2\left(\frac{\partial u}{\partial x}\right)^2 + 2\left(\frac{\partial v}{\partial y}\right)^2 + \left(\frac{\partial v}{\partial x} + \frac{\partial u}{\partial y}\right)^2\right\}, \tag{14}$$

where T is the mean temperature of the small control volume. [See, for example, Bird *et al.* (1960) or Bejan (1982) for a derivation of Eq. (14).]

Energy dissipation at the plate surface can be calculated from

$$\dot{e}_{\text{diss}} = \frac{1}{4}\frac{(p_1)^2}{\rho_m a^2}\delta_\kappa\frac{\gamma-1}{1+\epsilon_s}\omega + \frac{1}{4}\rho_m(u_1)^2\delta_\nu\omega, \tag{15}$$

where γ is the specific heat ratio and δ_ν is the viscous penetration depth $(=\sqrt{2\nu/\omega})$. This analytical expression was derived by Swift (1988) for the short engine model with a boundary layer approximation $(y_0 \gg \delta_\kappa)$.

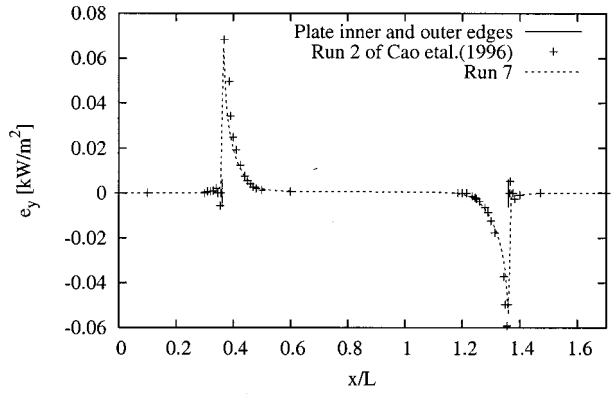

FIG. 3. Time-averaged energy flux density at the plate surface for run 2 of Cao *et al.* (1996) and run 7 of the current work.

VII. "LONG PLATE" SIMULATIONS

Figure 3 shows the energy flux at the plate surface for run 7 compared with run 2 of Cao *et al.* (1996). The time-averaged energy flux at the plate surface is positive for a heat flux leaving the domain through the plate and negative for it entering the domain. These sharp peaks in heat flux at the plate edges were also observed by Worlikar *et al.* (1998) numerically and by Mozurkewich (1998b) analytically.

In Fig. 4, the time-averaged energy flux distributions at the plate surface for various plate spacings are shown. Figure 4 shows that the width of the peak in the energy flux decreases as the plate spacing is reduced when $\delta_k/y_0 \geqslant 1.0$. The total energy flux leaving the outer edge of the plate and flowing through the gas and into the inner edge also reduces as the plate spacing is decreased. Figure 4 also shows some interesting trends with the plate spacing, especially at the outer plate edge, that were not identified previously.

The characteristic result in which energy flux leaves the outer edge of the plate and enters the inner edge changed to one in which energy flux entered each end of the plate at a plate spacing of $\delta_{km}/y_0 = 1.2$. The energy transfer is dis-

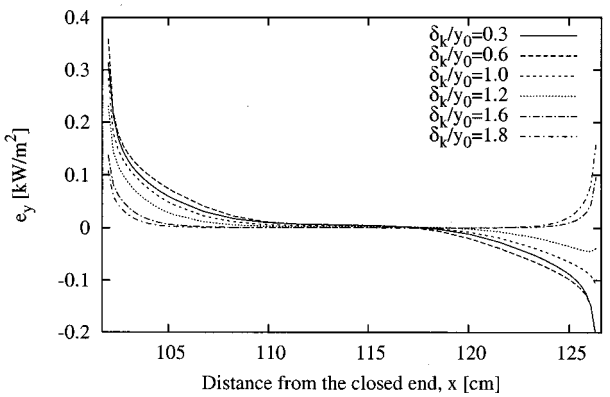

FIG. 4. Time-averaged energy flux entering the plate for different plate spacings (run 1; $\delta_k/y_0=0.3$, run 2; $\delta_k/y_0=0.6$, run 3; $\delta_k/y_0=1.0$, run 4; $\delta_k/y_0=1.2$, run 5; $\delta_k=1.6$, run 6; $\delta_k=1.8$).

played in terms of energy vectors in Figs. 5 and 6. Note that only the simulation domain near the plate is shown.

When $\delta_{km}/y_0=0.3$ (Fig. 5), the time-averaged energy vectors leaving the plate outer edge head towards BC_{os} near the plate surface and turn back towards the inner plate edge at approximately the thermal penetration distance from the plate ($\delta_{km}=0.24$ cm in Fig. 5). Energy vectors near the inner plate edge also start to point towards the plate edge at the thermal penetration depth away from the surface. When $\delta_{km}/y_0=1.2$ [Fig. 6(a)], the time-averaged energy vectors leaving the plate outer edge start to head towards the inner plate edge soon after they leave the outer edge. Energy vectors near the inner plate edge also head directly towards the plate. When $\delta_{km}/y_0=1.6$ [Fig. 6(b)], the energy vectors at both plate edges are directed towards the plate surface and there is no cycle-averaged net heat carried from the outer edge to the inner plate edge. This is attributed to increased energy dissipation as the plate spacing is reduced. This is further discussed later in this section.

Both Figs. 5 and 6 indicate a small amount of energy flux through the oscillatory boundary (to compensate for the energy dissipated in the simulation domain) which subsequently leaves the domain in the form of heat transferred to the plate. In fixing the oscillating variables at BC_{os} to be those of the 1D standing wave, the first two terms of Eq. (10)

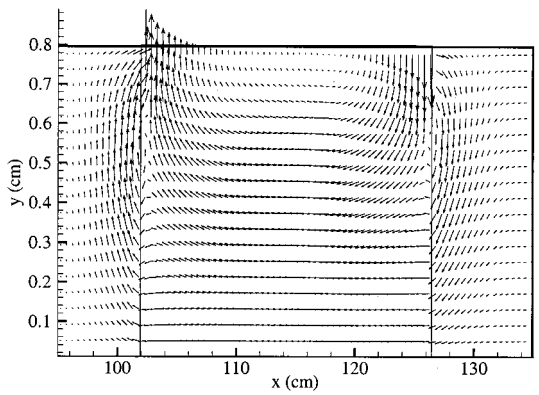

FIG. 5. Time-averaged energy vectors for $\delta_{km}/y_0=0.3$ (run 1), $M=0.03$.

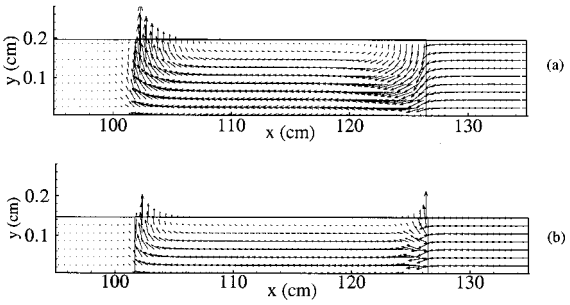

FIG. 6. Time-averaged energy vectors when (a) $\delta_{km}/y_0=1.2$ (run 4) and (b) $\delta_{km}/y_0=1.6$ (run 5). $M=0.03$.

and all but the fourth term of Eq. (11) are zero. Therefore, energy can only enter the domain through BC_{os} in the form of heat flux or flux due to internal friction. The magnitude of the total energy flux through this boundary is very small compared to the level of fluctuating energy flux within the domain (typically less than 1%). It is noted that specifying the boundary conditions in this way, which is quite different from how the conditions were specified in Cao *et al.*, resulted in good agreement between the two simulations (see Fig. 3).

For the simulation of thermoacoustic couples, an oscillating solid-wall boundary would be suitable. However, the boundary conditions used in the current work were chosen with an extension of the work to simulation of only the heat exchanger section in mind. In that case there will be an energy flux through the oscillating boundary.

The movement of the gas near the plate is shown by the paths taken by particles 1 to 9 for runs 1 and 5 in Figs. 7 and 8, respectively. x_E is the distance from the closed end of the tube, $x=0$, to the inner plate edge, point 3 in Fig. 2. The particle paths for run 4 were almost identical to those for run 5 and are not shown here. Particles 7, 8, and 9 in Figs. 7 and 8 start traveling just at the outer edge of the plate and the distance they travel in the x direction is approximately the particle displacement length.

There are some obvious differences in traces for particles at different locations in the domain. All particles, except 2 and 8, move mainly in the x direction with very little

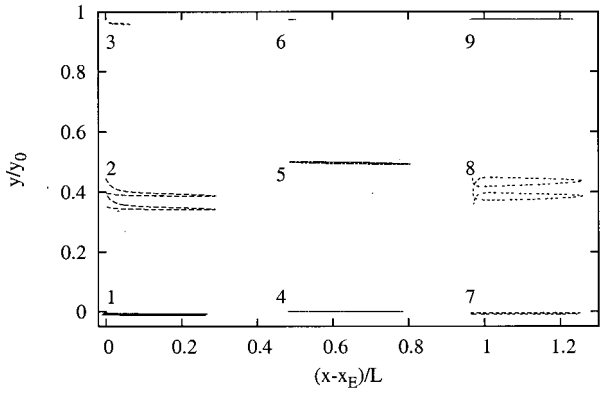

FIG. 7. Particle paths for nine particles when $\delta_{km}/y_0=0.3$ (run 1). $L=22u_1/\omega$.

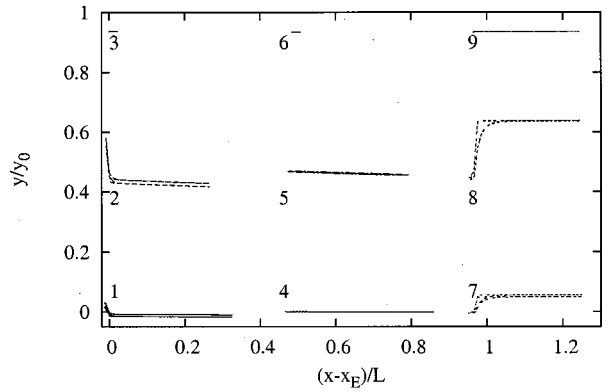

FIG. 8. Particle paths for nine particles when $\delta_{km}/y_0=1.6$ (run 5). $L=22u_1/\omega$.

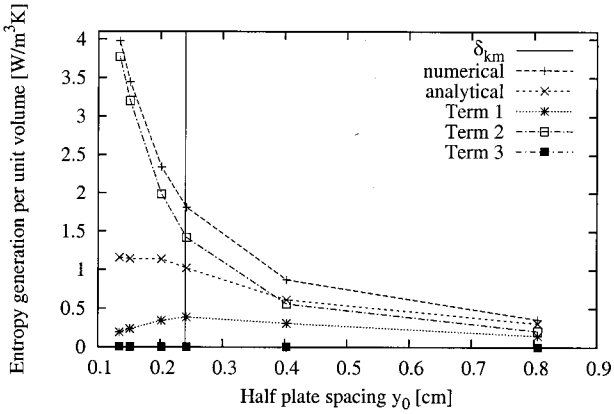

FIG. 9. Entropy generation rates for different plate spacings. (run 1; $y_0\simeq 0.81$ cm, run 2; $y_0\simeq 0.41$ cm, run 3; $y_0\simeq 0.24$ cm, run 4; $y_0\simeq 0.20$ cm, run 5; $y_0\simeq 0.15$ cm, run 6; $y_0\simeq 0.13$ cm).

y movement, although, for the smaller plate spacing, there is more *y* movement for particles 1 and 7. Particles 3 and 6, strongly influenced by viscous effects, move less than a quarter of the distance of the other particles for both test cases.

The largest differences are found in the movements of particles 2 and 8. When $\delta_{km}/y_0=1.6$, the particle traces show that particles 2 and 8 return to within less than $0.03y_0$ and $0.02y_0$, respectively of their starting positions. However, when $\delta_{km}/y_0=0.3$, the difference between the initial and the final positions is $0.05y_0$, and it is noted that y_0 is approximately five times that when $\delta_{km}/y_0=1.6$. Tests using two different time steps indicated that the difference between the starting and finishing points for particles 2 and 8 when $\delta_{km}/y_0=0.3$ is too great to be due to numerical errors in the tracking calculations.

This indicates that over a number of cycles, particles are moving away from the plate at these locations which must be compensated for by other particles replacing them from elsewhere in the domain. This is indicative of a larger scale, lower-frequency vortical motion just outside the plate edges.

This is similar to phenomena observed by Ozawa *et al.* (1999). Ozawa *et al.* visualized acoustic streaming in resonators with or without plates, at a drive ratio of 0.2%. Without plates, there are well-known large-scale vortices between the pressure node and antinode due to acoustic streaming. When Ozawa introduced a single plate or a multiple layer of plates spaced much wider apart than the thermal penetration depth, he observed a large vortex at either edge of the plates for both cases.

Ozawa's plate lengths were approximately 1/10th of the wavelength, which is of a similar order to the current ''long'' plates. It must be noted that the current work does not include the wall effect of the resonator in the simulation domain, yet the current simulation still indicated the possibility of vortical motion (of a scale set by the plate spacing) just outside both edges of the plate for smaller spacings.

In Fig. 9, the volume-averaged entropy generation rates versus plate spacing (runs 1 to 6) are shown, along with the analytically calculated entropy generation rates at the plate surface. (The vertical line in the figure indicates the magnitude of the thermal penetration depth.) To calculate the volume-averaged entropy generation, Eq. (14) was evaluated at each cell, multiplied by the cell volume, and summed over the whole domain. The sum was then divided by the domain volume. The analytical curve is generated from Eq. (15), which represents the energy dissipation at the plate surface, divided by the mean temperature and the domain volume.

In order to investigate what physical mechanisms contribute to entropy generation, terms in Eq. (14) are grouped and labeled as follows:

(i) Term 1: $(K/T^2)(\partial T/\partial y)^2$, entropy generation due to the dominant gradient in temperature.
(ii) Term 2: $(\mu/T)(\partial u/\partial y)^2$, entropy generation due to the dominant viscous effects.
(iii) Term 3: The remainder of the terms in Eq. (14).

These terms are plotted in Figs. 9 and 10.

The analytically calculated entropy generation rates agree with the numerical results at larger plate spacings, but not for smaller spacings. This is reasonable because the analytical expression was derived based on the assumption that $y_0 \gg \delta_{km}$. Note that the entropy generation is much higher than that predicted analytically for the smaller plate spacings. For all test cases, the difference between the entropy generation calculated over the whole domain and that in the plate

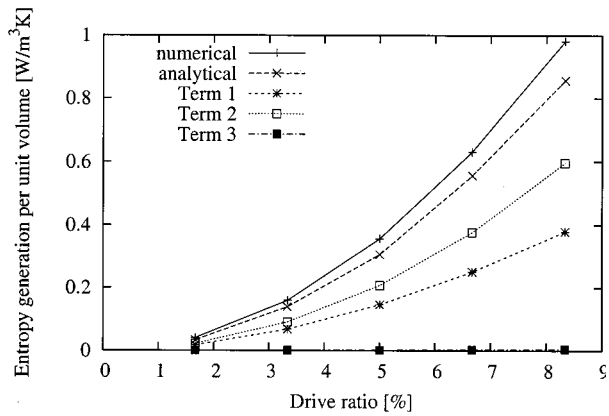

FIG. 10. Entropy generation for different drive ratios. $\delta_{km}/y_0=0.3$. (run 7; drive ratio$\simeq$1.7%, run 8; 3.4%, run 1; 5.1%, run 9; 6.8%, run 10; 8.5%).

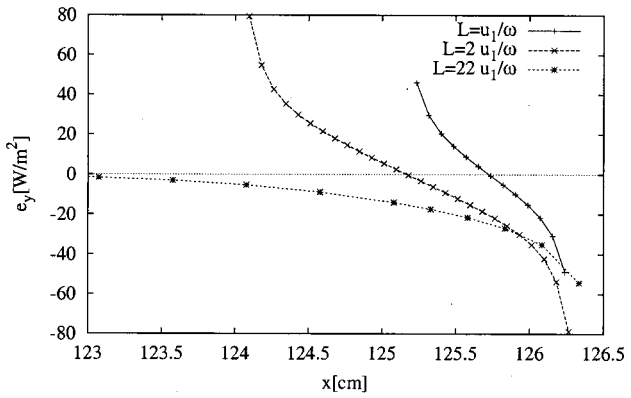

FIG. 11. Time-averaged energy flux density (y component) at the outer edge of the plate for three different plate lengths (run 14; $L=u_1/\omega$, run 11; $L=2u_1/\omega$, and run 7; $L=22u_1/\omega$). $y_0=3.3\delta_{km}$, $2u_1/\omega=2.3$ cm. The outer edges of all plates are at $x\simeq 126.2$ cm. The inner edges of the plates are at $x\simeq 124.2$, 125.2, and 101.2 cm, respectively.

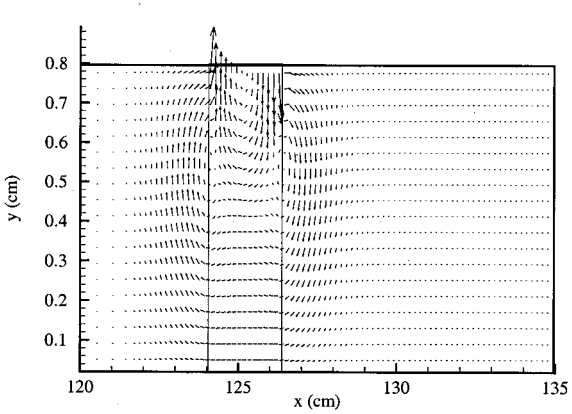

FIG. 12. Time-averaged energy vectors for run 11.

section was less than 1%. Thus, as would be expected, it is only in the vicinity of the plate that significant entropy generation occurs.

Figure 9 also shows that the dominant parameters leading to entropy generation are y gradients of temperature and y gradients in the x component of velocity (terms 1 and 2), respectively. The entropy generated due to temperature gradients in the y direction increases as the plate spacing increases. Note that this term decreases as y_0 increases beyond 0.24 cm. Although the total entropy generation in the simulation domain continues to increase as y_0 increase, term 1 (which is a per-unit volume term) does decrease. This indicates that the rate of increase in term 1 drops when the plate spacing is larger than twice the thermal penetration depth. This can be explained by the fact that the temperature gradient is large only within the thermal boundary layer. Term 2, the entropy generation due to dominant viscous effects, increases quadratically as the plate spacing is reduced.

As the plate spacing is reduced, the amount of heat pumped from one end of the plate to the other decreases (see Fig. 4). However, also as the plate spacing reduces, energy dissipation near the plate increases (see Fig. 9) and the highest rates of energy dissipation occur at the ends of the plates. The phenomenon of heat entering the plate at both ends for small plate spacings is attributed to a balance between these two effects.

The entropy generation over the whole simulation domain versus the drive ratio (or Mach number) is shown in Fig. 10 using the simulation results of runs 1 and 7 to 10 when $y_0=3\delta_{km}$. The figure also shows terms 1 to 3 of Eq. (14). The quadratic dependence was expected from the fact that the dominant terms in Eq. (14) vary with the square of temperature and velocity. The analytically calculated energy dissipation at the plate surface and the numerically calculated entropy generation over the whole domain agree at all drive ratios to within approximately 10%. This shows that most dissipation occurs at the plate surface for this plate spacing and for all drive ratios tested. Again, terms 1 and 2 are dominant and the magnitudes of each increase as the drive ratio increases.

VIII. "SHORT PLATE" SIMULATIONS

The time-averaged heat flux at the plate surface, $\dot{e}_y$, is plotted in Fig. 11 for plate lengths of $2u_1/\omega$ and u_1/ω when $y_0=3.3\delta_{km}$. The corresponding energy flux vectors are shown in Figs. 12 and 13. The long plate (run 7) result is also shown in Fig. 11 but only results at the outer end of the plate are shown. The results show that the heat transfer is in opposite directions at the inner and outer plate edges. This indicates that heat is pumped from the outer to the inner edge of the plate. This is in qualitative agreement with results of Worlikar and Knio (1999). The shapes of the curves in Fig. 11 are very similar to those for the long plates, except that for the short plates there is no flat region (where $\dot{e}_y$ is near zero).

Figure 11 shows that the distance from the plate edge where significant heat transfer occurs is approximately the particle displacement distance. For the operating conditions tested, this suggests that when the plate is more than four times longer than the particle displacement distance, the net amount of heat transfer from one end of the plate to the other is equal if the plate spacings are the same.

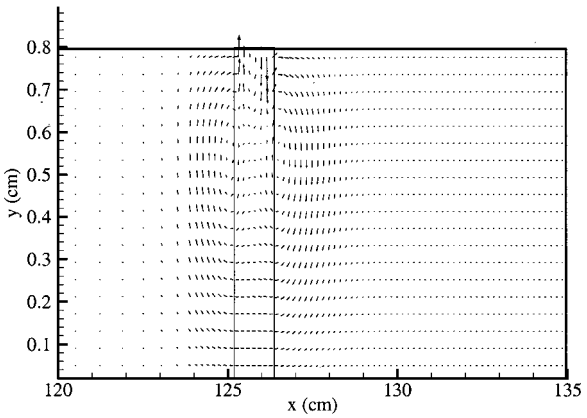

FIG. 13. Time-averaged energy vectors for run 14.

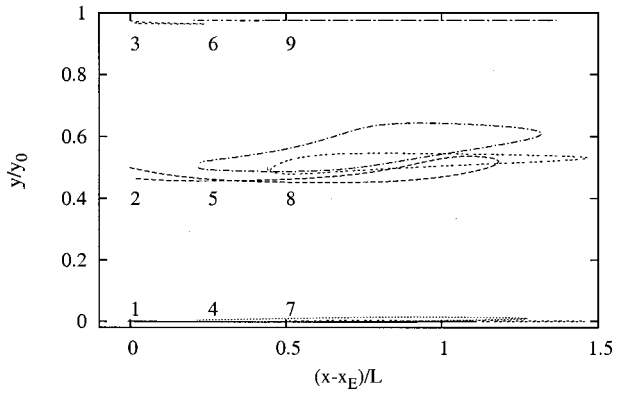

FIG. 14. Particle paths for nine particles for run 11 where $L=2u_1/\omega$.

The particle traces for run 11 are shown in Fig. 14. The results for run 14 were almost identical to those for run 11. The particle displacements are the same as the plate length in Fig. 14. These are in good agreement with the preliminary estimates of particle displacement distance which were calculated for ideal standing waves at the same location. The figures also show that particles 2, 5, and 8 (those at a quarter of the interplate spacing) have a large y movement resulting in looped paths. The maximum difference between the initial and the final locations are approximately 2% of the y-domain length and, given the accuracy of the particle traces, the fact that particles 2, 5, and 8 of Fig. 14 do not return to their original positions is again an indication of a possible vortical motion outside the plate edge.

The time-averaged heat flux to the plates, presented in Fig. 15 when $y_0=3\delta_{km}$, shows that a heat-pumping effect exists at the plate surface even though the plate spacing is equal to the thermal penetration depth. However, when the plate spacing is further reduced to $y_0=\delta_{km}/3$, the energy dissipation is dominant and the heat-pumping effects are no longer seen. The energy vector pattern for $y_0=\delta_{km}/2$ is similar to that for $y_0=3\delta_{km}$. However, the pattern changes significantly at smaller plate spacings. The energy vectors when

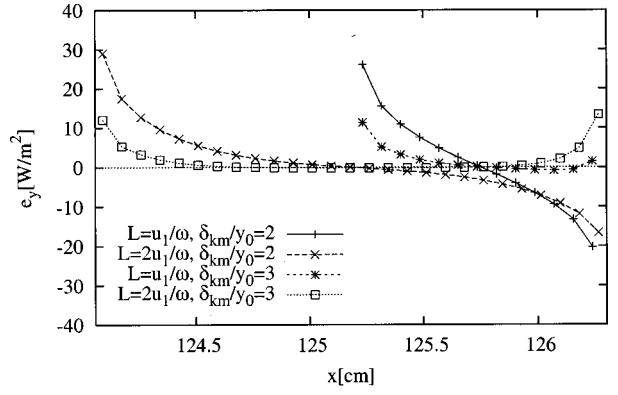

FIG. 15. Time-averaged energy flux density in the y direction at the surface of the short plates when $\delta_{km}/y_0=2$ (run 15; $L=u_1/\omega$, run 12; $L=2u_1/\omega$) and $\delta_{km}/y_0=3$ (run 16; $L=u_1/\omega$, run 13; $L=2u_1/\omega$). The outer edges of all plates are at $x\simeq 126.2$ cm. The inner edges of the plates are at $x\simeq 125.2$ and 124.2 cm, respectively.

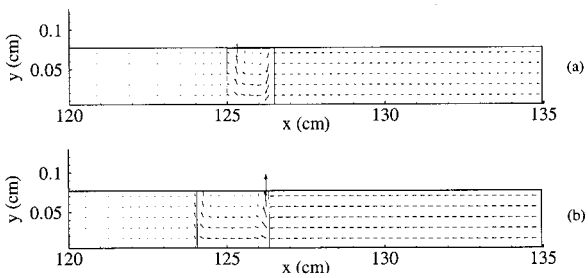

FIG. 16. Time-averaged energy vectors when $\delta_{km}/y_0=3$ for (a) run 16 where $L=u_1/\omega$; (b) run 13 where $L=2u_1/\omega$.

$y_0=\delta_{km}/3$ for $L=u_1/\omega$ and $L=2u_1/\omega$ are presented in Figs. 16(a) and (b).

The particle traces for the cases when $y_0=\delta_{km}/2$ are almost identical to those in Fig. 14, but the characteristic shapes of the particle traces change when $y_0=\delta_{km}/3$, as shown in Fig. 17. Traces for particles 2, 5, and 8 have y displacements but there are no loops in their tracks.

IX. CONCLUSION

The simulation results show that a heat-pumping effect can be seen, not only on the long plates but also on the shortest plates tested, when plate spacings are greater than the thermal penetration depth. As the plate spacing approaches the thermal penetration depth, energy dissipation near the plate increases quadratically and no heat-pumping effect is observed. The energy dissipation increases quadratically with Mach number.

The time-averaged heat transfer to and from the plates is concentrated at the edges of the plates for all test cases. At constant Mach number, the width of the region where there is substantial heat transfer decreases as the plate spacing is reduced.

Particle traces for the test case with the largest plate spacing and a long plate show evidence of vortical motion outside both edges of the plate. The short plate simulations also indicate this vortical motion outside the plates. In addition, particle traces indicate that the gas between the plate surface and the symmetrical boundary prescribes a path with

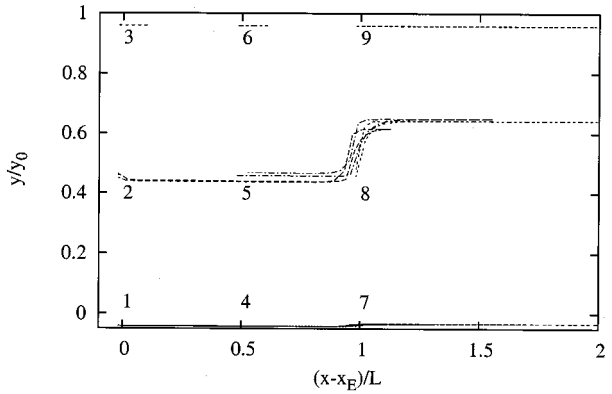

FIG. 17. Particle paths for nine particles for run 13 where $L=2u_1/\omega$, $\delta_{km}/y_0=3$.

a loop in it. However, to confirm the presence of vortical motion outside the plates (especially for the short plate), more particles should be traced, and visualization experiments are required. As the plate spacing is reduced, evidence for vortical motion diminishes.

A number of suggestions for the design of regenerators and heat exchangers can be drawn from these simulation results. The results show that, in terms of the total amount of heat pumped, it is not necessary to have plates longer than four times the particle displacement distance. Any extra surface area contributes to energy dissipation. However, when a certain temperature difference is required along the plate, as is the case of the regenerator plate, short plates will result in large temperature gradients along the plate, in which case there will be heat conduction losses along the plate.

For the design of heat exchangers, plate spacings of the order of the thermal penetration depth may not be appropriate, since the energy dissipation increases with the inverse square of the plate spacing. Therefore, plate spacing should be determined carefully using second law analysis to minimize the entropy generation (Ishikawa and Hobson, 1996).

ACKNOWLEDGMENTS

The authors are grateful for discussions with Professor. M. Ozawa and Dr. A. Tominaga, and suggestions from Dr. G. Swift.

Bejan, A. (**1982**). *Entropy Generation Through Heat and Fluid Flow* (Wiley, New York).

Bird, R. B., Stewart, W. E., and Lightfoot, E. N. (**1960**). *Transport Phenomena* (Wiley, New York).

Cao, N., Olson, J. R., Swift, G. W., and Chen, S. (**1996**). ''Energy flux density in a thermoacoustic couple,'' J. Acoust. Soc. Am. **99**, 3456–3464.

Chapman, S., and Cowling, T. G. (**1970**). *The Mathematical Theory of Non-uniform Gases*, 3rd ed. (Cambridge University Press, London).

Ishikawa, H. (**2000**). ''Investigations of optimum design of heat exchangers of thermoacoustic engines,'' Ph.D. thesis, The University of Queensland. Available at http://adt.caul.edu.au

Ishikawa, H., and Hobson, P. A. (**1996**). ''Optimization of heat exchanger design in a thermoacoustic engine using a second law analysis,'' Int. Commun. Heat Mass Transfer **23**(3), 325–334.

Landau, L. D., and Lifshitz, E. M. (**1959**). *Fluid Mechanics* (Pergamon, London).

Merkli, P., and Thomann, H. (**1975**). ''Transition to turbulence in oscillating pipe flow,'' J. Fluid Mech. **68**, 567–575.

Mozurkewich, G. (**1998a**). ''A model for transverse heat transfer in thermoacoustics,'' J. Acoust. Soc. Am. **103**, 3318–3326.

Mozurkewich, G. (**1998b**). ''Time-average temperature distribution in a thermoacoustic stack,'' J. Acoust. Soc. Am. **103**, 380–388.

Ozawa, M., Kunihiro, K., and Kawamoto, A. (**1999**). ''Flow visualization of acoustic streaming in a resonance tube refrigerator,'' in Technology Reports of Kansai University, March, (41):35–44.

Patankar, S. V., and Spalding, D. B. (**1972**). ''A calculation procedure for heat, mass and momentum transfer in three-dimensional parabolic flows,'' Int. J. Heat Mass Transf. **15**, 1787–1806.

Spalding, D. B. (**1981**). ''Mathematical modelling of fluid-mechanics, heat-transfer, and chemical-reaction processes. A lecture course,'' CFDU Report HTS 180/1, Imperial College, London.

Spalding, D. B. (**1991**). *The* PHOENICS *Beginner's Guide TR100*, CHAM, Bakery House, 40 High Street, Wimbledon Village, London SW19 5AU, UK.

Swift, G. W. (**1988**). ''Thermoacoustic engines,'' J. Acoust. Soc. Am. **84**, 1145–1180.

Swift, G. W. (**1999**). ''Thermoacoustics: A unifying perspective for some engines and refrigerators,'' Los Alamos. Available at http://www.lanl.gov/projects/thermoacoustics/Book/index.html

Watanabe, M., Prosperetti, A., and Yuan, H. (**1997**). ''A simplified model for linear and nonlinear processes in thermoacoustic prime movers. I. Model and linear theory,'' J. Acoust. Soc. Am. **102**, 3484–3496.

Wheatley, J., Hofler, T., Swift, G. W., and Migliori, A. (**1983**). ''Experiments with an intrinsically irreversible acoustic heat engine,'' Phys. Rev. Lett. **50**(7), 499–502.

Worlikar, A. S., and Knio, O. M. (**1996**). ''Numerical modeling of thermoacoustic refrigerator. I. Unsteady flow around the stack,'' J. Comput. Phys. **127**(5), 424–451.

Worlikar, A. S., and Knio, O. M. (**1999**). ''Numerical study of oscillatory flow and heat transfer in a loaded thermoacoustic stack,'' Numer. Heat Transfer, Part A **35**, 49–65.

Worlikar, A. S., Knio, O. M., and Klein, R. (**1998**). ''Numerical modeling of thermoacoustic refrigerator. II. Stratified flow around the stack,'' J. Comput. Phys. **144**, 299–324.

Yuan, H., Karpov, S., and Prosperetti, A. (**1997**). ''A simplified model for linear and nonlinear processes in thermoacoustic prime movers. I. Nonlinear oscillations,'' J. Acoust. Soc. Am. **102**, 3497–3506.

A model and experimental study of fiber orientation effects on shear wave propagation through composite laminates

Dong Fei and David K. Hsu[a)]
Center for Nondestructive Evaluation, Iowa State University, Ames, Iowa 50011-3042

(Received 28 June 2000; revised 12 October 2001; accepted 1 November 2001)

The strong elastic anisotropy of the discrete unidirectional plies in a composite laminate interacts sensitively with the polarization direction of a shear ultrasonic wave propagating in the thickness direction. The transmitted shear wave can therefore be used to detect errors in the ply orientation and stacking sequence of a laminate. The sensitivity is particularly high when the polarization directions of the shear wave transmitter and receiver are orthogonal to each other. To understand the interaction between normal-incident shear waves and ply orientations in a laminate, a complete analytical model was developed using local and global transfer matrices. The model predicted the transmitted signal amplitude as a function of polarization angle of the transmitter and time (or frequency) for a given laminate and input signal. To alleviate the experimental problems associated with shear wave coupling, electromagnetic acoustic transducers (EMATs) and metal delay lines were used in the angular scan of the transmitted signal. The EMAT system had the added advantage of being applicable to uncured composite laminates. Experiments were performed on both cured and uncured laminates with common layups for model verification. The sensitivity of the measured shear wave signals to fiber misorientation and stacking sequence errors was also demonstrated. [DOI: 10.1121/1.1430685]

PACS numbers: 43.35.Zc [SGK]

I. INTRODUCTION

Composite laminates with continuous fiber reinforcement are multilayered structures in which each ply contains numerous fibers oriented along the same direction. Such laminates are fabricated by stacking a number of plies of the starting material, usually in the form of preimpregnated tapes known as pre-pregs, in a specified orientation and sequence called for in the design of the laminate. The stack of uncured pre-pregs is then cured in an autoclave under pressure and at elevated temperatures according to some prescribed cure cycles to produce a composite component. Based on the load requirements, there are a variety of layups for composite laminates. Carbon fiber reinforced composites (e.g., graphite/epoxy) are widely used in aerospace applications due to their desirable strength-to-weight and stiffness-to-weight ratios and the flexibility for achieving the required elastic anisotropy. When the pre-pregs are used to lay up a composite structure, it is imperative that no errors are present in the fiber orientation and stacking sequence of the laminate. In a traditional hand layup, however, layup errors sometimes occur due to inadvertent mistakes. Even in an automated layup, such errors can be introduced to the laminate because the machine is incorrectly programmed. Methods for ensuring correct layup and stacking sequence are therefore needed.

Various means[1–12] have been employed for checking the layup of a laminate. Destructive inspection includes optical microscopic examination of cut and polished cross sections from a waste edge. Ultrasonic approaches[1–4,6–12] were investigated. In the immersion test of a laminate plate, a normal incidence longitudinal wave has no sensitivity to the fiber orientation of the plies; oblique incidence backscattering methods[1,13,14] were therefore used. Bar-Cohen *et al.*[1] invented the polar backscattering method. The backscattered signal amplitude as a function of the plate's orientation angle usually showed a series of peaks that are often correlated with fiber orientation in the plate. A peak occurred when the ultrasonic beam was perpendicular to a group of fibers. However, the angular pattern can be complicated and distorted for laminates of complex ply layups. Another ultrasonic method that showed sensitivity toward fiber orientation was the ''acousto-ultrasonic'' method,[2–4] where two longitudinal mode contact transducers were coupled to the same surface of the plate; the receiving transducer was rotated around the transmitting transducer and the signal amplitude was recorded as a function of angle. A peak occurred when the path between the transducers was aligned with a group of fibers in the laminate. Lamb waves were also used on composite laminates, but usually for determining the elastic properties of the laminate[15] and not for detecting fiber misorientation or stacking sequence errors. Finally, microwaves[5] have also been used to study the fiber orientation in graphite/epoxy and glass/epoxy composites. The angular dependence of the reflected or transmitted microwave signal amplitude was used to detect layup errors.

In an elastically anisotropic composite laminate, the propagation of oblique incidence ultrasonic waves is quite complex. There are generally three bulk wave modes and the phase velocity is generally different from the group velocity; the wave propagation is governed by the slowness surface of the laminate. For linearly polarized normal incidence shear waves, there are only two ''pure'' shear wave modes in each ply: polarized parallel and perpendicular to the fiber direc-

a)Author to whom correspondence should be addressed; electronic mail: dhsu@cnde.iastate.edu

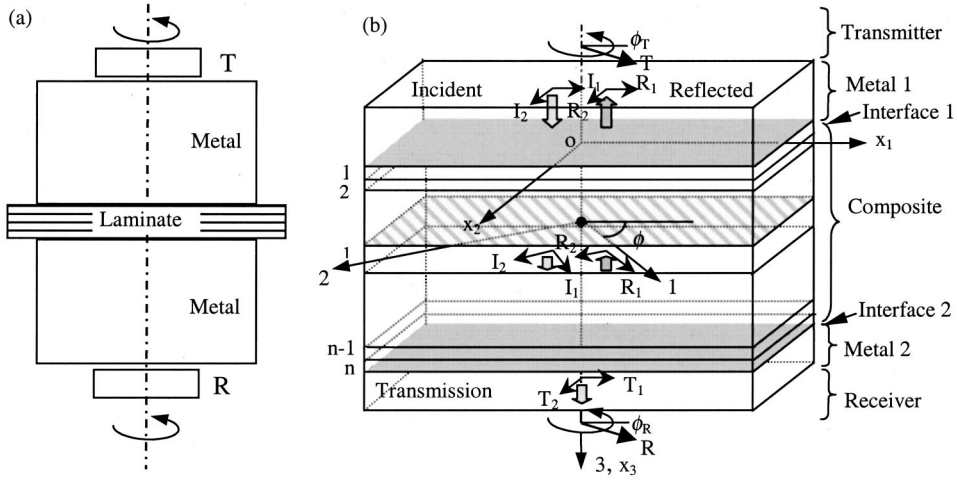

FIG. 1. Model idealization: (a) measurement configuration; (b) model.

tion, respectively. The orientation of the fibers in each ply strongly affects the propagation of the shear waves through the thickness of a laminate; as a result, the transmitted shear wave signal carries with it the information about the fiber orientation and stacking sequence of the ply layup. Hsu and Margetan[6] showed that ultrasonic shear wave velocity could be used to determine the ratio of the 0° and 90° plies in a cross-ply laminate. Komsky *et al.*[7,8] used a pair of 5 MHz contact shear wave transducers to make transmission measurements for layup characterization in thick laminates. A neural network was used to help determine the ply orientation.[8] Fischer and Hsu[9] were the first to take advantage of the high sensitivity of the ''crossed polarization'' toward the changes in fiber orientation and stacking sequence. In this configuration the polarization directions of the transmitting and receiving shear wave transducers were perpendicular to each other. They found that the angular pattern of the transmitted shear wave amplitude in the crossed geometry was very sensitive to errors in ply layup and stacking sequence. They also developed a ply-to-ply vector decomposition model[9,10] based on the displacement continuity at each ply interface to interpret the transmission results. The model was found to provide useful qualitative guide in data interpretation and prediction. Experimentally these researchers conducted angular scans using contact-mode shear wave transducers coupled to the opposite faces of the composite laminate with shear wave couplant. It was found that, even with great care, it was difficult to maintain a constant and reproducible coupling condition with repeated rotation of the transducers in an angular scan. To alleviate the coupling problem, Hsu *et al.*[11,12] employed electromagnetic acoustic transducers (EMATs) to generate and receive normal incidence shear waves. In the EMAT setup, the composite laminate was sandwiched between two aluminum delay blocks and the EMAT transducers were placed on the outer surfaces of the aluminum blocks where the transducers can rotate freely in a noncontact manner. For uncured composite laminates, the coupling was provided by pressing the blocks against the laminate, without the use of the couplant. For cured laminates, shear wave couplant was still used between the specimen and blocks, but the coupling condition was much easier to maintain constant because the bonds between the specimen and blocks were not disturbed by the rotation of the EMAT transducers.

It is evident that the interaction of shear wave polarization with the fiber orientation in a composite laminate can be exploited as a sensitive probe for characterizing the ply layup, particularly for the detection of certain errors in ply orientation and stacking sequence. However, it is also clear that an analytical model would greatly aid the understanding and facilitate the interpretation and prediction of experimental results for the great variety of laminate designs. In this work, a complete analytical model was developed for the propagation of EMAT-generated shear waves through a composite laminate of arbitrary layup. The model was based on the continuity of the shear wave velocity and stress fields at the ply interfaces and treated both the transmitted and reflected wave components in each ply. Local and global transfer matrices[16,17] were used in the model, leading to compact and tractable analytical expressions for the output signal of the receiving EMAT. The model permitted the prediction of the received signal for any laminate layup and orientation of the transmitting and receiving EMATs. With an experimentally measured shear wave wave-form as a reference signal, the model was used to predict the angular patterns of the received signal amplitude as a function of the transducer orientation and time (or frequency). Using a motorized data acquisition system, angular scans were performed on both cured and uncured laminates. The experimental results for a number of layups were compared with model predictions. In both the model and experimental studies, errors in ply orientation and stacking sequence were intentionally introduced and the detection sensitivity for such errors was evaluated.

II. MODEL DEVELOPMENT

A. Measurement configuration and model assumptions

The measurement configuration is shown in Fig. 1(a). The composite laminate sample, either cured or uncured, is sandwiched between two metal (for example, aluminum) blocks. The metal blocks serve as the conducting media for the generation and detection of shear waves by EMATs and as acoustic delay lines. For a cured laminate sample, a shear

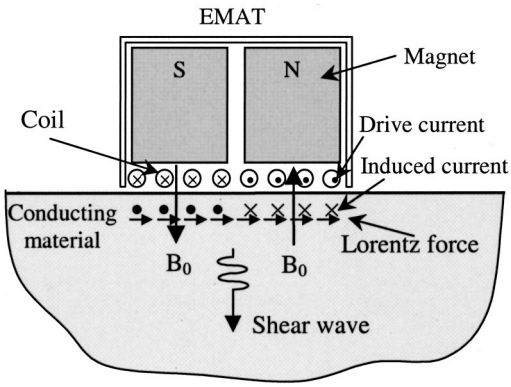

FIG. 2. Generation of normal-incident shear waves by the EMAT.

wave couplant can be used between the sample and the metal blocks. For an uncured laminate, which is a layup of tacky pre-pregs, shear wave coupling between the sample and metal blocks can be achieved simply by exerting a pressure on the laminate, owing to the tack of the pre-pregs at room temperature. The transmitter and receiver can be rotated freely and independently in an angular transmission measurement. Because of the noncontact generation and detection of the shear waves by EMATs at the surface of the metal blocks, the angular measurement can be done in a highly reproducible manner.

An idealized layered model, shown in Fig. 1(b), was established to model the shear wave transmission measurement shown in Fig. 1(a). The EMAT transmitter and receiver were modeled as linearly polarized plane shear wave generator and receiver, respectively. The metal blocks were modeled as two isotropic half spaces, as far as the transmitting and receiving EMATs are concerned, and the composite specimen was modeled as a material structure that contained multiple plies, each of which is a homogeneous, transversely isotropic, lossless layer with the plane of isotropy normal to the fiber direction. All the boundaries, including the ply-to-ply interfaces in the laminate and the metal–laminate interfaces, were assumed to be rigid so that the continuity conditions of velocity (or displacement) and stress can be applied.

B. Shear wave generation and detection by EMATs

The normal-incidence shear wave EMAT used in this work has a simple internal structure. As shown in Fig. 2, it consists of a flat spiral coil and a pair of permanent magnets. When this type of EMAT is placed near a conducting surface and driven by a pulsed electric current, eddy currents will be induced in the surface layer of the conducting material, and experience a Lorentz force owing to the presence of the static magnetic field. Due to charge neutrality requirement, this force can be simply assumed to be applied directly to the conducting material and serve as the body force source that excites shear waves, which then propagate away normal to the surface. The reception process is the reverse of the generation process. When the shear wave propagates and reaches the conducting surface, it moves the conducting material in the static magnetic field. Currents are generated near the surface and inductively coupled to the coil, producing a received voltage proportional to the amplitude of the ultrasonic shear wave. A good review of the principle and applications of EMATs can be found in Ref. 18.

In a rigorous analysis of the generation and reception process of EMAT, one needs to consider the magnetic field distribution, the eddy current pattern, the finite transducer size effect, and the conducting surface condition. However, when the separation distance between the transmitting and receiving EMATs is not too small, as is the case in this work, the generated shear wave can be simply assumed to be proportional to the drive current, and can be idealized as a linearly polarized plane wave. For the receiver side, the output signal can be simply assumed to be proportional to the displacement amplitude along the polarization direction of the receiving EMAT. We will present some experimental results in the latter part of this paper to show that the linear polarization assumption of the EMATs is a good approximation in this work.

As shown in Fig. 1(a), when the EMAT transmitter is driven by an electric pulse, a normal-incident shear wave is generated in metal medium 1. This shear wave is then decomposed into two components, respectively, along axes 1 and 2. Under the linear polarization assumption, the two displacement components of the generated incident shear wave are expressed in the frequency domain as

$$\begin{bmatrix} I_1 \\ I_2 \end{bmatrix}_{M_1}^{+} = V_i \beta_T(\omega) \begin{bmatrix} \cos\phi_T \\ \sin\phi_T \end{bmatrix}, \tag{1}$$

where I_1 and I_2 are the displacement components of the incident shear wave, V_i is the frequency component of the source voltage, ω is the angular frequency, $\beta_T(\omega)$ is the efficiency factor for the transmitter, and ϕ_T is the polarization direction of the transmitter with respect to axis 1. The subscripts of the variable or the matrix denote the medium in which the variable or the matrix is defined. In Eq. (1), for example, M_1 denotes metal block 1. The superscripts, "+" or "−," denote, respectively, the lower surface or the upper surface of the medium in which the variable or the matrix is defined. The same convention is followed in the rest of the model calculation.

Under the assumption of linear polarization, the reception is simply a projection process. The frequency component of the output voltage of the EMAT receiver, V_o, is therefore given by

$$V_o = \beta_R(\omega)[T_1 \;\; T_2] \begin{bmatrix} \cos\phi_R \\ \sin\phi_R \end{bmatrix}, \tag{2}$$

where T_1 and T_2 are the displacement components of the transmitted shear wave, $\beta_R(\omega)$ is the efficiency factor for the receiving EMAT, and ϕ_R is the polarization direction of the receiver.

C. Partial wave solutions in one ply

The wave field in each ply of the laminate can always be expressed as a summation of fundamental planar harmonic bulk-wave solutions. To obtain the fundamental solutions for the normal incidence elastic waves, one can solve the Christ-

offel equations in orthotropic media[16] with the wave vector specified along x_3. This leads to three pure-mode solutions:

$$c_1=\sqrt{\frac{C_{44}}{\rho}},\quad \hat{u}_1=[1,0,0];\quad c_2=\sqrt{\frac{C_{55}}{\rho}},$$
$$\hat{u}_2=[0,1,0];\quad c_3=\sqrt{\frac{C_{33}}{\rho}},\quad \hat{u}_3=[0,0,1], \tag{3}$$

where c_i and $\hat{u}_i$ $(i=1,2,3)$ are phase velocities and the corresponding unit displacement polarization vectors, respectively; C_{33}, C_{44}, and C_{55} are the components of the stiffness matrix of the ply material; and ρ is the mass density of the ply material. The first two solutions are the shear wave solutions and the third is the longitudinal wave solution that will not be considered further. In a unidirectional ply, the shear wave polarized along the fibers (direction 1) propagates faster than the one normal to the fibers (direction 2). For a typical unidirectional graphite/epoxy ply, for example, the ratio of the slow shear wave velocity to the fast shear wave velocity is about 3:4.

D. Transfer matrices

The transfer matrix approach,[16,17] a well-known method for modeling acoustic waves propagating through layered structures, has been used here to solve the transmitted shear wave field through the composite laminate. To apply this approach, we first expressed the shear wave field in each ply as a summation of four partial wave fields: two fast shear waves polarized along the fibers and propagating in the positive and negative thickness direction, and two slow shear waves polarized normal to the fibers and propagating in the positive and negative thickness direction. We then considered the velocity and stress fields of the shear waves and calculated the associated local and global transfer matrices. Finally, equations were established based on the velocity and stress continuity conditions at each interface, and were used to solve the transmitted shear wave fields. A brief description of the transfer matrices is given in the following; a more detailed derivation can be found in Appendix A.

For convenience, let vector P denote the velocity and stress components associated with the normal incidence shear wave field. P is defined as

$$P=[v_1 \quad v_2 \quad \sigma_{13} \quad \sigma_{23}]^T, \tag{4}$$

where v_1 and σ_{13} are, respectively, the velocity and stress of the fast shear wave field, v_2 and σ_{23} are, respectively, the velocity and stress of the slow shear wave field, and T denotes ''transpose.'' Velocity, instead of displacement, is used so that the final equations can be expressed in terms of acoustic impedances, which is more compact and physically meaningful.

The velocity–stress vectors at the top and the bottom interfaces of the jth ply in the laminate are related by a local transfer matrix B_j, as follows:

$$P_j^-=B_jP_j^+. \tag{5}$$

Local transfer matrix B_j is a 4×4 matrix whose components are given by Eq. (A5).

Applying the velocity and stress continuity conditions at each interface in the composite laminate, one can relate the velocity–stress vectors at the top and bottom interfaces of the laminate through a global transfer matrix B, as follows:

$$P_S^-=BP_S^+, \tag{6}$$

where $B=B_1B_2\cdots B_{n-1}B_n$ is the product of all the local transfer matrices in the n-ply laminate.

E. Transfer functions

In metal medium 1, the velocity–stress vector at interface 1 is given by

$$P_{M_1}^+=(-i\omega)\begin{bmatrix}1&0&1&0\\0&1&0&1\\-Z&0&Z&0\\0&-Z&0&Z\end{bmatrix}_{M_1}\begin{bmatrix}I_1\\I_2\\R_1\\R_2\end{bmatrix}_{M_1}, \tag{7}$$

where Z, which is equal to ρ_Mc_s (ρ_M is the mass density of metal and c_s is the shear wave velocity in metal), is the acoustic impedance of the shear wave in metal, and R_1 and R_2 are the displacement components of the reflected shear wave in the x_1 and x_2 directions, respectively.

In metal medium 2, there are only two transmitted partial waves. The velocity–stress vector at the top interface is given by

$$P_{M_2}^-=(-i\omega)\begin{bmatrix}1&0\\0&1\\-Z&0\\0&-Z\end{bmatrix}_{M_2}\begin{bmatrix}T_1\\T_2\end{bmatrix}_{M_2}. \tag{8}$$

The bonding conditions at the metal–sample interfaces are assumed to be rigid so that the velocity–stress continuity conditions, i.e., $P_{M_1}^+=P_S^-$ and $P_S^+=P_{M_2}^-$, can be applied. Combining Eqs. (6)–(8), we obtain the following equations for the unknown reflected and transmitted components in the metal media:

$$\begin{bmatrix}1&0&D_{11}&D_{12}\\0&1&D_{21}&D_{22}\\Z&0&D_{31}&D_{32}\\0&Z&D_{41}&D_{42}\end{bmatrix}\begin{bmatrix}R_1\\R_2\\T_1\\T_2\end{bmatrix}=\begin{bmatrix}-1&0\\0&-1\\Z&0\\0&Z\end{bmatrix}\begin{bmatrix}I_1\\I_2\end{bmatrix}, \tag{9}$$

where matrix D is given by Eq. (B3). Solving Eq. (9), one gets the transmitted components T_1 and T_2 in the form of

$$\begin{bmatrix}T_1\\T_2\end{bmatrix}=\begin{bmatrix}F_{11}&F_{12}\\F_{21}&F_{22}\end{bmatrix}\begin{bmatrix}I_1\\I_2\end{bmatrix}, \tag{10}$$

where F_{ij}'s $(i,j=1,2)$ are the transfer functions that relate an arbitrary incident input with the transmission output. These transfer functions [given by Eq. (B1)] are functions of frequency, material properties, and ply layup, and are independent of the orientations of the transmitter and receiver. Note that Eq. (9) can also be used to solve the reflected fields R_1 and R_2, which also carry ply layup information and can

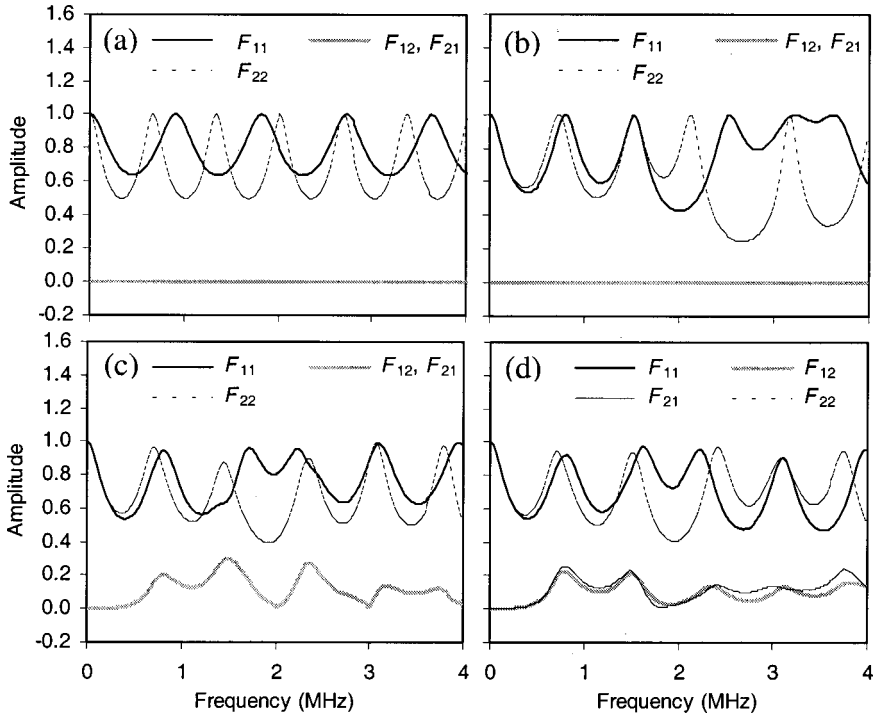

FIG. 3. Examples of transfer functions for graphite/epoxy laminates: (a) unidirectional, $[0]_8$; (b) cross-ply, $[0/90]_{2S}$; (c) quasi-isotropic, $[0/45/90/-45]_S$; (d) general, $[0/45/90/-45]_S$ with plies 1 and 2 interchanged.

therefore be utilized for layup characterization.

A special case where the laminate is an n-ply unidirectional composite laminate is discussed in Appendix C, giving a consistent result with that of classic theories.

F. Output voltage

Combining Eqs. (1), (2), and (10), one has the following expression for the output voltage of the receiving EMAT:

$$V_o = V_i \beta_T(\omega)\beta_R(\omega)[\cos\phi_R \quad \sin\phi_R]\begin{bmatrix} F_{11} & F_{12} \\ F_{21} & F_{22} \end{bmatrix}\begin{bmatrix} \cos\phi_T \\ \sin\phi_T \end{bmatrix}. \tag{11}$$

In Eq. (11), V_i, $\beta_T(\omega)$, and $\beta_R(\omega)$ are difficult to model individually, but the product of these three terms can be determined from the spectrum of a reference signal. The reference signal can be obtained with the EMAT transmitter and receiver aligned to each other and with the two metal blocks coupled directly by a shear couplant. Note here that the effect of the coupling layer is ignored because the coupling layer is thin compared to wavelength.

Equation (11) shows the essence of the shear wave transmission measurement. The laminate layup information is contained in the four transfer functions; therefore, there is no simple relationship between the transmission output and the ply layup. In addition, the transfer functions contain all the information that can possibly be extracted from the transmission measurement. These transfer functions can be determined in principle by four measurements: (1) $\phi_T = \phi_R = 0°$; (2) $\phi_T = 0°$, $\phi_R = 90°$; (3) $\phi_T = 90°$, $\phi_R = 0°$; and (4) $\phi_T = \phi_R = 90°$, respectively. If one makes these four "primary" measurements and obtains the four "primary" time-domain transmission signals, $V_{11}(t)$, $V_{12}(t)$, $V_{21}(t)$, and $V_{22}(t)$, respectively, one can predict the transmission output for arbitrary orientations of the transmitter and receiver according to

$$V_o(t) = [\cos\phi_R \quad \sin\phi_R]\begin{bmatrix} V_{11}(t) & V_{12}(t) \\ V_{21}(t) & V_{22}(t) \end{bmatrix}\begin{bmatrix} \cos\phi_T \\ \sin\phi_T \end{bmatrix}. \tag{12}$$

III. NUMERICAL CALCULATION AND DISCUSSIONS

In this section, we used the above-mentioned model to investigate the interaction between the fiber orientation and normal incidence shear waves and their potential for layup characterization in composite laminates. Owing to the importance of transfer functions, the model was first used to study the transfer functions of several typical types of laminates with common layups. The model was then used to predict the transmission output as a function of the orientation angle of the transmitter and receiver for a single or multiple frequencies, with the purpose of seeking the appropriate quantity for indicating layup errors. In all the numerical calculation, the metal material was aluminum with a density of 2.70×10^3 kg/m^3 and a shear wave velocity of 3.13×10^3 m/s. The ply material was graphite/epoxy with a density of 1.60×10^3 kg/m^3, a ply thickness of 1.30×10^{-4} m, a fast shear wave velocity of 1.89×10^3 m/s, and a slow shear wave velocity of 1.40×10^3 m/s.

A. Transfer functions

The transfer functions are determined for a given composite laminate and metal block material; they are independent of transducers and measurement system settings. Figure 3 shows the magnitude of the transfer functions for four types of composite laminates. In Fig. 3(a), the laminate is an 8-ply unidirectional graphite/epoxy laminate with fibers in the x_1 direction. It can be seen that F_{11} and F_{22} exhibit a simple resonance behavior, owing to the fact that an 8-ply unidirectional laminate is equivalent to a thick single layer in the idealized model. The resonance frequencies for F_{11} and

F_{22} are different due to the velocity difference of the fast and slow shear waves. Both F_{12} and F_{21} are zero because there is no coupling between the shear waves polarized along and normal to the fibers as they propagate through a unidirectional laminate.

For the transfer functions shown in Fig. 3(b) the laminate is a cross-ply graphite/epoxy laminate with a layup of $[0/90]_{2S}$ (S indicates that the layup is symmetric with respect to the midplane of the laminate). Comparing with Fig. 3(a), we see that transfer functions F_{11} and F_{22} are more complicated due to the additional resonance caused by the conversions between the fast and slow shear waves in the laminate, in either x_1 or x_2 directions. Transfer functions F_{12} and F_{21} remain zero, again because there is no coupling between the shear waves in directions x_1 and x_2. In fact, the above statement for F_{12} and F_{21} is valid for any cross-ply laminates (including the unidirectional laminate case), as long as the 0° of the laminate is aligned to either x_1 or x_2 directions.

Figure 3(c) shows the transfer functions of a quasi-isotropic graphite/epoxy laminate with a layup of $[0/45/90/-45]_S$. A significant difference from the previous unidirectional and cross-ply cases is that transfer functions F_{12} and F_{21} are no longer zero. This is because the input shear wave components in x_1 or x_2 directions have been coupled to the respective outputs in x_2 or x_1 directions, through the $\pm 45°$ plies in the laminate. Cross-ply and quasi-isotropic laminates can therefore be distinguished from each other by measuring F_{12} or F_{21}.

In all the three cases mentioned previously, F_{12} and F_{21} are either zero or the same. They are, however, not necessarily equal for a general laminate layup. Figure 3(d) gives one example. The layup of the laminate is $[0/45/90/-45]_S$ with plies 1 and 2 interchanged. One can see that F_{12} and F_{21} are no longer equal due to the break of ply layup symmetry. A comparison of F_{12} and F_{21} can therefore be used to reveal errors in stacking sequence. Here one can also see that the transfer functions of a composite laminate with a general layup are complicated, due to the mode conversions between the fast and slow shear waves and the resonance associated with different thickness of groups of plies or the whole laminate.

B. Angular patterns at different frequencies

When a normal-incidence shear wave propagates through a composite laminate, it interacts strongly with the fiber orientations in different plies. The transmitted shear wave can therefore be used in the detection of the errors in ply layup. As one can see from Eq. (11), the transmission output for a given composite laminate depends on the transducer orientation and frequency. There are therefore a number of possible ways to measure the transmitted signal and use it to indicate laminate layup errors. One convenient way is to perform an angular scan. Using the transmission setup shown in Fig. 1, one can perform an angular scan with the transmitting and receiving EMATs either ''aligned'' or ''crossed.'' Here, ''aligned'' means that the two transducers are oriented with their polarization directions parallel to each other, and ''crossed'' means perpendicular to each other. In either case, the two transducers are rotated synchronously in the same rotation direction over a full circle. The received signal is measured at every angular position, yielding an angular pattern after a scan. Previous study[9–11] showed that the changes in layup orientation and stacking sequence could sometimes drastically alter the angular pattern of the peak–peak amplitude of the transmitted signal.

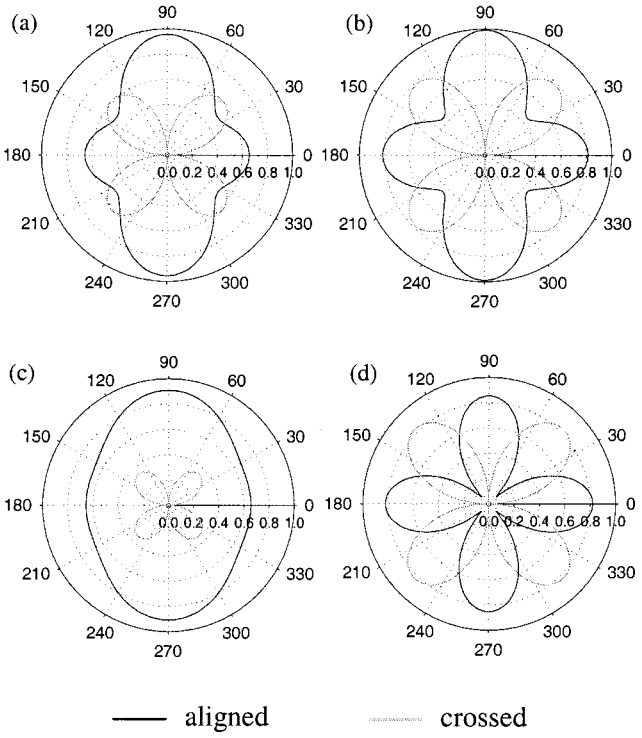

FIG. 4. Angular patterns for a 16-ply unidirectional graphite/epoxy laminate at different frequencies: (a) 1.0 MHz, (b) 2.0 MHz, (c) 3.0 MHz, and (d) 4.0 MHz.

With the developed analytical model, we simulated the angular scan and calculated the angular pattern for different frequencies. Using Eq. (11), we calculated the normalized output voltage, $V_o/(V_i\beta_R(\omega)\beta_R(\omega))$, so that the results were independent of the measurement system. Figure 4 shows the calculated angular patterns at selected frequencies of (a) 1.0 MHz, (b) 2.0 MHz, (c) 3.0 MHz, and (d) 4.0 MHz, for a 16-ply unidirectional graphite/epoxy laminate. It can be seen that the shapes of the aligned patterns (solid lines) vary greatly with frequency, from nearly elliptical to four equal lobes. All the crossed patterns (gray lines), however, have four equal lobes. This is actually valid for all the cross-ply laminates and can be easily proven using Eq. (11) with $F_{12}=F_{21}=0$ and $\phi_R=\phi_T-90°$. It is also seen that the absolute size (magnitude) of the aligned and crossed patterns and the relative size between the aligned and crossed patterns are very sensitive to frequency.

Another example is shown in Fig. 5. The laminate is a quasi-isotropic graphite/epoxy laminate with a layup of $[0/45/90/-45]_{2S}$. Compared with the angular patterns shown in Fig. 4, the main difference here is the tilting of both the aligned and crossed patterns. The tilting is caused by the nonzero transfer functions F_{12} and F_{21}, or the coupling between the shear wave fields in the x_1 and x_2 directions through the 45° plies in the laminate. The shape, absolute

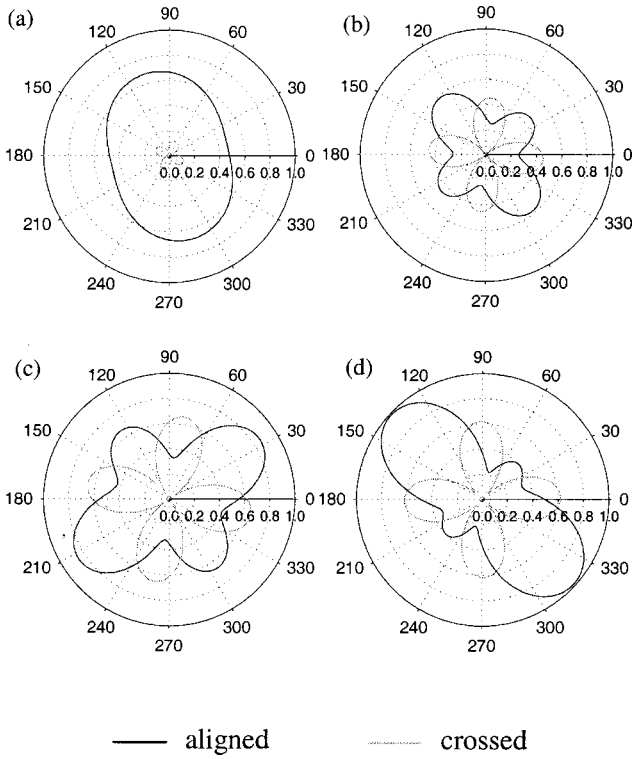

FIG. 5. Angular patterns for a quasi-isotropic graphite/epoxy laminate with a layup of $[0/45/90/-45]_{2S}$ at different frequencies: (a) 1.0 MHz, (b) 2.0 MHz, (c) 3.0 MHz, and (d) 4.0 MHz.

size, and relative size of both aligned and crossed patterns again change greatly with frequency.

C. Angle–frequency patterns

Because the angular pattern at a single frequency is very sensitive to frequency itself, as has been demonstrated previously, a more robust approach to show the laminate layup errors is to collect the angular patterns of the received signal at different frequencies and display them in a grayscale or color image. Such an image has frequency on the horizontal axis and angle of the transmitting transducer angle on the vertical axis; it was referred to as the ''angle–frequency pattern.'' Experimentally, we can use pulse excitation and record the transmitted shear wave signals in the time domain at every scan step in an angular scan. The obtained scan data can be displayed in grayscale or color image with time on the horizontal axis and transducer angle on the vertical axis, or the ''angle–time pattern.'' The angle–time and angle–frequency patterns are equivalent; they can be transformed from one to the other through a Fourier or inverse Fourier transform. Some of the features associated with laminate layup errors may be more prominent in the angle–frequency pattern while others may be more easily detected in the angle–time pattern.

The model has been used to calculate the angle–frequency patterns and to study their sensitivity to ply layup errors. The first example is given in Fig. 6. Before layup errors are introduced, the layup of the laminate is $[0/90]_{2S}$. The aligned and crossed angle–frequency patterns are shown in (a-A) and (a-C), respectively. If ply 2 is by mistake placed at 0° instead of at 90°, the patterns become those shown in (b-A) and (b-C). By comparison, one can easily see the changes of the angle–frequency patterns caused by the single-ply misorientation. The changes are especially evident in the crossed pattern. When the ply misorientation takes place at the fourth ply, the resultant aligned and crossed patterns are shown in (c-A) and (c-C), respectively. We see that the angle–frequency patterns are also sensitive to the depth of the misplaced ply. Finally, if the laminate is laid up as a nonsymmetric laminate, $[0/90]_4$, both aligned and crossed patterns change drastically, as shown in (d-A) and (d-C), respectively. The aligned pattern shows the stopping band between 2.5 and 3 MHz, which is caused by the periodic nature of the laminate. The crossed pattern is identically zero owing to the special properties of the layup. The layup takes the form of $[0_m/90_m]_n$ (where m, n are positive integers). For this special type of layup, $F_{11}=F_{22}$ and $F_{12}=F_{21}=0$, which explains why the crossed output is zero. This example also shows that the sensitivity of the angle–frequency patterns to layup errors is not constant over the entire frequency range: different layup errors cause changes in different frequency ranges. This shows the advantage of the angle–frequency pattern over the individual angular patterns for detecting layup errors.

The second example is shown in Fig. 7. The laminate has a quasi-isotropic layup of $[0/45/90/-45]_{2S}$. When the laminate is free of layup errors, the aligned and crossed angle–frequency patterns are shown in (a-A) and (a-C), respectively. The patterns change into (b-A) and (b-C) if ply 8 is placed at $+45°$ by mistake, into (c-A) and (c-C) if plies 7 and 8 are interchanged, and into (d-A) and (d-C) if the laminate is laid up as $[0/45/90/-45]_4$. From all these patterns, we again see that the crossed patterns are especially sensitive to ply misorientation and stacking sequence errors and that the sensitivity depends on frequency ranges for different layup errors. Analytically, it is difficult to prove that the aligned and crossed angle–frequency patterns are unique to a particular type of laminate. However, the two examples shown here and extensive model calculations performed for a variety of laminates with different layup errors have provided convincing evidence about the usefulness of the angle–frequency patterns (or equivalent angle–time patterns) for indicating ply layup errors.

The reason that the crossed pattern appears more sensitive to layup errors than the aligned pattern can be explained using the model. Substituting $\phi_R=\phi_T=\phi$ into Eq. (11), we can obtain the following normalized output $(V_o/(V_i\beta_R(\omega)\beta_R(\omega))$ for an aligned angular scan V_A:

$$V_A=\tfrac{1}{2}(F_{11}+F_{12})+\tfrac{1}{4}[(F_{11}-F_{22})-i(F_{12}+F_{21})]e^{i2\phi}+\tfrac{1}{4}[(F_{11}-F_{22})+i(F_{12}+F_{21})]e^{-i2\phi}. \quad (13)$$

Similarly, substituting $\phi_T=\phi$ and $\phi_R=\phi-90°$ in Eq. (11) leads to the following expression for the normalized output for a crossed scan V_C:

$$V_C=\tfrac{1}{2}(F_{12}-F_{21})+\tfrac{1}{4}[-i(F_{11}-F_{22})-(F_{12}+F_{21})]e^{i2\phi}+\tfrac{1}{4}[i(F_{11}-F_{22})-(F_{12}+F_{21})]e^{-i2\phi}. \quad (14)$$

Equations (13) and (14) show that both the aligned and crossed patterns contain only nonzero dc and $\pm 2\phi$ angular

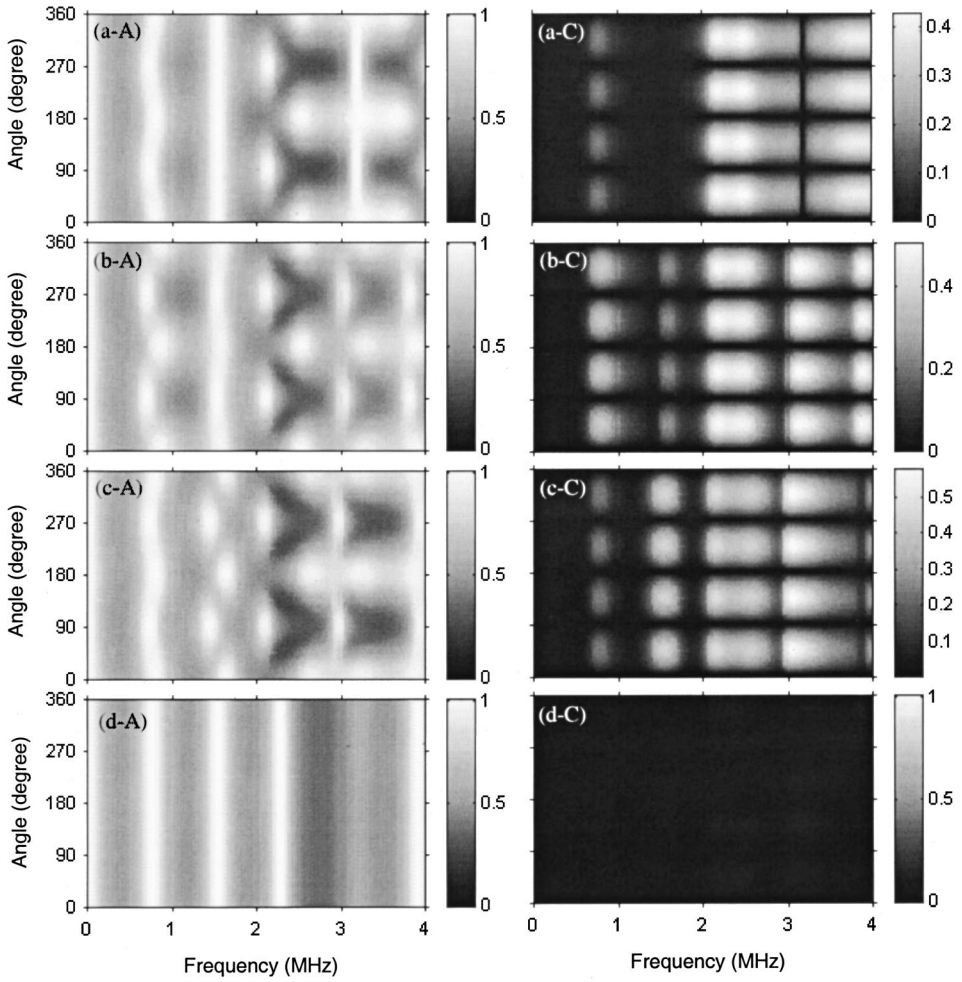

FIG. 6. Angle–frequency patterns for cross-ply graphite/epoxy laminates with and without errors. Layup: $[0/90]_{2S}$. (a-) without errors; (b-) ply 2 is placed at 0°; (c-) ply 4 is placed at 0°; (d-) $[0/90]_4$. (-A) aligned; (-C) crossed.

spectrum components. While the 2ϕ components of the aligned and crossed patterns have the same magnitude but a reversed phase, their dc components are very different. For shear wave measurements at one or several MHz, the wavelength is usually large compared with the laminate thickness. As a result, the values of transfer functions F_{11} and F_{22} are often close to unity, and transfer functions F_{12} and F_{21} are usually small. In the aligned patterns, the components that are sensitive to layup errors, F_{12}, F_{21}, and $F_{11}-F_{22}$, are superimposed on a strong dc background, $\frac{1}{2}(F_{11}+F_{22})$. In the crossed patterns, however, the dc background, $\frac{1}{2}(F_{12}-F_{21})$, is much smaller, making the sensitive components easily observed.

IV. EXPERIMENTAL PROCEDURE

A. Experimental system

Experiments were performed using a computer-controlled motorized EMAT scanning system whose schematic diagram is shown in Fig. 8. The composite sample is sandwiched between two aluminum blocks. For cured composite laminates, a shear couplant, such as honey, is used at the composite–metal interfaces. In the case of uncured laminates, no couplant is used and the shear wave can be coupled effectively via the pressure applied on the sample. The EMAT transmitter and receiver both have a 1.3 in.$\times$0.7 in. flat spiral coil, a pair of 0.7 in.$\times$0.35 in.$\times$0.5 in. Nd–Fe–B magnets, a central frequency of about 1.3 MHz, and a frequency bandwidth of about 1.0 MHz. The EMAT transmitter is driven by a burst pulser (Ritec, BP-9400). The output signal of the EMAT receiver, after being amplified ($\sim$10 dB), is digitized by the data acquisition card in the PC. Averaging (up to 256 times) is used to reduce the noise in the received signal caused by the currents in the stepper motors. The stepper motors are controlled by the computer through the motor driver; they are used to rotate the two EMATs simultaneously in an angular scan. The maximum angular resolution is 0.9°. The angular scans are done in either aligned or crossed configuration. A typical angular scan takes about 3 min. A more detailed description of the experimental system can be found in Ref. 4.

B. Calibration of the EMAT orientation

In the angular measurement, especially with crossed EMATs, the transmitted signal is very sensitive to the orientation of the EMATs. It is therefore necessary to calibrate the polarization directions of the EMATs. The calibration procedure consists of two steps in order: (1) to ensure that the polarization directions of the transmitter and receiver are normal to each other for crossed scans, and (2) to ensure that the polarization of the transmitting EMAT is along the zero

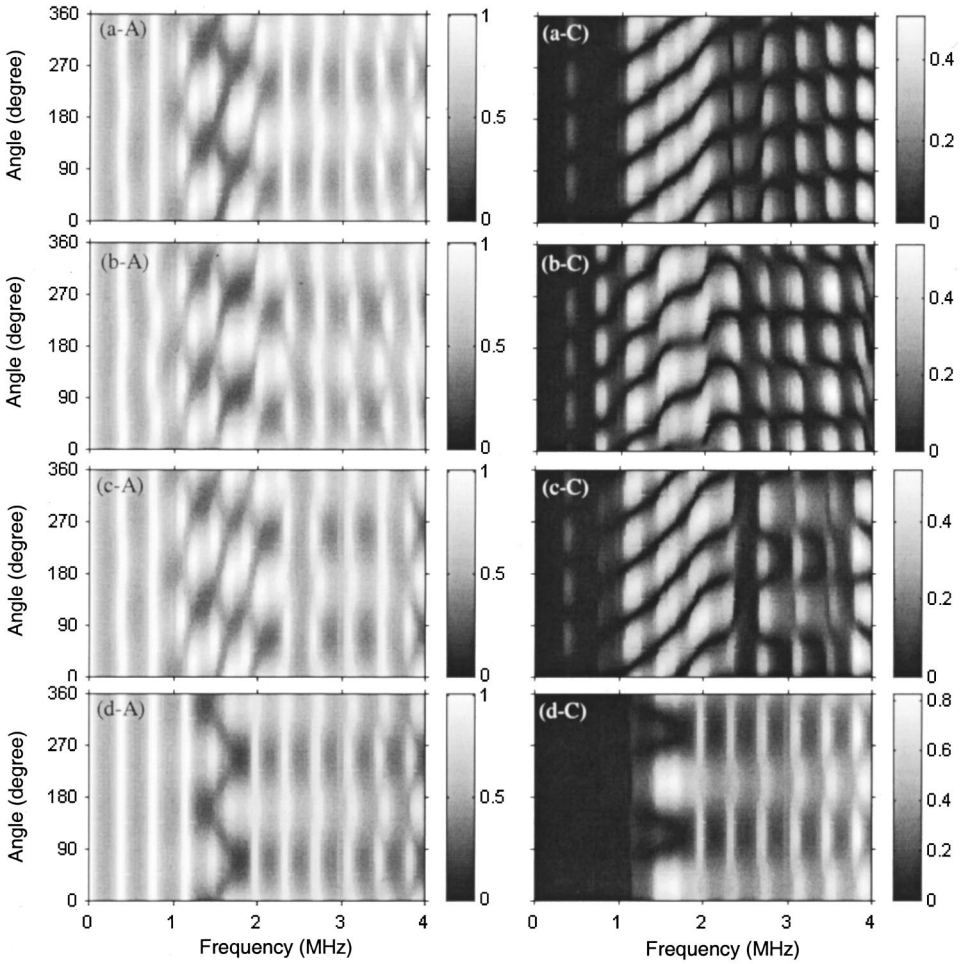

FIG. 7. Angle–frequency patterns for quasi-isotropic graphite/epoxy laminates with and without errors. Layup: $[0/45/90/-45]_{2S}$. (a-) without errors; (b-) ply 8 is placed at $+45°$; (c-) plies 7 and 8 are interchanged; (d-) placed as $[0/45/90/-45]_4$. (-A) aligned; (-C) crossed.

degree direction of the system when it is at 0°. For the first step, we used a thin isotropic rubber sheet as the sample. With the transmitter held fixed, the receiver was rotated 360° and the transmitted signals were acquired. The computer searched for the minimum of peak–peak amplitude of the acquired data. If initially the two transducers were parallel to each other, the minima would occur at 90° and 270°. If not, the angle of the receiver was automatically adjusted by a proper amount to make it so. In the second step, a fiducial mark was made on one of the aluminum blocks to serve as the system zero. To align the transmitting EMAT with the system zero, we used a unidirectional composite laminate as the sample and placed it in between the aluminum blocks with the fibers in the system zero direction. The transmitter and receiver were then rotated simultaneously in a crossed configuration. Because the transmitter and receiver were crossed, the received signal reached a minimum when the transmitter was along the fiber direction. Based on this criterion, the transmitter and receiver were rotated simultaneously so that the EMAT transmitter was oriented in the system zero direction after calibration.

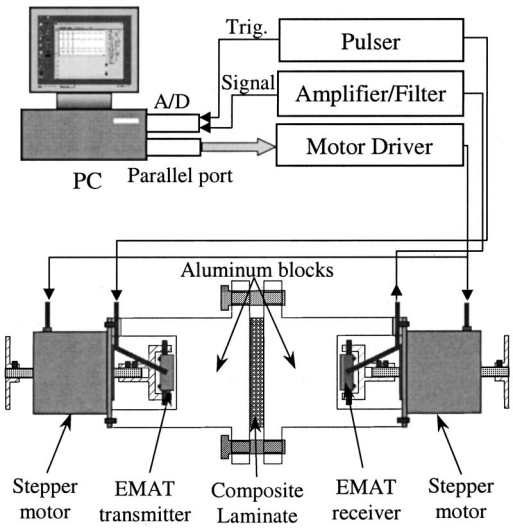

FIG. 8. A schematic diagram showing the azimuthal EMAT scanning system.

C. Samples

The laminates used in this work were fabricated using IM7-8551-7A graphite/epoxy pre-preg tapes, manufactured by Hercules, Inc. The sample set contains both cured and uncured laminates. Solid laminates were cured in a heated press. To make the uncured laminates, the prepreg was first warmed to room temperature and then cut and stacked by hand according to the required layup. The testing of uncured laminates was carried out right away while the laminate still had adequate ''tack.'' The physical properties of the cured and uncured unidirectional plies were measured using a 24-

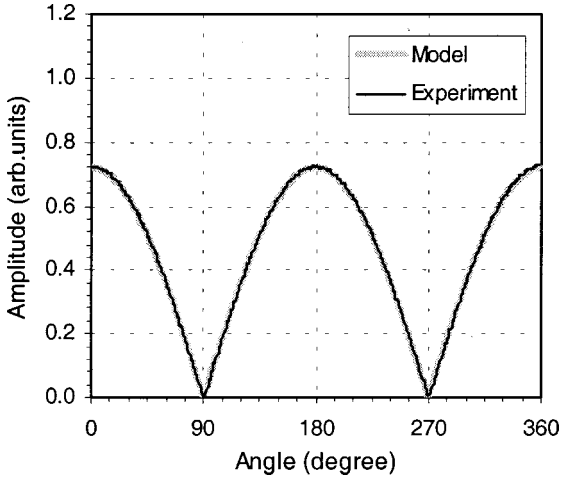

FIG. 9. Verification of linear polarization assumption of EMATs.

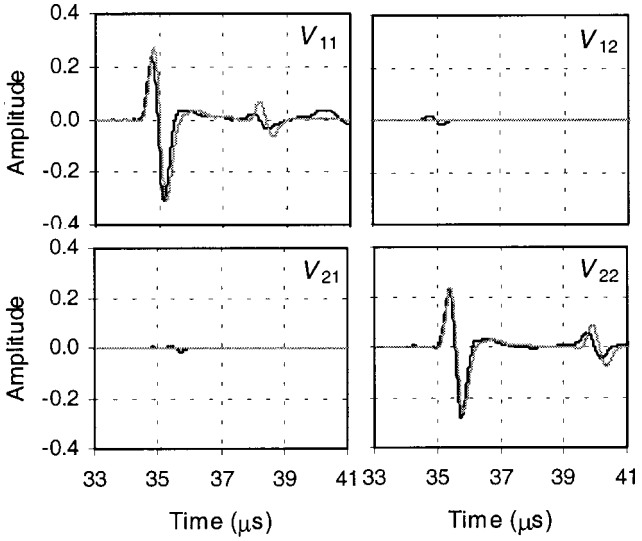

FIG. 10. Primary transmission wave forms for a 24-ply unidirectional graphite/epoxy laminate. Black lines: experiment; gray lines: model.

ply unidirectional laminate. The measured density, fast shear velocity, slow shear velocity, and ply thickness of the cured ply are the same as that used in the numerical calculation in Sec. III. The uncured ply has a measured density of 1.47×10^3 kg/m^3, a fast shear wave velocity of 1.43×10^3 m/s, a slow shear wave velocity of 1.25×10^3 m/s, and a thickness of 1.46×10^{-4} m. Both cured and uncured sample sets contain unidirectional, cross-ply and quasi-isotropic laminates, with and without various types of layup errors.

V. EXPERIMENTAL RESULTS AND DISCUSSION

A. Model verification

In the derivation of the model in Sec. II, it was assumed that the transmitting and receiving EMATs are linearly polarized and that any effects associated with their finite aperture size were ignored. In order to test experimentally the validity of this assumption, we held the aluminum blocks together with shear couplant (without any sample), held the transmitter fixed, and rotated the receiver to measure the amplitude of the transmitted signal. Figure 9 shows the measured peak-to-peak amplitude of the transmitted signal and its comparison with the model prediction based on the linear polarization assumption, which is simply $|\cos\phi_R|$. The excellent agreement between the experimental and model results indicates that the linear polarization assumption of the EMAT is a good approximation.

The analytic model was tested for four different types of laminates by comparing the experimentally measured and model-predicted received signals in the time domain. To pre-

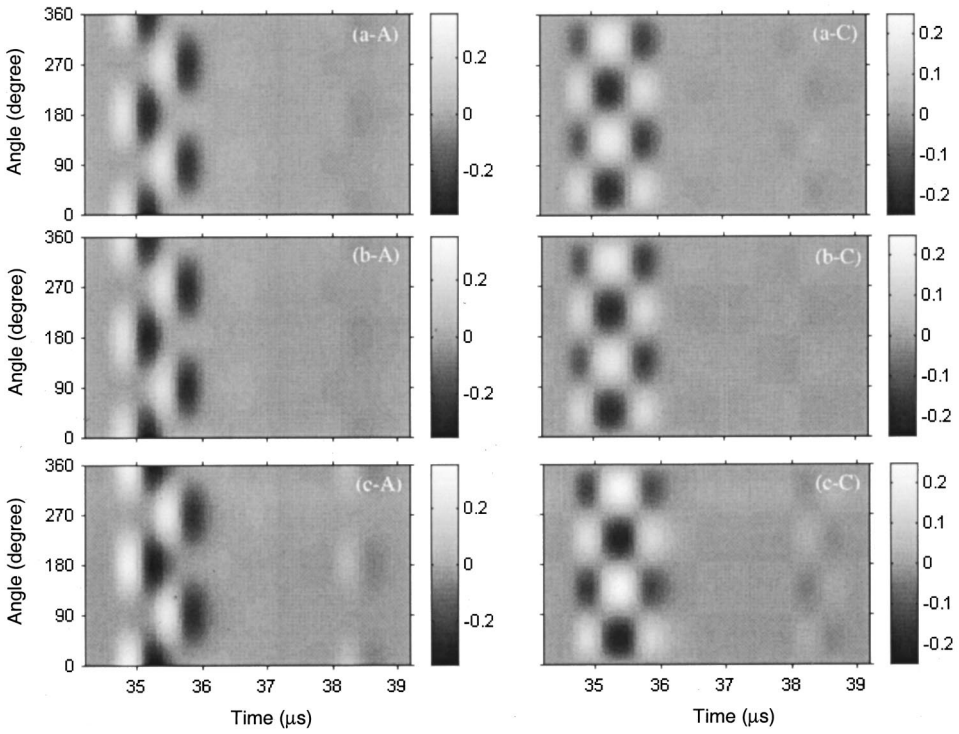

FIG. 11. Angle–time patterns for a 24-ply unidirectional graphite/epoxy laminate: (a-) experimental patterns; (b-) predicted patterns based on four primary wave forms; (c-) model prediction. (-A) aligned; (-C) crossed.

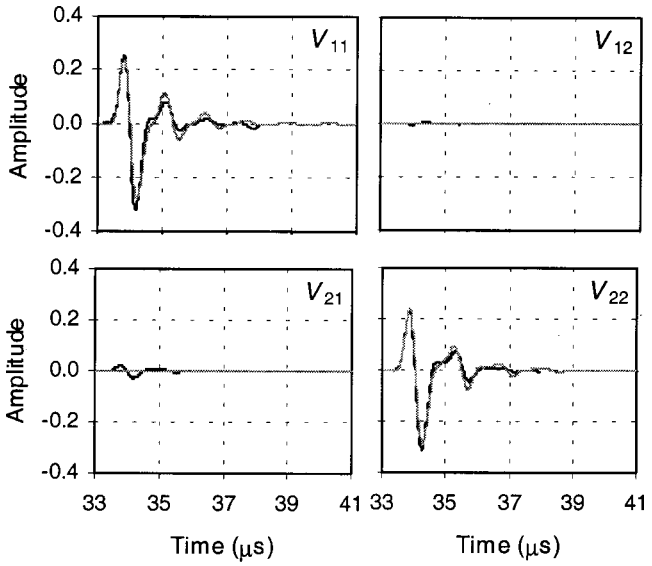

FIG. 12. Primary transmission wave forms for a cross-ply graphite/epoxy laminate. Layup: $[0/90]_{2S}$ with the fourth ply at 0°. Black lines: experiment; gray lines: model.

dict the time-domain signal using the model, a reference transmission signal was first recorded with the EMAT transmitter and receiver aligned to each other and the two aluminum blocks coupled directly together with shear couplant and no sample. The frequency spectrum of the reference signal, which is essentially $V_i\beta_R(\omega)\beta_R(\omega)$, was then used in Eq. (11) for a particular laminate sample. Finally, the calculated frequency spectrum of the output signal was transformed into the time domain through an inverse fast Fourier transform. The reference signal showed an effective frequency bandwidth of about 1.0 MHz.

The first example is a 24-ply cured unidirectional graphite/epoxy laminate. Figure 10 shows a comparison of the experimental wave forms and the model predictions for the four primary transmission signals V_{11}, V_{22}, V_{12}, and V_{21}. The experimental results and model predictions agree well with each other. The direct arrival pulse and its three-pass echo in the laminate can be clearly identified in both V_{11} and V_{22}. The experimental V_{12} and V_{21} are not strictly zero; this can be due to the receiver being not exactly normal to the transmitter and the imperfect alignment of the 24 plies. Figure 11 shows a comparison between experimental and calculated angle–time patterns for this laminate. In Fig. 11, (a-A) and (a-C) are experimental angle–time patterns for the aligned and crossed configurations, respectively; (b-A) and (b-C) are the synthetic patterns using the four experimental primary transmission wave forms and Eq. (12); and (c-A) and (c-C) are model predictions based on Eq. (11) using the reference signal only. It is clear that the three sets of patterns agree with each other very well.

The second example is a cured graphite/epoxy laminate with a layup of $[0/90]_{2S}$ except that the fourth ply was intentionally placed at 0°. The experimentally obtained primary transmission wave forms, V_{11}, V_{22}, V_{12}, and V_{21}, and their model predictions are shown in Fig. 12. The agreement is quite good. Compared to the results shown in Fig. 10, the pulses here are not well separated because the laminate is thinner. The comparison for the angle–time patterns is given in Fig. 13, from which one can see again the good agreement between the experimental results and model predictions. In the experimental patterns shown in (a-A) and (a-C), the signal decays more rapidly than that the model predicted. This is mainly due to the material attenuation and beam spreading effects.

The next example is a cured quasi-isotropic graphite/epoxy laminate with a layup of $[0/45/90/-45]_{2S}$. The four experimentally obtained primary transmission wave forms and their respective model predictions are shown in Fig. 14. The model predicted that V_{12} and V_{21} are equal and nonzero. The comparison for the angle–time patterns is shown in Fig. 15. Both Figs. 14 and 15 show that the model worked reasonably well for a quasi-isotropic laminate.

The last example is an uncured 8-ply quasi-isotropic graphite/epoxy laminate with a layup of $[0/45/90/-45]_S$. The comparison for the four primary transmission wave forms and the angle–time patterns is given in Figs. 16 and 17, respectively. For uncured laminates, the ''tack'' of the pre-preg material and the less intimate ply–ply interface contacts are expected to contribute to signal attenuation. Therefore, the discrepancies between the experimental and calcu-

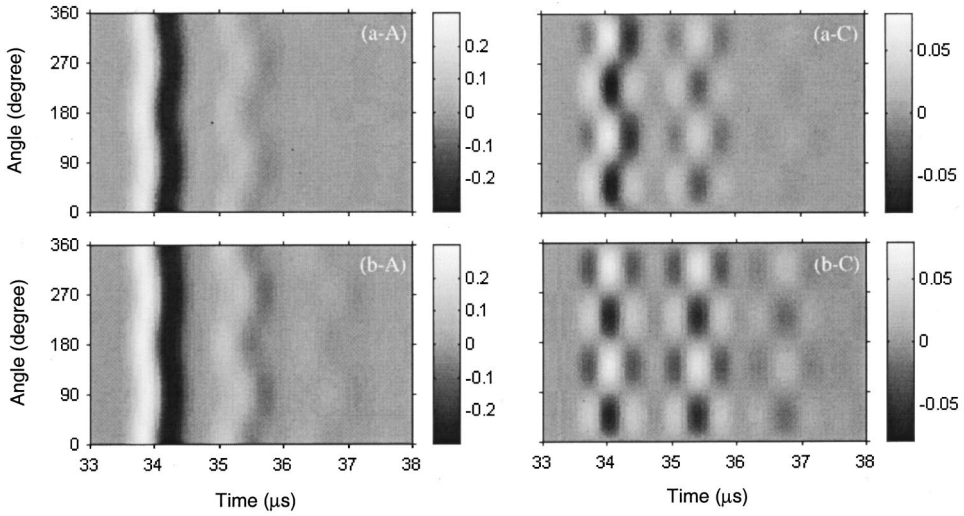

FIG. 13. Angle–time patterns for a cross-ply graphite/epoxy laminate. Layup: $[0/90]_{2S}$ with the fourth ply at 0°: (a-) experiment; (b-) model. (-A) aligned; (-C) crossed.

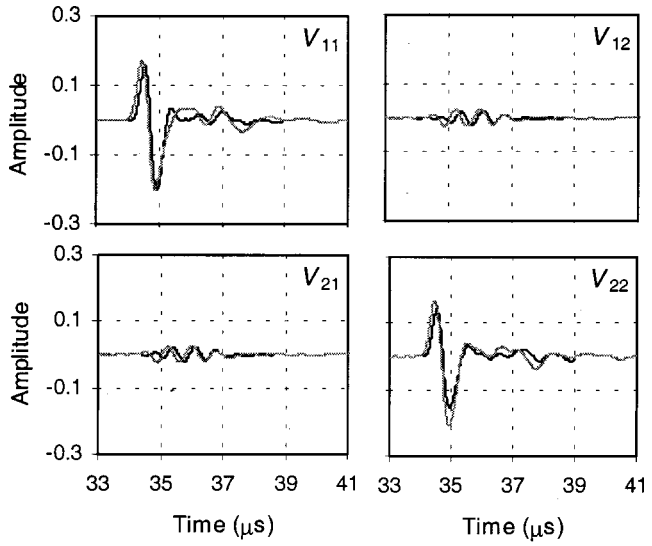

FIG. 14. Primary transmission wave forms for a quasi-isotropic graphite/epoxy laminate. Layup: $[0/45/90/-45]_{2S}$. Black lines: experiment; gray lines: model.

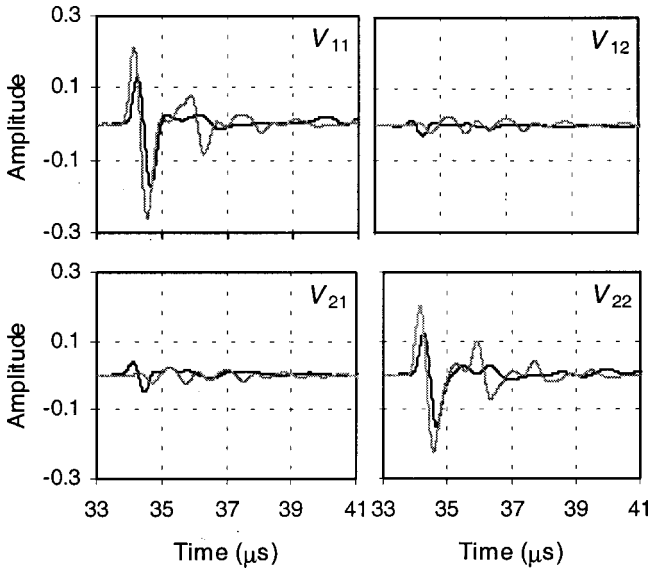

FIG. 16. Primary transmission wave forms for an uncured graphite/epoxy laminate. Layup: $[0/45/90/-45]_{S}$. Black lines: experiment; gray lines: model.

lated results shown in Figs. 16 and 17 were believed to come mainly from the model assumptions that led to higher amplitudes and more prominent multiple echoes. Other than the difference in signal intensity, the model predicted the angle–time patterns reasonably well.

The four examples mentioned previously, covering a variety of laminate layup designs, an intentional layup error, and both cured and uncured laminates, have amply demonstrated the agreement between the experimental results and model prediction. In addition to the cases shown here, other layups have also been studied, with similar agreement between experiment and model. The comparison between the experiment and model can also be conducted in the frequency domain using angle–frequency patterns, but it would be equivalent to the angle–time patterns. It is evident that the model has correctly treated the major physical behavior governing the shear wave propagation in a laminated composite. Further improvement of the model should include the effects due to the material attenuation, the nonideal interface conditions (especially the coupling layer between the laminate and metal), the beam spreading and responses of the EMATs. For uncured laminates, this could be challenging because the ply-to-ply interface conditions, shear wave velocities, ply thickness, and attenuation cannot be precisely characterized.

B. Detection of layup errors

The main motivation for using the transmission of linearly polarized, normal-incident shear waves in a composite laminate was to exploit the effects of fiber direction on the propagation of shear waves for detecting errors or anomalies in the layup and stacking sequence of the laminate.[10,12] It has been demonstrated by the model analysis in Sec. III that the angle–frequency patterns of the transmitted shear wave, especially for crossed EMATs, are able to show distinct changes when a number of layup errors occurred. In this section we present examples of layup errors occurring in two different laminates, one cross-ply and one quasi-isotropic, and show the experimentally obtained angle–time patterns,

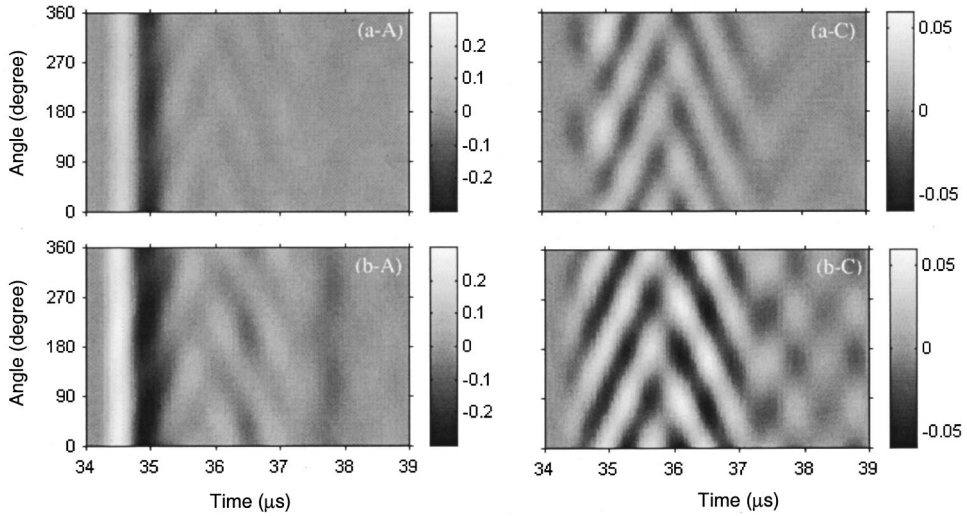

FIG. 15. Angle–time patterns for a quasi-isotropic graphite/epoxy laminate. Layup: $[0/45/90/-45]_{2S}$: (a-) experiment; (b-) model. (-A) aligned; (-C) crossed.

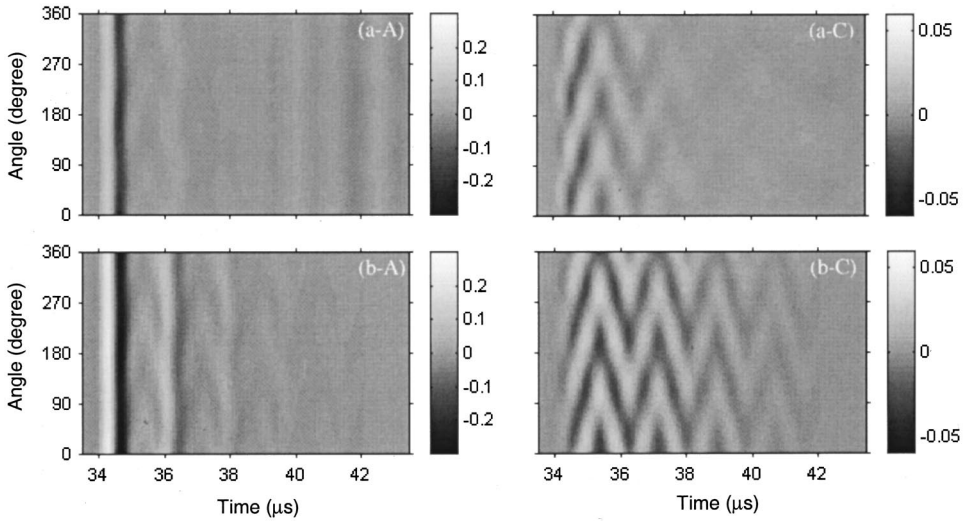

FIG. 17. Angle–time patterns for an uncured graphite/epoxy laminate. Layup: $[0/45/90/-45]_S$: (a-) experiment; (b-) model. (-A) aligned; (-C) crossed.

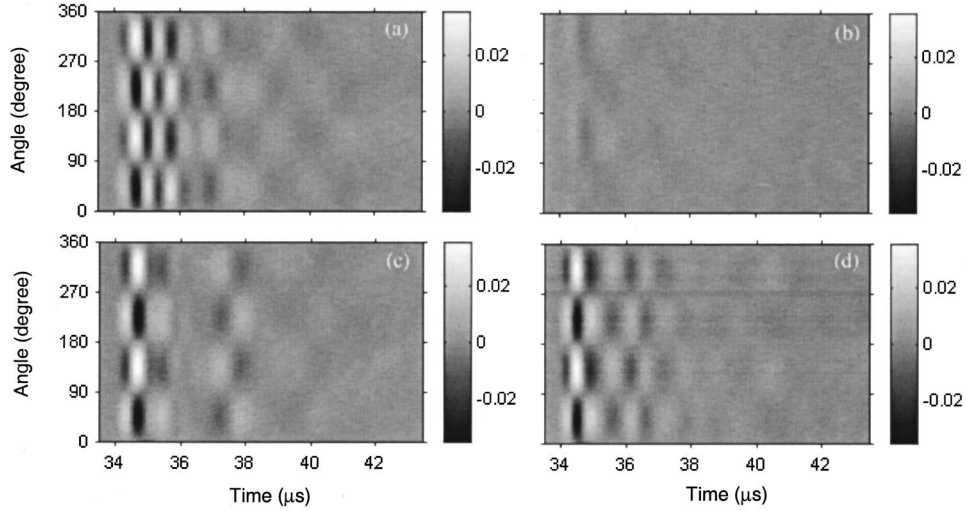

FIG. 18. Crossed-EMAT angle–time patterns for uncured graphite/epoxy laminates with and without various types of layup errors. Layup: $[0/90]_{2S}$: (a) without errors; (b) $[0/90]_4$; (c) ply 2 is placed at 0°; (d) ply 4 is placed at 0°.

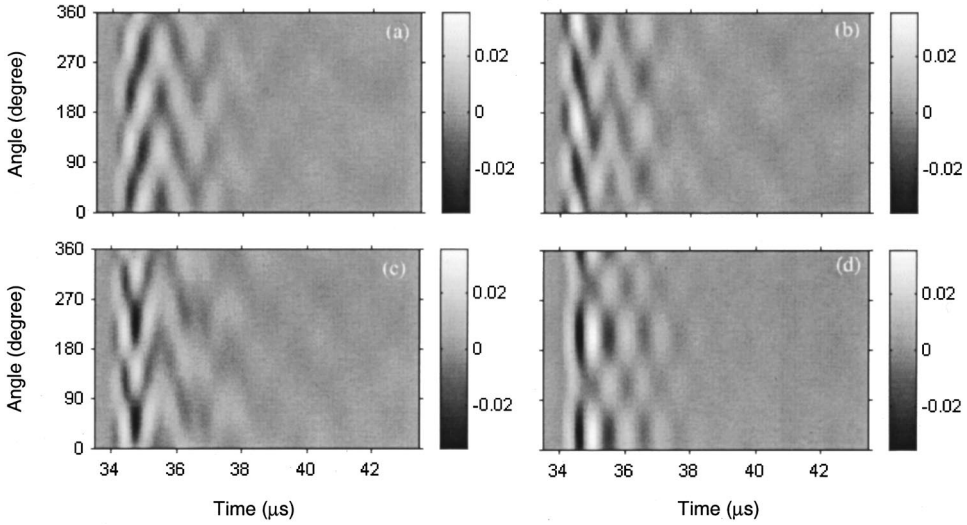

FIG. 19. Crossed-EMAT angle–time patterns for uncured graphite/epoxy laminates with and without various types of layup errors. Layup: $[0/45/90/-45]_S$: (a) without errors; (b) ply 4 is placed at 0°; (c) ply 4 is placed at 90°; (d) $[0/45/90/-45]_2$.

which are the time-domain presentation of the angle–frequency patterns. Only crossed patterns were shown because they are much more sensitive than the aligned ones. To show the changes, the patterns were given for both the case without error and the case with error.

The first example is for an 8-ply uncured cross-ply graphite-epoxy laminate $[0/90]_{2S}$. As shown in Fig. 18, the angle–time patterns obtained with crossed EMATs are given for the error-free case (a), for the case where the laminate was laid up asymmetrically $[0/90]_4$ (b), when the second ply was misplaced at 0° (c), and when the fourth ply was misplaced at 0° (d). When the symmetric layup $[0/90]_{2S}$ was made asymmetric $[0/90]_4$, the amplitude of the transmitted signal decreased dramatically. In fact, as we have discussed in Sec. III, because of the special properties of the layup $[0_m/90_m]_n$ (where *m,n* are positive integers), the crossed angle–time pattern of $[0/90]_4$ should have zero amplitude everywhere. The weak but nonzero angle–time pattern shown in (b) can be attributed to a number of nonideal conditions including imperfect alignment of the plies, imperfect orthogonality between the transmitting and receiving EMATs, beam spreading and others. Patterns (c) and (d) show that not only the errors were detectable, but the angle–time patterns were sensitive to the depth of the misoriented plies.

The second example was for an 8-ply uncured quasi-isotropic graphite-epoxy laminate $[0/45/90/-45]_S$. When the laminate layup was free of errors, the angle–time pattern is shown in Fig. 19(a). When the fourth ply was mistakenly placed at 0° and 90°, the resulting patterns showed discernable changes, as illustrated in Figs. 19(b) and (c), respectively. When the laminate was laid up as $[0/45/90/-45]_2$ without a mirror symmetry with respect to the midplane, the resulting angle–time pattern, Fig. 19(d), was characteristically different.

In addition to the two examples mentioned previously, extensive experiments were conducted for laminates with many likely and conceivable layup errors. The results also showed the sensitive changes in the crossed angle–time patterns for most of the ply misorientation and stacking sequence errors.

VI. CONCLUSIONS

The effects of fiber orientations on normal-incident shear waves propagating through a composite laminate have been studied both theoretically and experimentally, with the purpose of developing a nondestructive evaluation tool for detecting laminate layup errors. A complete analytical model was developed using transfer matrices for the shear waves transmitted through a laminate with an arbitrary layup and for arbitrary transducer orientations. The model led to compact and tractable results based on four transfer functions that can be measured experimentally. It was found that the transfer functions contain all the information obtainable from the transmission measurement and the minimum measurement data are the four primary transmission wave forms at 0° and 90°. The model has proven to be of substantial value in predicting the sensitivity of transmitted shear waves to various ply layup errors or stacking sequence anomalies.

On the experimental side, a motorized EMAT scan system was developed. Experimental results were obtained for a number of possible errors in both cured and uncured composite laminates. The good agreement with experimental results and model predictions has confirmed that the model has described the major physical behaviors of the normal-incidence shear waves propagating in a composite laminate. The experimental results also demonstrated that the transmitted shear wave signals for crossed EMAT transmitter and receiver, when displayed as angle–time patterns, have great sensitivity to various ply misorientation and stacking sequence errors in the laminate.

The shear wave transmission method developed thus far holds considerable potential for manufacturing process monitoring and quality assurance for composite laminates. It utilizes the strong interaction between shear wave polarization and fiber directions in a laminate to indicate effectively the anomalies associated with the ply layup. At the same time, the shear wave transmission method is based on mode conversions between fast and slow shear waves and shear wave resonances in a composite laminate and is by nature an indirect method for ply layup characterization. No simple relationship exists between the layup and the transmission data. A general and complete layup inversion based on the transmitted shear wave signal is expected to be difficult. Pattern recognition approaches may help to solve the inverse problem when the total number of possibilities is small and known. Further work should include an investigation for the feasibility of using the reflected shear waves for layup characterization in composite laminates, for which only a single-sided access is needed.

ACKNOWLEDGMENTS

This work was supported by the NSF Industry/University Cooperative Research Center for Nondestructive Evaluation at Iowa State University. D.F. acknowledges the support of a graduate fellowship from the Institute for Physical Research and Technology at Iowa State University. The authors would also like to thank Dr. Dale E. Chimenti for some helpful discussions on modeling.

APPENDIX A: DERIVATION OF LOCAL TRANSFER MATRIX

As stated previously, for a normal incidence shear wave field in an arbitrary jth layer, there are generally four partial waves. The corresponding velocity–stress vector of the shear wave field can be expressed in terms of the amplitudes of the four partial waves, as follows:

$$P_j=(-i\omega)X_jE_j(x_3)Y_j, \tag{A1}$$

where

$$X_j=\begin{bmatrix} \cos\phi & -\sin\phi & \cos\phi & -\sin\phi \\ \sin\phi & \cos\phi & \sin\phi & \cos\phi \\ -Z_1\cos\phi & Z_2\sin\phi & Z_1\cos\phi & -Z_2\sin\phi \\ -Z_1\sin\phi & -Z_2\cos\phi & Z_1\sin\phi & Z_2\cos\phi \end{bmatrix}_j,$$

$$E_j(x_3)=\begin{bmatrix} e^{ik_1x_3} & 0 & 0 & 0 \\ 0 & e^{ik_2x_3} & 0 & 0 \\ 0 & 0 & e^{-ik_1x_3} & 0 \\ 0 & 0 & 0 & e^{-ik_2x_3} \end{bmatrix}_j, \tag{A2}$$

$$Y_j=[U_1 \quad U_2 \quad U_3 \quad U_4]^T,$$

where $i=\sqrt{-1}$, ϕ is the fiber orientation, Z_1 and Z_2 are the acoustic impedances for the fast and slow shear waves, respectively, k_1 and k_2 are the fast and slow shear wave numbers, respectively, and Y is a vector that contains U_1, U_2, U_3, and U_4, the four displacement amplitudes, respectively, associated with the fast shear partial wave propagating downward, the slow shear partial wave propagating downward, the fast shear partial wave propagating upward, and the slow shear partial wave propagating upward. All the quantities are defined in the jth ply, as indicated by the subscripts of the variables and the matrices. Note that the $\exp(-i\omega t)$ harmonic sign convention is used. From the above equation, one can see the advantage of using velocity instead of displacement: the frequency-dependent term $(-i\omega)$ can be moved out of the matrix X_j, which can now be expressed in terms of fiber orientation and acoustic impedances only; otherwise matrix X_j is also frequency dependent. By letting the acoustic impedance be complex, material attenuation can also be modeled; although the attenuation effects are not included in the present model.

The velocity–stress vectors at the top and the bottom interfaces of a ply can be related by a local inverse transfer matrix B_j,

$$P_j^-=B_jP_j^+, \tag{A3}$$

with B_j given by

$$B_j=X_jE_j(-h_j)X_j^{-1}, \tag{A4}$$

where h_j is the thickness of the jth ply. The explicit expressions for the components of B_j can be obtained through symbolic calculation and simplication of Eq. (A4). The results are given below,

$$\begin{aligned}
B_{11}&=B_{33}=\cos(k_2h)+\cos^2\phi[\cos(k_1h)-\cos(k_2h)],\\
B_{12}&=B_{21}=B_{34}=B_{43}\\
&\quad=\sin\phi\cos\phi[\cos(k_1h)-\cos(k_2h)],\\
B_{13}&=i\{\sin(k_2h)/Z_2+\cos^2\phi[\sin(k_1h)/Z_1\\
&\quad-\sin(k_2h)/Z_2]\},\\
B_{14}&=B_{23}=i\sin\phi\cos\phi[\sin(k_1h)/Z_1-\sin(k_2h)/Z_2],\\
B_{22}&=B_{44}=\cos(k_1h)+\cos^2\phi[\cos(k_2h)-\cos(k_1h)],\\
B_{24}&=i\{\sin(k_1h)/Z_1+\cos^2\phi[\sin(k_2h)/Z_2\\
&\quad-\sin(k_1h)/Z_1]\},\\
B_{31}&=i\{\sin(k_2h)Z_2+\cos^2\phi[\sin(k_1h)Z_1-\sin(k_2h)Z_2]\},\\
B_{32}&=B_{41}=i\sin\phi\cos\phi[\sin(k_1h)Z_1-\sin(k_2h)Z_2],\\
B_{42}&=i\{\sin(k_1h)Z_1+\cos^2\phi[\sin(k_2h)Z_2-\sin(k_1h)Z_1]\}.
\end{aligned} \tag{A5}$$

APPENDIX B: TRANSFER FUNCTIONS

The four transfer functions are given by

$$\begin{aligned}
F_{11}&=2Z(-D_{42}+D_{22}Z)/\Delta,\\
F_{12}&=2Z(D_{32}-D_{12}Z)/\Delta,\\
F_{21}&=2Z(D_{41}-D_{21}Z)/\Delta,\\
F_{22}&=2Z(-D_{31}+D_{11}Z)/\Delta,
\end{aligned} \tag{B1}$$

where

$$\begin{aligned}
\Delta=&-D_{31}D_{42}+D_{32}D_{41}+(-D_{21}D_{32}+D_{22}D_{31}+D_{11}D_{42}\\
&-D_{12}D_{41})Z+(-D_{11}D_{22}+D_{12}D_{21})Z^2,
\end{aligned} \tag{B2}$$

and

$$D=B\begin{bmatrix} -1 & 0 \\ 0 & -1 \\ Z & 0 \\ 0 & Z \end{bmatrix}=\begin{bmatrix} -B_{11}+B_{13}Z & -B_{12}+B_{14}Z \\ -B_{21}+B_{23}Z & -B_{22}+B_{24}Z \\ -B_{31}+B_{33}Z & -B_{32}+B_{34}Z \\ -B_{41}+B_{43}Z & -B_{42}+B_{44}Z \end{bmatrix}. \tag{B3}$$

APPENDIX C: UNIDIRECTIONAL LAMINATE CASE

For an n-ply unidirectional laminate, the local transfer matrix given by Eq. (A5) can be reduced to

$$B_j=\begin{bmatrix} \cos(k_1h) & 0 & i\sin(k_1h)/Z_1 & 0 \\ 0 & \cos(k_2h) & 0 & i\sin(k_2h)/Z_2 \\ i\sin(k_1h)Z_1 & 0 & \cos(k_1h) & 0 \\ 0 & i\sin(k_2h)Z_2 & 0 & \cos(k_2h) \end{bmatrix}_j. \tag{C1}$$

The global inverse transfer matrix is simply B_j with h_j replaced by the thickness of the sample h, which is equal to nh_j. The transfer functions can then be simplified to

$$F=\begin{bmatrix} \dfrac{2Z_1Z}{2\cos(k_1h)Z_1Z-i\sin(k_1h)(Z^2+Z_1^2)} & 0 \\ 0 & \dfrac{2Z_2Z}{2\cos(k_2h)Z_2Z-i\sin(k_2h)(Z^2+Z_2^2)} \end{bmatrix}. \tag{C2}$$

Transfer functions F_{11} and F_{22} are exactly the same as the classical transmission coefficients for normal-incident longitudinal (or shear) wave propagating through an isotropic layer embedded in an isotropic medium, as given in Ref. 19. This agreement is expected because in this special case the shear waves involved are fast shear waves only in F_{11} and slow shear waves only in F_{22}. In either function, there are no mode conversions between the fast and slow shear waves. The transmission behavior should be a simple resonance as what one would expect for normal incidence longitudinal (or shear) wave propagating through an isotropic layer.

[1] Y. Bar-Cohen and R. L. Crane, ''Acoustic-backscattering imaging of subcritical flaws in composites,'' Mater. Eval. **40**, 970–975 (1982).

[2] *Acousto-ultrasonics: Theory and Application*, edited by J. C. Duke, Jr. (Plenum, New York, 1988).

[3] D. K. Hsu, ''Material properties characterization for composites using ultrasonic methods,'' in *Proceedings of Noise-Con 94*, edited by J. M. Cuschieri, S. A. Glegg, and D. M. Yeager (Noise Control Foundation, New York, 1994), pp. 821–830.

[4] D. Fei and D. K. Hsu, ''Development of motorized azimuthal scanners for ultrasonic NDE of composites,'' in *Review of Progress in Quantitative NDE*, edited by D. O. Thompson and D. E. Chimenti (Kluwer Academic/Plenum, New York, 1999), Vol. 18, pp. 1385–1392.

[5] K. Urabe and S. Yomoda, ''Non-destructive testing method of fiber orientation and fiber content in FRP using microwave,'' in *Progress in Science and Engineering of Composites*, edited by T. Hayashi, K. Kawata, and S. Umekawa (Japan Society for Composite Materials, Tokyo, 1982), pp. 1543–1550.

[6] D. K. Hsu, and F. J. Margetan, ''Examining CFRP laminate layup with contact-mode ultrasonic measurement,'' Adv. Composite Lett. **2**, 51–54 (1993).

[7] I. N. Komsky, I. M. Daniel and Y. C. Yee, ''Ultrasonic determination of layer orientation in ulti-layer multi-directional composite laminates,'' in *Review of Progress in Quantitative NDE*, edited by D. O. Thompson and D. E. Chimenti (Plenum, New York, 1992), Vol. 11, pp. 1615–1622.

[8] I. N. Komsky, K. Zgnoc, and I. M. Daniel, ''Ultrasonic determination of layer orientation in composite laminates using adaptive signal classifiers,'' in *Review of Progress in Quantitative NDE*, edited by D. O. Thompson and D. E. Chimenti (Plenum, New York, 1994), Vol. 13, pp. 787–794.

[9] B. A. Fisher and D. K. Hsu, ''Application of shear waves for composite laminate characterization,'' in *Review of Progress in Quantitative NDE*, edited by D. O. Thompson and D. E. Chimenti (Plenum, New York, 1996), Vol. 15, pp. 1191–1198.

[10] B. A. Fischer, ''Interaction of shear wave polarization and composite laminate layup: Experiment and modeling,'' M. S. thesis, Iowa State University, 1996.

[11] D. K. Hsu, B. A. Fisher, and M. Koskamp, ''Shear wave ultrasonic technique as an NDE tool for composite laminate before and after curing,'' in *Review of Progress in Quantitative NDE*, edited by D. O. Thompson and D. E. Chimenti (Plenum, New York, 1997), Vol. 16, pp. 1975–1982.

[12] D. Fei and D. K. Hsu, ''EMAT-generated shear wave transmission for NDE of composite laminates,'' in *Review of Progress in Quantitative NDE*, edited by D. O. Thompson and D. E. Chimenti (AIP, New York, 2000), Vol. 19, pp. 1159–1166.

[13] D. E. Yuhas, C. L. Vorres, and R. A. Roberts, ''Variations in ultrasonic backscatter attributed to porosity,'' in *Review of Progress in Quantitative NDE*, edited by D. O. Thompson and D. E. Chimenti (Plenum, New York, 1986), Vol. 5, pp. 1275–1284.

[14] R. A. Roberts, ''Porosity characterization in fiber-reinforced composites by use of ultrasonic backscatter,'' in *Review of Progress in Quantitative NDE*, edited by D. O. Thompson and D. E. Chimenti (Plenum, New York, 1987), Vol. 6, pp. 1147–1156.

[15] D. E. Chimenti, ''Guided waves in plates and their use in materials characterization,'' Appl. Mech. Rev. **50**, 247–284 (1997).

[16] A. H. Nayfeh, *Wave Propagation in Layered Anisotropic Media with Applications to Composites* (Elsevier, Amsterdam, 1995).

[17] M. J. S. Lowe, ''Matrix techniques for modeling ultrasonic waves in multilayered media,'' IEEE Trans. Ultrason. Ferroelectr. Freq. Control **UFFC-42**, 525–542 (1995).

[18] R. B. Thompson, ''Physical principles of measurements with EMAT transducers,'' in *Physical Acoustics* (Academic, New York, 1990), Vol. XIX, pp. 157–200.

[19] L. M. Brekhovskikh, *Acoustics of Layered Media I. Plane and Quasi-plane Waves*, 2nd ed. (Springer, Berlin, 1998), Chap. 2.

Research into an integrated intelligent structure—A new actuator combining piezoelectric ceramic and electrorheological fluid

Li Quanlu
College of Physics and Information Technology, Shaanxi Normal University, Xi'an, 710062, People's Republic of China

(Received 28 March 2001; accepted for publication 2 October 2001)

The design, preparation, and application of high-performance piezoelectric ceramics, e.g., FD_3–PZT and FD_4–PZT, then preparation, performance measurement, and applications of composite electrorheological fluids have been studied, respectively. The integrated intelligent structure (i.e., a new actuator) combining the piezoelectric ceramic and the electrorheological fluids, and their applications have been investigated, and emphasis was given to the applications in acoustics and vibration control, etc. as may be noted. © *2002 Acoustical Society of America.*
[DOI: 10.1121/1.1421343]

PACS numbers: 43.38.Ar, 43.38.Fx [SLE]

I. INTRODUCTION

Multifunctional electronic materials and integrated intelligent devices are needed in the development of advanced technologies, especially mechano-electronic integrative units. This work describes the preparation of new piezoelectric ceramic and composite electrorheological fluids and the testing of their properties, respectively. These materials will be of great significance for antiseismic structures, shock absorbers, reducers, dampers, electro-mechanical integrative joiners of high-speed brakes, and recoil-less weapons, and other uses.[1] In a situation where there is no movable power source, an electrorheological fluid may be useful. All applications of the above must use new-type actuators (electromechanical transducing device). However, an integrated intelligent structure (i.e., a new actuator) made of the piezoelectric ceramic and the composite electrorheological fluid is the example chosen for this study. In the new and unique intelligent structure, when piezoelectric ceramic elements are applied to produce a transient time impulsive force, an output high voltage (dc current) is set to the electrorheological fluid for a very short duration, where it is simultaneously changed from liquid phase to solid and may there counteract an impulsive force. Therefore, especially, the integrated intelligent structure (i.e., a new actuator) can be used to resist destructiveness of shock waves, etc. in the vibration control applications, and to protect against the perniciousness of infrasound, acoustic shock waves, explosive waves, etc. in the acoustical applications. In the present work, we have modeled the integrated intelligent structure (a new actuator) with the piezoelectric ceramic (FD_3–PZT or FD_4–PZT) and the composite electrorheological fluid. Our investigations of the electromechanical transducing function of the intelligent structure and phase change of the composite electrorheological fluids have shown good progress and results.

II. EXPERIMENTAL PROCEDURE

A. Preparation of high-performance piezoelectric ceramics

The formula for the high-performance piezoelectric ceramic[1] FD_3–PZT is expressed as

$$x\mathrm{Pb}(\mathrm{Mg}_{1/3}\mathrm{Nb}_{2/3})\mathrm{O}_3 - y\mathrm{PbTiO}_3 - z\mathrm{PbZrO}_3$$

$$(x+y+z=1;\ \ x=0.36-0.38;\ \ y=0.36-0.38), \tag{1}$$

with small amounts of MnO_2, SrO, and K_2O added.

FD_4–PZT is expressed as

$$\mathrm{Pb}_x\mathrm{Sr}_y\mathrm{Ba}_z[(\mathrm{Zn}_{1/3}\mathrm{Nb}_{2/3})_m(\mathrm{Sn}_{1/3}\mathrm{Nb}_{2/3})_n(\mathrm{Zr}_p\mathrm{Ti}_q)]\mathrm{O}_3$$

$$(x+y+z=1;\ \ m+n+p+q=1;\ \ x=0.94-0.96;$$

$$y=0.02-0.03;\ \ m=0.05-0.07;\ \ n=0.05-0.07;$$

$$p=0.43-0.45), \tag{2}$$

with small amounts of MnO_2 and Sb_2O_3 added.

TABLE I. Principal properties of FD_3–PZT and FD_4–PZT. Nomenclature of properties of piezoelectric ceramics: k_p planar electromechanical coupling factor; Q_m mechanical quality factor; $\epsilon_{33}^T/\epsilon_0$ relative dielectric constant; C capacitance; d_{33} piezoelectric strain constant; g_{33} piezoelectric voltage constant; $tg\,\delta$ dielectric loss; ρ density. Properties in the planar mode are measured on disks 20-mm diameter and 1-mm thick.

Materials symbol	k_p	Q_m	$\epsilon_{33}^T/\epsilon_0$	C (pF)	d_{33} ($\mathrm{pC\cdot N^{-1}}$)	g_{33} (10^{-3} $\mathrm{V\cdot m\cdot N^{-1}}$)	$tg\,\delta$ ($\times 10^{-3}$)	ρ (10^3 $\mathrm{kg\cdot m^{-3}}$)
FD_3–PZT	0.68	1100	1600	3850	460	32	3.0	7.7
FD_4–PZT	0.62	1230	2400	4120	670	40	1.5	7.8

Note: The above formula is based on our long-term investigation and study for PZT. Such complicated composition can be obtained by adding foreign matter in the make-up of a formulation to improve the properties of PZT.

1. Flow chart of technological process

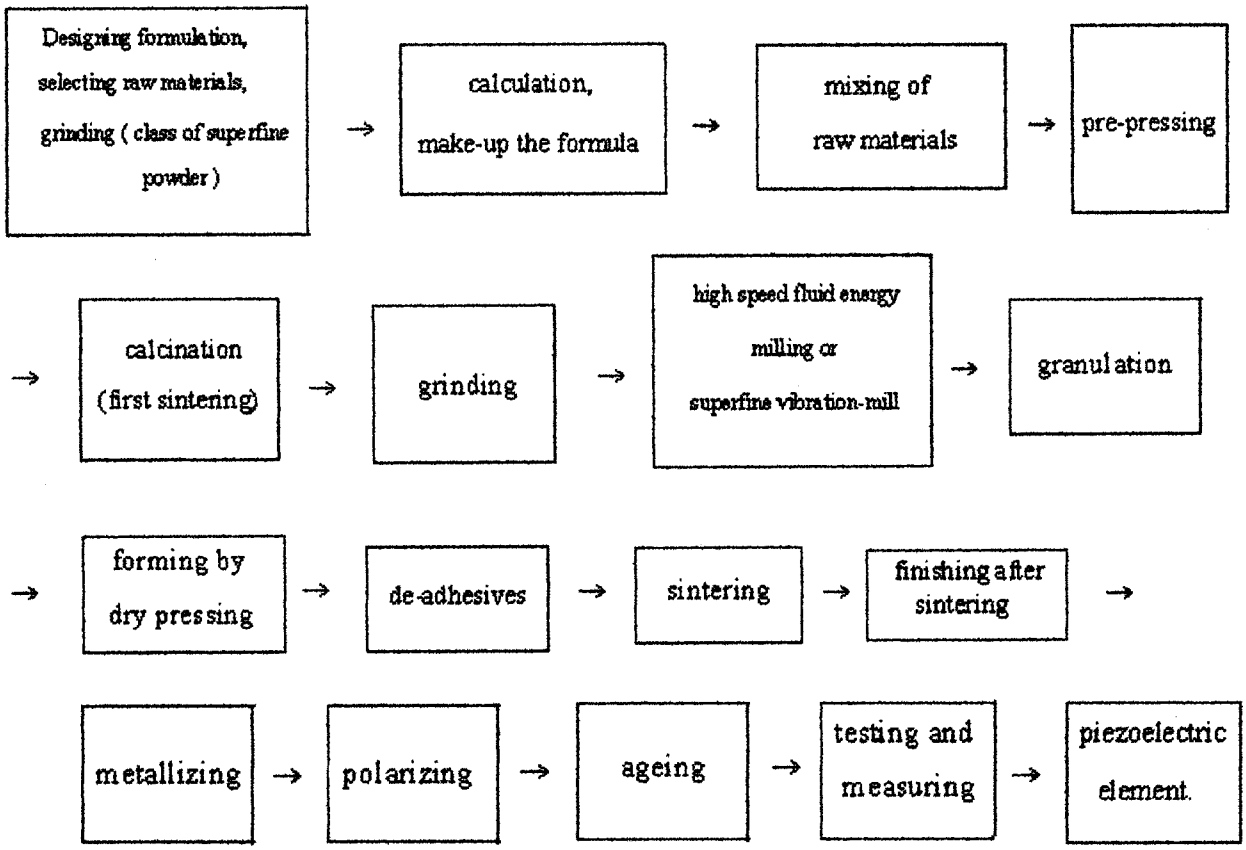

2. Principal properties of FD_3–PZT and FD_4–PZT

After fabrication and metallization, piezoelectric ceramic crystals cannot possess piezoelectricity and become piezoelectric elements when polarized. As these PZT crystalline pellets have all passed aging, their properties must be tested and measured in accordance with the IEEE standard on piezoelectricity. The properties of FD_3–PZT and FD_4–PZT in the present work are shown in Table I.

3. Applications

The two kinds of piezoelectric materials FD_3–PZT and FD_4–PZT, with which we worked, have been used in piezoelectric ceramic gas-sparking plugs, fuses for explosives, the trigger of electronic dry powder fire-extinguishing guns, sonars, buzzers, and high-power ultrasonic generators, such as an ultrasonic cleaning machine and an ultrasonic dispersion machine where they worked well. The same materials were also applied to ultrasonic motors, and to acoustic levitation techniques. The specific feature of the present work is the application of piezoelectric ceramic and electrorheological fluid in an integrated intelligent structure.

B. Preparations and performance measurement of composite electrorheological fluid

A composite electrorheological fluid (abbreviated as ERF) with high multiproperty was prepared in this work. The main specific characteristic of the electrorheological fluid is that which could have occurred during phase change (liquid state $\rightleftarrows$ solid state), under the electric field action. Response time (i.e., the states change time) of the ERF only is of the order of milliseconds, and is a reversible phase change. Because of the characteristics of the ERF and their broad application prospects, researchers are tending to attach more and more importance to the ERF. The present paper mainly used the characteristics of the ERF to make an integrated intelligent structure (a new actuator) with the piezoelectric ceramic for applications in acoustics and vibration control.

1. Preparing methods and technical measures of composite ERF

The experimental procedure of preparation of composite ERF in general is as follows:

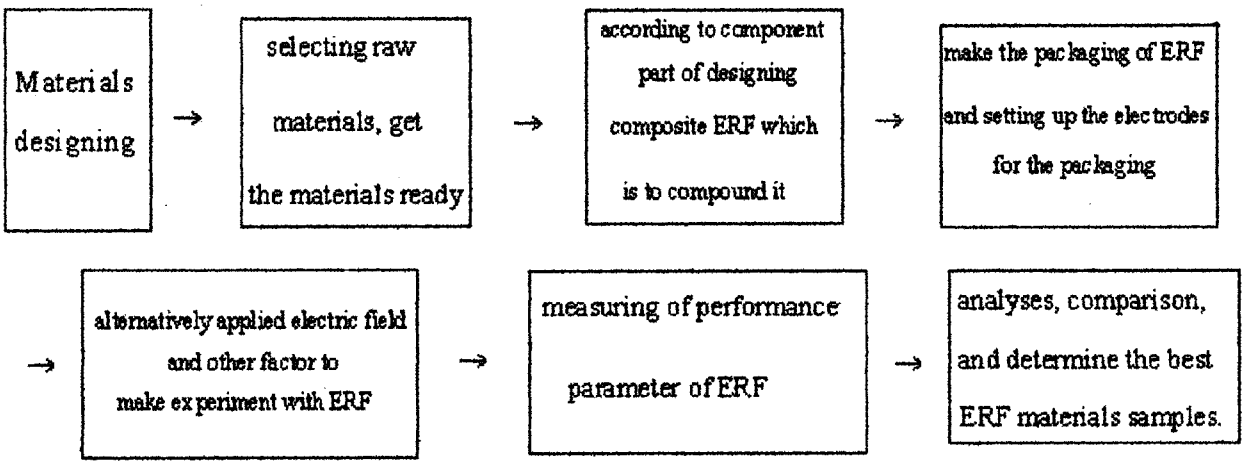

The preparation steps are roughly as follows:

(1) The main dispersing grains in the ERF are processed by using strongly polarized piezoelectric ceramic (such as FD_3–PZT or FD_4–PZT), which is ground to 50 μm or so by machines, and then to less than 10 μm by ultrasonic dispersion.
(2) Strongly polarized piezoelectric liquid crystal materials[2] are selected as an additive for liquid phase of ERF.
(3) The third phase included organic silicone oil and mineral oil, used as a dispersing medium of composite ERF, made up of the single- or muticomponent (series).
(4) To select activator and stabilizer of composite ERF: halogenated hydrocarbon, alcohol, amine, etc. and some surface active agent.
(5) In proportion to the designed part component, whose volume percentage concentration of the disperse phase is at 10%–30%, compound composite ERF is prepared in groups and is then treated with ultrasonic emulsification, which prevents the precipitation of dispersing grains in composite ERF.
(6) To design and process the package of ERF, and to set up the electrodes for them (as is shown in Fig. 1). The composite ERF is grouped to pack in the packaging of ERF.
(7) To test the basic performance parameter of composite ERF.
(8) To perform experiments with electric field (frequency, and other conditions) alternatively on ERF, measuring properties of the composite ERF (at ac is 1–41 kV, dc is 1–30 kV).

2. Principal properties of composite ERF in present work

Principal properties of this composite ERF are as follows:

Viscosity	$\eta_0 < 100$ mP$_a$·s	(at zero electric field),
Yield stress	$\tau_y < 4$ kP$_a$	(at E=3.5 kV·mm^{-1}),
Current density	$J > 100$ mA·cm^{-2}	(at E=3.5 kV·mm^{-1}),
Response time	$t < 1$ ms	

Antiprecipitate, nonpoisonous, and the composite ERF does not contain water.

3. General applications of ERF

Recently, researchers all over the world have thought highly of the ERF, which has broad applied prospects in electrical controlled driver, exciter, brake, clutches, recoilless equipment, and varied shock absorber and damper,[3,4] etc.; they are among the vibration control applications. These applications can be found in the fields of natural defense, electronics, aviation-spaceflight, machinery, traffic, chemical industry, robot and medical equipment. In the present work, the composite ERF is used for the research on and the development of the intelligent structure.

III. RESULTS AND DISCUSSION

The intelligent structure integrated with piezoelectric ceramic and ERF is a novel electro-mechanical integrated device (i.e., a new actuator) and has very important uses. In the present work, we have first developed high-performance piezoelectric ceramic and composite ERF, respectively. Then, we have made further study of the integrated intelligent structure, to suit the needs of the applications in acoustics and vibration control.

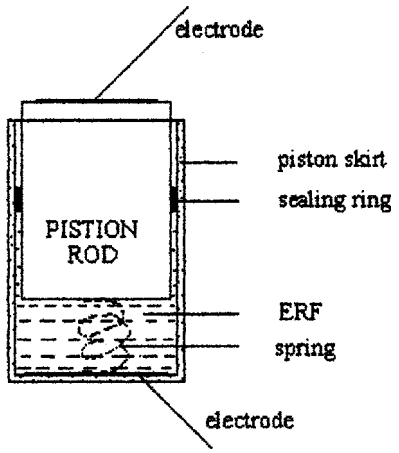

FIG. 1. Schematic diagram of the principle of the packaging of the ERF. Notes: (1) the spring is used to strut the dead weight of the piston rod (at zero electric field); (2) the sealing ring is made of insulating rubber; (3) the piston skirt is made of glass fiber reinforced plastic.

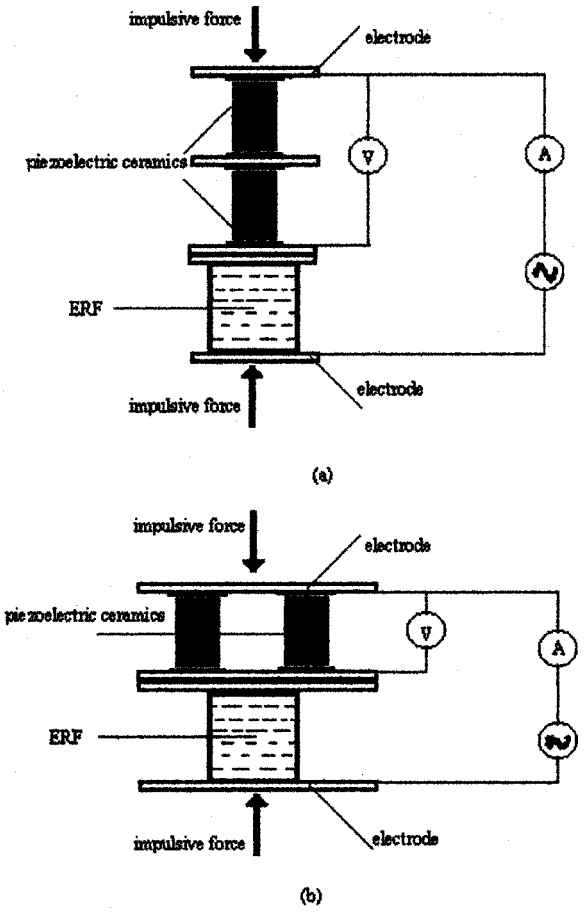

FIG. 2. Schematic diagram of the principle of the model of the integrated intelligent structure: (a) two piezoelectric ceramics in series; (b) two piezoelectric ceramics in parallel.

A. Theoretical design and calculation of integrated intelligent structure of piezoelectric ceramic with composite ERF

On the basis of the linear theory of piezoelectricity (i.e., piezoelectric effect, discovered in 1880 by Jacques and Pierre Curie),[5,6] when piezoelectric ceramic element is subjected to stress the potential difference between its upper and lower electrodes is generated in the anisotropy piezoelectric ceramic element, the voltage of which is equated as[6]

$$V = d_{33} T_3 A/C + \epsilon_{33}^T A/t. \tag{3}$$

where d_{33} stands for the piezoelectric strain constant (i.e., piezoelectric charge constant) of the piezoelectric ceramic element, T_3 for the applied axial stress on a piezoelectric ceramic surface in the 3 direction, A for the area of the piezoelectric ceramic element, C for the capacitance of the piezoelectric ceramic element at low frequency, ϵ_{33}^T for the dielectric constant, and t for the piezoelectric ceramic element thickness.

Considering the case of a cylindrical piezoelectric ceramic element of length which is poled in the axial direction and with electrodes on its ends. If an axial stress T_3 is applied, the voltage V_3 between the electrodes, under open circuit condition, is given by

$$V_3 = -g_{33} l T_3, \tag{4}$$

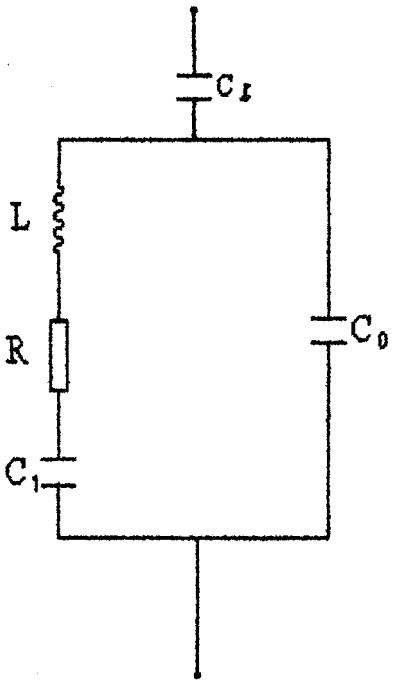

FIG. 3. The electromechanical equivalent electrical circuit of the piezoelectric ceramic in the model of the integrated intelligent structure.

where g_{33} stands for the piezoelectric voltage constant of the piezoelectric ceramic element and l for the length of the cylindrical piezoelectric ceramic element.

When piezoelectric ceramic elements have a transient impulse force applied to them, acoustic shock waves begin to move in from the ends of the piezoelectric ceramic cylinder. Their propagation speed is about 4 $\text{mm}\cdot\mu\text{s}^{-1}$, so that this deformation is complete within a few microseconds (depending on the length of the piezoelectric ceramic cylinder). It will output voltage (corresponding to 15–25 kV) in very short duration to ERF, which will simultaneously (at several tenths of a millisecond) change from liquid phase to solid and therefore counteract the impulsive force, as is shown in Fig. 2. In this case (in series) the time constant of the circuit is given by

$$\tau = RC, \tag{5}$$

where R is the series resistance in the equivalent circuit ($>10^{10}$ Ω), and C is the series capacitance in equivalent circuit (>3000 pF). The equivalent circuit in its simplest form is shown in Fig. 3. Since the four element of this circuit, i.e., resistance R, inductance L, capacitance C (in the so-called dynamic or mechanical branch of the circuit), the capacitance C_0 do not exist as individual elements, their respective values must be determined by indirect measurement. We applied a transmission circuit for determining the series resonance frequency f_s and the series resonance frequency f_{sL} with a load capacitance C_L connected in series with the resonator (Note: for the series resonance frequency f_{sL} of a loaded resonator, as a first approximation, this frequency is equal to corresponding minimum-impedance frequency). Since the value we calculated for the inductance L [as Eq. (6)] as very small (it was approximately 20 mH), the voltage of piezoelectric resonator in the model of the inte-

grated intelligent structure is irrelevant and can be omitted. The value of inductance L is calculated as:

$$L = \frac{1}{4\pi^2 f_s^2 (C + C_c)} \cdot \frac{f_{sL}^2}{f_{sL}^2 - f_s^2}. \tag{6}$$

Under these conditions the time constant is at least several seconds, so that transformation of the composite ERF from liquid state to solid is fully completed.

B. Preliminary experiment of the intelligent structure

In the present work, we have modeled the integrated intelligent structure (a new actuator) with piezoelectric ceramic (FD_3–PZT or FD_4–PZT) and the composite ERF. And, when the structure exerts an impulsive force of 20 kg of the dead weight of the upper punch pin of the oil press on the piezoelectric ceramic element (either two PZT cylinders or one PZT cylinder are 10-mm diameter and 40-mm length), a remarkable phase transition of ERF occurs in the packaging of ERF. The result of preliminary experiment of the integrated intelligent structure to which is applied the impulsive force, basically coincides with the theoretical design. In this model of the integrated intelligent structure, which is made of the piezoelectric ceramic and the composite ERF, the device does respond linearly. The response time of the ERF is the time undergone for the phase change from liquid state to solid (it is less than 1 ms generally). In the process, a transient voltage appears across the ERF and a transient current passes through the ERF. The time for the impulsive force to act on the piezoelectric ceramic is of the order of seconds, the piezoelectric response time is of the order of microseconds, and the response time of the composite ERF is of the order of milliseconds; therefore, time (t_1) for the impulsive force to act on the piezoelectric ceramic is far greater than the sum of the piezoelectric response time (t_2) and the response time of composite ERF (t_3); thus, there is

$$t_1 > t_2 + t_3. \tag{7}$$

IV. CONCLUSION

The research work on the integrated intelligent structure of piezoelectric ceramics and ERF shows that it is feasible in theory, and we have certainly made some progress in the experimental technique. But, there are other technologically difficult problems that require future research work and solutions to, such as the stacking form (it is series, parallel, or series–parallel connection) of piezoelectric ceramic elements, sealing of the piston ring of the packages of ERF, the insulating system of the whole intelligent structure, and the standard measuring of the properties of the ERF, etc. However, important applications of this kind of integrated intelligent structure which will pass through the further improvement of their design and manufacture must be pointed out: (1) The fist applicable aspects of the integrated intelligent structure will be an effective technique in the vibration control aspect, such as antiseismic structure, reducer, damper, and recoil-less weapons (equipment), and varied shock absorber, etc. These applications can be found in the fields of national defense, electronics, aviation-spaceflight, machinery, traffic, chemical industry, robot and medical equipment, nuclear installations, bridge seats, optic engineering, etc.; (2) in the acoustic applications, the integrated intelligent structure will be the potential to resist destructiveness of shock waves, and to protect against the perniciousness of infra sound, acoustic shock waves, explosive waves, etc., and, for a collision avoidance system of a future intelligent automobile, the surface protection of modern aircraft to fly at high speeds,[7] etc.; (3) this integrated intelligent structure (a new actuator) having the other important application is, where no power source (including no moveable high-voltage power source) to use ERF also is available; (4) the present work opens up and suggests further broad applied fields for piezoelectric ceramics and electrorheological fluids, etc.

[1] L. Quanlu, ''Research and their applications of high-performance piezoelectric ceramics,'' Proceedings of the First China International Conference on High-Performance Ceramics, Tsinghua University Press, Beijing, China (1999) **305**.

[2] A. Inoue, S. Maniwa, Y. Ide, and H. Oda, Int. J. Mod. Phys. B **10**, 23–24 (1996).

[3] Y. Akagami, S. Nisimara, Y. Ogasawara, T. Fujita, B. Jeyadevan, K. Nari, and K. Itoh, *Proceedings of the 6th International Conference on Electro-Rheological Fluids*, Magnetic-Rheological Suspensions and Their Applications (World Scientific, Singapore, 1988), p. 803.

[4] K. A. Alsweify, F. A. Kolkailak, and S. H. Farghaly, ''Active and passive damping control of intelligent structure,'' 43rd International SAMPE Symposium and Exhibition, Materials and Process Affordability, USA: Soc. Adv. Matter. & Process Eng., 1998, Vol. 1, p. 413.

[5] J. van Randeraat and R. E. Setterington, *Piezoelecric Ceramics* (Mullard House, London, 1974), p. 23.

[6] IEEE Standard Board, IEEE Standard on Piezoelectricity, IEEE Trans. Ultra. Ferroelectr. and Freq. Control **43**, No. 5, 719–772 (1996) (under revision ANSI/IEEE Std. 176–1987, 1–54).

[7] Adam Bogue, Brian D. Mulcahey, and Ronald L. Spangler, Jr., ''Piezoelectric Applications for Product Vibration Control,'' Sound & Vibration, Noise and Vibration Control, 1998, p. 26.

Noise in miniature microphones[a)]

Stephen C. Thompson,[b)] Janice L. LoPresti, Eugene M. Ring, Henry G. Nepomuceno, John J. Beard, William J. Ballad, and Elmer V. Carlson
Knowles Electronics, LLC, 1151 Maplewood Drive, Itasca, Illinois 60143

(Received 9 July 2001; accepted for publication 28 November 2001)

The internal noise spectrum in miniature electret microphones of the type used in the manufacture of hearing aids is measured. An analogous circuit model of the microphone is empirically fit to the measured data and used to determine the important sources of noise within the microphone. The dominant noise source is found to depend on the frequency. Below 40 Hz and above 9 kHz, the dominant source is electrical noise from the amplifier circuit needed to buffer the electrical signal from the microphone diaphragm. Between approximately 40 Hz and 1 kHz, the dominant source is thermal noise originating in the acoustic flow resistance of the small hole pierced in the diaphragm to equalize barometric pressure. Between approximately 1 kHz and 9 kHz, the noise originates in the acoustic flow resistances of sound entering the microphone and propagating to the diaphragm. To further reduce the microphone internal noise in the audio band requires attacking these sources. A prototype microphone having reduced acoustical noise is measured and discussed. © *2002 Acoustical Society of America.* [DOI: 10.1121/1.1436072]

PACS numbers: 43.38.Bs [SLE]

I. INTRODUCTION

Noise that is present in the electrical outputs of a microphone may originate as an acoustical noise in the environment or as a noise generated within the microphone. This paper deals with the estimation and measurement of the internal noise in miniature microphones. The particular microphones used in this study are a type that is normally used in the manufacture of hearing aids. The internal noise may be generated in the electrical circuits of the microphone, in the mechanical motion of the microphone diaphragm, or in the acoustical propagation paths within the structure of the microphone. This study will measure the total internal noise of the microphone in its normal operating state, and separately measure the microphone noise in a vacuum, where the acoustical noise sources are eliminated. An empirical model of the noise and its separate electrical, mechanical, and acoustical components will be presented. Finally, a modified microphone configuration having lower internal noise will be shown.

The methods of measurement and analysis used in this study have all been previously described and used, although apparently not all for the same microphone. Olsen[1] made a similar study of the noise in a ribbon microphone, including a vacuum measurement that eliminates all sources of acoustical noise leaving only the electrical noise and mechanical noise. Bevan *et al.*[2] describe an analogous circuit noise model for an electret condenser microphone. Gabrielson[3] has presented a comprehensive review of thermal noise sources in acoustic and vibration sensors, and another paper[4] with particular application to micromachined microphones. Zuckerwar and Ngo[5] measured the total internal nose and the purely electrical noise in separate experiments to determine the frequency dependence of the remaining acoustical and mechanical noise.

The present study was undertaken to understand the design features of the microphone that effect its internal noise level with the hope of identifying design changes that would provide a practical microphone with reduced internal noise.

II. THE MICROPHONE

The microphone used in this study is the model EM-3346 microphone from Knowles Electronics, shown in Fig. 1. The EM-3346 is similar to all microphones presently used in the manufacture of modern hearing aids, and is among the lowest in internal noise. Figure 2 is a cross sectional view showing its internal structure. Acoustic pressure from the environment enters the microphone through the sound coupling tube, and then passes through a thin slit in the outer microphone case into a small cavity called the microphone front volume. The use of a sound coupling tube has been desirable for hearing aid microphones because it allows the microphone to be mounted with its smallest area side toward the hearing aid case. In many hearing aid designs, the tube is a convenient feature to attach the microphone to the aid. The data of this study show, however, that this feature contributes to the internal noise of the microphones.

Referring again to Fig. 1, the inner wall of the front volume is a thin polymer diaphragm that is driven into motion by the acoustic pressure in the front volume. Not shown in the figure is a small hole pierced in the diaphragm to equalize the back volume with barometric pressure. Without this equalization, barometric pressure changes would cause very large displacements of the diaphragm that would degrade or damage the microphone.

The diaphragm is metalized on one surface, and this metalization is electrically connected to the metal parts of the case. The diaphragm moves near a metal backplate whose

[a)]Portions of this work were presented in "Internal noise in miniature electret microphones" at the 139th meeting of the Acoustical Society of America, Atlanta, Georgia [J. Acoust. Soc. Am. **107**, 2789(A) (2000)].

[b)]Electronic mail: steve.thompson@knowlesinc.com

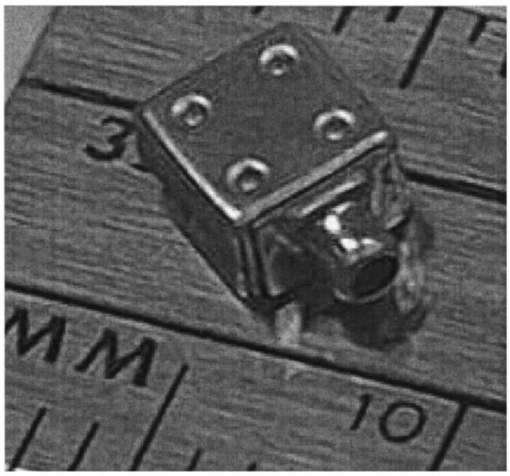

FIG. 1. The Knowles microphone model EM-3346 is an example of the miniature microphone discussed in this paper. This microphone is commonly used as the acoustic sensor in hearing aids.

surface is coated with an electrically charged electret material. The diaphragm and the backplate form a parallel plate capacitor that is charged to a relatively high voltage by the static charge stored in the electret. As the diaphragm moves, a small voltage is induced on the backplate, which is electrically isolated from the case. A wire connects between the backplate and the gate of a FET that buffers the high electrical impedance of the backplate to provide a useful output signal.

A number of features of the microphone will later be seen to be important in understanding the internal noise. First, the acoustic flow path from the external environment to the front volume contains several sections. Sound travels through the coupling tube and enters the front volume through a thin slot in the side of the microphone case. It then spreads across the width of the front volume and along its length. The acoustic flow impedance for this path is partly

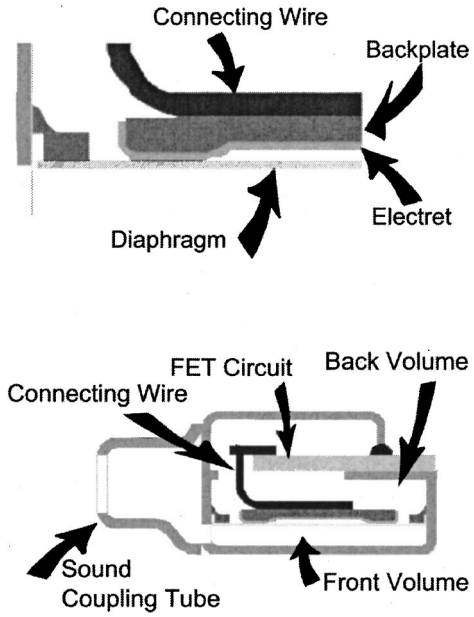

FIG. 2. Cross sectional view if the EM-3346 microphone showing its internal structure.

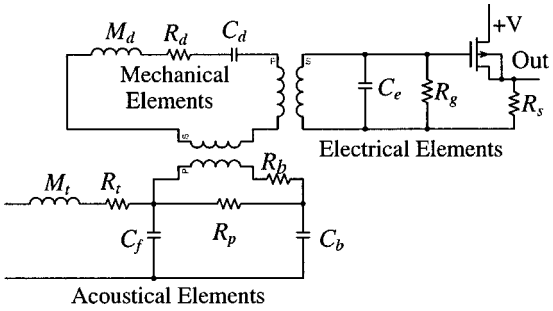

FIG. 3. Equivalent circuit of the electret microphone. The meaning of the circuit components is given in the text.

inertance (masslike impedance) and partly resistance. The motion of the diaphragm causes another acoustic flow of the air between the diaphragm and backplate into the larger part of the back volume. There is a significant acoustical resistance to this flow because of the smallness of the gap between the diaphragm and backplate. Often this resistance is reduced somewhat by ''venting'' the backplate with one or more small holes. There is also a significant acoustical resistance associated with flow through the barometric relief hole in the diaphragm. Altering the size of the hole can change the magnitude of this resistance.

A model of the microphone that includes these features is shown in the analogous circuit of Fig. 3. The components in this circuit are

M_t	inertance of the sound entry port
R_t	resistance of the sound port
R_p	resistance of barometric relief hole pierced in the diaphragm
C_f	compliance of the front volume
C_b	compliance of the back volume
R_b	flow resistance between diaphragm and backplate
M_d	effective mass of the diaphragm
C_d	compliance of the diaphragm including the negative compliance from the attractive force between diaphragm and backplate
R_d	mechanical resistance of the diaphragm
C_e	capacitance of the diaphragm including stray capacitances in the microphone and circuit
R_g	bias resistance at gate of FET
R_s	FET source resistor

The various impedances are of three types: acoustical, mechanical, and electrical. The variables in each domain have different units. The transformers in the equivalent circuit have transformation ratios that include the unit conversion factors. The transformation ratio from acoustical to mechanical variables is simply the effective area S_d of the diaphragm. The transformation ratio from mechanical to electrical variables is q/L where q is the charge stored in the electret and L is the equilibrium separation of the diaphragm and backplate.

III. SOURCES OF NOISE

The three main noise mechanisms in any type of sensing device are *thermal noise*, *shot noise*, and *flicker noise*.[6,7] The

measurements presented later in this paper show that thermal noise is the dominant noise mechanism in the miniature microphones at all frequencies between 20 Hz and at 10 kHz. Thus the investigation of thermal noise sources has been the primary interest in this study. Shot noise is associated with current flow across a potential barrier, and originates solely within the semiconductor device. In a FET device, shot noise is present only in the gate leakage current. This leakage and the associated noise are expected to be quite low in the CMOS FET. Flicker noise is a type of noise found in all active devices as well as some passive devices. It is associated with fluctuations in the resistance of circuit elements, and its value is related to the level of DC current in the element. It is often called $1/f$ noise because its power spectrum varies as $1/f^{\alpha}$ where α is approximately equal to unity. Observed values for α vary between 0.8 and 1.3 for most systems of interest.

Thermal noise in the microphone originates in the random motion of particles in the materials of the device. In the electrical elements. The random motion of electrons in the conductors generates noise. In the mechanical elements, it is the random motion of molecules in the solid lattice of the diaphragm material. In the acoustical elements, it is the random motion of the molecules in the air. In each case, the random flow generates a noise across any resistive element in the analogous circuit. The acoustical and mechanical noises generate motion of the diaphragm that is faithfully converted to electrical signals, just as any other signal is converted in the transducer.

The spectral density of thermal noise voltage is given by[8]

$$N = \sqrt{4kTR},$$

where k is Boltzmann's constant, T is the absolute temperature, and R is the resistance. Thermal noise has a flat spectrum at the location where it is generated. However, each noise source is filtered by all successive analogous circuit elements before it appears at the output of the microphone. Since each noise source is filtered differently, it may be possible to empirically determine the dominant source of the noise in a particular frequency band from the shape of the noise spectrum.

IV. NOISE MEASUREMENT EXPERIMENTS

When measuring the internal noise in a microphone, it is necessary to shield the microphone from all external sources of acoustical signals and noise to a level at least several decibels below that of the internal noise being measured. This must be done without changing the mechanical or acoustical properties of the microphone. In a microphone such as that shown in Fig. 1, it is *not* correct to block the sound entry port. While doing so might eliminate external acoustical noise from the measurement, it would also alter the reactive impedances in the acoustical part of the equivalent circuit. This, in turn, would change the filter function applied to some of the acoustical noise components and thus alter the spectrum of the noise being measured. The noise measurement must be done with the sound port open, while

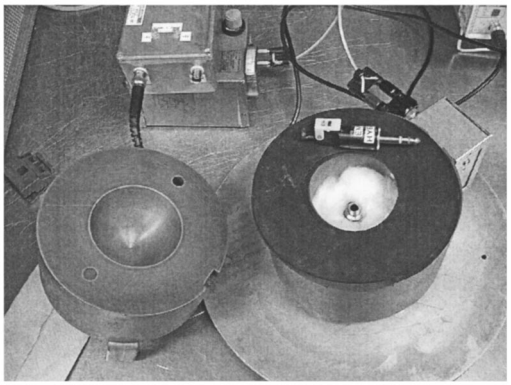

FIG. 4. Acoustical isolation housing for microphone noise measurement is a thick walled steel cylinder mounted on a small rubber bladder to shield from building vibrations as well as acoustical signals.

the unit is shielded from all environmental noise. The chamber used for the noise measurement reported here is shown in Fig. 4. It is composed of two steel cylinders each with a diameter of 6 in. and a length of approximately 3 in. Each cylinder is hollowed at one end to create a cavity with a diamter of 3 in. and a depth of approximately 2 in. The cylinders are placed together with the two cavities forming an internal volume of over 200 ml. This assures that the chamber will not affect the frequency response of the microphone. Visible in the bottom chamber section in Fig. 4 is a small amount of cotton wool that acts as acoustical damping. This eliminates the possibility that resonant modes of the otherwise hard-walled chamber might affect the measurement.

The two halves of the chamber are set together with a thin rubber gasket forming an acoustic seal. This stacked cylinder is set on a plate and a rubber air bladder to isolate the chamber from low frequency vibrations of the building and table. The entire chamber is electrically grounded, and shielded cables are run from the device under test to the measurement equipment to eliminate electromagnetic interference from the measurement. The electrical noise floor of the measurement system was quickly verified to be acceptable by connecting a 1 kΩ resistor across the measurement terminals. The A-weighted electrical noise in this case was well under 1 μV. This is equivalent to an input sound pressure level of approximately 5 dBA for the sensitivity of the microphone that is measured. This is at least 15 dB less than the measured microphone noise level.

The acoustical noise floor of the measurement chamber is not known in detail because it is not possible to fit micro-

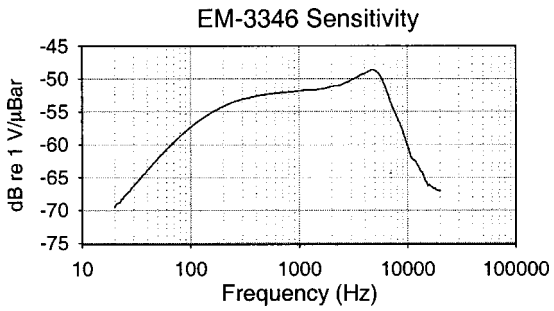

FIG. 5. Frequency response of the microphone sensitivity for the Knowles EM-3346 microphone.

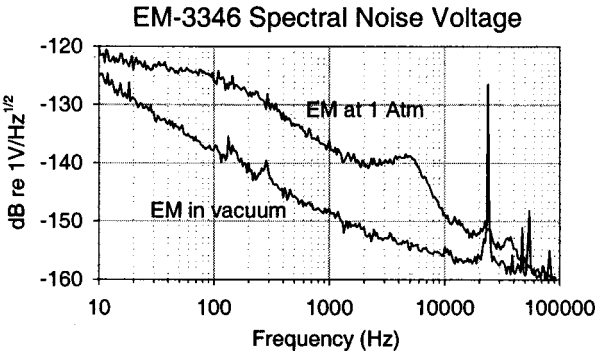

FIG. 6. Measured noise level of the EM-3346 microphone. The darker curve is the noise measured under normal operation at 1 atm. The lighter curve is the noise measured in a vacuum chamber where the acoustical noise sources have been eliminated.

phones with lower internal noise into the chamber. As a qualitative check, it is known that speaking in a loud voice near the chamber with a microphone installed does not produce a detectable voice signal in the microphone output.

The microphones used for this test are Knowles model EM-3346 units, whose typical frequency response is shown in Fig. 5. Figure 6 shows the noise level of the microphone as measured under normal operating conditions in the chamber of Fig. 4. This noise peak at approximately 5 kHz is at the same frequency as the peak in the sensitivity. This is a hint that the noise, at least in this frequency region, is of acoustical origin, since acoustical noise is filtered by the transfer function of the sensitivity. To investigate this hypothesis, we can measure the microphone noise in a vacuum chamber. The vacuum measurement eliminates all acoustical noise sources, so the remaining noise is entirely of electrical and mechanical origin. Figure 7 shows a small vacuum chamber that is used to measure the vacuum noise of the microphone.

Figure 6 shows the noise of the microphone measured in a vacuum in comparison to the noise in normal operation. A number of features can be different from the shape of these curves.

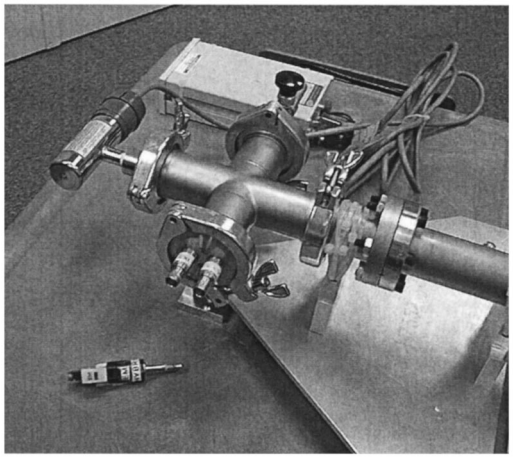

FIG. 7. Small vacuum chamber for the measurement of the electrical noise of the microphone. The microphone holding fixture at the lower left is placed into the chamber, and electrical connections emerge through the BNC connectors.

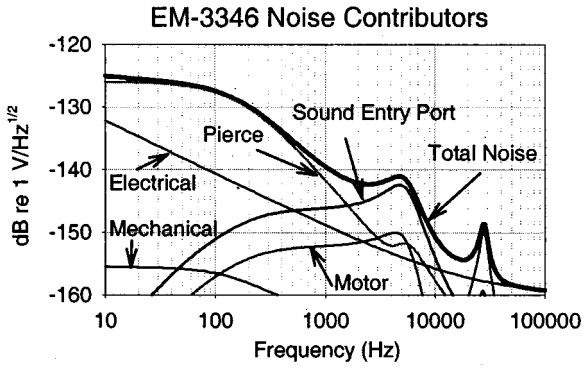

FIG. 8. The total noise at the output of the microphone is made up of several independent sources. Dominant sources are the resistance of the hole pierced in the diaphragm and the resistance of the flow in the sound entry port.

In the frequency range from 20 Hz to 10 kHz, the total microphone noise in normal operation is dominated by acoustical noise. By removing the acoustical noise in the vacuum measurement, the total noise level drops by more than 5 dB.

Electrical noise is not a significant part of the total internal noise except possibly at the extreme low and high frequencies in the figure. The spectrum of the electrical noise varies approximately as $1/f$ in the frequency range below 1 kHz.

The very tall peak in the vacuum noise near 25 kHz is the mechanical resonance of the diaphragm when the acoustical impedance of the air confined in the microphone does not load it.

V. EMPIRICAL MODEL OF THE NOISE

The analogous circuit of Fig. 3 can also be used to model the noise of the microphone. In the work reported here, the PSPICE circuit analysis code was used to model both the sensitivity and the noise of the microphone. Thermal noise is modeled by placing a noise voltage generator with spectral density $\sqrt{4kTR}$ in series with each resistor, whether the resistor is in the electrical, the mechanical or the acoustical sections of the circuit. The semiconductor noise contributions are modeled using the Type 1 FET model of PSPICE[9] using parameter values that have been fit to the characteristics of the custom CMOS FET in the microphone. Figure 8 shows the model results for the total noise of the EM-3346 microphone. Both the shape of this curve and the level of the noise are a good match for the measurement shown in Fig. 6. By independently ''turning on'' the noise of the separate sources, it is possible to calculate the contribution of each source. This process was performed for each of the resistances in the analogous circuit of Fig. 3 to produce the noise contribution curves of Fig. 8. The curves are labeled as listed in Table I.

It is seen in Fig. 8 that two sources of noise dominate within the audio band. At frequencies below 1 kHz, the dominant source is thermal noise from the resistance of the hole pierced in the diaphragm. Between 1 kHz and 10 kHz, the dominant source is the acoustical resistance in the flow through the sound entry tube and port. The electrical noise from the FET and the electrical resistances is an important

TABLE I. Correspondence between labels on curves in Figs. 11 and 12 and the microphone resistance that causes the noise.

Curve label	Circuit resistance	Description
Pierce	R_p	Flow resistance of diaphragm pierce hole
Sound entry port	R_t	Flow resistance through sound entry port and across diaphragm
Motor	R_b	Flow resistance between diaphragm and backplate
Mechanical	R_d	Mechanical resistance to motion of the diaphragm
Electrical	R_s,FET	FET bias and source resistors, semiconductor noise

contributor to the total noise only above 10 kHz, and at *very* low frequencies (below 10 Hz which is not shown in the figure).

VI. INTERNAL NOISE REDUCTION

Because the dominant noise in much of the frequency spectrum is acoustical noise, changes to the acoustical design of the microphone are necessary to further reduce its internal noise. The preceding section shows that the major sources of acoustical resistance in the microphone are as follows:

(1) Flow through the sound inlet tube and then through the small slot in the outside case that allows sound entry from the tube into the front volume.
(2) Flow within the confined space of the front volume.
(3) Flow through the hole pierced in the diaphragm to allow barometric pressure relief.
(4) Flow between the diaphragm and backplate within the back volume of the microphone.

Reductions in any of these flow resistances will affect both the internal noise level and the shape of the microphone sensitivity. As an experiment, the authors attempted to remove as much as possible of the acoustic flow resistance in the microphone without changing the dimensions or design

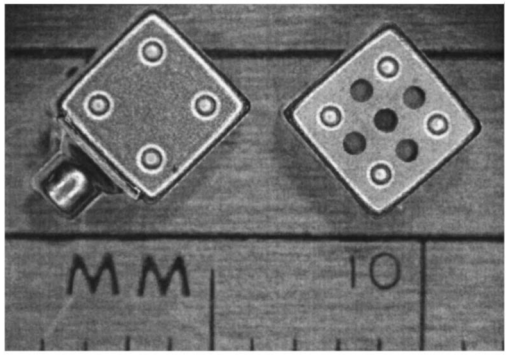

FIG. 9. Left: Standard EM-3346. Right: ''Saltshaker'' configuration that is modified for lower acoustic flow resistances between the far field and the diaphragm.

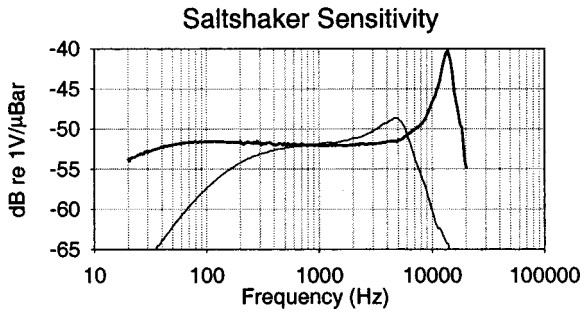

FIG. 10. Frequency response of the sensitivity for the microphone shown on the right-hand side of Fig. 9. The lighter curve is the response of the EM-3346 for comparison.

of the microphone motor. An attempt was made to reduce the first three sources of acoustical noise listed above. This involved removing the sound tube and opening the front volume of the microphone directly to the external acoustic field, and also decreasing the diameter of the barometric relief hole pierced in the diaphragm. With reference to the circuit analog of Fig. 3, the changes attempt to eliminate R_f and M_f, and to increase the value of R_p.

Figure 9 show the comparison of the standard microphone with the microphone as modified to open the front volume directly to the external acoustic field. This is called a ''saltshaker'' configuration because of the appearance of the several small holes in the wall of the front volume. Figure 10 shows the sensitivity of this microphone. Notice that the acoustical resistance plays an important part in determining the frequency response of the system. The design changes removed a significant amount of both flow resistance and inertance (masslike impedance), which causes the primary resonance to increase in frequency and to be significantly less damped. The change in the resistance of the barometric relief hole causes the frequency response to remain flat to a lower frequency. Figure 11 shows the noise spectrum for the saltshaker microphone. The spectral shape has changed along with the changes in the sensitivity, and the spectral level of the noise has decreased by approximately 6–8 dB over much of the audio frequency band. The noise measured in a vacuum is also shown. The vacuum noise is composed of the electrical and mechanical noise components, with no contribution from the acoustical noise. More insights of this kind

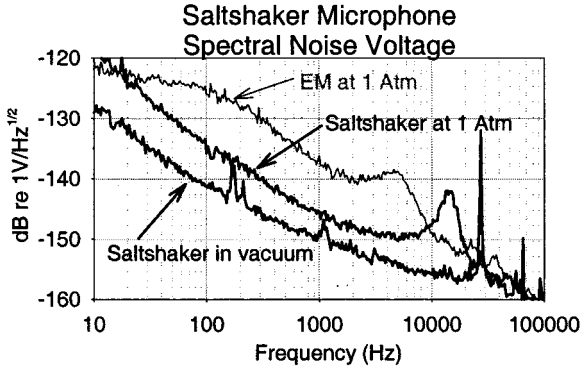

FIG. 11. Spectral nose of the ''Saltshaker'' microphone, compared to the standard EM-3346. Also shown is the vacuum noise of the saltshaker microphone.

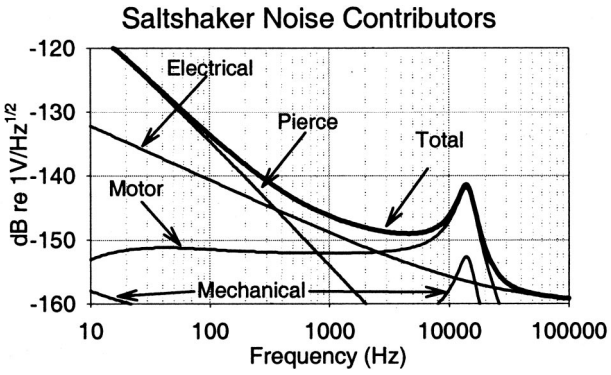

FIG. 12. The saltshaker configuration eliminates noise from the sound entry port and reduces the pierce noise above 50 Hz. The dominant sources are pierce noise below 300 Hz, motor noise from 3 kHz to 25 kHz, and electrical noise at other frequencies.

can come from a model of the noise components.

The noise contribution curves for the saltshaker microphone are shown in Fig. 12. The saltshaker design has eliminated the sound tube and enlarged the sound entry ports to the point that the flow impedance is negligible compared to the remaining flow resistance. Thus the noise contribution from the sound entry port is not present in Fig. 12.

The other modification in the saltshaker microphone from the standard EM-3346 is a reduced size for the barometric relief hole pierced in the diaphragm. This significantly increases the resistance R_p of the hole. It is, perhaps, not intuitively clear that *increasing* a thermal resistance should result in a noise reduction at the microphone output. In fact, at low frequencies, it does not. At frequencies below about 40 Hz, the thermal noise from the larger resistance of the pierce hole causes increased noise at the output. Above 40 Hz, the noise from the pierce resistance is shunted by the acoustical compliance of the back volume, C_b, and is greatly reduced in the output. The total noise of the saltshaker microphone remains below that of the standard microphone from 40 Hz to about 9 kHz, where the diaphragm resonance causes the flow resistance of the motor to dominate.

VII. CONCLUSIONS

The miniature microphones discussed in this paper are a type that is customarily used as a component in hearing aids. The internal noise in these microphones is predominantly the thermal noise associated with acoustic flow resistances in the small passages within the microphone. Testing of the microphone noise in a vacuum, which eliminates the noise sources of acoustical origin, verifies that the purely electrical noise is a small contributor to the total noise at all frequencies in the audible range.

An empirical model using an electrical circuit analog has been used to identify the noise contribution from the various acoustic flow resistances. In the EM-3346 microphone, the resistance associated with flow into the microphone port is the dominant source for audible frequencies above about 1 kHz. Below 1 kHz, the dominant source is the resistance associated with the flow through the hole pierced in the microphone diaphragm to equalize barometric pressure.

An experimental microphone was built and tested that reduced the noise from both of these sources. The sound tube and sound entry port were replaced by several larger holes in the front volume. This essentially eliminates the flow resistance from the sound entry path, and gives the microphone the characteristic appearance that gives it the name ''saltshaker.'' The hole pierced in the diaphragm was also reduced in size to change the frequency response of the noise from that resistance. Together these two changes result in a microphone having lower noise than the standard configuration from approximately 40 Hz to 9 kHz. The dominant sources of noise remaining in the saltshaker microphone are the flow resistance between the diaphragm and backplate at frequencies above 2.5 kHz, noise from the diaphragm pierce resistance for frequencies below 300 Hz, and electrical noise between 300 Hz and 3.5 kHz. Further significant reduction in microphone internal noise must deal with all three of these sources.

The removal of the sound coupling tube to achieve lower internal noise may be a difficult change to accommodate in the manufacture of hearing aids. Current hearing and manufacturing practice is to mount the microphone by its coupling tube with the smallest side of the microphone in contact with the inside of the case. Effective use of the salt shaker microphone would require that the largest side of the microphone be in contact with the case wall. It may be difficult to accommodate this change in hearing aid design. However, it is clear that microphone design changes of the type discussed in this paper are necessary to reduce the dominant sources of internal noise in this type of miniature microphone.

[1] H. F. Olsen, ''Microphone thermal agitation noise,'' J. Acoust. Soc. Am. **51**, 425–432 (1972).
[2] W. R. Bevan, R. B. Schulein, and C. E. Seeler, ''Design of a studio-quality condenser microphone using electret technology,'' J. Audio Eng. Soc. **26**, 947–957 (1978).
[3] T. B. Gabrielson, ''Fundamental noise limits for miniature acoustic and vibration sensors,'' ASME J. Vibr. Acoust. **117**, 405–410 (1995).
[4] T. B. Gabrielson, ''Mechanical-thermal noise in micromachined acoustic and vibration sensors,'' IEEE Trans. Electron Devices **40**, 903–909 (1993).
[5] A. J. Zuckerwar and K. C. Ngo, ''Measured $1/f$ noise in the membrane motion of condenser microphones,'' J. Acoust. Soc. Am. **95**, 1419–1425 (1994).
[6] C. D. Motchenbacher and F. C. Fitchen, *Low Noise Electronic Design* (Wiley, New York, 1973), pp. 9–21.
[7] P. Horowitz and W. Hill, *The Art of Electronics*, 2nd ed. (Cambridge University Press, New York, 1989), p. 432.
[8] Leo L. Beranek, *Acoustical Measurements* (American Institute of Physics, New York, 1993), p. 190.
[9] *PSpice Reference Guide*, 2nd online ed. (a part of the online documentation for the Orcad PSpice Version 9.2 software), Cadence Design Systems, Inc., Palo Alto.

Acoustic radiation impedance of rectangular pistons on prolate spheroids

Jeffrey E. Boisvert and A. L. Van Buren[a)]
Naval Undersea Warfare Center, Newport, Rhode Island 02841-5047

(Received 20 February 2001; accepted for publication 25 September 2001)

The self and mutual radiation impedances for rectangular piston(s) arbitrarily located on a rigid prolate spheroidal baffle are formulated. The pistons are assumed to vibrate with uniform normal velocity and the solution is expressed in terms of a modal series representation in spheroidal eigenfunctions. The prolate spheroidal wave functions are obtained using computer programs that have been recently developed to provide accurate values of the wave functions at high frequencies. Results for the normalized self and mutual radiation resistance and reactance are presented over a wide frequency range for different piston sizes and spheroid shapes. © *2002 Acoustical Society of America.* [DOI: 10.1121/1.1420384]

PACS numbers: 43.38.Hz, 43.20.Rz, 43.30.Jx [SLE]

I. INTRODUCTION

The acoustic radiation impedance of sources on baffles has been considered in the literature for various baffle geometries such as planes, spheres, and cylinders.[1–5] For prolate spheroidal baffles, however, results are limited, most likely due to the difficulties associated with the calculation of the required spheroidal wave functions. Van Buren[6] considered the radiation impedance of caps and rings mounted on a rigid prolate spheroidal baffle for relatively low frequencies. The present work considers the self and mutual radiation impedance of rectangular pistons conformal to a rigid prolate spheroidal baffle and vibrating with uniform normal velocity.

II. MATHEMATICAL FORMULATION

A prolate spheroidal surface is generated by the rotation of an ellipse about its major axis. The prolate spheroidal coordinate system (ξ,η,ϕ) is illustrated in Fig. 1. The relationship to Cartesian coordinates is given by

$$x=\frac{d}{2}[(1-\eta^2)(\xi^2-1)]^{1/2}\cos\phi,$$

$$y=\frac{d}{2}[(1-\eta^2)(\xi^2-1)]^{1/2}\sin\phi, \tag{1}$$

$$z=\frac{d}{2}\eta\xi,$$

where d is the interfocal distance of the generating ellipse, and the ranges of variables are

$$1\leqslant\xi<\infty,\quad -1\leqslant\eta\leqslant 1,\quad 0\leqslant\phi\leqslant 2\pi. \tag{2}$$

The surface of constant ξ is an ellipsoid of revolution about the z axis with a major axis of length ξd and a minor axis of length $(\xi^2-1)^{1/2}d$. Varying the value of the shape parameter ξ produces a wide range of shapes for the prolate spheroid, ranging from a straight line $(\xi=1)$ of length d to a sphere $(\xi\to\infty)$.

Consider a conformal region S_i that is assumed to vibrate with normal velocity v_i on an otherwise rigid prolate spheroidal baffle $(\xi=\xi_0)$, immersed in an unbounded fluid of density ρ and sound speed c, as shown in Fig. 2. Assuming time harmonic $(e^{i\omega t})$ wave fields, the acoustic field exterior to $(\xi=\xi_0)$ is governed by the Helmholtz equation

$$\nabla^2\Psi+k^2\Psi=0, \tag{3}$$

where ∇^2 is the Laplacian in prolate spheroidal coordinates, $k=\omega/c$, ω is the angular frequency, and $\Psi(\xi,\eta,\phi)$ denotes the spatial portion of the acoustic velocity potential. The Helmholtz equation is separable in prolate spheroidal coordinates, and solutions are expressible in eigenfunction expansions of spheroidal wave functions,

$$\Psi_{ml}=R_{ml}^{(4)}(h,\xi)S_{ml}^{(1)}(h,\eta)\begin{Bmatrix}\sin m\phi\\ \cos m\phi\end{Bmatrix}, \tag{4}$$

where

$$R_{ml}^{(4)}(h,\xi)=R_{ml}^{(1)}(h,\xi)-iR_{ml}^{(2)}(h,\xi) \tag{5}$$

denotes the prolate spheroidal radial function of the fourth kind that satisfies the radiation condition for outgoing waves, and $h=kd/2$ is the size parameter. The definitions for the prolate spheroidal radial functions of the first and second kind appearing in Eq. (5) and the prolate spheroidal angle function of the first kind $S_{ml}^{(1)}(h,\eta)$ in Eq. (4) are found in Flammer.[7] Because of the asymmetry of region S_i in Fig. 2, both $\sin m\phi$ and $\cos m\phi$ eigenfunctions are required in the solution, hence,

$$\Psi(\xi,\eta,\phi)=\Psi_1(\xi,\eta,\phi)+\Psi_2(\xi,\eta,\phi), \tag{6}$$

where

$$\Psi_1(\xi,\eta,\phi)=\sum_{m=0}^{\infty}\sum_{l=m}^{\infty}A_{ml}R_{ml}^{(4)}(h,\xi)S_{ml}^{(1)}(h,\eta)\cos m\phi, \tag{7}$$

and

a)Electronic mail: vanburenal@npt.nuwc.navy.mil

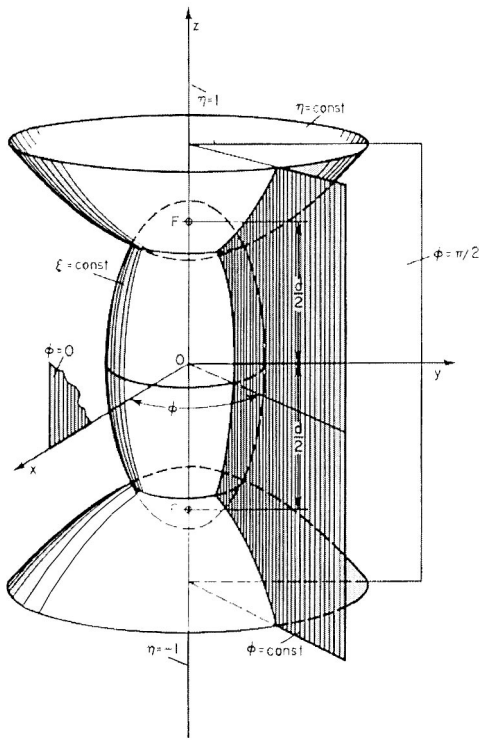

FIG. 1. Prolate spheroidal coordinate system.

$$\Psi_2(\xi,\eta,\phi)=\sum_{m=1}^{\infty}\sum_{l=m}^{\infty} B_{ml}R_{ml}^{(4)}(h,\xi)S_{ml}^{(1)}(h,\eta)\sin m\phi. \tag{8}$$

The boundary condition of continuity of normal particle velocity at the spheroid–fluid interface is given by

$$\frac{1}{\Delta_\xi}\left(\frac{\partial\Psi}{\partial\xi}\right)_{\xi=\xi_0}=\begin{cases} v_i(\eta,\phi) & \text{on } S_i \\ 0 & \text{elsewhere,}\end{cases} \tag{9}$$

where $\Delta_\xi=(d/2)(\xi^2-\eta^2)^{1/2}(\xi^2-1)^{-1/2}$ denotes the scale factor in the ξ direction. Substitution of Eq. (6) into Eq. (9) yields

$$\begin{aligned}(\xi_0^2-\eta^2)^{1/2}&v_i(\eta,\phi)\\ &=\frac{2}{d}(\xi_0^2-1)^{1/2}\sum_{m=0}^{\infty}\sum_{l=m}^{\infty} R_{ml}^{(4)\prime}(h,\xi_0)S_{ml}^{(1)}(h,\eta)\\ &\quad\times[A_{ml}\cos m\phi+B_{ml}\sin m\phi,\end{aligned} \tag{10}$$

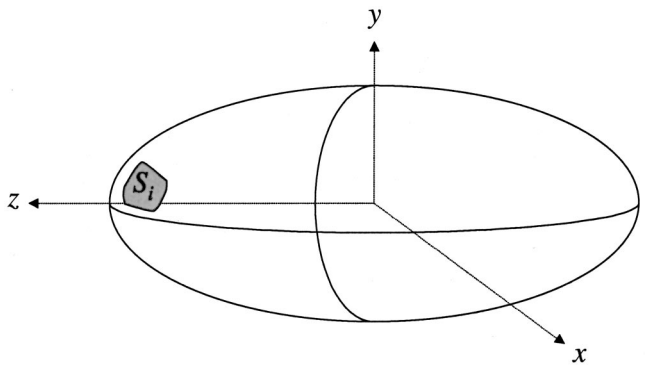

FIG. 2. Conformal region S_i vibrating on a rigid prolate spheroidal baffle.

where the prime on $R_{ml}^{(4)}$ denotes the first derivative with respect to ξ.

The A_{ml} coefficients are obtained by the multiplication of both sides of Eq. (10) by $S_{pq}^{(1)}(h,\eta)\cos p\phi$, and integrating over ϕ from 0 to 2π and over η from -1 to $+1$, yielding

$$A_{ml}=\frac{\int\int_{S_i} v_i(\eta,\phi)(\xi_0^2-\eta^2)^{1/2}S_{ml}^{(1)}(h,\eta)\cos m\phi\, d\eta\, d\phi}{\frac{2}{d}(\xi_0^2-1)^{1/2}\frac{2\pi}{\epsilon_m}R_{ml}^{(4)\prime}(h,\xi_0)N_{ml}}, \tag{11}$$

where

$$N_{ml}=\int_{-1}^{+1}[(S_{ml}^{(1)}(h,\eta)]^2 d\eta \tag{12}$$

defines the normalization of the prolate spheroidal angle wave functions, and $\epsilon_m=1$ when $m=0$, and $\epsilon_m=2$ when $m\neq 0$ (Neumann's number). In a similar manner, the B_{ml} coefficients are given by

$$B_{ml}=\frac{\int\int_{S_i} v_i(\eta,\phi)(\xi_0^2-\eta^2)^{1/2}S_{ml}^{(1)}(h,\eta)\sin m\phi\, d\eta\, d\phi}{(2/d)(\xi_0^2-1)^{1/2}\pi R_{ml}^{(4)\prime}(h,\xi_0)N_{ml}}. \tag{13}$$

Since the acoustic pressure is related to the velocity potential by

$$p_i(\xi,\eta,\phi)=-\rho\frac{\partial\Psi}{\partial t}=-i\omega\rho\Psi(\xi,\eta,\phi), \tag{14}$$

the solution for the acoustic pressure may be written in compact form as

$$\begin{aligned}p_i(\xi,\eta,\phi)=&\frac{-ih}{2\pi}\frac{\rho c}{(\xi_0^2-1)^{1/2}}\\ &\times\sum_{m=0}^{\infty}\sum_{l=m}^{\infty}\epsilon_m\frac{R_{ml}^{(4)}(h,\xi)S_{ml}^{(1)}(h,\eta)}{R_{ml}^{(4)\prime}(h,\xi_0)N_{ml}}\\ &\times[I_{ml}^{is}\cos m\phi+I_{ml}^{ic}\sin m\phi],\end{aligned} \tag{15}$$

where

$$\begin{aligned}I_{ml}^{is}=&\int\int_{S_i} v_i(\eta,\phi)(\xi_0^2-\eta^2)^{1/2}S_{ml}^{(1)}(h,\eta)\\ &\times\cos m\phi\, d\eta\, d\phi,\\ I_{ml}^{ic}=&\int\int_{S_i} v_i(\eta,\phi)(\xi_0^2-\eta^2)^{1/2}S_{ml}^{(1)}(h,\eta)\\ &\times\sin m\phi\, d\eta\, d\phi.\end{aligned} \tag{16}$$

Equations (15) and (16) thus represent the general form of the acoustic pressure for a source of arbitrary shape and location vibrating on a rigid prolate spheroidal baffle.

A piston is defined by the special case where the source on the baffle vibrates with uniform normal velocity, $v_i(\eta,\phi)=V_i$. Thus for a piston, Eq. (15) is expressible as

$$p_i(\xi,\eta,\phi)=\frac{-ih}{2\pi}\frac{\rho c V_i}{(\xi_0^2-1)^{1/2}}\times\sum_{m=0}^{\infty}\sum_{l=m}^{\infty}\epsilon_m\frac{R_{ml}^{(4)}(h,\xi)S_{ml}^{(1)}(h,\eta)}{R_{ml}^{(4)'}(h,\xi_0)N_{ml}}\times[\tilde{I}_{ml}^{is}\cos m\phi+\tilde{I}_{ml}^{ic}\sin m\phi], \tag{17}$$

where

$$\tilde{I}_{ml}^{is}=\int\int_{S_i}(\xi_0^2-\eta^2)^{1/2}S_{ml}^{(1)}(h,\eta)\cos m\phi\, d\eta\, d\phi,$$
$$\tilde{I}_{ml}^{ic}=\int\int_{S_i}(\xi_0^2-\eta^2)^{1/2}S_{ml}^{(1)}(h,\eta)\sin m\phi\, d\eta\, d\phi. \tag{18}$$

It is noted that the integrals residing in Eq. (18) define the size, shape, and location of the piston on the spheroidal baffle.

Consider a second region S_j (distinct from S_i) located on the surface of the spheroid. The acoustic force F_{ij} acting on region S_j due to the pressure originating from region S_i is given by

$$F_{ij}=\int_{S_j}p_i(\xi,\eta,\phi)|_{\xi=\xi_0}dS, \tag{19}$$

where the area element on the spheroidal surface is defined by

$$dS=(d/2)^2(\xi_0^2-\eta^2)^{1/2}(\xi_0^2-1)^{1/2}d\eta\, d\phi. \tag{20}$$

The acoustic mutual radiation impedance is defined by

$$Z_{ij}=F_{ij}/V_i, \tag{21}$$

and this quantity represents the acoustic impedance (force per unit normal velocity) acting on region S_j due to the motion of region S_i. The self-radiation impedance Z_{ii} is defined by the condition when S_i and S_j are the same region, and represents the acoustic radiation force per unit normal velocity acting on region S_i due to its own motion.

The normalized acoustic mutual radiation impedance z_{ij} is defined by

$$z_{ij}=\frac{Z_{ij}}{\rho c A_j}=\frac{1}{\rho c A_j V_i}\int_{S_j}p_i(\xi,\eta,\phi)|_{\xi=\xi_0}dS, \tag{22}$$

where A_j is the area given by the integration of Eq. (20) over region S_j, i.e.,

$$A_j=\int\int_{S_j}(d/2)^2(\xi_0^2-\eta^2)^{1/2}(\xi_0^2-1)^{1/2}d\eta\, d\phi. \tag{23}$$

The substitution of Eq. (17) into Eq. (22) yields

$$z_{ij}=\frac{-ih}{2\pi A_j}\left(\frac{d}{2}\right)^2\sum_{m=0}^{\infty}\sum_{l=m}^{\infty}\epsilon_m\frac{R_{ml}^{(4)}(h,\xi_0)}{R_{ml}^{(4)'}(h,\xi_0)N_{ml}}\times[\tilde{I}_{ml}^{is}\tilde{I}_{ml}^{js}+\tilde{I}_{ml}^{ic}\tilde{I}_{ml}^{jc}], \tag{24}$$

where the $\tilde{I}_{ml}^{js}$ and $\tilde{I}_{ml}^{jc}$ integrals are given by Eq. (18) with i replaced by j. The impedance is dependent upon the size, shape, and location of each of the two pistons. It depends implicitly on their separation through the products of the integrals $\tilde{I}_{ml}^{is}\tilde{I}_{ml}^{js}$ and $\tilde{I}_{ml}^{ic}\tilde{I}_{ml}^{jc}$ appearing in Eq. (24). The normalized acoustic self-radiation impedance is directly obtained from Eq. (24) with the substitution $j=i$.

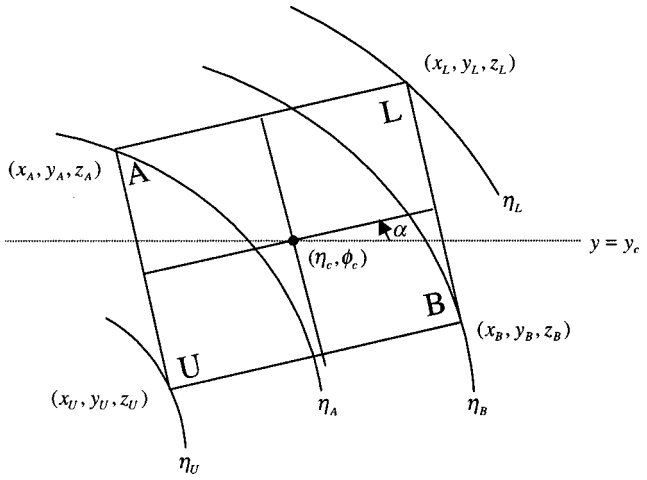

FIG. 3. Rectangular piston corner points on the surface of the spheroid with $\eta_U>\eta_A>\eta_B>\eta_L$.

III. RECTANGULAR PISTONS

Of special interest in this paper is the case where the pistons are quasirectangular in shape, conformal to the surface of the spheroid, and relatively small compared to the spheroid. It is noted that the use of constant values of η and ϕ to define the piston sides would result in pistons that become progressively more wedge-shaped as they approach the tip of the spheroid. Hence, the methodology adopted here to define the conformal piston is to first specify the center-point location (η_c,ϕ_c), width W, height H, and orientation angle α, of a *planar* rectangular piston, tangent to the surface of the spheroid at the point $(\eta_c,\phi_c,\xi=\xi_0)$. The conformal piston is then defined by the projection of this rectangular piston onto the spheroidal surface $\xi=\xi_0$. Using the methods of analytic geometry (see the Appendix), the projection in the $-\hat{\xi}$ direction of the (planar) piston onto the surface of the spheroid provides the (conformal) piston corner coordinates and the lines (curves) corresponding to the perimeter of the piston, as shown in Fig. 3. Here at each corner, the x,y,z value along with the corresponding value of η is designated, where $\eta_U>\eta_A>\eta_B>\eta_L$. Now the integral over ϕ in Eq. (18) is performed with limits that are functions of η as follows:

$$\tilde{I}_{ml}^{is}=\int_{\eta_{iL}}^{\eta_{iU}}\int_{\phi_L(\eta)}^{\phi_U(\eta)}(\xi_0^2-\eta^2)^{1/2}S_{ml}^{(1)}(h,\eta)\cos m\phi\, d\phi\, d\eta$$
$$=\int_{\eta_{iL}}^{\eta_{iU}}(\xi_0^2-\eta^2)^{1/2}S_{ml}^{(1)}(h,\eta)\phi^s(\eta)d\eta, \tag{25}$$

where

$$\phi^s(\eta)=\begin{cases}\frac{1}{m}[\sin m\phi_U(\eta)-\sin m\phi_L(\eta)], & m\neq 0\\ \phi_U(\eta)-\phi_L(\eta), & m=0.\end{cases} \tag{26}$$

Similarly,

$$\tilde{I}^{ic}_{ml} = \int_{\eta_{iL}}^{\eta_{iU}} \int_{\phi_L(\eta)}^{\phi_U(\eta)} (\xi_0^2 - \eta^2)^{1/2} S^{(1)}_{ml}(h,\eta) \sin m\phi \, d\phi \, d\eta$$

$$= \int_{\eta_{iL}}^{\eta_{iU}} (\xi_0^2 - \eta^2)^{1/2} S^{(1)}_{ml}(h,\eta) \phi^c(\eta) d\eta, \tag{27}$$

where

$$\phi^c(\eta) = \begin{cases} \dfrac{1}{m}[\cos m\phi_U(\eta) - \cos m\phi_L(\eta)], & m \neq 0 \\ 0, & m = 0. \end{cases} \tag{28}$$

Thus the double integral in Eq. (18) has been reduced to a single integral over η, and the task remains to determine the functions $\phi^s(\eta)$ and $\phi^c(\eta)$ that appear in Eqs. (25) and (27).

From Fig. 3 it is seen that the integration over η may conveniently be divided into three regions, thus Eq. (25) may be written as

$$\tilde{I}^{is}_{ml} = \int_{\eta_L}^{\eta_B} (\xi_0^2 - \eta^2)^{1/2} S^{(1)}_{ml}(h,\eta) \phi^s(\eta) d\eta$$

$$+ \int_{\eta_B}^{\eta_A} (\xi_0^2 - \eta^2)^{1/2} S^{(1)}_{ml}(h,\eta) \phi^s(\eta) d\eta$$

$$+ \int_{\eta_A}^{\eta_U} (\xi_0^2 - \eta^2)^{1/2} S^{(1)}_{ml}(h,\eta) \phi^s(\eta) d\eta, \tag{29}$$

and Eq. (27) can be written in a similar form. For the first integral in Eq. (29), the function $\phi_U(\eta)$ or $\phi_L(\eta)$ over the region $\eta_L \leqslant \eta \leqslant \eta_B$ is determined from the intersection of curve *BL* with the η=const curve. For curve *BL* let

$$t = \frac{x - x_L}{x_B - x_L} = \frac{y - y_L}{y_B - y_L} = \frac{z - z_L}{z_B - z_L}, \tag{30}$$

then

$$x = x_L + t(x_B - x_L), \quad y = y_L + t(y_B - y_L),$$
$$z = z_L + t(z_B - z_L). \tag{31}$$

The curve η=const is a hyperboloid of two sheets given by

$$\frac{x^2}{(d/2)^2(1-\eta^2)} + \frac{y^2}{(d/2)^2(1-\eta^2)} - \frac{z^2}{(d/2)^2\eta^2} = -1. \tag{32}$$

The substitution of Eq. (31) into Eq. (32) yields a quadratic equation in t as follows:

$$t = \frac{-b \pm \sqrt{b^2 - 4ac}}{2a}, \tag{33}$$

where

$$a = \eta^2[(x_B - x_L)^2 + (y_B - y_L)^2 + (z_B - z_L)^2]$$
$$- (z_B - z_L)^2,$$
$$b = \eta^2[2x_L(x_B - x_L) + 2y_L(y_B - y_L) + 2z_L(z_B - z_L)]$$
$$- 2z_L(z_B - z_L), \tag{34}$$
$$c = \eta^2[x_L^2 + y_L^2 + z_L^2 + (d/2)^2] - z_L^2 - (d/2)^2\eta^4.$$

Of the two roots of Eq. (33), the root satisfying the condition $0 \leqslant t \leqslant 1$ is selected. The x, y, z coordinates (dependent on η) are obtained from Eq. (31), and the function $\phi_{BL}(\eta)$ is given by

$$\phi_{BL}(\eta) = \tan^{-1}(y/x). \tag{35}$$

A similar procedure is followed to yield the $\phi_{AL}(\eta)$ intersection of curve *AL* with the η=const curve. Now referring to Eq. (26), the η-dependent functions are given by

$$\phi_U(\eta) = \max[\phi_{BL}(\eta), \phi_{AL}(\eta)], \quad \eta_L \leqslant \eta \leqslant \eta_B,$$
$$\phi_L(\eta) = \min[\phi_{BL}(\eta), \phi_{AL}(\eta)], \quad \eta_L \leqslant \eta \leqslant \eta_B. \tag{36}$$

The procedure is repeated for the remaining integrals in Eq. (29), and also for Eq. (27) upon its division into three integrals. Finally it is noted that the (conformal) piston area [Eq. (23)] is also evaluated in the same manner as described previously.

IV. NUMERICAL COMPUTATION

The calculation of the (normalized) self and mutual radiation impedance for rectangular pistons by the use of Eq. (24) requires values of the prolate spheroidal wave functions $R^{(4)}_{ml}$, $R^{(4)'}_{ml}$, and $S^{(1)}_{ml}$. Although computer programs developed at the Naval Research Laboratory provide accurate values for these functions,[8–10] the parameter ranges of these algorithms are limited to relatively low orders of m and l and small to moderate acoustic sizes. Since one of the objectives of the present effort is to provide results at high frequencies (large acoustic size), a parallel effort to develop algorithms to calculate spheroidal wave functions over a wider range of parameters than previously available has been undertaken, with the results of that study to be reported in the future.[11] The newly developed algorithms were employed in the present study.

The $\tilde{I}_{ml}$ integrals were evaluated numerically (Gauss quadrature) using the following procedure. Each individual integral [see Eq. (29) for example] can be expressed in the following generic form:

$$\tilde{I}_{ml} = \int_{\eta_{\rm lo}}^{\eta_{\rm up}} \chi(\eta) S^{(1)}_{ml}(h,\eta) d\eta, \tag{37}$$

where $\chi(\eta)$ includes the functions $\phi_U(\eta)$ and $\phi_L(\eta)$, as discussed in Sec. III, and where $\eta_{\rm up}$ and $\eta_{\rm lo}$ denote the upper and lower limits of the region under consideration. Upon defining the weight factors w_i and the abscissas u_i for an n-point Gauss quadrature, Eq. (37) is written as

$$\tilde{I}_{ml} \cong \left[\frac{\eta_{\rm up} - \eta_{\rm lo}}{2}\right] \sum_{i=1}^{n} w_i \chi(\eta_i) S^{(1)}_{ml}(h,\eta_i), \tag{38}$$

where

$$\eta_i = \frac{\eta_{\rm up} + \eta_{\rm lo}}{2} + u_i \left[\frac{\eta_{\rm up} - \eta_{\rm lo}}{2}\right] \quad -1 \leqslant u_i \leqslant 1. \tag{39}$$

Similarly, the partial area of the piston [Eq. (23)] is determined as follows:

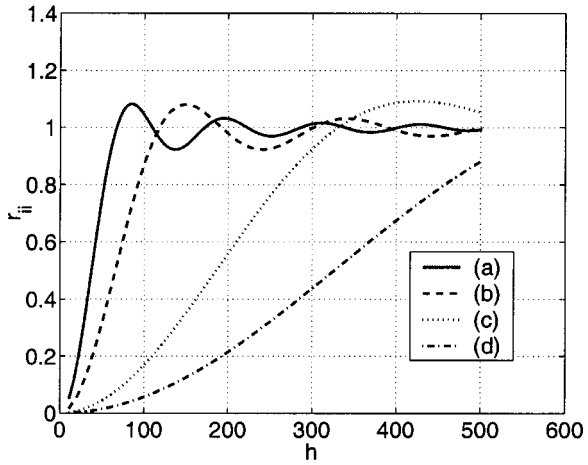

FIG. 4. Normalized self-radiation resistance vs h of square pistons on prolate spheroid ends for (a) spheroid shape parameter $\xi_0=1.72$, piston size parameter $W/[(\xi_0^2-1)^{1/2}d]=0.0191$, (b) spheroid shape parameter $\xi_0=1.35$, piston size parameter $W/[(\xi_0^2-1)^{1/2}d]=0.0168$, (c) spheroid shape parameter $\xi_0=1.72$, piston size parameter $W/[(\xi_0^2-1)^{1/2}d]=0.0038$, and (d) spheroid shape parameter $\xi_0=1.35$, piston size parameter $W/[(\xi_0^2-1)^{1/2}d]=0.0034$.

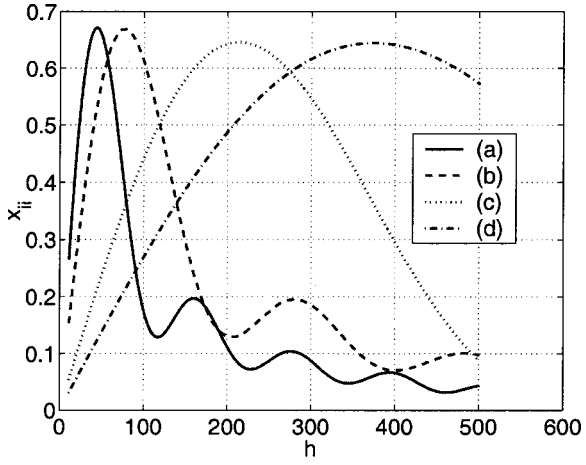

FIG. 5. Normalized self-radiation reactance vs h of square pistons on prolate spheroid ends for (a) spheroid shape parameter $\xi_0=1.72$, piston size parameter $W/[(\xi_0^2-1)^{1/2}d]=0.0191$, (b) spheroid shape parameter $\xi_0=1.35$, piston size parameter $W/[(\xi_0^2-1)^{1/2}d]=0.0168$, (c) spheroid shape parameter $\xi_0=1.72$, piston size parameter $W/[(\xi_0^2-1)^{1/2}d]=0.0038$, and (d) spheroid shape parameter $\xi_0=1.35$, piston size parameter $W/[(\xi_0^2-1)^{1/2}d]=0.0034$.

$$A\cong\frac{d^2}{4}(\xi_0^2-1)^{1/2}\left[\frac{\eta_{\rm up}-\eta_{\rm lo}}{2}\right]\sum_{i=1}^{n} w_i(\xi_0^2-\eta_i^2)^{1/2}\times[\phi_{\rm up}(\eta_i)-\phi_{\rm lo}(\eta_i)], \tag{40}$$

where the total area is given by the sum of the contributions from each region (three regions), as discussed in Sec. III.

The angle function normalization factor N_{ml} defined in Eq. (12) can be obtained without the need for numerical integration by employing the normalization scheme of Meixner and Schäfke,[12] where the prolate angle functions have the same normalization as the associated Legendre functions. The relationship is given by

$$N_{ml}=\int_{-1}^{1}[S_{ml}^{(1)}(h,\eta)]^2 d\eta=\int_{-1}^{1}[P_l^m(\eta)]^2 d\eta=\frac{2(l+m)!}{(2l+1)(l-m)!}. \tag{41}$$

The number of l and m values required for convergence of the sums appearing in Eq. (24) increases with the acoustic size of the spheroid. They also depend upon the shape parameter of the spheroid and the size of the piston relative to the spheroid. In general, for a fixed spheroid size, smaller pistons require higher values for both m and l. The numerical algorithms used in the current study remained stable and computationally efficient over a wide frequency range up to $h=500$, orders up to $m=250$ and degrees up to $l=2000$, for various combinations of piston sizes and spheroidal baffle shapes.

V. RESULTS AND DISCUSSION

The above-mentioned equations have been used to find the normalized self and mutual radiation resistance and reactance of square pistons as a function of the size parameter h for various sized pistons and spheroidal baffles. Figures 4 and 5 give examples for the normalized self-radiation resistance r_{ii} [real part of Eq. (24) evaluated with $j=i$] and reactance x_{ii} [imaginary part of Eq. (24) evaluated with $j=i$] of a square piston located at the tip $(\eta_c=1,\phi_c=0)$ of the spheroid with $\alpha=0$. Results are given for two different spheroidal shapes: $\xi_0=1.35$ and $\xi_0=1.72$, corresponding to a ratio of major axis to minor axis of 1.48 and 1.23, respectively. Two piston sizes (defined by the ratio of piston width/spheroid minor axis) are considered for each spheroidal shape. For the $\xi_0=1.35$ spheroid, the width of the pistons are 0.34% and 1.68%, respectively, of the spheroid minor axis, i.e., $W/[(\xi_0^2-1)^{1/2}d]=0.0034$ and 0.0168. For the $\xi_0=1.72$ spheroid, the corresponding widths are 0.38% and 1.91%, respectively, i.e., $W/[(\xi_0^2-1)^{1/2}d]=0.0038$ and 0.0191. For the relatively small pistons considered in the current study, it was determined that an eight-point Gauss quadrature provided sufficient accuracy for all numerical integrations conducted.

It is seen that the resistance is small for low values of h and rises (at a different rate for each case) as h increases. The rate of increase of the resistance versus h in each case is a function of the acoustic size of the piston relative to the spheroidal surface $\xi=\xi_0$, and is ordered by the numerical value of $W/[(\xi_0^2-1)^{1/2}d]$. The reactance, while larger than the resistance for small values of h, rises to a peak value somewhat smaller than unity then decreases as h increases. In all cases, when the piston becomes acoustically large, the radiation resistance tends to unity, and the radiation reactance tends to zero, a result consistent with the radiation impedance of pistons on the other baffle geometries (planar, spherical, cylindrical, etc.).

Figure 6 illustrates results for the normalized mutual radiation impedance $z_{ij}=r_{ij}+ix_{ij}$ for a pair of adjoining square pistons located at the end of the spheroid, as a function of h with $\alpha=0$. The first piston is located at the tip $(\eta_c=1,\phi_c=0)$ of the spheroid, and the second piston adjoins the first along one of its sides. For this case, the spheroid is defined by $\xi_0=1.72$, and the piston size is defined by $W/[(\xi_0^2-1)^{1/2}d]=0.0191$. It is seen that substantial interac-

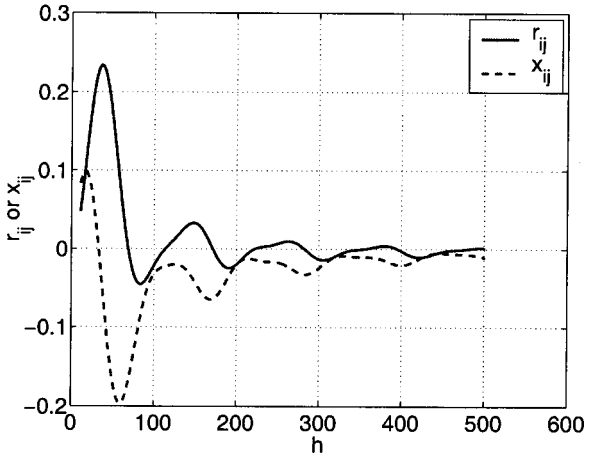

FIG. 6. Normalized mutual radiation impedance vs h for two adjoining square pistons on spheroid end for spheroid shape parameter $\xi_0=1.72$, and piston size parameter $W/[(\xi_0^2-1)^{1/2}d]=0.0191$.

tion occurs in the region below $h\approx 100$, and above that, the interaction decreases appreciably and approaches zero. Hence, although the pistons are adjoining, when the frequency is high enough, the fields are spatially localized. Thus, essentially no acoustic coupling occurs, the pistons ''see'' only their self-radiation impedance.

Results for the normalized mutual radiation resistance and reactance for square pistons as a function of separation angle ϕ at three locations on the spheroid are shown in Figs. 7 and 8, respectively. These results are for a spheroid defined by $\xi_0=1.35$ and piston size $W/[(\xi_0^2-1)^{1/2}d]=0.0168$, at $h=60$ with $\alpha=0$. In all cases, the center point of the first piston is held at $(\eta_c=\text{const},\phi_c=0)$, and the second piston initially adjoins the first piston, then traverses the $(\eta=\text{const})$ curve in the direction of increasing ϕ forming a circular path. The abscissa denotes the absolute separation $\Delta\phi$ in degrees between the piston center points. The results at $\eta=0.8$ illustrate the behavior near the tip of the spheroid, while those at $\eta=0.1$ apply to the region near the equator. It is seen that the interaction decreases more rapidly for the case nearest the

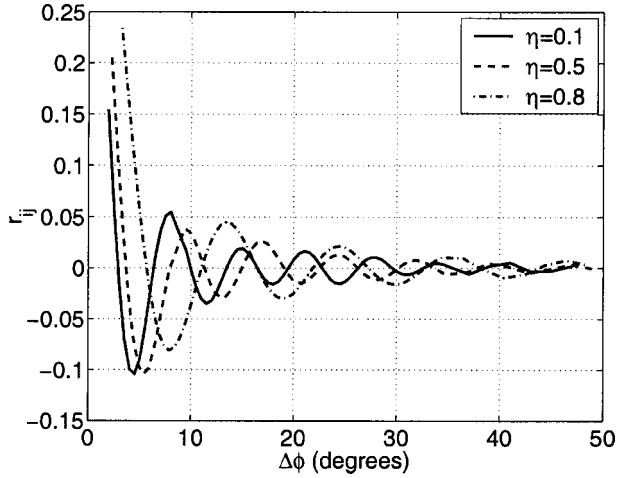

FIG. 7. Normalized mutual radiation resistance at $h=60$ for square pistons with size parameter $W/[(\xi_0^2-1)^{1/2}d]=0.0168$, on a spheroid with shape parameter $\xi_0=1.35$, as a function of separation angle $\Delta\phi$, for (a) $\eta=0.1$, (b) $\eta=0.5$, and (c) $\eta=0.8$.

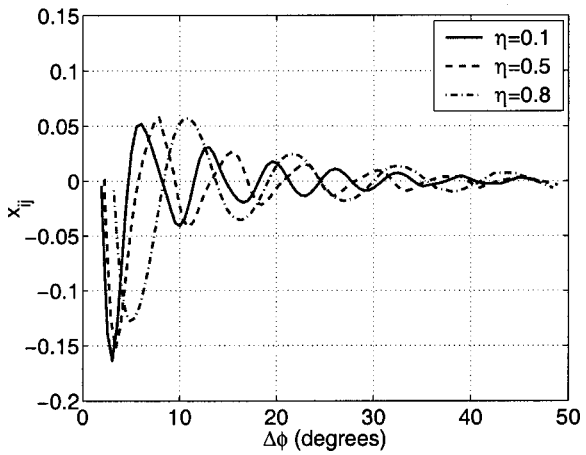

FIG. 8. Normalized mutual radiation reactance at $h=60$ for square pistons with size parameter $W/[(\xi_0^2-1)^{1/2}d]=0.0168$, on a spheroid with shape parameter $\xi_0=1.35$, as a function of separation angle $\Delta\phi$, for (a) $\eta=0.1$, (b) $\eta=0.5$, and (c) $\eta=0.8$.

equator. This occurs because near the equator, a given separation angle corresponds to a greater separation *distance* between pistons than that near the tip of the spheroid.

For the same spheroid and piston geometry, Fig. 9 gives normalized radiation impedance results for the case where the separation distance between pistons is measured along the η coordinate, at $\phi=0$. Here, the center point of the first piston is fixed at the tip of the spheroid $(\eta_c=1,\phi_c=0)$, and the second piston traverses the $(\phi=0)$ curve in the direction of decreasing η along the spheroid. Note the abscissa plots the quantity $(1-\eta)$, where $\eta=1$ at the tip and $\eta=0$ at the equator of the spheroid. In contrast to the results in Figs. 7 and 8 (where the separation distance is measured in the ϕ direction), the results in Fig. 9 (separation distance measured in the η direction) show a more rapid decrease in the interaction as one moves away from the tip toward the equator.

VI. SUMMARY

Expressions for the self and mutual radiation impedance for piston sources vibrating on a rigid prolate spheroidal baffle have been developed. The special case of rectangular

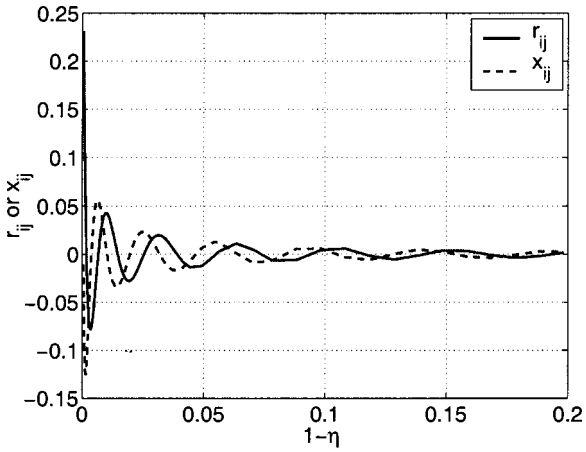

FIG. 9. Normalized mutual radiation impedance at $h=60$ for square pistons with size parameter $W/[(\xi_0^2-1)^{1/2}d]=0.0168$, on a spheroid with shape parameter $\xi_0=1.35$, as a function of separation distance $1-\eta$ for $\phi=0$.

pistons was derived and is given by Eq. (24). Sample results have been presented that illustrate the behavior of the radiation impedance for different pistons and spheroids over a wide frequency range. In addition, results were presented that show the variation of the mutual impedance between two pistons as a function of their separation distance. It is noted that the radiation impedance for pistons of other shapes on prolate spheroids is readily obtainable using the equations derived in this paper.

ACKNOWLEDGMENTS

This work was supported by the Office of Naval Research Code 321 and the Naval Undersea Warfare Center ILIR Program.

APPENDIX: GEOMETRICAL DESCRIPTION OF A RECTANGULAR PISTON CONFORMAL TO A PROLATE SPHEROIDAL BAFFLE

Consider a planar rectangular piston of width W and height H whose center point (x_c, y_c, z_c) is tangent to the surface of the spheroid at the point $(x_c, y_c, z_c, \xi = \xi_0)$, as illustrated in Fig. 10. The angle α denotes the orientation of the piston relative to its intersection with the $y = y_c$ plane. The equation of the plane containing the piston is given by

$$A(x - x_c) + B(y - y_c) + C(z - z_c) = 0, \tag{A1}$$

where A, B, and C are the direction cosines of the normal to the spheroid $\xi = \xi_0$ at the point (x_c, y_c, z_c). This normal $\hat{e}_n$ can be obtained from the cross product of the covariant vectors $\hat{e}_\eta$ and $\hat{e}_\phi$ as follows:

$$\hat{e}_n = \hat{e}_\phi \times \hat{e}_\eta, \tag{A2}$$

where

$$\begin{aligned} \hat{e}_\eta &= \frac{\partial x}{\partial \eta}\hat{e}_x + \frac{\partial y}{\partial \eta}\hat{e}_y + \frac{\partial z}{\partial \eta}\hat{e}_z, \\ \hat{e}_\phi &= \frac{\partial x}{\partial \phi}\hat{e}_x + \frac{\partial y}{\partial \phi}\hat{e}_y + \frac{\partial z}{\partial \phi}\hat{e}_z. \end{aligned} \tag{A3}$$

The substitution of Eq. (1) into Eq. (A3) followed by the evaluation of Eq. (A2) yields

$$\begin{aligned} \hat{e}_n = \frac{d^2}{4}[&\xi(1-\eta^2)^{1/2}(\xi^2-1)^{1/2}\cos\phi\ \hat{e}_x \\ &+ \xi(1-\eta^2)^{1/2}(\xi^2-1)^{1/2}\sin\phi\ \hat{e}_y + \eta(\xi^2-1)\ \hat{e}_z]. \end{aligned} \tag{A4}$$

The unit normal vector is defined by

$$\hat{u} = \frac{\hat{e}_n}{|\hat{e}_n|} = A\hat{e}_x + B\hat{e}_y + C\hat{e}_z, \tag{A5}$$

where the direction cosines are given by

$$\begin{aligned} A &= \xi(1-\eta^2)^{1/2}(\xi^2-\eta^2)^{-1/2}\cos\phi, \\ B &= \xi(1-\eta^2)^{1/2}(\xi^2-\eta^2)^{-1/2}\sin\phi, \\ C &= \eta(\xi^2-1)^{1/2}(\xi^2-\eta^2)^{-1/2}. \end{aligned} \tag{A6}$$

Now the equation of the line of intersection of the plane $y = y_c$ with the piston is given by

$$\frac{x - x_c}{C} = \frac{z - z_c}{-A}. \tag{A7}$$

Rotating this line an angle α about the normal $\hat{e}_n$ produces the piston midline ab expressed by

$$\frac{x - x_c}{A''} = \frac{y - y_c}{B''} = \frac{z - z_c}{C''}, \tag{A8}$$

where the direction cosines are given by

$$\begin{aligned} A'' &= \frac{1}{\sqrt{A^2 + C^2}}[-AB\sin\alpha + C\cos\alpha], \\ B'' &= \sqrt{A^2 + C^2}\ \sin\alpha, \\ C'' &= \frac{1}{\sqrt{A^2 + C^2}}[-BC\sin\alpha - A\cos\alpha]. \end{aligned} \tag{A9}$$

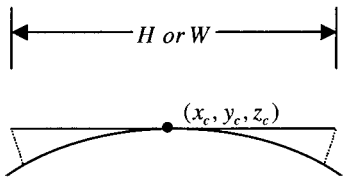

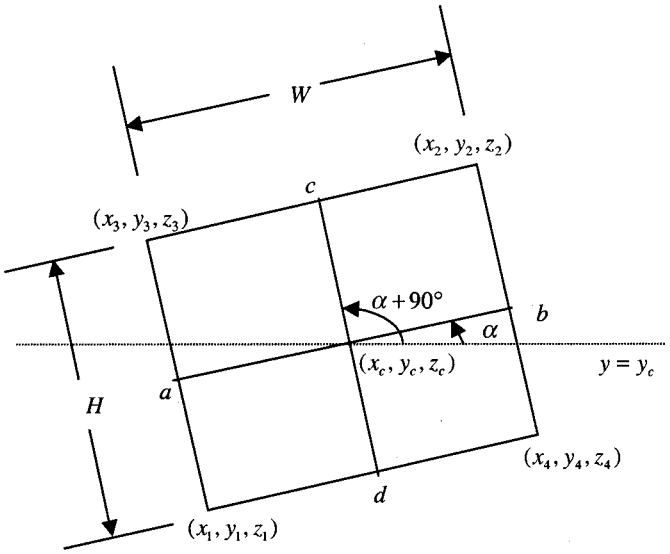

FIG. 10. Normal projection of the perimeter of a planar rectangular piston of width W and height H with its center point tangent to the spheroid at (x_c, y_c, z_c).

Letting $\alpha \rightarrow \alpha + 90°$ and following a similar procedure for the midline *cd* yields the direction cosines

$$A''' = \frac{1}{\sqrt{A^2 + C^2}}[-AB\cos\alpha - C\sin\alpha],$$
$$B''' = \sqrt{A^2 + C^2}\cos\alpha, \tag{A10}$$
$$C''' = \frac{1}{\sqrt{A^2 + C^2}}[-BC\cos\alpha + A\sin\alpha].$$

Now having obtained the direction cosines for the two midlines, the corner points *on the surface* of the spheroid corresponding to the normal projection of the perimeter of the planar piston of width W and height H [tangent to the spheroid at the point (x_c, y_c, z_c)] are given by

$$x_1 = x_c - (W/2)A'' - (H/2)A''',$$
$$y_1 = y_c - (W/2)B'' - (H/2)B''', \tag{A11}$$
$$z_1 = z_c - (W/2)C'' - (H/2)C''',$$

for corner 1,

$$x_2 = x_c + (W/2)A'' + (H/2)A''',$$
$$y_2 = y_c + (W/2)B'' + (H/2)B''', \tag{A12}$$
$$z_2 = z_c + (W/2)C'' + (H/2)C''',$$

for corner 2,

$$x_3 = x_c - (W/2)A'' + (H/2)A''',$$
$$y_3 = y_c - (W/2)B'' + (H/2)B''', \tag{A13}$$
$$z_3 = z_c - (W/2)C'' + (H/2)C''',$$

for corner 3, and

$$x_4 = x_c + (W/2)A'' - (H/2)A''',$$
$$y_4 = y_c + (W/2)B'' - (H/2)B''', \tag{A14}$$
$$z_4 = z_c + (W/2)C'' - (H/2)C''',$$

for corner 4. Finally, at each corner the value of η is given by

$$\eta_i = \frac{\sqrt{x_i^2 + y_i^2 + (z_i + d/2)^2} - \sqrt{x_i^2 + y_i^2 + (z_i - d/2)^2}}{d}, \tag{A15}$$

where $i = 1-4$.

[1] D. H. Robey, "On the radiation impedance of an array of finite cylinders," J. Acoust. Soc. Am. **27**, 706–710 (1955).
[2] C. H. Sherman, "Mutual radiation impedance of sources on a sphere," J. Acoust. Soc. Am. **31**, 947–952 (1959).
[3] R. L. Pritchard, "Mutual acoustic impedance between radiators in an infinite rigid plane," J. Acoust. Soc. Am. **32**, 730–737 (1960).
[4] J. E. Greenspon and C. H. Sherman, "Mutual-radiation impedance and near field pressure for pistons on a cylinder," J. Acoust. Soc. Am. **36**, 149–153 (1964).
[5] E. M. Arase, "Mutual radiation impedance of square and rectangular pistons in an infinite baffle," J. Acoust. Soc. Am. **36**, 1521–1525 (1964).
[6] A. L. Van Buren, "Acoustic radiation impedance of caps and rings on prolate spheroids," J. Acoust. Soc. Am. **50**, 1343–1356 (1971).
[7] C. Flammer, *Spheroidal Wave Functions* (Stanford University Press, Stanford, CA, 1957).
[8] B. J. King, R. V. Baier, and S. Hanish, "A Fortran computer program for calculating the prolate spheroidal radial functions of the first and second kind and their first derivatives," Naval Res. Lab. Report No. 7012, 1970.
[9] B. J. King and A. L Van Buren, "A Fortran computer program for calculating the prolate and oblate angle functions of the first kind and their first and second derivatives," Naval Res. Lab. Report No. 7161, 1970.
[10] B J. Patz and A. L. Van Buren, "A Fortran computer program for calculating the prolate spheroidal angular functions of the first kind," Naval Res. Lab. Memo. Report No. 4414 (1981).
[11] A. L. Van Buren and J. E. Boisvert, "Accurate calculation of prolate spheroidal radial functions of the first kind and their first derivatives," Quarterly Appl. Math (to be published).
[12] J. Meixner and F. W. Schäfke, *Mathieusche Funckionen und Sphäroidfunckionen* (Springer, Berlin, 1954).

Acoustic streaming induced by ultrasonic flexural vibrations and associated enhancement of convective heat transfer

Byoung-Gook Loh
Precision Engineering Center, North Carolina State University, Raleigh, North Carolina 27695-7910

Sinjae Hyun
Mechanical and Aerospace Engineering Department, North Carolina State University, Raleigh, North Carolina 27695-7910

Paul I. Ro
Precision Engineering Center, North Carolina State University, Raleigh, North Carolina 27695-7910

Clement Kleinstreuer
Mechanical and Aerospace Engineering Department, North Carolina State University, Raleigh, North Carolina 27695-7910

(Received 29 January 2001; accepted for publication 31 October 2001)

Acoustic streaming induced by ultrasonic flexural vibrations and the associated convection enhancement are investigated. Acoustic streaming pattern, streaming velocity, and associated heat transfer characteristics are experimentally observed. Moreover, analytical analysis based on Nyborg's formulation is performed along with computational fluid dynamics (CFD) simulation using a numerical solver CFX 4.3. Two distinctive acoustic streaming patterns in half-wavelength of the flexural vibrations are observed, which agree well with the theory. However, acoustic streaming velocities obtained from CFD simulation, based on the incompressible flow assumption, exceed the theoretically estimated velocity by a factor ranging from 10 to 100, depending upon the location along the beam. Both CFD simulation and analytical analysis reveal that the acoustic streaming velocity is proportional to the square of the vibration amplitude and the wavelength of the vibrating beam that decreases with the excitation frequency. It is observed that the streaming velocity decreases with the excitation frequency. Also, with an open-ended channel, a substantial increase in streaming velocity is observed from CFD simulations. Using acoustic streaming, a temperature drop of 40 °C with a vibration amplitude of 25 μm at 28.4 kHz is experimentally achieved. [DOI: 10.1121/1.1433811]

PACS numbers: 43.40.At [PJR]

I. INTRODUCTION

Acoustic streaming is a steady circular airflow occurring in a high-intensity sound field. Two factors have been known to induce acoustic streaming: spatial attenuation of a wave in a free space and the friction between a medium and a vibrating object (cf. Lee and Wang, 1990). When sound waves propagate, they are attenuated by absorption and scattered. This attenuation is, in general, insignificant in a short distance of propagation. However, the propagation of a high-intensity sound wave results in the attenuation of pressure significant enough to create steady bulk airflow. This type of streaming is usually associated with a medium of high viscosity. The other type of acoustic streaming is attributed to the friction between a vibrating medium in contact with a solid wall (cf. Ingard and Labate, 1950; Nyborg, 1958). As long as there is an oscillating tangential relative velocity, it is not important whether the source of a relative motion arises from either acoustic oscillations in the fluid or vibrations of the solid. Both cases lead to frictional dissipation within Stokes boundary layer. Unlike acoustic streaming resulting from spatial attenuation, this streaming has two components: inner and outer streaming. The inner streaming is created within the boundary layer due to the friction between the medium and the wall. Then, the inner streaming, in turn, induces relatively large-scale steady streaming outside the boundary layer. This process can be compared to the generation of electromagnetic field by a surface current on a conductor (cf. Lee and Wang, 1990). It is reported that the acoustic streaming is especially effective in promoting certain kinds of rate process occurring on the solid and fluid interface including convective heat transfer, electrical effects, changes in biological cells, and removal of loosely adhering surface layers (cf. Nyborg, 1958).

Faraday (1831) found that currents of air rise at displacement anti-nodes on plates and descend at the nodes. Rayleigh (1945) performed the first theoretical analysis of the acoustic streaming phenomenon. Further developments of the theory were made by Schlichting (1955), Nyborg (1958), and Lighthill (1978), where emphasis was placed on the fundamental role of dissipation of the acoustic energy in the evolution of the gradients in the momentum flux. In the study of Jackson and Nyborg (1960), acoustic streaming induced by sonic longitudinal vibration is investigated. Acoustic streaming induced by ultrasonic flexural traveling waves is studied for a micropump application and negligible heat transfer capability of acoustic streaming is reported (cf. Nguyen and White, 1999). Fand and Kave (1960) and Gould

(1966) studied heat transfer across a solid–liquid interface in the presence of sonically induced acoustic streaming and found that the effect of acoustic streaming was to cause the convective heat transfer rate from the heated cylinder to increase by a factor of 3. Gopinath and Mills (1993, 1994) investigated convective heat transfer due to acoustic streaming across the ends of a Kundt tube. Selected references give an overview of the works done for investigating the heat transfer characteristics of acoustic streaming (cf. Uhlenwinkel *et al.*, 1994; Vainshtein *et al.*, 1995; Chen *et al.*, 1998).

Most previous studies concentrated on acoustic streaming induced by sonic longitudinal vibration in an enclosed space such as a Kundt tube. Not much research on acoustic streaming induced in an open space by ultrasonic flexural vibration has been carried out. Ultrasonic excitation significantly increases acoustic streaming velocity. As a result, corresponding convective heat transfer rate can grow to the extent equal to that of conventional fan-based cooling. In addition, ultrasonic excitation permits silent operation. Employing flexural vibrations as a source of acoustic streaming allows for a slim profile and low power operation because flexural impedance of an elastic beam is generally far smaller than longitudinal impedance. To take full advantage of this promising technology, it is imperative to understand the nature of formation of acoustic streaming, its transient characteristics, streaming velocity, and associated enhancement of convective heat transfer.

Therefore, the objective of this article is to investigate the momentum and heat transfer due to the acoustic streaming induced by ultrasonic flexural vibrations in an open environment. A primary focus is placed on experimental observations of the phenomenon, simulations employing computational fluid dynamics software (CFX4), comparison with the existing analytical solution by Nyborg (1958), and cooling property.

II. EXPERIMENTAL OBSERVATIONS

A. Experimental apparatus

The experimental setup shown in Fig. 1 consists of a beam and modules that contain a piezoelectric actuator and a horn. The beam and horn are made of 6061-T6 aluminum due to its excellent acoustical characteristics. The piezoelectric actuator is a bolted Langevin type transducer (BLT) designed to resonate at 28 kHz (Sashida, 1993). The conical horn is used to increase the amplitude of vibration provided by the actuator. A conical geometry was chosen because it not only gives a desired amplification ratio but also can be easily machined. A mounting flange was included in the design of the horn and is located at the nodal lines where the velocity of vibration of the horn goes to zero. This allowed the mounting of the horn and BLT assembly onto a supporting base plate that was in turn bolted to the surface of an air-driven vibration absorption table. The small end of the horn was threaded to connect the beam with the horn using a machine screw. The dimension of the beam is determined such that one of the natural frequencies of the beam is located in the vicinity of the resonant frequency of the actuator,

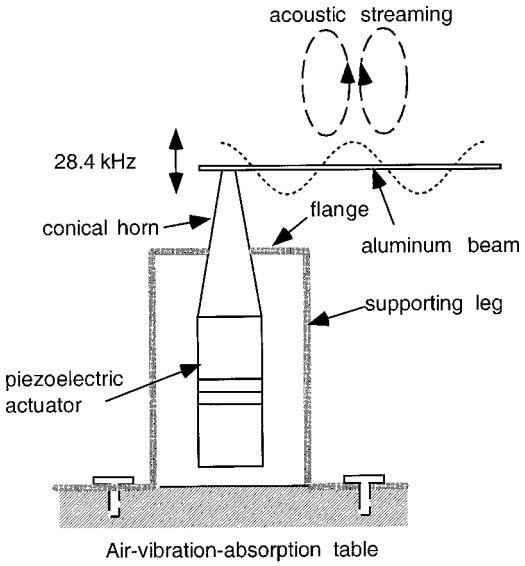

FIG. 1. Experimental setup.

thereby maximizing the displacement of the beam for a given power supply. The determined dimension is 10 mm wide, 1 mm thick, and 128 mm long. Frequency spectrum analysis of the system reveals that at an excitation frequency of 28.4 kHz, maximum vibration amplitude of the beam is achieved.

B. Acoustic streaming near the vibrating beam

To visualize acoustic streaming near the beam, the beam is excited at 28.4 kHz with the vibration amplitude of 10 μm. Acetone is sprayed onto the vibrating beam. When acetone comes in contact with the beam, it becomes small droplets and follows the airflow pattern near the beam until it completely evaporates. A fiber optic lamp locally illuminates the region near the vibrating beam. Light is reflected from only acetone droplets and the beam, making ambient air appear black. The whole process is videotaped using a camcorder. Figure 2 shows a snap shot of the process. Unique features of acoustic streaming are observed. First, air rises above the antinodes and descends toward the nodes. Since vibration amplitude is not uniform along the length of the beam, the maximum distance to which acetone droplets rise above the antinodes are not uniform either. Second, there exist two

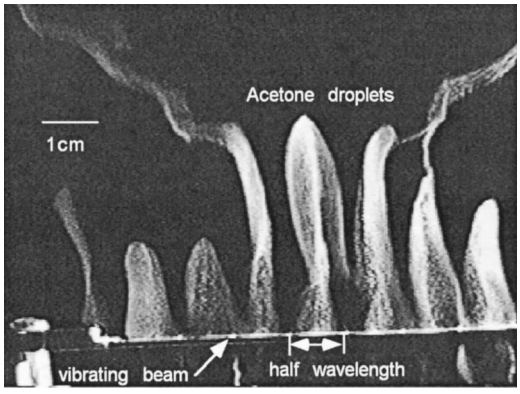

FIG. 2. Acoustic streaming over a ultrasonically vibrating beam.

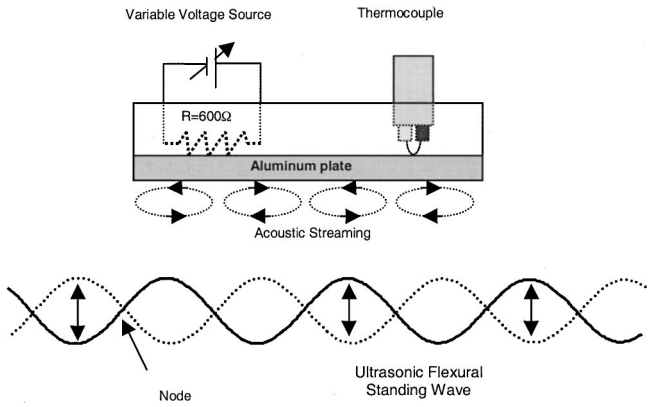

FIG. 3. Experimental setup for measuring enhancement of heat transfer.

distinctive circular airflows within the half-wavelength of the beam (1 cm for this case). Clearer acoustic streaming is observed with bigger vibration amplitude.

C. Streaming in the gap

One interesting application of acoustic streaming considered in this study is the enhancement of convective heat transfer. To this end, it is possible to envision that a heated object is placed over a vibrating beam near which acoustic streaming is induced. Then, the temperature of the heated object is decreased due to forced convection caused by acoustic streaming. Therefore, for heat transfer application, it is important to study how the acoustic streaming pattern changes when there is a stationary upper beam that represents a heat source.

A beam that is 1 cm wide, 2.5 cm thick, and 11 cm long is placed 1 cm over the vibrating beam. The same visualization process used for the case without an upper stationary beam is performed at the gaps ranging from 2 mm to 1 cm. It is observed that acoustic streaming in the gap is strong enough to blow most acetone droplets out of the gap, making it almost impossible to perform visual observation of acoustic streaming pattern. Therefore, CFD simulation presented in Sec. IV is used to estimate acoustic streaming pattern and velocity in the gap.

D. Enhancement of convective heat transfer

To measure the enhancement of convective heat transfer due to acoustic streaming, a heat source containing an aluminum plate, a resistor, and a thermocouple is made. A detailed schematic drawing of the plate is shown in Fig. 3. The bottom of the plate is made of aluminum. The top is made of Plexiglas that contains a 600-Ω resistor and a thermocouple. The resistor is connected to a variable voltage power supply and serves as a heater.

With the 600 Ω resistor, the temperature of the plate can be increased to 98 °C with the available power supply of 3.4 W. During the experiment, the room temperature was kept at 20 °C. The heat source is placed 1.5 mm above the vibrating beam. As the temperature of the heat source reaches a steady-state value of 98 °C, acoustic streaming is generated by vibrating the beam at 28.4 kHz with the vibration amplitude of 10 μm. Then, the temperature changes of the plate

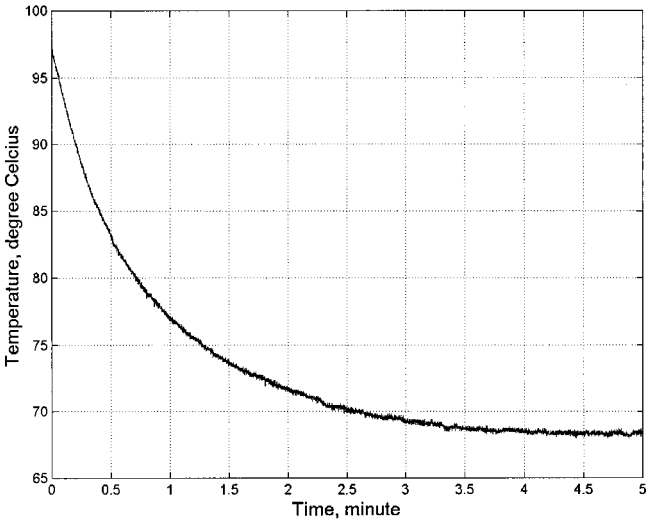

FIG. 4. Measurement of temperature drop of the heat source.

are measured using a thermocouple. Due to the inherent noises in the voltage signal from the thermocouple, the signal is filtered through a low-pass filter and sampled at 20 Hz using a data acquisition board. A temperature drop of 30 °C is achieved in 4 min and maintained as shown in Fig. 4. As the vibration amplitude is further increased to 25 μm, a temperature drop of 40 °C is achieved that is the maximum temperature drop obtained with the current experimental setup.

When acoustic streaming is induced in the gap, there are two possible major heat flow paths. The first one is convective heat transfer to ambient air in the direction parallel to the heat source marked as heat flow path 1 in Fig. 5. In this path, the heat from the heat source is taken away by airflow near the heat source and transferred to ambient air at both sides of the gap. The second path is convective heat transfer through the vibrating beam marked as heat flow path 2. Due to the recirculating nature of acoustic streaming flow pattern, in the second path the heat from the heat source is transferred to the vibrating beam and dissipated to ambient air.

To measure the heat transfer in path 1, the space between the heat source and the vibrating beam is enclosed along the perimeter of heat source, thereby allowing heat to flow only in path 2. As shown in Fig. 6, for the enclosed gap case, the achieved temperature drop is 10 °C less than for the open gap system, which is about a 33% decrease in the tem-

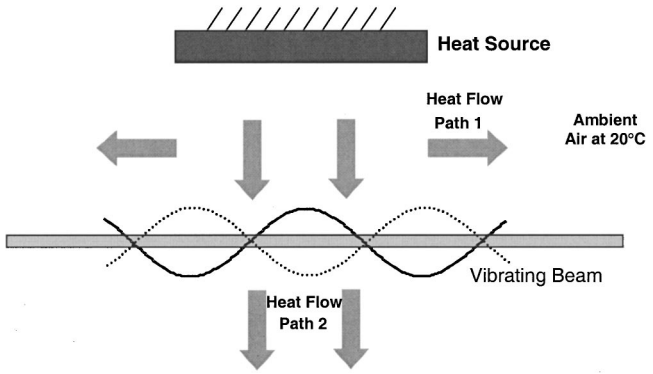

FIG. 5. Heat flow paths.

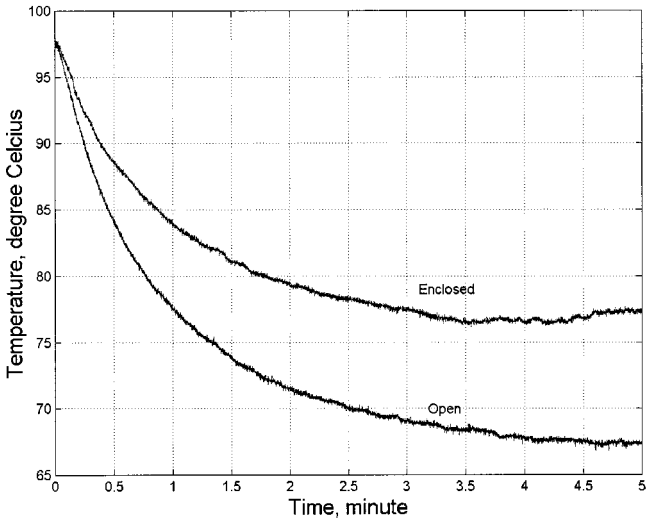

FIG. 6. Effect of enclosing the heat source.

perature drop. In addition, to estimate the heat transfer in path 2, changes in the temperature of the vibrating beam are measured as shown in Fig. 7. When the heat source is heated to 98 °C, the temperature of the lower beam is increased to 36 °C as a result of heat transfer through air. When induced, acoustic streaming causes the temperature of the vibrating beam to drop to 26 °C in 2 min, which is 6 °C higher than the room temperature. It is also observed that the resulting temperature drop changes with the gap.

III. THEORY

Nyborg (1958) formulated the equation for near-boundary acoustic streaming using successive approximation method as

$$\mu\nabla^2 u_2 - \nabla P_2 + F = 0, \tag{1}$$

$$F \equiv -\rho_0 \langle (u_1 \cdot \nabla) u_1 + u_1 (\nabla \cdot u_1) \rangle, \tag{2}$$

where μ is kinematic viscosity, ρ_0 is constant equilibrium density, u_1 is oscillatory particle velocity, u_2 is acoustic streaming velocity, P_2 is a steady-state "dc" pressure, F is

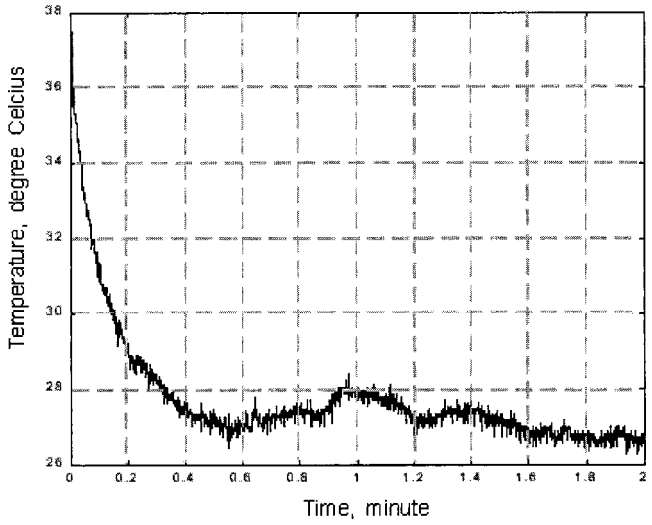

FIG. 7. Temperature drop of the vibrating beam.

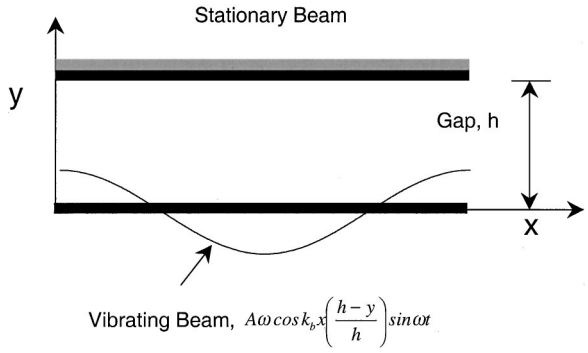

FIG. 8. Simulation schematic drawing.

nonlinear driving forcing term, and $\langle\ \rangle$ means a time average over a large number of cycles. Without averaging, F contains a dc part and harmonically varying terms. The former induces acoustic streaming. When averaged over a relatively long period of time, the effect of harmonically varying forcing terms disappears and only the contributions from the dc part appear in the solution. The acoustic streaming velocity, u_2, approaches a constant value as the distance from the vibrating beam approaches infinity. This time-independent limiting velocity, U_L, is given by

$$U_L = -\frac{3}{4\omega} U_0 \left(\frac{dU_0}{dx}\right), \tag{3}$$

where ω is excitation frequency and U_0 is amplitude of the irrotational velocity tangent to the boundary (cf. Andres and Ingard, 1953). To calculate outer acoustic streaming motion, the limiting velocity, U_L, is used as a slip velocity at the solid surface by assuming Stoke boundary layer thickness negligible (cf. Lighthill, 1978).

The amplitude of the tangential irrotational velocity, U_0, is obtained from the normal irrotational velocity, V, imposing the zero-divergence condition assumed in the Nyborg's formulation. For a relatively small gap, the normal irrotational velocity is assumed to be

$$V = A\omega \cos k_b x \left(\frac{h-y}{h}\right) \sin \omega t = V_0 \sin \omega t, \tag{4}$$

where A is the peak vibration amplitude of an elastic beam, k_b is the bending wave number of the beam defined as $2\pi/\lambda_b$ where λ_b is the wavelength of the beam, and h is the gap between the vibrating beam and the stationary beam as shown in Fig. 8. Equation (4) satisfies the boundary conditions that V at $y=0$ is equal to the velocity of the vibrating beam and V at $y=h$ is zero. By making use of the zero-divergence condition, $\partial U_0/\partial x + \partial V_0/\partial y = 0$, the amplitude of the tangential velocity, U_0, is given by

$$U_0 = \frac{A\omega}{2\pi} \left(\frac{\lambda_b}{h}\right) \sin k_b x. \tag{5}$$

Upon substitution of Eq. (5) into Eq. (3), U_L can be rewritten as

$$U_L = -\frac{3}{8} f \lambda_b \left(\frac{A}{h}\right)^2 \sin 2k_b x, \tag{6}$$

where f is excitation frequency in Hertz.

First, note that, from Eq. (6), any explicit dependence of acoustic streaming velocity on μ disappears although it originates from the viscosity. Also, note that acoustic streaming velocity is a function of the wavelength of the beam and the gap in addition to the excitation frequency and the vibration amplitude.

IV. COMPUTATIONAL FLUID DYNAMICS (CFD) SIMULATION

The length of the two plates for the computational simulations is the same as the wavelength of the ultrasonic flexural standing wave (UFSW). The gap between the two plates is small, i.e., 2–20 mm, and the maximum speed of the air is less than 2 m/s. Thus, the Reynolds number based on the given conditions is less than 1800, which is in the range of laminar flow. The air speed in the gap is under Mach 0.3, so that the incompressible fluid flow assumption may be applicable for a first-order approximation. The governing equations (cf. Kleinstreuer, 1997) for incompressible transient laminar Newtonian fluid flow are continuity,

$$\nabla \cdot \vec{\mathbf{v}} = 0, \tag{7}$$

and linear momentum

$$\frac{\partial \vec{\mathbf{v}}}{\partial t} + (\vec{\mathbf{v}} \cdot \nabla)\vec{\mathbf{v}} = \frac{1}{\rho}(-\nabla p + \mu \nabla^2 \vec{\mathbf{v}}). \tag{8}$$

The boundary condition for the lower vibrating plate of the CFD simulation is the vertical displacement defined by

$$y_p(x,t) = A(t) \cdot \cos(2\pi x/\lambda)$$

$$\text{where } A(t) = A_0 \cdot \sin(\omega t). \tag{9}$$

Here $A(t)$ is the vibration amplitude, λ is the wavelength, A_0 is the maximum vibration amplitude, $\omega = 2\pi f$ is the angular velocity of the wave, f is the frequency, and t is the time. The two open sides constitute natural symmetry planes with zero-gradient conditions.

The simulation covers more than 4000 periods with 16 time steps each to get the quasi-steady state solution. The velocity $\vec{\mathbf{v}}$, which contains harmonic terms and a ''dc'' term, is calculated from Eqs. (7) and (8). The acoustic streaming velocity ($\overline{v}_{a,i}$, $i = x$, y, and z) is obtained by averaging $\vec{\mathbf{v}}$ over a period as follows:

$$\overline{v}_{a,i} = \frac{1}{T_a}\int_0^{T_a} v_i \, dt, \quad i = x, \; y, \; \text{and} \; z, \tag{10}$$

where T_a is the period of ultrasonic vibration.

A. Numerical analysis

The computational fluid dynamics package CFX 4 (AEA Technology, Bethel Park, PA) was used for the numerical simulation. CFX 4 is a control-volume-based solver and employs a structured, multi-block, body-fitted coordinate discretization scheme, which uses the SIMPLEC algorithm for the pressure correction. The CFD simulation was run on a SGI Origin 2000 (400 MHz; multiple R12000 processors) at the North Carolina Supercomputing Center (NCSC, RTP). Simulations consisted of first determining the instantaneous velocity field, governed by Eqs. (7) and (8) with the moving boundary condition defined by Eq. (1). The time-averaged velocity, i.e., acoustic streaming velocity, was calculated with Eq. (10). CFX 4.3 employs a particular implementation of an Algebraic Multi-Grid called Additive Correction. This approach takes advantage of the fact that the discrete equations are representative of the balance of conserved quantities over a finite volume, making it ideally suited for the discretization used. Coarser mesh equations can be generated by merging the original finite volumes into larger ones. Thus, they impose conservation requirements over larger volumes and in so doing reduce the error components at longer wavelengths. The size and configuration of the computational domain used in this study were adjusted until an acceptable level of grid independence of the final solution was achieved, i.e., $\varepsilon \leqslant 10^{-4}$, where ε represents the mass and momentum residuals.

The algebraic equations are discretized with respect to the computational space coordinates with implementation of the appropriate boundary conditions, i.e., no-slip at the walls and zero-gradients at the symmetry planes. A time-dependent moving grid option was employed, based on a user-supplied FORTRAN program, to solve for the airflow field induced by ultrasonic flexible waves (UFW) at the vibrating plate boundary. This program allows specifying time-dependent grid positions on the lower wall surface at each time step as defined in Eq. (1). The typical size of the computational mesh at about 2000 control volumes and about 3.0 CPU hours on the SGI Origin 2000 were required to obtain the quasi-equilibrium flow field solution. The time-dependent waveform for the UFW was discretized nonlinearly into about 16 time steps for each period. The numerical accuracy of the model is further documented with validation results discussed in the next section.

B. CFD results

Figure 9 shows the time evolution of vortices in the gap between two infinite beams due to acoustic streaming. At time $t = 0$, no airflow exists in the gap, and then the lower beam starts to vibrate with the frequency $f = 28.4$ kHz, vibration amplitude $A = 20\,\mu$m, and wavelength of $\lambda_b = 2.0$ cm in a 2-mm gap between two beams. Four vortices over a single wavelength emerge near the lower vibrating beam [cf. Fig. 9(a)]. They appear between nodal points and antinodal points of the vibrating beam with the two in the center moving closer to each other [cf. Figs. 9(a)–(l)]. The airflow patterns show an upward motion at antinodal points and downward at nodal points, which is similar to the experimental visualization shown in Fig. 2. After 610 pulses, a steady streaming flow field is achieved [cf. Figs. 9(f)–(l)].

Figure 10 represents the acoustic streaming velocity tangent and normal to the beam along a fictitious vertical line passing through a vortex center. The tangential and normal velocities are zero at the vortex center (about $y = 0.072$ cm). The tangential velocity reaches 70 cm/s near the lower vibrating beam and 30 cm/s near the upper beam. The normal velocity is significant only near the nodal and antinodal points, and near zero along the vertical line through the vortex center as shown in the flow field of the converged solution in Fig. 9(l).

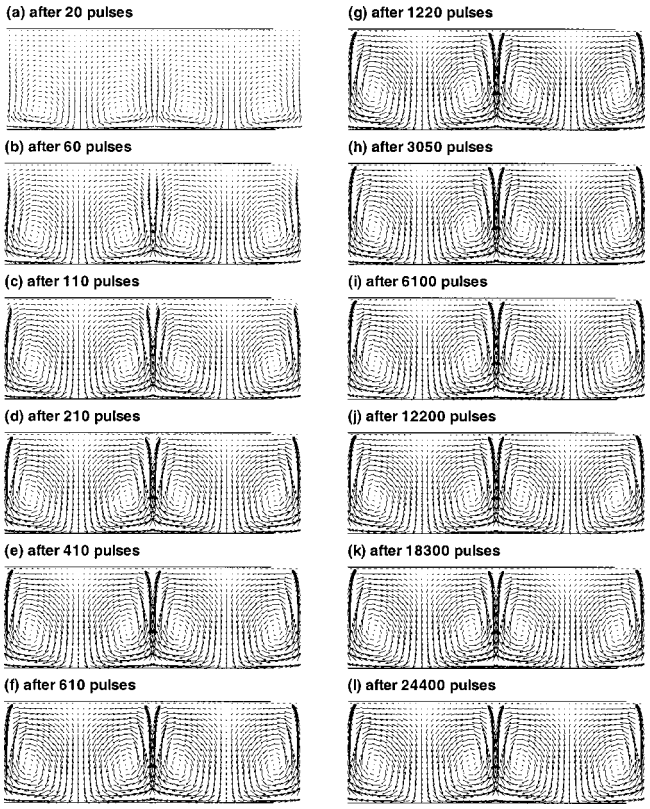

FIG. 9. Time evolution of the streaming velocity field for the base case.

To observe the effect of changing excitation frequency, vibration amplitude, and gap on the streaming velocity and its patterns, a series of simulations was conducted. It is observed that the vortical flow patterns are not influenced by the simulation conditions but the magnitude of the acoustic streaming velocity is strongly influenced. Therefore, for the following analyses, only the variations of the streaming velocity magnitude along a vortex center are compared and discussed, except for the case of open ends in Sec. IV B 3.

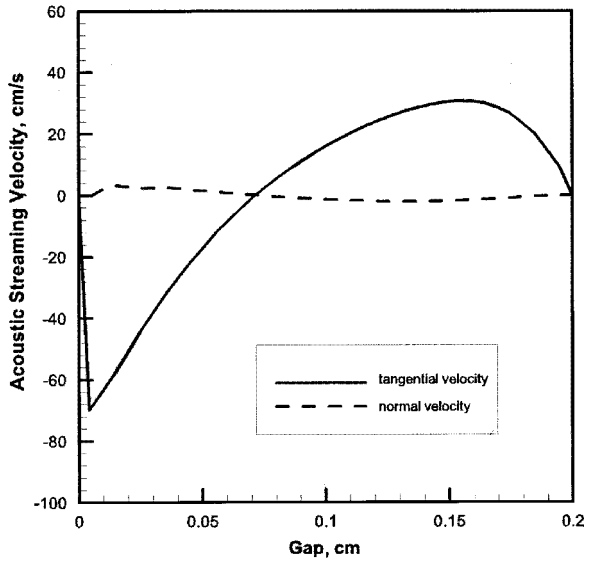

FIG. 10. The streaming velocity through the vortex center.

TABLE I. System characteristics for CFD simulation.

Frequency (kHz)	Vibration amplitude (μm)	Velocity of vibrating beam (m/s)	Wavelength (mm)
6.0	93.0	3.5	48.0
12.0	47.0	3.5	34.0
18.0	31.0	3.5	28.0
28.4	20.0	3.5	20.0
50.0	11.0	3.5	17.0

1. Effect of vibration frequency

The effect of the excitation frequency on the acoustic streaming velocity is measured. Of particular interest is to observe a change in acoustic streaming velocity when the excitation frequency becomes ultrasonic. If the excitation frequency of the beam increases, the irrotational velocity would also increase with the excitation frequency. This results in an increase in acoustic streaming velocity because acoustic streaming velocity is proportional to the square of the irrotational velocity (cf. Nyborg, 1958). Therefore, the effect of excitation frequency can be properly measured only when the velocity of the vibrating beam is maintained at a constant value. This can be achieved by decreasing the vibration amplitude to an appropriate value. Detailed test conditions are shown in Table I.

Figure 11 shows the maximum acoustic streaming velocity in the 2-mm gap at an excitation frequency of 6, 12, 18, 28.4, and 50 kHz with corresponding vibration amplitude values detailed in Table I. The results are obtained from CFD simulation and the analytical solution based on Eq. (6). It is observed that the maximum streaming velocities decrease with the excitation frequency. The maximum streaming velocities at 28.4 kHz near the lower and upper beams are 66.2 and 30.6 cm/s, respectively. While the streaming patterns around the lower beam are directly influenced by the beam motion, those near the upper beam are induced by the streaming flows from the lower beam. It is observed that the airflow is attenuated in the process of inducing streaming motions near the upper beam. As a result, the larger streaming velocities are observed near the lower beam. As shown in

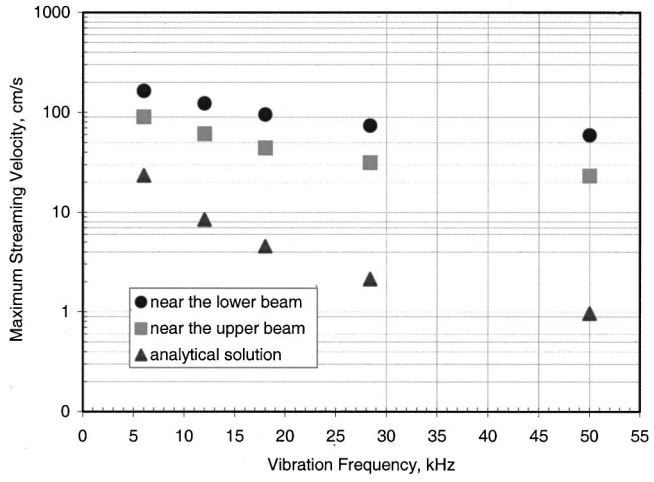

FIG. 11. The maximum acoustic streaming velocity for constant vibration velocity of the beam.

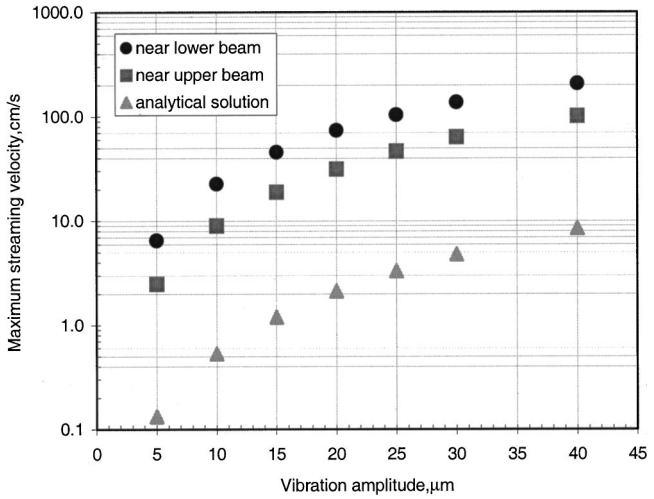

FIG. 12. The maximum acoustic streaming velocity for different vibration amplitude.

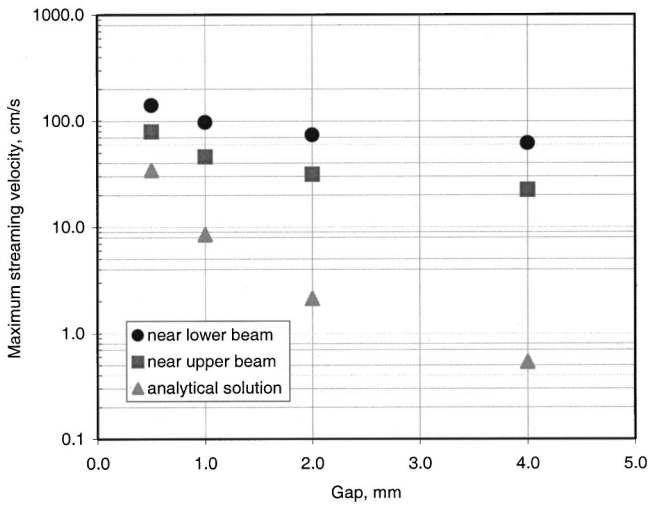

FIG. 13. The maximum acoustic streaming velocity for different gap size.

Eq. (6), the acoustic streaming velocity is proportional to the square of the vibration amplitude and the wavelength of the vibrating beam that decreases with the excitation frequency. Although the excitation frequency grows, a decrease in wavelength and vibration amplitude offsets the increase in the acoustic streaming velocity due to frequency increase. As a result, both CFD simulation and the analytical solution indicate that the maximum streaming velocity decreases with excitation frequency.

Moreover, no significant change in acoustic streaming velocity is observed as the excitation frequency becomes ultrasonic. The analytical solution does not include the attenuation of flow, resulting in uniform streaming velocities across the gap. Therefore the analytical solution can be compared to the streaming velocity near the lower beam obtained from CFD simulation. It is noted that an analytical solution formulated based on Nyborg's theory underestimates the acoustic streaming velocity when compared to the CFD results, which are based on the assumption of air incompressibility for $\mathrm{Ma} < 0.3$.

2. Effect of vibration amplitude and gap

Figure 12 shows the maximum streaming velocities near the beams for vibration amplitudes of 5, 10, 15, 20, 25, 30, and 40 μm with a gap of 2 mm at an excitation frequency of 28.4 kHz. The wavelength is 20 mm. The maximum streaming velocity increases as the vibration amplitude increases due to increase in the irrotational velocity. The maximum irrotational velocity near the lower vibrating beam can be calculated with the excitation frequency, the vibration amplitude and wavelength of the beam, and the gap.

For vibration amplitude of 25 μm, the maximum streaming velocities near the lower and upper beams from CFD simulation reach 100 and 45 cm/s, respectively. For the same vibration amplitude, a maximum streaming velocity of 3.3 cm/s is obtained from the analytical solution. It is observed that as the vibration amplitude grows, maximum streaming velocity from both CFD simulation and the analytical solution increase in a similar trend, an increase with the square of the amplitude but the analytical solution predicts significantly smaller acoustic streaming velocity. An explanation for this discrepancy requires further investigation.

Figure 13 represents the maximum acoustic streaming velocity as a function of the gap between the vibrating beam and the upper stationary beam. The maximum streaming velocity decreases with the growth of the gap for both CFD simulation and the analytical solution. It is also observed that the analytical solution underestimates acoustic streaming velocity as opposed to CFD simulation result. The difference between the analytical and numerical results grows as the gap increases because the analytical model is developed with an assumption that the gap is small enough to presume a linear variation of the normal irrotational velocity across the gap.

3. Effect of beam end openings

Figure 14 shows the streaming velocity fields for the 2 mm gap, considering the lower beam to be one-and-a-half-wavelength long (3 cm) and the upper beam one-wavelength long (2 cm) to observe the effect of an open-ended channel. Vortical flow and flow entrainment are observed near the

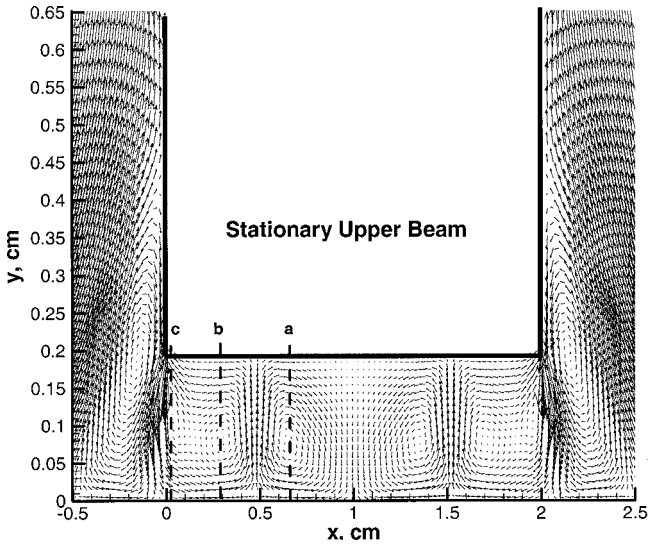

FIG. 14. The streaming velocity considering the entire system.

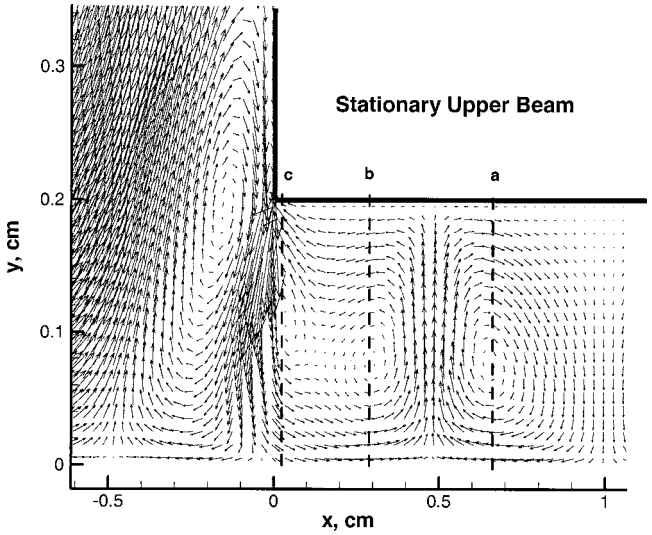

FIG. 15. Enlarged view of the streaming velocity fields near the end.

ends of the upper beam. The vortex centers in the channel are located at $x=0.3$ and 0.65 cm with a symmetry condition at $x=1$ cm. Due to air entrainment, the flow field near the end is disturbed, forming a small vortex (cf. enlarged Fig. 15). Figure 16 shows the magnitude of the acoustic streaming velocity in the gap from a three-dimensional perspective. A maximum streaming velocity occurs right at the openings of the gap near the upper beam, which enhances the mixing of flow between inside and outside the gap. The streaming velocities near the lower beam are generally greater than those near the upper beam except the maximum streaming velocity occurring at the openings. The velocities observed with an open-ended channel are greater than those without an opening (cf. Fig. 13). The velocity near the lower beam reaches up to 130 cm/s due to the flow entrainment and is almost twice that of the 2-mm gap case without flow entrainment. From this, one concludes that flow entrainment enhances the flow speed and changes the flow pattern, resulting in enhanced cooling capability.

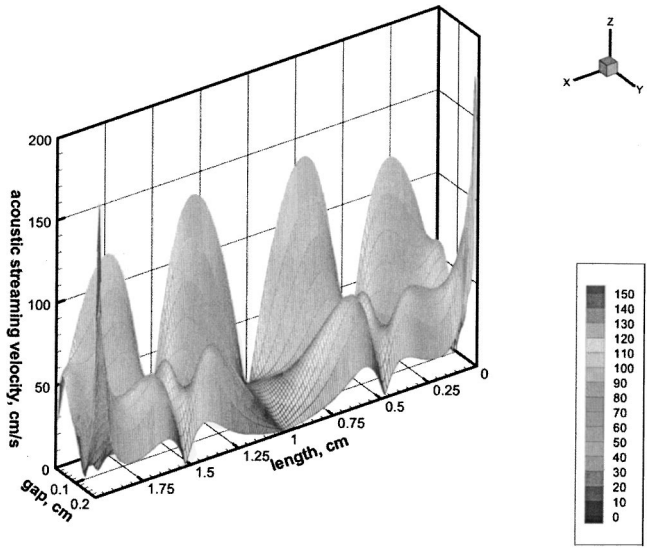

FIG. 16. The 3-D streaming velocity contours inside the gap between two plates.

V. CONCLUSIONS

An investigation of acoustic streaming induced by the ultrasonic flexural vibration is presented. The investigation includes acoustic streaming pattern and its velocity along with associated heat transfer characteristics. Acoustic streaming patterns visualized using acetone corresponded well with the prediction by Nyborg's theory. Using acoustic streaming, a notable temperature drop of 40 °C was obtained in 4 min and maintained. Tests identifying major heat flow paths indicated that both gaps and the vibrating beam serve as crucial heat flow paths.

Employing CFD simulations assuming laminar incompressible flow, it was shown that the vortical flows, observed by experiment and predicted by acoustic streaming theory, could be reproduced. Also, it was found that the streaming velocity from the CFD simulation is far greater than the estimation from the analytical solution based on sonically induced acoustic streaming assuming inviscid flow and a linear variation of the normal (irrotational) velocity across a very small gap (cf. Nyborg, 1958; Vainshtein *et al.*, 1995). This result proves that the theoretical calculations based on sonically induced acoustic streaming may not be extended to estimate ultrasonically induced acoustic streaming velocities. In other words, more comprehensive CFD simulations considering turbulent and/or compressible flow may be needed to accurately predict ultrasonically induced acoustic streaming flows.

With an open-ended channel, simulation revealed the existence of large flow entrainment at the channel ends, which enhances convective heat transfer but cannot be captured with the analytical solution due to the complexity of boundary conditions. With a computational control volume mesh of 2000, the CFD simulation of the flow field induced by a beam vibrating at an ultrasonic frequency is computationally very intensive. It takes almost 10 CPU hours on the Cray T-90 supercomputer and 90 CPU hours on SGI Origin 2000 to obtain a fully developed acoustic streaming flow field. Although the CFD simulations are expensive, more accurate and realistic results can be obtained including a three-dimensional effect of acoustic streaming and the open-ended channel.

Andres, J. M., and Ingard, U. (**1953**). ''Acoustic streaming at high Reynolds numbers,'' J. Acoust. Soc. Am. **25**(5), 928–937.

Chen, Z. D., Taylor, M. P., and Chen, J. J. J. (**1998**). *Heat Transfer on a Surface Affected by an Air/Water Interface Undergoing Wave Motion* (The Minerals, Metals & Materials Society), pp. 429–435.

Fand, R. M., and Kave, J. (**1960**). ''Acoustic streaming near a heated cylinder,'' J. Acoust. Soc. Am. **32**(5), 579–584.

Faraday, M. (**1831**). Philos. Trans. **121**, 229.

Gopinath, A., and Mills, F. (**1993**). ''Convective Heat Transfer From a Sphere Due to Acoustic Streaming,'' J. Heat Transfer **115**, 332–341.

Gopinath, A., and Mills, F. (**1994**). ''Convective Heat Transfer Due to Acoustic Streaming across the Ends of Kundt Tube,'' J. Heat Transfer **116**, 47–53.

Gould, R. K. (**1966**). ''Heat transfer across a solid-liquid interface in the presence of acoustic streaming,'' J. Acoust. Soc. Am. **40**(1), 219–225.

Hamilton, M. F., and Blockstock, D. T. (**1998**). *Nonlinear Acoustics* (Academic, New York).

Ingard, U., and Labate, S. (**1950**). ''Acoustic circulation effects and the nonlinear impedance of orifices,'' J. Acoust. Soc. Am. **22**(2), 211–218.

Jackson, F. J., and Nyborg, W. L. (**1960**). ''Sonically induced microstreaming near a plane boundary. I. The sonic generator and associated acoustic fields,'' J. Acoust. Soc. Am. **32**(10), 1243–1250.
Kays, W. M., and Crawford, M. E. (**1993**). *Convective Heat and Mass Transfer* (McGraw–Hill, New York).
Kleinstreuer, C. (**1997**). *Engineering Fluid Dynamics–An Interdisciplinary Systems Approach* (Cambridge U.P., New York).
Lee, C. P., and Wang, T. G. (**1990**). ''Outer acoustic streaming,'' J. Acoust. Soc. Am. **88**(5), 2367–2375.
Lighthill, J. (**1978**). ''Acoustic Streaming,'' J. Sound Vib. **61**(3), 391–418.
Nguyen, N. T., and White, R. M. (**1999**). ''Design and Optimization of an Ultrasonic Flexural Wave Micropump using Numerical Simulation,'' Sensors Actuators **77**, 229–236.
Nyborg, W. L. (**1958**). ''Acoustic Streaming near a Boundary,'' J. Acoust. Soc. Am. **30**(4), 329–339.
Rayleigh, Lord (**1945**). *Theory of Sound* (Dover, New York).
Ro, P. I., and Loh, B. (**2001**). ''Feasibility of using Ultrasonic Flexural Waves as a Cooling Mechanism,'' *IEEE Industrial Electronics* Vol. 48, No. 1, pp. 143–150.
Sashida, T. (**1993**). *An Introduction to Ultrasonic Motors* (Clarendon, Oxford).
Schlicting, H. (**1955**). *Boundary Layer Theory* (McGraw–Hill, New York).
Uhlenwinkel, V., Meng, R., Bauckhage, K., Schreckenber, P., and Andersen, O. (**1994**). ''Heat Transfer to Cylindrical Bodies and Small Particles in an Ultrasonic Standing-Wave Fields of Melt Atomizer,'' in *Multiphase-Flow and Heat Transfer in Materials Processing*, ASME, FED-Vol. 201/HTD-Vol. 297, pp. 19–24.
Vainshtein, P., Fichman, M., and Cutfinger, C. (**1995**). ''Acoustic enhancement of heat transfer between two parallel plates,'' Int. J. Heat Mass Transf. **38**(**10**), 1893–1899.

Grazing instabilities and post-bifurcation behavior in an impacting string

K. D. Murphy and T. M. Morrison
Department of Mechanical Engineering, University of Connecticut, Storrs, Connecticut 06269-3139

(Received 27 June 2001; revised 21 October 2001; accepted 13 November 2001)

A theoretical and experimental investigation of the nonlinear dynamic response of a periodically excited string subject to a knife-edge amplitude restraint is presented. The amplitude restraint creates an impact condition as the amplitude of the response grows. The focus of this work is on the influence of a grazing instability; this zero-velocity impact event leads to complicated, post-bifurcation behavior ranging from multifrequency, periodic motion to chaos. In addition to looking at the response numerically, parameter combinations leading to an incidence of grazing are clearly identified in the excitation force excitation frequency parameter space using a multiple scales perturbation analysis. Modeling issues, numerical difficulties, and experimental limitations are also discussed. © *2002 Acoustical Society of America.* [DOI: 10.1121/1.1433806]

PACS numbers: 43.40.Cw [ANN]

I. INTRODUCTION

A wide variety of problems in science and engineering involve impact events. Some simple examples include engine valve closure, gears experiencing backlash, a moored ship bumping into a dock, a pendulum contacting an amplitude restraint, and a ball bouncing on a table, see Refs. 1–4. The principle feature of these *impact oscillators* is that there is a discontinuity in the stiffness at the onset of contact. This highly nonlinear contact event is at the heart of the diverse response characteristics previously reported.

Many studies of impacting systems have involved discrete, single degree-of-freedom (DOF) models and have shown a host of complicated behavior including period doubling bifurcations, quasiperiodicity, high-period impacting orbitals, and, of course, chaos. For the sake of numerically computing the response of these single DOF systems, a two model approach, shown in Fig. 1, is commonly taken. In the free-play region [Fig. 1(b)], the standard 1 DOF linear oscillator is used. At the moment of impact ($x=\sigma$), the equation of motion switches to the two spring model shown on the right-hand side of Fig. 1(c). As contact is achieved and lost between the mass and the wall, the governing equations are toggled between these two single DOF models.

Early exceptions to studying low-dimensional, single DOF systems have considered the motion of a continuous beam subject to amplitude constraints at the tip.[5–8] However, even these models are 1 DOF in nature, since the beam is discretized using a single mode Galerkin projection (resulting in a single ordinary differential equation). In the free-play region, a cantilevered shape function is used in the discretization. In the contact region, a clamped–pinned shape function is used. So, once again, the solution is found by switching between two governing ODE's as contact is initiated and lost.

More recently, solitary wave solutions have been investigated for a piecewise linear beam model.[9] This particular analysis did not involve a single mode discretization of the governing equation and rendered two generic solution types.

The present work takes a theoretical, numerical, and experimental approach to examine the response of a tensioned string subject to harmonic excitation and a knife edge amplitude restraint. Practical realizations of an impacting string system include moving textile threadlines, the fiber optic cable drawing process, and wire electro-discharge machining. The idealized system under consideration is shown schematically in Fig. 2. The principle objectives of this study are (i) to identify parameter combinations which lead to the zero-velocity grazing instability[10,11] and (ii) to examine the post-bifurcation behavior of the system.

II. EQUATIONS OF MOTION

To begin, the string is assumed to be a homogeneous, 1D elastic continuum. The knife-edge amplitude constraint is modeled as a localized, stiff spring which is set off from the equilibrium position of the string by a distance σ. In this case, the strain energy per unit length of the system may be expressed as

$$U=\int_0^L\left[\frac{1}{2}EA\epsilon^2+\frac{1}{2}K\delta(x-x_r)(v(x)-\sigma)^2\right]dx, \tag{1}$$

where $\epsilon=u_{,x}+v_{,x}^2/2+P/EA$ is the axial strain, u and v are the axial and transverse deflections, respectively, E is the elastic modulus, A is the cross-sectional area of the string, P is the applied axial tension, L is the length of the string, δ is the Dirac delta function, and x_r is the location of the restraint. The discontinuous restraint stiffness is given by

$$K=\begin{cases}0 & -\infty<v(x_r)<\sigma,\\ \text{Large} & \sigma\leqslant v(x_r)<\infty.\end{cases} \tag{2}$$

The kinetic energy of the system is

$$T=\frac{1}{2}\int_0^L m[v_{,t}^2+u_{,t}^2]dx, \tag{3}$$

where m is the mass per unit length. Finally, the work done on the string by the externally applied force is

 0001-4966/2002/111(2)/884/9/$19.00

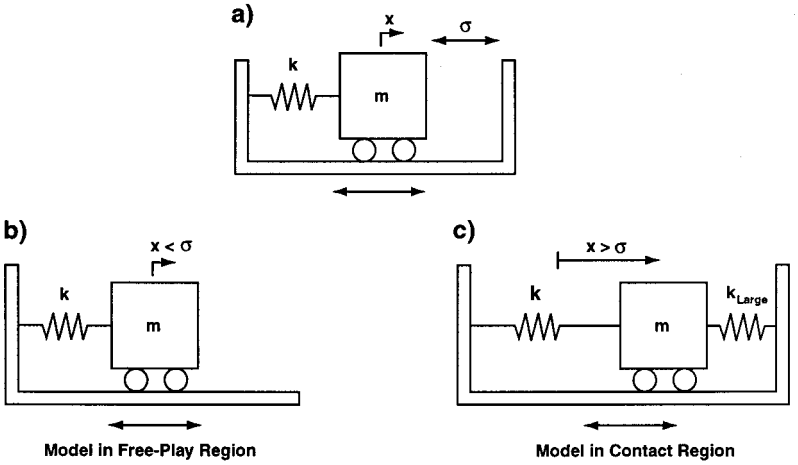

FIG. 1. A schematic of a common single degree-of-freedom model for impact problems.

$$W=\int_0^L F\,\sin(\omega t)\,\delta(x-x_0)v(x)dx, \tag{4}$$

where F is the excitation amplitude, ω is the excitation frequency, and x_0 is the point of application of the force.

Using these expressions in Hamilton's principle leads to two partial differential equations of motion governing the axial and transverse motion of the string. To further simplify matters, the axial motion of the string is assumed to take place quasistatically. This assumption is justified since our attention will be focused near the first transverse resonant frequency, which is typically much lower than the first axial frequency. With this quasistatic stretching assumption, the transverse equation of motion for the string is

$$mv_{,tt}+cv_{,t}-\left[\int_0^L\frac{1}{2}\frac{EA}{L}v_{,x}^2\,dx+P\right]v_{,xx}+K\delta(x-x_r)(v(x)-\sigma)=F\,\sin(\omega t)\,\delta(x-x_0). \tag{5}$$

Viscous structural damping, given by $cv_{,t}$, has been added to capture the dissipative nature of the system. It should also be noted that, with the exception of the amplitude restraint stiffness, this equation is identical to the nonlinear string model developed from a Newtonian point-of-view by Narasimha.[12] This equation is recast in nondimensional form

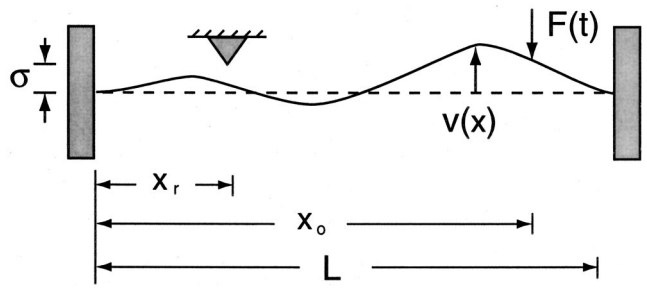

FIG. 2. An overhead schematic of the vibrating string system, including the knife-edge amplitude restraint and periodic excitation $F(t)$.

$$V_{,\tau\tau}+2\zeta\omega_1 V_{,\tau}-\left[\int_0^1\frac{1}{2}\frac{EA}{P\pi^2}V_{,\xi}^2\,d\xi+\frac{1}{\pi^2}\right]V_{,\xi\xi}+\frac{KL^2}{P\pi^2}\delta(\xi-\xi_r)(V(\xi)-\overline{\sigma})=\frac{\delta(\xi-\xi_0)}{P\pi^2}F\,\sin(\Omega\tau), \tag{6}$$

where the displacement is $V=v/L$, the axial coordinate is $\xi=x/L$, the gap size is $\overline{\sigma}=\sigma/L$, ζ is the damping ratio, $\Omega=\omega/\omega_1$ is the nondimensional forcing frequency, and time is rescaled to $\tau=t\sqrt{P\pi^2/mL^2}$. This equation is discretized spatially using a Galerkin procedure along with the expansion

$$V(\xi,\tau)=\sum_{j=1}^{n}a_i(\tau)\sin(i\pi\xi). \tag{7}$$

The ith equation of motion, resulting from that procedure, is

$$\ddot{a}_i+2\zeta\omega_1\dot{a}_i+\left[\frac{EA}{P}\sum_{j=1}^{n}\frac{(j\pi)^4}{4}a_j^2+i^2\right]a_i+\frac{KL^2}{P\pi^2}\left[\sum_{j=1}^{n}a_j\,\sin(j\pi\xi_r)-\overline{\sigma}\right]\sin(i\pi\xi_r)=\frac{2\sin(i\pi\xi_0)}{\pi^2}\frac{F}{P}\sin(\Omega\tau). \tag{8}$$

Nonlinearities arise in this equation from two sources: (i) geometric nonlinearities associated with large deflections and (ii) the restraint stiffness K, as defined by Eq. (2). Also, note that the ith linear natural frequency is $\omega_i=\sqrt{i^2P\pi^2/mL^2}$ rad/s and that time has been rescaled with the first natural frequency.

III. NUMERICAL SIMULATION

In the impacting regime, numerical solutions to Eq. (8) will be sought. However, before proceeding, it is important to ensure that reliable solutions are obtained. There are four primary challenges to obtaining such solutions. The first stems from the large stiffness discontinuity which occurs at impact; the governing equations [Eq. (8)] often become numerically stiff at impact, meaning that the eigenvalues of the local Jacobian matrix range over several orders of magni-

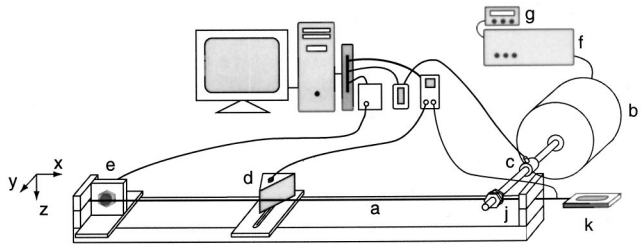

FIG. 3. A diagram of the components comprising the experimental setup.

tude. To remedy this problem, an adaptive step, hybrid integration routine is used. This routine uses Geer's method during nonstiff portions of the solution and automatically switches to a backwards difference method, which is slower but extremely stable, during the stiff portions. Second, it is crucial to determine the exact moment of impact, since this will have a tremendous influence on the computed response. However, it is also computationally inefficient to use an extremely small time step throughout the simulation. To overcome this difficulty, the equations of motion are recast as described by Henon.[13] In this new form, the instant of impact is easily determined without having to resort to an extremely small time step. Third, due to the finite expansion of the displacement field in Eq. (7), the issue of modal convergence arises. Typically, 20 terms ($n=20$) were retained; the addition of more terms did not change the qualitative character of the response or the parameter values associated with the observed bifurcations. The final challenge involves the transient dynamics. Transient oscillations, induced at the start of impacting, die slowly in this lightly damped system. In all cases presented, 250 forcing cycles are allowed to elapse before the response is considered to be at steady state.

IV. EXPERIMENTAL STUDY

A. Experimental system

A schematic of the experimental setup is shown in Fig. 3. It consists of a tensioned bass guitar string (a), an electromechanical shaker (b), a force transducer (c), a knife-edge constraint (d), and a displacement sensor (e). The shaker was driven by a power amplifier (f) and a wave form generator (g). This system also employed a control system that helped maintain a constant forcing amplitude, even during large amplitude deflections of the string.

The sinusoidal force was provided by an electromechanical shaker in the y direction, such that motion occurred in the (x,y) plane. A lightweight aluminum stinger was attached to the shaker armature and used to deliver the periodic force to the string. The threaded end of the stringer was connected to the string by means of two nuts, which were sinched down to pinch the wire (j). A PCB force transducer was attached to the stringer to monitor the force supplied by the shaker. The data acquisition software was able to monitor the amplitude of the applied load to two decimal places. However, distortions in the *shape* of the wave form, occurring during impacts, could not be monitored quantitatively. Fortunately, the onset of these distortions were dramatic and easily identifiable.

The impact condition was realized by a wedge-shaped aluminum block (d). The block was mounted to a fixture that allowed the wedge location to be moved (varying ξ_r) and the gap separation to be changed (varying $\overline{\sigma}$).

The planar displacement of the string was monitored using a noncontacting displacement sensor (e). The sensor produced a voltage proportional to the displacement of the wire from its equilibrium position. Because the sensor can only detect small motion, it was mounted at $\xi=0.035$, where the motion was expected to be small.

The string was made of a solid wire core of diameter 0.31 mm. Wire windings around this core increased the net string diameter to 2.31 mm. Because the inner core was primarily responsible for sustaining the axial tension (the windings are expected to take up very little of the axial load), the axial rigidity EA was calculated using only the inner core area. An axial tension of $P=45$ N was applied by mounting the left end of the string and using a spring scale (k) to deliver the load to the right end. With this load applied, the right end was clamped down.

The parameters of the system under consideration include the string length $L=0.6$ m; the load applied at $\xi_0=0.933$; the knife-edge restraint located at $\xi_r=0.3$; the displacement sensor at the right end of the string at $\xi_s=0.035$. The wire has a Young's modulus of $E=205\times10^3$ MPa and a mass per unit length of $m=0.020\,95$ kg/m^2. Using the log–dec method, the damping ratio was found to be $\zeta=0.005$. Under these conditions, the fundamental linear natural frequency is $\omega_1=38.6$ Hz.

B. Experimental procedure

There were two experimental goals. The first was to determine the nonimpacting amplitude-frequency response diagram. This would validate the governing equations in the freeplay region. The second goal involved measuring the parameter combinations of the forcing amplitude and driving frequency (F,ω) that led to the initiation of impacts. The procedures for obtaining the necessary data are outlined below.

For the first series of tests, the system was setup as described in the preceding section, but with the knife-edge restraint removed. A sinusoidal excitation was applied to the wire and the frequency was swept in order to determine experimentally the natural frequency. Having completed this, the excitation frequency was then set at 40% of the first natural frequency. The system was driven at this frequency for approximately 30 s to ensure transients had decayed. The voltage from the displacement sensor was then read by a LabVIEW data acquisition program, which recorded the peak-to-peak displacement of the string at the sensor. The excitation frequency was incremented by 1 Hz and the procedure was carried out again. This process was continued until the frequency reached approximately $\Omega=1.4$. In an attempt to capture any dramatic hysteresis, the entire procedure was repeated, starting at a frequency of $\Omega=1.4$ and gradually decreasing through resonance.

The second series of tests involved predicting the parameter combinations (F,ω) that correspond to the transition from no-impact to impact. To accomplish this, the displace-

ment sensor was removed and the knife-edge amplitude restraint was attached to the system. The positive terminal of a DC power supply was attached to the right end of the string, which was hanging through the end support (see Fig. 3). The negative terminal of that same power supply was connected to a light bulb, which was also in electrical contact with the amplitude restraint. If the vibration caused the string to contact the restraint, the circuit would be completed and the light would blink. This closed circuit was also connected to the LabVIEW software, which recorded the first incidence of contact. To develop the required parameter plot, the frequency was fixed and the forcing amplitude was increased (quasistatically) until contact was detected. The force was turned down and the frequency was incremented. After transients died out, the force was gradually increased again until contact was detected. Repeating this process, gives the required parameter diagram.

V. PARAMETER STUDY—INITIATION OF GRAZING

Consider gradually increasing the excitation frequency from a small value. As the first natural frequency is approached, the response amplitude at ξ_r will grow until it eventually equals the gap separation $\bar{\sigma}$. At the peak of this motion, the string *grazes* the knife edge. This zero velocity impact can lead to a variety of post-grazing responses as the frequency is increased; this will be demonstrated in Sec. VI. As a result, it would prove useful to know *a priori* what combinations of the forcing amplitude and frequency lead to grazing.

Grazing occurs when the response amplitude at ξ_r equals to the gap distance $\bar{\sigma}$. These parameter combinations are found using two methods: (i) a linear analysis for small gap separations where the response amplitude need not be large for impact and (ii) a multiple scales perturbation analysis for moderate gap separations, where the motion is weakly nonlinear.

A. Linear motion

If it is assumed that the displacement is less than one diameter, $\bar{\sigma}<\mathcal{O}(d)$, it is reasonably safe to assume that the motion is nearly linear. For simplicity, it is also assumed that only one mode (the ith) participates. Under these assumptions, the nonlinear terms are eliminated from Eq. (8) and only the ith equation of motion remains. Letting the amplitude $|V(\xi_r)|$ equal $\bar{\sigma}$ gives the grazing condition

$$\frac{2\sin(i\pi\xi_r)}{\pi^2}\frac{F}{P}=\frac{\bar{\sigma}}{\sin(i\pi\xi_r)}\sqrt{[i^2-\Omega^2]^2+[2\zeta\Omega]^2}. \tag{9}$$

It is important to recognize that the actual deflection of the string is made up of the sum of all of the modes. Hence, this one-mode-at-a-time approach does not give a completely accurate picture of the motion, since modes may sum constructively or destructively at different locations. Nonetheless, near the ith resonant frequency, these results should prove satisfactory since the ith mode will dominate the response.

B. Nonlinear motion: A perturbation analysis

The method of multiple time scales is used to obtain the response amplitude of the string in the free-play region. Again, a single mode approach is taken. The analysis presented here is limited to first nonlinear order, though higher order solutions could easily be found. To begin, the equation of motion is rescaled. Specifically, the modal amplitude is recast as $a_i=\epsilon^{1/2}A_i$ which leads to

$$\ddot{A}_i+\beta\dot{A}_i+i^2A_i+k\epsilon A_i^3=\epsilon^{-1/2}\mathcal{F}\sin(\Omega\tau), \tag{10}$$

where ϵ is a small positive parameter, β is a damping coefficient,

$$\mathcal{F}=\frac{2\sin(i\pi\xi_r)}{\pi^2}\frac{F}{P}$$

is a nondimensional forcing amplitude [see Eqs. (8) and (9)], and

$$k=\frac{EA}{P}\frac{(i\pi)^4}{4}$$

is the coefficient to the cubic nonlinearity [see Eq. (8)]. Two new time scales are also introduced,

$$T_n=\epsilon^n\Omega\tau,\quad n=0,1. \tag{11}$$

T_0 is the fast time scale and T_1 is a slow time scale that captures the effects of damping, nonlinearity, and the external excitation. Derivative operators on the original time scale τ may be expressed in terms of the derivatives on the new time scales as

$$\frac{d}{d\tau}=\Omega(D_0+\epsilon D_1+\cdots), \tag{12}$$

$$\frac{d^2}{d\tau^2}=\Omega^2(D_0^2+2\epsilon D_0D_1+\cdots), \tag{13}$$

where D_i is a derivative operator on the ith time scale. Next, the rescaled modal amplitude is expressed to first nonlinear order as a uniform expansion in the new time scales,

$$A_i=\sum_{n=0}^{1}\epsilon^n\alpha_n(T_0,T_1). \tag{14}$$

The excitation amplitude and the damping coefficients are intentionally reordered so that they will appear at the first nonlinear order: $F=\epsilon^{3/2}F_1$ and $\Omega\beta=\epsilon\beta_1$. Finally, only excitation frequencies near the ith nondimensional natural frequency are considered. In other words,

$$\Omega^2=i^2+\epsilon\sigma_1, \tag{15}$$

where σ_1 represents the amount of detuning from the ith resonant frequency. These definitions are substituted into the discretized equation of motion, Eq. (10), and collected into groups with like powers of ϵ. The linear order equation, $\mathcal{O}(\epsilon^0)$, is

$$D_0^2\alpha_0+\alpha_0=0. \tag{16}$$

The solution to Eq. (16) is

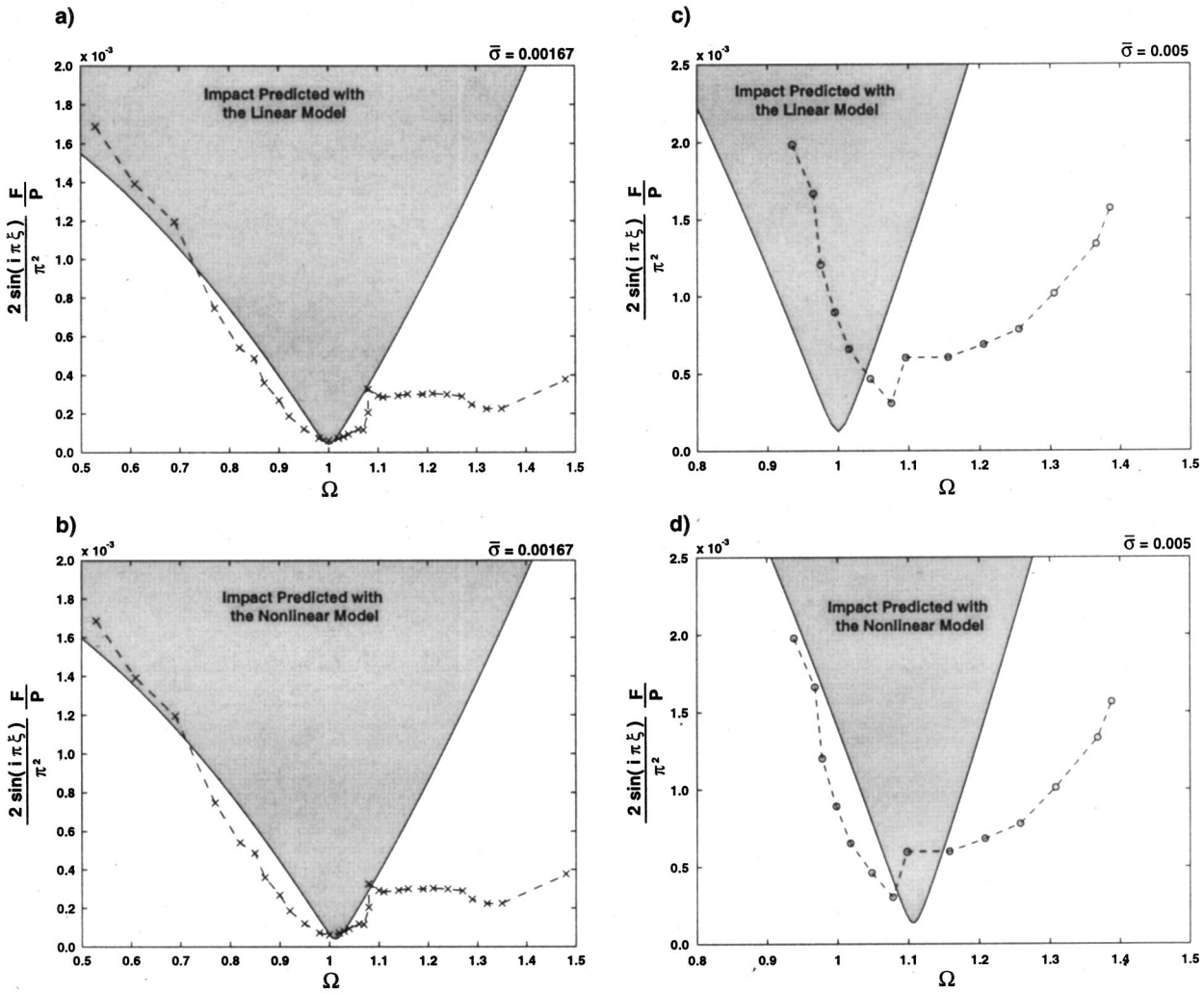

FIG. 4. Parameter combinations leading to the initiation of impacting motion. (a) and (b) Correspond to a small gap size $\bar{\sigma}=0.001\,67$ (linear and nonlinear, respectively), while (c) and (d) correspond to a larger gap size $\bar{\sigma}=0.005$ (linear and nonlinear, respectively).

$$\alpha_0 = C_0(T_1)e^{j\omega t} + \bar{C}_0(T_1)e^{-j\omega t}, \tag{17}$$

where $j=\sqrt{-1}$ is the imaginary number and the overbar denotes the complex conjugate. The unknown coefficient, C_0, is a slowly varying complex amplitude which will be determined at the next order. The first nonlinear order equation, $\mathcal{O}(\epsilon)$, is

$$D_0^2\alpha_1+\alpha_1=\frac{1}{i^2}\Bigg[-\beta_1 D_0\alpha_0-2i^2D_1D_0\alpha_0-k\alpha_0^3 - \sigma_1 D_0^2\alpha_0+\frac{F_1}{2}(e^{jT_0}+e^{-jT_0})\Bigg]. \tag{18}$$

Substituting α_0, as given in Eq. (17), into the right-hand side of Eq. (18) enables a solution for α_1. However, there are terms on the right-hand side that are proportional to $e^{\pm jT_0}$, creating a resonance condition for α_1. To ensure that α_1 remains bounded, these *secular* terms are set to zero. This procedure yields

$$-\beta_1 jC_a-2i^2jD_1C_a-3kC_a^2C_a+\sigma_1C_a+\tfrac{1}{2}F_1=0. \tag{19}$$

For steady motion, the derivative on the T_1 time scale is zero: $D_1C_a=0$. Also, because C_a is complex, it may be expressed in polar form as $C_a=\frac{1}{2}Me^{j\phi}$. Substituting this expression into the secular equation renders two algebraic equations (arising from the real and imaginary parts of the equation) for the amplitude M and the phase ϕ:

$$-\Omega\beta M-F\,\sin(\phi)=0, \tag{20}$$

$$-\tfrac{3}{4}kM^3+(\Omega^2-i^2)M+F\,\cos(\phi)=0. \tag{21}$$

These nonlinear algebraic equations may be solved using a Newton–Raphson solution technique.

These equations may be used in two ways. First, by prescribing the forcing frequency and amplitude, the response may be determined (M and ϕ). Alternatively, the frequency and amplitude may be specified (i.e., M could be set equal to $\bar{\sigma}$), and the necessary force could be determined. It is the second approach which will be used to develop the desired parameter diagrams.

C. Parameter study—Results

Figures 4(a) and (b) show the parameter combinations that lead to impact for a separation of $\bar{\sigma}=0.001\,67$ ($\sigma=1.0$

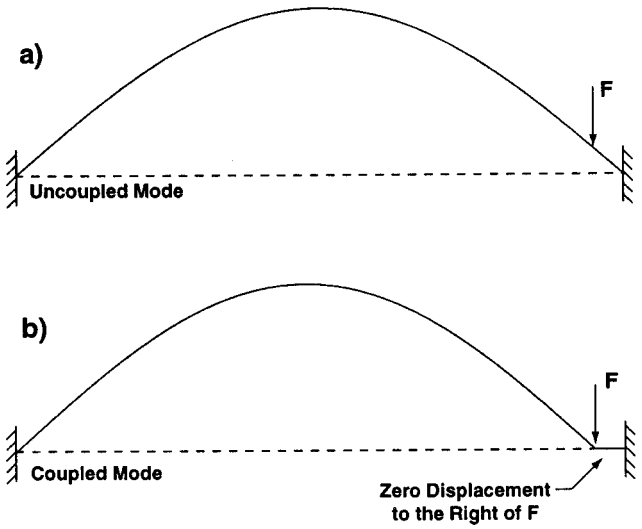

FIG. 5. Two different *first mode* vibration patterns. The first is the traditional first mode. The second has a dead zone to the right of the applied force and is caused by string-shaker coupling.

mm). Experimental results are given by the $\times$ symbols while the linear and perturbation results are given by the solid lines in Figs. 4(a) and (b), respectively. For this small separation size, where linear motion is expected to dominate, both analytical techniques render good predictions below resonance. As the frequency approaches $\Omega=1$, the force required to cause impact decreases because of the amplitude amplification associated with resonance. Above resonance (say, above $\Omega=1.1$), neither predicts impact accurately. This loss of consistency occurs because of shaker-string coupling in the experimental system. This coupling produced another weak resonance; it's mode shape has a node at the point of applications of the force and zero deflection to the right. This is sketched in Fig. 5(b). However, this mode is not resonant in the typical sense. There was not a peak in the amplitude as the frequency was changed. Rather, it's amplitude stayed roughly constant over a range of frequencies ($1.1 \leqslant \Omega \leqslant 1.5$).

For a slightly larger gap size, $\bar{\sigma}=0.005$ ($\sigma=3$ mm), the parameter diagrams are shown in Figs. 4(c) and (d). The linear analysis [Fig. 4(c)] predicts that the minimum required force level occurs at the linear resonance $\Omega=1$. But the minimum for the experimental results occurs at a higher frequency and at a higher force level. This may be explained as follows: the larger gap separation suggests that larger (nonlinear) oscillations must take place for impact to occur. The hardening characteristics of the string system imply that more force will be required to reach this amplitude (since the system has stiffened) and that the maximum amplitude is achieved above the linear resonance (see Fig. 6 in the next section). The perturbation results [Fig. 4(d)] clearly demonstrate these trends, as the minimum has shifted up and to the right of $\Omega=1$. As with the small gap separation tests, agreement between theory and experiments breaks down at higher frequencies as the weak shaker-string coupled resonance begins to take effect.

VI. RESPONSE CHARACTERISTICS

A. Vibrations in the absence of the amplitude restraint

In the absence of the amplitude restraint, the system returns to the classic nonlinear string. Figure 6 shows both the experimental and analytical amplitude versus frequency response diagram for the string, under an excitation amplitude of 1 N. The $\bigcirc$ $(+)$ symbols indicate an increasing (decreasing) frequency sweep. The solid lines were generated using the perturbation solution. The experiments and analysis show reasonable qualitative and quantitative agreement. In terms of their qualitative trends, both clearly show that the response diagram bends to the right of the traditional linear (upright) response diagram, indicating a hardening system.

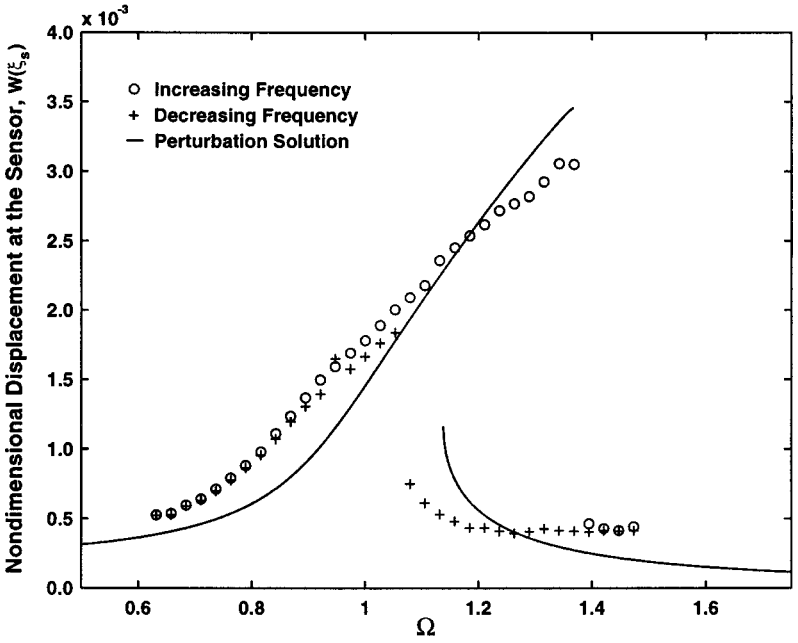

FIG. 6. The amplitude versus excitation frequency response diagram in the absence of impacts. Results from the experiment and the perturbation analysis are shown.

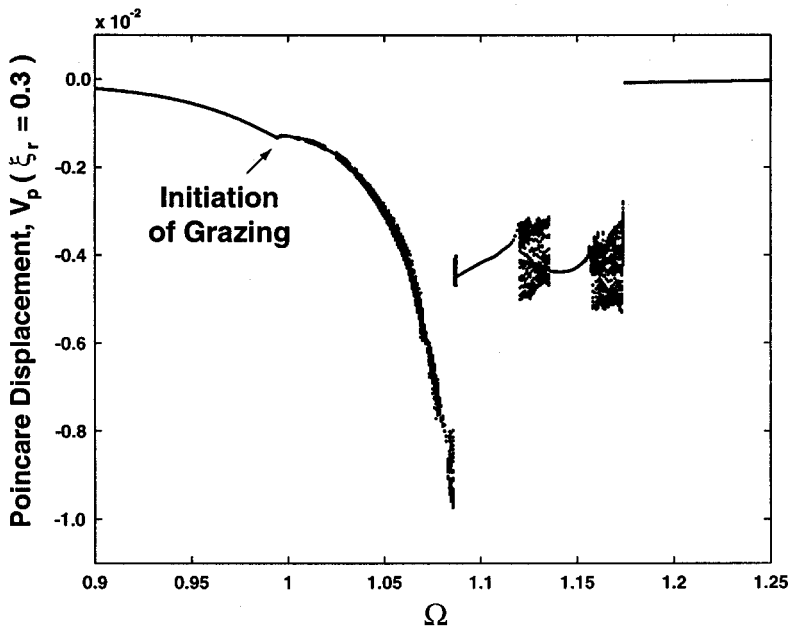

FIG. 7. A numerically generated amplitude versus excitation frequency response diagram, which includes impacts. Note the apparently chaotic portions as well as the periodic windows in the response.

Furthermore, both demonstrate an obvious dynamic hysteresis region, in which multiple periodic solutions coexist. Quantitatively, the amplitudes are close together over a range of frequencies. Also, the bifurcation frequencies, which produce the jump-in-amplitude, show reasonable agreement—though agreement is better for the jump down than for the jump up.

B. Impacting response behavior

The remainder of the results presented here are based purely on the numerical simulation of the equation of motion. Although attempts were made to obtain experimental results, it became impossible to maintain a constant force amplitude due to the coupling between the string and the shaker. This coupling distorted the shape and amplitude of the input force wave form, and became stronger as the response grew and became less periodic. Hence, any agreement between the theoretical and experimental results would have been mere coincidence.

Figure 7 shows the steady-state string response as a function of the nondimensional excitation frequency. The response is taken at $\xi=\xi_r=0.3$ and is Poincaré sampled (once per forcing period) at zero phase relative to the excitation. At a frequency ratio of $\Omega=0.9$ the string is not contacting the knife edge and it is undergoing a period-one response. As the frequency ratio is increased, grazing occurs at $\Omega=0.9936$. Immediately thereafter, the response ceases to be a simple, single frequency period-one oscillation. Higher period motion and chaos ensue (as will be discussed, shortly). However, several period-one windows emerge, notably in the ranges $1.088<\Omega<1.12$ and $1.1360<\Omega<1.155$. At still higher frequencies, the response jumps down to a simple periodic motion.

Figure 8 shows some of the individual responses depicted in the response diagram. Figures 8(a), (b), and (c) correspond to $\Omega=0.9936$, which is the grazing frequency where impacts are initiated. The time response is shown in Fig. 8(a) and appears to be a period one oscillation. Figure 8(b) shows the associated velocity versus displacement trajectory (the pseudo-phase plane) for 40 orbits. This diagram, more than any other, clearly demonstrates the idea of grazing. The trajectory *grazes* the amplitude restraint [at $V(\xi_r)=\bar{\sigma}=5\times10^{-3}$] with zero velocity before moving away. The associated power spectrum is shown in Fig. 8(c) and indicates that this response is dominated by a single frequency.

Figures 8(d), (e), and (f) give the response at ξ_r inside one of the periodic windows: $\Omega=1.100\,37$. In Figs. 8(d) and (e), the displacement never exceeds $\bar{\sigma}=0.005$, as required by the stiff impact condition. Again, 40 cycles are shown in Fig. 8(e), demonstrating the complicated, yet periodic, character of the response. The power spectrum indicates that this periodic impacting motion has many frequencies participating.

Finally, Figs. 8(g), (h), and (i) show a nonperiodic response at $\Omega=1.124\,87$. While the gross motion of Fig. 8(g) looks somewhat periodic, Fig. 8(h) clearly shows that the motion is nonperiodic. The power spectrum of this response, Fig. 8(i), has the broadband characteristics commonly associated with chaos.

One hallmark of a chaotic oscillation is that the phase space experiences both folding and stretching—giving the attractor a fractal structure. This can be described by the exponential divergence of nearby trajectories over short times in the phase space. The exponential divergence accounts for the stretching of the attractor. The expression ''for short times'' implies that these trajectories do not wander off indefinitely, since the attractor must be bounded; this accounts for the folding. Hence, quantifying this divergence (or, alternately, convergence) is one of the few definitive tests for chaotic motion. This is done in terms of Lyapunov exponents.

The technique for computing the Lyapunov exponents is described briefly here. A more thorough discussion may be found in the papers by Wolf *et al.*[14] and Abarbanel.[15] To begin, the system is integrated to steady state using the full

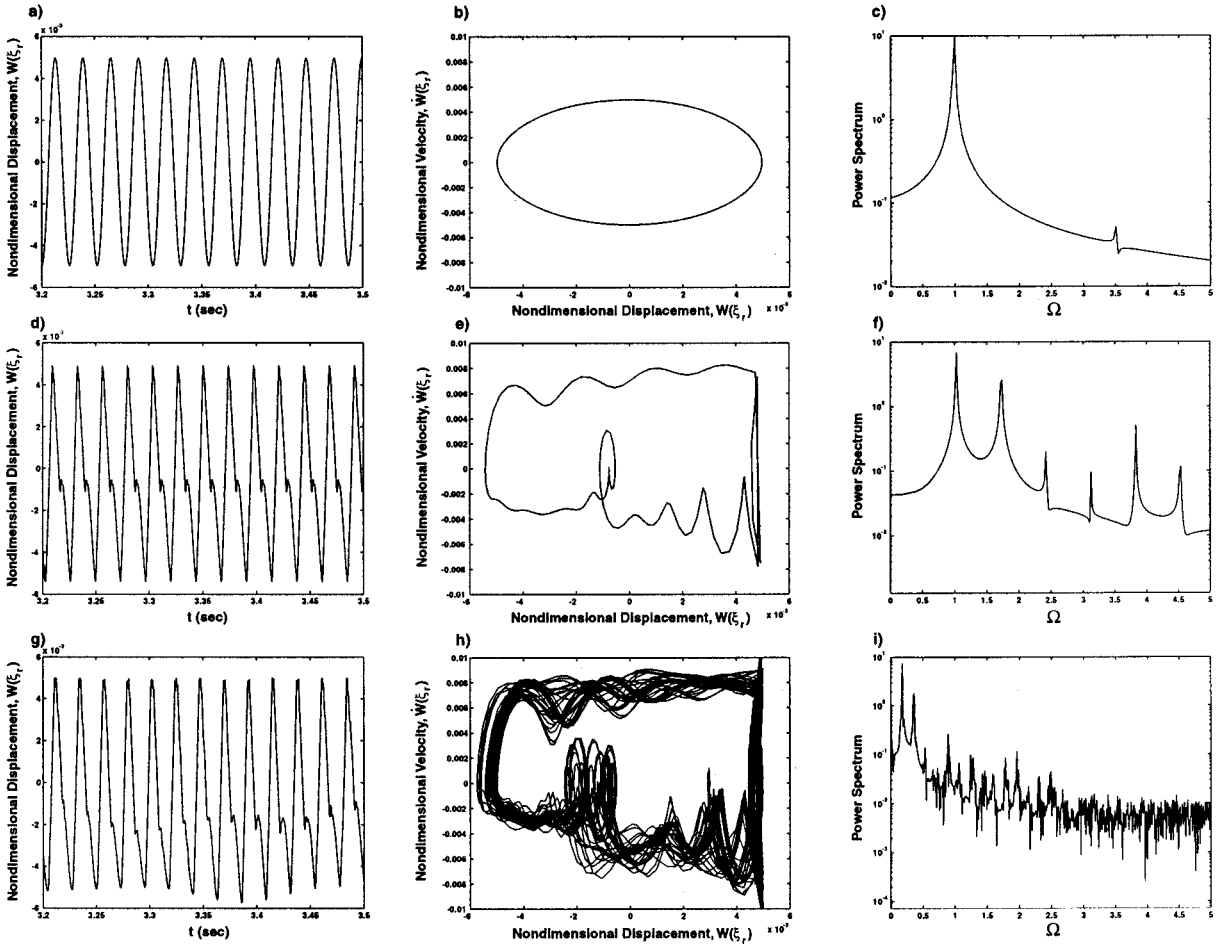

FIG. 8. Three numerical responses are shown. (a)–(c) Show the grazing response, where the trajectory impacts the restraint with zero velocity $-\Omega=0.9936$. (d)–(f) Is the response in one of the periodic windows, $\Omega=1.00\,37$. (g)–(i) Shows the aperiodic (chaotic) response, $\Omega=1.124\,87$.

nonlinear equations of motion, Eq. (8). Again, 20 modes have been incorporated, meaning that the phase space is 40 dimensional. Integration is temporarily stopped and the current time is defined as t_0. Forty initial conditions are prescribed $\delta(t_0)$ away from the steady state solution—one along each of the phase space directions. This forms a 40-dimensional hypersphere, whose center is the actual trajectory of the string (dubbed the *fiducial* trajectory). Integration is resumed, with the fiducial trajectory being integrated with the full nonlinear equations. The equations governing the

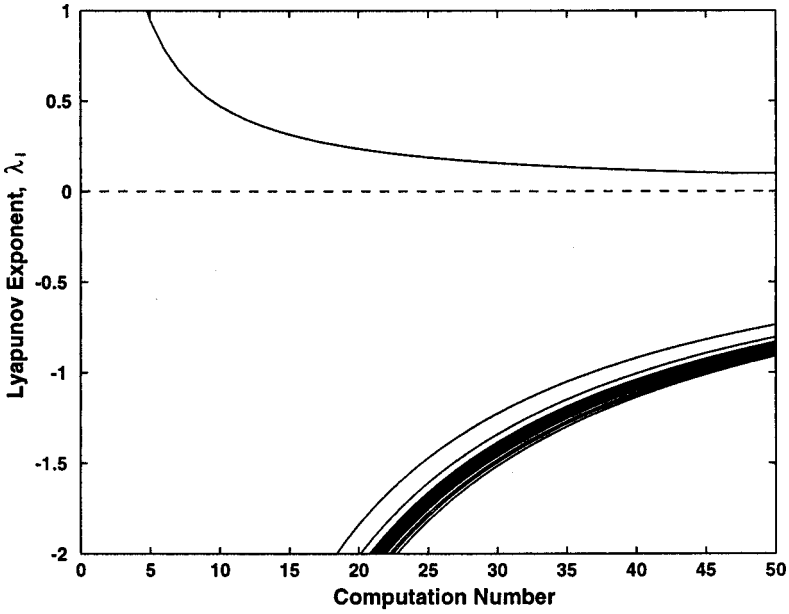

FIG. 9. The Lyapunov spectrum for the response at $\Omega=1.124\,87$ [see Figs. 8(g)–(i)].

motion of the perturbed trajectories are linearized about the fiducial. As the sphere of initial conditions deforms under the action of the equations of motion, the relative stretching or compression of these axes may be computed by the formula

$$\lambda_i = \frac{1}{t - t_0} \ln\left(\frac{\delta_i(t)}{\delta(t_0)} \right). \tag{22}$$

These are the Lyapunov exponents for the motion. Of course, the exponents are calculated a number of times and averaged. This simply allows the results to be averaged over the attractor to give a more representative measure of the divergence.

The Lyapunov exponents have been calculated for the response $\Omega = 1.124\,87$ [Figs. 8(g)–(i)] and are shown in Fig. 9. Here the 40 exponents are plotted as a function of the number of times the exponents are calculated. This figure shows that 39 are negative and one is positive with a value of 0.945. As a result, the aperiodic response is confirmed to be chaotic. But since only one exponent is positive and it is small, it is evident that the divergence is not very strong and the motion may be classified as weakly chaotic. This is consistent with the rather periodic looking response shown in Fig. 8(g).

VII. CONCLUSIONS

This paper details some new results on the vibrations of a periodically excited string subject to an amplitude restraint. The amplitude restraint sets up an impacting condition, which provides a discontinuity in the stiffness. The principle focus of this work is to examine the grazing instability and the post-bifurcation response. First, this involves describing approximately the excitation parameter combinations (F, Ω) that lead to grazing. The response is then considered at a variety of excitation frequencies. It is shown that the grazing event leads to a nonperiodic response at higher frequencies, though periodic windows do appear in some frequency ranges. Typical responses are examined using its time response, pseudo-phase plane projection, and the power spectrum. These responses ranged from the grazing incidence, to periodic impacts, to chaos. In the case of chaos, the response was confirmed by a Lyapunov exponent calculation. In all, these results shed light on some of the complicated response behavior that occurs in a periodically excited string subject to an amplitude restraint.

ACKNOWLEDGMENTS

The support of the National Science Foundation (Grant No. CMS-9625319) is gratefully acknowledged.

[1] F. Pfeiffer and A. Kunert, "Rattling models from deterministic to stochastic processes," Nonlinear Dyn. **1**, 63–74 (1990).
[2] J. M. T. Thompson, "Complex dynamics of compliant off-shore structures," Proc. R. Soc. London, Ser. A **387**, 407–427 (1983).
[3] P. V. Bayly and L. N. Virgin, "An experimental study of an impacting pendulum," J. Sound Vib. **164**, 364–374 (1993).
[4] P. J. Holmes, "The dynamics of repeated impact with a sinusoidally vibrating table," J. Sound Vib. **84**, 173–189 (1982).
[5] F. C. Moon and S. W. Shaw, "Chaotic vibrations of a beam with nonlinear boundary conditions," Int. J. Non-Linear Mech. **18**, 465–477 (1983).
[6] S. W. Shaw, "Forced vibrations of a beam with one-sided amplitude constrain: theory and experiment," J. Sound Vib. **99**, 199–212 (1985).
[7] T. Watanabe, "Forced vibrations of continuous system with non-linear boundary condition," J. Mech. Des. **100**, 487–491 (1978).
[8] S. Foale and S. R. Bishop, "Bifurcations in impact oscillators: Theory and experiments," in *Nonlinearity and Chaos in Engineering Dynamics*, edited by J. M. T. Thompson and S. R. Bishop (Wiley, New York, 1994).
[9] A. R. Champneys and P. J. McKenna, "On solitary waves of a piecewise linear suspended beam model," Nonlinearity **10**, 1763–1782 (1997).
[10] C. Budd, F. Dux, and A. Cliffe, "The effect of frequency and clearance variations on single-degree-of-freedom impact oscillators," J. Sound Vib. **184**, 475–502 (1995).
[11] A. B. Nordmark, "Non-periodic motion caused by grazing incidence on an impact oscillator," J. Sound Vib. **145**, 279–297 (1991).
[12] R. Narasimha, "Nonlinear vibration of an elastic string," J. Sound Vib. **8**, 134–146 (1968).
[13] M. Henon, "On the numerical computation of Poincaré maps," Physica D **5**, 412–414 (1982).
[14] A. Wolf, J. B. Swift, H. L. Swinney, and J. A. Vastano, "Determining Lyapunov exponents from a time series," Physica D **16**, 285–317 (1985).
[15] H. D. I. Abarbanel, "The analysis of observed chaotic data in physical systems," Rev. Mod. Phys. **65**, 1331–1390 (1993).

Scattering and active acoustic control from a submerged spherical shell

Clyde Scandrett
Naval Postgraduate School, Monterey, California 93943

(Received 2 August 2001; revised 24 October 2001; accepted 29 October 2001)

This paper is concerned with the scattering from a submerged (heavy fluid) bilaminate spherical shell composed of an outer layer of steel, and an inner layer of radially polarized piezoelectric material. The methodology used includes separation formulas for the stresses and displacements, which in turn are used (coupled with spherical harmonics) to reduce the governing equations to linear systems of ordinary differential equations. This technique uses the full equations of elasticity rather than any of the various thin-shell approximations in determining the axisymmetric scattering from a shell, normal modes of vibration for the shell, as well as voltages necessary for annihilation of a scattered pressure due to insonification of the shell by an incident plane wave. © *2002 Acoustical Society of America.* [DOI: 10.1121/1.1428749]

PACS numbers: 43.40.Fz, 43.40.Rj, 43.40.Vn [EGW]

I. INTRODUCTION

Piezoelectric materials have for some time been important in the study of transducers, and of particular interest to the Navy in the area of underwater acoustics.[1] Use of piezoelectric materials in applications involving active acoustic control of structures has more recently become an important area of research,[2–4] and while there has been much written on the subject of active acoustic control for light fluid-loaded structures, there has been decidedly fewer publications regarding active control of structures constrained by a ''heavy'' fluid.[5,6]

In a recent article, Chen[7] considered the free vibrations of laminated piezoelectric hollow spheres by applying a normal-modes methodology involving a decomposition of the stress and displacement fields referred to as the ''state-space'' method. In addition to spherical geometries considered here, the state-space methodology has been used to find modes of vibrations for circular and rectangular plates as well.[8,9] The decomposition of field variables, as it applies to spherical geometry originated with the work of Hu.[10] In most of the papers that apply state-space methods, *in vacuo* natural frequencies are the sought-after quantities. An exception is the paper by Ding and Chen,[11] which reports on the natural frequencies for an elastic spherically isotropic hollow sphere, submerged in a heavy fluid. That paper does not, however, consider the scattering problem, nor is the issue of applying a piezoelectric layer for the purpose of active acoustic control addressed.

In many ways, the state-space method used by Chen is reminiscent of wave-number integration techniques used for acoustic wave propagation in marine layers[12] and the Thomson–Haskell method[13] originally used in seismology. In each of these methods, a system of first-order differential equations is derived with thickness coordinate as the independent variable, while dependent variables are combinations of stresses and displacements. Unlike ''flat,'' layered media, which may be comprised of isotropic or anisotropic elastic materials for which constant coefficient Stroh matrices[14] are produced, the spherical geometry of the present problem introduces a matrix with variable coefficients. Furthermore, for the flat, layered media, the lateral extent of the layers is usually taken to be infinite with the result that all dependent field variables are represented by plane waves that have equivalent functional dependence in terms of the lateral independent variables in order to phase match across layers. With this assumption, an ordinary differential equation with constant coefficients results for each layer. For the spherically layered structure, expanding all field variables in terms of spherical harmonics eliminates lateral variable dependence. The primary difference between state-space methods and other matrix techniques is the decomposition of field variables into two groups prior to the application of normal modes. For the problem addressed in this report, this decomposition is particularly useful, since in calculations involving the scattering and radiation of acoustic pressures into the fluid medium encompassing the sphere, only one of the two ''groups'' need be considered.

The paper is summarized as follows. The governing equations are derived in the next section, followed by a short description of the solution methods and comparisons to previously reported results. Determinations of the scattering properties for the spherical shell as well as modal voltage potentials necessary to actively cancel scattered pressures from the shell are then given. Numerical results applied to the particular case of a bilaminate sphere are reported.

II. GOVERNING EQUATIONS

Governing equations for an elastic spherical shell are given below. From these, it is a relatively simple matter to include the piezoelectric effects as additive terms to the governing equations for a piezoelectric shell. Ultimately, both will be needed in the analysis of a bilaminate shell. Using abbreviated subscripts,[15] strain variables in spherical coordinates are

$$\mathbf{S}=\begin{bmatrix} S_{rr} \\ S_{\theta\theta} \\ S_{\phi\phi} \\ 2S_{\theta\phi} \\ 2S_{r\phi} \\ 2S_{r\theta} \end{bmatrix}$$

$$=\begin{bmatrix} \partial w/\partial r \\ w/r+(1/r)\partial u/\partial\theta \\ w/r+(\cot\theta/r)u+(1/r\sin\theta)\partial v/\partial\phi \\ (1/r\sin\theta)\partial u/\partial\phi+(1/r)\partial v/\partial\theta-(\cot\theta/r)v \\ (1/r\sin\theta)\partial w/\partial v+\partial v/\partial r-(1/r)v \\ (1/r)\partial w/\partial\theta+\partial u/\partial r-(1/r)u \end{bmatrix}, \quad (1)$$

where w, u, and v are displacements in the radial, longitudinal, and latitudinal directions, respectively.

The stress/strain relationship for an isotropic homogeneous elastic substance is given by

$$\begin{aligned} T_{rr}&=(\lambda+2\mu)S_{rr}+\lambda(S_{\theta\theta}+S_{\phi\phi}),\\ T_{\theta\theta}&=(\lambda+2\mu)S_{\theta\theta}+\lambda(S_{rr}+S_{\phi\phi}),\\ T_{\phi\phi}&=(\lambda+2\mu)S_{\phi\phi}+\lambda(S_{\theta\theta}+S_{rr}),\\ T_{\theta\phi}&=2\mu S_{\theta\phi}, \quad T_{r\phi}=2\mu S_{r\phi}, \quad T_{r\theta}=2\mu S_{r\theta}, \end{aligned} \quad (2)$$

while the governing equilibrium equations are

$$\nabla\cdot\mathbf{T}=\rho\frac{\partial^2}{\partial t^2}\begin{bmatrix} w \\ u \\ v \end{bmatrix}. \quad (3)$$

Introducing new dependent variables related to the stress

$$\boldsymbol{\sigma}=\mathbf{rT}, \quad (4)$$

and multiplying the equations of motion by r^2, they become

$$\begin{aligned} &\nabla_2\sigma_{rr}+\sigma_{rr}-(\sigma_{\theta\theta}+\sigma_{\phi\phi})+\frac{1}{\sin\theta}\frac{\partial\sigma_{r\phi}}{\partial\phi}+\cot\theta\sigma_{r\theta}\\ &\quad+\frac{\partial\sigma_{r\theta}}{\partial\theta}=\rho_e r^2\frac{\partial^2 w}{\partial t^2}\\ &\nabla_2\sigma_{r\theta}+2\sigma_{r\theta}+\cot\theta(\sigma_{\theta\theta}-\sigma_{\phi\phi})+\frac{\partial\sigma_{\theta\theta}}{\partial\theta}+\frac{1}{\sin\theta}\frac{\partial\sigma_{\theta\phi}}{\partial\phi}\\ &\quad=\rho_e r^2\frac{\partial^2 u}{\partial t^2}\\ &\nabla_2\sigma_{r\phi}+2\sigma_{r\phi}+\frac{1}{\sin\theta}\frac{\partial\sigma_{\phi\phi}}{\partial\phi}+2\cot\theta\sigma_{\theta\phi}+\frac{\partial\sigma_{\theta\phi}}{\partial\theta}\\ &\quad=\rho_e r^2\frac{\partial^2 v}{\partial t^2}, \end{aligned} \quad (5)$$

where $\nabla_2=r(\partial/\partial r)$.

A similar set of equations can be derived for the piezoelectric shell. The strain elastic equations and the divergence of the stress are equivalent, but the stress quantities must now be amended due to the fact that the material is radially anisotropic, and because the additional piezoelectric effect must be accounted for.

For radial polarizations of the piezoelectric layer, one can introduce a Bond matrix to transform the constitutive relationships from those of a flat piezoelectric layer with polarization in the z direction, to a radial polarization. Applying these transformations, the piezoelectric, dielectric, and stiffness matrices for a 6-mm crystal (PZT) can be determined. For the piezoelectric equations,[15] using stress and electric displacements as dependent variables, total stresses acting on the piezoelectric material are

$$\begin{aligned} T_{rr}&=c_{33}S_{rr}+c_{13}(S_{\theta\theta}+S_{\phi\phi})+e_{33}\frac{\partial\Phi}{\partial r},\\ T_{\theta\theta}&=c_{11}S_{\theta\theta}+c_{13}S_{rr}+c_{12}S_{\phi\phi}+e_{31}\frac{\partial\Phi}{\partial r},\\ T_{\phi\phi}&=c_{11}S_{\phi\phi}+c_{12}S_{\theta\theta}+c_{13}S_{rr}+e_{31}\frac{\partial\Phi}{\partial r},\\ T_{\theta\phi}&=2c_{66}S_{\theta\phi},\\ T_{r\phi}&=2c_{44}S_{r\phi}+e_{15}\frac{1}{r\sin\theta}\frac{\partial\Phi}{\partial\phi},\\ T_{r\theta}&=2c_{44}S_{r\theta}+e_{15}\frac{1}{r}\frac{\partial\Phi}{\partial\theta}, \end{aligned} \quad (6)$$

where the electric field has been represented by the negative gradient of an electric potential under the quasistatic approximation[15] ($\mathbf{E}=-\nabla\Phi$). The electric displacement vector in terms of the strains and electric potential function of the new coordinate system is

$$\begin{aligned} D_r&=e_{33}S_{rr}+e_{31}(S_{\theta\theta}+S_{\phi\phi})-\varepsilon_3\frac{\partial\Phi}{\partial r},\\ D_\phi&=2e_{15}S_{r\phi}-\varepsilon_1\frac{1}{r\sin\theta}\frac{\partial\Phi}{\partial\phi},\\ D_\theta&=2e_{15}S_{r\theta}-\varepsilon_1\frac{1}{r}\frac{\partial\Phi}{\partial\theta}. \end{aligned} \quad (7)$$

The governing equation for the electric displacement given the quasistatic approximation is that the divergence of the electric displacement vanishes

$$\frac{1}{r^2}\frac{\partial}{\partial r}\left(r^2\frac{\partial D_r}{\partial r}\right)+\frac{1}{r\sin\theta}\frac{\partial}{\partial\theta}(\sin\theta D_\theta)+\frac{1}{r\sin\theta}\frac{\partial D_\phi}{\partial\phi}=0. \quad (8)$$

As was done for the isotropic, homogeneous elastic equations, the equations of motion (and electric displacement equation) are scaled by r^2 and new dependent variables for the stress and electric displacement are introduced

$$\boldsymbol{\tau}=\mathbf{rT} \text{ and } \boldsymbol{\delta}=\mathbf{rD}. \quad (9)$$

The equations of motion for the piezoelectric layer can then be written

$$\nabla_2\tau_{rr}+\tau_{rr}-(\tau_{\theta\theta}+\tau_{\phi\phi})+\frac{1}{\sin\theta}\frac{\partial\tau_{r\phi}}{\partial\phi}+\cot\theta\tau_{r\theta}+\frac{\partial\tau_{r\theta}}{\partial\theta}$$
$$=\rho_p r^2\frac{\partial^2 w_p}{\partial t^2}$$
$$\nabla_2\tau_{r\theta}+2\tau_{r\theta}+\cot\theta(\tau_{\theta\theta}-\tau_{\phi\phi})+\frac{\partial\tau_{\theta\theta}}{\partial\theta}+\frac{1}{\sin\theta}\frac{\partial\tau_{\theta\phi}}{\partial\phi}$$
$$=\rho_p r^2\frac{\partial^2 u_p}{\partial t^2} \tag{10}$$
$$f\nabla_2\tau_{r\phi}+2\tau_{r\phi}+\frac{1}{\sin\theta}\frac{\partial\tau_{\phi\phi}}{\partial\phi}+2\cot\theta\tau_{\theta\phi}+\frac{\partial\tau_{\theta\phi}}{\partial\theta}$$
$$=\rho_p r^2\frac{\partial^2 v_p}{\partial t^2}$$
$$\nabla_2\delta_r+\delta_r+\frac{\partial\delta_\theta}{\partial\theta}+\cot\theta\delta_\theta+\frac{1}{\sin\theta}\frac{\partial\delta_\phi}{\partial\phi}=0.$$

III. SEPARATION OF VARIABLES USING POTENTIAL FUNCTIONS AND THE STATE-SPACE METHOD

For both the elastic and piezoelectric layers the same procedure of ''separation'' will be performed. Hu[10] was evidently the first to employ the separation method, with other researchers more recently adopting and modifying the procedure for special cases.[7,16] In this technique, new displacement and stress potentials are introduced in order to reduce the order and coupling of the governing equations. In Hu's original paper, displacements were separated to produce two sets, one set with zero dilatation and zero radial displacement, and a second with the property that the radial component of the curl of the displacements is zero. In this paper, the application of the state-space method closely follows that found in Chen's paper.[7] Displacement and stress potentials ψ, G, Σ_1, and Σ_2, are introduced in the following fashion:

$$u=-\frac{1}{\sin\theta}\frac{\partial\psi}{\partial\phi}-\frac{\partial G}{\partial\theta},\quad v=-\frac{1}{\sin\theta}\frac{\partial G}{\partial\phi}+\frac{\partial\psi}{\partial\theta},$$
$$\tau_{r\theta}\ \text{ or }\ \sigma_{r\theta}=-\frac{1}{\sin\theta}\frac{\partial\Sigma_1}{\partial\phi}-\frac{\partial\Sigma_2}{\partial\theta}, \tag{11}$$
$$\tau_{r\phi}\ \text{ or }\ \sigma_{r\phi}=-\frac{1}{\sin\theta}\frac{\partial\Sigma_2}{\partial\phi}+\frac{\partial\Sigma_1}{\partial\theta}.$$

Replacing all expressions in the above shear stresses with the new values for the displacements u and v, one obtains the coupled equations for the piezoelectric case

$$\frac{1}{\sin\theta}\frac{\partial A}{\partial\phi}=\frac{\partial B}{\partial\theta},\quad -\frac{1}{\sin\theta}\frac{\partial B}{\partial\phi}=\frac{\partial A}{\partial\theta},$$
$$A=\Sigma_2+c_{44}w-c_{44}\nabla_2 G+c_{44}G+e_{15}\Phi, \tag{12}$$
$$B=\Sigma_1-c_{44}\nabla_2\psi+c_{44}\psi.$$

Choosing A and B to have a common potential function V, as follows:

$$A=\frac{\partial V}{\partial\phi},\quad B=\sin\theta\frac{\partial V}{\partial\theta}\Rightarrow\nabla_1^2 V=0,$$
$$\nabla_1^2=\frac{\partial^2}{\partial\theta^2}+\cot\theta\frac{\partial}{\partial\theta}+\frac{1}{\sin^2\theta}\frac{\partial^2}{\partial\phi^2}, \tag{13}$$

one typically chooses $V=0$, and is left with the two first-order equations

$$\nabla_2 G=\frac{1}{c_{44}}\Sigma_2+w+G+\frac{e_{15}}{c_{44}}\Phi,\quad \nabla_2\psi=\frac{1}{c_{44}}\Sigma_1+\psi. \tag{14}$$

The corresponding elastic equations that result are

$$\nabla_2 G=\frac{1}{\mu}\Sigma_2+w+G,\quad \nabla_2\psi=\frac{1}{\mu}\Sigma_1+\psi. \tag{15}$$

With the above expressions, some of the dependent variables in the original sets of equations can be eliminated. In particular, the stress variables $\tau_{\theta\phi}$, $\tau_{\theta\theta}$, $\tau_{\phi\phi}$ (and the elastic expressions $\sigma_{\theta\phi}$, $\sigma_{\theta\theta}$, $\sigma_{\phi\phi}$) can be rewritten as functions of the new potentials, normal displacement, and electric potential. These intermediate expressions can then be used in the equations for radial components of the electric displacement and stress. For the elastic case there is no electric potential, so only one equation is produced by the substitution.

The remaining four equations for the piezoelectric material (three for the elastic material) come from manipulating the equations of motion. The two shear-stress equations of motion are transformed into the familiar coupled system

$$\frac{1}{\sin\theta}\frac{\partial A}{\partial\phi}=-\frac{\partial B}{\partial\theta},\quad \frac{1}{\sin\theta}\frac{\partial B}{\partial\phi}=\frac{\partial A}{\partial\theta},$$
$$A=\nabla_2\Sigma_1+2\Sigma_1+c_{66}(\nabla_1^2\psi+2\psi)-\rho_p r^2\frac{\partial^2\psi}{\partial t^2},$$
$$B=\nabla_2\Sigma_2+2\Sigma_2-\beta\tau_{rr}-k_2\nabla_1^2 G+2c_{66}G-\rho_p r^2\frac{\partial^2 G}{\partial t^2}$$
$$+k_1 w_p-\gamma\delta_r, \tag{16}$$
$$k_1=2(\beta c_{13}+\gamma e_{31})-(c_{11}+c_{12}),$$
$$k_2=\beta c_{13}+\gamma e_{31}-c_{11},$$

whereby in applying the same argument as before, a potential function equal to zero can be hypothesized that ultimately leads to the vanishing of both A and B above, and an equivalent set for the elastic case. The final two equations for the piezoelectric case (one for the elastic case) are straightforward (but tedious) substitutions.

The final sets of equations are consolidated into matrix form, and a time-harmonic frequency dependence of the

form $e^{-i\omega t}$ is assumed throughout. The decoupled sets of equations for the elastic material are given first, followed by those for the piezoelectric material.

$$r\frac{\partial}{\partial r}\begin{bmatrix}\Sigma_1\\ \psi\end{bmatrix}=\begin{bmatrix}-2 & -\mu(\nabla_1^2+2)-r^2\omega^2\rho_e\\ 1/\mu & 1\end{bmatrix}\begin{bmatrix}\Sigma_1\\ \psi\end{bmatrix}$$

$$r\frac{\partial}{\partial r}\begin{bmatrix}\sigma_{rr}\\ \Sigma_2\\ G\\ w\end{bmatrix}=\begin{bmatrix}2\beta_e-1 & \nabla_1^2 & k_{1e}\nabla_1^2 & -2k_{1e}-\rho_e r^2\omega^2\\ \beta_e & -2 & k_{2e}\nabla_1^2-2\mu-\rho_e r^2\omega^2 & -k_{1e}\\ 0 & 1/\mu & 1 & 1\\ 1/\alpha_e & 0 & \beta_e\nabla_1^2 & -2\beta_e\end{bmatrix}\begin{bmatrix}\sigma_{rr}\\ \Sigma_2\\ G\\ w\end{bmatrix} \tag{17}$$

$$r\frac{\partial}{\partial r}\begin{bmatrix}\Sigma_1\\ \psi\end{bmatrix}=\begin{bmatrix}-2 & -c_{66}(\nabla_1^2+2)-r^2\omega^2\rho_p\\ 1/c_{44} & 1\end{bmatrix}\begin{bmatrix}\Sigma_1\\ \psi\end{bmatrix}$$

$$r\frac{\partial}{\partial r}\begin{bmatrix}\tau_{rr}\\ \Sigma_2\\ G\\ w_p\\ \delta_r\\ \Phi\end{bmatrix}=\begin{bmatrix}2\beta-1 & \nabla_1^2 & k_1\nabla_1^2 & -2k_1-\rho_p r^2\omega^2 & 2\gamma & 0\\ \beta & -2 & k_2\nabla_1^2-2c_{66}-\rho_p r^2\omega^2 & -k_1 & \gamma & 0\\ 0 & \dfrac{1}{c_{44}} & 1 & 1 & 0 & \dfrac{e_{15}}{c_{44}}\\ \varepsilon_3/\alpha & 0 & \beta\nabla_1^2 & -2\beta & \dfrac{e_{33}}{\alpha} & 0\\ 0 & \dfrac{e_{15}\nabla_1^2}{c_{44}} & 0 & 0 & -1 & k_3\nabla_1^2\\ e_{33}/\alpha & 0 & \gamma\nabla_1^2 & -2\gamma & -\dfrac{c_{33}}{\alpha} & 0\end{bmatrix}\begin{bmatrix}\tau_{rr}\\ \Sigma_2\\ G\\ w_p\\ \delta_r\\ \Phi\end{bmatrix}. \tag{18}$$

The piezoelectric equations are identical to those reported in Chen's paper,[7] and as done in Chen's work, the dependent variables are scaled

$$\Sigma_{1,n}^s(\xi)=\Sigma_{1,n}(r)/a_1c_{44},$$

$$\psi_n^s(\xi)=\psi_n(r)/a_1,\quad \tau_{rr,n}^s(\xi)=\tau_{rr,n}(r)/a_1c_{44},$$

$$\Sigma_{2,n}^s(\xi)=\Sigma_{2,n}(r)/a_1c_{44},\quad G_n^s(\xi)=G_n(r)/a_1, \tag{19}$$

$$w_n^s(\xi)=w_n(r)/a_1,$$

$$\delta_{r,n}^s(\xi)=\delta_{r,n}(r)/a_1e_{33},\quad \Phi_n^s(\xi)=\Phi_n(r)/a_1e_{33}.$$

Normal modes in the form of spherical harmonics are introduced (with axisymmetry assumed a representative of the expansions is the radial displacement w)

$$w=\sum_{n=0}^{\infty}\sum_{m=-n}^{n}w_{nm}(r)P_n^m(\cos\theta)e^{im\phi}$$

$$\xrightarrow[\text{assuming axisymmetry}]{}\sum_{n=0}^{\infty}w_n(r)P_n(\cos\theta), \tag{20}$$

and the independent variable "r" is altered by the simple substitution

$$r=a_ie^{\xi}\Rightarrow\begin{cases}r\dfrac{d}{dr}=\dfrac{d}{d\xi}\\ r^2=a_i^2e^{2\xi}\end{cases}. \tag{21}$$

Using the property that $\nabla_1^2P_n(\cos\theta)=-LP_n(\cos\theta)$ where $L=n(n+1)$ (and n refers to the particular mode of the expansion), the matrix equations result in systems of ordinary differential equations in the new radial variable ξ.

For the piezoelectric layer, the matrices are

$$\frac{d}{d\xi}\begin{bmatrix}\Sigma_{1,n}^s\\ \psi_n^s\end{bmatrix}=\begin{bmatrix}-2 & c_{66}(L-2)/c_{44}-J_p\\ 1 & 1\end{bmatrix}\begin{bmatrix}\Sigma_{1,n}^s\\ \psi_n^s\end{bmatrix}$$

$$\frac{d}{d\xi}\begin{bmatrix} \tau^s_{rr,n} \\ \Sigma^s_{2,n} \\ G^s_n \\ w^s_{p,n} \\ \delta^s_{r,n} \\ \Phi^s_n \end{bmatrix} = \begin{bmatrix} 2\beta-1 & -L & -\frac{k_1 L}{c_{44}} & -\frac{2k_1}{c_{44}}-J_p & \frac{2\gamma e_{33}}{c_{44}} & 0 \\ \beta & -2 & -\frac{(k_2 L+2c_{66})}{c_{44}}-J_p & -k_1/c_{44} & \frac{\gamma e_{33}}{c_{44}} & 0 \\ 0 & 1 & 1 & 1 & 0 & \frac{e_{15}e_{33}}{c_{44}\varepsilon_3} \\ \frac{\varepsilon_3 c_{44}}{\alpha} & 0 & -\beta L & -2\beta & e^2_{33}/\alpha & 0 \\ 0 & -\frac{e_{15}L}{e_{33}} & 0 & 0 & -1 & -\frac{k_3 L}{\varepsilon_3} \\ \frac{c_{44}\varepsilon_3}{\alpha} & 0 & -\gamma L\varepsilon_3/e_{33} & -\frac{2\gamma\varepsilon_3}{e_{33}} & -\frac{c_{33}\varepsilon_3}{\alpha} & 0 \end{bmatrix} \begin{bmatrix} \tau^s_{rr,n} \\ \Sigma^s_{2,n} \\ G^s_n \\ w^s_{p,n} \\ \delta^s_{r,n} \\ \Phi^s_n \end{bmatrix},$$

$$J_p=\Omega^2 e^{2\xi}, \quad \Omega^2=\omega^2 a^2_{\text{inner}}\rho_p/c_{44}, \tag{22}$$

while the matrices for an outer elastic layer, assuming the inner layer is piezoelectric, are

$$\frac{d}{d\xi}\begin{bmatrix} \Sigma^s_{1,n} \\ \psi^s_n \end{bmatrix} = \begin{bmatrix} -2 & \mu(L-2)/c_{44}-J_e \\ c_{44}/\mu & 1 \end{bmatrix} \begin{bmatrix} \Sigma^s_{1,n} \\ \psi^s_n \end{bmatrix}$$

$$\frac{d}{d\xi}\begin{bmatrix} \sigma^s_{rr,n} \\ \Sigma^s_{2,n} \\ G^s_n \\ w^s_n \end{bmatrix} = \begin{bmatrix} 2\beta_e-1 & -L & -k_{1e}L/c_{44} & -2k_{1e}/c_{44}-J_e \\ \beta_e & -2 & -(k_{2e}L+2\mu)/c_{44}-J_e & -k_{1e}/c_{44} \\ 0 & c_{44}/\mu & 1 & 1 \\ c_{44}/\alpha_e & 0 & -\beta_e L & -2\beta_e \end{bmatrix} \begin{bmatrix} \sigma^s_{rr,n} \\ \Sigma^s_{2,n} \\ G^s_n \\ w^s_n \end{bmatrix} \tag{23}$$

$$J_e=\frac{\rho_e}{\rho_p}\left(\frac{a_{\text{interface}}}{a_{\text{inner}}}\right)^2 \Omega^2 e^{2\xi}.$$

When there are two layers of differing material, only the material parameters for the innermost layer are used for the entire structure, as in Chen.[7] If the material is composed of an isotropic, homogeneous elastic material, the last two variables relevant only for piezoelectric material are absent, and the stiffness parameter c_{44} becomes μ. The distance scale a_1 is the radius of the inner surface of the hollow sphere.

Note that the matrices just developed collapse somewhat when one considers the fundamental mode $n=0$. In this case, the potential functions introduced earlier can have amplitudes equal to zero without loss of generality because only their derivatives are used in the definition of the displacements and stresses. Therefore, for the $n=0$ case, the two piezoelectric matrix equations collapse to a single four-by-four matrix system, and the elastic equations collapse to a single three-by-three matrix system. These are again equivalent to those given in Chen for the purely piezoelectric layer.

IV. FUNDAMENTAL OR PROPAGATOR MATRICES

The matrix formulations are exact within the theory of linear elasticity as they stand, and can be used to solve radiation and scattering problems from structures that enjoy spherical symmetry. What is sought essentially is the propagator matrix for each layer, which can be used to translate a given set of boundary conditions in the form of stresses and displacements at the bottom of a given layer to a second set of values at the top of the layer. Gilbert and Backus introduced the propagator matrix method to seismology as a more general case of the Thomson–Haskell matrix method,[13] but the more generic mathematical name for the special matrix is the fundamental matrix of the system of ordinary differential equations found in standard textbooks.[17]

Chen[7] uses a Neumann series approach in his determination of the fundamental matrices, which is entirely appropriate provided the layer is "thin" ($\xi \ll 1$) relative to the radius of the sphere or layer. An alternative technique is to apply a simple ordinary differential equation (ODE) solver with a constrained tolerance. If the Neumann series approach is adopted, one must split a thick layer into several thin layers, each of which must necessarily find fundamental matrices. A matrix for the entire layer is then found by simply multiplying the matrices of each of the sublayers together. By comparison, use of an ODE solver requires many more function evaluations, but a single fundamental matrix is found without further substructuring of the layer.

To demonstrate the effectiveness of the Neumann series method, while comparing it to the use of an ODE solver, consider the simple, first-order ordinary differential equation that has a form similar to the radially dependent entry from the governing matrices

$$\frac{dy}{d\xi}=e^{2\xi}y, \quad y(0)=1 \Rightarrow y(\xi)=e^{(e^{2\xi}-1)/2}. \tag{24}$$

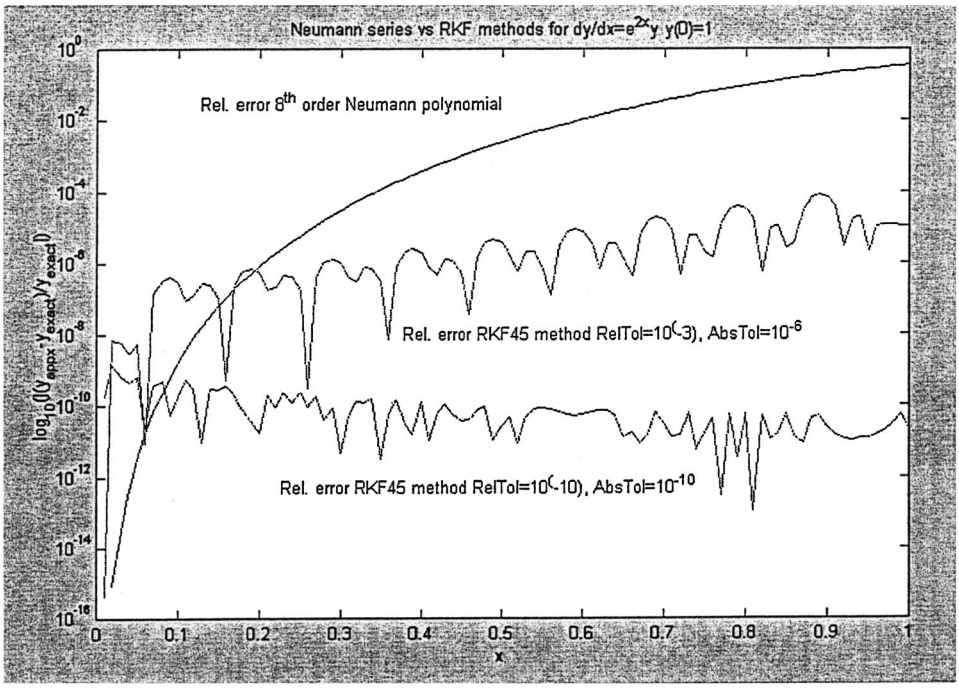

FIG. 1. Comparison of Neumann series and RKF errors for model scalar equation.

In the Neumann series technique, a nine-term expansion is compared with a solution found using a Runge–Kutta–Fehlberg (RKF) algorithm of orders 4 and 5.[18] The standard application of this algorithm in MATLAB, applies a scalar relative error tolerance of 10^{-3}, and a vector absolute error tolerance of 10^{-6}. The tolerance level in MATLAB is set by these two parameters by maintaining the following inequality, where the subscript "i" refers to the particular component of the solution vector:

$$\text{estimated error}_i \leqslant \max\{\text{RelTol}*|y_i|, \text{AbsTol}_i\}.$$

The first few terms of the Neumann series are given below

$$\begin{aligned}
&\mathbf{T}(0)=\mathbf{T}_0,\\
&\mathbf{T}'=N\mathbf{T}\Rightarrow\mathbf{T}'(0)=N(0)\mathbf{T}_0,\\
&\mathbf{T}''=N'\mathbf{T}+N\mathbf{T}'=(N'+NN)\mathbf{T}\\
&\qquad\Rightarrow\mathbf{T}''(0)=(N'(0)+N(0)N(0))\mathbf{T}_0,\\
&\mathbf{T}'''=N''\mathbf{T}+2N'\mathbf{T}'+N\mathbf{T}''\\
&\quad=(N''+2N'N+N(N'+NN))\mathbf{T}\\
&\quad\Rightarrow\mathbf{T}'''(0)=[N''(0)+2N'(0)N(0)+N(0)N'(0)\\
&\qquad+N(0)N(0)N(0)]\mathbf{T}_0,
\end{aligned}\tag{25}$$

and the Neumann series terms so constructed can be used to find values of the dependent variables as a polynomial in the independent variable ξ.

The errors in solving the model first-order scalar differential equation using the ODE solvers are plotted against errors using a nine-term Neumann series over the interval from zero to one on a semilog graph (Fig. 1). For this simple example, one can see that the Neumann series does quite well for short intervals, but as expected its error grows dramatically compared to the two RKF solutions over longer intervals.

In performing the scattering calculations to be considered in subsequent sections of this paper, thicknesses of each layer are on the order of one-hundredths of the radius of the shell, so that either method works well. However, for thicker shells, it may be advisable to use an ODE solver rather than a Neumann series to avoid accuracy issues, and programming difficulties in sublayering thick layers.

In the matter of determining free modes of vibration, the use of applying an ODE solver versus the series solution is considered. Labeling the propagator or fundamental matrices for $n>0$, T_{1n}, and T_{2n}, and the fundamental matrices for $n=0$, T_{10}, and T_{20}, one can find the mechanical resonances of the shell by finding zeros of the real part of certain components or submatrices of the fundamental matrices after application of the appropriate boundary conditions. In the case of an anisotropic elastic or piezoelectric shell, the two independent classes of vibrations correspond to the vanishing of the (1,2) component of T_{1n}, (first class), vanishing of the (1,2) component of T_{20} for the second class $n=0$ case, and for the second class $n>0$ cases (open-circuit modes), the vanishing of the three-by-three determinant

$$\begin{vmatrix} T_{2n,13} & T_{2n,14} & T_{2n,16} \\ T_{2n,23} & T_{2n,24} & T_{2n,26} \\ T_{2n,53} & T_{2n,54} & T_{2n,56} \end{vmatrix} = 0, \quad n=1,2,3,\ldots. \tag{26}$$

The boundary conditions that lead to the above conditions for the eigenfrequency calculations are vanishing from the stresses on both inner and outer surfaces, with the additional constraint that the normal component of the electric displacement vector (open-circuit case) vanish at both surfaces when the material is piezoelectric. Symbolically, these conditions are

TABLE I. Comparison of results for an elastic hollow sphere.

n		0	1	2	3	4	5
RKF45	First class	0	3.5558	2.3919	3.6966	4.8732	5.9375
Tol=$(10^{-3},10^{-6})$	Second class	5.1514	3.3933	1.7823	2.4971	3.2849	3.6242
RKF45	First class	0	3.5558	2.3919	3.6966	4.8732	5.6171
Tol=$(10^{-5},10^{-8})$	Second class	5.1514	3.3933	1.7822	2.4963	3.1045	3.6740
RKF45	First class	0	3.5558	2.3919	3.6966	4.8732	5.6171
Tol=$(10^{-8},10^{-11})$	Second class	5.1514	3.3933	1.7822	2.4963	3.1045	3.6733
Chen's results (9 terms in		0	3.5558	2.3919	3.6966	4.8732	5.9974
series, using 5 sublayers)		5.1514	3.3933	1.7823	2.4963	3.1047	3.6744
Cohen *et al.* (Ref. 19) and		0	3.5558	2.3919	3.6966	4.8732	5.9974
Chen and Ding (Ref. 20) results		5.1514	3.3933	1.7822	2.4963	3.1045	3.6733

$\sigma_{rr}=\sigma_{r\theta}=\sigma_{r\phi}=0$ for elastic material,

$\tau_{rr}=\tau_{r\theta}=\tau_{r\phi}=\delta_r=0$

for piezoelectric material (open circuit),

$\tau_{rr}=\tau_{r\theta}=\tau_{r\phi}=\Phi=0$

for piezolectric material (short circuit).

A two-by-two matrix consisting of the first two rows and columns of the three-by-three matrix replaces the three-by-three determinant used in calculating the upper branch eigenfrequencies of a piezoelectric layer for the elastic case.

Normal modes of vibration of an elastic anisotropic thick shell (thickness=0.5 m, outer radius=1 m), with stiffness parameters: $c_{11}=20\times10^{10}$, $c_{12}=12\times10^{10}$, $c_{13}=2\times10^{10}$, $c_{33}=2\times10^{10}$, $c_{44}=10^{10}$, and density $\rho=7500$ were reported in the work of Chen,[7] in which he varied the number of terms in the Neumann series, as well as the number of sublayers for the thick shell. In Table I are some results reported in that paper, as well as the result of applying the RKF45 ordinary differential equation solver with various tolerances.

As can be seen in Table I, the Runge–Kutta–Fehlberg method works quite well in determining modal eigenfrequencies. These have been nondimensionalized in the same fashion as done in Chen's paper, namely, by the inner radius divided by the shear wave speed ($\Omega_n=\omega_n a/c_T$). The largest discrepancy appears for the first class, $n=5$ mode, for which the results in the paper by Chen differs from the RKF solution by about 5%.

A comparison is also made for the eigenfrequencies of a piezoelectric hollow sphere in Table II. The sphere in this instance has inner and outer radii of 0.5 and 1 m, respectively. The stiffness constants, piezoelectric constants, and dielectric constants are the same as those used by Chen: $c_{11}=13.9\times10^{10}$, $c_{12}=7.8\times10^{10}$, $c_{13}=1.4\times10^{10}$, $c_{33}=33.64\times10^{10}$, $c_{44}=16.25\times10^{10}$, $e_{15}=12.7$, $e_{31}=-5.2$, $e_{33}=15.1$, $\varepsilon_1=650\times10^{-11}$, $\varepsilon_3=560\times10^{-11}$, and density $\rho=7500$. Again, the results using the RKF method with tolerances shown in the table compare well to the values reported in Chen's paper for which a nine-term Neumann series is used, with presumably five sublayers. The results differ by less than one percent in all cases, with the first-class values being identical.

V. FLUID-LOADING EFFECTS

When a heavy fluid surrounds a sphere, the effects of this loading must be taken into account in the determination of the mechanical resonances of the sphere, as well as in calculations involving radiation or scattering from the sphere. The fluid motion and structural displacements are coupled at the fluid–solid interface in a complicated way. In the previous examples for which mechanical resonances of *in vacuo* spheres were determined, all matrix components are real. With fluid loading, the matrices become complex due to the fluid loading, and the decay of energy caused by pressure radiating into the surrounding fluid medium. The state-space methods are particularly useful in that they have decoupled the structural equations of motion into those that act independently (first-class modes from those that are directly affected by the loading (the second-class modes). For the very special geometry of spherical coordinates, the fluid-loaded normal modes of the structure remain uncoupled. This is not true for more general geometries, where an infinite set of normal modes would need to be truncated and solved simultaneously.

Because of the aforementioned decoupling, only ''second-class modes'' from the previous section are considered in the fluid-loading problem. Scattered or radiated pressures are expanded in terms of spherical Hankel functions

TABLE II. Comparison of results for a piezoelectric hollow sphere.

n		0	1	2	3	4	5
RKF45	First class	0	3.5558	0.5308	0.8374	1.1203	1.3927
Tol=$(10^{-5},10^{-8})$	Second class	1.0961	1.2059	0.4950	0.9576	1.5013	2.0723
Chen's results (9 terms in		0	3.5558	0.5308	0.8374	1.1203	1.3927
series, using 5 sublayers)		1.0893	1.2082	0.4947	0.9551	1.4972	2.0691

TABLE III. Comparison of eigenfrequencies for an elastic hollow sphere.

n		0	1	2	3	4	5
Elastica theory	Low branch		0	610	725	777	814
(*in vacuo*)	High branch	1403	1717	2367	3160	3996	4846
Elastica theory	Low branch		0	390	481	549	605
(fluid loaded)	High branch	1313	1668	2350	3154	3993	4845
Thin-shell theory	Low branch		0	601	711	754	776
(*in vacuo*)	High branch	1382	1692	2332	3114	3938	4776
Thin-shell theory	Low branch		0	390	479	541	584
(fluid loaded)	High branch	1294	1643	2315	3108	3935	4775

$$p_{\text{scattered or radiated}}=\sum_{n=0}^{\infty} B_n h_n^{(1)}(k_f r) P_n(\cos\theta), \tag{27}$$

with unknown modal amplitudes. Applying Euler's equation, the pressure at the fluid–solid interface is related to the radial surface displacement by a modal-specific acoustic impedance term[21]

$$p_n=-i\omega z_n w_n, \quad z_n=i\rho_f c_f \frac{h_n^1(k_f a_{\text{outer}})}{h_n^{1\prime}(k_f a_{\text{outer}})}, \tag{28}$$

where a_{outer} is the radius at which the fluid–solid interface resides, and p_n, w_n are the nth modal amplitudes for pressure and normal displacement at the interface.

For the elastic hollow sphere, the natural frequencies can be found from the fundamental matrices. For the $n=0$ case one has the two-by-two system

$$\begin{aligned}(T_{20})_{12} w_{\text{inside surface}} &= (\sigma_{rr})_{\text{fluid/solid interface}},\\ (T_{20})_{22} w_{\text{inside surface}} &= w_{\text{fluid/solid interface}}.\end{aligned} \tag{29}$$

Applying the modal-specific acoustic impedance for a radiation problem, one obtains the homogeneous system

$$\begin{bmatrix} T_{20,12} & \dfrac{-i\omega z_0}{a_1\mu} \\ T_{20,22} & -1 \end{bmatrix} \begin{bmatrix} w_{\text{inside surface}} \\ w_{\text{fluid/solid interface}} \end{bmatrix} = \begin{bmatrix} 0 \\ 0 \end{bmatrix}, \tag{30}$$

and the $n=0$ mechanical resonance occurs at that frequency for which the real part of the two-by-two determinant vanishes. Equivalently for the $n>0$ case, the fundamental matrix T_{2n} matrix is used in conjunction with the specific modal impedance, producing a three-by-three matrix

$$\begin{bmatrix} T_{2n,13} & T_{2n,14} & \dfrac{-i\omega z_n}{a_1\mu} \\ T_{2n,23} & T_{2n,24} & 0 \\ T_{2n,43} & T_{2n,44} & -1 \end{bmatrix} \begin{bmatrix} G_{\text{inside surface}} \\ w_{\text{inside surface}} \\ w_{\text{fluid/solid interface}} \end{bmatrix} = \begin{bmatrix} 0 \\ 0 \\ 0 \end{bmatrix}, \tag{31}$$

and again mechanical resonance frequencies occur when the real part of the three-by-three matrix determinant vanishes.

Table III includes the results of comparing the above methodology to thin-shell theory in determining the *in vacuo* and fluid-loaded mechanical resonance frequencies. The lowest-order thin-shell theory is used in this comparison, and upper-and lower-branch frequencies correspond to the two roots of the thin-shell theory equations.[21] The fluid and elastic material parameters are: fluid: $c_f=1500$, $\rho_f=1000$; and for the elastic layer (steel): $E=2.07\times10^{11}$, $\upsilon=0.30$, $\rho_e=7850$. The shell has an outer radius of 1 m, and a thickness of 3 cm. As seen in the table, the thin-shell values compare favorably with those of the above theory since the shell thickness relative to the shear wavelengths is quite small.

The natural mechanical resonances for the bilaminate sphere has an inner layer of piezoelectric material, and an outer layer of elastic material is found in much the same way, except that the product of propagator matrices for each of the layers must be multiplied prior to the imposition of boundary conditions. Additionally, since the elastic layer does not have electric potential or electric displacement degrees of freedom, these must be split off, with the appropriate open- or short-circuit boundary condition placed at inner and outer surfaces of the piezoelectric layer. Open-circuit boundary conditions were used in the comparison of the previous section. Because a voltage potential will be applied for the problem of scattered pressure suppression, the formulation for mechanical resonances of the short-circuited case will be given.

The imposition of the short-circuit condition at the interface between the elastic and piezoelectric layers does nothing more than provide the value of the electric displacement component in terms of the normal displacement of the hollow sphere at its interior surface. The electric displacement degree of freedom is therefore eliminated in favor of the inside normal displacement for $n=0$, and in terms of the inside normal displacement and potential function G for $n>0$. In particular, the relationships are

$$\begin{aligned}\delta_{r,0} &= -\frac{T^p_{20,42}}{T^p_{20,43}} w_{0,\text{inside surface}}, \quad n=0\\ \delta_{r,n} &= -\frac{T^p_{2n,64}}{T^p_{2n,65}} w_{n,\text{inside surface}} - \frac{T^p_{2n,63}}{T^p_{2n,65}} G_{n,\text{inside surface}}, \quad n>0.\end{aligned} \tag{32}$$

Not all entries in the fundamental matrix for the piezoelectric matrix are needed in subsequent calculations. With superscripts "e" and "p" that correspond to elastic and piezoelectric terms, respectively, the $n=0$, and $n>0$ matrices needed in calculating the mechanical resonances of the bilaminate are given by

$$S_0=T^e_{20}T^p_{20(1:2,1:4)} \quad \text{and} \quad S_n=T^e_{2n}T^p_{2n(1:4,1:6)}. \tag{33}$$

The additional subscripts refer to the rows and columns needed in the matrix multiplications. For the $n=0$ case, the two-by-two matrix equation that results is

TABLE IV. Resonant frequencies for a bilaminate hollow sphere.

n		0	1	2	3	4	5
Short-circuit case	Low branch		0	509	601	640	663
(*in vacuo*)	High branch	1137	1396	1936	2595	3287	3990
Short-circuit	Low branch		0	295	368	417	454
(fluid loaded)	High branch	967	1305	1906	2584	3282	3987
Open-circuit case	Low branch		0	513	609	648	669
(*in vacuo*)	High branch	1222	1499	2058	2741	3460	4193
Open-circuit	Low branch		0	298	373	422	458
(fluid loaded)	High branch	1064	1414	2029	2729	3455	4190

$$\begin{bmatrix} S_{0,12}-qS_{0,13} & \dfrac{-i\omega z_n a_0}{a_1 c_{44}} \\ S_{0,22}-qS_{0,23} & -1 \end{bmatrix} \begin{bmatrix} w_{\text{inside surface}} \\ w_{\text{fluid/solid interface}} \end{bmatrix} = \begin{bmatrix} 0 \\ 0 \end{bmatrix},$$

$$q = \frac{T^p_{20,42}}{T^p_{20,43}}. \tag{34}$$

Just as with the elastic hollow sphere, the mechanical resonance occurs when the real part of the two-by-two determinant vanishes. For $n>0$, one has

$$\begin{bmatrix} S_{n,13}-q_1S_{n,15} & S_{n,14}-q_2S_{n,15} & \dfrac{-i\omega a_0 z_n}{a_1 c_{44}} \\ S_{n,23}-q_1S_{n,25} & S_{n,24}-q_2S_{n,25} & 0 \\ S_{n,43}-q_1S_{n,45} & S_{n,44}-q_2S_{n,45} & -1 \end{bmatrix} \times \begin{bmatrix} G_{n,\text{inner surface}} \\ w_{n,\text{inner surface}} \\ w_{n,\text{fluid/solid interface}} \end{bmatrix} = \begin{bmatrix} 0 \\ 0 \\ 0 \end{bmatrix} \quad q_1 = \frac{T^p_{2n,63}}{T^p_{2n,65}}, \quad q_2 = \frac{T^p_{2n,64}}{T^p_{2n,65}}, \tag{35}$$

and the mechanical resonances are when the real part of the three-by-three determinant vanishes. It should be noted that the *in vacuo* resonances for the bilaminate can be found from each of the above matrices by simply setting the modal impedance value to zero and following the same procedure.

In Table IV, *in vacuo* and fluid-loaded mechanical resonance frequencies are given for the bilaminate sphere. The sphere is of radius 1 m, and has equal thickness for elastic and PZT4 layers of 1 cm. The pertinent material parameters are for the fluid: $c_f=1500$, $\rho_f=1000$; for the elastic layer (steel): $E=2.07\times10^{11}$, $v=0.29$, $\rho_e=7850$; and for the PZT4 layer: $c_{11}=13.9\times10^{10}$, $c_{12}=7.784\times10^{10}$, $c_{13}=7.428\times10^{10}$, $c_{33}=11.541\times10^{10}$, $c_{44}=2.564\times10^{10}$, $e_{15}=12.718$, $e_{31}=-5.203$, $e_{33}=15.08$, $\varepsilon_1=650\times10^{-11}$, $\varepsilon_3=560\times10^{-11}$, and density $\rho_p=7500$.

VI. SCATTERING AND CANCELLATION BY ACTIVE CONTROL

Consider scattering of an incident plane wave propagating in the positive z direction from the fluid-loaded bilaminate sphere described in the previous section. The incident plane wave can be expressed in terms of spherical Bessel functions[22]

$$e^{ik_f z} = I\sum_{n=0}^{\infty}(2n+1)i^n j_n(k_f r)P_n(\cos\theta), \quad k_f = a\omega/c_f. \tag{36}$$

The *scattered* pressure is expanded in terms of outgoing spherical Hankel functions

$$p_{\text{scattered}} = \sum_{n=0}^{\infty} B_n h_n^{(1)}(k_f r)P_n(\cos\theta), \tag{37}$$

and the applied voltage in terms of spherical harmonics

$$\Phi = V = \sum_{n=0}^{\infty} V_n P_n(\cos\theta). \tag{38}$$

With the introduction of an incident plane wave, the total pressure on the surface of the sphere is the sum of incident and scattered pressures. This sum represents the negative normal stress on the surface of the fluid-loaded sphere, while from Euler's equation, there is a relationship between the normal acceleration and pressure gradient at the fluid–solid interface. In terms of the normal modes and previously mentioned scaling of the problem, the pertinent boundary conditions can be written

$$\begin{aligned} \sigma^s_{rr,n}(a_{\text{outer}}) &= \frac{-a_{\text{outer}}}{a_{\text{inner}}c_{44}} \times [A_n j_n(k_f a_{\text{outer}}) + B_n h_n(k_f a_{\text{outer}})], \\ w^s_n(a_{\text{outer}}) &= \frac{k_f}{a_{\text{inner}}\omega^2\rho_f} \times [A_n j_n'(k_f a_{\text{outer}}) + B_n h_n'(k_f a_{\text{outer}})], \\ \Sigma^s_{2,n}(a_{\text{outer}}) &= 0, \\ A_n &= I(2n+1)i^n j_n(k_f a_{\text{outer}}). \end{aligned} \tag{39}$$

With subscripts "p" and "e" referring to piezoelectric and elastic variables, the remaining relevant interface and boundary conditions for the bilaminate are

$$\begin{aligned} &\tau^s_{rr,n}(a_{\text{inner}}) = 0, \quad \Sigma^s_{2,n}(a_{\text{inner}}) = 0, \quad \Phi^s_n(a_{\text{inner}}) = 0, \\ &\tau^s_{rr,n}(a_{\text{inter}}) = \sigma^s_{rr,n}(a_{\text{inter}}), \quad \Sigma^s_{2,n}(a_{\text{inter}}) = \Sigma^s_{e2,n}(a_{\text{inter}}), \\ &\Phi^s_n(a_{\text{inter}}) = \frac{V_n\varepsilon_3}{a_{\text{inner}}e_{33}}, \\ &w^s_{p,n}(a_{\text{inter}}) = w^s_n(a_{\text{inter}}), \quad G^s_n(a_{\text{inter}}) = G^s_{e,n}(a_{\text{inter}}). \end{aligned} \tag{40}$$

Solution of the scattering problem is found by applying the above conditions in conjunction with the fundamental matrices of each layer. Consider the modes for $n \geqslant 0$. At the inner surface, three of the unknown values of the dependent variables are known. Writing the values for the six terms at the inner surface, using the piezoelectric fundamental matrix, gives the values of these dependent variables at the interface between the elastic and piezoelectric layers. The equation that provides the electric displacement at the interface is ignored in subsequent calculations since it can be found in terms of the remaining unknowns determined by other equations. The voltage potential value is assigned to its interface value, and constitutes one of the final four equations. The remaining four dependent variables at the interface are the initial values for the elastic material. When these are used as inputs to the elastic fundamental matrix, values at the fluid solid interface can be applied. In mathematical terms

$$\begin{bmatrix} \sigma^s_{rr,n}(a_{\text{outer}}) \\ \Sigma^s_{e2,n}(a_{\text{outer}}) \\ G^s_{e,n}(a_{\text{outer}}) \\ w^s_n(a_{\text{outer}}) \end{bmatrix} = \underbrace{M^e_{2n} M^p_{2n}(1{:}4,{:})}_{=S_n} \begin{bmatrix} \tau^s_{rr,n}(a_{\text{inner}}) \\ \Sigma^s_{2,n}(a_{\text{inner}}) \\ G^s_n(a_{\text{inner}}) \\ w^s_{p,n}(a_{\text{inner}}) \\ \delta^s_{r,n}(a_{\text{inner}}) \\ \Phi^s_n(a_{\text{inner}}) \end{bmatrix} \Rightarrow \begin{bmatrix} -a_{\text{outer}}[A_n j_n(k_f a_{\text{outer}}) + B_n h_n(k_f a_{\text{outer}})]/(a_{\text{inner}} c_{44}) \\ 0 \\ k_f a_{\text{outer}}[A_n j'_n(k_f a_{\text{outer}}) + B_n h'_n(k_f a_{\text{outer}})]/(a_{\text{inner}} \omega^2 \rho_f) \end{bmatrix}$$

$$= \begin{bmatrix} S_{n,13} & S_{n,14} & S_{n,15} \\ S_{n,23} & S_{n,24} & S_{n,25} \\ S_{n,43} & S_{n,44} & S_{n,45} \end{bmatrix} \begin{bmatrix} G^s_n(a_{\text{inner}}) \\ w^s_n(a_{\text{inner}}) \\ \delta^s_{r,n}(a_{\text{inner}}) \end{bmatrix} \tag{41}$$

$$\Phi^s_n(a_{\text{inter}}) = T^p_{2n}(6,{:}) \begin{bmatrix} \tau^s_{rr,n}(a_{\text{inner}}) \\ \Sigma^s_{2,n}(a_{\text{inner}}) \\ G^s_n(a_{\text{inner}}) \\ w^s_{p,n}(a_{\text{inner}}) \\ \delta^s_{r,n}(a_{\text{inner}}) \\ \Phi^s_n(a_{\text{inner}}) \end{bmatrix} \Rightarrow \frac{V_n \varepsilon_3}{a_{\text{inner}} e_{33}} = (T^p_{2n})_{63} G^s_n(a_{\text{inner}}) + (T^p_{2n})_{64} w^s_{p,n}(a_{\text{inner}}) + (T^p_{2n})_{65} \delta^s_{r,n}(a_{\text{inner}}).$$

Depending upon whether the applied voltage necessary to cancel the scattered pressure is to be found, or if the amplitude

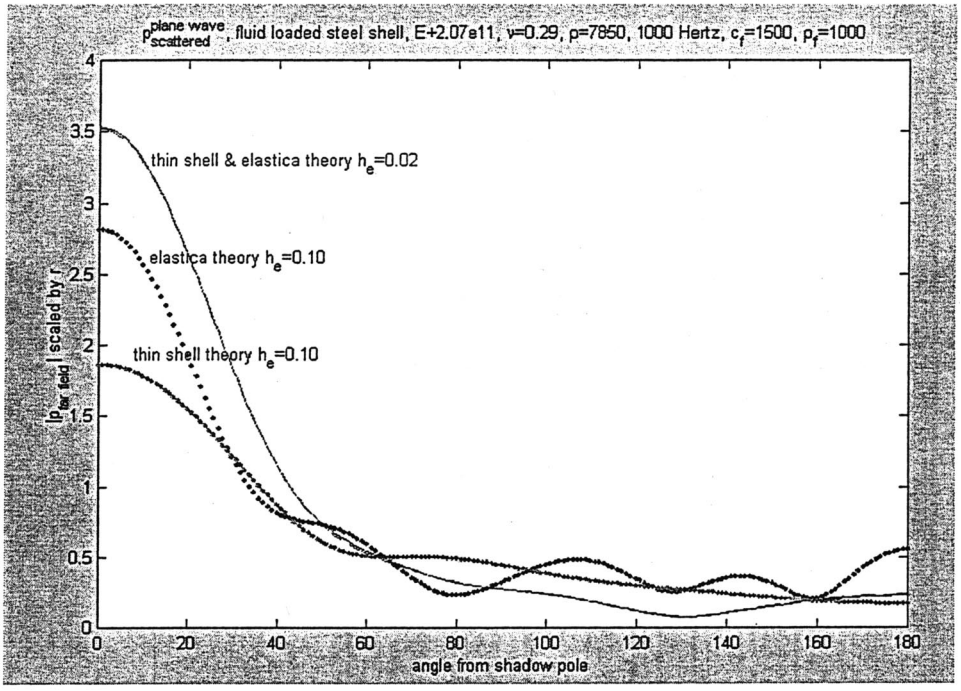

FIG. 2. Far-field scattered pressure for two elastic fluid-loaded shells.

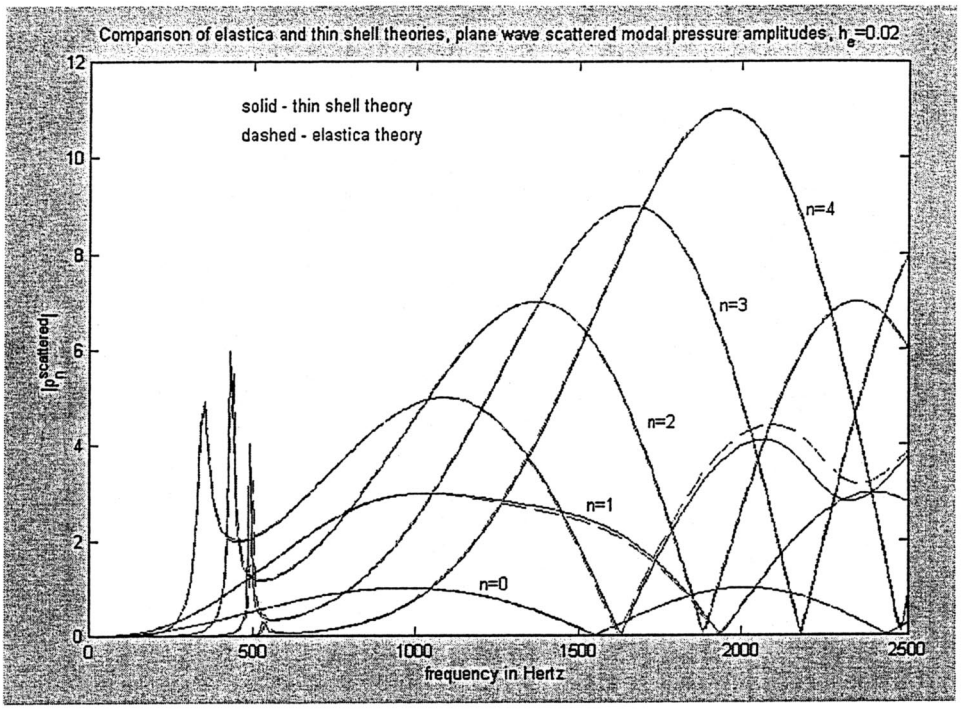

FIG. 3. Modal amplitudes of scattered pressure for a thin elastic shell versus frequency.

of the scattered pressure with a prescribed voltage and incident pressure is to be found, one obtains slightly different matrix equations. To find the scattered pressure amplitudes (B_n), the four-by-four system of equations for a given mode is

$$\begin{bmatrix} S_{n,13} & S_{n,14} & S_{n,15} & a_{\text{outer}} h_n(k_f a_{\text{outer}})/a_{\text{inner}} c_{44} \\ S_{n,23} & S_{n,24} & S_{n,25} & 0 \\ S_{n,43} & S_{n,44} & S_{n,45} & -k_f h_n'(k_f a_{\text{outer}})/a_{\text{inner}} \omega^2 \rho_f \\ (T^p_{2n})_{63} & (T^p_{2n})_{64} & (T^p_{2n})_{65} & 0 \end{bmatrix} \begin{bmatrix} G^s_{p,n} \\ w^s_{p,n} \\ \delta^s_{r,n} \\ B_n \end{bmatrix} \begin{bmatrix} -A_n a_{\text{outer}} j_n(k_f a_{\text{outer}})/a_{\text{inner}} c_{44} \\ 0 \\ A_n k_f j_n'(k_f a_{\text{outer}})/a_{\text{inner}} \omega^2 \rho_f \\ V_n \varepsilon_3 / a_{\text{inner}} e_{33} \end{bmatrix}. \tag{42}$$

The above equation can be solved to determine the value of the scattered pressure amplitude. To determine the modal voltage necessary to *cancel* the scattered pressure, we take the original set of four equations, but set B_n to zero, and solve for the unknown V_n. This leads to the equations

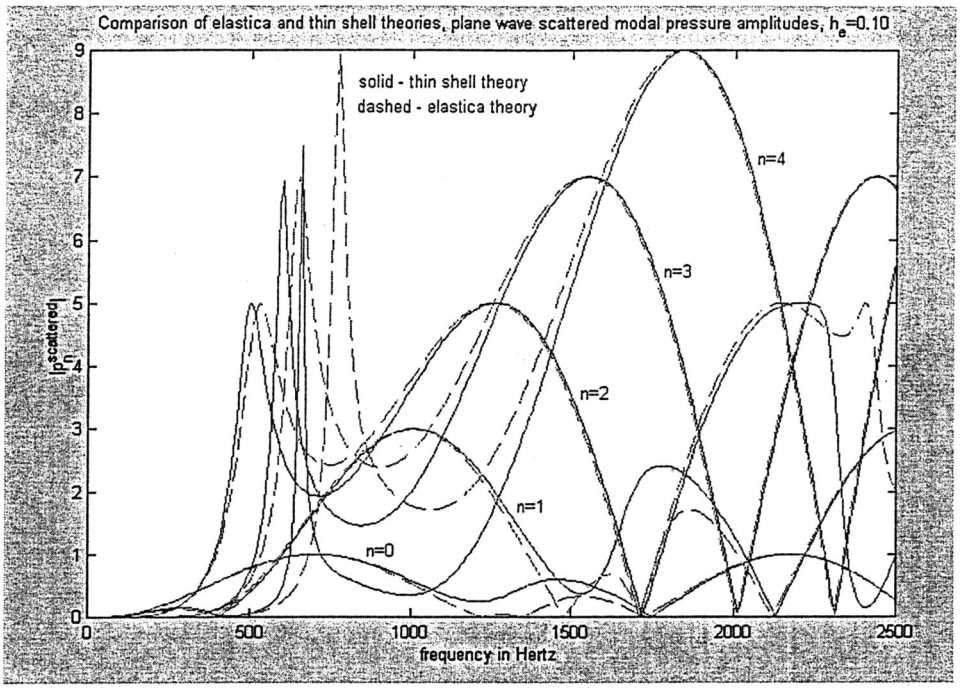

FIG. 4. Modal amplitudes of scattered pressure for a thick elastic shell versus frequency.

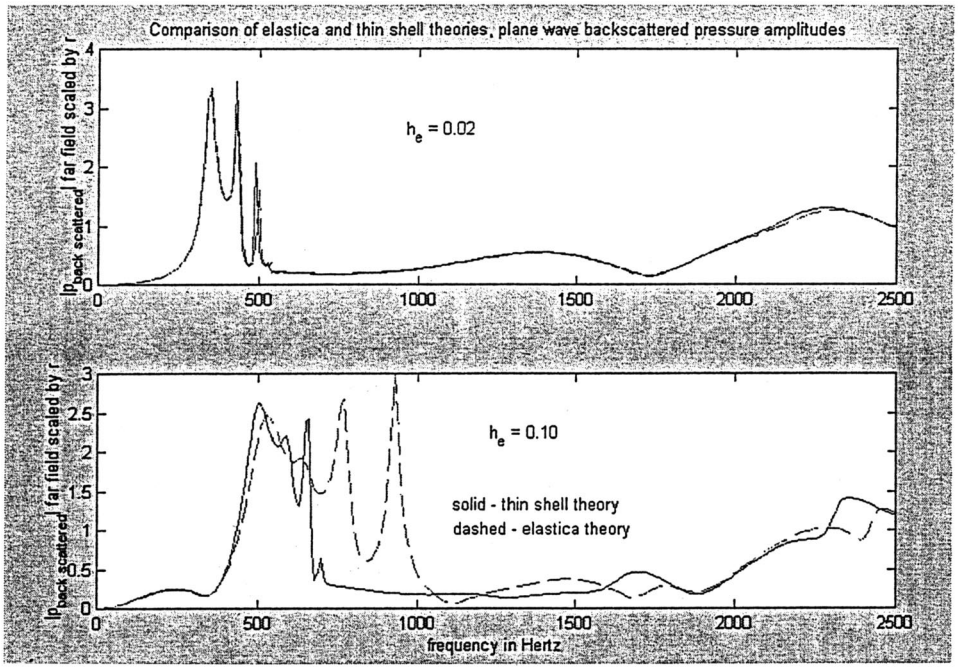

FIG. 5. Backscattered pressure for thin and thick elastic shells versus frequency.

$$\begin{bmatrix} S_{n,13} & S_{n,14} & S_{n,15} & 0 \\ S_{n,23} & S_{n,24} & S_{n,25} & 0 \\ S_{n,43} & S_{n,44} & S_{n,45} & 0 \\ (T^p_{2n})_{63} & (T^p_{2n})_{64} & (T^p_{2n})_{65} & \varepsilon_3/a_{\text{inner}}e_{33} \end{bmatrix} \begin{bmatrix} G^s_{p,n} \\ w^s_{p,n} \\ \delta^s_{r,n} \\ V_n \end{bmatrix} = \begin{bmatrix} -A_n a_{\text{outer}}\, j_n(k_f a_{\text{outer}})/a_{\text{inner}} c_{44} \\ 0 \\ A_n k_f j_n'(k_f a_{\text{outer}})/a_{\text{inner}} \omega^2 \rho_f \\ 0 \end{bmatrix}. \tag{43}$$

VII. RESULTS

As a first example, we consider the plane-wave scattering at 1000 Hz from a fluid-loaded thin steel shell, with pertinent parameters given by: $c_f = 1500$, $\rho_f = 1000$, $E = 2.07 \times 10^{11}$, $v = 0.29$, $\rho_e = 7850$. Results from the full elastica theory, compared to those using thin-shell theory for a sphere of radius 1 m, with two different thicknesses, 2 and 10 cm, are shown in Fig. 2. As can be seen, the thin-shell theory and elastica theory results coincide in the first case, and differ considerably in the second. The discrepancy at 10-cm thickness is in spite of the fact that at 1000 Hz, and thickness 10 cm, the ''rule of thumb''

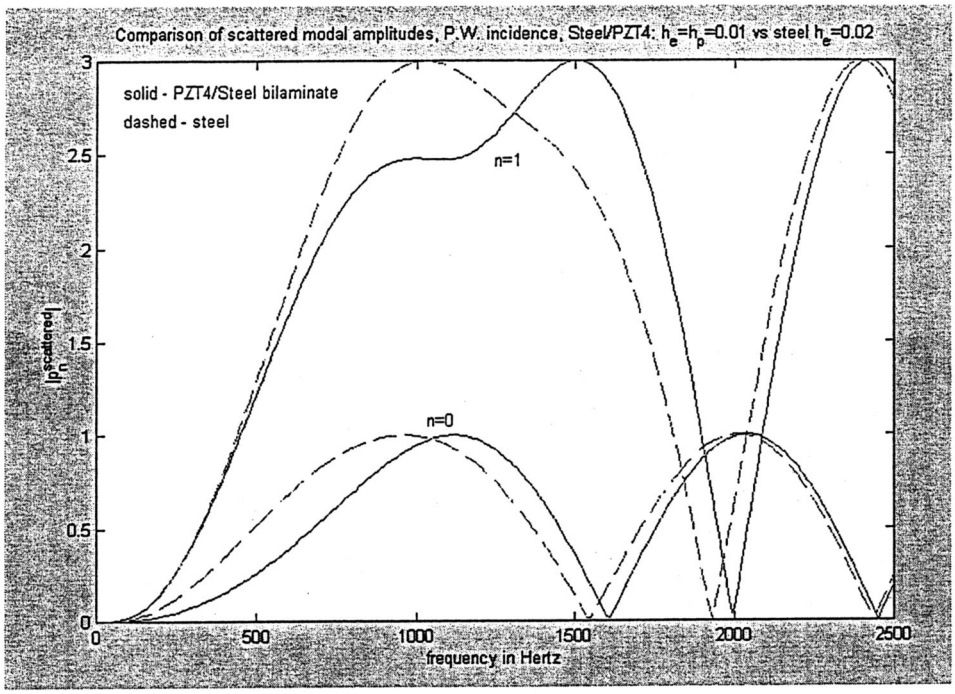

FIG. 6. Modal amplitudes of scattered pressure for a PZT4/steel bilaminate and 2-cm-thick steel shell versus frequency (modes 0 and 1).

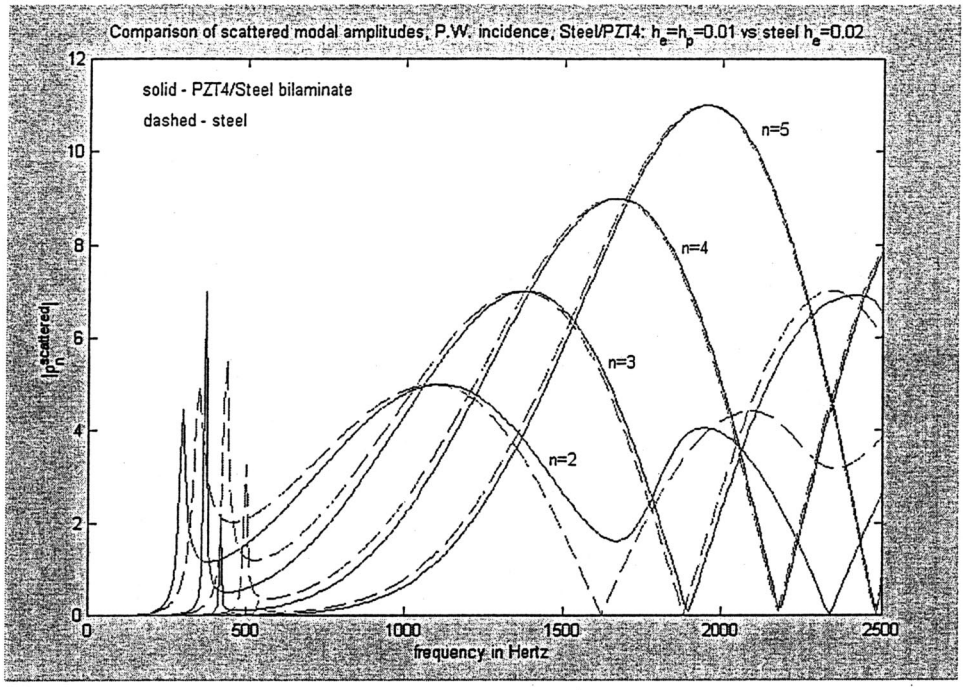

FIG. 7. Modal amplitudes of scattered pressure for a PZT4/steel bilaminate and 2-cm-thick steel shell versus frequency (modes 2 through 5).

governing the applicability of thin-shell theory that the thickness must be less than one-twentieth of the shear wavelength[22] is satisfied. Amplitude of the scattered pressure at 100 m from the spherical shell, scaled by the distance from the sphere as a function of angle measured from the shadow pole of the sphere, is shown in the figure.

In Figs. 3 and 4, scattered pressure modal amplitudes are compared for the same two spheres over a frequency range from 0 to 2500 Hz. Again, for the thinner shell, thin-shell theory does quite well, but for the thicker shell, the thin-shell theory results seem to have a downward shift in the mechanical resonance frequencies for the lower-branch modes. However, note that the thin-shell theory matches well with the full elastica theory for upper-branch modes of the thicker shell.

Considering the backscattered pressure for the two elastic spheres given in Fig. 5, one again sees a near perfect match at 1-cm thickness, with large errors for the 10-cm-thick shell at frequencies corresponding to the mechanical resonance frequencies of the lower-branch modes.

Figures 6 and 7 show results corresponding to that given for the elastic spherical shell in Figs. 3 and 4, for a bilaminate spherical shell of radius 1 m with elastic and piezoelectric layers of thickness equal to 1 cm. Material parameters are the same as those given for the mechanical resonance frequency results displayed in Table IV. The solid lines in these graphs are modal amplitudes for a steel shell of thick-

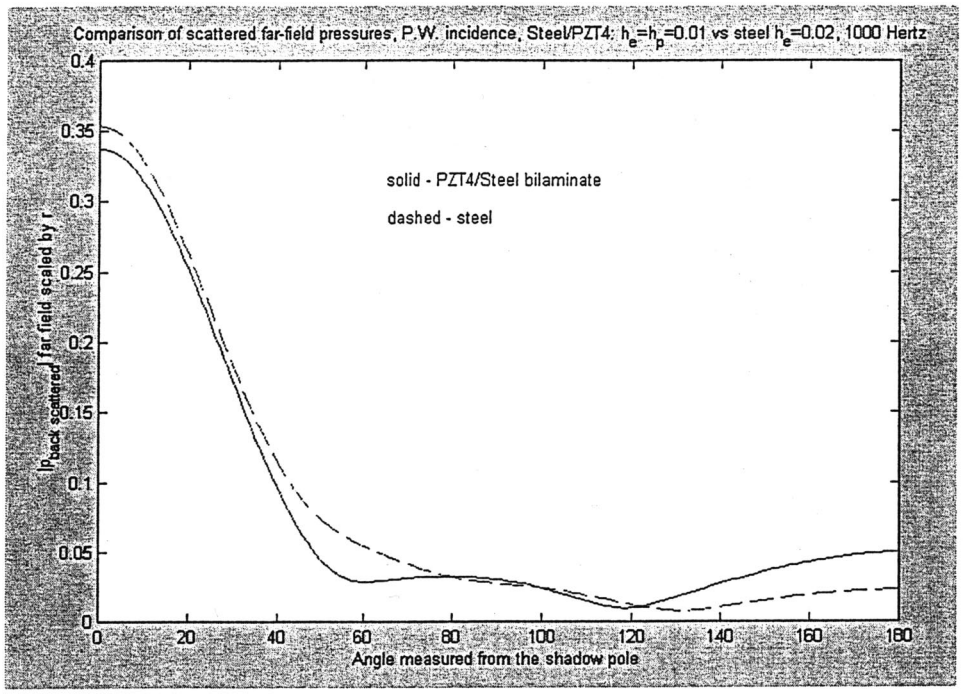

FIG. 8. Far-field scattered pressure for a PZT4/steel bilaminate and 2-cm-thick steel shell.

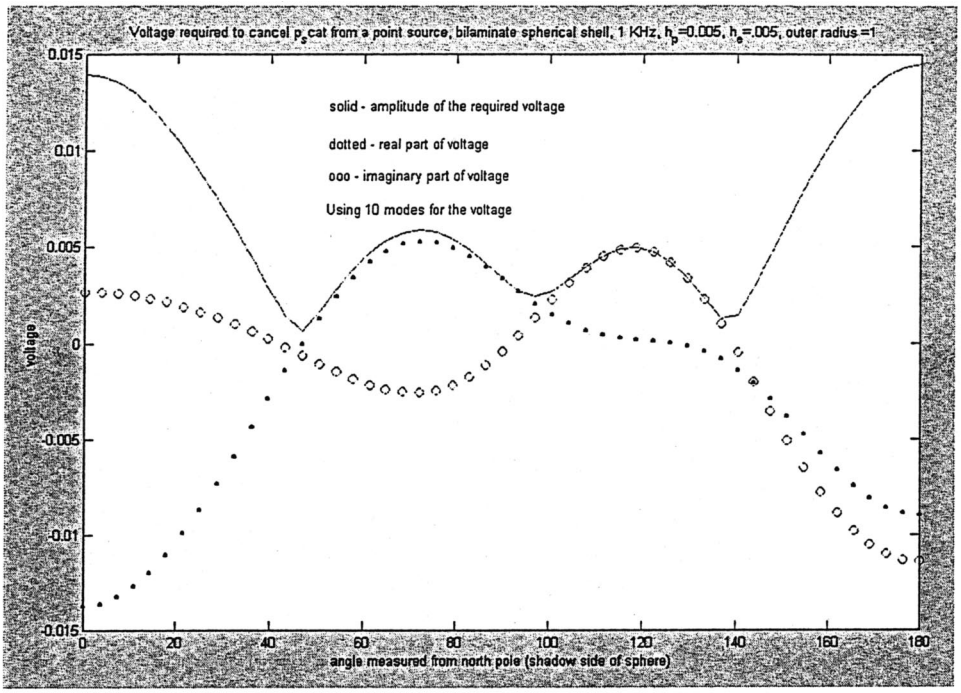

FIG. 9. Voltage necessary as a function of angle from shadow pole to cancel scattered pressure from a unit incident plane pressure wave.

ness 2 cm, and are presented only for comparison purposes. The case displayed in Figs. 6 and 7 is for a piezoelectric layer that has been short-circuited. The net effect of the piezoelectric/steel composite compared to a purely steel layer is the reduction of the mechanical resonances of the lower-branch modes, and an increase in the frequencies of the first two upper-branch peaks. In considering the far-field scattered pressure at 1000 Hz, shown in Fig. 8, there is little difference between the elastic and bilaminate spherical shells.

With the application of a voltage potential across the piezoelectric layer for the purpose of canceling the scattered pressure, Fig. 9 plots the voltage necessary, as a function of angle measured from the shadow pole of the sphere, to cancel a unit amplitude plane pressure wave at 1000 Hz. The dotted and circled plots in this graph are for the real and imaginary parts of the voltage as a function of position, respectively, while the solid line refers to the amplitude of the voltage. The voltages are actually quite small, as can be seen. Amplitudes of the first ten modal voltages are: $V_0=0.0073$, $V_1=0.0125$, $V_2=0.3927$, $V_3=0.3442$, $V_4=0.1615$, $V_5=0.0761$, $V_6=0.0322$, $V_7=0.0129$, $V_8=0.0057$, and $V_9=0.0056$.

More illuminating are Figs. 10 and 11, displayed on

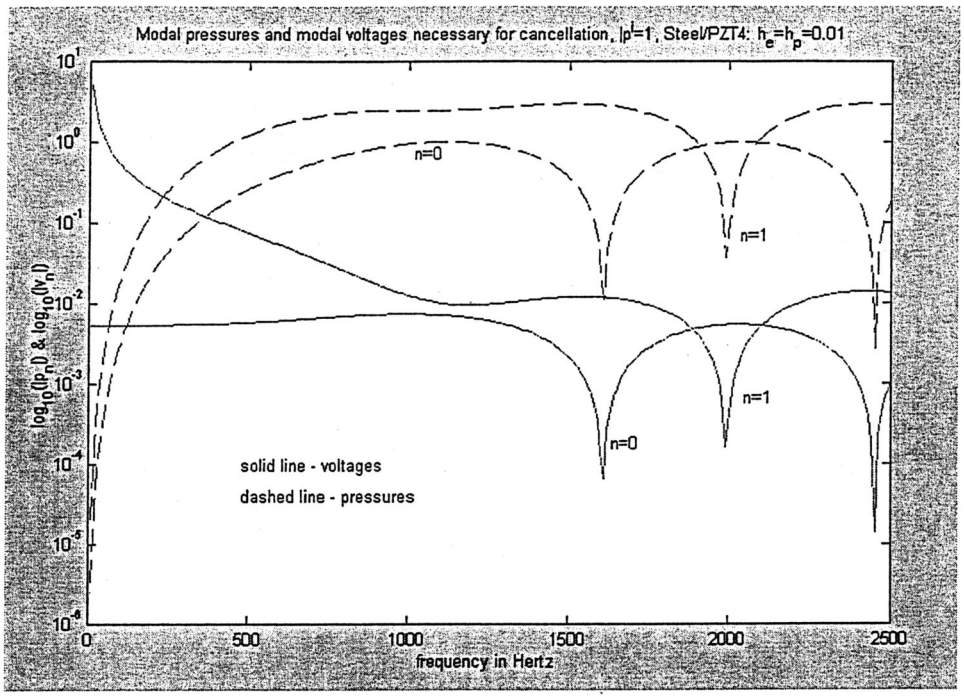

FIG. 10. Modal amplitudes of scattered pressure and cancellation voltage for a PZT4/steel bilaminate versus frequency (modes 0 and 1).

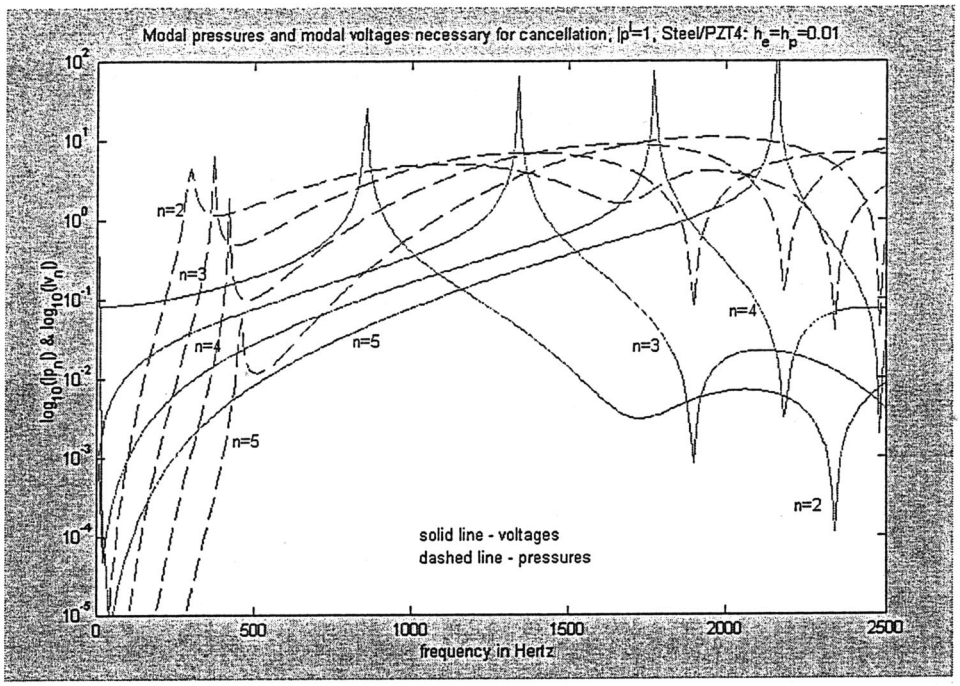

FIG. 11. Modal amplitudes of scattered pressure and cancellation voltage for a PZT4/steel bilaminate versus frequency (modes 2 through 5).

semilog graphs, showing the log of the modal voltage amplitudes necessary to cancel the scattered pressure modal amplitudes over a frequency range from 0 to 2500 Hz. One can see that drops in the modal pressure amplitudes necessarily drop the magnitude of the modal voltage necessary to cancel the scattered pressure. The periodic large spikes in the voltage amplitude for the higher-order modes appear to be instances of large electrical impedance similar physically to an electrical antiresonance phenomenon.

In conclusion, the results and methodology presented could be used to study geometrically simple shapes that lend themselves to normal-mode analysis. Perhaps more importantly, however, the results and application given are valuable insofar as they can be used as diagnostic or test cases for purely numerical techniques that try to combine elastic, piezoelectric, and fluid-loading effects.

[1] O. B. Wilson, *Introduction to Theory and Design of Sonar Transducers* (Peninsula, Los Altos, CA, 1988).

[2] S. D. Snyder, N. Tanaka, and Y. Kikushima, ''The Use of Optimally Shaped Piezoelectric Film Sensors in the Active Control of Free Field Structural Radiation, Part 1: Feedforward Control,'' J. Vibr. Acoust. **117**, 311–322 (1995).

[3] Z. Chaudhry and C. Rogers, ''Actuators for Smart Structures,'' in *Fiber-Optic Smart Structures*, edited by Eric Udd (Wiley, New York, 1995).

[4] J. Tani and J. Qui, ''Smart composite cylindrical shells without vibration,'' Third International Conference on Intelligent Materials, held in Lyon, France, 3–5 June 1996, edited by P. F. Gobin and J. Tatibouët (1996).

[5] P. Z. Barbone and A. M. B. Braga, ''Influence of electrode size on the active suppression of sound reflection from submerged plates using distributed piezoelectric actuators,'' First European Conference on Smart Structures and Materials, Glasgow, Scotland, 12–14 May 1992, edited by B. Culshaw, P. T. Gardiner, and A. McDonach (1992), pp. 325–328.

[6] J. Kim, V. V. Varadan, and V. K. Varadan, ''Finite element modeling of a finite piezoelectric sensor/actuator embedded in a fluid-loaded plate,'' Mathematics and Control in Smart Structures, Orlando, FL, February 1994, edited by H. T. Banks (1994), pp. 273–280.

[7] W. Q. Chen, ''Free vibration analysis of laminated piezoceramic hollow spheres,'' J. Acoust. Soc. Am. **109**, 41–50 (2001).

[8] W. Q. Chen, R. Q. Xu, and H. J. Ding, ''On free vibration of a piezoelectric composite rectangular plate,'' J. Sound Vib. **218**, 741–748 (1998).

[9] H. J. Ding, R. Q. Xu, Y. W. Chi, and W. Q. Chen, ''Free axisymmetric vibration of transversely isotropic piezoelectric circular plates,'' Int. J. Solids Struct. **36**, 4629–4652 (1999).

[10] H. C. Hu, ''On the general theory of elasticity for a spherically isotropic medium,'' Acta Sci. Sin. **3**, 247–260 (1954).

[11] H. J. Ding and W. Q. Chen, ''Natural frequencies of an elastic spherically isotropic hollow sphere submerged in a compressible fluid medium,'' J. Sound Vib. **192**, 173–198 (1996).

[12] F. B. Jensen, W. A. Kuperman, M. B. Porter, and H. Schmidt, *Computational Ocean Acoustics* (AIP, New York, 1994).

[13] K. Aki and P. G. Richards, *Quantitative Seismology Theory and Methods* (Freeman, New York, 1980), Vol. 1.

[14] A. N. Stroh, ''Steady state problems in anisotropic elasticity,'' J. Math. Phys. **41**, 77–103 (1962).

[15] B. A. Auld, *Acoustic Fields and Waves in Solids* (Krieger, Malabar, FL, 1990), Vol. I.

[16] N. A. Shul'ga, ''Harmonic electroelastic oscillations of spherical bodies,'' Int. Appl. Mech. **29**, 812–817 (1993).

[17] W. E. Boyce and R. C. DePrima, *Elementary Differential Equations and Boundary Value Problems* (Wiley, New York, 2001).

[18] J. Stoer and R. Bulirsch, *Introduction to Numerical Analysis* (Springer, New York, 1980).

[19] H. Cohen, A. H. Shah, and C. V. Ramakrishnan, ''Free vibrations of a spherically isotropic hollow sphere,'' Acustica **26**, 239–333 (1972).

[20] W. Q. Chen and H. J. Ding, ''Natural frequencies of a fluid-filled anisotropic spherical shell,'' J. Acoust. Soc. Am. **105**, 174–182 (1999).

[21] M. C. Junger and D. Feit, *Sound, Structures, and Their Interaction* (MIT Press, Cambridge, MA, 1986).

[22] D. S. Jones, *Acoustic and Electromagnetic Waves* (Oxford University Press, New York, 1986).

Active vibroacoustic control with multiple local feedback loops

Stephen J. Elliott,[a] Paolo Gardonio, Thomas C. Sors, and Michael J. Brennan
Institute of Sound and Vibration Research, University of Southampton, Highfield, Southampton SO17 1BJ, United Kingdom

(Received 30 March 2001; accepted for publication 31 October 2001)

When multiple actuators and sensors are used to control the vibration of a panel, or its sound radiation, they are usually positioned so that they couple into specific modes and are all connected together with a centralized control system. This paper investigates the physical effects of having a regular array of actuator and sensor pairs that are connected only by local feedback loops. An array of 4×4 force actuators and velocity sensors is first simulated, for which such a decentralized controller can be shown to be unconditionally stable. Significant reductions in both the kinetic energy of the panel and in its radiated sound power can be obtained for an optimal value of feedback gain, although higher values of feedback gain can induce extra resonances in the system and degrade the performance. A more practical transducer pair, consisting of a piezoelectric actuator and velocity sensor, is also investigated and the simulations suggest that a decentralized controller with this arrangement is also stable over a wide range of feedback gains. The resulting reductions in kinetic energy and sound power are not as great as with the force actuators, due to the extra resonances being more prominent and at lower frequencies, but are still worthwhile. This suggests that an array of independent modular systems, each of which included an actuator, a sensor, and a local feedback control loop, could be a simple and robust method of controlling broadband sound transmission when integrated into a panel. [DOI: 10.1121/1.1433810]

PACS numbers: 43.40.Vn [PJR]

I. INTRODUCTION

The vibration of a structure can be actively controlled by feeding back the signals measured by sensors on the structure to integrated actuators.[1,2] Sound radiation from structures can also be actively controlled,[3] although in this case it is most important to control the components of vibration which radiate sound most efficiently, which has been termed active structural acoustic control.

Active control systems are usually designed by selecting the number and position of the actuators, the number and position of the sensors, and the controller response. The positions of the actuators and sensors used in active vibroacoustic control systems are often chosen so that they can couple into the structural modes that dominate the vibration or the sound radiation.[1–3] As the frequency of excitation increases, however, the detailed shape of these structural modes become increasingly sensitive to the boundary conditions and external loads on the structure and hence become more uncertain. It may thus be preferable to use a larger number of actuators and sensors than are strictly required, arranged in a regular array so that the structural modes are controlled whatever their shape.

There are considerable advantages in collocating the actuators and the sensors in such a feedback control system. When the actuator and sensor are also dual, in the sense that the product of the actuator input and the sensor response is proportional to the power supplied to the structure,[4] the plant response, from actuator input to sensor output, will have a positive real part, since the uncontrolled structure is passive. If a collocated force actuator and velocity sensor were used, for example, the plant response would be proportional to the input, or point, mobility of the structure, which must have a positive real part. The bandwidth over which this passivity property holds will, in practice, be limited by the dynamics of the transducers used. Provided the frequency response of the feedback controller also has a positive real part, the polar plot of the open loop frequency response function, i.e., the Nyquist plot, must stay in the right-hand half of the complex plane and so the system is unconditionally stable, since the polar plot cannot encircle the Nyquist point. The generalization of this simple passivity property to multichannel systems is discussed in the following, where it is shown that if the collocated actuators and sensors are coupled only by local feedback control loops with positive feedback gains, then the controller is passive and stability is assured for a passive plant. Such an array of locally acting feedback loops is referred to as a decentralized control system. It may also be possible to economically implement such an array of integrated transducers using micro-electromechanical systems technology.

In this paper, an initial version of which was published in Ref. 5, we investigate the consequences of a decentralized feedback control strategy, which uses a set of 16 collocated actuators and sensors on a panel, when the panel is subject to an incident acoustic excitation. Each actuator is driven individually by the output of the corresponding sensor so that only local feedback control is implemented, with each actuator, sensor, and controller operating independently.

The objective is to investigate the effect on both the vibration of the panel, as quantified by its kinetic energy, and the sound radiated by the panel, as quantified by the sound power it radiates. It will be assumed that each of the sensors

[a]Electronic mail: sje@isvr.soton.ac.uk

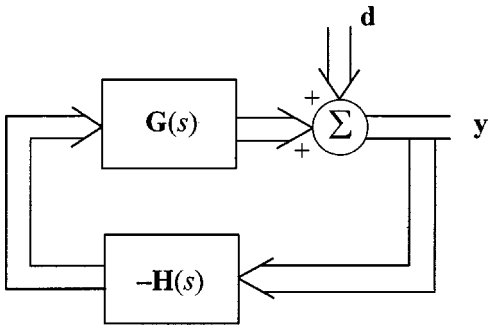

FIG. 1. Multichannel feedback control system, which for a passive plant response, $\mathbf{G}(s)$, and a passive controller $\mathbf{H}(s)$, is unconditionally stable.

measures the panel velocity at the corresponding point, which could be achieved in practice by integrating the output of a small accelerometer for example. Initially, the actuators will be assumed to be collocated devices which generate out of plane forces, as discussed previously. Although such actuators have useful theoretical properties, they require an inertial base to react off. It would be more useful in practice to have actuators that are fully integrated with the panel. In the latter parts of the paper the corresponding results will be described with velocity sensors and small strain actuators directly underneath them, such as could be implemented using piezoelectric devices. The similarity between the behavior of the ''ideal'' force actuator and velocity sensor control system will be compared with that of the ''practical'' control system with piezoelectric actuators and velocity sensors.

In Sec. II the performance of such a multichannel decentralized system is investigated, together with the conditions for stability. Section III describes the theoretical model used to calculate the panel vibration and sound radiation. Sections IV and V discuss the results of feedback control using force actuators and piezoelectric actuators, respectively, and the overall conclusions are summarized in Sec. VI.

II. MULTICHANNEL FEEDBACK CONTROLLERS

In this section we consider multichannel feedback control systems with equal numbers of collocated actuators and sensors.[4,6,7] In this case, the plant and controller responses are square matrices, $\mathbf{G}(s)$ and $\mathbf{H}(s)$, and the control objective is disturbance rejection, as illustrated by the block diagram in Fig. 1. Provided the control system is stable, the vector of spectra for the residual signals at the sensor outputs, $\mathbf{y}(j\omega)$, is related to that of the sensor outputs before control, $\mathbf{d}(j\omega)$, by

$$\mathbf{y}(j\omega)=[\mathbf{I}+\mathbf{G}(j\omega)\mathbf{H}(j\omega)]^{-1}\mathbf{d}(j\omega). \tag{1}$$

Similarly the vector of control inputs to the actuators, $\mathbf{u}(j\omega)$, is given by

$$\mathbf{u}(j\omega)=\mathbf{H}(j\omega)[\mathbf{I}+\mathbf{G}(j\omega)\mathbf{H}(j\omega)]^{-1}\mathbf{d}(j\omega). \tag{2}$$

In the case under consideration here, $\mathbf{G}(j\omega)$ is the fully populated matrix of input and transfer responses between the actuators and sensors on the panel and $\mathbf{H}(j\omega)$ is a diagonal matrix, which we will assume to have constant gains on each channel so that $\mathbf{H}(j\omega)=h\mathbf{I}$, where h is the feedback gain. Thus, given a set of panel responses, $\mathbf{G}(j\omega)$, and a feedback gain, h, the actuator signals can be calculated and hence the total response of the panel to both the primary and secondary excitations can be found. These results rely on the control system being stable, and the conditions for stability in this application are discussed in the following.

If collocated and dual transducers are used, then the real part of $\mathbf{G}(j\omega)$ must be positive definite, since the total power supplied to the uncontrolled system by all the actuators must be positive. If force actuators and velocity sensors are used, for example, then $\mathbf{u}(j\omega)=\mathbf{f}(j\omega)$, where $\mathbf{f}(j\omega)$ is the vector of applied forces and $\mathbf{y}(j\omega)=\mathbf{v}(j\omega)$, where $\mathbf{v}(j\omega)$ is the vector of measured velocities, and the power supplied by the actuators to the system at a frequency ω can be written as

$$\Pi(\omega)=\tfrac{1}{2}\mathrm{Re}[\mathbf{f}^H(j\omega)\mathbf{v}(j\omega)], \tag{3}$$

where Re denotes the real part and H denotes the Hermitian (conjugate) transpose. Since $\mathbf{v}(j\omega)=\mathbf{G}(j\omega)\mathbf{f}(j\omega)$ in this case, then Eq. (3) can be written as

$$\Pi(\omega)=\tfrac{1}{2}\mathrm{Re}[\mathbf{f}^H(j\omega)\mathbf{G}(j\omega)\mathbf{f}(j\omega)]. \tag{4}$$

Assuming reciprocity, $\mathbf{G}(j\omega)$ is also symmetric, so that

$$\Pi(\omega)=\tfrac{1}{2}\mathbf{f}^H(j\omega)\mathrm{Re}[\mathbf{G}(j\omega]\mathbf{f}(j\omega), \tag{5}$$

and it is clear that $\mathrm{Re}[\mathbf{G}(j\omega]$ must be positive definite if $\Pi(\omega)$ is to remain positive for all combinations of applied force, and the real parts of all the eigenvalues of $\mathbf{G}(j\omega)$ must be positive for all ω, so that the system is passive.[7,8] We assume that there is always some level of damping in the structure, so that $\Pi(\omega)$ can never be exactly zero unless $\mathbf{f}(\omega)$ is identically zero.

We also assume that the controller is designed so that it too has a positive definite real part at all frequencies, as would be the case if $\mathbf{H}(j\omega)=h\mathbf{I}$ and $h>0$. The plant and controller are thus both passive and the feedback control system illustrated in Fig. 1 must be unconditionally stable.[7,8] Thus if multiple local feedback loops are implemented with fixed gains then the system is stable provided each of the individual feedback gains is positive. Under these conditions the feedback gains can, in principle, be increased without limit and the signals from the control sensors can be driven to zero.

It should also be noted in passing that if an independent reference signal is available and feedforward control was implemented on such a system with collocated transducers, then independent loops could also be used for the adaptation of each actuator signal, using only the error signal from the corresponding sensor.[9] Because each of the eigenvalues of the matrix of plant responses has a positive real part, the stability of such a decentralized feedforward controller is guaranteed for slow convergence, provided the estimated plant responses used by the individual adaptation loops also had a positive real part.

Although the multichannel plant response is guaranteed to be passive if collocated point force actuators and velocity sensors are used, this property cannot be guaranteed with piezoelectric actuators and velocity sensors. The stability of a general multichannel control system can, however, always be determined[10] by examining whether the locus of the de-

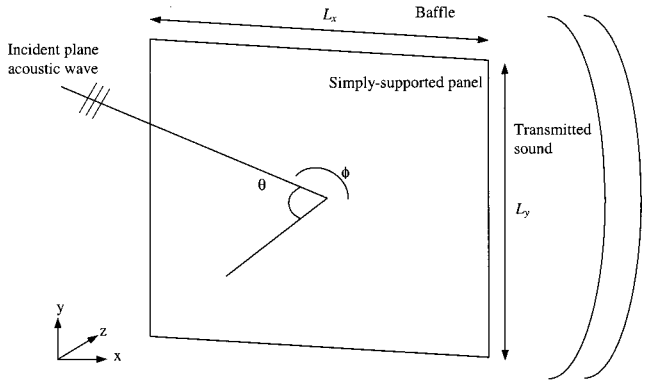

FIG. 2. Physical arrangement for the computer simulations, in which the vibration of a simply supported panel is excited by a plane acoustic wave on one side and radiates sound into an anechoic half space on the other side of the panel.

terminant of $[\mathbf{I}+\mathbf{G}(j\omega)\mathbf{H}(j\omega)]$ encloses the origin as ω varies from $-\infty$ to ∞. Alternatively the fact that the determinant of a matrix is the product of its eigenvalues can be used to derive a series of polar plots, each of which are analogous to the single channel Nyquist criteria. Specifically we note that

$$\det[\mathbf{I}+\mathbf{G}(j\omega)\mathbf{H}(j\omega)]=(1+\lambda_1(j\omega))(1+\lambda_2(j\omega))\cdots, \tag{6}$$

where $\lambda_i(j\omega)$ is the ith eigenvalue of $\mathbf{G}(j\omega)\mathbf{H}(j\omega)$, and so provided the locus of none of the eigenvalues encloses the Nyquist point $(-1,0)$ as ω varies from $-\infty$ to ∞, the system will be stable.

III. SIMULATION STUDY

The arrangement used in this simulation study is shown in Fig. 2, in which a thin aluminum panel, 278 mm $\times$247 mm$\times$1 mm, is subject to an incident plane acoustic wave of unit pressure. The plane wave is assumed to be incidental at azimuthal and lateral angles of 45° and 45° and thus excites all the structural modes of the panel.[11] The panel is assumed to be driven into motion by the incident acoustic wave and then to radiate sound on the other side. A weakly coupled analysis is used, in that the radiated pressure is assumed to have no effect on the panel vibration, which is a reasonable assumption in air for this thickness of panel. The panel is assumed to be simply supported and its velocity distribution is represented by the finite modal series

$$v(x,y,\omega)=\sum_{n=1}^{N} a_n(\omega)\psi_n(x,y), \tag{7}$$

where x and y are the spatial coordinates on the panel, $a_n(\omega)$ is the frequency-dependent amplitude of the nth mode, and $\psi_n(x,y)$ is its mode shape. The mode shape is assumed to be real and normalized so that the surface integral of its square value is equal to the surface area, so that in this simply supported case

$$\psi_n(x,y)=4\sin\left(\frac{n_1\pi x}{L_x}\right)\sin\left(\frac{n_2\pi y}{L_y}\right), \tag{8}$$

where L_x and L_y are the dimensions of the panel and n_1 and n_2 are the two modal integers, which are denoted above by the single index n.

The modal amplitude is given by the product of a second-order resonance term, $A_n(\omega)$, and the modal excitation term, $F_n(\omega)$,

$$a_n(\omega)=A_n(\omega)F_n(\omega), \tag{9}$$

where

$$A_n(\omega)=\frac{j\omega}{m(\omega_n^2-\omega^2+j2\zeta_n\omega\omega_n)}, \tag{10}$$

and m is the total mass of the panel, ζ_n is the modal damping ratio, which was taken to be 0.01 (1%) for all modes in these simulations, and ω_n is the natural frequency of the nth mode which is given by

$$\omega_n=\sqrt{\frac{Eh^2}{12\rho(1-\nu^2)}}\left[\left(\frac{n_1\pi}{L_x}\right)^2+\left(\frac{n_2\pi}{L_y}\right)^2\right], \tag{11}$$

where ρ is the density of the material, E is its Young's modulus of elasticity, ν is the Poisson's ratio, and h is the panel's thickness.

The modal excitation term will have a component due to the incident plane wave, $F_{np}(\omega)$, and a component due to each of the M secondary actuators, $F_{nm}(\omega)$, so that

$$F_n(\omega)=F_{np}(\omega)+\sum_{m=1}^{M} F_{nm}(\omega). \tag{12}$$

For the plane acoustic wave excitation assumed here, $F_{np}(\omega)$ is given by Wang *et al.*,[12] who also analyze the modal excitation terms for the plate when driven by a point force or the line moments generated by a piezoelectric actuator, which were used here to calculate $F_{nm}(\omega)$, as summarized in Ref. 3. The size of each of the piezoelectric actuators is 25$\times$25 mm.

The total kinetic energy of the panel is defined to be

$$E(\omega)=\frac{m}{4S}\int_S |v(z,y,\omega)|^2 dx\,dy, \tag{13}$$

where S is the surface area of the panel. Using the orthonormal properties of the mode shapes the kinetic energy is also equal to

$$E(\omega)=\frac{1}{4m}\sum_{n=0}^{N} |a_n(\omega)|^2. \tag{14}$$

The sound power radiated by the panel is calculated using an elemental approach.[13] The velocities at the center of each of a dense grid of elements is calculated using Eq. (7) to form the vector $\mathbf{v}$, and it is assumed that the vector of pressures in front of each element on the panel, $\mathbf{p}$, is related to $\mathbf{v}$ by the acoustic impedance matrix $\mathbf{Z}$, so that

$$\mathbf{p}=\mathbf{Z}\mathbf{v}. \tag{15}$$

The radiated sound power can then be approximated by

$$W=\frac{\Delta S}{2}\mathrm{Re}[\mathbf{v}^H\mathbf{p}], \tag{16}$$

where ΔS is the area of each element, and this can also be written as

$$W = \frac{\Delta S}{2} \mathrm{Re}[\mathbf{v}^H \mathbf{Z} \mathbf{v}] = \mathbf{v}^H \mathbf{R} \mathbf{v}, \tag{17}$$

where $\mathbf{R} = (\Delta S/2)\mathrm{Re}[\mathbf{Z}]$, which has a particularly simple form for planar radiators.[13] 52×52 elements were used in these simulations so that their spacing is small compared with the acoustic wavelength at the highest frequency of interest.

Although the sound power radiated by the panel usefully quantifies the far-field pressure it generates, high levels of vibration in weakly radiated modes can give rise to significant pressure levels in the near field of the panel. It has been shown that the total kinetic energy of a panel provides a better measure of near-field pressure than radiated sound power,[11] and so if there is any possibility that listeners may be in close proximity to the panel, as well as being further away, then both of these criteria are important for active structural acoustic control.

For practical computations only a finite number of modes can be used in the expansion for the velocity, Eq. (7). The convergence of the modal series can be investigated by calculating the ratio of the velocity computed at a point on the panel with a modal summation using N modes, to that computed with a large number of modes, such as 500, with natural frequencies up to 38 kHz. For excitation at 300 Hz, for example, which is not a resonant frequency of the panel, the results show that for a point force actuator, the velocity at the measured point converges to within 1% of the result with 500 modes when about 100 modes are included in the modal summation, whereas 200 modes are required to reach this level of accuracy with the piezoelectric actuator.[14] This result can be misleading, however, for the active control simulations presented here since very high levels of attenuation are predicted at some frequencies and so the residual components of the vibration may be more sensitive to modal truncation. The results presented here were obtained by taking values of both n_1 and n_2 in Eq. (5) from 1 to 17, i.e., about 300 modes, with natural frequencies up to about 20 kHz. This was chosen since none of the results presented here was significantly altered if the upper limit of the modal summation was increased to n_1 and $n_2 = 25$, i.e., about 600 modes.

A large number of modes is required to accurately model the velocity with a collocated actuator because the velocity is influenced by the near field of the actuator, which is more intense for the piezoelectric actuator than it is for the point force. It should be noted that only the line moment excitation of the piezoelectric actuator[12] has been taken into account in the model, not the local stiffening effect.

A uniform array of 4×4 actuators and sensors was modeled on the panel and control systems were investigated for which each pair of the 16 individual actuators and sensors were connected in 16 control loops, as illustrated in Fig. 3 for the case of piezoelectric actuators. The transducers were uniformly arranged on the panel so that their centers were $\frac{1}{8}$, $\frac{3}{8}$, $\frac{5}{8}$, and $\frac{7}{8}$ of the plate length and breadth away from the edges.

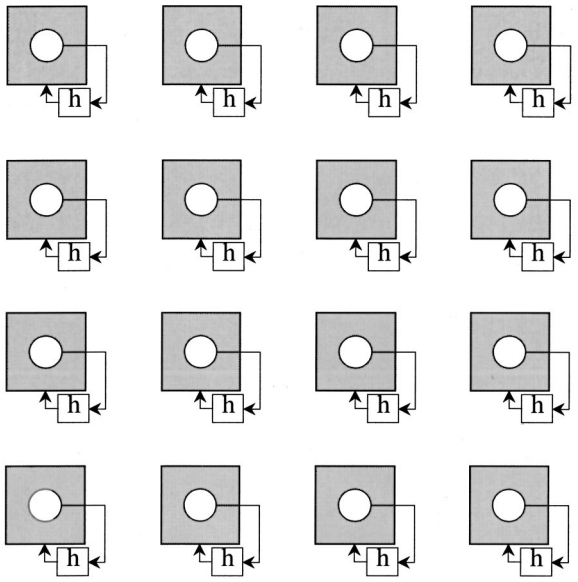

FIG. 3. Arrangement of 16 piezoelectric actuators, as shown by squares, driven locally by the output of 16 velocity sensors, as shown by circles, via individual control loops with a gain of h.

IV. RESULTS WITH POINT FORCE ACTUATORS

Figure 4 shows the total kinetic energy of the panel excited by the plane wave before control and when subject to control with 16 individual single channel control system with various feedback gains, h.

The modal response of the panel is clearly seen in the plot of the kinetic energy against frequency before control, with the resonance associated with the first, (1,1), mode occurring at about 72 Hz. As the gains of the feedback loops are increased, the resonances in the response become more heavily damped, as one would expect with velocity feedback control. If the gains of the feedback loops are increased beyond a certain value, however, the closed loop response displays new peaks, such as that at about 600 Hz, for example, which become more pronounced as the feedback gain is in-

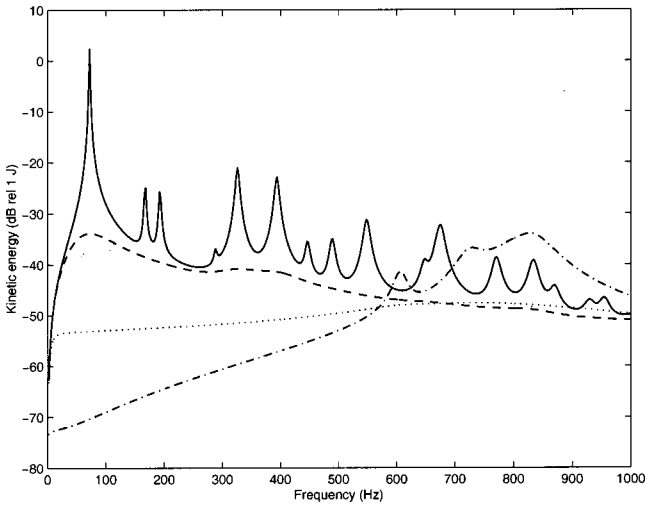

FIG. 4. Kinetic energy of the plane wave-excited panel with no control (solid line) and with a 16 channel decentralized feedback controller using force actuators and having feedback gains of 10 (dashed line), 100 (dotted line), and 1000 (dot-dashed line).

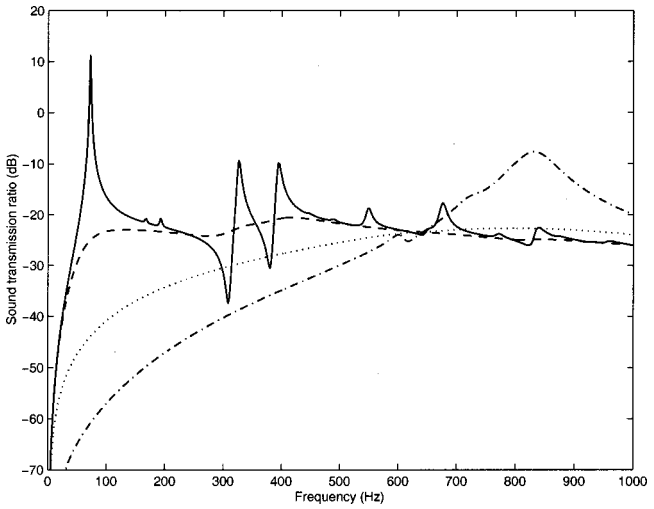

FIG. 5. Sound transmission ratio of the plane wave-excited panel with no control (solid line) and with a 16 channel decentralized feedback controller using force actuators and having feedback gains of 10 (dashed line), 100 (dotted line), and 1000 (dot-dashed line).

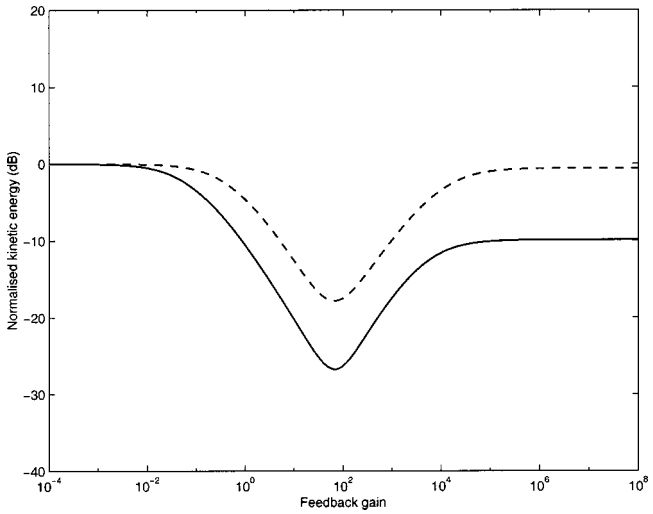

FIG. 6. Normalized kinetic energy level of the panel, integrated from 0 Hz to 1 kHz, plotted against the gain in the decentralized feedback controller, h, for the force actuators (solid line) and the piezoelectric actuators (dashed line).

creased further. These extra peaks are due to the resonances of the controlled dynamic system, which is effectively pinned at the sensor positions with high feedback gain. If feedback controllers having very high gain were used, the velocities at each sensor could be driven to zero and the physical result would be equivalent to that of perfect control of the sensor outputs with a feedforward control system, which could have been implemented if a suitable reference signal were available. With force actuators and velocity sensors the feedback gains have the same units as a mechanical impedance ($\mathrm{N\,s\,m^{-1}}$).

Figure 5 shows the ratio of the sound power radiated on one side of the panel to the incident sound power due to the plane wave excitation on the other side, which is termed the sound transmission ratio, T. Before control only the modes whose modal integers are both odd radiate sound significantly at low frequencies and also antiresonances appear, due to destructive interference between the sound pressures radiated by adjacent odd–odd modes. As the feedback gains are increased, similar trends are observed in the reduction of the sound transmission ratio as in the reduction of the panel's kinetic energy, except that the new resonance at about 830 Hz has the greatest prominence, since its velocity distribution has the greatest net volume velocity.

The panel's kinetic energy, integrated across the bandwidth shown in Fig. 4 (up to 1 kHz), is plotted against feedback gain as the solid line in Fig. 6, and a clear minimum is observed, for a gain of about 100. It should be emphasized that the individual outputs of the velocity sensors monotonically decrease as the feedback gains are increased, and that this is the only information available to the control system about the panel's vibration. These velocities give rise to a poor estimate of the panel's response when the feedback gains are high enough for the new resonances to become significant. Figure 7 shows the result for the sound transmission ratio integrated across this bandwidth, which corresponds to the total radiated sound power if the plate is subject to broadband excitation by a plane wave up to a frequency of 1 kHz, and which also has a minimum value for a feedback gain of about 100. Note also that at high feedback gains the overall sound power radiated after control is some 8 dB higher than it was with no control, because of the effect of the new resonance at about 830 Hz. The optimum feedback gain to minimize both kinetic energy or sound transmission is thus about 100 $\mathrm{N\,s\,m^{-1}}$, and the control system essentially synthesises an array of 16 mechanical dampers with this damping coefficient. It is interesting to note that the input or point impedance of an infinite 1 mm aluminum panel is real, frequency independent, and has a value of about 34 $\mathrm{N\,s\,m^{-1}}$.

V. RESULTS WITH PIEZOELECTRIC ACTUATORS

Although we can theoretically guarantee the unconditional stability of the 16 channel decentralized feedback control system in the case of point force actuators and velocity

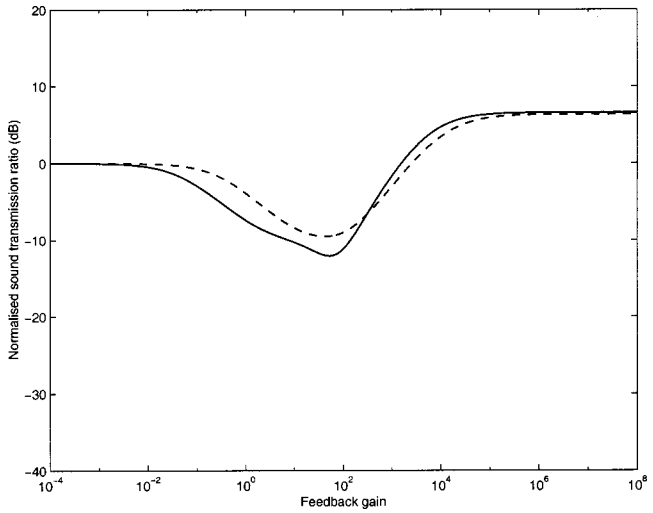

FIG. 7. Normalized sound transmission ratio level, integrated from 0 Hz to 1 kHz, plotted against the gain in the decentralized feedback controller, h, for the force actuators (solid line) and the piezoelectric actuators (dashed line).

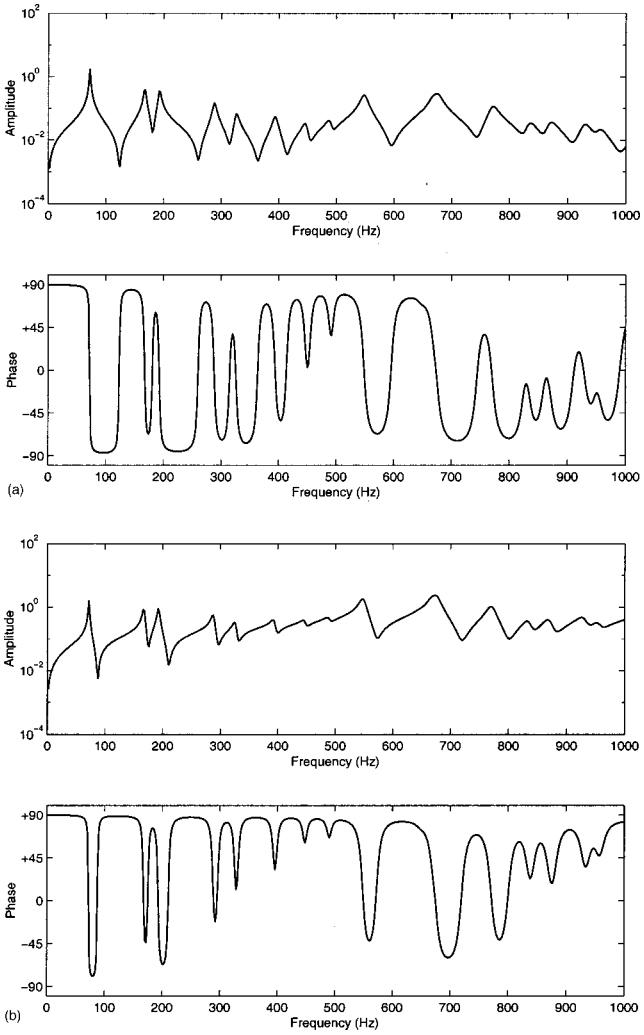

FIG. 8. Frequency responses between an individual force actuator and velocity sensor (a) and piezoelectric actuator and velocity sensor (b).

sensors, since this system is passive, the stability range of this controller must be determined when piezoelectric actuators are used before the control performance can be calculated. The stability of the decentralized feedback control system using piezoelectric actuators has been determined by examining the loci of the 16 eigenvalues of $\mathbf{G}(j\omega)$. This investigation was carried out on the simulated frequency responses up to 10 kHz and showed that within the accuracy of the simulation, all eigenvalues had positive real parts and so, in principle, the control system is again unconditionally stable. A practical investigation of this result is currently under way[15] in order to establish the upper limit imposed on the gain due to unmodeled effects in the interaction between the actuator, sensor, and structure. Rather than present the rather complicated eigenvalue loci referred to previously, the frequency response of a single diagonal element of the plant response up to 1 kHz is illustrated in Fig. 8 for both a force actuator (a) and a piezoelectric actuator (b), to illustrate the features of one of the individual control loops. The phase of both responses is confined to between $-90°$ and $+90°$, so that the real part of both responses has a positive real part. The absolute magnitude of the response between the piezoelectric actuator and the velocity sensor will depend on the

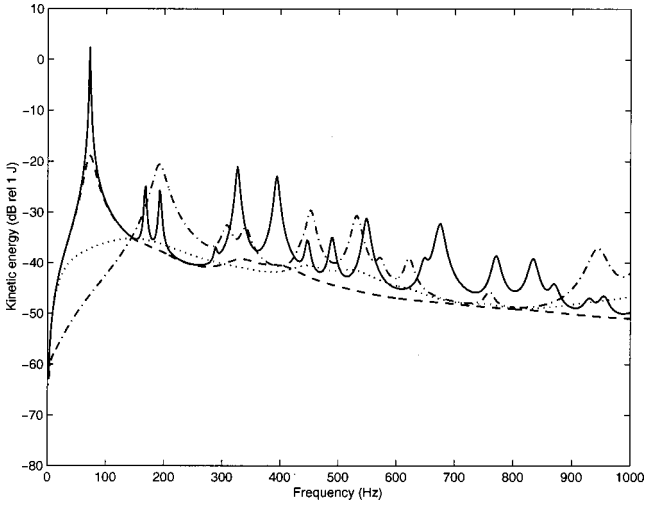

FIG. 9. Kinetic energy of the plane wave-excited panel with no control (solid line) and with a 16 channel decentralized feedback controller using piezoelectric actuators and with feedback gains of 1 (dashed line), 10 (dotted line), and 100 (dot-dashed line).

piezoelectric constants of the actuator, but the response in Fig. 8(b) has been normalized to have a similar value of that with the force actuator at the first resonance peak, at about 72 Hz.

Note that although the high frequency response using the piezo actuator is then about 20 dB greater than that using the force actuator, the shapes of the two frequency responses are surprisingly similar. When the piezoceramic actuator is small compared with the flexural wavelength in the panel, then at a given frequency and with these boundary conditions the moment excitation at the edges of the actuator thus has a similar effect to that of a point force. The theoretically dual sensor for a piezoceramic actuator would be a strain-measuring device of the same size and shape as the actuator. In order to collocate such a sensor it would typically be positioned on the other side of the panel, immediately opposite the actuator.[16] Unfortunately, such an actuator-sensor pair is then coupled by the in-plane motion of the panel as well as the flexural motion we are hoping to control. The in-plane motion can become dominant at high frequencies and destroy the passive property of the frequency response between such an actuator and sensor.[17,18] Another advantage of using the velocity derived from inertial accelerometers, rather than using strain sensors, is that the former is sensitive to any rigid body motion of the panel, whereas the latter is not.

The kinetic energy of the panel when using 16 individual single channel control systems with 16 piezoelectric actuators having velocity sensors at their centers are shown for various feedback gains in Fig. 9. Compared with the results using point force actuators, Fig. 4, the levels of reduction are somewhat smaller, although still very worthwhile below about 100 Hz. The frequencies at which extra resonances are induced at higher feedback gains are also significantly lower with the piezoelectric actuators than with the point forces, and the peak value of the first extra resonance, at about 200 Hz, is higher.

Figure 10 shows the sound transmission ratio when the

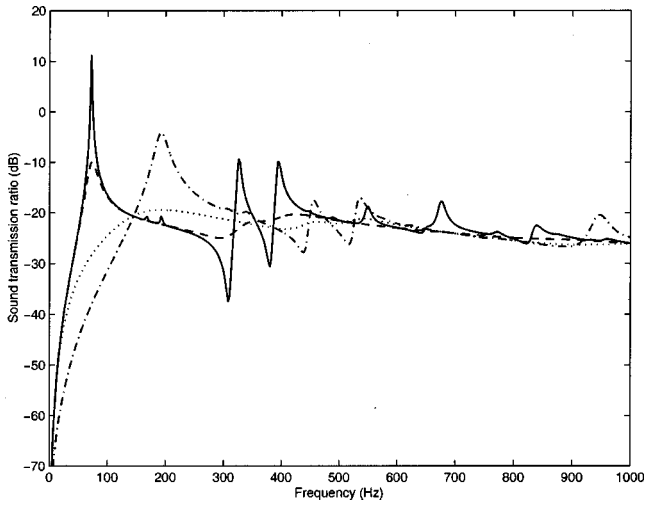

FIG. 10. Sound transmission ratio of the plane wave-excited panel with no control (solid line) and with a 16 channel decentralized feedback controller using piezoelectric actuators and with feedback gains of 1 (dashed line), 10 (dotted line), and 100 (dot-dashed line).

velocities are controlled by the piezoelectric actuators using 16 individual control systems with various feedback gains. Once again the performance is good for moderate feedback gains below about 100 Hz, but not as good as with force actuators, and the additional resonance at about 200 Hz degrades the performance for higher feedback gains.

The variation of the kinetic energy, integrated up to 1 kHz, with the feedback gain for piezoelectric actuators has been plotted in Fig. 6, together with this variation for force actuators. A clear minimum in the integrated kinetic energy is again seen for one value of feedback gain. This value of feedback gain is about the same as it was when using the force actuators, although it should be remembered that the piezoelectric responses have been scaled to be similar to force responses at the first resonance, as described previously. Of more importance is that at high feedback gains the integrated kinetic energy is not decreased when using piezoelectric actuators, due to the extra resonance at 200 Hz, whereas with force actuators reductions of about 10 dB in integrated kinetic energy are achieved even at high gains, because the extra resonances occur at higher frequencies and are not so prominent.

A similar comparison for the integrated sound transmission ratio is shown in Fig. 7, which again shows a clear minimum for a certain feedback gain, although the amplification for high feedback gains is now about the same when using piezoelectric actuators and when using force actuators.

VI. CONCLUSIONS

This paper reports the results of an initial simulation study of active vibroacoustic control using an array of collocated actuators and sensors and local feedback. It is shown that if perfect point force actuators and velocity sensors are used, such a feedback system is unconditionally stable.

The physical consequences of this control strategy are then investigated in a simulation of a panel excited by a plane acoustic wave and having a 4×4 array of force actuators and collocated velocity sensors. It is shown that both the kinetic energy of the panel and its transmitted sound power can be significantly reduced in the bandwidth up to 1 kHz provided an appropriate feedback gain is chosen. If the feedback gain is too large, the control systems will tend to pin the panel at the sensor locations, generating new resonance frequencies which can increase the response of the panel at higher frequencies.

Although an array of point force actuators has attractive theoretical properties, it cannot be implemented in practice without reacting the forces off a separate structure. Piezoelectric strain actuators, on the other hand, which generate line moments at their edges, can easily be integrated into a structure. Such an actuator cannot, strictly speaking, be collocated with a velocity sensor, and the stability of a control system using piezoelectric actuators and velocity sensors cannot be guaranteed in the same way as with force actuators and velocity sensors. The computer simulation has been used to calculate the responses from each of 16 small piezoelectric actuators on the panel to each of 16 velocity sensors at the center of these actuators, which form the matrix of plant responses for the feedback loop in this case. These responses have then been used to calculate the range of gains for which the 16 single channel feedback controllers will be stable, which was found to be unlimited in these idealized simulations.

Having established the stability of this control strategy with piezoelectric actuators, the performance has been calculated for various feedback gains. Once again significant reduction can be achieved with appropriate feedback gains in both the vibration of the panel, as quantified by the kinetic energy, and in its sound radiation, as quantified by the sound transmission ratio. With higher values of feedback gain not only is there a danger of instability due to unmodeled dynamics, but the feedback control systems again tend to pin the panel causing additional resonances, which now occur at much lower frequencies than was the case with point force actuators.

The overall performance of the various control strategies can be estimated by integrating the kinetic energy and the sound transmission ratio over the bandwidth considered, up to 1 kHz. Using this criterion, the maximum reduction in vibration which can be obtained with point force actuators is about 28 dB, whereas the maximum attenuation with piezoelectric actuators is about 18 dB. The maximum attenuation in the sound power transmission integrated over this bandwidth is about 12 dB with point force actuators and about 9 dB with piezoelectric actuators. It is emphasized that the reductions in the panel's kinetic energy may give a better indication of the change in sound pressure close to the panel than the sound power radiated into the far field.

This initial investigation thus suggests that useful reductions can be obtained in both the near-field and the far-field sound radiated from a panel using this decentralized feedback control approach, which is able to control broadband random primary fields as well as impulsive or tonal disturbances. Since each pair of actuators and sensors is only connected by local, constant-gain, feedback controllers, no coupling is necessary between each actuator and sensor pair, which could potentially be manufactured as identical modular units with simple integrated electronics.

[1] L. Meirovitch, *Dynamics and Control of Structures* (Wiley, New York, 1990).
[2] A. Preumont, *Vibration Control of Active Structures* (Kluwer Academic, Dordrecht, 1997).
[3] C.R. Fuller, S.J. Elliott, and P.A. Nelson, *Active Control of Vibration* (Academic, New York, 1996).
[4] J.Q. Sun, ''Some observations on physical duality and collocation of structural control sensors and actuators,'' J. Sound Vib. **194**, 765–770 (1996).
[5] S.J. Elliott, P. Gardonio, T.C. Sors, and M.J. Brennan, ''Active vibro-acoustic control with multiple local feedback loops,'' *Proceedings of the Eighth SPIE International Symposium on Smart Structures and Materials*, 2001, pp. 720–731.
[6] M.J. Balas, ''Direct velocity feedback of large space structures,'' J. Guid. Control **2**, 252–253 (1979).
[7] S.M. Joshi, *Control of Large Flexible Space Structures* (Springer, Berlin, 1989).
[8] K.J. Åström and B. Wittenmark, *Adaptive Control*, 2nd ed. (Addison–Wesley, Reading, MA, 1995).
[9] S.J. Elliott and C.C. Boucher, ''Interaction between multiple feedforward active control systems,'' IEEE Trans. Speech Audio Process. **2**, 521–530 (1994).
[10] S. Skogestad and I. Postlethwaite, *Multivariable Feedback Control* (Wiley, New York, 1996).
[11] M.E. Johnson and S.J. Elliott, ''Active control of sound radiation using volume velocity cancellation,'' J. Acoust. Soc. Am. **98**, 2174–2186 (1995).
[12] B.T. Wang, C.R. Fuller, and E.K. Dimitriadis, ''Active control of noise transmission through rectangular plates using multiple piezoelectric or multiple point force actuators,'' J. Acoust. Soc. Am. **90**, 2820–2830 (1991).
[13] S.J. Elliott and M.E. Johnson, ''Radiation modes and the active control of sound power,'' J. Acoust. Soc. Am. **94**, 2194–2204 (1993).
[14] T. Sors, ''Active structural acoustic control of sound transmitted through a plate,'' Ph.D. Thesis, University of Southampton, 2000.
[15] E. Bianchi, P. Gardonio, and S.J. Elliott, ''Smart panel with an array of 16 sensor-actuator pairs for the control of sound transmission,'' *Proceedings of the International Conference On Smart Technology Demonstrators and Devices*, Edinburgh, United Kingdom, December 2001 (to be published).
[16] B. Petitjean and I. Legrain, ''Feedback controllers for active vibration suppression,'' J. Struct. Control **3**, 111–127 (1996).
[17] S.Y. Yang and W.H. Huang, ''Is a collocated piezoelectric sensor/actuator pair feasible for an intelligent beam?,'' J. Sound Vib. **216**, 529–538 (1998).
[18] P. Gardonio, Y.-S. Lee, S.J. Elliott, and S. Debost, ''A panel with matched polyvinylidene fluoride volume velocity sensor and uniform force actuator for the active control of sound transmission,'' Proc. Inst. Mech. Eng., J. Aerospace Eng. **215**(G), 187–206 (2001).

Reduction of electronic delay in active noise control systems—A multirate signal processing approach

Mingsian R. Bai,[a] Yuanpei Lin, and Jienwen Lai
Department of Mechanical Engineering, National Chiao-Tung University, 1001 Ta-Hsueh Road, Hsin-Chu 300, Taiwan, Republic of China

(Received 30 November 2000; accepted for publication 5 November 2001)

Electronic delay has been a critical problem in active noise control (ANC) systems. This is true whether a feedforward structure or a feedback structure is adopted. In particular, excessive delays would create a causality problem in a feedforward ANC system of a finite-length duct. This paper suggests a multirate signal-processing approach for minimizing the electronic delay in the control loop. In this approach, digital controllers are required in decimation and interpolation of discrete-time signals. The computation efficiency is further enhanced by a polyphase method, where the phases of low-pass finite impulse response (FIR) filters must be carefully designed to avoid unnecessary delays. Frequency domain optimization procedures based on H_1, H_2, and H_∞ norms, respectively, are utilized in the FIR filter design. The proposed method was implemented by using a floating-point digital signal processor. Experimental results showed that the multirate approach remains effective for suppressing a broadband (200–600 Hz) noise in a duct with a minimum upstream measurement microphone placement of 20 cm.
[DOI: 10.1121/1.1432980]

PACS numbers: 43.50.Ki [MRS]

NOMENCLATURE

p_{sp}	equivalent primary pressure source
p_{sa}	equivalent secondary pressure source
Z_{sp}	equivalent primary source impedance
Z_{sa}	equivalent secondary source impedance
Z_0	radiation impedance at the duct opening
$C(z)$	digital filter of active controller
$H_{\mathrm{d}}(e^{j\omega})$	frequency response template
Bl	electromagnetic transduction constant
z_{M}	mechanical mobility of loudspeaker
$u_{\mathrm{c}}, f_{\mathrm{c}}$	cone velocity and force

I. INTRODUCTION

Active control for noise in ducts has been investigated by researchers in the area of active noise control (ANC) for decades.[1–4] A great majority of ANC systems to date has been realized by digital systems.[4] Although digital systems provide many advantages over the analog counterpart, they suffer from several design constraints. In particular, the electronic delay during analog-to-digital (AD) conversion and digital-to-analog (DA) conversion, low-pass antialiasing and reconstruction (or smoothing) filtering has been a critical problem in active noise control systems. These delays along with other inherent delays resulting from computation and transducer dynamics might pose design constraints on ANC systems, which could become quite severe when the application of interest has strict space limitation, e.g., active mufflers for motorcycles. These design constraints apply to both feedback control and feedforward control. Specifically, excessive delays would limit the achievable performance and stability margin in a feedback ANC system.[5] Causality is usually not a problem for periodic signals so long as the controller has a long enough impulse response to produce the properly phased cancellation filter. In conventional signal-processing applications, delay is usually not an important issue. Pure delay is usually tolerated because the waveform is preserved. However, delay becomes crucial in control systems, especially for ANC applications that generally involve relatively large bandwidth. Excessive delays could create causality problems in a feedforward ANC system of a finite length duct if the noise of concern is broadband and random in nature. Causality constraint refers to the condition under which the delay in the acoustical path is greater than the electronic path such that the resulting controller is causal and hence implementable. Under the causality constraint, delays in low sampling rate systems generally result in impractical requirement on physical dimension.[1,4]

To combat the delay problem in the control loop, this paper proposes a digital signal-processing scheme based on the multirate concept that is a fast growing area in many applications.[6,7] In this approach, digital controllers are required in decimation and interpolation of discrete-time signals. To enhance computation efficiency, a polyphase method is employed in filter design.[8–10] In the multirate ANC system, a factor of 8 was used for upsampling and downsampling. This resampling process raises the nominal sampling frequency of controller 2 kHz to 16 kHz during AD/DA conversion, which significantly reduces the sample delays. As a crucial part in the polyphase design, the phases of low-pass finite impulse response (FIR) filters must be carefully designed to avoid unnecessary delays. To this end, optimization

[a]Electronic mail: msbai@cc.nctu.edu.tw

procedures in frequency domain based on H_1, H_2, and H_∞ norms, respectively, are utilized in the design.[11–13]

One fundamental question may be naturally raised: why not simply run the ANC system at a very high sampling rate? Delay would then be low, and there would be no need for the multirate filters at all. Unfortunately, there are several subtle points that may prohibit the use of this seemingly straightforward approach. First, the effective control bandwidth for the physical system would only be in a small portion of the total frequency span. This causes an ill-conditioned eigenvalue spread and poor frequency resolution. Second, numerical problems may arise so that a filter with lightly damped poles may easily become unstable. Third, impractically long taps may be needed to implement a FIR filter for very high sampling rate operation, and the computations may not be completed within one sample. Therefore, we chose to take the indirect approach, multirate signal processing. It was also pointed out by the reviewer that the idea of using multirate, or oversampling, has been applied to ANC by Brammer *et al.* for headsets.[14] In their work, a digital ANC headset based on adaptive feedforward control has been developed, and the performance measured on human subjects using helicopter noise reproduced in a reverberation room. Their system demonstrated more than 10-dB noise reduction at frequencies 16 to 250 Hz. A dual-rate sampling structure is used. The signals at the reference and error microphones were oversampled, and the control signal computation and updating were performed at a decimated rate. This technique reduces the delay in the control path by increasing the sampling frequency of AD and DA converters and, at the same time, permits the low-frequency performance of the FIR filter to be improved. This paper is based on the same motivation, but different from the work of Brammer *et al.* in the following aspects. First, the nature of the problem in this paper is quite different from the headset problem. The problem investigated in this paper is a one-dimensional duct problem where the complexity of its plant dynamics is much higher than the zero-dimensional headset problem. Second, the ANC structure examined in this paper is the spatially feedforward structure with strong acoustic feedback (from the actuator to the upstream sensor). Acoustic feedback creates a undesirable positive feedback and may destabilize the system, which calls for different controller design than the headset problem. In headset problems, acoustic feedback is virtually negligible and conventional filtered-X LMS is sufficient. On the other hand, the significance of delay to the spatially feedforward system is examined in the paper. How to reduce delay becomes a critical issue due to the causality constraint imposed by the feasible physical dimension. Third, in the paper details of how one would implement the multirate scheme are presented, and the effectiveness of the approach with regard to physical dimension is quantitatively evaluated. As pointed out by Brammer *et al.*, electronic delay can be reduced by running IO operations at a high sampling rate, while performing computation at a low sampling rate. However, cautions must be taken to implement this idea properly. Two digital low-pass filters are needed to eliminate the artifacts in the decimation and interpolation processes. Without these protection measures, one might get erroneous results from the up/down sampling. Unlike typical multirate signal processing, however, these low-pass filters entail special design in the context of active control, where delay within the control bandwidth has profound effects on performance and stability. Another key step regarding implementation is the enhancement of computational efficiency by polyphase filters. As compared to the primitive up/down sampling scheme, where idling of CPU power arises due to redundancies such as dropping of data during decimation and convolution with zero during interpolation, great saving of computations can be obtained by reformulating the filters by polyphase structures. These implementation techniques are not trivial but extremely important to a properly functioning multirate system. Without handling these crucial steps correctly, the system may result in poor efficiency and even failure of performance.

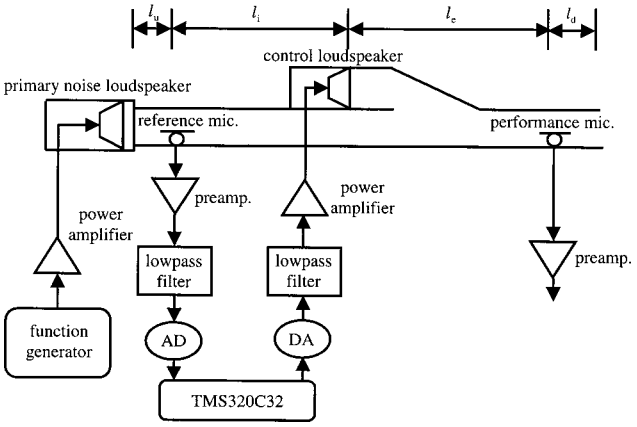

FIG. 1. The spatially feedforward structure of ANC system.

The proposed method was implemented by using a floating-point digital signal processor (DSP). Experimental results indicated that the multirate approach is effective for suppressing broadband noise in a spatially feedforward duct ANC system. Some technical considerations involved in implementation will also be addressed in the paper.

II. EFFECTS OF DELAY ON A SPATIALLY FEEDFORWARD SYSTEM

The ANC system chosen for investigation in this work is the *spatially feedforward structure*[15] for ducts, which has been a prevailing ANC structure in that it can be used when a nonacoustical reference is unavailable and broadband attenuation is desired. In what follows, only key results relevant to the discussion are presented and detailed derivations can be found in the literature[16] and are thus omitted for brevity.

Figure 1(a) depicts a duct ANC system with spatially feedforward structure. In this structure, an upstream microphone is employed to measure the sound field near the primary noise source. The signal from the upstream microphone is fed to the controller, which produces a control signal to drive a downstream control speaker that generates an antifield to interact with the primary noise field. The goal of active control is to minimize the residual noise downstream of the control speaker. The definitions of symbols can be found in the Nomenclature and Ref. 15.

TABLE I. The electro-mechanical parameters of a moving-coil speaker.

Electro-mechanical constants	
M_M	13.83 g
R_M	1.3 ohms
C_M	874 μm/N
R	6.88 ohms
L	0.68 mH
Bl	4.85 T-m

Munjal and Eriksson[16] derived the ideal controller capable of achieving global noise cancellation downstream of the control source in a finite-length duct

$$C=-\frac{Z_{sa}}{Y_0}\left(\frac{e^{-jkl_i}}{1-e^{-2jkl_i}}\right)=C_0\cdot C_r, \tag{1}$$

where Z_{sa} is the equivalent acoustic impedance of the control source, $Y_0=c/S$ is the characteristic impedance of the duct, c is the sound speed, S is the cross-sectional area of the duct, k is the wave number, and l_i is the distance between the upstream measurement microphone and the control source. In Eq. (1), $C_0\equiv -Z_{sa}/Y_0$ is a function of the finite impedance Z_{sa}, which depends only on the electro-mechanical parameters of the control source. On the other hand, $C_r \equiv e^{-jkl_i}/1-e^{-2jkl_i}$ takes the form of the so-called *repetitive controller*.[17] Due to the infinite number of poles on the imaginary axis, both frequency response and impulse response of the ideal controller exhibit patterns of comb-typed periodic peaks ($\Delta f=c/2l_i, \Delta t=2l_i/c$). The fundamental reason for the repetitiveness is essentially rooted in the acoustic feedback.

In the course of analysis, we shall develop some physical insights into the causality of the ANC system by examining the aforementioned ideal controller. It is observed from Eq. (1) that the implementation of the ideal controller requires the knowledge of the control source impedance Z_{sa}. In what follows, Z_{sa} will be expressed explicitly in terms of the electro-mechanical parameters of speaker. Detailed analysis will show that Z_{sa} can be expressed as[15]

$$Z_{sa}=\frac{1}{\rho S^2}\left(\frac{1}{z_M}+\frac{B^2l^2}{R+j\Omega L}\right), \tag{2}$$

where R is the total equivalent resistance of the coil, L is the equivalent inductance of the coil, Bl is the coil constant, z_M is the mechanical mobility, and Ω is the analog frequency in rad/s. In the expression of Eq. (2), Z_{sa} depends solely on the speaker parameters R, L, and Bl that can be identified in advance.[18] In the experimental setup in our case, these parameters were identified and listed in Table I. With the transducer dynamics taken into account, it has been shown in Ref. 15 that the resulting controller is

$$C'=-\frac{1}{G_{XDCR}}\left(\frac{e^{-jkl_i}}{1-e^{-2jkl_i}}\right), \tag{3}$$

where

$$G_{XDCR}=(g_p g_m G_s)\frac{Y_0}{Z_{sa}} \tag{4}$$

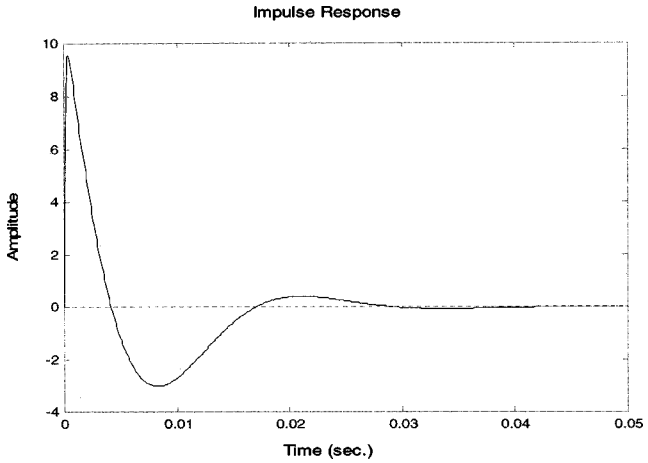

FIG. 2. The impulse response of transducer dynamics G_{XDCR}.

represents the overall transducer dynamics, where g_p and g_m denote the constant gains of the power amplifier and the microphone, respectively, and G_s is the frequency response function of the speaker

$$G_s=\frac{Bl}{S(R+j\Omega L)}. \tag{5}$$

Inspection of Eq. (3) reveals that the transducer response must compete with the propagation delay e^{-jkl_i} in the acoustic path. More precisely, the condition under which the resulting controller is causal is that the term e^{-jkl_i}/G_{XDCR} must be causal. This is an important causality constraint one must observe, particularly for the spatially feedforward structure.

Omitting the constants g_p, g_m, and Y_0 in Eq. (4), G_{XDCR} can be written as a third-order system

$$\begin{aligned} G_{XDCR}\sim (BlR_MC_Ms)/[&M_MR_MC_MLs^3 \\ &+(C_ML+M_MR_MC_MR)s^2 \\ &+(C_MR+R_ML+B^2l^2R_MC_M)s+R_MR], \end{aligned} \tag{6}$$

where M_M, R_M, C_M are mechanical mass, viscous damping, and mechanical compliance, respectively. For example, we can use the data in Table I and plot the impulse response of G_{XDCR}, as shown in Fig. 2. The first peak is at 0.3 ms, which amounts to 0.6 delay samples at 2-kHz sampling rate. Using this as a criterion of transducer delay, the length of the duct must be greater than 343 m/s (at 20 °C) $\times 0.3$ ms $=0.103$ m to meet the causality condition.

In addition to transducer delay, other types of electronic delay include all possible delays in the antialiasing/smoothing filters (denoted as δ_F), AD/DA conversion, and the one-sample processing time (provided computations are completed within one sample), where the last two terms can be lumped into a single term δ_T. These delays, together with the group delays of transducer and the digital controller (denoted as δ_X and δ_W, respectively), constitute the total electronic delay

$$\delta_E=\delta_X+\delta_F+\delta_T+\delta_W. \tag{7}$$

The electronic delays are summarized in Fig. 3. The transducer delay δ_X is estimated according to the first peak of the impulse response of Eq. (6). The analog filter delay can be

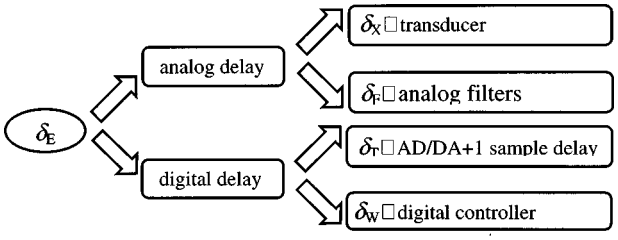

FIG. 3. The elements of electronic delay δ_E.

estimated by $\delta_F = n/8f_c$, where n is the filter order and f_c is the cutoff frequency.[19] The one-sample delay and the AD/DA delay together can be estimated by $\delta_T = \Delta\Phi/360\Delta f$, where Φ is the unwrapped phase (in degrees) of the DSP frequency response in "echo" operation.

A formal statement of the causality constraint on the spatially feedforward ANC system can now be written as

$$\delta_A \geq \delta_E, \tag{8}$$

where the acoustical delay $\delta_A = l_i/c$, l_i being the distance between the upstream microphone and the control speaker. Violation of the causality constraint, i.e., the electronic delay is greater than the acoustical delay, will result in a noncausal controller. An optimal causal approximation to a noncausal controller may well exist theoretically and converge to the Wiener filter solution.[20] However, in practice, violation of causality would give rise to performance degradation of an ANC system, depending on the degree of violation. For the compensators to be implementable, the acausal part must be truncated to construct FIR filters. Physically, the causality constraint sets the minimum length of duct for which random noise can be effectively canceled

$$(l_i)_{\min} \geq c\,\delta_E. \tag{9}$$

Therefore, a system with large electronic delay will generally lead to impractical length of duct, especially when the sampling rate is low. For example, the sampling rate is selected to be 2 kHz in our experiment, rendering an estimated electronic delay of 4.3 samples. This corresponds to a minimal duct length of 73 cm. From the delay components listed in Table II, it can be observed that δ_F and δ_T contribute most significantly to the overall delay. Given a length limitation of a duct, one must strive to minimize the electronic delay in order to meet the causality constraint. To this end, a multirate signal-processing technique is developed in this work for reducing the delays δ_F and δ_T.

TABLE II. The elements of electronic delay measured in samples (on a 2-kHz basis).

Delay elements	Conventional implementation (samples)	Multirate implementation (samples)
δ_X	0.6	0.6
δ_F	2.2	0.3[a]
δ_T	1.5	0.7
Total delay	4.3	1.6

[a]Includes the delay of digital LPF = 0.1 samples.

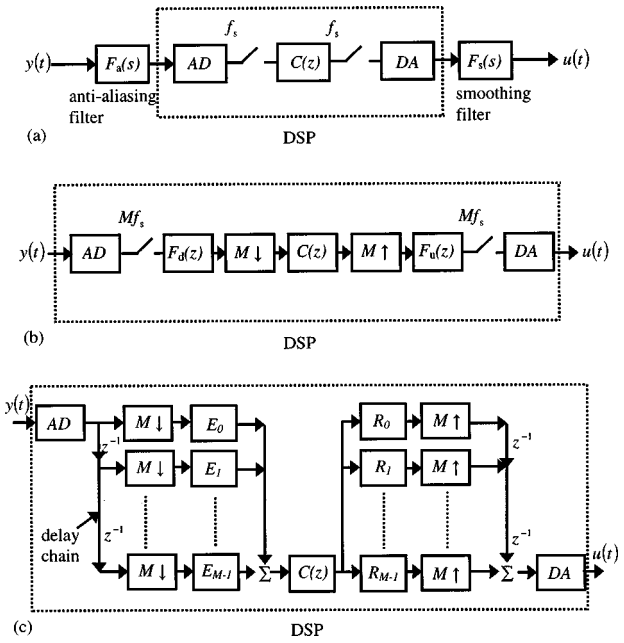

FIG. 4. The structures of implementation for a duct ANC system. (a) The conventional structure; (b) the original multirate structure; (c) the multirate structure using polyphase representation.

III. MULTIRATE SIGNAL PROCESSING BY POLYPHASE FILTERS

To reduce electronic delay, this paper proposes a digital signal-processing scheme based on the multirate concept. In this approach, only inexpensive analog filters with high cutoff frequency, e.g., 8 kHz, are required. To enhance computation efficiency, a polyphase method is employed in filter design. This technique reduces the delay in the control loop by increasing the sampling frequency of AD and DA converters and, at the same time, permits the low-frequency performance of the FIR filter to be improved.

The block diagram of a conventional ANC system is depicted in Fig. 4(a). The system generally suffers from excessive electronic delay, especially for low sampling rate and/or low filter cutoff frequencies. It may create a causality problem in the ANC system, particularly for the control of broadband random noise where upstream microphone spacing is limited, such as short ducts. It is then highly desirable to minimize, whenever possible, the group delay in the electronic path. To this end, an ANC system based on multirate digital signal processing is developed in the work. The general idea of the multirate ANC system is depicted in Fig. 4(b). In the new structure, the sampling rate of AD and DA converters is raised to a much higher rate, say, $M f_s$, with M being the decimation factor. The continuous-time signal $y(t)$ from the sensor is discretized by an AD converter at a high sampling rate, filtered by a low-pass digital filter, and decimated by a downsampler. The signal is then processed by a low sampling rate (f_s) digital controller $C(z)$ to produce an output signal that is in turn interpolated by an expander to the high sampling rate, $M f_s$. In this paper, a fixed controller $C(z)$ is synthesized for the spatially feedforward duct problem. The frequency response samples of the controller are calculated by using Eq. (3). Then, the discrete-time transfer

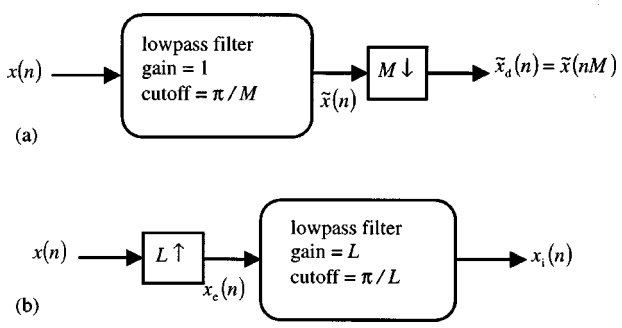

FIG. 5. The decimator and the interpolator. (a) Decimator for sampling rate reduced by a factor M; (b) interpolator for sampling rate increased by a factor L.

function of the controller $C(z)$ is obtained simply by curve-fitting the frequency response samples, using the MATLAB command *invfreqz*. The details of implementation can be found in Ref. 15. The upsampled signal is low-pass filtered before DA conversion into the continuous-time actuating signal $u(t)$. It is noted that, in this multirate scheme, hardware complexity and the associated delay are reduced because low-pass filtering is all done by software and analog low-pass filters are no longer needed. Efficient implementation of the interpolation and decimation filters forms the basis of a delay-reduced ANC system. Optimization methods can be utilized to calculate the filter coefficients, as will be detailed in the next section. In addition to the reduction of hardware complexity, the AD/DA delay and the one-sample computation delay are almost negligible because the critical processes are operated at a much higher sampling rate, hence the saving of δ_T and δ_F.

As a final touch, computation efficiency of the multirate ANC system can be drastically enhanced by polyphase filters, as shown in Fig. 4(c), where the decimation factor M and the interpolation factor L are identical. Note that the decimation filter and the interpolation filter both contain delay chains that function essentially as rotating switches.[7]

IV. FILTER DESIGN BY FREQUENCY-DOMAIN OPTIMIZATION

The decimation and interpolation processes in the foregoing multirate ANC system involve the design of two digital low-pass filters. In order to avoid aliasing in downsampling by a factor of M, a low-pass filter is required with a cutoff frequency

$$\omega_N < \pi/M, \tag{10}$$

as illustrated in Fig. 5(a). If the discrete-time input $x(n)$ is filtered by such a filter, then the output $\tilde{x}(n)$ can be downsampled without aliasing. Such a system is called a decimator. On the other hand, to reconstruct the sequence by upsampling with a factor of L requires another low-pass filter with cutoff frequency π/L and gain L, as shown in Fig. 5(b). Such a system is called an interpolator. In general, FIR filters are employed as the low-pass filters due to the fact that they are inherently stable.

To further improve the computation efficiency, optimization techniques[11] in frequency domain are developed for minimizing the filter length. In terms of H_1, H_2, and H_∞ norms, the optimization problem of the filter design can be written as follows:[12]

$$\min_{h(k)\in R} \left\| \sum_{k=0}^{K-1} h(k)e^{-j\omega k} - H_d(e^{j\omega}) \right\|_{1,2,\infty}, \tag{11}$$

where $\|\ \|$ denotes the norm, ω is the digital frequency, K is the tap length of the FIR filter, $h(k)$ is the impulse response (or the filter coefficients) of the FIR filter, and $H_d(e^{j\omega})$ is a low-pass frequency response template. The objective here is to find the filter coefficients $h(k)$ such that the "difference" (measured by 1, 2, or ∞ norm) between the desired and the resulting frequency responses is minimized. Globally optimal solutions exist for these problems because they all fall into the class of convex problems.[12,13]

The optimization problem of Eq. (11) can now be solved numerically by subroutines *fminu* (1 norm and 2 norm) and *minimax* (∞ norm) in the MATLAB optimization toolbox.[13] Among these, the H_2 optimization problem can also be solved via the least-square method. Express the desired frequency response into a FIR form

$$H_d(z) = \sum_{k=0}^{K-1} h(k)z^{-k}. \tag{12}$$

Substituting the frequency samples $z = e^{j\omega_n}$, $n = 1,2,...,N$, in Eq. (12) leads to the following linear system of equations:

$$\begin{bmatrix} H_d(e^{i\omega_1}) \\ H_d(e^{i\omega_2}) \\ \vdots \\ H_d(e^{i\omega_N}) \end{bmatrix} = \begin{bmatrix} e^{-j\omega_1\times 0} & e^{-j\omega_1\times 1} & \cdots & e^{-j\omega_1\times(K-1)} \\ e^{-j\omega_2\times 0} & \ddots & & e^{-j\omega_2\times(K-1)} \\ \vdots & & \ddots & \vdots \\ e^{-j\omega_N\times 0} & e^{-j\omega_N\times 1} & \cdots & e^{-j\omega_N\times(K-1)} \end{bmatrix} \times \begin{bmatrix} H(0) \\ h(1) \\ \vdots \\ h(K-1) \end{bmatrix}. \tag{13}$$

In matrix notation, Eq. (13) can be written in a more compact form

$$\mathbf{b} = \mathbf{A}\mathbf{x}. \tag{14}$$

The least-square solution of Eq. (14), corresponding to the H_2 optimization of Eq. (11), simply reads

$$\mathbf{x} = \mathbf{A}^+\mathbf{b}, \tag{15}$$

where $\mathbf{A}^+ = (\mathbf{A}^H\mathbf{A})^{-1}$, $\mathbf{A}^H\mathbf{b}$ being the *pseudoinverse*[21] of $\mathbf{A}$.

To end this section, an important point regarding how to choose the desired filter response for multirate implementation needs to be addressed. A common practice in multirate signal processing is to employ low-pass filters with linear phase property, where waveform distortion is the only concern. Unfortunately, such an approach did not work for our ANC application because of the undesired group delay intro-

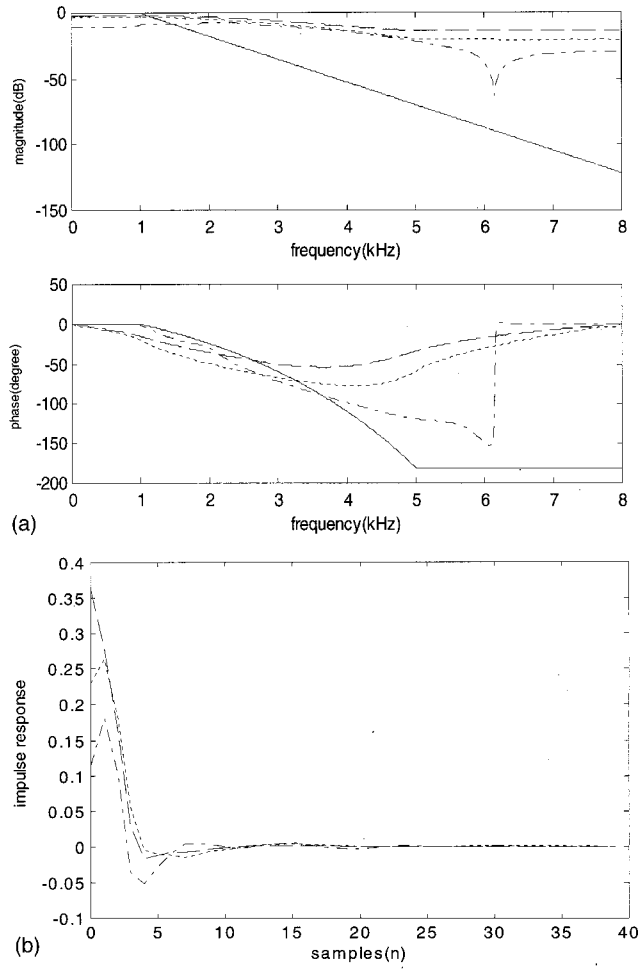

FIG. 6. Comparison of optimal filter designs using H_1, H_2, H_∞ norms, respectively. (a) The frequency responses; (b) the impulse responses. template (—), 1-norm (–·–), 2-norm (···), ∞-norm (––).

duced by the filters. Instead, we selected the templates H_d with minimal phase shifts within the passband. The best compromise between the stopband roll-off rate and the passband phase shift must be sought to choose the template. If there is not enough stopband roll-off, an aliasing problem will arise. On the other hand, increasing the filter roll-off will increase phase shift and degrade the performance. Once an appropriate template is chosen, it can be amended to the aforementioned optimal filter design procedure.

The model-matching criterion described in Eq. (11) is a general-purpose frequency-domain FIR filter design method. It is a simple technique that enables one to find the filter coefficients in an optimal fashion, given the frequency response specification. Different from FFT-based methods, this approach does not require the numbers of frequency samples and filter coefficients to be equal (we generally want the latter as small as possible). In this work, the frequency-domain optimization technique is employed to design both the low-pass filters required in decimation and interpolation processes, and the ANC filter $C(z)$ as well. That is, the filter template H_d can be low-pass filters or $C(z)$, depending on what one is after.

An example of the optimal filter design is shown in Fig. 6. From the results, it can be observed that the H_2 and H_∞ filters have similar trends in both frequency response and impulse response. The filter obtained from H_1 optimization has larger phase shift at high frequency than the other filters.

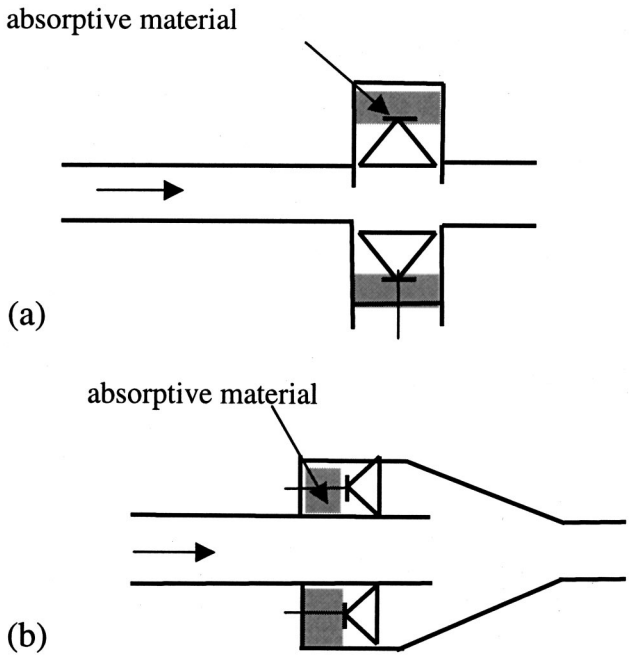

FIG. 7. Two arrangements of control loudspeaker. (a) Sideway loudspeaker; (b) backward loudspeaker.

V. EXPERIMENTAL INVESTIGATIONS

Experiments were undertaken to compare the performance of spatially feedforward duct ANC systems with and without multirate implementation. In addition, the effects of different optimal filter designs on the control performance are also examined. A wooden duct of length 440 cm and cross section 25×25 cm was constructed for the experiments. If the control loudspeaker is oriented like Fig. 7(a), the controller frequency response is expressed as Eq. (3), in which an infinite number of poles will be present on the imaginary axis as a result of acoustic feedback. To mitigate the acoustic feedback, we faced the control loudspeaker towards the opening of the duct, as shown in Fig. 7(b). A practical loudspeaker differs from an ideal one-dimensional omnidirectional point source. In this configuration, Eq. (3) should be modified into

$$C' = -\frac{1}{G_{\mathrm{XDCR}}}\left(\frac{e^{-jkl_i}}{1-De^{-2jkl_i}}\right), \tag{16}$$

where $|D|<1$ signifying the ''directivity factor'' of the transducer, which is generally frequency dependent with increasing attenuation as frequency is increased. Such an approach would effectively reduce the repetitiveness of the controller impulse response (because the poles are moved away from the imaginary axis) and improve the performance as well. An extensive investigation on this technique can be found in Ref. 22. A TMS320C32 DSP equipped with four 16-bit analog IO channels is utilized to implement the controller. The sampling frequency is chosen to be 16 kHz. The up/down sampling factor is selected to be 8, rendering a nominal sampling rate of 2 kHz for the digital controller $C(z)$. Consid-

ering the cutoff frequency of the duct (approximately 700 Hz) and the poor response of the control speaker at low frequency, we chose as the control bandwidth 200 to 600 Hz. It is noted that the delays introduced by the multirate low-pass filters have been compensated by a simple ''preview'' procedure[15] in implementing $C(z)$ as follows:

(a) Measure the frequency response of the DSP in the ''echo'' mode (with only AD/DA conversions and the multirate filters), and estimate the effective delay (in samples) by $N=\Delta\Phi/360T\Delta f$, where f is frequency (in Hz), Φ is the unwrapped phase (in degrees), and T is the sampling period.
(b) Compensate the controller $C(z)$ by multiplying its frequency response with $\exp(j\theta N)$.
(c) Calculate the discrete-time transfer function of the compensated controller by using the MATLAB command *invfreqz*. This would effectively ''phase-lead'' compensate the controller by a phase shift $\pi f\Delta\Phi/180\Delta f$. It is also tantamount to advancing the impulse response of the controller; hence the name preview.

The active noise controller of Eq. (3) was implemented on the platform of the above-mentioned hardware system. The distance between the upstream measurement microphone and the control speaker is 2.8 m to avoid any causality problem.

In order to examine if the multirate approach is an effective method for designing low-speed digital filters in conjunction with high-speed IO channels, an experiment is conducted for comparing the conventional low sampling rate method and multirate rate method with H_2 optimal filter. Figure 8(a) shows the experimental results obtained from DSP implementation of both methods. Good agreement can be found in the magnitude response within the control bandwidth 200–600 Hz. However, the phase response deserves more explanation. At low sampling rate (2 kHz), the IO delay (δ_T) of the conventional implementation is approximately 1.5 samples. The controller must be advanced using samples previewed by 1.5 to compensate for the delay. By multirate implementation, where the sampling rate is raised to 16 kHz, the IO delay can be reduced to only 0.7 samples (on a 2-kHz basis). The controller is then previewed by 0.7 samples to compensate for the delay. These two compensated phase responses are shown in Fig. 8(b). Good agreement can be seen in the phase response within the control bandwidth 200–600 Hz, while the discrepancy below 200 Hz could be due to the poor signal-to-noise ratio outside the band.

An experiment is then undertaken to compare various optimal filter designs used in multirate implementation (16 kHz). The result of the conventional low sampling rate implementation (2 kHz) is also included for reference. Broadband random noise is used as the primary noise. Various systems are implemented by this scenario: the first case is the conventional ANC without multirate implementation, while the next three cases are multirate ANC with H_1, H_2, H_∞ optimal filters, respectively. The experimental results are shown in Fig. 8(c). Significant attenuation of noise has been obtained throughout the control bandwidth. The results are also summarized in Table III. Note that the delays introduced

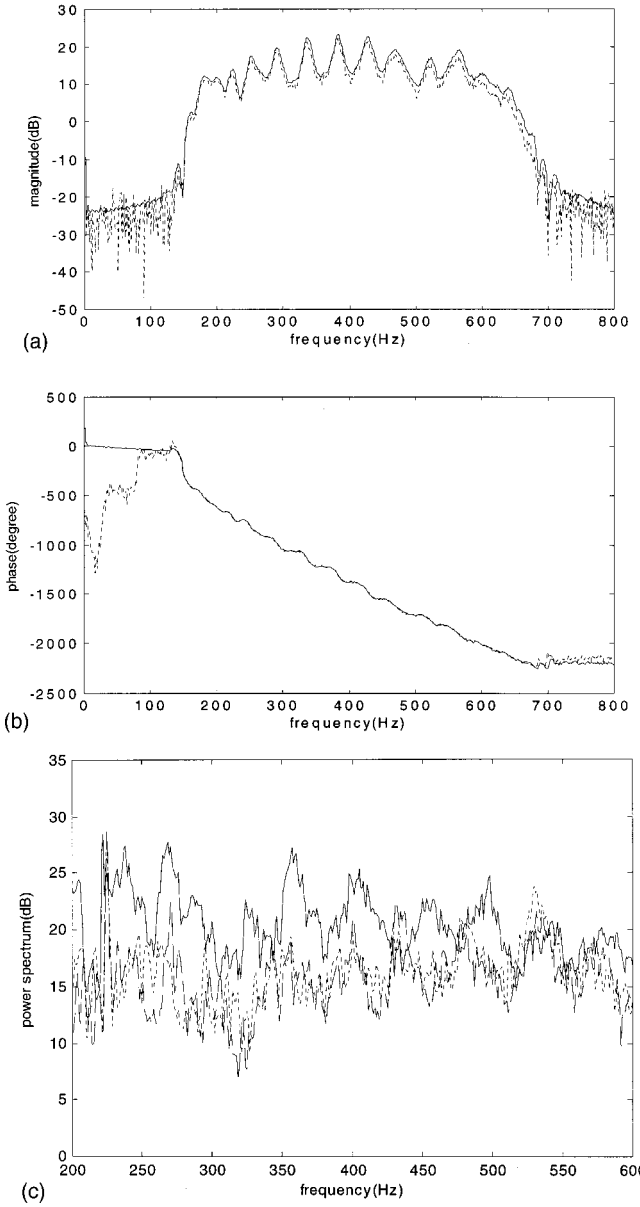

FIG. 8. The experimental results of comparison of ANC systems with and without multirate approach, using H_2 optimal filter. (a) The magnitude responses of controller; (b) the phase responses of controller [without multirate (———); with multirate (···)]; (c) the ANC performance [control off (—); control on, without multirate (···); control on, with multirate (––)].

by the multirate low-pass filters have been compensated by the preview procedure in implementing $C(z)$ that are optimally designed for each test case in the table. As indicated in the results, the multirate approach is able to provide better performance with less hardware complexity than the conven-

TABLE III. Summary of ANC performance for conventional and multirate implementations ($l_i=2.8$ m).

Method	Sampling rate (kHz)	IO delay on DSP (2 kHz) (samples)	Maximum attenuation (dB)	Total attenuation (dB)
Conventional	2	1.5	15.3	7.4
Multirate H_1	16	0.4	16.8	6.6
Multirate H_2	16	0.7	17.1	7.6
Multirate H_∞	16	0.7	15.2	7.3

TABLE IV. Attenuation versus distance l_i for conventional and multirate implementations using H_2 filter. The word "ineffective" in the table refers to the case where no attenuation was observed in the experiment.

Implementation methods	The distance l_i between upstream sensor and control source (cm)					
	80	65	50	40	30	20
Conventional	5.4 dB	1.8 dB	ineffective	ineffective	ineffective	ineffective
Multirate	6.8 dB	6.5 dB	6.3 dB	5.2 dB	2.5 dB	1.2 dB

tional implementation. The multirate structure based on the polyphase representation achieves not only reduction of electronic delay but also enhancement of performance of the ANC controller. In particular, the multirate ANC with H_2 optimal filter appears to yield the best performance (total attenuation 4.8 dB and maximum attenuation 17.3 dB). Thus, in the next experiment, we shall focus our discussion only on the multirate ANC with H_2 optimal filter.

At this point, one question will naturally arise. What is the limit of shortest length that one is able to achieve by using the multirate approach in the spatially feedforward duct ANC system? On the basis of the delay estimation procedure depicted in Fig. 3, the total electronic delay is estimated as 1.6 samples (with details presented in Table II). To ensure a causal controller, this in turn renders the minimal length $l_i = 23$ cm, which is a remarkable improvement owing to the considerable reduction in the analog filter delay and digital IO delay. To justify the above theoretical prediction, the experiment is repeated for $l_i = 80$, 65, 50, 40, 30, and 20 cm, respectively. The results are summarized in Table IV. Both the conventional approach and multirate approach with the H_2 optimal filter have produced attenuation for $l_i = 80$ and 65 cm. However, for shorter lengths the conventional method begins to lose performance, whereas the multirate method remains effective in achieving broadband attenuation, as shown in Fig. 9. The word "ineffective" in the table refers to the case where no attenuation was observed in the experiment. For brevity, only the results for $l_i = 50$ and 20 cm are shown. As expected, the performance deteriorates with decreasing length.

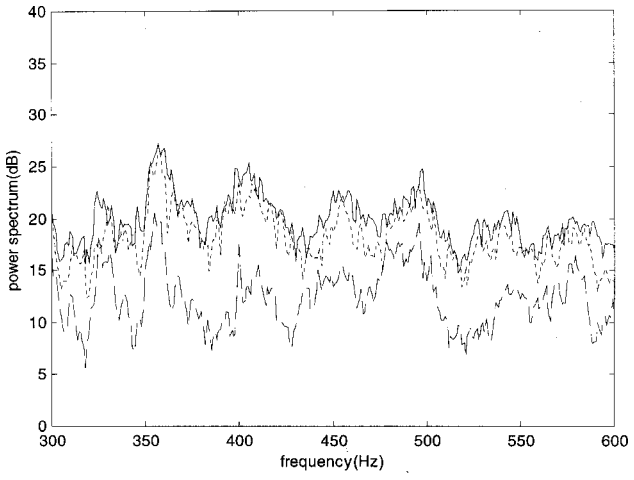

FIG. 9. The experimental results of ANC performance for $l_i = 20$ and 50 cm, using multirate implementation with H_2 optimal filter. control off (—), on (20 cm) (···), control on (50 cm) (––).

VI. CONCLUSIONS

This paper suggests three potential contributions. First, this work represents the first application of a multirate ANC system to duct problems. Second, the significance of delay to the spatially feedforward system with strong acoustic feedback is thoroughly examined in the paper. Third, details of how one should implement the multirate scheme in the context of ANC applications are presented, and how effective the approach would be with regard to physical dimension is quantitatively evaluated. A detailed analysis of causality for spatially feedforward ANC systems reveals that electronic delay dictates the minimal upstream measurement microphone spacing l_i. A multirate approach has been developed in this work for reducing the electronic delay in the control loop. Analog low-pass filters were replaced by direct decimation and interpolation, through the use of digital filters. The computation efficiency is further enhanced by a polyphase representation, where the phases of low-pass filters must be carefully designed to avoid unnecessary delays. Frequency domain optimization procedures based on H_1, H_2, and H_∞ norms, respectively, are utilized to facilitate the FIR filter design. Experimental results demonstrated the effectiveness of the multirate approach in suppressing a broadband random noise in a spatially feedforward duct ANC system. In particular, the H_2 design yielded the best results because it has the smallest phase shift in low-pass filtering.

However, some possibilities remain for improvement of the proposed techniques. For instance, better FIR filter design should be sought, concentrating on the vicinity of cutoff where distortions are likely to arise. The up/down sampling factor (currently 8) should be increased to further reduce the delay. The active controller was implemented as a fixed digital filter in this paper. However, in an adaptive system, this multirate technique can be highly useful. On the basis of this work, these aspects shall be explored in the future research.

ACKNOWLEDGMENTS

The work was supported by the National Science Council in Taiwan, Republic of China, under the Project Number NSC 89-2212-E-009-007. The authors also thank the technical editor, Dr. M. Stinson, for providing the faxed copy of Ref. 14.

[1] S. J. Elliott and P. A. Nelson, "Active noise control," IEEE Signal Process. Mag. **10**, 12–35 (1993).
[2] R. F. La. Fontaine and I. C. Shepherd, "An experimental study of a broadband active attenuator for cancellation of random noise in ducts," J. Sound Vib. **91**, 351–362 (1983).
[3] M. A. Swinbanks, "The active control of sound propagation in long ducts," J. Sound Vib. **27**, 411–436 (1973).

[4] S. M. Kuo and D. R. Morgan, *Active Noise Control Systems: Algorithms and DSP Implementations* (Wiley, New York, 1995).
[5] J. C. Doyle, B. A. Francis, and A. R. Tannenbaum, *Feedback Control Theory* (Macmillan, New York, 1992).
[6] R. E. Crochiere and L. R. Rabiner, *Multirate Digital Signal Processing* (Prentice-Hall, Englewood Cliffs, NJ, 1983).
[7] P. P. Vaidyanathan, *Multirate Systems and Filter Banks* (Prentice-Hall, Englewood Cliffs, NJ, 1993).
[8] P. P. Vaidyanathan, ''Design and implementation of digital FIR filters,'' in *Handbook on Digital Signal Processing*, edited by D. F. Elliott (Academic, Cambridge, UK, 1987), pp. 55–172.
[9] M. Bellanger, G. Bonnerot, and M. Coudreuse, ''Digital filtering by polyphase network: Application to sample rate alteration and filter banks,'' IEEE Trans. Acoust., Speech, Signal Process. **ASSP-24**, 109–114 (1976).
[10] P. P. Vaidyanathan and V. C. Liu, ''Classical sampling theorems in the context of multirate and polyphase digital filter bank structures,'' IEEE Trans. Acoust., Speech, Signal Process. **ASSP-36**, 1480–1495 (1988).
[11] J. S. Arora, *Introduction to Optimum Design* (McGraw-Hill, New York, 1989).
[12] S. Boyd, L. Vandenberghe, and M. Grant, ''Efficient convex optimization for engineering design,'' in Proceedings of the IFAC Symp. Robust Contr. Design, Rio de Janeiro, Brazil, Sept. 1994.
[13] A. Grace, MATLAB *optimization toolbox* (The Mathworks, 1995).
[14] A. J. Brammer, G. J. Pan, and R. B. Crabtree, ''Adaptive feedforward active noise reduction headset for low-frequency noise,'' Proceedings ACTIVE 97 (Budapest, Hungary, August, 1997).
[15] M. R. Bai, Y. J. Lin, and J. D. Wu, ''Analysis and DSP implementation of a broadband duct ANC system using spatially feedforward structure,'' ASME J. Vibr. Acoust. **123**, 129–136 (2001).
[16] M. L. Munjal and L. J. Eriksson, ''An analytical, one-dimensional, standing-wave model of a linear active noise control system in a duct,'' J. Acoust. Soc. Am. **84**, 1086–1093 (1988).
[17] M. T. S. Tomizuka and K. K. Chew, ''Analysis and synthesis of discrete-time repetitive controllers,'' ASME J. Dyn. Syst., Meas., Control **111**, 353–358 (1989).
[18] R. H. Small, ''Closed-box loudspeaker systems. I. Analysis,'' J. Audio Eng. Soc. **20**, 798–808 (1972).
[19] P. A. Nelson and S. J. Elliott, *Active Control of Sound* (Academic, San Diego, 1992).
[20] R. A. Burdisso and C. R. Fuller, ''Causality analysis of feedforward controlled systems,'' J. Acoust. Soc. Am. **94**, 234–242 (1993).
[21] B. Noble, *Applied Linear Algebra* (Prentice-Hall, Englewood Cliffs, NJ, 1969).
[22] J. D. Wu and M. R. Bai, ''Effects of directional microphone and transducer in spatially feedforward active noise control system,'' Jpn. J. Appl. Phys. **40**, 6133–6137 (2001).

Sweeping echoes perceived in a regularly shaped reverberation room

Kenji Kiyohara[a] and Ken'ichi Furuya
NTT Cyber Space Laboratories, 3-9-11 Midori-cho, Musashino-shi, Tokyo 180-8585, Japan

Yutaka Kaneda
Tokyo Denki University, 2-2 Kanda-Nishiki-cho, Chiyoda-ku, Tokyo 101-8457, Japan

(Received 15 January 2001; revised 30 October 2001; accepted 12 November 2001)

A very interesting new phenomenon that we call a sweeping echo is described and investigated. When we clap hands in a regularly shaped reverberant room, we hear sweeping echoes whose frequency increases linearly with time. An example of sweeping echoes observed in a rectangular reverberation room is first described. Then, the mechanism that generated the sweeping echoes is investigated by assuming a cubic room and using number theory. The reflected pulse sound train is found to have almost equal intervals between pulses on the squared-time axis. This regularity of arrival times of the reflected pulse sounds is shown to generate the sweeping echoes. Computer simulation of room acoustics shows good agreement with the theoretical results. © *2002 Acoustical Society of America.* [DOI: 10.1121/1.1433808]

PACS numbers: 43.55.Br, 43.55.Ka, 43.20.El [JDQ]

I. INTRODUCTION

A new, interesting acoustical phenomenon is described, and its generation mechanism is investigated theoretically.

When we clap hands once between parallel, hard walls, we hear a sound called a ''fluttering echo.''[1] A single hand clap sound (i.e., an impulsive sound) is reflected by the walls repeatedly, and a train of pulses with periodic intervals is generated. This pulse train causes a specific sound sensation; that is, a fluttering echo.

In the fluttering echo, reflected sounds go forward and backward in a one-dimensional pattern between parallel hard walls. What happens, then, when we clap hands in a three-dimensional reflective space? We found that sweep sound (Audio illustrations are available at: http://www.asp.c.dendai.ac.jp/sweep/ and http://www.ntt.co.jp/cclab/info/sweep.html) which we call ''sweeping echoes,'' were perceived when we generated a pulse sound in a regularly shaped reverberation room. The perceived frequencies of the sweep sounds increased with time at different speeds. Other researchers have also noticed the sweeping echoes in squash courts, which also had hard regularly shaped walls.

There are some other types of sweeping (or sliding) echoes. One is caused by frequency dispersion. The frequency dispersion assumes some special sound field where the phase velocity of a sound varies with its frequency. This is not the case here; the sweeping echoes presented in this paper occur in a normal sound field, without dispersion.

Knudsen[2] reported another type of frequency shift in reverberated sound. He reported that the pitch of a tone in a small, resonant room might change perceptibly during the decay of the tone. The pitch of the emitted sound is considered to be changed to that of a resonance frequency. On the other hand, our sweeping echoes are clearly explained in the time domain based on the number theory.

In this paper, the sweeping echoes observed in a rectangular parallelepiped reverberation room are described first with their time-frequency analysis in Sec. II. Then, the generation mechanism of the sweeping echoes in a cubic room is investigated using number theory in Secs. III and IV. The theoretical results are compared with simulation results in Sec. V. Sweeping echoes in a rectangular parallelepiped room are discussed in Sec. VI and Sec. VII concludes the paper.

II. SWEEPING ECHOES PERCEIVED IN A RECTANGULAR PARALLELEPIPED REVERBERATION ROOM

Sweeping echoes are perceived in relatively large, regularly shaped three-dimensional rooms with highly reflective surfaces; i.e., walls, ceiling, and floor. We first describe the sweeping echoes measured in a rectangular parallelepiped reverberation room along with their time-frequency analysis.

A. Measurement conditions and sweeping echoes

The dimensions of the rectangular parallelepiped reverberation room were 11 m (width) × 8.8 m (depth) × 6.6 m (height).[3] The measurement conditions are shown in Fig. 1. Figures 1(a) and (b) show the plan view and cross section of the reverberation room, respectively. The symbols *S* and *R* represent the source and reception positions, respectively. As shown in Fig. 1(a), both *S* and *R* were located on the center line of the floor. *S* was located 3.2 m from the wall and 1.2 m high, and *R* was 1.1 m from the opposite wall and 1.5 m high as shown in the figure, respectively.

When hands were clapped once at position *S*, the first sweep sound whose frequency increased over a short time (called the main sweeping echo) was perceived at position *R*. Multiple sweep sounds whose frequency increased relatively slowly (called subsweeping echoes) were then perceived, along with ordinary reverberation sounds.

[a]Electronic mail: kiyohara.kenji@lab.ntt.co.jp

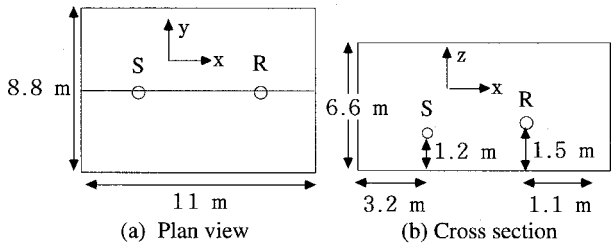

FIG. 1. Layout for sweep-sound measurement. (a) Plan view, (b) cross section, *S*, source position, *R*, reception position.

Although sweep sounds were perceived at other source and reception positions, the sounds were perceived more clearly at positions that were symmetrical with respect to the room, such as those shown in Fig. 1. To analyze these sweep sounds, they were recorded with a microphone placed at position *R*.

B. Time-frequency analysis of the sweeping echoes

Figure 2 shows the results of analyzing the recorded echoes by using short-time Fourier transformation. The horizontal axis represents time, and the time when hands were clapped is set to the origin. The figure shows the spectrogram for the first 2 seconds. The vertical axis represents frequency, up to 2 kHz, which was the range within which the sweep sounds were clearly perceived. The analysis conditions were the following: the sampling frequency was 16 kHz, a 16-ms rectangular window (62.5 Hz frequency resolution) was used, and the window was shifted in steps of 8 ms.

In Fig. 2, the main sweeping echo appears clearly from 0 to about 400 ms [line (*A*)]. The frequency of the main sweeping echo increased linearly with time, and it rose to about 1500 Hz during the first 400 ms. This result corresponds with hearing perception. Following the main sweeping echo, multiple subsweeping echoes whose frequencies rose linearly at relatively slow speeds, also appear in Fig. 2.

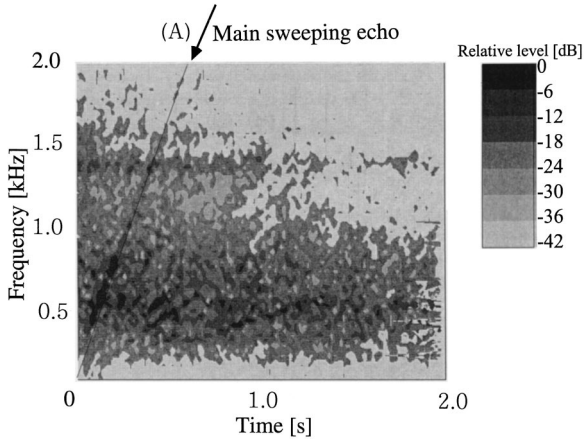

FIG. 2. Spectrogram of the recorded data. The main sweeping echo appears clearly from 0 to about 400 ms [line (*A*)]. The frequency of the main sweeping echo increased linearly with time, and it rose to about 1500 Hz during the first 400 ms. Following the main sweeping echo, multiple subsweeping echoes also appeared whose frequency rose linearly at relatively slow speeds.

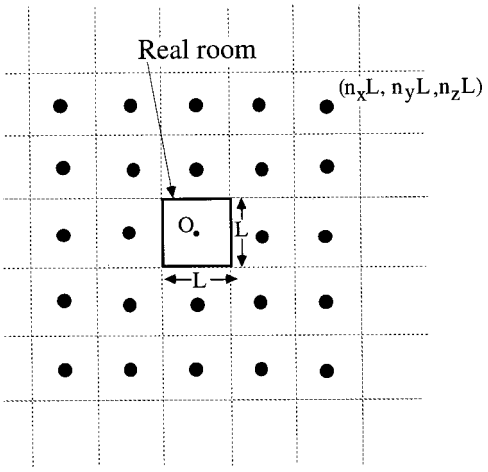

FIG. 3. Mirror image sources of a cubic room. The figure shows a top view, and the size of the room is denoted by *L*. The reflected sounds are treated as the sounds from the image sources. The coordinate origin O is set to the center of the room. The location of each image source is represented by (n_xL, n_yL, n_zL) where n_x, n_y, n_z are positive and negative integers.

III. GENERATION MECHANISM OF THE MAIN SWEEPING ECHO

In this section, we investigate the generation mechanism of the main sweeping echo, based on geometrical acoustics and number theory. As the first step in this investigation, a cubic room is assumed in this paper.

A. Intervals of reflected sounds in a cubic room

First, the regularity of arrival time of reflected sounds in a cubic room is described. To simplify the issue, the source and reception points are both assumed to be located at the center of the room. Figure 3 shows the mirror image sources generated in a cubic room based on geometrical acoustics.[4] The figure shows a top view, and the edge length of the room is denoted by *L*. When a pulse sound is generated at the center of the room, the arrival times and amplitudes of the observed reflected sounds are the same as those of the sounds that would be generated from the image sources shown in Fig. 3. In other words, the reflected sounds can be treated as the sounds from the image sources.

The coordinate origin O is set at the center of the room. Then, the location of each image source is represented by (n_xL, n_yL, n_zL), where n_x, n_y, n_z are integers. The distance *d* between the origin (reception position) and an image source of (n_xL, n_yL, n_zL) is represented by

$$d=\sqrt{(n_xL)^2+(n_yL)^2+(n_zL)^2}=\sqrt{n_x^2+n_y^2+n_z^2}\cdot L. \quad (1)$$

Thus, the arrival time of the sound from the image source is obtained by dividing *d* by the sound velocity *c*, as in the following equation:

$$t=d/c=\sqrt{n_x^2+n_y^2+n_z^2}\left(\frac{L}{c}\right). \quad (2)$$

Next, consider the arrival time on the squared-time axis. The squared arrival time is derived by squaring Eq. (2):

$$t^2=(n_x^2+n_y^2+n_z^2)\left(\frac{L}{c}\right)^2=M\left(\frac{L}{c}\right)^2, \quad (3)$$

where

$$M = n_x^2 + n_y^2 + n_z^2. \tag{4}$$

Thus, the squared arrival time t^2 is represented by an integer M times a constant $(L/c)^2$. Equation (3) represents the position on the squared-time axis at which the reflected sound exists.

From number theory,[5] the sum of the squared integers $(n_x^2+n_y^2+n_z^2)$ expresses all integers, except the "forbidden numbers," i.e.,

$$M \neq 4^k(8m+7), \tag{5}$$

where $k, m = 0,1,2,\ldots$.

Since these forbidden numbers account for 1/6 of all positive integers, we first disregard the forbidden numbers and assume that M includes approximately all positive integers. Then, Eq. (3) indicates that reflected sounds (pulse sounds) exist at $(L/c)^2$, $2(L/c)^2$, $3(L/c),\ldots$; that is, they exist at equal intervals of $(L/c)^2$ on the squared-time axis.

B. Relationship between the squared-time axis and the time axis

We represent the arrival times of two adjacent pulses (reflected sounds) as t_a and t_b $(t_a < t_b)$. The interval between these pulses on the squared-time axis is $(L/c)^2$. Namely

$$t_b^2 - t_a^2 = \left(\frac{L}{c}\right)^2. \tag{6}$$

By factoring the left-hand side of Eq. (6), we obtain

$$(t_b - t_a)(t_b + t_a) = \left(\frac{L}{c}\right)^2. \tag{7}$$

The average arrival time t_v of the two pulses is defined by

$$t_v = (t_b + t_a)/2. \tag{8}$$

By substituting Eq. (8) into Eq. (7) and modifying it, the interval between pulses on the time axis is represented by the following equation:

$$t_b - t_a = \left(\frac{L^2}{2c^2}\right)\left(\frac{1}{t_v}\right). \tag{9}$$

Equation (9) clarifies that the interval between the two pulses is inversely proportional to the time t_v.

Thus, a pulse series with equal intervals on the squared-time axis has intervals inversely proportional to time on the time axis. Figure 4 illustrates this relationship.

C. Main sweeping echo

A periodic pulse series has a fundamental frequency represented by the reciprocal of its interval.[6] Therefore, when the interval of pulses is represented by Eq. (9), the fundamental frequency of the pulses at time t_v is expressed by the following equation:

$$f(t_v) = \frac{1}{t_b - t_a} = \left(\frac{2c^2}{L^2}\right) t_v. \tag{10}$$

Equation (10) indicates that the fundamental frequency f is proportional to the time t_v. In other words, humans perceive

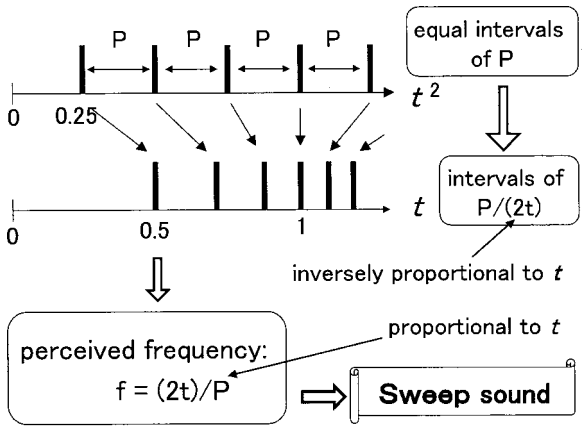

FIG. 4. A pulse series with equal intervals on the squared-time axis has intervals inversely proportional to time on the time axis.

an increasing sweep sound. This proves that a reflective pulse train in a cubic room produces a sweep sound sensation.

IV. GENERATION MECHANISM OF THE SUBSWEEPING ECHOES (INFLUENCE OF THE FORBIDDEN NUMBERS)

As described above, a pulse series from the image sources of a cubic room does not have completely equal intervals on the squared-time axis because of the forbidden numbers. The influence of the forbidden numbers can be explained as the addition of a forbidden numbers pulse train which has pulses corresponding to forbidden numbers on the squared-time axis with negative amplitudes. Figure 5 conceptually illustrates this phenomenon. Figure 5(a) shows a pulse series on the time axis of a cubic room for equal amplitudes, where the dimension L of the cubic room was assumed to be 10 m. Some pulses are missing because of the

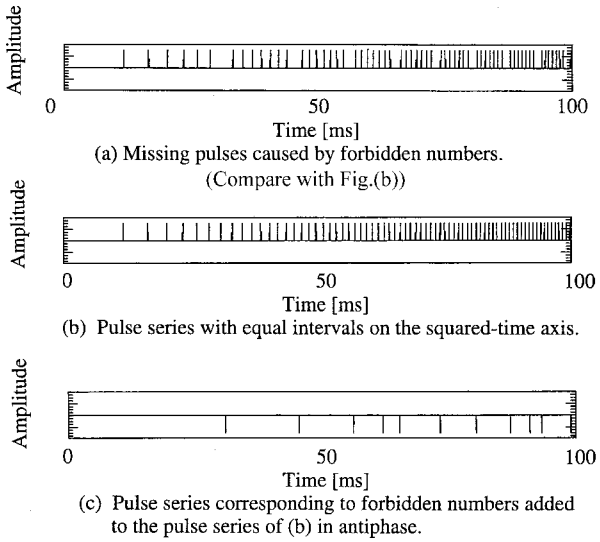

FIG. 5. The influence of the forbidden numbers. (a) A pulse series on the time axis of a cubic room for equal amplitudes. (b) A pulse series with completely equal intervals on the squared-time axis. (c) A pulse series corresponding to the forbidden numbers with the negative amplitude of the same values. The gaps of (a) are considered to be generated by adding (c) to (b), where the dimension L of the cubic room was assumed to be 10 nm.

forbidden numbers. These gaps were considered to be generated by adding a pulse series corresponding to the forbidden numbers with negative amplitude of the same values [Fig. 5(c)] to a pulse series with completely equal intervals on the squared-time axis [Fig. 5(b)].

From Eqs. (3) and (5), the squared arrival time for the pulse series corresponding to the forbidden numbers is represented by the following equation:

$$t^2 = 4^k(8m+7)\left(\frac{L}{c}\right)^2, \tag{11}$$

where $k,m=0,1,2,3,\ldots$.

The pulse series has equal intervals of $4^k 8(L/c)^2$, for $k=0,1,2,\ldots$, on the squared-time axis as m changes. For a typical example, corresponding to $k=0$ and $m=0,1,2,\ldots$, the period of the pulse series becomes $8(L/c)^2$. The fundamental frequency at the mean time t_v of two adjacent pulses corresponding to this example is represented by the following equation:

$$f_b(t_v) = \left(\frac{2c^2}{L^2}\right)\frac{1}{8}t_v. \tag{12}$$

For $k=1$ and $m=0,1,2,\ldots$, the period of the pulses becomes $32(L/c)^2$, and its fundamental frequency is represented by the following equation:

$$f_b(t_v) = \left(\frac{2c^2}{L^2}\right)\frac{1}{32}t_v. \tag{13}$$

For $k=2,3,4,\ldots$, the fundamental frequency is represented in a similar way.

The pulses series corresponding to the forbidden numbers thus consists of multiple pulse series with different periods on the squared-time axis. Since these periods are longer than that of the main sweeping echo, the fundamental frequencies of the pulse series corresponding to the forbidden numbers increase more slowly. Thus, subsweeping echoes are generated.

V. NUMERICAL SIMULATION

The theoretical results derived in the preceding sections were confirmed by time-frequency analysis. Figure 6(a) shows the spectrogram of the pulse series shown in Fig. 5(b). The spectrogram was calculated by FFT with a 16-ms rectangular time window and an 8-ms shift. In Fig. 6(a), the main sweeping echo (*A*) appears clearly. The lines (*B*) are its harmonics. Calculating the slope (or frequency rising speed, or sweep speed) of the main sweeping echo from Eq. (10) with sound velocity $c=340$ m/s gave $2c^2/L^2=2312$ Hz/s. This value is consistent with the slope of the main sweeping echo (*A*) shown in Fig. 6(a).

Figure 6(b) shows the spectrogram of the pulse series shown in Fig. 5(c). The subsweeping echo (*C*) corresponding to $k=0$ appears clearly, and its harmonics (*D*) also appear. Calculating the slope of the subsweeping echo for $k=0$ from Eq. (12) gave $(2c^2/L^2)/8=289$ Hz/s. This value is consistent with the slope of the subsweeping echo (*C*) shown in Fig. 6(c).

Figure 7 shows the spectrogram of the pulse series shown in Fig. 5(a). The spectrogram is almost the power sum of the spectra shown in Figs. 6(a) and (b). The main sweeping echo (*A*) and its harmonics (*B*), and the subsweeping echo (*C*) corresponding to $k=0$ and its harmonics (*D*) all appear in Fig. 7. Thus, the main sweeping echo and the subsweeping echoes corresponding to the forbidden numbers were perceived for the pulse series shown in Fig. 5(a).

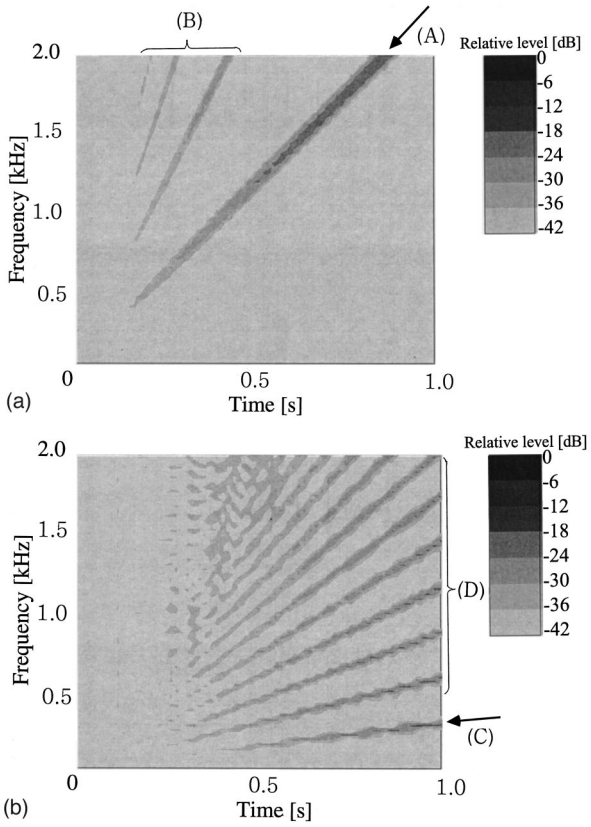

FIG. 6. (a) Spectrogram of the pulse series shown in Fig. 5(b). The main sweeping echo (*A*) appears clearly. The lines (*B*) are its harmonics. (b) Spectrogram of the pulse series shown in Fig. 5(c). The subsweeping echo (*C*) appears clearly, and its harmonics (*D*) also appear.

Next, the reflected sounds of a pulse sound (i.e., an impulse response) in the cubic room were simulated by the

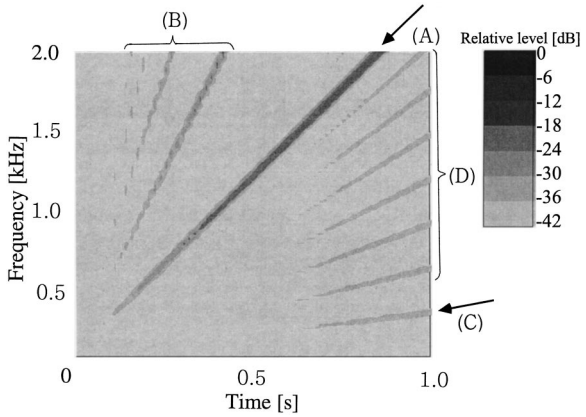

FIG. 7. Spectrogram of the pulse series shown in Fig. 5(a). The spectrogram is almost the power sum of the spectra shown in Figs. 6(a) and (b). The main sweeping echo (*A*) and its harmonics (*B*), and the subsweeping echo (*C*) and its harmonics (*D*) all appear.

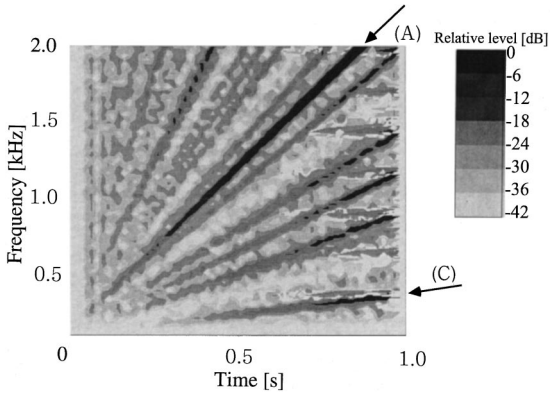

FIG. 8. Spectrogram of the impulse response in a cubic reverberation room whose dimension L is 10 m. Multiple sweep sounds appear, and just as in Fig. 7, the main sweeping echo (A) appear clearly. The subsweeping echo (C) also appears.

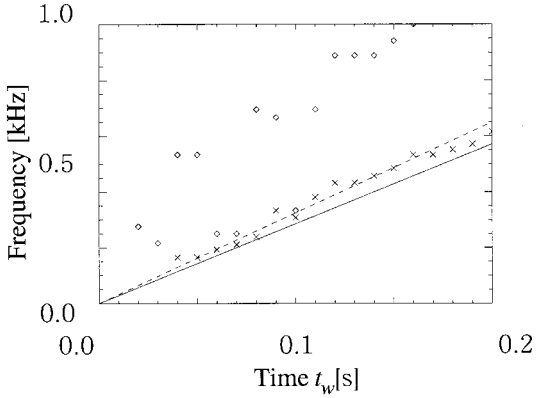

FIG. 9. Reciprocal of peak time of short-time autocorrelation $\rho(\tau)$ of recorded data shown in Fig. 2. $\diamond$, the first high peak of $\rho(\tau)$. $\times$, the second high peak of $\rho(\tau)$. Solid line, theoretical frequency. The solid line is close to the $\times$ symbols. Broken line, the line of main sweeping echo observed in Fig. 2. It is also close to the theoretical line plot.

mirror image source method.[7] Dimension L for the room was 10 m. The calculated reflected pulses were convolved with a sinc function and overlap added[8] to derive sampling data. Figure 8 shows the spectrogram of the simulated sounds. Multiple sweep sounds appear, and just as in Fig. 7, the main sweeping echo (A) appears clearly. The subsweeping echo (C) also appears.

Since the sound source and reception point were located at the center of the room, different numbers of multiply reflected pulses arrived at the same time due to the degeneracy of the mirror image sources. Therefore, the amplitudes of the reflected-pulse series were not equal. This caused the random noisy spectrum that was superposed on the time-spectrum plot. As a result, the sweeping echoes shown in Fig. 8 are somewhat obscure. However, the same sweeping echoes shown in Fig. 7 can also be recognized in Fig. 8.

The slopes of lines (A) and (C) in Fig. 8 are similar to the theoretical values 2312 Hz/s and 289 Hz/s, respectively, calculated above. Thus, the theoretical results developed in the preceding section adequately explain the sweeping echo phenomenon that appeared in the computer simulation of room acoustics.

VI. RECTANGULAR PARALLELEPIPED REVERBERATION ROOM

Unlike a cubic room, all the side lengths of a rectangular parallelepiped room are not equal. Therefore, the arrival time of a reflected sound from an image source cannot be represented by a simple formula like Eq. (2). This makes theoretical analysis using number theory difficult.

Therefore, we attempted a qualitative explanation by analyzing experimental data. A pulse sound was generated by hand clapping under the conditions shown in Fig. 1. Then, the periodicity of the received pulse train (reverberation sound) was studied based on the short-time autocorrelation method. The short-time autocorrelation function $\rho(\tau,t_w)$ was calculated from the windowed data centered at time t_w, and it was calculated repeatedly with sliding time t_w. The sampling frequency was 16 kHz, and the window length was 10 ms.

When the reflected pulses contain periodic pulses, the autocorrelation function $\rho(\tau,t_w)$, as a function of time τ with fixed t_w, has peaks at times, τ s, corresponding to the pulse periods. These peak times, or pulse periods were calculated as a function of t_w. The results are shown in Fig. 9, as the reciprocals of the detected periods, which correspond to the frequencies.

In Fig. 9, the horizontal axis represents the time t_w and the vertical axis represents the reciprocal of the peak of the autocorrelation function by frequency. The $\diamond$ symbol denotes the frequencies that correspond to the first high peaks of $\rho(\tau,t_w)$ for each t_w, and the $\times$ symbol denotes the frequencies that correspond to the second high peaks.

The root-mean-square L_m of the side lengths of the rectangular parallelepiped room was calculated using the following equation:

$$L_m=\sqrt{(L_x^2+L_y^2+L_z^2)/3}. \tag{14}$$

Substituting the dimension of the experimental room ($L_x=11$ m, $L_y=8.8$ m, $L_z=6.6$ m from Fig. 1) gave $L_m=8.98$ m. A function derived by substituting L_m into Eq. (10), representing the theoretical frequency of a main sweeping echo for a cubic room with side length of L_m, is shown as a solid line in Fig. 9. This solid line is close to the $\times$. The line of the main sweeping echo observed in Fig. 2 is also plotted in Fig. 9, by a broken line, and it is also close to the theoretical line plot.

This result indicates that the calculated frequency line of a sweeping echo based on L_m matches the observed sweeping echo, and its sweeping frequency corresponds to the periodicity in the pulse train appearing as the second high peak of the short-time autocorrelation function. It is left for future study to answer the questions why the second high peaks but not the fist ones, and what do the first high peaks represent.

Thus, the main sweeping echo in a rectangular parallelepiped room has reflected pulse periods close to those of a cubic room with the same mean side length L_m as the rectangular parallelepiped room. This implies that the pulse train

in a rectangular parallelepiped room has a regularity similar to that in a cubic room, and this regularity causes sweeping sounds.

VII. CONCLUSION

When a pulse sound is generated in a rectangular parallelepiped reverberation room, a peculiar phenomenon is observed in that the frequency components of the reflected sounds increase linearly (called ''sweeping echoes''). These sweeping echoes consist of a ''main sweeping echo,'' whose frequency component increases over a short time, and ''subsweeping echoes,'' whose frequency components increase slowly. Investigating the sweeping echoes assuming a cubic room showed that the arrival times of the pulse sounds from mirror image sources had almost equal intervals on the squared-time axis, and this regularity of the pulse intervals generated the main sweeping echo. The pulse train does not have exactly equal intervals on the squared-time axis, but rather has some missing pulses corresponding to ''forbidden numbers'' based on number theory. These missing pulses were shown to have relatively long, equal intervals. This regularity causes the subsweeping echoes. Computer simulation based on the image method produced results in good agreement with the theoretical results.

ACKNOWLEDGMENTS

We thank Kazuhiko Yamamori, Dr. Nobuhiko Kitawaki, and Junji Kojima for their support of our work. We thank Masashi Tanaka for his useful advice. We thank our colleagues for their help in measuring the sounds.

[1] E. Meyer and E.-G. Neumann, *Physical and Applied Acoustics* (Academic, New York, 1972), pp. 92–94.
[2] V. O. Knudsen, ''Resonance in small rooms,'' J. Acoust. Soc. Am. **3**, 20–37 (1932).
[3] M. Tohyama and S. Yoshikawa, ''Approximate formula of the averaged sound energy decay curve in a rectangular reverberant room,'' J. Acoust. Soc. Am. **70**, 1674–1678 (1981).
[4] H. Kuttruff, *Room Acoustics* (Elsevier Applied Science, London, 1991), pp. 81–95.
[5] M. R. Shroeder, *Number Theory in Science and Communication* (Springer-Verlag, Berlin, 1984), pp. 97–99.
[6] A. Papoulis, *The Fourier Integral and Its Application* (McGraw-Hill, New York, 1962), pp. 43–44.
[7] J. B. Allen and D. A. Berkley, ''Image method for efficiently simulating small-room acoustics,'' J. Acoust. Soc. Am. **65**, 943–950 (1979).
[8] A. V. Oppenheim and R. W. Schafer, *Digital Signal Processing* (Prentice-Hall, New Jersey, 1975), pp. 26–30.

Effect of noise and occupancy on optimal reverberation times for speech intelligibility in classrooms

Murray Hodgson[a] and Eva-Marie Nosal
School of Occupational and Environmental Hygiene and Department of Mechanical Engineering, University of British Columbia, 2206 East Mall, Vancouver, British Columbia V6T 1Z3, Canada

(Received 30 May 2001; revised 15 October 2001; accepted 23 October 2001)

The question of what is the optimal reverberation time for speech intelligibility in an occupied classroom has been studied recently in two different ways, with contradictory results. Experiments have been performed under various conditions of speech-signal to background-noise level difference and reverberation time, finding an optimal reverberation time of zero. Theoretical predictions of appropriate speech-intelligibility metrics, based on diffuse-field theory, found nonzero optimal reverberation times. These two contradictory results are explained by the different ways in which the two methods account for background noise, both of which are unrealistic. To obtain more realistic and accurate predictions, noise sources inside the classroom are considered. A more realistic treatment of noise is incorporated into diffuse-field theory by considering both speech and noise sources and the effects of reverberation on their steady-state levels. The model shows that the optimal reverberation time is zero when the speech source is closer to the listener than the noise source, and nonzero when the noise source is closer than the speech source. Diffuse-field theory is used to determine optimal reverberation times in unoccupied classrooms given optimal values for the occupied classroom. Resulting times can be as high as several seconds in large classrooms; in some cases, optimal values are unachievable, because the occupants contribute too much absorption.
 [DOI: 10.1121/1.1428264]

PACS numbers: 43.55.Br, 43.55.Hy, 43.55.Ka [JDQ]

I. INTRODUCTION

A major concern regarding the acoustical characteristics of classrooms is speech intelligibility. This is known to be mainly determined by the signal-to-noise level difference (SN)—the difference between the speech-signal and background-noise levels at a receiver—and the amount of reverberation.[1] When speech intelligibility is the concern, the amount of reverberation is best quantified by the early-to-late energy ratio.[2] However, it is more usual to characterize the amount of reverberation in a room by the reverberation time, *T*, which will be used here.

Speech intelligibility is directly related to signal-to-noise level difference and is inversely related to the reverberation time. However, in rooms the situation is complicated by the fact that reverberation and steady-state levels are interrelated. Increased reverberation, while decreasing the ratio of early-to-late energy ratio to the detriment of speech intelligibility, has the additional effect of increasing steady-state levels by increasing the reverberant sound energy, to the benefit of speech intelligibility.

In this paper, literature on determining optimal reverberation times in classrooms, to optimize speech intelligibility, is reviewed. Fundamental contradictions in the literature are revealed and explained. A new, more physically realistic theoretical approach to predicting the optimal reverberation time in a classroom, considering single and multiple noise sources inside the classroom, is presented and used to corroborate the explanation for the differences in previous results. More realistic optimal reverberation times are derived using the methods developed. How to achieve optimal and satisfactory conditions for speech is discussed. Finally, the optimal reverberation times in the unoccupied classrooms, corresponding to the optimal values in the occupied classroom, are presented.

[a]Electronic mail: hodgson@mech.ubc.ca

II. OPTIMAL CLASSROOM REVERBERATION TIMES

A. Literature review

There are two main approaches that have been taken to determine the optimal reverberation time for speech intelligibility in published work—experimental methods and theoretical prediction.

1. Experimental methods

The first approach taken is an experimental one, in which the speech intelligibility of a group of listeners is tested in different acoustical conditions. The conditions that result in the highest speech intelligibility are identified. In one such test by Nabelek and Robinson,[3] modified-rhyme speech tests were recorded in a number of different anechoic and reverberant acoustical environments, and played to test subjects through earphones. A table from the work is reproduced in Table I. The table gives mean word-recognition scores (in percent correct) for monaural and binaural listening at 70 dB speech levels, for various reverberation times and six groups of ten normal-hearing subjects. Note that identification scores decrease as reverberation time increases in all cases; that is, the optimal reverberation time for speech intelligibility is zero. This is as might be expected, since this test procedure did not incorporate noise; it only considered

TABLE I. Mean word-recognition scores in percent found by Nabelek and Robinson (Ref. 3).

Listening mode	Age (years)	$T=0.0$ s	$T=0.4$ s	$T=0.8$ s	$T=1.2$ s
Binaural	10	-	93.9	85.2	87.8
	27	-	98.8	96.7	93.0
	42	-	96.1	91.6	90.2
	54	-	96.1	91.2	88.2
	64	-	89.9	79.8	82.4
	72	-	88.0	80.7	78.0
Monaural	10	99.0	91.6	80.0	82.6
	27	99.7	97.0	92.5	87.7
	42	99.9	91.8	86.9	85.2
	54	99.6	93.3	87.4	83.8
	64	97.2	87.9	70.6	75.6
	72	96.1	83.6	73.1	69.5

the direct effect of reverberation on speech intelligibility, neglecting the effect of signal-to-noise level differences.

Some experimental tests of speech intelligibility did consider signal-to-noise level differences and reverberation together. These tests were performed with the speech and noise generated by one or more loudspeakers at some constant distance from the listener in a room. This approach was taken by Nabelek and Pickett,[4] who found that speech intelligibility decreases with increased reverberation time; that is, they found an optimal reverberation time of zero. Table II is reproduced from their study. It shows the mean perception scores for binaural and monaural hearing through hearing aids. The authors tested five subjects with normal hearing and five subjects with impaired hearing. Results for one normal-hearing subject are given in parentheses. Speech levels for the normal-hearing subjects were presented at 50 dB while those for the hearing impaired were at 60 dB. The results shown are for reverberation times of 0.3 and 0.6 s, and for signal-to-noise level differences of $+10$ to -15 dB.

Finitzo-Hieber and Tillman[5] did tests similar to those of Nabelek and Pickett, and also found optimal reverberation times of zero. Their results, presented in Table III, give mean monosyllabic word-discrimination scores in percent correct for monaural hearing of normal-hearing children between the ages of 8 and 14 years, for different reverberation times and signal-to-noise differences. Once again, word-discrimination scores decrease as reverberation times increase from zero.

2. Theoretical prediction

The second approach predicts optimal reverberation times from various speech-intelligibility metrics. Values of each metric are determined for various signal and noise levels, and their differences, and for various room characteristics (reverberation time, volume, surface area, absorption, and so forth). The metrics used are considered to be good predictors of speech intelligibility.[1,6] Plomp, Steeneken, and Houtgast[7] predicted nonzero optimal reverberation times by applying method-of-image procedures to predict the modulation transfer function. The audience was assumed to be the main source of noise (with subjects evenly covering the floor at a density of one per square meter, and with each audience member generating a noise level 35 dB below the speech level of the speaker). They found optimal reverberation times increasing from about 0.3 s for a small hall ($10\,\text{m}\times 15\,\text{m}\times 5\,\text{m}$), to about 1.7 s for a large hall ($40\,\text{m}\times 60\,\text{m}\times 20\,\text{m}$)!

Bistafa and Bradley[2] used a number of metrics to again predict nonzero values for the optimal reverberation time (that is, the reverberation time that predicted the highest

TABLE II. Mean-word recognition scores in percent found by Nabelek and Pickett (Ref. 4).

		Normal		Impaired	
Listening mode	SN (dB)	$T=0.3$ s	$T=0.6$ s	$T=0.3$ s	$T=0.6$ s
Binaural	Quiet	(98.0)	(95.5)	64.9	57.1
	+10	-	-	60.7	55.2
	+5	-	-	57.4	49.9
	0	-	82.5	49.7	42.4
	−5	76.6	60.7	38.2	31.6
	−10	48.7	38.3	-	-
	−15	26.0	-	-	-
Monaural	Quiet	(95.5)	(95.5)	59.8	54.9
	+10	-	-	57.4	49.6
	+5	-	84.9	54.4	48.9
	0	82.5	72.8	46.7	38.8
	−5	64.0	45.7	33.0	23.3
	−10	25.4	-	-	-

TABLE III. Monosyllabic word-discrimination scores in percent from Finitzo-Hieber and Tillman (Ref. 5).

SN (dB)	$T=0.0$ s	$T=0.4$ s	$T=1.2$ s
∞	94.5	92.5	76.5
12	89.2	82.8	68.8
6	79.7	71.3	54.2
0	60.2	47.7	29.7

value of the metric). Their work assumed diffuse-field theory to be applicable in classrooms. Moreover, they made a number of simplifying assumptions—ratio of classroom volume to surface area equal to 1 m, distance from the speech source to the receiver much greater than the classroom reverberation radius, and negligible air absorption. Table IV is taken from their work; it presents the optimal reverberation which predicts the highest value of the U_{50} speech-intelligibility metric (defined in the following) for rooms of various volumes, V, and signal-to-noise differences, $L_{sf1}-L_n$. Here, L_{sf1} is the long-term anechoic (free-field) speech level at 1 m directly in front of the talker, and L_n is the total noise level at the listener position. Note that the optimal values are nonzero; an optimal reverberation time of zero is predicted only if $L_{sf1}-L_n=\infty$, i.e., if there is negligible noise.

The physical explanation for the nonzero optimal reverberation times predicted by Bistafa and Bradley is as follows. In the absence of reverberation, background noise reduces intelligibility. Increased reverberation increases early energy, which can compensate for noise and increase intelligibility. However, too much reverberation decreases the early-to-late energy ratio, decreasing intelligibility.

3. Explaining the contradiction

Why do experimental methods predict an optimal reverberation time of zero while theoretical methods predict nonzero values? Which is correct? The contradictory results for the experimental and theoretical approaches for determining optimal reverberation time require explanation.

It would appear that the difference in the results stems from the different ways in which the methods incorporate noise and, consequently, signal-to-noise level difference. The study by Nebelek and Robinson[3] did not consider the case when noise was present; thus, their results cannot be generalized to conclude that zero reverberation is always optimal. Indeed, Bistafa and Bradley[2] argued that reverberation increases speech levels and, therefore, signal-to-noise level differences, leading to nonzero optimal reverberation times.

By design, the experimental methods employed by Nabelek and Pickett[4] and those by Finitzo-Hieber and Tillman,[5] involved speech and noise generated at positions at the same distance from the listener. More importantly, the signal-to-noise level difference was fixed at the location of the listener's head before each test. In this way, the effect of reverberation on signal-to-noise level differences and, consequently, the possible positive effect of reverberation on speech intelligibility, were eliminated.

TABLE IV. Optimal reverberation times in seconds using U_{50} predicted by Bistafa and Bradley (Ref. 2).

$L_{sf1}-L_n$ (dB)	$V=100$ m^3	$V=300$ m^3	$V=500$ m^3
10	0.4	0.5	0.6
15	0.3	0.4	0.4
20	0.2	0.3	0.3
25	0.2	0.2	0.2
30	0.1	0.2	0.2

Bistafa and Bradley,[2] on the other hand, assumed total noise levels which did not vary with position or reverberation. The positive effect of reverberation on total speech levels was included by way of a reverberant speech-sound term. However, this method did not consider the analogous negative effect of reverberation on total noise levels. In particular, Bistafa and Bradley used $L_{sf1}-L_n$ as the input parameter describing signal-to-noise level difference. L_{sf1} is a measure of the speech-source output independent of room effects. In fact, it is analogous to the output power level, L_{ws}; for a point source with directivity index q_s, $L_{sf1}=L_{ws}-10\log(q_s)+11$ dB. It was held constant for a given prediction. The effect of the room was taken into account as an increase in speech levels due to reverberation. However, L_n was the total noise level (including the effect of reverberation). Since, for a given prediction, L_{sf1} and $L_{sf1}-L_n$ were constants, so, effectively, was L_n. Thus, the total noise level did not increase with increasing reverberation; the adverse effect on speech intelligibility, resulting from an increased noise level with increased reverberation time, was not modeled. In principle, the adverse effect of reverberation on noise could be strong enough to cause a decrease in the predicted optimal reverberation times, possibly even to zero.

An alternative way to consider the physical implications of holding L_n constant in the work of Bistafa and Bradley[2] is to assume that the effect of reverberation on noise levels does, in fact, contribute to L_n. Then, as the reverberation time (thus, the reverberant-field contribution to L_n) increases, the power of the noise source effectively decreases, to keep L_n constant. From this perspective, it is likely the fact that the noise-source output effectively decreases with increasing reverberation time, which leads to predictions of nonzero optimal reverberation time. In reality, however, the inherent sound-level output of the noise source does not change. This begs the question of whether this method would still predict nonzero optimal reverberation times if the noise-source output were kept constant?

The method-of-images approach of Plomp, Steeneken, and Houtgast[7] allowed arbitrary (rectangular) room geometries and absorption coefficients, thus considerably reducing the limitations associated with diffuse-field theory, by predicting the spatial propagation characteristics of the rooms more realistically. In their work, noise was incorporated by considering the audience as a collection of individual noise sources.

B. Theoretical prediction of optimal reverberation time

1. Basic equations

To address the issue of the differences in the predicted optimal reverberation times, we focus on noise sources inside the classroom (projectors, ventilation outlets, and occu-

pants), and consider the U_{50} speech-intelligibility metric that has been shown to be best suited for the evaluation of speech intelligibility in classrooms.[1] U_{50} is among the metrics that make use of the acoustical energy-ratio concept. This concept divides received acoustical energy into useful and detrimental parts. The useful part consists of the direct energy from the speaker, E_d, and the early arriving, reflected energy from the speaker, E_e. In U_{50}, reflected energy that arrives at the listener within 0.05 s of the signal is classified as early (useful) reflected energy. The remaining reflected, or late-arriving, energy, E_l, is considered detrimental. In addition to late-arriving reflected energy, noise energy, E_n, is included as detrimental. In summary, the useful-to-detrimental energy ratio Q is defined as

$$Q=\frac{E_d+E_e}{E_l+E_n}. \tag{1}$$

U_{50} in decibels is given by

$$U_{50}=10\log(Q). \tag{2}$$

To determine Q, let us follow previous work[2] by considering each of the four components of energy defined previously. Assuming point sources, and applying diffuse-field theory which assumes an exponential sound decay and a spatially invariant reverberant field, it can be shown that the direct and total-reflected energy densities ($E_r=E_c+E_l$) in w s/m^3 are, respectively, given by[8]

$$E_d=\frac{q_s W}{4\pi c r_s^2}, \tag{3}$$

and

$$E_r=\frac{q_s W}{4\pi c r_h^2}, \tag{4}$$

where q_s is the directivity index of the source, W is the output sound power of the point acoustic source (assumed, for now, to be a speaker) in w, c is the speed of sound in m/s, r_s is the distance from the source to the listener in m, and r_h is the reverberation radius in m. The reverberation radius is that distance at which the total reflected sound energy equals the direct sound energy ($E_d=E_r$). To find r_h, consider Eyring's reverberation formula:

$$T=\frac{24V\ln(10)}{c[4mV-S\ln(1-\alpha)]}, \tag{5}$$

where T is the reverberation time in s, V is the room volume in m^3, S is the room surface area in m^2, α is the average surface absorption coefficient, and m is the air-absorption exponent in Np/m. After appropriate manipulation we obtain

$$1-\alpha=\exp[(4V/S)(m-k/c)], \tag{6}$$

with $k=\ln(10^6)/T$.

Using the formula for reflected energy density given by Kuttruff:[8]

$$E_r=-\frac{4W(1-\alpha)}{S\ln(1-\alpha)}, \tag{7}$$

and setting $E_d=E_r$ with $r_s=r_h$ in the expression for E_d, then solving for r_h^2 we obtain:

$$r_h^2=\frac{qV(k-mc)\exp[(4V/S)(k/c-m)]}{4\pi c}. \tag{8}$$

It can further be shown[1] that

$$E_e=E_r(1-e^{-k/20}), \tag{9}$$

from which it follows that

$$E_l=E_r e^{-k/20}. \tag{10}$$

Now consider L_{sf1}, the long-term anechoic speech level at 1 m directly in front of the speaker (analogous to the speaker output-power level). If L_d denotes the direct sound pressure level, and E_s denotes the sound energy density in w s/m^3 at 1 m, we have

$$L_d-L_{\mathrm{sf1}}=10\log\left(\frac{E_d}{E_s}\right)=10\log\left(\frac{1}{r_s^2}\right) \tag{11}$$

from which it follows that

$$\frac{\rho c^2 E_d}{p_0^2}=\frac{10^{L_{\mathrm{sf1}}/10}}{r_s^2} \tag{12}$$

with $p_0=2\times10^{-5}$ Pa. Similarly:

$$\frac{\rho c^2 E_r}{p_0^2}=\frac{10^{L_{\mathrm{sf1}}/10}}{r_{h_s}^2}. \tag{13}$$

2. Improved treatment of noise

In this improved analysis, noise due to a source inside the classroom is treated as generated by a point source at distance r_n from the listener. First, we note from Eq. (8) that

$$\frac{r_{h_s}^2}{q_s}=\frac{r_{h_n}^2}{q_n}, \tag{14}$$

where the subscripts s and n refer to the speech and noise sources, respectively. Then, following the same steps as for the speaker, we find:

$$\frac{\rho c^2 E_n}{p_0^2}=\frac{\rho c^2}{p_0^2}(E_{\mathrm{nd}}+E_{\mathrm{nr}})=10^{L_{\mathrm{nf1}}/10}\left(\frac{1}{r_n^2}+\frac{1}{r_{h_n}^2}\right), \tag{15}$$

where E_{nd} is the direct-energy density from the noise source, E_{nr} is the reflected-energy density from the noise source, and L_{nf1} is the long-term anechoic noise level at one meter directly in front of the noise source (analogous to the noise-source output-power level). Combining the above-given results and simplifying yields

$$U_{50}=10\log\left(\frac{(r_{h_s}^2/r_s^2)+1-e^{-k/20}}{e^{-k/20}+10^{(L_{\mathrm{nf1}}-L_{\mathrm{sf1}})/10}\left(\frac{r_{h_s}^2}{r_n^2}+\frac{q_s}{q_n}\right)}\right). \tag{16}$$

This equation allows for the calculation of U_{50} as a function of reverberation time, speaker-to-listener distance and speech-source output level, noise-source-to-listener distance and noise-source output level, and speech- and noise-

source directivity indices, for a given room (in particular, for a given volume, surface area and air-absorption exponent). Thus, given any room and its characteristics, and given the distances of the speech and noise sources from the listener, and their directivities, we can predict the optimal reverberation time for given speech- and noise-source output levels, by finding the value of T that maximizes U_{50}. Note, however, that Eq. (16) is still based on diffuse-field theory; in particular, it assumes a spatially invariant reverberant field.

It is important to emphasize here that, in Eq. (16), signal-to-noise level difference is defined in terms of values inherent to the speech- and noise-source outputs, independent of their acoustical environments, and not, as is common, in terms of the values at a receiver position which are, of course, strongly dependent on the acoustical environment. Source-related values will be indicated by SNS, received values by SNR. Output-power levels of typical speakers can be determined from published data;[9] total *A*-weighted values vary with vocal effort from about 60 to 75 dB. Output-power levels of UBC-classroom projectors and ventilation outputs have been measured.[10] Typical total *A*-weighted values are in the range 40–60 dB. These data suggest that SNS would be expected to range from about 0 to 40 dB in typical classrooms.

3. U_{50} prediction

U_{50} predictions were done using Eq. (16) for six classrooms with volumes $V=50$, 100, 300, 500, 1000, and 4000 m^3, the range found at the University of British Columbia (UBC). Corresponding surface areas were determined from $S=5.36\ V^{0.7104}$, the equation describing the best-fit regression between V and S for 279 UBC classrooms involved in another study.[11] Various distances from the speech source and the noise source to the receiver were used, as detailed in the following. Predictions were made for SNS=0, 10, 20, 30, and 40 dB (again, $\mathrm{SNS}=L_{\mathrm{sf1}}-L_{\mathrm{nf1}}$; the actual noise- and speech-source output levels do not matter). The values of the other prediction parameters were as follows: $q_s=2$, $q_n=1$, $m=0.0012$ Np/m, $c=344$ m/s. Note that noise sources were assumed to be omni-directional, an assumption that may not be accurate. Ventilation ducts and projectors would be expected to be directional at higher frequencies. However, their orientations in the classroom, and the positions of receivers with respect to them, are highly variable. Thus, an assumption of omni-directionality is a reasonable one to make from a practical point of view.

Two interesting general results were found when U_{50} was maximized for various rooms and for various speech and noise levels and listener distances:

(1) In any case for which the speech source was at a distance equal to or less than the distance from the noise source to the listener, an optimal reverberation time of zero was predicted.

(2) When the noise source was closer to the listener than the speaker, nonzero optimal reverberation times were, in general, predicted. The optimal reverberation time increased with classroom volume. It decreased with increased signal-to-noise level difference, tending to zero as the level difference tends to infinity. For a given r_s, the optimal reverberation time increased with decreasing r_n.

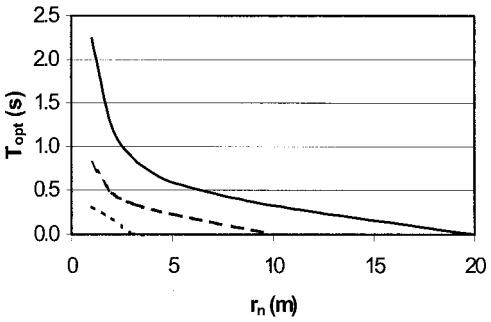

FIG. 1. Predicted variation of the optimal reverberation time T_{opt} with the distance from the noise source to the receiver, r_n, for classrooms with three volumes: (—) 4000 m^3; (---) 500 m^3; (···) 50 m^3, and SNS=0 dB. The speaker is at the front, the receiver at the back, of the classroom.

Figures 1 and 2 illustrate the results. Figure 1 represents a "worst-case" scenario with large r_s and small r_n. Here r_s was chosen to represent the largest likely distance from the speech source to the receiver—that for a speaker at the front of the classroom and the receiver at the back. Values of r_s were calculated as a function of volume using $r_s=0.7145\ V^{0.417}$, the equation describing the best-fit regression between V and the distance to the center, rear of the classroom (seating area F) for 279 UBC classrooms involved in another study;[11] the values used are shown in Table V. The noise-source-to-receiver distance was $r_n=1$ m corresponding, for example, to a receiver seated close to a noisy ventilation outlet or projector. Shown in Fig. 1 are the optimal reverberation times in the classrooms with $V=50$, 500, and 4000 m^3, for the case of SNS=0 dB. Figure 2 shows the same results for a receiver seated at distances one half those used in Fig. 1. Table V summarizes the worst-case predictions of optimal reverberation time. The optimal reverberation time increases with increasing volume from about 0.3 s to several seconds with low signal-to-noise level difference, and from 0.1 to 0.3 s with near optimal signal-to-noise level difference. In fact, the results are similar to, but slightly lower than, those of Bistafa and Bradley[2]—see Table IV.

These results can be explained physically in an approximate way as follows. A given increase in reverberation, while inherently tending to decrease speech intelligibility,

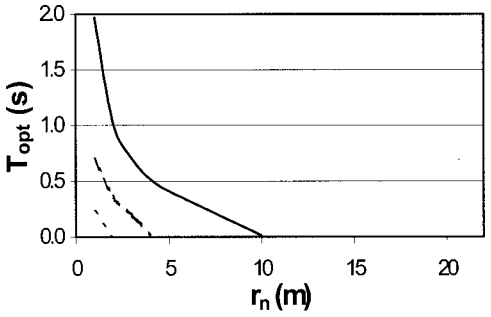

FIG. 2. Predicted variation of the optimal reverberation time T_{opt} with the distance from the noise source to the receiver, r_n, for classrooms with three volumes: (—) 4000 m^3; (---) 500 m^3; (···) 50 m^3, and SNS=0 dB. The speaker is at the front, the receiver in the middle, of the classroom.

TABLE V. Optimum reverberation times (T_{opt} in s—first line), received signal-to noise level differences (SNR in dB—second line) and U_{50}'s in dB (third line), determined using Eq. (16). Also shown are the optimum average surface-absorption coefficients (α_{opt}—fourth line) calculated from T_{opt} using diffuse-field theory.

SNS (dB)	Quantity	$V=50$ m^3 $r_s=3.7$ m	$V=100$ m^3 $r_s=4.9$ m	$V=300$ m^3 $r_s=7.7$ m	$V=500$ m^3 $r_s=9.5$ m	$V=1000$ m^3 $r_s=12.7$ m	$V=4000$ m^3 $r_s=22.7$ m
	T_{opt} (s)	0.08	0.08	0.10	0.11	0.12	0.17
40	SNR (dB)	34.23	31.35	27.35	25.42	22.60	17.62
	U_{50} (dB)	30.73	28.13	23.91	21.91	19.20	13.93
	α_{opt}	0.69	0.76	0.79	0.81	0.84	0.86
	T_{opt} (s)	0.10	0.14	0.14	0.16	0.19	0.29
30	SNR (dB)	25.03	22.65	18.92	17.22	14.83	10.47
	U_{50} (dB)	21.61	19.22	15.23	13.36	10.82	5.94
	α_{opt}	0.61	0.64	0.67	0.68	0.69	0.68
	T_{opt} (s)	0.14	0.17	0.23	0.27	0.35	0.61
20	SNR (dB)	16.18	14.49	11.43	10.02	8.28	4.97
	U_{50} (dB)	12.69	10.69	7.22	5.56	3.33	−1.08
	α_{opt}	0.48	0.49	0.49	0.49	0.47	0.41
	T_{opt} (s)	0.23	0.29	0.43	0.53	0.72	1.42
10	SNR (dB)	7.54	6.38	4.25	3.25	1.92	−0.54
	U_{50} (dB)	3.85	2.30	−0.56	−2.01	−4.06	−8.42
	α_{opt}	0.33	0.32	0.30	0.29	0.26	0.20
	T_{opt} (s)	0.34	0.43	0.72	0.91	1.27	2.85
0	SNR (dB)	−1.69	−2.58	−3.95	−4.69	−5.73	−7.39
	U_{50} (dB)	−5.43	−6.69	−9.22	−10.59	−12.62	−17.09
	α_{opt}	0.24	0.23	0.19	0.18	0.15	0.10

also results in a constant position-invariant increase in steady-state reverberant speech and noise levels which add to direct levels to give the total speech and noise levels. For both the speech and the noise, the magnitude of the total-level increases depends on the relative contributions of the direct and reverberant levels. At low source/receiver distance, the direct sound dominates, and the increase is small; at large distance the reverberant sound dominates and the increase is large. Thus, the constant increase in reverberant level results in an increase in the total level which increases with source/receiver distance. The relative amounts by which the speech and noise levels increase with increased reverberation determine whether the resulting speech-to-noise level difference increases (tending to increase intelligibility), decreases (tending to decrease intelligibility), or remains the same. This depends on the relative distances of the speech and noise sources from the receiver. If the distances are the same, both the speech and noise levels vary with reverberation in the same way, and the level difference does not change; the only effect on intelligibility is a decrease due to increased reverberation. If, on the other hand, the noise source is farther from the receiver than the speech source, then noise levels increase more with reverberation than do speech levels; resulting level differences decrease, tending to decrease intelligibility. This reinforces the effect of reverberation on intelligibility, and leads to an optimal reverberation time of zero. Finally, if the speech source is farther from the receiver than the noise source, then speech levels increase more with reverberation than do noise levels, and the level difference increases with reverberation, tending to increase intelligibility. This trend tends to counteract the decrease in intelligibility due to temporal reverberation, leading to the highest intelligibility occurring at a nonzero optimal reverberation time.

It is of interest to consider the results in terms of the more commonly used received signal-to-noise level difference, SNR. Values corresponding to T_{opt} are shown in Table V. It is generally considered that SNR$>$15 dB is required for excellent speech intelligibility.[2] Table V shows that SNSs greater than about 20, 28, and 38 dB, respectively, are required to achieve this in small, medium, and large classrooms.

It is also of interest to consider the results in terms more directly relevant to classroom design—for example, the amount of sound absorption required to achieve the optimal reverberation times. Table V shows the optimal average surface-absorption coefficients, α_{opt}, corresponding to the T_{opt} values, calculated using diffuse-field theory. In quiet classrooms, requiring low reverberation times and, in general, high absorption, the optimal coefficient increases with volume from about 0.7 to 0.9. In moderately noisy classrooms, it varies between about 0.4 and 0.5. In noisy classrooms, requiring higher reverberation and, generally, low absorption, α_{opt} decreases with volume from about 0.2 to 0.1 s. The classroom sound-absorptive features that can be used to achieve these various values of α_{opt} can be determined from absorption-coefficient data published elsewhere.[12,13]

4. Reverberation time for satisfactory speech intelligibility

It should be noted that, although the reverberation times recommended previously do not provide optimal speech intelligibility for listeners closer to the speaker than to the

TABLE VI. Ranges of sufficient reverberation time in seconds for satisfactory speech intelligibility, for the "worst case" of large r_s and $r_n = 1$ m. "Na" indicates that satisfactory speech intelligibility cannot be achieved.

SNS (dB)	$V = 50$ m^3 $r_s = 3.7$ m	$V = 100$ m^3 $r_s = 4.9$ m	$V = 300$ m^3 $r_s = 7.7$ m	$V = 500$ m^3 $r_s = 9.5$ m	$V = 1000$ m^3 $r_s = 12.7$ m	$V = 4000$ m^3 $r_s = 22.7$ m
40	0–0.9	0–0.9	0–0.9	0–0.9	0–0.9	0–0.9
30	0–0.9	0–0.9	0–0.9	0–0.9	0–0.9	0–0.9
20	0–0.8	0–0.8	0–0.8	0.1–0.8	0.2–0.8	Na
10	0.1–0.6	0.2–0.5	Na	Na	Na	Na
0	Na	Na	Na	Na	Na	Na

noise source (we have found optimal values of zero in this case), U_{50} tends to be high for these listeners. In Table V, U_{50} values corresponding to the optimal reverberation times are shown; they are as higher than 30. Optimal reverberation times may not be necessary for satisfactory speech intelligibility. For example, it has been suggested that $U_{50} \geqslant 1.0$ is sufficient for satisfactory speech intelligibility.[1] Following this suggestion, Table VI gives the ranges of reverberation times which result in satisfactory speech intelligibility for the same worst-case configurations considered previously. $U_{50} \geqslant 1.0$ can generally be achieved with SNS greater than about 15 dB, and T in the range 0 to 0.9 s; it generally cannot be achieved if SNS < 0 dB. "Na" entries indicate conditions for which $U_{50} = 1.0$ cannot be obtained, regardless of reverberation time. Table V indicates the combinations of classroom volume and source-related signal-to-noise level difference, SNS, which correspond to $U_{50} \geqslant 1.0$. In classrooms with low, medium, and high volume SNS must exceed about 5, 15, and 25 dB, respectively, to achieve satisfactory speech intelligibility.

5. Extension to multiple noise sources

Classrooms usually contain only one main speech source, but they may contain many sources of noise (e.g., ventilation outlets, projectors, occupants). The above-mentioned work assumed only one noise source. However, we can account for multiple noise sources (say, m of them, where n_i refers to the ith noise source) in the present analysis by simply adding the energy contributions E_{ni} $(i = 1,2,...,m)$ of all sources to give the total-noise energy density:

$$E_n = \sum_{i=1}^{m} E_{ni} = \sum_{i=1}^{m} 10^{L_{\mathrm{nf1}i}/10} \left(\frac{1}{r_{ni}^2} + \frac{1}{r_{h_{ni}}^2} \right), \tag{17}$$

where $L_{\mathrm{nf1}i}$ is the long-term anechoic noise level at 1 m directly in front of the ith noise source, and r_{ni} is the distance of the ith noise source to the listener. This gives

$$Q = \frac{(r_{h_s}^2 / r_s^2) + 1 - e^{-k/20}}{e^{-k/20} + \sum_{i=1}^{m} 10^{(L_{\mathrm{nf1}i} - L_{\mathrm{sf1}})/10} \left(\frac{r_{h_s}^2}{r_{ni}^2} + \frac{q_s}{q_{ni}} \right)}. \tag{18}$$

When this method is applied to multiple noise sources, those further from the listener than the signal have negligible effect in the prediction of optimal reverberation time. For example, when a noise source (regardless of output level) is added at 30 m from the listener in the example in the previous section (where the signal was 20 m from the listener and the first noise source was 1 m from the listener), optimal reverberation-time predictions remain exactly the same. This result suggests that, for multiple noise sources, only those closer to the listener than the speech source need to be considered. Also, as might be expected, adding noise sources that are closer to the listener than the signal results in an increase in the predicted optimal reverberation time.

6. Further explanation of the contradiction in the literature

Different treatments of noise were suggested as the reason why empirical methods find an optimal reverberation time of zero while theoretical methods predict nonzero values. We can use Eq. (16) to corroborate this explanation. First, as noted previously, experimental methods effectively ignore the positive effect of reverberation on signal-to-noise level differences. This is equivalent to replacing the $(r_{h_s}^2 / r_n^2 + 1)$ term in the denominator of Eq. (16) with one, resulting in optimal reverberation times of zero. If the signal-to-noise level difference were allowed to vary with changing reverberation, the design of experimental methods (with noise and speech generated at the same distances from the listener) would correspond to $r_n = r_s$. In this case, Eq. (16) predicts an optimal reverberation time of zero.

In the treatment of noise by Bistafa and Bradley,[2] the r_n variable was eliminated, because there was no source of noise. Also, the effect of reverberation on noise was included in L_{nf1}, which was the total noise level. This is equivalent to replacing the $(r_{h_s}^2 / r_n^2 + 1)$ term in the denominator of Eq. (16) with $r_{h_s}^2$. To apply our model in this case, we treat the uniform and stationary noise as originating from a noise source close to the listener—say $r_n = 1$ m. Then $r_n \ll r_s$, and Eq. (16) predicts nonzero optimal reverberation times (see Table V).

In the work of Plomp, Steeneken, and Houtgast,[7] a listener had several point noise sources nearby. In particular, there was a noise source that was closer to the listener than the speaker. From our discussion of multiple noise sources, we see that our method predicts nonzero optimal reverberation times in this situation. This is consistent with the findings of Plomp, Steeneken, and Houtgast.

III. OPTIMAL REVERBERATION TIMES IN UNOCCUPIED CLASSROOMS

The optimal classroom reverberation times discussed previously (e.g., as presented in Table V) are those experienced by the occupants of the classroom when in use—that

TABLE VII. Predictions of optimal reverberation time in seconds in unoccupied classrooms from the values when occupied from Table V. N is the number of classroom occupants.

SNS (dB)	$V=50$ m^3 $N=12$	$V=100$ m^3 $N=25$	$V=300$ m^3 $N=70$	$V=500$ m^3 $N=115$	$V=1000$ m^3 $N=230$	$V=4000$ m^3 $N=400$
40	0.1	0.1	0.1	0.1	0.1	0.2
30	0.1	0.1	0.2	0.2	0.2	0.3
20	0.2	0.2	0.3	0.4	0.6	0.9
10	0.3	0.5	0.9	1.4	4.3	5.0
0	0.6	0.9	4.7	-	-	-

is, in the occupied classroom. It would be convenient, however, to be able to specify optimal reverberation times for the unoccupied classroom, since unoccupied values are those to which designers can more readily design. This can be accomplished by calculating the reverberation times in the unoccupied classrooms from those that are optimal in the occupied classrooms, given the number of occupants and their absorption characteristics. This can be done using diffuse-field theory, according to which the occupied reverberation time T_o in seconds is given by

$$T_o=\frac{0.161V}{A_u+NA_p}, \tag{19}$$

in which V is classroom volume in m^3, A_u is the unoccupied room absorption in m^2, N is the number of occupants, and A_p is the absorption per occupant (the 1 kHz value of 0.81 m^2 is used here).[13]

Now, according to diffuse-field theory, for the unoccupied classroom, $T_u=0.161V/A_u$; thus, $A_u=0.161V/T_u$. Substituting this into Eq. (19) and rearranging gives

$$T_u=\frac{1}{\frac{1}{T_o}-\frac{A_pN}{0.161V}}. \tag{20}$$

Note that, according to this expression, classrooms of different volumes with the same occupied T_o's and the same numbers of occupants per unit volume, have the same unoccupied T_u's (and vice versa).

Consider classrooms with volumes of 50, 100, 300, 500, 1000, and 4000 m^3, as discussed previously. Assume that these classrooms contain 12, 25, 70, 115, 230, and 400 occupants, respectively (these were again determined from typical data for 279 UBC classrooms considered in another study[11] on the assumption of 70% occupancy, typical of UBC classrooms). Table VII shows, for various source-related signal-to-noise level differences, the optimal unoccupied T_u 's associated with the optimal occupied T_o's in Table V. In the case of the low optimal T_o's associated with high signal-to-noise level difference, the optimal T_u's are almost the same. However, in the case of the higher optimal T_o's associated with low signal-to-noise level difference and large volume, optimal T_u's can be as high as several seconds. In several of these cases the optimal T_u was negative (in Table VII, this is indicated by a dash). The explanation of this nonphysical result is that the amount of absorption provided by the classroom occupants exceeded that required to obtain the optimal occupied reverberation time; that is, the optimal occupied reverberation time cannot be achieved if the classroom is 70% occupied.

IV. CONCLUSION

Our work indicates that the question of optimal reverberation time is ultimately reduced to the question of how to incorporate noise in a physically realistic manner. Here we have considered noise sources located in the classrooms. To treat noise as it is treated in the experimental methods—where its level is adjusted with changing reverberation to keep the signal-to-noise level difference at the listener constant—is not realistic. In a real classroom, it is the inherent output-power level of the noise source and of the speaker that is constant, regardless of reverberation, not the levels at the listener position. Nor is it realistic to treat noise as generated at a single point somewhere within the classroom at a distance from the listener equal to the distance between the speaker and the listener. Sources of ventilation and student-activity noise are very easily, and most likely, located much closer to the listener than is the speaker. Consequently, the way in which noise is incorporated in the theoretical methods is, in this respect, more realistic than in experimental methods. In using theoretical methods, however, we must still be careful to incorporate the effect of reverberation on noise. Bistafa and Bradley[2] did not do this, while Plomp, Steeneken, and Houtgast[7] did.

A physically realistic treatment of noise incorporates both the nearby noise source and the effect of reverberation on noise—for example, by setting $r_n<r_s$ in Eq. (16). The results of such an analysis are given in Table V. We see that when noise is incorporated in a more physically realistic manner, nonzero reverberation times, in the range of 0.1 s to several seconds, are found to be optimal.

There are numerous reasons why a reverberation time of zero may not, in practice, be desirable. First, the cost of reducing reverberation times to very low values may be prohibitively expensive and impractical. Second, it is unnatural to be in an environment in which there is very little reverberation. A listener in such an environment may feel uncomfortable, while speakers may have difficulty monitoring their voices (since no energy is returned). Also, since speech is directional (directed predominantly in front of the speaker), listeners in an anechoic situation who are not positioned directly in front of the speaker will receive relatively little direct speech signal. Further, since the rate of spatial decrease of direct energy is inversely proportional to the square

of the distance between the listener and the speaker, listeners far from the speaker (near the back of a large classroom, for example) will also receive little direct speech signal. These listeners rely on reflected sound energy to hear what is being said.

For all of the above-mentioned reasons—in particular, because physically realistic incorporation of noise leads to predictions of nonzero optimal reverberation time—it is safe to conclude that one should aim for nonzero reverberation times in occupied classrooms. Reverberation times varying from 0 to 1 s with increasing noise level and classroom size appear to be appropriate; these correspond to optimal values in unoccupied classrooms which are as high as several seconds. However, optimal values may, in fact, be impossible to achieve in well-occupied classrooms, since the absorption provided by the occupants may exceed that required for optimal reverberation times.

The above-presented work is by no means conclusive and points to other areas that should be explored. The use of other metrics to predict optimal reverberation time is one natural extension of the work done here with U_{50}. Although such work has been done,[2] it would be beneficial to seek results when noise is incorporated in a more physically realistic manner and which eliminates the assumption of diffuse-field theory. To do so, and to improve the current work, it is necessary to accurately model noise in classrooms (or, if this has already been done, to apply these models to the predictions). Another interesting approach would be to realistically incorporate noise into the experimental methods. For obvious reasons, this may be quite difficult (or even impractical) and, again, demands an accurate model of noise in classrooms.

It is also important to note that increased reverberation times and background noise may have more adverse effects on children, older listeners, and the hearing impaired than on normal-hearing, adult listeners.[3,5] Consequently, the above-presented results may not apply to these listeners. Also of importance would be to find U_{50} levels which correspond to acceptable speech intelligibility for various groups of special listeners (children, elderly, hearing impaired), and to use these to suggest ideal and acceptable reverberation levels in classrooms designed to teach these people.

Finally, further work is required to revise the prediction models to reduce their reliance on diffuse-field theory. In particular, it would be of interest to incorporate more realistic decreases of steady-state levels with source–receiver distance.[12,13]

[1] J. S. Bradley, "Speech intelligibility studies in classrooms," J. Acoust. Soc. Am. **80**, 846–854 (1986).
[2] S. R. Bistafa and J. S. Bradley, "Reverberation time and maximum background-noise level for classrooms from a comparative study of speech intelligibility metrics," J. Acoust. Soc. Am. **107**, 861–875 (2000).
[3] A. K. Nabelek and P. K. Robinson, "Monaural and binaural speech perception in reverberation for listeners of various ages," J. Acoust. Soc. Am. **71**, 1242–1248 (1982).
[4] A. K. Nabelek and J. M. Pickett, "Monaural and binaural speech perception through hearing aids under noise and reverberation with normal and hearing-impaired listeners," J. Speech Hear. Res. **7**, 724–739 (1974).
[5] T. Finitzo-Hieber and T. W. Tillman, "Room acoustics effects on monosyllabic word discrimination ability for normal and hearing-impaired children," J. Speech Hear. Res. **21**, 440–458 (1983).
[6] J. S. Bradley, "Predictors of speech intelligibility in rooms," J. Acoust. Soc. Am. **80**, 837–845 (1986).
[7] T. Houtgast, H. J. M. Steeneken, and R. Plomp, "Predicting speech intelligibility in rooms from the modulation transfer function. II. Mirror image computer model applied to rectangular rooms," Acustica **46**, 73–81 (1980).
[8] H. Kuttruff, *Room Acoustics*, 3rd ed. (Elsevier Applied Science, London, 1991), pp. 114–123.
[9] "American National Standard Methods for Calculation of the Speech Intelligibility Index," ANSI S3.5-1997.
[10] R. Wang, "Sound-intensity measurements of the sound-power outputs of classroom projectors and ventilation outlets," Technical report, University of British Columbia, 2001.
[11] M. R. Hodgson, "Rating, ranking and explaining the acoustical quality of university classrooms," J. Acoust. Soc. Am. (submitted).
[12] M. R. Hodgson, "Empirical prediction of speech levels and reverberation in classrooms," J. Build. Acoust. **8**, 1–14 (2001).
[13] M. Hodgson, "Experimental investigation of the acoustical characteristics of university classrooms," J. Acoust. Soc. Am. **106**, 1810–1819 (1999).

On the sampling conditions for reconstruction of an acoustic field from a finite sound source

Makoto Tabei
Department of Electrical and Computer Engineering, University of Rochester, Rochester, New York 14627

Mitsuhiro Ueda
Department of International Development Engineering, Tokyo Institute of Technology, Tokyo 152-8552, Japan

(Received 10 May 2000; revised 8 November 2001; accepted 14 November 2001)

A simple and accurate method for the estimation of ultrasonic transducer fields is developed. In the method, the angular spectrum is employed to evaluate the three-dimensional propagation from a measured plane to an arbitrary parallel plane. The implementation uses a discrete convolution that is described in detail. Relative to conventional spatial-frequency representations, the implementation of the angular spectrum method in this paper has the advantage of being free from artifacts, enabling sample spacing to be greater than one half wavelength, using memory efficiently, and interpolating the measured data. The loosened sampling requirement and natural interpolation of the method permit efficient reconstruction of the full three-dimensional acoustic field from a coarse sound pressure measurement on single plane. © *2002 Acoustical Society of America.*
[DOI: 10.1121/1.1434946]

PACS numbers: 43.60.Sx, 43.30.Yj, 43.20.Ye, 43.35.Yb [JCB]

I. INTRODUCTION

The acoustic field of an ultrasonic transducer determines the quality of imaging and sensing that the transducer can provide. Although direct three-dimensional (3D) measurement of the acoustic field may be impractical, the 3D sound field can in theory be reconstructed from the sound pressure distribution measured on a plane orthogonal to the axis of the transducer.[1–3] The method is known as angular spectrum method or acoustical holography.[4,5] An advantage of angular spectrum method is that volumetric diffraction between parallel planes is represented as a linear filtering operation efficiently implementable by a fast Fourier transform (FFT) without explicit account of geometry or boundary conditions.

Although in principle straightforward, the 3D acoustic field reconstruction using an angular spectrum method has not been reported to our knowledge. This is perhaps because artifacts and stringent sampling requirements arise from the spatial-frequency implementation of filtering when the spatial-frequency characteristic of the propagation function has a sudden jump or singularity.[6,7]

In this paper that extends a previous conference paper[8] by the inclusion of a theoretical basis and includes further data as well as a more formal presentation of results, a reconstruction technique based on a discrete convolution of the input data with a transfer function represented in the spatial domain[6] rather than the conventional manipulation of the input data in the frequency domain is proposed. Although a similar technique known as the convolution backprojection (CBP) method is used in x-ray computer tomography,[9,10] a two-dimensional convolution based reconstruction in acoustical holography has not apparently been reported.

The implementation of acoustical holography by convolution may have been thought impractical because the filter has infinite extent in the spatial domain. However, if the output has finite extent, the unnecessary part of the filter response can be truncated. Then, the overlap-save method,[10] which is a convolution based algorithm designed for implementing finite impulse response (FIR) filters, can be used.

This paper also shows that when the finite sound source is reconstructed from the sampled acoustic field, the sampling interval in measurements can be taken to be significantly greater than half a wavelength without loss of precision.[11–17] Using this property along with the overlap-save method allows an efficient algorithm for the reconstruction of the acoustic field. By taking the pixel interval of the reconstructed source image to be less than or equal to half a wavelength, the acoustic field at an arbitrary point can be evaluated by a successive forward propagation of the source image. The sampling interval depends on the ratio of the source size and the observation distance. Since the measurement of a field by scanning a hydrophone is generally a slow process, use of a coarse sampling interval can reduce the measurement by an order of magnitude if the time for measurement is assumed proportional to the square of the reciprocal of the sampling interval.

In Sec. II, a spatial-domain expression for the propagation is introduced and sampling conditions in the general case as well as backpropagation are discussed. Section III explains the implementation that incorporate the overlap-save method and the interpolation of the measured data on the source plane as well as successive reconstruction of acoustic field. Finally, Sec. IV presents experimental results and compares the precision and sampling requirements for conventional and convolutional techniques.

II. SPATIAL DOMAIN REALIZATION OF ANGULAR SPECTRUM

The angular spectrum method is commonly described in the spatial-frequency domain because the expressions are simple. A spatial domain representation is obtained by the inverse Fourier transform of frequency domain representation[6] or by forming an appropriate Green's function. Although these two representations are mathematically equivalent, they have a distinct difference when implemented with finite arithmetic. In the following, the spatial-domain representation and its features are discussed because this approach is not susceptible to artifacts.

A. Representation of transfer function in spatial domain

An acoustic wave propagating in the positive direction of z-axis is considered here. The fields are represented in x-y planes. The propagation of sound pressure between two planes, one at $z=z_1$ and the other at $z=z_2$, is expressed by the following convolution:[6]

$$p(x,y,z_2)=\int_{-\infty}^{+\infty}\int_{-\infty}^{+\infty} p(\xi,\eta,z_1) \cdot h(x-\xi,y-\eta,z_2-z_1)\,d\xi\,d\eta \tag{1}$$

in which

$$h(x,y,z)=\frac{z(1+jkr)}{2\pi r^3}\exp(-jkr), \qquad r=\sqrt{x^2+y^2+z^2}, \tag{2}$$

and k is the wave number given by $2\pi f/c$. (The symbol f denotes temporal frequency in Hertz and c is the sound speed.) In practice, the sound pressure distribution cannot be measured over an infinite extent. Thus, $p(\xi,\eta,z_1)$ and $p(x,y,z_2)$ in Eq. (1) are limited to finite ranges, i.e.,

$$\xi_0\leqslant\xi\leqslant\xi_1, \quad \eta_0\leqslant\eta\leqslant\eta_1,$$

and

$$x_0\leqslant x\leqslant x_1, \quad y_0\leqslant y\leqslant y_1.$$

In this case, only a finite range

$$x_0-\xi_1\leqslant x-\xi\leqslant x_1-\xi_0, \quad y_0-\eta_1\leqslant y-\eta\leqslant y_1-\eta_0$$

in $h(x-\xi,y-\eta,z_2-z_1)$ is required for evaluation of Eq. (1). This is important when the data are treated in spatial domain. In the frequency domain, an infinite extent of $h(x-\xi,y-\eta,z_2-z_1)$ is used implicitly and this leads to artifacts.

B. Discrete representation and general sampling conditions

The convolution integral in Eq. (1) can be approximated by a summation of values at discrete points:

$$p(x,y,z_2)\simeq\Delta x\Delta y\sum_{i_\eta=-\infty}^{\infty}\sum_{i_\xi=-\infty}^{\infty} p(\Delta x i_\xi,\Delta y i_\eta,z_1) \times h(x-\Delta x i_\xi,y-\Delta y i_\eta,z_2-z_1), \tag{3}$$

where Δx and Δy are the sampling interval in the x and y coordinates, respectively. To calculate $p(x,y,z_2)$ accurately using Eq. (3) instead of Eq. (1), the sampling intervals Δx and Δy need to be smaller than the reciprocal of the maximum spatial frequency of the integrand of Eq. (1) in each dimension. (See Appendix A for a sufficient condition that the integral and summation are equal.)

The spatial-frequency characteristics of $h(x,y,z)$ determine the maximum frequency not only for $p(x,y,z_2)$ but also for $p(\xi,\eta,z_1)$ because the pressure field $p(\xi,\eta,z_1)$ is filtered before observation in either numerical calculations or physical experiments. The 2D Fourier transform of $h(x,y,z)$ in x and y may be expressed[6]

$$H(u,v,z)=\begin{cases}\exp(j2\pi z\sqrt{(f/c)^2-(u^2+v^2)}), & (u^2+v^2)\leqslant(f/c)^2,\\ \exp(-2\pi z\sqrt{(u^2+v^2)-(f/c)^2}), & (u^2+v^2)>(f/c)^2.\end{cases} \tag{4}$$

Here, the latter term on the right-hand side describes an evanescent wave that decays exponentially with propagation distance.

The spatial-frequency range of the integrand in Eq. (1), i.e., $p(\xi,\eta,z_1)h(x-\xi,y-\eta,z_2-z_1)$, is bounded by the sum of the range for $p(\xi,\eta,z_1)$ and for $h(x-\xi,y-\eta,z_2-z_1)$. Assuming that the input pressure field $p(\xi,\eta,z_1)$ is observed more than a few wavelengths away from the sound source prior to the evaluation of Eq. (1) and that z_2-z_1 is also larger than a few wavelengths, the evanescent wave components over f/c become negligible in each term. Then, $\Delta x<c/(2f)$ and $\Delta y<c/(2f)$ become sufficient conditions to satisfy the constraint that sampling intervals be smaller than the reciprocal of the maximum spatial frequency of the integrand in Eq. (1).

However, even if $p(\xi,\eta,z_1)$ is properly bandlimited, the calculation of propagation using Eq. (1) for extremely small distances, i.e., $|z_2-z_1|<c/f$, is a problem because $h(x-\Delta x i_\xi,y-\Delta y i_\eta,z_2-z_1)$ has undesired high spatial-frequency components and suitable interpolation of the pulse train $p(\Delta x i_\xi,\Delta y i_\eta,z_1)$ is not possible.

C. Sampling conditions needed for reconstruction of a point source

The maximum spatial frequency of the integrand in Eq. (1) becomes smaller than the simple sum of frequency range for $p(\xi,\eta,z_1)$ and $h(x-\xi,y-\eta,z_2-z_1)$ in some special cases. For example, suppose that a point pressure source is located at (0,0,0). The sound pressure caused by this point source in the plane $z=z_1$ is described by

$$p(x,y,z_1)=\int_{-\infty}^{+\infty}\int_{-\infty}^{+\infty}\delta(\xi,\eta)h(x-\xi,y-\eta,z_1)\,d\xi\,d\eta =h(x,y,z_1). \tag{5}$$

Then, from $p(x,y,z_1)$, a diffraction limited point source distribution on $z=0$ can be reconstructed by backpropagating the field using a complex conjugate propagator $h^*(x,y,z)$ instead of $h(x,y,z)$. The expression for this is

$$p(x,y,0)=\int_{-\infty}^{+\infty}\int_{-\infty}^{+\infty} h(\xi,\eta,z_1)\cdot h^*(x-\xi,y-\eta,z_1)d\xi\, d\eta. \tag{6}$$

When $|x|$ and $|y|$ are small, $h(\xi,\eta,z_1)$ and $h^*(x-\xi,y-\eta,z_1)$ have almost opposite phase and they cancel each other. In fact, the highest spatial frequency of $h(\xi,\eta,z_1)h^*(x-\xi,y-\eta,z_1)$ is dependent on x and y. These spatial frequencies are given by

$$(f/c)/[(1/2)^2+(z_1/x)^2]^{1/2},$$

and

$$(f/c)/[(1/2)^2+(z_1/y)^2]^{1/2}.$$

(See Appendix B for this calculation.) By limiting the range of reconstruction to $|x|\leqslant x_{\max}$ and $|y|\leqslant y_{\max}$, the sampling requirements become

$$\Delta x<(c/f)[(1/2)^2+(z_1/x_{\max})^2]^{1/2}, \tag{7}$$

and

$$\Delta y<(c/f)[(1/2)^2+(z_1/y_{\max})^2]^{1/2}. \tag{8}$$

III. METHOD OF CALCULATIONS

A. Implementation using the overlap-save method

If the input pressure field has finite extent, Eq. (3) can be rewritten using the finite sum

$$\begin{aligned} &p(\Delta x i_x+x_0,\Delta y i_y+y_0,z_2)\\ &\simeq\Delta x\Delta y\sum_{i_\xi=0}^{N_\xi-1}\sum_{i_\eta=0}^{N_\eta-1} p(\Delta x i_\xi+\xi_0,\Delta y i_\eta+\eta_0,z_1)\\ &\quad\times h(\Delta x(i_x-i_\xi)+(x_0-\xi_0),\Delta y(i_y-i_\eta)\\ &\quad+(y_0-\eta_0),z_2-z_1),\\ &\quad 0\leqslant i_x\leqslant N_x-1,\quad 0\leqslant i_y\leqslant N_y-1, \end{aligned} \tag{9}$$

in which Δx and Δy are sampling intervals, and N_ξ, N_η, and N_x, N_y are the number of samples in observation and reconstruction data, respectively.

Equation (9) can be implemented using a DFT based fast convolution. To ensure that the every point in the input affects each point in the output, $(N_\xi+N_x-1)\times(N_\eta+N_y-1)$ samples of h are required. The result is that the linear convolution of $N_\xi\times N_\eta$ and $(N_\xi+N_x-1)\times(N_\eta+N_y-1)$ extends to $(2N_\xi+N_x-2)\times(2N_\eta+N_y-2)$. The storage requirements for computation can be reduced by the use of the overlap-save method.[10] The original method was designed to evaluate the discrete convolution of infinite input sequences with finite impulse response filters; the use here is instead with a finite sequence and an infinite response filter. Both the input pressure field and the transfer function should be stored in an $(N_\xi+N_x-1)\times(N_\eta+N_y-1)$ 2D array. The input pressure field should be in the lower left corner of the array and the rest of the array should be filled with zeroes. The DFTs of these two arrays are multiplied in the frequency domain; the output pressure field is in the upper-right corner of the corresponding IDFT and starts at $(N_\xi-1,N_\eta-1)$. The upper and right ends of the convolution that exceed the DFT size are wrapped around and overlapped on the lower and left ends of the array.

The abovementioned convolution may be done by using either a $(N_\xi+N_x-1)$ column by $(N_\eta+N_y-1)$ row 2D FFT or a $(N_\xi+N_x-1)\times(N_\eta+N_y-1)$ 1D FFT. In the latter, the one-dimensional sequence is formed by arranging columns end to end.[9] The difference between these methods is in the wrapped portion of the result. The $N_x\times N_y$ output that originates at $(N_\xi-1,N_\eta-1)$ is, however, identical. Further details can be found in Ref. 8.

When using a typical FFT with a data length that is not a power of two, zero padding is required. For a 2D FFT, the data should be filled with zeroes to a power of 2 in each dimension. For a 1D FFT, only the total length of the data need to be padded to power of 2. The 2D FFT implementation requires, consequently, double the storage in the worst case and is computationally more complex than the 1D FFT. Prime factor FFT packages that have recently become available, however, make the choice of data size less critical.[18]

B. Point source reconstruction with a fine resolution

The discussion in Sec. II C shows a point-source field that is measured with a large sampling interval $[>c/(2f)]$ can be backpropagated to the source plane. However, the sample interval for the reconstruction must be less than a half wavelength to avoid loss of information and to form an equivalent source for successive use. This is accomplished by evaluating Eq. (9) repeatedly with a fractional increments of x_0 and y_0 relative to measurement sampling interval. Then, merging each reconstruction with different x_0 and y_0 forms a fine resolution reconstruction. Alternatively, this may be done of the expense of memory in one step by storing measurement data in appropriate position of a finely spaced array.

Why can an image be reconstructed with finer resolution than the measured data? The reason is that the measurement has far larger extent than the reconstruction and this has the effect of preserving the total amount of information in a diverging field. The wave front converges during backpropagation to the source, which decreases the effective sample spacing. Noteworthy is that application of ordinary polynomial or bandlimited type interpolation schemes to a coarse reconstruction does not reproduce the source accurately because these schemes simply smooth out the distribution and do not supply missing information.

Numerical examples of point-source reconstructions are shown in Fig. 1.[8] First, the field is calculated on a coarse sampling interval obeying Eq. (5). Then, the field is backpropagated to the source plane using Eq. (9) with the complex conjugate propagator h^*. The distance between the source and the point of observation is 100 wavelengths and the measurement sampling interval is eight wavelengths [16 times the Nyquist interval $c/(2f)$]. This permits accurate reconstruction within the range of $x_{\max}=y_{\max}=12.5$ wavelengths using Eqs. (7) and (8).

A virtually infinite aperture size, i.e., 960×960 wavelengths, is used in the reconstruction shown in Fig. 1. The shape of the diffraction limited impulse response is clearly

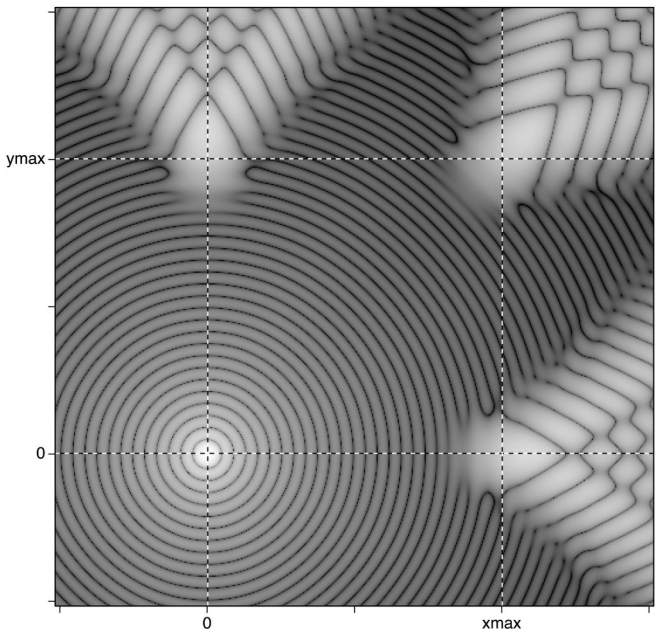

FIG. 1. Back-propagated image of point source. $\Delta x=\Delta y=8c/f$, $z_1=100\ c/f$, and $\Delta xN_\xi=\Delta yN_\eta=9.6z_1$. (Dynamic range=60 dB.)

represented by a reconstruction sampling interval of 1/10 of the wavelength. The field from the point source is stored in lower left 120×120 portion of 128×128 array and upper right 8×8 regions are reserved for the reconstruction. To perform the interpolation, this process is repeated 80 times in each direction with wavelength/10 increments of x_0 and y_0 and results are merged. The largest amplitude at the edge of aperture is 4% of the amplitude at the center. Since this factor applies also in the backpropagation, the effect of finite aperture is negligible. The reconstructed image has the characteristic form of a Bessel function because the measurement aperture is very large and the theoretical resolution limit is almost achieved.

The artifacts beyond $\pm x_{\max}$ and $\pm y_{\max}$ are from aliasing due to the sampling procedure. However, the aliasing is not present within the region of interest in the reconstruction.

C. Finite source reconstruction and successive forward propagation

A finite sound source can be interpreted as a superposition of point sources. Therefore, the above discussion can also be applied to the reconstruction of finite sound source. The image of a point source can be obtained accurately in the range of $2x_{\max}\times 2y_{\max}$. For the reconstruction of a finite source, the accurate range becomes $(2x_{\max}-x_{\text{source\_size}})\times(2y_{\max}-y_{\text{source\_size}})$ because the aliasing or grating lobe artifact of the other part of finite source also interferes in the reconstruction, i.e., the following relations must be satisfied:

$$x_{\text{source\_size}}<2x_{\max}-x_{\text{source\_size}},$$

and

$$y_{\text{source\_size}}<2y_{\max}-y_{\text{source\_size}}.$$

As a result, maximum source size reconstructable without artifact becomes $x_{\max}\times y_{\max}$ for a given Δx and Δy.

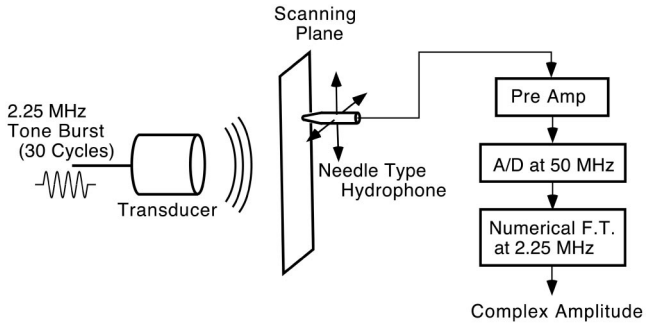

FIG. 2. Apparatus for measurement using PVDF hydrophone.

By taking the sampling intervals of the source reconstruction less than $c/(2f)$, the data can then be used for forward propagation to an arbitrary point for field reconstruction since the data now satisfies general sampling requirements. In most cases, this process can reduce data requirements by an order of magnitude in comparison to direct reconstruction from measured data that satisfy the general $c/(2f)$ sampling criterion.

IV. RESULTS

A. Measurement methods

The source images and the acoustic fields of actual transducers were reconstructed. In these reconstructions, the data were obtained from measurements in water and the transducers were driven by 30 cycles of a 2.25 MHz sine wave. The wave field was sampled by mechanically scanning a 1 mm diam PVDF hydrophone (see Fig. 2). The temporal signal from the hydrophone was sampled at a 50 MHz rate and the complex amplitude at 2.25 MHz was extracted from a Fourier transform of the sampled sequence.

B. Reconstruction of finite sound source and its acoustic field

For the reconstruction shown in Fig. 3(a), a 50×50 point measurement was made at a range of 50 mm from a 25.4 mm diam disk transducer. The sampling increment of the measurement was 0.9 mm (nearly three times larger than the Nyquist interval, since the wavelength c/f is 0.667 mm in water). Two zeroes were inserted in the measured data between each point to form a 148×148 point data set with a 0.3 mm sampling interval. The resulting data were then backpropagated to the source plane using Eq. (9). The size of reconstruction was chosen to be 100×100. A 65 536 point 1D FFT was performed after zero padding the sequence. (The minimum DFT size for this situation is 247×247 in 2D or 61 009 in 1D.) The interpolated reconstructed source image is shown on the left side of Fig. 3(a). In spite of the coarse measurement interval, no grating artifacts are present in the 100×100 point reconstruction. [The absolute maximum sampling interval given by Eqs. (7) and (8) is around 1.35 mm so a 0.9 mm sampling interval still is less than the maximum.] Finally, the reconstructed image of the source was used for the successive calculation of the acoustic field by forward propagation. The result is shown on the right side of Fig. 3(a). In this figure, the cross-sectional acoustic field

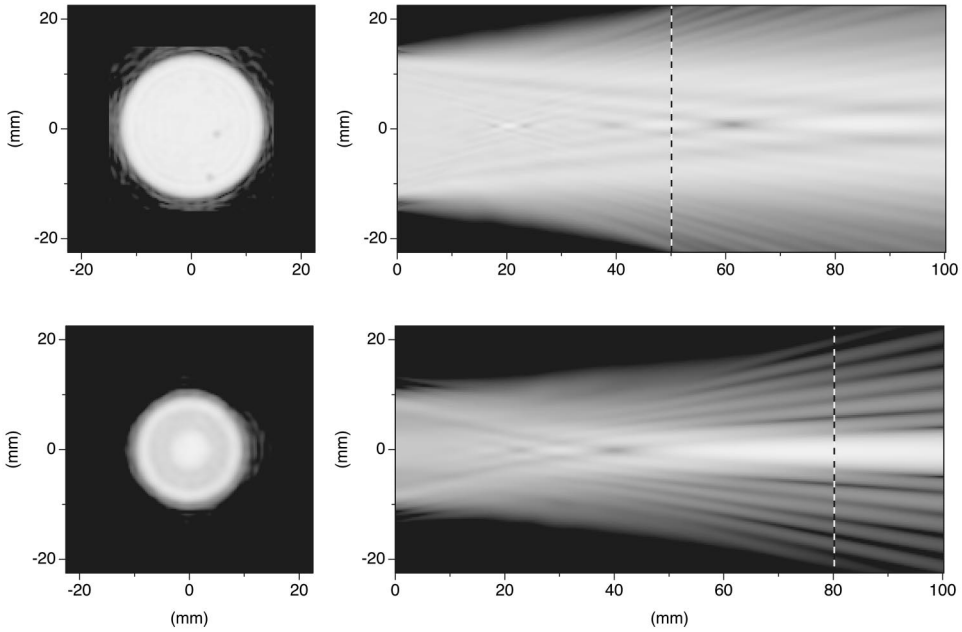

FIG. 3. Reconstructed source image and acoustic field obtained by forward propagation; (a) 25.4 mm flat transducer, (b) 19 mm focal transducer (focal length=100 mm). (Dynamic range=40 dB.)

along the transducer axis is displayed. The size of reconstruction is 150×1 and was obtained by repeating the reconstructions at 0.3 mm intervals up to 100 mm distance from the source plane. Since the absolute half-wavelength sampling requirements are satisfied, an artifact free image is obtained over the entire range. In this case, a smaller size FFT could be used because only a one-line reconstruction along the transducer axis was sought. A 32 768 point 1D FFT was used for the reconstruction in the figure. (The minimum DFT size is 249×100 for the 2D case or 24 900 for 1D case.)

In Fig. 3(b), the reconstructed source image and acoustic field of a 19 mm diam focused transducer are shown. The measurements were made at 80 mm from the transducer surface in 25×25 point grid with a sampling interval of 1.8 mm. Five zeroes were inserted between each measurement point to yield a 145×145 point array. A 100×100 point source image was then reconstructed using 0.3 mm sampling intervals. The source reconstruction has a nonuniform ringlike distribution. This is caused by the acoustic lens in front of the transducer. The lens material acted like a matching layer between the water and the PZT material and transmitted energy most efficiently when the thickness was an odd multiple of a quarter wavelength. As expected from this phenomenon, the difference of the acoustic path between the central maximum and the second maximum is approximately a half wavelength. The axial acoustic field was reconstructed in the same manner as for the previous figure.

Figure 4 shows a direct reconstruction of an acoustic field without first calculating the source under the same circumstances described for Fig. 3(b) to demonstrate the advantage of a two-step reconstruction. The measured data were expanded to 145×145 points and the field evaluated directly from these data. Because the field was undersampled, several grating lobes are present along with the true acoustic beam from the measurement plane. The key to the two-step reconstruction is the separation of the source image from the artifacts due to the sampling conditions and the use of only the artifact-free information for the subsequent reconstruction. Equations (7) and (8) specify the conditions that ensure the image of the source is not corrupted by the sampling artifacts. In Fig. 4, the source image is completely free of artifacts at the source plane.

A comparison of the convolution based propagation described here with a conventional frequency-domain imple-

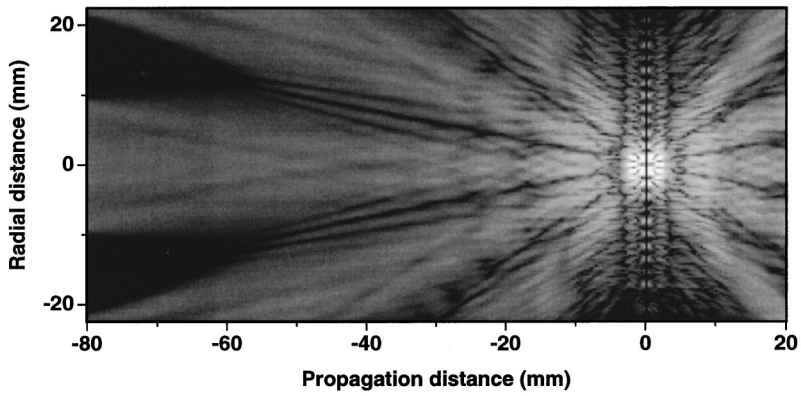

FIG. 4. Direct reconstruction of 19 mm focal transducer using a spatial-domain convolution from the measurement at 80 mm. (Dynamic range=30 dB.)

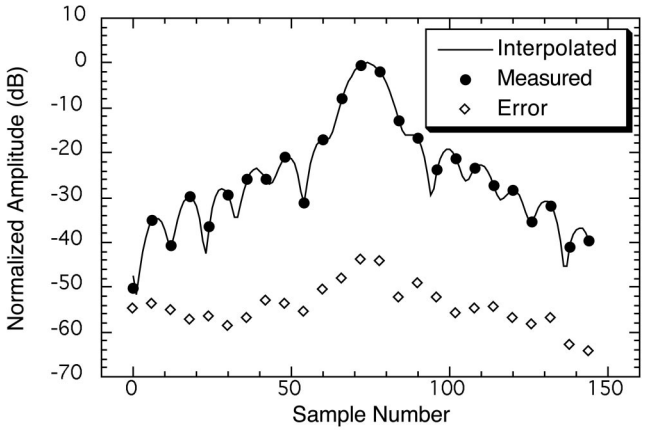

FIG. 5. Measured and interpolated fields and interpolation error.

mentation shows that artifacts in the convolution based approach are significantly less than in the frequency-domain approach.[8]

The accuracy of the two-step reconstruction was tested by comparing the forward propagated data with the original data. The results are shown in Fig. 5. The backpropagation and forward propagation were used to interpolate the data in the plane of observation. In this case, a 145×145 point set of data was obtained from a 25×25 point set of data. Although the data were obtained experimentally, the interpolated data agree almost perfectly with the original. (The error is the absolute of difference between complex amplitude of the original data and the interpolated data.) This shows that no information was lost in the two-step reconstruction by the addition of second propagation step. The reason is that the convolution based method propagates all the frequency components that originate from the geometry of the measurement aperture in which the data are acquired.

V. CONCLUSIONS

A discrete convolution-based holographic reconstruction of acoustic fields has been presented. Since convolution-based reconstruction does not have wraparound error, the reconstruction is robust compared to the conventional frequency-domain manipulation of the transfer function.

The sampling requirements were analyzed using the concept of the spatial-frequency bandwidth of the integrand of the convolution. The resulting sampling condition is a function of the ratio of the propagation distance and the source size with the general $c/(2f)$ condition as the limit for a infinite sound source. This sampling condition is combined with the interpolation property of the propagation to create a two-step reconstruction. A major advantage is that the amount of measured data is reduced by more than an order of magnitude compared to a method based on the conventional sampling requirements.

Examples showed that when the measured acoustic field is backpropagated to the source plane, the sampling interval can be taken to be much larger than the well known half wavelength condition because of phase cancellation in the combination of the forward and the backward propagation.

A pulse wavefield can be decomposed into frequency components that can be treated by the described method.

Although the method presented here is based on linear acoustic theory, the method can also be used as a guide for the analysis of nonlinear acoustic fields. The nonlinear acoustic field generated by the propagation of a high amplitude fundamental wave in a homogeneous medium behaves as if it were emitted by the same finite sound source. Therefore, the acoustic field of the harmonic wave can also be interpolated using the proposed backward and forward propagation method. This is particularly useful when higher order components have shorter wavelengths that make the conventional half-wavelength sampling requirement more difficult to satisfy.

ACKNOWLEDGMENTS

The authors thank Dr. Masahito Goto and Dr. Daniel B. Phillips for helpful discussions and Professor Robert C. Waag for editorial help during the preparation of the paper.

APPENDIX A

Use of a sampling interval smaller than the reciprocal of the maximum spatial frequency of the integrand in Eq. (1) is shown here to be a sufficient condition to make Eq. (3) an equality.

Let the Fourier transform of an arbitrary function $f(\xi,\eta)$ as $F(u,v)$ be denoted

$$F(u,v)=\int_{-\infty}^{\infty}\int_{-\infty}^{\infty}f(\xi,\eta)\exp(-j2\pi(\xi u+\eta v))d\xi\, d\eta. \tag{A1}$$

Poisson's sum formula states[19]

$$\sum_{i_u=-\infty}^{\infty}\sum_{i_v=-\infty}^{\infty}F\left(\frac{i_u}{\Delta x},\frac{i_v}{\Delta y}\right)$$

$$=\Delta x\Delta y\sum_{i_\eta=-\infty}^{\infty}\sum_{i_\xi=-\infty}^{\infty}f(\Delta x i_\xi,\Delta y i_\eta). \tag{A2}$$

Therefore, if $F(u,v)=0$ when $|u|>\Delta x$ and $|v|>\Delta y$, then

$$\int_{-\infty}^{\infty}\int_{-\infty}^{\infty}f(\xi,\eta)d\xi\, d\eta$$

$$=F(0,0)=\Delta x\Delta y\sum_{i_\eta=-\infty}^{\infty}\sum_{i_\xi=-\infty}^{\infty}f(\Delta x i_\xi,\Delta y i_\eta). \tag{A3}$$

APPENDIX B

The maximum spatial-frequency of the integrand in Eq. (6) is given in the following.

The x component of the instantaneous frequency of $h(\xi,\eta,z_1)h^*(x-\xi,y-\eta,z_1)$ can be written

$$\phi_x(\xi,\eta)=\frac{(f/c)\xi}{(\xi^2+\eta^2+z_1^2)^{1/2}}-\frac{(f/c)(\xi-x)}{((\xi-x)^2+(\eta-y)^2+z_1^2)^{1/2}}. \tag{B1}$$

For simplicity, assume the maximum of $|\phi_x(\xi,\eta)|$ is at $y=\eta=0$. (Otherwise, the analysis becomes a multi-variable

problem and very complicated.) The numerical results demonstrate the validity of this assumption. The limiting value of $\phi_x(\xi,0)$ is zero at $\xi=\pm\infty$. Therefore, the maximum of $|\phi_x(\xi,\eta)|$ is obtained when $\partial\phi_x(\xi,\eta)/\partial\xi=0$. The expression for this derivative is

$$\frac{\partial}{\partial\xi}\phi_x(\xi,0)=\frac{(f/c)z_1^2}{(\xi^2+z_1^2)^{3/2}}-\frac{(f/c)z_1^2}{((\xi-x)^2+z_1^2)^{3/2}}. \tag{B2}$$

The maximum occurs when $\xi=x/2$ and is obtained by substituting $y=\eta=0$ and $\xi=x/2$ into Eq. (B1).

[1] P. R. Stepanishen and K. C. Benjamin, "Forward and backward projection of acoustic fields using FFT methods," J. Acoust. Soc. Am. **71**, 803–812 (1982).

[2] M. E. Schafer and P. A. Lewin, "Transducer characterization using the angular spectrum method," J. Acoust. Soc. Am. **85**, 2202–2214 (1989).

[3] C. J. Vecchio and P. A. Lewin, "Finite amplitude acoustic propagation modeling using the extended angular spectrum method," J. Acoust. Soc. Am. **95**, 2399–2408 (1994).

[4] J. A. Goodman, *Introduction to Fourier Optics* (McGraw-Hill, New York, 1968), Chap. 3, pp. 55–61.

[5] K. Nagai, *Ultrasonic Holography* (in Japanese) (Nikkan Kogyo Shinbunsha, Tokyo, Japan, 1989).

[6] R. C. Waag, J. A. Campbell, J. Ridder, and P. R. Mesdag, "Cross-sectional measurements and extrapolations of ultrasonic fields," IEEE Trans. Sonics Ultrason. **SU-32**, 26–35 (1985).

[7] P. T. Christopher and K. J. Parker, "New approaches to the linear propagation of acoustic fields," J. Acoust. Soc. Am. **90**, 507–521 (1991).

[8] M. Tabei and M. Ueda, "Holographic reconstruction of acoustic fields by discrete convolution," in *Proceedings of the 23rd International Symposium on Acoustical Imaging* (Plenum, New York, 1997), pp. 453–458.

[9] D. E. Dudgeon and R. M. Mersereau, *Multidimensional Digital Signal Processing* (Prentice-Hall, Englewood Cliffs, NJ, 1984), Chap. 2, p. 110.

[10] J. S. Lim, *Two-Dimensional Signal and Image Processing* (Prentice-Hall, Englewood Cliffs, NJ, 1990), Chap. 3, pp. 145–149.

[11] H. Lee, "Optimal reconstruction algorithm for holographic imaging of finite-size objects," J. Acoust. Soc. Am. **80**, 195–198 (1986).

[12] H. Lee, "Formulation for quantitative performance evaluation of holographic imaging," J. Acoust. Soc. Am. **84**, 2103–2108 (1988).

[13] Z. G. Hah and K. M. Sung, "Effect of spatial sampling in the calculation of ultrasonic fields generated by piston radiators," J. Acoust. Soc. Am. **92**, 3403–3408 (1992).

[14] D. P. Orofino and P. C. Pedersen, "Efficient angular spectrum decomposition of acoustic sources—Part I: Theory," IEEE Trans. Ultrason. Ferroelectr. Freq. Control **40**, 238–249 (1993).

[15] D. P. Orofino and P. C. Pedersen, "Efficient angular spectrum decomposition of acoustic sources—Part II: Results," IEEE Trans. Ultrason. Ferroelectr. Freq. Control **40**, 250–257 (1993).

[16] P. Wu, R. Kazys, and T. Stepinski, "Analysis of the numerically implemented angular spectrum approach based on the evaluation of two-dimensional acoustic fields. Part I. Errors due to the discrete Fourier transform and discretization," J. Acoust. Soc. Am. **99**, 1339–1348 (1996).

[17] P. Wu, R. Kazys, and T. Stepinski, "Analysis of the numerically implemented angular spectrum approach based on the evaluation of two-dimensional acoustic fields. Part II. Characteristics as a function of angular range," J. Acoust. Soc. Am. **99**, 1349–1359 (1996).

[18] M. Frigo and S. G. Johnson, "FFTW 2.1.3," http://www.fftw.org (1999).

[19] A. Papoulis, *Signal Analysis* (McGraw-Hill, New York, 1977), pp. 24–25.

Factors contributing to bone conduction: The middle ear[a)]

Stefan Stenfelt,[b)] Naohito Hato, and Richard L. Goode
Division of Otolaryngology—Head and Neck Surgery, Stanford University Medical Center, Stanford, California 94305-5328

(Received 15 March 2001; revised 17 May 2001; accepted 5 November 2001)

Measurement of the motion of the malleus umbo and stapes footplate during bone conduction (BC) stimulation was conducted *in vitro* in 26 temporal bones using a laser Doppler vibrometer over the frequency range 0.1 to 10 kHz. For lower frequencies, both ossicular sites followed the motion of the temporal bone. The differential motion between the malleus and the surrounding bone was greater than the differential motion of the stapes footplate; both resonated near 1.5 kHz. Different lesions were shown to affect the response: (1) a mass attached to the umbo lowered the resonance frequency of the ossicular vibration; (2) fixation of either the malleus or stapes increased the stiffness and shifted the resonance frequency upward; and (3) dislocation of the incudo-stapedial joint did not significantly affect the ossicular vibration. The sound radiated from the tympanic membrane was approximately 85 dB SPL at an umbo differential velocity of 1 mm/s for low frequencies in an open ear canal and about 10 dB higher for an occluded one; at higher frequencies (above 2 kHz) resonances of the canal determine the response. It was also found that the motion between the footplate and promontory was within 5 dB when the specimen was stimulated orthogonal to the vibration direction of the ossicles than in line with the same. Measurement of the differential motion of the umbo in one live human skull gave similar response as the average result from the temporal bone specimens.
[DOI: 10.1121/1.1432977]

PACS numbers: 43.64.Bt, 43.66.Ba, 43.66.Ts [LHC]

I. INTRODUCTION

Bone conduction (BC) hearing as a physical phenomenon can be divided into three general routes (Tonndorf, 1966):

(1) the sound radiated into the external ear canal, named the osseotympanic route,
(2) compression and expansion of the petrous bone yielding displacement of the fluid in the cochlea and consequently basilar membrane motion, and
(3) the inertial effect of the middle ear ossicles and inner ear fluids.

It is the latter route that is the scope of this investigation, in particular the relative motion of the middle ear ossicles compared with the motion of the temporal bone when stimulated by a BC signal.

The role of the middle ear in BC was clarified mainly by the work of Bárány (1938). Briefly, when the skull is vibrated, the middle ear ossicles, being only loosely coupled to the skull, will participate in this vibration due to their own moment of inertia with respect to translational motion. This is the ossicular inertial mode of BC. The phase and amplitude differences bring about a relative difference in displacement between the bony annulus of the oval window and the stapes footplate; this in turn results in stimulation of the inner ear in essentially the same manner as following transmission of air conduction (AC) sound across the ossicular chain.

When any of the bones of the skull are subjected to a vibratory stimulus, it is transmitted to the temporal bone containing the external ear canal, the middle ear with its ossicles, and the inner ear. Even if the transmission is more efficient when the stimulus is placed on the mastoid, as long as the stimulus is above the threshold of hearing, it is heard as a BC sound wherever it is applied on the skull. Some of the differences in BC hearing thresholds for different locations of stimulation (e.g., mastoid versus forehead) can be explained by the lesser sound energy transmitted but also to a less efficient mode of vibration of the ossicles of the middle ear or some other part contributing to the whole BC response.

The AC and BC thresholds are used to distinguish between a sensorineural and conductive hearing loss; the BC thresholds are considered to reflect the cochlear reserve. However, it has been shown that the BC thresholds, to a lesser extent than the AC, are also affected by the middle ear status. The first one to make a major investigation of this effect was Bárány (1938), who studied BC thresholds after loading the TM with small spirals of copper wire as well as controlling the air pressure in the ear canal. The limitation of his investigation was that he only used stimulation at one frequency, 435 Hz. Huizing (1960) made thorough studies of the influence of middle ear on BC thresholds for frequencies up to 8 kHz; he used mass loading of the TM, air pressure changes, and occlusion of the ear canal. Similar measurements were performed by Kirikae (1959), Legouix and Tarab

[a)]Portions of this work were presented at the 24th Association for Research in Otolaryngology meeting in St. Petersburg Beach, Florida, 2001.
[b)]Present address: Department of Signals and Systems, Chalmers University of Technology, SE-412 96 Goteborg, Sweden. Electronic mail: stenfelt@s2.chalmers.se

(1959), and Tonndorf (1966). Tonndorf made his measurements in cats using cochlear microphonics.

Investigations have been conducted to study the differences between BC stimulation on the mastoid bone and the mid-forehead. Studebaker (1962) investigated BC thresholds in patients with defective middle ears; he found the BC thresholds to be about 5 dB worse for frequencies between 0.5 and 4 kHz when stimulating on the mastoid than at the forehead. Dirks and Malmquist (1969) also found an average 5 dB worse BC thresholds for patients with various middle ear lesions when stimulating at the mastoid as compared with the forehead. Further, Goodhill *et al.* (1970) found that for frequencies up to 4 kHz, BC is more sensitive to the condition of the middle ear when stimulating at the mastoid than on the frontal bone. These studies suggest that the ossicles are more sensitive to vibration in line with the axis of ossicular motion than at orthogonal directions. Dirks and Malmquist (1969), however, argued that this does not hold for all middle ear impairments.

The studies mentioned so far have not directly measured the relative vibration of the middle ear ossicles upon BC stimulation. The response has been either the subjective or objective measurement of the cochlear response, but not the vibrations of the ossicles. Recently, an investigation of the occlusion effect during BC stimulation using temporal bone specimens and a laser Doppler vibrometer measurement of ossicular vibration has been reported (Hofmann *et al.*, 1996). This approach makes it possible to accurately measure the relative vibration of the temporal bone and ossicles without the problems associated with mass loading as when using accelerometers.

Several recent investigations concerning AC middle ear transmission have shown that the middle ear ossicles do not, as anticipated, rotate only around a given axis yielding a pistonlike motion of the stapes; for frequencies above 1 to 2 kHz the ossicles translate and rotate in all three dimensions in space (Decraemer *et al.*, 1994; Khanna and Decraemer, 1996). Similar modes of vibration could also be present for BC stimulation, making the ossicular inertia component difficult to predict. In addition, at higher frequencies the joints in the ossicular chain, particularly the incudo-stapedial joint, may have an influence.

The aim of this study is to investigate the contribution of the ossicular chain to BC stimulation in the human and to answer the following questions:

(i) What is the relative translational motion between stapes footplate and temporal bone as well as the relative difference between umbo and temporal bone for a normal intact middle ear?
(ii) How do different abnormalities of the middle ear affect the above measurements of ossicular inertia?
(iii) How do different vibration directions of the temporal bone influence the resulting ossicular inertia?

II. MATERIALS AND METHODS

A. Temporal bone experiments

For the experimental measurements it is desirable to use live human material but for obvious reasons this is impossible. A reasonable substitute for the live human head is to use temporal bone cores extracted from human cadavers; this has been shown to yield reliable data when used properly (Goode *et al.*, 1993). The temporal bones were extracted from human cadavers within 48 hours of death using a Schuknecht bone saw at the time of autopsy. The temporal bone specimens were wrapped in gauze, placed in a 1:10 000 merthiolate solution in normal saline and stored at 5 °C. All measurements on individual bones were conducted on the same day within 6 days of death. The tympanic membrane (TM) and middle ear were inspected in each bone using an operating microscope; bones with abnormal TMs or middle ears were excluded from the investigation. Twenty-six temporal bones were studied consisting of 25 males and 1 female with an average age of 73.8 years and a range from 53 to 89 years.

The temporal bones were prepared slightly differently depending on the type of measurement. For all preparations, the attached connective tissue was removed and the bony wall of the external ear canal was drilled down to 2 mm from the tympanic annulus. A simple mastoidectomy (opening the mastoid antrum and removal of the mastoid air cells) and posterior hypotympanotomy (widely opening the facial recess) were performed, including removal of the mastoid portion of the facial nerve and surrounding bone, providing a good view of the stapes and stapes footplate. The ossicular ligaments, chorda tympani, tensor tympani, and stapedius muscle were left intact. See Fig. 1(a) for a schematic of the specimen.

A 25-mm-long plastic artificial external ear canal of 8.5-mm-internal diam was placed against the bony ear canal remnant; it was placed so that the axis of the tube was approximately perpendicular to the TM. In order for the laser beam of the vibrometer to reach the footplate in a direction almost perpendicular to the footplate surface, a small hole of approximately 1-mm diameter was cut in the TM. This hole was covered by a small piece of clear, thin plastic film. It was found that this hole had a slight effect on the sound pressure produced in the ear canal by BC. Therefore, the making of the hole was always done after the measurements of the ear canal sound pressure were finished. However, the umbo motion produced by BC was not altered by this patched hole in the TM. The artificial external ear canal was held in place with clay and also the majority of the temporal bone was covered with clay. This prevented the temporal bone from drying and sealed any small openings.

In order to investigate the middle ear mechanics with BC stimulation, manipulations of the temporal bone specimens were conducted. After the sound pressure measurement in the ear canal was conducted and the small hole in the TM was made, the umbo and the stapes footplate vibrations with an intact middle ear were measured. As reference velocity of the temporal bone, the promontory of the cochlea was used and this site was measured with every new measurement of the footplate and umbo. Next, a glass cover was placed on the artificial ear canal enabling the laser beam to reach the target, and measurements with the ear canal occluded and removed were conducted; the ear canal was reattached and a 100-mg mass was applied to the umbo. So far no destruction

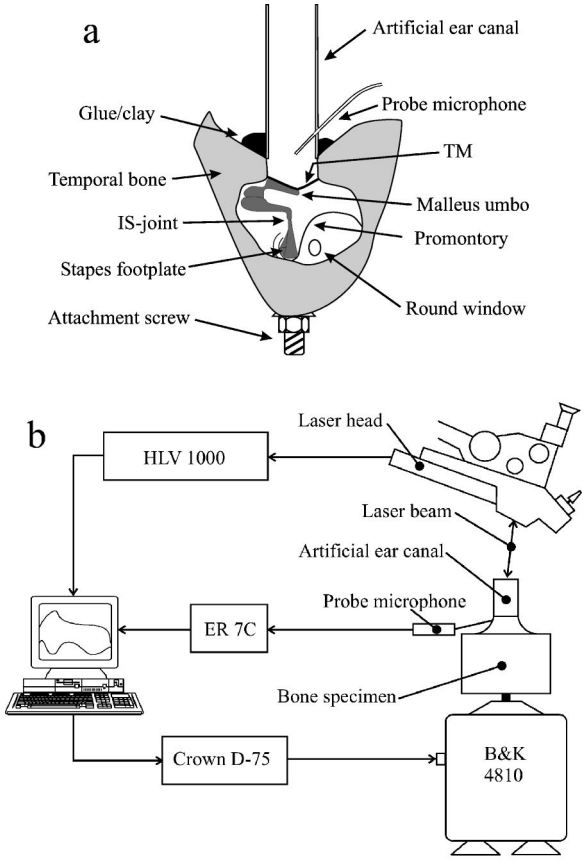

FIG. 1. (a) Cross-sectional view of the temporal bone specimen. The figure is slightly unphysical for better view of the important structures for the present measurements. The opening into the middle ear cavity was sealed with a glass cover after the preparations were made. (b) Schematic of the experimental measurement setup. The B&K 4810 mini-shaker provided the vibrations to the rigidly attached temporal bone specimen. An ER 7C probe microphone was applied 2 mm from the TM in the artificial ear canal for the measurements of the ear canal sound pressure and the HLV 1000 laser-Doppler vibrometer measured the velocity of the malleus umbo, stapes footplate, and cochlea promontory through the artificial ear canal. A PC equipped with a signal-processing card controlled all measurements.

of the middle ear structures was made, but after the effect of mass loading was measured, either the stapes footplate or the malleus was glued into the surrounding bone. After that measurement the incudo-stapedial joint was severed. If it was a specimen where the malleus had been glued, a 20-mg mass was glued onto the stapes and the footplate was measured and, finally, the cochlea was drained and the 20-mg mass was removed from the stapes.

B. Measurement system

The vibration stimuli were provided by a PC based software, SYSid 6.5, using a DSP-16+ signal processing card (Ariel Corp., Cranbury, NJ). The measurement system is shown in Fig. 1(b). The output from the computer was fed through a power amplifier (D-75, Crown, Elkhart, IN) to a B&K type 4810 mini-shaker (Brüel and Kjær, Nærum, Denmark). The mini shaker piston was rigidly coupled to the temporal bone by a threaded connector attached to a threaded hole in the temporal bone. To further ensure a rigid connection the connector was also glued to the bone specimen by cyanoacrylate glue (Garf Reef glue™, Garf, Inc., Boise, ID).

The vibrations, either of the temporal bone or the ossicles, were measured with a laser Doppler vibrometer, the HLV-1000 (Polytec, Waldbronn, Germany). The sensor head was mounted with a joystick-controlled mirror on an operating microscope enabling easy control of the laser beam. The ear canal sound pressure was measured with a probe tube microphone (ER-7C, Etymotic Research, Elk Grove Village, IL) positioned 2 mm from the TM in the artificial ear canal. In order to achieve good reflection of the laser light and ensure that the same specific position was measured after any rearrangements of the setup, reflective micro spheres about 5 μm in diameter were positioned on the center of the footplate, promontory, and tip of the umbo.

The stimulus was a swept sine signal with a logarithmically spaced resolution of 50 frequencies per decade. The frequency range for each measurement was 0.025 to 25 kHz; only frequencies between 0.1 and 10 kHz were used in the postprocessing of the data. Each frequency was measured and averaged 20 times before the next frequency was measured; the measurement time for each sweep was approximately 1 min. During each measurement, the second and third harmonic distortion components were measured to ensure that distortion did not corrupt the data.

C. Calibration

The HLV-1000 is precalibrated by the manufacturer and stated to have an amplitude accuracy better than 0.1 dB in the frequency range of interest. However, to limit any high frequency noise or overloading by low frequency vibrations, the filters of the HLV-1000 were used. The low-pass filter cutoff frequency was set at 15 kHz and the high-pass filter cutoff frequency at 100 Hz. These settings affected the frequency response of the HLV-1000 which was calibrated against a B&K type 4371 accelerometer. Below 10 kHz this accelerometer has, according to the manufacturer, a maximum level deviation of 0.2 dB and a maximum phase deviation of 5 degrees. The accelerometer was mounted on the B&K 4810 mini shaker and the laser aimed on the surface of the accelerometer in a line perpendicular to the accelerometer surface. This was used for calibration of the HLV-1000 for the frequency range 0.1 to 10 kHz (50 frequencies/decade). The ER-7C probe tube microphone was calibrated against a B&K type 4138 1/8 inch microphone. The sensitivity of the 1/8-in. microphone was first determined in a B&K type 4230 sound level calibrator. Both microphones were then placed 1 mm apart in a small cavity, a sound introduced, and the calibration curve of the ER-7C obtained for the frequency range 0.1 to 10 kHz (50 frequencies/decade).

The test-retest variability of the setup was also investigated. First, two consecutive measurement runs were performed. The results were within 0.2 dB of each other. Next, the entire assembly was taken down and put together again before a second measurement. With this change, the measurements were within 1.5 dB of each other. However, since the measurements depended on taking the difference between two velocities, errors of 1.5 dB limit the ability to detect small differences. Therefore, it was made sure that

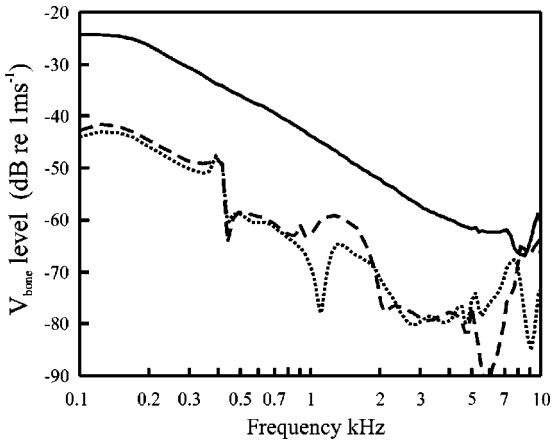

FIG. 2. Absolute velocity in a temporal bone specimen measured on the bone close to the TM in three directions. Straight line: velocity in line with ossicular vibration, same as the stimulation direction. Dashed and dotted lines: velocities in the two orthogonal directions. Similar stimulation level was used for all preparations tested. Frequency resolution is 50 points/decade.

during a measurement session nothing was moved, otherwise that whole session was remeasured.

D. Temporal bone vibration

The vibration mode of the specimen is of vital importance in this investigation. The desirable vibration mode would be a one-dimensional translational vibration in the line of the ossicular vibration; this is unfortunately very difficult to achieve. First, there are limited places for the attachment of the specimen to the vibrator; drilling at several places can destroy vital structures of the middle and inner ear, and the laser beam must be able to reach the target. Second, a slight misalignment between the vibration axis and the specimens' center of gravity yields additional rotational components. Third, the stimulation source itself is not purely one- dimensional but has small vibrational components in the plane orthogonal to the main axis of vibration. However, precautions were taken to decrease these problems. A small hole was drilled and threaded in the temporal bone specimen on the cranial side close to the internal auditory canal. This place had good quality of the bone for the threads and gave a good alignment to the specimens' center of gravity. A connector with a screw of 3-mm diameter was inserted into the threaded hole in the specimen to connect it to the shaker. Further, the attachment between the shaker and the temporal bone was made very rigid; in addition to the screw that connects the two, cyanoacrylate glue was used to make the bond even more rigid.

Figure 2 displays the typical vibration level of a specimen during excitation; the solid line is the vibration level in the measurement direction and the other two (dashed and dotted) are the two orthogonal directions. The measurement position is the bone close to the TM on the opposite side of the specimen to where the attachment screw is situated. As can be seen, the level difference between the main stimulation direction and the other two is about 20 dB for almost the entire frequency range of 0.1 to 10 kHz. At the higher frequencies, the difference often becomes smaller due to some additional rotational vibration mode of the specimen.

III. RESULTS

In what follows, all the velocities (footplate and umbo) are relative to the velocity of the promontory of the cochlea in the temporal bone measured in the same direction as the stapes footplate and umbo motion. Relative velocity V^{rel}, either of the stapes footplate or umbo, is calculated as

$$V^{\mathrm{rel}}_{\mathrm{footplate}} = \frac{V_{\mathrm{footplate}}}{V_{\mathrm{promontory}}} \tag{1a}$$

and

$$V^{\mathrm{rel}}_{\mathrm{umbo}} = \frac{V_{\mathrm{umbo}}}{V_{\mathrm{promontory}}}, \tag{1b}$$

whereas a differential relative velocity V^{diff} is in a similar way calculated as

$$V^{\mathrm{diff}}_{\mathrm{footplate}} = \frac{V_{\mathrm{footplate}} - V_{\mathrm{promontory}}}{V_{\mathrm{promontory}}} \tag{2a}$$

and

$$V^{\mathrm{diff}}_{\mathrm{umbo}} = \frac{V_{\mathrm{umbo}} - V_{\mathrm{promontory}}}{V_{\mathrm{promontory}}}. \tag{2b}$$

The phase is calculated as the phase difference between the stapes footplate or umbo and the promontory of the cochlea, i.e.,

$$\mathrm{Phase}_{\mathrm{footplate}} = P(V_{\mathrm{footplate}}) - P(V_{\mathrm{promontory}}) \tag{3a}$$

and

$$\mathrm{Phase}_{\mathrm{umbo}} = P(V_{\mathrm{umbo}}) - P(V_{\mathrm{promontory}}), \tag{3b}$$

where $P(\,)$ stands for phase calculation. The relative velocity [V^{rel}, Eq. (1)] gives an indication of the mechanics of the middle ear ossicles with BC stimulation, for example, $V^{\mathrm{rel}} = 1$ indicates that the ossicle is rigidly coupled to the temporal bone whereas $V^{\mathrm{rel}} = 0$ indicates that the ossicle is totally decoupled from the temporal bone and stands still in space. V^{rel} is naturally a function of frequency. The differential relative velocity [V^{diff}, Eq. (2)] gives an indication of the hearing stimulation by the ossicle (similar to AC stimulation), for example, $V^{\mathrm{diff}} = 0$ indicates no hearing stimulation at all and $V^{\mathrm{diff}} = 1$ means a hearing stimulation level that equals the vibration level of the temporal bone itself.

A. Stimulation in one direction

1. Footplate motion

Figures 3(a)–(c) show the results from 26 temporal bones with intact middle and inner ears. Figure 3(a) shows the relative footplate velocity level ($V^{\mathrm{rel}}_{\mathrm{footplate}}$); Fig. 3(b) shows the differential relative footplate velocity level ($V^{\mathrm{diff}}_{\mathrm{footplate}}$); and the phase of the relative footplate velocity ($\mathrm{Phase}_{\mathrm{footplate}}$) is plotted in Fig. 3(c). In the figures, a thin line represents the individual result from each specimen and the thick lines are the mean results from all the specimens. The results show that the individual specimens vary a great deal, particularly at higher frequencies. The large variations in the

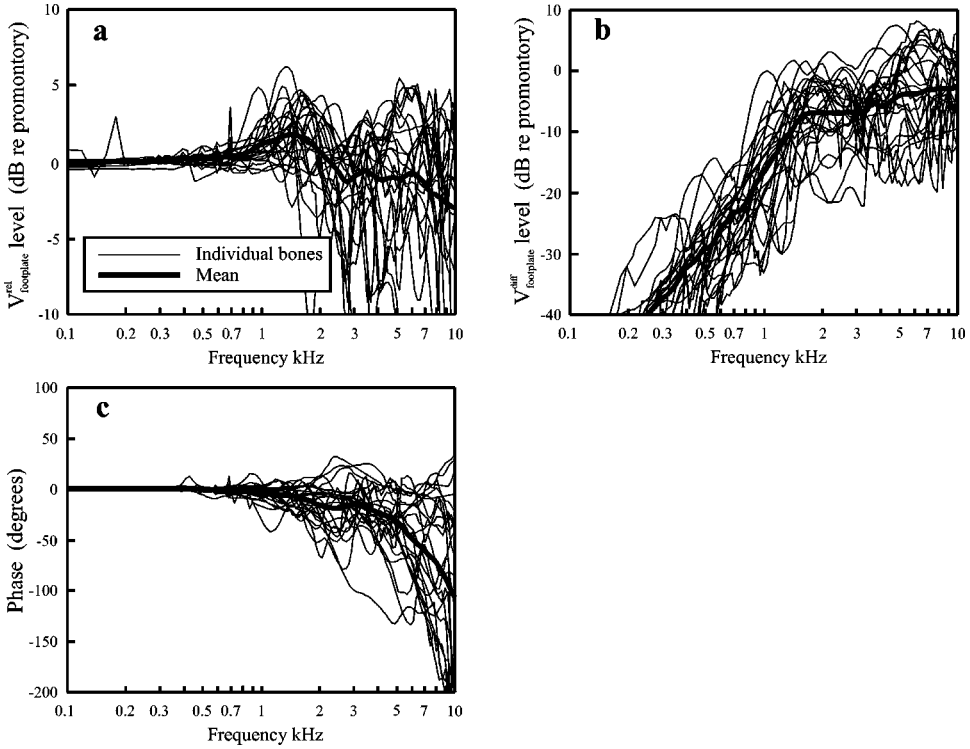

FIG. 3. Footplate motion upon BC stimulation for 26 temporal bone specimens with the stimulation direction in line with the ossicular vibration. The measurements are made in line with the stimulation direction. (a) Relative footplate velocity level, (b) differential relative velocity level between footplate and promontory bone, and (c) phase between footplate and promontory bone velocity. Thin lines—individual results; thick lines—mean results. Frequency resolution is 50 points/decade.

individual measurements may be the result of complicated local modes of ossicular vibration, and less than ideal one-dimensional stimulation of the preparation. The average relative velocity has a slight overshoot of around 2 dB between 1 and 2 kHz and then starts to roll off. The roll-off is slow and the average relative velocity does not go below −5 dB in the frequency range studied here. The differential relative velocity can be considered the input to the cochlea since it is a measure of the fluid displacement in the vestibule. Here, the differential relative velocity increases at approximately 40 dB/decade for frequencies below the resonance at 1.5 kHz. Above the resonance the average curve flattens out around −5 dB. This indicates that the stimulation of the cochlea by the stapes footplate with BC stimulation is 5 dB lower than the vibration of the temporal bone itself. The phase response in Fig. 3(c) stays close to 0° for frequencies below 1 kHz. At higher frequencies the phase drops slowly but generally stays above −100 degrees below 10 kHz. This indicates that the stapes footplate is not totally decoupled from the surrounding promontory bone at the highest frequencies tested here.

In Fig. 4, the mean footplate results for the normal condition and the three manipulations: stapes glued into the oval window, malleus glued into the attic, and mass loading (100 mg) of the umbo are shown. As in Fig. 3, Figs. 4(a)–(c) show the relative velocity, differential relative velocity, and phase, respectively. An additional plot [Fig. 4(d)] is added showing the average change between the $V^{\text{diff}}_{\text{footplate}}$ for the manipulated conditions and the $V^{\text{diff}}_{\text{footplate}}$ for the normal intact middle ear condition. The bars in Figs. 4(b) and (d) indicate the standard error of the mean for all conditions. Gluing the stapes into the oval window yields a stiffer connection between the footplate and the bone; consequently, the footplate velocity is similar to that of the promontory. This manifests itself as a lower differential relative velocity and a phase of almost 0 degrees throughout the test frequency range. As seen in Fig. 4(d), the change obtained upon gluing the stapes gives 20 to 30 dB less differential relative velocity of the footplate. Gluing the malleus gives less effect than gluing the stapes, only a loss of 5–10 dB below 3 kHz. This is a result of the freedom of motion of the stapes due to the ossicular joints. The increase in ossicular stiffness caused by gluing increases the ossicular resonance frequency and leads to an increase of the stapes footplate differential relative velocity near the new resonance frequency.

The effect of occluding the artificial ear canal is not shown in the figure, but no significant difference from the normal condition was found. Furthermore, no significant change was seen between the normal condition and measurements done with the artificial ear canal removed. Loading the umbo with a small lead ball of 100 mg shifts the resonance frequency downward. This leads to an increased differential relative velocity of 15 to 20 dB below 1 kHz. Further, a slight loss of some 5 dB is seen around 1.5 kHz upon loading the umbo, originating in the absence of the resonance that gives a boost for the normal intact middle ear around this frequency.

The curves in Fig. 5 represent the stapes footplate velocity with an interrupted ossicular chain: the incudo-stapedial joint has been incised and the lenticular process of the incus removed. Figure 5 includes the result of the normal intact middle ear condition for comparison. In Fig. 5(d) the results are compared with those obtained with the incised incudo-stapedial joint (IS-joint cut), except for IS-joint cut itself, where the comparison was made with the result from the intact middle ear. The differential relative velocity of the stapes footplate with the incised IS-joint was about 10 dB less as compared with the normal condition between 1.5 and

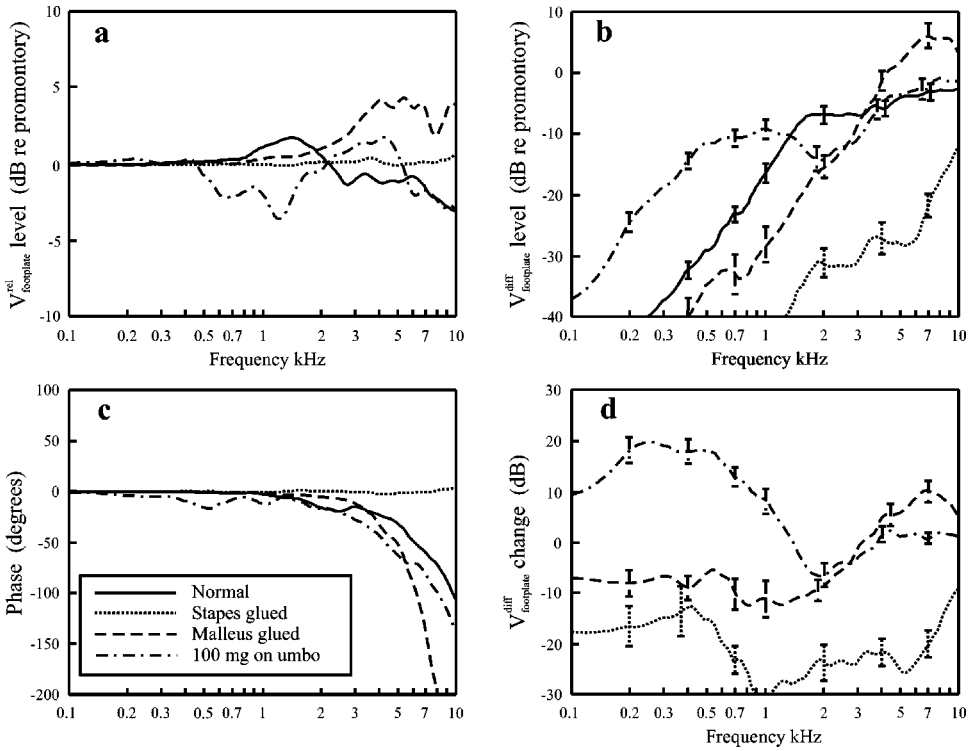

FIG. 4. Comparison of average stapes footplate motion with BC stimulation for four conditions: Intact middle ear (straight line, 26 bones), stapes glued (dotted line, 10 bones), malleus glued (dashed line, 11 bones), and mass loading 100 mg on umbo (dash-dotted line, 20 bones). Stimulation and measurement direction are in line with the ossicular vibration. (a) Relative footplate velocity level, (b) differential relative velocity level between footplate and promontory bone, (c) phase between footplate and promontory bone velocity, and (d) level of velocity change compared to the intact middle ear condition. The bars in (b) and (d) indicate ±1 standard error of the mean. Frequency resolution is 50 points/decade.

3 kHz. The cause may be due to a lesser constraint on the stapes without attachment to the incus: rotational motion of the stapes is more likely to appear. However, except at the midfrequencies, no significant difference between stapes alone and an intact ossicular chain was found; the lower mass of the ossicles appears to be compensated by less stiffness from the suspensory ligaments. With a small mass of 20 mg added to the stapes, the resonance frequency was lowered and consequently a higher differential relative footplate velocity was obtained. This stapes footplate velocity level was approximately 10 dB higher for frequencies below 3 kHz; above this frequency the addition of the mass made no difference on the differential relative footplate velocity level. With the cochlea drained (and incised IS-joint), the differential relative velocity became 5 to 10 dB greater for frequencies above 1.5 kHz. The stapes footplate interfaces the cochlear fluid in the oval window of the cochlea, and any motion originating from the fluid influences the motion of the stapes footplate. With the cochlea drained, the inertial effect of the cochlear fluid is removed and the inertial effects

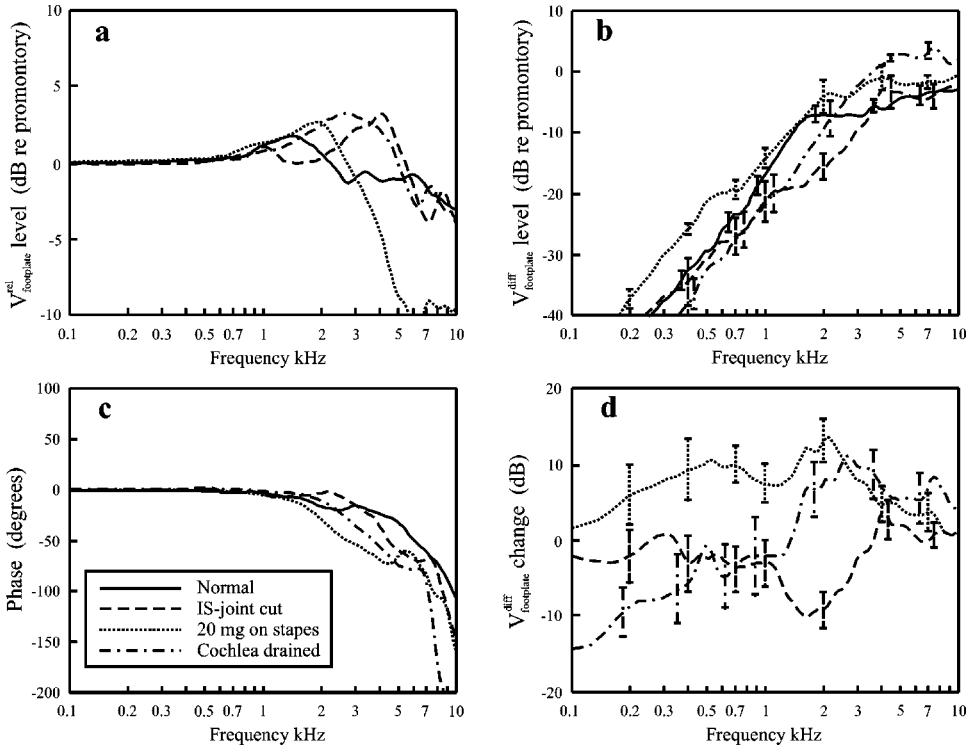

FIG. 5. Comparison of average stapes footplate motion with BC stimulation for four conditions: Intact middle ear (straight line, 26 bones), IS-joint cut (dashed line, 13 bones), mass loading 20 mg on the stapes and severed IS-joint (dotted line, 10 bones), and cochlea drained and severed IS-joint (dash-dotted line, 6 bones). (a) Relative footplate velocity level, (b) differential relative velocity level between footplate and promontory bone, (c) phase between footplate and promontory bone velocity, and (d) level of velocity change between IS-joint cut and the intact middle ear, between 20 mg loading and IS-joint cut, and cochlea drained and IS-joint cut. Stimulation and measurement direction are in line with the ossicular vibration. The bars in (b) and (d) indicate ±1 standard error of the mean. Frequency resolution is 50 points/decade.

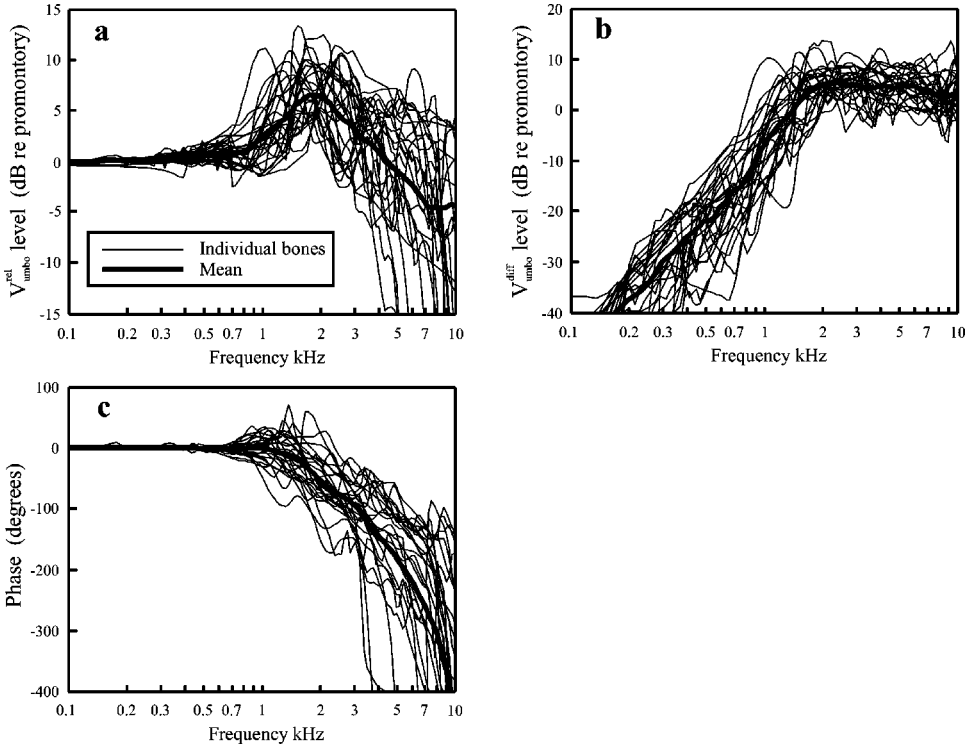

FIG. 6. Umbo motion upon BC stimulation for 26 temporal bone specimens with the stimulation direction in line with the ossicular vibration. The measurements are made in line with the stimulation direction. (a) Relative umbo velocity level, (b) differential relative velocity level between umbo and promontory bone, and (c) phase between umbo and promontory bone velocity. Thin lines—individual results; thick lines—mean results. Frequency resolution is 50 points/decade.

in the cochlear fluid therefore no longer affect the stapes footplate. If fluid inertia is dominating over middle ear ossicle inertia, a major change in the stapes footplate response could be anticipated following draining of the cochlea. The response in Fig. 5 with intact cochlea (IS-joint cut) and drained cochlea show similar response, both in amplitude and phase. This suggests that the motion of the ossicles is mainly caused by their own inertia rather than a motion due to the fluid inertia.

2. Umbo motion

Results from the measurement of umbo velocity in a normal middle ear are presented in Fig. 6. As with the measurement of footplate velocity (Fig. 3), there were large individual differences. However, the general shape of the curves was similar and the result similar to that obtained for the stapes footplate. From Fig. 6(a), it appears that the umbo does not follow the vibration of the temporal bone as well as the footplate does; the roll-off is more pronounced and resembles the expected −20 dB/decade. The phase shows a considerable lag starting at 1.5 kHz and reaches −400 degrees at 10 kHz. This suggests that the umbo and footplate actually move 180 degrees out of phase at certain frequencies above 7 kHz.

Figure 7 shows the mean results of umbo velocity for various lesions of the ossicles: intact ossicular chain, stapes glued, malleus glued, 100 mg mass loading on the umbo, and cutting and separating the incudo-stapedial joint. Occluded ear canal and ear canal removal were also investigated; no significant difference occurred with either case. Upon gluing the stapes into the oval window the differential relative velocity of the umbo diminished by 10 dB below 1 kHz. This is a considerably lesser effect than seen at the stapes footplate after immobilization of the stapes. We again attribute this behavior to the two ossicular joints. This result is consistent with increased stiffness and the corresponding higher resonance frequency corresponds well with the results seen in Figs. 7(b) and (c). With the malleus glued the result is, as expected, more pronounced with a 20-dB differential relative velocity loss for frequencies below 3 kHz. Once more, this appears due to an increased stiffness that produces a higher resonance frequency of the ossicles. The opposite occurs when a mass of 100 mg is placed on the umbo; the resonance frequency is lowered and the resulting differential relative velocity becomes 20 dB greater below 1 kHz. Above 2 kHz, however, the differential relative velocity with 100 mg on the umbo is 5 dB less than the normal ear. The loading produces a roll-off at a lower frequency [Fig. 7(a)] and, thus, the boost between 1 and 4 kHz seen in the normal ear is not present.

When the IS-joint is cut, only the lenticular process of the incus is removed, the remainder of the incus is left untouched. This means that for vibration of the umbo, incising the IS-joint removes only the impedance of the stapes annular ligament (stiffness), the cochlea (damping), and the small mass of the stapes. The only change upon incising the IS-joint is a slightly larger response around 2 kHz and a slightly lesser differential relative velocity in the low frequencies. A higher response around 2 kHz can be a result of the removal of the damping produced by the intact cochlea. The resonance frequency, however, appears to remain the same. Consequently, the motion of the umbo is minimally influenced by a normal annular ligament but is restricted primarily by the TM and the malleus and incus suspensory ligaments.

3. Sound pressure in the ear canal and middle ear cavity

Figure 8 shows the mean results from nine temporal bone specimens of the sound pressure in the artificial ear

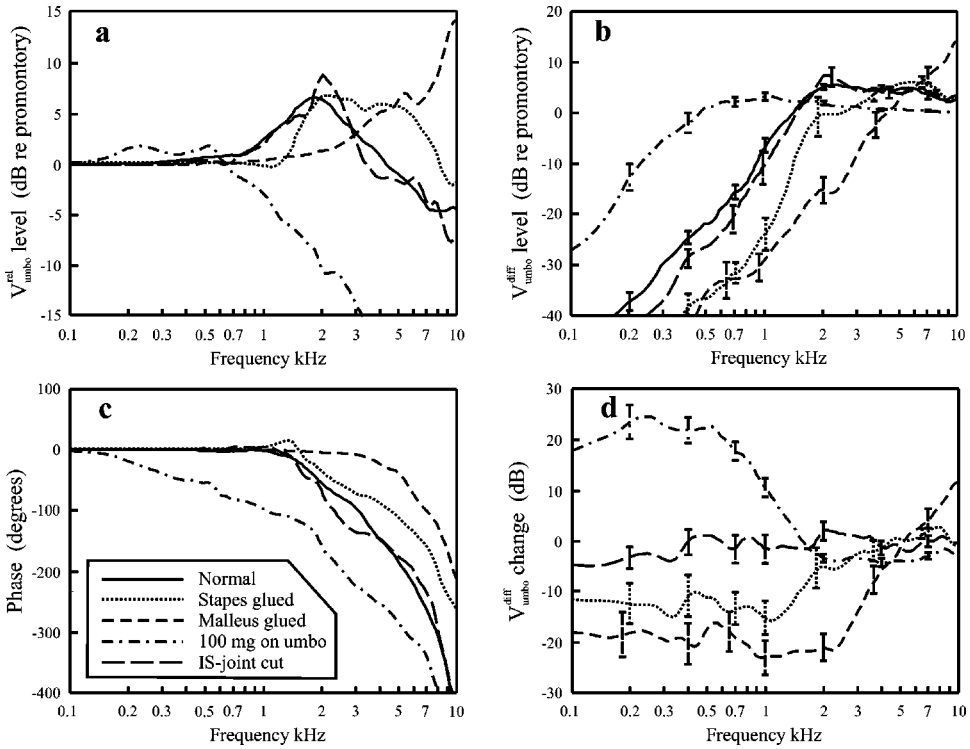

FIG. 7. Comparison of average umbo motion with BC stimulation for five conditions: Intact middle ear (straight line, 26 bones), stapes glued (dotted line, 10 bones), malleus glued (dashed line, 11 bones), mass loading 100 mg on umbo (dash-dotted line, 20 bones), and IS-joint cut (long dashed line, 10 bones). (a) Relative umbo velocity level, (b) differential relative velocity level between umbo and promontory bone, (c) phase between umbo and promontory bone velocity, and (d) level of velocity change compared to the intact middle ear. Stimulation and measurement direction are in line with the ossicular vibration. The bars in (b) and (d) indicate ±1 standard error of the mean. Frequency resolution is 50 points/decade.

canal upon BC stimulation. The graphs (Fig. 8) demonstrate the sound pressure divided by the absolute velocity between the umbo and the bony annulus at the TM ($V_{\text{umbo}} - V_{\text{bone}}$). It should be noted here that these results are not the same as the sound pressure produced with BC stimulation in an intact skull. The walls of the normal external ear canal are believed to be responsible for the major contribution of the sound pressure in the ear canal when the skull is subjected to a BC sound; here they are removed and replaced by a plastic tube. The structure that is still able to move and radiate sound is the TM. With the ear canal open, the sound pressure was approximately 85 dB SPL at an umbo differential velocity of 1 mm/s for frequencies below 2 kHz. When the ear canal was occluded, the sound pressure increased with about 10 dB for frequencies below 1 kHz. Above 1 kHz, the sound pressure with the ear canal occluded falls off with approximately 20 dB/decade. At higher frequencies, the canal resonances dominated the results. For the open ear canal, two resonances were present: the quarter wavelength resonance at 2.7 kHz and the three-quarter wavelength resonance around 8 kHz. With the ear canal occluded, the only resonance in the frequency range measured was the half-wavelength resonance at 5.5 kHz. The fact that the occluded condition gave a higher sound pressure in the ear canal indicates that the sound source was the TM and not airborne sound radiating from the specimen or the shaker.

Sealing the entire specimen with dental cement to ensure that no external sound would leak into the middle ear cavity assessed the sound pressure in the middle ear cavity produced by BC stimulation. The remnant of the ear canal was also filled with dental cement which immobilized the TM. Hence, the setup differs from the measurements of the ear canal sound pressure. The microphone probe tube was inserted through the Eustachian tube and sealed with clay. We concluded that the sound pressure in the middle ear cavity was lower than the noise level since the same results were obtained with the microphone tube sealed. When analyzing the vibration patterns at different locations in the middle ear measured by the laser vibrometer, we found identical phase responses up to at least 10 kHz. Hence, the bone executed rigid body motion and no sound was radiated from the walls of the middle ear or from the bony part of the outer ear canal.

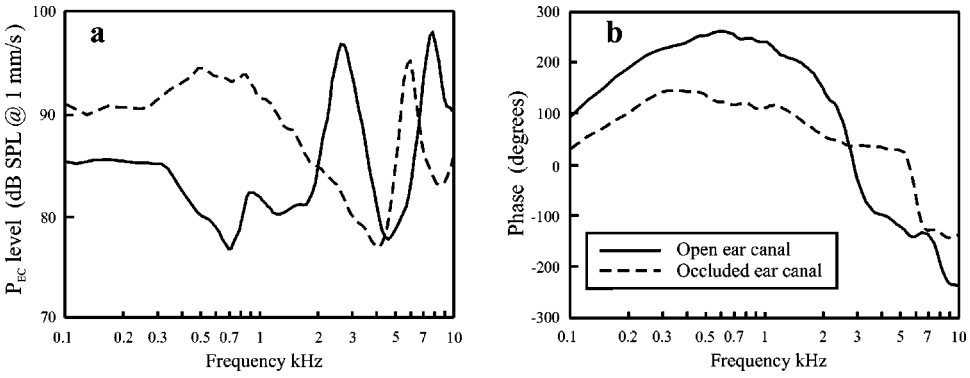

FIG. 8. Mean (a) level and (b) phase of the ear canal pressure divided by the differential velocity between the umbo and bone in temporal bone specimens equipped with an artificial ear canal (9 bones). Results are shown for the ear canal open (straight line) and occluded (dashed line). BC stimulation direction is in the line of normal ossicular vibration. Frequency resolution is 50 points/decade.

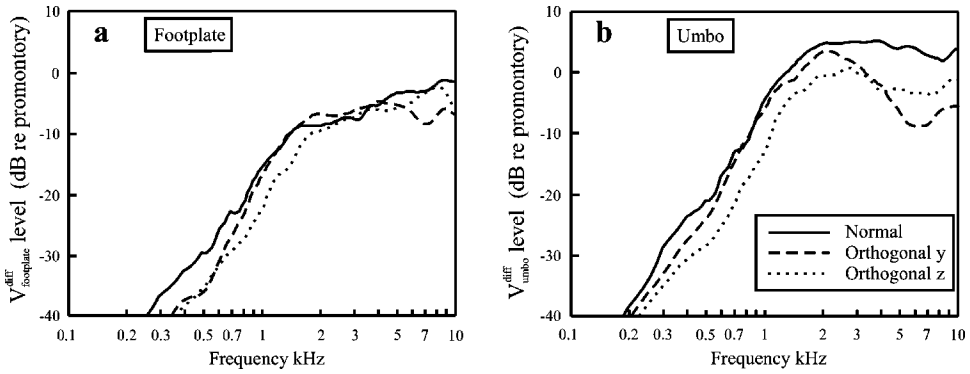

FIG. 9. Mean differential relative velocity level between footplate and promontory bone (a) and umbo and promontory bone (b) (13 bones). Results are shown for three orthogonal stimulation directions: in line with normal ossicular vibration (straight line), stimulation direction in line with the long axis of the malleus handle (*y*, dashed line), and stimulation direction orthogonal to the two (*z*, dotted line). The results are calculated as the velocity difference between the footplate or umbo and promontory bone and divided with the velocity of the specimen in the stimulation direction. Frequency resolution is 50 points/decade.

In a live human, however, the sound radiation into the middle ear cavity might be different. The tegmen wall is a thin plate of bone that separates the middle ear space from the cranial cavity. This bone plate is very thin and could radiate sound transmitted as pressure waves through the cerebrospinal fluid.

B. Stimulation in three directions

Measurements of the stapes footplate and umbo velocity made with BC excitation in three different orthogonal directions are shown in Fig. 9. The figure shows the average differential relative velocities when stimulation of the specimens was in line with the vibration direction of the ossicles, when stimulation was in line with the long axis of the malleus handle, and when stimulation was orthogonal to the two. For stimulation in line with normal ossicular vibration the results are calculated as described previously; for the other two modes of stimulation the results are calculated as the difference velocity between the footplate (or umbo) and the promontory bone in the normal vibration direction and then divided by the velocity of the temporal bone in the excitation direction.

Figure 9(a) revealed that the effective vibration of the stapes footplate was similar regardless of stimulation direction. For the whole frequency range measured, the results of the three curves are within 5 dB of each other. The results from the umbo vibration measurement in Fig. 9(b) show a similar response as for the footplate in Fig. 9(a) except above 3 kHz, where the difference for the umbo vibration measurement was greater.

C. Umbo measurement in a living human head

Figure 10 shows the result of the umbo differential relative velocity and phase measured in one live human skull. For this measurement a bone transducer Radioear B-71 was attached to the mastoid to supply the BC stimuli. The reference bone-vibration was measured with the HLV-1000 in the bony part of the external ear canal close to the TM; the umbo motion was measured in a similar way as in the temporal bone specimens. The skull has more complex vibration modes than the one-dimensional motion that dominated the vibrations of the preparations. However, the result of the umbo differential relative velocity and phase of the whole head is close to the average results obtained in the temporal bone specimens.

IV. DISCUSSION

A. Method validity

Vogel *et al.* (1996) reported nonlinear distortion when measuring BC response with laser vibrometry on a temporal

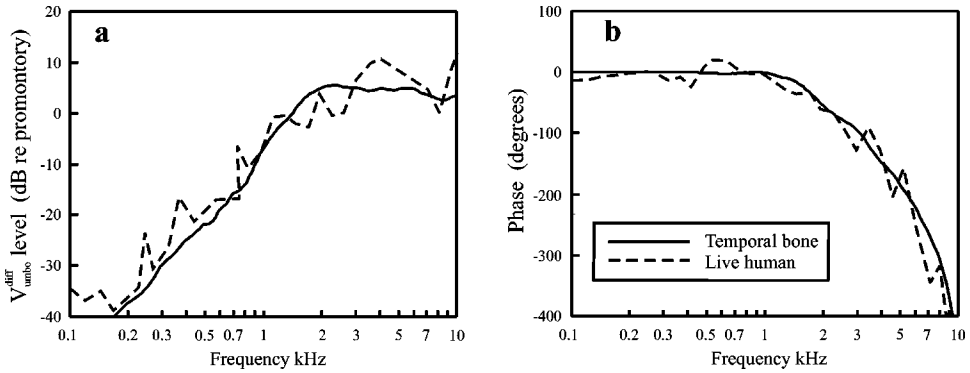

FIG. 10. Mean results from umbo measurements in 26 temporal bone specimens with the stimulation and measurement direction in line of normal ossicular direction, and one measurement of the umbo motion with BC stimulation at the mastoid portion of the temporal bone in a live human skull. The measurement direction for the human skull is in line with the external ear canal and the reference position for the vibration of the skull bone is the bony part of the ear canal close to the TM. Results are presented as differential relative velocity (a) and phase between the umbo and bone (b). Frequency resolution is 50 points/decade.

bone specimen. They suggest this was the result of the difference between a temporal bone specimen compared to a whole skull. However, a different geometry is not a source for nonlinear distortion and the transmission of the BC sound in a skull has been reported to be linear for sound levels adequate for normal hearing (Håkansson *et al.*, 1996). The nonlinearities revealed in the study of Vogel *et al.* (1996) could be a result of the stimulation source or the interface between the exciter and specimen. Throughout the experiments reported the second and third harmonic distortion components were so low as to not be measurable.

The result of measurements in a cored temporal bone specimen is naturally different from measurements on a whole skull. However, this investigation aims to evaluate the middle ear, in particular the ossicles, contribution to BC. Hence, it is of lesser importance what the vibration modes of the intact skull were like. The reference was the vibration of the promontory in the temporal bone and, thus, the results can be compared using the transfer function from the stimulation position to the promontory bone in an intact skull. This transfer function has been given for a dry skull (Stenfelt *et al.*, 2000) where it was shown that above the first skull resonance (0.8–1 kHz, Håkansson *et al.*, 1994) the vibratory response of the promontory is three dimensional without any dominant vibration direction. This was also observed by Kirikae (1959); he stated that at higher frequencies the vibrations of the skull become extremely complex. A benefit of using a temporal bone specimen instead of a whole skull is the ability to vibrate the bone in one direction. Even if this is not the case in the skull, where the temporal bone vibrates and rotates in all directions, it enables analysis of the sensitivity to different directions.

A more serious problem using the current preparation could arise if the mode of vibration is different for the petrous part of the temporal bone in the intact skull compared with the specimen. In the intact skull, the petrous part of the temporal bone encapsulating the middle ear and the cochlea is situated in the base of the skull. The bone in the upper part of the skull is thin whereas the base of the skull consists of thick bone. Most measurements of the vibration characteristics of the skull have been conducted on the thin upper part of the skull that resembles a thin shell of a sphere (von Békésy, 1932; Zwislocki, 1953; Franke, 1956). Tonndorf and Jahn (1981) suggested that the wave propagation of the cranial vault occurs as plate waves, which constitutes both longitudinal and transverse components. Tonndorf (1966), arguing for a compressional response of the cochlea, saw some evidence in his study as well as in the study by Kirikae (1959) that along the base of the skull with thick, solid bones, vibrations might propagate in the form of distortional waves. However, at low frequencies below the first resonance frequency (0.8–1.0 kHz) the skull moves as a rigid body and no wave motion is present. No such compression and expansion of the bone was present at the preparations used in this study; they executed rigid body motion for the whole frequency range investigated. Such discrepancy in mode of vibration would mainly affect the sound pressure in the middle ear cavity and the pressure in the cochlear fluid and only slightly affect the ossicular inertia results. Consequently, some caution must be made when comparing the results in this study with live human physiological data.

B. Middle ear ossicle inertia

Tonndorf (1966), using temporal bone specimens of cats, postulated that the relative vibration of the footplate in relation to the absolute vibration of the promontory bone is on the order of -50 to -70 dB. In his experiments he positioned a silver electrode in a drained vestibule to form a capacitor with the footplate and vestibular wall. The large discrepancy between those measurements and the measurements here cannot entirely be accounted for by the use of cat temporal bone specimens in the experiments of Tonndorf and human specimens in this investigation. It is more likely that the method used by Tonndorf and colleagues is not sensitive enough to yield valid data for this measurement. It has further been stated that the differential relative motions of the TM are several magnitudes smaller, at least a factor of 20 dB, than the vibrations of the head (Tonndorf and Tabor, 1962). This study shows that the differential relative vibration of the umbo and the TM are equal or larger than the vibration of the head for frequencies above 1 kHz. Further, Hudde and Weistenhöfer (2000) presented BC measurements of the stapes footplate using temporal bone specimen. They report results comparable to the ones presented in this study.

In another experiment, Tonndorf (1966) examined the contribution to BC by sound radiation into the middle ear cavity in the cat. In their BC experiment, they opened the bulla and expected less low frequency response due to the leakage of sound out of the middle ear cavity. In their investigation, as well as in this one, there was no evidence for an important middle ear sound radiation component. However, they state that the closed middle ear cavity acts as a spring on the TM and affects the BC response in that way. In our experiments, the vibration of the middle ear cavity walls was also investigated. In doing so, we found that the entire temporal bone specimen moved as a rigid body up to 10 kHz and therefore no sound would be radiated into the middle ear cavity. In an intact human head, compression and expansion of the cavity walls could be present and give a sound pressure in the middle ear cavity that could influence the perception of BC sounds.

Groen (1962) also pointed out that the response of the ossicular chain is modified by the action of the air enclosed in the middle ear. The latter would act like a spring upon the TM, and to a lesser degree upon the round window membrane: the middle ear compliance effect. However, Brinkman *et al.* (1965) found only a minor effect on the BC response with perforations of the TM, small as well as large ones. We found that the BC response did not change whether the middle ear cavity was open or not. Hence, the spring effect of the air in the enclosed middle ear cavity seems to be minimal. Zwislocki (1962) pointed out that the middle ear air space is so large that its compliance has little effect on middle ear mechanics. The importance of ossicular inertia has been disputed over the years. Some have postulated that ossicular inertia together with inner ear fluid inertia is the most important contributor to BC (Brinkman *et al.*, 1965). Kirikae (1959) states that the inertia of the ossicular chain is

dominant in the low frequency range, a result not found examining the differential relative velocity of the stapes footplate in this study. The results in this study with differential relative footplate motion indicate that the inertial effects of the ossicles with BC stimulation would mainly influence the BC response in the mid-frequencies.

C. Lesions of the ossicles

To simulate the results of footplate fixation (otosclerosis) and malleus fixation, the footplate and the malleus were glued to the bone, respectively, with cyanoacrylate glue developed for underwater use (Garf Reef glue™, Garf, Inc., Boise, ID). In theory, after footplate and malleus fixation the two are considered immobile. However, even if the glue did impede the vibratory motion of both the footplate and malleus, they were movable after being glued to the bone (Figs. 4 and 7). The result of gluing is a stiffer attachment of the stapes footplate to the promontory or of the malleus to the attic bone. With the stapes footplate glued, the malleus is still movable; a higher resonance frequency produces about 10 dB less differential relative velocity of the malleus below the resonance frequency (Fig. 7). The same occurs when gluing the malleus; the differential relative velocity of the stapes footplate is about 10 dB lower below the resonance frequency (Fig. 4). This difference between the stapes footplate and malleus is clearly a result of the compliance in the joints between the ossicles, especially the incudo-stapedial joint. Goodhill (1966) reported it was only when the incudo-stapedial joint has become a participant in total ossicular fixation that a fixed malleus produces an air-bone gap comparable to that seen in otosclerosis of the stapes.

That addition of a mass to the ossicles or TM yields increased low frequency sensitivity for BC is well known and has been reported extensively in the literature (Bárány, 1938; Huizing, 1960; von Békésy, 1960; Tonndorf, 1966). Figures 4 and 7 demonstrate that adding a mass lowers the resonance frequency of the ossicular chain: the stiffness is constant whereas the mass increases. In particular, the umbo becomes vibrationally decoupled from the bone at a lower frequency and thus yields a greater differential relative motion at lower frequencies. At the footplate level, the mass also lowers the resonance frequency and the vibration of the stapes footplate begins to roll off above the new resonance frequency. However, at higher frequencies, the velocity of the stapes footplate becomes close to that of the promontory bone. At these frequencies, above 2 kHz, the phase of the stapes footplate lags that of the promontory bone and the differential relative velocity is therefore close to that of the normal condition.

Legouix and Tarab (1959) removed the malleus in cats and measured the cochlear microphonics when stimulating by BC. They found a decrease in the cochlear microphonics and an advance of phase; adding a mass to the incus restored the response. Dirks and Malmquist (1969) noted that in patients who have had a radical mastoidectomy, the greatest reduction in BC response was around 2 kHz, where the ossicles normally resonate. They suggested, as proposed by Tonndorf (1966) earlier, that it was due to the elimination of the ossicular inertial component yielding a maximum loss at the resonance frequency of the ossicular chain. Some of the loss can be due to the lack of resonance at that frequency, however, our results with the IS-joint cut in Fig. 5 also suggest that some of the loss can be a result of a different mode of vibration, e.g., rotational motion of the stapes due to less restriction of stapes motion.

D. Occlusion of the ear canal

The effect on BC produced sound in the external ear canal after occlusion has been explained by Khanna *et al.* (1976). Two phenomena are seen. First, an increase in sound pressure at the low frequencies occurs due to the fact that an open canal acts as a high pass filter; the low frequency energy leaks out of the opening. By obstructing the canal opening this effect is eliminated, which is seen as a low frequency sound increase. It is generally agreed that the BC produced sound is radiated into the ear canal through the walls, but the increase in low frequency sound with occlusion of the ear canal should be the same even if the sound is radiated from the TM, as in this study. Second, another effect that occurs upon occluding the ear canal is the alteration of its normal resonances: with an open canal the first resonance is a quarter wavelength resonance at around 2.7 kHz, whereas in the occluded canal, the first resonance is a half wavelength resonance at approximately 5.5 kHz. These effects with occlusion of the ear canal are clearly shown in Fig. 8. However, the low frequency gain as a result of the occlusion is similar or slightly lower than those reported in human subjects (e.g., Huizing, 1960; Goldstein and Hayes, 1971; Khanna *et al.*, 1976).

The subjective occlusion effect was postulated by Tonndorf (1966) to be due to an elevation of sound pressure in the ear canal and a change of impedance at the TM due to the enclosed air column within the ear canal affecting the inertial effects of the ossicles. We found no significant effect on umbo or footplate motion after occluding or even removing the artificial ear canal. It seems, therefore, that the subjective occlusion effect in a normal human head is due to elevation of the sound pressure level in the ear canal alone and not to any change in the ear canal impedance.

E. Implications for BC measurements in humans

An important question is how these results can be interpreted in BC measurements of humans. Even if there are several issues that can differ between BC stimulation of the specimens and a human head as discussed in Sec. IV A, the results of BC stimulation in a human presented in Fig. 10 show that the specimen results can, at least as a first order approximation, be extrapolated to live humans. It is not possible to find the absolute contribution to BC sound by ossicular inertia from the experiments. However, some overall findings can be stated. It is well known that with otosclerosis of the stapes and a functioning inner ear, the BC loss is concentrated to frequencies around 2 kHz; above and below this frequency the BC hearing is almost normal (Carhart, 1950). When examining the results of gluing the stapes footplate in Fig. 4 it shows that the stapes footplate motion is greatly attenuated for the low frequencies. This indicates that

ossicular inertia is not significant for frequencies below 1 kHz. It does not necessarily imply that ossicular inertia is dominating around 2 kHz either. Otosclerosis does not only remove inertial effects of the ossicles with BC sound but it also alters the status of the oval window for BC effects of the inner ear: the normally movable stapes footplate is now stiff and cannot provide a fluid flow. It was shown that with a fenestration of the vestibuli as a treatment of otosclerosis, the BC hearing thresholds almost returned to normal (Walsh, 1962). With a fenestration, the influence of the middle ear ossicles is removed.

It can also be noted that the contribution to BC sound by the ossicles at the low frequencies is close to that of other BC contributing parts. When a mass is added to the ossicles (a 100 mg mass on the umbo) the differential motion of the stapes footplate is increased at frequencies below 1 kHz. This is similar to the gain in BC sensitivity seen in subjective measurements in humans with a small mass added to the TM (Bárány, 1938; Huizing, 1960; von Békésy, 1960). Since such a manipulation only influences the inertia of the middle ear ossicles positively (other contributors is affected negatively or not at all), the contribution to BC sound by the ossicles must be close to that of other contributors. Moreover, it was found that the stapes footplate motion was similar regardless of stimulation direction. This finding, together with the finding by Stenfelt *et al.* (2000) that the temporal bone constitutes motion in all three directions in space with BC stimulation, disproves the hypothesis that BC measurements at the mastoid is more affected by the status of the middle ear than measurements at the forehead (Studebaker, 1962; Dirks and Malmquist, 1969; Goodhill *et al.*, 1970).

V. CONCLUSIONS

It was found that it is feasible to use human temporal bone specimens and sensitive non-contact measurement techniques for investigation of the response of middle ear structures to BC produced stimuli. Care must be taken as to the method of attachment between the specimen and the BC shaker in order to achieve one-dimensional translational vibrations.

Comparison of BC induced vibration of the malleus umbo, stapes footplate, and the promontory bone showed that for low frequencies the ossicles move in phase and with equal magnitude as the bone; above the resonance frequency of 1.5 kHz, the phase of the ossicles starts to lag that of the bone. The footplate appears rather closely coupled to the temporal bone and its velocity is typically within 5 dB of the bone; this is true even if the cochlea is drained. The malleus, on the other hand, is more loosely coupled to the temporal bone, which manifests itself as a larger phase lag and greater velocity roll-off at higher frequencies as compared with the footplate.

Neither occlusion nor removal of the artificial ear canal affected the motion of the ossicles produced by BC stimulation. However, a mass attached to the ossicles lowered the resonance frequency, yielding a higher response at the low frequencies. Modeling malleus or stapes fixation by gluing either structure to the adjacent bone produced increased stiffness of the ossicular chain, resulting in a higher resonance frequency and consequently a lower response for BC produced vibration below this frequency. Further, dislocating the incudo- stapedial joint decreased the response of the footplate only between 1 and 3 kHz, probably due to a difference in vibration modes of the stapes caused by less restriction of stapes motion.

The ear canal sound pressure produced by the relative TM motion was approximately 85 dB SPL at an umbo differential velocity of 1 mm/s in the low frequencies for an open ear canal; occluding the canal yielded a 10 dB higher result. At higher frequencies, the response was dominated by the resonances of the ear canal: a quarter wavelength resonance at 2.7 kHz for the open ear canal and a half wavelength resonance at 5.5 kHz for the occluded one. Moreover, when the vibration of the temporal bone was applied in a direction orthogonal to the vibration direction of the ossicles, the results were within 5 dB for the differential relative footplate and umbo velocity.

Care must be taken when interpreting these results with BC response in a live human, since these results are based on temporal bone specimens with mainly a translational vibration pattern whereas the temporal bone in a human skull constitutes complex vibration patterns upon BC stimulation. Further, removal of the soft tissues and the removal of the loading from the cranial cavity could also bias the results obtained here compared with BC response in a live human. However, it was found that the motion of the umbo with BC stimulation was similar whether the umbo was measured in a specimen or a live human skull.

ACKNOWLEDGMENTS

This work was supported in part by a V.A. merit review grant (GDE0010ARG) and the Swedish Institute.

Bárńy, E. (**1938**). ''A contribution to the physiology of bone conduction,'' Acta Oto-Laryngol., Suppl. **26**, 129.

Brinkman, W., Marres, E., and Tolk, J. (**1965**). ''The mechanism of bone conduction,'' Acta Oto-Laryngol. **59**, 109–115.

Carhart, R. (**1950**). ''Clinical application of bone conduction audiometry,'' Arch. Otolaryngol. **51**, 798–807.

Decraemer, W., Khanna, S. M., and Funnell, W. (**1994**). ''A method for determining three-dimensional vibration in the ear,'' Hear. Res. **77**, 19–37.

Dirks, D., and Malmquist, C. (**1969**). ''Comparison of frontal and mastoid bone-conduction threshold in various conductive lesions,'' J. Speech Hear. Res. **12**, 725–746.

Franke, E. (**1956**). ''Response of the human skull to mechanical vibrations,'' J. Acoust. Soc. Am. **24**, 142–146.

Goldstein, D., and Hayes, C (**1971**). ''The occlusion effect in bone-conduction hearing,'' in *Hearing Measurement: A Book of Readings*, edited by I. Ventry, J. Chaiklin, and R. Dixon (Appleton-Century-Crofts, New York), pp. 150–157.

Goode, R. L., Ball, G., and Nishihara, S. (**1993**). ''Measurements of umbo vibration in human subjects—method and possible clinical applications,'' Am. J. Otol. **14**, 247–251.

Goodhill, V. (**1966**). ''External conductive hypacusis and the fixed malleus syndrome,'' Acta Oto-Laryngol., Suppl. **217**, 39.

Goodhill, V., Dirks, D., and Malmquist, C. (**1970**). ''Bone-conduction thresholds. Relationships of frontal and mastoid measurement in conductive hypacusis,'' Arch. Otolaryngol. **91**, 250–256.

Groen, J. (**1962**). ''The value of the Weber test,'' in *Otosclerosis*, edited by H. Schuknecht (Little, Brown, Boston), pp. 165–174.

Håkansson, B., Brandt, A., Carlsson, P., and Tjelström, A. (**1994**). ''Resonance frequency of the human skull *in vivo*,'' J. Acoust. Soc. Am. **95**, 1474–1481.

Håkansson, B., Carlsson, P., Brandt, A., and Stenfelt, S. (**1996**). ''Linearity of sound transmission through the human skull *in vivo*,'' J. Acoust. Soc. Am. **99**, 2239–2243.
Hofmann, G., Vogel, U., Zahnert, T., Offergeld, C., and Hüttenbrink, K.-B. (**1996**). ''Are there objective criterions for experimental evidence of WEBER's test?'' in *Middle Ear Mechanics in Research and Otosurgery*, edited by K.-B. Hüttenbrink (UniMedia GmbH, Dresden), pp. 134–138.
Hudde, H., and Weistenhöfer, C. (**2000**). ''Circuit models of middle ear function,'' in *The Function and Mechanics of Normal, Diseased and Reconstructed Middle Ears*, edited by J. Rosowski and S. Merchant (Kugler, The Hauge), pp. 39–58.
Huizing, E. H. (**1960**). ''Bone conduction—The influence of the middle ear,'' Acta Oto-Laryngol., Suppl. **155**, 99.
Khanna, S. M., and Decraemer, W. F. (**1996**). ''Vibration modes and the middle ear function,'' in *Middle Ear Mechanics in Research and Otosurgery*, edited by K.-B. Hüttenbrink (UniMedia GmbH, Dresden), pp. 21–26.
Khanna, S. M., Tonndorf, J., and Queller, J. (**1976**). ''Mechanical parameters of hearing by bone conduction,'' J. Acoust. Soc. Am. **60**, 139–154.
Kirikae, I. (**1959**). ''An experimental study on the fundamental mechanism of bone conduction,'' Acta Oto-Laryngol., Suppl. **145**, 110.
Legouix, J. P., and Tarab, S. (**1959**). ''Experimental study of bone conduction in ears with mechanical impairment of the ossicles,'' J. Acoust. Soc. Am. **31**, 1453–1457.
Stenfelt, S., Håkansson, B., and Tjellström, A. (**2000**). ''Vibration characteristics of bone conducted sound *in vitro*,'' J. Acoust. Soc. Am. **107**, 422–431.
Studebaker, G. (**1962**). ''Placement of vibrator in bone-conduction testing,'' J. Speech Hear. Res. **4**, 321–331.
Tonndorf, J., and Tabor, J. (**1962**). ''Closure of the cochlear windows: Its effect upon air and bone conduction,'' Ann. Otol. Rhinol. Laryngol. **71**, 5–29.
Tonndorf, J. (**1966**). ''Bone conduction. Studies in experimental animals,'' Acta Oto-Laryngol., Suppl. **213**, 132.
Tonndorf, J., and Jahn, A. F. (**1981**). ''Velocity of propagation of bone-conducted sound in human head,'' J. Acoust. Soc. Am. **70**, 1294–1297.
Vogel, U., Zahnert, T., Hofmann, G., Offergeld, C., and Hüttenbrink, K.-B. (**1996**). ''Laser vibrometry of the middle ear: Opportunities and limitations,'' in *Middle Ear Mechanics in Research and Otosurgery*, edited by K.-B. Hüttenbrink (UniMedia GmbH, Dresden), pp. 128–133.
von Békésy, G. (**1932**). ''Zur theorie des hörens bei der shallaufnahme durch knochenenleitung,'' Ann. Phys. **13**, 111–136.
von Békésy, G. (**1960**). *Experiments in Hearing*, edited by E. G. Wever (McGraw–Hill, New York), p. 745.
Walsh, T. (**1962**). ''Fenestration: Results, indication, limitations,'' in *Otosclerosis*, edited by H. Schuknecht (Little, Brown, Boston), pp. 245–250.
Zwislocki, J. (**1953**). ''Wave motion in the cochlea caused by bone conduction,'' J. Acoust. Soc. Am. **25**, 986–989.
Zwislocki, J. (**1962**). ''Analysis of the middle-ear function. Part I: Input impedance,'' J. Acoust. Soc. Am. **34**, 1514–1523.

Mapping ear canal movement using area-based surface matching[a)]

Malcolm J. Grenness[b)]
Discipline of Anatomy and Physiology, University of Tasmania, Australia

Jon Osborn
Lecturer, Center for Spatial Information Science, University of Tasmania, Australia

W. Lee Weller
Senior Lecturer, Discipline of Anatomy and Physiology, University of Tasmania, Australia

(Received 18 June 2001; revised 30 October 2001; accepted 31 October 2001)

Movement of the external ear canal, associated with jaw motion, relative to the concha region of the pinna has been studied. Pairs of open-jaw and closed-jaw impressions were taken of 14 ears from 10 subjects. Three-dimensional coordinate data were obtained from the concha and the anterior surface of the canal using a reflex microscope. Proprietary area-based matching software was used to evaluate distortion of the two surfaces between the two jaw positions. The canal data from each pair were placed into the same coordinate system with their respective concha regions aligned. Difference maps of the canal data were used to demonstrate the amount of anterior–posterior (A–P), superior–inferior (S–I), and medial–lateral (M–L) movement, relative to the concha, that occurred between the open- and closed-jaw impressions. The concha regions did not undergo significant deformation. The canal regions underwent varying amounts of deformation with all canals conforming within an rms of 136 μm across the entire surface. The majority of canals underwent significant movement relative to the concha. M–L movement ranged from +2.0 to −3.8 mm; eight canals moved laterally, five moved medially, and two showed no movement. S–I movement ranged from +3.7 to −2.7 mm; nine canals moved inferiorly, two moved superiorly, and three showed no movement. A–P movement ranged between +7.5 and −8.5 mm, with five canals moving anteriorly, three posteriorly, and four in a mixed fashion. This study has shown the variability of canal movement relative to the concha and does not support previous reports that suggest that the ear canal only widens with jaw opening.
[DOI: 10.1121/1.1430682]

PACS numbers: 43.64.Ha [BLM]

I. INTRODUCTION

Ear canal morphology changes upon smiling, talking, and chewing (Morgan, 1987). *Cunningham's Textbook of Applied Anatomy* (1972), when discussing the external ear canal, simply states, ''When the head of the mandible moves forward e.g. on opening the mouth, the cartilaginous part is widened.'' Anecdotal reports suggest that the canal can narrow during functional movements and create difficulties in fitting hearing aids (Grenness, 1990). How this is possible is not immediately clear. Cunningham's description does not seem adequate to explain this observation, which provided the impetus to investigate movement in the ear canal related to jaw movements.

A. The external ear

The external ear consists of the auricle (pinna) (Fig. 1), and the external auditory meatus (ear canal) leading from it to the tympanic membrane. The auricle is attached to the side of the head via ligaments and muscles whose actions have not been described. The external auditory meatus assumes an ''S'' shape in adulthood and has been described as having a first bend or ''conchomeatal angle'' (Abel *et al.*, 1990) and a second bend or ''cartilaginous-bony angle'' (Alvord and Farmer, 1997) (Fig. 2).

B. Movements of the external ear

The auricle contains six intrinsic muscles; however, none of these involves the concha region. It is assumed that for practical purposes the concha area does not deform during movements of the entire pinna and canal. This assumption was tested during this study.

A horizontal section through the external ear shows the relation of the canal to the temporo-mandibular joint (TMJ). Reviewing Fig. 2 and simple observation suggests that as the condyle of the mandible moves forwards, that portion of the canal adjacent to the condyle may also move forward. At the same time the tragus may be pulled anteriorly, and/or medially. Flexion of the cartilage of the anterior wall of the canal would be likely to occur principally at the notches in the cartilage of the ear canal. When subsequent ear impressions are taken with the mouth in closed and open positions, the first bend in the impression becomes more clearly defined (Grenness, 1990).

[a)]A brief summary of results of the paper was presented orally to the 3rd Biennial Congress of the Australian College of Audiology held in Melbourne, Australia in March 2001.
[b)]Electronic mail: grenness@tassie.net.au

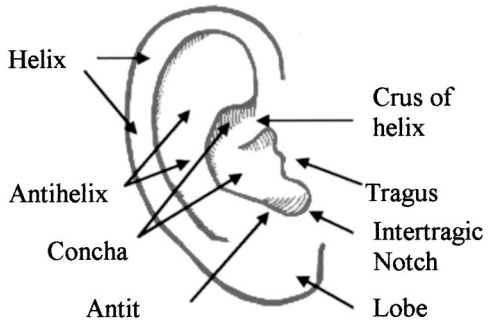

FIG. 1. Auricle. Lateral view.

However, anterior movement of the tragus may not be an automatic consequence of anterior movement of the condyle. Wilkinson and Crowley (1994) conducted a histological study of the TMJ retrodiscal tissues of the temporomandibular joint in the open and closed jaw positions. They found that the upper stratum of the retrodiscal tissues was folded on itself in the closed position and only became stretched near maximal opening. They concluded that the primary role of the retrodiscal tissues was to provide a volumetric compensatory mechanism for pressure equilibration during jaw opening. Their study did not support the concept of a recoil mechanism to control TMJ disc movement. Therefore, it cannot be assumed that as the condyle moves forward, it must take all that is behind it forward.

Movements of the pinna as a whole must also be considered. Should the pinna as a whole be pulled anteriorly at a greater rate than the anterior wall of the canal, the result would be a narrowing of the canal.

C. Previous studies

Van Willigan (1976) showed changes in ear canal shape and position relative to the position of the maxilla by sectioning the canal at 2-mm intervals. He found that opening jaw movement caused an increase in volume of the ear canal. It also appeared that, with a change in mandibular position, not only the ventral wall of the external ear but the entire meatus changed form. However, an increase in volume does not equate with an increase in size in all dimensions. Examination of the diagrams in Van Willigan (1976) clearly shows

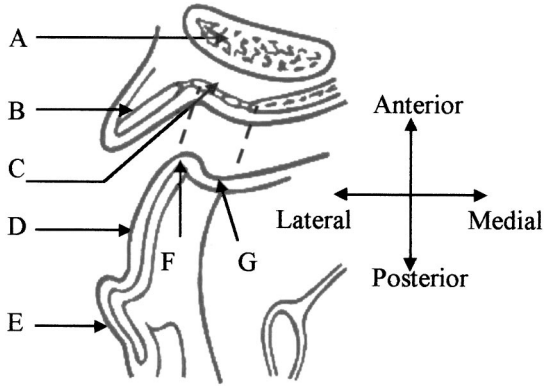

FIG. 2. Horizontal section through right ear, viewed from above. (A) Mandibular condyle; (B) Tragus; (C) Notches in cartilage of acoustic meatus; (D) Concha; (E) Antihelix; (F) First bend; (G) Second bend.

that there is an increase in size in the superior–inferior (S–I) dimension. At best, it is difficult to evaluate whether there is an increase or decrease in the anterior–posterior (A–P) dimension. Many of the diagrams do suggest a decrease in this dimension upon jaw opening.

If the anterior wall of the canal is generally moving forward, then a reduction in the A–P dimension can only be reasonably explained by a greater movement forward of the entire pinna, including the posterior wall of the canal. A study of movement of the canal relative to the pinna is therefore warranted.

Oliveira *et al.* (1992) obtained silicon impressions of a subject at varying degrees of jaw opening. Transaxial diameters of the impression canals were measured with a digital caliper. Approximately 25% change in this subject's ear canal with different jaw positions was observed in the (A–P) plane with essentially no change in the (S–I) plane. This was equivalent to an average increase, in the A–P direction, of about 0.7 mm in a typical adult over the length of the canal. They also reported a case with asymmetrical changes in which a 6% change occurred in the right ear, and a 21% change in the left ear.

Pirzanski (1996) described an ''open-jaw'' impression technique and inserted closed-jaw ear impressions into open-jaw impression negatives to demonstrate movement in the ear canal. He reported that: (1) Mandibular movement affected 20% to 60% of subjects having impressions taken for hearing aids; (2) The cartilage in some subjects stretched up to 2 mm; (3) The majority of changes in the ear canal occurred in the anterior direction; (4) Minor changes were observed in the inferior direction; and (5) No changes or minimal changes were found in the posterior and superior part of the canal.

Oliveira (1997) reported on MRI studies using an MRI enhancer fluid in the ear canal, measuring volumetric changes in the ear canal at varying degrees of mandibular opening and relating these changes to underlying tissues. The biomechanics of the jaw was used to explain changes in ear canal dimension as the jaw opens. He concluded that the most significant changes that occurred in ear canal dimension with jaw motion were between the first and second bends of the canal.

These studies reveal an increasing awareness and reportage of ear canal movement and its impact upon hearing-aid fitting and comfort. They indicate that the major deformation of the canal occurs in the anterior wall. Very small changes occur in the S–I plane and in the posterior wall of the canal. No mention has been made of the medio–lateral (M-L) plane. There is no information about a possible reduction in ear canal dimension or movement within the concha region. Quantitative data of morphological changes of the external ear canal relative to the concha region of the pinna associated with facial and mandibular movement are required.

In addition to the fit, comfort, and acoustic seal of hearing aids, ear canal movement is also relevant during audiometry (Ventry *et al.*, 1961; Creston, 1965); it affects the sound attenuation of earplugs (Smith *et al.*, 1980; Abel *et al.*, 1990); and it may affect the development of acoustical mod-

els of the ear canal (Zemplenyl *et al.*, 1985; Stinson and Lawton, 1989).

D. Aim

The aim of this investigation was to study

(1) Movement within the concha region of the ear in order to determine whether this region undergoes deformation;
(2) Movement within the anterior wall of the ear canal in order to determine the range of deformation; and
(3) Movement of the canal region of the ear canal relative to the concha area in order to determine the range of movements in the A–P, S–I, and M–L directions.

II. METHOD

A. Impressions

Pairs of ear impressions were taken from 14 ears of 10 subjects with the jaw in the ''closed'' and ''open'' position as described by Pirzanski (1996). Impressions were taken to the depth of the second bend. Subjects were selected on an *ad hoc* basis to provide male and female subjects, a wide age range (15 to 58 years), known hearing-aid fitting difficulty, existing hearing-aid users, and non-hearing-aid users. Subject selection was not intended to be representative of any group or the population as a whole.

Impressions were taken with a medium-viscosity condensation silicone dental impression material [Xantopren H (green), Heraeus/Kulzer, Germany]. It gives good surface detail without causing trauma to the lining epidermis upon removal. The manufacturer reports recovery from deformation equal to or greater than 98.0% and linear dimensional change of equal to or less than -0.90%.

B. Measurement of geometry

The concha and the anterior surface of the canal regions of the impressions were mapped using a Reflex microscope. The Reflex microscope is a noncontacting instrument enabling direct measurement in 3D of small objects (up to 110 mm) which can lead to 3D computer representations, also called digital surface models. The observer views the object through an ordinary stereoscopic microscope. A small light spot appears in the field of view, and it can be guided to coincide with desired points on the surface. The *x*, *y*, and *z* coordinates are monitored by Moiré fringe encoders, and a counting interface passes the position on request to a computer.

The object is carried on a conventional two-dimensional (*x*, *y* axis) slide. The slide was first translated to give the observer a view of the point to be measured by a trackball (free-format routine) or computer program (ordered-grid routine). The microscope and measuring spot are carried on a vertical (*z*-axis) slide, and the observer alters the plane of focus with a finger slide until the measuring spot and the object point coincide. Multiple views of an object can be recorded and combined where there are common points to each view. This measurement system has the advantage that where defects are present on the surface of an impression, due to air inclusions, wax, or hair, the operator is able to judge the plane of the tissue surface. A full description and explanation of the reflex principle, the Reflex microscope, and examples of its application may be found in a paper by Scott (1981).

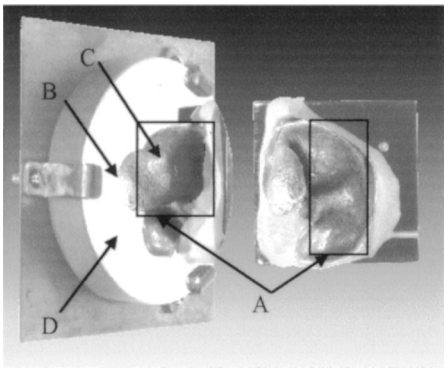

FIG. 3. Object mount with fixed mirror and impression seated, viewed from above, showing the impression and the concha field viewed directly (right rectangle) and canal field viewed via the fixed mirror (left rectangle). (A) Southern border; (B) Canal at second bend; (C) Canal at first bend; (D) Fixed mirror.

The microscope was calibrated according to the manufacturer's instruction. All measurements were taken using $\times 20$ magnification and a 20-μm measuring spot. Precision in the *x* and *y* axes is determined by the precision of the Moiré fringe encoders, reported by the manufacturer as 1 μm. The precision of the *z*-axis scale is dependent on the capacity of the operator to place the measuring mark upon the surface of the object. The mean of the standard deviations of the differences (30 points on an ear impression were plotted 14 times) on the *z* axis was measured during several sessions and found to be 36.0, 33.6, 19.9, and 16.3 μm. This indicated a progressive improvement in precision with familiarity with the measuring system (as also noted in Speculand *et al.*, 1988). All ear impression measurements were taken on or after session 4. The value of 20 μm was taken as the precision of the *z*-axis measurements.

The ear impressions were seated on an object mount with the concha region approximately horizontal and the canal region pointing vertically. The object mount included a 50-mm-diameter optical flat mirror, lambda 4, set at 45 deg. When viewed through the microscope, the concha region could be seen directly, on the right, and the anterior surface of the canal could be seen through the mirror, on the left (Fig. 3). Both regions were mapped in the same coordinate system without need for remounting the impressions.

C. Alignment and securing of object

The ear impressions from each impression pair were seated onto the object mount with their concha regions aligned in the same orientation. This was done with the aid of an impression negative made from dental bite registration material (Automix Bite Registration material, 3M). The tragus and canal regions of the impressions were not included in the negative. Separate negatives were made for each pair of impressions.

TABLE I. Precision of mirror transformation, by *x*, *y*, and *z* axes.

Session	No. of points	Standard deviations		
		x axis (μm)	*y* axis (μm)	*z* axis (μm)
1	30	26.3	9.2	33.4
2	28	33.9	13.4	33.8
3	18	23.7	26.9	24.7
4	18	41.0	17.7	49.6
Mean		30.9	15.5	35.0

D. Collection of 3D coordinate data

Coordinate data were recorded from the impressions as ASCII files of *x*, *y*, and *z* columns of numbers. Each field was plotted using ordered-grid routines. Fields were plotted on a 1000-μm×1000-μm grid, with points along the edge of the southern border of each field recorded every 500 μm (Fig. 3).

E. Determination of mirror transformation

A triangular calibration block was placed on the object mount so that calibration marks could be plotted with the reflex microscope directly and also through the mirror. At the beginning of each measurement session, between 18 and 30 common marks were measured using a free-format routine. These coordinates were used to solve for a three-dimensional transformation from the mirror coordinate system to the direct coordinate system (Parslow, 1994). This resulted in the canal fields being in the correct spatial relationship with their respective conchae.

The precision of the mirror transformation was taken as the standard deviation from the mean of the differences between the direct points and the same points plotted through the mirror and transformed into direct points (i.e., calculated direct points) (Table I). The rms of the standard deviations for the three axes was on the order of 30 μm.

To determine whether there was any systematic error, the mean of the differences between the direct and calculated points was calculated (Table II). The mean of the differences for the *x*, *y*, and *z* axes was close to 0 μm. This indicated that the error was random in nature and did not favor any one axis.

On the basis of these tests the precision of mirror transformation was taken to be $\pm$30 μm in each of the *x*, *y*, and *z* axes. This led to an rms standard deviation of 52 μm for the three axes combined.

TABLE II. Precision of mirror transformation, assessment of systematic error.

Session	No. of points	Mean of differences		
		x axis (μm)	*y* axis (μm)	*z* axis (μm)
1	30	−2.11	0.45	2.49
2	28	−0.97	−1.25	0.89
3	18	2.37	−3.87	0.87
4	18	4.01	1.75	−2.01
Mean diff.		0.26	−0.63	0.84

F. Alignment of concha regions

To measure movement in the ear canal relative to the concha region, it was necessary to precisely align the datasets of the concha fields of each impression pair. Care was taken in the alignment of the impressions during the mounting procedure so that any misalignment was minimized. The alignment could be further enhanced using computer software utilizing common surface features between both datasets. Skin pores were readily identifiable on individual impressions. However, attempts to identify common pores on impression pairs failed and attempts to mark suspected common points were unsuccessful, so feature-based surface matching was unsuccessful.

Area-based surface matching using proprietary software DS MATCH (version 23, Mitchell, 1995) was tried and found to be successful. Area-based surface matching involved finding the orientation of best fit between corresponding fields in surfaces that are being matched. In this case the entire surface was used in the matching process. One surface was translated and rotated by an iteration process until the differences between the two surfaces were minimized (convergence). Iteration stopped when the most recent corrections to the translation parameters were less than 0.01 μm, and the rotation parameters were less than $\pm$0.000 01 decimal degrees. When convergence occurred, the mean of the differences between the two surfaces was zero.

DS MATCH required a ''threshold for exclusion of points,'' in addition to the two input files to be matched. This enabled the exclusion of points where the fields did not overlap and of points that were grossly divergent from the rest of the field, either through measurement error or gross distortion of the surface.

The solution of the matching process was comprised of

(i) The transformation parameters, the rotations and translations derived by the matching process.
(ii) The number of points included in the solution, a measure of the amount of overlap or gross divergence between the two surfaces.
(iii) The differences between the two surfaces after they had been aligned, presented as 3D coordinates (difference data).
(iv) The root-mean-square of the differences (rms diff.) between the two surfaces, a measure of the coincidence or deformation of the two surfaces after they had been aligned.

G. Movement within the concha

Area-based matching was applied to the concha datasets of open- and closed-jaw impressions with threshold exclusion limits of 100, 200, 300, and 400 μm. The solution derived from the matching process was used to evaluate the changes that occurred in the concha upon opening the mouth.

The difference data were mapped with SURFER 3D analysis and visualization software (Golden Software, version 6.04, 1997) and overlaid with a closed-jaw contour map of the concha. The difference data were gridded on a 1-mm interval with triangulation and interpolation, and contoured between −0.2 and +0.2 mm with contour intervals of 0.1

mm. The closed-jaw data contour map was gridded on a 0.5-mm grid with triangulation and interpolation.

H. Movement within the canal

Area-based matching was applied to the canal datasets with threshold exclusion limits of 100, 200, 300, and 400 μm. The solution derived from the matching process was used to evaluate the distortion that had occurred in the canal.

The difference data were mapped and overlaid with a closed-jaw data contour map of the canal. The difference data were gridded on a 1-mm interval with triangulation and interpolation, and contoured between -0.4 and $+0.4$ mm with contour intervals of 0.2 mm. The overlaid contour maps of the closed-jaw canal data were gridded on a 0.5-mm grid with triangulation and interpolation.

I. Movement of canal relative to the concha

The transformation parameters derived to precisely align the concha datasests were applied to the corresponding canal datasets using the Bursa–Wolf seven-parameter similarity transformation equations (Harvey, 1995). The datasets from each pair of canal regions, with their concha fields aligned, were further analyzed using SURFER software. The imported datasets were orientated as horizontal surfaces.

1. Movement in the M–L and S–I directions

Data sets were converted to ''grid files'' using SURFER. Gridding parameters were set at 500 μm for both x and y axes. Fields were plotted as contour maps with contours at 500-μm intervals. Open- and closed-jaw maps were superimposed. The open-jaw contour map was then clicked and dragged over the closed-jaw map until an alignment of best fit was achieved. Best fit was determined subjectively by balancing considerations of

(i) The highest contour of the plot (first bend in canal);
(ii) The ridge extending from the highest point to the inferior aspect of the canal; and
(iii) The superior and inferior borders of the canal.

The translations that occurred while manually aligning the two maps were determined. These represented movement in the M–L and S–I directions.

2. Movement in the A–P direction

Gridding parameters were set as above. Difference contour maps were generated with a contour interval of 500 μm and overlaid with a contour map of the corresponding closed-jaw dataset. The difference maps represented movement in the A–P plane. The range of values along a horizontal line through the center of the map was taken as an approximation of the movement in the A–P direction.

III. RESULTS

A. Movement within the concha

Fourteen impression pairs were area-matched using DS MATCH. The mean values on the 14 datasets for the percentage of points included in the solution and rms diff. values for the 100, 200, 300, and 400-μm exclusion limits are presented in Table III.

TABLE III. Concha area-matching, varying the exclusion limit.

Exclusion limit (μm)	Mean % of points	Mean rms diff. (μm)
100	58	49
200	82	78
300	87	97
400	90	108

Error in the solutions was dependent on the surface shape, the perimeter shape, the number of points used to determine the solution and the coincidence of the two surfaces (rms diff.). The percentage of points included in the solution for exclusion limits of 200 to 400 μm was in excess of 80% (Table III). Each profile of the concha fields accounted for between 8 and 10 percent of the total number of points. If a pair of concha fields did not overlap by one profile, then 10 percent of the points would be lost to the solution. Along the inferior, posterior, and superior borders of the concha field the surface fell away very steeply. Points recorded in these areas were subject to increased measurement error due to the steep angle at which the surface intersected with the measuring mark. The error associated with this phenomenon was not tested. However, many of these edge points are likely to have been excluded from the solution. The number of points excluded for this reason could approach 10 percent. It was also accepted that the coordinates of a number of points would be recorded incorrectly because of operator error. No attempt was made to assess the percentage of points that fell into this category but an upper limit of 5 percent would seem a conservative estimate, one point in a profile of 20 points.

In summary, loss of points from the solutions were due to

(i) Lack of overlap at the first or last profiles; $<10\%$
(ii) Steep inclines at southern and northern border; $<10\%$
(iii) Operator observation error; $<5\%$.

An exclusion of approximately 20% of points is consistent with a correct match between two closely fitting surfaces.

Thus, the figure of 82% for the 200-μm exclusion limit is consistent with the data and measuring system. The figures of 87% for the 300-μm exclusion limit and 90% for the 400-μm exclusion limit are consistent with inclusion of a further 5% and 8% of points as more inaccurate points and more edge points are included by the higher exclusion limit. On the basis of the data in Table III, the need to include the highest number of points was balanced with the need to keep the value of the rms diff. as low as possible. Transformation parameters based on a exclusion limit of 200 μm were accepted as inputs into further analysis.

The rms diff. and the percentage of points involved in the matching with an exclusion limit of 200 μm are given in Table IV. Table IV shows that the concha region of open-jaw and closed-jaw impression sets 2–14 conform, with a mean rms diff. of 78 μm derived from coordinate data with a mea-

TABLE IV. Concha area-matching, % points, and rms differences. Note: *Data set 1 was excluded from the calculation of the mean because the area-matching result was unreliable, with a lower number of points and higher rms differences value.*

Imp. no.	Total no. of points	No. of points in solution	% points in solution	rms diff. (μm)
1	442	202	46	102
2	237	177	75	71
3	380	334	88	64
4	283	181	64	91
5	319	252	79	73
6	236	215	91	75
7	301	250	83	87
8	314	256	82	73
9	254	219	86	87
10	234	197	84	77
11	262	211	81	77
12	206	169	82	70
13	270	215	80	90
14	321	286	89	73
Mean			82	78

surement error of 20 μm and plotted on a 1-mm grid.

Figure 4 shows difference data from the matching solution from impression no. 13, mapped using SURFER with the closed-jaw contour map to aid orientation. Examination reveals broad areas of residual data between $\pm$0.1 mm, discrete areas of residual data between $\pm$0.1 and 0.2 mm, principally the crus of the helix and some edges, and blank areas at some edges where data points have been excluded.

B. Movement within the canal

Fourteen pairs of canal regions were matched using DS MATCH. Applying an exclusion limit of 200 μm produced the following table (Table V) with a mean percentage of points of 66% and mean rms residuals of 96 μm.

Six impressions (numbers: 5, 7, 10, 11, 12, and 14) converged with a high number of points included in the solution

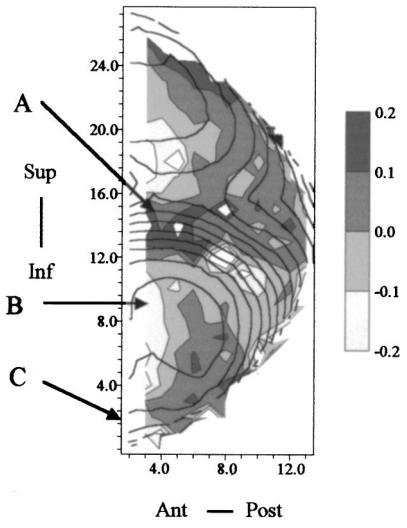

FIG. 4. Impression no. 13. Concha field, area-matching difference data map, overlaid with closed-jaw contour map. (A) Crus of helix; (B) first/left-hand profile; (C) region adjoining antitragus. All units in mm.

TABLE V. Canal area-matching, 200-μm exclusion limit, % points, and rms differences, ranked by % equations.

Imp. no.	Total no. of points	No. of points in solution	% points in solution	rms diff. (μm)
10	208	182	88	85
11	210	175	83	80
7	276	220	80	94
5	342	270	79	91
14	208	164	79	82
12	218	169	78	81
1	619	396	64	81
9	145	90	62	101
4	306	184	60	91
6	297	179	60	89
13	267	153	57	89
8	340	183	54	97
2	195	86	44	97
3	247	101	41	106
Mean			66	96

(>78%). Six impressions (numbers: 1, 4, 6, 8, 9, and 13) converged with a moderate number of points (between 50% and 75%). Two impressions (numbers: 2 and 3) converged with a very low number of points (<50%).

The higher than normal loss of points is attributed to a difference in the shape of the canal at the inferior and superior borders, as a result of distortion of the canal during jaw opening. As with the concha fields, a loss of around 20% of points from the solutions of matching the canal fields is consistent with a correct match of two closely fitting surfaces.

Applying an exclusion limit of 400 μm produced the following table (Table VI) with a mean percentage points of 85% and a mean rms residual of 136 μm.

Eleven impressions (numbers: 2–5, 7–12, and 14) converged with a high number of points (>75%). Three impressions (numbers: 1, 6, and 13) converged with a moderate number of points (between 50% and 75%).

In summary, six of the impression pairs matched with an exclusion limit of 200 μm, a mean 81% of points included in

TABLE VI. Canal area-matching, 400-μm cutoff, % exclusion limit, and rms differences, ranked by % points.

Imp. no.	Total no. of points	No. of points in solution	% points in solution	rms diff. (μm)
2	97	192	98	139
10	85	199	96	116
11	80	193	92	107
5	91	316	92	141
12	81	198	91	120
7	94	251	91	130
14	82	185	89	114
3	106	221	89	153
9	101	119	82	134
4	91	239	78	150
8	97	261	77	168
6	89	215	72	153
13	89	189	71	150
1	81	408	66	123
Mean			85	136

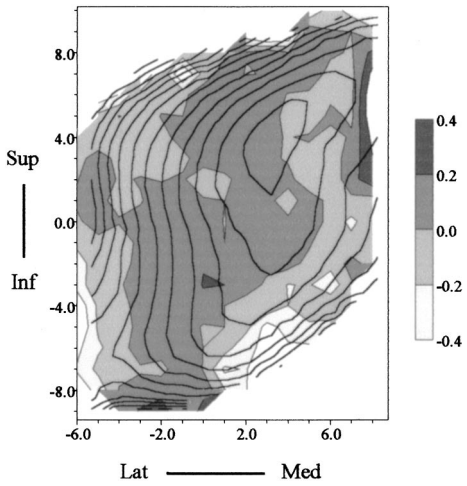

FIG. 5. Impression no. 5. Canal field, 400-μm exclusion limit, area-matching difference data map, overlaid with closed-jaw map. There is good overlap between the difference data map and the closed-jaw map consistent with the 92% of points included in the solution. All units in mm. *Note: different scale from Fig. 4.*

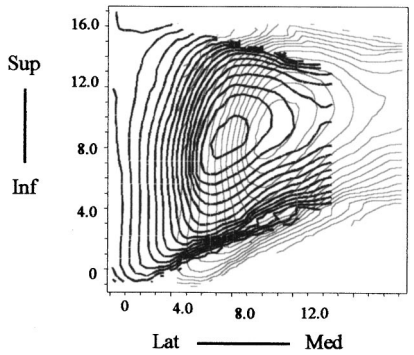

FIG. 6. Impression no. 4. Canal field, overlaid contour maps. Closed-jaw data (light), open-jaw data (heavy). Maps overlaid into the same coordinate system with concha fields coincident, significant M–L movement. All units in mm.

the solution and an rms diff. value of 86 μm. Five impression pairs matched moderately well with an exclusion of 400 μm, a mean 85% of points, and rms diff. value of 149 μm. Three impression pairs matched with an exclusion of 400 μm, a mean 70% of points, and a mean rms diff. value of 142 μm.

This points to increased distortion of the canal field when compared to the concha in 8 out of 14 impressions. Successful matching of fields generally occurred only when the exclusion limit was increased to 400 μm with a mean rms diff. of 136 μm (compared with a mean rms diff. of 78 μm for concha matching).

Figure 5 shows canal difference data from impression no. 5, mapped and overlaid with a closed-jaw contour map to aid orientation. Examination shows good overlap between the difference data map and the closed-jaw map consistent with the 92% of points included in the solution. Distortion of the canal could occur in two general areas, within the body of the field and at the edges. The above table and examination of all the overlaid contour maps indicate that the influence of loss of data at the edges was significant.

C. Movement of the canal relative to the concha

1. Movement in the M–L and S–I directions

Contour maps of the canal fields were generated with their respective concha aligned. The precision of the points on which the contour plots were based was calculated from

Precision of recorded points: 20 μm,

Precision of mirror transformed points: 52 μm,

Precision of area-based matching: 78 μm.

Because the closed-jaw data were recorded, then transformed through the mirror, they had an estimated accumulated error of 56 μm. By comparison, the open-jaw data were recorded, transformed through the mirror, and further transformed using parameters derived from the concha area matching, and so had an estimated accumulated error of 97 μm. Contour intervals of 500 μm could be reliably plotted from these data. Displacements of 500 μm or greater are therefore clearly significant. Figure 6 shows the open- and closed-jaw canal maps of impression 5. There has been significant M–L movement in impression 5.

The M–L and S–I translations were recorded in μm (Table VII). Negative figures represent movement to the inferior or lateral. The mean of the absolute values of the M–L and S–I translations were 1450 and 1210 μm, respectively, with a range of +2022 to −3839 μm and +2372 to −3712 μm.

In general terms, upon opening, the canal moved in the S–I plane

Inferiorly in impressions: 2, 4, 6, 7, 8, 11, 13, 14 (8 ears),

Superiorly in impressions: 3, 9, 10 (3 ears),

No S–I movement in impressions: 1, 5, 12 (3 ears).

In general terms, upon opening, the canal moved in the M–L plane

Laterally in impressions: 2, 3, 4, 6, 11, 12, 13, 14 (9 ears),

Medially in impressions: 7, 8, 9, 10 (4 ears),

No M–L movement in impressions: 1, 5 (2 ears).

TABLE VII. M–L and S–I movements of canal relative to the concha.

Imp no.	Subject	Medial–lateral (μm)	Superior–inferior (μm)
1	1	0	0
2	2	−3839	−1592
3	3	−364	+823
4	4	−3231	−588
5	5	0	0
6	5	−1248	−1006
7	6	1458	−2716
8	6	2022	−811
9	7	1595	3712
10	7	1489	2372
11	8	−1190	−440
12	8	−2075	0
13	9	−775	−1270
14	10	−647	−1616
Mean absolute		1450	1210

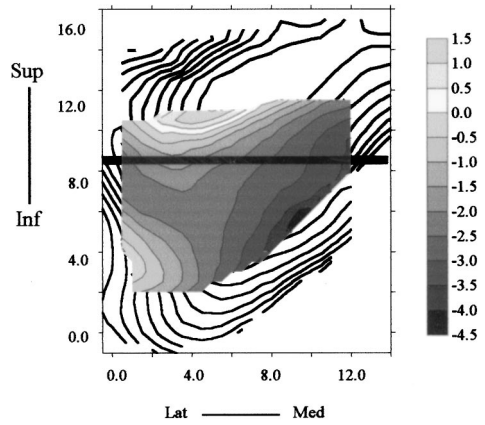

FIG. 7. Impression no. 10. Canal field, closed-jaw data (light), open-jaw data (black), and closed–open-jaw difference data contour map. Maps overlaid into the same coordinate system with concha fields coincident. All units in mm.

2. Movement in the A–P direction

Difference contour maps were generated on a 500-μm grid. Issues of error and significance are the same as in the previous section. Positive values represent movement in the anterior direction upon opening (e.g., Fig. 7).

The range of values along a horizontal line through the center of the map was taken as an approximation of the movement in the A–P direction (Table VIII). The horizontal line in Fig. 7 was the region through which difference values were accepted as the A–P movement. This line passes through contour levels of -4.0 to -0.5 mm. Movement ranged from -8.5 to $+7.5$ mm. Movement in 10 of the 14 ears occurred between -3.0 and $+3.5$ mm. The absolute mean of the range was 3.1 mm.

In general, upon opening, the canal moved in the A–P plane

Anteriorly in impressions: 1, 3, 5, 7, 9, and 13 (6 ears),

Posteriorly in impressions: 2, 6, 10 (3 ears),

Mixed in impressions: 4, 8, 11, 12, and 14 (4 ears).

In the mixed group, impressions 4, 11, and 12 showed anterior movement (widening of the canal) lateral to the first bend and posterior movement (narrowing of the canal) medial to the first bend. Impression 8 showed the reverse.

TABLE VIII. A–P movements of canal relative to the concha.

Imp. no.	Subject	Anterior–posterior (mm)	Range (mm)
1	1	4.5 to 5.0	0.5
2	2	−8.5 to −3.0	5.5
3	3	−0.5 to 2.0	2.5
4	4	−2.5 to 3.0	5.5
5	5	0 to 2.0	2.0
6	5	−3.0 to −1.0	2.0
7	6	3.5 to 7.5	4.0
8	6	−2.0 to 3.0	5.0
9	7	1.0 to 3.5	2.5
10	7	−4.0 to −0.5	3.5
11	8	−1.0 to 2.0	3.0
12	8	−1.0 to 2.5	3.5
13	9	1.0 to 3.5	2.5
14	10	1.0 to 2.5	1.5
Mean			3.1

Transformation parameters derived from matching the canal fields could not be used to evaluate movements of the canal. The matching solution contained both rotations and translation. Rotations of the fields had significant translation effects. There was no correlation between translation parameters derived from matching and the translations determined above. There was also no correlation between the rotation parameters and the quantum of movements.

IV. DISCUSSION

A. Impressions and accuracy

Mapping was designed to be sufficiently accurate to be relevant to clinical practice and the manufacture of hearing aids. Clinically, the accuracy of ear impressions can be hampered by the presence of hairs and cerumen. During manufacture of ear molds, factors such as impression modification, the nature of the materials used, and ear mold polishing results in differences between the impression and the final mold/shell that is fitted. Changes in external ear morphology of less than 200 μm are unlikely to have a significant impact upon the dimensions of hearing aids and earplugs. Differences of 0.5 mm have been shown to exert a dramatic effect on sound attenuation of earplugs (Smith *et al.*, 1980). In the study an error on the order of 100 μm in ear impression maps was accepted as a level of accuracy consistent with clinical and manufacturing practice.

In order to achieve accuracy on the order of 100 μm in the ear impression maps, it was necessary to achieve accuracy in data collection on the order of 30 μm. This level of error was achieved with the Reflex microscope.

The repeatability of ear impressions was not tested in this study. Distortion of the external ear by the impression material and technique is possible. Comparison of repeat impressions at the same jaw position is possible using area matching as described above. This is an area for future study.

B. The concha field: Area-based matching

During the initial matching of concha fields it was apparent that area-based matching could be unreliable. The circular nature of the concha fields allowed several different ''good matches,'' with widely varying parameters being derived from the same pair of impressions. This phenomenon could be described as ''barreling.'' Two identical cylinders can be matched in an infinite number of ways when their long axes coincide. This problem was overcome by enlarging the area of the concha being plotted, and including elements that were less subject to barreling. The most important elements were the edge of the impression, and the hollow of the crus of the helix. The area mapped in this study has generally been sufficient for reliable area-based matching.

C. Impression alignment

A comparison of the transformation parameters for matching the concha fields gives an indication of the effectiveness of the use of an impression negative in aligning each

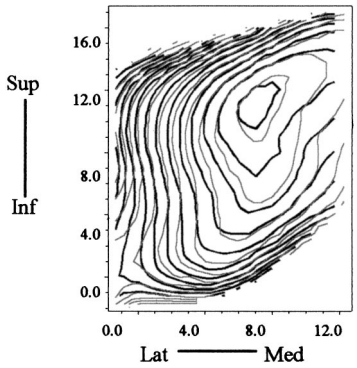

FIG. 8. Impression no. 5. Canal field, overlaid contour maps. Closed-jaw data (light), open-jaw data (heavy). Maps overlaid into the same coordinate system with concha fields coincident. No M–L or S–I movement resulting in no movement along the lower border of the canal. All units in mm.

pair of impressions. The absolute mean of the translations on the M–L, S–I, and A–P planes was on the order of 1000 μm, and the rotations were on the order of 2 deg. These values were larger than expected, and may have been the result of an inherent problem with the method or in its application.

The region of the impression most likely contributing to this problem was the tragus. In the current study, the anterior surface of the tragus and canal regions was excluded from the register because it was known to move relative to the concha. Examination of the maps reveals large movements along the inferior border of the canal/tragus in this region in the majority of maps (e.g., Fig. 6). Interestingly, maps that show the least movement along the inferior border in the S–I and M–L planes (Nos. 3, 5, 6, and 11) also show smaller translations and rotations for all six area-matching parameters. Figure 8 shows the open- and closed-jaw canal maps of impressions 5. There has been no change along the lower border of the canal.

The lateral–inferior aspects of the canal contour plots represent the region leading to the antitragic notch and the antitragus. It can be concluded that where there was not significant movement in the intertragic notch region in the S–I and M–L planes, there was less error in the manual alignment of the impressions with a register.

These movements do not appear to have resulted in distortion of the area of the concha that was plotted, as shown by the high number of equations included in all the matching solutions.

Examination of the concha difference data contour plots (e.g., Fig. 4) shows a small loss of difference data along the inferior border of the map in the region of the antitragus in about half of the datasets. This loss of data, commented upon in the results section, was due to the increased slope in the region leading to increased measurement error and reduction in effective sampling rate, and possibly distortion in the region.

However, the posterior wall of the intertragic notch, i.e., the antitragus region, was included in the register to provide sufficient contact with the impression to aid in the alignment of the impressions. There was a suspicion of movement in this region. Casual inspection of ear impressions frequently shows changes in this area. However, the extent and significance of these changes has not been reported or commented on previously and did not form a part of this study. The plane of the antitragus part of the ear impressions was typically at close to right angles to the plane of the concha (Fig. 9), and was therefore not mapped.

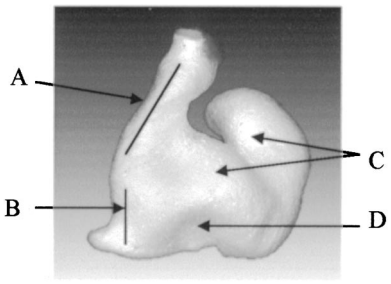

FIG. 9. Ear impression. (A) Inferior border of tragus; (B) Antitragic notch; (C) Concha; (D) Antitragus region.

D. The canal field: Multiple best-fit solutions

Area-based matching of the canal region had a propensity to produce multiple solutions. In order to determine the solution of best fit the data were repeatedly iterated with different combinations of three, four, and six parameters until the highest number of equations included in the solution was determined. For example, Fig. 10 shows the residual data of area matching the canal of impression no. 5, mapped as a contour map, overlaid with a contour map of the closed-jaw data. An exclusion limit off 400 μm was used, and convergence achieved with 62% of points and an rms diff. of 134 μm. Clearly, the difference data contour map and the overlaid closed-jaw map do not coincide at the superior and inferior borders.

Further iteration of the closed- and open-jaw data produced convergence with 92% of equations and an rms residual of 141 μm. The resultant map in Fig. 5 shows good alignment of the residual data contour map and the corresponding closed-jaw impression. Clearly, this second solu-

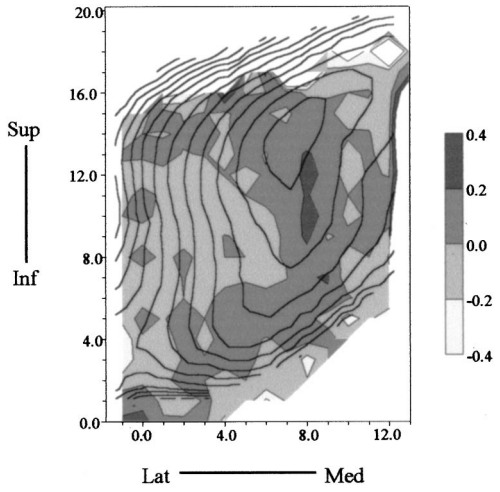

FIG. 10. Impression no. 5. Canal field, 400-μm exclusion limit, area-matching difference data map, overlaid with closed-jaw map. Solution contains 62% of points. The difference data map does not coincide well with the closed-jaw contour map at the superior and inferior borders. All units in mm.

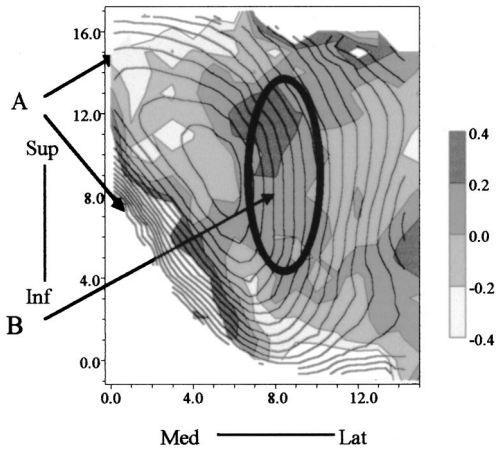

FIG. 11. Distortion of canal, loss of data. Impression no. 8, difference data (400 mm exclusion limit) contour map overlaid with closed-jaw data contour map. (A) Loss of data due to lack of overlap/distortion of region; (B) Difference data generally positive in region around bend in canal (heavy oval).

tion provides a better match than the first. Whether this result is the correct match is a matter of clinical judgment, as is whether the result provides meaningful information about the relationship between the two surfaces.

E. Increased flexion at the first bend

Distortion of the canal could occur in two general areas: within the body of the field and at the edges. Figure 11 shows loss of data due to distortion at the superior and inferior border of the canal. Figure 11 also shows a central region near or around the bend in the canal where the difference data are generally positive, whereas the remainder of the data are generally negative. Figure 12 represents an interpretation of the general form of Fig. 11. Where the form of the open-jaw impression data (thick line) passes above the closed-jaw impression data (thin line), the difference data are positive. Where the open-jaw data passes below the closed-jaw data, the difference data are negative.

This finding does seem to support the observation (Grenness, 1990) that open-jaw and closed-jaw impressions can be readily identified due to an increased definition of the first bend in the canal.

However, Fig. 12 does not represent the movement that has occurred. Area matching has matched the surfaces over their entire surface. The medial aspect of the canal, on the other hand, is fixed as it merges into the bony part of the

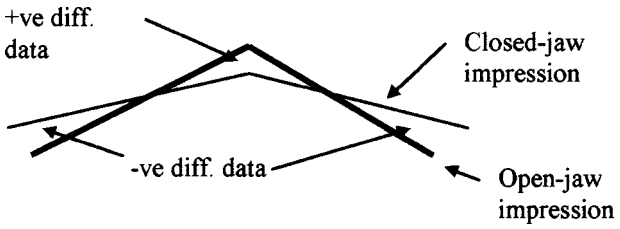

FIG. 12. Line drawing representing a horizontal slice through the anterior surface of canal. Increased flexion of the canal leads to a change in sign of the difference data as shown in Fig. 11.

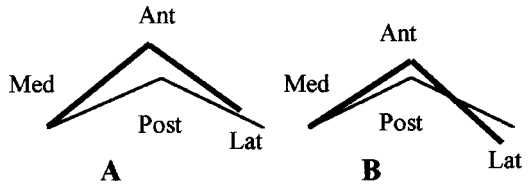

FIG. 13. Line drawing representing a horizontal slice through the anterior surface of canal. Left ends (medial) coincide. (A) Larger anterior movement at bend, small anterior movement in canal; (B) smaller anterior movement at bend, posterior movement of tragus.

canal. When Fig. 12 is redrawn such that the medial part of the canals coincide, two general possibilities arise (Fig. 13).

Flexion at the bend in the canal may occur in conjunction with a larger anterior movement at the bend and a smaller anterior movement of the tragus [Fig. 13(A)], or a smaller anterior movement at the bend and a posterior movement of the lateral part of the tragus [Fig. 13(B)]. Area matching the medial part of the field is needed in order to differentiate between these two general possibilities. However, because of the essentially cylindrical nature of the canal in this region, area matching is likely to result in significant barreling and widely variant multiple solutions and was therefore not trialed. The most likely means of matching this portion of the canal would involve including data from surrounding anatomical structures not directly a part of the external ear.

If the difference data map in Fig. 11 had a common factor of 300 μm added across the entire field, this would have the approximate effect of aligning the medial part of the canal into the same frontal plane. The region at the bend in the canal would now show differences up to 600 μm. This is consistent with Oliveira (1997), who found that the average increase in A–P direction in adults was 0.7 mm.

F. Direction of movements

A summary of the combinations of movements appears in Table IX. Movement of the canal inferiorly, laterally, and in a mixed anterior/posterior is the most common movement of the ears studied. The sample size was not large enough to draw conclusions in this regard. However, the distribution of movements does hint at trends.

Comparing the distribution of movement in Table IX with the canal area-matching results (Tables V and VI) does not give any indication of a direct relationship between an increased amount of distortion and direction of movement. In particular, there is no obvious trend between increased distortion and mixed A–P movement.

Each of the movements was recorded as movement of the canal relative to the concha. It is expected that a substantial component of the movement was a result of the concha moving relative to the canal. For example, it is not thought that the canal region moves significantly in the S–I plane. It is more likely that it is the pinna as a whole that moves in the S–I-plane in these cases.

In the A–P direction, the absolute mean of the range of movement was 3.1 mm (Table VIII). This figure combines anterior, posterior, and mixed movements; however, it does give a measure of the quantum of movement. As noted

TABLE IX. Distribution of movements.

Movement	Inferior			Superior		No S–I
A–P	Ant	Mixed	Post	Ant	Post	Ant
Lateral	13	4,11,14	2,6	3		
Medial	7	8		9	10	
No M–L		12				1,5

above, flexion in the canal may account for 0.7-mm average movement across the entire field. If movements are considered relative to the skull, up to 80% of the movement may be provided by the pinna and 20% or greater by the canal.

Posterior movement of the canal relative to the concha will result in force being applied to the surface of an ITE hearing aid if present. These findings do not show that the canal itself has narrowed in the A–P direction. However, while a CIC hearing aid may not extend into the bowl of the concha, the cartilage that forms the concha also provides a portion of the posterior wall of the canal. Thus, it is possible that anterior movement of the concha (and a portion of the posterior wall of the canal e.g., Fig. 14) is responsible for some CICs sliding out of the ear as described by Pirzanski (1996).

G. Symmetry

A review of the overlaid contour plots of left and right ears, subjects 5 to 8, demonstrates a degree of symmetry in both the direction and quantum of movement. The difference in movement between right and left ears in the same subject was approximately 100 to 1200 μm in the x axis (S–I) and 440 to 1300 μm in the y axis (M–L). In no case was there movement in opposite directions between ears, although there was no movement in some cases.

None of the subjects studied had a history of TMJ dysfunction. No subject had a jaw deviation from the center line upon opening, an indication of restricted joint mobility on the side to which the jaw deviates. If the sample size was increased or subjects selected who had a known history of TMJ dysfunction with a deviation, it could be expected that greater asymmetry between the right and left ears might be found.

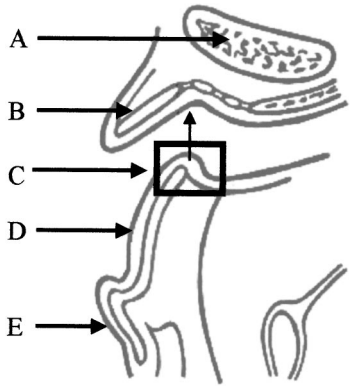

FIG. 14. Horizontal section through right ear. Anterior movement of part of concha that forms the posterior wall of the canal. (A) Mandibular condyle; (B) Tragus; (C) That part of concha forming posterior wall of canal; (D) Concha; (E) Antihelix.

Movements have also been shown in the S–I and M–L directions. These were of a smaller magnitude, approximately 1.5 mm, but are still of clinical significance. M–L movements may provide an additional mechanism for the dislodgement of hearing aids.

H. Clinical evaluation of movement

The quantum, direction, and combination of movements demonstrated in this study point to the need for a protocol and method of clinical evaluation and/or technique that aids clinicians and hearing-aid users. Further study is required to determine whether correlations exist between specific patterns of movement and specific clinical problems. Further detailed study of morphologic change in the external ear, especially the posterior wall, related to jaw and facial movements should yield further insights into the problems associated with the wearing of hearing aids.

V. CONCLUSION

Area-based matching has been found to be a reliable method of enhancing the alignment of coordinate data and evaluating the conformation/distortion between surfaces.

The mapped concha regions did not undergo clinically significant deformation during jaw movement. The anterior wall of the canal generally underwent greater deformation than the concha regions. However, the amount of deformation was not in itself clinically significant.

Movement of the anterior wall of the canal relative to the concha was significant. This study has demonstrated a range of movement combinations of the anterior wall of the canal relative to the concha in three dimensions. Most significantly, the canal has moved anteriorly in five cases, posteriorly in three cases, and a combination of anteriorly and posteriorly in four cases.

Narrowing or partial narrowing of the ear canal has occurred during jaw opening in 7 out of 14 ears studied. This study does not support previous reports that suggest that the ear canal only widens with jaw opening.

Movement of the canal relative to the bony meatus could not be evaluated in this study. The most likely means of matching this portion of the canal would involve including data from surrounding bony anatomical structures not directly a part of the external ear. Mapping of the entire tissue surface of ear impressions or the actual external ear, together with cranial reference areas, remains a valuable project for study.

ACKNOWLEDGMENTS

We thank Susan Grenness and the Tasmanian Center for Hearing for the recruitment of subjects and taking impressions, Gordon Sanson for assistance with the Reflex microscope, and Harvey Mitchell for the use of DS MATCH proprietary software.

Abel, S. M., Rockley, T., Goldfarb, D., and Hawke, M. (**1990**). ''Outer ear canal shape and its relation to the effectiveness of sound attenuating earplugs,'' J. Otolaryngol. **19**(2), 92–95.

Alvord, L. S., and Farmer, B. L. (**1997**). ''Anatomy and orientation of the human external ear,'' J. Am. Acad. Audiol. **8**, 383–390.

Creston, J. E. (**1965**). ''Collapse of the ear canal during routine audiometry,'' J. Otolaryngol. Otol. **79**, 893–901.

Grenness, S. K. (**1990**). Personal communication. Tasmanian Centre for Hearing, Hobart.

Harvey, B. R. (**1995**). *Practical Least Squares* (The School of Geometric Engineering, University of NSW, Sydney).

Mitchell, H. (**1995**). DS MATCH, Version 23.

Morgan, R. (**1987**). ''The foundation—a good impression,'' Hear. Instrum. **38**(4), 20–57.

Oliveira, R. J., Hammer, B., Stillman, A., Holm, J., Jons, C., and Margolis, R. H. (**1992**). ''A look at ear canal changes with jaw motion,'' Ear Hear. **13**(6), 464–466.

Oliveira, R. (**1997**). ''The active ear canal,'' J. Am. Acad. Audiol. **8**, 401–410.

Parslow, J. (**1994**). Personal communication. CSIRO, Hobart.

Pirzanski, C. Z. (**1996**). ''An alternative impression-taking technique: The open-jaw impression,'' Hearing J. **49**(11), 30–33.

Romanes, G. J. (editor) (**1972**). *Cunningham's Textbook of Anatomy*, 11th ed. (Oxford University Press, London).

Scott, P. J. (**1981**). ''The reflex plotters: Measurement without photographs,'' Photogramm. Rec. **10**(58), 435–446.

Smith, C. R., Borton, T. E., Patterson, L. B., Mozo, B. T., and Camp, R. T. (**1980**). ''Insert hearing protector effects,'' Ear Hear. **1**(1), 263–2.

Speculand, B., Butcher, G. W., and Stephens, C. D. (**1988**). ''Three-dimensional measurement: The accuracy and precision of the reflex microscope,'' Br. J. Oral Maxillofac. Surg. **26**, 276–283.

Stinson, M. R., and Lawton, B. W. (**1989**). ''Specification of the geometry of the human ear canal for the prediction of sound-pressure level distribution,'' J. Acoust. Soc. Am. **85**, 2492–2503.

SURFER 3D (**1997**). Golden Software, Version 6.04.

Van Willigan, J. (**1976**). ''Some morphological aspects of the meatus acusticus externus in connection with mandibular movements,'' J. Oral Rehabil. **3**, 299–304.

Ventry, I., Chaiklin, J., and Boyle, W. (**1961**). ''Collapse of the ear canal during audiometry,'' Arch. Otolaryngol. **73**, 727–731.

Wilkinson, T. M., and Crowley, C. M. (**1994**). ''A histologic study of retrodiscal tissues of the temporomandibular joint in the open and closed position,'' J. Orofac. Pain **8**(1), 7–17.

Zemplenyi, J., Gilman, S., and Dirks, D. (**1985**). ''Optical method for measurement of ear canal length,'' J. Acoust. Soc. Am. **78**, 2146–2148.

On the detection of early cochlear damage by otoacoustic emission analysis

M. Lucertini
Italian Air Force—CSV Aerospace Medicine Department, Pratica di Mare AFB, 00040 Pomezia (Roma), Italy

A. Moleti
Dipartimento di Fisica, Università di Roma "Tor Vergata," Via della Ricerca Scientifica, 1, 00133 Roma, Italy

R. Sisto
Dipartimento Igiene del Lavoro, ISPESL, Via Fontana Candida, 1, 00040 Monte Porzio Catone (Roma), Italy

(Received 18 July 2001; revised 7 October 2001; accepted 12 November 2001)

Theoretical considerations and experimental evidence suggest that otoacoustic emission parameters may be used to reveal early cochlear damage, even before it can be diagnosed by standard audiometric techniques. In this work, the statistical distributions of a set of otoacoustic emission parameters chosen as candidates for the early detection of cochlear damage (global and band reproducibility, response level, signal-to-noise ratio, spectral latency, and long-lasting otoacoustic emission presence) were analyzed in a population of 138 ears. These ears have been divided, according to a standard audiometric test, in three classes: (1) ears of nonexposed bilaterally normal subjects, (2) normal ears of subjects with unilateral noise-induced high-frequency hearing loss, and (3) their hearing impaired ears. For all analyzed parameters, a statistically significant difference was found between classes 1 and 2. This difference largely exceeds the difference observed between classes 2 and 3. This fact suggests that the noise exposure, which was responsible for the unilateral hearing loss, also caused subclinical damage in the contralateral, audiometrically normal, ear. This is a clear indication that otoacoustic emission techniques may be able to early detect subclinical damages. © *2002 Acoustical Society of America.* [DOI: 10.1121/1.1432979]

PACS numbers: 43.64.Jb, 43.64.Wn [BLM]

I. INTRODUCTION

The application of otoacoustic emission (OAE) pass–fail tests to neonatal screening is already a widespread and successful technique (e.g., Tognola *et al.*, 2001). As regards other possible clinical applications of OAEs, namely the early detection of subclinical cochlear damage and the objective determination of the hearing threshold, much work has still to be done.

OAE parameters have been shown to be sensitive to noise (Norton *et al.*, 1989; Furst *et al.*, 1992; Mansfield *et al.*, 1999) and ototoxic drugs, such as aspirin (Long and Tubis, 1988; Long *et al.*, 1991) and quinine sulfate (McFadden and Pasanen, 1994). This is not surprising, if one considers that OAEs are produced by the sensitive feedback mechanism, located in the outer hair cells, which is responsible for the excellent amplification and frequency selection performance of the human ear, and that the outer hair cells are the first part of the system to be damaged by ototoxic agents.

Among the several experimental techniques available for studying the OAE properties, in this work only transiently evoked OAEs (TEOAEs) and synchronized spontaneous OAEs (SSOAEs) will be considered. Correlation between hearing sensitivity, expressed by the audiometric threshold, and the OAE presence and level has been established by many authors: as regards spontaneous OAEs (SOAEs), Moulin *et al.* (1991) and McFadden and Mishra (1993) found a correlation between the global presence of SOAEs and good hearing sensitivity. In the studies by Probst *et al.* (1987) and Sisto *et al.* (2001) it was shown that this correlation is local in the frequency domain; as regards TEOAEs, Probst *et al.* (1987), Attias *et al.* (1995), and Lucertini *et al.* (1996), among many others, demonstrated the absence of TEOAEs in the audiometrically impaired frequency range, for hearing threshold levels higher than 20 dB. Prieve *et al.* (1993) and Hussain *et al.* (1998) showed also that the separation between normal-hearing and hearing-impaired ears was effectively performed above 1 kHz only, by analyzing TEOAE parameters such as response, signal-to-noise ratio (SNR), and reproducibility.

In a study on a population of workers exposed to high levels of industrial noise, Kowalska and Sulkowski (1997) found that also in the frequency ranges in which the hearing threshold of the exposed subjects was normal, their average TEOAE response was lower by 3 dB than that of a nonexposed control population. Attias *et al.* (1995) also found reduced TEOAE power and narrower frequency range in exposed normal subjects as compared with nonexposed normal subjects. Hall and Lutman (1999) have recently shown, by comparing the sensitivity and test–retest repeatability of several techniques, that OAE measures (and, particularly, maximum-length sequences TEOAEs) are more effective

than pure-tone audiometry in detecting mild hearing loss. These results may be considered a strong indication that the reduced TEOAE reponse could be a good indicator of early cochlear damage in audiometrically normal ears. On the other hand, interpersonal variability and test–retest fluctuations of the measured quantities, evaluated for TEOAEs by Harris *et al.* (1991), Marshall and Heller (1996), and Hall and Lutman (1999), either intrinsic or due to instrumental factors, make it difficult to demonstrate the practical applicability of these research findings to the early detection of subclinical cochlear damage. However, in the light of the above results, it is expected that a statistical correlation between exposure to noise and OAE parameters could be observed, particularly by using frequency band selective indicators.

In this work, a set of OAE measurable parameters has been analyzed on a population of audiometrically normal and impaired young males. Standard OAE parameters, such as global and band reproducibility, response level, and SNR were used. Other parameters were also used, such as the OAE spectral latency and the presence of long-lasting OAEs, which had also been recently shown to be correlated to audiometrically determined hearing loss (Sisto *et al.*, 2001; Sisto and Moleti, 2002). All the impaired subjects had been exposed to noise during their military training with firearms. The impaired population (22 subjects) showed unilateral hearing loss, with an audiometrically normal contralateral ear. It is reasonable to assume that occurrence of subclinical cochlear damage should be expected in the normal ears of these exposed and unilaterally impaired subjects more frequently than in the ears of nonexposed bilaterally normal subjects. In this case OAE parameters should permit us to show a difference between these two populations, which would fall in the same audiometric category, according to a standard dichotomous criterion. To test this hypothesis, a statistical analysis has been performed, comparing the distributions of a set of OAE parameters, among three classes of ears: (1) ears of nonexposed bilaterally normal subjects, (2) normal ears of exposed subjects with unilateral audiometric high-frequency hearing loss, and (3) their impaired ears. The aim of the work was to understand if the OAE average parameters of these three subsets showed any significant ordering, and, particularly, if those of class 1 were significantly different from those of class 2.

II. METHOD

In this work a population of 138 ears has been studied. The ears belong to 69 young male subjects (age ranging from 18 to 25 years). They were classified, according to a standard tonal audiometric test, in three classes: (1) ears of nonexposed bilaterally normal subjects (47 subjects), (2) audiometrically normal ears of subjects affected by unilateral high-frequency hearing loss (22 subjects), caused by impulsive noise exposure, and (3) the impaired ears of the same subjects. All subjects were selected on the basis of their statement that they have had no previous exposure to either occupational or recreational noise. Exposed subjects had served for one year in the army. None of them had preexisting hearing loss. During their service they had been exposed, without ear protection, to firearm noise. Thus hearing loss was in all cases presumably related to training with firearms, because the subjects had not been previously exposed to other ototoxic agents. All subjects underwent an otoscopy with removal of debris and wax from the ear canal, and an impedance test, before being analyzed for OAEs, to rule out possible bias due to the external and/or middle ear dysfunction. Possible bias due to a side effect on otoacoustic emissions was ruled out by the presence in our sample of the same number of right and left impaired ears in the subjects affected by unilateral hearing loss (McFadden, 1993). The equal number of right and left ear losses is due to the use of either guns or rifles, which, in right-handed people, tend to cause damage in the left and right ear, respectively.

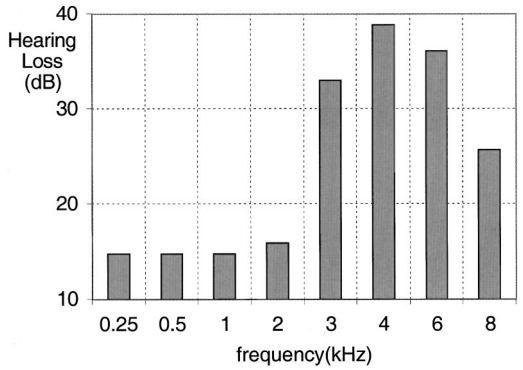

FIG. 1. Average audiometric hearing loss of the impaired ears. The loss pattern is that typical of impulsive noise-induced hearing loss.

Pure tone audiograms were recorded in an acoustically shielded room, using a clinical audiometer Amplaid A-460, equipped with TDM-39 headphone, according to the procedure described by Yantis and Katz (1994). The audiometric test frequencies are 0.25, 0.5, 1, 2, 3, 4, 6, and 8 kHz. The examined ear is conventionally defined ''normal'' if no threshold shift larger than 20 dB is found over the whole frequency range. For threshold shifts larger than 20 dB in any audiometric range $f \geqslant 3$ kHz, the ear is defined ''high-frequency impaired.'' The global audiometric behavior of the impaired ears belonging to class 3 is reported in Fig. 1, to show that the audiometric hearing loss pattern is indeed that characteristic of noise-induced high-frequency hearing impairment.

For threshold values exceeding 20 dB an accurate threshold search was performed, increasing the stimulus by steps of 5 dB. Unfortunately, as these data were originally recorded for clinical screening purposes, in the normal ears no accurate threshold search was performed below 10–15 dB, so, in the normal range, the recorded threshold value is just an upper limit for the real one. As a consequence, a significant difference between the average audiometric thresholds of the ears of classes 1 and 2 cannot be excluded, the only constraint being that the real average threshold shift is in both cases below 15 dB over the whole frequency range.

TEOAE recordings were obtained using the standard ILO-96 system in the nonlinear mode of acquisition, with a stimulus intensity of 80 ± 3 dB. The standard ILO window (from 2.5 to 20 ms, with a linear ramp from 2.5 to 5 ms) was

applied to the data. The TEOAE recordings were processed off-line by using a dedicated software developed in LabVIEW (National Instruments) to compute the standard OAE parameters (global and band reproducibility, response and SNR) and the TEOAE spectral latency. Two average waveforms $A(t)$ and $B(t)$ are independently registered by the ILO System. In this work, the OAE parameters have been computed starting from the ILO raw data $A(t)$ and $B(t)$, and it has been verified that the computed values of the parameters defined below coincide within 1% (for reproducibility) or within 0.1 dB (for signal and noise levels) with the corresponding ILO parameters.

The global reproducibility of the response is defined here as the correlation coefficient of $A(t)$ and $B(t)$:

$$\text{GRepro} = \frac{\langle A(t)B(t)\rangle}{\sigma(A)\sigma(B)}, \tag{1}$$

or, equivalently, from the FFTs of $A(t)$ and $B(t)$, respectively indicated here as $A'(f)$ and $B'(f)$, as

$$\text{GRepro} = \frac{\int_0^{f_{\max}} \text{Re}(A'^{*}B')\,df}{\sqrt{\int_0^{f_{\max}}|A'|^2\,df \int_0^{f_{\max}}|B'|^2\,df}}. \tag{2}$$

The global response is defined here as the acoustic level in dB SPL of the correlation function of $A(t)$ and $B(t)$:

$$\text{GResp} = 10\log\left\langle \frac{A(t)B(t)}{p_0^2}\right\rangle, \tag{3}$$

where p_0 is the standard pressure level $=2\times10^{-5}$ Pa, or, equivalently,

$$\text{GResp} = 10\log\left(\int_0^{f_{\max}} \text{Re}\left(\frac{A'^{*}(f)B'(f)}{p_0^2}\right) df\right). \tag{4}$$

A rough noise estimate may be obtained from the difference between the waveforms A and B. In this work the noise global level is estimated from the rms value of $(A-B)$:

$$\text{Noise} = 10\log\left\langle \frac{(A(t)-B(t))^2}{2p_0^2}\right\rangle, \tag{5}$$

or, in the frequency domain, by

$$\text{Noise} = 10\log\left(\int_0^{f_{\max}} \frac{|A'(f)-B'(f)|^2}{2p_0^2} df\right). \tag{6}$$

The global SNR is of course defined as

$$\text{SNR} = \text{GResp} - \text{Noise}. \tag{7}$$

Reproducibility, response, and SNR within nth-octave bands have also been evaluated, using the frequency domain formulation, and integrating over the desired frequency band. The frequency analysis was performed in nth-octave bands, with $n=2,3,6$.

Spectral latency was measured by means of a wavelet transform technique based on the iterative application of filter banks to the TEOAE waveform. It is defined as the delay between the stimulus and the maximum of the wavelet component of a given octave band. Fast wavelet transform (Mallat, 1998) was performed by iterative application of perfect reconstruction FIR filter banks. The wavelet transform $W(f_i,t)$ of a signal s is obtained by computing the inner product of s with a set of basis functions ζ_i, named wavelets, as a function of the time shift t:

$$W(f_i,t) = \int s(t')\zeta_i(t'-t)\,dt'. \tag{8}$$

The wavelet functions $\zeta_i(t)$ are scaled (compressed) versions of a mother wavelet $\phi(t)$, whose Fourier transform is that of a band-pass filter, so the convolution integrals of Eq. (8) perform the band-pass filtering of s around the frequencies f_i. The functions $W(f_i,t)$, which will be called wavelet coefficients in the following, give a time-frequency representation of the evolution of the signal s. Filters corresponding to linear spline biorthogonal wavelets have been used in this work. Four octave bands were analyzed: 0.39–0.78 kHz, 0.78–1.56 kHz, 1.56–3.12 kHz, and 3.12–6.25 kHz.

SSOAEs of the same subjects were also recorded by the ILO-96 system. The 80-ms recordings have been off-line analyzed, to search for long-lasting OAEs, according to the method described in Sisto *et al.* (2001). The method consists in dividing the 80-ms interval in seven 50% overlapping time intervals of duration $T\sim20$ ms. Each interval is Hanning windowed and FFT analyzed. The first time interval is not used because it is perturbed both by linear ringing (because SSOAE are recorded using the linear paradigm) and by the OAE delay. The resulting six low resolution spectra allow for roughly estimating the characteristic decay time of the excited spectral lines in the 80 ms following the stimulus. In this analysis, OAEs are conventionally defined ''long-lasting'' if their spectral line amplitude exceed local noise for at least 40 ms after the click stimulus subministration.

For the three classes of ears, the statistical distributions of all the above parameters, over the whole set of registrations belonging to each class, have been analyzed, and the statistical significance of the differences between contiguous

TABLE I. Average global and half-octave-band SNR for the three classes of ears. Statistical comparison of the SNR distributions of contiguous classes of ears. Quoted errors represent one standard deviation of the average.

Class	Global SNR	SNR					
		1 kHz	1.4 kHz	2 kHz	2.8 kHz	4 kHz	5.6 kHz
1	12.7±0.5	16.2±0.7	16.5±0.6	12.9±0.5	10.7±0.6	8.4±0.6	−2.7±0.6
2	9.0±1.4	14.4±1.8	14.0±1.3	6.8±1.9	4.0±1.8	2.6±1.5	−5.8±1.4
3	8.1±1.1	12.7±1.1	13.4±1.1	6.0±1.8	−1.3±2.4	−1.4±1.6	−7.9±1.3
$P_{1\text{-}2}(t)$	2×10^{-2}	ns	ns	5×10^{-3}	3×10^{-3}	2×10^{-3}	ns
$P_{2\text{-}3}(t)$	ns	ns	ns	ns	ns	ns	ns

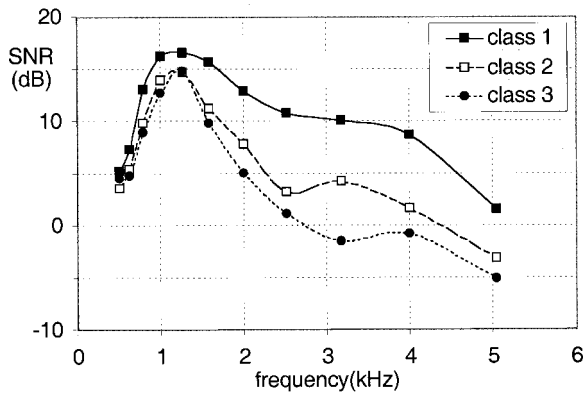

FIG. 2. Third-octave-band average OAE SNR for the three classes of ears. Above 1 kHz there is a clear difference between class 1 (ears of nonexposed bilaterally normal subjects), class 2 (audiometrically normal ears of subjects affected by unilateral noise-induced hearing loss), and class 3 (hearing-impaired ears of the same subjects). A very similar behavior is observed for reproducibility and response.

classes has been evaluated according to Student's *t*-test. A 95% confidence level ($P<0.05$) was arbitrarily chosen as a criterion of significance.

III. RESULTS

As it is evident from their definitions, SNR, reproducibility, and response are strictly correlated parameters, because the noise level is almost independent of the response level, and reproducibility is just a different definition of the SNR. Thus it is not surprising that very similar results are obtained using any of these parameters. In Table I the average values of SNR, both global and relative to frequency bands, are shown for the three classes of ears. There is a clear trend indicating that SNR gradually decreases going down from class 1 through 3. The statistical comparison between the distributions of contiguous classes, shown in Table I, indicates that the difference between classes 1 and 2 is significant while that between classes 2 and 3 is not. This could partly be due also to the smaller impaired sample. In Fig. 2 the band SNR is shown with a slightly higher frequency resolution, in thirds of octave. The difference between classes 1 and 2 is evident for $f>1$ kHz. Due to the above-mentioned correlation with the SNR, very similar results have been obtained for the reproducibility, as shown in Table II, and for the signal response, as shown in Table III.

As shown in Tables I–III, statistically significant differences between classes 1 and 2 can be evidenced by using parameters of the global TEOAEs response (reproducibility, response, and SNR), but more significant differences can be found using the corresponding spectral parameters, excluding the lowest frequency bands, in which all ears were audiometrically normal.

As regards the spectral latency, an analogous result can be found, in the octave-band immediately below the audiometric damage. In Fig. 3 the average OAE spectral latencies in the four octave bands are shown for the three classes of ears. The only significant difference is observed between classes 1 and 2 in the 1.56–3.12-kHz frequency band, with a probability for the student's parameter $P_{1,2}(t)=2\times10^{-3}$.

In a previous study (Sisto *et al.*, 2001) it had been shown that long-lasting OAEs (including SOAEs) are absent in audiometrically impaired frequency bands and that the average total number of long-lasting OAEs in impaired ears is significantly smaller than in normal ears. In this study, the average total number of long-lasting OAEs in the ears of class 1 (2.32) resulted larger than that found in the ears of classes 2 and 3 (1.57 and 1.14, respectively). This decreasing trend going from class 1 to 3 is in qualitative agreement with all the above results, and the difference between classes 1 and 3, evaluated with Student's *t*-test, is significant, but, in this case, the difference between the distributions of classes 1 and 2 is not statistically significant, due to their large variances and to the small number of exposed subjects.

IV. DISCUSSION

All the examined OAE parameters showed a clear monotonic behavior going from class 1 to 3. The difference between classes 1 and 3 was expected, because all these OAE parameters had already proven to be significantly correlated to audiometric hearing loss. It is natural to assume that the exposed normal ears with a contralateral impaired ear are more probable candidates for subclinical early impairment than the ears of nonexposed bilaterally normal subjects are. The main result of this work is that, for all the examined OAE parameters, classes 1 and 2 (nonexposed and exposed normal ears, respectively) proved to be significantly different from each other, though, from a clinical point of view, all these ears would fall in the normal ear category, according to a standard dichotomous audiometric criterion [hearing loss (HL)$<$20 dB]. Furthermore, the difference between classes 1 and 2 was always more significant than that between classes 2 and 3. This result confirms and extends the findings by Attias *et al.* (1995) and Kowalska and Sulkowski (1997), and is a clear indication that OAE parameters may be

TABLE II. Average global and half-octave-band reproducibility (%) for the three classes of ears. Statistical comparison of the reproducibility distributions of contiguous classes of ears. Quoted errors represent one standard deviation of the average.

Class	Global repro	Repro					
		1 kHz	1.4 kHz	2 kHz	2.8 kHz	4 kHz	5.6 kHz
1	92±1	94±1	95±1	92±1	87±2	81±2	36±3
2	81±4	86±5	93±3	69±7	53±8	57±7	23±6
3	82±3	93±2	93±2	67±7	36±9	32±7	13±5
$P_{1\text{-}2}(t)$	2×10^{-2}	ns	ns	5×10^{-3}	4×10^{-4}	2×10^{-3}	5×10^{-2}
$P_{2\text{-}3}(t)$	ns	ns	ns	ns	ns	2×10^{-2}	ns

TABLE III. Average global and half-octave-band response for the three classes of ears. Statistical comparison of the response distributions of contiguous classes of ears. Quoted errors represent one standard deviation of the average.

Class	Global response	Response					
		1 kHz	1.4 kHz	2 kHz	2.8 kHz	4 kHz	5.6 kHz
1	11.1±0.5	3.1±0.7	4.4±0.6	1.9±0.6	1.4±0.6	−2.4±0.7	−16.2±0.6
2	7.0±1.4	0.6±1.9	1.2±1.3	−4.7±1.9	−5.4±1.8	−8.0±1.6	−19.5±1.4
3	6.2±1.1	−0.6±1.4	0.9±1.2	−5.8±1.7	−11.2±2.4	−12.2±1.5	−22.1±1.3
$P_{1\text{-}2}(t)$	10^{-2}	ns	3×10^{-2}	3×10^{-3}	3×10^{-3}	4×10^{-3}	5×10^{-2}
$P_{2\text{-}3}(t)$	ns	ns	ns	ns	ns	ns	ns

used to reveal subclinical damage due to noise exposure in audiometrically normal ears. It should be noted that, in this study, the TEOAE global response difference between normal exposed ears and nonexposed normal ears is 4.1 dB (see Table III), and reaches a maximum value of 6.8 dB in the 2.8-kHz half-octave band. These differences are much larger than those reported by Kowalska and Sulkowski (1997), and largely exceed the typical test–retest fluctuations [2 dB at 3 kHz, according to Hall and Lutman (1999)]. As shown in the previous section, very similar results have also been obtained for SNR and reproducibility. This suggests that OAE parameters be particularly sensitive to subclinical cochlear damage. This fact may be explained by considering that the OAE signals are dominated by the contribution of a few resonant emissions, with fine-tuned cochlear parameters, which are significantly modified also by a very mild cochlear damage, while the global cochlear functionality, which is randomly probed by audiometric techniques looking at fixed frequencies uncorrelated to the OAE frequencies, is affected by higher levels of exposure.

As already mentioned, reproducibility, response level, and SNR are strictly correlated to each other, and the choice between them is not obvious. Response level is perhaps a more intrinsic parameter, as it is independent of the noise level of the recording apparatus, but it is still sensitive to the systematic errors associated to probe positioning. Another interesting result is related to the use of global or frequency band OAE parameters. It has been shown that the differences between the three classes are more clearly observed by separately analyzing the frequency bands in which the hearing impairment is typically found, or those contiguous to them. The lowest frequency bands' results were typically less significant, as already found by Prieve *et al.* (1993) and Hussain *et al.* (1998), also because the hearing loss is generally at higher frequencies. As a consequence, global parameters are often less significant than band parameters, also due to the large low-frequency contribution that is typically present in adult subjects.

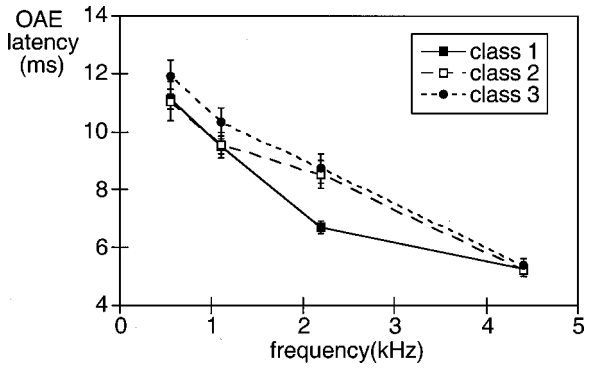

FIG. 3. Octave-band average OAE spectral latency for the three classes of ears. Error bars represent one sample standard deviation of the average. The difference between nonexposed normal ears and exposed (either normal or impaired) ears is visible in the 1.56–3.12-kHz frequency band, immediately below the impaired frequency range.

In the case of the OAE spectral latency, the interpretation of the results is more involved, and requires the use of cochlear transmission models to be meaningful. In fact, localized cochlear damage produces a frequency-dependent variation of the latency by affecting both the transmission properties of the cochlear membrane (Talmadge *et al.*, 1998) and the response time of the resonant active filter, as suggested by Don *et al.* (1998) in a study of the auditory brainstem response (ABR) latencies. However, the statistically significant difference observed also in this case between classes 1 and 2 means that also this parameter could be useful for the early detection of hearing impairment. It should be mentioned that latency is an intrinsic parameter, as response level is, and has the additional advantage of being quite insensitive to the absolute level uncertainties associated to probe positioning.

It would have been very interesting to compare the "normal" hearing threshold distributions of populations 1 and 2. This would have needed an accurate (±2 dB) determination of the audiometric threshold in the 0–20-dB range. Unfortunately, as explained in Sec. II, the audiometric thresholds have been determined with a standard clinical accuracy (±5 dB) and only in the impaired range. For this reason, a statistically significant difference between the audiometric thresholds of classes 1 and 2 cannot be excluded, even if it can be stated that all thresholds are lower than 15 dB HL. Thus the conclusion that the OAE parameters, which have been shown to be sensitive to exposure, should also be more sensitive than audiometry would not be fully motivated by the present data. However, this point has already been demonstrated by Hall and Lutman (1999), and their results may be used to complement the present work. According to the slope of the TEOAE response–audiometric threshold relation reported by Hall and Lutman (1999), the expected difference between the average thresholds of populations 1 and 2 may be estimated to be on the order of 8 dB at 3–4 kHz, to be compared to a test–retest uncertainty on the order of 5 dB at these frequencies (Atherley and Dingwall-Fordyce, 1963; Hall and Lutman, 1999). These estimates may be compared

to the results of this work, in which a difference on the order of 6 dB has been found between the 2–4-kHz responses, to be compared with the typical 2-dB test–retest fluctuations (Hall and Lutman, 1999). The clear separation between the band parameters of the three classes also suggests that a dichotomous risk assessment criterion based on the measurement of these OAE parameters could be proposed for exposed populations. For example, in the examined sample, a reproducibility lower than 60% in the 2.8-kHz band was observed in 14 out of 22 exposed normal ears, and only in 7 out of 94 nonexposed normal ears. For this sample, a reproducibility lower than 60% in the 2.8-kHz band is therefore an indication of probable exposure-induced early cochlear damage, and would suggest adopting some precaution regarding the further exposure of that subject. Of course, the determination of a threshold level providing an adequately low level of false alarms and a sufficient protection of the exposed subjects would need a much larger statistical sample and an accurate quantification of the exposure. The standard dichotomous audiometric criterion (HL$<$20 dB) would have put all these ears in the same category, and using a lower cutoff audiometric threshold would face the problem of the test–retest variability, which for audiometry is particularly large [5–10 dB within the 0.5–4-kHz range and even larger outside (Atherley and Dingwall-Fordyce, 1963)].

V. CONCLUSIONS

In this work a set of OAEs parameters was analyzed in a population of ears divided in three classes: (1) ears of nonexposed, bilaterally normal subjects, (2) audiometrically normal ears of subjects affected by noise-induced unilateral high-frequency hearing loss, and (3) impaired ears of the same last subjects.

For the whole set of OAE parameters analyzed, a statistically significant difference was generally found between classes 1 and 2, confirming and extending previous results of Attias *et al.* (1995) and Kowalska and Sulkowski (1997). This difference largely exceeds the differences observed between classes 2 and 3, which are not statistically significant, with the only exception of the 4-kHz reproducibility. In other words, the audiometrically normal ears of exposed subjects affected by a unilateral hearing loss resulted more similar, as regards all OAE parameters, to the impaired ears than to the ears of nonexposed bilaterally normal subjects. This fact suggests that the noise exposure, which was responsible for the unilateral hearing loss, also caused a subclinical (from the audiometric point of view, using the standard dichotomous criterion HL$<$20 dB) damage in the contralateral ear. Thus OAE techniques seem to be useful to early detect such a kind of subclinical damage in exposed populations.

It is also important to point out that statistically significant differences between classes 1 and 2 can be evidenced by using parameters of the global TEOAEs response (reproducibility, response level, and SNR, indifferently), but much more significant differences can be found using the corresponding spectral parameters, excluding the lowest frequency bands. As regards the spectral latency, an analogous result can be found, in the spectral band immediately below the audiometric damage. As regards the long-lasting OAEs, their average number decreases from class 1 to 3.

All the results of this work support the idea that OAE parameters can be used to successfully discriminate a population of normal ears from one of early damaged, but still audiometrically normal, ears.

The application of this analysis method to a larger statistical sample and an accurate determination of the audiometric threshold are necessary to confirm the results of this work. This would permit us to quantitatively compare the effectiveness of the OAE and audiometric techniques, and to determine the threshold levels of the OAE parameters to be used for the early diagnosis of probable cochlear damage in exposed subjects. This diagnosis could be important to suggest performing other clinical tests, and to limit the subject's exposure before the occurrence of irreversible damage.

Atherley, G. R., and Dingwall-Fordyce, I. (**1963**). ''The reliability of repeated auditory threshold determination,'' Br. J. Ind. Med. **20**, 231–235.

Attias, J., Furst, M., Furman, V., Reshef, I., Horowitz, G., and Bresloff, I. (**1995**). ''Noise-induced otoacoustic emission loss with or without hearing loss,'' Ear Hear. **16**, 612–618.

Don, M., Ponton, C. W., Eggermont, J. J., and Kwong, B. (**1998**). ''The effects of sensory hearing loss on cochlear filter times estimated from auditory brainstem response latencies,'' J. Acoust. Soc. Am. **104**, 2280–2289.

Furst, M., Reshef, I., and Attias, J. (**1992**). ''Manifestations of intense noise stimulation on spontaneous otoacoustic emission and threshold microstructure: Experiment and model,'' J. Acoust. Soc. Am. **91**, 1003–1014.

Hall, A. J., and Lutman, M. E. (**1999**). ''Methods for early identification of noise-induced hearing loss,'' Audiology **38**, 277–280.

Harris, F. P., Probst, R., and Wenger, R. (**1991**). ''Repeatability of transiently evoked otoacoustic emissions in normally hearing humans,'' Audiology **30**, 135–141.

Hussain, D. M., Gorga, M. P., Neely, S. T., Keefe, D. H., and Peters, J. (**1998**). ''Transient evoked otoacoustic emissions in patients with normal hearing and in patients with hearing loss,'' Ear Hear. **19**, 434–449.

Kowalska, S., and Sulkowski, W. (**1997**). ''Measurements of click-evoked otoacoustic emissions in industrial workers with noise-induced hearing loss,'' Int. J. Occup. Med. Environ. Health **10**, 441–459.

Long, G. R., and Tubis, A. (**1988**). ''Modification of spontaneous and evoked otoacoustic emissions and associated psychoacoustic microstructure by aspirin consumption,'' J. Acoust. Soc. Am. **84**, 1343–1353.

Long, G. R., Tubis, A., and Jones, K. L. (**1991**). ''Modeling synchronization and suppression of spontaneous otoacoustic emissions using Van der Pol oscillators: Effects of aspirin administration,'' J. Acoust. Soc. Am. **89**, 1201–1212.

Lucertini, M., Bergamaschi, A., and Urbani, L. (**1996**). ''Transient evoked otoacoustic emissions in occupational medicine as an auditory screening test for employment,'' Br. J. Audiol. **30**, 79–88.

Mallat, S. (**1998**). *A Wavelet Tour of Signal Processing*, 2nd ed. (Academic, San Diego), pp. 255–272.

Mansfield, J. D., Baghurst, P. A., and Newton, V. E. (**1999**). ''Otoacoustic emissions in 28 young adults exposed to amplified music,'' Br. J. Audiol. **33**, 211–222.

Marshall, L., and Heller, L. M. (**1996**). ''Reliability of transient-evoked otoacoustic emissions,'' Ear Hear. **17**, 237–254.

McFadden, D. (**1993**). ''A speculation about the parallel ear asymmetries and sex differences in hearing sensitivity and otoacoustic emissions,'' Hear. Res. **68**, 143–151.

McFadden, D., and Mishra, R. (**1993**). ''On the relation between hearing sensitivity and otoacoustic emissions,'' Hear. Res. **71**, 208–213.

McFadden, D., and Pasanen, E. G. (**1994**). ''Otoacoustic emissions and quinine sulfate,'' J. Acoust. Soc. Am. **95**, 3460–3474.

Moulin, A., Collet, L., Delli, D., and Morgon, A. (**1991**). ''Spontaneous otoacoustic emissions and sensory-neural hearing loss,'' Acta Oto-Laryngol. **111**, 835–841.

Norton, S. J., Mott, J. B., and Champlin, C. A. (**1989**). ''Behavior of spontaneous otoacoustic emissions following intense ipsilateral acoustic stimulation,'' Hear. Res. **38**, 243–258.

Prieve, B. A., Gorga, M. P., Schmidt, A., Neely, S., Peters, J., Schultes, L., and Jesteadt, W. (**1993**). ''Analysis of transient-evoked otoacoustic emissions in normal-hearing and hearing-impaired ears,'' J. Acoust. Soc. Am. **93**, 3308–3319.

Probst, R., Lonsbury-Martin, B. L., Martin, G. K., and Coats, A. C. (**1987**). ''Otoacoustic emissions in ears with hearing loss,'' Am. J. Otolaryngol. **8**, 73–81.

Sisto, R., and Moleti, A. (**2002**). ''On the frequency dependence of the otoacoustic emission latency in ipoacousic and normal ears,'' J. Acoust. Soc. Am. **111**, 297–308.

Sisto, R., Moleti, A., and Lucertini, M. (**2001**). ''Spontaneous otoacoustic emissions and relaxation dynamics of long decay time OAEs in audiometrically normal and impaired subjects,'' J. Acoust. Soc. Am. **109**, 638–647.

Talmadge, C. L., Tubis, A., Long, G. R., and Piskorski, P. (**1998**). ''Modeling otoacoustic emission and hearing threshold fine structures,'' J. Acoust. Soc. Am. **104**, 1517–1543.

Tognola, G., Grandori, F., and Ravazzani, P. (**2001**). ''Data processing options and response scoring for OAE-based newborn hearing screening,'' J. Acoust. Soc. Am. **109**, 283–290.

Yantis, P. A., and Katz, J. **(1994).** ''Puretone air-conduction threshold testing,'' in *Handbook of Clinical Audiology*, 4th ed. (Williamson and Wilkins, Baltimore), pp. 97–108.

The mechanical waveform of the basilar membrane. IV. Tone and noise stimuli[a)]

Egbert de Boer[b)]
Room D2-226, Academic Medical Center, University of Amsterdam, Meibergdreef 9, 1105 AZ, Amsterdam, The Netherlands

Alfred L. Nuttall[c)]
Oregon Hearing Research Center, NRC04, Oregon Health & Science University, 3181 SW Sam Jackson Park Road, Portland, Oregon 97201-3098 and Kresge Hearing Research Institute, University of Michigan, 1301 East Ann Street, Ann Arbor, Michigan 48109-0506

(Received 6 April 2001; revised 10 July 2001; revised 20 October 2001; accepted 29 October 2001)

Analysis of mechanical cochlear responses to wide bands of random noise clarifies many effects of cochlear nonlinearity. The previous paper [de Boer and Nuttall, J. Acoust. Soc. Am. **107**, 1497–1507 (2000)] illustrates how closely results of computations in a nonlinear cochlear model agree with responses from physiological experiments. In the present paper results for tone stimuli are reported. It was found that the measured frequency response for pure tones differs little from the frequency response associated with a noise signal. For strong stimuli, well into the nonlinear region, tones have to be presented at a specific level with respect to the noise for this to be true. In this report the nonlinear cochlear model originally developed for noise analysis was modified to accommodate pure tones. For this purpose the efficiency with which outer hair cells modify the basilar-membrane response was made into a function of cochlear location based on *local* excitation. For each experiment, the modified model is able to account for the experimental findings, within 1 or 2 dB. Therefore, the model explains why the type of filtering that tones undergo in the cochlea is essentially the same as that for noise signals (provided the tones are presented at the appropriate level). © *2002 Acoustical Society of America.* [DOI: 10.1121/1.1428548]

PACS numbers: 43.64.Kc, 43.64.Bt [LMC]

I. INTRODUCTION

In the three preceding papers of the present series (de Boer and Nuttall, 1997, 2000a, 2000b), henceforth to be called Part I, Part II, and Part III, respectively, results of experiments were reported on movements of the basilar membrane (BM) in the cochlea of the guinea pig. Measurements were done with a laser velocimeter, at a cochlear location showing tuning to frequencies in the region of 15 to 18 kHz. Measured responses were compared to the response of a suitably chosen nonlinear bio-mechanical model of the cochlea. In Parts II and III it was demonstrated that via ''resynthesis'' this model can be given a response that closely matches the response of the real cochlea. The analysis includes effects of model geometry (Part II) as well as general and subtle effects of nonlinearity in the cochlea due to variations in stimulus level (Part III).

The basic stimulus signal in the experiments described was always wideband noise. This was so because we used a nonlinear cochlear model for which noise signals are optimum stimuli. The mechanical variables and operations acting in a cross section of that model are sketched in Fig. 1. For simplicity only one outer hair cell (OHC) is shown. Each OHC has an input signal, the ciliary deflection $d_{\mathrm{cil}}(x,t)$, which is directly derived from the BM velocity $v_{\mathrm{BM}}(x,t)$ by the transformation H_1. The dynamic variable x denotes position along the length of the model, and t is time; for reasons of clarity these independent variables have been omitted from the figure. The transformation H_1 is assumed to be linear, but will be frequency- and location dependent.[1] The output signal of the OHCs is the local OHC pressure $p_{\mathrm{OHC}}(x,t)$. This pressure can be considered to arise from OHC motility, or, alternatively, as resulting from a reaction force produced by the stereocilia; for the functioning of the model these alternatives are equivalent. The pressure $p_{\mathrm{OHC}}(x,t)$ gives rise to an *additive* component $p_{\mathrm{add}}(x,t)$ of the sound pressure $p(x,t)$ near the BM, again via a linear (and possibly location- and frequency-dependent) transformation, H_2. In the case where OHC activity occurs via somatic motility, most of the frequency selectivity involved in the feedback loop will be included in H_1. In the case where active reactions of stereocilia are the main source of feedback, the frequency selectivity will be more or less equally divided between H_1 and H_2 (because of reciprocity). Over a certain range of locations and frequencies the loop shown in Fig. 1 produces positive feedback, whereby the pressure $p_{\mathrm{add}}(x,t)$ acts to enhance the response (''local activity''). Transduction in the OHCs, from ciliary deflection $d_{\mathrm{cil}}(x,t)$ to local OHC pressure $p_{\mathrm{OHC}}(x,t)$, is described as a memoryless compressive nonlinearity. In the model, the nonlinearity of the OHCs is considered to be responsible for all nonlinear mechanical effects that have been observed over the normal

[a)]Preliminary data on tone versus noise responses were reported at the ARO 2000 Midwinter Meeting (Abstract No. 705).
[b)]Electronic mail (new): e.d.boer@hccnet.nl
[c)]Electronic mail: nuttall@ohsu.edu

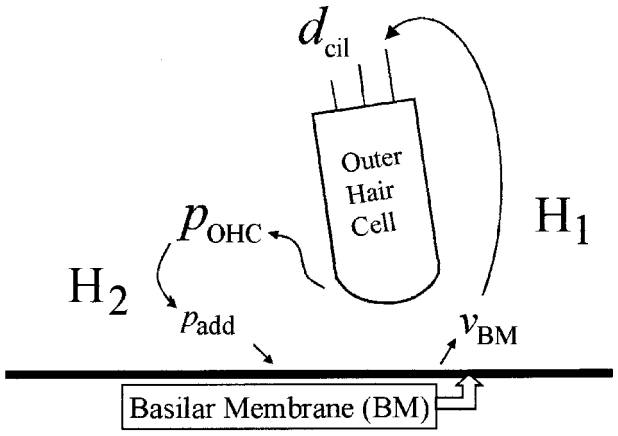

FIG. 1. Signal transformations in a cross section of the model. See the text for the meaning of symbols.

operating range of the cochlea. Note that OHCs described as memoryless nonlinearities are present throughout the cochlea, all embedded in structures with different frequency responses. This means that a model with memoryless nonlinearities can exhibit frequency-dependent nonlinearity.

The EQ-NL theorem can be applied to a nonlinear model of this type (de Boer, 1997a). This theorem is formulated in terms of input-output cross-correlation functions (ccfs) for wideband noise signals, and this is where the requirement of using noise stimuli stems from. (A short description of the theorem can be found in Appendix A of Part III.) All conclusions from the analysis relate only to responses to wideband noise signals.

If the model of Fig. 1 is a valid model, it should be equally well applicable to the case where stimuli are sinusoidal signals. This is the subject studied in the present paper. The main characteristic of the model is that the degree of saturation is fully determined by the *total* signal $d_{cil}(x,t)$ acting at the input of the OHCs. For a noise stimulus this signal will contain many components, and will be (nearly) Gaussian, but for sinusoidal stimulation it contains one dominant component and a few weaker ones, and is non-Gaussian. Furthermore, strong pure tones and noise signals have quite different distributions of the degree of OHC saturation over the length of the cochlea. For strong wideband noise signals saturation is evenly distributed, whereas for a strong tone it is more localized to the region of the response peak.

Our hypothesis is that noise components and sinusoidal signals are handled in an identical way when the average degree of saturation they evoke in the OHCs are the same. We will investigate whether the same model, with the same parameters and the same nonlinearity, can predict responses to sinusoidal signals as well as to noise signals. If it does, we can apply that model to the consideration of many more types of signal than wideband flat-spectrum noise, to formants and formant transitions in speech stimuli, for instance. Furthermore, the value of the model for predicting distortion products on the basilar membrane can be studied. In none of these applications should it be necessary to resort to time-domain computations.

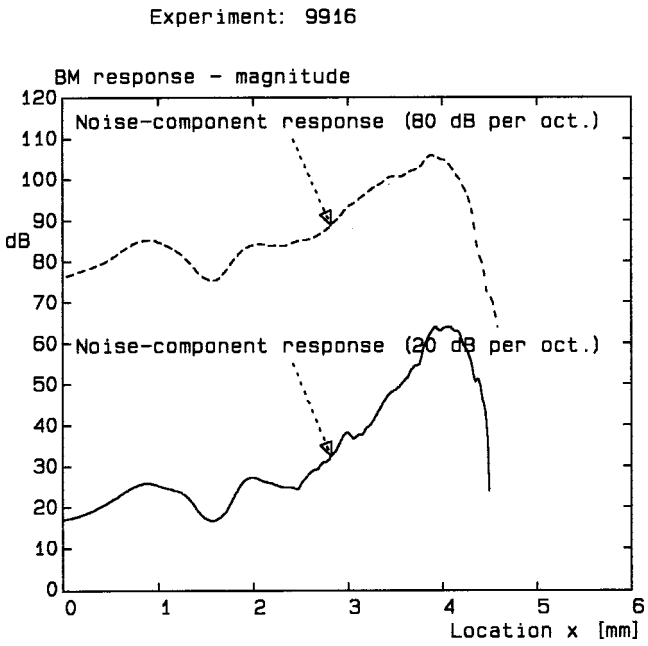

FIG. 2. Propagation of a single component of a noise stimulus (16.8 kHz) in a cochlear model. Amplitude of the response, corrected for the stapes response (see the text). On the ordinate the ratio 1 corresponds to 0 dB. Abscissa: distance from stapes/round-window location. Two stimulus levels, 60 dB apart. For the lower one, (solid line) propagation is a linear process. For the higher one (dashed line) partial saturation causes nonlinearity.

II. GENERAL CONSIDERATIONS: A STRATEGY

Let us first consider what happens to a single-frequency component of a noise signal inside the cochlea. The noise response has been measured at one location x, and has been analyzed into its frequency components.[2] The lower curve in Fig. 2 (solid line) illustrates the amplitude of the wave produced by one of the frequency components—as we imagine it to propagate in the cochlea. In this case the stimulus had a low intensity (20 dB per octave). The measured response has been transformed to a function of location x by assuming that the cochlea ''scales,'' i.e., that different frequencies (f) project to different locations (x) along the length of the cochlea. In particular, we assume that the log of the frequency f transforms linearly to location x [for more details see de Boer and Nuttall (1999)]. The abscissa in Fig. 2 denotes location x starting at the stapes. The figure shows the amplitude of the noise component at 16.7 kHz. Because this is a high frequency, and does not travel far, it is not necessary to make the model longer than 6 mm. The phase is omitted from the figure and is not considered in this report.[3]

For the solid line the noise signal was presented at 20 dB (SPL) per octave. For each frequency the spectral component is normalized with respect to the stapes velocity as if the stapes response were measured at the same frequency and *at the same spectral level*. If the cochlea operates linearly, the solid line of Fig. 2 will also show the response pattern of a 16.7-kHz *pure tone*, at least when it is plotted normalized to the stapes response *for the same stimulus*.

The BM velocity is seen to rise gradually with increasing x from the stapes location ($x=0$). In a spatial region that is specific to the frequency, the BM velocity rises more rap-

idly to reach a maximum. In that region the cochlear wave is amplified by the BM and its associated cell structures—positive feedback resulting from the loop shown in Fig. 1. After having passed that region the wave extinguishes rapidly. In the peak region, size and form of the response are controlled by the feedback loop; outside the peak region the influence of the feedback is small. As stated above, the pattern is shown for the frequency 16.7 kHz. For a component or a tone with a higher frequency the response maximum will lie more to the left, nearer to the stapes; for a lower frequency it will lie more to the right. Frequency- and place-dependent properties of the BM and the feedback loop are responsible for this type of scaling.

With stronger stimulation the cochlea will react in a nonlinear way. While the *solid* line in Fig. 2 shows the propagation of the 16.7-kHz component of a noise signal presented at 20 dB per octave, the *dashed* line shows the response to a signal at 80 dB (SPL) per octave, transformed by the same frequency-to-place (f-to-x) transformation. The response is normalized with respect to the same stapes noise response at 20 dB (SPL) per octave so that the leftmost part of the dashed curve lies 60 dB higher than the solid line. Clearly, the peak of the high-level response is depressed in size, the bandwidth is increased, and the location of the maximum has moved to the left. All three effects are well-known properties of cochlear nonlinearity. In terms of the model, the nonlinear effects are attributed to *partial saturation* of the outer hair cells (OHCs).

For a strong wide band of *noise*, the average amplitude of vibration of the BM will be about the same for all locations along the length of the cochlea. Consequently, all OHCs will be excited to about the same extent, and will be saturated to about the same degree. The 80-dB response pattern shown by the dashed line in Fig. 2 is associated with such an even distribution of saturation. For stimulation by a strong *tone* the situation is entirely different. In the initial part of the wave, near the stapes, there will be only little saturation because the wave amplitude is small. When the wave is nearing the peak, saturation becomes more and more pronounced until it reaches a maximum at the response peak. After the wave has passed the peak, saturation rapidly vanishes. The tone response should show a peak of the same general shape as a noise component when the degrees of saturation are the same. It should be clear, now, that we have to modify the formalism that we used to explain noise responses in order to accommodate tones. To explain noise responses by our nonlinear model, we used a coefficient γ, signifying the degree of saturation, $\gamma=1$ for no saturation and $\gamma=0$ for complete saturation (or absence of OHCs). See Part III of this series. The parameter γ is independent of x. In the case of tone stimulation, we have to replace this by a function $\gamma(x)$ of x. The local value of $\gamma(x)$ reflects the *local* excitation.

The principal questions we are asking and trying to answer in this paper are: (a) What is the frequency response of the cochlea measured for tones compared to that for noise? and (b) Can the nonlinear model that we used to explain noise responses be extended (in the way we just indicated) to account for the data? Finally, there probably will be differences between the responses to tones and noise. Can we explain these by the same mechanism?

III. DATA ACQUISITION AND PROCESSING

We collected data on movements of the basilar membrane (BM) in the basal turn of the guinea-pig cochlea with a laser velocimeter (see Nuttall *et al.*, 1991 and Part I).[4] In the earlier described experiments *bands of flat-spectrum pseudorandom noise* were used as acoustical stimuli and the velocity of the BM at a location tuned to a frequency between 15 and 18 kHz was measured as a function of time. One period of the noise signal contains 4096 samples, presented at the rate of 208 kHz. As a consequence, the frequency components are spaced by 50.78 Hz. Noise-response data were collected in the form of input–output cross-correlation functions (ccfs). For greater accuracy we collected ''composite ccf spectra'' responses; we this did by combining sections of ccf spectra measured with flat-spectrum stimuli of different bandwidths, central frequencies, and intensities in the same animal. The high-frequency part was measured with a noise signal 1 octave wide, presented at stimulus level L. In the lower frequency ranges the cochlea is (nearly) linear, and filtered noise bands at higher stimulus levels could be used. See de Boer and Nuttall (1999) for details. The resulting composite ccf spectrum represents the response to a noise signal that covers more than 5 octaves, from below 1 kHz to well over 40 kHz. The spectral level (in dB SPL per octave) associated with the response is the level L employed in measuring the highest frequency band.

Responses to *tones* were gathered with sinusoidal stimuli. Tone bursts were 380 ms in duration, and had by default an abrupt onset. Except for extremely strong stimuli well above the best frequency (BF) the abrupt onset had no effect on amplitude and phase of the averaged response. We verified that this was the case. All data, for noise and tone stimuli, are corrected for the stapes response.[5] Tones were presented in steps of 5 dB. In the processing of responses data could be interpolated in steps of 1 dB.

As regards inverse solution and resynthesis, the ''stylized'' three-dimensional model of Part III was used, with the same parameters. The model equations were solved by the efficient solution method described by de Boer (1998). The inverse solution produces the BM impedance, to be denoted by $Z_{\mathrm{BM}}(x,\omega)$, where the independent variable x is the longitudinal coordinate of the model and ω is constant (made equal to 2π times the best frequency for low-level signals).

IV. RESULTS I: THE MEASURED FREQUENCY RESPONSE

Figure 3 shows a typical result, response amplitudes for tones and noise, plotted together as functions of frequency, for experiment 9924. All noise response data are normalized by the stapes response measured with wideband noise presented at 50 dB (SPL) per octave. Upper and lower parts of the figure refer to two values for the noise stimulus level, 50 and 80 dB (SPL) per octave, respectively. Recall that the

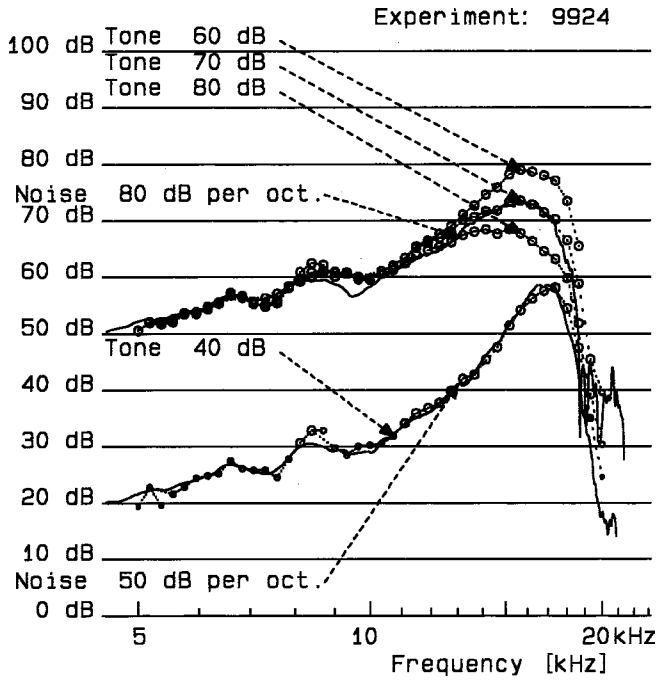

FIG. 3. Comparison of measured responses to tones (circles) and noise signal components (solid line). Experiment 9924 (amplitudes shown only). Data are corrected for the stapes response (see the text). Two stimulus levels for the noise signal, 50 and 80 dB SPL per octave. The response to the stronger noise stimulus is compared with responses to tones presented at three levels, 60, 70, and 80 dB SPL. The 70-dB response gives the best fit.

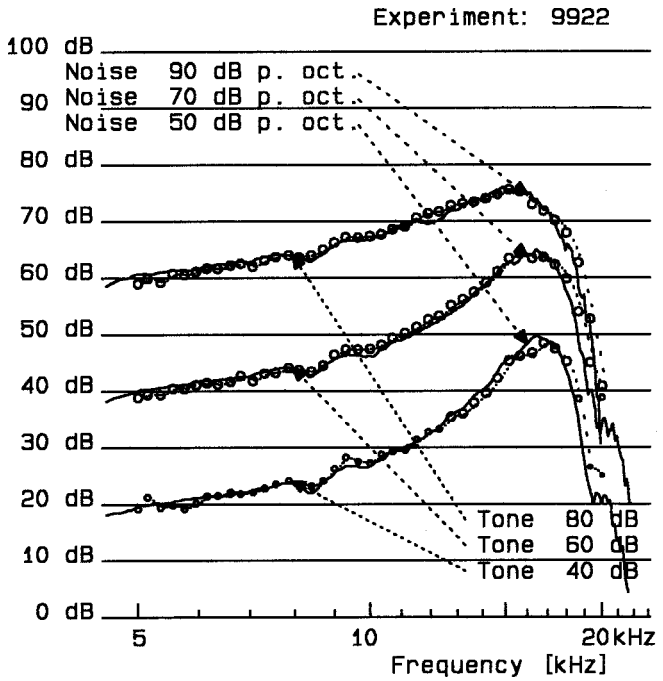

FIG. 4. Comparison of measured responses to tones (circles) and noise signal components (solid line). Experiment 9922. High-, medium-, and low-level responses superimposed (amplitudes shown only). Levels as indicated. For amplitude scaling see the text.

responses have been measured at a cochlear location that has 16.7 kHz as its best frequency for low stimulus levels.

Consider first the lowermost part of the figure; it represents weak-signal stimulation. The *solid line* shows the amplitude of the frequency response for a wideband noise signal presented at 50 dB (SPL) per octave. Each spectral component, when presented alone, would be equivalent to a tone of approx. 17 dB (SPL). The data shown are derived from a ''composite-spectrum'' file as described in Sec. III. For the solid line the amplitude plotted corresponds to the ratio of BM velocity to stapes velocity. The *small circles* show the response to single pure tones presented at 40 dB (SPL)—weak enough to render the cochlea linear. Forty-one frequencies distributed over two octaves were selected, and presented one by one. The tone responses are shown scaled as if each tone were presented at the same level (17 dB SPL) as one component of the noise stimulus. Outside the peak region some circles are drawn smaller, denoting that in the tone measurements the signal-to-noise ratio decreased to below 30 dB. Over the entire frequency range the circles practically lie on the solid curve, indicating that the cochlea is indeed reacting in a linear way. For all stimulus levels in the linear range we can expect the same type of relation between tone and noise responses. Hence, if we were to plot responses to 20- or 30-dB tones, *with appropriate scaling*, the circles would again nearly lie on the continuous line.

The upper sets of curves in Fig. 3 illustrate noise (solid line) and tone results (circles) for a higher level of the noise stimulus (80 dB SPL per octave). The scaling of the noise response is the same as before so that in the low-frequency region the solid curve (noise response) lies 30 dB above the curve for 50 dB per octave. Three sets of tone-response data are shown, measured at three stimulus levels, 60, 70, and 80 dB (SPL). For each set the tone response is scaled with respect to the stapes response at its own level minus 30 dB so that the low-frequency part of the graph nearly coincides with the noise response. This is not so in the peak region, where the sharpness depends on level. The tone response measured at 70 dB (SPL) produces the best agreement with the noise-response curve. Tones at 80 dB (SPL) produce a response that is too flat, tones at 60 dB (SPL) a response that is too sharp. For the optimum stimulus level (70 dB SPL) the frequency selectivity of the cochlea for tones is virtually the same as for noise. In other words, for that level the effect of nonlinearity is the same for single pure tones as for components of a noise signal.

Other examples of tone-to-noise comparison are shown by Figs. 4, 5, and 6. The solid lines show the noise responses, the sets of circles the tone responses. For all figures the reference level is taken from the noise record with the lowest level (for this record the amplitude is plotted as the ratio of BM to stapes velocity). In these figures three levels of stimulation are illustrated, one in the linear range and two high enough to cause appreciable nonlinearity. At the two higher levels the tone response that produces the best agreement with the noise response has been selected. For optimal agreement the stimulus level of the higher-level tones has to be 5 to 10 dB lower than that of the noise per octave. The four figures also illustrate the variability between experiments.

The results of Figs. 4–6 confirm the conclusion from Fig. 3: for a specific stimulus level the frequency response for tones is almost the same as for noise. We do observe deviations, however, that seem systematic. On the high-

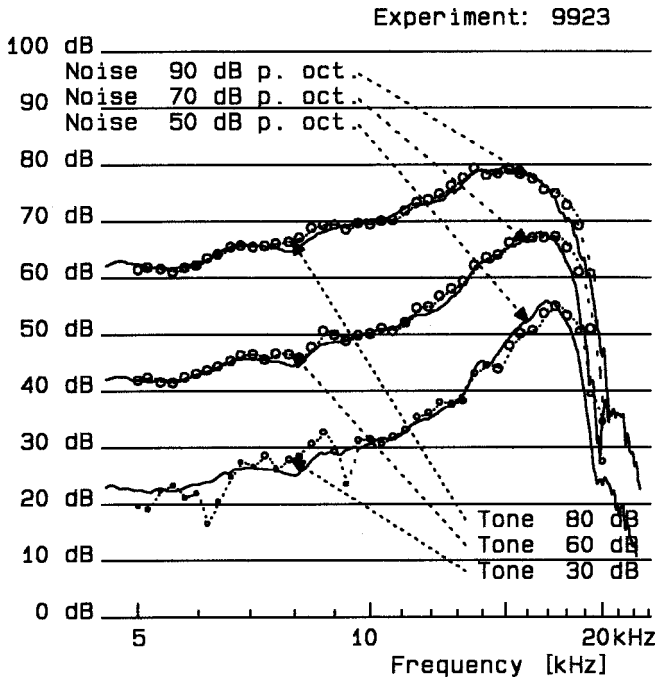

FIG. 5. Comparison of measured responses to tones (circles) and noise signal components (solid line). Experiment 9923. Layout as Fig. 4.

frequency side, the tone responses have a tendency to be a few dB higher than the noise response. In the way of the reasoning presented in Sec. II, some systematic deviations would be expected. When a sinusoidal wave starts to approach the region of the response peak, it will find a region with less saturation than with a noise stimulus. The pure tone may here be amplified somewhat more than a noise component of the same frequency and level. Let us call this effect "α." When the tone-evoked wave has passed the peak, it again encounters a region where OHC saturation is less for a tone than for noise. In that region we may again expect the tone response to be slightly stronger than a noise component response, and we will call this effect "β." Apparently, in Figs. 3–6 evidence of effect "β" is small but visible, but effect "α" cannot be seen. Why does this near-equivalence in frequency response between tones and noise exist? And why are the expected effects "α" and "β" so small? To explain these results it is necessary to go into modeling of the cochlea in more detail.

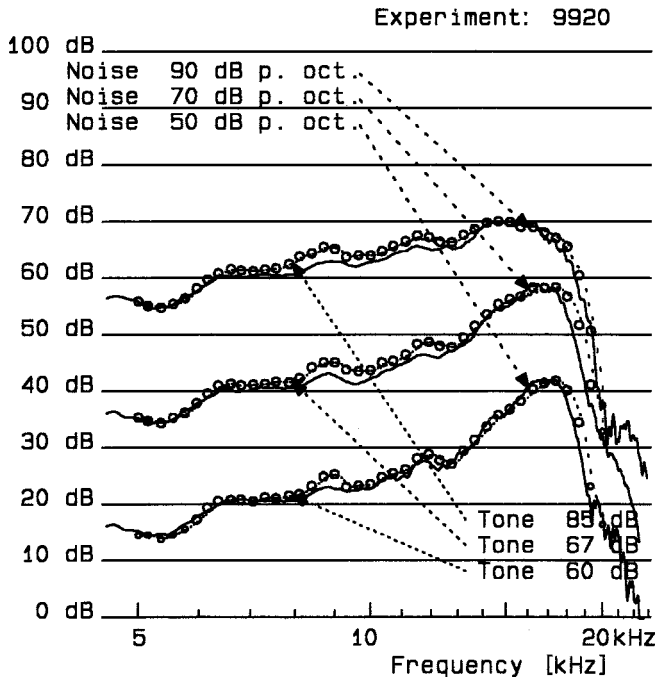

FIG. 6. Comparison of measured responses to tones (circles) and noise signal components (solid line). Experiment 9920. Layout as Fig. 4.

V. PROPAGATION OF SINUSOIDAL WAVES IN A NONLINEAR MODEL

We will apply the same "locally active" model (see Fig. 1) as used in preceding papers of the present series to the case of tonal stimulation. As stated in the Introduction, the OHCs are assumed to be nonlinear for strong stimuli as a result of (partial) saturation. In contrast, the two transformations H_1 and H_2 are linear. Both transformations may well be frequency- and place dependent and thus act as filters. In Appendix A a number of relevant relations are derived which will be used in what follows.

In order to develop a method to compute the propagation of a sinusoidal signal in this nonlinear model, two basic principles will be needed. The first one is that in the major part of the model the degree of distortion will be small so that some form of approximation method (or variational analysis) can be applied. For noise stimulation—as studied earlier—combination tones formed by the multitude of frequency components are neglected (shown as justified in de Boer, 1997a). For tone stimulation second- and higher-order harmonics can be neglected so that for the first harmonic the model acts as a *linear* model (see for further justification Kanis and de Boer, 1993, 1997). The second principle is that the *local* propagation of a cochlear wave is mainly determined by the *local* BM impedance $Z_{\mathrm{BM}}(x,\omega)$ and its variation with x. The "classical" LG or WKB[6] solution utilizes that notion in the computation of waves in complicated cochlear models [key papers: Steele and Taber (1979, 1981), generalized analyses of two- and three-dimensional models: de Boer and Viergever (1982, 1984)].

It is easy to understand that the pressure component $p_{\mathrm{add}}(x,\omega)$, when divided by the BM velocity $v_{\mathrm{BM}}(x,\omega)$, produces an *additive* contribution to the basilar-membrane (BM) impedance $Z_{\mathrm{BM}}(x,\omega)$. In other words, the BM impedance is intrinsically built up from two components, the second of which being generated by OHCs, is subject to saturation. In Part III the effect of saturation was expressed by the efficiency coefficient γ that is equal to 1 for weak stimuli and a viable cochlea, and approaches zero for stronger stimuli or in the case of cochlear pathology. The two-component concept of the BM impedance is expressed by Eq. (A8b) of Appendix A. Application of the two principles of the preceding paragraph leads to the assumption that, at every location x, the BM impedance is composed of two terms but that *for tone stimulation* the efficiency coefficient γ depends on *local* stimulation and thus is a function $\gamma(x)$ *of* x. This is expressed by the following modification of the aforementioned equation:

$$Z_{\mathrm{BM}}(x,\omega)=Z^{\mathrm{pass}}(x,\omega)+\gamma(x)Z^{\mathrm{mact}}(x,\omega). \tag{1}$$

The function $Z^{\mathrm{pass}}(x,\omega)$ is derived from the postmortem response. The function $Z^{\mathrm{mact}}(x,\omega)$ is found as the difference of the BM impedances corresponding to (a) a low-level response from a viable cochlea and (b) the postmortem response. It is repeated that the additivity of the terms in Eq. (1) stems from the fact that the pressure $p_{\mathrm{add}}(x,t)$ in Fig. 1 is to be *added* to the local pressure $p(x,t)$. Once we know $\gamma(x)$ as a function of x, and thus the form of $Z_{\mathrm{BM}}(x,\omega)$, propagation of a pure tone in the (nonlinear) model can be computed from a linear model.

Let us now briefly recapitulate how the two-component theory was used in Part III to account for the effect of stimulus level and how individual experiments were handled. That information is needed in order to develop the method to compare responses to tones and noise in the present paper. The stimulus signal in the earlier work was a wide band of noise. The OHC input signal (deflection of the stereocilia) was assumed to be proportional to v_{rms}, a ''synthetic'' rms value, which served as a kind of normalized BM velocity amplitude. In the first instance v_{rms} was made proportional to the stimulus amplitude A_1, but a correction factor C_1 was included to express amplitude compression

$$v_{\mathrm{rms}}=A_1C_1. \tag{2}$$

Both factors depend on stimulus level L. For 0-dB stimulation level A_1 equals 1, for 20 dB 10, for 40 dB 100, and so on. The compression factor C_1 gradually decreases from 1 to zero for increasing stimulus level, and is around 0.5 for levels of 80 to 90 dB (Part III, Figs. 7 and 8). Neither of the two factors depends on x because for wideband noise the rms BM velocity is (approximately) the same at all locations. Each experiment was characterized by an individual normalization factor v_1 by which v_{rms} was scaled. According to the EQ-NL theorem (de Boer, 1997a), the efficiency γ of OHC transduction is proportional to the average slope of the transducer's transfer function, averaged over the OHC input signal's excursions, i.e., averaged over a Gaussian noise signal with v_{rms}/v_1 as its rms value. The nonlinear OHC transduction function is assumed to be the same for all experiments. Taken together, these steps were sufficient to compute γ as a function of stimulus level L for each individual experiment. It was shown in Part III that for noise responses the model response resynthesized from the two-component BM impedance agrees well with experimental data, over the entire range of stimulus levels (L) explored. For different experiments v_1 had to be different, and this was the only parameter to distinguish one experiment from another.

All this applies to (broadband) noise stimuli. The procedure now needs to be adapted to tones. Instead of v_{rms} (valid for uniformly exciting noise) we will define a synthetic rms value $v_{\mathrm{tone}}(x)$ for tone stimulation, but this is no longer a constant. It has become a function of location x. In lieu of Eq. (2) we write

$$v_{\mathrm{tone}}(x)=A_1C_2(x), \tag{3}$$

where the factor A_1 is proportional to the signal amplitude, but now that of the stimulating tone. The factor $C_2(x)$ is normalized in such a way that, when it would be evaluated for noise stimulation (at the appropriate stimulus level), and summed over all contributing frequency components, $C_2(x)$ would be equal to C_1. The method for this summation is detailed in Appendix A. The quotient $v_{\mathrm{tone}}(x)/v_1$ is used to find the effective degree of saturation, in other words, the value of $\gamma(x)$. Appendix B gives details of this transformation (the result of which is slightly different for tones and noise signals).

The *variations* of $C_2(x)$ for tones with x should parallel the *variations* of the ciliary excitation signal $d_{\mathrm{cil}}(x,\omega)$. Appendix A describes how the signal $d_{\mathrm{cil}}(x,\omega)$ depends on the BM velocity $v_{\mathrm{BM}}(x,\omega)$. We repeat Eq. (A9)

$$d_{\mathrm{cil}}(x,\omega)=-\frac{Z^{\mathrm{mact}}(x,\omega)}{2S_0(x)}v_{\mathrm{BM}}(x,\omega), \tag{4}$$

where $S_0(x)$ is a parameter with the character of stiffness. To conform with response scaling (frequency versus location), the parameter $S_0(x)$ should be proportional to the square of the local frequency associated with x. However, in the summation over frequency components $S_0(x)$ in Eq. (4) remains constant. Relation (4) holds true when the transformation H_2 from $p_{\mathrm{OHC}}(x,t)$ to $p_{\mathrm{add}}(x,t)$ is taken to be unity. It will be shown further on that in the context of the present paper elaborations on other choices for H_2 are not strictly necessary.

The procedure is now as follows. Start by assuming that the local tone response $v_{\mathrm{BM}}(x,\omega)$—as a function of x—is like that for the corresponding component of a noise signal, presented at an appropriate stimulus level. Compute $v_{\mathrm{tone}}(x)$ from $v_{\mathrm{BM}}(x,\omega)$ using Eqs. (4) and (3), and derive $\gamma(x)$ for all locations x. Finally, generate the BM impedance $Z_{\mathrm{BM}}(x,\omega)$ from Eq. (1), and compute the response of the model to the tone (do ''resynthesis''). The result, again a function $v_{\mathrm{BM}}(x,\omega)$ of x, will differ somewhat from the initially assumed response. Compute $v_{\mathrm{tone}}(x)$ and $\gamma(x)$ again, and perform a few iterations (as is characteristic of the work of Kanis and de Boer) until sufficient convergence is obtained. As long as $\gamma(x)$ faithfully represents how the first harmonic of the signal is compressed, the implied approximation is accurate. When indeed noise and tone responses are comparable, using the appropriately chosen noise-derived function $v_{\mathrm{BM}}(x,\omega)$ in the first step already produces an acceptable result. For experiments 9920, 9922, 9923, and 9924 that first step produces a tone-response result that is not more than 5 dB different from the ultimate result.

We found that three steps of iteration are sufficient to reduce variations to less than 2 dB. We interpret this rapid convergence as confirming the validity of the model used. We do not believe that a different ''division of labor'' between the two transformations H_1 and H_2 would lead to a materially different result. Therefore, in view of the present findings there is no need to investigate other choices for the transformation H_2.

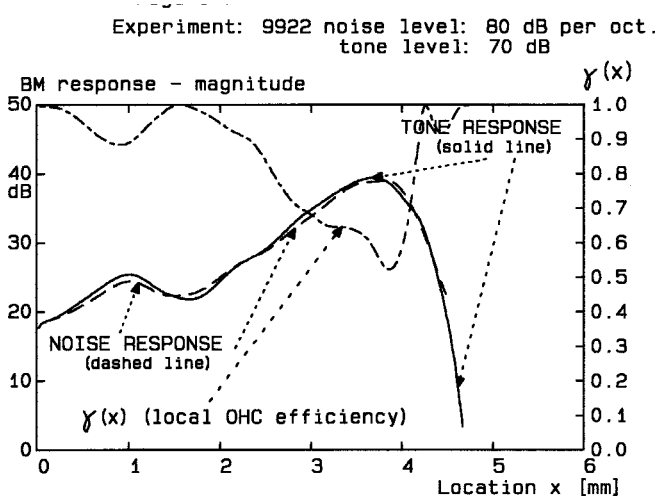

FIG. 7. Propagation of a pure tone (16.6 kHz) in a cochlear model (amplitude shown only). Noise-response data from experiment 9922. Dashed line: resynthesized response with uniform gamma ($\gamma = 0.67$), representative for a single component of a noise signal. Solid line: computed for pure tone. Dash-dot line: the location-dependent OHC efficiency $\gamma(x)$, scale (0 to 1) on the right.

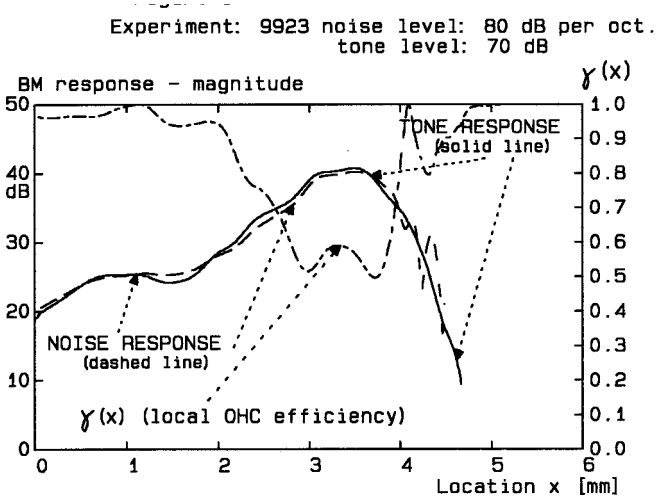

FIG. 8. Propagation of a pure tone (16.9 kHz) in a cochlear model (amplitude shown only). Noise-response data from experiment 9923. Dashed line: resynthesized response with uniform gamma ($\gamma = 0.61$), representative for a single component of a noise signal. Solid line: computed for pure tone. Dash-dot line: the location-dependent OHC efficiency $\gamma(x)$, scale (0 to 1) on the right.

VI. RESULTS II. COCHLEAR PATTERNS FOR TONE AND NOISE

Figure 7 shows as an example of a result, the amplitude of the model response to a sinusoidal stimulus compared to that for a wideband noise signal, both plotted as functions of location x. The dashed line shows (as in Fig. 2) the propagation of a component of the noise signal (80 dB per octave), for experiment 9922 (the same experiment as was used for Fig. 4). The solid line illustrates the solution of the model equation for a sinusoidal stimulus (presented at 70 dB). From the figure it is apparent that the computed tone response is very close in amplitude to the noise response. A similar agreement will exist in the frequency domain. A third curve is present: the dash-dot line, which shows the local effective OHC efficiency $\gamma(x)$. This curve has its ordinate scale, going from zero to 1, on the right. It is seen that $\gamma(x)$ starts on the left near 1 (corresponding to weak excitation) and decreases to appreciably lower values in the region of the response peak.

For the preceding figures the "high" noise levels were selected as 70 and 90 dB per octave. For the present and later figures we used 80 dB per octave because that yields a value for the average γ between 0.6 and 0.8. As can be seen from Fig. 11 (Appendix B), in this region γ is the most sensitive to variations in excitation. Hence, this is the best region for exploring deviations between noise and tone responses. See the legends to this and the following figures for the values of γ applying to the noise responses.

Figures 8, 9, and 10 show results derived from basic data for three other experiments. Compare these figures with Figs. 5, 6, and 3, respectively. Note that for both Figs. 6 (experiment) and 9 (theory) a smaller level difference between tone and noise was used than in the other figures. From all four figures we can draw the same conclusion, but we also observe that there is a wide variation in the course of $\gamma(x)$ as a function of x. In the final section of this paper we return to this finding.

VII. INTERPRETATION AND CONCLUSION

In this report we have demonstrated that the response of the cochlea to tones is, to a good approximation, equivalent to that of components of a noise signal. As a matter of fact, stimuli of the appropriate levels have to be compared; see Fig. 3. We found that equivalence in the data and have corroborated it by theory. Briefly: insofar as frequency filtering (the differential treatment of frequencies) is concerned, the cochlea is not "more nonlinear" or "less nonlinear" for tones than for noise. For tone stimulation the signal at the input of the OHCs is (nearly) sinusoidal. For a noise stimulus

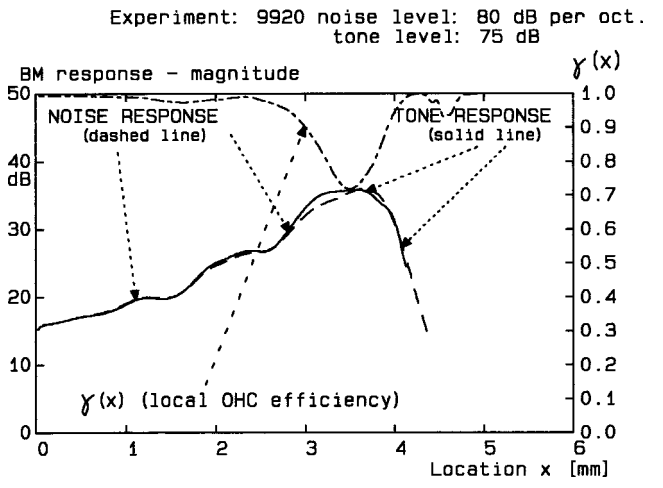

FIG. 9. Propagation of a pure tone (17.1 kHz) in a cochlear model (amplitude shown only). Noise-response data from experiment 9920. Dashed line: resynthesized response with uniform gamma ($\gamma = 0.82$), representative for a single component of a noise signal. Solid line: computed for pure tone. Dash-dot line: the location-dependent OHC efficiency $\gamma(x)$, scale (0 to 1) on the right.

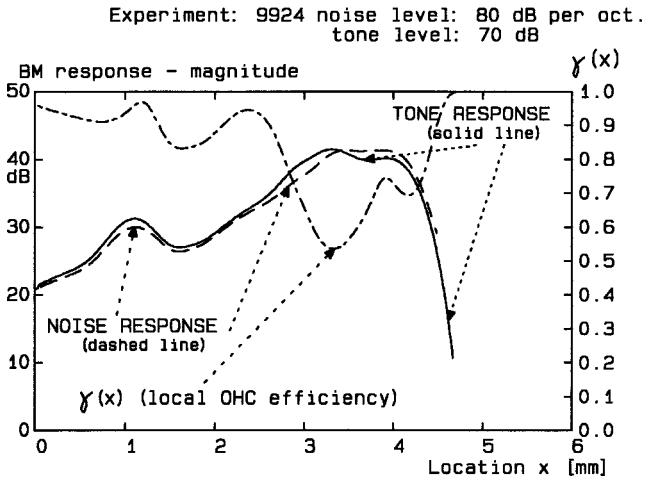

FIG. 10. Propagation of a pure tone (16.7 kHz) in a cochlear model (amplitude shown only). Noise-response data from experiment 9924. Dashed line: resynthesized response with uniform gamma ($\gamma = 0.69$), representative for a single component of a noise signal. Solid line: computed for pure tone. Dash-dot line: the location-dependent OHC efficiency $\gamma(x)$, scale (0 to 1) on the right.

it is a multicomponent signal. In both cases the degree of saturation is determined by the (average) rms amplitude of the *total* signal at the input to the OHCs. Here lies the root of the comparison between tone and noise responses. Note that with the model that we use—in which the efficiency coefficient $\gamma(x)$ is a function of location x—the full extent of the variations of the response with stimulus level L can now be explained. This holds for noise as well as for tones. With respect to frequency filtering of stationary signals, the cochlea acts almost as an intensity-dependent linear filter.

As described in Sec. IV, we may have expected small differences in level between noise and tone responses, effects "α" and "β." Effect α is not found in the experimental data, and appears only as very small in the model results. The explanation why effect α is so small can be found from the course of the local efficiency function $\gamma(x)$. This function is not only well below 1 in the peak region but also more basally. Apparently, the domain over which a pure tone causes saturation (nonlinearity) extends sufficiently far to the left of the peak region to make the difference between excitation by tones and by noise minimal. In this respect, it may be expected that variations in $\gamma(x)$ would cause corresponding variations in suppression of high-frequency by low-frequency tones, upward suppression. Note that in the field of psychophysics, upward suppression would contribute to upward spread of masking (increased nonlinearity above a suppressing tone's frequency). It is worthwhile to delve deeper into this topic.

As regards effect β, we found evidence of it in the data but detected it also in the low-level data.[7] It is not present in the model results; on the contrary, the theoretical tone responses seem to have a small negative effect β, even at low levels. This may indicate an inadequacy of the model. We should realize that our computation method has been chosen as the one that corresponds most closely to our insight. It is a hybrid method, based on one of the principles of the LG or WKB method, but it does not utilize the concept of the wave number $k(x)$ at all. In fact, the actual model computation is performed not as in the WKB or LG approximation but in the "exact" way, via solution of a matrix equation. In view of this we should not pay particular attention to deviations of 1 to 2 dB.

A single, very strong sinusoid will be distorted heavily (by the OHCs) but the harmonics cannot propagate (their frequencies are above the local best frequency). That has been the main reason why, in computing wave propagation, we could concentrate on the first harmonic. When *two tones* are presented, there will arise a host of distortion products (DPs) and many of them (intermodulation products) can and will propagate. With the experience gained by the present work, the propagation of these DPs can be computed according to the same modeling concept. It is in this area where we might need to investigate the possible influence of the transformation H_2, namely, whether or not DPs undergo a second filtering (cf. Allen and Fahey, 1993 versus Kanis and de Boer, 1997).

In one respect tones, signals consisting of a finite number of fixed frequency components, and random-noise signals are similar: all are stationary signals. Our understanding of how the cochlea processes stationary signals is fairly complete now. It is for *non*-stationary (rapidly varying) signals that we have to extend our repertoire of mathematical operations in order to formulate and verify a satisfactory theory.

ACKNOWLEDGMENTS

Experiments have been performed in close cooperation with the cochlea research team of the Oregon Hearing Research Center (OHRC). Special thanks are due to Jiefu Zheng and Edward Porsov. This work has been supported by NIH (No. NIDCD-DC-00141) and is a logical continuation of project No. SLW 01.011 (NWO, The Netherlands).

APPENDIX A: THE INPUT SIGNAL OF OUTER HAIR CELLS

In this Appendix the effective strength of excitation of OHCs is computed. The model on which this is based is briefly described in the Introduction, and illustrated by Fig. 1. Input to the OHCs is the signal $d_{\mathrm{cil}}(x,t)$, the deflection of the OHC stereocilia, and output the pressure $p_{\mathrm{OHC}}(x,t)$ developed in the immediate surroundings of these cells. The instantaneous nonlinear transduction function of the OHCs is expressed by

$$p_{\mathrm{OHC}}(x,t) = S_0 d_1 F\,[d_{\mathrm{cil}}(x,t)/d_1], \tag{A1}$$

where d_1 is a scaling factor for $d_{\mathrm{cil}}(x,t)$, $F(\cdot)$ is a saturating, no-memory, nonlinear real function, and S_0 is a constant. The function $F(\cdot)$ is assumed to be equal to its argument for very small values of the argument and to remain finite for extreme values of the argument. Equation (A1) is identical to Eq. (B1) of Appendix B in Part III. For very small signals Eq. (A1) reads

$$p_{\mathrm{OHC}}(x,t) = S_0 d_{\mathrm{cil}}(x,t) \quad \text{when } |d_{\mathrm{cil}}(x,t)| \ll d_1, \tag{A2}$$

where S_0 is the only factor relating $p_{\mathrm{OHC}}(x,t)$ to $d_{\mathrm{cil}}(x,t)$. It is assumed that $d_{\mathrm{cil}}(x,t)$ is a *linear* transform of the BM velocity $v_{\mathrm{BM}}(x,t)$

$$d_{\mathrm{cil}}(x,t)=[H_1^{(\mathrm{op})}]v_{\mathrm{BM}}(x,t), \tag{A3}$$

where $H_1^{(\mathrm{op})}$ is a linear operator (it includes the integration operator transforming velocity into displacement) corresponding to the transformation H_1 in Fig. 1. The filtering in $H_1^{(\mathrm{op})}$ will be frequency- and place dependent. In a more general setting, $H_1^{(\mathrm{op})}$ may operate over a certain range of x values—such as in a ''non-classical'' model (Steele *et al.*, 1993; Geisler and Sang, 1995; Fukazawa, 1997; de Boer, 1997b), but we restrict ourselves here to the simpler case of a ''classical'' model where $H_1^{(\mathrm{op})}$ operates on the *local* velocity. We will use symbols with time t replaced by radian frequency ω to denote the corresponding variables in the frequency domain and tacitly imply that a Fourier transformation has taken place. In the frequency domain, Eq. (A3) is then written as

$$d_{\mathrm{cil}}(x,\omega)=H_1(x,\omega)v_{\mathrm{BM}}(x,\omega), \tag{A4}$$

where $H_1(x,\omega)$ is the transfer function corresponding to $H_1^{(\mathrm{op})}$. Notice that $H_1^{(\mathrm{op})}$ and $H_1(x,\omega)$ do not depend on stimulus level since the transformation H_1 is linear. The relation between $p_{\mathrm{OHC}}(x,t)$ and the pressure $p_{\mathrm{add}}(x,t)$ near the BM is expressed in a similar way by

$$p_{\mathrm{add}}(x,t)=[H_2^{(\mathrm{op})}]p_{\mathrm{OHC}}(x,t), \tag{A5}$$

with its frequency-domain counterpart

$$p_{\mathrm{add}}(x,\omega)=H_2(x,\omega)p_{\mathrm{OHC}}(x,\omega). \tag{A6}$$

$H_2^{(\mathrm{op})}$ and $H_2(x,\omega)$ represent the filtering from $p_{\mathrm{OHC}}(x,t)$ to $p_{\mathrm{act}}(x,t)$ which, again, is linear. For reasons of simplicity we assume that $H_2^{(\mathrm{op})}$ is the unity operator so that $H_2(x,\omega)$ is identically equal to 1. This choice means that we consider all frequency- and place dependence of the feedback loop in Fig. 1 as concentrated in the transformation $H_1(x,\omega)$. Possible effects of this restriction would only be expected in the treatment of distortion products, which is outside the scope of this paper.

All parameters and variables that are functions of both x and ω are assumed to ''scale,'' i.e., any change in ω can be offset by a change in x. This transformation implies a ''cochlear map'' which, again for reasons of simplicity, is assumed to be linear from x to the logarithm of ω. The factor S_0 in Eq. (A1) has the dimension and the character of stiffness, and S_0 is assumed to vary (exponentially) with x but not to depend on ω. Therefore, in what follows it is written as $S_0(x)$.

The pressure component $p_{\mathrm{add}}(x,\omega)$, when divided by the BM velocity $v_{\mathrm{BM}}(x,\omega)$, produces an *additive* contribution to the basilar-membrane (BM) impedance $Z_{\mathrm{BM}}(x,\omega)$ that we call $Z^{\mathrm{add}}(x,\omega)$; it is defined by

$$Z^{\mathrm{add}}(x,\omega)=\frac{-2p_{\mathrm{add}}(x,\omega)}{v_{\mathrm{BM}}(x,\omega)}. \tag{A7}$$

The concept of an impedance is relevant in a linear system, i.e., in the weak-signal case. If we introduce $Z^{\mathrm{mact}}(x,\omega)$ for the maximum value of $Z^{\mathrm{add}}(x,\omega)$ (associated with the weakest stimuli), and call the BM impedance without the contribution of the OHCs $Z^{\mathrm{pass}}(x,\omega)$, the total BM impedance $Z_{\mathrm{BM}}(x,\omega)$ in the weak-signal case is equal to the sum of two components

$$Z_{\mathrm{BM}}(x,\omega)=Z^{\mathrm{pass}}(x,\omega)+Z^{\mathrm{mact}}(x,\omega). \tag{A8a}$$

In the more general case, where the OHCs partly saturate, the concept of impedance can be retained for wideband noise stimulation [the EQ-NL theorem (de Boer, 1997a)]. The term $Z^{\mathrm{add}}(x,\omega)$ will then include the real coefficient γ so that Eq. (A8a) changes into

$$Z_{\mathrm{BM}}(x,\omega)=Z^{\mathrm{pass}}(x,\omega)+\gamma Z^{\mathrm{mact}}(x,\omega). \tag{A8b}$$

For very weak signals γ equals 1, and with increasing signal strength it decreases towards zero; see Part III where this ''two-component theory of the BM impedance'' is worked out in detail. The parameter γ is the only factor that varies with stimulus level; the basic parameter functions $Z^{\mathrm{pass}}(x,\omega)$ and $Z^{\mathrm{mact}}(x,\omega)$ do *not* depend on stimulus level. Furthermore, for wideband, flat-spectrum noise signals γ does not depend on ω or x.

Returning to the weak-signal case, we can combine Eq. (A2) with Eqs. (A6) and (A7) and arrive at the following expression for the signal $d_{\mathrm{cil}}(x,\omega)$ at the input to the OHCs:

$$d_{\mathrm{cil}}(x,\omega)=-\frac{Z^{\mathrm{mact}}(x,\omega)}{2S_0(x)}v_{\mathrm{BM}}(x,\omega). \tag{A9}$$

Although this relation is derived for weak signals it remains valid for any stimulus level and any stimulus type because the transformation H_1 is linear. The impedance $Z^{\mathrm{mact}}(x,\omega)$ can be estimated from an experiment with a weak *noise* stimulus and an experiment postmortem [Eq. (A8a)]. We would only need an estimate of $S_0(x)$ to know the transformation (A9) completely.

For stimulation with a *noise* signal all frequency components of the noise have to be taken into account. When the noise signal has components at radian frequencies ω_j ($-\infty<j<\infty$), Eq. (A9) must be summed over all frequency components of the noise and Fourier transformed to find the time function $d_{\mathrm{cil}}(x,t)$. The variance of $d_{\mathrm{cil}}(x,t)$ is found as the sum of the intensities of all the components, Eq. (A9) with ω_j substituted for ω. In the summation $S_0(x)$ remains the same. For this operation we need to scale the impedance $Z^{\mathrm{mact}}(x,\omega)$ (which has been determined as a function of x for constant ω to become a function of ω for constant x. Location x is scaled to radian frequency ω according to the inverse of the transformation from ω to x; for the impedance a factor ω has to be included.

APPENDIX B: OHC TRANSDUCTION FUNCTION

For a no-memory transducer with transducer function $F(\cdot)$ and input signal u, the average efficiency coefficient γ of OHC transduction is given by

$$\gamma=\int_{-\infty}^{\infty}F'(u)P(u)\mathrm{d}u, \tag{B1}$$

where $P(u)$ is the probability density of the signal u, $F'(\cdot)$ is the derivative of $F(\cdot)$, which should be a monotonically

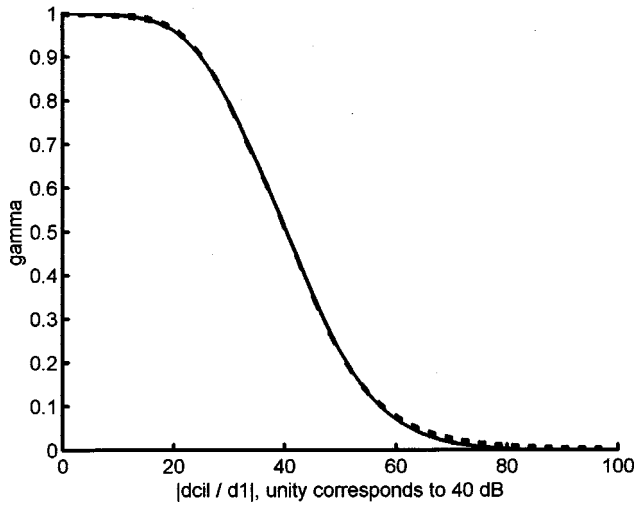

FIG. 11. Gamma (γ_G for Gaussian noise and γ_S for tones) as a function of $|d_{\mathrm{cil}}|/d_1$ (abscissa in dB). *Solid* line: γ_G (for Gaussian noise), *dotted* line: γ_S (for a tone) but in this case $|d_{\mathrm{cil}}|/d_1$ is taken as 1.78 times the value on the abscissa. In the text this factor is rounded off to 2.

decreasing function of the magnitude of its argument, and $F'(0)$ is assumed to be equal to 1. Then, for very small signals the coefficient γ is equal to 1. For stronger signals γ expresses, by its reduction from 1, the average state of saturation in the system.

For stimulation with noise the probability distribution of $d_{\mathrm{cil}}(x,t)$ will be nearly Gaussian. The efficiency coefficient γ_G is the average slope $F'(u)$ of $F(u)$ over the values of $[d_{\mathrm{cil}}(x,t)/d_1]$ for a Gaussian distribution

$$\gamma_G = \int_{-\infty}^{\infty} F'(a d_{\mathrm{cil}}/d_1) P_g(a) da, \tag{B2}$$

where $P_g(\cdot)$ stands for the Gaussian probability density function with unity variance. The normalizing factor d_1 plays the same role as in Part III. In Sec. V of the present paper $[d_{\mathrm{cil}}(x,t)/d_1]$ is expressed in the "synthetic" forms $[v_{\mathrm{rms}}/v_1]$ and $[v_{\mathrm{tone}}(x)/v_1]$, for noise and tone, respectively, and by way of the factor ν_1 it is adapted to an individual experiment.

For sinusoidal stimulation the corresponding efficiency coefficient γ_S will be equal to the first Fourier component of the distorted signal $F[d_{\mathrm{cil}}(x,t)/d_1]$ divided by the original signal's amplitude

$$\gamma_S(x) = (2/\pi) \int_0^{\pi} F[|d_{\mathrm{cil}}(x)/d_1| \cdot \sin\varphi] \times \sin\varphi \, d\varphi / |(d_{\mathrm{cil}}(x)/d_1)|. \tag{B3}$$

In Sec. V it is explained how the quotient $[d_{\mathrm{cil}}(x,t)/d_1]$ is estimated in the form of $[v_{\mathrm{tone}}(x)/v_1]$, again adapted to an individual experiment.

Our function $F(u)$ is based on the hyperbolic tangent function used by Kanis and de Boer (1993). A weighted sum of two such functions has a two-stage variation of the slope which corresponds better to the nonlinear odd-order character of measured hair-cell transfer functions (cf. Geisler, 1998, Figs. 8.3 and 8.5)

$$F(u) = [\tanh w + c \tanh(w/c)]/(1+c), \tag{B4}$$

where

$$w = (1+c)u/2. \tag{B5}$$

The parameter c is a constant which must be nonzero. For every (nonzero) value of c the function $F(u)$ has unity slope at $u=0$ and it reaches $+1$ for $u \to \infty$ and -1 for $u \to -\infty$. For $c=1$ $F(u)$ reduces to a single tanh function. The parameter c is taken equal to 0.2. For $u=1$, $F(u)$ is equal to 0.613.

It is illuminating to compare γ_G for Gaussian noise with γ_S for tones. In Fig. 11 the *solid* line shows γ_G from Eq. (B2) (for Gaussian noise) as a function of $|d_{\mathrm{cil}}|/d_1$(on a log scale). The *dashed* line illustrates γ_S from Eq. (B3) (for a tone) but $|d_{\mathrm{cil}}|/d_1$ is taken as 1.78 times the value on the abscissa. The two curves are nearly coincident; the differences are of the order of 2%. Apparently, the two functions demonstrate very similar behavior of the efficiency coefficient as a result of OHC saturation. The sinusoidal signal is about half as effective in reducing the efficiency γ as a noise signal of the same rms value. This is easily understood from the shape of the signal distribution function: the waveform of the sine signal never exceeds the maximum value, whereas signal values for a noise signal cover a large range outside the rms value. The ratio of 1.78 and 2.0 amounts to approx. 1 dB and will be neglected.

[1]In this paper we assume that the transformation H_1 is a local one. Equivalently, we assume a classical model (cf. Appendix A and de Boer, 1997b).
[2]We have presented pseudorandom noise which has a periodic waveform and, therefore, analyzes into discrete components. In our case the components were separated by 50.78 Hz.
[3]In comparing responses to tones and noise the effective stimulus levels are similar, therefore, phase differences will be minimal.
[4]The present study was consistent with NIH guidelines for humane treatment of animals and was reviewed and approved by the Oregon Health Sciences Committee on the Use and Care of Animals.
[5]The stapes response was measured postmortem. We acquired the stapes response in the form of a cross-correlation function (ccf) for wideband noise. This stapes ccf can serve to normalize noise as well as tone responses.
[6]LG stands for Liouville–Green, WKB for Wentzel, Kramers, and Brillouin.
[7]One possible influence in the data could be due to efferent effects.

Allen, J. B., and Fahey, P. F. (**1993**). "A second cochlear-frequency map that correlates distortion product and neural tuning measurements," J. Acoust. Soc. Am. **94**, 809–816.
de Boer, E. (**1997a**). "Connecting frequency selectivity and nonlinearity for models of the cochlea," Aud. Neurosci. **3**, 377–388.
de Boer, E. (**1997b**). "Classical and nonclassical models of the cochlea," J. Acoust. Soc. Am. **101**, 2148–2150.
de Boer, E. (**1998**). "A method for forward and inverse solutions of a 3-dimensional model of the cochlea," J. Acoust. Soc. Am. **103**, 3725–3728.
de Boer, E., and Nuttall, A. L. (**1997**—Part I). "The mechanical waveform of the basilar membrane. I. Frequency modulations (glides) in impulse responses and cross-correlation functions," J. Acoust. Soc. Am. **101**, 3583–3592.
deBoer, E., and Nuttall, A. L. (**1999**). "The inverse problem solved for a three-dimensional model of the cochlea. III. Brushing-up the solution method," J. Acoust. Soc. Am. **105**, 3410–3420.
de Boer, E., and Nuttall, A. L. (**2000a**—Part II). "The mechanical waveform of the basilar membrane. II. From data to models—and back," J. Acoust. Soc. Am. **107**, 1487–1496.
de Boer, E., and Nuttall, A. L. (**2000b**—Part III). "The mechanical waveform of the basilar membrane. III. Intensity effects," J. Acoust. Soc. Am. **107**, 1497–1507.
de Boer, E., and Viergever, M. A., (**1982**). "Validity of the Liouville-Green (or WKB) method for cochlear mechanics," Hear. Res. **8**, 131–155.

de Boer, E., and Viergever, M. A. (**1984**). ''Wave propagation and dispersion in the cochlea,'' Hear. Res. **13**, 101–112.
Fukazawa, T. (**1997**). ''A model of cochlear micromechanics,'' Hear. Res. **113**, 182–190.
Geisler, C. D. (**1998**). *From Sound to Synapse* (Oxford University Press, Oxford).
Geisler, C. D., and Sang, C. (**1995**). ''A cochlear model using feed-forward outer-hair-cell forces,'' Hear. Res. **86**, 132–146.
Kanis, L. J., and de Boer, E. (**1993**). ''Self-suppression in a locally active nonlinear model of the cochlea: A quasi-linear approach,'' J. Acoust. Soc. Am. **94**, 3199–3206.
Kanis, L. J., and de Boer, E. (**1997**). ''Frequency dependence of acoustic distortion products in a locally active model of the cochlea,'' J. Acoust. Soc. Am. **101**, 1527–1531.
Nuttall, A. L., Dolan, D. F., and Avinash, G. (**1990**). ''Measurements of basilar membrane tuning and distortion with laser Doppler velocimetry,'' in *The Mechanics and Biophysics of Hearing*, edited by P. Dallos, C. D. Geisler, J. W. Matthews, M. A. Ruggero, and C. R. Steele (Springer, Berlin), pp. 288–295.
Steele, C. R., and Taber, L. A. (**1979**). ''Comparison of WKB and finite difference calculations for a two-dimensional cochlear model,'' J. Acoust. Soc. Am. **65**, 1001–1006.
Steele, C. R., and Taber, L. A. (**1981**). ''Three-dimensional model calculations for guinea pig cochlea,'' J. Acoust. Soc. Am. **69**, 1107–1111.
Steele, C. R., Baker, G., Tolomeo, J., and Zetes, D. (**1993**). ''Electromechanical models of the outer hair cell,'' in *Biophysics of Hair-Cell Sensory Systems*, edited by H. Duifhuis, J. W. Horst, P. van Dijk, and S. M. van Netten (World Scientific, Singapore), pp. 207–214.

Neural activity associated with distinguishing concurrent auditory objects

Claude Alain,[a] Benjamin M. Schuler, and Kelly L. McDonald
Rotman Research Institute, Baycrest Centre for Geriatric Care, 3560 Bathurst Street, Toronto, Ontario M6A 2E1, Canada and Department of Psychology, University of Toronto, Sidney Smith Hall, 100 St. George Street, Toronto, Ontario M5S 1A1, Canada

(Received 25 September 2001; accepted for publication 20 November 2001)

The neural processes underlying concurrent sound segregation were examined by using event-related brain potentials. Participants were presented with complex sounds comprised of multiple harmonics, one of which could be mistuned so that it was no longer an integer multiple of the fundamental. In separate blocks of trials, short-, middle-, and long-duration sounds were presented and participants indicated whether they heard one sound (i.e., buzz) or two sounds (i.e., buzz plus another sound with a pure-tone quality). The auditory stimuli were also presented while participants watched a silent movie in order to evaluate the extent to which the mistuned harmonic could be automatically detected. The perception of the mistuned harmonic as a separate sound was associated with a biphasic negative–positive potential that peaked at about 150 and 350 ms after sound onset, respectively. Long duration sounds also elicited a sustained potential that was greater in amplitude when the mistuned harmonic was perceptually segregated from the complex sound. The early negative wave, referred to as the object-related negativity (ORN), was present during both active and passive listening, whereas the positive wave and the mistuning-related changes in sustained potentials were present only when participants attended to the stimuli. These results are consistent with a two-stage model of auditory scene analysis in which the acoustic wave is automatically decomposed into perceptual groups that can be identified by higher executive functions. The ORN and the positive waves were little affected by sound duration, indicating that concurrent sound segregation depends on transient neural responses elicited by the discrepancy between the mistuned harmonic and the harmonic frequency expected based on the fundamental frequency of the incoming stimulus.
[DOI: 10.1121/1.1434942]

PACS numbers: 43.64.Qh, 43.64.Ri, 43.66.Lj [LHC]

I. INTRODUCTION

In most everyday situations, there is often more than one audible sound source at any given moment. Given that the acoustic components from simultaneously active sources impinge upon the ear at the same time, how does the auditory system sort which elements of the mixture belong to a particular source and which originate from a different sound source?

Psychophysical research has identified several factors that can help listeners to segregate co-occurring events. For example, sound components that are harmonically related or that rise and fall in intensity together usually arise from a single physical source and tend to be grouped into one perceptual object. Conversely, sounds are more likely to be assigned to separate objects (i.e., sources) if they are not harmonically related and if they differ widely in frequency and intensity (for a review, see Bregman, 1990; Hartmann, 1988, 1996). The present study focuses on concurrent sound segregation based on harmonicity.

One way of investigating concurrent sound segregation based on harmonicity is by means of the mistuned harmonic experiment. Usually, the listener is presented with two stimuli sucessively, one of them with perfectly harmonic components, the other with a mistuned harmonic. The task of the listener is to indicate which one of the two stimuli contains the mistuned harmonic. Several factors influence the perception of the mistuned harmonic as a separate tone, including degree of inharmonicity, harmonic number, and sound duration (Hartmann, McAdams, and Smith, 1990; Lin and Hartmann, 1998; Moore, Peters, and Glasberg, 1985).

This effect of mistuning on concurrent sound segregation is consistent with Bregman's account of auditory scene analysis (Bregman, 1990). Within this model, the acoustic wave is first decomposed into perceptual groups (i.e., objects) according to Gestalt principles. Partials that are harmonically related are grouped together into one entity, while the partial that is sufficiently mistuned stands out as a separate object. It has been proposed that the perception of the mistuned harmonic as a separate object depends on a pattern-matching process that attempts to adjust a harmonic template, defined by a fundamental frequency, to fit the spectral pattern (Goldstein, 1978; Hartmann, 1996; Lin and Hartmann, 1998). When a harmonic is mistuned by a sufficient amount, a discrepancy occurs between the perceived frequency and that expected on the basis of the template. The purpose of this pattern-matching process could be to signal to higher auditory centers that more than one auditory object might be simultaneously present in the environment.

One important question concerns the nature of the mismatch process that may underlie concurrent sound segrega-

[a]Electronic mail: calain@rotman-baycrest.on.ca

tion. For instance, it is unclear whether the mismatch process is transient in nature or whether it remains present for the whole duration of the stimulus. Previous behavioral studies have shown that perception of the mistuned harmonic as a separate tone improved with increasing sound durations (e.g., Moore *et al.*, 1986). This suggests that perception of concurrent auditory objects may depend on a continuous analysis of the stimulus rather than on a transient detection of inharmonicity.

Event-related brain potentials (ERPs) provide a powerful tool for exploring the neural mechanisms underlying concurrent sound segregation. In a series of experiments, Alain, Arnott, and Picton (2001) measured ERPs to complex sounds that either had all harmonics in tune or included one mistuned harmonic so that it was no longer an integer multiple of the fundamental. When individuals reported perceiving two concurrent auditory objects (i.e., a buzz plus another sound with a pure-tone quality), a phasic negative deflection was observed in the ERP. This negative wave peaked around 180 ms after sound onset and was referred to as the object-related negativity (ORN) because its amplitude correlated with perceptual judgment, being greater when participants reported hearing two distinct perceptual objects. The ORN was also present even when participants were asked to ignore the stimuli and read a book of their choice. This suggests that this component indexes a relatively automatic process that occurs even when auditory stimuli are not task relevant.

Distinguishing concurrent auditory objects was also associated with a late positive wave that peaked at about 400 ms following stimulus onset (P400). Like the ORN, the P400 amplitude correlated with perceptual judgment, being larger when participants perceived the mistuned harmonic as a separate tone. However, in contrast with the ORN, this component was present only when participants were required to respond whether they heard one or two auditory stimuli.

The aim of the present study was to further investigate the nature of the neural processes underlying concurrent sound segregation using sounds of various durations. In Alain *et al.*'s study, it was unclear whether the ORN and P400 indexed a transient or a sustained process because the sound duration was always kept constant. Examining the ORN and P400 for sounds of various duration can give clues about the processes involved in concurrent sound segregation. If concurrent sound segregation depends on a transient process that detects a mismatch between the mistuned harmonic and the harmonic template, then these ERP components should be little affected by sound duration. However, if concurrent sound segregation depends on the ongoing analysis of the stimulus, then the effect of mistuning on ERPs should vary with sound duration. Because the stimuli in Alain *et al.*'s study were always 400 ms in duration, it was also difficult to determine the contributions of the offset responses and the response selection processes to the P400 component. In the present study, participants were presented with sounds of various durations and were asked to respond at the end of the sound presentation to reduce contamination by response processes. If the P400 component received contribution from the offset reponses and/or from the response processes, then the P400 amplitude should vary as a function of stimulus duration.

II. METHOD

A. Participants

Thirteen adults provided written informed consent to participate in the study. The data of three participants were excluded from further analysis because they showed extensive ocular contaminations or had extreme difficulty in distinguishing the different stimuli. Four women and six men form the final sample (aged between 22 and 37 years, mean age $= 25.7 \pm 4.67$ years). All participants were right-handed and had pure-tone thresholds within normal limits for frequencies ranging from 250 to 8000 Hz (both ears).

B. Stimuli and task

All stimuli had a fundamental frequency of 200 Hz. The tuned stimuli consisted of a complex sound obtained by combining 12 pure tones with equal intensity. In the mistuned stimuli the third harmonic was shifted either up- or downwards by 16% of its original value (696 or 504 Hz instead of 600 Hz). The intensity level of each sound was 80 dB SPL. The durations of the sounds were short (100 ms), medium (400 ms), or long (1000 ms), including 5-ms rise/fall time. The sounds were generated digitally with a sampling rate of 50 kHz and presented binaurally through Sennheiser HD 265 headphones. Participants were presented with 18 blocks of trials. Each block consisted of 130 stimuli of short, medium, or long duration sounds. Half of the stimuli in each block were tuned while the other half were mistuned. Tuned and mistuned stimuli were presented in a random order. The short, medium, and long duration blocks were presented in a random order across participants.

Each participant took part in active and passive listening conditions (nine blocks of trials in each condition). In the active listening condition, participants indicated whether they perceived one tuned sound or two sounds (i.e., a buzz plus another sound with a pure-tone quality) by pressing one of two buttons on a response box using the right index and middle fingers. Participants were asked to withhold their response until the end of the sound to reduce motor-related potentials during sound presentation. The intertrial interval, i.e., the interval between the participant's response and the next trial, was 1000 ms. No feedback was provided after each response. In the passive condition, participants watched a silent movie with subtitles and were asked to ignore the auditory stimuli. In the passive listening condition, the interstimulus interval varied randomly between 800 and 1000 ms. The order of the active and passive conditions was counterbalanced across participants.

C. Electrophysiological recording and analysis

The electroencephalogram (EEG) was digitized continuously (bandpass 0.05–50 Hz; 250-Hz sampling rate) from an array of 64 electrodes using NeuroScan SynAmps and stored for offline analysis. Eye movements were monitored with electrodes placed at the outer canthi and at the superior and

inferior orbit. During the recording, all electrodes were referenced to the midline central electrode (i.e., *Cz*); for data analysis they were re-referenced to an average reference and the electrode *Cz* was reinstated.

The analysis epoch included 200 ms of prestimulus activity and 800, 1000, or 1600 ms of poststimulus activity for the short, medium, and long duration sounds, respectively. Trials contaminated by excessive peak-to-peak deflection ($\pm 200\ \mu$V) at the channels not adjacent to the eyes were automatically rejected before averaging. ERPs were then averaged separately for each site, stimulus duration, stimulus type, and listening condition. ERPs were digitally low-pass filtered to attenuate frequencies above 15 Hz. For each individual average, the ocular artifacts (e.g., blinks, saccades, and lateral movements) were corrected by means of ocular source components using the Brain Electrical Source Analysis (BESA) software (Picton *et al.*, 2000).

The ERP waveforms were quantified by computing mean values in selected latency regions, relative to the mean amplitude of the 200-ms prestimulus activity. The intervals chosen for the ORN and P400 mean amplitude were 100–200 ms and 300–400 ms, respectively. To ease the comparison between active and passive listening, the ERPs for correct and incorrect trials in the active listening condition were lumped together. Trials with an early response (i.e., response during sound presentation) were excluded from the analysis.

The effects of sound duration on perceptual judgment were subjected to a repeated measures within-subject analysis of variance (ANOVA) with sound duration and stimulus type as factors. Accuracy was defined as hits minus false alarms. For the ERP data, the independent variables were participants' listening condition (active versus passive), sound duration (short, medium, long), stimulus type (tuned versus mistuned), and electrode (Fz, F1, F2, FCz, FC1, FC2, Cz, C1, and C2). Scalp topographies using the 61 electrodes (omitting the periocular electrodes) were statistically analyzed after scaling the amplitudes to eliminate amplitude differences between stimuli and conditions. For each participant and each condition, the mean voltage measurements were normalized by subtracting the minimum value from each data point and dividing by the difference between the maximum and minimum value from the electrode set (McCarthy and Wood, 1985). Whenever appropriate, the degrees of freedom were adjusted with the Greenhouse–Geisser epsilon. All reported probability estimates are based on these reduced degrees of freedom.

III. RESULTS

A. Behavioral data

Overall, participants were more likely to report hearing two concurrent stimuli when the complex sound included a mistuned harmonic. Conversely, they were more likely to report perceiving one complex sound when the sound components were all harmonically related. The main effects of stimulus type and sound duration on perceptual judgment were not significant. However, there was a significant interaction between sound duration and stimulus type, $F(2,18) = 5.75$, $p < 0.02$ (Fig. 1). Analyses of simple main effects revealed that participants were significantly less likely to report hearing one complex sound when the tuned stimuli increased in duration, $F(2,36) = 5.63$, $p < 0.01$. In comparison, the perception of the mistuned harmonic as a separate tone was little affected by increasing sound duration, $F(2,36) = 1.97$.

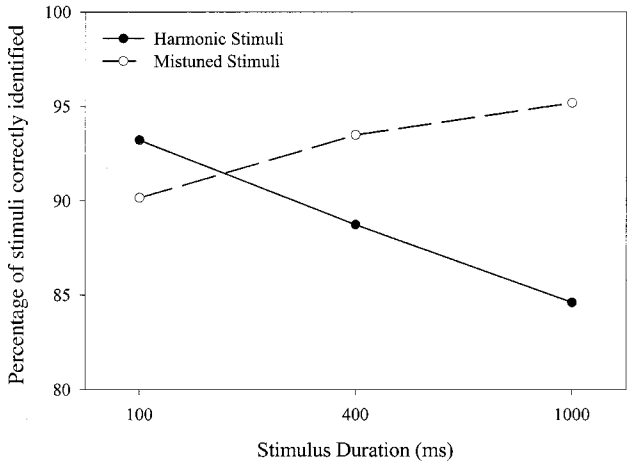

FIG. 1. Probability of reporting hearing one sound or two sounds as a function of stimulus duration.

B. Electrophysiological data

Figure 2 shows the group mean ERPs elicited by tuned and mistuned stimuli as a function of sound duration during passive and active listening. In both listening conditions, tuned and mistuned stimuli elicited a clear N1–P2 complex. At the midline frontocentral site (i.e., FCz), the N1 and P2 deflections peaked at about 125 and 195 ms after sound onset, respectively. Middle and long duration sounds generated a sustained potential and a small offset response. The N1 amplitude was larger during active than passive listening, $F(1,9) = 21.48$, $p < 0.001$. The effect of sound duration on the N1 amplitude was not significant nor was the interaction

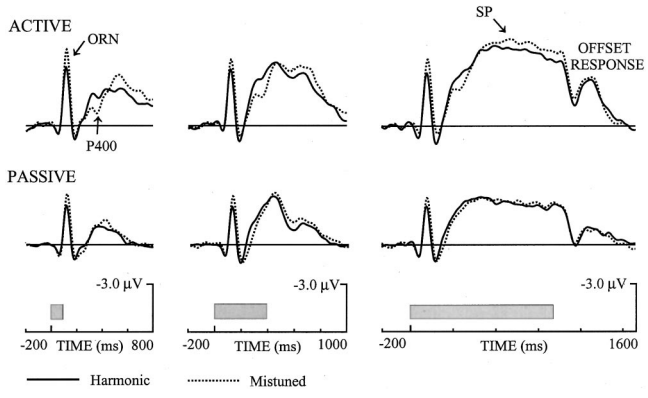

FIG. 2. Group mean event-related brain potentials (ERPs) from the midline frontocentral site (FCz) as a function of sound duration and harmonicity. Top: ERPs recorded when individuals were required to decide whether one sound or two sounds were present (active listening). Bottom: ERPs recorded when individuals were asked to watch a movie and to ignore the auditory stimuli (passive listening). The gray rectangle indicates the duration of the stimulus.

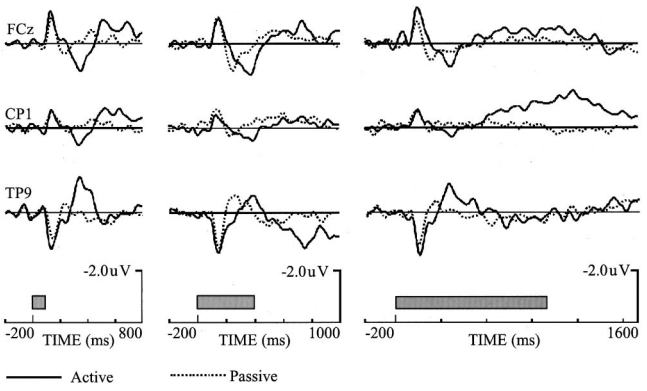

FIG. 3. Group mean difference waves between ERPs elicited by harmonic and inharmonic stimuli during passive and active listening at the midline frontocentral site (FCz), the left central parietal site (CP1), and the left inferior and posterior temporal site (TP9). The tick marks indicate 200 ms for the short and middle duration sounds, and 300 ms for the long duration sound.

between sound duration and listening condition. The P2 wave amplitude and latency were not significantly affected by the listening condition or sound duration.

The ERPs to mistuned stimuli showed a negative displacement compared to those elicited by tuned stimuli. The effects of mistuning on ERPs can best be illustrated by subtracting ERPs to tuned stimuli from ERPs elicited by mistuned stimuli (Fig. 3). In the active listening condition, the difference waves revealed a biphasic negative–positive potential that peaked at about 160 and 360 ms poststimulus. The negative wave, referred to as the ''object-related negativity'' (ORN), was maximum at frontocentral sites and inverted in polarity at inferior temporal sites. ANOVA with stimulus type, listening condition, stimulus duration, and electrode as factors yielded a main effect of stimulus type, $F(1,9)=20.54$, $p<0.001$, and a main effect of listening condition, $F(1,9)=16.48$, $p<0.01$. The interaction between listening condition and stimulus type was not significant, $F(1,9)=3.69$, $p=0.09$. A separate ANOVA on ERP data recorded during passive listening yielded a main effect of stimulus type, $F(1,9)=17.16$, $p<0.01$. This indicates that a significant ORN was present during passive listening. In both listening conditions, the ORN amplitude and latency was little affected by sound duration.

In the active listening condition, the ORN was followed by a positive wave peaking at 350 ms poststimulus referred to as the P400. Like the ORN, the P400 was biggest over frontocentral sites and was inverted in polarity at occipital and temporal sites (see Figs. 3 and 4). Complex sounds with the mistuned harmonic generated greater positivity than tuned stimuli, $F(1,9)=7.90$, $p<0.05$. The interaction between stimulus type and listening condition was significant, $F(1,9)=7.32$, $p<0.05$, reflecting greater P400 amplitude during active than passive listening. A separate ANOVA on the ERPs recorded during passive listening yielded no main effect of stimulus type, $F(1,9)=0.28$. Like the ORN, there was no significant interaction between sound duration and stimulus type, $F(2,18)=1.69$, $p=0.214$, indicating that P400 amplitude was not significantly affected by the duration of the mistuned stimulus.

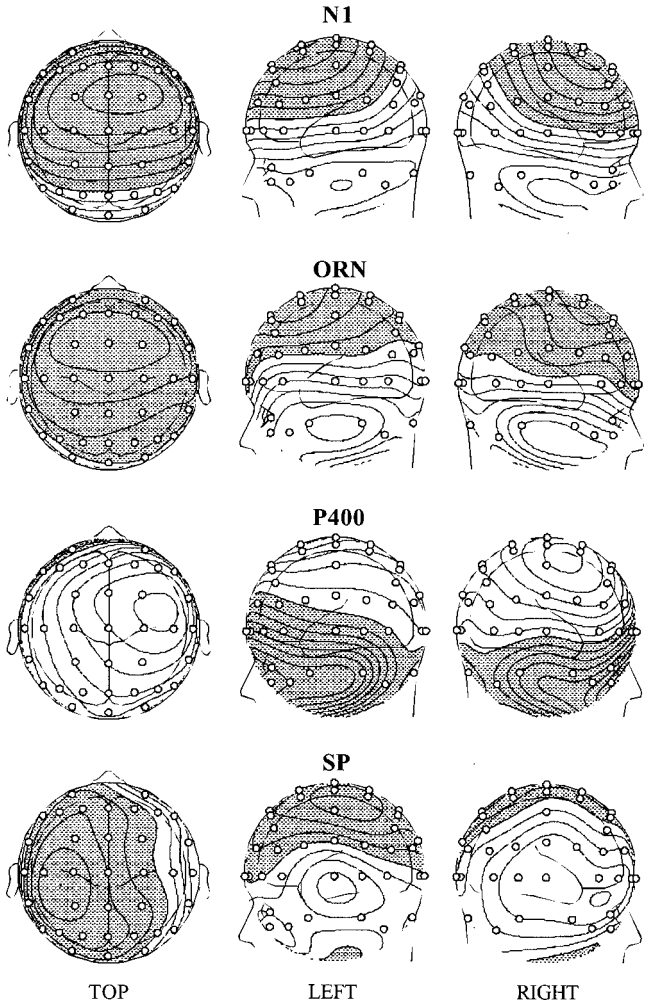

FIG. 4. Contour maps for the N1 (120 ms), ORN (160 ms), P400 (360 ms), and sustained potential (800 ms). The N1, ORN, and P400 topographies represent the peak amplitude measurement for the short duration signal (i.e., 100 ms). The sustained potential (SP) topography represents the amplitude measurement for the long duration signal (i.e., 1000 ms). Shade indicates negativity, whereas light indicates positivity. For the N1 wave the contour spacing was set at 0.6 μV. For the ORN, P400, and sustained potential the contour spacing was set at 0.2 μV. The negative polarity is illustrated by the shaded area. The open circle indicates electrode position.

A visual inspection of the data revealed a positive wave that peaked at 245 ms following sound onset that was present during the passive listening. This positive wave peaked earlier than the P400 and was more frontally distributed than the P400. The positive wave recorded during passive listening was affected by sound duration, $F(2,18)=8.99$, $p<0.01$, being larger for middle than the short or the long duration sounds ($p<0.05$, in both cases).

1. Sustained potentials

Long duration stimuli elicited a large and widespread sustained potential that was maximum at frontocentral sites. To take into account the widespread nature of the sustained response, the effects of mistuning and listening condition on the sustained potentials were quantified using a larger array of electrodes (i.e., F1, F2, F3, F4, F5, F6, FC1, FC2, FC5, FC6, C1, C2, C3, C4, C5, C6). ANOVA for the 600–1200-ms interval following sound onset yielded a main effect

of listening condition, $F(1,9)=12.12$, $p<0.01$, reflecting greater amplitude during active than passive listening (Fig. 3). The main effect of mistuning was not significant nor was the interaction between listening condition and mistuning. However, there was a significant interaction between mistuning and hemisphere, $F(1,9)=6.34$, $p<0.05$, and a three-way interaction including listening condition, mistuning, and hemisphere, $F(1,9)=9.64$, $p<0.02$. Therefore, the effect of mistuning on the sustained potential was examined separately for the left and right hemispheres. The effect of mistuning on the sustained potential was significant only over the left hemisphere, $F(1,9)=7.25$; $p<0.05$ (Fig. 4). The interaction between listening condition and mistuning was not significant for the selected electrodes. However, it was highly significant for central electrodes near the midline [e.g., C1 and C3, $F(1,9)=10.77$, $p<0.01$].

2. Scalp distribution

Scalp distributions are an important criterion in identifying and distinguishing between ERP components. The assumption is that different scalp distributions indicate different spatial configurations of intracranial current sources. In the present study, we analyzed scalp distributions to examine whether the observed ERP component generation (i.e., N1, ORN, P400, sustained potentials) depends on distinct neural networks.

Figure 4 shows the amplitude distribution for the N1, ORN, P400, and mistuning-related changes in the sustained potential. The N1 was largest at frontocentral sites and inverted polarity at inferior temporal sites. The ORN amplitude distribution was not significantly different from that of the N1 wave. There was no significant difference in N1 and ORN amplitude distribution elicited by short, medium, and long duration sounds. In comparison with the N1 and the ORN, the P400 response was more lateralized over the right central areas. This difference in topography was present for short, medium, and long duration sounds, $F(60,540)>9.50$, $p<0.001$, in all cases. The N1, ORN, and P400 scalp distributions were not significantly affected by sound durations. Last, the mistuning-related change in sustained potential was greater over the left central parietal area than the N1, ORN, and P400 responses, $F(60,540)>5.00$, $p<0.01$ in all cases.

IV. DISCUSSION

Participants were more likely to report hearing two distinct stimuli when the complex sound contained a mistuned harmonic. This is consistent with previous research (e.g., Alain *et al.*, 2001; Hartmann *et al.*, 1990; Moore, Glasberg, and Peters, 1986), and shows that frequency periodicity provides an important cue in parsing co-occurring auditory objects.

The ability to perceive the mistuned harmonic as a separate tone was little affected by increasing sound duration. Given that the amount of mistuning was well above threshold, it is not surprising that sound duration had little impact on perceiving the mistuned harmonic as a separate tone. More surprising was the finding that for tuned stimuli participants were more likely to report hearing two auditory objects when the complex sound was long rather than short. Because the third harmonic was the only harmonic that was mistuned in the present study, participants may have realized that the only changing component was always in the same frequency region and therefore listened more carefully for sounds at that particular frequency. It has been shown that individuals are able to identify a single harmonic in a complex sound if they have previously listened to that harmonic presented alone (for a review, see Bregman, 1990). A similar effect could have taken place in the present study. Participants could have heard the mistuned partial as a separate tone and this tone may have primed them to hear, in the tuned stimuli, the third harmonic which was the most similar in frequency with the mistuned harmonic. Hence, the relevant figure, which was identified by the attention processes, was not the whole Gestalt of the complex sound but the changing third harmonic over different trials.

Two ERP components were associated with the perception of the mistuned harmonic as a separate tone. The first one was the ORN, which was maximum at frontocentral sites and inverted in polarity at inferior parietal and occipital sites. This amplitude distribution is consistent with generators in auditory cortices along the Sylvian fissure. Like participants' perception of the mistuned harmonic as a separate tone, the ORN amplitude and latency were little affected by increasing sound duration. This suggests that concurrent sound segregation depends on a transient neural response triggered by the automatic detection of inharmonicity. As previously suggested by Alain *et al.*, the ORN may index an automatic mismatch detection process between the mistuned harmonic and the harmonic frequency expected based upon the harmonic template extrapolated from the incoming stimulus.

Mistuned stimuli generated a significant ORN even when participants were not actively attending to the stimuli. In addition, the ORN amplitude was similar in both active and passive listening conditions. These findings replicate those of Alain *et al.* (2001), and are consistent with the proposal that this component indexes a relatively automatic process. The results are also consistent with the proposal that the ORN indexes primarily bottom-up processes and that concurrent sound segregation may occur independently of listener's attention. However, the role of attention in detecting a mistuned harmonic will require further empirical research. In the present study, listeners' attention may have wandered to the auditory stimuli while they watched the subtitled movie, thereby contributing to the ORN recorded during passive listening.

The ORN presents some similarities in latency and amplitude distribution with another ERP component called the mismatch negativity, or MMN. The MMN is elicited by the occurrence of rare deviant sounds embedded in a sequence of homogeneous standard stimuli. Like the ORN, the MMN has a frontocentral distribution and its latency peaks at about 150 ms after the onset of deviation. Both ORN and MMN can be recorded while listeners are reading or watching a video and therefore are thought to index bottom-up processing of auditory scene analysis. A crucial difference between the two components is that while the MMN generation is highly sensitive to the perceptual context, the ORN generation is not.

That is, the MMN is elicited *only* by rare deviant stimuli, whereas the ORN is elicited by mistuned stimuli whether they are presented occasionally or frequently (Alain *et al.*, 2001). Thus, the MMN reflects a mismatch between the incoming auditory stimulus and what is expected based on the previously occurring stimuli, whereas the ORN indexes a discrepancy between the mistuned harmonic and the harmonic template that is presumably extrapolated from the incoming stimulus. As mentioned earlier, scalp distributions and dipole source modeling are important criteria in identifying and distinguishing between ERP components. Thus, further research comparing the scalp distributions of the ORN and MMN may provide evidence that these two ERP components index different processes and recruit distinct neural networks.

The second component associated with concurrent sound segregation was the P400, which was present only when participants were asked to make a response. The P400 has a more lateralized and widespread distribution than the N1 or the ORN and seems to be more related to perceptual decisions. Given that participants indicated their response after the sound was presented, the P400 generation cannot be easily accounted for by motor processes. The P400 may index the perception and recognition of the mistuned harmonic as a separate object, distinct from the complex sound. As with the ORN, the P400 amplitude was little affected by sound duration, although the P400 tended to be smaller for long than middle or short duration stimuli. This result suggests that for shorter and intermediate duration sounds, the P400 amplitude may be partly superimposed by the offset response elicited by the end of the stimulus.

Long duration sounds generated a sustained potential, which was larger during active than passive listening. This enhanced amplitude may reflect additional attentional resources dedicated to the analysis of the complex sounds. Within the active listening condition, the perception of the mistuned harmonic as a separate sound generated greater sustained potential amplitude than sounds that were perceived as a single object. This suggests that concurrent sound segregation can involve both transient and sustained neural events when individuals are required to pay attention to the auditory scene. The role of the transient neural event may be to signal to higher auditory centers that more than one sound source is present in the mixture. In comparison, the enhanced sustained potential for mistuned stimuli may reflect an ongoing analysis of both sound sources for an eventual response, context updating, or a second evaluation of the mistuned harmonic. Interestingly, the mistuning-related changes in the sustained potential were lateralized to the left hemisphere and could partly reflect motor-preparation processes because participants were required to indicate their response with their right hand. However, this cannot easily account for the differences between tuned and mistuned stimuli because both stimuli required a response from the right hand, unless the differences in sustained potentials between tuned and mistuned stimuli reflect the activation of different motor programs. It is also possible that the enhanced sustained potential to mistuned stimuli reflects enhanced processing allocated to the mistuned harmonic. Perhaps there is an additional and ongoing analysis of the sound quality when one partial stands out from the complex as a separate object.

V. CONCLUSION

In summary, the perception of concurrent auditory objects is associated with two neural events that peak, respectively, at about 160 and 360 ms poststimulus. The scalp distribution is consistent with generators in auditory cortices, reinforcing the role of primary and secondary auditory cortex in scene analysis. Although it cannot be excluded that concurrent sound segregation may have taken place at some stage along the auditory pathway before auditory cortices, the perception of the mistuned harmonic as a separate sound does involve primary and secondary auditory cortices.

The ORN was little affected by sound duration and was present even when participants were asked to ignore the stimuli. We propose that this component indexes a transient and automatic mismatch process between the harmonic template extrapolated from the incoming stimulus and the harmonic frequency expected based upon the fundamental of the complex sound. As with the ORN, the P400 was little affected by sound duration. However, the P400 is present only when individuals are required to discriminate between tuned and mistuned stimuli, suggesting that the P400 generation depends on controlled processes responsible for the identification of the stimuli and the generation of the appropriate response. Last, the perception of the mistuned harmonic generated larger sustained potentials than the perception of tuned stimuli. The effect of mistuning on the sustained potential was present only during active listening, suggesting that attention to complex auditory scenes recruits both transient and sustained processes but that scene analysis of sounds presented outside the focus of attention may depend primarily on transient neural events.

Alain, C., Arnott, S. R., and Picton, T. W. (**2001**). ''Bottom-up and top-down influences on auditory scene analysis: Evidence from event-related brain potentials,'' J. Exp. Psychol. Hum. Percept. Perform. **27**(5), 1072–1089.

Bregman, A. S. (**1990**). *Auditory Scene Analysis: The Perceptual Organization of Sounds* (The MIT Press, London).

Goldstein, J. L. (**1978**). ''Mechanisms of signal analysis and pattern perception in periodicity pitch,'' Audiology **17**(5), 421–445.

Hartmann, W. M. (**1988**). ''Pitch, perception and the segregation and integration of auditory entities,'' in *Auditory Function: Neurobiological Bases of Hearing*, edited by G. M. Edelman, W. E. Gall, and W. M. Cowan (Wiley, New York), pp. 623–645.

Hartmann, W. M. (**1996**). ''Pitch, periodicity, and auditory organization,'' J. Acoust. Soc. Am. **100**, 3491–3502.

Hartmann, W. M., McAdams, S., and Smith, B. K. (**1990**). ''Hearing a mistuned harmonic in an otherwise periodic complex tone,'' J. Acoust. Soc. Am. **88**, 1712–1724.

Lin, J. Y., and Hartmann, W. M. (**1998**). ''The pitch of a mistuned harmonic: Evidence for a template model,'' J. Acoust. Soc. Am. **103**, 2608–2617.

McCarthy, G., and Wood, C. C. (**1985**). ''Scalp distributions of event-related potentials: An ambiguity associated with analysis of variance models,'' Electroencephalogr. Clin. Neurophysiol. **62**, 203–208.

Moore, B. C., Glasberg, B. R., and Peters, R. W. (**1986**). ''Thresholds for hearing mistuned partials as separate tones in harmonic complexes,'' J. Acoust. Soc. Am. **80**, 479–483.

Moore, B. C., Peters, R. W., and Glasberg, B. R. (**1985**). ''Thresholds for the detection of inharmonicity in complex tones,'' J. Acoust. Soc. Am. **77**, 1861–1867.

Picton, T. W., van Roon, P., Armilio, M. L., Berg, P., Ille, N., and Scherg, M. (**2000**). ''The correction of ocular artifacts: A topographic perspective,'' Clin. Neurophysiol. **111**(1), 53–65.

Quantifying the implications of nonlinear cochlear tuning for auditory-filter estimates

Michael G. Heinz[a)]
Speech and Hearing Sciences Program, Division of Health Sciences and Technology, Massachusetts Institute of Technology, 77 Massachusetts Avenue, Cambridge, Massachusetts 02139 and Hearing Research Center, Biomedical Engineering Department, Boston University, 44 Cummington Street, Boston, Massachusetts 02215

H. Steven Colburn and Laurel H. Carney[b)]
Hearing Research Center, Biomedical Engineering Department, Boston University, 44 Cummington Street, Boston, Massachusetts 02215

(Received 25 April 2001; revised 26 October 2001; accepted 19 November 2001)

The relation between auditory filters estimated from psychophysical methods and peripheral tuning was evaluated using a computational auditory-nerve (AN) model that included many of the response properties associated with nonlinear cochlear tuning. The phenomenological AN model included the effects of dynamic level-dependent tuning, compression, and suppression on the responses of high-, medium-, and low-spontaneous-rate AN fibers. Signal detection theory was used to evaluate psychophysical performance limits imposed by the random nature of AN discharges and by random-noise stimuli. The power-spectrum model of masking was used to estimate psychophysical auditory filters from predicted AN-model detection thresholds for a tone signal in fixed-level notched-noise maskers. Results demonstrate that the role of suppression in broadening peripheral tuning in response to the noise masker has implications for the interpretation of psychophysical auditory-filter estimates. Specifically, the estimated psychophysical auditory-filter equivalent-rectangular bandwidths (ERBs) that were derived from the nonlinear AN model with suppression always overestimated the ERBs of the low-level peripheral model filters. Further, this effect was larger for an 8-kHz signal than for a 2-kHz signal, suggesting a potential characteristic-frequency (CF) dependent bias in psychophysical estimates of auditory filters due to the increase in strength of cochlear nonlinearity with increases in CF.
[DOI: 10.1121/1.1436071]

PACS numbers: 43.66.Ba, 43.64.Bt, 43.66.Dc [MRL]

I. INTRODUCTION

The ability of the auditory system to partially resolve frequency components in a complex stimulus has been widely used as the basis for many fundamental theories of auditory perception (e.g., von Helmholtz, 1863; Fletcher, 1940, 1953). Thus, much effort has gone into developing psychophysical techniques for the measurement of auditory frequency selectivity. Fletcher (1940) observed that the detection threshold for a tone in bandlimited noise increases as the bandwidth of the noise increases up to a *critical bandwidth*, beyond which detection threshold is roughly constant. This observation led to the concept of the psychophysical *auditory filter*, which forms the basis for many modern psychophysical methods for estimating auditory tuning (for a review see Moore, 1995a).

Most psychophysical methods for measuring auditory frequency selectivity are based on the power-spectrum model of masking, which assumes that performance for tone-in-noise detection is constant when the long-term signal-to-noise power ratio is constant at the output of a linear filter centered at (or close to) the frequency of the tone (Moore, 1995a). Fletcher (1940) noted that the auditory-filter bandwidth could be estimated as the ratio of the signal power at masked threshold to the power-spectral density of a broadband noise, now referred to as the critical ratio (Moore, 1995a), if it were assumed that threshold corresponded to a signal-to-noise ratio of 0 dB at the output of the auditory filter. Auditory-filter bandwidths have also been estimated from Fletcher's band-widening experiment as the noise bandwidth (critical band) beyond which detection thresholds are constant, based on the assumption of rectangular filters. Psychophysical tuning curves have been derived by measuring the level of a variable-frequency tone or narrow-band masker that is required to just mask a low-level tone signal at the frequency of interest (e.g., Moore, 1978; Vogten, 1978). Despite the relative simplicity of these methods, the use of notched-noise maskers to estimate auditory-filter shapes has proven to be a much more reliable psychophysical method (Moore, 1995a). In the notched-noise method, detection thresholds are measured for a tone in the presence of two bandlimited noise maskers that are above and below the tone frequency (Patterson, 1976; Glasberg and Moore, 1990, 2000; Rosen *et al.*, 1998). Detection threshold is measured as

[a)]Current address: Department of Biomedical Engineering, Johns Hopkins University, 505 Traylor Building, 720 Rutland Avenue, Baltimore, MD 21205. Electronic mail: mgheinz@bme.jhu.edu
[b)]Current address: Department of Bioengineering and Neuroscience, Institute for Sensory Research, 621 Skytop Road, Syracuse University, Syracuse, NY 13244-5290.

a function of the separation between the two noise bands (i.e., the notch width), and the power-spectrum model is used to derive an auditory-filter shape that accounts for the rate of threshold decrease as notch width is increased. Asymmetric notches are often used to derive the upper and lower sides of the auditory filter separately, and thus allow estimates of auditory-filter asymmetry to be made. While the notched-noise method provides estimates of auditory filters that are successful in predicting detection performance in a variety of masking conditions (e.g., Derleth and Dau, 2000), a fundamental question is whether the frequency selectivity measured psychophysically is primarily determined by peripheral tuning.

Glasberg and Moore (1990) derived equations that describe the variation in psychophysical estimates of auditory-filter equivalent-rectangular bandwidths (ERBs) with characteristic frequency (CF) and with masker level. The variation in auditory-filter ERB with CF was consistent with the idea that a psychophysical ERB represents a constant distance along the basilar membrane (Greenwood, 1961). The variation in psychophysical estimates of auditory filters with stimulus level was consistent with the well-established result that cochlear tuning broadens with increases in stimulus level (e.g., Patuzzi and Robertson, 1988; Ruggero *et al.*, 1997). In addition, psychophysical estimates of auditory filters were typically broader for hearing-impaired listeners than for normal-hearing listeners (Glasberg and Moore, 1986; Moore, 1995b; Moore *et al.*, 1999b), consistent with the loss of sharp frequency tuning in basilar-membrane and auditory-nerve (AN) responses of damaged cochleae (Patuzzi *et al.*, 1989; Ruggero and Rich, 1991; Liberman and Dodds, 1984). Moore *et al.* (1999b) have shown that psychophysical estimates of auditory-filter ERB from the notched-noise method are correlated with several other psychophysical measures assumed to be related to cochlear nonlinearity. Thus, it appears that psychophysical estimates of frequency selectivity from the notched-noise method are closely related to peripheral tuning in humans. Consistent with this conclusion, Evans *et al.* (1992) found a high degree of correspondence between psychophysical and physiological ERBs both measured in guinea pigs.

In spite of this general agreement about the importance of psychophysical auditory filters, there is continued debate about the proper method for psychophysically estimating auditory-filter shapes as a function of level (Lutfi and Patterson, 1984; Moore and Glasberg, 1987; Glasberg and Moore, 1990, 2000; Rosen and Baker, 1994; Moore, 1995a; see Rosen *et al.*, 1998 for a review). This debate has focused on which aspect of the stimulus, signal or masker level, controls the auditory filter shape. Moore (1995a) has proposed masker level per ERB as the controlling variable, rather than overall masker level or spectrum level. Rosen and Baker (1994) and Rosen *et al.* (1998) argued that deriving auditory filters across a range of fixed noise spectrum levels (e.g., Glasberg and Moore, 1990) is only appropriate if the level dependence of the auditory filter is determined by the noise spectrum level. If auditory filters were to vary with signal level rather than masker level, then the auditory filter would vary across notch widths because the signal level decreases as notch width is increased, and the psychophysically estimated auditory filter would represent an average auditory filter across a range of signal levels. Rosen *et al.* (1998) have shown that notched-noise detection data across a wide range of levels were fitted better by the power-spectrum model when the auditory filter was assumed to depend on the signal level rather than on the masker level. Glasberg and Moore (2000), who used uniformly exciting noise that was designed to provide equal excitation for each psychophysical ERB, also concluded that models in which the signal level was assumed to control auditory-filter shape were better able to predict the detection data. Despite the debate over whether the signal or masker level controls auditory-filter shape, methods based on both views result in nonlinear changes in auditory-filter shapes that qualitatively match nonlinear trends in physiologically measured tuning. While the debate has focused on assumptions about which aspects of the stimulus control nonlinear tuning, a direct comparison between psychophysical measures of frequency selectivity and physiological measures of nonlinear peripheral tuning has not been made in the same subject.

The present study uses a computational AN model to relate peripheral tuning to estimates of frequency selectivity from psychophysical methods. This phenomenological AN model provides a useful description of nonlinear peripheral tuning (Heinz *et al.*, 2001c; see also Zhang *et al.*, 2001) and is used to evaluate how different nonlinear AN properties affect psychophysical methods for estimating auditory filters.

Many of the observed nonlinear AN response properties appear to result from a single physiologically vulnerable mechanism that controls peripheral tuning (Sachs and Abbas, 1974; Sewell, 1984; Patuzzi *et al.*, 1989; Ruggero and Rich, 1991; Ruggero *et al.*, 1992; see the review by Ruggero, 1992). This mechanism is widely believed to be related to outer-hair-cell (OHC) electromotility; however, the underlying biophysical basis for the role of the OHCs in this mechanism is still unknown (Allen, 2001). The most prevalent view is that the OHCs provide the high sensitivity and sharp tuning that characterize normal hearing through an active process, often referred to as the *cochlear amplifier*, which enhances the vibration of the basilar membrane in response to low-level sounds (e.g., Yates, 1995; Moore, 1995b). The results from the present study do not depend on the biophysical basis for the underlying mechanism; rather, they depend only on the idea that a single physiologically vulnerable mechanism produces many of the nonlinear peripheral response properties that have been described. Basilar-membrane tuning has been shown to broaden with increases in level and to demonstrate associated compressive magnitude responses and nonlinear phase responses near CF (Ruggero *et al.*, 1997). These three nonlinear properties are related in terms of a filter gain/bandwidth trade-off, i.e., the peripheral filter gain at CF decreases as the bandwidth increases with increases in stimulus level. The nonlinear phase shifts correspond to the peripheral-filter phase-versus-frequency response becoming shallower as level increases, and have also been observed in inner-hair-cell (IHC) responses (Cheatham and Dallos, 1998) and AN responses (Anderson *et al.*, 1971). Recio *et al.* (1998) have shown that

the dynamics of cochlear compression are extremely fast, with a time constant on the order of 200 μs.

Two-tone suppression, another response property of the auditory periphery associated with nonlinear cochlear tuning, refers to suppression of basilar-membrane and AN responses to CF tones by an off-CF tone (Sachs and Kiang, 1968; Delgutte, 1990b; Ruggero *et al.*, 1992). Delgutte (1990a) demonstrated that AN suppression plays an important role in the masking of signals by off-frequency stimuli, a finding that has been supported by related psychophysical experiments (Oxenham and Plack, 1998). Suppression has been hypothesized to play a role in psychophysical estimates of auditory tuning based on the common finding that psychophysical estimates of frequency selectivity are sharper when using nonsimultaneous masking than when using simultaneous masking (e.g., Houtgast, 1977; Moore, 1978; Moore and Glasberg, 1981, 1982, 1986; Moore and O'Loughlin, 1986; Moore *et al.*, 1987). The role of suppression is often discussed in terms of how the reduction in signal response due to the off-frequency masker may affect psychophysical estimates of auditory tuning. However, Moore and O'Loughlin (1986) argue that this simple-attenuation view is not as well justified as a distributed-attenuation view, which is supported by both psychophysical (e.g., Moore and Glasberg, 1982) and physiological (Pickles, 1984) studies. A direct measure of the effect of off-frequency noise on the underlying peripheral tuning was reported by Kiang and Moxon (1974), who showed that the tuning curves of high-CF AN fibers became broader and CF-tone thresholds were raised when a near-threshold, low-frequency masking noise band was presented simultaneously with the tone. The phenomenological AN model used in the present study (Heinz *et al.*, 2001c; see also Zhang *et al.*, 2001) represents suppression as the ability of off-frequency energy to reduce the excitatory-filter gain at CF and thus to broaden peripheral tuning.

Thus, consideration of the peripheral response properties associated with nonlinear cochlear tuning suggests that psychophysical methods would have difficulty in directly estimating AN-fiber frequency selectivity. This does not necessarily pose a problem for psychophysical studies that aim to characterize behavioral frequency selectivity without regard for the underlying mechanisms. However, this issue is important for interpreting changes in psychophysical estimates of frequency selectivity as a function of level or cochlear state, as well as for modeling studies that use human psychophysical data to specify peripheral tuning.

The present study relates many of the response properties associated with nonlinear cochlear tuning to estimates of psychophysical auditory filters by combining a phenomenological AN model with signal detection theory (SDT). Peripheral tuning (as specified in the AN model) can be directly compared to estimates of psychophysical auditory filters based on SDT analysis of AN-model population discharge patterns. Previous studies have used SDT with analytical AN-population models to quantify psychophysical performance limits based on the stochastic nature of AN discharge patterns (e.g., Siebert, 1968, 1970; Colburn, 1973, 1981; Delgutte, 1987; Heinz *et al.*, 2001b). A benefit of this approach is that the AN forms a bottleneck in the information pathway from the periphery to the brain, and thus the effects of peripheral response properties can be characterized based on the total information that is available to the central nervous system for the psychophysical task. A second benefit of considering AN information is that the effects of several significant peripheral transformations (between the basilar membrane and AN) are included, e.g., that AN information is encoded by intrinsically random all-or-none action potentials that have a spontaneous rate, and that the driven rate of AN fibers typically saturates about 30–40 dB above threshold. Heinz *et al.* (2001b) used this approach to demonstrate that compressive magnitude responses and nonlinear phase responses associated with nonlinear cochlear tuning are significant for the encoding of sound level based on responses of a narrow range of CFs; however, their analytical AN model was limited to pure-tone stimuli, and several extensions of this approach were necessary to evaluate detection in random notched-noise maskers in the present study. Heinz *et al.* (2001a) demonstrated the use of computational AN models with this SDT approach, and a theoretical extension of the SDT analysis was developed to quantify the influence of random stimulus variation (in addition to AN variability) on psychophysical performance (Heinz, 2000).

In the present study, psychophysical auditory filters were estimated from the AN model using the notched-noise method by predicting psychophysical detection thresholds based on the information available in the population discharge patterns of AN-model fibers. Two specific questions were addressed: (1) How closely are estimates of psychophysical auditory filters related to peripheral tuning, given that psychophysical detection is based on a population of 30 000 AN fibers that have a wide range of CFs, different spontaneous rates (SRs), and different thresholds (Liberman, 1978)? (2) How do AN response properties associated with nonlinear cochlear tuning influence estimates of psychophysical auditory filters? Notched-noise maskers with a fixed spectrum level (as in Glasberg and Moore, 1990) were used in order to present the most straightforward demonstration of the expected effects of nonlinear AN properties on estimates of psychophysical auditory filters. Four versions of the computational AN model were used to demonstrate the separate contributions of compression and suppression to the estimates of psychophysical auditory filters.

II. METHODS

A. Computational auditory-nerve model

Zhang *et al.* (2001) developed a phenomenological model for cat AN responses. This model has a single nonlinear mechanism that accounts for many nonlinear AN response properties, including the on- and off-frequency control of peripheral tuning, i.e., compression and suppression. Heinz *et al.* (2001c) modified the original model in several ways to make it more appropriate for evaluating human psychophysical performance. These modifications included a description of human tuning, implementation of three SR groups (Liberman, 1978), and several implementations of peripheral-tuning control to allow the separate effects of compression and suppression to be evaluated. The AN model

used in the present study was identical (including all parameter values) to the Heinz *et al.* (2001c) model. The model properties that are relevant to the current study are described below, while the details of the model implementation are described elsewhere (Heinz *et al.*, 2001c; Zhang *et al.*, 2001).

The AN model has a signal path that consists of a nonlinear, third-order narrow-band filter followed by a broader linear, first-order filter and an IHC/synapse module that produces the time-varying discharge rate $r(t)$ for a given CF. The bandwidth and gain of the nonlinear signal-path filter are varied according to the output of a control path, which consists of a nonlinear wideband filter followed by an OHC module. As the level of the stimulus energy that passes through the control-path filter increases, the bandwidth of the nonlinear signal-path filter is increased and the filter gain at CF is reduced, representing the reduction in cochlear gain at CF as stimulus level is increased above roughly 20 dB SPL (Ruggero *et al.* 1997). This single control mechanism in the AN model produces nonlinear tuning with both compression and suppression. Compression represents the reduction in cochlear gain at CF as the level of the stimulus near CF is increased (Ruggero *et al.*, 1997). Suppression represents the ability of off-CF energy to reduce the cochlear gain at CF (Ruggero, 1992). Stimulus energy that passes through the wideband control-path filter but not the narrow-band excitatory filter causes suppression (e.g., Geisler and Sinex, 1980). The wideband control-path filter was centered slightly higher in frequency than the signal-path filter (a basal shift of 1.2 mm along the basilar membrane; Heinz *et al.*, 2001c; see Zhang *et al.*, 2001 for details). The size of the basal shift and the bandwidth of the control-path filter were chosen to match AN two-tone suppression tuning curves from the literature (e.g., Sachs and Kiang, 1968; Delgutte, 1990b). The dynamics of the AN-model control path are extremely fast, with the ability of the control signal to follow cycle-by-cycle fluctuations in the stimulus determined by an 800-Hz low-pass filter in the OHC module. The fast dynamics in the model control path are consistent with the 200-μs basilar-membrane compression time constant reported by Recio *et al.* (1998) and the nearly instantaneous effects of two-tone suppression (e.g., Arthur *et al.*, 1971).

The low-level tuning of the nonlinear AN model was set based on low-level psychophysical estimates of human auditory tuning (Glasberg and Moore, 1990). The ERBs of the nonlinear signal-path filters at low levels were set to be 1.2 times smaller than the standard midlevel psychophysical estimates of auditory-filter ERBs described by Glasberg and Moore (1990) as a function of CF, a factor that is roughly consistent with their more complicated level-dependent equation for auditory-filter ERB (see Heinz *et al.* 2001c for details). High-level tuning in the AN model is broadened because the cochlear gain at CF is reduced as stimulus level increases, i.e., due to the filter gain/bandwidth trade-off. The maximal reduction in cochlear gain at CF across level (often referred to as the cochlear-amplifier gain), ranges from 20 dB at and below 500 Hz to roughly 55 dB at and above 8 kHz, which is consistent with basilar-membrane data from the chinchilla basal and apical turns (Ruggero *et al.*, 1997; Cooper and Rhode, 1997) and with human psychophysical data (Hicks and Bacon, 1999; Glasberg and Moore, 2000). The bandwidth of the linear, first-order filter in the signal path equaled the time-averaged bandwidth of the nonlinear signal-path filter at high levels, i.e., with full reduction of the cochlear gain (Heinz *et al.*, 2001c; Zhang *et al.*, 2001). The effective ERB of the total signal-path filter at low levels was calculated computationally to be about 20% larger than the low-level ERB of the nonlinear signal-path filter for a 2-kHz CF, and about 25% larger for an 8-kHz CF.

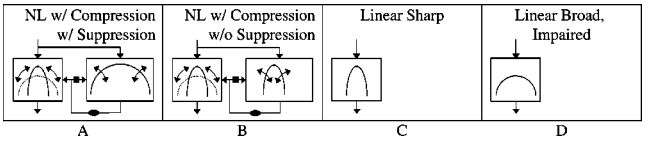

FIG. 1. Four versions of the phenomenological auditory-nerve model used to isolate the effects of compression and suppression on tuning. Only the section of the model that includes the peripheral tuning is illustrated; it includes the signal path (in A, B, C, D; only the initial third-order signal-path filter is shown; see the text) and the control path (in A, B; filled squares and ovals represent control-path modules that are the same in both nonlinear model versions). The curved arrows in A and B indicate that the filters fluctuate with level. A: The *nonlinear with compression and suppression* model version has a broad control-path filter. B: The *nonlinear with compression and without suppression* model has a narrow control-path filter. C: The *linear-sharp* model has sharp tuning and high gain at all stimulus levels, consistent with models A and B at low levels. D: The *linear-broad, impaired* model has broad tuning and low gain, consistent with the average tuning in models A and B at high stimulus levels.

Predictions from four versions of the AN model (Fig. 1) are compared to evaluate the role of several response properties associated with nonlinear cochlear tuning, including compression and suppression (Heinz *et al.*, 2001c). (1) The *nonlinear with compression and suppression* AN model is the standard version of the model with a level-dependent broad control-path filter [Fig. 1(A)]. (2) The *nonlinear with compression and without suppression* AN model controls the level-dependent gain and bandwidth of the signal-path filter by the stimulus energy within a narrow-band control-path filter that has the same level-dependent bandwidth and center frequency as the nonlinear signal-path filter [Fig. 1(B)]. The nonlinear models (#1 and 2) differ from one another in the spectral content of the stimulus that controls the level-dependent tuning. (3) The *linear-sharp* version of the AN model has low thresholds and linear signal-path filters with bandwidths set to the low-level tuning in the nonlinear AN model [Fig. 1(C)]. (4) The *linear-broad, impaired* version of the AN model has high thresholds and linear filters with broad bandwidths that match the time-averaged high-level tuning in the nonlinear AN model [Fig. 1(D)]; this model represents an impaired cochlea in which the cochlear-amplifier mechanism is absent (e.g., total OHC loss). Loss of the cochlear-amplifier gain, which increases as a function of CF (as discussed above), produces a sloping high-frequency hearing loss for this version of the AN model (Heinz *et al.*, 2001c).

Each version of the AN model was used to generate a population response for each of the three SR groups described by Liberman (1978). All AN fibers within an SR group had the same SR, threshold, and dynamic range for a CF-tone response (Heinz *et al.*, 2001c). Spontaneous rates of

60, 5, and 1 spikes/s were used for the high-, medium-, and low-SR populations, respectively. The physiological thresholds for high-SR fibers were chosen for simplicity to be near 0 dB SPL at all CFs, i.e., no external- or middle-ear filtering was included in this AN model. The lowest physiological thresholds observed in cat AN fibers are roughly 0 dB SPL and are found for high-SR fibers (Liberman, 1978; Miller *et al.*, 1997). Auditory-nerve thresholds were inversely related to SR in the model (Liberman, 1978). The elevated thresholds for low-SR fibers ($\sim$20 dB above the high-SR class) resulted in wide dynamic ranges for the low-SR fibers due to the compression in the signal-path filter response (Sachs and Abbas, 1974). The increased amount of compression at high CFs resulted in ''straight'' rate-level curves for high-CF low-SR fibers and ''sloping saturation'' rate-level curves at low CFs, consistent with the lack of straight rate-level curves observed for CFs below 1.5 kHz in guinea pigs (Winter and Palmer, 1991).

Sixty model CFs ranging from 200 Hz to 20 kHz were used to simulate the AN population response and were uniformly spaced in location according to a human cochlear map (Greenwood, 1990; as in Heinz *et al.*, 2001a).[1] This spacing of fiber CFs corresponded to roughly a 0.5-mm separation on the basilar membrane and is estimated to be about one-half of a human psychophysical ERB (Glasberg and Moore, 1990). The tone frequency was always chosen to be equal to one of the model CFs (e.g., the closest model CFs to the 2- and 8-kHz conditions used in the present study were 1927 and 8079 Hz, respectively, based on the roughly log-spaced cochlear map). Populations of high-, medium-, and low-SR fibers were simulated by assuming that 200 high-SR, 75 medium-SR, and 50 low-SR fibers were represented by each model CF. This represents all AN fibers within the frequency range from 200 Hz to 20 kHz [based on a total population of 30 000 AN fibers from 20 Hz to 20 kHz in human (Rasmussen, 1940; Heinz *et al.*, 2001a)], and is consistent with the 61%, 23%, and 16% distributions for high-SR, medium-SR, and low-SR fibers reported by Liberman (1978). All AN fibers were assumed to have independent Poisson discharge-generating mechanisms. Thus, the model AN-fiber responses were treated as conditionally independent stochastic point processes given the stimulus (Heinz *et al.*, 2001a); however, there were correlations across AN-fiber responses due to random stimulus fluctuations associated with the noise maskers (see below).

B. Signal detection theory

Heinz *et al.* (2001a) used SDT analysis with computational AN models to predict psychophysical performance limits based on the intrinsic variability in AN-discharge responses; however, this analysis was limited to deterministic stimuli. For masking studies with random-noise maskers, the effects of random stimulus fluctuations on the variability of AN responses must also be taken into account. The present study used the SDT analysis developed by Heinz (2000) to quantify detection performance limits due to random variations in the notched-noise stimuli as well as in the AN responses. Predicted performance was calculated for a processor based on *rate-place* information (as shown in Fig. 2 of Heinz *et al.*, 2001a). In the rate-place analysis, the observations on which the detection decision is made are the population of spike counts $\{K_i\}_{i=1,\ldots,M}$, where M is the total number of AN fibers. The counts are produced by M homogeneous Poisson processes (conditionally independent, given the stimulus) with rates equal to the average rates r_i produced by the AN model. This section provides an overview of the detection-in-noise analysis for rate-place information that was used in the current study, while the details of this approach for both rate-place information and *all information* (both temporal and average-rate information) are described by Heinz (2000).

A likelihood-ratio test (LRT) can be used to derive the form of an optimal processor based on a set of random observations (van Trees, 1968). For the case considered here in which the stimulus is random in addition to the AN discharges, the form of the optimal population processor can only be specified analytically if the processor is assumed to have knowledge of the average AN discharge rates $r_i(n)$ for each noise waveform n from the random-noise ensemble (Heinz, 2000); however, this is an unrealistic assumption for human listeners in a random-noise masking task. In order to remove this assumption, the same processor form as the optimal processor was used with the assumption that the processor only has knowledge of the *average-noise-response* properties (i.e., $x_i = E_n[r_i(n)]$, where E_n represents the expected value across the random-noise ensemble), and not the individual-noise responses $r_i(n)$. Thus, the predictions in the present study represent a *suboptimal* processor that is assumed to have knowledge of the average (across noise waveforms) AN discharge properties in response to the masked tone $[x_i(SN)]$ and in response to the notched-noise masker alone $[x_i(N)]$. The processor uses this knowledge of average noise responses in the same way that the optimal processor uses the knowledge of individual-noise responses.

The form of this general processor, which evaluates the number of observed discharges from the ith AN fiber based on the assumed *a priori* knowledge, $x_i(SN)$ and $x_i(N)$, is given by

$$Y_i(K_i) \triangleq \left[\ln \frac{x_i(SN)}{x_i(N)}\right] K_i + T\,[x_i(N) - x_i(SN)], \tag{1}$$

where T is the duration of the stimulus. The decision variable $Y_i(K_i)$ is a function of the random AN discharge count K_i, and thus is a random variable itself that depends on both the stimulus and AN variability. The reliability of this decision variable for indicating the presence of the tone depends on the difference in the mean value of $Y_i(K_i)$ between the signal-plus-masker (SN) and masker-alone (N) observation intervals, and on the variance of $Y_i(K_i)$. A useful metric for quantifying the sensitivity of a decision variable Y is

$$Q = \frac{(E[Y|SN] - E[Y|N])^2}{\mathrm{Var}[Y|N]}, \tag{2}$$

where detection threshold is defined as the signal level for which the sensitivity index $Q = 1$. This sensitivity metric Q is similar to $(d')^2$, and represents a complete characterization of performance when the decision variable Y is Gaussian and has equal variance in both observation intervals

(Green and Swets, 1966; van Trees, 1968). These two assumptions are reasonably accurate for characterizing just-detectable differences in decision variables that are based on the total population of all AN discharges (Siebert, 1968, 1970; Colburn, 1969, 1973, 1981; Heinz *et al.*, 2001a). Actual deviations from these assumptions do not significantly affect the characterization of performance based on the sensitivity metric Q (Colburn, 1981).

Performance based on M AN fibers was calculated for a population decision variable

$$Y=\sum_{i=1}^{M} Y_i(K_i). \tag{3}$$

The equal-weighting combination in Eq. (3) behaves in an intuitive way based on Eq. (1). Fibers for which the signal does not (on average) change the discharge rate in response to the masker [i.e., $x_i(SN)=x_i(N)$] do not contribute to the population decision variable Y because $Y_i(K_i)=0$ for any observed discharge count K_i. However, as described above the equal-weighting combination is not necessarily optimal, because across-fiber correlations are not accounted for in the way information is combined across fibers. The population sensitivity index Q based on this suboptimal processor [Eqs. (1) and (3)] is given by

$$Q=\left\{\sum_{i=1}^{M}\left[\ln\frac{x_i(SN)}{x_i(N)}\right][x_i(SN)-x_i(N)]\right\}^2 \Bigg/ \left(\frac{1}{T}\sum_{i=1}^{M}\left[\ln\frac{x_i(SN)}{x_i(N)}\right]^2 x_i(N)+\mathrm{Var}_n\left\{\sum_{i=1}^{M}\left[\ln\frac{x_i(SN)}{x_i(N)}\right]r_i(n|N)\right\}\right), \tag{4}$$

where Var_n represents the variance across the random-noise ensemble (Heinz, 2000). Note that the variance of the decision variable Y [the denominator of Eq. (4)] is separated into two terms, where the first term represents the contribution of *AN variability* and the second term represents the contribution of *stimulus variability*.

Detection performance was predicted based on the individual high-, medium-, and low-SR populations of AN fibers (as described above), as well as on the total AN-fiber population. For predictions based on a population of AN fibers, the effect on performance of any potential correlation between AN fibers of different SR or CF due to a common random-stimulus drive was accounted for by including all AN fibers in the three summations in Eq. (4). The summation across AN fibers in the numerator and in both denominator terms differs from summing individual values of Q_i. The sensitivity indices Q_i for individual fibers cannot be simply added to obtain the total sensitivity because the fibers' responses are potentially correlated when stimulated with random-noise stimuli (see Heinz, 2000). In general, if the stimulus-induced contribution to the variance [second denominator term in Eq. (4)] of the decision variable Y dominates the intrinsic-AN contribution [first denominator term in Eq. (4)], then AN fibers with similar CFs will be correlated.

Psychophysical detection thresholds based on the AN model were simulated using Eq. (4). For a fixed signal level and masker notch width, the sensitivity index Q was estimated based on AN-population responses to the signal-plus-masker and masker-alone conditions for ten individual noise waveforms n from the random-noise ensemble. The adequacy of using only ten noise waveforms to estimate E_n and Var_n was evaluated by verifying in several conditions that the results did not change significantly when more noise waveforms (20–40) were used. The sensitivity index Q was evaluated as a function of level for each notch width. The signal level at which $Q=1$ was defined as representing the psychophysical detection threshold and was determined by interpolation.

C. Notched-noise method for estimating auditory filters

Most psychophysical methods for estimating auditory-filter shapes use the power-spectrum model of masking to derive the best auditory filter to explain a set of detection data (Moore, 1995a). The power-spectrum model assumes that the psychophysical detection threshold corresponds to a fixed long-term signal-to-noise ratio (SNR) at the output of the auditory filter. To estimate the psychophysical auditory filter, signal power at detection threshold, P_S, is measured for various masker spectra $N(f)$, and the best auditory-filter shape $W(f)$ to explain the set of detection data is derived based on the constant-SNR assumption. To simplify the fitting of the detection data, a class of auditory-filter shapes $W(f)$, which can be specified by a few parameters, is often assumed.

In the present study, psychophysical detection thresholds were predicted from the AN model (as described above) for a tone in the presence of two noise bands that were above and below the tone frequency f, had bandwidths equal to $0.4f$, and had a *fixed* noise spectrum level ($N_0=20$ dB SPL). The tone was always centered arithmetically between the two noise bands, i.e., only symmetric notches were used in the present study. The notch width Δf was defined as the frequency separation between the tone and the edge of each noise band that was closest to the tone frequency, and is referred to in terms of the normalized frequency separation $\Delta f/f$. Psychophysical detection thresholds were predicted for normalized frequency separations of 0.0, 0.1, 0.2, 0.3, 0.4, 0.5, and 0.6.

The predicted AN-model detection thresholds were then used to derive an estimate of the psychophysical auditory filter $W(f)$ from a common class of auditory filters using the power-spectrum model in the usual manner (Glasberg and Moore, 1990). The class of rounded-exponential filters, $\mathrm{roex}(p,r)$, is specified by a parameter p that describes the slope of the filter and a parameter r that controls the filter dynamic range (Patterson *et al.*, 1982; also see Moore, 1995a).[2] The estimated psychophysical auditory filter represents the $\mathrm{roex}(p,r)$ filter that best describes the AN-model detection thresholds predicted from the SDT analysis. The goodness of fit is quantified in terms of the root-mean-squared deviation in dB between the predicted thresholds from the power-spectrum model and the AN-model de-

tection thresholds. The estimated psychophysical auditory filters from the fitting procedure are described in terms of the roex-filter parameters p and r, and the ERB (which equals $4f/p$). The power-spectrum model also includes the variable K_{psm}, which represents the constant signal-to-noise ratio at the output of the auditory filter at detection threshold. The corrections described by Glasberg and Moore (1990) for the transmission characteristics of the middle and external ear and for the earphone frequency response were not needed in the fitting procedure because the AN model had constant thresholds as a function of frequency (Heinz *et al.*, 2001c).

III. RESULTS

A. The relation between model peripheral filters and estimates of psychophysical auditory filters

First, estimates of psychophysical auditory filters were derived from predicted detection performance based on the total AN population using a version of the AN model with linear tuning. The ERBs of these estimated psychophysical auditory filters can be compared directly to the ERBs of the linear peripheral filters of the AN model at the signal frequency.

Predicted performance for the *linear-sharp* version of the AN model is shown in Fig. 2 for the three SR populations (triangles) as well as for the total AN population (circles). Detection thresholds for the rate-place model are plotted as a function of notch width for fixed-spectrum-level ($N_0 = 20$ dB SPL) notched-noise maskers. Note that the predicted detection thresholds for the total-AN population did not correspond to one SR group for all notch widths. Rather, detection performance was dependent on the low-SR population for small notch widths and on the high-SR population for large notch widths due to the differences in threshold and dynamic range across SR groups. The on-frequency masker energy in the zero-notch-width condition drove the high- and medium-SR fibers closer to saturation than the low-SR fibers, which have a higher threshold and wider dynamic range. The dependence of performance on low-SR fibers was stronger at higher levels (not shown), consistent with AN-fiber responses to tones in noise (Young and Barta, 1986). Thus, estimates of psychophysical auditory filters are derived from detection performance that is based on different AN fibers as a function of notch width. It is unlikely that estimated auditory filters based on individual AN fibers (or on single SR classes, as discussed below) would consistently correspond with those estimated psychophysically. However, this does not necessarily imply that psychophysical estimates of auditory filters do not represent peripheral tuning, because same-CF AN fibers with different SRs have similar tuning as a function of CF (Liberman, 1978).

The power-spectrum model was used to derive estimates of psychophysical auditory filters from the AN model predictions based on the total population (combined across all three SR groups). The resulting fit is shown in Fig. 2 (solid curve), and a summary of the roex-filter parameters used by the power-spectrum model to fit these data (circles) is given in Table I. The fit of the power-spectrum model to the predicted AN-model detection thresholds is quite good (1.4 dB rms deviation). Shailer *et al.* (1990) reported rms deviations between power-spectrum model fits and human psychophysical detection thresholds that were typically between 0.9 and 2.2 dB and were always less than or equal to 2.7 dB. The ERB of

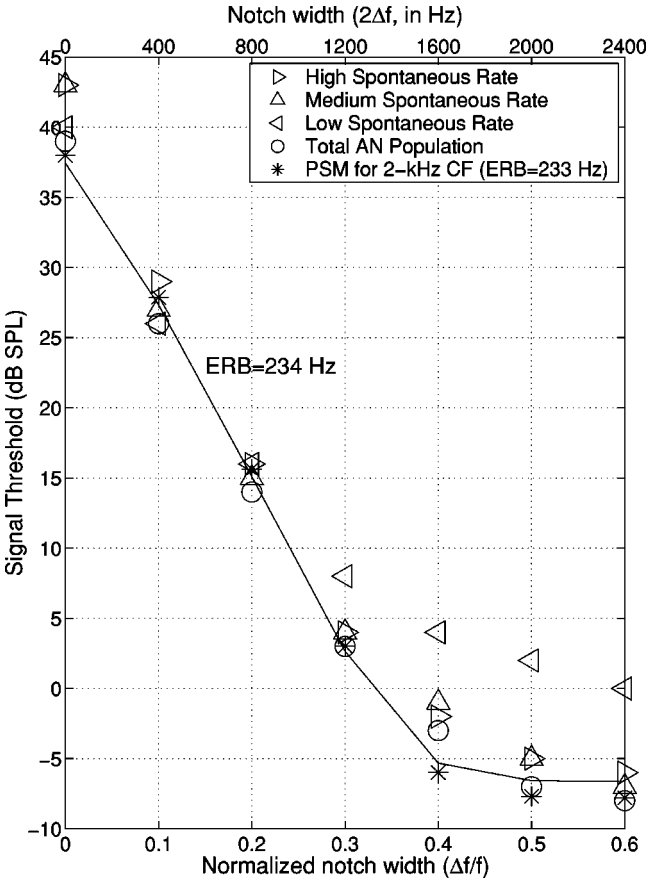

FIG. 2. Predicted detection thresholds for a tone in a notched-noise masker as a function of notch width based on the *linear-sharp* AN model. Model predictions are for a 2-kHz, 100-ms (20-ms rise/fall) tone presented simultaneously with the masker, which had a spectrum level of $N_0 = 20$ dB SPL. Predicted thresholds for the AN model are shown for each of the three SR populations (triangles), as well as for the combination of all three SR groups (circles). The solid curve represents the best fit from the power-spectrum model to the total-AN-population detection thresholds (circles) that were used to derive the estimated psychophysical auditory filter [ERB given in the figure; all auditory-filter parameters given in Table I]. The detection thresholds and estimated psychophysical-auditory-filter ERB derived from the AN model match very closely to the predicted thresholds (stars) from the power-spectrum model (PSM) based on the effective ERB of the 2-kHz peripheral model filter (see the text), which was 233 Hz.

TABLE I. Psychophysical-auditory-filter parameters derived from the power-spectrum model for Fig. 2. The derived estimate of the psychophysical auditory filter represents the roex(p,r) filter that best describes the rate-place detection thresholds predicted from the AN model. The roex-filter parameters used to predict thresholds from the power-spectrum model based on the effective 2-kHz peripheral model filter bandwidth (stars, Fig. 2) are also listed. ERB: equivalent-rectangular bandwidth; rms: root-mean-squared error; p: filter slope; r: filter dynamic range; K_{psm}: signal-to-noise at the auditory-filter output required for detection threshold.

	ERB (Hz)	rms (dB)	p	r (dB)	K_{psm} (dB)
Rate-place model	234	1.4	33.0	−52.3	−6.2
2-kHz peripheral model filter	233	⋯	33.1	−54.0	−5.7

the estimated psychophysical auditory filter derived from the total-population AN-model thresholds was 234 Hz. This estimate of the psychophysical-auditory-filter ERB matches very closely to the effective ERB (233 Hz; see Sec. II) of the 2-kHz-CF peripheral filter in the linear-sharp AN model. As discussed above, detection performance predicted from the total AN population was based on different SR classes at different notch widths. Thus, as expected, none of the estimated psychophysical-auditory-filter ERBs derived from individual SR classes [e.g., ERB(HSR)=214 Hz, ERB(MSR) =216 Hz, or ERB(LSR)=245 Hz, not shown] corresponded to the 234-Hz ERB of the estimated psychophysical auditory filter based on the total AN population.

For reference, detection thresholds predicted from the power-spectrum model based on the effective 2-kHz peripheral model filter with ERB=233 Hz are shown in Fig. 2 (stars). The roex-filter parameters used to predict the detection thresholds are given in Table I and were chosen to be consistent with critical ratios and absolute thresholds. Detection threshold for the zero-notch-width condition was set to 38 dB SPL, which is equal to the masker spectrum level (20 dB SPL) plus the human critical ratio at 2 kHz (18 dB, Fletcher, 1940), by adjusting the variable K_{psm}. Asymptotic detection thresholds for large notch widths, controlled by the parameter r, were set to be consistent with the AN-model rate-place absolute threshold of roughly -7 dB SPL at 2 kHz. The rate-place detection threshold is slightly less than the lowest AN-fiber physiological threshold because the threshold definitions differ and because information is combined across many AN fibers in the rate-place model.

Overall, the detection thresholds based on the total AN population were very close to the detection thresholds predicted from the power-spectrum model based on the 2-kHz peripheral model filter. Thus, estimates of psychophysical auditory filters based on rate-place detection thresholds from the linear-sharp AN model appear to be closely related to peripheral tuning at the signal frequency.[3]

B. The influence of compression and suppression on estimates of psychophysical auditory filters

If estimates of psychophysical auditory filters are directly related to peripheral tuning, as shown above for the linear-sharp AN model, then it is expected that changes in peripheral tuning associated with compression and suppression would affect psychophysical methods for estimating auditory filters. A demonstration of how AN response properties associated with nonlinear cochlear tuning influence estimates of psychophysical auditory filters is provided by comparing auditory-filter estimates based on detection thresholds from the four versions of the AN model.

Predicted detection thresholds for the four versions of the AN model are compared in Fig. 3 for a 2-kHz signal and a fixed masker spectrum level of $N_0=20$ dB SPL. Performance was predicted based on the combination of the three AN-model SR groups and plotted as a function of notch width. The power-spectrum model was used to derive estimates of psychophysical auditory filters from the AN-model detection thresholds, and the resulting fits (curves) and ERBs are shown in Fig. 3. A summary of the roex-filter parameters

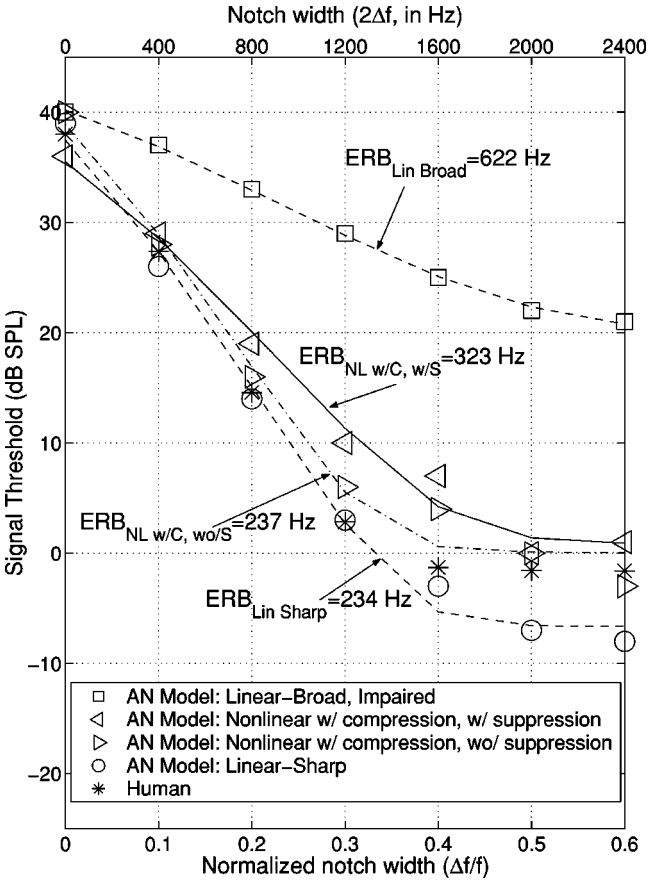

FIG. 3. Predicted detection thresholds for a 2-kHz tone in a notched-noise masker as a function of notch width for the four versions of the AN model. Same conditions as in Fig. 2. Predicted thresholds for the AN model are based on the combination of discharge counts across the three SR populations. Curves represent the best fits from the power-spectrum model [auditory-filter parameters given in Table II]. Also shown are typical human detection thresholds (stars) for $N_0=20$ dB SPL predicted from the power-spectrum model (see the text; Glasberg and Moore, 1990). The 2-kHz peripheral filter in the linear-sharp AN model had an effective ERB of 233 Hz and corresponds to the low-level tuning in the nonlinear AN models. The ERB of the peripheral filter in the linear-broad, impaired AN model was 613 Hz, corresponding to the ERB of the filter that represents a full reduction in the cochlear gain. The ERB of the estimated psychophysical auditory filter derived for the nonlinear AN model with compression and suppression was 323 Hz, corresponding to an overestimation of the ERB of the peripheral model filter describing low-level tuning to the signal.

used by the power-spectrum model to fit the AN-model detection thresholds is given in Table II. Also shown in Fig. 3 are typical human psychophysical detection thresholds (stars) for a masker spectrum level of $N_0=20$ dB SPL predicted from the power-spectrum model based on a psychophysical-auditory-filter ERB of 223 Hz (Glasberg and Moore, 1990). The roex-filter parameters used to predict typical human detection thresholds are given in Table II and were chosen to be consistent with human critical ratios (as in Fig. 2) and with an absolute threshold of 0 dB SPL at 2 kHz (Robinson and Dadson, 1956).

The lowest predicted detection threshold for each notch width (except zero) was for the linear-sharp AN-model version, while the highest threshold was always for the linear-broad, impaired version (Fig. 3). Detection thresholds from the two nonlinear versions of the AN model (with and without suppression) were in between those for the two linear

TABLE II. Psychophysical-auditory-filter parameters derived from the power-spectrum model for the 2-kHz (Fig. 3) and the 8-kHz (Fig. 4) signals. The roex-filter parameters used to predict typical human detection thresholds (stars) from the power-spectrum model for $N_0=20$ dB SPL are also listed (Glasberg and Moore, 1990).

	ERB (Hz)	rms (dB)	p	r (dB)	K_{psm} (dB)	Peripheral model filter ERB (Hz)
2 kHz						
Linear-sharp	234	1.4	33.0	−52.3	−6.2	233
Nonlinear, w/o suppression	237	1.9	32.6	−46.9	−4.9	233–613
Nonlinear, w/suppression	323	1.4	23.9	−41.4	−9.6	233–613
Linear-broad, impaired	622	0.2	12.6	−24.5	−7.6	613
Human	223	⋯	34.6	−48.0	−5.5	⋯
8 kHz						
Linear-sharp	932	2.1	34.7	−53.5	−6.4	934
Nonlinear, w/o suppression	931	1.7	34.7	−57.1	−2.0	934–6168
Nonlinear, w/suppression	1486	0.4	21.8	−48.7	−8.3	934–6168
Human	889	⋯	36.4	−57.0	−2.5	⋯

model versions and were within 5 dB of one another for all notch widths. Furthermore, for all notch widths except zero, the detection thresholds for the nonlinear AN model with suppression were higher than those for the nonlinear model without suppression, which in turn were higher than those for the linear-sharp model. Thus, for all off-frequency masking conditions, both compression and suppression in the AN model led to higher predicted psychophysical thresholds for detecting a tone in a notched-noise masker.

The fits from the power-spectrum model to the predicted AN-model detection thresholds in Fig. 3 were good for all versions of the AN model (Table II). For both linear versions of the AN model, the ERBs of the estimated psychophysical auditory filters were close to the ERBs of the peripheral model filters for the 2-kHz CF. The peripheral filters in the nonlinear versions of the AN model vary with level and time. At low stimulus levels, the tuning in the nonlinear AN model is linear and corresponds to the tuning in the linear-sharp AN model version. As stimulus level increases, tuning in the nonlinear AN model tends to broaden as the signal-path-filter gain is reduced; however, the fast dynamics of the control path result in a peripheral filter in the nonlinear AN model that fluctuates as a function of time. Thus, the instantaneous ERB of the 2-kHz nonlinear signal-path filter in the AN model can vary between 233 Hz, corresponding to the effective ERB of the filter that describes low-level tuning, and 613 Hz, corresponding to the ERB of the filter that represents a full reduction of the signal-path-filter gain (i.e., the filter in the linear-broad, impaired AN-model version). The time-average value of the nonlinear signal-path-filter ERB increases as the stimulus level through the control-path filter increases. Thus, the peripheral tuning in the nonlinear AN model with compression and suppression can be expected to be broader when the masker is present than when the signal is alone.

Despite higher predicted detection thresholds at all notch widths, the ERB of the estimated psychophysical auditory filter for the nonlinear AN model without suppression (237 Hz) was essentially the same as the ERB of the estimated psychophysical auditory filter derived for the linear-sharp AN model (234 Hz). In contrast, the ERB of the estimated psychophysical auditory filter derived for the nonlinear AN model with both compression and suppression (323 Hz) was a factor of 1.38 larger than the ERB of the estimated psychophysical auditory filter for the linear-sharp AN model. This result suggests that the presence of suppression results in an estimated psychophysical-auditory-filter ERB that overestimates the ERB of the peripheral tuning to the signal alone at low levels. In response to the tonal signal alone at levels below roughly 20 dB SPL, the tuning in the nonlinear AN model equals the tuning in the linear-sharp AN model because the compression threshold for CF tones is 20 dB SPL (Heinz *et al.*, 2001c; see also Zhang *et al.*, 2001). Although the signal level at detection threshold for the nonlinear AN models was below 20 dB SPL for notch widths of 0.2 and greater (Fig. 3), the notched-noise masker contains energy that passes through the wideband control path and thus acts to broaden the peripheral tuning in the AN model.

While there was a clear effect of the AN-model nonlinearity on the detection thresholds and estimated psychophysical-auditory-filter ERBs for the 2-kHz CF (Fig. 3), a larger effect could be expected for higher-frequency CFs due to the increased strength of cochlear nonlinearity at higher frequencies. The maximal reduction in cochlear gain at CF across level was 30 dB at 2 kHz in the AN model and 55 dB at 8 kHz (Heinz *et al.*, 2001c). Figure 4 shows predicted detection thresholds for an 8-kHz signal as a function of notch width for the four versions of the AN model. Detection thresholds were predicted for a fixed-level masker ($N_0=20$ dB SPL) based on the combination of all three SR groups.

The relative roles of the SR groups across different notch widths (not shown) were the same as for the 2-kHz signal, i.e., low-SR fibers accounted for detection performance at small notch widths, while high-SR fibers accounted for detection at large notch widths. Detection thresholds for the linear-broad, impaired AN model were essentially invariant with notch width and represent the absolute rate-place threshold for an 8-kHz tone in the impaired model (Heinz *et al.*, 2001c). Full reduction of the cochlear gain by 55 dB at

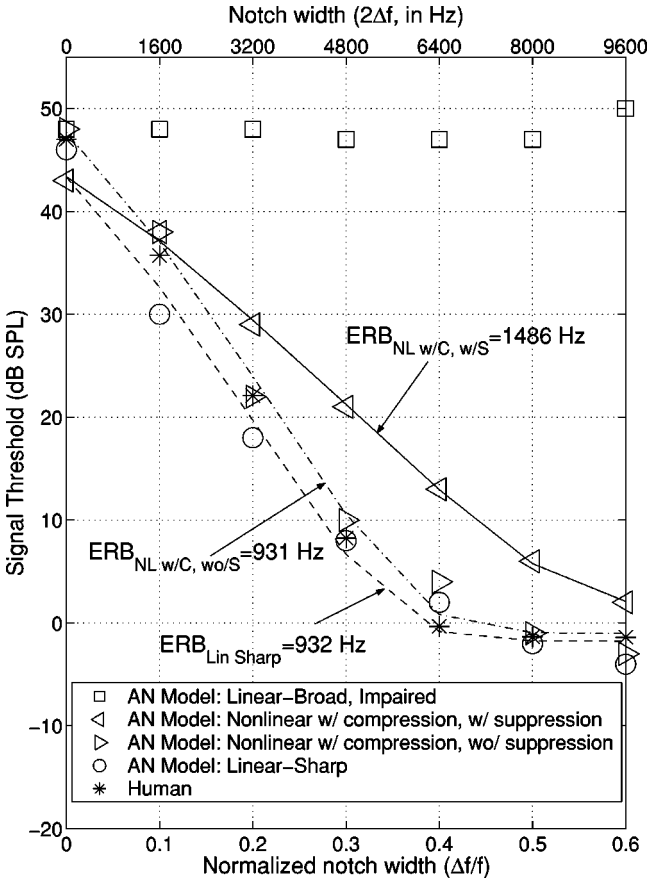

FIG. 4. Predicted detection thresholds for an 8-kHz tone in a notched-noise masker as a function of notch width for the four versions of the AN model (as in Fig. 3). Curves represent the best fits from the power-spectrum model [auditory-filter parameters given in Table II]. Also shown are typical human detection thresholds (stars) for $N_0 = 20$ dB SPL predicted from the power-spectrum model (see the text; Glasberg and Moore, 1990). The 8-kHz peripheral filter in the linear-sharp AN model had an effective ERB of 934 Hz, while the ERB of the peripheral filter in the linear-broad, impaired AN model was 6168 Hz. The factor by which the ERB of the estimated psychophysical auditory filter derived for the nonlinear AN model with suppression overestimated the ERB of the peripheral model filter describing low-level tuning to the signal was greater for the 8-kHz CF than for the 2-kHz CF (Fig. 3).

the 8-kHz CF raised the absolute rate-place detection threshold from roughly −7 dB SPL in the nonlinear AN model to 48 dB SPL in the impaired model. Typical human detection thresholds (stars in Fig. 4) for a masker spectrum level of $N_0 = 20$ dB SPL were predicted from the power-spectrum model based on a psychophysical-auditory-filter ERB of 889 Hz (Glasberg and Moore, 1990). The roex-filter parameters used to predict typical human psychophysical detection thresholds were chosen to be consistent with the 8-kHz human critical ratio (27 dB, Fletcher, 1940) and an absolute threshold of roughly 0 dB SPL. The use of an absolute threshold of 0 dB SPL in the present study is a simplification to match the absolute threshold of the AN model. Human absolute threshold at 8 kHz is about 18 dB SPL (Robinson and Dadson, 1956), primarily due to middle-ear filtering, which is not considered in the present study. The current predictions thus isolate the frequency-dependent effects of cochlear nonlinearity from those of middle-ear filtering; however, the potential effects of frequency-dependent audibility could be evaluated in future studies by including a middle-ear filter in the AN model. Table II summarizes the power-spectrum-model fits (curves) to the predicted AN-model detection thresholds shown in Fig. 4 and the roex-filter parameters used to predict typical human detection thresholds. The power-spectrum model was not fit to the predicted detection thresholds for the linear-broad, impaired AN model because the thresholds were approximately invariant with notch width due to the high absolute tone threshold for this model version.

The same relative effects between predicted psychophysical detection thresholds for the different versions of the AN model were demonstrated for the 8-kHz signal (Fig. 4) as were observed for the 2-kHz signal (Fig. 3). The lowest detection threshold at each notch width except zero was for the linear-sharp AN model. Predicted thresholds for the nonlinear AN model without suppression were only slightly higher than for the linear-sharp model, but the detection thresholds for the nonlinear AN model with suppression were substantially higher for the middle notch widths. The large difference between the nonlinear AN models with and without suppression for notch widths larger than 0.1 was due to off-frequency masking energy passing through the wide-band control-path filter and acting to reduce the signal-path-filter gain, and thus to broaden the peripheral tuning in the model.

The ERB of the estimated psychophysical auditory filter for the linear-sharp AN model (932 Hz) was very close to the effective ERB of the 8-kHz peripheral model filter (934 Hz), similar to the result for the 2-kHz CF (Table II). Again, none of the estimated psychophysical auditory filters derived from the individual SR classes [e.g., ERB(HSR) = 850 Hz, ERB(MSR) = 864 Hz, or ERB(LSR) = 1022 Hz, not shown] provided as accurate an estimate of the underlying peripheral tuning as the estimated psychophysical auditory filter based on the total AN population.

The instantaneous ERB of the 8-kHz peripheral model filter in the nonlinear AN models can vary between 934 Hz at low levels and 6168 Hz at high levels based on the output of the control-path filter. Similar to the 2-kHz signal condition, the ERB of the estimated psychophysical auditory filter for the nonlinear AN model without suppression (931 Hz) was very close to the ERB of the estimated psychophysical auditory filter derived for the linear-sharp AN model (932 Hz). In contrast, when suppression was included in the nonlinear AN model, the ERB of the estimated psychophysical auditory filter (1486 Hz) was a factor of 1.59 larger than the ERB of the estimated psychophysical auditory filter derived for the linear-sharp AN model. This factor was larger than the corresponding factor of 1.38 for the 2-kHz CF; thus, as expected, the degree by which the estimated psychophysical-auditory-filter ERB overestimates the low-level peripheral tuning bandwidth was larger for the 8-kHz CF than for the 2-kHz CF. The larger difference at higher frequencies was due to the increased strength of cochlear nonlinearity at high frequencies in the AN model.

IV. DISCUSSION

For the AN model with linear tuning, the estimated psychophysical auditory filters were shown to be closely related to the peripheral filters in the AN model. Thus, detection predictions from the rate-place model were used in the present study to evaluate the effects of compression and suppression on estimates of psychophysical auditory filters.

A. The influence of nonlinear cochlear tuning on estimates of psychophysical auditory filters

The primary benefit of the modeling approach taken in the present study was to provide a quantitative framework in which to explore the effect of nonlinear AN response properties on estimates of psychophysical-auditory-filter bandwidths. It is not surprising that the inclusion of nonlinear AN response properties associated with broadened peripheral tuning resulted in broader estimates of psychophysical auditory filters. However, the specific properties related to the nonlinear control of peripheral tuning have potentially important implications for the interpretation of psychophysical-auditory-filter estimates. While several of the fundamental implications were demonstrated directly in the present study, many others are clearly suggested from this initial demonstration and it will be important to investigate these quantitatively in future studies.

1. Nonlinear control of peripheral tuning

Many nonlinear AN response properties, often described separately, are consistent with a single underlying mechanism that controls peripheral tuning (e.g. Sachs and Abbas, 1974; Sewell, 1984; Patuzzi *et al.*, 1989; Ruggero and Rich, 1991; Ruggero *et al.*, 1992; see the review by Ruggero, 1992). The phenomenological AN model used in the present study included both compression and suppression properties by accounting for the general property that both on- and off-frequency stimulus energy can act to control peripheral tuning. This property suggests that both the signal and the masker can influence peripheral tuning, and the fast dynamics of nonlinear cochlear tuning (Arthur *et al.*, 1971; Recio *et al.*, 1998) implies that both the temporal and spectral relation of the signal and masker must be considered when interpreting the results of psychophysical masking studies. Thus, it is improper to discuss the tuning at a given CF without specifying the stimulus configuration. For example, Kiang and Moxon (1974) showed that AN tuning curves in cat were broader and CF thresholds were higher in the presence of a bandpass noise centered well below CF than they were in the presence of the signal alone. This effect is consistent with the difference in human psychophysical frequency selectivity estimated using simultaneous masking (for which both the signal and the masker influence the peripheral tuning) and nonsimultaneous masking (for which the signal and the masker influence peripheral tuning independently) (e.g., Houtgast, 1977; Moore, 1978; Moore and Glasberg, 1981, 1982, 1986; Moore *et al.*, 1987). Thus, the nonlinear control of cochlear tuning poses a basic problem for the interpretation of psychophysical estimates of frequency selectivity because the noise maskers affect the tuning of the peripheral filter that is being measured.

2. Implications of the nonlinear control of peripheral tuning for the interpretation of psychophysical-auditory-filter estimates

The results from the present study show that suppression produces an estimated psychophysical auditory filter with an ERB that overestimates the ERB of peripheral tuning to the signal alone at low levels. The low masker spectrum level used in the present study ($N_0 = 20$ dB SPL) was chosen to evaluate whether compression and suppression influenced estimates of psychophysical auditory filters near the lowest spectrum levels that have been used in psychophysical studies. The phenomenological AN model suggests that any condition for which enough stimulus energy (signal and masker) passes through the wideband suppression filter to reduce the cochlear gain would result in estimates of psychophysical auditory filters that were broader than low-level peripheral tuning. The compression threshold for CF tones is about 20 dB SPL in the model, consistent with physiological measures of basilar-membrane compression (Ruggero *et al.*, 1997). Thus, any noise masker that produces roughly 20 dB SPL or more of overall level through the suppression filter would be expected to reduce the cochlear gain and thus to broaden peripheral tuning. Psychophysical studies that estimate auditory filters rarely use noise spectrum levels less than 20 dB SPL, and AN suppression bandwidths are much larger than 100 Hz for both low and high CFs (Delgutte, 1990b). Thus, it is likely that most psychophysical estimates of auditory filters include the effects of suppression, and therefore overestimate the bandwidth of low-level peripheral tuning to the signal alone. Consistent with this prediction, Rosen *et al.* (1998) found that psychophysical estimates of auditory filters were nonlinear down to the lowest stimulus levels that they could measure. A consequence of this limitation is that the difference between the frequency selectivity of normal and impaired listeners may be underestimated using current psychophysical methods, because the largest difference would be expected to occur for stimulus levels just above absolute threshold, where suppression was not invoked.

The debate over how to estimate psychophysical auditory filters as a function of level has focused on which aspect of the stimulus controls the level dependence of the psychophysical auditory filter, e.g., signal or masker level, overall level or level per ERB (Moore, 1995a). In addition, the debate has included whether the dependence is on the stimulus level prior to filtering (e.g., Glasberg and Moore, 1990) or on the level of the filtered stimulus (e.g., Rosen and Baker, 1994; Rosen *et al.*, 1998). Glasberg and Moore (2000) have recently suggested that the gain of their tip (sharp) filter might depend on the output of their tail (broad) filter. The current results suggest that none of these views is entirely correct because they fail to account for the effect of suppression on peripheral tuning. Contrary to the current debate, peripheral tuning depends on both the signal and the masker, and the level dependence is based on the stimulus energy that passes through the suppression filter rather than the excitatory filter. This property suggests that the underlying peripheral tuning is likely to vary across the different notch widths used to estimate psychophysical auditory filters (also see Sinex and Havey, 1986; Delgutte, 1990a). Thus, as suggested

by Rosen *et al.* (1998) for fixed-level masking conditions, psychophysical estimates of auditory filters are likely to represent some sort of average auditory filter over the different notch widths. Future modeling studies that evaluate the effect of stimulus level on estimates of psychophysical auditory filters are needed to investigate this issue further.

The present study predicts that the increase in strength of cochlear nonlinearity with CF could introduce a CF-dependent bias in psychophysical estimates of auditory filters such that the bandwidth of high-CF peripheral tuning is overestimated to a greater extent than the bandwidth of low-CF tuning. This predicted CF-bias is consistent with recent noninvasive measures of human cochlear tuning based on the phase response of stimulus-frequency otoacoustic emissions. Shera and Guinan, (2000) and Shera *et al.* (2002) described the frequency dependence of an emission-based measure of the sharpness of tuning derived from the theory of coherent reflection filtering (Shera and Zweig, 1993; Zweig and Shera, 1995) for humans, cats, and guinea pigs. The emission-based measure of sharpness of tuning increased with frequency for all three species, consistent with neural measures of sharpness ($Q = \mathrm{CF/ERB}$) for cats and guinea pigs (e.g., Liberman, 1978; Miller *et al.*, 1997). In contrast, the increase in the human emission-based measure of sharpness with frequency was inconsistent with the essentially constant sharpness of tuning above 1 kHz described by the frequency dependence of psychophysical estimates of auditory-filter ERBs (Glasberg and Moore, 1990).

The role of suppression in broadening peripheral tuning suggests an important implication for the use of asymmetric notched-noise maskers to estimate psychophysical-auditory-filter asymmetry. Studies that have used asymmetric notch widths have consistently shown that psychophysical estimates of auditory filters derived from the power-spectrum model become more asymmetric as stimulus level increases, with the low-frequency side of the derived auditory filters becoming shallower as level increases (Moore and Glasberg, 1987; Glasberg and Moore, 1990, 2000; Rosen and Baker, 1994; Moore, 1995a; Rosen *et al.*, 1998). However, the results from the present study suggest that the relative influence of suppression above and below the signal frequency must be considered in an interpretation of psychophysical estimates of auditory filters derived using asymmetric notch widths. Delgutte (1990b) systematically measured the growth of two-tone suppression in AN fibers as a function of suppressor level and found that suppression growth was asymmetric above and below CF. The growth rate of suppression was much higher for suppressor frequencies below CF (ranging from 1–3 dB/dB) than for suppressor frequencies above CF (ranging from 0.15–0.7 dB/dB). The much faster growth rate of suppression below CF than above CF is consistent with the much greater effect of level on broadening the low-frequency side of psychophysical estimates of auditory filters than the high-frequency side. In addition, the asymmetry in psychophysical estimates of auditory filters for 2- and 4-kHz signals was reported to be greater than that for lower-frequency signals (Glasberg and Moore, 2000), which is consistent with the greater asymmetry in AN suppression growth rates for CFs above 2 kHz (Delgutte, 1990b). The combination of faster growth rates and higher thresholds for suppression below CF than above CF produces suppression that is stronger above CF at low levels and stronger below CF at high levels (Delgutte, 1990b). This result is consistent with psychophysical estimates of auditory filters having shallower high-frequency slopes at low levels, shallower low-frequency slopes at high levels, and symmetric slopes at medium levels (Moore, 1995a). Thus, the present study suggests that the reported changes in the asymmetry of psychophysical-auditory-filter estimates as a function of level may be due to (or at least influenced by) the asymmetry in the growth rate of suppression above and below CF, and not solely to actual changes in excitatory-filter asymmetry. Future studies are needed to explore this issue quantitatively.

The nonlinear control of peripheral tuning may have implications for comparing estimates of frequency selectivity derived from different psychophysical methods. Techniques such as Fletcher's (1940) band-widening (critical-band) method, the critical ratio, psychophysical tuning curves, and the notched-noise method have all been criticized based on methodological issues, such as the role of off-frequency listening, the varying influence of random-noise fluctuations as a function of masker bandwidth, and the assumption of rectangular filters (Moore, 1995a). However, a more fundamental issue is whether the underlying peripheral tuning at the frequency of interest is the same in each experiment, given that these methods use different stimulus configurations that may affect the control of peripheral tuning in different ways. The critical-band and critical-ratio methods use noise maskers of different bandwidths centered at the tone frequency, while the notched-noise and psychophysical-tuning-curve methods primarily use off-frequency maskers. Each of these methods involves the physiological mechanisms of compression and suppression in vastly different ways, and thus it is likely that the bandwidths of the underlying peripheral filters are different for these common psychophysical methods for estimating auditory frequency selectivity. For example, different bandwidths of the underlying peripheral filters are likely to be the cause for the common finding that frequency selectivity measured psychophysically using nonsimultaneous masking is typically sharper than when measured using simultaneous masking (e.g., Houtgast, 1977; Moore, 1978; Moore and Glasberg, 1981, 1982, 1986; Moore and O'Loughlin, 1986; Moore *et al.*, 1987; see Moore, 1995a for a review). Thus, differences in psychophysical estimates of frequency selectivity across methods must be evaluated both in terms of methodological issues and in terms of the underlying peripheral tuning (e.g., Lentz *et al.*, 1999).

B. What do current psychophysical estimates of auditory filters represent?

Despite the complications that cochlear nonlinearity places on the interpretation of psychophysical estimates of auditory filters, these estimates have proven useful in predicting psychophysical data from a variety of masking conditions (Moore, 1995a). Derleth and Dau (2000) have suggested that their linear filter bank was successful in predicting masking patterns at midlevels because the effects

of cochlear nonlinearities were likely to be included in the psychophysical-auditory-filter bandwidths estimated using simultaneous notched-noise maskers, and that these filter bandwidths could be considered to represent ''effective'' auditory filters. The present study suggests that psychophysical auditory filters estimated using simultaneous masking may be appropriate for representing the average peripheral tuning in the presence of *both* the signal and the masker (i.e., the ''effective'' tuning), which is consistent with their success in accounting for similar masking conditions. Alternatively, nonsimultaneous masking may be more appropriate for estimating peripheral tuning in response to the *signal alone* by allowing the masking noise to be used primarily as an excitatory masker due to the fast dynamics of nonlinear cochlear tuning. However, the signal and the masker may pass through peripheral filters with different bandwidths in nonsimultaneous masking experiments, which would have important implications for comparing the amount of excitation produced by the signal and by the masker. A similar idea was used to model the additivity of nonsimultaneous masking based on the independent effects of compression on the signal and on the masker (Oxenham and Moore, 1994). Thus, even though psychophysical estimates of auditory filters based on nonsimultaneous masking may provide a better estimate of peripheral tuning in response to the signal alone, these estimates are likely to depend on peripheral tuning both in response to the signal alone and to the masker alone. Potential differences between signal-alone and masker-alone peripheral tuning can be minimized by measuring masked detection at stimulus levels as close to absolute threshold as possible.

The predicted detection thresholds in the present study were based on peripheral AN-model filters that were specified according to low-level psychophysical estimates of auditory filters (Glasberg and Moore, 1990); however, the present results suggest that these psychophysical estimates of auditory filters are likely to be broader than human peripheral tuning at low levels. A strength of the present study comes from demonstrating the issues that need to be considered to interpret the effects of cochlear nonlinearity on psychophysical estimates of auditory filters, and this demonstration does not depend significantly on the accuracy of the peripheral-filter ERBs in the AN model. In order to determine the appropriate ERBs to use for low-level human peripheral tuning, the variation in the strength of cochlear nonlinearity as a function of frequency and the bandwidth of the suppression filter must be determined for human listeners. Determination of whether the current model parameters are appropriate for human listeners will require future studies that can evaluate the strength of human cochlear nonlinearity by quantitatively relating physiological response properties to human psychophysical performance. The related physiological and psychophysical masking studies by Delgutte (1990a) and Oxenham and Plack (1998) provide a good basis for relating the strength of compression and suppression in cats and humans. Physiological and psychophysical measures of basilar-membrane compression (e.g., Ruggero *et al.*, 1997; Cooper and Rhode, 1997; Oxenham and Plack, 1997; Plack and Oxenham, 1998) provide useful data for relating the strength of compression in chinchilla, guinea pig, and humans.

C. Implications of the cochlear-amplifier mechanism for comparing normal and impaired hearing

The present study demonstrated that the nonlinear response properties associated with the physiologically vulnerable cochlear-amplifier mechanism influence estimates of psychophysical auditory filters. This result suggests that a better quantitative understanding of these influences may allow for a direct psychophysical characterization of cochlear status in human listeners. Loss of the cochlear-amplifier mechanism in hearing-impaired listeners is likely to be caused by the loss of OHCs, and it represents a form of sensorineural hearing loss that is likely to be common in humans (Pickles, 1988; Patuzzi *et al.*, 1989; Ruggero and Rich, 1991; van Tasell, 1993; Moore, 1995b). The results from the current study are consistent with the view that listeners with OHC loss have broader psychophysical auditory filters than normal-hearing listeners, but that reduced frequency selectivity is not the only difference between normal and impaired listeners (Moore, 1995b).

The phenomenological AN model used in the present study highlights the idea that the difference between a normal-hearing listener with a cochlear-amplifier mechanism and a hearing-impaired listener without a cochlear-amplifier mechanism is not simply a difference between one system in two states, i.e., with low or high thresholds, narrow or broad tuning, compressive or linear magnitude responses. Rather, the difference is between two different systems: an impaired system that is static, insensitive, and has broad tuning, and a normal system with fast, dynamic tuning that is continuously changing in response to the stimulus. This view is different than the view that has arisen from the power-spectrum model of masking, i.e., that the primary differences in the impaired system are higher thresholds and broader tuning.

The difference between these two views is likely to be most significant for rapidly changing complex stimuli and may be less significant for steady-state stimuli. Peters *et al.* (1998) and Moore *et al.* (1999a) have reported that the difference between the ability of normal-hearing and hearing-impaired listeners to understand speech is much larger in the presence of temporally and spectrally varying backgrounds than for stationary broadband backgrounds, even when advanced amplification algorithms were provided to the hearing-impaired listeners. This result has been interpreted as representing a deficit in the ability of hearing-impaired listeners to ''listen in the dips'' (e.g., Peters *et al.*, 1998; Moore *et al.*, 1999a). This deficit has been suggested to result from degraded frequency selectivity and reduced temporal resolution, which have been accounted for in terms of broadened tuning and loss of compression, respectively (see Moore, 1995b, and Moore and Oxenham, 1998, for reviews). Thus, the absence of the dynamic peripheral tuning provided by the cochlear-amplifier mechanism is likely to be significant for stimulus conditions in which current amplification algorithms have the most limited benefit. The present modeling approach provides a quantitative method that could be used

in future studies to investigate the significance of the loss or degradation of dynamic cochlear tuning in hearing-impaired listeners.

V. CONCLUSIONS

(1) The ERB of the estimated psychophysical auditory filter that was derived based on the total AN-model population was closely related to the ERB of the peripheral AN-model filter at the signal frequency for model versions with linear peripheral tuning.
(2) The predicted detection performance that was used to derive estimates of psychophysical auditory filters was based on different AN-fiber SR classes at different notch widths due to the variation of threshold and dynamic range across SR. None of the estimated psychophysical auditory filters derived from individual SR classes provided as accurate an estimate of the underlying peripheral tuning as the estimated psychophysical auditory filter based on the total AN population.
(3) The ERBs of the estimated psychophysical auditory filters derived from the nonlinear AN model with suppression were always larger than the ERBs of the estimated psychophysical auditory filters from the linear-sharp AN model. This result suggests that psychophysically estimated auditory-filter ERBs represent an overestimate of the bandwidth of low-level peripheral tuning in response to the signal alone.
(4) The factor by which the ERB of the estimated psychophysical auditory filter derived from the nonlinear AN model overestimated the ERB of the peripheral AN-model filter was larger at 8 kHz (factor of 1.59) than at 2 kHz (factor of 1.38). This results suggests a potential CF-dependent bias in psychophysical estimates of auditory filters due to the increased strength of cochlear nonlinearity at high CFs.
(5) The role of suppression in broadening peripheral tuning in response to the noise masker has important implications for the interpretation of psychophysical-auditory-filter estimates. The present study suggests that psychophysical estimates of auditory filters depend on the level of the signal and masker energy at the output of the wideband suppression filter. Thus, psychophysical auditory filters estimated using simultaneous masking are likely to represent some sort of average tuning in the presence of both the signal and the masker.

ACKNOWLEDGMENTS

The authors would like to thank Ian Bruce, Bertrand Delgutte, and Susan Early for constructive comments on an earlier version of this manuscript, and Torsten Dau and Andy Oxenham for valuable discussions on this work. Ray Meddis and Brian Moore provided very helpful comments and suggestions in their reviews. This study was part of a graduate dissertation in the Speech and Hearing Sciences Program of the Harvard-MIT Division of Health Sciences and Technology (Heinz, 2000). Supported by NIH Grants Nos. T32DC00038, R01DC01641 and R01DC00100, and NSF Grant No. 9983567. The simulations in this study were performed on computers provided by the Scientific Computing and Visualization Group at Boston University.

[1]The human cochlear map described by Greenwood (1990) was used in the present study, and is given by $f(x)=165.4(10^{0.06x}-0.88)$, where x is the distance (in mm) along the basilar membrane from the apex, and $f(x)$ is the frequency (in Hz) corresponding to the position x.

[2]The equation for the roex(p,r) filter shape is given by $W(g)=(1-r)(1+pg)\exp(-pg)+r$, where $g=|f-f_c|/f$ represents the normalized frequency relative to the filter center frequency f_c (Moore, 1995a). The parameter p determines the filter slope and bandwidth, while the parameter r controls the filter dynamic range.

[3]Estimates of psychophysical auditory filters derived from the all-information model (based on discharge times and counts) did not represent a good measure of peripheral tuning (see Heinz, 2000), and thus are not presented in this report. The all-information estimates of psychophysical auditory filters were typically narrower than the AN-model peripheral filters due to the differential effects of the random-noise masker on the temporal signal information for on- versus off-frequency masking conditions. In the zero-notch-width condition, the on-frequency random-masker energy degraded the temporal signal information, resulting in an all-information detection threshold that was only about 10 dB below the rate-place threshold. For the off-frequency conditions (0.1–0.6 notch widths), the temporal information about the signal was much more reliable, producing all-information thresholds that were roughly 25–30 dB below the rate-place thresholds.

Allen, J.B. (**2001**). "Nonlinear cochlear signal processing," in *Physiology of the Ear*, edited by A.F. Jahn and J. Santos-Sacchi (Singular Thomson Learning, San Diego), pp. 393–442.
Anderson, D.J., Rose, J.E., Hind, J.E., and Brugge, J.F. (**1971**). "Temporal position of discharges in single auditory nerve fibers within the cycle of a sinewave stimulus: Frequency and intensity effects," J. Acoust. Soc. Am. **49**, 1131–1139.
Arthur, R.M., Pfeiffer, R.R., and Suga, N. (**1971**). "Properties of 'two-tone inhibition' in primary auditory neurons," J. Physiol. (London) **212**, 593–609.
Cheatham, M.A., and Dallos, P. (**1998**). "The level dependence of response phase: Observations from cochlear hair cells," J. Acoust. Soc. Am. **104**, 356–369.
Colburn, H.S. (**1969**). "Some physiological limitations on binaural performance," Ph.D. dissertation, Massachusetts Institute of Technology, Cambridge, MA.
Colburn, H.S. (**1973**). "Theory of binaural interaction based on auditory-nerve data. I. General strategy and preliminary results on interaural discrimination," J. Acoust. Soc. Am. **54**, 1458–1470.
Colburn, H.S. (**1981**). "Intensity perception: Relation of intensity discrimination to auditory-nerve firing patterns," Internal Memorandum, Research Laboratory of Electronics, Massachusetts Institute of Technology, Cambridge, MA.
Cooper, N.P., and Rhode, W.S. (**1997**). "Mechanical responses to two-tone distortion products in the apical and basal turns of the mammalian cochlea," J. Neurophysiol. **78**, 261–270.
Delgutte, B. (**1987**). "Peripheral auditory processing of speech information: Implications from a physiological study of intensity discrimination," in *The Psychophysics of Speech Perception*, edited by M.E.H. Schouten (Nijhoff, Dordrecht, The Netherlands), pp. 333–353.
Delgutte, B. (**1990a**). "Physiological mechanisms of psychophysical masking: Observations from auditory-nerve fibers," J. Acoust. Soc. Am. **87**, 791–809.
Delgutte, B. (**1990b**). "Two-tone rate suppression in auditory-nerve fibers: Dependence on suppressor frequency and level," Hear. Res. **49**, 225–246.
Derleth, R.P., and Dau, T. (**2000**). "On the role of envelope fluctuation processing in spectral masking," J. Acoust. Soc. Am. **108**, 285–296.
Evans, E.F., Pratt, S.R., Spenner, H., and Cooper, N.P. (**1992**). "Comparisons of physiological and behavioral properties: Auditory frequency selectivity," in *Auditory Physiology and Perception*, edited by Y. Cazals, L. Demany, and K. Horner (Pergamon, New York), pp. 159–169.
Fletcher, H. (**1940**). "Auditory patterns," Rev. Mod. Phys. **12**, 47–65.
Fletcher, H. (**1953**). *Speech and Hearing in Communication* (Van Nostrand, New York).
Geisler, C.D., and Sinex, D.G. (**1980**). "Responses of primary auditory fi-

bers to combined noise and tonal stimuli,'' Hear. Res. **3**, 317–334.
Glasberg, B.R., and Moore, B.C.J. (**1986**). ''Auditory filter shapes in subjects with unilateral and bilateral cochlear impairments,'' J. Acoust. Soc. Am. **79**, 1020–1033.
Glasberg, B.R., and Moore, B.C.J. (**1990**). ''Derivation of auditory filter shapes from notched-noise data,'' Hear. Res. **47**, 103–138.
Glasberg, B.R., and Moore, B.C.J. (**2000**). ''Frequency selectivity as a function of level and frequency measured with uniformly exciting notched noise,'' J. Acoust. Soc. Am. **108**, 2318–2328.
Green, D.M., and Swets, J.A. (**1966**). *Signal Detection Theory and Psychophysics* (Wiley, New York; reprinted 1988 by Peninsula, Los Altos, CA).
Greenwood, D.D. (**1961**). ''Critical bandwidth and the frequency coordinates of the basilar membrane,'' J. Acoust. Soc. Am. **33**, 1344–1356.
Greenwood, D.D. (**1990**). ''A cochlear frequency-position function for several species—29 years later,'' J. Acoust. Soc. Am. **87**, 2592–2605.
Heinz, M.G. (**2000**). ''Quantifying the effects of the cochlear amplifier on temporal and average-rate information in the auditory nerve,'' Ph.D. dissertation, Massachusetts Institute of Technology, Cambridge, MA.
Heinz, M.G., Colburn, H.S., and Carney, L.H. (**2001a**). ''Evaluating auditory performance limits. I. One-parameter discrimination using a computational model for the auditory nerve,'' Neural Comput. **13**, 2273–2316.
Heinz, M.G., Colburn, H.S., and Carney, L.H. (**2001b**). ''Rate and timing cues associated with the cochlear amplifier: Level discrimination based on monaural cross-frequency coincidence detection,'' J. Acoust. Soc. Am. **110**, 2065–2084.
Heinz, M.G., Zhang, X., Bruce, I.C., and Carney, L.H. (**2001c**). ''Auditory-nerve model for predicting performance limits of normal and impaired listeners,'' ARLO **2**, 91–96.
Hicks, M.L., and Bacon, S.P. (**1999**). ''Psychophysical measures of auditory nonlinearities as a function of frequency in individuals with normal hearing,'' J. Acoust. Soc. Am. **105**, 326–338.
Houtgast, T. (**1977**). ''Auditory-filter characteristics derived from direct-masking data and pulsation-threshold data with a rippled-noise masker,'' J. Acoust. Soc. Am. **62**, 409–415.
Kiang, N.Y.S., and Moxon, E.C. (**1974**). ''Tails of tuning curves of auditory-nerve fibers,'' J. Acoust. Soc. Am. **55**, 620–630.
Lentz, J.J., Richards, V.M., and Matiasek, M.R. (**1999**). ''Different auditory filter bandwidth estimates based on profile analysis, notched noise, and hybrid tasks,'' J. Acoust. Soc. Am. **106**, 2779–2792.
Liberman, M.C. (**1978**). ''Auditory-nerve response from cats raised in a low-noise chamber,'' J. Acoust. Soc. Am. **63**, 442–455.
Liberman, M.C., and Dodds, L.W. (**1984**). ''Single-neuron labeling and chronic cochlear pathology. III. Stereocilia damage and alterations of threshold tuning curves,'' Hear. Res. **16**, 55–74.
Lutfi, R.A., and Patterson, R.D. (**1984**). ''On the growth of masking asymmetry with stimulus intensity,'' J. Acoust. Soc. Am. **76**, 739–745.
Miller, R.L., Schilling, J.R., Franck, K.R., and Young, E.D. (**1997**). ''Effects of acoustic trauma on the representation of the vowel /ε/ in cat auditory nerve fibers,'' J. Acoust. Soc. Am. **101**, 3602–3616.
Moore, B.C.J. (**1978**). ''Psychophysical tuning curves measured in simultaneous and forward masking,'' J. Acoust. Soc. Am. **63**, 524–532.
Moore, B.C.J. (**1995a**). ''Frequency analysis and masking,'' in *Hearing*, edited by B.C.J. Moore (Academic, New York), Chap. 5.
Moore, B.C.J. (**1995b**). *Perceptual Consequences of Cochlear Damage* (Oxford University Press, New York).
Moore, B.C.J., and Glasberg, B.R. (**1981**). ''Auditory filter shapes derived in simultaneous and forward masking,'' J. Acoust. Soc. Am. **70**, 1003–1014.
Moore, B.C.J., and Glasberg, B.R. (**1982**). ''Interpreting the role of suppression in psychophysical tuning curves,'' J. Acoust. Soc. Am. **72**, 1374–1379.
Moore, B.C.J., and Glasberg, B.R. (**1986**). ''Comparisons of frequency selectivity in simultaneous and forward masking for subjects with unilateral cochlear impairments,'' J. Acoust. Soc. Am. **80**, 93–107.
Moore, B.C.J., and O'Loughlin, B.J. (**1986**). ''The use of nonsimultaneous masking to measure frequency selectivity and suppression,'' in *Frequency Selectivity in Hearing*, edited by B.C.J. Moore (Academic, London), pp. 179–250.
Moore, B.C.J., and Glasberg, B.R. (**1987**). ''Formulae describing frequency selectivity as a function of frequency and level, and their use in calculating excitation patterns,'' Hear. Res. **28**, 209–225.
Moore, B.C.J., Poon, P.W.F., Bacon, S.P., and Glasberg, B.R. (**1987**). ''The temporal course of masking and the auditory filter shape,'' J. Acoust. Soc. Am. **81**, 1873–1880.
Moore, B.C.J., and Oxenham, A.J. (**1998**). ''Psychoacoustic consequences of compression in the peripheral auditory system,'' Psychol. Rev. **105**, 108–124.
Moore, B.C.J., Peters, R.W., and Stone, M.A. (**1999a**). ''Benefits of linear amplification and multichannel compression for speech comprehension in backgrounds with spectral and temporal dips,'' J. Acoust. Soc. Am. **105**, 400–411.
Moore, B.C.J., Vickers, D.A., Plack, C.J., and Oxenham, A.J. (**1999b**). ''Inter-relationship between different psychoacoustic measures assumed to be related to the cochlear active mechanism,'' J. Acoust. Soc. Am. **106**, 2761–2778.
Oxenham, A.J., and Moore, B.C.J. (**1994**). ''Modeling the additivity of nonsimultaneous masking,'' Hear. Res. **80**, 105–118.
Oxenham, A.J., and Plack, C.J. (**1997**). ''A behavioral measure of basilar-membrane nonlinearity in listeners with normal and impaired hearing,'' J. Acoust. Soc. Am. **101**, 3666–3675.
Oxenham, A.J., and Plack, C.J. (**1998**). ''Suppression and the upward spread of masking,'' J. Acoust. Soc. Am. **104**, 3500–3510.
Patterson, R.D. (**1976**). ''Auditory filter shapes derived with noise stimuli,'' J. Acoust. Soc. Am. **59**, 640–654.
Patterson, R.D., Nimmo-Smith, I., Weber, D.L., and Milroy, R. (**1982**). ''The deterioration of hearing with age: Frequency selectivity, the critical ratio, the audiogram, and speech threshold,'' J. Acoust. Soc. Am. **72**, 1788–1803.
Patuzzi, R., and Robertson, D. (**1988**). ''Tuning in the mammalian cochlea,'' Physiol. Rev. **68**, 1009–1082.
Patuzzi, R.B., Yates, G.K., and Johnstone, B.M. (**1989**). ''Outer hair receptor currents and sensorineural hearing loss,'' Hear. Res. **42**, 47–72.
Peters, R.W., Moore, B.C.J., and Baer, T. (**1998**). ''Speech reception thresholds in noise with and without spectral and temporal dips for hearing-impaired and normally hearing people,'' J. Acoust. Soc. Am. **103**, 577–587.
Pickles, J.O. (**1984**). ''Frequency threshold curves and simultaneous masking functions in single fibres of the guinea pig auditory nerve,'' Hear. Res. **14**, 245–256.
Pickles, J.O. (**1988**). *An Introduction to the Physiology of Hearing* (Academic, New York).
Plack, C.J., and Oxenham, A.J. (**1998**). ''Basilar-membrane nonlinearity and the growth of forward masking,'' J. Acoust. Soc. Am. **103**, 1598–1608.
Rasmussen, G.L. (**1940**). ''Studies of the VIIIth cranial nerve in man,'' Laryngoscope **50**, 67–83.
Recio, A., Rich, N.C., Narayan, S.S., and Ruggero, M.A. (**1998**). ''Basilar-membrane responses to clicks at the base of the chinchilla cochlea,'' J. Acoust. Soc. Am. **103**, 1972–1989.
Robinson, D.W., and Dadson, R.S. (**1956**). ''A redetermination of the equal-loudness relations for pure tones,'' Br. J. Appl. Phys. **7**, 166–181.
Rosen, S., and Baker, R.J. (**1994**). ''Characterising auditory filter nonlinearity,'' Hear. Res. **73**, 231–243.
Rosen, S., Baker, R.J., and Darling, A. (**1998**). ''Auditory filter nonlinearity at 2 kHz in normal hearing listeners,'' J. Acoust. Soc. Am. **103**, 2539–2550.
Ruggero, M.A. (**1992**). ''Physiology and coding of sound in the auditory nerve,'' in *The Mammalian Auditory Pathway: Neurophysiology*, edited by A.N. Popper and R.R. Fay (Springer, New York), pp. 34–93.
Ruggero, M.A., and Rich, N.C. (**1991**). ''Furosemide alters organ of Corti mechanics: Evidence for feedback of outer hair cells upon the basilar membrane,'' J. Neurosci. **11**, 1057–1067.
Ruggero, M.A., Robles, L., and Rich, N.C. (**1992**). ''Two-tone suppression in the basilar membrane of the cochlea: Mechanical basis of auditory-nerve rate suppression,'' J. Neurophysiol. **68**, 1087–1099.
Ruggero, M.A., Rich, N.C., Recio, A., Narayan, S.S., and Robles, L. (**1997**). ''Basilar-membrane responses to tones at the base of the chinchilla cochlea,'' J. Acoust. Soc. Am. **101**, 2151–2163.
Sachs, M.B., and Kiang, N.Y.S. (**1968**). ''Two-tone inhibition in auditory-nerve fibers,'' J. Acoust. Soc. Am. **43**, 1120–1128.
Sachs, M.B., and Abbas, P.J. (**1974**). ''Rate versus level functions for auditory nerve fibers in cats: Tone burst stimuli,'' J. Acoust. Soc. Am. **56**, 1835–1847.
Sewell, W.F. (**1984**). ''The effects of furosemide on the endocochlear potential and auditory-nerve fiber tuning curves in cats,'' Hear. Res. **14**, 305–314.
Shailer, M.J., Moore, B.C.J., Glasberg, B.R., Watson, N., and Harris, S. (**1990**). ''Auditory filter shapes at 8 and 10 kHz,'' J. Acoust. Soc. Am. **88**, 141–148.
Shera, C.A., and Zweig, G. (**1993**). ''Order from chaos: Resolving the para-

dox of periodicity in evoked otoacoustic emission,'' in *Biophysics of Hair Cell Sensory Systems*, edited by H. Duifhuis, J. W. Horst, P. van Dijk, and S. M. van Netten (World Scientific, Singapore), pp. 54–63.

Shera, C.A., and Guinan, J.J., Jr. (**2000**). ''Frequency dependence of stimulus-frequency-emission phase: Implications for cochlear mechanics,'' in *Recent Developments in Auditory Mechanics*, edited by H. Wada, T. Takasaka, K. Ikeda, K. Ohyama, and T. Koike (World Scientific, Singapore), pp. 381–387.

Shera, C.A., Guinan, Jr., J.J., and Oxenham, A.J. (**2002**). ''Revised estimates of human cochlear tuning from otoacoustic and behavioral measurements,'' Proc. Natl. Acad. Sci. USA, in press.

Siebert, W.M. (**1968**). ''Stimulus transformations in the peripheral auditory system,'' in *Recognizing Patterns*, edited by P.A. Kolers and M. Eden (MIT Press, Cambridge, MA), pp. 104–133.

Siebert, W.M. (**1970**). ''Frequency discrimination in the auditory system: Place or periodicity mechanisms?,'' Proc. IEEE **58**, 723–730.

Sinex, D.G., and Havey, D.C. (**1986**). ''Neural mechanisms of tone-on-tone masking: Patterns of discharge rate and discharge synchrony related to rates of spontaneous discharge in the chinchilla auditory nerve,'' J. Neurophysiol. **56**, 1763–1780.

van Tasell, D.J. (**1993**). ''Hearing loss, speech, and hearing aids,'' J. Speech Hear. Res. **36**, 228–244.

van Trees, H.L. (**1968**). *Detection, Estimation, and Modulation Theory: Part I* (Wiley, New York), Chap. 2.

Vogten, L.L.M. (**1978**). ''Low-level pure-tone masking: A comparison of 'tuning curves' obtained with simultaneous and forward masking,'' J. Acoust. Soc. Am. **63**, 1520–1527.

von Helmholtz, H.L.F. (**1863**). *Die Lehre von den Tonempfindungen als Physiologische Grundlage für die Theorie der Musik* (F. Vieweg und Sohn, Braunschweig, Germany). Translated as: *On the Sensations of Tone as a Physiological Basis for the Theory of Music*, by A.J. Ellis from the 4th German edition, 1877, Leymans, London, 1885 (reprinted by Dover, New York, 1954).

Winter, I.M., and Palmer, A.R. (**1991**). ''Intensity coding in low-frequency auditory-nerve fibers of the guinea pig,'' J. Acoust. Soc. Am. **90**, 1958–1967.

Yates, G.K. (**1995**). ''Cochlear structure and function,'' in *Hearing*, edited by B.C.J. Moore (Academic, New York), pp. 41–74.

Young, E.D., and Barta, P.E. (**1986**). ''Rate responses of auditory-nerve fibers to tones in noise near masked threshold,'' J. Acoust. Soc. Am. **79**, 426–442.

Zhang, X., Heinz, M.G., Bruce, I.C., and Carney, L.H. (**2001**). ''A phenomenological model for the responses of auditory-nerve fibers. I. Nonlinear tuning with compression and suppression,'' J. Acoust. Soc. Am. **109**, 648–670.

Zweig, G., and Shera, C.A. (**1995**). ''The origin of periodicity in the spectrum of evoked otoacoustic emissions,'' J. Acoust. Soc. Am. **98**, 2018–2047.

Effects of a limited class of nonlinearities on estimates of relative weights

Virginia M. Richards
Department of Psychology, 3815 Walnut Street, University of Pennsylvania, Philadelphia, Pennsylvania 19104

(Received 15 September 2000; revised 22 August 2001; accepted 16 November 2001)

Perturbation analyses have been applied in recent years to determine the relative contribution of individual stimulus components in detection and discrimination tasks. Responses to stimulus samples are compared to stimulus parameters to determine the details of the decision rule. Often, a linear model is assumed and it is of interest to determine the relative contribution of different stimulus elements to the decision. Here, biases in estimated relative weights are considered for the case where the decision variable is given by $D=(\Sigma(\alpha_i X_i^n)^k)^m$ and the stimulus components, the X_i, are normally distributed, of equal variance, and mutually independent. The α_i are the ''true'' combination weights, and n, k, and m are positive reals. The method used to estimate relative weights is the correlation coefficient between the X_i and the observer's responses. Estimates of relative α_i do not depend on m but may depend on the mean values of the X_i and the values of n and k (a dependence on the variance, σ_i^2, holds even for linear transformations). © *2002 Acoustical Society of America.* [DOI: 10.1121/1.1434944]

PACS numbers: 43.66.Ba, 43.66.Gf [MRL]

I. INTRODUCTION

Perturbation, or micro-, analyses provide a suite of empirical methods that can be exploited to examine details of observers' categorization decisions. In constrained psychophysical experiments, the class of response categories available is usually S and N, signal and no signal. An observer is presented with an l-dimensional sample, X_i, $i=1$ to l, and indicates whether the sample is drawn from the S or N distribution. It is assumed that the decision variable, D, is a linear combination of the X_i, $D_L=\Sigma\beta_i X_i$, where the X_i are normally distributed and mutually independent, the β_i are the combination weights, and the subscript ''L'' indicates that the assumed decision rule is linear. The observer is assumed to make a decision, either signal or no signal, depending on the value of D_L relative to some criterion. Coding the signal and no-signal responses as 1 and 0, respectively, an observer's responses yields a response vector T. The correlation coefficient between each X_i and T for each i, $\rho_{X_i,T}$, is proportional to β_i, i.e., provides an estimate of the relative weights (Richards and Zhu, 1994; Lutfi, 1995). The basis of this method is straightforward: the squared correlation coefficient indicates the proportion of variance in the responses (T) accounted for by the random variable X_i. In the simplest condition, when the X_i have equal variance, changes in the correlation coefficients across i indicate the relative differences in the β_i. If the X_i are of unequal variance the relative weights may be adjusted to take into account the differences in variance.

In psychophysics, correlation or related methods (cf. Ahumada and Lovell, 1970; Berg, 1989; Knill, 1998) have been used to examine the decision processes for X_i presented both sequentially (cf. Berg, 1989) and simultaneously (cf. Berg and Green, 1992). The method can be applied in either two-interval forced-choice or yes–no tasks. For the former, the X_i are differences between samples presented in the two intervals. For the latter, the stimuli are expressed in terms of the X_i. As an example, consider a profile analysis experiment in which an observer indicates whether the single stimulus is the sum of tones with equal mean amplitudes (N) vs a stimulus in which one of the tones has larger mean amplitude than the others (S). In this case, the X_i are the levels of the simultaneous tones that comprise the stimuli, and the relative weights indicate the relative contribution of each tone to the category decision.

There are several concerns associated with correlation and allied methods. Errors in estimating the variance of the individual X_i lead to errors in the estimate of the relative weights. Thus, an experimenter must be confident in his/her knowledge of the variances of the X_i. It is clear that the experimenter can make reasonable guesses, and indeed control, the variance of the external, or *objective* variables. The larger problem is that there is less certainty regarding the effective, or *subjective* variables. Here, the term subjective variables refers to the ''internal'' variables combined to form the presumed decision variable D. If the externally presented X_i are altered by the sensory system such that the objective and subjective variables have different variances, the resulting relative weights are not assured to be correct.

If a nonlinearity is present, the objective and subjective variables may differ in terms of variance. Imagine that an observer is presented sequentially with lX_i's and indicates whether the sequence is drawn from the S or N distribution. For stimuli with X_i's of equal variance but *unequal mean*, squaring the objective variables to form the subjective variables will lead to subjective variables with unequal variances. In this example, X_i is the objective variable and Y_i is the subjective variable (e.g., $Y_i=X_i^2$ and $D=\Sigma\alpha_i Y_i$). The variance of the Y_i depends on the mean of the X_i.[1] Because the decision variable depends on Y_i, whose variances are not

equal, the correlation between the observers' responses and the X_i will lead to an incorrect estimate of relative weight (see Lutfi, 1995, for analysis methods that might be applied when such nonlinearities are suspected). Thus, when the X_i are squared there is no reason to expect linear methods to provide accurate estimates of relative weights.

In the current paper a nonlinearity of the form $D=(\Sigma(\alpha_i X_i^n)^k)^m$ is considered. The primary question is the degree to which the experimenter will under- or overestimate the combination true weights (the α_i) when a linear combination is assumed (i.e., the assumption $D_L=\Sigma\beta_i X_i$). The terms *relative weights* and *estimated relative weights* will be used to denote the estimated relative values of the β_i, i.e., the weights estimated using a linear assumption. It is assumed that the estimated relative weights are based on correlation coefficients, $\rho_{x_i,T}$, between the magnitudes of the objective variables X_i and the vector of observers responses (T). The variables α_i will be referred to as the *true weights*. Using this terminology, the magnitude of the mismatch between the estimated relative weights and the true weights is addressed in the current paper.

A method introduced by Dai *et al.* (1996) may be used to approximate the relation between estimated relative weights and true weights when the decision rule includes a nonlinearity. In the following section, their approach is reviewed. Then, for the decision rule $D=(\Sigma(\alpha_i X_i^n)^k)^m$ the relation between estimated weights (as correlation coefficients) and true weights is derived for selected values of *n*, *k*, and *m*. Finally, results of computer simulations are presented. The simulations provide estimates of $\rho_{X_i,T}$ values for several values of *n*, *k*, and *m*.

II. RELATION BETWEEN ESTIMATED AND TRUE WEIGHTS: THE METHOD OF DAI *ET AL.* (1996)

Dai *et al.* (1996) used both Taylor's series and computer simulations to estimate the relation between true and estimated relative weights when the decision process included nonlinearities. Their approach is summarized here. First, consider the Taylor's series for a ''regular'' function of a single variable, $f(x)$. The Taylor's series for $f(x)$ near $x=x_o$ is given by

$$f(x)=\sum_{n=0}^{\infty}\left.\frac{\partial^n f}{\partial x^n}\right|_{x=x_o}\frac{1}{n!}(x-x_o)^n,$$

where $\partial^n f/\partial x^n$ is the nth derivative of $f(x)$. Truncating at $n=N$, the series becomes

$$f(x)=\sum_{n=0}^{N}\left.\frac{\partial^n f}{\partial x^n}\right|_{X=X_o}\frac{1}{n!}(x-x_o)^n+\varepsilon,$$

where ε is an error term. A similar form of a Taylor's series is available for functions of several variables (cf. Dai *et al.*, 1996; Hildebrand, 1976). For an l-dimensioned vector X in the region $X=X_o$, the Taylor's series expanded only to the first-order derivatives ($N=1$) is given by

$$f(X)=f(X_o)+\sum_{i=1}^{l}\left.\frac{\partial f}{\partial X_i}\right|_{X=X_o}(X_i-X_{oi})+\varepsilon. \quad (1)$$

Note that in Eq. (1) the summation is across the elements of the vector X, not across higher derivatives. Higher-order derivatives and their interactions are present in the error term, ε.

Dai *et al.* [1996; their Appendix—the current Eq. (1) is their Eq. (A1)] recognized that this form of the Taylor's series is the linear approximation assumed in perturbation studies; i.e., $D=\Sigma\beta_i X_i$. This can be appreciated by replacing

$$\left.\frac{df}{dX_i}\right|_{X=X_o}$$

with β_i. The term $f(X_o)$ is an additive constant which has no impact on relative weights. Thus, estimates of relative weights generated using correlation coefficients are also estimates of the first derivative of the decision rule in the region $X=X_o$. Due to the presence of the error term, ε, the correlation coefficient is not assured to provide an accurate estimate of the derivative of *f*.

The approximation used by Dai *et al.* (1996), i.e., that estimates of relative weights derived using correlation coefficients provide the derivative of the underlying decision rule, is very general. For example, consider a decision rule of the form $D=(\Sigma(\alpha_i X_i^n)^k)^m$

$$\rho_{T,X_i}\overset{\approx}{\propto}\left.\frac{\partial D}{\partial X_i}\right|_{X=X_o}=m\left(\sum\ (\alpha_i X_{oi}^n)^k\right)^{m-1}\cdot nk\cdot\alpha_i^k X_{oi}^{nk-1}, \quad (2)$$

where the symbol $\overset{\approx}{\propto}$ implies that the derivative is approximately proportional to the correlation coefficient (proportionality misses due to the presence of the error term ε). For psychophysical perturbation studies, X_o is the mean of the vector X, so each X_{oi} is the mean of random variable X_i. Equation (2) provides considerable information regarding the relation between the estimated weights, the true weights, and the impact of the nonlinearity. Note that the first two terms, $m(\Sigma(\alpha_i X_{oi}^n)^k)^{m-1}$ and nk, are constants. Thus, Eq. (2) may be rewritten as

$$\rho_{T,X_i}\overset{\approx}{\propto}\left.\frac{\partial D}{\partial X_i}\right|_{X=X_o}\propto\alpha_i^k X_{oi}^{nk-1}. \quad (2a)$$

There are several implications of Eq. (2a). First, note that *m* does not appear in Eq. (2). This means that *m* has no impact on the relation between the estimated and true weights. Second, because *n* raises X_i but not α_i, if the X_i are equal and if $k=1$, relative weights will be proportional to the true weights. When *k* has a power other than 1, the estimated relative weights are not likely to be predictive of the true weights because α_i is directly raised to the power *k*.

Equation (2a) also provides potential psychophysical applications. For example, taking the logarithm of both sides of Eq. (2a) yields

$$\log(\rho_{T,X_i})\approx k\log(\alpha_i)+(nk-1)\log(X_{oi}), \quad (2b)$$

where the symbol $\approx$ indicates that the two sides of the equation are known to within an additive constant (the logarithm

shifts the proportionality to additivity; ε is assumed to be small, and so is treated as an additive constant). Imagine that a psychophysical experiment is repeated for several different values of the stimulus vector X. To the degree that the functions relating $\log(\rho_{T,X_i})$ and $\log(X_i)$ are linear, the slope of the line provides an estimate of nk-1. Note that n and k are present as a product. If both the X_i and the α_i are systematically varied, n and k can be separated. In most experiments, however, the experimenter can control the X_i but not the α_i, and so Eq. (2b) provides an estimate of the product nk.

As demonstrated by considering the decision rule $D=(\Sigma(\alpha_i X_i^n)^k)^m$, the method used by Dai *et al.* [1996; Eq. (2b)] provides substantial information regarding the relation between estimated and true weights. Moreover, this method provides potential procedures by which tests for nonlinearities may follow (e.g., Dai *et al.*, 1996). One issue to be considered is the magnitude of the error term, ε. When the decision rule includes high-order nonlinearities, or when the range of stimulus perturbations applied by the experimenter is large [thus increasing the magnitude of $X-X_o$ in Eq. (1)], the error term may be large. As a point of comparison, in the next section exact solutions are presented for several values of n, k, and m when the decision rule is given by $D=(\Sigma(\alpha_i X_i^n)^k)^m$.

III. n, k, OR $m=2$; $k=3$; ANALYTIC SOLUTIONS

For a decision variable of the form $D=(\Sigma(\alpha_i X_i^n)^k)^m$, where n, k, and m are positive integers, it is relatively straightforward, if arduous, to derive the relation between the estimated and true weights. It is assumed that the X_i are independent, of equal variance, and normally distributed. It is mathematically advantageous to consider the relative weights in terms of the covariance between X_i and D rather than the correlation between X_i and T. In Appendix A it is shown that $\mathrm{cov}(X_i,D)$ and $\rho_{X_i,T}$ are proportional. This means that effects of nonlinearities on the psychophysically derivable $\rho_{X_i,T}$ are proportional to the effects of nonlinearities on the nonobservable, but mathematically tractable, $\mathrm{cov}(X_i,D)$. In Appendix B, four (n, k, m) combinations are considered: (2,1,1), (1,2,1), (1,1,2), and (1,3,1)

$$n=2:\ D=\sum\ \alpha_i X_i^2,$$

$$\rho_{X_i,T}\propto \mathrm{cov}(X_i,D)=\alpha_i\mu_i(2\sigma^2). \tag{3a}$$

$$k=2:\ D=\sum\ (\alpha_i X_i)^2,$$

$$\rho_{X_i,T}\propto \mathrm{cov}(X_i,D)=\alpha_i^2\mu_i(2\sigma^2). \tag{3b}$$

$$m=2:\ D=\left(\sum\ \alpha_i X_i\right)^2,$$

$$\rho_{X_i,T}\propto \mathrm{cov}(X_i,D)=\alpha_i\left(2\sigma^2\sum\ (\alpha_j\mu_j)\right). \tag{3c}$$

$$k=3:\ D=\sum\ (\alpha_i X_i)^3,$$

$$\rho_{X_i,T}\propto \mathrm{cov}(X_i,D)=\alpha_i^3\mu_i^2(3\sigma^2)+\alpha_i^3(3\sigma^4). \tag{3d}$$

When the μ_i are equal, the correlation coefficient provides accurate relative estimates of the true combination weights (α_i) when n *or* $m=2$. This result is apparent in Eqs. (3a) and (3c) because when $\mu_i=\mu$ the correlation coefficients are proportional to α_i. For $k=2$ (or $k=3$), the α_i are squared (cubed) so the relative weights are not accurately estimated by a linear model. When the means are unequal, the correlation coefficients provide accurate relative α_i's only when $m=2$ [Eq. (3c)]. This is because when $m=2$ the correlation coefficient depends on the summed means, not the individual means.

The results shown in Eq. (3) may be directly compared with results estimated using a Taylor's series and first-order derivatives [cf. Dai *et al.*, 1996, Eq. (2) above]. For the same four (n, k, m) combinations, Eq. (2) becomes

$$n=2:\quad D=\sum\ \alpha_i X_i^2,\quad \frac{\partial D}{\partial X_i}=2\alpha_i X_{oi}. \tag{4a}$$

$$k=2:\quad D=\sum\ (\alpha_i X_i)^2,\quad \frac{\partial D}{\partial X_i}=2\alpha_i^2 X_{oi}. \tag{4b}$$

$$m=2:\quad D=\left(\sum\ \alpha_i X_i\right)^2,\quad \frac{\partial D}{\partial X_i}=2\alpha_i\left(\sum\ \alpha_j X_{oj}\right). \tag{4c}$$

$$k=3:\quad D=\sum\ (\alpha_i X_i)^3,\quad \frac{\partial D}{\partial X_i}=3\alpha_i^3 X_{oi}^2. \tag{4d}$$

For n, k, and m of 2, the relation between the true weights (α_i) and relative weights is essentially the same regardless of the means of estimating the relative weights (either as $\rho_{X_i,T}$ or $\partial D/\partial X_i$). This is not surprising because the higher-order derivatives of the Taylor's series are constant when n, m, or k is set to 2.

For $k=3$ the impact of the error term becomes apparent; comparing Eqs. (3d) and (4d), the error term includes the added factor of $\alpha_i^3(3\sigma^4)$. If the range of perturbation is small, i.e., σ^2 is small, or if the X_i have large mean values, this added term will have little impact. When the X_i have mean values near zero, the correlation coefficient is mostly driven by the error term, and so the estimate provided by Eq. (4d) is a poor one. This is because the derivative of a simple cubic is a quadratic with a minimum of zero at zero, and the slope is positive for values of x slightly off-zero. As a result, the correlation coefficient or any other *estimate* of the slope in the region of the minimum is biased toward positive numbers.

IV. COMPUTER SIMULATIONS

Computer simulations were run to evaluate the relation between estimated and true weights for a nonlinear decision variable of the form $D=(\Sigma(\alpha_i X_i^n)^k)^m$. Values of n, k, and m ranged from 0.25 to 3. Expanding the results shown in Eqs. (3c) and (4c), simulations indicated that the value of m has no impact on the relation between estimated and true weights. Thus, results are shown only for the decision variable $D=\Sigma(\alpha_i X_i^n)^k$.

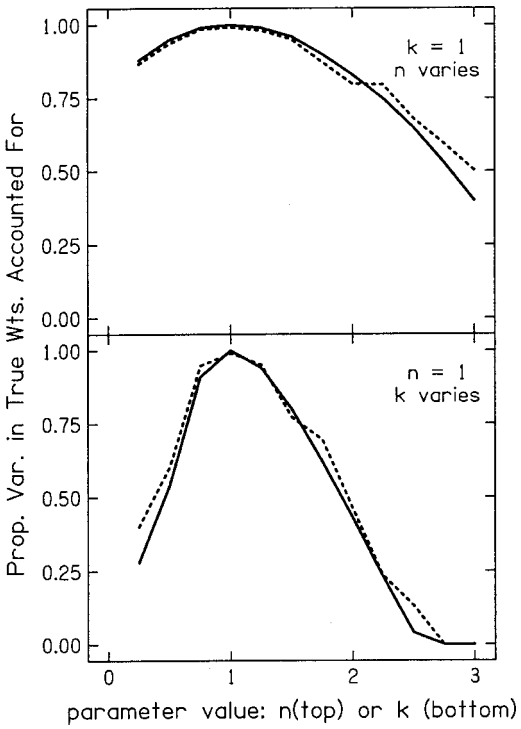

FIG. 1. The percentage of variance in the true relative weights that is accounted for using the linear model is plotted as a function of the values of n (top panel) and k (middle panel). The dashed lines are for simulation results and the solid lines are for the Taylor's series approximation [Eq. (2)]. The parameters n and k refer to the decision variable $D=\Sigma(\alpha_i X_i^n)^k$.

A. Methods

Computer simulations were run using MATLAB 5.3 (Math Works, 1996). Four normally distributed X_i were tested. The X_i either had means of [40, 50, 30, 40] or [0.1, 2, 1, 0.1]. The former case mimics values that might be encountered in yes–no tasks (i.e., the stimulus values are large positive numbers) and the later case mimics the situation in a two-interval, forced-choice task (where the X_i are differences between stimuli). Each X_i had a variance of 1. Four thousand four-dimensional ''stimulus'' vectors were generated, and the response to each sample was either 0 or 1, depending on whether the value of D fell short of or exceeded the criterion, respectively. The criterion was an estimate of the mean of D. Other criteria were also tested and the results were essentially the same. The correlation between simulated responses and each of the four X_i across all trials was the basis of the estimated weights. The true weights are {0.5, 1, 1.5, 2}. The statistic considered below is the proportion of variance in the true weights accounted for by the estimated relative weights.

B. Simulation results

Figure 1 shows the proportion of variance in the true weights accounted for by the estimated linear weights for two conditions: $(n,k)=(n,1)$ and $(1,k)$. n and k took on values ranging from 0.25 to 3 in steps of 0.25. The top panel shows changes in n and the bottom panel shows changes in k. The dashed line shows the relative weights estimated using computer simulations (correlation coefficients scaled so that the maximum is 1), and the solid line shows results for relative weights estimated using Eq. (2) (with $m=1$). The means of the X_i were [40, 50, 30, 40].

First, consider the simulation results shown in Fig. 1 (dashed line). When the decision variable is linear, the relative weights reflect the true weights (n, $k=1$; proportion of variance accounted for is near 1). When n deviates from 1, an effect of n is apparent (top panel). For equal-mean X_i (not shown) the magnitude of n has no impact on the relation between the true and relative weights. These simulation results parallel the analytical result derived for $n=2$ [Eq. (3a)].

Regardless of whether the means are equal (not shown) or unequal (bottom panel of Fig. 1), k's other than 1 lead to mismatches between true and estimated weights. This result is apparent in the analytical results for $k=2$ and $k=3$ [Eqs. (3b) and (3d)].

The solid lines show relative weights derived using first-order derivatives [Eq. (2)]. The Taylor's series approximation and the results generated using computer simulations of the actual decision rule are very similar. Thus, the proportion of the variance in the true weights accounted for by estimated relative weights is essentially the same whether the estimated relative weights are derived using computer simulations (dashed lines) or first-order derivatives (solid lines).

When the different X_i have a smaller range of expected values, e.g. [40, 42, 38, 40] rather than the [40, 50, 30, 40] values used for Fig. 1, errors in relative weight estimations are smaller. Using simulations similar to those described above and means of [40, 42, 38, 40], true weights were well estimated when values of k ranged from 1/3 to 3. This is of interest because psychophysical experiments often introduce only minor changes from equal-mean stimuli. For example, if the threshold signal level leads to small changes in one or more of the X_i, little impact of the nonlinearity is expected and relative weights estimated using a linear model are likely to provide good estimates of the true combination weights.

Figure 2 shows results for X_i's with means near zero: [0.1, 2, 1, 0.1]. The results are substantially different from those shown in Fig. 1. The proportion of variance in the true weights accounted for by the relative estimated weight estimates is low when $n\neq 1$ or $k\neq 1$. Additionally, relative weights estimated using first-order derivatives are poor predictors of relative weights derived using correlation coefficients obtained from computer simulations (solid vs dashed lines, respectively). Additional simulations indicate that for mean values near zero, the estimated weights vary substantially depending on the particular choice of means. In most simulations tested, the predictions were as poor as, or poorer than, those shown in Fig. 2.

When the X_i have near-zero means, a linear model fails in estimating relative weights. In addition, the Taylor's series approximation poorly predicts the estimated relative weights. There are two factors at work. First, when the means are small, modest errors loom large. This is apparent in Eqs. (3a)–(3d) in the product of μ_i and α_i. Second, for the nonlinearities considered here higher-order derivatives tend to change rapidly in the region of $X=0$. This leads to relatively large error terms (ε).

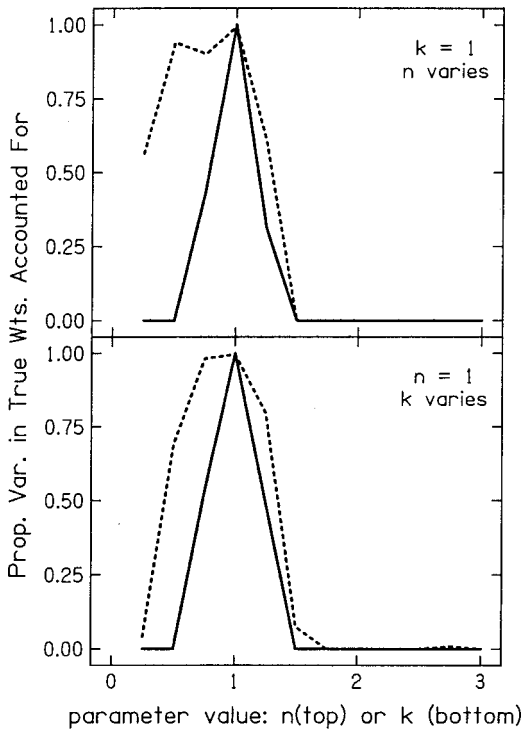

FIG. 2. As Fig. 1, except the means of the X_i are near zero.

V. DISCUSSION AND SUMMARY

Analytical and simulation results indicate that tests of linearity can be achieved by varying signal levels. This is the approach tested by Dai *et al.* (1996), who used correlation methods to examine decision nonlinearities. Another approach is to compare weights estimated using equal-mean and unequal-mean stimuli. A nonlinearity is indicated if relative weights vary with changes in means. For the detection of a tone added to a masker, shifts in relative weights associated with changes in mean (the addition of the signal) are notably present in Ahumada and Lovell (1970) and Matiasek and Richards (1999), but not in Richards and Buss (1996).

There is little cost in studying various stimulus levels to test for linearity. For a linear model the number of trials, not the distribution of signal levels, dictates the accuracy of the estimated relative weights. This suggests that tests such as those allowed by Eq. (2a) are empirically tractable.

For the nonlinearity considered in detail, $D=(\Sigma(\alpha_i X_i^n)^k)^m$, if the X_i have equal means the linear method accurately estimates the true combination weights (α_i) when $k=1$ and the n and m take on values other than 1. If the means are unequal, n's other than unity generate inaccurate relative weights. For $k\neq 1$, the weights estimated using a linear model and the α_i are not proportional because the power k is directly applied to the α_i.

ACKNOWLEDGMENTS

This work was supported by Grant No. RO1 DC 02012 from the National Institutes of Health. Dr. Jacob Nachmias, Zhongzhou Tang, and Tao Zeng provided helpful suggestions on an earlier draft of this manuscript. Two anonymous reviewers provided very helpful suggestions on an earlier version of this manuscript.

APPENDIX A: PROPORTIONALITY OF $\rho_{X_j,T}$ AND $\rho_{X_j,D}$

Consider $\rho_{X_j,D}=\mathrm{cov}(X_j,D)/\sqrt{\mathrm{var}(X_j)\mathrm{var}(D)}=\mathrm{cov}(X_j,D)/\sigma_j\sigma_D$. For $D=\Sigma\beta_i X_i$, $\mathrm{cov}(X_j,D)=\Sigma_{i=1}^n\beta_i\,\mathrm{cov}(X_j,X_i)=\Sigma_{i\neq j}\beta_i\,\mathrm{cov}(X_j,X_i)+\beta_j\,\mathrm{cov}(X_j,X_j)$. By independence, $\mathrm{cov}(X_j,X_i)=0$ when $i\neq j$. Noting $\mathrm{cov}(X_j,X_j)=\mathrm{var}(X_j)$ yields $\rho_{X_j,D}=\beta_j\sigma_j^2/\sigma_j\sigma_D=\beta_j\sigma_j/\sigma_D$. Richards and Zhu (1994; Theorem 1) showed that the correlation between the observers' responses, T, and X_j is given by $\rho_{X_j,T}=(1/\sqrt{2\pi})(1/\sqrt{pq})(\beta_j\sigma/\sigma_D)\times e^{-(1/2)(k-\mu_D)^2/\sigma_D^2}$, where p and q are the binomial probabilities and k is the criterion.

At present it is assumed that the $\mathrm{var}(X_j)$ are equal for all j. As a result, the ratio of $\rho_{X_j,D}$ and $\rho_{X_j,T}$ does not depend on j, and so the two correlation coefficients are proportional to one another. The assumption of equal variance also leads to the proportionality of $\mathrm{cov}(X_j,D)$ and $\rho_{X_j,D}$. Thus, factors effecting $\mathrm{cov}(X_j,D)$ have a parallel impact on $\rho_{X_j,T}$. In Appendix B, the easier computation, based on $\mathrm{cov}(X_j,D)$, is considered.

APPENDIX B: $\mathrm{cov}(X_i,D)$ FOR $m=1$, $k=2$, AND $n=2$

The correlation method assumes a decision variable of the form $D_L=\Sigma(\beta_i X_i)$. If D_L exceeds the criterion, the observer is assumed to respond, "signal;" otherwise a "no signal" response is provided. Denoting the responses to various stimulus samples in a vector T, the relative weights are derived by correlating, for each j, X_j, and T. Here, we consider decision variables of the form $D=(\Sigma(\alpha_i X_i^n)^k)^m$. As indicated in Appendix A, it is assumed the X_j are independent and of equal variance. As a result one obtains the same estimates of relative weights for the correlation between X_j and T (psychophysically available variables) and the covariance between X_j and D. Here, the latter approach is used.

The covariance between D, defined by $D=(\Sigma(\alpha_i X_i^n)^k)^m$, and X_i for the case of equal variance across i and for n, k or $m=2$ (the other parameters being set to 1) is derived below. Initially, various expected values, $E(X_j^2)$, $E(X_j^4)$, etc., are derived. The resulting expected values allow the derivation of the covariances of interest.

1. Expected values

If $X_j\sim N(\mu_j,\sigma^2)$ the moment generating function is given by: $\phi(t)=e^{(\mu_j t+[\sigma^2 t^2/2])}$ (e.g., Ross, 1989). By definition, the expected value for X_j^n is given by

$$E(X_j^n)=\partial^n\phi(t)/\partial t^n\big|_{t=0}.$$

For powers of 1–4, the expected values are

$$\frac{\partial\phi(t)}{\partial t}=\phi'(t)=(\mu_j+\sigma^2 t)e^{(\mu_j t+[\sigma^2 t^2/2])}$$

$$=(\mu_j+\sigma^2 t)\phi(t),$$

so

$$E(X_j)=\left.\frac{\partial\phi(t)}{\partial t}\right|_{t=0}=\mu_j. \tag{B1}$$

$$\frac{\partial^2\phi(t)}{\partial t^2}=\phi''(t)=\sigma^2\phi(t)+(\mu_j+\sigma^2 t)\phi'(t),$$

so

$$E(X_j^2)=\left.\frac{\partial^2\phi(t)}{\partial t^2}\right|_{t=0}=\sigma^2+\mu_j^2. \tag{B2}$$

$$\frac{\partial^3\phi(t)}{\partial t^3}=\phi'''(t)=\sigma^2\phi'(t)+\sigma^2\phi'(t)+(\mu_j+\sigma^2 t)\phi''(t)$$

$$=2\sigma^2\phi'(t)+(\mu_j+\sigma^2 t)\phi''(t),$$

so

$$E(X_j^3)=\left.\frac{\partial^3\phi(t)}{\partial t^3}\right|_{t=0}=3\sigma^2\mu_j+\mu_j^3. \tag{B3}$$

$$\frac{\partial^4\phi(t)}{\partial t^4}=2\sigma^2\phi''(t)+\sigma^2\phi''(t)+(\mu_j+\sigma^2 t)\phi'''(t)$$

$$=3\sigma^2\phi''(t)+(\mu_j+\sigma^2 t)\phi'''(t),$$

so

$$E(X_j^4)=\left.\frac{\partial^4\phi(t)}{\partial t^4}\right|_{t=0}=3\sigma^4+6\sigma^2\mu_j^2+\mu_j^4. \tag{B4}$$

2. Covariances

Next, the covariance between X_j and D is derived. Recall the general form of the decision variable is $D=(\Sigma(\alpha_i X_i^n)^k)^m$.

(i) $D=\Sigma\alpha_i X_i^2$ $n=2$; $k=1$; $m=1$.
Consider $\mathrm{cov}(D,X_j)=\mathrm{cov}(\Sigma\alpha_i X_i^2,X_j)=\Sigma\alpha_i\mathrm{cov}(X_i^2,X_j)=\Sigma\alpha_i[E(X_i^2X_j)-E(X_i^2)E(X_j)]$. Due to independence (cf. Ross, 1989), this becomes $\Sigma_{i\neq j}\,\alpha_i[E(X_i^2)E(X_j)-E(X_i^2)E(X_j)]+\alpha_j[E(X_j^3)-E(X_j^2)E(X_j)]$. The first term is zero. Substituting expected values from Eqs. (B1)–(B3), yields $\mathrm{cov}(D,X_j)=\alpha_j[3\sigma^2\mu_j+\mu_j^3-\sigma^2\mu_j-\mu_j^3]=\alpha_j\mu_j(2\sigma^2)$.

(ii) $D=\Sigma(\alpha_i X_i)^2$ $n=1$; $k=2$; $m=1$.
Note that $\mathrm{cov}(D,X_j)=\mathrm{cov}(\Sigma\alpha_i^2X_i^2,X_j)=\Sigma\alpha_i^2\mathrm{cov}(X_i^2,X_j)$. This is identical to (i) above, save for the presence of α_i^2 rather than α_i. The steps used above yield: $\mathrm{cov}(D,X_j)=\alpha_j^2\mu_j(2\sigma^2)$. Thus, for this case, $\mathrm{cov}(D,X_j)$ is not proportional to α_j, but to α_j^2.

(iii) $D=(\Sigma\alpha_i X_i)^2$ $n=1$; $k=1$; $m=2$.
Here, $\mathrm{cov}(D,X_j)=\mathrm{cov}((\Sigma_i\alpha_i X_i)^2,X_j)=\mathrm{cov}(\Sigma_i\alpha_i^2X_i^2+2\Sigma_i\Sigma_{k>i}\alpha_i\alpha_kX_iX_k,X_j)=\Sigma\alpha_i^2\mathrm{cov}(X_i^2,X_j)+2\Sigma_i\Sigma_{k>i}\alpha_i\alpha_k\mathrm{cov}(X_iX_k,X_j)$. From (ii) above the first term is given by $\Sigma\alpha_i^2\mathrm{cov}(X_i^2,X_j)=\alpha_j^2\mu_j(2\sigma^2)$. Next, consider the second term. When $i\neq j\neq k$, $\mathrm{cov}(X_iX_k,X_j)=0$, so one need only consider $\mathrm{cov}(X_iX_j,X_j)$, meaning that $\mathrm{cov}(\Sigma_i\Sigma_{k>i}\alpha_i\alpha_kX_iX_k,X_j)$ becomes $\mathrm{cov}(\Sigma_i\alpha_i\alpha_jX_iX_j,X_j)$. By the independence of i and j, $\mathrm{cov}(X_iX_j,X_j)=E(X_iX_jX_j)-E(X_iX_j)E(X_j)=E(X_i)E(X_j^2)-E(X_i)E(X_j)E(X_j)=E(X_i)E(X_j^2)-E(X_i)E(X_j)^2=E(X_i)[E(X_j^2)-E(X_j)^2]=\mu_i\sigma^2$.
Combining terms $\mathrm{cov}(D,X_j)=\mathrm{cov}((\Sigma\alpha_iX_i)^2,X_j)=\alpha_j^2\mu_j(2\sigma^2)+2\Sigma_{i\neq j}\alpha_i\alpha_j\mu_i\sigma^2=2\alpha_j\sigma^2(\Sigma\alpha_i\mu_i)$, or $\mathrm{cov}(D,X_j)=\alpha_j2\sigma^2\Sigma\alpha_i\mu_i$.

(iv) $D=\Sigma(\alpha_iX_i)^3$ $n=1$; $k=3$; $m=1$.
Note that $\mathrm{cov}(D,X_j)=\mathrm{cov}(\Sigma\alpha_i^3X_i^3,X_j)=\Sigma\alpha_i^3\mathrm{cov}(X_i^3,X_j)$. This is similar to (i) and (ii) above. Following the same logic, $\mathrm{cov}(D,X_j)=\alpha_j^3[E(X_j^4)-E(X_j^3)E(X_j)]$ or $\mathrm{cov}(D,X_j)=\alpha_j^3\mu_j^2(3\sigma^2)+\alpha_j^3(3\sigma^4)$.

[1]For $Y_i=X_i^2$, the expected value and variance of Y_i may be determined using results of Appendix B. $E(Y_i)=E(X_i^2)=\sigma^2+\mu_i^2$, and $\mathrm{var}(Y_i)=E(Y_i^2)-E(Y_i)^2=E(X_i^4)-E(X_i^2)^2=2\sigma^2+4\sigma^2\mu_i^2$.

Ahumada, Jr., A., and Lovell, J. (**1970**). "Stimulus features in signal detection," J. Acoust. Soc. Am. **49**, 1751–1756.

Berg, B. G. (**1989**). "Analysis of weights in multiple observation tasks," J. Acoust. Soc. Am. **86**, 1743–1746.

Berg, B. G., and Green, D. M. (**1992**). "Discrimination of complex spectra: Spectral weights and performance efficiency," *Auditory Physiology and Perception*, edited by Y. Cazals, L. Demany, and K. Horner (Pergamon, London), pp. 373–379.

Dai, H., Nguyen, Q., and Green, D. M. (**1996**). "Decision rules of listeners in spectral-shape discrimination with or without signal-frequency uncertainty," J. Acoust. Soc. Am. **99**, 2298–2306.

Hildebrand, F. B. (**1976**). *Advanced Calculus for Applications*, 2nd ed. (Prentice-Hall, Englewood Cliffs, NJ).

Knill, D. C. (**1998**). "Ideal observer perturbation analysis reveals human strategies for inferring surface orientation from texture," Vision Res. **38**, 2635–2656.

Lutfi, R. A. (**1995**). "Correlation coefficients and correlation ratios as estimates of observer weights in multiple-observation tasks," J. Acoust. Soc. Am. **97**, 1333–1334.

The Math Works, Inc. (**1996**). MATLAB: *The Language of Technical Computing* (The Math Works, Inc., Natick, MA).

Matiasek, M. R., and Richards, V. M. (**1999**). "Relative weights for three different psychophysical tasks," J. Acoust. Soc. Am. **106**, 2209(A).

Richards, V. M., and Buss, E. (**1996**). "Frequency correlation functions for the detection of a tone added to modulated noise maskers," J. Acoust. Soc. Am. **99**, 1645–1652.

Richards, V. M., and Zhu, S. (**1994**). "Relative estimates of combination weights, decision criteria and internal noise based on correlation coefficients," J. Acoust. Soc. Am. **95**, 423–434.

Ross, S. M. (**1989**). *Introduction to Probability Models*, 4th ed. (Academic, San Diego).

Modeling the influence of inherent envelope fluctuations in simultaneous masking experiments[a)]

Jesko L. Verhey[b)]
Graduiertenkolleg Psychoakustik, AG Medizinsche Physik, Carl-von-Ossietzky Universität Oldenburg, Postfach 2503, D-26111 Oldenburg, Germany

(Received 21 February 2001; revised 22 October 2001; accepted 30 October 2001)

Masked thresholds are measured and simulated for bandpass-noise signals ranging in bandwidth from 4 to 256 Hz in the presence of a masking bandpass noise also ranging in bandwidth from 4 to 256 Hz. Signal and masker are centered at 2 kHz. To investigate the role of temporal processing in simultaneous masking, simulations were performed with the modulation-filterbank model by Dau *et al.* [J. Acoust. Soc Am. **102**, 2906–2919 (1997)]. For a fixed masker bandwidth, thresholds are independent of the signal bandwidth as long as the signal bandwidth does not exceed the masker bandwidth and thresholds decrease with increasing masker bandwidth in those conditions. A simple modulation-low-pass filter (energy integrator) would be sufficient to describe the experimental results in those conditions. In contrast, the processing by a modulation filterbank is necessary to account for the conditions of ''asymmetry of masking,'' where thresholds for signals with bandwidths larger than the masker bandwidth are much lower than those for the reversed condition. In those conditions, the modulation-filterbank model is able to use the inherent higher modulation frequencies of the signal as an additional cue. [DOI: 10.1121/1.1430690]

PACS numbers: 43.66.Fe, 43.66.Ba, 43.66.Dc [MRL]

I. INTRODUCTION

Fletcher (1940) proposed a model to describe detection thresholds in spectral masking experiments. This model, known as the power-spectrum model assumes (i) that the peripheral auditory system consists of a bank of overlapping critical-band filters, and (ii) that the thresholds are determined by the overall long-term energy of the masker in the peripheral filter centered at the signal frequency. Thus, a power-spectrum model is not sensitive to variations of the temporal structure of signal and masker. However, several experiments in the literature indicate that the temporal properties of the stimuli may affect the detection thresholds.

For example, several authors have reported a decrease in the intensity difference limen for bandpass-noise signals with increasing bandwidth for subcritical bandwidth (e.g., Zwicker, 1956a; Bos and de Boer, 1966; Zwicker and Fastl, 1999; Buus, 1990). The same trend is observed for masked thresholds of a pure tone spectrally centered in the bandpass-noise masker (e.g., Bos and de Boer, 1966; Kohlrausch *et al.*, 1997; van de Par and Kohlrausch, 1999).

A power-spectrum model would predict a constant threshold independent of the noise bandwidth. Zwicker (1956a) and de Boer (1962) suggested that the statistical properties of the envelope fluctuations of narrow-band noise explain the increased thresholds. De Boer (1966) showed that a model which analyzes the energy distribution, i.e., the mean and standard deviation of the energy, can account for intensity discrimination of fluctuating signals. According to de Boer's model, the increase in threshold with decreasing bandwidth is a consequence of the increase in the standard deviation of the energy (relative to the mean) with decreasing bandwidth.

Another phenomenon, which cannot be described by the power-spectrum model, is related to the difference in the masking properties of a bandpass noise and a sinusoid. Several studies concerning spectral masking have persistently shown that the amount of masking produced by sinusoidal maskers is less than that obtained for bandpass-noise maskers (Egan and Hake, 1950; Greenwood, 1961; Hellman, 1972; Hirsh *et al.*, 1950; Zwicker, 1956b; Young and Wenner, 1967; Moore *et al.*, 1998). Especially puzzling was the result that the different masking properties of noise and sinusoids were still observed when the bandwidth of the noise did not exceed the critical bandwidth and its center frequency was equal to the frequency of the sinusoid. For example, Hellman (1972) found that a bandpass-noise signal with a subcritical bandwidth is audible at signal-to-masker ratios as low as -20 to -30 dB when it is masked by a sinusoid at the center frequency of the noise signal. In the reversed condition, with a sinusoidal signal and a bandpass-noise masker, the signal is audible at a signal-to-masker ratio as high as -4 dB. These values are comparable to those reported by Greenwood (1961, 1971) and more recently by Hall (1997) and Moore *et al.* (1998).

Hall (1997) investigated this asymmetry of masking for a combination of signal and masker bandwidth ranging from 256 to 0 Hz, i.e. a sinusoid. The center frequency of the stimuli was 1 kHz. Using frozen-noise stimuli, Hall (1997) found that thresholds decreased markedly with increasing signal bandwidth when the signal bandwidth was larger than

[a)]Part of this work was presented at the joint ASA-EAA meeting, 1999, Berlin, Germany.

[b)]Current address: Center for the Neural Basis of Hearing, The Physiological Laboratory, University of Cambridge, Downing Street, Cambridge CB2 3EG, United Kingdom.

the masker bandwidth, whereas thresholds were essentially independent of signal bandwidth when it was equal or smaller than the masker bandwidth. Hall (1997) concluded that the detection is based on the long-term average energy as long as the bandwidth is equal to or less than the masker bandwidth, but that other cues are utilized when the signal bandwidth exceeds the masker bandwidth. He suggested that a model which operates on the temporal structure of the stimuli may account for the results. However, no simulations were performed to test this hypothesis.

In the present study, an experiment is performed which is similar to the experiment conducted by Hall (1997). In contrast to Hall's experiment, signal and masker have a higher center frequency and are running-noise signals (instead of frozen noise as used in Hall's study). A difference between Hall's data and the data in the present study may already be expected for the equal-bandwidth condition, since Buus (1990) found that the level-discrimination thresholds for bandpass running noise with subcritical bandwidth can be significantly higher than those for frozen noise (see Sec. IV). In the present study, running noise is primarily used to prevent the subjects from using a cue related to the specific time structure of the signals. This may be especially important for conditions where the envelope fluctuation could provide additional signal information, as hypothesized by Hall (1997) for conditions where the signal bandwidth exceeds the masker bandwidth. In addition, by using running noise, it is possible to investigate the influence of energy fluctuations on the intensity difference limen within the same experiment.

The experimental results are compared to simulated data obtained with the modulation-filterbank model proposed by Dau *et al.* (1997a). It has been shown that this model can describe modulation detection and masking experiments (Dau *et al.*, 1997a, b), as well as spectral masking experiments with sinusoidal signals and noise maskers (Verhey, 1999; Verhey *et al.*, 1999; Derleth and Dau, 2000).

II. MODEL STRUCTURE

The model consists of several preprocessing stages. The first stage of the model is the linear gammatone-filterbank model of Patterson *et al.* (1987). The signal at the output of each peripheral filter is half-wave rectified and low-pass filtered at 1000 Hz. Thus, at high center frequencies only the signal envelope is further processed. A chain of five consecutive nonlinear feedback loops is incorporated (Püschel, 1988; Dau *et al.*, 1996) to account for adaptation and compression in the auditory system. A linear modulation filterbank further analyzes the amplitude fluctuations of the envelope. As proposed by Verhey *et al.* (1999), the center frequency of the highest modulation filter is set to a quarter of the center frequency of the respective peripheral filter. The frequency selectivity for modulation frequencies is based on physiological findings (Langner and Schreiner, 1988) and psychoacoustical data from modulation-masking and modulation-detection studies (Houtgast, 1989; Dau *et al.*, 1999). To model a limit of resolution, an internal (Gaussian) noise with a constant variance was added to the output of each modulation channel. A multichannel version of the model is used, where information from peripheral filters in an octave range around the center frequency of the stimuli is combined across frequency. An optimal detector is used as the decision device that combines the information across time, center frequency of the peripheral filter, and center frequency of the modulation filter. In the decision process, a stored temporal representation of the signal to be detected (the template) is compared with the actual activity pattern by calculating the unnormalized cross correlation between the two temporal patterns (Dau *et al.*, 1996, 1997a). This is comparable to a ''matched filtering'' process. The template is derived once at a clearly suprathreshold signal value. The idea is that at the beginning of an experiment the signal is usually presented at a highly detectable level where the subject is assumed to be able to get an ''image'' of the signal. A detailed description of the model is given in Dau *et al.* (1997a, b).

III. METHODS

A. Procedure

A three-interval, forced-choice procedure (3 IFC) was used for measurements and simulations. A trial consisted of three intervals separated by 500 ms of silence. Two intervals contained the masker alone, and one randomly chosen interval contained the masker plus signal. The subject's task was to indicate the signal interval by pressing the corresponding key on a keyboard. Feedback was provided after each trial. The level of the signal was varied adaptively according to a 1-up, 2-down procedure. A single run of the adaptive procedure consisted of 14 reversals. The step size was 8 dB for the first two reversals, reduced to 4 dB for the following two reversals, and set to 2 dB for the rest of ten reversals that made up one run. The threshold was determined by calculating the median of the levels during these ten reversals. The final threshold estimate was taken as the mean over three runs.

B. Stimuli and apparatus

Bandpass-filtered Gaussian-noise stimuli arithmetically centered at 2 kHz was used as masker and signal. The bandwidth of signal and masker was 4, 16, 64, and 256 Hz. All combinations of masker and signal bandwidth were tested. The masker duration was 700 ms. The signal had a duration of 500 ms and was temporally centered in the masker. Cosine ramps of 100 ms were applied to the masker and the signal. Both signal and masker were randomly cut out from fixed long noise waveforms which were generated separately for signal and masker at the beginning of each experiment. To generate the long bandpass-noise stimuli, a 4-s-long broadband noise was digitally filtered by (i) calculating the Fourier transform of the 4-s-long broadband noise; (ii) setting the Fourier components to zero outside the desired passband; and (iii) calculating the inverse Fourier transform. Thus, the resulting noise waveform had a periodicity of 4 s. The overall level of the long masker waveform was 70 dB SPL.

Thresholds are expressed in terms of signal-to-masker ratio, i.e., the overall intensity of the long signal waveform relative to the overall intensity of the long masker waveform. Note that the level of the 4-s-long masker waveform was

fixed while the level of each realization of the 700-ms-long masker undergoes some fluctuations (cf. Sec. V C). Similar level variations occur for the signal realizations.

The stimuli were generated digitally with a sampling rate of 32 kHz. Stimulus generation and presentation were controlled by a Silicon Graphics workstation (INDY), which also sampled the listener's responses and controlled the procedure. The software package SI, which was developed at the University of Göttingen, was used for signal generation and controlled the experiments. The stimuli were converted into analog signals with the on-board 16-bit D/A converter, and then preamplified and low-pass filtered at 16 000 Hz with a computer-controlled audiometric amplifier. The subjects sat in a double-walled, sound-attenuating booth. The stimuli were presented diotically via Sennheiser HD 25 headphones.

C. Subjects

Four subjects (three male, one female) participated in the experiment. One of them was the author JV. The author had extensive prior listening experience in spectral masking experiments. The other three subjects (JD, MT, OW) were inexperienced listeners. The subjects ranged in age from 24 to 29. One subject (MT) was paid for her participation in the experiments. All subjects had normal hearing (absolute threshold in quiet $\leqslant$15 dB HL) and no previous history of any hearing problems. All listeners received training before any data were recorded. At the beginning of the experiment, subjects were instructed to detect the sound which was perceived as being different from the other two stimuli in an interval and practice trials were run with all combinations of the two extreme signal bandwidths with the two extreme masker bandwidths. Already after a few trials (usually less than ten), all subjects reported no difficulties concerning the (different) detection cues in the different conditions. None of the subjects showed a learning effect, i.e., a progressive decrease in thresholds with increasing number of runs.

IV. RESULTS

Figure 1 shows individual data and intraindividual standard deviations for four subjects (upper and middle panels), mean data across subjects, and interindividual standard deviations (lower left panel) and simulated data (lower right panel). The figure shows the signal-to-masker ratio in dB as a function of the masker bandwidth. The parameter is the signal bandwidth: 4 Hz (circles), 16 Hz (triangles), 64 Hz (squares), and 256 Hz (diamonds).

In general, for all signal bandwidths larger than 4 Hz, two observations can be made: (i) For signal bandwidths less than or equal to a given masker bandwidth, thresholds do not depend on the signal bandwidth; (ii) For signal bandwidths larger than the masker bandwidth, threshold decreases with increasing signal bandwidth. Thus, an asymmetry of masking can be observed for all bandpass-noise combinations with different bandwidths, and masking asymmetry increases with increasing bandwidth difference. In the present study, the largest asymmetry (24 dB) is found for the 4-Hz bandpass-noise signal masked by a 256-Hz broad masker compared to the reversed condition, i.e., 256-Hz-wide bandpass noise masked by a 4-Hz-wide bandpass noise.

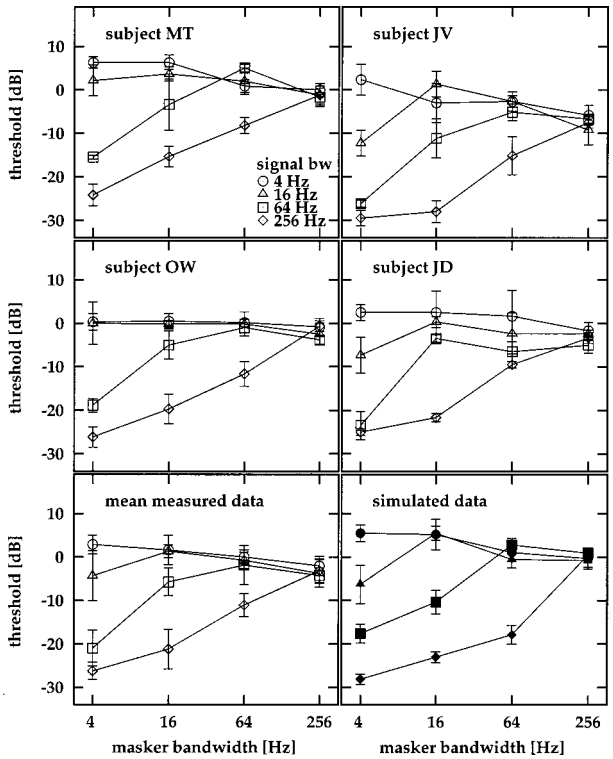

FIG. 1. Masked threshold of a bandpass-noise signal masked by a bandpass-noise masker as a function of masker bandwidth. Parameter is the signal bandwidth: 4 Hz (○), 16 Hz (△), 64 Hz (□), and 256 Hz (◇). Upper and middle panels: individual data for four normal-hearing subjects. Lower right panel: Mean data and interindividual standard deviation across the four subjects. Lower right panel: Simulated data obtained with a multi-(peripheral-)channel model with a modulation filterbank.

For three of four subjects, thresholds for a signal bandwidth of 4 Hz decrease slightly with increasing masker bandwidth (subject JV, MT, JD), whereas for one subject (OW), thresholds are independent of the masker bandwidth. On average, the threshold for a signal bandwidth of 4 Hz is 3 dB for a masker bandwidth of 4 Hz and -2 dB for a masker bandwidth of 256 Hz. The corresponding level increment, $10\log(I_{S+M}/I_M)$, is approximately 4.7 dB for the masker bandwidth of 4 Hz and 2.1 dB for a masker bandwidth of 256 Hz.[1] This corresponds to data in the literature for tonal signals masked by bandpass noise with different bandwidth (e.g., Bos and de Boer, 1966). In the present study, a similar decrease in threshold with increasing bandwidth as found for the 4-Hz signal is also observed for conditions where signal and masker have the same bandwidth. This finding is in agreement with the decrease in intensity difference limen with increasing bandwidth that is observed for subcritical bandpass-noise stimuli (e.g., Buus, 1990).

Buus (1990) obtained a difference limen of about 3 to 4 dB for a 50-Hz bandpass running noise at 60 and 90 dB SPL. It was about 1 dB less for the 150-Hz bandpass noise, which is comparable to the difference limens obtained in the present study (see above). The difference limens in the present study are higher than those in Hall (1997). The difference between the level discrimination thresholds in the

two studies amounts to about 1.5 to 2.5 dB with the tendency to decrease towards larger bandwidths. This difference is probably due to the use of running noise in the present study, whereas Hall used frozen noise. In fact, Buus (1990) obtained 1.5-dB higher thresholds for a 90-dB, 50-Hz broad bandpass noise when he used running noise instead of frozen noise. He also found a decreasing effect of the statistics on the thresholds with increasing bandwidth in agreement with the present data.

The thresholds for the conditions where the signal bandwidth exceeds the masker bandwidth are not systematically different from the data in Hall (1997). For example, 5-dB higher thresholds are measured in the present study compared to Hall's data for 16-Hz-wide signal in a 4-Hz-wide masker, whereas about 5-dB lower thresholds are obtained for a 64-Hz-wide signal in a 4-Hz-wide masker. The difference between the results of the two studies is probably due to interindividual differences that are larger for conditions where the signal bandwidth exceeds the masker bandwidth than for the reversed conditions. However, in general, the threshold pattern in Hall (1997) is very similar to the pattern in the present study.

The simulated thresholds (lower right panel) are in good agreement with experimental results. An asymmetry of masking can be predicted for all bandpass-noise combinations. The predicted asymmetry increases with increasing bandwidth difference of the stimuli. This is also seen in the measured data. The lowest measured threshold (-26 dB), obtained with a 256-Hz signal masked by a 4-Hz-wide bandpass noise, can be predicted quantitatively by the model. Furthermore, for signal bandwidths smaller than the masker bandwidth, simulated thresholds decrease with increasing signal bandwidth by about 5 dB, which agrees well with the experimental data.

V. DISCUSSION

To investigate the role of inherent envelope fluctuations of the masker and signal, simulations with a modulation-filterbank model were performed and compared to experimental data. It was shown that the model accounts for (i) the decrease in threshold with increasing masker bandwidth for signals with bandwidths less than or equal to that of the masker; and (ii) the low thresholds obtained when the signal bandwidth exceeds the masker bandwidth (asymmetry of masking).

A. Role of modulation processing in asymmetry of masking conditions

To account for asymmetry of masking, Hall (1997) proposed that the temporal structure is utilized as an additional cue for the detection of signals with bandwidths greater than the masker bandwidth, whereas in the reversed condition (for frozen stimuli) thresholds are consistent with the predictions of the energy-detector model. In the model proposed by Dau *et al.* (1997a), the temporal structure is analyzed by a modulation filterbank. To quantify the effect of the modulation-frequency selectivity in the model, simulations were performed with a modified model where instead of an analysis of the envelope with a modulation filterbank, only a low-pass-filtered envelope is processed in each peripheral filter. The cutoff frequency of the modulation-low-pass filter was 8 Hz. Figure 2 shows predicted thresholds obtained with this modified model. The simulated threshold curves are nearly independent of the signal bandwidth. This shows that a model which is mainly based on the energy of the output of the different peripheral filters is inadequate to account for the data. Thus, the experimental data in the conditions of asymmetry of masking can only be described with information from modulation filters tuned to higher modulation rates.

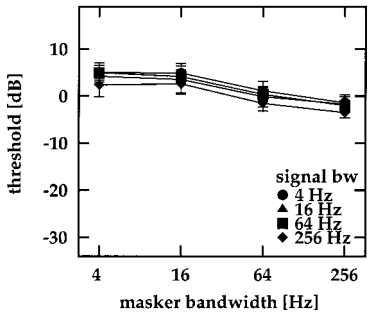

FIG. 2. Simulated thresholds obtained with a multi-(peripheral-) channel version of the model with an 8-Hz modulation low-pass filter instead of a modulation filterbank. Symbols are the same as in Fig. 1.

To illustrate the detection cues in the different masking conditions in the framework of the model, the difference between the internal representation of signal plus masker and that of the masker alone in the critical band at 2 kHz is shown in Fig. 3 for two extreme conditions. In the upper panel of the figure, the signal and the masker have the same bandwidth of 4 Hz. In the lower panel, the signal bandwidth is 256 Hz and the masker bandwidth is 4 Hz. In both conditions, the signal level was 15 dB above the level of the masker, i.e., in both conditions the signal was presented well above threshold. The figure shows the internal ''activity'' as a function of time and center frequency of the modulation filters. The ordinate is scaled in model units (MU).

The two activity patterns differ markedly. For a 4-Hz-wide signal, the signal mainly activates the modulation-low-pass filter. In addition, the onset (100 ms after masker onset) and offset (600 ms after masker onset) of the signal are also represented in the modulation filters centered at higher modulation frequencies.[2] In contrast, the activity pattern for the 256-Hz-wide signal is dominated by high modulation frequencies. This indicates that in conditions where the signal bandwidth is larger than the masker bandwidth, higher modulation frequencies are probably used by the subject as an additional cue. For Gaussian bandpass noise (as used in the present experiment), the envelope of the signal will fluctuate with rates from 0 to the bandwidth of the noise (cf. Lawson and Uhlenbeck, 1950; Dau *et al.*, 1999). Thus, in conditions, where the signal bandwidth is larger than the masker bandwidth, the modulation spectrum of the signal will be broader than that of the masker. In these conditions, the higher (unmasked) modulation frequencies of the signal will offer an additional detection cue. In contrast, when the signal bandwidth is smaller than the masker bandwidth, the detection is mainly based on the energy within the critical band filter, since the inherent envelope fluctuations of the

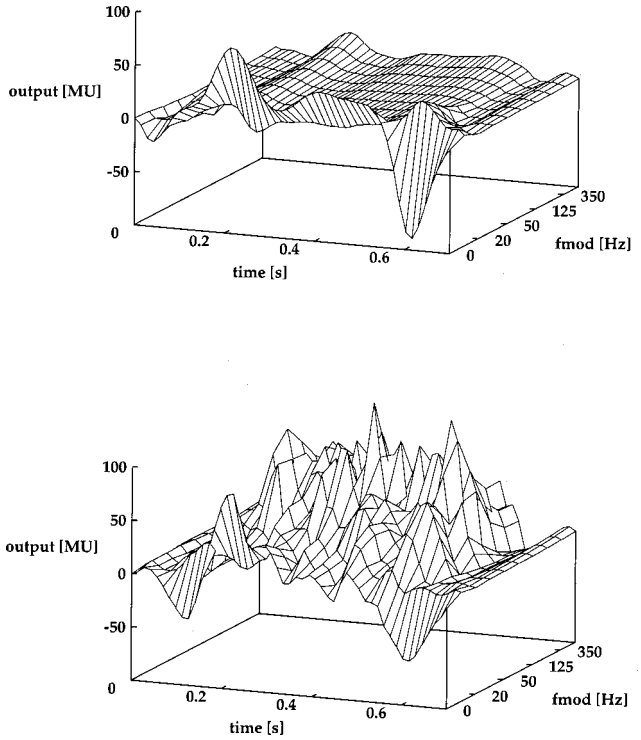

FIG. 3. Internal representation of the signal calculated as the difference between the actual internal representation of the signal plus masker and the stored mean internal representation of the masker alone. The upper panel shows the internal representation of a signal with a bandwidth of 4 Hz; in the lower panel the signal bandwidth was 256 Hz. In both conditions the masker bandwidth was 4 Hz and the signal level was 15 dB above the masker level of 70 dB SPL.

signal are completely masked by the inherent envelope fluctuations of the masker.

Note that the ability of the modulation-filterbank model to describe asymmetry of masking is a consequence of the modulation-frequency selectivity in the model. A model which instead of a modulation filterbank combines the information out of an ac-coupled modulation low-pass filter, as proposed by Viemeister (1979), with information of the overall energy in each critical band would not be able to describe asymmetry-of-masking effects, since such an approach cannot separate the higher inherent signal fluctuations from the inherent masker fluctuations.

In the present study, only stochastic signals (bandpass noises) were used for both signal and masker. In the first studies concerning asymmetry of masking, the masking of a tone by a narrow-band noise was compared to the reversed condition, i.e., masking of a narrow-band noise by a tone (e.g., Hellman, 1972; Greenwood, 1961, 1971; Moore *et al.*, 1998). However, the arguments delineated above also hold for those conditions. In fact, Hellman (1972) and Moore *et al.* (1998) explained the asymmetry of masking between a tone and a noise in a similar way. They argued that the lower threshold for a noise signal in the presence of a sinusoidal masker may be attributed to the availability of a within-channel cue of fluctuations in level. In a recent study concerning spectral masking patterns, Derleth and Dau (2000) showed that the modulation-filterbank model is able to predict the asymmetry of masking between a 1-kHz tone masked by a 80-Hz-wide bandpass-noise masker centered at 1 kHz compared to the reversed condition. Note that in order to predict the lower threshold in the noise-in-tone condition, it is crucial (as it is in the present study) that energy and the (ac-coupled) envelope are separate sources of information for the auditory system. However, the data in Derleth and Dau (2000) could also be predicted by combining the information of a energy detector with the output of an ac-coupled low-pass-filter as proposed by Viemeister (1979), since in the noise-in-tone condition it is sufficient to use the information that the noise envelope fluctuates over time, whereas the tone has a flat envelope. Thus, in contrast to the present study, it is not necessary to differentiate between the modulations of the masker and those of the signal by means of a modulation filterbank.

The arguments delineated above also hold for a similar asymmetry, which was found when the masking of a two-tone complex on a bandpass-noise signal spectrally centered between the two tones was compared to the masking of noise with a spectral notch on a sinusoidal signal spectrally centered in the notch (Patterson and Henning, 1977; Zwicker and Fastl, 1999). Although the shape of the masking patterns in these two conditions was similar, the overall level in the two-tone masking experiment was −12 dB lower than in the comparable notched-noise experiment. Again, when the signal is a noise, subjects will use the envelope fluctuation of the signal as an additional cue. This cue is not available in the ''classical'' notched-noise condition, where a tone is masked by two bands of noise.

B. Role of off-frequency information

It is argued in the literature that in some spectral masking experiments the listener can extract useful information from the stimulus out of (off-frequency) filters that are adjacent to the (on-frequency) filter at the signal frequency (e.g., Patterson and Nimmo-Smith, 1980; Leshowitz and Wightman, 1971; Schacknow and Raab, 1976).

Hall (1997) quantified the role of signal energy exciting off-frequency filters for his experimental data concerning asymmetry of masking. He showed that using the same peripheral filter form as used in the present study (gammatone filter), a small proportion of asymmetry of masking (about 6 dB) could already be predicted for the largest bandwidth (256 Hz). However, since Hall performed his experiment at 1 kHz this bandwidth is already considerably larger than the critical bandwidth. In contrast, in the present study the (broadest) bandwidth of 256 Hz is only slightly larger than the critical bandwidth, expressed as an equivalent rectangular bandwidth (ERB).[3] Thus, even for the broadest bandwidth, the energy falling into the off-frequency filters is very small. In fact, as shown in Fig. 2, nearly the same thresholds are obtained in the extreme conditions, i.e., for a 256-Hz-wide signal masked by a 4-Hz-wide masker and a 4-Hz-wide signal masked by a 4-Hz-wide masker. Thus, within the complete multichannel modulation-filterbank model, the energy in the off-frequency filters does not contribute to the predicted asymmetry of masking.

However, it is still possible that the temporal information in off-frequency filters may contribute to the detectabil-

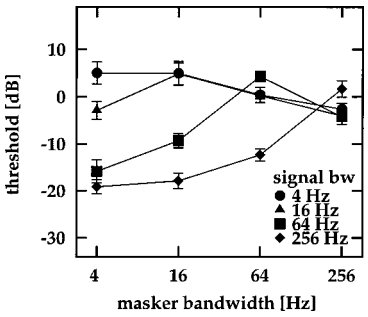

FIG. 4. Simulated data obtained with a single-(peripheral-) channel version of the modulation-filterbank model. Symbols are the same as in Fig. 1.

ity of the signal in some condition. To quantify the role of temporal off-frequency information, the simulations with the complete model are compared to simulations with a single-(peripheral-)channel version of the modulation-filterbank model, where only the information from the single gammatone filter tuned to the center frequency of the signals is processed. Thresholds obtained with the single-channel version of the model are shown in Fig. 4. There is a good qualitative agreement between the simulated and mean measured data as shown in the lower left panel of Fig. 1. There is also a good qualitative agreement between the simulated data of the single-channel version and the multichannel version of the model (lower right panel of of Fig. 1). For signal bandwidths below or equal to 64 Hz, the differences between the predictions of the single-channel version and the multichannel version of the model are smaller than 3.5 dB. In contrast, for the 256-Hz broad signal, a smaller decrease in thresholds with decreasing masker bandwidth is predicted with the single-channel version of the model compared to the multichannel model. For the smallest masker bandwidth, the single-channel model predicts 9-dB higher thresholds than the multichannel model. For a masker bandwidth of 64 Hz, the difference still amounts to 5 dB. This indicates that for the broadest signal bandwidth, the temporal information in off-frequency filters contributes additional information in the conditions where the signal bandwidth is larger than the masker bandwidth.

C. Difference limen for narrow-band noise

Since the noise signals have a finite duration, they differ in level compared to the long-term average level of the noise (de Boer, 1966). In fact, for the smallest bandwidth of 4 Hz, the level of the different masker realizations can differ by as much as 5 dB. In contrast, the level of the different realizations do not differ markedly ($<$2 dB) for the broadest bandwidth of 256 Hz.[4] Thus, the thresholds are measured in a quasi-intensity-roving condition for small masker bandwidths, whereas for the 256-Hz condition, the masker has a nearly constant level.

In Fig. 1, it was shown that the present model predicts a decrease in thresholds with increasing bandwidth in conditions where signal and masker had the same bandwidth, i.e., the model accounts for the increase in difference limen with decreasing noise bandwidth. Interestingly, the model predictions based only on the low-pass-filter output of the envelope agree well with the data (Fig. 2), indicating that processing of modulations plays only a minor role in these experiments. Thus, as in the analytical calculations by de Boer (1966), the increasing standard deviation of the energy with decreasing bandwidth is the reason for the increasing threshold. However, in the present model the standard deviation of the signal energy is not calculated explicitly as in de Boer (1966) (see Sec. I.). Instead, the statistics was taken into account by simulating the experiment, i.e., using the same stochastic stimuli and the same psychoacoustical procedure as were used in gathering the psychoacoustical data.

This explanation is in line with Buus (1990). He argued that, on the basis of the comparison of the data obtained with frozen and running noise, at least for narrow bandwidth and high levels, the level discrimination is almost entirely determined by the external statistics.

D. Possible role of modulation processing in level-roving conditions

In order to reduce the salience of the energy difference as a detection cue, Hall (1997) performed a second experiment, where he randomly varied the intensity of the (frozen-noise) stimuli in a $\pm$5-dB intensity range. He found a substantial increase in thresholds in conditions where signal and masker have the same bandwidth. In contrast, thresholds were not increased compared to the unroved condition for signal bandwidths larger than the masker bandwidth. For signal bandwidths smaller than the masker bandwidth, the effect of the level roving on the signal threshold decreases with decreasing signal bandwidth.

A modulation-filterbank model should be able to account for these findings. The model would predict an increase in threshold in the level-roving conditions where masker and signal have the same bandwidth, since in those conditions detection in the model is based on energy changes. In contrast, no increase in threshold is expected when signal bandwidth exceeds masker bandwidth, since level roving will not affect the modulation-frequency content of the stimuli. Thus, as in the unroved condition, the model will use the higher modulation frequency of the signal as an additional cue (see Sec. V A). For signal bandwidths smaller than the masker bandwidth, the higher amplitude of low-modulation frequencies in the modulation spectrum of the signal-plus-masker stimulus compared to that of the masker alone will contribute to signal detection. The effect of level roving decreases as the difference between masker bandwidth and signal bandwidth increases, since the difference in the shape of the modulation spectrum between the signal-plus-masker stimulus and masker-alone stimulus becomes more salient. These changes in modulation spectrum are not used in the unroved condition, since the energy changes provide the most consistent detection cue for signal bandwidths smaller than or equal to the masker bandwidth in this condition (see Sec. V C).

In order to test if the modulation-filterbank model is able to account for the roving effect, simulations (with a single-channel model) were performed for signal bandwidths of 16 and 256 Hz and masker bandwidths of 16 and 256 Hz and compared to the experimental data presented in Hall (1997).

Frozen noise with the same center frequency, duration, and gating as used in Hall (1997) were used in the simulations. The frozen noise was either unroved or roved in a range -5 to $+5$ dB. The predicted threshold difference between roved and unroved condition is 7 dB when signal and masker have the same bandwidth. This is comparable to the measured difference of 6.8 dB for 16 Hz and 10.5 dB for 256 Hz (Hall, 1997). For the condition where the signal bandwidth is different from the masker bandwidth (i.e., a 16-Hz-wide signal in a 256-Hz-wide masker or a 256-Hz-wide signal in a 16-Hz-wide masker), a 0.5-dB difference between roved and unroved condition is predicted. This predicted difference is similar to the measured difference of -0.8 dB for a 16-Hz-wide signal in a 256-Hz-wide masker and 1 dB for the reversed condition in Hall's data. In summary, the good correspondence between predicted and measured data indicates that the modulation-filterbank model is able to predict (i) the large effect of masker-level roving on the thresholds in conditions where the signal bandwidth is equal to the masker bandwidth; and (ii) the negligible effect of masker-level roving on the thresholds for considerably different signal and masker bandwidths.

VI. SUMMARY AND CONCLUSIONS

The present study examined the ability of the modulation-filterbank model to account for the influence of inherent envelope fluctuations in simultaneous masking conditions. The model accounts for the dependence of the intensity difference limen on the bandwidth of the noise for subcritical bandwidths. In agreement with the data, it also predicts the same thresholds for all signal bandwidths less than or equal to the masker bandwidth. In those conditions the random intensity fluctuations of the masker determine thresholds. The present model accounts for the effect of the masker intensity fluctuations by simulating the experiment explicitly. It was shown that a modulation low-pass filter (energy integrator) instead of a modulation filterbank is sufficient to account for the data in those conditions. In contrast, asymmetry of masking can only be predicted if the modulation spectrum is analyzed. For signal bandwidths that exceed the masker bandwidth, the modulation-filterbank model uses the higher unmasked modulation frequencies of the signal as an additional detection cue.

ACKNOWLEDGMENTS

Torsten Dau made several helpful suggestions concerning the interpretation of the results. Thanks to Birger Kollmeier for helpful hints and discussion and to Katrin Krumbholz and Carsten Zerbs for comments on an earlier version of this manuscript. Marjorie Leek, Søren Buus, and one anonymous reviewer made helpful suggestions on a previous version of this manuscript. This work was supported by the Deutsche Forschungsgemeinschaft.

[1]In contrast to Hall (1997), the intensity of the masker with signal I_{M+S} can be calculated by adding the intensity of the signal alone, I_S, and the masker intensity I_M because the stimuli are not correlated.

[2]The internal representation of the masker alone is similar to the representation shown in the upper panel of Fig. 3, since the masker bandwidth and signal bandwidth are the same in this condition. The masker mainly excites as the 4-Hz-wide signal the modulation-low-pass filter of the modulation filterbank. Note that the signal is shorter and temporally centered in the masker, i.e., the masker onset and offset response are before and after the respective signal onset and offset responses.

[3]The ERB for a center frequency of 2 kHz is 240 Hz (Moore and Glasberg, 1983; Moore, 1997). Note that the critical bandwidth in bark for a center frequency of 2 kHz is 300 Hz (Zwicker and Fastl, 1999). Thus, the broadest bandwidth used in the present study (256 Hz) is slightly broader than the bandwidth in ERB, but is still smaller than the critical bandwidth in bark at 2 kHz.

[4]An analytic expression of the standard deviation of the intensity for realizations of bandpass noise with a finite duration was given by de Boer (1966). He showed that the standard deviation σ of the intensity relative to the mean intensity I is equal to $1/(\Delta f * T)^{0.5}$, where Δf represents the bandwidth and T represents the duration of the signal. In the present experiment the calculated standard deviations relative to the mean for the different realizations of the masker range from about 0.07 ($\Delta f = 256$ Hz, $T = 700$ ms) to about 0.6 ($\Delta f = 4$ Hz, $T = 700$ ms). Thus, the difference between $I + \sigma$ and $I - \sigma$ ranges from about <1 dB to 6 dB.

Bos, C. E., and de Boer, E. (**1966**). "Masking and discrimination," J. Acoust. Soc. Am. **39**, 708–715.

Buus, S. (**1990**). "Level discrimination of frozen and random noise," J. Acoust. Soc. Am. **87**, 2643–2654.

Dau, T., Püschel, D., and Kohlrausch, A. (**1996**). "A quantitative model of the effective signal processing in the auditory system. I. Model structure," J. Acoust. Soc. Am. **99**, 3615–3622.

Dau, T., Kollmeier, B., and Kohlrausch, A. (**1997a**). "Modeling auditory processing of amplitude modulation. I. Detection and masking with narrow-band carriers," J. Acoust. Soc. Am. **102**, 2892–2905.

Dau, T., Kollmeier, B., and Kohlrausch, A. (**1997b**). "Modeling auditory processing of amplitude modulation. II. Spectral and temporal integration," J. Acoust. Soc. Am. **102**, 2906.

Dau, T., Verhey, J., and Kohlrausch, A. (**1999**). "Intrinsic envelope fluctuations and modulation-detection thresholds for narrow-band noise carriers," J. Acoust. Soc. Am. **106**, 2752–2760.

de Boer, E. (**1962**). "Note on the critical bandwidth," J. Acoust. Soc. Am. **34**, 985–986.

de Boer, E. (**1966**). "Intensity discrimination of fluctuating signals," J. Acoust. Soc. Am. **40**, 552–560.

Derleth, R. P., and Dau, T. (**2000**). "On the role of envelope fluctuation processing in spectral masking," J. Acoust. Soc. Am. **108**, 285–296.

Egan, J. P., and Hake, H. W. (**1950**). "On the masking patterns of simple auditory stimuli," J. Acoust. Soc. Am. **22**, 622–630.

Fletcher, H. (**1940**). "Auditory patterns," Rev. Mod. Phys. **12**, 47–65.

Greenwood, D. D. (**1961**). "Auditory masking and the critical band," J. Acoust. Soc. Am. **33**, 484–502.

Greenwood, D. D. (**1971**). "Aural combination tones and auditory masking," J. Acoust. Soc. Am. **50**, 502–543.

Hall, J. L. (**1997**). "Asymmetry of masking revisited: Generalization of masker and probe bandwidth," J. Acoust. Soc. Am. **101**, 1023–1033.

Hellman, R. P. (**1972**). "Asymmetry of masking between noise and tone," Percept. Psychophys. **11**, 241–246.

Hirsh, I. J., Rosenblith, W. A., and Ward, W. (**1950**). "The masking of clicks by pure tones and bands of noise," J. Acoust. Soc. Am. **22**, 631–637.

Houtgast, T. (**1989**). "Frequency selectivity in amplitude-modulation detection," J. Acoust. Soc. Am. **85**, 1676–1680.

Kohlrausch, A., Fassel, R., van der Heyden, M., Kortekaas, R., van de Par, S., Oxenham, A. J., and Püschel, D. (**1997**). "Detection of tones in low-noise noise: Further evidence for the role of envelope fluctuations," Acta Acust. (Beijing) **83**, 659–669.

Langner, G., and Schreiner, C. (**1988**). "Periodicity coding in the inferior colliculus of the cat. I. Neuronal mechanism," J. Neurophysiol. **60**, 1799–1822.

Lawson, J. L., and Uhlenbeck, G. E., editors (**1950**). *Threshold Signals*, Radiation Laboratories Series, Vol. 24 (McGraw Hill, New York).

Leshowitz, B., and Wightman, F. L. (**1971**). "On-frequency masking with continuous sinusoids," J. Acoust. Soc. Am. **49**, 1180–1190.

Moore, B. C. J., and Glasberg, B. R. (**1983**). "Suggested formulae for calculating auditory-filter bandwidth and excitation patterns," J. Acoust. Soc. Am. **74**, 750–753.

Moore, B. C. J., Alcántara, J. I., and Dau, T. (**1998**). "Masking patterns for

sinusoidal and narrow-band noise maskers,'' J. Acoust. Soc. Am. **104**, 1023–1038.
Moore, B. C. J. (**1997**). *An Introduction to the Psychology of Hearing*, 4th ed. (Academic, New York).
Patterson, R. D., and Henning, G. B. (**1977**). ''Stimulus variability and auditory filter shape,'' J. Acoust. Soc. Am. **62**, 649–664.
Patterson, R. D., and Nimmo-Smith, I. (**1980**). ''Off-frequency listening and auditory-filter shape,'' J. Acoust. Soc. Am. **67**, 229–245.
Patterson, R. D., Nimmo-Smith, J., Holdsworth, J., and Rice, P. (**1987**). ''An efficient auditory filterbank based on the gammatone function,'' Paper presented at a meeting of the IOC Speech Group on Auditory Modelling at RSRE.
Püschel, D. (**1988**). ''Prinzipien der zeitlichen Analyse beim Hören,'' Ph.D. thesis, Universität Göttingen.
Schacknow, P. N., and Raab, D. H. (**1976**). ''Noise intensity discrimination: Effects of bandwidth conditions and mode of masker presentation,'' J. Acoust. Soc. Am. **60**, 893–905.
van de Par, S., and Kohlrausch, A. (**1999**). ''Dependence of binaural masking level differences on center frequency, masker bandwidth, and interaural parameters,'' J. Acoust. Soc. Am. **106**, 1940–1947.
Verhey, J., Dau, T., and Kollmeier, B. (**1999**). ''Within-channel cues in comodulation masking release (CMR): Experiments and model predictions using a modulation-filterbank model,'' J. Acoust. Soc. Am. **106**, 2733–2745.
Verhey, J. L. (**1999**). ''Psychoacoustics of Spectro-temporal Effects in Masking and Loudness Perception,'' Ph.D. thesis, Universität Oldenburg, BIS-Verlag, Oldenburg.
Viemeister, N. F. (**1979**). ''Temporal modulation transfer functions based upon modulation thresholds,'' J. Acoust. Soc. Am. **66**, 1364–1380.
Young, I. M., and Wenner, C. H. (**1967**). ''Masking of white noise by pure tone, frequency modulated tone, and narrow-band noise,'' J. Acoust. Soc. Am. **41**, 700–706.
Zwicker, E., and Fastl, H. (**1999**). *Psychoacoustics*, 2nd ed., Springer Series in Information Sciences (Springer, Berlin).
Zwicker, E. (**1956a**). ''Die elementaren Grundlagen zur Bestimmung der Informationskapazität des Gehörs,'' Acustica **6**, 365–381.
Zwicker, E. (**1956b**). ''Über die Lautheit von ungedrosselten und gedrosselten Schallen,'' Acustica **8**, 237–258.

Discrimination of sound source velocity in human listeners

Simon Carlile[a)]
Auditory Neuroscience Laboratory, Department of Physiology, and Institute for Biomedical Research, University of Sydney, NSW 2006, Australia

Virginia Best
Auditory Neuroscience Laboratory, Department of Physiology, University of Sydney, NSW 2006, Australia

(Received 30 April 2001; accepted for publication 27 November 2001)

The ability of six human subjects to discriminate the velocity of moving sound sources was examined using broadband stimuli presented in virtual auditory space. Subjects were presented with two successive stimuli moving in the frontal horizontal plane level with the ears, and were required to judge which moved the fastest. Discrimination thresholds were calculated for reference velocities of 15, 30, and 60 degrees/s under three stimulus conditions. In one condition, stimuli were centered on 0° azimuth and their duration varied randomly to prevent subjects from using displacement as an indicator of velocity. Performance varied between subjects giving median thresholds of 5.5, 9.1, and 14.8 degrees/s for the three reference velocities, respectively. In a second condition, pairs of stimuli were presented for a constant duration and subjects would have been able to use displacement to assist their judgment as faster stimuli traveled further. It was found that thresholds decreased significantly for all velocities (3.8, 7.1, and 9.8 degrees/s), suggesting that the subjects were using the additional displacement cue. The third condition differed from the second in that the stimuli were ''anchored'' on the same starting location rather than centered on the midline, thus doubling the spatial offset between stimulus endpoints. Subjects showed the lowest thresholds in this condition (2.9, 4.0, and 7.0 degrees/s). The results suggested that the auditory system is sensitive to velocity *per se*, but velocity comparisons are greatly aided if displacement cues are present. [DOI: 10.1121/1.1436067]

PACS numbers: 43.66.Qp, 43.66.Pn [LRB]

I. INTRODUCTION

There has been considerable research concerned with human sound localization, the vast bulk of which has been concerned with the localization of static sources (for review see Middlebrooks and Green, 1991; Carlile, 1996a, b). It is noteworthy, however, that sound source motion relative to the head is a far more common experience in a normal listening environment, resulting from both moving sources and motion of the listener.

Sensitivity to moving stimuli has been compared with sensitivity to variations in the location of stationary stimuli. The minimum audible angle (MAA) is defined as the smallest perceivable angular separation between two stationary sounds and is about 1 degree for broadband noise stimuli at locations in the frontal hemisphere (Mills, 1958; Harris and Sargent, 1971; Grantham, 1986). Extending this idea, the minimum audible movement angle (MAMA) has been defined as the smallest angle a sound must travel before its direction is correctly discriminated. Harris and Sargeant (1971) were the first to report MAMAs that were consistently larger than the static MAA (generally 2–4 degrees of arc) using both noise bursts and tones emitted from a moving speaker. Perrott and Musicant (1977) used pure tone stimuli only and noted that increased source velocity resulted in a larger MAMA. Grantham (1986) also reported a degradation of performance with increasing velocity when simulating motion by varying the relative intensity between two external loudspeakers (stereobalancing). He also noted that the apparent loss in spatial acuity with rapidly moving sources might indicate a minimum integration time required to perform these tasks.

However, there is a range of difficulties in directly comparing localization precision (MAA) for stationary sources to the dynamic sound field (MAMA) because the parameters of velocity, time, and displacement co-vary with a moving stimulus. Despite this, some researchers have used the fact that the MAMA is generally higher than the MAA to argue that the auditory system is relatively insensitive to motion, and that motion detection may be merely a degraded localization task. By contrast, Perrott and Marlborough (1989) presented a relatively broadband (500–8000 Hz) noise from a moving speaker at 20 degrees/s and reported MAMAs of 1 degree which is equal to the average MAA reported in a static task.

Several neurophysiological studies have provided evidence that there are motion sensitive areas in the auditory system. Altman and colleagues found direction sensitive single neurons in the inferior colliculus and medial geniculate body of the cat (Altman, 1968; Altman *et al.*, 1970), and directionally selective units have also been demonstrated in the auditory cortex of the monkey (Ahissar *et al.*, 1992). Griffiths *et al.* (1996) reported of a patient with a right hemisphere stroke who was unable to detect sound movement defined by interaural phase or intensity differences. They proposed that this deficit reflects damage to a distinct cortical

[a)]Electronic mail: s.carlile@vcc.usyd.edu.au

area that is specialized for sound motion detection. This is consistent with a positron emission topography (PET) study in normal individuals, which showed the activation of a specific area of cortex on the right side upon exposure to simulated auditory motion (Griffiths *et al.*, 1994). A more recent study using functional magnetic resonance imaging defined a specific region of right auditory cortex that seemed to be responsible for distinguishing between static and dynamic sound stimuli (Baumgart *et al.*, 1999).

It is reasonable to predict that if a listener can detect auditory motion, then there may also be some sense of the *rate* of movement of the source, but surprisingly few auditory motion studies have focused on the perception of velocity. Altman and Viskov (1977) simulated movement over headphones using binaurally presented click trains and measured the smallest change in velocity that could be detected accurately for several different velocities. The authors reported that discrimination was poorer with increasing velocity, and this was confirmed by Grantham (1986) who simulated motion using stereobalancing with 500-Hz tones. A methodological problem concerns the fact that velocity covaries with displacement and time: when pairs of constant duration stimuli were presented and subjects were asked to decide which moved faster, it is possible that the faster stimulus could simply be selected on the basis that it moved further, i.e., on the basis of a *displacement* cue. Grantham noted that subjects did tend to perform the task by judging which sound traveled further, and consequently suggested that displacement, not velocity, is the more salient cue in motion perception.

Waugh and colleagues (1979) took a different approach and asked subjects to make subjective velocity judgments in miles/hour of single moving sound stimuli (bandwidth 100–1000 Hz). Performance for velocities of 15–360 degrees/s was tested under conditions of complete darkness, as well as with lights on such that the sound source was clearly visible. It was found that velocity estimates were surprisingly similar for the two conditions, despite significant errors in their absolute values. The authors interpreted these results as suggesting that the auditory system has a capacity to resolve velocities that is as good as the visual system, which is generally assumed to be a superior in this regard [for example, compare audition (Altman and Viskov, 1977; Grantham, 1986) to vision (Watamaniuk and Duchon, 1992; Matthews and Qian, 1999)].

The diversity of published data is likely a result of the variety of experimental paradigms employed in auditory motion experiments, making straightforward comparisons between studies difficult. A number of studies have opted for headphone stimulus presentation to avoid difficulties associated with moving speakers in space. These have generally simulated motion by dynamically varying the interaural time and intensity differences, which results in auditory images being perceived intracranially or within the head (e.g., Grantham and Wightman, 1979). The experiment reported here made use of virtual auditory space (VAS) where sounds presented over headphones can be externalized and accurately localized in space (Carlile, 1996a, b). The benefit of this approach is that listeners can be presented with realistic sound stimuli, containing a consistent and complete set of localization cues. Furthermore, stimuli can be moved smoothly and noiselessly on *any* trajectory in virtual space.

Using the capabilities of this stimulus paradigm, velocity discrimination was revisited in order to gain a better understanding of how sensitive the auditory system is to this parameter of motion. It was clear from previous studies that effects on motion perception of velocity, time, and displacement, *per se*, are difficult to partition. To overcome this interdependence, stimulus durations were randomized within a carefully restricted range, ensuring that relative displacement and duration did not bear a consistent relation to relative velocity (see Sec. II D). In this way, the experimental design forced subjects to make an estimate of velocity for each stimulus rather than using associated spatial or temporal cues to make comparisons.

II. METHODS

A. Subjects and general conditions

The six human subjects participating in these experiments (four females and two males, 21 to 28 years) all had normal hearing assessed auditometrically, and three had previous experience in auditory psychophysics. Stimuli were broadband sounds created in virtual auditory space (see Sec. II B) such that they moved on a horizontal plane at the level of the ears in front of the listener. These were presented over earphones to subjects seated in a darkened, sound-attenuating room at a level approximately 50 dB above the average hearing threshold of the subjects for sounds in this region of space.

Before commencing experiments, subjects were familiarized with the virtual auditory stimuli to ensure that they were externalized and moving smoothly. No formal training regime was employed for the velocity discrimination experiments; however, testing was organized in such a way that any effects of practice would be evenly distributed within and across conditions. Subjects were not told which test they were doing and had no idea of the details of the stimulus conditions.

B. Stimulus generation

The generation of individualized virtual auditory space (VAS) is based on an accurate simulation of the head-related transfer function (HRTF) and has been described in detail elsewhere (Pralong and Carlile, 1996). Briefly, subjects were seated in an anechoic chamber within which a hoop system carrying a loudspeaker could be moved to position the loudspeaker at any location on an imaginary sphere of radius 1 m. The subject's head was positioned in the center of this sphere by fixing a laser from the front (0°,0°) on the nose, and a laser from the left side (−90°,0°) on the ear canal entrance. Subjects were required to keep their head in this position for the duration of the recording process (about 30 min) with the assistance of a chin-rest and a small LED display that signaled deviations from the calibrated position. Impulse responses were recorded from microphones placed in the ear canal (''blocked-ear canal recording'': Middlebrooks *et al.*, 1989; Moller *et al.*, 1995) for 393 positions

evenly spaced on the sphere. The recording stimulus was a 1024 bit golay code pair presented 12 times, with the resultant input averaged to increase the signal-to-noise ratio.

Microphone (Sennheiser KE 4-211-2) and system transfer functions were removed from the impulse response functions by deconvolving the microphone transfer function, and HRTFs were extracted. Location-independent components were removed to leave only the directional transfer functions (DFTs) for each ear (see Middlebrooks *et al.*, 1989). The two DTF filters corresponding to a particular location could then be convolved with broadband noise (300–14 000 Hz) and delivered via in-ear headphones (Etymotic Research ER-2) to the subject to give rise to a virtual externalized sound stimulus at the original location. Digital-to-analog conversion occurred at a sampling rate of 80 kHz [Tucker-Davis Technologies (TDT) System II]. Stimuli were then delivered to an amplifier via a programmable attenuator (TDT: PA4). Stimulus synthesis and delivery as well as data recording and visualization made use of MATLAB 5.3 software (Mathworks Inc.).

In order to validate the recorded HRTFs, subjects' localization ability in VAS was compared to their free field localization ability. The localization paradigm requires a subject to stand in darkness in the center of the anechoic chamber and indicate his/her perceived location of a series of 150-ms noise bursts presented from random locations on the sphere. Responses involve a noise-pointing technique which is described in detail elsewhere (Carlile *et al.*, 1997). Localization performance was quantified using the spherical correlation coefficient, a global measure of accuracy. When performance under VAS conditions was as accurate as performance in the free field (as determined by this coefficient) and subjects reported a clear externalized percept, the HRTFs obtained for that subject were assumed to be physiophysically valid. This was the case for all subjects used in this study.

To create stimuli moving in VAS, sequential segments of a sound were filtered with HRTFs corresponding to closely spaced locations along the intended path of movement. For continuous motion, a spatial separation of 1 degree was chosen, based on the minimum audible angle for stationary broadband stimuli reported in previous studies (Mills, 1958; Harris and Sergeant, 1971; Grantham, 1986). Recent work in this laboratory has confirmed that this spatial sampling size is well within the range required for the perception of smooth, continuous motion (Leung and Carlile, 2001). To ensure smooth transitions between filtered segments, the final filter conditions for each segment were incorporated as the initial conditions of the next filter. Stimuli were ramped by applying a raised cosine to the first and last 10 ms of the signal.

As spacing of 1 degree was desired between HRTFs used in generating the moving stimulus, and the recorded HRTFs were spaced at 13 degrees, a spatial interpolation technique was employed based on the method of spherical thin-plate splines (Wahba, 1981). This allowed the description of the HRTF at any location on the sphere based on the data from a discrete set of actual recordings (393 positions on the sphere). The acoustical accuracy (in terms of the structure of the filters) and psychophysical validity (localization performance) of this interpolation technique have been tested previously in this laboratory (Carlile *et al.*, 2000, 2001). As a result of the arrangement of recorded locations on the sphere of space, moving stimuli created in this way were restricted to motion on the same sphere.

C. Psychophysical paradigm

The aim of the experiment was to examine the ability of subjects to detect changes in the velocity of moving stimuli. The general task took the form of a two-interval forced choice, in which the subject was required to indicate which of two successive intervals contained the faster moving sound source by pushing one of two response buttons. The interstimulus interval (between the end of the first stimulus and the start of the second) was approximately 1 s, and the next pair of stimuli was presented approximately 2 s after a response.

Experiments were arranged in blocks, with each block having a particular reference velocity that was presented once in every pair. Three reference velocities were employed; 15, 30, and 60 degrees/s. The comparison (''test'') velocity was chosen randomly from a set of 12 velocities in a range centered on the reference velocity and the order of presentation of the two stimuli was randomized. The range of test stimuli was chosen, on the basis of extensive preliminary tests using one of the authors, to fall in a suitable testing range about the reference velocity (2, 5, 8, 10, 12, 14, 16, 18, 20, 22, 25, and 28 degrees/s for the 15 degrees/s reference velocity; 5, 13, 20, 25, 27, 29, 31, 33, 35, 40, 47, and 55 degrees/s for the 30 degrees/s reference velocity; 20, 30, 39, 45, 51, 57, 63, 69, 75, 81, 90, and 100 degrees/s for the 60 degrees/s reference velocity). Within each testing block, the reference velocity was presented with each of its 12 test velocities a total of ten times in a random fashion. To avoid any adaptation to stimuli moving repeatedly in one direction (see Kurilowich and Carlile, 1998), rightward and leftward directions of motion were interleaved. This gave a total of 240 trials in each block (12 test velocities, 10 repetitions, and 2 directions of motion). There were three velocities and three stimulus conditions (see below), resulting in a total of nine testing blocks. Each block was broken down into six tests of 40 trials, and a single test took approximately 15 min. A short break was provided between consecutive tests to avoid fatigue and loss of concentration.

For each test stimulus velocity the percentage of trials in which the subject indicated that the test stimulus moved faster than the reference stimulus was calculated, and Probit analysis (Finney, 1971) was used to fit a psychophysical curve to the observed data. Discrimination thresholds were calculated as half the stimulus increment required to change the response rate from 25% to 75%.

D. Stimulus conditions

Three separate stimulus conditions were used in an attempt to reveal the contribution of displacement-related cues to velocity perception. In the first condition, the aim was to investigate discrimination performance based purely on sensitivity to changes in velocity of auditory targets. To achieve

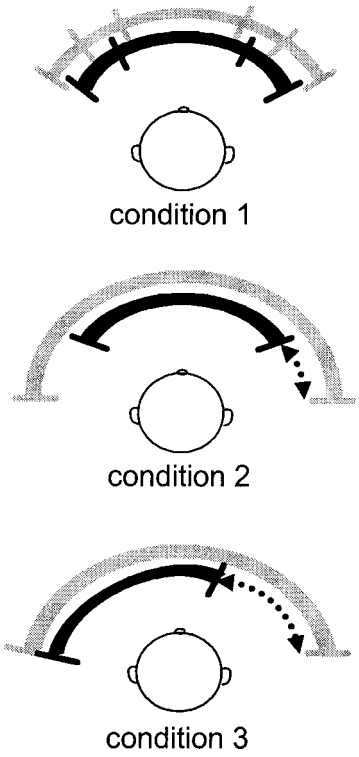

FIG. 1. Stimuli moved to the left or right on an arc in the frontal region of space. In condition 1 the gray and black bars illustrate the arc swept out by the reference and test stimuli (in no particular order). In this case both stimuli were centered on the midline and stimulus duration was randomized such that the distance traveled by a stimulus was jittered (as indicated schematically by the staggered bars) and unrelated to its velocity. In condition 2, stimuli were again centered but duration was held at a constant value. Thus the faster stimulus (in this condition the gray bar) traveled a greater distance and a spatial offset was available at the endpoints which could indicate relative velocity (indicated by black arrow). In condition 3, stimuli were identical to condition 2 with the exception that they were ''anchored'' on a common starting point, and hence the spatial offset at the endpoints was doubled for a given velocity pair.

this, it was necessary to eliminate, as far as possible, potential displacement and duration cues. In the second and third conditions, the effect of providing a direct displacement cue was examined.

Condition 1: In condition 1, the trajectories of all stimuli (both reference and test) were chosen in a pseudo-random way with practical constraints placed on both the displacement and duration. Duration was restricted within the range 600–5000 ms and it was assumed that stimuli in this temporal range would surpass any minimum integration time for the detection of motion (Grantham, 1986; Chandler and Grantham, 1992). In addition, if a stimulus velocity/duration pair was chosen and it corresponded to a displacement greater than 180 degrees/s, the duration was rejected and a new one randomly chosen. The result was that duration and displacement varied unpredictably with velocity and thus these variables were eliminated as potential cues to relative velocity. All stimulus trajectories were centered on the midline for this condition and the same set of trajectories was used for all subjects. Figure 1 depicts the trajectories of the reference and test stimuli (black and gray bars), and demonstrates how the displacement of each could vary from trial to trial regardless of their relative velocities.

Condition 2: In order to examine the influence of displacement-related cues on velocity judgments, stimuli in condition 2 were presented for a constant duration resulting in stimuli with higher velocities traveling further. In effect, relative velocity was correlated with relative displacement, and thus velocity discrimination could be based on this displacement cue. Stimulus trajectories were centered on the midline, and hence any displacement differences would emerge as differences in the starting point and endpoint locations. Figure 1 illustrates the stimulus trajectories for this condition, where the faster stimulus (gray bar) travels a greater distance than the slower stimulus (black bar) and produces a spatial offset (arrow) that is related to the relative velocities. Within a velocity condition, the constant duration value was chosen to be the average of the random durations employed in condition 1 (3000, 1800, and 1700 ms for the 15, 30, and 60 degrees/s reference velocities, respectively).

Condition 3: Condition 3 was designed to imitate condition 2 in all respects (duration and spatial extent of stimuli) except that stimulus trajectories were ''anchored'' on a common starting location rather than centered on the midline. This arrangement removed any starting point differences, but produced a spatial offset of endpoints twice as large as that provided by condition 2, as can be seen by the size of the arrow in Fig. 1. Thus the effective contribution of this particular cue could be estimated by examining the effect of doubling it. The location of the starting point for both stimuli was the same as the starting point of the reference stimulus in condition 2 ($\pm$22.5 degrees for the 15 degrees/s block; $\pm$27 degrees for the 30 degrees/s block; $\pm$51 degrees for the 60 degrees/s block). In addition, this stimulus configuration was similar to that simulated in some previous velocity discrimination studies (Altman and Viskov, 1977; Altman and Romanov, 1988).

III. RESULTS

A. General observations

The performance levels varied across the six subjects in this experiment: three subjects (1, 2, and 3) appeared more sensitive to stimulus velocity, performing more consistently and achieving an overall higher number of correct responses. Two of these subjects had previous experience in auditory experiments (subjects 2 and 3). The remaining three subjects (4, 5, and 6) performed, in general, less consistently and their overall number of correct responses was lower. Out of these three subjects, only subject 6 had experience in auditory experiments.

Despite the overall differences in sensitivity to velocity, each subject demonstrated the same pattern of sensitivity across the three different stimulus conditions. A typical set of results (obtained from subject 1) is shown in Fig. 2. Psychophysical curves are shown for each of the reference velocities in separate rows, and leftward (negative) and rightward (positive) directions of motion are depicted in separate panels. Within each panel, differences in curves for the three stimulus conditions can be seen. For this subject, and indeed each of the six subjects, judgments were poorest in the first condition (''random'') where stimulus duration varied ran-

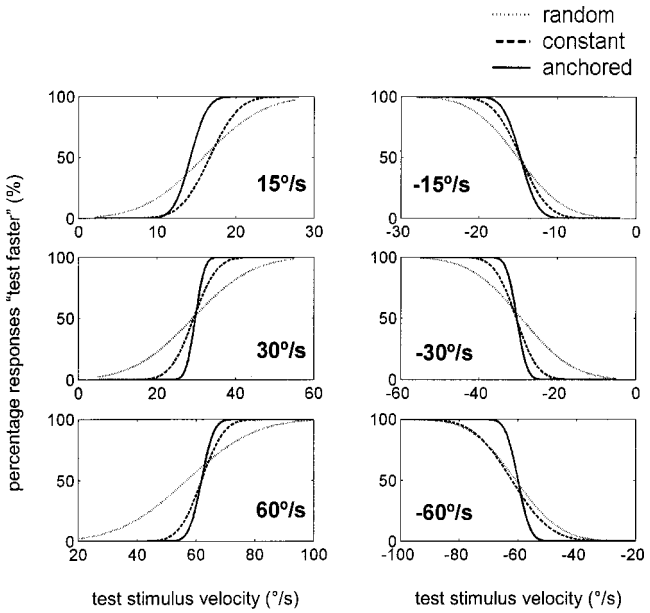

FIG. 2. Representative psychophysical curves fitted to the data from subject 1 showing all three stimulus conditions at each of the three reference velocities (leftward and rightward motion shown in left and right panels, respectively; reference velocity indicated on each graph). Dotted lines indicate fitted curves for the ''random'' condition (condition 1), dashed lines the ''constant'' condition (condition 2), and solid lines the ''anchored'' condition (condition 3).

domly with velocity (gray line). This was reflected in the relatively shallow psychophysical curves. When duration was held constant, i.e., condition 2 (''constant''—dashed line), a relative improvement in performance was observed, and psychophysical curves were steeper in the majority of cases. Discrimination was aided considerably in the third stimulus condition (''anchored''—black line) where the displacement cue had been enhanced.

B. Thresholds for velocity discrimination

The variations in the slope of the psychophysical curves were quantified by calculating discrimination thresholds (see Sec. II C). Threshold values for each subject in all conditions are presented in Fig. 3 with the data for each subject plotted in a separate panel. These are plotted for both leftward (negative) and rightward (positive) motion for each of the three reference velocities. Thresholds for condition 1 (''random'') are plotted as unfilled bars, condition 2 (''constant'') as gray bars, and condition 3 (''anchored'') as black bars. Plotted in this way, the individual differences in sensitivity discussed above are obvious from the variation in the mean height of the histograms from panel to panel. Subjects 1, 2, and 3 show threshold values that are somewhat lower than the other subjects, indicating a higher sensitivity to velocity changes.

Furthermore, in nearly every case, a decrease in absolute threshold for each velocity can be seen when comparing the ''random'' condition to the ''constant'' condition and then to the ''anchored'' condition. Another feature of these data is that absolute thresholds show a general decrease with decreasing stimulus velocity, indicated by the ''u-shaped'' distribution with velocity.

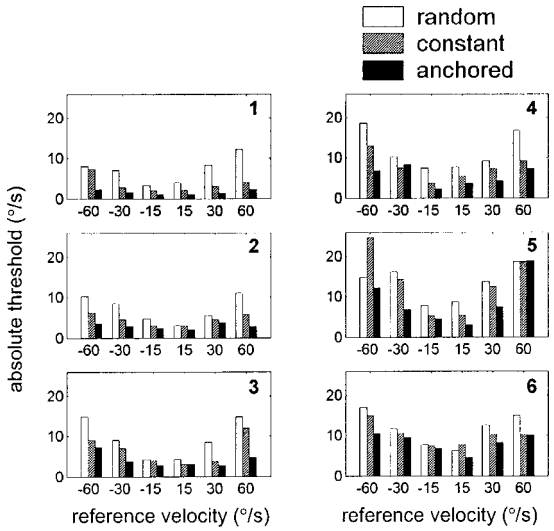

FIG. 3. Thresholds for each stimulus condition at all reference velocities (positive velocities indicating rightward motion, negative velocities indicating leftward motion). Each of the six subjects are shown in separate panels. The unfilled bars indicate threshold for the ''random'' condition (condition 1), the gray bars the ''constant'' condition (condition 2), and the black bars the ''anchored'' condition (condition 3).

Calculation of the Weber fraction (in this case, division of the threshold by the reference velocity) provides one means by which the magnitude dependence of threshold can be normalized. The threshold data are replotted as Weber fractions in Fig. 4. When presented this way, it can be seen that the ''u-shaped'' effect is inverted, indicating that *relative* discrimination thresholds *decrease* with increasing velocity, whereas *absolute* discrimination thresholds were seen to *increase*. In other words, subjects became relatively more sensitive to velocity changes as velocity was increased from 15 to 60 degrees/s. However, not surprisingly, the previously observed differences between conditions in any velocity block are preserved: i.e., Weber fractions, in nearly all cases, are highest for the ''random'' condition and lowest in the ''anchored'' condition.

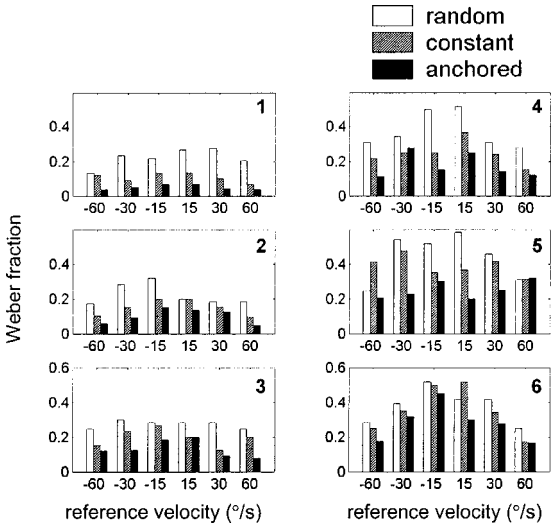

FIG. 4. Weber fractions for each stimulus condition at all reference velocities. Other details as for Fig. 3.

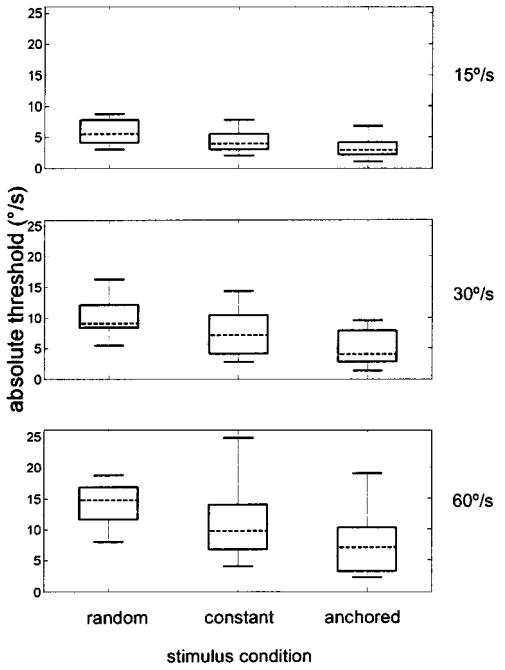

FIG. 5. Boxplots of threshold data pooled across subjects and direction. Dotted lines indicate the median, box ends illustrate upper and lower quartiles of population, and whiskers show extent of data.

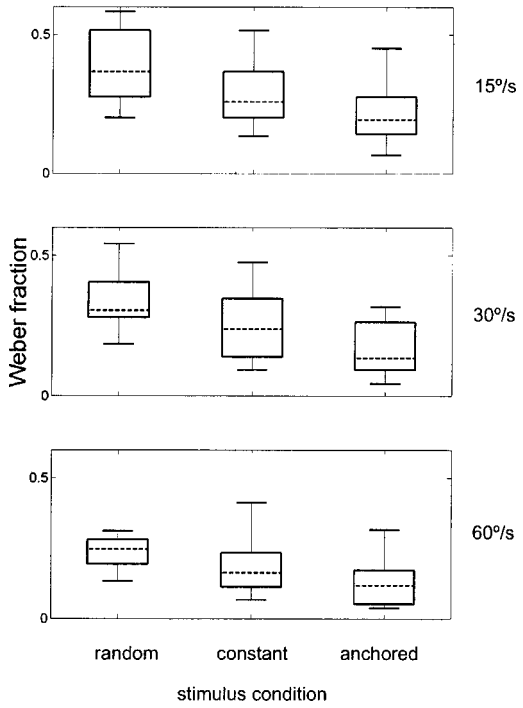

FIG. 6. Boxplots of Weber fractions pooled across subjects and direction. Details as for Fig. 5.

C. Effect of direction

As both directions of motion (left-to-right and right-to-left) were tested in this experiment, the data were investigated to see if direction had any impact on velocity discrimination. Thresholds were pooled across subjects and stimulus conditions and each velocity range in turn was examined for any effect of direction. Data were not normally distributed, so a nonparametric approach was utilized (Kolmogorov-Smirnov two-sample test: Massey, 1951). It was confirmed that there were no significant differences (confidence 99.95%) between results for the two directions of motion for any of the three velocity ranges. This is consistent with the finding of Chandler and Grantham (1992) that there was no effect of direction on the minimum audible movement angle (see the Introduction). It was therefore possible to collapse the current data across direction for statistical purposes. As there was a range of sensitivities across subjects within a stimulus condition, a large spread was observed in the pooled data. However, it was still useful to examine these data for trends, as the covariation across conditions was obvious.

D. Effect of stimulus conditions

In order to determine whether the observed differences in discrimination performance under the three stimulus conditions were statistically significant, pooled thresholds were compared. Boxplots of these, as well as the corresponding Weber fractions, are shown in Figs. 5 and 6, where the box edges represent upper and lower quartiles of the data, and the dotted lines indicate the median. Median thresholds were highest in condition 1, with values of 5.5, 9.1, and 14.8 degrees/s for the 15, 30, and 60 degrees/s velocities, respectively. In condition 2 median thresholds decreased for all velocities to 3.8, 7.1, and 9.8 degrees/s. Subjects showed the lowest thresholds in condition 3, and median values were 2.9, 4.0, and 7.0 degrees/s. From the uneven spread of values about the medium, it appeared that few of these populations were normally distributed. To make statistical comparisons, a Kruskal–Wallis one-way analysis of variance by ranks was employed (Kruskal and Wallis, 1952). Using a significance level of 0.05, the three conditions were determined to be different in all velocity ranges (15 degrees/s, $p=0.039$; 30 degrees/s, $p=0.026$; 60 degrees/s, $p=0.034$). As the transformation from absolute thresholds to Weber fractions is linear, this significance applies to both representations.

IV. DISCUSSION

A. Thresholds for velocity discrimination

The data presented indicate that subjects could discriminate between auditory stimuli moving at different velocities, but thresholds were largest when duration varied randomly to prevent displacement being used as an indicator of velocity. When displacement was related directly to velocity (by presenting stimuli at a constant duration) it was found that performance improved according to the magnitude of the resulting displacement cue. Figure 7 shows the relative ''improvement'' offered by the constant duration conditions, which was calculated by comparing the Weber fractions obtained under these conditions to the random duration condition. It was found that introducing a spatial offset cue (condition 2, ''constant'') resulted in a 25% reduction of threshold, and doubling this spatial offset (condition 3, ''anchored'') resulted in a 50% reduction of threshold. Interestingly, there was no significant difference in this improvement as a function of the reference velocity, as is clear from Fig. 7.

Altman and Viskov (1977) also used a two-interval forced choice paradigm to examine velocity discrimination

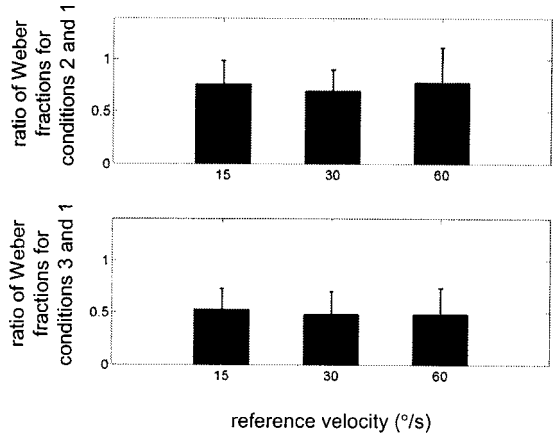

FIG. 7. Ratio of Weber fractions calculated in the constant duration conditions to those calculated in the random condition. The top panel indicates the reduction of Weber fractions seen in condition 2 compared to condition 1 for each of the three reference velocities. The bottom panel shows similar values for condition 3 compared to condition 1. Standard deviations are shown as error bars.

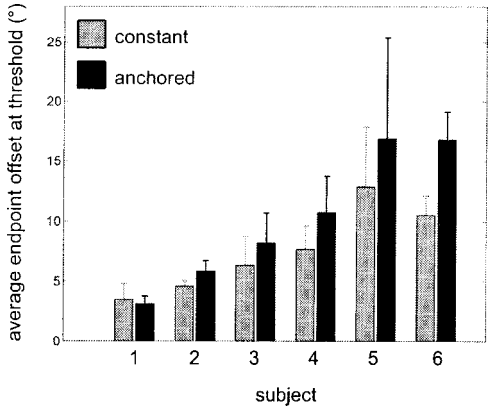

FIG. 8. Average spatial offset of stimulus endpoints at threshold. Values are pooled across velocities and the two constant duration conditions for each of the six subjects. Shown are individual means and standard deviations.

and used constant duration stimuli (3-s duration, anchored on the midline) with a reference velocity of 14 degrees/s. These conditions are comparable to condition 3 for the 15 degrees/s reference velocity in the present study, as the velocity is similar and a reliable displacement cue is provided. Altman and Viskov reported a difference limen (corresponding to a 75% correct response rate) of 10.8 degrees/s for their four subjects in this velocity range. This is much greater than the median threshold values obtained in the present study (2.9 degrees/s for condition 3) and greater even than the value obtained when stimulus duration was randomized (5.5 degrees/s, condition 1). This disparity is most likely due to differences in the stimuli employed. Altman and Viskov used binaural click trains with varying interaural time differences (ITDs) presented over headphones to simulate auditory motion. These stimuli were lateralized within the head, not externalized as the virtual auditory stimuli employed here were. In the present experiment VAS stimuli were externalized and listeners had the benefit of the full range of localization cues (interaural time and level differences and spectral cues) whereas Altman and Viskov's subjects were provided with stimuli based only on varying interaural time differences, with no level cues or spectral information.

In a later study, Altman and Romanov (1988) revisited velocity discrimination using click trains, but simulated motion by varying interaural level differences (ILDs), and the results are much more comparable to those presented here. For a reference velocity of 14 degrees/s presented for a period of 4 s, these authors reported a threshold of 2 degrees/s. This is in closer agreement with the 3.06 degrees/s value presented here for the anchored 15-degrees/s condition. However, in the Altman and Romanov study listeners indicated the perceived velocity of a single reference stimulus by ''choosing'' from a range of stimuli, to match the reference velocity, and they were given as much time as they wished to do so. Threshold in that study was defined as the variance of 20 such ''choices,'' complicating a direct comparison with the results reported here. Despite these differences, these results suggest that dynamic ILD may be a more salient cue to the perception of velocity than dynamic ITD. This idea is supported by the work of Blauert (1972) and Grantham (1984), who attempted to compare the sensitivity of listeners to fluctuations in ITD and ILD and concluded that the binaural system can follow the latter more efficiently.

Grantham (1986) employed a two-interval stimulus paradigm to investigate velocity discrimination with 500-Hz tones and all stimuli were presented for a constant duration of up to 600 ms. The thresholds reported for discrimination were much larger than those presented in this study and others. For a reference velocity of 10 degrees/s, approximately 10 degrees/s change in velocity was needed for a difference to be detected, giving an unusually high Weber fraction of 1.0. Again the difference between this result and those reported here most likely reflect differences in the methodology. Grantham's subjects were judging the motion of pure tones, and the lack of spectral information for localization may have increased the difficulty of the task. Additionally, moving sounds with 600-ms duration or less may be insufficient to allow the auditory system to properly sample their rate of change of location. Interestingly, for greater reference velocities in Grantham's 600-ms condition (up to 40 degrees/s), threshold did not change very much. This is consistent with the notion that for relatively brief moving stimuli, discrimination may be based on displacement alone. In other words, velocity thresholds can be expressed as the displacement difference required between two stimuli for them to be accurately discriminated. If this is the case, Grantham reports that his subjects could discriminate stimuli on this basis when one stimulus traveled approximately 4 to 10 degrees further than the other. This is also consistent with the current study where listeners tended to use a displacement cue if it was available. For the subjects in the present study, endpoint differences at threshold were calculated for the two constant duration conditions. Marked individual differences were observed and the mean values (across all velocities) for each subject are shown in Fig. 8. These range from about 3 to 7 degrees. However, within subjects the values were fairly constant, as shown by the relatively small error bars, suggesting that displacement was a salient cue. A feature that was evident for all subjects except for subject 1, however, was that the average endpoint difference at threshold was

slightly lower in condition 2 (''constant''—gray bars) than in condition 3 (''anchored''—black bars). It is likely that this is explained by the fact that only endpoint offsets have been taken into account, whereas in condition 2 (''constant''), there was an additional offset cue at the starting point. In other words, it appears that the extra ''look'' at the offsets of the reference and test stimuli available in condition 2 aids in their comparison and ultimately produces a lower threshold. Both of these studies then suggest that the auditory system readily utilizes displacement as an indicator, if it is available, to significantly improve on a moderate capability to detect velocity *per se*.

Overall, based on the data presented here, the auditory system does not appear to be as sensitivity to velocity as the visual system. Many studies have calculated thresholds for vision, both foveally and peripherally, using various moving stimuli. In all cases reported, Weber fractions were found to be less than 0.2 and in the majority of studies reported values were between 0.05 and 0.1 (e.g., Watamaniuk and Duchon, 1992; Matthews and Qian, 1999). This suggests a much more acute sense of velocity in the visual modality, as the lowest Weber fraction obtained for auditory motion is 0.14 (Altman and Romanov, 1988) and in general the reported range is 0.2–0.7. In fact, only one study in the literature has reported a similar capability in these two modalities for a velocity task (Waugh *et al.*, 1979; see the Introduction). In that study, it was found that subjects gave similar velocity estimates for moving auditory stimuli whether or not visual input was also provided. However, the task there was a subjective judgment rather than an objective discrimination and large errors in these estimates were consistently observed. The literature on velocity discrimination indicates overwhelmingly that the visual system is more sensitive than the auditory system to this parameter.

B. Relating auditory motion to auditory space.

The fact that the auditory system must derive a representation of space indirectly from a set of acoustical cues has important implications for the perception of motion in this modality. In the visual system, the direct representation of space provided by the receptors allows a motion detection system based on a sequential shift in activation across this array. In the auditory system, however, the detection of motion must rely on extensive central processing of dynamic acoustical cues.

There is some evidence in the literature suggesting the existence of detectors that are specialized for auditory motion (Spitzer and Semple, 1991, 1993; Griffiths *et al.*, 1996; Baumgart *et al.*, 1999). The current data is consistent with this notion, as subjects were indeed capable of making reasonable velocity estimates. However, the data in this study also indicate that motion judgments may be based on displacement cues when available, as velocity discrimination was affected by the spatial disparity between a pair of stimulus trajectories. The displacement difference required to distinguish two stimulus velocities, however, was certainly greater than any reported minimum audible angle (Mills, 1958; Harris and Sargeant, 1971; Grantham, 1986). It could be the case that the endpoints are simply being compared in order to perform the task, but the judgments of their locations are degraded as a result of the motion of the stimulus. This is consistent with the general finding that the minimum audible movement angle is larger than the minimum audible angle (see the Introduction). Alternatively, the finding could suggest that, in fact, some continuous processing is required in addition to a significant amount of spatial information, to make accurate decisions about velocity. We are unable from these data to discriminate between these two possibilities.

A study by Grantham (1997) compared motion detection with a continuous moving target (minimum audible movement angle, MAMA) to a similar task in which sound was only produced by the target for two brief bursts at the start and end of the trajectory (marked endpoints, ME). The aim was to identify whether information in the ongoing portion of the target was helpful for judgments, or whether motion perception could be simply explained by localization of the endpoints (a ''snapshot'' mechanism). It was found that for faster velocities (60 degrees/s) the MAMA and ME thresholds were not significantly different whereas for slower velocities (20 degrees/s), the MAMA threshold was lower than the ME threshold. This suggests that information in the ongoing signal aided judgments at lower velocities whereas, at the higher velocities, displacement alone was sufficient to determine the MAMA.

To test if any velocity effect could be observed in the present data, the Weber fractions were compared for the ''random'' and ''constant'' conditions. The ratio of the Weber fractions in conditions 2 and 1 was calculated as a measure of the *improvement* afforded by keeping duration constant (Fig. 7). This analysis indicates a constant improvement in performance for the three velocities, suggesting that the spatial cues available in this study contributed equally to velocity discrimination at each of the velocity ranges tested. This is in contrast to Grantham's finding as discussed above for similar velocities. However, as a measure of motion sensitivity, the stimulus paradigm in the current study differs from the MAMA paradigm in that it disambiguates velocity, duration, and displacement (see the Introduction). In this light, the constant change in velocity discrimination performance seen across velocity given a displacement cue (Fig. 7) suggests a single underlying process for the velocities examined.

C. Final considerations

The actual nature of velocity perception is a question that has arisen repeatedly in both the auditory and visual motion literature. The debate concerns whether velocity is perceived directly, or whether it is a derived statistic based on a computation of the stimulus displacement to duration ratio. It is possible, for example, that subjects in the current experiment calculated the total displacement traveled by a stimulus, and the duration of the motion, and from these computed a velocity estimate. It is an interesting but difficult question to probe experimentally, but there have been several clever attempts. As an example, Lappin *et al.* (1975) compared the discriminabilities of moving visual stimuli that varied in the spatial extent of their trajectories, temporal duration, or redundant combinations of both variables, and found that velocity discrimination was too accurate to be attributed

only to discriminations of the temporal and spatial extents. They proposed that velocity is perceived directly, as a *relation* between time and space. The experiments described here did not attempt to address this question, but rather were designed to examine how accurate the velocity estimate is, regardless of how it is acquired.

The general finding that the auditory system in humans is not highly sensitive to changes in velocity is somewhat surprising. Anecdotally, there are certainly indications that auditory cues can provide accurate information regarding the motion of real objects, such as the judgment of the speed of moving vehicles. Perhaps the difference here is that these environmental stimuli have a component of motion towards or away from the listener. In contrast, most of the experiments in this area, including the present study, have used (or simulated) stimuli moving on an arc at a constant distance from the head. The importance of this difference is that stimuli moving towards or away from a listener elicit a Doppler effect. As most environmental stimuli are influenced by the Doppler shift, it may be that this is a strong indicator of motion, and velocity in particular. A recent study by Lufti and Wang (1999) attempted to reveal the relative importance of the various acoustical cues for the perception of linear motion. The authors repeated that for discrimination of the velocity of a moving stimulus (five harmonics of a 100-Hz tone), the Doppler shift as a cue was weighted more heavily by subjects than overall intensity and interaural time difference. The influence of Doppler on broadband stimuli such as those used in the present study is uncertain, however. In addition, stimulus velocities were relatively high in the Lufti and Wang study compared to the study reported here, and it remains to be seen if the Doppler shift would improve velocity discrimination performance at relatively slow velocities.

ACKNOWLEDGMENTS

This work was supported by Australian Research Council Grant No. A79905421. The assistance of Johahn Leung and André van Schaik at various stages in the project is warmly acknowledged.

Ahissar, M., Ahissar, E., Bergman, H., and Vaadia, E. (**1992**). ''Encoding of sound-source location and movement: activity of single neurons and interactions between adjacent neurons in the monkey auditory cortex,'' J. Neurophysiol. **67**(1), 203–215.

Altman, J. A. (**1968**). ''Are there neurons detecting direction of sound source motion?'' Exp. Neurol. **22**, 13–25.

Altman, J. A., and Romanov, V. P. (**1988**). ''Psychophysical characteristics of the auditory image movement perception during dichotic simulation,'' Int. J. Neurosci. **38**, 369–379.

Altman, J. A., and Viskov, P. V. (**1977**). ''Discrimination of perceived movement velocity for fused auditory image in dichotic stimulation,'' J. Acoust. Soc. Am. **61**, 816–819.

Altman, J. A., Syka, J., and Shmigidina, G. W. (**1970**). ''Neuronal activity in the medial geniculate body of the cat during monaural and binaural stimulation,'' Exp. Brain Res. **10**, 81–93.

Baumgart, F., Gaschler-Markefski, B., Woldorff, M. G., Heinze, H., and Scheich, H. (**1999**). ''A movement-sensitive area in auditory cortex,'' Nature (London) **400**, 724–726.

Blauert, J. (**1972**). ''On the lag of lateralization caused by interaural time and intensity differences,'' Audiology **11**, 265–270.

Carlile, S. (**1996a**). ''Auditory space,'' in *Virtual Auditory Space: Generation and Applications*, edited by S. Carlile (Landes, Austin).

Carlile, S. (**1996b**). ''The physical and psychophysical basis of sound localization,'' in *Virtual Auditory Space: Generation and Applications*, edited by S. Carlile (Landes, Austin).

Carlile, S., Jin, C., and van Raad, V. (**2000**). ''Continuous virtual auditory space using HRTF interpolation: acoustic and psychophysical errors,'' Proc. IEEE-PCM **1**, 220–223.

Carlile, S. and Leung, J. (**2001**). ''Rendering sound sources in high fidelity virtual auditory space: some spatial sampling and psychophysical factors,'' in Usability Evaluation and Interface Design: Cognitive Engineering, Intelligent Agents and Virtual Reality, edited by M. Smith, G. Salvendy, D. Harris, and R. Koubek (Erlbaum, NJ)

Carlile, S. and Leong, P., and Hyams, S. (**1997**). ''The nature and distribution of errors in sound localization by human listeners,'' Hear. Res. **114**, 179–196.

Chandler, D. W., and Grantham, D. W. (**1992**). ''Minimum audible movement angle as a function of stimulus frequency and bandwidth, source azimuth, and velocity,'' J. Acoust. Soc. Am. **91**(3), 1624–1636.

Finney, D. J. (**1971**). *Probit Analysis* (Cambridge U. P., Cambridge).

Grantham, D. W. (**1984**). ''Discrimination of dynamic interaural intensity differences,'' J. Acoust. Soc. Am. **76**(1), 71–76.

Grantham, D. W. (**1986**). ''Detection and discrimination of simulated motion of auditory targets in the horizontal plane,'' J. Acoust. Soc. Am. **79**(6), 1939–1949.

Grantham, D. W. (**1997**). ''Auditory motion perception: snapshots revisited,'' in *Binaural and Spatial Hearing in Real and Virtual Environments*, edited by R. H. Gilkey and T. R. Anderson (Erlbaum, Mahwah, NJ).

Grantham, D. W., and Wightman, F. L. (**1979**). ''Detectability of a pulsed tone in the presence of a masker with time-varying interaural correlation,'' J. Acoust. Soc. Am. **65**(6), 1509–1517.

Griffiths, T. D., Bench, C. J., and Frackowiak, R. S. J. (**1994**). ''Cortical areas in man selectivity activated by apparent sound movement,'' Curr. Biol. **4**, 892–895.

Griffiths, T. D., Rees, A., Witton, C., Shakir, R. A., Henning, G. B., and Green, G. G. R. (**1996**). ''Evidence for a sound movement area in the human cerebral cortex,'' Nature (London) **383**, 425–427.

Harris, J. D., and Sergeant, R. L. (**1971**). ''Monaural/binaural minimum audible angles for a moving sound source,'' J. Speech Hear. Res. **14**, 618–629.

Kruskal, W. H., and Wallis, W. A. (**1952**). ''Use of ranks in one-criterion variance analysis,'' J. Am. Stat. Assoc. **4**, 583–621.

Kurilowich, R., and Carlile, S. (**1998**). ''Effects of prolonged exposure to moving auditory stimuli,'' Proc. Aust. Neurosci. Soc. **9**, 167.

Lappin, J. S., Bell, H. H., Harm, O. J., and Kottas, B. (**1975**). ''On the relation between time and space in the visual discrimination of velocity,'' J. Exp. Psychol. Hum. Percept. Perform. **1**(4), 383–394.

Leung, J., and Carlile, S. (**2001**). ''The granularity of Virtual Auditory Space and the perception of auditory motion,'' Proc. Aust. Neurosci. Soc. **12**, 215.

Lufti, R. A., and Wang, W. (**1999**). ''Correlational analysis of acoustic cues for the discrimination of auditory motion,'' J. Acoust. Soc. Am. **106**(2), 919–928.

Massey, F. J. (**1951**). ''The distribution of the maximum deviation between two sample cumulative step functions,'' Ann. Math. Stat. **22**, 125–128.

Matthews, N., and Qian, N. (**1999**). ''Axis-of-motion affects direction discrimination, not speed discrimination,'' Vision Res. **39**, 2205–2211.

Middlebrooks, J. C., and Green, D. M. (**1991**). ''Sound localization by human listeners,'' Annu. Rev. Psychol. **42**, 135–159.

Middlebrooks, J. C., and Green, D. M. (**1989**). ''Directional sensitivity of sound-pressure levels in the human ear canal,'' J. Acoust. Soc. Am. **86**(1), 89–108.

Mills, A. W. (**1958**). ''On the minimum audible angle,'' J. Acoust. Soc. Am. **30**, 237–246.

Moller, H., Sorensen, M. F., Hammershoi, D., and Jensen, C. B. (**1995**). ''Head-related transfer functions of human subjects,'' J. Audio Eng. Soc. **43** (5), 300–321.

Perrott, D. R., and Marlborough, K. (**1989**). ''Minimum audible movement angle: Marking the end points of the path traveled by a moving sound source,'' J. Acoust. Soc. Am. **85**(6), 1773–1775.

Perrott, D. R., and Musicant, A. D. (**1977**). ''Minimum audible movement angle: Binaural localization of moving sound sources,'' J. Acoust. Soc. Am. **62**(6), 1463–1466.
Pralong, D., and Carlile, S. (**1996**). ''Generation and validation of Virtual Auditory Space,'' in *Virtual Auditory Space: Generation and Applications*, edited by S. Carlile (Landes, Austin).
Spitzer, M. W., and Semple, M. N. (**1991**). ''Interaural phase coding in auditory midbrain: influence of dynamic stimulus features,'' Science **254**, 721–724.
Spitzer, M. W., and Semple, M. N. (**1993**). ''Responses of inferior colliculus neurons to time-varying interaural phase disparity: effects of shifting the locus of virtual motion,'' J. Neurophysiol. **69**(4), 1245–1263.
Wahba, G. (**1981**). ''Spline interpolation and smoothing on the sphere,'' SIAM (Soc. Ind. Appl. Math.) J. Sci. Stat. Comput. **2**(1), 5–16.
Watamaniuk, S. N. J., and Duchon, A. (**1992**). ''The human visual system averages speed information,'' Vision Res. **32**(5), 931–941.
Waugh, W., Strybel, T. Z., and Perrott, D. R. (**1979**). ''Perception of moving sounds: velocity discrimination,'' J. Aud Res. **19**, 103–110.

Frequency-to-electrode allocation and speech perception with cochlear implants

Colette M. McKay[a] and Katherine R. Henshall
The University of Melbourne, Department of Otolaryngology, Parkville, Australia

(Received 21 May 2001; accepted for publication 23 November 2001)

The hypothesis was investigated that selectively increasing the discrimination of low-frequency information (below 2600 Hz) by altering the frequency-to-electrode allocation would improve speech perception by cochlear implantees. Two experimental conditions were compared, both utilizing ten electrode positions selected based on maximal discrimination. A fixed frequency range (200–10 513 Hz) was allocated either relatively evenly across the ten electrodes, or so that nine of the ten positions were allocated to the frequencies up to 2600 Hz. Two additional conditions utilizing all available electrode positions (15–18 electrodes) were assessed: one with each subject's usual frequency-to-electrode allocation; and the other using the same analysis filters as the other experimental conditions. Seven users of the Nucleus CI22 implant wore processors mapped with each experimental condition for 2-week periods away from the laboratory, followed by assessment of perception of words in quiet and sentences in noise. Performance with both ten-electrode maps was significantly poorer than with both full-electrode maps on at least one measure. Performance with the map allocating nine out of ten electrodes to low frequencies was equivalent to that with the full-electrode maps for vowel perception and sentences in noise, but was worse for consonant perception. Performance with the evenly allocated ten-electrode map was equivalent to that with the full-electrode maps for consonant perception, but worse for vowel perception and sentences in noise. Comparison of the two full-electrode maps showed that subjects could fully adapt to frequency shifts up to ratio changes of 1.3, given 2 weeks' experience. Future research is needed to investigate whether speech perception may be improved by the manipulation of frequency-to-electrode allocation in maps which have a full complement of electrodes in Nucleus implants. [DOI: 10.1121/1.1436073]

PACS numbers: 43.66.Sr, 43.66.Ts, 43.71.Ky [CWT]

I. INTRODUCTION

Cochlear implants now provide a useful aid to communication for a large number of severely to profoundly deaf individuals. Although advances in implant technology have resulted in significant improvements in the ability of implant users to understand speech, there still remains a large variability among implantees, with some achieving nearly perfect scores on open-set speech tests in quiet, and others needing to combine listening with lip reading to understand conversations. A recent report (Henry *et al.*, 2000) showed that the speech perception ability of implantees was correlated to their ability to discriminate adjacent electrodes. Those authors measured the amount of transferred speech information in different frequency regions and correlated this with the subjects' ability to discriminate electrodes (in the presence of random level changes) which were allocated to the same frequency regions. They found that, for frequencies below 2.6 kHz, these two measures were correlated, and that there was, on average, a significant reduction in speech information in this formant-frequency region compared to that perceived by normally hearing listeners. For frequencies above 2.6 kHz, however, the speech information was less reduced than for lower frequencies, and was not correlated with electrode discrimination in that frequency region. If the correlations reflect a causal relationship between electrode discrimination and speech information transfer, it can be hypothesized that speech perception would be improved if discrimination of electrodes allocated to the low-to-mid frequencies was improved. The aim of the present study was to test this hypothesis by altering the allocation of frequencies along the electrode array to provide wider perceptual distances between electrodes coding lower frequencies.

There have been several recent studies which investigated the effects on speech perception of altering the pattern of frequency-to-electrode mapping in multiple-electrode implants. Fu and Shannon (Fu and Shannon, 1999a, 1999b, 1999c) have completed three such studies with three or five users of the Nucleus CI22 implant and the Speak strategy (McDermott *et al.*, 1992; Seligman and McDermott, 1995). In these studies four-electrode maps were tested, either using a CIS strategy (Wilson *et al.*, 1991) with four wide analysis filters allocated to the four electrode positions, or using the Speak strategy with five of the 20 analysis filters allocated to each of the four electrodes. The range of frequencies allocated to each electrode and/or the electrode location was varied and the effects on consonant and vowel perception were measured. In general, the studies showed a significant effect of both frequency range and electrode place. The experiments showed that electrode location was more important for vowel perception than for consonant perception, perhaps indicating that vowel information is more dependent than con-

[a]Electronic mail: colette@unimelb.edu.au

sonant information on the perception and resolution of place-of-stimulation information. The implantees could discriminate vowels best when the frequency-to-electrode allocation was most similar to that in their clinical speech processor map.

The clear deleterious effect on vowel perception seen when the frequency-to-electrode allocation was altered so that it differed from the one used in the clinical map of the patient, made it difficult to assess possible additional effects in the Fu and Shannon studies due to the electrode or analysis-frequency configurations. This deleterious effect is similar to that seen with frequency-shifted speech in normally hearing listeners when the analysis and carrier bands are mismatched in frequency (Shannon *et al.*, 1998; Fu and Shannon, 1999b). It seems likely that cochlear implantees adapt over time to the frequency-to-electrode configuration that is initially fitted in the speech processor, and that if the frequency allocation is subsequently shifted, their perception of speech is degraded. If so, then it is possible that further adaptation to a new frequency-to-electrode configuration could be possible given an appropriate amount of time and experience. The experiments described above did not provide any training before the speech perception testing, and so the results may not accurately predict the longer-term results of any changes in frequency allocation. It is unclear, however, how much experience is necessary to fully adapt to frequency shifts or whether such adaptations are ever complete. Rosen *et al.* (1999) have found that normally hearing subjects significantly improve their perception of shifted-frequency speech even with relatively small amounts of training (a total of 3 h spread over 9 test sessions), thus suggesting that experiments which do not provide any training at all seriously exaggerate the long-term effects of frequency shifts.

Two studies have examined the longer-term effects of changes in frequency-to-electrode allocation in experimental designs in which the subjects used the experimental map at home for periods of time. In both cases, improvements in speech perception were obtained with a shift in frequency allocation. Skinner *et al.* (1995) tested the effect of altering the set of filters from the then-default filter set 9 to filter set 7 with users of the Speak strategy, which extended the low-frequency range of analysis filters and provided an extra one or two filters to the $F1$ formant region of speech (up to 800 Hz). (In the Spectra processor, and later processors for Nucleus implants, there are alternative sets of analysis filters that can be selected by the clinician. These sets of filters are usually referred to as tables, but in this paper they will be referred to as filter sets to avoid confusion. The center frequencies of the filters are shifted by constant ratios from one filter set to the next so that the overall frequency range also differs across filter sets. The filter sets referred to in the present paper are detailed in Table I.) Subjects in their experiment had alternating take-home experience of 2 or 3 weeks with each of the two filter sets before testing. They found that the perception of vowels and nasality in consonants was improved by changing to filter set 7.

Whitford *et al.* (1993) tested the effect, in four users of the MSP(Multipeak) strategy, of changing the frequency allocation so that the higher-frequency analysis filters (3 kHz and above) were allocated to electrodes closer to the characteristic place (in normal hearing) for these frequencies along the cochlea. This had the effect of compressing the overall frequency range onto a smaller electrode set, positioned at the apical end of the array. The patients had alternating take-home experience of 1 week or 2 weeks before each of eight test sessions. This study also found improvements for the experimental maps, even though frequency-to-electrode allocation had been changed from the pattern the subject was used to.

TABLE I. The filter sets used in the Speak processor which are referred to in this paper. These sets are usually referred to as frequency tables. The two numbers refer to the lower and upper frequency boundary of each filter in Hz.

Filter set 7	Filter set 9	Filter set 10	Filter set 11
120–280	150–350	171–400	200–466
280–440	350–550	400–628	466–733
440–600	550–750	628–857	733–1 000
600–760	750–950	857–1085	1000–1 266
760–920	950–1150	1085–1314	1266–1533
920–1080	1150–1350	1314–1542	1533–1800
1080–1240	1350–1550	1542–1771	1800–2066
1240–1414	1550–1768	1771–2020	2066–2357
1414–1624	1768–2013	2020–2321	2357–2708
1624–1866	2013–2333	2321–2666	2708–3110
1866–2144	2333–2680	2666–3062	3110–3573
2144–2463	2680–3079	3062–3518	3573–4105
2463–2856	3079–3571	3518–4081	4105–4761
2856–3347	3571–4184	4081–4781	4761–5578
3347–3922	4184–4903	4781–5603	5578–6537
3922–4595	4903–5744	5603–6564	6537–7658
4595–5384	5744–6730	6564–7691	7658–8973
5384–6308	6730–7885	7691–9011	8973–10 513
6308–7390	7885–9238	9011–10 557	
7390–8658	9238–10 823		

In the present study three experimental maps were tested with take-home experience, all of which differed in frequency-to-electrode allocation from the subjects' own clinical map. These maps used an identical set of 18 analysis filters in filter set 11 (spanning 200 to 10 513 Hz). Two maps which differed only in the frequency-to-electrode allocation pattern were designed using ten electrodes which spanned the electrode array and were optimally spaced perceptually. The effect of expanding the spatial allocation to the low-frequency filters, compared to an even allocation of frequencies across the electrode array, was tested by dividing the 18 filters in two different patterns across the ten electrodes. The third experimental map was a reference map using the same 18 filters and all available electrode positions from each subject's clinical map.

II. PROCEDURES

A. Subjects

Seven users of the Nucleus CI22 implant and the SPEAK strategy participated in the study. Each had a minimum of 3 years' experience with their speech processor. The details of their etiology and implant use are listed in Table II.

TABLE II. Subject details.

Subject	Age	Etiology	Years of profound deafness	Years of implant use	SIT sentence score in quiet (% correct)
S1	74	Infection	23	14	11.7
S2	69	Genetic	30	13	36.3
S3	63	Otosclerosis	21	7	50
S4	44	Otosclerosis	15	7	92.5
S5	62	Otosclerosis	16	11	95
S6	53	Genetic	5	11	67.5
S7	50	Unknown	2	3	62

B. Selection of ten electrodes

As the hypothesis to be tested in this study was based on electrode discriminability, it was important that the electrode positions used in the two 10-electrode experimental maps were optimally discriminable. Therefore, in selecting the ten electrodes for these maps, we did not select every second electrode position (for example), but instead selected them so that the perceptual distances between adjacent electrode positions were maximized.

The result of a multidimensional scaling (MDS) procedure was used to select the ten electrodes. Each stimulus in the MDS procedure was a 250-Hz-rate pulse train of duration 500 ms, presented on one of the active electrodes in the subject's clinical map. The stimuli were loudness balanced at a comfortable loudness before use. All possible pairs of stimuli were presented to the subject, and, after each presentation, the subject rated the dissimilarity of the pair of stimuli along a scale from ''exactly the same'' to ''the most different.'' The position along the scale was converted to a number between 0 and 100. The result of the procedure is a dissimilarity matrix. Two such matrices were obtained for each subject, and were analyzed using repeated-measures nonparametric multidimensional scaling (Kruskal, 1964). The result of such an analysis is a stimulus space in which the distances among the stimulus representations are related to the relative perceptual dissimilarity of the stimuli.

The data were analyzed in a two-dimensional stimulus space, as previous work has shown that the best way of representing this kind of one-dimensional data is in a two-dimensional stimulus space, where the stimuli are usually arranged around a single horseshoe curve (Collins and Throckmorton, 2000; McKay *et al.*, 1996; McKay and Carlyon, 1999). Collins and Throckmorton demonstrated that this horseshoe shape (rather than the expected straight line for one-dimensional data) may be due to subjects' inability to distinguish between different large dissimilarities. Figure 1 illustrates the stimulus space obtained for subject S4. The arrows point to the electrodes chosen for the ten-electrode map for subject S4. The aim was to select a set of stimuli which was relatively evenly spaced perceptually across the electrode array, instead of evenly separated spatially, thus optimizing the discriminability of the electrode set. Any electrodes which were not tonotopically ordered in the array (for example, electrode 6 for subject S4) were also avoided in the selection. The electrode positions selected for each subject's ten-electrode experimental maps are listed in Table III.

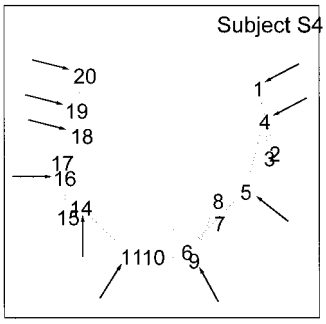

FIG. 1. The stimulus space for subject S4 which resulted from the multidimensional scaling procedure. Each number represents a stimulus on the corresponding electrode. The arrows point to the ten electrodes chosen for S4's 10-electrode experimental maps. Note that electrodes 2, 3, and 6 are not in the correct tonotopic position for this subject, and electrodes 12 and 13 are not used in his clinic map.

C. Experimental maps and speech perception tests

Four maps were compared in the speech perception experiment: the subject's own clinical map, and three experimental maps. The details of these four maps for each subject are summarized in Table III. The subjects' clinical maps usually utilized filter set 9 (except S6 and S7; see Table III). As is the usual practice in clinic maps, the number of filters used matched the number of electrodes, so that one or more of the highest-frequency filters were not used when there were less than 20 active electrodes. The highest frequency boundary was greater than 5384 Hz in all clinic maps.

The three experimental maps all utilized the same (complete) set of analysis filters for each subject. Filter set 11 was selected (except for S6; see below) because there are nine filters available in the frequency region below 2708 Hz, and the goal was to allocate this frequency region to nine out of the ten electrodes (with one filter per electrode) in the low-frequency allocation ten-electrode map. In this map, the remaining nine filters (covering the range 2708–10 513 Hz) were all allocated to the most basal of the ten selected electrodes. The even-allocation ten-electrode map distributed the 18 filters of filter set 11 across the same ten electrodes using two filters per electrode except for the first- and sixth-most apical of the ten electrodes, each of which had a single filter allocated. The reference map utilized the same full-electrode set as each subject's clinic map, but utilized all the filters from frequency filter set 11. For subjects who had fewer than 18 active electrodes in their clinic map (see Table III), one filter was allocated for each electrode in the reference map up to the most-basal electrode, which was allocated all remaining high-frequency filters (between one and three filters depending on the subject). Thus, the reference and clinic map differed mostly in the filter set used, corresponding to a constant ratio shift of frequency allocation.

For subject S6, the first 18 filters of filter set 9 (150–7885 Hz) were used in the three experimental maps. This subject used filter set 7 in her clinic map, and found the shift to filter set 11 too great to tolerate when wearing the experimental maps away from the laboratory. The pattern of filter allocation was changed slightly in her even-allocation ten-electrode map, so that the fifth- and tenth- (instead of first-

TABLE III. Map details for each subject. The distribution of filters across the electrode positions is described in the text. The electrode numbers refer to the most-basal member of a bipolar (BP) pair (where electrodes are numbered basal-to-apical), or the active electrode in common-ground mode (CG).

Subject	Map	Active electrodes	Frequency set	Mode
S1	Clinic & reference	1 2 3 4 5 6 7 8 9 10 11 12 13 14 15 16 17 18	9 & 11	BP+2
	10-electrode maps	1 2 8 9 11 12 13 14 16 18	11	
S2	Clinic & reference	4 5 6 7 8 9 10 11 12 14 15 16 17 18 19 20	9 & 11	BP+1
	10-electrode maps	10 11 12 14 15 16 17 18 19 20	11	
S3	Clinic & reference	1 2 3 4 5 6 7 8 9 10 11 12 13 14 15 16 20	9 & 11	Mixed
	10-electrode maps	3 5 6 8 9 10 11 12 13 20	11	Bipolar
S4	Clinic & reference	1 2 3 4 5 6 7 8 9 10 11 14 15 16 17 18 19 20	9 & 11	BP+1
	10-electrode maps	1 4 5 9 11 14 16 18 19 20	11	
S5	Clinic & reference	1 2 4 5 6 7 8 9 10 11 12 13 15 16 17 20 22	9 & 11	CG
	10-electrode maps	2 4 7 8 9 11 13 15 20 22	11	
S6	Clinic & reference	1 2 3 4 5 6 7 8 9 10 11 12 13 14 15 16 17	7 & 9	BP+3
	10-electrode maps	4 6 7 9 10 11 13 14 15 16	9	
S7	Clinic & reference	6 7 8 9 10 11 12 13 14 15 16 17 18 19 20	10 & 11	BP+1
	10-electrode maps	7 8 9 10 14 15 16 17 18 20	11	

and sixth-) most apical electrodes were allocated a single filter rather than a pair of filters. This change made the even-frequency allocation closer to that for the other subjects. It should also be noted that the first nine filters of filter set 9 cover a frequency range up to 2013 Hz rather than 2708 Hz, so that, in comparison to other subjects, a portion of vowel formant information (between 2013 and 2708 Hz) was included in the high-frequency allocation to the single basal electrode in the low-frequency allocation ten-electrode map for this subject.

Speech perception data with each subject's clinical map were collected at the start of the study, and again at the end of the study (following a further 2-weeks experience with the clinical map). The subjects used each of the three experimental maps at home for periods of 2 weeks over a 14-week period, and their speech perception was tested with each map in a test session at the end of the corresponding 2-week period. The order of testing of the three maps was arranged so that learning effects were minimized. The experience/test periods followed an ABCACBA pattern, where A, B, and C were periods with the reference map, the low-frequency allocation ten-electrode map, and the even-allocation ten-electrode map, respectively. An additional period with the reference map (A) was inserted into the center of the experimental period to avoid having two adjoining periods with the even-frequency allocation (C). A total of four repeated measures of two speech perception assessments (see below) was obtained with each map, two in each of two test sessions for all maps except the reference map. Since there were three test sessions with the reference map, two measures were obtained in the middle session, and one in each of the first and last sessions.

Recordings of the Consonant–Nucleus–Consonant (CNC) word test and the SIT sentence test (Magner, 1972) were used to assess speech perception. The CNC word lists comprise 50 lists of 50 words each, each list containing a similar phoneme set as the original lists of Peterson and Lehiste (1962), but adapted for Australian usage. The SIT sentences are 40 lists of 15 sentences each. Both sets of speech material used a single (but different) female speaker. All speech materials were presented at an average level of 70 dB SPL. The sensitivity of the subject's speech processor was held constant throughout the experiment. In each test session, two CNC word lists were presented in quiet.

During each subject's first test session (with the clinic map), a list of SIT sentences was presented in quiet. These sentence scores are listed in Table II. Subjects whose score was less than 50% (S1 and S2) were tested using two lists of SIT sentences in quiet in this and all subsequent test sessions. For the remaining subjects (who scored greater than or equal to 50% in quiet), an adaptive task in noise was performed, whereby the noise level was adapted until the score converged on a value 70% of the individual subject's score in quiet. The adaptive procedure was based on a method described by Levitt (1970). The speech stimulus was set so the average (fast) meter reading for keywords in the sentences was 70 dB SPL. The first sentence was presented in speech-shaped masking noise at a signal-to-noise ratio of 21 dB. The percentage of words correctly identified for that sentence was calculated and compared to the target score (70% of the score in quiet). When the score in noise was lower than the target score, the noise level was reduced, and when it was higher, the noise level was increased, and the process repeated for each subsequent sentence. For example, subject S7 obtained 62% correct in quiet; therefore, her target score was 43.4% (i.e., 70% of 62), and the noise was adjusted up or down after each sentence depending on whether the score for that sentence was greater or smaller than 43.4%. The step sizes for the noise level were 5 dB until two level reversals were recorded, and 3 dB until a further six reversals were recorded. The signal-to-noise ratios at the last six turning points were averaged. For the purposes of this test, the sentence lists were concatenated (in random order) to allow the procedure to run smoothly regardless of the number of sentences needed to reach the criterion number of turning points.

All speech test data were analyzed with repeated-measures two-way analysis of variance (ANOVA), with subject and map as factors. Significant map effects were further investigated with *post hoc* Tukey tests with a family error

rate of 0.05. For analysis of individual subject data, repeated measures one-way ANOVA with *post hoc* Tukey tests were used.

III. RESULTS

Figure 2 shows the results of the CNC word test (means and standard deviations of initial and final consonants and vowels) with the clinic map and the three experimental maps for each subject, and the mean results for all seven subjects. The CNC scores were divided into vowels and consonants for analysis, since the test hypothesis predicted differential effects of the experimental maps on vowel and consonant perception, and initial data inspection confirmed this possibility. Statistically significant effects of map are marked with an asterisk for individual or mean scores. It can be seen that the difference in mean scores with the four different maps is generally very small and there is a large degree of subject variability.

Data analysis showed a significant effect of map on the vowel scores ($p<0.001$) with the even-allocation ten-electrode map producing reduced scores compared to all other maps. There was a highly significant subject/map interaction ($p<0.001$). Analysis of the initial consonant scores revealed no significant effect of map ($p=0.09$), but a mildly significant subject/map interaction ($p=0.01$). Analysis of the final consonant scores showed a highly significant map effect ($p<0.001$) with the low-frequency allocation ten-electrode map producing scores significantly poorer than the two full-electrode maps, although not significantly different from the even-allocation ten-electrode map. Once again, there was a significant subject/map interaction ($p=0.001$). In summary, the results showed that, in general, vowel perception was degraded in the even-allocation ten-electrode map, and consonant perception was degraded in the low-frequency allocation ten-electrode map compared to the full-electrode maps, but the effects were not consistent across all subjects.

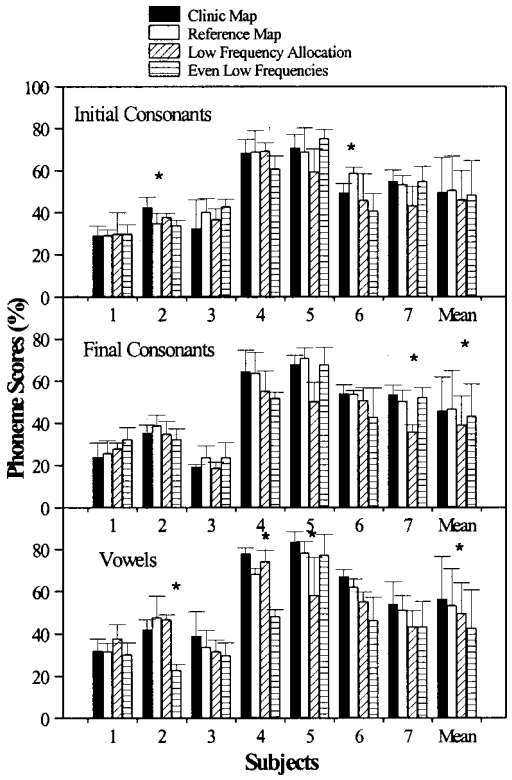

FIG. 2. The results of the CNC word test for the four maps for each subject. The scores for initial and final consonants and vowels are separated into the three panels. Error bars denote standard deviations. Asterisks denote conditions where there were significant map differences for individual subjects or group data.

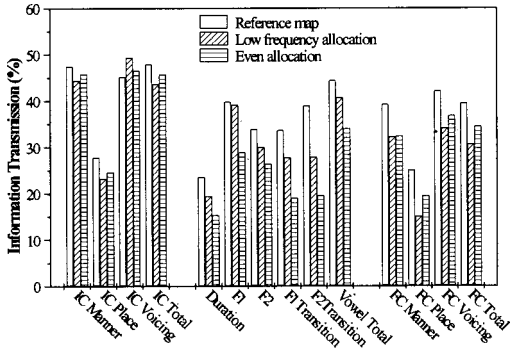

FIG. 3. The results of information transmission analysis for vowel and consonant features in the CNC word test in quiet. The data for the seven subjects were combined in this analysis.

These differential effects of the two 10-electrode maps on vowel and consonant perception are further illustrated by analysis of the scores as percentage of phonemes correct. In this case, both ten-electrode maps [means and standard errors of 44.2 (5.0) and 43.9 (6.1) for low-frequency and even allocations, respectively] produced significantly lower scores than both full-electrode maps [49.4 (6.5) and 50.4 (6.9) for reference and clinical maps, respectively] with the pair of ten-electrode maps and the pair of full-electrode maps not being significantly different.

The phoneme confusions in the responses of the subjects to the CNC word tests were analyzed using information transmission analysis (Miller and Nicely, 1995). The phoneme feature categories used in this analysis were as follows: consonant voicing (yes or no), consonant place of articulation (seven categories), consonant manner of articulation (five categories), vowel duration (short or long), first formant frequency and second formant frequency (low, mid, or high within each formant range), and the first and second formant changes that define diphthongs or steady vowels (rising, falling, or steady for each formant). The responses for all subjects were combined in this analysis, the results of which are shown in Fig. 3. In view of the nonsignificant differences between the clinic and reference maps found above, only the reference map and the two 10-electrode maps were included (all of which used the same set of analysis filters). There are two general observations which can be made about these data. First, when comparing the two frequency allocations with ten electrodes, there is less final-consonant information (mostly attributed to reduced place-of-articulation information) transmitted by the low-frequency allocation map compared to the even-frequency allocation map. Conversely, there was less vowel formant information transmitted (particularly $F1$ information and formant transition information) within the even-frequency allocation map compared to the

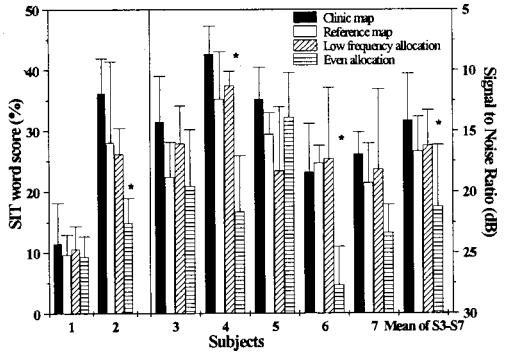

FIG. 4. The results of the SIT sentence test. Two subjects performed this test in quiet, and their % correct scores are shown in the left panel. The remaining subjects performed an adaptive test in noise, and the signal-to-noise ratios which resulted in the reduction of their scores to 70% of the corresponding values in quiet are plotted. The error bars denote standard deviations.

low-frequency allocation map. Second, when comparing the full-electrode reference map to the ten-electrode maps, it appears that final consonant information (but not initial consonant information) is degraded by having ten rather than more electrodes, and that vowel information is severely degraded in those conditions having fewer than nine electrodes allocated to the formant regions.

The results of the SIT sentence test with the clinic map and the three experimental maps are shown for each subject in Fig. 4. Subjects S1 and S2 performed this test in quiet (left panel of the figure). Their individual results were consistent with their corresponding results for CNC words. Subject S1 showed no significant effects of map on either test. Subject S2 scored the most poorly with the even-allocation ten-electrode map in both cases. The results for the group of five subjects who completed the adaptive test in noise (right panel in Fig. 4) showed a significant map effect ($p < 0.001$), with the even-allocation map producing poorer results (greater signal-to-noise ratio) compared to the low-frequency allocation ten-electrode map and both the full-electrode maps. The results for these last three maps were not significantly different. As with the CNC scores, there was a significant subject/map interaction ($p = 0.015$).

In summary, the reference and clinical maps (both using all the active electrodes) did not lead to different speech perception ability in quiet or in noise. In comparing the results for the two 10-electrode maps, it is clear that, in quiet, the two ways of allocating filters to the electrode positions affected speech perception in different ways for vowels and consonants, and the effect was not uniform across subjects. In background noise there was a group advantage for the low-frequency allocation ten-electrode map over the even-allocation map, with no individual performing significantly better with the even-allocation map.

IV. DISCUSSION

A. Effect of change in filter set

The data for the two full-electrode maps showed no effect of the shift in frequencies between the two filter sets used (see Table III). When moving between filter sets all electrode positions experience the same ratio change of frequency allocation. Thus, in this experiment all subjects experienced a shift to higher frequencies in the reference map compared to their clinical map (ranging from a constant ratio increase of 1.33 for those using filter set 9 clinically, to 1.25 for subject S6 and 1.16 for subject S7). A side effect of this shift is that the range of frequencies is restricted at the low-frequency end, with some low frequencies (150–200 Hz for those changing from filter set 9 to filter set 11) no longer represented in the output of the processor, and fewer electrodes are allocated to the $F1$ formant range.

The results of the present experiment, together with those of Skinner *et al.* (1995) and Whitford *et al.* (1993) suggest that implantees can, given listening experience, adapt to a shift up or down in frequency from the frequency allocation in their normal map. In the Skinner *et al.* study and the present study, the shift in frequency allocation was only moderate (ratio changes up to 1.33). It is possible that greater shifts in frequency allocation may be more difficult to adapt to. For example, subject S6 would not tolerate the shift from filter set 7 to filter set 11 (ratio of 1.66) for this experiment, although it is not known whether she would have adapted to this larger shift given experience.

B. Effect of frequency-allocation pattern

The two 10-electrode maps in our experiment differed only in the pattern of allocation of the filters across electrode positions (factors such as number of electrodes and frequency analysis range did not differ in these two conditions). A comparison of these two conditions tests the hypothesis that increasing the discriminability of low-frequency information (at the expense in this case of discriminability of high-frequency information) will improve the speech perception of implantees. The low-frequency allocation map represents the extreme case, in which all but one electrode are devoted to frequencies in the range of the first and second formants, and only one electrode position represents the remaining high frequencies. Our hypothesis was that the reduction of information derived from the high frequencies would be offset by a larger improvement in information from the low frequencies. Our rationale for this hypothesis was based on the proposition that frequency resolution is important in the low frequencies but less important in the high frequencies.

The comparison of results with the two 10-electrode maps only partially supported this hypothesis. It is clear that, in general, the allocation of low frequencies to all but one electrode improved the perception of vowel information and degraded the perception of consonant information as expected from the hypothesis. This was supported by information transmission analysis, with vowel formant perception being improved by spreading out the low frequencies over a greater cochlear extent, and consonant perception only marginally degraded by allocating all frequencies above 2600 Hz to a single electrode position. However, the balance of these two effects when listening to words in quiet did not consistently favor the low-frequency allocation. When listening to sentences in noise there was a more consistent advantage for the low-frequency allocation.

TABLE IV. The ratio of frequency shift from the clinic map for electrodes allocated to three frequencies in the two 10-electrode maps for each subject. The maps which produced significantly better performance for individuals in the CNC word test are marked in bold. Note that for S6, three slightly different frequencies were used for the calculations (642, 1447, and 2177 Hz).

Subject/Map	584-Hz position	1393-Hz position	2207-Hz position
S1 low-frequency map	0.91	0.96	0.88
even map	0.91	1.33	1.54
S2 **low-frequency map**	**1.33**	**1.33**	**1.33**
even map	1.33	2.17	2.13
S3 low-frequency map	0.56	0.84	0.77
even map	0.56	0.96	1.33
S4 **low-frequency map**	**1.33**	**0.96**	**0.57**
even map	1.33	2.17	1.54
S5 low-frequency map	1.33	0.84	0.77
even map	**1.33**	**1.33**	**1.33**
S6 **low-frequency map**	**0.95**	**0.95**	**0.70**
even map	1.25	1.72	1.64
S7 low-frequency map	0.79	0.98	0.67
even map	**0.79**	**1.45**	**1.56**

One feature of the data is that the map changes had a different pattern of effects for different subjects (as shown by the significant subject/map interactions). An obvious potential source of this variability is the individual degree of frequency shift of the experimental maps from the clinically used frequency allocation. Perhaps some subjects had more difficulty than others in adapting to the frequency shifts. This possibility is made less likely by the fact that no significant degradation was observed for any subject when going from the clinic map to the reference map. In the ten-electrode maps, however, some of the frequency shifts were greater than that between the reference and clinic maps, and the frequency shifts also varied in degree across electrode positions.

To test the hypothesis that subjects were merely performing better with whichever ten-electrode map minimized the frequency shift from their clinical map, the amount of frequency shift was calculated at three representative electrode positions for each map and subject. The electrode positions were chosen to evenly sample those electrodes allocated to the vowel formant frequencies in each experimental map. The results of the calculations are shown in Table IV. It can be seen from the table that the ten-electrode map which resulted in significantly higher scores in quiet (marked in bold) for each subject was not consistently the one in which the frequency shift was less, or more constant across electrode position. It is unlikely, therefore, that the subject/map interaction found in the experimental results is due to subject differences in the pattern of frequency allocation shift in the two experimental maps.

An alternative source of the subject/map interaction may be that subjects differ in the relative importance of frequency resolution in the low- and high-frequency regions of the speech signal. That is, subjects may differ in which cues they attend to in order to discriminate consonants. For example, cues for place of articulation can be provided by the formant frequencies either in the consonant itself (semivowels, glides, and nasals) or in the surrounding vowels (i.e., the transitions caused by coarticulation), but can also be provided by the spectral shape of the high-frequency noise associated with consonant production (except for the vowel-like consonants mentioned above). Thus, the ten-electrode low-frequency allocation map has the potential to either improve or degrade place-of-articulation perception compared to the ten-electrode even-frequency allocation map, depending on whether implantees are attending more to spectral cues in the formant regions or in the high-frequency region.

It is interesting to note that the two subjects (S1 and S3) who did not show any significant effects of map on any speech test were also subjects with poor speech perception. This result perhaps indicates that these two subjects did not gain as much information from the spectral content of the speech signal (compared to amplitude envelope cues) as the other subjects, and hence the adjustment of frequency-to-electrode allocation did not have a large effect on them. In summary, the results with the two 10-electrode maps suggest that using more electrodes (nine compared to five in these experimental maps) to represent the vowel formant frequency region (up to 2600 Hz) can lead to improved vowel perception, and improved perception of speech in the presence of background noise. However, the restriction of high-frequency information to a single electrode position may cause a deterioration in consonant perception which can outweigh any corresponding benefit of increased low-frequency resolution when listening in quiet.

C. Effect of number of electrodes

In this study ten-electrode maps were used in order to be able to create alternative frequency-allocation patterns for the same set of analysis filters. The results of the study, however, do provide further information related to the question of how many electrodes or analysis filters are required to reach optimal performance with a cochlear implant. Previous research which has addressed this question can be divided into two broad categories: simulation experiments with normally hearing listeners, and speech perception experiments with cochlear implantees.

Simulation experiments using amplitude-modulated noise bands and normally hearing listeners show a rapid improvement of speech perception with increasing number of bands up to about 4–6 bands (Shannon *et al.*, 1995), with further increases up to at least eight bands when listening to more-difficult speech material (Loizou *et al.*, 1999), and up to at least 20 bands when listening in background noise (Dorman *et al.*, 1998; Fu *et al.*, 1998; Friesen *et al.*, 2001). Experiments with implantees have generally been consistent with the findings of experiments using normally hearing listeners, if the additional and subject-dependent perceptual difficulty in resolving the features of the electrically represented spectral shape is considered. For example, Fishman *et al.* (1997) showed no average improvement in perception of speech in quiet with increases in electrode numbers over seven. Zeng and Galvin (1999) investigated, with four implantees, the interaction of number of electrodes used in the Speak strategy with perception of vowels and consonants in different signal-to-noise ratios, and found that ten or 20 elec-

trodes were significantly better than four in all conditions. Friesen *et al.* (2001) measured the perception of vowels, consonants, words, and sentences in various signal-to-noise conditions and numbers of electrodes (without listening experience). For Speak users (who had up to 20 active electrodes), there was no average improvement in vowel and consonant perception above seven electrodes, and for words and sentences above ten electrodes.

The present experiment differs from all the above experiments in that the electrodes were selected in the reduced-electrode map to optimize their discriminability, rather than being selected on a spatial distribution criterion. Also, take-home experience was provided with the reduced-electrode maps, which should have reduced any impact of lack of adaptation to frequency shifts in the new maps. These factors should theoretically have provided an advantage for the ten-electrode maps in the present study. However, our group results for both types of speech test are consistent in showing that an even allocation of the 18 filters across ten (maximally discriminable) electrode positions leads to poorer vowel perception in quiet and sentence perception in noise than the full-electrode maps (with numbers of electrodes from 15 to 18).

There are three potential reasons for the significant result in this experiment in spite of nonsignificant results for more than ten electrodes in the previous experiments. First, the ''perceptually even'' method of selecting the 10 electrodes may have produced poorer speech perception than a 'spatially even' method. Second, our experimental procedures involved multiple test sessions for each condition, as well as test procedures which avoided ceiling and floor effects, thus leading to greater statistical power, and allowing small effects on speech perception to be statistically significant. Third, is it quite probable that the benefit of greater number of electrode positions is dependent on each subject's ability to perceptually resolve the stimulation on different electrode positions. Since each study used only a small number of subjects, this variability can be reflected in variability of test outcome.

The results of this experiment indicate that the question regarding ''optimal number of electrodes'' cannot be asked in isolation. The answer may depend both on how the range of frequencies is distributed across the electrode positions, and on how the electrodes are distributed along the cochlea. In this experiment, ten optimally discriminable electrode positions produced a significantly poorer result than 15–18 electrode positions. There was also evidence that the optimal number of electrodes may differ for high-and low-frequency regions. The low-frequency allocation ten-electrode map had the same number of electrode positions (nine) allocated to the vowel formant region as the full-electrode reference map. Subjects with this map could perceive vowels and understand speech in noise at level equivalent to their reference map performance, whereas with five electrodes (in the even-allocation map) their perception of these speech features was degraded. Conversely, for consonant perception, five electrodes allocated to high frequencies (in the even-allocation ten-electrode map) provided equivalent performance to nine electrodes in the reference map, and better performance than one electrode (in the low-frequency allocation map). Thus, the optimal number of electrode positions may be quite different for the low-and high-frequency regions, with a larger number of electrodes required in the low-frequency region than in the high-frequency region for optimal perception.

The results of this experiment shed some further light on the results of Henry *et al.* (2000), in which perceived speech information for Speak users (with 16 electrode positions) was highly correlated with adjacent-electrode discrimination for the 11 electrodes (using filter set 9) allocated to the vowel-formant region. If these subjects had only a few (3 or 4) ''perceptual'' channels in this low-frequency region, then it is hard to see why the discrimination of adjacent electrodes would be highly correlated with speech perception scores. On the other hand, the present experiment demonstrates that a larger number of electrodes for the low-frequency region may be beneficial for speech perception, provided they are discriminable. Further research is required using maps with more than a total of ten electrodes, to see if altering the frequency-to-electrode allocation to improve low-frequency resolution has a beneficial effect on speech perception.

V. CONCLUSIONS

This study has investigated the effect of changes to the frequency-to-electrode allocation in speech processor maps for users of the Speak strategy. The main conclusions are

(1) Subjects can fully adapt to a mild constant-ratio shift in frequency allocation (up to a ratio change of 1.3) given 2 weeks of experience with the altered map.
(2) When 18 filters are allocated in two different ways across the same ten electrodes (which have been selected to maximize their discriminability), there is a significant but subject-dependent effect on speech perception ability in most subjects. When listening in noise, there is generally a significant advantage for the low-frequency range (up to 2.6 kHz) to be allocated across the nine instead of five of electrodes. In quiet, vowel information is generally improved and consonant information degraded by the allocation of the low-frequency information to nine rather than five electrodes, and allocation of high-frequency information to one rather than five electrodes.
(3) The optimal number of electrodes for speech perception may differ for high-and low-frequency information. In this study, nine electrodes were better than five for the perception of information below 2.6 kHz, and five electrodes were better than one and equivalent to nine for perception of frequencies above 2.6 kHz.

In the present experiment the number of electrodes was restricted, and multiple filters assigned to each electrode, in order to be able to manipulate the pattern of frequency allocation. Thus, the experimental maps did not represent clinically useful conditions. In addition, subjects with neither experimental map were able to exceed their performance with their clinical map. The results of this experiment indicate, however, that it may be useful to investigate of the effects of electrode discriminability and distribution of analysis filter

bandwidths using the full electrode array in the Nucleus implants (20 electrode positions), to see if speech perception can be improved from that with the clinical maps. Current commercially available speech processors for the Nucleus implants do not provide the flexibility in design of individual filter bandwidths which would be required to do this research.

ACKNOWLEDGMENTS

This research was supported by the Garnett Passe and Rodney Williams Memorial Foundation, and by the Australian National Health and Medical Research Council. The authors wish to thank Dr. Hugh McDermott for useful discussions about the research and manuscript, Stuart Rosen, Chris Turner, and an anonymous reviewer for helpful comments on previous versions of the manuscript, and all the cochlear implantees who gave their time to participate in this research.

Collins, L. M., and Throckmorton, C. S. (**2000**). ''Investigating perceptual features of electrode stimulation via a multidimensional scaling paradigm,'' J. Acoust. Soc. Am. **108**, 2353–2365.

Dorman, M. F., Loizou, P. C., Fitzke, J., and Tu, Z. (**1998**). ''The recognition of sentences in noise by normal-hearing listeners using simulations of cochlear-implant signal processors with 6–20 channels,'' J. Acoust. Soc. Am. **104**, 3583–3585.

Fishman, K. E., Shannon, R. V., and Slattery, W. H. (**1997**). ''Speech recognition as a function of the number of electrodes used in the SPEAK cochlear implant speech processor,'' J. Speech Hear. Res. **40**, 1201–1215.

Friesen, L. M., Shannon, R. V., Baskent, D., and Wang, X. (**2001**). ''Speech recognition in noise as a function of the number of spectral channels: Comparison of acoustic hearing and cochlear implants,'' J. Acoust. Soc. Am. **110**, 1150–1163.

Fu, Q. J., Shannon, R. V., and Wang, X. S. (**1998**). ''Effects of noise and spectral resolution on vowel and consonant recognition: Acoustic and electric hearing,'' J. Acoust. Soc. Am. **104**, 3586–3596.

Fu, Q. J., and Shannon, R. V. (**1999a**). ''Effects of electrode location and spacing on phoneme recognition with the Nucleus-22 cochlear implant,'' Ear Hear. **20**, 321–331.

Fu, Q. J., and Shannon, R. V. (**1999b**). ''Recognition of spectrally degraded and frequency-shifted vowels in acoustic and electric hearing,'' J. Acoust. Soc. Am. **105**, 1889–1900.

Fu, Q.-J., and Shannon, R. V. (**1999c**). ''Effects of electrode configuration and frequency allocation on vowel recognition with the Nucleus-22 cochlear implant,'' Ear Hear. **20**, 332–344.

Henry, B. A., McKay, C. M., McDermott, H. J., and Clark, G. M. (**2000**). ''The relationship between speech perception and electrode discrimination in cochlear implantees,'' J. Acoust. Soc. Am. **108**, 1269–1280.

Kruskal, J. B. (**1964**). ''Nonmetric multidimensional scaling: A numerical method,'' Psychometrika **29**, 115–129.

Levitt, H. (**1970**). ''Transformed up–down methods in psychoacoustics,'' J. Acoust. Soc. Am. **49**, 467–477.

Loizou, P. C., Dorman, M., and Tu, Z. (**1999**). ''On the number of channels needed to understand speech,'' J. Acoust. Soc. Am. **106**, 2097–2103.

Magner, M. E. (**1972**). *A Speech Intellibility Test for Deaf Children* (Clarke School for the Deaf, Northampton, MA).

McDermott, H. J., McKay, C. M., and Vandali, A. E. (**1992**). ''A new portable sound processor for the University of Melbourne/Nucleus Limited multielectrode cochlear implant,'' J. Acoust. Soc. Am. **91**, 3367–3371.

McKay, C. M., and Carlyon, R. P. (**1999**). ''Dual temporal pitch percepts from acoustic and electric amplitude-modulated pulse trains,'' J. Acoust. Soc. Am. **105**, 347–357.

McKay, C. M., McDermott, H. J., and Clark, G. M. (**1996**). ''The perceptual dimensions of single-electrode and nonsimultaneous dual-electrode stimuli in cochlear implantees,'' J. Acoust. Soc. Am. **99**, 1079–1090.

Miller, G. A., and Nicely, P. E. (**1955**). ''An analysis of perceptual confusions among some English consonants,'' J. Acoust. Soc. Am. **27**, 301–315.

Peterson, G., and Lehiste, I. (**1962**). ''Revised CNC lists for auditory tests,'' J. Speech Hear Disord. **27**, 62–70.

Rosen, S., Faulkner, A., and Wilkinson, L. (**1999**). ''Adaptation by normal listeners to upward spectral shifts of speech: Implications for cochlear implants,'' J. Acoust. Soc. Am. **106**, 3629–3636.

Seligman, P., and McDermott, H. (**1995**). ''Architecture of the Spectra 22 speech processor,'' Ann. Otol. Rhinol. Laryngol. Suppl. 166 **104**, 139–141.

Shannon, R. V., Zeng, F. G., Kamath, V., Wygonski, J., and Ekelid, M. (**1995**). ''Speech recognition with primarily temporal cues,'' Science **270**, 303–304.

Shannon, R. V., Zeng, F.-G., and Wygonski, J. (**1998**). ''Speech recognition with altered spectral distribution of envelope cues,'' J. Acoust. Soc. Am. **104**, 2467–2476.

Skinner, M. W., Holden, L. K., and Holden, T. A. (**1995**). ''Effect of frequency boundary assignment on speech recognition with the SPEAK speech-coding strategy,'' Ann. Otol. Rhinol. Laryngol. Suppl. 16 **104**, 307–311.

Whitford, L. A., Seligman, P. M., Blamey, P. J., McDermott, H. J., and Patrick, J. F. (**1993**). ''Comparison of current speech coding strategies,'' Adv. Oto-Rhino-Laryngol. **48**, 85–90.

Wilson, B. S., Finley, C. C., Lawson, D. T., Wolford, R. D., Eddington, D. K., and Rabinowitz, W. M. (**1991**). ''Better speech recognition with cochlear implants,'' Nature (London) **352**, 236–238.

Zeng, F. G., and Galvin III, J. J. (**1999**). ''Amplitude mapping and phoneme recognition in cochlear implant listeners,'' Ear Hear. **20**, 60–74.

On the influence of laryngeal pathologies on acoustic and electroglottographic jitter measures[a)]

Maurílio N. Vieira[b)]
Departamento de Física/ICEx, Universidade Federal de Minas Gerais, CP 702, CEP 30.161-970, Belo Horizonte, Minas Gerais, Brazil

Fergus R. McInnes and Mervyn A. Jack
Centre for Communication Interface Research, Department of Electronics and Electrical Engineering, University of Edinburgh, 80 South Bridge, Edinburgh EH1 1HN, Scotland, United Kingdom

(Received 18 April 2001; accepted for publication 29 October 2001)

This study compared acoustic and electroglottographic (EGG) jitter from [a] vowels of 103 dysphonic speakers. The EGG recordings were chosen according to their intensity, signal-to-noise ratio, and percentage of unvoiced intervals, while acoustic signals were selected based on voicing detection and the reliability of jitter extraction. The agreement between jitter measures was expressed numerically as a normalized difference. In 63.1% (65/103) of the cases the differences fell within ±22.5%. Positive differences above +22.5% were associated with increased acoustic jitter and occurred in 12.6% (13/103) of the speakers. These were, typically, cases of small nodular lesions without problems in the posterior larynx. On the other hand, substantial rises in EGG jitter leading to differences below −22.5% took place in 24.3% (25/103) of the speakers and were related to hyperfunctional voices, creaky-like voices, small laryngeal asymmetries affecting the arytenoids, or small-to-moderate glottal chinks. A clinically relevant outcome of the study was the possibility of detecting gentle laryngeal asymmetries among cases of large unilateral increase in EGG jitter. These asymmetries can be linked with vocal problems that are often overlooked in endoscopic examinations. [DOI: 10.1121/1.1430686]

PACS numbers: 43.70.Dn, 43.70.Aj, 43.70.Jt [AL]

I. INTRODUCTION

Automated measures from acoustic and electroglottographic (EGG) signals have been increasingly used in the clinical assessment of voice disorders. Perturbation measures such as jitter (cycle-to-cycle fundamental frequency perturbation), shimmer (cycle-to-cycle amplitude perturbation), or harmonics-to-noise ratio can aid in the evaluation of laryngeal pathologies, but care should be taken because there are various sources of measurement error and intrasubject variability. Acoustic measures can be corrupted by microphone type and positioning, recording equipment, fundamental-frequency (F_0) demarcation algorithm, or vowel type (see the summary in Titze, 1995), while EGG signals are sensitive to electrode placement, changes in laryngeal height, or head movements during phonation (e.g., Colton and Conture, 1990). Moreover, the occurrence of perturbations and their respective levels of severity are episodic. Intrasubject measures can vary during the course of the day or week (Hall, 1995; Bough *et al.*, 1996), can depend on vocal-fold hydration condition (Verdolini-Martson *et al.*, 1994; Hemler *et al.*, 1997), hormonal changes (Hirson and Roe, 1993), etc. The pathology can also give rise to different temporal perturbation patterns. For example, dysphonias related to gastroesophageal reflux tend to be more severe early in the morning (Sataloff, 1991; p. 180), whereas vocal disturbances associated with nodules can increase towards the end of the day after vocal demand, although not all measures will necessarily reveal this trend (Hall, 1995). Having these sources of variability in mind, it cannot be expected, *a priori*, that any single measure will be representative of the dysphonic voice. Utterances such as sustained vowels, glides of pitch, loudness, or register (Titze, 1995; Robinson, 1993), should be viewed as vocal tasks to probe the laryngeal dynamics.

Vowels prolonged with ''comfortable levels of pitch and loudness'' are attractive from the clinical point of view because they are easy to collect. In the authors' experience, long sustained vowels have favored the occurrence of abnormalities (e.g., increased cycle-to-cycle perturbations, involuntary register changes, voicing interruption, vocal tremor, bifurcations) that seem to relate to poor respiratory-phonatory control and usually do not occur in short vowels. It should be noted that ''comfortable levels'' imply a lack of control in vocal parameters, particularly fundamental frequency and intensity, which can also affect perturbation measures (Orlikoff and Kahane, 1991; Gelfer, 1995). However, in clinical practice, rigorous control of the vocal emission seems unrealistic because many pathologies limit the patient's ability to control fundamental frequency (e.g., Reinke's edema), intensity (e.g., hypofunctional dysphonia), and even vocal register (e.g., mutational dysphonia). Besides, the change of such vocal features can be the goal of treatment (see the related discussion in Bless and Baken, 1992; p. 203).

This paper investigates the discrepancies between acous-

[a)]An earlier version of this paper was presented in ''Detecting arytenoid cartilage misplacement through acoustic and electroglottographic jitter analysis,'' Proceedings of the 4th International Conference on Spoken Language Processing (ICSLP 96), Philadelphia, PA, October 1996.

[b)]Electronic mail: maurilio@fisica.ufmg.br

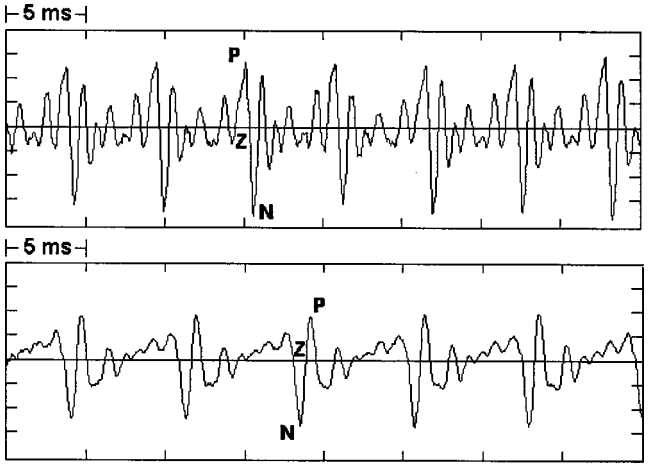

FIG. 1. Zero-crossing patterns observed in sustained [a] vowels. Top: Positive-to-negative (PZN) crossing. Bottom: Negative-to-positive (NZP) crossing. P and N indicate positive and negative significant peaks, respectively, and Z is a zero crossing.

tic and EGG jitter. A certain vowel-independent agreement between these measures exists in nondysphonic speakers (Orlikoff, 1995), but unilateral increase in EGG jitter can be caused, for example, by the cardiovascular pulse (Orlikoff and Baken, 1989). The influence of fundamental period demarcation methods and vowel type was investigated by Vieira *et al.* (1997). Their results indicate that currently available methods for jitter extraction are not reliable for [i] and [u] vowels and, as a corollary of that, for running speech. By analyzing sustained vowels ([i], [a], [u]) from 15 dysphonic speakers, these authors reported large discrepancies between acoustic and EGG jitter in [i] and [u] vowels, independently of F_0 extraction methods using peaks, zero crossings, or a wave-matching technique. In [a] vowels, though, consistent values were obtained between EGG jitter based on zero crossings in the closing phase and acoustic jitter based on positive-to-negative (PZN) or negative-to-positive (NZP) zero crossings. Acoustic jitter based on such zero crossings was more reliable than measures from a wave-matching algorithm, which underestimated jitter for values above $\approx$0.6%. Wave-matching methods are intrinsically sensitive to fluctuations in the radiated signal amplitude or shape. These fluctuations can be caused, for instance, by overlaps in the vocal-tract responses to glottal pulses relatively close in time (Hillenbrand, 1987) or by source jitter, which leads to ''harmonic shimmer'' as the harmonics shift in frequency and undergo an uneven vocal-tract filtering (Murphy, 1999), similarly to what occurs in amplitude vibrato (Sundberg, 1987; p. 164).

A dominant PZN or NZP pattern (Fig. 1) can be robustly detected in sustained [a] because the largest peak in each glottal cycle is sharper in [a] than in [u] and [i]. Additionally, the steep zero crossings in [a], associated with first formants having relatively high frequencies, provide better immunity to glottal noise. The superiority of zero crossings in [a] has been recently exploited in a comparative study of high-precision F_0 extraction methods in dysphonic [a] vowels, where the reference F_0 values were obtained with a semiautomatic identification of the patterns described above (Parsa and Jamieson, 1999).

It is well known that acoustic measures of jitter, shimmer, and glottal noise can be strongly correlated (Hillenbrand, 1987) and much research has been devoted to uncouple them (e.g., Cox *et al.*, 1989; Qi, 1992; Qi *et al.*, 1995; Murphy, 1999; Lucero and Koenig, 2000). Independent perturbation indices may improve the correlations between acoustic measures and perceptual ratings of voice quality if, for instance, vocal breathiness is associated with increased harmonics-to-noise ratio only, and vocal harshness with jitter only. However, acoustic jitter and shimmer can be intrinsically interdependent due to harmonic shimmer, as discussed above. The measures of acoustic and EGG jitter used in this study anchor in a common phonatory event, namely, the relatively fast closing phase of the glottal cycle. Sources of jitter inflation in only one of the signals were intentionally avoided in the analysis routines. For instance, aerodynamic turbulences produced by glottal chinks were regarded as artifacts in acoustic jitter extraction, although the quantification of such noise is of major interest in acoustic harmonics-to-noise ratio measures.

It is of clinical interest to know whether pathologies give rise to deviations between acoustic and EGG jitter or if these values can be used without distinction. To help answer this question, this study compared measures from sustained [a] in a large group of speakers suffering from various laryngeal pathologies. The agreement between measures held for most cases in which comparison was possible, but discrepant values occurred despite adequate signals. As detailed in subsequent sections, some of the discrepant measures can be associated with laryngeal anatomic or physiologic anomalies of clinical relevance.

II. METHOD

A. Data acquisition

The subjects were adult outpatients of the Voice Clinic of the Royal Infirmary of Edinburgh who attended sessions from May 1994 to August 1995. Each person was seated in an Amplivox-Burgess audiometer booth and fitted with a Shure SM10A head-worn microphone, laterally positioned at about 4 cm from the lips, and amplified by a Shure FP11 microphone-to-line amplifier. A portable laryngograph (Laryngograph Ltd., London) provided line-level EGG signals. Subjects were not using metallic necklaces during the recordings and, as is common in electroglottography, difficulties in obtaining adequate signals arose mostly in women, men with beards or wide necks, and pathologies that reduce the vocal contact. The microphone and EGG signals were monitored in an analog oscilloscope, and a Sony 55ES digital audio tape (DAT) recorder simultaneously digitized the waveforms at 48 000 samples per second, 16 bits per sample. The background acoustic noise, as monitored in the DAT, was below -60 dB *re*: FS (referenced to full scale). The amplification was adjusted to keep the average recording levels at about -6 dB *re*: FS (acoustic) or between -20 and -12 dB *re*: FS (EGG). The EGG level was relatively smaller to avoid clipping caused by excessive baseline fluctuation prior

to digitization due to insufficient high-pass filtering by the laryngograph, which had a flat response between 10–5000 Hz. Later, the signals were resampled through a Sound Blaster 16 personal computer audio card at 22 050 samples per second, 16 bits per sample.

The recordings were taken during the maximum sustained phonation of [a],[1] each patient being instructed to take a deep breath and prolong the vowel as long as possible at comfortable levels of pitch and loudness; maximum phonation times ranged from 3 to 42 s. The computer algorithms processed the whole utterance and no segment (such as voice onset or offset) was manually excluded from analysis, although an upper limit of 10% was applied to EGG jitter measures, as discussed later.

After the voice recording session, each subject was submitted to an endoscopic examination with a 70° oral telescope connected to a B&K 4914 stroboscope, a Panasonic CCD WV-KS152 color digital microcamera, and a Panasonic NV-SD40B VHS (video home system) four-head recorder. Video clips with 160×120 pixels, 16 bits for colors, were created from the VHS tapes through a Movie Machine Pro card (FAST Electronic GmbH, Munich). Data from 222 patients were collected but many subjects were excluded from the study due to poor EGG signals or unreliable acoustic jitter measures, as discussed further below.

B. EGG-signal selection and processing

The inadvertent use of automated measures from noisy or highly irregular signals is a major risk of the EGG technique. Before relying on automated ''objective'' measures, it is of primary importance to certify that the signals have not been corrupted by poor vocal-fold contact, inaccurate placement of electrodes, or signal-processing artifacts such as phase distortion, system bandwidth, or clipping (Watson, 1995). In the study reported here, each waveform was visually examined at the initial-, mid-, and final portions, 65 recordings being excluded for presenting small amplitudes (i.e., peak-to-peak amplitude less than 14 000 units) or aberrations (Vieira *et al.*, 1997) that could deceive the signal-processing algorithms. Next, to remove baseline drift, 50-Hz hum, or noise above the 5000-Hz upper limit of the laryngograph, the recordings were bandpass filtered (60–5000 Hz) with zero phase shift (Kormylo and Jain, 1974). Then, F_0 contours based on zero crossings in the closing phase (Vieira *et al.*, 1996) and a measure of the signal-to-noise ratio (SNR) were extracted.

A noise measure named Normalized Noise Energy (NNE, Kasuya *et al.*, 1986) was used by Watson (1995) to select EGG signals adequate for automated measures. He suggested that recordings should be discarded if NNE >-15 dB. The study reported here used an alternative signal-to-noise ratio (SNR) defined as

$$\mathrm{LSNR}(j)=10\cdot\log_{10}\left[\frac{\Sigma_{k=0}^{T_j-1}[\frac{1}{2}\cdot(x_{z_j+k}+x_{z_j+T_j+k})]^2}{\Sigma_{k=0}^{T_j-1}[\frac{1}{2}\cdot(x_{z_j+k}-x_{z_j+T_j+k})]^2}\right], \tag{1a}$$

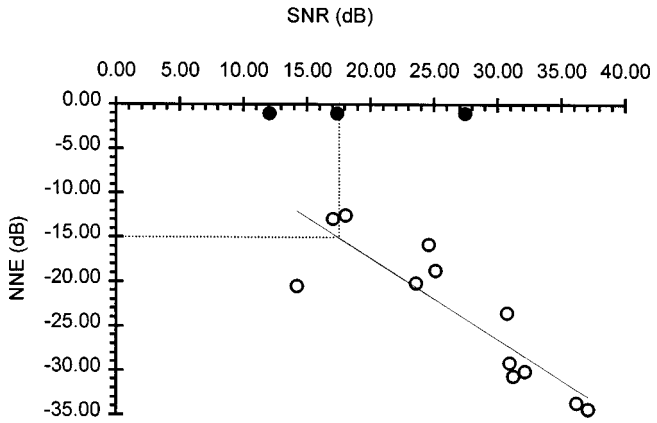

FIG. 2. EGG signal selection based on SNR values. A comparison of measures of SNR [Eq. (1)] and NNE taken with the commercial package DR. SPEECH SCIENCE (Tiger Electronics, Seattle), across 15 patients resulted in a correlation of -0.87 between measures. Watson's (1995) rejection criterion, NNE>-15 dB, corresponds to SNR$<$17.5 dB. Three recordings (filled dots at NNE$=-1$ dB) were rejected by the commercial package.

$$\underset{(\mathrm{EGG})}{\mathrm{SNR}}=\frac{1}{N-1}\sum_{j=0}^{N-2}\mathrm{LSNR}(j), \tag{1b}$$

where LSNR(j) is the local signal-to-noise ratio of the jth glottal cycle, z_j is the index of the sample closest to the jth cycle's zero-crossing instant, T_j is the number of samples in the jth cycle's fundamental period, and N is the number of detected cycles. It can be shown (e.g., Taylor, 1994; p. 426) that the numerator of Eq. (1a) behaves like a comb filter, selecting energy around F_0 and its harmonics, while the denominator is a comb filter at interharmonic energy. The condition NNE>-15 dB is equivalent to SNR$<$17.5 dB (Fig. 2) and excluded seven noisy recordings that were not detected in the visual inspection.

Unvoiced segments are common in sustained vowels of dysphonic speakers. To take this into account, an objective criterion based on voicing detection was used to select recordings. For reasons explained later, 20 EGG recordings with unvoiced intervals totaling more than 25% of the utterance were rejected. At the end, EGG data from 130 out of 222 patients were left for jitter analysis.

Instantaneous jitter was calculated according to the first-order perturbation function, PF1 (Titze, 1995), but mean values included only instantaneous measures not higher than 10%, that is

$$\mathrm{PF1}(i)=\frac{|F_0(i+1)-F_0(i)|}{\frac{1}{2}\cdot[F_0(i+1)+F_0(i)]}\times 100\%, \tag{2a}$$

$$\mathrm{PF1}_{10}=\frac{1}{N_{10}}\sum_{i=1}^{N_{10}}\mathrm{PF1}_{10}(i), \tag{2b}$$

where $F_0(i)$ is an instantaneous fundamental frequency value, $\mathrm{PF1}_{10}(i)$ is an instantaneous jitter $\leqslant$10%, and N_{10} is the number of such values in each time series. The 10% restriction aimed to limit EGG and acoustic measures to the same range because acoustic values above 10% were automatically rejected by the acoustic processing (Schäfer-Vincent, 1983), whereas instantaneous EGG values above this limit (e.g., in creaky voice) could be measured with con-

fidence. Although previous research by the authors suggests that mean acoustic jitter measures ($PF1_{10}$) above ≈2.5% can be unreliable, the 10% limit was kept to allow the detection of large unilateral increase in EGG jitter.

In summary, 130 EGG recordings were selected according to visual inspection, voicing detection, and SNR measures. Details on the processing of the acoustic data are given next.

C. Acoustic signal processing and selection

Acoustic recordings of the 130 selected patients were analyzed by a fully automated F_0 and jitter extraction algorithm (Schäfer-Vincent, 1983; Vieira *et al.*, 1997). Briefly, during jitter extraction two sets of values were initially taken from each recording: when searching for NZP patterns (Fig. 1), auxiliary jitter values were calculated from the first zero crossings after negative significant peaks, $PF_{10}(\vec{N})$, and before positive significant peaks, $PF_{10}(\overleftarrow{P})$; notice that these values can differ in noisy waveforms. Similarly, in the PZN searching mode auxiliary measures were based on zero crossings after positive peaks, $PF_{10}(\vec{P})$, and before negative peaks, $PF_{10}(\overleftarrow{N})$. Two jitter candidates associated with each pattern were then calculated as follows:

$$PF1_{10}(PZN) = \tfrac{1}{2}[PF1_{10}(\vec{P}) + PF1_{10}(\overleftarrow{N})], \tag{3a}$$

$$PF1_{10}(NZP) = \tfrac{1}{2}[PF1_{10}(\vec{N}) + PF1_{10}(\overleftarrow{P})]. \tag{3b}$$

To end the procedure, one of the candidates was elected according to the parameter ''ratio''

$$\text{ratio(PZN)} = \min[PF1_{10}(\vec{P})/PF1_{10}(\overleftarrow{N}),\ PF1_{10}(\overleftarrow{N})/PF1_{10}(\vec{P})] \times 100\%, \tag{4a}$$

$$\text{ratio(NZP)} = \min[PF1_{10}(\vec{N})/PF1_{10}(\overleftarrow{P}),\ PF1_{10}(\overleftarrow{P})/PF1_{10}(\vec{N})] \times 100\%. \tag{4b}$$

The maximum ratio value above 80% adequately selected the most reliable zero-crossing pattern but recordings from 19 out of 130 patients were abandoned due to ratio values less than 80%.

Last, eight acoustic recordings with more than 25% of unvoiced intervals were excluded, leaving 103 acoustic measures for comparison with the respective EGG values. The voicing criterion guaranteed that at least 50% of the utterance provided EGG and acoustic measures. Considering a minimum effective length of 1.5 s (50% of 3 s) and $F_0 = 120$ Hz (male average), at least 180 cycles, approximately, would be analyzed. This harmonizes with the study of Karnell (1991), suggesting that mean jitter in speakers with moderate levels of hoarseness asymptotes after approximately 190 cycles. In another related study, Scherer *et al.* (1995) investigated the number of voice tokens required to determine representative voice perturbation values but recommended a number of cycles higher than 190. In their investigation, each token consisted of 100 consecutive glottal cycles, taken at least 200 ms after phonation onset in a prolonged steady [ɑ] vowel. By analyzing the cumulative average of each perturbation measure as a function of the number of tokens used in the respective average, they recommend at least 15 tokens to yield representative perturbation values in voices with high levels of instability (i.e., perturbation values greater than one standard deviation above the normative mean). As noted by Scherer and colleagues (p. 1266), ''There should be a trade-off relation between the number of tokens required for a stable average of a perturbation measure and the number of consecutive cycles used in the analysis of each token.'' Thus, fifteen 200-ms tokens would correspond to a single 3-s token (15×200 ms), or 360 cycles at $F_0 = 120$ Hz, which is twice the minimum value suggested by Karnell (1991). There is a possibility that the recommendation in Scherer *et al.* (1995) was inflated by outliers in the cumulative averages, as suggested by data in their Fig. 2 (p. 1263).

D. Comparison of EGG and acoustic jitter

According to the criteria above, acoustic and EGG jitter were measured in 103 patients. A normalized difference, $\overleftrightarrow{\Delta}$, was used to compare the measures from each subject, where

$$\overleftrightarrow{\Delta} = \frac{PF1_{10}(\text{acoustic}) - PF1_{10}(\text{EGG})}{PF1_{10}(\text{EGG})} \times 100\%. \tag{5}$$

So, negative $\overleftrightarrow{\Delta}$ values indicate inflation in EGG jitter while positive values indicate increase in acoustic jitter.

III. RESULTS AND DISCUSSION

A. On signal selection

In Titze (1995) many recommendations on *acoustic* voice analysis were summarized. In particular, signals were classified as type 1 (nearly periodic with perturbation measures less than about 5%), type 2 (with intermittency, strong subharmonics or modulations), or type 3 (chaotic or with no apparent periodic structure). It seems difficult to discriminate between type 2 and type 3 signals considering that the existence of chaos in real voices remains to be proved and that the extraction of rigorous indicators of chaotic dynamics is affected by small sample lengths and nonstationarity in the voice production system (e.g., Behrman and Baken, 1997).

Behrman *et al.* (1998) reported a study where clinicians used the 3-type scheme mentioned above to visually classify voice signals. These authors acknowledged that the recommendations in Titze (1995) refer to acoustic analysis but applied them to EGG signals also. It should be noted, though, that irregular vibrations do not necessarily result in noisy or inadequate EGG signals because they can still provide reliable demarcation of glottal cycles in segments where automatic tracking of acoustic signals fails. Electroglottographic signals have been used, for example, to investigate subharmonic vocal-fold vibratory patterns that resemble creaky voice in certain aspects (Švec *et al.*, 1996).

Regarding standardization, Titze (1994) observed that standards are helpful because they educate newcomers to the field, they simplify procedures, and they help to certify. On

TABLE I. Overview of the pathologies in the original and selected group of recordings. M=male, F=female, MTD=muscular tension dysphonia, NAD=no abnormality detected, rec.=recurrent laryngeal nerve.

	Original			Selected		
Laryngeal problem	F	M	F+M	F	M	F+M
acid laryngitis	2	5	7	2	3	5
carcinoma	1	3	4	0	1	1
cyst	8	1	9	5	1	6
granuloma	0	1	1	0	1	1
leukoplakia	0	2	2	0	1	1
mutational dysphonia	0	2	2	0	1	1
myopathy	2	7	9	0	2	2
NAD	15	9	24	11	7	18
nodules	23	2	25	11	2	13
papillomas	3	4	7	1	3	4
polyp	2	2	4	1	1	2
presbyphonia	3	5	8	1	2	3
functional/abuse/MTD	45	13	58	21	6	27
rec. paralysis (unilateral)	14	13	27	5	2	7
rec. paralysis (bilateral)	1	0	1	0	0	0
Reinke's edema	3	0	3	2	0	2
sulcus vocalis	3	1	4	0	0	0
scar	5	4	9	1	2	3
web	1	2	3	0	0	0
others	9	6	15	4	3	7
Totals:	140	82	222	65	39	103

the other hand, they are not helpful in the sense that (p. 2) ''premature standardization or overstandardization can be a hindrance to progress. (...) Standards should therefore not be a threat to those who do not wish to conform; they should at most be a slight inconvenience. (...) In addition, standards may be confusing or erroneous. (...) For this reason, standards require frequent reviewing and updating.''

In our study, acoustic jitter was extracted from nearly type 1 portions of the sustained vowel but EGG measures were not necessarily limited to segments of this type. The exclusion of non-type 1 segments from perturbation statistics was discussed by Behrman *et al.* (1998) but they also pointed out that the removal of aperiodicities could result in a complete distortion of the data. A compromise, adopted here, was to exclude utterances in which the proportion of non-type 1 (i.e., unvoiced) segments was above a certain value, guaranteeing that at least 1.5 s were successfully tracked by the F_0 detection algorithm. The average number of cycles used in the estimation of acoustic jitter in the 103 selected patients was 1892 (standard deviation: 113; range: 157–5939). In three cases, the total of cycles was less than the 360 cycles recommended by Scherer *et al.* (1995), the respective values being 157, 190, and 244.

B. Overview of the results

The incidence of disorders in the original and selected recordings is presented in Table I. As seen, most of the rejections occurred in cases of paralyses, nodules, and functional/abuse/MTD (muscular tension dysphonia). The latter group included cases of psychogenic dysphonias, which are often hypofunctional states characterized by poor respiratory support, longitudinal chinks, and vocal-fold bowing (e.g., Stemple, 1993), leading to poor EGG signals and

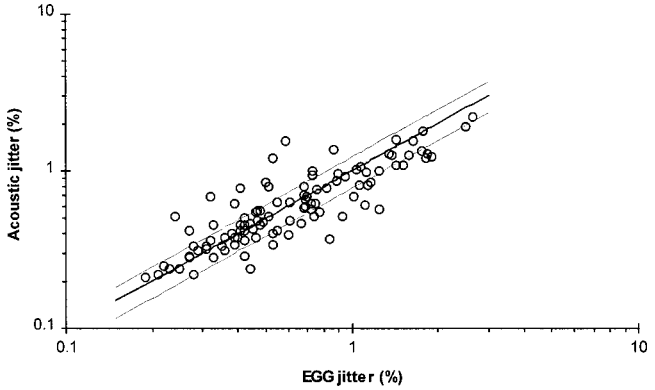

FIG. 3. Scatter plot of acoustic and EGG jitter from 103 dysphonic speakers. The three lines in the plot indicate the conditions where the normalized differences, $\overleftrightarrow{\Delta}$, are +22.5% (top), 0% (mid), and −22.5% (bottom).

breathy voices. A similar scenario was seen in cases of myopathy and presbyphonia. A high rate of rejections also occurred in the few cases of anterior webs and scarred vocal folds, which resulted in severe voice problems and aphonic speakers.

A scatter plot of the jitter measures is presented in Fig. 3, showing agreement between acoustic and EGG jitter for values up to ≈2.7%. The correlation coefficient between measures was $r=0.86$, strongly suggesting that they represent the underlying mechanical perturbations, particularly because they were derived from physiologically related events in different signals. It appears that there are no reported data confronting EGG and acoustic measures in dysphonic speakers, but comparisons between independent measures of acoustic jitter in pathological voices show poorer agreement than those in Fig. 3. For instance, Rabinov *et al.* (1995) compared acoustic jitter estimated with three commercial packages and found low correlations (0.20 to 0.66) between values. As they observed (p. 27), ''...even systems whose jitter measurements were moderately correlated did not necessarily produce the same numbers for a given voice.'' Despite the relatively high correlation between measures in Fig. 3, marked differences occurred in the midrange of jitter values (≈0.25%–1.3%). To find possible explanations for these discrepancies, a careful inspection of acoustic and EGG waveforms, plots of jitter time series, videoendoscopic images, and medical history details, was carried out, as described below.

A histogram of $\overleftrightarrow{\Delta}$ values was used in this investigation. As seen in Fig. 4, in most cases (65/103=63.1%) the differences fell within ±22.5%. The hatched bins at the right-hand side of Fig. 4 represent the cases (13/103=12.6%) in which acoustic jitter was markedly larger than EGG jitter (i.e., $\overleftrightarrow{\Delta}$ >22.5%). The hatched bins at the left side indicate the patients (25/103=24.3%) with acoustic jitter marked smaller than EGG jitter (i.e., $\overleftrightarrow{\Delta}<-22.5\%$).

The ±22.5% range was adopted as reference because a number near this interval (±23.81%) encompassed all jitter differences in the former study with 15 dysphonic speakers. There are other data in the literature supporting this choice. Normative EGG and acoustic jitter values from normal speakers were reported by Orlikoff (1995), who compared

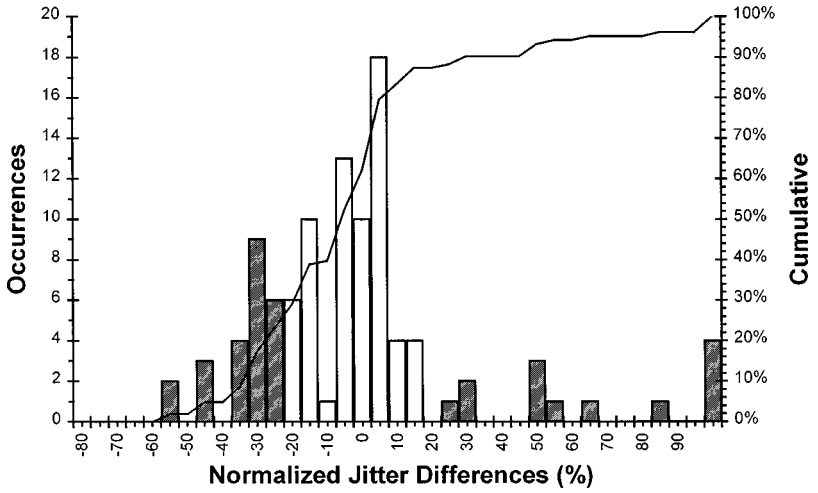

FIG. 4. Distribution of normalized differences. Differences between EGG and acoustic jitter, $\overleftrightarrow{\Delta}$, for 103 dysphonic speakers. The rightmost bin accumulates all differences between 97.5% and 162.5%. The hatched bins are discussed in the text. The width of the bins was 5% and the central bin was symmetrically positioned around zero so that the ±22.5% range could be delimited.

acoustic and EGG jitter from eight vowels [i ɛæ ʌ ɑ ɔ o u], produced with controlled values of intensity and fundamental frequency. The [a] vowel used here is closest to [ɑ], considering that [a] differs from [ɑ] only in the front–back dimension, whereas it differs from [æ] and [ʌ] in the front–back and open–close dimensions (Schwartz *et al.*, 1997; p. 236). The variability in jitter measures can be expressed by the coefficient of variation (CV), i.e., the standard deviation divided by the respective mean; jitter estimates that deviate by more than one standard deviation above the normative mean have been regarded as ''large'' in the literature (Scherer *et al.*, 1995). Using Orlikoff's measures (in ms) for [ɑ], the CV values for male subjects become 0.009/0.041=22.0% (acoustic) and 0.010/0.044=22.7% (EGG), the corresponding values for females being 0.007/0.038=18.4% (acoustic) and 0.006/0.040=15.0% (EGG). The 22.5% range is thus equivalent to the maximum CV (22.7%) from the nondysphonic normative open vowel. In general, the coefficient of variation in Orlikoff (1995) tended to be larger for other vowels, indicating that the measures from the open vowel were more stable.

C. Increased acoustic jitter ($\overleftrightarrow{\Delta}>+22.5\%$)

Large acoustic jitter ($\overleftrightarrow{\Delta}>+22.5\%$) occurred in 13 subjects, with a predominance of small nodular lesions: 2 cysts, 4 nodules, 2 polyps, and 1 papilloma; in the latter, videoendoscopic images revealed only one small lump affecting the anterior part of one fold. The other cases were 1 functional dysphonia, 1 leukoplakia, and 2 Reinke's edemas (postsurgery). The acoustic signals of patients with $\overleftrightarrow{\Delta}>+22.5\%$ were affected by noise due to incomplete glottal closure. Although Eq. (4) provided high ratio values, indicating that the zero crossings were detected with confidence, noise contaminated the regularity of the crossings, as exemplified in Fig. 5. Since this problem is a pure acoustic artifact, there was no corresponding increase in EGG jitter.

Unilateral rise in acoustic jitter can occur in the breathy voices of paralyzed vocal folds. In general, though, jitter comparison cannot be carried out in such voices because EGG signals tend to be inadequate. Nevertheless, there were two cases of recovering paralyses among the 103 selected patients. The corresponding $\overleftrightarrow{\Delta}$ values were 0.56% and −13.04%, suggesting that acoustic jitter measures were, possibly, not inflated by aerodynamic noise. In one case there was actually a certain increase in EGG jitter. As will be justified later, EGG jitter can increase substantially in certain mild paralyses and other anomalies that affect the posterior larynx.

D. Increased EGG jitter ($\overleftrightarrow{\Delta}<-22.5\%$)

Twenty-five patients had normalized differences below −22.5%. The diagnoses, detailed in the third column of Table II, can be grouped into three classes: (1) Structurally normal or almost normal larynges (no abnormality detected, acid laryngitis, functional dysphonia, myopathy); (2) Abnormalities in the posterior glottis (laryngeal trauma, intubation granuloma, and paralysis); and (3) Lesions of the vocal-fold mucosa (scar and dysplasia). The cases of cyst do not fit in the above classification.

The observation of waveforms and a careful frame-by-frame analysis of videoendoscopic images of the 25 patients revealed a more complex scenario than in the group with $\overleftrightarrow{\Delta}>+22.5\%$. Nonetheless, combinations of the following features were common (Table II): laryngeal hyperfunction, posterior glottal chink, asymmetries in the posterior part of the larynx, creaky-like voice, and some increase in EGG noise. Each factor contributed to jitter in a peculiar way.

Many hyperfunctional laryngeal patterns have been described in the literature (Morrison *et al.*, 1986; Morrison and Rammage, 1993). Eight patients (Table II) had a laryngeal hyperfunction pattern where, as described by Hirano and

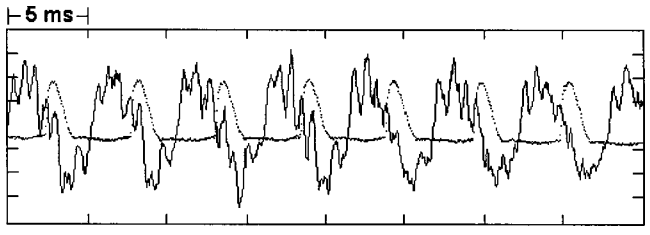

FIG. 5. Increase in acoustic jitter. Notice noise affecting acoustic zero crossings (solid line) and also the reduced closed quotient in the EGG signal (dotted line), typical of breathy voices. Upward changes in EGG signals represent increasing vocal-fold contact. Data from a patient with leukoplakia and $\overleftrightarrow{\Delta}=+57.64\%$.

TABLE II. Large-EGG-jitter group ($\overleftrightarrow{\Delta} < -22.5\%$). ID=patient identification; NAD=no abnormality detected, SNR=EGG signal-to-noise ratio. The criteria adopted to detect hyperfunction, posterior glottal chinks, laryngeal asymmetries, creaky-like EGG, and EGG noise are described in the text.

ID	$\overleftrightarrow{\Delta}$(%)	Diagnosis	Hyper-function	Post. chink	Laryngeal asymmetry	Creaky-like EGG	EGG noise	SNR (dB)
1	−23.86	NAD		√	√	√	√	20.72
2	−28.29	trauma		√	√		√	22.49
3	−30.95	NAD		√	√		√	26.38
4	−23.81	cyst				√		21.62
5	−45.54	paralysis	√	√	√	√		28.45
6	−33.52	granuloma		√		√	√	24.34
7	−35.79	functional[a]					√	18.68
8	−44.09	scar		√	√		√	27.38
9	−23.64	papilloma	√	√		√	√	32.67
10	−22.64	Reinke's edema	√	√		√	√	22.16
11	−28.57	functional		√	√	√		28.50
12	−31.34	dysplasia					√	25.35
13	−29.73	functional	√	√			√	29.01
14	−31.35	scar	√			√	√	19.95
15	−32.35	functional	√			√	√	28.73
16	−45.45	cyst		√			√	24.00
17	−35.85	cyst	√			√	√	29.81
18	−24.31	acid laryngitis		√	√		√	22.52
19	−35.00	functional[a]					√	25.99
20	−28.21	presbyphonia					√	24.99
21	−28.07	rec. paralysis	√	√	√		√	24.04
22	−24.53	NAD			√	√		33.69
23	−55.95	NAD			√		√	25.85
24	−54.40	presbyphonia		√		√	√	24.26

[a]Videoendoscopic images not available.

Bless (1993; p. 179), the ''false folds are often excessively adducted. The epiglottis is strongly pulled backward and the arytenoids are markedly pulled forward during phonation. The vocal folds are often shortened.'' Moreover, a lessening of the acute angle defined by the edges of the aryepiglottic folds and the posterior commissure is also typical (Fig. 6), and the arytenoids may fall inward due to fatigue of the posterior cricoarytenoid muscle (Harris and Lieberman, 1993) because the activity of this muscle will be necessary in order to counterbalance the increased activity of the adductors (Hirose and Gay, 1972, 1973; Hirano, 1981).[2] These laryngeal hyperfunction features seem capable of inflating EGG jitter by means of fluctuations in the contact area between the arytenoids or between the corniculate cartilages (the latter being small cartilages that rest on top of the arytenoids and behaving like cushions to absorb the adductive impact of the arytenoids).[3] Trembling of the arytenoids could be observed in stroboscopic sequences but the delineation of the cartilages was often unclear.

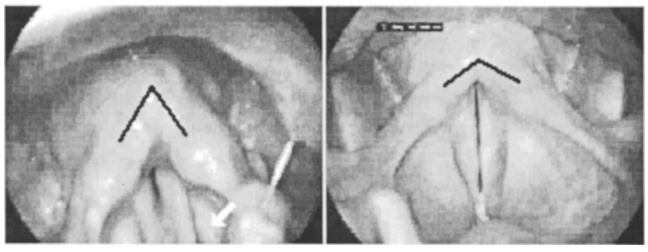

FIG. 6. Laryngeal hyperfunction. The drawn angle is more acute in a tense (left) than in a nontense larynx (right). In the left panel the arytenoids are pulled towards the glottal midline. In clinical practice, it is not always possible to obtain highly symmetrical images. In the left panel, for instance, the patient's right arytenoid is slightly closer to the lens than the left arytenoid, but the acute angle is not a consequence of image distortion. In particular, the pressed ventricular folds are useful signs of hyperfunction. Note that the false folds (arrow) are tight and elongated due to increased medial compression and longitudinal tension, respectively.

Images from 11 patients provided other indications of instabilities in the contact of the arytenoids. The main features were asymmetries in the phonatory position of these cartilages and/or in their maneuvers during glottal opening or closing. These features can be easily detected in videoendoscopic sequences (Sulter *et al.*, 1996) provided that clinicians give attention to the laryngeal framework. Asymmetries affecting the arytenoids were seen in (a) Two cases of recovering paralyses and one case of laryngeal trauma due to an anesthetic intubation that dislocated the left arytenoid; and (b) Seven cases of nearly normal larynges (four patients with no abnormality detected, one functional dysphonia, one acid laryngitis, and one scar postsurgery).

In general, the human body, including the larynx (Hirano *et al.*, 1989), is not symmetrical across the midline, but the medical literature shows that asymmetries involving the arytenoids can originate from a number of laryngeal disorders. Among the ten observed cases of asymmetries, some resembled descriptions of (1) selective paralysis, or paresis, of the recurrent laryngeal nerve (Sasaki *et al.*, 1980); (2) gentle states of paradoxical vocal-fold dysfunction (Powell *et al.*, 2000); (3) laryngeal synkinesis, i.e., the unintentional movement of one muscle due to the voluntary action of another muscle, which is caused by cross innervations and can lead to trembling of the arytenoids (Crumley, 1989); (4) unilateral paralysis of the superior nerve, which can cause a

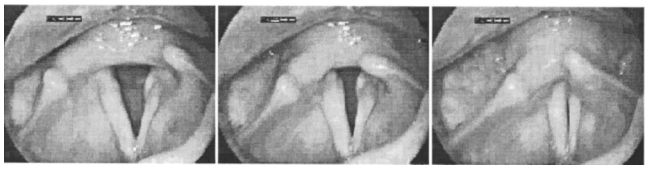

FIG. 7. Laryngeal asymmetry. Notice the limited movement of the patient's right arytenoid during adduction. Images from patient 23 (Table II), with $\overleftrightarrow{\Delta} = -55.95\%$.

lowering of the fold in the affected side and the rotation of the posterior glottis towards the paralyzed side (Arnold, 1961; Tanaka, Hirano and Umeno, 1994); and (5) fixation of the cricoarytenoid joint due, e.g., to prolonged intubation (Sasaki *et al.*, 1980), laryngeal manifestations of rheumatoid arthritis (Brooker, 1988), or anatomical asymmetries in the cricoarytenoid joints (Sellars and Keen, 1978; Kahane and Hommons, 1987). A clinical confirmation of the anomalies would require electromyographic (EMG) evaluation, but this was not carried out in the subjects. Even if multichannel EMG equipment had been available, electromyography would have been tried in just a few patients and probably only in the cricothyroid and thyroarytenoid muscles, because other intrinsic laryngeal muscles are difficult to reach (Hirose and Gay, 1972). An example of what appeared to be a partially recovered paralysis or a mechanic fixation of the right cricoarytenoid joint is given in Fig. 7. The image was taken from patient 23 in Table II. This case exemplifies a situation that commonly occurs in videoendoscopic examination: the clinician focuses his attention on the phonatory movement of the folds, giving little importance to small changes in the structure of the larynx.

As a word of caution, care should be taken with apparent asymmetries in the posterior larynx caused by optical artifacts. Remembering that an oral telescope was used in this research, false asymmetries were seen in three situations: (1) when the endoscope was not aligned with the glottal midline; (2) when it was rotated in relation to its longitudinal axis; and (3) when its tip was closer to one arytenoid than the other. Similar artifacts have been reported in connection with nasal fiber optic endoscopy (Casper *et al.*, 1988).

Laryngeal gentle asymmetries can have phonatory implications. Asymmetries can cause differences between the longitudinal tensions of the vocal folds, facilitating left–right desynchronizations that can lead to voice breaks and creaky voice (Berry *et al.*, 1994). This can occur, for example, if the lax fold vibrates with a strong, second-order longitudinal mode, whereas the other fold vibrates in the fundamental longitudinal mode only. Under such conditions, mechanical transients can be triggered by desynchronized collisions of the folds. The relative phase of the folds' oscillations and the site of the impacts seem to play an important role in the production of transients (Fig. 8). Clinical practice reveals that the anterior third is a highly sensitive region: the closer a problem is situated toward the anterior commissure, the greater the vocal problem (Luchsinger and Arnold, 1965; p. 282). A type of collision in asymmetrical folds that can lead to mechanical transients is represented pictorially in Fig. 8 (right). This drawing was based on stroboscopic frames seen

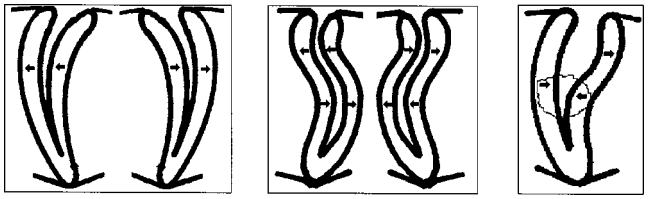

FIG. 8. Asymmetrical vocal-fold vibration and voice breaks. The arrows indicate the directions of movement. The left- and midpanels schematically show two asymmetrical patterns that are stable during phonation and do not lead to voice breaks, whereas the pattern on the right panel is unstable. Left: both folds vibrate in the fundamental longitudinal mode but there is a phase difference of 180° in the medial-lateral excursion of the folds. Mid: both folds vibrate in the second longitudinal mode, a phase difference of 180° also existing between them. Right: one fold vibrates in the first longitudinal mode and the other in the second mode; the surrounded part is the local of collisions that initiate mechanical transients and voice breaks. As the collision occurs near the anterior commissure, it is potentially harmful to phonation.

just before the beginning of mechanical transients leading to spells of irregular creaky-like voice; notice that the interpretation of stroboscopic sequences during the highly irregular transients is meaningless. Similar voice breaks have been described in association with subharmonic vibratory patterns of the vocal folds (Švec *et al.*, 1996) and with jumps between modal voice and falsetto (Švec *et al.*, 1999). A question on the importance of laryngeal asymmetries has actually been raised by these authors (p. 1529): ''As no larynx is ideally symmetrical, however, the question remains unresolved as to whether, and to what extent, asymmetry is an important factor (...) in the occurrence of spontaneous chest-falsetto jumps.'' Emphasizing that the transients illustrated in Fig. 8 (right) occurred in a kind of modal-to-creaky phonation, it seems advisable that clinical protocols for videoendoscopic examination include slow F_0 glides to probe such breaks along the patient's phonatory range.

As a final aspect concerning the posterior larynx, 14 patients, shown in Table II, had small-to-moderate posterior glottal chinks, i.e., from chinks limited to the cartilaginous glottis up to chinks extending into the membranous part, as described by Hertegård and Gauffin (1995). In these cases, mucus spots, which can interfere with the EGG signal (Childers *et al.*, 1986), could be seen moving in the cartilaginous glottis during endoscopy. This may have also contributed to the ''EGG noise'' indicated in Table II and exemplified in Fig. 9, which was present throughout the recordings of 19 patients. This noise did not decrease the SNR substantially, compared with the 28.19-dB average, but introduced

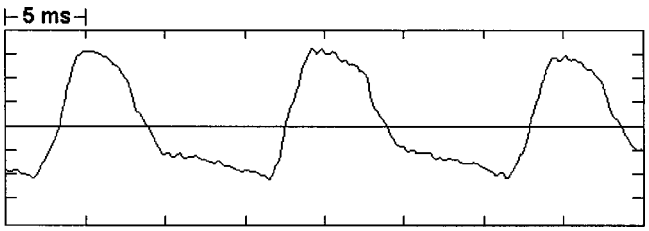

FIG. 9. Irregularities in the EGG closing phase. Example of a patient with $\overleftrightarrow{\Delta} = +35.85\%$, showing cycle-to-cycle changes in the slope of the closing phase and high-frequency noise throughout the electroglottogram. Upward changes in EGG signals represent increasing vocal-fold contact.

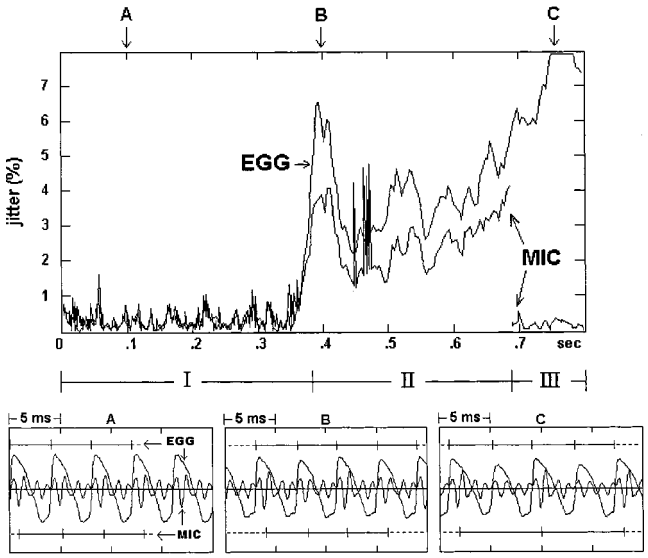

FIG. 10. Increased EGG jitter in creaky-like vibrations. Top: comparison of acoustic (Mic) and EGG jitter. Bottom: acoustic and EGG waveforms taken in points A, B, and C of regions I, II, and III, respectively. In the lower panels, segments (⊢—⊣) indicate the fundamental periods detected acoustically and upward changes in EGG signals represent increasing vocal-fold contact. Data from subject 11 (Table II).

irregularities in the slope of the closing phase leading, eventually, to jitter. Notice how the inflection in the closing phase of the second glottal cycle differs from the others. In a few patients this irregular aspect of the EGG signal was not observed though, and the source of EGG jitter was creaky-like phonation only.

It is known that creaky voice (or vocal fry) is produced with relatively low fundamental frequencies (≈50 Hz), reduced airflow, low EGG contact quotients, and EGG amplitude perturbation patterns ranging from increased shimmer to multiple and irregular peaks per EGG cycle (Hollien, 1974; Dejonckere and Lebacq, 1983; Blomgren *et al.*, 1998). A related irregular vibratory pattern was reported by Švec *et al.* (1996), who described a subharmonic oscillation pattern similar to vocal fry but produced with increased airflows. Irregular creaky-like vibrations can also be caused by vocal-fold asymmetries in tension or mass (Ishizaka and Isshiki, 1976; Isshiki *et al.*, 1977; Wong *et al.*, 1991). It does not seem simple to discriminate these creaky-like vibrations solely based on the analyses of acoustic, electroglottographic, and standard videoendostroboscopic recordings.

Inspection of the EGG and acoustic jitter time series of all patients in Table II revealed 11 cases (indicated by ''creaky-like EGG'' in the table) with long segments of EGG jitter systematically larger than acoustic values, as exemplified in Fig. 10. The voices sounded creaky in such segments. Three regions of interest are indicated in the upper panel of Fig. 10. In region I, acoustic and EGG jitter nearly overlapped and, as seen in the sample waveforms (lower panel A), there was no increase in EGG shimmer along this region. This pattern was also present in the time series of the patients with $\overleftrightarrow{\Delta}$ values within ±22.5%. In region II, EGG and acoustic jitter were correlated, as seen in the figure, but EGG values were mostly ≈1%–3% above the acoustic measures. Instabilities in acoustic tracking can be seen from ≈4.5–4.7 s. The rise in EGG jitter was related to increased EGG shimmer, as seen in the lower panel B, which also reveals increased acoustic shimmer. Nevertheless, the fundamental periods acoustically detected in region II were close to the corresponding EGG periods. In region III, EGG jitter was more than ≈4% above acoustic jitter. As seen in the lower panel C, acoustic shimmer increased further and the acoustic tracking followed the more regularly spaced subharmonic pattern. A situation, not represented in Fig. 10, also occurred in other patients. In such cases, only acoustic F_0 detection failed, producing unvoiced intervals that were excluded from acoustic jitter average, resulting in increased EGG jitter.

In summary, consistency between acoustic and EGG jitter held in most patients, but a number of factors led to large normalized differences. As discussed above, it was possible to speculate on the laryngeal behavior according to the magnitude and sign of $\overleftrightarrow{\Delta}$ values.

IV. CONCLUDING REMARKS

This study investigated sources of differences between jitter measures, and the results indicated that acoustic and EGG jitter could differ significantly in the presence of laryngeal disorders. Therefore, acoustic and EGG jitter should not be used interchangeably to describe a dysphonic voice. Discrepancies between measures due to increased acoustic jitter ($\overleftrightarrow{\Delta} > +22.5\%$) occurred mostly in cases of small nodular lesions with moderate breathiness, noisy acoustic signals, no posterior glottal chink, and no abnormality affecting the position or movement of the arytenoids. Measures from patients with highly breathy voices were not compared because, as the vocal-fold contact is reduced in such cases, the EGG signal is inadequate for jitter extraction. Regarding divergences caused by increased EGG jitter ($\overleftrightarrow{\Delta} < -22.5\%$), they were associated with hyperfunctional voices with certain asymmetries affecting the arytenoids, small-to-moderate glottal chinks, and creaky-like voices. It is possible that small jitter differences ($|\overleftrightarrow{\Delta}| \leqslant 22.5\%$) can occur in the presence of laryngeal features that inflate EGG jitter simultaneously with factors that increase acoustic jitter. In this series of patients, this actually happened in cases with an asymmetry in the arytenoids and a moderate posterior chink.

Asymmetrical vocal folds can lead to irregular subharmonic vibratory patterns and other vocal problems. Approximately 1 out of 10 patients (10/103) in the study had laryngeal asymmetries that could help understand the nature of the dysphonia. If such minute laryngeal changes are not detected in videoendoscopic examination, patients can be discharged without an adequate and reassuring explanation or can be referred to speech therapy with an inappropriate or vague description of the problem. The $\overleftrightarrow{\Delta}$ measure used in this study may have some clinical relevance. Always bearing in mind that artifacts can affect the measure and the measure can fail in the detection of disorders, large negative $\overleftrightarrow{\Delta}$ values can bring the clinician's attention to possible laryngeal asymmetries and to the underlying causes.

ACKNOWLEDGMENTS

Part of the study was carried out during Maurílio N. Vieira's research stays in the Center for Speech Communication Research, University of Edinburgh, and the Royal Infirmary of Edinburgh, Scotland, UK, between 1993 and 1997. Professor Arnold Maran and Dr. Colin Watson, from the Royal Infirmary of Edinburgh, gave invaluable assistance. The commentaries by Dr. Anders Löfqvist and two anonymous reviewers were greatly appreciated. This research was supported by Grant No. 200068/93-8 from CNPq, Brazil.

[1]The [a] is not a monophthong in American English but it occurs in British English, as reported, e.g., for the English spoken in Glasgow (Scobbie *et al.*, 1999) or Berwick upon Tweed, England's northernmost town, near the Scottish/English border (Watt and Ingham, 2000). Moreover, according to Jones (1997, pp. iv–xv), ''The pronunciation of any language is constantly changing, and a dictionary ... should reflect such changes. However, there is a general reluctance among users of phonemic transcription to change the symbols used too frequently, as this causes existing teaching materials and textbooks to become out of date.'' Referring to the so-called BBC (British Broadcast Corporation) pronunciation, he observed that ''The vowel /æ/, classified as a short vowel, is nevertheless generally lengthened before /b, d, g, dʒ, m, n/. Thus, /æ/ in 'bag' is considerably longer than /æ/ in 'back.' The quality of this vowel is now more open than it used to be, and the symbol /a/ might one day be considered preferable. We have retained the /æ/ symbol partly because it is phonetically appropriate for the corresponding American vowel.''

[2]There appears to be no electromyographic study on hyperfunctional voices, but there are reports of increased activity of the posterior cricoarytenoid (PCA) muscle in situations of increased laryngeal tension. Hirose and Gay (1972; p. 159) carried out EMG studies on the laryngeal muscles and stated that an ''... interesting finding is the small PCA peak just before the onset of an initial or medial stressed vowel. Interpretation of this transient PCA activity is not perfectly clear as yet, but it is conceivable that the PCA acts to counterbalance the strong contraction of the adductors ... .'' In another study (Hirose and Gay, 1973), these authors found similar patterns of PCA activity in the voice onset during hard glottal attacks. Hirano (1981) also found increased PCA activity in high-pitched sung vowels and stated that (p. 161) ''This activity of PCA may be required in order to brace the arytenoid cartilage against the strong anterior pull of the CT [cricothyroid muscle].''

[3]Referring to the corniculate cartilage, Fink and Demarest (1978; p. 3) stated that, ''This conical piece of elastic cartilage projects backward and medially and, when compressed against its fellow of the opposite side, functions as a spring whose recoil aids in pushing the adducted arytenoids apart (...).'' Further details are given in this book. The same idea has been adopted in the biomechanical laryngeal model of Farley (1996; p. 3796), where the ''cartilages are represented, primarily as passive springs that resist arytenoid rotation when brought into contact.''

Arnold, G. E. (**1961**). ''Physiology and pathology of the cricothyroid muscle,'' Laryngoscope **71**, 687–753.

Behrman, A., Agresti, C. J., Blumstein, E., and Lee, N. (**1988**). ''Microphone and electroglottographic data from dysphonic patients: Type 1, 2 and 3 signals,'' J. Voice **12**, 249–260.

Behrman, A., and Baken, R. J. (**1997**). ''Correlation dimension of electroglottographic data from healthy and pathologic subjects,'' J. Acoust. Soc. Am. **102**, 2371–2379.

Berry, D. A., Herzel, H., and Titze, I. R. (**1994**). ''Interpretation of biomechanical simulations of normal and chaotic vocal fold oscillations with empirical eigenfunctions,'' J. Acoust. Soc. Am. **95**, 3595–3604.

Bless, D. M., and Baken, R. J. (transcribers and editors) (**1992**). ''International Association of Logopedics and Phoniatrics (IALP) voice committee discussion of assessment topics,'' J. Voice **6**, 194–210.

Blomgren, M., Chen, Y., Ng, M. L., and Gilbert, H. R. (**1998**). ''Acoustic, aerodynamic, physiologic, and perceptual properties of modal and vocal fry registers,'' J. Acoust. Soc. Am. **103**, 2649–2658.

Bough, I. D., Heuer, R. J., Sataloff, R. T., Hills, J. R., and Cater, J. R. (**1996**). ''Intrasubject variability of objective voice measures,'' J. Voice **10**, 166–174.

Brooker, D. S. (**1988**). ''Rheumatoid arthritis: otorhinolaryngological manifestations,'' Clin. Otolaryngol. **13**, 239–246.

Casper, J. K., Brewer, D. W., and Colton, R. H. (**1988**). ''Pitfalls and problems in flexible videolaryngoscopy,'' J. Voice **1**, 347–352.

Childers, D. G., Hicks, D. M., Moore, G. P., and Alsaka, Y. A. (**1986**). ''A model for vocal fold vibratory motion, contact area, and the electroglottogram,'' J. Acoust. Soc. Am. **80**, 1309–1320.

Colton, R. H., and Conture, E. G. (**1990**). ''Problems and pitfalls of electroglottography,'' J. Voice **4**, 10–24.

Cox, N. B., Ito, M. R., and Morrison, M. D. (**1989**). ''Technical considerations in the computation of spectral harmonics-to-noise ratios for sustained vowels,'' J. Speech Hear. Res. **32**, 203–218.

Crumley, R. L. (**1989**). ''Laryngeal synkinesis: Its significance to the laryngologist,'' Ann. Otol. Rhinol. Laryngol. **98**, 87–92.

Dejonckere, P. H., and Lebacq, J. (**1983**). ''An analysis of the diplophonia phenomenon,'' Speech Commun. **2**, 47–56.

Farley, G. R. (**1996**). ''A biomechanical laryngeal model of voice F_0 and glottal width control,'' J. Acoust. Soc. Am. **100**, 3794–3812.

Fink, B. R., and Demarest, R. J. (**1978**). *Laryngeal Biomechanics* (Harvard University Press, Cambridge, MA).

Gelfer, M. P. (**1995**). ''Fundamental frequency, intensity, and vowel selection: Effects on measures of phonatory stability,'' J. Speech Hear. Res. **38**, 1189–1198.

Hall, K. D. (**1995**). ''Variation across time in acoustic and electroglottographic measures of phonatory function in women with and without vocal nodules,'' J. Speech Hear. Res. **38**, 783–793.

Harris, T., and Lieberman, J. (**1993**). ''The cricothyroid mechanism, its relation to vocal fatigue and vocal dysfunction,'' Voice: The Journal of the British Voice Association **2**, 89–96.

Hemler, R. J. B., Wieneke, G. H., and Dejonckere, P. H. (**1997**). ''The effect of relative humidity on inhaled air on acoustic parameters of voice in normal subjects,'' J. Voice **11**, 295–300.

Hertegård, S., and Gauffin, J. (**1995**). ''Glottal area in vibratory patterns studied with simultaneous stroboscopy, flow glottography, and electroglottography,'' J. Speech Hear. Res. **38**, 85–100.

Hillenbrand, J. (**1987**). ''A methodological study of perturbations and additive noise in synthetically generated voice signals,'' J. Speech Hear. Res. **30**, 448–461.

Hirano, M. (**1981**). ''The function of the intrinsic laryngeal muscles in singing,'' in *Vocal Fold Physiology*, edited by K. N. Stevens and M. Hirano (University of Tokyo Press, Tokyo), pp. 155–170.

Hirano, M., and Bless, D. M. (**1993**). *Videostroboscopic Examination of the Larynx* (Singular, San Diego).

Hirano, M., Kurita, S., Yukizane, K., and Hibi, S. (**1989**). ''Asymmetry of the laryngeal framework: A morphologic study of cadaver larynges,'' Ann. Otol. Rhinol. Laryngol. **98**, 135–140.

Hirose, H., and Gay, T. (**1972**). ''The activity of the intrinsic laryngeal muscles in voicing control: An electromyographic study,'' Phonetica **25**, 140–164.

Hirose, H., and Gay, T. (**1973**). ''Laryngeal control in vocal attack: An electromyographic study,'' Folia Phoniatr. **25**, 203–213.

Hirson, A., and Roe, S. (**1993**). ''Stability of voice and periodic fluctuations in voice quality through the menstrual cycle,'' Voice (British Voice Association) **2**, 78–88.

Hollien, H. (**1974**). ''On vocal registers,'' J. Phonetics **2**, 125–143.

Ishizaka, K., and Isshiki, N. (**1976**). ''Computer simulation of pathological vocal-cord vibration,'' J. Acoust. Soc. Am. **60**, 1193–1198.

Isshiki, N., Tanabe, M., Ishizaka, K., and Broad, D. (**1977**). ''Clinical significance of asymmetrical vocal cord tension,'' Otol. Rhinol. Laryngol. **86**, 58–66.

Jones, D. (**1997**). ''Introduction,'' in *English Pronouncing Dictionary*, 15th ed., edited by P. Roach and J. Hartman (Cambridge University Press, Cambridge), pp. iv–xv.

Kahane, C. J., and Hammons, J. (**1987**). ''Developmental changes in the articular cartilage of the human cricoarytenoid joint,'' in *Laryngeal Function in Phonation and Respiration*, edited by T. Baer, C. S. Sasaki, and K. S. Harris (College Hill, Boston), pp. 15–28.

Karnell, M. P. (**1991**). ''Laryngeal perturbation analysis: Minimum length of analysis window,'' J. Speech Hear. Res. **34**, 544–548.

Kasuya, H., Ogawa, S., Kikuchi, Y., and Ebihara, S. (**1986**). ''An acoustic analysis of pathological voices and its application to the evaluation of laryngeal pathology,'' Speech Commun. **5**, 171–181.

Kormylo, J. J., and Jain, V. K. (**1974**). ''Two-pass recursive digital filter with zero phase shift,'' IEEE Trans. Acoust., Speech, Signal Process. **22**, 384–387.
Lucero, J. C., and Koenig, L. (**2000**). ''Time normalization of voice signals using functional data analysis,'' J. Acoust. Soc. Am. **108**, 1408–1420.
Luchsinger, R., and Arnold, M. D. (**1965**). *Clinical Communicology: Its Physiology and Pathology* (Wadsworth, Belmont).
Morrison, M. D., Nichol, H., and Rammage, L. A. (**1986**). ''Diagnostic criteria in functional dysphonia,'' Laryngoscope **94**, 1–8.
Morrison, M. D., and Rammage, L. A. (**1993**). ''Muscle misuse voice disorders: Description and classification,'' Acta Oto-Laryngol. (Stokh.) **113**, 428–434.
Murphy, P. J. (**1999**). ''Perturbation-free measurement of the harmonics-to-noise ratio in voice signals using pitch synchronous harmonic analysis,'' J. Acoust. Soc. Am. **105**, 2866–2881.
Orlikoff, R. F. (**1995**). ''Vocal stability and vocal tract configuration: An acoustic and electroglottographic investigation,'' J. Voice **9**, 173–181.
Orlikoff, R. F., and Baken, R. J. (**1989**). ''The effect of the heartbeat on vocal fundamental frequency,'' J. Speech Hear. Res. **32**, 576–582.
Orlikoff, R. F., and Kahane, J. C. (**1991**). ''Influence of mean sound pressure level on jitter and shimmer measures,'' J. Voice **5**, 113–119.
Parsa, V., and Jamieson, D. G. (**1999**). ''A comparison of high precision F_0 extraction algorithms for sustained vowels,'' J. Speech Lang. Hear. Res. **42**, 112–126.
Powell, D. M., Karanfilov, B. I., Beechler, K. B., Treole, K., Trudeau, M. D., and Forrest, L. A. (**2000**). ''Paradoxical vocal cord dysfunction in juveniles,'' Arch. Otolaryngol. Head Neck Surg. **126**, 29–34.
Qi, Y. (**1992**). ''Time normalization in voice analysis,'' J. Acoust. Soc. Am. **92**, 2569–2576.
Qi, Y., Weinberg, B., Bi, N., and Hess, W. J. (**1995**). ''Minimizing the effect of period determination on the computation of amplitude perturbation in voice,'' J. Acoust. Soc. Am. **97**, 2525–2532.
Rabinov, C. R., Kreiman, J., Gerrat, B. R., and Bielamowicz, S. (**1995**). ''Comparing reliability of perceptual ratings of roughness and acoustic measures of jitter,'' J. Speech Hear. Res. **38**, 26–32.
Robinson, H. F. (**1993**). ''Assessment of voice problems,'' in *Assessment in Speech and Language Therapy*, edited by J. R. Beech and L. Harding with D. Hilton-Jones (Routledge, London), pp. 68–84.
Sasaki, C. T., Horiuchi, M., Ikari, T., and Kirchner, J. A. (**1980**). ''Vocal fold positioning by selective denervation. Old territory revisited,'' Otol. Rhinol. Laryngol. **89**, 541–546.
Sataloff, R. T. (**1991**). *Professional Voice: The Science and Art of Clinical Care* (Raven, New York).
Schäfer-Vincent, K. (**1983**). ''Pitch period detection and chaining: Method and evaluation,'' Phonetica **40**, 177–202.
Scherer, R. C., Vail, V. J., and Guo, C. G. (**1995**). ''Required number of tokens to determine representative voice perturbation values,'' J. Speech Lang. Hear. Res. **38**, 1260–1269.
Schwartz, J. L., Boë, L. J., Vallée, N., and Abry, C. (**1997**). ''Major trends in vowel system inventories,'' J. Phonetics **25**, 233–253.
Scobbie, J. M., Turk, A. E., and Hewlett, N. (**1999**). ''Morphemes, phonetics and lexical items: The case of the Scottish vowel length rule,'' Proceeding of the XVth International Conference on Phonetic Sciences (San Francisco), pp. 1617–1620.
Sellars, I. E., and Keen, E. N. (**1978**). ''The anatomy and movements of the cricoarytenoid joint,'' Laryngoscope **88**, 667–674.
Stemple, J. C. (**1993**). *Voice Therapy: Clinical Studies* (Mosby-Year, St. Louis).
Sulter, A. M., Schutte, H. K., and Miller, D. G. (**1996**). ''Standardized laryngeal videostroboscopic rating: Differences between untrained and trained male and female subjects, and effects of varying sound intensity, fundamental frequency, and age,'' J. Voice **10**, 175–189.
Sundberg, J. (**1987**). *The Science of the Singing Voice* (Northern Illinois University Press, DeKalb).
Švec, J. G., Schutte, H. K., and Miller, D. G. (**1996**). ''A subharmonic vibratory pattern in normal vocal folds,'' J. Speech Lang. Hear. Res. **39**, 135–143.
Švec, J. G., Schutte, H. K., and Miller, D. G. (**1999**). ''On pitch jumps between chest and falsetto register in voice: Data from living and excised human larynges,'' J. Acoust. Soc. Am. **106**, 1523–1531.
Tanaka, S., Hirano, M., and Umeno, H. (**1994**). ''Laryngeal behaviour in unilateral superior nerve paralysis,'' Ann. Otol. Rhinol. Laryngol. **103**, 93–97.
Taylor, F. J. (**1994**). *Principles of Signals and Systems* (McGraw-Hill, New York).
Titze, I. R. (**1994**). ''Toward standards in acoustic analysis of voice,'' J. Voice **8**, 1–7.
Titze, I. R. (**1995**). *Workshop on Acoustic Voice Analysis: Summary Statement* (National Center for Voice and Speech, Iowa City).
Verdolini-Marston, K., Sandage, M., and Titze, I. R. (**1994**). ''Effect of hydration treatments on laryngeal nodules and polyps and related voice measures,'' J. Voice **8**, 30–47.
Vieira, M. N., McInnes, F. R., and Jack, M. A. (**1996**). ''Analysis of the effects of electroglottographic baseline fluctuation on the F_0 estimation in pathological voices,'' J. Acoust. Soc. Am. **99**, 3171–3178.
Vieira, M. N., McInnes, F. R., and Jack, M. A. (**1997**). ''Comparative assessment of electroglottographic and acoustic measures of jitter in pathological voices,'' J. Speech Lang. Hear. Res. **40**, 170–182.
Watson, C. (**1995**). ''Quality analysis of laryngography in a busy hospital ENT voice clinic,'' Eur. J. Disord. Commun. **30**, 132–139.
Watt, D., and Ingham, C. (**2000**). ''Durational evidence of the Scottish vowel length rule in Berwick English,'' in Leeds Working Papers in Linguistics 8, edited by D. Nelson and P. Foulkes, pp. 205–228.
Wong, D., Ito, M. R., Cox, N. B., and Titze, I. R. (**1991**). ''Observation of perturbations in a lumped-element of the vocal folds with application to some pathological cases,'' J. Acoust. Soc. Am. **89**, 383–394.

Synchrony capture hypothesis fails to account for effects of amplitude on voicing perception

Andrew J. Lotto[a)]
Department of Psychology, Washington State University, PO Box 644820, Pullman, Washington 99164

Keith R. Kluender
Department of Psychology, University of Wisconsin—Madison, 1202 West Johnson Street, Madison, Wisconsin 53706

(Received 5 July 2001; revised 8 November 2001; accepted 13 November 2001)

Kluender *et al.* [J. Acoust. Soc. Am. **97**, 2552–2567 (1995)] reported that overall stimulus amplitude affects perception of the voicing contrast in syllable-initial stops as a function of frequency separation between the first formant (F1) and higher formants (F2, F3). These results were offered as support for a hypothesis that [−voice] could be signaled by a shift in the temporal pattern of neural firing from synchronizing to energy at frequencies of F2 and F3 to synchronizing to energy near F1. Several predictions from this ''synchrony capture hypothesis'' were tested in the current study. In all cases the hypothesis was not supported. Effect of stimulus amplitude (increased voiceless responses with higher amplitude) was maintained when there was no cutback in F1 or when F2 and F1 energy bands were presented dichotically. In further tests of the hypothesis, voice–voiceless series were created that maintained periodic energy throughout the syllable (with F1 cutback signaling voicing). Energy just below the frequency of F2 and energy above F1 were presented dichotically. Thus, at the periphery there was no competition between frequencies near F2 and lower frequencies. In contrast to predictions of the ''synchrony capture hypothesis,'' overall amplitude still had an effect on voice–voiceless identifications. © *2002 Acoustical Society of America.* [DOI: 10.1121/1.1433809]

PACS numbers: 43.71.Es [CWT]

I. INTRODUCTION

The voicing contrast in syllable-initial stop consonants has been a major interest of speech perception researchers for many years. This is due in part to the ubiquity of the voicing distinction in languages (Maddieson, 1984) and in part to the apparent complexity of the mapping from stimulus attributes to perception of the contrast. There are a number of spectral and temporal acoustic attributes that have been shown to affect the identification of a stop as voiced or voiceless (Stevens and Klatt, 1974; Lisker, 1975; Summerfield and Haggard, 1977; Soli, 1983; Kluender and Lotto, 1994).

One attempt to account for the joint effects of some of these spectral and temporal cues is the synchrony capture hypothesis (SCH) offered by Kluender *et al.* (1995). This hypothesis was developed from consideration of the neural response to voiced and voiceless stops and was inspired, in particular, by the work of Sinex and his colleagues on auditory nerve (AN) responses to consonant-vowel (CV) stimuli (Sinex and Geisler, 1983; Sinex and McDonald, 1988, 1989; Sinex *et al.*, 1991). In investigations of synchronization patterns in chinchilla AN fibers, Sinex and MacDonald (1989) demonstrated that mid- and high-CF fibers often responded in synchrony to frequencies near the second formant (F2) of the CV prior to the onset of voicing.[1] These same fibers changed their dominant synchronization to components near the frequency of the first formant (F1) following the onset of voicing. Kluender *et al.* (1995) proposed that this change in dominant synchronization for a population of fibers at the onset of periodicity was a potential signal for voicelessness. Prior to voicing in *voiceless* stops, there is little energy near F1 and the vocal tract is excited by an aperiodic aspiration source. As a result, mid-CF fibers have an opportunity to synchronize to frequencies near F2 and F3 prior to being ''captured'' by F1 energy. In contrast, the release of occlusion and onset of voicing in *voiced* stops (in English) tend to be near simultaneous. Thus, there is energy near F1 from the onset of the consonant and no time for mid-CF AN fibers to synchronize to F2 prior to a change in dominant synchronization. Therefore, according to the SCH, *change* in dominant synchronization of a large population of mid- and high-CF fibers is potential information to the voice contrast at the neural level.

Several predictions were derived from this hypothesis based on previous empirical work on neural synchrony (Sachs and Abbas, 1976; Javel *et al.*, 1983). These predictions were tested by presenting listeners series of synthesized CV syllables that varied from voiced to voiceless. The first prediction was that increases in overall amplitude of CVs should result in more stimuli being identified as voiceless. This prediction arises because synchrony capture, the relative dominance of the synchronization by one frequency component over others, increases with increased amplitude (Javel *et al.*, 1983). In addition, increases in intensity lead to an extension of the low-frequency tails of the response area for a neuron. That is, as amplitude increases, the likelihood of a mid-CF fiber being sensitive to (and becoming synchronized to) com-

a)Electronic mail: alotto@wsu.edu

 0001-4966/2002/111(2)/1056/7/$19.00

ponents near F1 increases. If this change signals voicelessness, as proposed by the SCH, then higher amplitudes should result in more voiceless identifications. In agreement with this prediction, Kluender *et al.* (1995) reported that voiceless identifications increased monotonically as CV amplitude increased from 40 to 60 to 80 dB.[2]

The second prediction was that a decrease in the frequency separation of F1 and F2 would enhance the effect of amplitude on voicing judgments. The rationale for this prediction was that if F1 and F2 were closer in frequency, then energy from F1 would be more likely to fall within the low-frequency tails of a larger population of the fibers that originally synchronized to F2 at stimulus onset. At the onset of voicing, this large group of fibers would more likely switch dominant synchronization to F1, resulting in a more robust signal for voicelessness. Kluender *et al.* reported the results of several experiments that upheld this prediction. When F1 onset frequency was increased or F2 frequency decreased (by changing place of articulation of consonant or identity of following vowel) the effect size of amplitude on identifications was increased.

The SCH is appealing because it relates neural representations to behavior and it appears to account for some of the interaction of spectral and temporal attributes in determining the voice contrast judgment. The results of Kluender *et al.* (1995) related above matched novel predictions made by the hypothesis. In addition, Kluender *et al.* ruled out differential masking of aspiration energy as a cause for the effect of amplitude on identifications because the effect of aspiration level was shown not to interact with overall stimulus level. The SCH seems to be well supported.

The purpose of the experiments reported in this article is to further test the hypothesis by examining some additional predictions of the SCH. The studies reviewed above tested the viability of the SCH by manipulating stimulus parameters thought to enhance the likelihood of synchrony capture. The predictions of the hypothesis would be that these manipulations should lead to more voiceless judgments and that these effects would be a function of overall stimulus level. The present experiments attempt to eliminate the possibility of mid-CF fibers changing their dominant synchronization in CV stimuli. This should eliminate synchrony capture as a cue for voicelessness. The prediction of the SCH is *not* that this will lead to the absence of voiceless responses. There are certainly other attributes that can signal voicelessness, and synchrony capture was never meant to be the sole determiner of the perception of the contrast. Instead, the SCH would predict that without major shifts in temporal encoding from F2 to F1, overall stimulus amplitude should have a reduced or nonexistent effect on voice judgments. That is, if the explanation for the amplitude effect is due to synchrony capture, then one should see a substantially reduced effect when changes in dominant synchronization are limited.

II. EXPERIMENT 1: LACK OF F1 CUTBACK

The SCH of Kluender *et al.* (1995) suggests that the *change* in dominant synchronization for mid-CF fibers from components near F2 to components near F1 during a CV is a cue to voicelessness. The reason this change occurs in voiceless stimuli is because there is little or no energy in the region of F1 prior to voicing (referred to as F1-cutback). One way to eliminate or diminish this potential cue is to present CVs with energy present in the region of F1 throughout the stimulus. With the elimination of F1-cutback most mid-CF fibers should synchronize to F1 from stimulus onset. Thus, there will be a greatly diminished *change* in synchronization to act as a cue. If modulation of the strength of the synchronization cue is the explanation for amplitude effects on voicing judgments, then CV series without F1-cutback should show a smaller identification shift with change in amplitude.

A. Methods

1. Stimuli

Two series of three-formant syllables were created based on the series used in experiment 2 of Kluender *et al.* (1995). One series varied perceptually from /ba/ to /pa/ (labial). The other series varied perceptually from /ga/ to /ka/ (velar). Stimuli were generated using the parallel branch of the Klatt (1980) software synthesizer. The only difference between stimuli in the two series was the frequency of F2 onset. For the labial series, F2 began at 800 Hz, increasing linearly to a steady state of 1220 Hz after 45 ms. For the velar series, F2-onset frequency was 1950 Hz, decreasing linearly to a steady state of 1220 Hz after 45 ms. F1 and F3 parameters were the same for both series. The frequency of F1 at stimulus onset was 300 Hz, rising to 750 Hz over the 45-ms transition duration. F3 began at 1200 Hz, increasing to a steady state of 2600 Hz over the same period. Fundamental frequency ($f0$) was 128 Hz at the beginning of the syllable and decreased to 100 Hz over the last 50 ms. Overall stimulus duration was 300 ms.

For each series, there were 13 stimuli differing in the duration between stimulus onset and voicing onset (5–65 ms in 5-ms steps). Prior to the onset of voicing, all formants were excited with a noise source (amplitude of aspiration synthesizer control parameter AH=65). Note that, while Kluender *et al.* (1995) covaried F1-cutback with the aspiration energy, onset of F1 energy and the onset of energy near F2 and F3 are contemporaneous for these stimuli. All stimuli were matched in rms amplitude of the steady-state portion of the vowel.

Stimuli were synthesized with 12-bit resolution at a 10-kHz sampling rate and stored on computer disk. Stimulus presentation and data collection were under the control of a microcomputer. Following D/A conversion (Ariel DSP-16), stimuli were low-pass filtered (Frequency Devices 677, cutoff frequency 4.8 kHz) prior to being attenuated (Analog Devices AD7111 digital attenuator), amplified (Stewart HDA4), and played over headphones (Beyer DT-100). For each stimulus, the rms energy of the steady-state vowel was matched to a 1000-Hz sine wave of 40, 60, or 80 dB SPL (A) intensity. Calibration of the audio presentation was accomplished by using a Brüel & Kjaer system consisting of a flat-plate adapter (type DB0843) on an artificial ear (type 4153) with $\frac{1}{2}$-in. microphone (type 4134) and sound level meter (type 2203).

2. Subjects

Fourteen college-aged adults participated. All subjects learned English as their first language and reported normal hearing. Each participant received class credit in an Introductory Psychology course.

3. Procedure

One to three subjects were run at one time in three single-subject soundproof chambers (Suttle Equipment Corp.) during a single experimental session consisting of 12-min test periods separated by brief breaks. During each of the three test periods, the two series (labial and velar) of 13 stimuli (5- to 65-ms aspiration noise duration in 5-ms steps) were presented three times in random order at each of the three intensity levels (40, 60, and 80 dB). This yielded a total of nine presentations of each stimulus at each intensity level. Participants were instructed to press a button labeled "BDG" if they heard the syllable as beginning with one of these consonants or to press a button labeled "PTK" to indicate that they perceived one of these consonants. The alveolar responses (D,T) were included in the unlikely case that the participants happened to hear some of the stimulus exemplars as /da/ or /ta/. Thus, responses were generally in terms of voiced versus voiceless.

B. Results and discussion

Kluender *et al.* (1995) did not include in analyses data from any subject who was not able to correctly label the endpoint stimuli (i.e., 5 ms as voiced and 65 ms as voiceless) at least 90% of the time. This was done to exclude participants who may have had difficulty with presentations of syllables at 40 dB. The same criterion was used for inclusion of data in the present experiments. In experiment 1, 6 of 14 subjects failed to respond correctly for at least 90% of the presentations across the 12 end-point stimuli. This ratio of subject loss is slightly higher than that of Kluender *et al.* This may be due in part to the unnaturalness of the stop consonants with no F1-cutback.[3]

Boundary values for each of the six series (labial/velar $\times$presentation level) were calculated for each subject using probit analysis. The SCH would lead to the prediction that for each series (labial and velar) boundary values should remain fairly constant across presentation level. This is because the cue that is proposed to vary with amplitude, synchrony change, has been diminished or eliminated. The mean boundary for each condition is displayed in Fig. 1. As can be seen, the data do not support the prediction of the SCH. For each series, boundaries shift as a function of presentation level. This shift is similar to that reported by Kluender *et al.*, i.e., more voiceless responses at higher overall amplitudes.

Separate one-way within-subjects ANOVA were run on data for each series. These tests revealed that amplitude-based boundary shifts were evident for both the labial [$F(2,14)=49.35$, $p<0.0001$] and the velar [$F(2,14)=20.21$, $p<0.0005$] series. Calculation of protected least significant difference (Keppel, 1982) revealed that identification boundaries differed for each amplitude level in each series ($\alpha=0.05$). An analysis of the mean percentage of [+voice] ("BDG") responses in each condition (as opposed to the boundaries) provided an equivalent pattern of results. Greater stimulus amplitude led to significantly more "voiceless" responses [$F(2,14)=52.11$, $p<0.0001$]. In agreement with the results of Kluender *et al.*, the effect of amplitude was slightly greater for the labial series [$F(2,14)=9.01$, $p<0.005$ for the interaction between place of articulation and stimulus amplitude]. The data clearly demonstrate that the effect of amplitude on voicing judgments is present even for CV stimuli that lack F1-cutback, in opposition to predictions of the SCH.

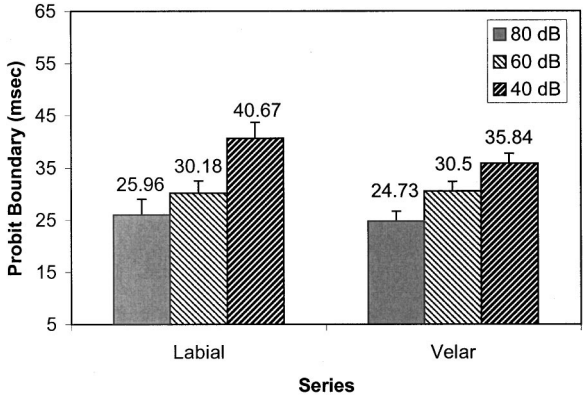

FIG. 1. Mean boundary values (and attendant standard errors) for each series (labial and velar) from experiment 1. The parameter is the overall presentation level (80, 60, or 40 dB).

A more lenient test of the SCH would be to demonstrate that the effect of amplitude decreases substantially with no F1-cutback even if it does not disappear outright. However, the boundary shifts for these series were comparable to the ones obtained by Kluender *et al.* In the present experiment the mean boundary shift for the labial series was 14.71 ms compared to 12.24 ms for Kluender *et al.* (1995, experiment 2). The respective values for the velar series are 11.11 and 3.77 ms. Thus, there is no support here for the predictions of the SCH.

One way to salvage the SCH given these results is to suggest that despite the presence of energy near F1 during the aspiration portion of the CV, this energy was not sufficiently intense to capture the synchronization of mid-CF fibers. The spectrum for the aspiration source in the Klatt (1980) synthesizer is relatively flat. As a result, the relative amplitude of the F1 peak will not differ as much from the amplitude of the F2 and F3 peaks as when the voicing source is used. Perhaps, this reduced difference in amplitude minimized synchrony to F1 by mid-CF fibers. If this were the case, then temporal responses of these fibers would still be dominated by energy near F2 and F3. At onset of voicing, amplitude of energy near F1 increases and could capture the dominant synchronization of these fibers. That is, despite the lack of F1-cutback, change in synchronization may remain a viable cue to voicing.

III. EXPERIMENT 2: DICHOTIC PRESENTATION

Experiment 1 attempted to eliminate the synchrony change cue to voicing by encouraging neurons to encode frequencies near F1 for the duration of the stimulus. Experi-

ment 2 takes a complementary tack. The stimuli are manipulated to eliminate the possibility of mid-CF fibers synchronizing to F1 frequencies at any time during the duration of the CV syllable. This was accomplished by filtering the stimulus and presenting low-frequency energy around F1 to one ear and energy around F2 and F3 to the opposite ear. Because there is no possible opportunity for AN fibers to shift synchronization from F2 to F1, changing stimulus amplitude cannot make the shift more or less likely. According to the SCH, this lack of amplitude affect on synchronization change should eliminate or greatly reduce the effect of amplitude on voicing judgments.

A. Methods

1. Stimuli

Again, velar and labial series of 13 synthesized CVs were created. These stimuli were identical to the original series used by Kluender *et al.* (1995, experiment 2). Unlike experiment 1, energy in the region of F1 was attenuated during the aspirated portion of the signal as occurs in natural productions. This was accomplished by manipulating the amplitude of the filter associated with F1 (parameter A1 set to 0 at syllable onset and to 55 at voicing onset). Each CV was filtered twice using a sharp (eight-pole) elliptical digital filter. For both filters, the cutoff frequency was 1000 Hz. One filter was high pass, resulting in a filtered CV that contained only the second and higher formants. The other filter was low pass, resulting in a filtered CV containing predominantly F1 information. For velar stimuli, this low-pass filtered stimulus contained no appreciable information about F2 as this formant started at 1950 Hz and decreased to 1200 Hz. For the labial stimuli, there was some F2 energy present in this low-pass filtered CV due to the low F2-onset frequency of these syllables (800 Hz). Given the formant structure of the labial syllables, this residue F2 energy was unavoidable. Other than this case, discrete FFTs demonstrated that the filtering resulted in the desired segregation of spectral energy. Filtering was performed off-line and stimuli were saved to disk. The two filtered portions of the CVs were presented time-aligned to opposite ears at 80, 60, and 40 dB (amplitude of entire stimulus prior to filtering).

2. Subjects

Twenty-two college-age adults participated for Psychology course credit. All reported normal hearing and learned English as a first language.

3. Procedure

The procedure was identical to that used in experiment 1. On each trial, the participants were presented both portions (high and low pass) of the filtered CVs at one of three amplitudes (80, 60, or 40 dB). The low-pass portion was always presented to the left ear. Participants identified the syllable-initial consonant as ''BDG'' or ''PTK.''

B. Results and discussion

Two subjects failed to meet the criterion listed for experiment 1 of 90% correct identification across endpoints. Their data were not included in the analyses. Probit boundaries were computed from the identification curves of the remaining 20 subjects. Mean boundaries for each series (labial and velar) at each amplitude (80, 60, and 40 dB) are presented in Fig. 2.

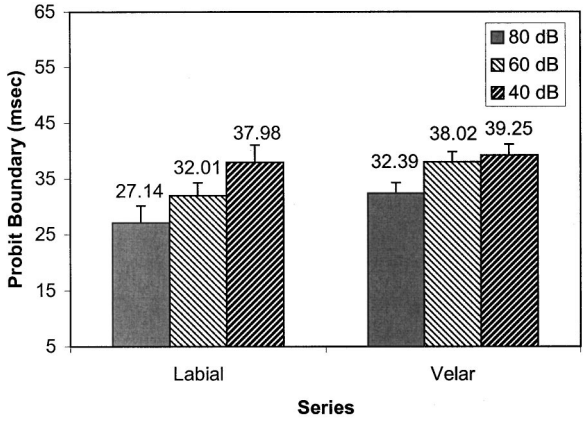

FIG. 2. Mean boundary values (and attendant standard errors) for each series (labial and velar) from experiment 2. The parameter is the overall presentation level (80, 60, or 40 dB).

A one-way ANOVA was computed on boundary values for each series separately. Boundary values decreased (more voiceless responses) with increases in overall amplitude for both the labial series [$F(2,38)=111.68$, $p<0.0001$] and the velar series [$F(2,38)=51.12$, $p<0.0001$]. *Post hoc* tests revealed that the boundaries differed significantly at all three presentation levels for labial stimuli. For velar stimuli, the identification boundary for 40 dB presentation level differed from both the 80 and 60 dB levels, but the two higher-level conditions did not reliably differ from each other. An equivalent pattern of results is present in the mean percentage of [+voice] (''BDG'') responses. Across place, there is a significant effect of stimulus amplitude [$F(2,38)=87.71$, $p<0.0001$].

These data do not support the predictions of the SCH. Mid-CF fibers in the right ear should have synchronized to the components of F2 and F3 at stimulus onset and there would be no opportunity to change synchronization to F1 because there was no energy near F1 presented to that ear. In the left ear, for velar stimuli, there was little or no energy at stimulus onset followed by energy near F1 at the onset of voicing. Thus, mid-CF fibers would again have no opportunity to shift dominant synchronization. For velar stimuli, there should be no change-in-synchrony cue in the firing patterns of the VIIIth nerve for either ear. The SCH would, therefore, predict no effect of amplitude. However, there was an average boundary shift of about 7 ms for the velar series, which is even larger than that obtained in the original experiments of Kluender *et al.*

The results of experiments 1 and 2 provide little evidence supporting the notion that modulation of the shift in synchronization of AN fibers from F2/F3 to F1 is the basis for the effect of amplitude on voicing judgments. However, an alternative synchronization shift cue may account for these data. At the onset of voicing in a CV syllable, there is not only onset of F1 energy but also onset of energy at the

fundamental frequency. Mid-CF fibers could change their dominant synchronization from F2/F3 to $f0$ at voicing onset. This shift could potentially serve as a cue to voicelessness. This slightly modified version of the synchrony capture hypothesis (mod-SCH) would be compatible with the results of experiment 1. The lack of F1 cutback would not affect this shift. What is important for mod-SCH is "$f0$ cutback," so to speak. The aspirated portion of the syllable would allow AN fibers to fire in synchrony to components near F2/F3. Then, the fibers' temporal patterns may encode $f0$ at voicing onset.

The mod-SCH may also be compatible with the results of experiment 2. Despite the filtering of lower frequencies, $f0$ remains present in the high-pass CV stimuli in the harmonics. Theoretically, mid-CF AN fibers in the right ear could first synchronize to F2 and F3 and then switch synchronization to $f0$ at onset of voicing. The likelihood of this shift would be dependent on amplitude, with more fibers shifting synchronization at louder presentation levels. Thus, if the change in temporal synchronization were a cue to voicelessness, one would predict more voiceless judgments at higher intensities. This is exactly the pattern of results in experiment 2.[4] In order to test the SCH-mod, experiment 3 was designed as a variation of experiment 2.

IV. EXPERIMENT 3: DICHOTIC PRESENTATION, NO *f0* CUTBACK

In order to eliminate the possibility of mid-CF fibers *changing* dominant synchronization to $f0$, stimuli were created that signaled voicelessness only through cutback in F1 energy. That is, periodic energy was present throughout the CVs. Absence or presence of energy in the region of F1 remained as a cue to the voicing contrast. These stimuli were then filtered and presented dichotically as in experiment 2. These manipulations should, in tandem, significantly reduce the possibility of sharp changes in synchronization during the CVs. It is clear in this case that the SCH (and the mod-SCH) would predict that the effect of amplitude on voicing judgments should be reduced significantly or should disappear completely.

A. Methods

1. Stimuli

Two series of CVs were synthesized that were identical to those employed in experiment 2 except that periodic energy excited the formants throughout the syllable. That is, there was no aspirated portion in the initial stops (AH=0 throughout). Each step of the series differed in the timing between syllable onset and the onset of significant energy in the region of F1 (controlled by the amplitude of the filter for the first formant; A1 parameter). This duration varied from 5 to 65 ms in 5-ms steps. Each syllable was filtered using the same filters as described in experiment 2. Because high-pass-filtered syllables of each series did not change with varying F1 cutback, the same base labial and velar high-pass-filtered stimuli served as one of the dichotic inputs for each member of the series (the 5-ms F1-cutback stimulus in each case). Thus, the input to this ear provided no information about the voice contrast.

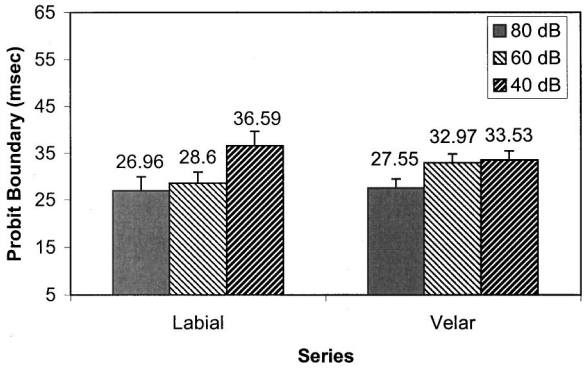

FIG. 3. Mean boundary values (and attendant standard errors) for each series (labial and velar) from experiment 3. The parameter is the overall presentation level (80, 60, or 40 dB).

2. Subjects

Twenty-eight college-aged adults participated in the experiment for class credit. All reported normal hearing and English as their native language. None of the subjects had participated in experiments 1 or 2.

3. Procedure

The procedure was identical to experiment 2. Only the stimuli were changed.

B. Results and discussion

The stimuli used in experiment 3 were very unnatural. The lack of delay in the onset of periodicity eliminates one of the most salient attributes of voiceless stimuli. In addition, the syllables were filtered and presented dichotically; a decidedly unlikely acoustic event outside the laboratory. Not surprisingly, many participants had difficulties consistently labeling these stimuli. What may be surprising is that 25% of the subjects (7 out of 28) were able to label the syllable-initial consonants well enough to pass the rather strict criterion of 90% correct across endpoints. Identification functions from these subjects allowed for the computation of probit boundaries, which can be compared to the results from experiments 1 and 2. Given the large number of subjects failing to reach criterion, both sets of data will be examined separately below.

Mean identification boundaries for each condition were computed from the data of the subjects who passed criterion. Means and standard errors of these boundaries are displayed in Fig. 3. These boundaries were entered into separate one-way ANOVA for each series. The analyses reveal that the effect of amplitude is statistically significant for both the labial [$F(2,18)=5.64$, $p<0.05$] and velar series [$F(2,18)=6.03$, $p<0.01$]. According to *post hoc* comparisons, the boundary for the labial series presented at 40 dB differed significantly from both the 80- and 60-dB boundaries, which did not differ from each other. For the velar series, the 80-dB boundary differed from both the 60- and 40-dB boundaries, which did not differ from each other. Again, the effect of amplitude can also be seen in analyses of the mean percentage of [+voice] responses [$F(2,12)=12.15$, $p<0.005$ across place of articulation].

TABLE I. Mean percentages of [+voice] responses for subjects failing to meet criterion in experiment 3. The atypical data from one subject are presented. Results of one-way ANOVA are included for all subjects failing criterion (df=2,57) and for the same group without the data of the atypical subject (df=2,54).

	80 dB mean	60 dB mean	40 dB mean	*F*-statistic	*p* value
Labial series (all subjects)	56.07	65.22	68.98	3.16	0.097
Velar series (all subjects)	55.91	62.40	66.84	1.31	0.28
Labial series (atypical subject)	94.88	54.71	13.66		
Velar series (atypical subject)	88.05	55.56	10.25		
Labial series (without atypical)	54.03	65.77	71.89	5.37	0.0074
Velar series (without atypical)	54.22	62.76	69.82	2.87	0.065

Because the number of subjects who did not reach criterion was so large, their data was analyzed separately to see if they demonstrated similar trends to those described above. Identification data from these subjects did not provide functions that were amenable to probit analysis. As a result, mean percent [+voice] responses (''BDG'' label) were calculated for each subject in each condition. These means were entered into separate one-way ANOVA for each series. The mean [+voice] judgments *increased* as overall amplitude *decreased* for both series. However, these differences did not reach statistical significance (see Table I). In examining the individual data, one subject's responses were clearly aberrant. This single subject showed a very large effect of amplitude in the opposite direction from the pattern present in the other 20 subjects' data. When this subject's data were eliminated from the analyses, the effects of amplitude on voicing judgments reached statistical significance (see Table I).

The data from both groups of subjects paint a fairly clear picture. The effect of amplitude is still present even for CV stimuli that do not offer an opportunity for mid-CF fibers to change dominant synchronization to components of F1 (experiments 1 and 2) or $f0$ (experiment 3). There isn't any evidence that these effects have been weakened by the stimulus manipulations for experiment 3. The original boundary shifts reported by Kluender *et al.* (1995) were 12.24 ms for the labial series and 3.77 ms for the velar series. For experiment 3, the respective shifts were 9.63 and 5.98 ms. The predictions of mod-SCH were not obtained.

V. GENERAL DISCUSSION

The synchrony capture hypothesis offered by Kluender *et al.* (1995) produced novel predictions about human responses to speech sounds based on data from encoding of CVs in the auditory nerve. The fact that SCH predictions were consistent with multiple empirical tests provided an example of the utility of integrating neurophysiological results into speech perception theory. The experiments presented here were designed to further test the validity of this hypothesis. In each experiment, CV stimuli were manipulated to reduce the probability that mid-CF auditory nerve fibers would change their dominant synchronization during the course of the stimulus. According to the SCH, these manipulations should reduce the shift in voiced–voiceless identifications that occur when overall stimulus amplitude changes. The results of these three experiments were unequivocal. Whether F1 cutback was eliminated or lower and higher frequencies were presented to opposite ears, the effect of amplitude on voicing judgments remained undiminished. Even the extreme manipulation of deleting the delay between stimulus onset and voicing onset (and presenting the stimuli dichotically) did not alter the effect of amplitude.

Absent an explanation from the SCH,[5] the robust effect of amplitude on voicing judgments as well as the details of effects related to frequency separation between F1 and higher formants remain unexplained. These identification shifts, first described by Van Tassell and Crump (1981), have obvious implications for speech amplification. The size and resiliency of these effects are remarkable when compared to other speech perception effects. Stimulus amplitude effects remained strong through all of the stimulus manipulations of Kluender *et al.* (1995) and the present set of experiments.

One alternative explanation for these shifts is that lower amplitudes compromise the detection of the onset of aspiration. The duration between aspiration onset and voicing onset is considered an important cue to the voicing distinction (Lisker and Abramson, 1964). Cortical potentials elicited from stop+vowel stimuli usually show a peak corresponding to aspiration or burst onset and a second peak corresponding to the onset of voicing (Koch *et al.*, 1997; Sharma and Dorman, 1999). It is possible that when the amplitude of the syllable is decreased, the neural representation of the aperiodic energy onset is more affected than the onset of voicing. Periodic energy in natural speech is typically higher in amplitude [it was in all of the stimuli used by Kluender *et al.* (1995)] and the predictable nature of the periodic signal may provide some protection from the effects of lower amplitude. In contrast, the onset of aspiration energy may be easily compromised. From a signal detection viewpoint, more temporal information may be required to detect the onset of the aspiration noise when the amplitude is decreased. This could lead to more [+voice] responses at lower amplitudes, which matches the effect as reported (Van Tassel and Crump, 1981; Kluender *et al.*, 1995). In addition, this explanation would predict less of an effect of amplitude for velar stimuli. Velar

consonants are distinguished by a compact concentration of aspiration energy as the frequencies of F2 and F3 begin close together. This should result in a clearer marking of the onset of the aspiration in those frequency bands. As a result, the deleterious effects of amplitude would be ameliorated. This prediction is supported in the current data and in data from Kluender *et al.*

As plausible as this explanation may seem, it also fails to account for all of the data. In experiment 4 of Kluender *et al.*, aspiration level was manipulated but did not interact with the effect of overall stimulus amplitude. In their experiment 5, natural tokens were used with bursts present or filtered off. Bursts should provide a compelling signal to stimulus onset, but burst presence did not modulate the effects of amplitude. In experiment 3 of this report, the voice contrast was signaled only by F1-cutback with periodic energy present throughout the stimulus. The resulting identification functions still showed boundary shifts that were dependent on amplitude. These three stimulus manipulations should have provided better markers for stimulus onset, yet none appeared to interact with overall amplitude.

The effect of amplitude on voicing judgments remains unexplained. Synchrony capture cannot explain the effect. While the present results most clearly eliminate synchrony capture as an explanation for effects of amplitude, it must be noted that the only perception data supporting the SCH relied critically upon amplitude effects being closely tied to changes in synchrony. As such, the SCH is left to rest solely upon physiological observations from cat and chinchilla. Absent compelling new data from humans, the SCH must be viewed with some skepticism.

ACKNOWLEDGMENTS

Some of the data were presented at the 131st Meeting of the Acoustical Society of America in Indianapolis, IN. The authors thank Quentin Summerfield for comments on the original synchrony capture paper that inspired some of these experiments. Research supported by NSF Grant No. DBS-9258482.

[1]We will use the term ''voicing'' to refer to the presence of periodic energy. This is somewhat imprecise because the term is articulatory and we are only concerned here with attributes of the acoustic signal regardless of the source. In addition, we use the terms ''labial'' and ''velar'' to refer to stimuli differing in F2 onset frequency. However, this manner of usage is common in the speech field and we have decided to sacrifice precision for ease of reading. We have avoided the articulatory term ''voice-onset time'' because its use has traditionally confounded several attributes of the signal (e.g., F1-cutback, duration of aspiration) that are manipulated independently in this study.

[2]The steady-state vowel portions of these stimuli were matched in rms energy to a 1000-Hz sine wave of 40, 60, or 80 dB intensity.

[3]The trends described in the results section were also obviously present in the data of the subjects who failed to pass criterion.

[4]Kluender *et al.* (1995) concentrate on synchrony capture by F1 and generally ignore $f0$. Part of the reason for this is that the computational models on which the SCH are based (Jenison *et al.*, 1991) use a synchrony measure that is fairly insensitive to $f0$.

[5]Here we are dismissing the hypothesis that modulation of synchrony capture by F1 (or $f0$) underlies the effects of amplitude on voicing judgments. We are *not* claiming that synchrony capture does not exist in the auditory nerve nor that synchrony capture has no effect on perception of auditory signals.

Javel, E., McGee, J., Walsh, E. J., Farley, G. R., and Gorga, M. P. (**1983**). ''Suppression of auditory nerve responses. II. Suppression threshold and growth, iso-suppression contours,'' J. Acoust. Soc. Am. **74**, 801–813.

Jenison, R. L., Greenberg, S., Kluender, K. R., and Rhode, W. S. (**1991**). ''A composite model of the auditory periphery for the processing of speech based on the filter response functions of single auditory-nerve fibers,'' J. Acoust. Soc. Am. **90**, 773–786.

Keppel, G. (**1982**). *Design & Analysis* (Prentice–Hall, Englewood Cliffs, NJ).

Klatt, D. H. (**1980**). ''Software for a cascade/parallel formant synthesizer,'' J. Acoust. Soc. Am. **67**, 971–995.

Kluender, K. R., and Lotto, A. J. (**1994**). ''Effects of first formant onset frequency on [-voice] judgments result from auditory processes not specific to humans,'' J. Acoust. Soc. Am. **95**, 1044–1052.

Kluender, K. R., Lotto, A. J., and Jenison, R. L. (**1995**). ''Perception of voicing for syllable-initial stops at different intensities: Does synchrony capture signal voiceless stop consonants?,'' J. Acoust. Soc. Am. **97**, 2552–2567.

Koch, D., Tremblay, K., Dunn, I., Dinces, E., Carrell, T., and Kraus, N. (**1997**). ''Speech-evoked N1 and mismatch neurophysiologic responses in cochlear implant users and normal listeners,'' Assoc. Res. Otolaryngol. Abstr. **20**, 80.

Lisker, L. (**1975**). ''Is it VOT or a first-formant transition detector?,'' J. Acoust. Soc. Am. **57**, 1547–1551.

Lisker, L., and Abramson, A. S. (**1964**). ''A cross-language study of voicing in initial stops: Acoustical measurements,'' Word **20**, 384–422.

Maddieson, I. (**1984**). *Patterns of Sounds* (Cambridge U.P., Cambridge).

Sachs, M. B., and Abbas, P. J. (**1976**). ''Phenomenological model for two-tone suppression,'' J. Acoust. Soc. Am. **60**, 1157–1163.

Sharma, A., and Dorman, M. (**1999**). ''Cortical auditory evoked potential correlates of categorical perception of voice-onset-time,'' J. Acoust. Soc. Am. **106**, 1078–1083.

Sinex, D. G., and Geisler, C. D. (**1983**). ''Responses of auditory-nerve fibers to consonant-vowel syllables,'' J. Acoust. Soc. Am. **73**, 602–615.

Sinex, D. G., and McDonald, L. P. (**1988**). ''Average discharge rate representation of voice-onset time in the chinchilla auditory nerve,'' J. Acoust. Soc. Am. **83**, 1817–1827.

Sinex, D. G., and McDonald, L. P. (**1989**). ''Synchronized discharge rate representation of voice-onset time in the chinchilla auditory nerve,'' J. Acoust. Soc. Am. **85**, 1995–2004.

Sinex, D. G., McDonald, L. P., and Mott, J. B. (**1991**). ''Neural correlates of nonmonotonic temporal acuity for voice onset time,'' J. Acoust. Soc. Am. **90**, 2441–2449.

Soli, S. (**1983**). ''The role of spectral cues in discrimination of voice onset time differences,'' J. Acoust. Soc. Am. **73**, 2150–2165.

Stevens, K. N., and Klatt, D. H. (**1974**). ''Role of formant transitions in the voiced-voiceless distinction for stops,'' J. Acoust. Soc. Am. **55**, 653–659.

Summerfield, Q., and Haggard, M. (**1977**). ''On the dissociation of spectral and temporal cues to the voicing distinction in initial stop consonants,'' J. Acoust. Soc. Am. **62**, 435–448.

Van Tassel, D. J., and Crump, E. S. A. (**1981**). ''Effects of stimulus level on perception of two acoustic cues in speech,'' J. Acoust. Soc. Am. **70**, 1527–1529.

Detecting stop consonants in continuous speech

P. Niyogi[a] and M. M. Sondhi
Bell Laboratories, Lucent Technologies, 600 Mountain Avenue, Murray Hill, New Jersey 07974

(Received 1 September 2000; revised 25 June 2001; accepted 25 June 2001)

The problem of implementing a detector for stop consonants in continuously spoken speech is considered. The problem is posed as one of finding an optimal filter (linear or nonlinear) that operates on a particular appropriately chosen representation, and ideally outputs a 1 when a stop occurs and 0 otherwise. The performance of several variants of a canonical stop detector is discussed and its implications for human and machine speech recognition is considered. © *2002 Acoustical Society of America.* [DOI: 10.1121/1.1427666]

PACS numbers: 43.72.Ar, 43.71.An, 43.72.Ne [DOS]

I. INTRODUCTION

We are exploring a framework for speech recognition that utilizes the notion of distinctive features (Jakobson *et al.*, 1952). Approaches based on such notions were previously developed primarily in rule-based, artificial intelligence frameworks (Lesser *et al.*, 1975; Wolf and Woods, 1977) that relied mainly on the intuition of expert phoneticians to define the acoustic phonetic features and their properties. While such systems showed some initial promise, they proved ultimately to be brittle in the face of the tremendous variability in real speech signals. Variability is best captured statistically and here we revisit the feature-based approach in a modern, statistical context where we attempt to derive detectors by optimizing recognition performance for labeled databases.

An important problem that needs to be solved for the success of such an approach is the accurate and robust detection of various phonetic classes. The acoustic cues for the different phonetic events are distributed nonhomogeneously in the time-frequency plane, so separate detectors need to be constructed for each phonetic class. These detectors need not all use the same representation. In principle, each such detector may use a different representation that is most suited for the phonetic event it is designed for. This is in contrast to approaches (e.g., most current approaches as in Rabiner and Juang, 1993 or Jelinek, 1997) that use the same representation for all sound classes without special attention to their particular attributes.

In this paper, we focus on the problem of detecting stop consonants[1] in continuous speech. Stops present a particularly challenging case because of their highly transient acoustic characteristics and surprisingly, we found very few extensive studies (see Liu, 1995 for discussion) that focus exclusively on this task. In future publications, we will present detectors for detecting other phonetic classes such as fricatives, nasals, and so on.

Progress on the problem of implementing feature detectors will be useful for a number of reasons. A good feature detector will certainly advance the state of the art in technological applications such as automatic speech recognition, segmentation, or alignment. We also hope it will be useful for researchers in human speech perception and acoustic phonetics. A satisfactory account of speech perception will ultimately need to specify a precise mechanism for successfully recovering the linguistic identity from the speech signal. We might view the current paper as an exploration of one such mechanism for a subtask of some importance in speech perception. It is therefore desirable for us to proceed in a manner that allows the performance of our detectors to be interpreted in a phonetically or perceptually meaningful manner.

Some aspects of the work presented in this paper are worth highlighting.

(1) The characteristic signature of a stop consonant is a complete closure of the vocal tract followed by a sharp release of broadband energy, especially at high frequencies. We therefore represent a stop by its spectral energies and its Wiener entropy, which provides a measure of spectral flatness, to characterize the broadband nature of the burst. All spectra have been computed using multitapered spectral[2] methods (Thomson, 1982).

(2) We propose to solve the problem of stop detection by constructing an optimal filter that operates on the above-mentioned representation such that the output is high when there is a stop and low otherwise. Previous attempts at stop detection have typically attempted to take time derivatives in appropriately chosen energy bands (Liu, 1995). While this is intuitively a reasonable thing to do, differential operators are a specific kind of linear operator and not necessarily optimal for this task. The filter derived by our method depends on the optimality criterion chosen. We compare the performance of several optimal filters with that of the differential operator, and show significant improvement.

(3) As a way to characterize the performance of our feature detection approach, we obtain ROC curves for the stop detection problem on the multispeaker TIMIT database. When the correct detection rates range from 70% to 90%, the insertion rates range from 5% to 20%. Previous published accounts of feature detection typically do not present ROC curves. It is also worthwhile to note in this context that the problem of *detecting* (with its associated type I and type II errors) an acoustic–phonetic feature in continuous speech has not been explicitly studied before to the best of our knowledge. Many recent acoustic–phonetic recognition stud-

[a]Electronic mail: niyogi@cs.uchicago.edu

ies have focused on *classification* where segmented data are available to the recognition algorithms (see, e.g., deMori and Flammia, 1993; Meng *et al.*, 1991; Djezzar and Haton, 1995). Notions of distinctive features have also been utilized as a way of structuring HMMs in continuous speech applications (Kirchhoff, 1996; Eide *et al.*, 1993) but without any attempt to detect the acoustic correlates of such features explicitly.

(4) Our optimal filters require only 33 parameters to achieve the above-quoted performance. Since the number of distinctive features in human language is small and of the order of 6–12, this encourages us to believe that a full-fledged speech recognizer based on feature detectors would require far fewer parameters than traditional HMM-based systems making the task of training and adapting such systems much easier.

(5) We perform a detailed analysis of the errors committed by our detection algorithms. We discuss the errors by phonetic class where we show that in the above-mentioned approach most of the false negatives (stops that are not detected) are due to poorly released stops. Many of the false positives (other phonetic events falsely detected as stops) can be explained as glottal stops or closures followed by strident fricatives (that are perceptually often like stops). On examining the errors by speaker identity, we find that the speakers on whom the detection algorithms fail often have[3] "vocal fry." On examining the errors by syllable structure, we see that stop consonants in syllable initial position are detected far more accurately than those in syllable final positions.

(6) It is well known that when there is a mismatch between training and test sets, automatic speech recognition performance rapidly deteriorates. We use distinctive feature detection as an entry point to understanding the causes of this deterioration and to this end, we study the performance of the stop detector derived from TIMIT on test sentences in the NTIMIT database, i.e., with a mismatch between training and test environments. Expectedly, there is degradation in performance. Our detectors rely heavily on finding a closure–burst transition in the speech signal. The burst is a low energy event and therefore this transition is greatly weakened by adding noise. We show that much of the degradation from TIMIT to NTIMIT is simply explained by degradation in local signal-to-noise ratio at the burst. This explanation is also supported by an analysis of stop detection performance in the presence of additive global and local noise that we conduct in this paper.

(7) While detailed results are presented for the case of stop detection, our overall approach can be utilized to detect other kinds of phonetic events as well. For example, nasals in the context of a neighboring vowel might be detected by looking for an abrupt change in energy in the region of the second formant.

Our study raises questions regarding the role of burst cues for the detection and perception of stop consonants in continuous speech, especially in the presence of noise. A considerable amount of literature exists on the role of burst cues and transient cues of this nature. One strand pertains to the role of durational quantities like voice onset time (VOT) in the voiced–unvoiced distinction for stop consonants. VOT is seen to be a perceptually salient quantity (Abramson and Lisker, 1970; Niyogi and Ramesh, 1998) and its accurate estimation would seem to require one to extract the time at which a closure–burst transition occurs. A second strand relates to the possible role that burst spectra play in the perception of place of articulation for stop consonants (Stevens and Blumstein, 1978; Blumstein and Stevens, 1979; Ohde and Stevens, 1983; Cassidy and Harrington, 1995; Smits *et al.*, 1996). The burst spectra and associated quantities (like the burst frequency) are usually measured with a short window (5–15 ms) centered on a point shortly after the onset of the burst. To do this reliably would also require one to estimate the time at which the burst onset occurs. Others (Furui, 1986) have also suggested that transitional quantities like the onset of the burst are important cues used in human phonetic perception.[4] Indeed, much of the phonetically motivated stop/plosive recognition literature uses burst spectra to classify the *place of articulation* of stop consonants showing good performance. Crucially, however, if the human perceptual apparatus is to use information contained in the burst to detect and classify stop consonants, it must have access to the onset of the burst and mechanisms for detecting it and estimating the time of its onset from continuous speech. Yet few systematic attempts to either provide an algorithmic framework for a burst detector or characterize the performance of such a detector (Liu, 1995 is a notable exception) exist. This paper might be viewed as a step in this direction.

II. THE STOP DETECTION PROBLEM

Stop consonants are produced by causing a complete closure of the vocal tract followed by a sudden release. Hence they are signaled in continuous speech by a period of extremely low energy (corresponding to the period of closure) followed by a sharp, broadband signal (corresponding to the release). As a result, stops consonants are highly transient (dynamic) sounds that have a varying duration lasting anywhere from 5 to 100 ms. In American English, the class of stops consists of the sounds {p,t,k,b,d,g}.

In order to build a detector for stop consonants in running speech, we have chosen to represent[5] the speech signal $s(t)$ by a time series of three-dimensional vectors, $\mathbf{x}(n) = [x_1(n)x_2(n)x_3(n)]'$ at a sampling rate of 1000/s. The index n thus represents time in milliseconds. The vector $\mathbf{x}(n)$ is derived from the short time spectrum $S(f,n)$ computed over a 5 ms segment of the speech signal centered at the sampling instant n. The first two components $x_1(n)$ and $x_2(n)$ are defined as $\log e(n)$ and $\log e_h(n)$, respectively, where $e(n)$ is the total energy and $e_h(n)$ is the energy above 3 kHz. The third component, $x_3(n)$ is chosen to be the Wiener entropy, $E(n)$, defined as

$$E(n) = \int \log(S(f,t))df - \log\left(\int S(f,t)df\right).$$

Measuring the feature vector $\mathbf{x}$ at 1 ms intervals potentially allows us to track rapid transitions that would otherwise be smoothed out by a coarser temporal resolution. This is particularly important since previous studies (e.g., Niyogi and Ramesh, 1998; Abramson and Lisker, 1970; Zue, 1976)

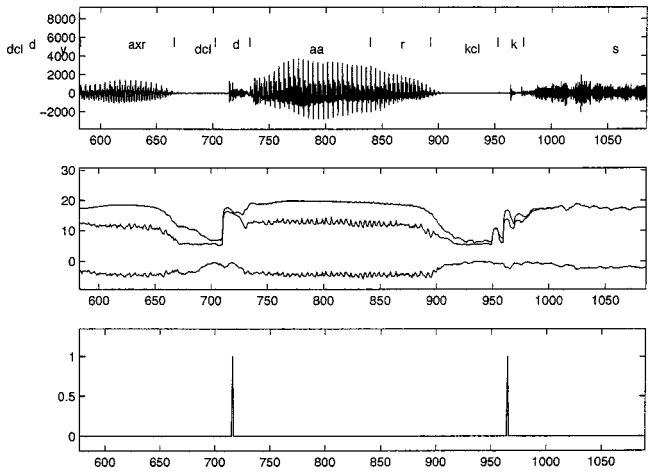

FIG. 1. Portion of the speech wave form $s(n)$ (top panel), the associated three-dimensional feature vector, $\mathbf{x}(n)$ (middle panel), and the desired output $y(n)$ bottom panel marking the times of the closure–burst transition.

indicate that burst durations for voiced stops could be as short as a few milliseconds. The Wiener entropy, which is a measure of spectral flatness, can be interpreted as a Kullback–Liebler divergence between $S(f,t)$ and a flat spectrum. It is also related to the predictability of the process $s(t)$. It therefore allows us to separate noisier parts of the speech signal (bursts, fricative, etc.) from more periodic, predictable parts (like vowels, nasals, etc.).

We need to find an operator on the feature vector time series that will return a single-dimensional time series that takes on large values around the times that stops occur and small values otherwise. The most natural points in time that mark the presence of stops are the transitions from closure to burst release. Shown in Fig. 1 is an example of a speech wave form $s(n)$, the associated feature vector time series $\mathbf{x}(n)$, and a desired output $y(n)$. The technical goal is to find an operator h on the time series $\mathbf{x}(n)$ that produces an output $y_h(n)=h\circ\mathbf{x}(n)$ such that $\|y-y_h\|$ is small in some sense. Specifically, we choose the optimal operator (from some class $\mathcal{H}$ of operators) so as to minimize a risk $R(h)$ associated with the operator h. We choose the risk to be the expected mean squared error between y and y_h. Thus we choose the optimal operator according to the criterion

$$h_{\text{opt}}=\arg\min_{h\in\mathcal{H}} R(h)=\arg\min_{h\in\mathcal{H}} E[\|y-y_h\|^2]$$
$$=\arg\min_{h\in\mathcal{H}} E[(y-y_h,y-y_h)]. \qquad (1)$$

Both y and y_h are random time series and we denote the inner product between two time series a and b by (a,b). We assume a probability distribution P on an ensemble $X\times Y$ according to which the paired time series $(\mathbf{x},y)$ can be drawn as random sample paths. The expectation shown in Eq. (1) is taken over P, i.e., it is an ensemble average in the usual sense. The distance metric on the space Y is given by $d(y_1,y_2)=\|y_1-y_2\|^2=(y_1-y_2,y_1-y_2)$ in the usual way. Now we see the following:

$$E[\|y-y_h\|^2]=E[(y-y_h,y-y_h)]$$
$$=E[(y-p+p-y_h,\ y-p+p-y_h)],$$

where p is the conditional mean, i.e., $p=E[y|\mathbf{x}]=\int yP(y|\mathbf{x})dy$ where the integration is performed over the ensemble space of possible time series. Thus p is (i) a time series and (ii) depends upon $\mathbf{x}$. Expanding the terms in the inner product, we get

$$E[\|y-y_h\|^2]=y-p\|^2+\|p-y_h\|^2+2E[(y-p,p-y_h)].$$

The cross-product term in the above-given expression is zero. To see this, we take the expectation first with respect to $P(y|\mathbf{x})$ (indicated by $E_{Y|X}$) and then with respect to $P(\mathbf{x})$ (indicated by E_X). Thus,

$$E[(y-p,p-y_h)]=E_XE_{Y|X}[(y-p,p-y_h)].$$

Note that p and y_h depend only upon $\mathbf{x}$ and therefore, by linearity, the expectation with respect to $P(y|\mathbf{x})$ can be taken inside the inner product giving

$$E_X[(E_{Y|X}[(y-p)],p-y_h)].$$

But $E_{Y|X}[y-p]=0$ since p is the conditional mean. Hence, we have

$$E[\|y-y_h\|^2]=E[\|y-p\|^2]+E[\|p-y_h\|^2].$$

Thus we see that minimizing $R(h)$ over all operators $h\in\mathcal{H}$ is equivalent to finding the operator h which minimizes the quantity $E[\|E[y|\mathbf{x}]-y_h\|^2]$. In other words, the operator h is chosen so that y_h is the best approximation to $E[y|\mathbf{x}]$ in the above-presented sense.

We have been denoting by $p(n)=E[y|\mathbf{x}]$ the fixed time series whose value at time n is given by $E[y(n)|\mathbf{x}]$. Since y is a time series that takes on values in $\{0, 1\}$ at each time instant, we see that

$$p(n)=1.P(y(n)=1|\mathbf{x})+0.P(y(n)=0|\mathbf{x})$$
$$=P(y(n)=1|\mathbf{x}).$$

In other words, $p(n)$ is simply the *a posteriori* probability that a closure–burst transition is present at time n given the entire speech data time series $\{\mathbf{x}(n)\}$. The purpose of the previous discussion was to show that it is this *a posteriori* probability that is approximated by y_h. Thus if an operator is trained by minimizing the risk $R(h)$ then its output can be interpreted as an approximation to the conditional probability of a stop at that point in time. This allows us to interpret the output of the stop detector (or feature detector in general) in a probabilistic fashion for integration into more general speech recognition systems at a later stage.

In this paper, we consider in detail only linear convolution operators $h\circ\mathbf{x}=h*\mathbf{x}$ although we demonstrate, in one section (Sec. III), the concrete improvements that can be obtained by nonlinear operators as well. In actual practice, we deviate from the formulation of Eq. (1) since we do not have access to the true distribution that generates the time series $\{\mathbf{x}(n),y(n)\}$ and so cannot compute $R(h)$. We actually approximate $R(h)$ by an empirical risk $R_{\text{emp}}(h)$ computed from labeled examples (training data). $R_{\text{emp}}(h)$ is defined as follows.

Let N be the number of sentences in the training set. Further, let N_k be the length of the kth sentence where each

sentence corresponds to a particular realization of the process $(\mathbf{x},y)$. Let the kth sentence in the training set have m_k stops with corresponding closure–burst transitions occurring at times n_{kl} $(l \in \{1,...,m_k\})$, respectively. Then define $y^{(k)}(n)$ to be the *desired* 0–1 valued time series that is 0 everywhere except for values of $n=n_{kl}$ where it takes the value 1. The approximation to this desired output is $y_h^{(k)}(n) = \Sigma_{i=1}^{3}\Sigma_j x_i^{(k)}(n-j)h_i(j)$. Then the empirical risk is defined as

$$R_{\text{emp}}(h)=\sum_{k=1}^{N}\sum_{n=1}^{N_k} w^{(k)}(n)(y^{(k)}(n)-y_h^{(k)}(n))^2.$$

Note that we have introduced a weighting function, $w^{(k)}(n)$, which is also 0–1 valued and is such that $w^{(k)}(n) = 1$ everywhere except for $0<|n-n_{kl}|<W$ where it takes the value 0. The reason for introducing such a weight function is discussed in remark (2) below.

Some remarks are in order.

(1) Our formulation is an optimal filter design problem. The filter coefficients are denoted by $h_i(j)$, where h_i refers to the ''subfilter'' acting on the ith dimension of the input time series $\mathbf{x}$. (In the case we consider here, there are three dimensions.) Its solution can be obtained by adaptive means using recursive least squares techniques. The filter can be trained from data to optimally match the desired output y. Taking derivatives of energy (correspondingly differences of energy at successive times) corresponds to a particular choice of the linear filter h.

(2) The function $w^{(k)}(n)$ serves to define a ''don't care'' region around each stop (specifically the closure–burst transition). It weights the data so that parts of the signal near a stop transition (but not exactly at it) are not taken into consideration. This is because it is not completely clear what a desirable output is near a transition. Further, from a numerical point of view, this allows the output $y_h^{(k)}$ some time to move smoothly from 0 to 1 and back again to 0 at the stops. In our experiments, the value of W was set at 6, i.e., a don't care region was effective from 5 ms before to 5 ms after a closure–burst transition. An optimal choice of W was not attempted.

(3) In our experiments, we set $h_i(m)$ to be zero if $|m| \geqslant 6$. Thus there were $(33=3\times11)$ free parameters for the filter that were then optimally learned from the training data in the manner described. On a test sentence, stops were detected by thresholding the output y_h obtained by filtering the feature vector $\mathbf{x}$ with h.

Finally, it is important to emphasize that the speech recognition problem can be decomposed into a collection of feature detection subproblems that have a structure very similar to that of the stop detection problem described previously. Consider, for example, the problem of detecting nasals in continuous speech. Nasals in American English always occur adjacent to vowels and the transition from a vowel to a nasal is marked, among other things, by a sharp drop of energy in the regions surrounding the second formant, a broadening of the bandwidth of the first formant, and a change in spectral tilt since most of the energy in the nasal is in the first formant region. These changes may be explained by the changing resonance patterns of the vocal tract and the associated coupling with the nasal cavity that is brought into play. Consequently, in a representation that measures the relevant acoustic properties, vowel nasal transitions would have a characteristic signature that may be detected using the approaches discussed in this paper. Or consider the problem of detecting a transition from an obstruent segment to a sonorant one. In this case, a detector might be built with a representation $\mathbf{x}$ consisting of dimensions like degree of periodicity in the signal, ratio of high frequency to low frequency energy, presence of formant structure, and so on. In general, the transition from one broad phonological (manner) class to another is the canonical problem that may be tackled using our approach. In contrast, other kinds of features like the vocalic features of [back/front] or [high/low] or features related to place of articulation of consonants might require a substantially different approach from that suggested here.

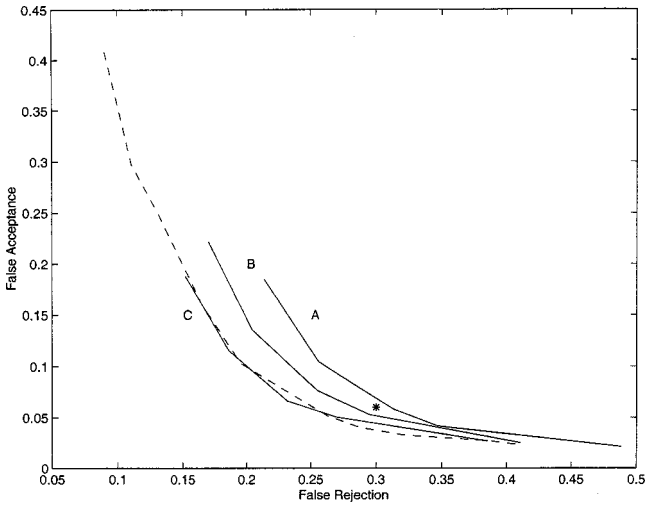

FIG. 2. ROC curves for detection of stop consonants using three different algorithms described in text.

III. EXPERIMENTAL RESULTS

We present results of several stop detection algorithms on the TIMIT database. All results are presented on dialect[6] region 4 of the test set containing 32 speakers, 16 male and 16 female saying ten sentences each, resulting in a total of 320 sentences. At every point in time (ms), the detection algorithm could potentially postulate the existence of a stop—clearly, as in any detection problem, one will need to balance the false acceptance rate (percentage of false detects, i.e., insertions) against the false rejection rate (percentage of stops not detected). This is done by varying the threshold for acceptance. As one varies this threshold one generates a ROC (receiver operating characteristic) curve. In Fig. 2, we show ROC curves for three different algorithms. The curves in Fig. 2 are for the following algorithms.

(1) *Algorithm A.* Here the detector h is simply a differential energy operator over log(energies) in the two subbands. The specific operation is given by $y_h=\Sigma_{i=1}^{2}(x_i(n) - x_i(n-1))$. This corresponds to a particular choice of filter h where the filter coefficients take values $+1$ and -1 at

successive times for each dimension and the length (support) of the filter is 2. Of course, such a choice of h is not optimal in the class of linear filters.

(2) *Algorithm B*. Here the detector h is an optimal linear operator over log(energies) in the two subbands. Thus $y_h = \Sigma_{i=1}^{2} \Sigma_j x_i(j) h_i(n-j)$ but the values of $h_i(m)$'s are now chosen optimally by minimizing $R_{\text{emp}}(h)$ constructed appropriately as in the formulation in Sec. II. The detector obtained by this method is similar in structure to the one obtained by algorithm A except that its coefficients have been optimally chosen.

(3) *Algorithm C*. Here the detector h is an optimal linear operator over all three components of the vector $\mathbf{x}$, i.e., the two energy components and the Wiener entropy. This is the complete formulation described in Sec. II.

The overall conclusion from these experiments is that it is possible to attain an equal error rate of about 16% on TIMIT speakers with a 33 parameter linear filter trained on 4 speakers.

Some further points need to be made here.

(1) In order to go from the output y_h to a set of candidate times n_i where stops are postulated, we need a decision rule. An appropriate one to use is to threshold y_h and pick peaks after thresholding. Each candidate peak n_i, was considered to be a correct detection if it was within 20 ms of the TIMIT labeling of the closure–burst transition, otherwise it was considered to be a false insert. The primary reason for having this 20 ms leeway is to compensate for inaccurate labelings that are present in the TIMIT database.

(2) Since there are only 33 parameters in the full-scale linear filter, the optimal parameters can be derived from very few training data. Specifically, in the present experiments, we selected 4 speakers at random (2 male and 2 female) from the TIMIT training database with 10 sentences from each, making a total of 40 sentences on which the detectors were trained. These 40 training sentences contained 133 stops in all. The ROC curves were tested on the much larger subset of the TIMIT database described previously. This test set contained 1376 stop consonants and 12 064 realizations of other phones. The false rejection rate was obtained by simply counting the total number of stops that were missed by the detector and dividing by 1376. The false acceptance rate was obtained by counting the total number of firings of the detector that was not associated with any stop and dividing by 12 064. It is important to recognize that the detector provides an output every frame, i.e., every millisecond. Therefore the false acceptance rate could also have been computed by counting how many nonstop frames were misclassified as stops. Since the total number of frames is much higher than the number of phones, this would provide a much lower number for false acceptance than that reported here. Researchers have considered the problem of detecting phonetic events in running speech (Glass and Zue, 1986; Liu, 1995; Mermelstein, 1977). Unfortunately, they have not published ROC curves, nor compared their performance to other methods.

(3) The asterisk shown in Fig. 2 corresponds to the performance of a full blown HMM (32 mixtures; 3 state left-to-right models; 47 phonemes; free grammar; 450 000 parameters). The HMM was trained on an extremely large database collected under similar acoustic conditions and tested on the TIMIT sentences. The HMM output was decoded to segment the signal into stops and nonstops. Each closure–burst transition was considered to be correctly detected if it fell *anywhere* within a segment postulated as a stop by the HMM. This is a concession to the fact that the HMM is not designed to specifically locate the closure–burst transition. The performance of an HMM for this experiment has been included just to serve as a point of reference to give a very rough idea on HMM-based performance. It should be interpreted really as a sanity check to make sure that the performance of the detectors discussed here is reasonable. Several additional caveats with respect to HMM-based performance should be noted. First, it may be possible to design specially tuned HMM-based systems for detection of stop consonants that perform better than the HMM-based system used by us. We have not encountered such an HMM-based stop detector in the literature so far. Second, the HMM-based system used here was not trained on TIMIT but on a much larger database with similar acoustic characteristics. This is mostly because much more data were required to train the full system than was available to us. Recall that the detectors designed in this paper were trained on exactly 40 sentences of TIMIT—this is much too inadequate for training a large HMM-based system.

(4) The procedure outlined previously can be extended to detection of other phonetic events, as well as to improve stop detection. From an algorithmic point of view what is needed for each such extension is a choice of representation, a choice of the class of operators $\mathcal{H}$, and a decision rule. We are currently investigating other broad class transitions, e.g., fricative–vowel and vowel–nasal transitions.

Further improvements in detector structure. The framework described previously is sufficiently general in that it allows one to choose an optimal operator ($h \in \mathcal{H}$) that yields an output that is high when closure–burst transitions occur and low otherwise. It is clear from the previous discussion that the problem reduces to separating two kinds of patterns from each other. Each pattern corresponds to an 11 ms patch of signal. One way to improve this further is by generalizing the class $\mathcal{H}$ to include nonlinear functions. Another way to improve is to consider alternative objective functions (as opposed to least squares) to minimize and obtain the optimal operator. These two ideas come together using the framework of structural risk minimization (Vapnik, 1998).

Recall that the true goal was to minimize $R(h)$ over the class $\mathcal{H}$. Since the true probability distribution P was not available, we approximated $R(h)$ by $R_{\text{emp}}(h)$ in the actual computations and hoped that the resulting empirically optimal operator would generalize well. The work of Vapnik and Chervonenkis (1981) (expounded at length in Vapnik, 1998) suggests that better generalization is obtained when the approximation also includes a regularization term. Thus, the following quantity is optimized instead:

$$\min_{h \in \mathcal{H}} R_{\text{emp}}(h) + \Phi(d;l).$$

The regularization term $\Phi(d;l)$ depends upon the com-

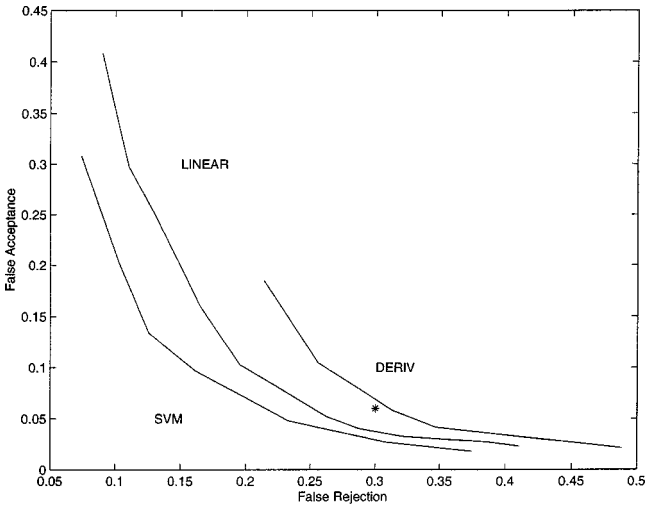

FIG. 3. ROC curves for stop detection using three different classes of operators (detectors)—differential operators, general linear operators, and nonlinear operators. Notice the steady improvement in performance. The asterisk denotes HMM performance.

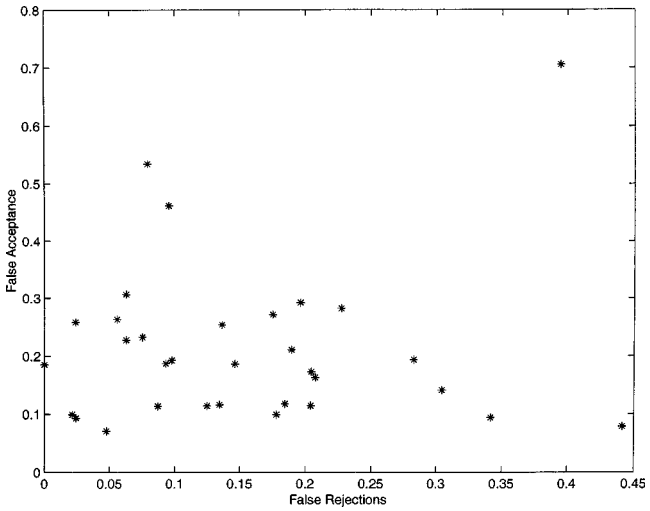

FIG. 4. False acceptance and rejection rates for the 32 speakers in the test set. Each point represents a particular speaker.

plexity of the class $\mathcal{H}$ and the number of datapoints available (l). The complexity of $\mathcal{H}$ is measured as the VC dimension (denoted by d), which is a combinatorial parameter that captures the ''expressive power'' of $\mathcal{H}$. This formulation leads to the so-called support vector machines (SVMs).

We do not describe the subtleties involved in utilizing SVMs effectively (see Niyogi *et al.*, 1999 for further details) but only observe that it involves two changes over the previous formulation: (i) the addition of a regularization term in the objective function, (ii) the utilization of a nonlinear class $\mathcal{H}$ for greater expressive power. As a result of this, detectors based on such SVMs have been constructed and the ROC curves for such nonlinear detectors are shown in Fig. 3. As we see, the equal error rate has improved from 16% to 11%. Figure 3 demonstrates the substantial improvement in detector performance that is obtained in moving from differential operators to linear operators to nonlinear operators (SVM). The underlying intuition of capturing a closure–burst transition and the underlying representation of energies and Wiener entropy have, however, remained the same.

IV. ANALYSIS OF ERRORS

Let us examine more closely the nature of the errors made by the detector of algorithm C noted previously.

A. Errors by speakers

Recall that there are 32 speakers in directory 4 of the TIMIT database. Here we examine how the stop detector performs on each of these speakers. We look at a few cases of poor performance to get some insight into the nature of these errors. Figure 4 shows the acceptance and rejection rates for each of the 32 speakers (using algorithm C) for a point (18% false rejection[7]) on the ROC curve of Fig. 2.

Notice that there are some speakers for whom the performance of the current detection algorithm is quite poor. It turns out that each of the speakers with high false acceptance rates was male with low pitch and occasionally creaky voice with considerable glottalization. False firings of the stop detector often occurred at the pitch pulses. Figure 5 shows the output of the stop detector (before thresholding) on a sentence on which performance is particularly bad.

Figure 6 shows the output of the detector on a vocalic segment of the speech corresponding to the vowel /aa/. The pitch period was of the order of 10 ms and each pitch pulse gives rise to a peak in the detector output. Strong pitch pulses often cause the detector output to cross the threshold. This is a common type of error that occurs with certain speakers.

Speakers with high false rejection rates typically had stop consonants that were highly attenuated in the speech signal. Figure 7 shows the portion of a sentence corresponding to the stop ''p.'' Notice that while the closure is quite pronounced, the burst is very weak (almost not realized in the signal). Naturally, our detector that looks for a transition from closure to burst does not detect the stop consonant. A more interesting case occurs in a ''k'' burst for the same speaker, shown in Fig. 8. Here, there is a gradual frication after the closure and then the sharp characteristic burst oc-

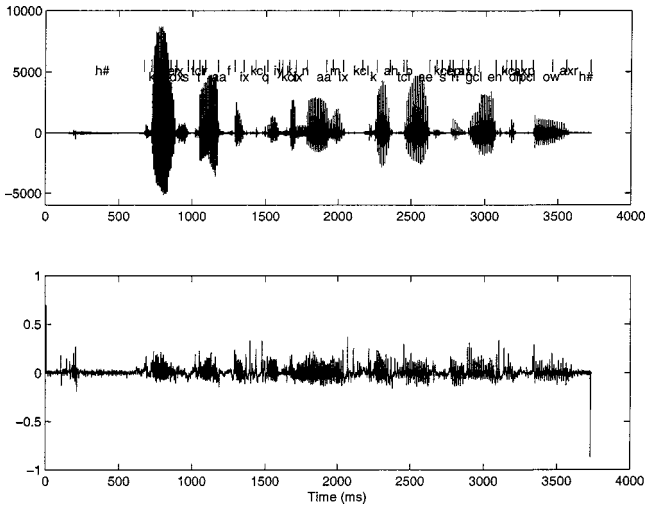

FIG. 5. Sentence (top) and detector output (bottom) for speaker for whom performance is poor.

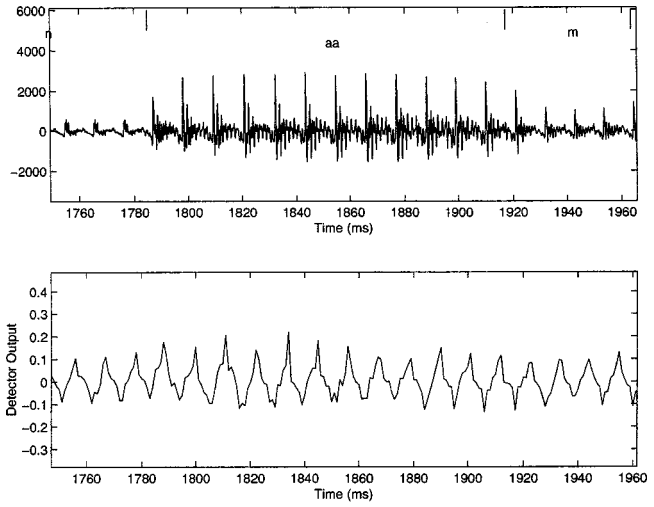

FIG. 6. A vocalic segment of the speech for which detector output firings occur at pitch pulses.

curs about 50 ms later. Because of the pre-frication, the transition from frication to burst is less sharp than the corresponding transition from closure to burst that we have been regarding to be the characteristic signature of a stop consonant. The detector output as seen in Fig. 8 is low at the closure–frication transition and modestly high at the frication–burst transition that occurs later. The labeling of the TIMIT speech is such that the boundary between the closure and the burst (kcl-k) is put at the transition between the closure and the pre-fricated part of the stop consonant. Therefore, the true burst when detected would be considered a false detect as it occurs more than 20 ms after the postulated boundary. Since there was no firing at the closure–frication boundary, one false rejection and one false insertion was declared according to the scoring scheme used in this paper.

B. Errors by phonetic class

Here we examine the correct detections and false insertions of the stop detector to get a sense of how often they

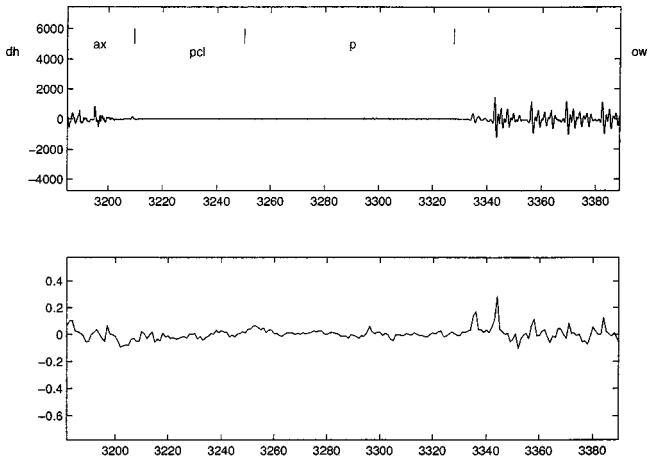

FIG. 7. The stop ''p'' (top) and detector output (bottom) for speaker for whom performance is poor. Short vertical lines on the top panel indicate the phonetic segments. There is a brief bit of vowel (''ax'') followed by a closure and burst (''pcl'' and ''p,'' respectively), and then another patch of vowel (''ow'').

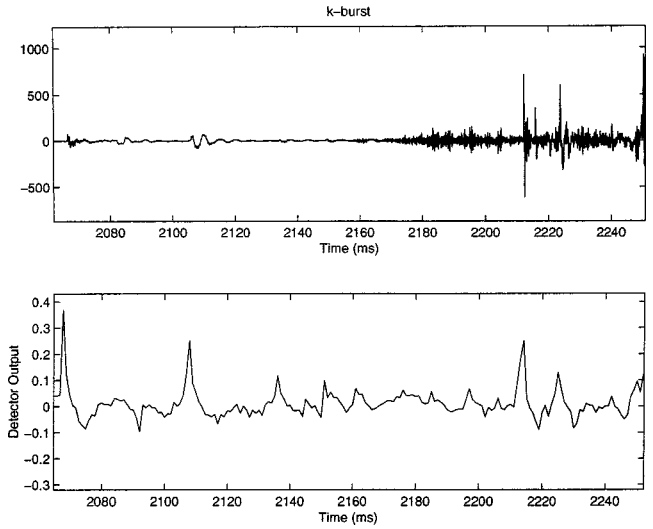

FIG. 8. A noncanonical *k* burst and associated detector output. The closure has a few blips (e.g., around 2110 ms). Prefrication starts at around 2160 ms and the burst at around 2210 ms.

occur during different phonetic events in the speech signal. For convenience, we pick a particular point on the ROC curve of detection algorithm C with false rejection of 23% and false acceptance of 5%. One can examine how often each kind of stop consonant is detected at this threshold. The false rejection rates for the stop consonants are: (i) ''b''—42%, (ii) ''p''—28%, (iii) ''d''—25%, (iv) ''t''—21%, (v) ''g''—26%, (vi) ''k''—23%. Clearly, ''b'' is detected least accurately while the rest are detected with roughly the same range of accuracy with unvoiced stop consonants being detected a little better than their voiced cognates.

One can examine more closely the nature of the false insertions obtained by the detection algorithm. For each point in time that was marked as a closure–burst transition by the stop detector, we located the nearest phonetic boundary (provided by the manual TIMIT segmentation) and noted the phonetic identity to the left and right of that boundary. Figures 9 and 10 show the number of times each phonetic class appears to the left and right, respectively, of a firing that was deemed false (therefore, false insertion) according

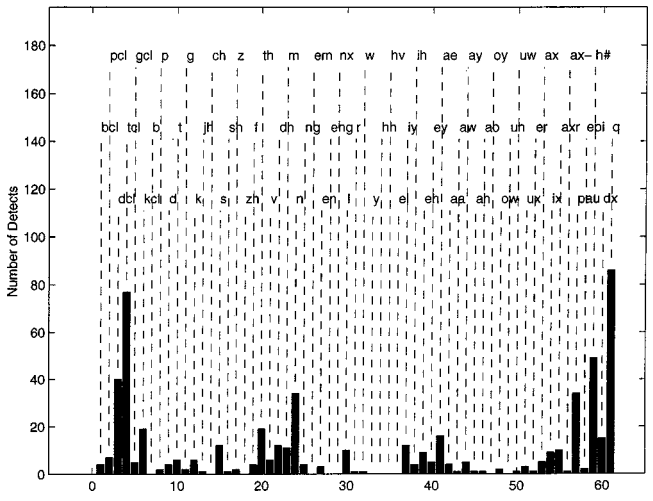

FIG. 9. False insertions, left phonemic context.

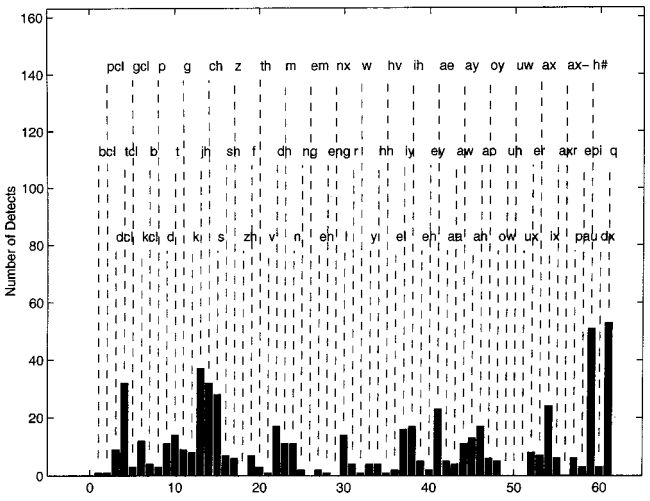

FIG. 10. False insertions, right phonemic context.

to the scoring convention. The TIMIT notation has been used to denote phoneme identity.

One notices some false insertions occurring during closures and releases of stops as indicated by the counts corresponding to closures and releases of stops in each of the figures. These correspond to firings of the detector that are more than 20 ms away from the closure–burst boundary as marked by the TIMIT labeling scheme. Some of these are indeed false insertions. Others are actually correct detections of real bursts that occurred more than 20 ms away from the closure–burst transition as marked in TIMIT. Some of these are due to multiple bursts being present in the articulation of the stop consonant; others are due to effects like pre-frication described earlier; yet others are simply due to mislabelings by the TIMIT labeler.

Excluding these, the most common left contexts for false insertions are the following.

(i) ''q'' (glottal stop). These have many stop-like characteristics and some phoneticians would even include them in the class of stops.

(ii) ''h#'' (silence). Sometimes the silence occurs before a stop, e.g., as in the TIMIT sentence /*Don't ask me to carry an oily rag like that*/. In such a case, the section before the stop burst is marked as a silence rather than a closure. In other cases, the silence might occur between words and if it is followed by a strident fricative or a vowel (glottalization) then the stop detector often fires.

(iii) ''pau'' (pause). This is exactly like silence.

(iv) ''n.'' These firings were of many sorts. One was presumably due to the oral closure that accompanies nasals leading to rapid transients. The nature of these transients is quite different from that of stops but nevertheless our algorithms are often unable to distinguish them from each other. A second sort occurs toward the end of the nasal release and may be due to a reduced or prematurely closed velic aperture causing a rise in intra-oral pressure and a resulting plosion. Additionally, the transition from a nasal to a following vowel is often accompanied by a sharp increase in overall energy and may be the cause of some false firings of the detector. (These can be eliminated by use of periodicity measures but we do not explore those directions here).

(v) ''th'' (dental fricative). This has a partial closure and a broadband nature. If the transition is sharp enough, it does cause a stop-like effect.

The most common right contexts are the following.

(i) ''q'' (glottal stop). See the previous list.

(ii) ''ch'' and ''jh'' (affricates). This is hardly surprising. These affricates have many stop-like properties.

(iii) ''s'' (strident fricative). The strong frication, especially if the transition is from something weaker leads to the impression of a stop consonant.

(iv) ''ae''; ''ix'' (vowels). Usually preceded by glottalization or silence or having noticeable pitch pulses.

Some of these errors occur with sounds that are perceptually like stops and in this sense are ''reasonable'' errors that might be harder to eliminate. Errors like those due to pitch pulses or sudden blips in the signal are clearly deficiencies in the current approach and ways to eliminate them need to be considered.

The errors in detecting stop consonants are strongly correlated with their location in the syllable structure of the utterance. Syllable initial stop consonants tend to be strongly articulated and detected with high accuracy by the algorithms developed in this paper. Stop consonants in syllable final position or in clusters tend to be more variable in their articulation and consequently detected with higher error rates. We did not perform a detailed analysis of this issue because syllable parses were not available with the TIMIT database. However, to provide the reader with a sense of the degree to which this factor affects recognition accuracy, we provide the following statistics:

The TIMIT *sa*2 sentence ''Don't ask me to carry an oily rag like that'' has been uttered by every single speaker in the database. In this particular sentence, the phoneme /k/ occurs in syllable initial position in the word ''carry,'' in syllable final position in the word ''like,'' and in a syllable final cluster in the word ''ask.'' The syllable initial /k/ was correctly detected with an error rate of 8% by algorithm C. The syllable final /k/ was detected with an error rate of 46% and the /k/ in the cluster was detected with an error rate of 42%. This illustrates the significant variation of closure–burst characteristics by syllable position.

The TIMIT *sa*1 sentence ''She had your dark suit in greasy wash water all year'' has the phoneme /d/ in syllable initial position in the word ''dark'' and syllable final position in the word ''had.'' The detection error rates for these two /d/'s were 2% and 41%, respectively.[8] This demonstrates again the significant effect of syllable location upon detection rates. We believe that this is due to the fact that stops in syllable initial positions are better articulated and therefore have more characteristic closure–burst transitions.

V. ASPECTS OF ROBUSTNESS

The previous experiments suggest that in a clean environment, the accurate detection of stop consonants can be achieved at rates that are competitive with current HMM-based systems. However, the significant problem with current ASR systems is the lack of robustness to changes in acoustic conditions that affect the human relatively little. One of the major motivations in studying the problem of

detecting a specific feature is to get a point of entry to understanding what goes wrong in the presence of an unfamiliar acoustic environment like channel changes, noise, reverberation, and so on. An entire speech recognition system typically has too many parameters and too many variables to yield readily to diagnostic analysis. By focusing on the smaller and more manageable task of detecting specific subclasses of sounds (distinctive features) and studying the degradation in performance as acoustic conditions are varied, one might be able to make more progress.

What is the nature of the degradation that happens? What might be done to recover the linguistic identity in the face of such degradation? Does this allow us to formulate relevant perceptual experiments that might inform us about processing strategies the human might use. Let us examine some of these questions under conditions of channel variation and noise.

A. NTIMIT

The NTIMIT database consists of TIMIT sentences sent out over a telephone channel and recollected and realigned with the original TIMIT sentences. The same labeling was therefore used for both TIMIT and NTIMIT. The NTIMIT speech differs from the TIMIT version in two important respects. The first is band limitation: the telephone speech is band limited to the range 300 Hz to 3.5 kHz. This bandwidth is about half of TIMIT's 8 kHz range. The energy above 3.5 kHz is particularly important for the accurate detection of some stop bursts and weak fricatives and therefore is likely to have a significant effect on the task considered in this paper. The second important effect is a reduced signal-to-noise ratio (SNR) in NTIMIT sentences. For example, the TIMIT sentences used in the test set have a mean SNR of 39.5 dB while the NTIMIT sentences have a mean only of 26.8 dB. Thus the NTIMIT database allows us to study the effect of channel variability on feature detection problems.

We begin by considering the performance of algorithm C for the stop detection task in three different modes: (i) trained on 4 TIMIT speakers and tested on 32 TIMIT speakers (as reported in the preceding experiments), (ii) trained on 4 TIMIT speakers and tested on 32 NTIMIT speakers, (iii) trained on 4 NTIMIT speakers (corresponding to the TIMIT training speakers) and tested on 32 NTIMIT speakers. Shown in Fig. 11 are the ROC curves that are generated in each of these three modes. Clearly the case where detection algorithms were trained and tested on clean TIMIT speech yields the best results with an equal error rate of 16%. Detection rates drop drastically when the same detector is used on NTIMIT speech with equal error rates of almost 35%.

To get a sense of why detection rates drop so dramatically, we examined the TIMIT and NTIMIT versions of several utterances. Shown in Fig. 12 are the TIMIT wave form and corresponding detector output for a typical sentence. In Fig. 13 are shown the NTIMIT wave form and corresponding detector output for the same sentence. The first obvious thing that strikes one is fall in the dynamic range of the detector output. The overall pattern of the two detector outputs is similar and one can often match the peaks corresponding to the same stop consonant in the two cases. However, the absolute value of the peaks on the NTIMIT version seem to have fallen to about 10%–40% of their original values on the TIMIT version of the same sentence.

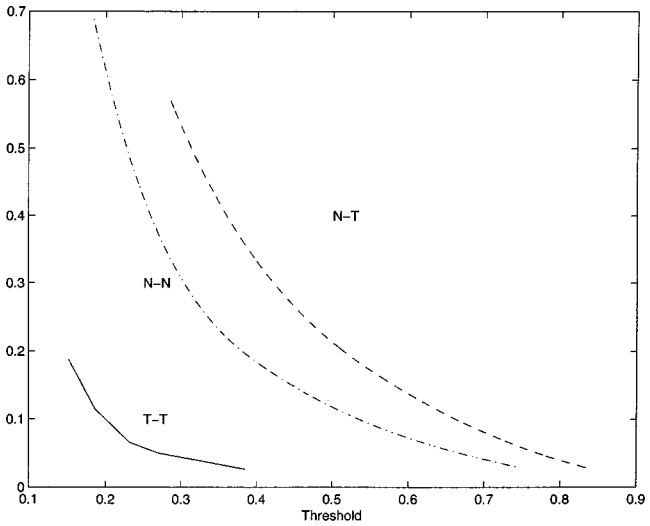

FIG. 11. ROC curves for algorithm C in three different modes of training-testing mismatch—(i) T-T, trained and tested on TIMIT (ii) N-N, trained and tested on NTIMIT, (iii) N-T, trained on TIMIT and tested on NTIMIT.

This indicates of course that one will need to adapt the value of the threshold from TIMIT to NTIMIT. It is clear that a threshold value for the detector output that is sufficient to detect stops at some detection rate (false rejection rate) now has to be lowered to achieve the same detection accuracies on the NTIMIT version. To see this more explicitly, we plot the false rejection rates and the false acceptance rates as a function of the threshold in Fig. 14. As the threshold increases, the false rejection rate increases while the false acceptance rate decreases. The point at which the two curves meet denotes the threshold value at which equal error rate is achieved for each detector.

Clearly, the change in the dynamic range of the detector output is not all. There are further differences. Examining the detector outputs in Figs. 12 and 13 more closely one notices that the strong peak corresponding to the final /tcl/-/t/ in the TIMIT version is completely absent in the NTIMIT version.

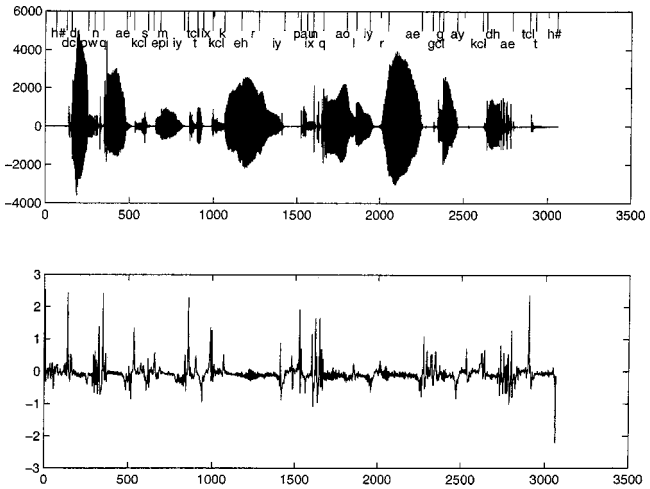

FIG. 12. Detector output for a TIMIT sentence. Wave form (top panel) and detector output (bottom panel).

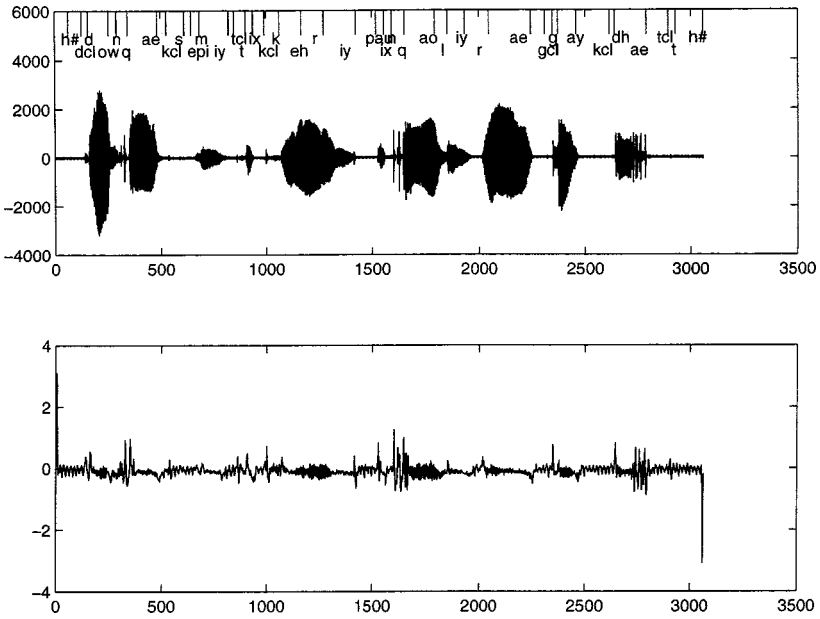

FIG. 13. Detector output for the NTIMIT version of the same sentence. Wave form (top panel) and detector output (bottom panel).

Shown in Fig. 15 is the portion of the signal corresponding to the final /tcl/-/t/ aligned in TIMIT and NTIMIT. While the stop consonant is clearly articulated and present in the TIMIT version of the signal, the telephone channel essentially wiped this stop consonant out so that only a faint trace remains in the NTIMIT version. It seems unreasonable to expect the stop detector to fire in the NTIMIT version of the speech signal where the presence of the stop consonant is so greatly reduced. While this is a particularly extreme case, there are a number of cases of stop consonants that are either eliminated or greatly reduced in intensity by the telephone channel. It is not clear whether to interpret the corresponding failure of the stop detector to fire in such cases as a positive or negative aspect of the detection algorithm. It is also not clear what human performance would be when stops are so greatly reduced in intensity. In order to measure this more quantitatively, psychophysical experiments are being conducted where multisyllable nonsense streams are presented to human subjects. Some of the nonsense streams have a plosive in a consonantal position and human detection rates are sought. We will measure the effect on detection rates of greatly reducing the intensity of the burst by filtering or reducing the prominence of the closure–burst transition by adding noise. The psychophysical results will be part of a separate paper.

As we have mentioned before, the two major differences between TIMIT and NTIMIT speech are (i) more noise (lower SNR) in NTIMIT speech, (ii) greatly reduced spectral energy above 3.5 kHz in NTIMIT speech. The reduction in high frequency energy is particularly debilitating because a characteristic signature of a canonical stop consonant includes a high frequency burst that is now harder to detect. To get greater insight into what might possibly be going on, we considered every single stop in the test set (there were 1376 of them in all) and obtained the detector output for the

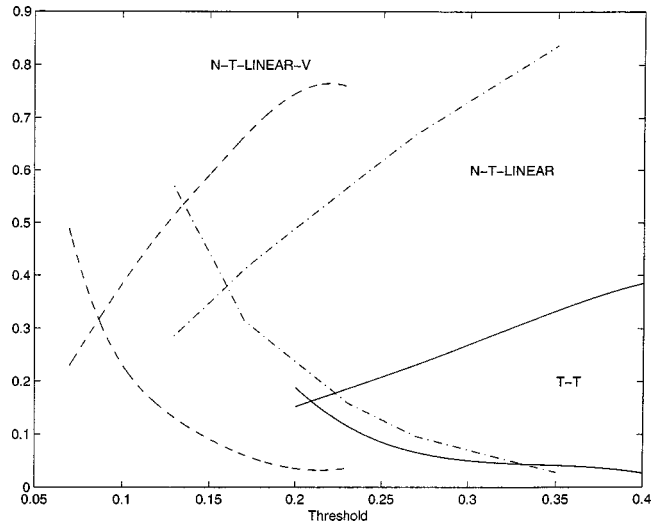

FIG. 14. False rejection rates and false acceptance rates as a function of the threshold for three different cases. (i) T-T, trained on TIMIT and tested on TIMIT, (ii) N-T-LINEAR, trained on TIMIT and tested on NTIMIT, (iii) N-T-LINEAR-V, trained on TIMIT and tested on NTIMIT using a voiced/unvoiced detector to augment the decision. As the threshold increases, the false rejection rate increases while the false acceptance rate decreases. We see that the equal error rate is met at different thresholds for each of the modes of use.

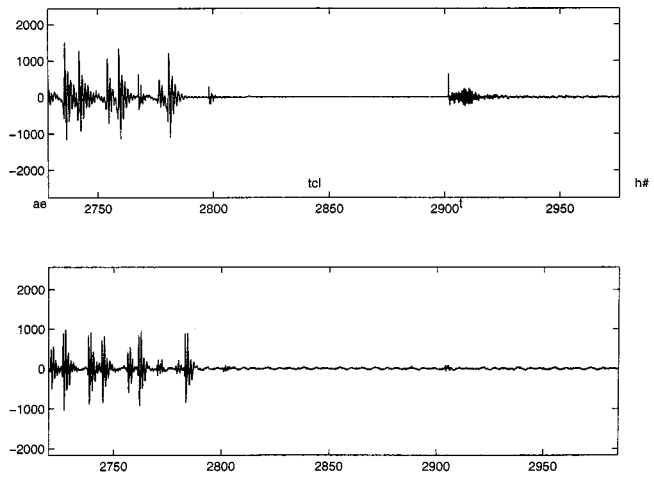

FIG. 15. An extreme case of a stop deletion.

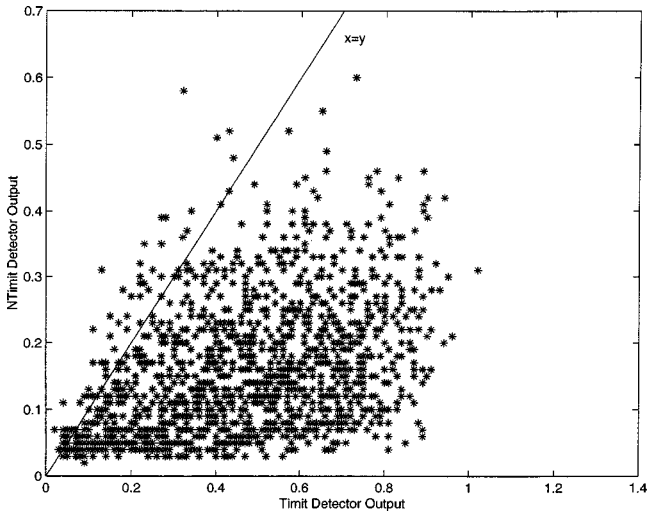

FIG. 16. For each stop consonant in the test set, the detector output on the NTIMIT version is plotted against the detector output in the TIMIT version. The straight line has slope=1. Clearly the NTIMIT detector output is on average much lower than the TIMIT detector output. The detector used (algorithm C) was trained on TIMIT data.

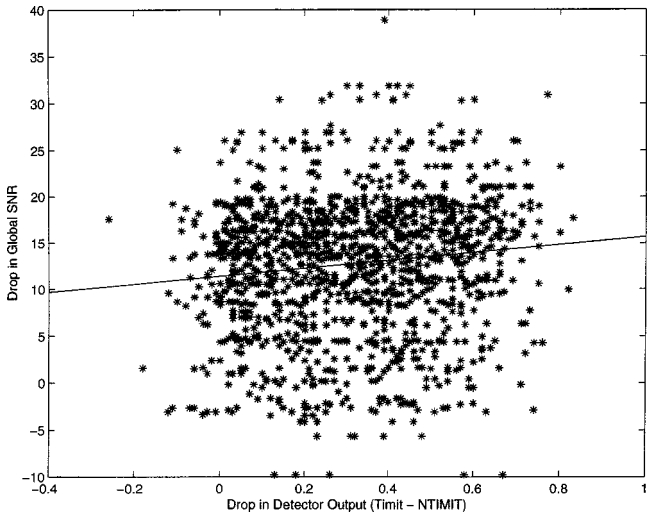

FIG. 17. Drop in global SNR plotted against the drop in detector outputs between TIMIT and NTIMIT for each sentence.

TIMIT version and the NTIMIT version. Shown in Fig. 16 is a plot of the TIMIT output against the NTIMIT output for each stop. Each point in this plot refers to a particular stop consonant in the test data set and its coordinates indicate the magnitude of the detector output for the TIMIT version and the NTIMIT version of that stop.

Clearly, the output of the detector for the NTIMIT version of the stop consonants is much lower on average than the output for the TIMIT version of those same stop consonants. Perfect invariance to the change in channel would require the points to all lie on the straight line $y=x$. This, of course, is not the case. The fact that the NTIMIT detectors outputs are lower is not entirely surprising—what is surprising perhaps are the cases when the NTIMIT version is actually higher than the TIMIT version. We examined several of these cases and they all fell into one of two cases: (i) the burst appeared from inspection to be as strong (not obviously stronger, though) in the the NTIMIT version, (ii) there was a local noise burst introduced by the telephone network near the true closure–burst transition and it was this noise burst that was actually detected.

This leads one to hypothesize that the drop in detector output from TIMIT to NTIMIT might simply reflect the deterioration in the overall strength of the stop burst. To this effect, we plot in Fig. 17, the drop in global SNR between TIMIT and NTIMIT for each stop as a function of the drop in the detector output between the two versions. A regression line has been plotted through the data points and has nonzero slope suggesting some correlation between the two.

However, it is pretty clear from examining Fig. 17 that this drop in global SNR is only very weakly correlated to the drop in detector outputs. In some respects, this is not surprising since the global SNR is determined mostly by the energy in the vocalic portions of the signal. It has the same value for every stop consonant in the sentence, although individual stop consonants in that sentence might deteriorate to different degrees over the telephone transmission. A better measure of the degree of preservation of the stop consonant is provided by a measure of the local SNR indicated in Fig. 18. An estimate of the local SNR was obtained by measuring the average energy in the burst and the average energy in the closure. The segmentation provided by the TIMIT labeling was used to calculate the average energy in the burst and closure, respectively. While the degree of correlation has increased, there is still considerable unexplained variance in the data as plotted.

Closer examination of this issue led to the feeling that much of the unexplained variance was simply due to poor segmentation of the consonants in the TIMIT data set. Since the segments in question (closures and bursts) are small in duration, misalignments of the order of 5–10 ms (which are quite common in the database) would have significant effect on the reliability of the estimates of local SNR. Relabeling all the stop consonants in the data set would require too much effort. Instead, we obtained an estimate of instantaneous SNR in the following manner. We found the point in time closest to the labeled closure–transition boundary that

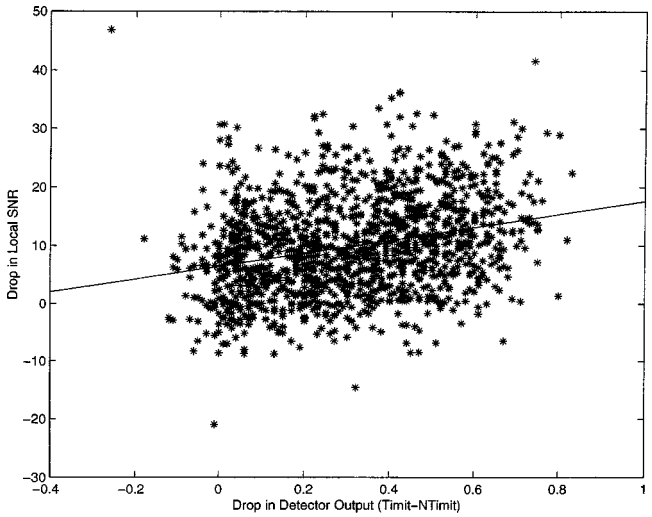

FIG. 18. Drop in local SNR plotted as a function of the drop in detector outputs between TIMIT and NTIMIT.

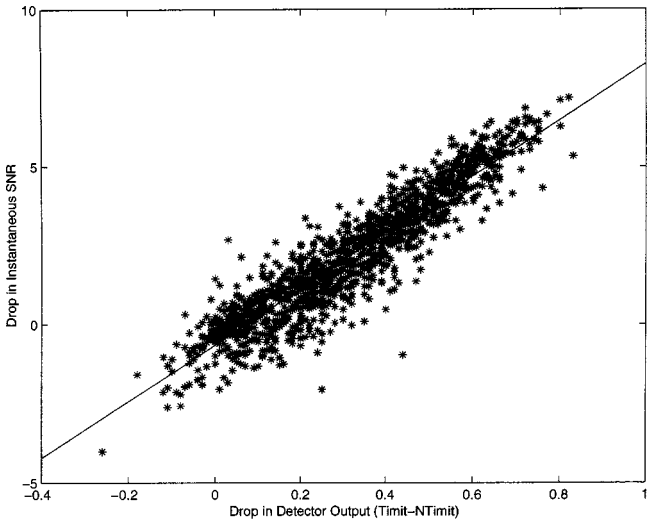

FIG. 19. Drop in instantaneous SNR as a function of the drop in detector outputs between TIMIT and NTIMIT.

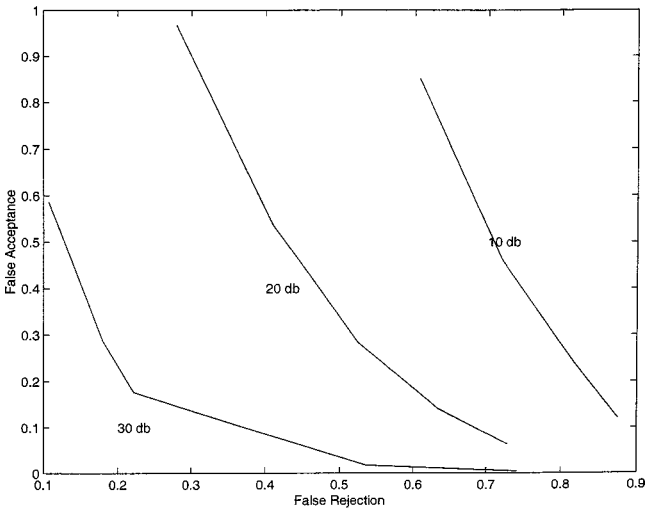

FIG. 20. ROC curves for stop detection at various values of global noise ranging from 30 dB SNR to 10 dB SNR.

had maximum change in energy $[E(n)-E(n-1)$ where $E(n)$ is energy at time $n]$. This point was declared the true closure transition boundary and energy of a 5 ms stretch to the left (energy in closure) and a 5 ms stretch to the right (energy in release) was taken. This provided an estimate of the local rise in energy (instantaneous SNR) for the closure–burst transition associated with that stop consonant. One can then compute the drop in instantaneous SNR from TIMIT to NTIMIT and shown in Fig. 19 is a plot of the drop in instantaneous SNR against the drop in detector outputs. Clearly, the correlation is now quite striking.

The results of this study suggest that much of the deterioration from TIMIT to NTIMIT can be simply explained by the deterioration in the strength of the burst, the addition of noise in the closure period, and overall degradation of the closure burst transition. Unfortunately, the acoustic degradation from TIMIT to NTIMIT is not under the control of the experimenter and therefore in Sec. V B, we study the degradation of the detector in the presence of controlled amounts of additive noise.

B. Noise

Automatic speech recognition performance is known to degenerate with additive noise. We examine the performance of the stop detection algorithm under two kinds of additive noise. All experimental results are reported with algorithm C for the stop detection task as usual.

1. Global white noise

White noise was added to the TIMIT speech wave forms by sampling from a zero mean random distribution. The variance of the distribution was set depending upon the level of *global* SNR we wished to obtain. Shown in Fig. 20 are the ROC curves generated when varying degrees of noise are added. As you can see, there is rapid deterioration due to noise. At 30 dB SNR, the equal error rate drops from 16% to around 20% but at 20 dB SNR, the equal error rate has dropped[9] to almost 50%.

At first glance, this might seem like an outrageous degradation but closer examination of this issue suggested that at 20 dB global SNR, the local SNR in the closure–burst region was actually quite high. The closures were very noisy and the transition from closure to burst was very indistinct. Figure 21 is a picture of the speech signal corresponding to a closure–burst transition in the clean and at signal-to-noise ratios of 20 and 10 dB, respectively. At 10 dB SNR, for example, the closure–burst transition seems to be essentially obscured.

This suggests that the success of the stop detector depended essentially on how well preserved the closure–burst transition was. To examine this in greater detail, we performed experiments with additive local noise in the following.

2. Local white noise

The clean speech signal $x(n)$ was corrupted by noise to yield the noisy signal $y(n)$ according to

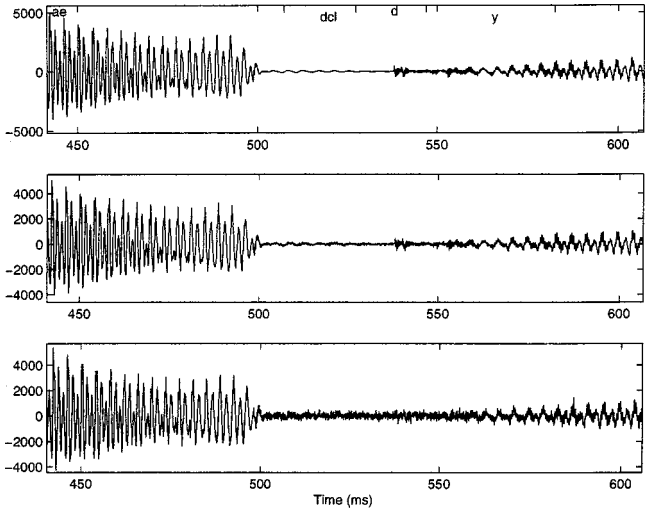

FIG. 21. The transition from closure to burst in clean speech (top), 20 dB SNR (middle) and 10 dB SNR (bottom).

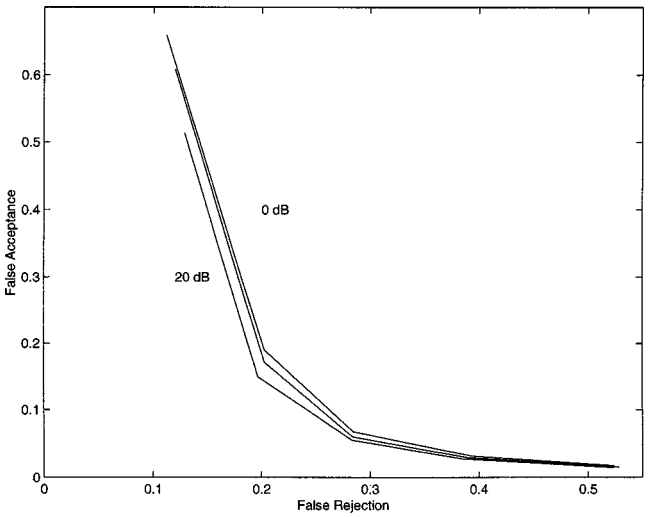

FIG. 22. ROC curves for stop detection at various values of local noise ranging from 20 dB SNR to 0 dB SNR.

$$y(n)=x(n)[1+\epsilon\eta(n)],$$

where $\eta(n)$ takes on values $+1$ and -1 with equal probability at each n. Furthermore $\eta(n_1)$ and $\eta(n_2)$ are independent for all n_1 and n_2. Therefore the noise will have a flat power spectrum.

In this model, the total additive noise $[\zeta(n)=\epsilon x(n)\eta(n)]$ scales as a function of signal energy at each point in time. One can make the following observations about $y(n)$ and $\zeta(n)$:

(1) $E[y(n)]=E[x(n)]$, i.e., the additive noise is zero mean.
(2) $E[\zeta(n_1)\zeta(n_2)]=0$ for $n_1\neq n_2$, i.e., the additive noise is white.
(3) $E[y^2(n)]=E[x^2(n)](1+\epsilon^2)$. Further, the signal-to-noise ratio at each time n (local SNR) is given by $20\log(1/\epsilon)$.

Such a model of noise is often referred to as Schroeder noise or MNRU in some communities.

Shown in Fig. 22 are the ROC curves for the detector of algorithm C that we have been studying in this paper for local SNR values from 20 to 0 dB SNR obtained by adding noise to clean TIMIT speech. Clean speech is approximately 40 dB SNR on average and recall that the ROC curve for clean speech has an equal error rate of approximately 16%. There is almost no deterioration when the SNR falls to 30 dB SNR. At 0 dB SNR, the equal error rate is 22%. Thus a drop from 40 to 0 dB SNR results in a corresponding drop in detector performance from 16% to 22% equal error rate. This drop seems much less dramatic now.

The experiments on telephone degradation in previous sections and those conducted here with controlled white noise seem to point to the same conclusions. The performance of the stop detector depends upon how clearly articulated the closure–burst transition is. This in turn is a function of the local signal-to-noise ratio at the closure–burst transition. Furthermore the detectors discussed in this paper can withstand local signal-to-noise ratios of up to 0 dB without significant deterioration. This is not obvious by simply studying the behavior of the stop detector with respect to the global signal-to-noise ratio. In this sense, we see that the local SNR is a good predictor of stop detection performance for the detectors that we have constructed. It is certainly a much better predictor than global SNR for the same task. The local SNR as we have constructed it is only a function of time. One could potentially consider the SNR locally as a function of both time and frequency and thus be able to pinpoint in greater detail the regions of the time–frequency plane that most affect stop detection. We do not pursue such a detailed analysis here.

VI. CONCLUSIONS

We have considered the problem of detecting stop consonants in continuous speech. We have utilized a simple representation using log-energies and Wiener entropy to characterize the speech signal. Stops correspond to certain characteristic transitions in this feature space and we show how to use a filtering framework to extract the stops with reasonable accuracy and very little training data.

Many phonetic events, particularly those characterized by transitions, e.g., broad class boundaries, nasals, etc., can be handled by a similar approach. While we have utilized a simple linear filter to extract the stop, one can, in principle, use more complex nonlinear filters to extract such phonetic events. We have experimented with such nonlinear filters and have reported part of those results in this paper. Finally, the output of the filters can be interpreted as an *a posteriori* density for the event and might be useful as an intermediate representation for other speech recognition and segmentation tasks.

We have analyzed the performance of the stop detector from a variety of perspectives. Variability with respect to speakers has been considered. The common errors have been analyzed in terms of their phonetic classes. Changes in acoustic environments due to channel (regular to telephone) and noise have been studied. We are led to conjecture that reliable burst detection is unlikely when the local signal-to-noise ratio is low.

Two important future directions for research need to be considered. First, we need to relate the performance of the automatic stop detectors with human performance on similar tasks. If human detection rates are demonstrably higher or more robust, it would be interesting to have some insight into what acoustic cues they use—cues that we have presumably ignored in our current approach. Second, we have pursued a largely bottom up strategy for stop detection. Clearly, higher level knowledge constrains the sequence of stops so that many false insertions can be eliminated by such means. We intend to explore such directions as part of future work.

[1]We use stop consonants to refer to the class containing the phonemes "p," "t," "k," "g," "b," "d," respectively. Thus we use stop consonants or plosives to refer to a class of phonemes and not to any particular acoustic attribute correlated with that class. As we see in this paper, the acoustic attributes that we focus on are those that accompany the transition from closure to burst that is correlated with the articulation of such a phoneme.
[2]A detailed description of multitapered methods is beyond the scope of this paper. The basic idea is that rather than computing a short time windowed Fourier transform using only a single window at each time step, the multi-

tapered approach computes spectra using several different windows (tapers) and combines them. Principled methods exist to choose the windows and combine them allowing one to obtain a more robust estimate of the spectrum and negotiate a more graceful bias-variance trade-off in spectral estimation.

[3]Vocal fry refers to an articulation mode where the vocal cords vibrate particularly slowly leading to a low pitch and a creaky voice.

[4]There is considerable literature also on the role of formant transitions in identifying the stop consonant, in particular its place of articulation. It was not clear to us whether and in what manner formant transitions play a role in determining the *manner* class of stop consonants as a whole. A preliminary attempt to include formant transitions did not yield positive results. Thereafter, we did not explore the possibility of using such cues.

[5]Clearly, we had to utilize our intuition and judgment in choosing such a representation. It seems to us that this is where acoustic phonetic knowledge is crucial. Once an appropriate representation is picked, one may explore various statistical detection frameworks that act on such a representation to separate the phonetic classes from each other.

[6]No particular reason should be attributed to the choice of this dialect region. Some additional experiments conducted on the entire TIMIT database confirm that the essential results presented in this paper generalize to the entire database.

[7]No particular significance should be attributed to the choice of the number 18. This was made purely for convenience.

[8]The syllable final /d/ is often palatalized due to the following /y/ leading to additional complications. We have excluded all such palatalizations in the current analysis.

[9]One might be puzzled by how the equal error rate can be above 50%. The reason is that we are measuring false acceptances (i.e., insertions) as a function of the total number of phonemes (excluding the stop consonants) in the database. Because this total number is much smaller than the total number of frames and the stop detector provides an output every frame, the equal error rate is artificially higher. We have discussed this in an earlier section. Of course, higher level constraints can be used to control the number of stop consonants hypothesized every sentence—such higher level constraints have not been explored here as our intent was to investigate the possibilities of a purely bottom up approach.

Abramson, A. S., and Lisker, L. (**1970**). ''Discriminability along the voicing continuum: Cross-language tests,'' *Proceedings of the Sixth International Congress of Phonetic Sciences* (Academia, Prague), pp. 569–573.

Blumstein, S. E., and Stevens, K. N., (**1979**). ''Perceptual invariance and onset spectra for stop consonants in different vowel environments,'' J. Acoust. Soc. Am. **67**, 648–662.

Cassidy, S., and Harrington, J. (**1995**). ''The place of articulation distinction in voiced oral stops: Evidence from burst spectra and formant transitions,'' Phonetica **52.4**, 263–284.

de Mori, R., and Flammia, G. (**1993**). ''Speaker independent consonant classification in continuous speech with distinctive features and neural networks,'' **94**, 3091–3103.

Djezzar, L., and Haton, J. P. (**1995**). ''Exploiting acoustic-phonetic knowledge and neural networks for stop recognition,'' Eurospeech, 2217–2220.

Eide, E., Rohlicek, J. R., Gish, H., and Mitter, S. K., (**1993**). ''A linguistic feature representation of the speech waveform,'' Proc. ICASSP **2**, 483–486.

Furui, S. (**1986**). ''On the role of spectral transitions for speech perception,'' **80**, 1016–1025.

Glass, J. R., and Zue, V. W. (**1986**). ''Detection and recognition of nasal Consonants in American English,'' Proc. ICASSP, 2767–2770.

Jakobson, R., Halle, M., and Fant, G., (**1952**). *Preliminaries to Speech Analysis: The Distinctive Features and their Correlates* (MIT, Cambridge).

Jelinek, F. (**1997**). *Statistical Methods for Speech Recognition* (MIT, Cambridge).

Kirchhoff, K. (**1996**). ''Phonologically structured HMMs for speech recognition,'' Proceedings of the SIGPHON Workshop for Computational Phonology in Speech Technology, pp. 45–50.

Klatt, D. H. (**1975**). ''Voice onset time, frication and aspiration in word-initial consonant clusters,'' J. Speech Hear. Res. **18**, 686–706.

Lesser, V., Fennell, R., Erman, L., and Reddy, D. R., (**1975**). ''The hearsay II speech understanding system,'' IEEE Trans. Acoust., Speech, Signal Process. **23**, 11–24.

Liu, S. (**1995**). ''Landmark detection for distinctive feature-based speech recognition,'' Ph.D. thesis. MIT, Cambridge, MA.

Meng, H. M., Zue, V. W., and Leung, H. C. ''Signal representation, attribute extraction and the use of distinctive features for phonetic classification,'' Fourth DARPA Speech and Natural Language Workshop, 19–22 February 1991, Pacific Grove, CA.

Mermelstein, P. (**1977**). ''On detecting nasals in continuous speech,'' J. Acoust. Soc. Am. **1**, 581–587.

Niyogi, P., Burges, C., and Ramesh, P., (**1999**). ''Distinctive feature detection using support vector machines,'' Proc. of ICASSP, Phoenix, AZ.

Niyogi, P., and Ramesh, P. (**1998**). ''Incorporating voice onset time to improve letter recognition accuracies,'' Proc. ICASSP.

Ohde, R. N., and Stevens, K. N. (**1983**). ''Effect of burst amplitude on the perception of place of articulation for stops,'' J. Acoust. Soc. Am. **74**, 706–714.

Rabiner, L. R., and Juang, B. H. (**1993**). *Fundamentals of Speech Recognition* (Prentice–Hall, Englewood Cliffs).

Smits, R., Ten Bosch, L., and Collier, R., (**1996**). ''Evaluation of various sets of acoustical cues for the perception of prevocalic stop consonants. I. Perception experiment,'' J. Acoust. Soc. Am. **100**, 3852–3864.

Stevens, K. N., and Blumstein, S. (**1978**). ''Invariant cues for place of articulation in stop consonants,'' J. Acoust. Soc. Am. **64**, 1358–1368.

Thomson, D. J. (**1982**). ''Spectrum estimation and harmonic analysis,'' Proc. IEEE **70**, 1055–1096.

Vapnik, V. N. (**1998**). *Statistical Learning Theory* (Wiley, New York).

Vapnik, V. N., and Chervonenkis, A. (**1981**). ''Necessary and sufficient conditions for the uniform convergence of the means to their expectations,'' Theory Probab. Appl. **26**, 532–553.

Wolf, J. J., and Woods, W. A. (**1977**). ''The HWIM speech understanding system,'' Proc. ICASSP, 784–787.

Zue, V. W. (**1975**). ''Duration of English stops in prestressed position,'' J. Acoust. Soc. Am. Suppl. 1 **58**, S96.

Zue, V. W. (**1976**). ''Acoustic study of stop consonants,'' Ph.D. dissertation, MIT.

Zue, V. W. (**1985**). ''The use of speech knowledge in automatic speech recognition,'' Proc. IEEE **73**, 1602–1615.

On application of adaptive decorrelation filtering to assistive listening

Yunxin Zhao[a)]
Department of Computer Engineering and Computer Science, University of Missouri-Columbia, Columbia, Missouri 65211

Kuan-Chieh Yen
Beckman Institute and Department of ECE, University of Illinois at Urbana-Champaign, Urbana, Illinois 61801

Sig Soli, Shawn Gao, and Andy Vermiglio
Human Communication Sciences and Devices Department, House Ear Institute, Los Angeles, California 90057

(Received 24 May 2000; revised 20 July 2001; accepted 12 November 2001)

This paper describes an application of the multichannel signal processing technique of adaptive decorrelation filtering to the design of an assistive listening system. A simulated ''dinner table'' scenario was studied. The speech signal of a desired talker was corrupted by three simultaneous speech jammers and by a speech-shaped diffusive noise. The technique of adaptive decorrelation filtering processing was used to extract the desired speech from the interference speech and noise. The effectiveness of the assistive listening system was evaluated by observing improvements in A-weighted signal-to-noise ratio (SNR) and in sentence intelligibility, where the latter was evaluated in a listening test with eight normal hearing subjects and three subjects with hearing impairments. Significant improvements in SNR and sentence intelligibility were achieved with the use of the assistive listening system. For subjects with normal hearing, the speech reception threshold was improved by 3 to 5 dBA, and for subjects with hearing impairments, the threshold was improved by 4 to 8 dBA. © *2002 Acoustical Society of America.* [DOI: 10.1121/1.1433815]

PACS numbers: 43.72.Ew, 43.72.Kb, 43.72.Dv [DOS]

I. INTRODUCTION

Conventional hearing aids have many limitations. In particular, hearing aid users experience difficulties in noisy acoustic environments with multiple sound sources and reverberation (Smedley and Schow, 1992). In conventional hearing aids, sound amplification is performed to compensate for the reduction of dynamic range and frequency response in hearing-impaired ears without discrimination between desired speech and interference sounds. Since hearing impairments are commonly accompanied by a reduced binaural directional hearing that enables selective reception of desired signal in a sound field, hearing aid users are more affected by the amplified noises. In the past, speech enhancement techniques were evaluated for attenuating noise and assisting listening. However, enhancement processing improves only quality but not intelligibility of speech (Deller *et al.*, 1993).

Since sound sources are in general spatially separated, multimicrophone based speech processing offers the promise of separating desired speech from interference sounds and thereby improving intelligibility of desired speech. Research efforts in this area have been focused on fixed or adaptive microphone-array beamforming to enhance speech in the desired direction and suppress jammer signals in undesired directions. Hearing aids utilizing fixed beamforming (Kates, 1993; Soede *et al.*, 1993a, 1993b; Stadler *et al.*, 1993) can realize useful directional gains with relatively simple and robust processing, and hearing aids employing adaptive processing can achieve very good interference cancellation under certain favorable conditions, in particular low reverberation (Peterson, 1989; Greenberg and Zurek, 1992; Hoffman *et al.*, 1994). Recent research efforts further investigate the incorporation of sound localization into hearing aids, which will not only assist speech comprehension but also facilitate a subjective sense of auditory space (Desloge *et al.*, 1997; Welker *et al.*, 1997).

In the current work, a new approach is taken in the design of an assistive listening system. This effort is motivated by recent developments of co-channel speech separation techniques in the field of speech and signal processing. Co-channel speech separation extracts source speech signals from their convolutive mixtures by reducing cross interferences among the speech signals, and therefore, the techniques offer the potential of improving speech comprehension in acoustic environments with multiple sound sources. Similarly automatic speech recognition systems suffer from performance degradation in the presence of competing speech (Cole *et al.*, 1995), and co-channel speech separation is therefore also important to real-world applications of spoken language technology.

Early research efforts on co-channel speech separation focused on separating competing speech from their additive mixture (Comon *et al.*, 1991; Jutten and Heuralt, 1991; Sorouchyari, 1991; Tong *et al.*, 1993). While these algorithms

a)Electronic mail: zhao@cecs.missouri.edu

are fast, simple, and capable of separating a large number of speech sources, they cannot deal with the convolutive effect of acoustic paths on mixtures of speech sources, referred to as convolutive mixtures. The convolutive effect depends on the durations of acoustic path impulse responses relative to the stationary periods of speech sound units, where a short response results in spectral distortion and a long response results in reverberation noise. Recently, research focus has been directed to the separation of convolutive mixtures. The methods can be categorized by using second-order statistics Weinstein *et al.*, 1993; Van Gerven and Van Compernolle, 1995) or higher-order statistics (Yellin and Weinstein, 1994; Shamsunder and Giannakis, 1997). The methods of the first category are easier to implement but may not guarantee uniqueness of solution (Weinstein *et al.*, 1993; Yellin and (Weinstein, 1994, 1996; Shamsunder and Giannakis, 1997). The methods in the second category can provide unique solutions but are more complicated to implement. In addition, empirical estimates of second-order statistics are usually more reliable than higher-order statistics, making the first-type algorithms preferable in certain applications.

In a previous work (Yen and Zhao, 1996, 1997, 1998, 1999a), Yen and Zhao developed a co-channel speech separation system based on the adaptive decorrelation filtering (ADF) algorithm proposed by Weinstein, Feder, and Oppenheim (Weinstein *et al.*, 1993). The system was effective in separating two speech source signals from their convolutive mixtures. Using the system as a processing front end, the accuracy of automatic speech recognition (Zhao, 1993, 1996) on co-channel speech was significantly improved. An informal subjective listening test on the processed speech also showed increased intelligibility. The ADF algorithm was subsequently generalized to the separation of co-channel speech signals from more than two sources (Yen and Zhao, 1999b) and was shown in a simulation to be effective in separating three speech sources. In addition, the generalized algorithm allows extraction of one or more source signals from convolutive mixtures of the full set of source signals, and it reduces computational complexity in such cases (Yen and Zhao, 1999b).

In the current work, the generalized ADF, simply referred to as ADF, is evaluated as a technique for assistive listening. A ''dinner table'' scenario is simulated in the study: a listener would like to hear a particular talker, but the intelligibility of the desired speech is reduced by jammer speech from other talkers at the table and by background diffusive noise. In each interference condition, the desired speech signals before and after ADF processing were evaluated. The objective measure was A-weighted signal-to-noise ratio (SNR), and the subjective measure was sentence intelligibility obtained from a formal listening test on eight normal-hearing subjects and three hearing-impaired subjects. Significant improvements in SNR and sentence intelligibility were observed, indicating the potential of ADF in the design of assistive listening systems.

This paper is organized into four sections. In Sec. II, a brief overview is made for ADF-based co-channel speech separation. Details of experimental conditions are described in Sec. III, and the test results are presented in Sec. IV. The implications of the findings of the current work to the design of assistive listening systems are discussed in Sec. V.

II. OVERVIEW OF ADAPTIVE DECORRELATION FILTERING

A. Mathematical model of co-channel environment

In a co-channel environment, several speech sources may be active simultaneously, and therefore each microphone acquires a mixture of these speech signals. Assume that there are M speech sources, and the source speech signals are zero-mean and uncorrelated to each other. Also assume that M microphones are used to acquire the speech signals, with the microphone i targeting the speech source i, $i=1,2,...,M$. Denote the speech signal generated by the source j as $x_j(t)$ and the signal acquired by the microphone i as $y_i(t)$, and denote the transfer function of the acoustic path from the speech source j to the microphone i by $H_{ij}(f)$. The co-channel speech environment can then be modeled in the frequency domain as

$$\underline{Y}(f)=\mathbf{H}(f)\underline{X}(f), \tag{1}$$

where the signal vectors are defined as $\underline{Y}(f)=[Y_i(f)]_{1\leqslant i\leqslant M}^T$, $\underline{X}(f)=[X_i(f)]_{1\leqslant i\leqslant M}^T$, with T denoting vector transpose, and the transfer function matrix is defined as $\mathbf{H}(f)=[H_{ij}(f)]_{1\leqslant i\leqslant M,1\leqslant j\leqslant M}$. Generally, the acoustic paths are unknown and time varying. As indicated by Eq. (1), the acquired signals $y_i(t)$ are convolutive mixtures of the source signals $x_i(t)$.

Each acquired signal $y_i(t)$ can be decomposed into a sum of two components as

$$y_i(t)=y_{i,T}(t)+y_{i,I}(t), \tag{2}$$

where $y_{i,T}(t)=H_{ii}\{x_i(t)\}$ represents the target speech component, and $y_{i,I}(t)$ represents the interfering component and is defined as $y_{i,I}(t)=\Sigma_{j=1,j\neq i}^{M}H_{ij}\{x_j(t)\}$. The objective of co-channel speech separation is to attenuate the interfering component $y_{i,I}(t)$ in each acquired signal $y_i(t)$, and hence extract the target component $y_{i,T}(t)$ from the convolutive mixture.

B. Adaptive decorrelation filtering

Given that the speech sources are zero-mean and mutually uncorrelated, output signals of a perfect co-channel speech separation system should also be mutually uncorrelated. Define $\underline{f}_{ij}^{(t)}$, $i,j=1,\ldots,M$, $i\neq j$, to be length-N FIR filters that are estimated at time t for separation of source speech signals (Yen and Zhao, 1999b). Then, the ADF algorithm processes the input $y_j(t)$, $j=1,...,M$ of Eq. (1) and generates output signals $v_i(t)$, $i=1,...,M$ according to the equation

$$v_i(t)=y_i(t)-\sum_{j=1,j\neq i}^{M}\underline{y}_j^T(t)\underline{f}_{ij}^{(t)}, \tag{3}$$

where $\underline{y}_j(t)$'s are length-N vectors defined as $\underline{y}_j(t)=[y_j(t-\tau)]_{0\leqslant\tau\leqslant N-1}^T$. Taking decorrelation as the separation criterion, i.e., $E\{v_i(t)v_j(t-\tau)\}=0$, $i\neq j$, $\forall\tau$, the FIR filters can be adaptively estimated as

$$\underline{f}_{ij}^{(t+1)} = \underline{f}_{ij}^{(t)} + \mu(t)\underline{v}_j(t)v_i(t), \quad i,j=1,\ldots,M, \quad i \neq j, \tag{4}$$

where $\mu(t)$ is an adaption gain. For system stability and efficiency, $\mu(t)$ is chosen as

$$\mu(t) = \frac{2\gamma}{(M-1)N\Sigma_{j=1}^{M}\hat{\sigma}_{y_j}^2(t)}, \tag{5}$$

where $0<\gamma<1$ is an empirical constant, and $\hat{\sigma}_{y_j}^2(t)$ is the variance of $y_j(t)$ estimated from the latest input samples. When the filters converge, the output signal $v_i(t)$ becomes the extracted source signal $x_i(t)$, subject to a certain linear transformation, $i=1,\ldots,M$.

Based on Robbins–Monro's stochastic approximation method, a theoretical analysis has been made on the applicability condition of ADF. The analysis shows that in order to effectively reduce cross interference among speech sources in a given acoustic environment, the multimicrophone configuration needs to satisfy the condition of $|H_{ij}(f)H_{ji}(f)| < |H_{ii}(f)H_{jj}(f)|, \ i \neq j, \ \forall f$ (Yen and Zhao, 1999b), i.e., the cross-coupled acoustic paths need to attenuate source signals more than the direct acoustic paths do. In the above assumed co-channel model, when each microphone is placed closer to its target source than to the interference sources, this condition is satisfied in general.

C. Applications

The proposed application of ADF to assistive listening in the ''dinner table'' scenario is but one of many possibilities. Some others include teleconference, robust speech recognition, stage sound processing, etc. For teleconference, a co-channel speech separation system can be used to separate multiple talkers' speech at one site of the meeting and the separated speech signals can be sent to remote sites for selective listening. For robust speech recognition inside a vehicle, for example, microphones can be distributively placed in accordance with the locations of speech and interference sources, such as driver, radio, engine, etc., and the extracted driver's speech would allow more accurate automatic recognition. For stage sound pick up, the recorded signals consisting of actors' voices and special sound effects can be separated, edited, and remixed to generate enhanced sound environments.

III. EXPERIMENTAL CONDITIONS

In simulating the ''dinner table'' scenario, the cross-coupled channel filters were measured in a sound booth, and the co-channel speech signals were computed according to Eq. (1) by using standard speech and noise materials (the simulation conditions were verified to be consistent with a real sound field recording). The estimation of separation filters and the filtering of acquired signals were implemented according to Eqs. (4) and (3), respectively.

A. Measurement of acoustic paths

The configuration of the sound booth for measuring the cross-coupled acoustic paths is shown in Fig. 1. As shown in the figure, five ''people'' sat at a round table with an equal spacing. The microphones were installed 9″ below the respective loud speakers that represented the mouth positions of the dinner partners. The acoustic paths between each pair of speaker–microphone locations were measured, yielding a total of 25 FIR filters. Based on the measured impulse responses, the direct-to-reverberant energy ratios at the listener and talker locations were computed over 20 TIMIT sentences. The ratios at the listener and talker locations were measured as −0.57 dB and 3.01 dB, respectively.

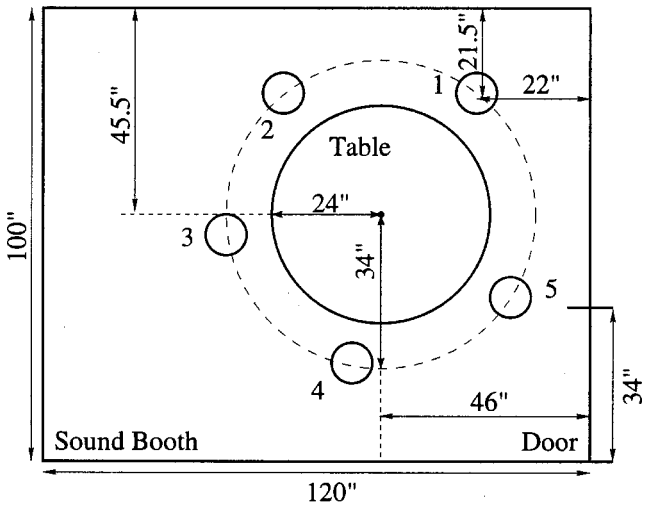

FIG. 1. Sound booth where the acoustic paths were measured for simulation of ''dinner table'' scenario.

B. Generation of speech, jammers and diffusive noise

Among the five locations shown in Fig. 1, location 1 was chosen for the listener and the cross-table location 4 was chosen for the talker. The locations 2, 3, and 5 were used for simultaneous jammers. For the designated talker, the speech materials of HINT sentences (Nilsson *et al.*, 1994) were played through a load-speaker, and for the designated jammers, the TIMIT speech sentences (Lamel *et al.*, 1986) were played. The HINT speech consists of short sentences spoken by a male talker, designed for measuring hearing thresholds of either normal or impaired hearing. The TIMIT speech was randomly taken from a database of sentences collected from over 600 male and female talkers. In forming each jammer, the silence periods before and after each TIMIT sentence were stripped off, and the extracted sentences were then concatenated. The two simulated interference conditions are described below.

Condition 1. Speech jammers

In this condition, the interference consisted of three simultaneous jammers. The signal-to-noise ratio (SNR) was measured at the listener's location as the ratio of the A-weighted energy of the desired speech to sum of A-weighted energies of the three jammers, where the short-time spectra of the desired speech and jammers were A-weighted by a bandpass filter (Pierce, 1994) to emphasize perceptually important frequency bands. It is noted that A-weighting is a standard method of characterizing noise environment, and as a contrast, articulation-index (AI) based weighting (French and Steinberg, 1947) is commonly used

for characterizing overall signal power as a result of array processing. AI-weighted SNR would be very similar to A-weighted SNR in the current study since the spectra of signal and noise were similar. The A-weighted SNR (simply referred to as SNR here) was designated the unit of dBA. Four levels of SNRs, −12, −15, −18, and −21 dBA, were produced at the listener's location, with the energies of desired speech and interference adjusted by the following procedure. A speech shaped noise was used for sound level calibration, where the spectrum of the speech-shaped noise matched the long-term spectrum of the HINT test speech materials. At the talker's location, calibration speech-shaped noise was first played and its level was adjusted to yield a fixed sound level of 65 dBA at the listener's location. The average root mean-squared value of each HINT speech sentence was adjusted to be the same as the calibration noise, i.e., when the sentences were played at the talker's location, the average received sound level was also 65 dBA at the listener's location. The sound levels of the three jammers were constrained to be identical at the listener's location. Again, the sound level of the listener's location was first calibrated by the speech-shaped noise, and the levels of jammer speech were then adjusted in a sentence-by-sentence fashion to match the root-mean-squared value of the noise. At the listener-location SNRs (LL−SNR) of −12, −15, −18, and −21 dBA, the sound level of each of the three jammers at the listener location was 72.2, 75.2, 78.2, and 81.2 dBA, respectively.

Condition 2: Speech jammers and diffusive noise

In this condition, the interference consisted of three simultaneous jammers as well as a speech-shaped diffusive noise. In generating the diffusive noise, the speech-shaped stationary noise as described above was played through four loud speakers that were placed close to the ceiling and at the four corners of the sound booth. The SNR was measured as the ratio of the A-weighted energy of the desired speech to sum of A-weighted energies of the jammers and the diffusive noise. The simulation procedure was similar to that described in Condition 1. At the listener's location, the talker's sound level was again fixed as 65 dBA, and the dBA levels of the three jammers and the diffusive noise were identical. At the LL−SNRs of −12, −15, −18, and −21 dBA, the sound level of each interference source at the listener location was 71.0, 74.0, 77.0, and 80.0 dBA, respectively.

C. Validation on the simulation conditions

In order to ensure the simulation conditions to be consistent with sound field recordings, a pilot test was carried out at the House Ear Institute before the formal listening test. In the pilot test, four subjects with normal hearing were provided with two sets of HINT speech sentences: one generated by the above simulation conditions and another recorded in the sound field, where the sound field was constructed according to the above described procedure. The correct word percentages measured from the two sets of speech over the four subjects were compared. The comparison indicated insignificant differences between the two sets of results and hence validated the simulation. Based on the consideration that simulation allows a more precise control of experimental parameters and is convenient to implement, the formal listening tests were conducted under the simulation conditions.

D. ADF implementation

The ADF algorithm was implemented to run in an online mode, i.e., the output signal samples of each time t were estimated by using the filter estimates obtained from the input signals up to t, and therefore processing was accomplished in one pass. As a contrast, in a multiple-pass processing, filter estimation would be made iteratively over a block of data and the filter estimates obtained in the last iteration would be used to perform source separation for the same data block. Although an iterative implementation in general leads to higher SNR gains, one-pass processing was chosen based on the consideration of computation load and delay, as well as the potential need for tracking time variation of acoustic paths within a block.

In a practical co-channel environment, jammer signals may not be always on. The issue of performing ADF estimation in the absence of jammers was investigated previously in a two-source separation problem (Yen and Zhao, 1999a). The finding is that if the cross-coupled acoustic paths are strong ($|H_{ij}(f)H_{ji}(f)| \approx |H_{ii}(f)H_{jj}(f)|$, $i \neq j$) and if the jammers are inactive for an extended period of time, then adaptive filter estimation may go wrong. As a consequence, significant distortion or cancellation effect may be observed in the estimated target speech signals. A coherence-function based active-source detection algorithm was developed for this case (Yen and Zhao, 1999a), where a coherence function between each pair of system output signals was used to detect the active regions of each speech source, and such regions formed the basis for on−off switching of filter estimation. Although the method may be extended to the M-source case along a similar line of idea, the algorithm has not been fully developed and is left for a future work. On the other hand, the interference conditions as considered in the ''dinner table'' scenario were moderate. When jammers were absent, the distortion or cancellation effect on target speech as introduced by the estimation algorithm was insignificant. Therefore, in processing the speech signals, the estimation algorithm was applied from beginning to end instead of being switched on or off from time to time.

IV. EXPERIMENTAL RESULTS

The assistive listening system was evaluated through the gains of A-weighted signal-to-noise ratio and the percentage of correctly recognized words by human subjects. It was assumed that a listener could choose a talker by selecting the assistive system's output that targets the talker. Since the SNR was highest at the selected talker's location, the SNR and word correct percentage were measured on speech acquired and processed at the talker's location, i.e., on $y_4(t)$ for conditions before ADF processing and on $v_4(t)$ for conditions after ADF processing. As such, the measured improvements represented the net effect of ADF processing. On the other hand, the SNRs at the listener location (LL−SNR)

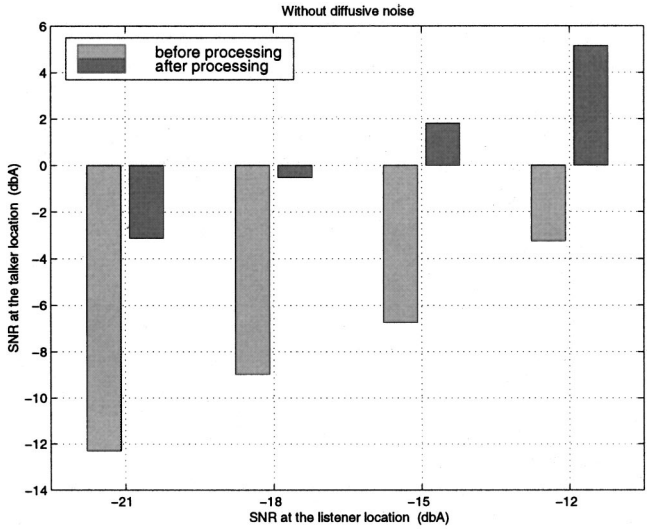

FIG. 2. The SNR at the talker's location before and after ADF processing in the jammers only condition.

represented the difficulty level as experienced by the listener without the assistive listening system, and therefore the LL–SNRs were used for identifying the testing conditions.

A. Signal-to-noise ratio

For each specified LL–SNR and under each interference condition, the SNRs at the talker's location (TL–SNR) were calculated before and after ADF processing. Each SNR value was obtained from one distinct list of 10 HINT sentences, with each list consisting of approximately 50 short words. The results for the three-jammer interference condition are shown in Fig. 2, and the results for the jammer and diffusive noise interference condition are shown in Fig. 3. In Fig. 3, the results are also summarized by signal-to-jammer ratio (SJR) before and after ADF where for each LL-SNR condition, the four bars ordered from left-to-right represent SNR before processing, SNR after processing, SJR before processing, and SJR after processing, respectively. Figure 2 shows that in the jammer-alone interference conditions, ADF

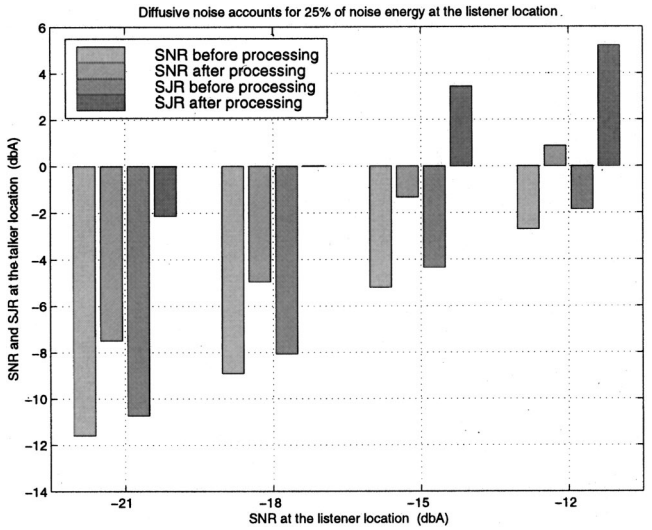

FIG. 3. The SNR and SJR at the talker's location before and after ADF processing in the jammers and diffusive noise condition.

improved the TL–SNR by 8.39 to 9.18 dBA for the initial LL–SNR conditions of −12, through −21 dBA. Figure 3 shows that in the presence of both jammers and diffusive noise, ADF improved the TL–SNR by 3.58 to 4.11 dBA for the initial LL–SNRs of −12 through −21 dBA, and it improved the SJR in the range of 7.03 to 8.61 dBA, which was close to the SNR gain in the jammer-alone case. These results indicate that the ADF technique was effective in attenuating jammers but ineffective in attenuating diffusive noise, which is not surprising since diffusive noise is spatially uncorrelated and decorrelation processing would not produce any impact.

B. Intelligibility

The listening subject test was conducted at the House Ear Institute. A total of 11 subjects were recruited in the study, eight with normal hearing and three with hearing impairments. Normal hearing is defined by having audiometric threshold <30 dBL across the wide band of speech spectrum, with threshold measurements made at the frequencies (in Hz) of 250, 500, 1000, 2000, 3000, 4000, 6000, and 8000. Every hearing-impaired subject has, to varying degrees, a severe high-frequency hearing loss. Of the three hearing-impaired subjects, one wore hearing aids, and the other two should be wearing hearing aids but have never tried them. In the subject listening test, none of the subjects wore hearing aids.

The speech data before and after ADF processing were recorded on CD. There were a total of 14 testing cases, resulting from the combination of two interference conditions, four LL–SNRs, and before and after ADF processing, where in the jammer and diffusive noise condition, the two cases of LL–SNR=−21 dBA (before and after ADF processing) were excluded due to extremely low scores of word correct percentages. In order to avoid effects of learning and memorization, the HINT lists were made distinct among the 14 testing conditions. Subjects were asked to listen to a CD under headphones and transcribe a HINT list for each testing condition. Prior to the transcription, subjects were instructed to listen to track number 1 and select a comfortable listening level with the CD volume control. They were then told to leave the volume control of the setting for the remainder of the experiment. It is noted that the test materials were not adjusted for frequency-dependent hearing loss. In each testing condition, the percentages of word correct were averaged separately for the normal-hearing group and the hearing-impaired group.

For the normal-hearing subjects, the listening test results are summarized in Figs. 4 and 5. In jammer alone interference and at the LL–SNR of −12, −15, −18, and −21 dBA, the absolute gains of word correct percentage were 7.3%, 20.2%, 46.6%, and 52.3%, respectively. In both jammers and diffusive noise and at the LL–SNRs of −12, −15, and −18 dBA, the absolute gains of word correct percentage were 11.0%, 43.3%, and 29.6%, respectively. For the hearing-impaired subjects, the listening test results are summarized in Figs. 6 and 7. In jammer alone interference and at the LL–SNRs of −12, −15, −18, and −21 dBA, the absolute gains were 32.7%, 59.0%, 55.2%, and 37.8%, respectively. In both

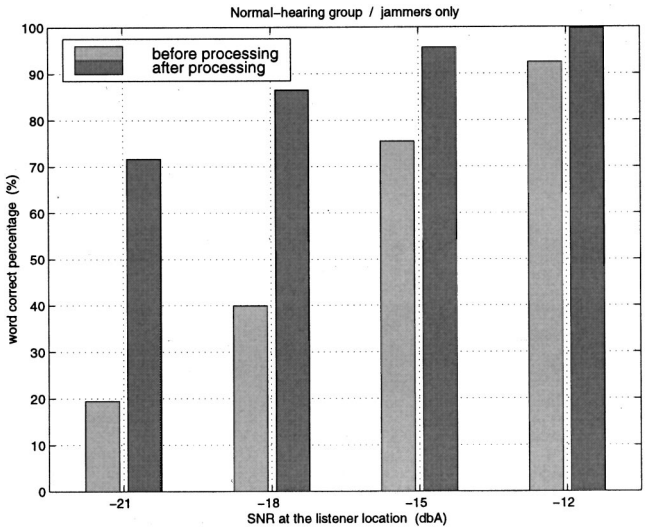

FIG. 4. The word correct percentage before and after ADF processing in the jammers only condition for the normal-hearing group.

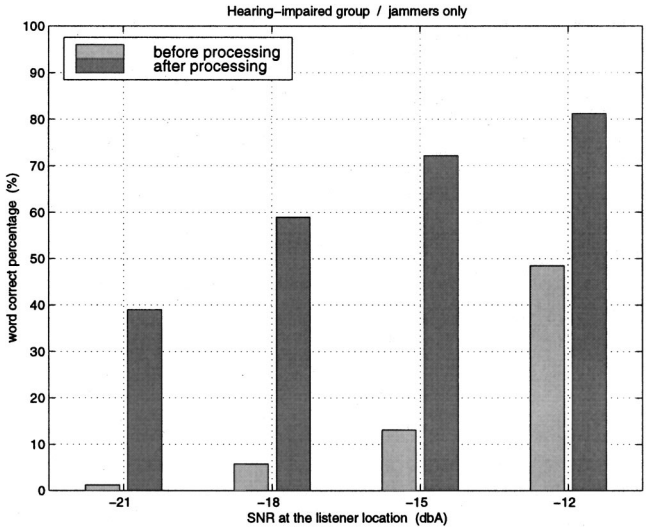

FIG. 6. The word correct percentage before and after ADF processing in the jammers only condition for the hearing-impaired group.

jammers and diffusive noise, and at the LL–SNRs of −12, −15, and −18 dBA, the absolute gains of word correct were approximately 38.0%, 29.1%, and 5.4%, respectively. Based on the results of Figs. 4–7, it is estimated that in jammer alone interference, ADF processing improved the speech reception threshold by 5 dBA for the normal-hearing subjects and by 8 dBA for the hearing-impaired subjects, and in the jammer and diffusive noise interference, ADF improved the speech reception threshold by 3 dBA for the normal-hearing subjects and by 4 dBA for the hearing-impaired subjects.

The means and standard deviations of word correct percentage in each testing condition are provided in Table I. For the normal-hearing group, ADF not only improved the mean values but it also reduced the standard deviations. For the hearing-impaired group, the standard deviations remained large due to the small number of hearing-impaired subjects.

C. Analysis of intelligibility improvement

A statistical significance test was made on the listening test results. The difference between the percentage word correct values measured after and before ADF processing is assumed to be a Gaussian random variable c with an unknown variance. The null hypothesis H_0 postulated an insignificant effect of ADF processing, i.e., $E[c]=0$, and the alternative hypothesis H_1 asserted a positive difference, i.e., $E[c]>0$. Denote the sample mean and sample variance of the listening evaluation data as $\overline{c}$ and s^2, and denote the number of subjects by n. The test statistic was $q=\overline{c}/(s/\sqrt{n})$, which had a t distribution with $n-1$ degrees of freedom (Papoulis, 1991).

Without diffusive noise and across the four LL–SNRs, H_0 can be rejected with the type-I errors of $\alpha<0.005$ ($t_\alpha=3.335$) and $\alpha<0.01$ ($t_\alpha=4.541$) for the two groups of normal hearing and hearing impaired, respectively. In diffusive noise and for the first group, $\alpha<0.005$ is held at the LL–SNRs of −15 and −18 dBA, and the level of type-I error was increased to $\alpha<0.025$ ($t_\alpha<2.306$) at −12 dBA, due to a larger variation of scores before ADF processing. In diffusive noise and for the second group, $\alpha<0.01$ is held at the LL–SNRs of −12 and −15 dBA, and the level of significance

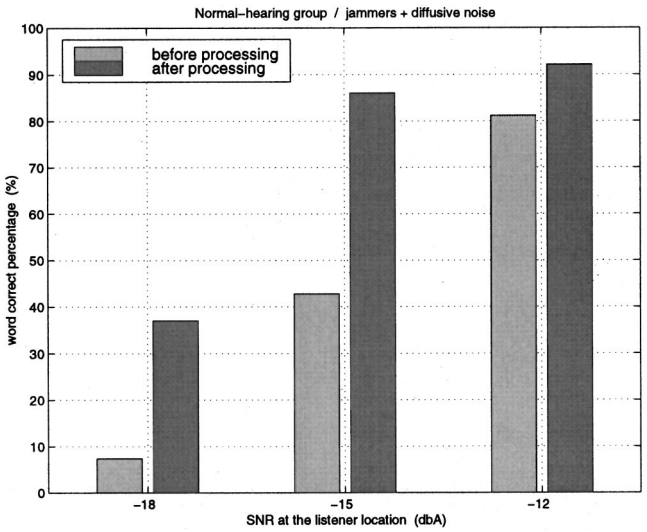

FIG. 5. The word correct percentage before and after ADF processing in the jammers and diffusive noise condition for the normal-hearing group.

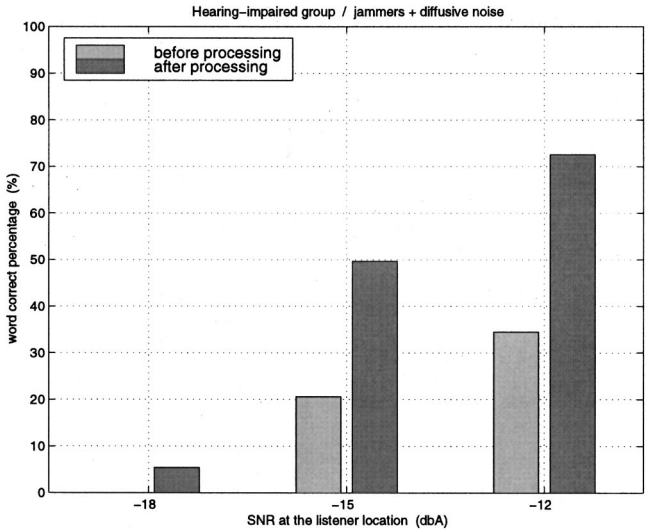

FIG. 7. The word correct percentage before and after ADF processing in the jammers and diffusive noise condition for the hearing-impaired group.

TABLE I. Means and standard deviations of word correct percentage before and after ADF processing for the two interfering conditions.

	Normal-hearing group				Hearing-impaired group			
	Before processing		After processing		Before processing		After processing	
LL-SNR	mean	s.d.	mean	s.d.	mean	s.d.	mean	s.d.
Condition 1: Jammers only								
−12 dBA	92.45%	4.62%	99.76%	0.67%	48.43%	15.25%	81.13%	14.74%
−15 dBA	75.49%	8.95%	95.68%	3.50%	13.07%	4.08%	72.12%	18.21%
−18 dBA	39.90%	11.43%	86.54%	8.66%	5.77%	1.92%	58.97%	13.64%
−21 dBA	19.44%	8.85%	71.70%	8.32%	1.23%	1.07%	38.99%	3.93%
Condition 2: Jammers and diffusive noise								
−12 dBA	81.14%	13.22%	92.16%	5.03%	34.50%	7.09%	72.55%	8.99%
−15 dBA	42.73%	10.51%	86.03%	6.66%	20.61%	10.01%	49.67%	13.06%
−18 dBA	7.35%	8.24%	36.99%	17.06%	0.00%	0.00%	5.44%	6.23%

was increased to $\alpha<0.1$ ($t_\alpha=1.638$) at LL-SNR of −18 dBA, due to a larger variation of scores after ADF processing. The increased α level in the hearing-impaired group was mainly attributed to the small number of subjects ($n=3$), as it was difficult recruiting hearing-impaired subjects at the time the listening test was carried out. In summary, the hypothesis test supports the notion that the ADF processing produced statistically significant improvement to speech intelligibility as perceived by both normal hearing and hearing-impaired subjects under the studied conditions.

D. System realization

The above experimental results show that the ADF algorithm can effectively reduce cross-interference among the speech sources. In constructing an assistive listening system for the ''dinner table'' scenario, microphones can be arranged on the table so that each microphone targets a dinner partner. Each listener can tune to a desired talker by selecting the corresponding system output. The ADF algorithm can be implemented on a digital signal processing board. The ADF algorithm as described in the current work is based on direct-form FIR filters, which requires floating-point DSP hardware to provide the needed numerical accuracy. The simulations described above, which worked with a 16 kHz sampling rate and employed 600-tap FIR filters, required about 270 MMPS (10^6 multiplications per second) to separate all four speech signals, or 154 MMPS to extract only one desired speech signal. As a result, it would require several high-end floating-point DSPs such as TMS320C44 (with 60 MFLOPS capability) working in parallel to implement such a system. Alternatively, a similar system working with a 10 kHz sampling rate and extracting only one desired speech signal could be implemented using a single TMS320C44. Recently, a lattice-ladder structured ADF algorithm has been formulated and developed (Yan and Zhao, 2000). In this formulation, numerical stability can be attained while using fixed-point DSP hardware, which would allow faster computation and lower power consumption.

The convergence behavior of the ADF algorithm depends on the number of speech sources in a co-channel speech system, the desired number of speech sources to be separated, and the condition of acoustic paths. In the above described experiments, the separation filters were initialized as zeros. In this cold-start adaptive mode, 5 and 10 seconds of adaptive estimation led to approximately 50% and 75% of converged SJR gain, respectively, and 30 seconds of adaptive estimation basically led to converged SJR gain. In a tracking mode, the system is expected to be able to quickly adapt to time variations of acoustic paths due to changes of sound source positions resulting from head turns, body movements, etc.

Beside the method of placing one microphone close to one target sound source, which may be overly constrictive in certain applications, there are alternative ways of designing microphone configurations to satisfy the theoretical condition described in Sec. II B. Two alternative methods that are planned for a future study are described below.

For example, in the ''dinner table'' scenario, if directional microphones are used instead of omnidirectional ones, then microphones may be placed at the center of the table, with each microphone's receiving pattern directed toward its target talker. Note that in such a case, the transfer functions $H_{ij}(f)$ represent the combined effect of room acoustic paths and the spatial–temporal response patterns of microphones.

A more flexible implementation is to combine adaptive array beamforming with co-channel speech separation. In the combined approach, beamforming is used for spatial-selective sound capturing, and multiple beams can be formed to capture simultaneous speech signals in different directions. It is known that small-sized beamformers suffer from limited beam resolution. With a further processing on the acquired speech signals by ADF, the jammer speech signals that are leaked into the beams can be attenuated. As such, beamforming and co-channel speech separation would potentially complement each other and relax the design constraints in each. It is noted that the requirement on system computation power may be increased due to the preprocessing stage of beamforming.

V. DISCUSSION

Overall, ADF processing has led to significant improvement in both the objective measure of signal-to-noise ratio and the subjective measure of sentence intelligibility. The

following observations are made from the experimental results.

ADF is effective in the separation of co-channel speech, even in the presence of diffusive noise. However, ADF is not able to attenuate diffusive noise. An integration of speech enhancement with ADF may provide a better solution to the interference condition with both jammers and diffusive noise, the requirement being that the enhancement step does not significantly distort speech signals.

As indicated by the current work, interference consisting of both jammers and diffusive noise was more detrimental to speech comprehension than interference with jammers alone. Informal evaluation also revealed that at each given SNR, three jammers were more detrimental to speech comprehension than one or two jammers, and a higher proportion of diffusive noise was more detrimental than a lower proportion of diffusive noise. This may be attributed to the fact that the energy envelopes of speech jammers are modulated rather than constant, allowing subjects to perceive words correctly in the low-energy intervals of jammers.

For subjects with normal hearing, the LL–SNR level of −12 dBA in the interference condition of three jammers appears to be the benefit threshold for the ADF; above −12 dBA, the subjects were able to comprehend the HINT sentence speech that was acquired by the talker-location microphone nearly perfectly without ADF processing. In both jammers and diffusion noise, the benefit threshold for ADF appears to be shifted by 3 dBA, i.e., the ADF processing should provide improvement in word correct percentage at −9 dBA as well. For subjects with hearing impairments, the benefit threshold of ADF could be shifted to −6 dBA, or even −3 dBA in both types of interference conditions. This shift of threshold also implied the degree of hearing impairments of the subjects who participated in the studies. In a practical dinner table scenario, the LL–SNRs of −6 to −3 dBA may be more realistic than −9 dBA or below, and the assistive listening system is expected to be useful mainly for users with hearing impairments. In other scenarios where more severe LL–SNR conditions are likely, or the target talker has a very soft voice, the system is expected to be useful for users with normal hearing as well.

Based on this ''dinner table'' study, a conclusion is drawn that ADF is a promising new technique for constructing assistive listening devices that will benefit both populations of normal hearing and hearing impairments. On the other hand, it is expected that in certain acoustic conditions and applications, processing techniques such as microphone array beamforming and speech waveform enhancement may be integrated with ADF to achieve flexibility and performance that cannot be achieved by ADF alone. The application conditions of various types of processing techniques and their potential integration will be investigated in a future work.

ACKNOWLEDGMENT

This work is supported in part by NSF under the grant NSF EIA 9911095 and a grant from the Whitaker Foundation.

Cole, R. *et al.* (**1995**). ''The challenge of spoken language systems: Research directions for the nineties,'' IEEE Trans. Speech Audio Process. **3**, 1–21.

Comon, P., Herault, J., and Jutten, C. (**1991**). ''Blind separation of sources, Part II: Problem statement,'' Signal Process. **24**, 11–20.

Deller, J. R., Proakis, J. G., and Hensen, J. H. (**1993**). *Discrete Time Processing of Speech Signals* (Prentice Hall, New York).

Desloge, J. G., Rabinowitz, W. M., and Zurek, P. M. (**1997**). ''Microphone-array hearing aids with binaural output—Part I: Fixed processing systems,'' IEEE Trans. Speech Audio Process. **5**, 529–542.

French, N. R., and Steinberg, J. C. (**1947**). ''Factors governing the intelligibility of speech sounds,'' J. Acoust. Soc. Am. **19**, 90–119.

Greenberg, J. E., and Zurek, P. M. (**1992**). ''Evaluation of an adaptive beam forming method for hearing aids,'' J. Acoust. Soc. Am. **91**, 1662–1676.

Hoffman, M. W., Trine, T. D., Buckley, K. M., and Van Tasell, D. J. (**1994**). ''Robust adaptive microphone array processing for speech enhancement,'' J. Acoust. Soc. Am. **96**, 759–770.

Jutten, C., and Heuralt, J. (**1991**). ''Blind separation of sources, Part I: An adaptive algorithm based on neuromimetic architecture,'' Signal Process. **24**, 1–10.

Kates, J. M. (**1993**). ''Superdirective arrays for hearing aids,'' J. Acoust. Soc. Am. **94**, 1930–1933.

Lamel, L. F., Kassel, R. H., and Seneff, S. (**1986**). ''Speech Database Development: Design and Analysis of the Acoustic Phonetic Corpus,'' *Proceedings of Speech Recognition Workshop (DARPA)*.

Nilsson, M., Soli, S. D., and Sullivan, J. A. (**1994**). ''Development of the hearing in noise test for the measurement of speech reception thresholds in quiet and in noise,'' J. Acoust. Soc. Am. **95**, 1085–1099.

Papoulis, A. (**1991**). *Probability, Random Variables, and Stochastic Processes*, 3rd ed. (McGraw-Hill, New York).

Peterson, P. M. (**1989**). Ph.D. dissertation, Massachusetts Institute of Technology, Cambridge, MA.

Pierce, A. D. (**1994**). *Acoustics, An Introduction to the Physical Principles and Applications*.

Shamsunder, S., and Giannakis, G. B. (**1997**). ''Multichannel blind signal separation and reconstruction,'' IEEE Trans. Speech Audio Process. **5**, 515–528.

Smedley, T. C., and Schow, R. L. (**1992**). ''Frustrations with Hearing Aid Use: Candid Reports from the Elderly,'' Hear. Res. **43**, 21–27.

Soede, W., Berkhout, A. J., and Bilsen, F. A. (**1993a**). ''Development of a directional hearing instrument based on array technology,'' J. Acoust. Soc. Am. **94**, 785–798.

Soede, W., Bilsen, F. A., and Berkhout, A. J. (**1993b**). ''Assessment of a directional hearing microphone array for hearing impaired listener,'' J. Acoust. Soc. Am. **94**, 790–808.

Sorouchyari, E. (**1991**). ''Blind separation of sources, Part III: Stability analysis,'' Signal Process. **24**, 21–29.

Stadler, R. W., and Rabinowitz, W. M. (**1993**). ''On the potential of fixed arrays for hearing aids,'' J. Acoust. Soc. Am. **94**, 1332–1342.

Tong, L., Inouye, Y., and Liu, R. (**1993**). ''Waveform preserving blind estimation of multiple independent sources,'' IEEE Trans. Signal Process. **41**, 2461–2470.

Van Gerven, S., and Van Compernolle, D. (**1995**). ''Signal separation by symmetric adaptive decorrelation: Stability, convergence, and uniqueness,'' IEEE Trans. Signal Process. **43**, 1602–1612.

Weinstein, E., and Oppenheim, A. V. (**1993**). ''Multi-channel signal separation by decorrelation,'' IEEE Trans. Speech Audio Process. **1**, 405–413.

Welker, D. P., Greenberg, J. E., Desloge, J. G., and Zurek, P. M. (**1997**). ''Microphone-array hearing aids with binaural output—Part II: A two-microphone adaptive system,'' IEEE Trans. Speech Audio Process. **5**, 543–551.

Yellin, D., and Weinstein, E. (**1994**). ''Criteria for multichannel signal separation,'' IEEE Trans. Signal Process. **42**, 2158–2168.

Yellin, D., and Weinstein, E. (**1996**). ''Multichannel signal separation: Methods and analysis,'' IEEE Trans. Signal Process. **44**, 106–118.

Yen, K., and Zhao, Y. (**1996**). ''Robust automatic speech recognition using a multi-channel signal separation front-end,'' Proc. ICSLP **3**, 1337–1340.

Yen, K., and Zhao, Y. (**1997**). ''Co-channel speech separation for robust automatic speech recognition: Stability and efficiency,'' Proc. ICASSP **2**, 859–862.

Yen, K., and Zhao, Y. (**1998**). ''Improvements on co-channel speech separation using ADF: Low complexity, fast convergence, and generalization,'' Proc. ICASSP **2**, 1025–1028.

Yen, K., and Zhao, Y. (**1999a**). ''Adaptive co-channel speech separation and recognition,'' IEEE Trans. Speech Audio Process. **7**, 138–151.
Yen, K., and Zhao, Y. (**1999b**). ''Adaptive decorrelation filtering for separation of co-channel speech signals from $M>2$ sources,'' Proc. ICASSP **2**, 801–804.
Yen, K., and Zhao, Y. (**2000**). ''Lattice-ladder structured adaptive decorrelation filtering for cochannel speech separation,'' Proc. ICASSP **1**, 388–391.
Zhao, Y. (**1993**). ''A speaker-independent continuous speech recognition system using continuous mixture Gaussian density HMM of phoneme-sized units,'' IEEE Trans. Speech Audio Process. **1**, 345–361.
Zhao, Y. (**1996**). ''Self-Learning Speaker and Channel Adaptation Based on Spectral Variation Source Decomposition,'' Speech Commun. **18**, 65–77.

An overlapping-feature-based phonological model incorporating linguistic constraints: Applications to speech recognition

Jiping Sun and Li Deng[a)]
University of Waterloo, Waterloo, Ontario N2L3G1, Canada

(Received 9 July 2000; revised 21 December 2000; accepted 27 August 2001)

Modeling phonological units of speech is a critical issue in speech recognition. In this paper, our recent development of an overlapping-feature-based phonological model that represents long-span contextual dependency in speech acoustics is reported. In this model, high-level linguistic constraints are incorporated in automatic construction of the patterns of feature-overlapping and of the hidden Markov model (HMM) states induced by such patterns. The main linguistic information explored includes word and phrase boundaries, morpheme, syllable, syllable constituent categories, and word stress. A consistent computational framework developed for the construction of the feature-based model and the major components of the model are described. Experimental results on the use of the overlapping-feature model in an HMM-based system for speech recognition show improvements over the conventional triphone-based phonological model. © *2001 Acoustical Society of America.* [DOI: 10.1121/1.1420380]

PACS numbers: 43.72.Ne, 43.72.Ar [DOS]

I. INTRODUCTION

Modeling phonological units of speech, also referred to as pronunciation or lexicon modeling, is a critical issue in automatic speech recognition. Over the past several years, we have been studying this issue from the perspective of computational phonology, motivated by some recent versions of nonlinear phonology.[1,2] The computational framework developed is based on subphonemic, overlapping articulatory features where the rule-governed overlap pattern is described mathematically as a finite-state automaton. Each state in the automaton corresponds to a feature bundle with normalized duration information specified.[3,4] In this paper, we report our new development of the feature-based phonological model which incorporates high-level linguistic (mainly prosodic) constraints for automatic construction of the patterns of feature overlapping and which includes new implementation of the model. We also report positive results of experiment on use of the feature-based model as the HMM-state topology generator for speech recognition.

In our feature-based phonological model, patterns of feature overlapping are converted to an HMM state-transition network. Each state encodes a bundle of overlapping features and represents a unique, symbolically coded articulatory configuration responsible for producing speech acoustics based on that configuration. When the features of adjacent segments (phonemes) overlap asynchronously in time, new states are derived which model either the transitional phases between the segments or the allophonic alternations caused by the influence of context. Since feature overlapping is not restricted to immediately neighboring segments, this approach is expected to show advantages over the conventional context-dependent modeling based on diphones or triphones. Use of diphone or triphone units necessarily limits the context influence to only immediately close neighbors, and demands a large amount of training data because of the large number of the units (especially triphone units) combinatorially generated. Such a drawback is completely eliminated in the overlapping-feature-based model described in this paper.

The feature-based phonological model and the conventional, triphone-based model currently most popular in speech recognition[5] are alternative ways of representing words in the lexicon and their pronunciation using HMM states. Their differences can be likened to ''atomic'' units versus ''molecular'' units—fine versus coarse scales in representing the fundamental building blocks of speech utterances. Consequences of such a disparity are that the feature-based model provides the long-span context-dependency modeling capability while the triphone model provides only the short-span one, and that the feature-based model is much more parsimonious and economical in lexical representation than the triphone model. This latter advantage is due to the fact that several distinct phones may share common features while feature overlapping concerns only the spreading of such features with no identity changes. As a result, the triphone model has much greater training-data requirements than the feature-based model for speech recognizer construction.

The feature-based model further permits construction of language-independent recognition units and portability of speech recognizers from one language to another in a principled way,[6] while the triphone model is not able to do the same. This is because articulatory features are commonly shared by different languages and play important mediating roles in mapping the underlying, perceptually defined phonological units to surface acoustic forms. A feature-overlapping model defined by general articulatory dynamics can potentially generate all possible transitory and allophonic states given canonical articulatory descriptions of phonemes and continuous speech contexts. The task of a training process against a particular language, on the other hand, is to determine a subset of feature bundles employed by the language so that the underlying units can be correctly ''perceived'' by

[a)]Current address: Microsoft Research, Redmond, WA 98052.

 0001-4966/2002/111(2)/1086/16/$19.00

the listener in terms of feature-bundle sequences. Therefore, feature bundles derived from context-induced overlapping can form a universal set for describing all sounds in all languages at a mediating level between acoustic signals and the lexical units. The main challenge for developing the feature-based phonological model is its implementation complexity, which is the main focus of this paper. To what extent the feature bundles obtained from one language's data is shared by another language is both a theoretical topic as well as an empirical issue, and demands further study beyond the scope of this paper.

In our previous work, the feature overlapping rules were constructed based only on the information about the phoneme (i.e., segment) identity in each utterance to be modeled.[3,7,8] It is well established[1,2,9,10] that a wealth of linguistic factors beyond the level of phoneme, in particular prosodic information (syllable, morpheme, stress, utterance boundaries, etc.), directly controls the low-level feature overlapping. Thus, it is desirable to use such high-level linguistic information to control and to constrain feature overlapping effectively. As an example, in pronouncing the word *display*, the generally unaspirated /p/ is constrained by the condition that an /s/ precedes it in the same syllable onset. On the other hand, in pronouncing the word *displace*, *dis* is a morphological unit of one syllable and the /p/ in the initial position of the next syllable subsequently tends to be aspirated.

In order to systematically exploit high-level linguistic information for constructing the overlapping-feature-based phonological model in speech recognition, we need to develop a computational framework and methodology in a principled way. Such a methodology must be sufficiently comprehensive to cover a wide variety of utterances (including spontaneous speech) so as to be successful in speech recognition. Development of such a methodology is the major thrust of the research reported in this paper.

II. A GENERAL FRAMEWORK OF FEATURE OVERLAPPING

A. Use of high-level linguistic constraints

Our general approach to pronunciation modeling is based on the assumption that high-level (e.g., prosodic) linguistic information controls, in a systematic and predictable way, feature overlapping across feature dimensions through long-span phoneme sequences. The high-level linguistic/prosodic information used in the current implementation of the feature-based model for constraining feature overlapping includes

(i) Utterance, word, morpheme, and syllable boundaries. (Syllable boundaries are subject to shifts via resyllabification.)
(ii) Syllable constituent categories: onset, nucleus, and coda.
(iii) Word stress and sentence accents.

Morpheme boundary and syllabification are key factors in determining feature overlapping across adjacent phonemes. For example, aspiration of voiceless stops in *dis-place* and in *mis-place* versus nonaspiration of the stop in *di-splay* are largely determined by morpheme boundary and syllabification in these words. In the former case, overlapping occurs at the larynx tier (see Sec. II B for the definition of articulatory feature tiers). Utterance and word boundaries condition several types of boundary phenomena. Examples of the boundary phenomena are glottalized word onset and breathy word ending at utterance boundaries, and the affrication rule at word boundaries (e.g., compare *at right* with *try*).[11] Likewise, association of a phoneme with its syllable constituent influences pronunciation in many ways. For example, stops are often unreleased in coda but not so in onset. An example of the effect of word-stress information on feature overlapping is the alveolar-flap rule, which only applies to the contextual environment where the current syllable is unstressed and the preceding syllable is stressed within the same word.

This kind of high-level linguistic constraint is applied to our framework through a predictive model which parses the training sentences into accent groups at the sentence level and syllabic components at the lexical level. The accent group identification is mainly through part-of-speech tagging information. The syllabic component identification is mainly through a context-free grammar parser based on rules of syllable composition by phonemes (see Appendix A). After this analysis, a sentence is represented by a sequence of symbolic vectors, each containing the phoneme symbol and its syllabic, boundary, and accent information which governs the pronunciation of each phoneme in continuous speech. For example, the utterance ''The other one is too big'' will be represented as

[dh ons ub] (ons = syllable onset, ub = utterance beginning)
[iy nuc we ust] (nuc = syllable nucleus, we = word end, ust = unstressed)
[ah nuc wb] (wb = word beginning)
[dh ons]
[ax nuc we ust]
[w ons wb]
[ah nuc ust]
[n cod we] (cod = syllable coda)
[ih nuc wb ust]
[s cod we]
[t ons wb]
[uw nuc we str] (str = stressed)
[b ons wb]
[ih nuc str]
[g cod ue] (ue = utterance end).

In the above and throughout this paper, we use the ARPAbet symbols to represent phonemes. In the later part of the paper we will explain how high-level information constrains feature overlapping, and thus influences speech recognition model building.

B. Feature specification for American English

We use a consistent feature-specification system for transforming segment symbols to feature bundles, which is

carried out after syllable parsing and before the application of feature overlapping rules. This system is characterized by the following key aspects:

(i) Five feature tiers are specified, which are: lips, tongue-blade, tongue-dorsum, velum, and larynx.
(ii) The feature specification of segments is context independent; it shows canonical articulatory properties coded in symbolic forms. (The total repertoire of the feature values we have designed is intended for all segments of the world languages. For a particular language, only a subset of the repertoire is used.)
(iii) Open (underspecified) feature values are allowed in the feature specification system. These underspecified feature values may be partially or fully filled by temporally adjacent (specified) features during the rule-controlled feature-overlapping process.

The feature specification system we have worked out for American English has the following specific properties. A total of 45 phonemes is classified into 8 categories: stops, fricatives, affricates, nasals, liquids, glides, (monophthong) vowels, and diphthongs. Each phoneme is specified with a five-dimensional feature bundle, corresponding to the five articulators: lips, tongue-blade, tongue-body, velum, and larynx. The values for each dimension are symbolic, generally concerning the place and manner of articulation (which are distinct from other phonemes) for the relevant articulator. The feature values for any (canonically) irrelevant articulator are underspecified (denoted by the value ''0'').

Continue with the above example. After the phonemes are replaced by articulatory features [before overlapping], the utterance ''The other one is too big'' becomes (the explanations of the prosodic symbols are given in the example in Sec. II A):

[dh(0 ClsDen 0 0 V+) ons ub] (ClsDen = dental closure, V+ = voiced)
[iy(0 0 D.iy 0 V+) nuc we ust] (D.iy = tongue dorsum position of /iy/)
[ah(0 0 D.ah 0 V+) nuc wb]
[dh(0 ClsDen 0 0 V+) ons]
[ax(0 0 D.ax 0 V+) nuc we ust]
[w(Rnd.u 0 D.w 0 V+) ons wb] (Rnd.u = lip rounding of /u/)
[ah(0 0 D.ah 0 V+) nuc ust]
[n(0 ClsAlv 0 N+ V+) cod we] (ClsAlv = alveolar closure, N+ = nasal)
[ih(0 0 D.ih 0 V+) nuc wb ust]
[s(0 CrtAlv 0 0 V−) cod we] (CrtAlv = alveolar critical, V− = unvoiced)
[t(0 ClsAlv 0 0 V−) ons wb]
[uw(Rnd.u 0 D.uw 0 V+) nuc we str]
[b(ClsLab 0 0 0 V+) ons wb] (ClsLab = labial closure)
[ih(0 0 D.ih 0 V+) nuc str]
[g(0 0 ClsVel 0 V+) cod ue] (ClsVel = velum closure)

Some further detail is given here on the featural representation of the segments. Generally, we use a single feature bundle to represent a segment in its canonical state. This, to some extent, ignores some finer structures. For example, the stops have at least two distinctive phases: the closure phase and the release phase. To account for this, finer structures are needed and they are modeled by the derived feature bundles. For instance, the release phase of the stops is represented by a derived feature bundle between the stop and an adjacent segment. The derived feature bundle for the release phase still contains such a feature as ClsAlv (e.g., for /t/) or ClsLab (e.g., for /p/), but it is understood differently as will be illustrated in the examples of Sec. II D.

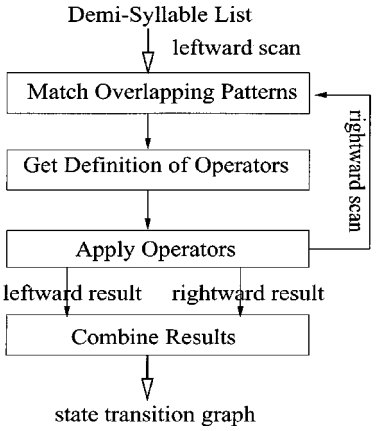

FIG. 1. The overlapping feature bundle generator.

C. A generator of overlapping feature bundles

An overlapping feature bundle generator is a program which (1) scans the input sequence of feature bundles with high-level linguistic information; (2) matches them to corresponding overlapping rules; (3) executes overlapping (or mixing) operations specified in the overlapping rules during two separate, leftward-scan and rightward-scan processes; the execution starts from the right-most phoneme for the leftward-scan process, and it starts from the left-most phoneme for the rightward-scan process; and (4) integrates the results of leftward-scan and rightward-scan to produce a state-transition network. A block diagram of the overlapping feature bundle generator is shown in Fig. 1.

Our feature-overlapping rules contain two types of information (or instruction): possibility information and constraint information. The possibility component specifies which features can overlap and to what extent, regardless of the context. The constraint component specifies various contexts to constrain feature overlapping. Below, we give some examples of possibility and constraint.

(i) Possibility of velum feature overlapping: A velum lowering feature can spread left and right to cause the phenomenon of nasalization in some phones, such as vowels.
(ii) Possibility of lip feature overlapping: A lip-rounding feature can spread mainly to the left to cause the phenomenon of lip-rounded allophones.
(iii) Possibility of tongue-body feature overlapping: A tongue-body feature can spread to cause such phenomenon in stops as advanced or retracted tongue body closures (as in /g iy/ versus /g uh/).

(iv) Possibility of larynx feature overlapping: A voicing/unvoicing feature can spread to cause such phenomena as voiced/unvoiced allophones.
(v) Possibility of tongue-tip feature overlapping: The tongue-tip feature of /y/ can spread into the release phase of a stop to cause the phenomenon of palatalization (as in ''did you'').
(vi) Constraint rule: A stop consonant blocks feature spreading of most features, such as lip feature, larynx feature, etc.
(vii) Constraint rule: A vowel usually blocks tongue-body features from spreading through it.

The above spreading-and-blocking model can account for many types of pronunciation variation found in continuous speech. But, there are some other common phenomena that cannot be described by feature spreading only. The most common among these are the reductive alternation of vowels (into schwa) and consonants (flapping, unreleasing, etc.). Therefore, our model needs to include a control mechanism that can utilize high-level information to ''impose'' feature transformation in specific contexts. We give some examples below.

(i) Context-controlled transformation: A stop consonant undergoes a flap transformation in such contexts as: [V stressed] ∗ [V unstressed] (where ''∗'' marks the position of the consonant in question).
(ii) Context-controlled transformation: A stop consonant deletes its release phase in a coda position.
(iii) Context-controlled transformation: A vowel undergoes a schwa transformation in an unstressed syllable of an unaccented word in the utterance.

The output of the generator is a state-transition network consisting of alternative feature bundle sequences as the result of applying feature-overlapping rules to an utterance. This structure directly corresponds to the state topologies of hidden Markov models of speech. Each distinctive HMM state topology can be taken as a phonological representation for a word or for a (long-span) context-dependent phone. The HMM parameters, given the topology, are then trained by cepstral features of the speech signal. In the following subsection, we give two examples of applying the feature-overlapping rules (details will be presented in Sec. III), and show the results in the form of the constructed overlapping feature bundles.

D. Examples: feature bundles generated by applying feature-overlapping rules

We present two examples to illustrate typical applications of the feature-overlapping rules utilizing high-level linguistic information before details of the rules are formally described. The first example shows how the words *display* and *displace* are endowed with different feature structures in the stop consonant /p/, despite the same phoneme sequence embedding the /p/. The difference is caused by different syllable structures. After syllable parsing and feature overlapping, the results in feature bundles, accompanied by the spectragrams of the two words, are shown in Fig. 2. Due to different syllable structures: (/d ih s · p l ey s/ versus /d ih · s p l ey/), different overlapping rules are applied. This simulates the phonological process in which the phoneme /p/ in *displace* tends to be aspirated but in *display* unaspirated.

The two relevant feature bundles are shown in the figure by the dashed vertical lines. The difference lies in the voicing feature at the larynx feature tier. The aspiration is indicated by a V feature in the feature bundle of the word *displace* between /p/ and /l/. Phonologically, this is called delayed voicing in the onset of /l/. In the model, this is realized through asynchronous leftward spreading of the tongue blade and larynx features of /l/, which overlap with the features of /p/.

The second example (Fig. 3) shows the word *strong*, which contains several feature overlaps and mixes. (Feature mixes are defined as feature overlaps at the same feature tier). Some of them have variable durations (in lip rounding and nasalization), represented by the dashed boxes. Such variability in the duration of feature overlapping gives rise to alternative feature-bundle sequences. By merging identical feature bundles, a network can be constructed, which we call the ''state-transition network.'' Each state in the network corresponds to a feature bundle. The network constructed by the overlapping feature-bundle generator for the word *strong* is shown in Fig. 4, where each state is associated with a set of symbolic features. The branches in the network result from alternative overlapping durations specified in the feature overlapping rules.

Generally, a derived feature bundle with overlapping features from adjacent segments represents a transitional phase (coarticulation) between phonemes in continuous speech. Overlapping in real speech can pass several phonemes and our feature-overlapping model effectively simulates this phenomenon. For example, in *strong* /s t r ao ng/, the lip-rounding feature of /r/ can spread through /t/ to /s/, and the nasal feature of /ng/ can also pass through /ao/ to /r/, as is shown in Fig. 3. This ability to model long-span phonetic context is one of the key characteristics of this model.

III. IMPLEMENTATION OF THE FEATURE-OVERLAPPING ENGINE

A. The demisyllable as the organizational unit in formulating feature-overlapping rules

Based on the information obtained by the syllable parser and the feature specification (including underspecification) of phonemes, demisyllables are constructed, which are operated upon by the feature-overlapping rules (formally defined below) to generate transition networks of feature bundles. A demisyllable in our system is a sequence of broad phoneme categories encompassing the phonemes in either syllable-onset plus nucleus, or nucleus plus syllable-coda formations, together with high-level linguistic information. When a syl-

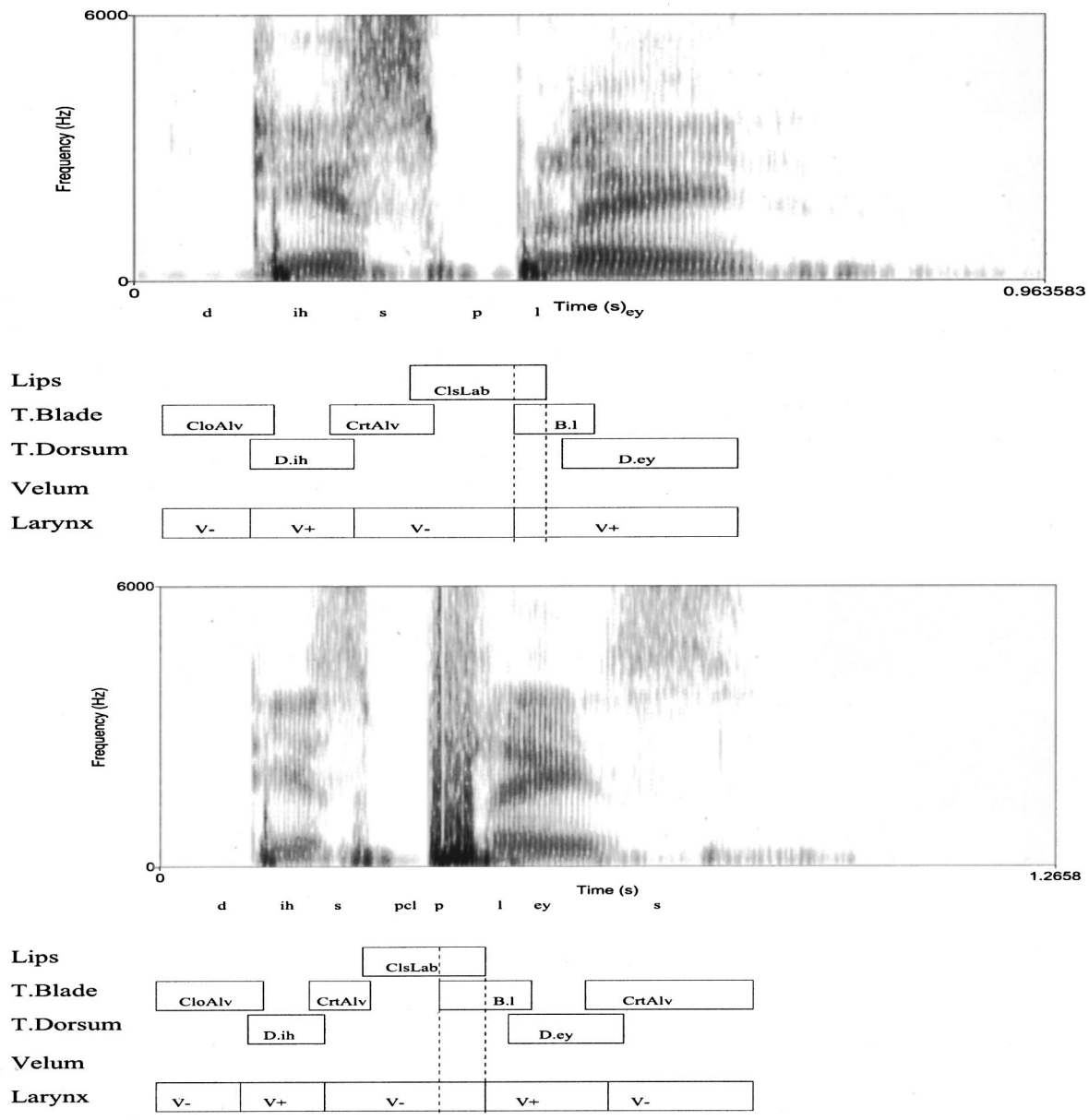

FIG. 2. Feature overlaps for words *display* (upper panel) and *displace* (lower panel).

lable has no onset or coda consonants, that demisyllable will be only a vowel. The broad phonetic categories we have used are defined as follows:

V—vowel,
GLD—glide,
LQD—liquid,
NAS—nasal,
AFR—affricate,
FRI1—voiced fricative,
FRI2—voiceless fricative,
STP1—voiced stop,
STP2—voiceless stop.

Other elements included in a demisyllable are related to the higher-level linguistic information. These include

ons—syllable onset,
nuc—syllable nucleus,
cod—syllable coda,
ub—utterance beginning,
ue—utterance end,
wb—word beginning,
we—word end,
str—stressed syllable in the utterance,
ust—unstressed syllable.

For instance, the demisyllables of the utterance ''The other one is too big,'' including high-level linguistic information, are as follows:

[FRI1 ons ub] [V nuc we ust] (dh-iy)
[[V, nuc, wb]] (ah)
[FRI1 ons] [V nuc we ust] (dh-ax)
[GLD ons wb] [V nuc ust]] (w-ah)

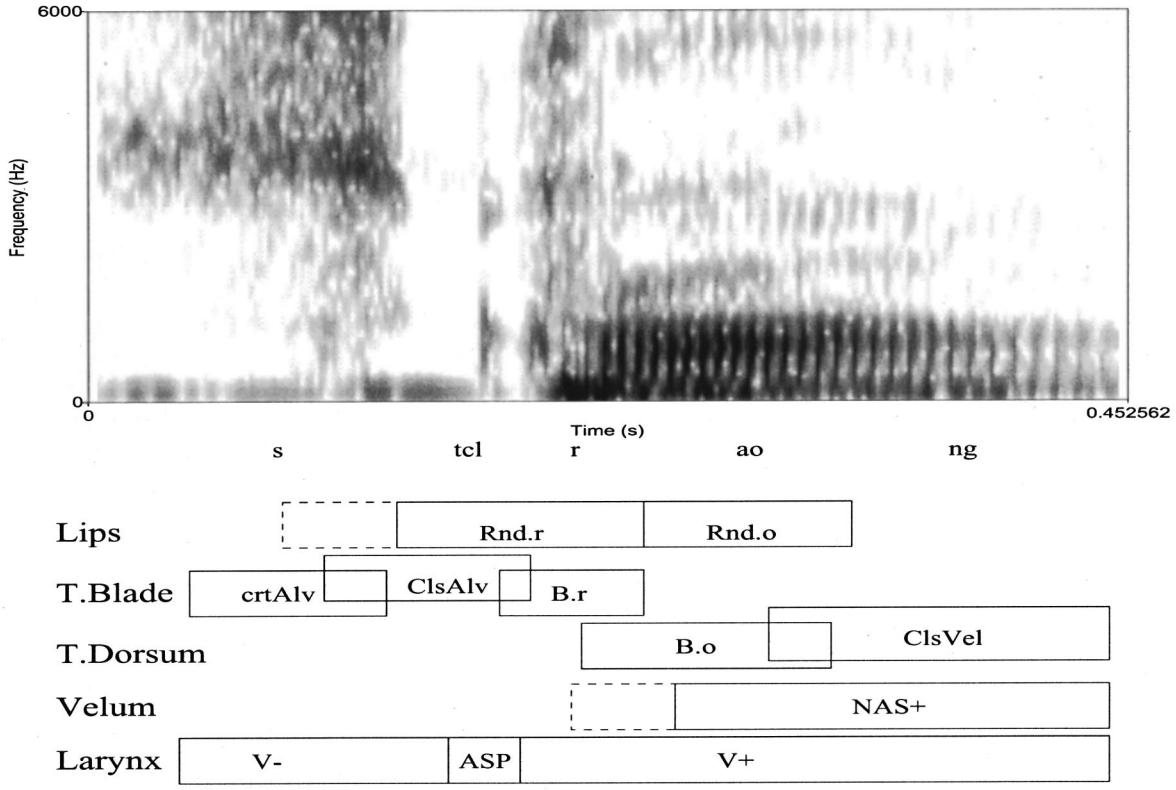

FIG. 3. Feature overlaps and mixes for word *strong*.

[V nuc ust] [NAS cod we]] (ah-n)
[V nuc wb ust] [FRI2 cod we] (ih-s)
[STP2 ons wb] [V nuc we str] (t-uw)
[STP1 ons wb] [V nuc str]] (b-ih)
[V nuc str] [STP1 cod ue] (ih-g).

Demisyllables split a full syllable (one with both onset and coda consonants) into two halves. The purpose of this splitting is to make a small set of units for practical rule development. Contextual constraints specified in the phonological rules are defined on the demisyllables. After parsing all 6110 words in the TIMIT corpus dictionary, we obtained 291 distinct word-based demisyllables (that is, without speci-

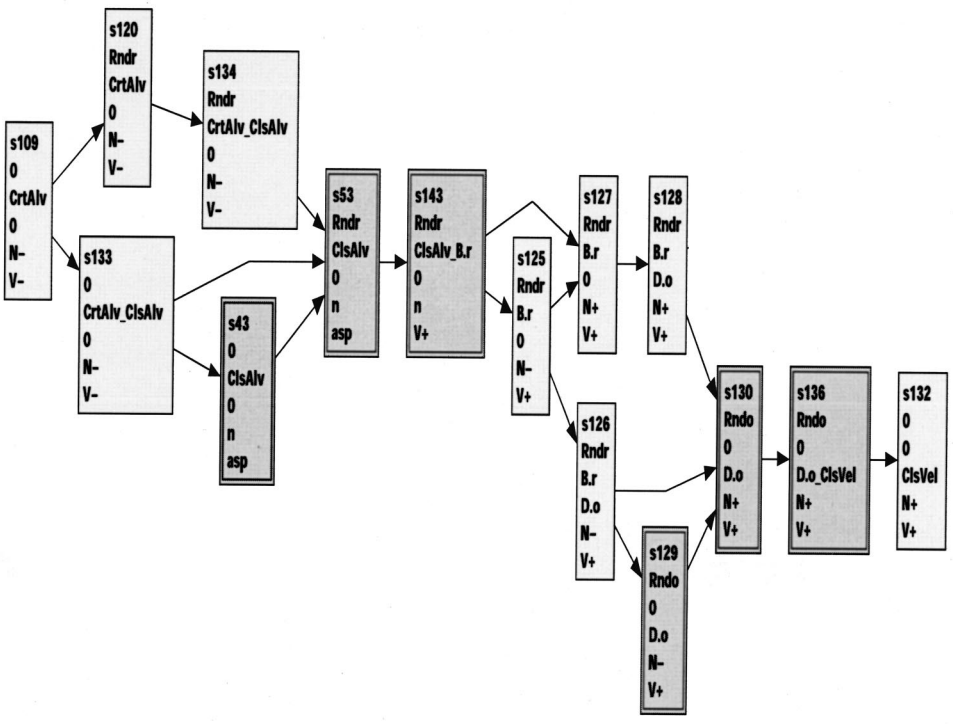

FIG. 4. State-transitional graph for word *strong*.

fying utterance boundaries and utterance accents, which can be included in later rule development). This is a compact set, facilitating the development of the overlapping rule system which we now describe in detail.

B. Overlapping phonological rule formulation

This subsection gives a detailed description of the phonological rules for articulatory feature overlapping. Appendix B presents a logical basis of our feature-overlapping system in the form of a temporal logic. This logic is based on autosegmental and computational phonological theories, presented in Refs. 12, 1, 2 and elsewhere. The phonological rules have been formulated systematically based on the behavior of articulatory features, especially under the influence of high-level linguistic structures. The phonological rules are used to map any utterance from its demisyllable representation into its corresponding feature bundle network (i.e., the state transition graph).

The data structure of feature-overlapping rules consists of ''overlapping patterns'' and ''overlapping operators.'' Each overlapping pattern is defined with respect to a demisyllable and contains the names of a number of overlapping operators. The demisyllable, as illustrated in the last subsection, contains both segmental information (broad phonetic categories) and high-level linguistic information (boundaries, accents, and syllable constituents). The construction of overlapping patterns starts from the 291 word-based demisyllables. Based on the temporal logic and particular phonological knowledge concerning coarticulation and phonetic alternations, necessary boundary and accent requirements are added. Further, a number of overlapping operators' names are added to form an overlapping pattern. Each operator corresponds to a broad phonetic category in the demisyllable.

The overlapping operators are defined on the phonemes based on phonological theory, describing how their articulatory features may overlap in speech. When an overlapping pattern is applied, an operator name will point to the actual definition, which then is applied to the corresponding phoneme matching a broad phonetic category. One definition of an operator may be pointed to by more than one overlapping pattern. Thus, the overlapping operators realize the possibilities while the overlapping patterns realize the constraints on the possibilities. (The concepts of possibility and constraint were discussed in Sec. II C.)

Let us denote a broad phone category in a demisyllable by DSC (standing for demisyllable constituent); then, a phonological rule is described by a list of DSCs in a demisyllable, together with all possible operators allowed to operate on each DSC. The overall data structure of a phonological rule is in this form

[DSC−1: operator1.1, operator1.2, operator1.3 . . .

(high-level information)]

[DSC−2: operator2.1, operator2.2, operator2.3 . . .

(high-level information)]

[DSC−3: operator3.1, operator3.2, operator3.3 . . .

(high-level information)]

. . . .

An operator describes how feature overlapping could happen on different articulatory tiers, as is described in phonological theory, such as ''lip rounding,'' ''jaw lowering,'' ''palatalization,'' etc. Each operator consists of four components: (1) action; (2) tier specification; (3) feature-value constraint; and (4) relative timing. Below we discuss each of these components. First, there are three choices for describing an action

(i) L or R: For leftward (look-ahead) or rightward (carry-over) feature spread from an adjacent phoneme onto an underspecified tier of the phoneme.
(ii) M or N: For leftward or rightward mixture of a feature from an adjacent phoneme on the same tier.
(iii) S: For substitution of a feature value by a different feature value.

Second, a tier indicator specifies at which feature tier an action takes place. A tier indicator is given by an integer as follows:

(1) the lips tier,
(2) the tongue-blade tier,
(3) the tongue-dorsum tier,
(4) the velum tier,
(5) the larynx tier.

Third, a value constraint can optionally be given to stipulate that a feature spread from an adjacent phoneme must have a specified value. If this value constraint is not given, the default requirement is that on this tier of an adjacent phoneme there must be a specified feature in order for the operator to be applicable.

Fourth, a relative-timing indicator is used to specify the temporal extent of a feature spreading. In the current implementation of the model, we use four relative-timing levels: 25%, 50%, 75%, and 100% (full) with respect to the entire duration of the phoneme.

The reader may wonder how long-span effects are realized in this model. This is realized by full (100%) feature spreading. Once an adjacent phoneme's feature is spread to the entire duration of the current phoneme, that feature is visible to the adjacent phoneme on the other side and may spread further. For example, a nasal feature from a right adjacent phoneme may be allowed to spread to the full duration of a vowel. The phoneme to the left of the vowel can ''see'' this feature and may allow it to spread into itself. This is the mechanism used by the model to pass a feature over several phonemes until it is blocked.

The naming of an operator follows a syntax which reflects its internal definition. The syntax for an operator name is given as

$$\text{Operator-Name} := Op N^{+} [@N^{+}]$$

$$N := 1|2|3|4|5,$$

where the numbers after ''Op'' reflect the tier indicators in the definition, and the optional numbers after the symbol @

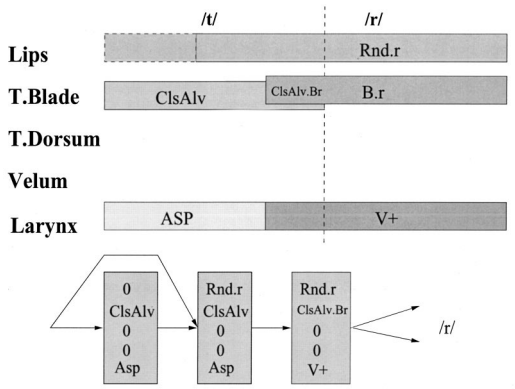

FIG. 5. Results of applying operator Op125@15 to /t/ before /r/ and the corresponding state-transition graph of /t/.

stands for the tiers at which feature-value constraints are imposed.

A phoneme can be given a number of operators. Whether an operator is allowed to apply to a phoneme depends on whether it is listed in a DSC of an overlapping pattern. Furthermore, whether an operator listed in an DSC can be fired or not depends on if the conditions in the operator definition are met. For example, for the operator with the name Op2 to fire, the second tier of the adjacent phoneme must have a specified feature value. As another example, for the operator of the name Op12@2 to fire, the adjacent phoneme (whether it is to the left or right depends on the action type of the operator) must have specified features at tier 1 and 2 and the feature value at tier 2 must match the value specified in its definition.

As an illustration, Fig. 5 shows the result of applying an operator named Op125@15 to the feature bundle of /t/ when it is followed by /r/. The operator is defined as

(125@15, tier_1.L.rnd, tier_2.M, tier_5.L.V+,

time:(0.5,0.25,0.25;1,0.25,0.25)).

According to this definition, the three tiers of the phoneme—lips (1); tongue-blade (2); and larynx (5) have actions M or L. Tiers 1 and 5 constrain the spreading feature values as *rnd* and *V+* that come from a right neighbor. There are two alternative timing specifications (0.5,0.25,0.25) and (1,0.25,0.25). Feature spreading at the three tiers will enter the feature bundle of /t/ in two possible ways: (1) Lips feature spreading to 50% of the entire duration, and tongue-blade and larynx features spreading to 25%, or (2) Lips feature spreading to the entire duration and the tongue-blade and larynx feature spreading to 25%. As a consequence, two new feature bundles are derived. The two possible ways for state transitions are shown in Fig. 5, which is automatically derived by a node-merging algorithm accepting parallel state sequences. Note how long-distance feature overlapping can be realized by the rule mechanism: Once a feature spreading covers an entire duration, this feature will be visible to the next phoneme. Now, we give an example of a phonological rule, which is defined on the demisyllable with high-level linguistic structure

[FRI2 ons wb] [STP2 ons] [LQD ons] [V nuc str].

This demisyllable can match the first four phonemes of the word *strong*. This rule is expressed as

[FRI2 (Op2, Op3, Op13@1) ons wb]

[STP2 (Op2, Op125@15) ons]

[LQD (Op3, Op34@4) ons]

[V (Op3, Op34@4) nuc str].

Each DSC in this rule is given a number of operators which can operate on the phonemes that are matched by the demisyllable. Notice the high-level linguistic structures (ons, wb, etc.) which constrain the application of the rule to certain prosodic context. In the current implementation of the feature-based model, we have the following operator inventory which consists of a total of 26 operators defined for the 44 English phonemes for the leftward scanning. A corresponding set of operators for rightward scanning is similarly defined. We list the leftward operators as follows:

(1) `(Op1,1.M,(0.25))` (transitional phase)
(2) `(Op1,1.L,(0.25))`
(3) `(Op2,2.M,(0.25))`
(4) `(Op2,2.L,(0.25))`
(5) `(Op3,3.M,(0.25))`
(6) `(Op3,3.L,(0.25))`
(7) `(Op5,5.S,())` (glottal substitution)
(8) `(Op2,2.S,())` (tongue-blade substitution)
(9) `(Op4,4.L.N+,(0.5;1))` (nasalization)
(10) `(Op12@1,1.L.rnd,2.M,(0.5,0.25;1,0.25))` (transition with lip rounding)
(11) `(Op13@1,1.M.rnd,3.L, (0.5,0.25;0.25,0.25))`
(12) `(Op13@1,1.L.rnd,3.M,(0.5,0.25;1,0.25))`
(13) `(Op13@1,1.L.rnd,3.L,(0.5,0.25;1,0.25))`
(14) `(Op14@4,1.L,4.L.N+,(0.25,0.5;0.25,1))` (transition with nasalization)
(15) `(Op24@4,2.L,4.L.N+,(0.25,0.5;0.25,1))`
(16) `(Op34@4,3.M,4.L.N+,(0.25,0.5;0.25,1))`
(17) `(Op23@2,2.S.TapAlv,3.L, (0.25,0.75;1,0.25))`
(18) `(Op34@4,3.M,4.l.N+,(0.25,0.5;0.25,1))`
(19) `(Op34@4,3.L,4.L.N+,(0.25,0.5;0.25,1))`
(20) `(Op35@5,3.M,5.L.V+,(0.25,0.25))` (transition with unaspiration)
(21) `(Op35@5,3.L,5.L.V+,(0.25,0.25))`
(22) `(Op125@15,1.L.rnd,2.M,5.L.V+, (0.5,0.25,0.25;1,0.25,0.25))` (more combinations)
(23) `(Op134@14,1.M.rnd,3.L,4.L.N+, (0.5,0.25,0.5;0.5,0.25,1;1,0.25,0.5))`
(24) `(Op134@14,1.L.rnd,3.L,4.L.N+, (0.5,0.25,0.5;0.5,0.25,1;1,0.25,0.5))`
(25) `(Op135@15,1.M.rnd,3.L,5.L.V+, (0.5,0.25,0.25;1,0.25,0.25))`
(26) `(Op135@15,1.L.rnd,3.L,5.L.V+, (0.5,0.25,0.25;1,0.25,0.25))`

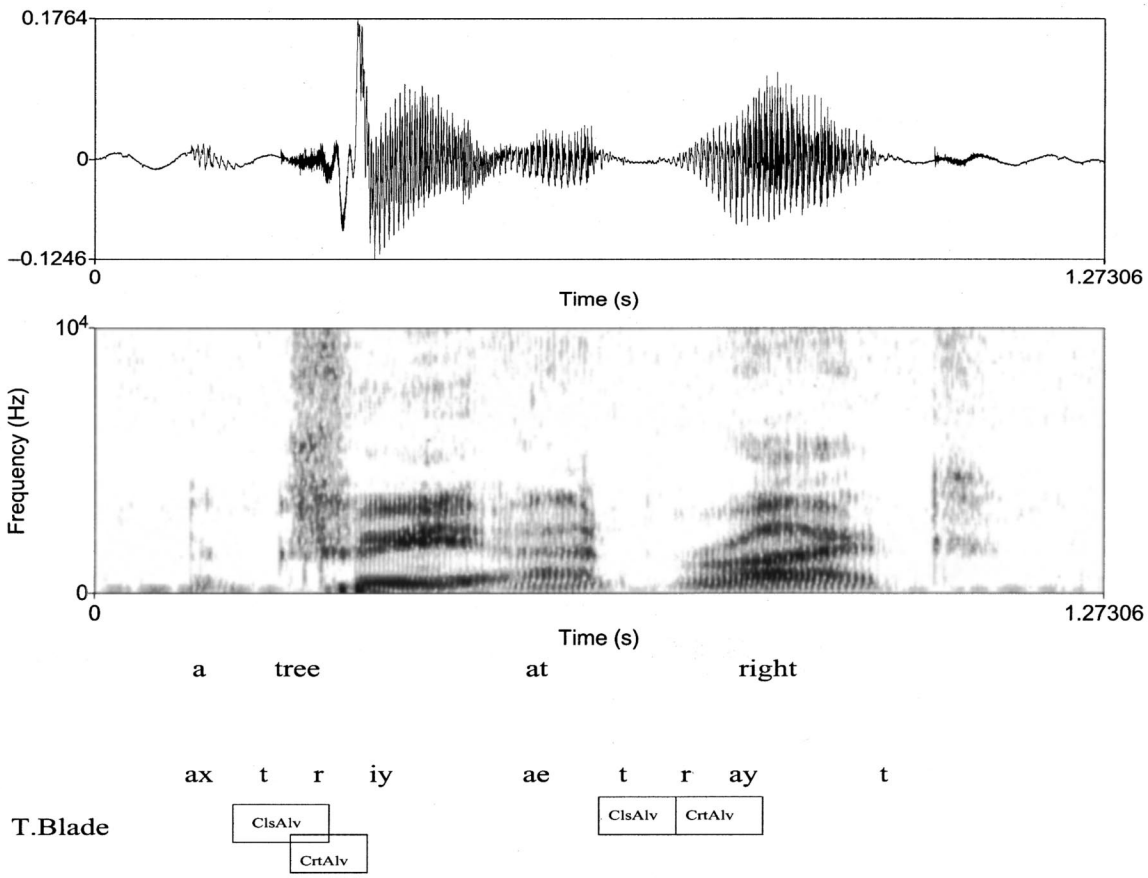

FIG. 6. Use of phonological rules and high-level linguistic information.

To illustrate the use of overlapping phonological rules and how high-level linguistic information is incorporated, we demonstrate with the example utterance ''a tree at right'' (the corresponding phoneme sequence is /ax t r iy ae t r ay t/). After prosodic processing, where part-of-speech tagging and shallow syntactic parsing is used for deriving the boundary and accent information, and following syllable parsing, the utterance is represented by a sequence of demisyllables

(1) [V nuc ub ust] (ax)
(2) [STP2 ons wb] [FRI1 ons] [V nuc we str] (t-r-iy)
(3) [V nuc wb ust] [STP2 cod we] (ae-t)
(4) [FRI1 ons wb] [V nuc str] (r-ay)
(5) [V nuc str] [STP2 cod ue] (ay-t).

Each demisyllable is matched by a phonological rule. The overlapping operators in each DSC are tried for firing. If the conditions are met, an operator is fired to derive feature bundles. During the derivation process, segment and word boundaries are recorded to ''cut up'' the derived network into word networks or phone networks, which are used to build word- or phone-based hidden Markov models.

In this example, we illustrate the use of syllable information to realize the ''affrication rule'' discussed earlier in Sec. II A. The utterance's wave form, spectrogram, and relevant features concerning the use of the affrication rule are shown in Fig. 6. To realize the affrication rule, the phonological rule matching the second demisyllable: [STP2 ons wb] [FRI1 ons] [V nuc we str] will have its first DSC assigned an operator: [Op2,2.L,(0.25)] which allows feature overlapping on the tongue-blade tier. The overlapping phonological rule matching the third demisyllable, on the other hand, will not assign this operator to the second DSC: [STP2 cod we], blocking affrication.

As another example of applying high-level linguistic information, consider the use of a substitution action in an operator at utterance beginning. For the above utterance, a rule matching the first demisyllable: [V nuc ub ust] can have an operator with a glottal substitution action: [Op5, 5.S.?, ()]. This simulates an utterance with a glottal stop at the outset. Similarly, an unreleased stop consonant at the end of a word or an utterance can be simulated by the phonological rule mechanism as well.

We have illustrated how ''possibilities'' and ''constraints'' can be implemented by the overlapping patterns and operators. With each DSC within a rule there may be a number of operators available for firing. When more than one operator can be fired, it is the more specific ones that are fired first. Depending on how complex we expect the generated network to be, the system is able to control how many operators are carried out.

IV. SPEECH RECOGNITION EXPERIMENTS

In this section we describe the speech recognition experiments using the phonological rules and the generator of

overlapping feature bundles described earlier in this paper. Our experiments are carried out using the TIMIT speech database and the tasks are both (continuous) word and phone recognition. Our preliminary experimental results show that this feature-based approach is a promising one with a number of new directions for future research.

A. Automatic creation of HMM topology with feature-bundle states

The feature-based speech recognizer we have constructed uses a special HMM topology to represent pronunciation variability in continuous speech. The variability is modeled by parallel feature-bundle state sequences as a result of applying the phonological rules to the canonical phoneme representations. The HMM topology is created automatically by rules, one for each word. Details of this process have been provided in Sec. III and we summarize this process as the following six steps for the TIMIT corpus:

(1) Parse each phoneme string in a sentence into a syllable sequence, and further into a demisyllable sequence with prosodic structure;
(2) Match the demisyllable sequence to a sequence of corresponding feature-overlapping patterns;
(3) Select the relevant feature-overlapping operators (defined in the feature-overlapping pattern) for each phoneme according to its featural context in the sentence;
(4) Apply the operators in the order from most specific to most general, with complexity control;
(5) Generate a full set of overlapped or mixed feature bundles (and use them as the HMM states), as the result of the applications of feature-overlapping rules; and
(6) Generate state-transition graphs for all the words (and sentences) in the TIMIT database based on the parallel feature-bundle transition paths.

The last step creates the feature-based pronunciation models in the form of word-HMMs for all 6110 TIMIT words. To show the parsimony of the feature-based approach, only 901 distinct HMM states (i.e., 901 distinct feature bundles) were derived and used to represent these 6110 words, in contrast to tens of thousands generated by the conventional triphone approach. Furthermore, long-span context dependence has been incorporated due to the application of long-span feature-overlapping rules.

Given the HMM topology automatically created for each word in TIMIT, we used the HTK tools to compute the speech features (MFCC) and to train the continuous-density HMM output-distribution parameters (means, variances, and mixture weights) for all 901 unique feature bundles (HMM states) using the training data in TIMIT. The HMMs trained were then used to automatically recognize the TIMIT test-set sentences, using HTK VITERBI decoder (HVite tool).

The training and recognition with network HMMs (see Fig. 4), which contain multipath graphs, is allowed by the HTK tool as it is designed for experimenting with different model structures including multipath topologies. We use the global mean and variance from the entire data set to initialize the models, and then use Baum–Welsh re-estimation to compute the parameters specific to each state. The re-estimation procedure (HERest tool) applied to the models avoids the alignment problem as may occur with multipath structures because of the following two reasons. First, all the states which are derived from the same feature bundle are tied from the beginning. Second, when a branch occurs in some model, the alignment between data and alternative states is resolved when there are similar data elsewhere in the corpus aligned with a nonbranching state which is tied with one of the alternative states.

B. Statistics in training and testing data

The TIMIT database used in our experiments consists of 630 speakers in 8 dialect regions, of which 462 are in the training set and 168 are in the testing set. The sentences in the training and the testing sets are disjointed, except for two sentences which were spoken once by every speaker. The training set contains 4620 sentences and the testing set 1680. The training set contains 4890 distinct words and the testing set 2375. Among the total 6110 words in TIMIT, 1155 words occur in both the training and testing sets and 1220 words are unique to the testing set (i.e., distinct from all words in training).

The entire set of TIMIT words (training and testing sets) gives rise to a total of 901 HMM states after the application of the overlapping rules described in Sec. III. Among all the 901 states, the testing set contains 754 states, of which 717 states also occur in the training set. This shows the advantage of the feature-based approach: in contrast to around 48% sharing of words (1155 out of 2375), the subphonemic, feature-bundle sharing is over 95% (717 out of 754) for the testing set. This means that with about 52% of the words unseen in the training model, when it comes to feature-bundle-based states, the unseen portion in the training set drops to only about 5%. For the 37 states occurring uniquely in the testing set, we synthesized them with the parameters of the states obtained from the training set which have similar features as the ''unseen'' states, using a feature vector similarity metric.

In short, in contrast to words, the training and testing sets differ less in terms of feature bundles. The 4890 words in the training set account for 95% of feature bundles in the words of the testing set, although they only account for 48% of the words in the testing set.

C. Speech recognition results

Using the embedded estimation tool HERest in the HTK, we trained the word-HMMs by direct tying. This means that the 901 states were used for all the words from the very beginning. Unlike the triphone training procedure, which undergoes a separate state-tying process, the direct tying training was efficient in terms of both training time and memory space requirements. We estimated single-Gaussian state models twice. Then, the mixture number was increased gradually to five, with one re-estimation for each increase.

This amounts to using the feature-overlapping model to construct the word-level HMMs. Since the testing set has half of the words distinct from that of the training set, these

TABLE I. Continuous speech recognizer performance on words and tested on all 1680 sentences in the TIMIT testing set. Feature-based phonological model is used to construct the word-level HMMs and bigram language model is used for word recognition. Each feature-defined HMM state was trained with a five-Gaussian mixture using HTK.

	Speech recognition decoding results							
Dial. reg.	No. sents	No. words	Corr %	Sub	Del	Ins	WER %	Sent. ER %
1	110	964	89	48	55	10	12	36
2	260	2281	92	97	71	17	9	33
3	260	2271	92	94	77	20	9	31
4	320	2714	90	141	114	21	11	33
5	280	2438	88	175	116	25	13	40
6	110	966	91	51	27	14	10	35
7	230	1967	91	107	62	9	10	33
8	110	956	91	61	23	2	10	29
Total/Ave.	1680	14557	90	752	567	120	10	34

unseen word-HMM models are synthesized with state macros (symbolic names pointing to the trained states). We have carried out speech recognition (decoding) experiments using the HMMs, obtained by the above training procedure. Details of the recognition performance are shown in Table I, where the word error rate (WER) and sentence error rate (Sent.ER), as well as the word substitution (Sub), deletion (Del), and insertion (Ins) rates, are shown as a function of the dialect regions (Dial.Reg.) in the TIMIT database. The size of the testing set in terms of the total number of test words and sentences in each of the dialect regions is also listed. These results are obtained on all the 1680 sentences in the TIMIT testing set covering all eight dialect regions of American English accents. A bigram language model was used, which was derived from the whole set of TIMIT prompt sentences, with one-gram probabilities lowered to -99. A five-Gaussian mixture was used as the output distribution for each of the 901 feature bundle-based HMM states.

The efficiency of the feature-based system was evident in the experiments. For example, the state set from the very beginning was compact and the training time was also much less compared to the triphone system, at the ratio of about 1/20.

In a further experiment, we used the data-driven state-clustering functionality provided by the HTK toolkit in the overlapping-feature framework with unified model topologies. We performed the TIMIT phone recognition task by using 39 three-state, left-to-right, no-skip phone models trained as quinphones. Compared with triphones, a quinphone incorporates contexts of up to two phones to its left and right. This gives the possibility of utilizing the predictions made by the feature-overlapping model. The predictions were used to form decision-tree questions for state tying.

The training set of TIMIT database resulted in 64 230 context-dependent quinphones. The overlapping features germinating from five-phone contexts were used in designing decision-tree questions for state tying. The contexts that affect the central phones through feature overlapping, as predicted by the model, form questions for separating a state pool (a technique of state tying with decision trees). For example, the nasal release of stop consonants in such contexts as /k aa t ax n/ and /l ao g ih ng/ (the /t/ in the first context and /g/ in the second context, influenced by /n/ and /ng/) will induce questions for tying the third state of the three-state model with the conditions expressed as *+ax2n, *+ax2ng, etc. (''2'' is used here to separate the first- and the second right context phones). With the aid of such decision-tree questions, the quinphone states were tied and re-estimated. The testing result is compared with the triphone baseline results for the 39-phone recognition defined in the TIMIT database. This comparison is shown in Table II, where both systems are used to recognize the same 1680 test utterances that consist of a total of 53 484 phone tokens. The results in Table II show that the feature-overlapping model outperforms the conventional triphone model. The feature-overlapping model is able to make meaningful predictions, which lead to increase of the efficiency of model organization and training process. Without this predictive model, it would have been impossible to form meaningful state-tying questions.

Our third experiment used phone-level HMMs to perform word recognition. This is done via a pronunciation dictionary in which each word is represented by one or more sequences of phone HMM models. We used four basic types of predefined phone models, representing stop consonants, other consonants, single vowels, and diphthongs, respectively. The design of the HMM topologies is based on the assumption that high-level linguistic structures can influence the acoustic properties of the pronounced phonemes and this is reflected in the model structures. The design of each of the four types of phone models is given below.

(1) Stop consonants: Three HMM states, one skip from the second state to the exit dummy state, modeling nonrelease of stop consonants, one skip from the first state to the exit state, modeling a very short duration without release. The loss of release phase is expected to occur mainly in the coda position.

TABLE II. TIMIT phone recognition results: Triphone baseline versus feature-overlapping model. The latter uses the feature-overlapping rules in the decision-tree-based state-tying process of phone-level HMMs.

	Phone recognition decoding results	
System	Correct %	Accuracy %
Triphone (baseline)	73.90	70.86
Overlapping feature	74.70	72.95

TABLE III. TIMIT word recognition results: Triphone baseline versus feature-overlapping model. The latter uses the feature-overlapping rules to construct context-dependent phone-level HMMs incorporating high-level linguistic constraints.

Speech recognition decoding results: Word correction and accuracy						
Dial. reg.	No. sents	No. words	Baseline corr.	Baseline acc.	Feature corr.	Feature acc.
1	110	964	81.98	80.42	82.92	81.88
2	260	2281	86.10	85.44	86.58	85.62
3	260	2271	85.78	85.16	86.35	85.78
4	320	2714	83.05	81.80	83.35	82.09
5	280	2438	80.31	79.16	80.84	79.61
6	110	966	85.92	85.51	85.20	84.47
7	230	1967	88.66	87.90	89.22	88.66
8	110	956	86.61	85.67	87.13	86.51
Total/Ave.	1680	14557	84.61	83.69	85.04	84.13

(2) Other consonants: Three HMM states, one skip from the first state to the third state, modeling a short duration in which the central state has no acoustic data, such as in fast spontaneous speech when the whole duration is influenced by the left and right contexts.
(3) Monophthongs (single vowels): Four HMM states. The middle two states are in parallel. These two middle states model stressed and unstressed phones, respectively, depending on the sentential accent of the phone. One skip from the first to the fourth state, modeling (optionally) faster speech.
(4) Diphthongs: Five HMM states. The second and third states are in parallel, modeling the stressed and unstressed phones, respectively, depending on the sentential accent of the phone. One skip from the first to the fifth state, modeling fast speech.

These models were first trained as monophones. Then, they were expanded into quinphones and re-estimated in their individual contexts. Next, their boundary states were tied by decision-tree-based state tying. The decision-tree questions were formed again by feature-based model predictions. Finally, the models were re-estimated with increased mixtures. The unseen quinphones were synthesized by the HTK state-tying algorithm.

The difference of this framework from a triphone baseline word recognition system lies in the topology design for utilizing high-level linguistic information and the state-tying questions used by decision trees. The results of testing with the TIMIT database are shown in Table III. These results demonstrate superior performance of the overlapping-feature-based approach over the triphone-based one.

In this experiment, we used a bigram language model similar to the one used in the first experiment. The only difference is that the one-gram word probabilities were not lowered, which accounted for the lower accuracy compared to the first experiment.

V. SUMMARY AND DISCUSSION

We have reported our recent theoretical development of an overlapping-feature-based phonological model which includes long-span contextual dependencies. Our most recent implementation of the model and some speech recognition experiments using the TIMIT data have been described. We extended our earlier work[3,4] by incorporating high-level linguistic structure constraint in the automatic construction of feature-based speech units. The linguistic information explored includes utterance and word boundaries, syllable constituents, and word stress. A consistent computational framework, based on temporal feature logic, has been developed for the construction of the phonological model.

One use of the feature-based phonological model in automatic speech recognition, which is reported in this paper, is to provide an HMM state topology for the conventional recognizers, serving as a pronunciation model that directly characterizes phonological variability. We have built a feature-based speech recognizer using the HTK toolkit for this purpose, and the implemented recognizer is reported in detail in this paper.

The overlapping-feature-based phonological model described in this paper is a significant improvement upon a number of earlier versions of the model. The earliest version of the model automatically created an HMM topology based on simple, heuristic rules to constrain feature overlaps.[3] A total of 1143 distinct HMM states are created for the TIMIT sentences. When that model was used for the task of phonetic classification (TIMIT database), the phone classification accuracy of 72% was achieved using as little as one-tenth of the full training data. The next version of the model improved the phonological rules for constraining feature overlaps, and interfaced the feature bundles with the HMM states which are nonstationary (polynomial).[7,8] The new rules created a total of 1209 distinct HMM states for the TIMIT sentences. Evaluation on TIMIT phonetic recognition (N-best) gave 74% phonetic recognition accuracy (and 79% correct rate excluding insertion errors). A further version of the model abandoned all rules to constrain feature overlaps, and allowed all features to freely overlap across the feature tiers.[13] This created an unmanageable number of distinct feature bundles which rendered the HMM recognizer untrainable. The solution to this problem as reported in Ref. 13 was to use an automatic decision-tree clustering or tying algorithm (based on the acoustic clustering criterion) to reduce the total number of distinct HMM states needed for reliable HMM training. Evaluation on TIMIT phonetic recognition showed the same performance as the decision-tree-clustered triphone units. This demonstrated the weaknesses of using acoustic information only without incorporating phonological information.

The current version of the model presented in this paper refocused on the phonological rules, and it differs from all the previous versions of the model in the following significant aspects: (1) It incorporates high-level (above phoneme level) linguistic information which is used to control, in a systematic and predictable way, the feature overlaps across feature tiers through long-span phoneme sequences; (2) It formulates the phonological rules in terms of actions of operators which determine detailed behavior of feature overlaps; and (3) It has been completely reimplemented in PROLOG (all the previous versions of the model were implemented in C).

The work reported in this paper initiates new efforts of systematic development of feature-based pronunciation modeling for automatic speech recognition. In this first stage of the work, we successfully implemented the theoretical constructs in terms of rule formalisms and programs generating state-transition graphs. The experimental results demonstrated feasibility of the model in speech recognition applications. In our future work, intensive efforts will be devoted to automatically acquiring more effective feature overlapping rules and to developing more effective ways of building speech recognition systems using feature-overlapping models. A data-driven feature-overlapping rule modification system will also be developed to test precision of the feature overlapping predictions and to automatically adjust the predicted articulatory feature bundles during the recognizer training and decoding phases.

ACKNOWLEDGMENTS

Discussions with Jeff Ma and Xing Jing are gratefully acknowledged. Support of this work has been provided by NSERC, Canada.

APPENDIX A: A PARSER FOR ENGLISH SYLLABLE STRUCTURE

The syllable structures of words are obtained by a recursive transition network-based phonological parser,[9] using a pronunciation dictionary. The transition network is derived from a set of context-free grammar (CFG) rules describing the syllable structure of English words. The CFG rules are obtained by reorganizing and supplementing several lists found in Ref. 11. These rules have been tested for all 6110 words in the TIMIT dictionary. The CFG rules used for constructing the transition network are as follows:

Word → [Init-Onset] V [CvCluster] [Final-Coda]
Init-Onset → C | p,l | p,r | p,w | p,y | b,l | b,r | b,w | b,y | t,r | t,w | t,y | d,r | d,w | d,y | k,l | k,r | k,w | k,y | g,l | g, r | g,w | g,y | f,l | f,r | f,y | v,l | v,r | v,y | th,r | th,w | th,y | s,p | s,p,y | s,t | s,t,y | s,k | s,k,y | s,f | s,m | s,n | s,l | s,w | s, y | s h,m | sh,l | sh,r | sh,w | hh,y | hh,w | m,y | n,y | l,y | s,p,l | s,p,r | s,t,r | s,k,l | s,k,r | s,k,w
CvCluster → [MidC] V [CvCluster]
MidC → MidC41 | MidC31 | MidC32 | MidC20 | MidC21 | C
MidC41 → C, s, C, C
MidC31 → s, C, C | C, s, C | Nas, Fri, Lqd | Nas, Stp, Gld, | Nas, Obs, r | Lqd, Fri, Lqd | Lqd, Obs, r | Gld, Fri, Lqd | Gld, Obs, r | Stp, Stp, Lqd | Stp, Stp, Gld | Stp, Fri, Lqd | Fri, Stp, Lqd | Fri, Stp, Gld
MidC32 → Nas, Stp, Lqd | Nas, Stp, Nas | Nas, Stp, Fri | Nas, Stp, Stp | Nas, Stp, Afr | Lqd, Fri, Stp | Lqd, Fri, Nas | Lqd, Fri, Fri | Lqd, Stp, Stp | Lqd, Stp, Lqd | Lqd, Stp, Fri | Lqd, Stp, Gld | Lqd, Stp, Afr | Fri, Fri, hh | r, C, C
MidC20 → p,l | p,r | p,w | p,y | b,l | b,r | b,w | b,y | t,r | t,w | t,y | d,r | d,w | d,y | k,l | k,r | k,w | k,y | g,l | g,r | g,w | g ,y | f,l | f,r | f,y | v,l | v,r | v, y | th,r | th,w | th, y | s,p | s,t | s,k | s,f | s,m | s,n | s,l | s,w | s, y | sh,p | sh,m | sh,l | sh,r | sh,w | hh,y | hh,w | m,y | n,y | l,y

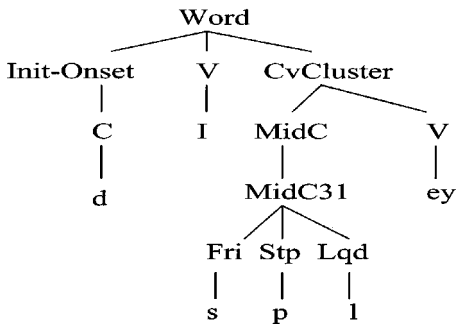

FIG. 7. Parse tree for word *display*.

MidC21 → C, C
Final-Coda → C | p, th | t, th | d, th | d,s,t | k,s | k,t | k,s,th | g, d | g , z | ch, t | jh, d | f, t | f, th | s, p | s, t | s, k | z, d | m, p | m, f | n, t | n, d | n, ch | n, jh | n, th | n, s | n, z | ng, k | ng, th | ng , z | l, p | l, b | l, t | l, d | l, k | l, ch | l , jh | l, f | l, v | l, th | l, s | l, z | l , sh | l, m | l, n | l,p | l,k,s | l,f,th | r, Stp | r,ch | r,jh | r,f | r,v | r,th | r,s | r,z | r,sh | r,m | r,n | r,l

The phoneme type categories are C (consonants), V (vowels), Nas (nasals), Gld (glides), Fri (fricatives), Afr (affricates), Obs (obstruents), Stp (stops), Lqd (liquids). The MidC categories are used for assigning word-internal consonant clusters to either the previous syllable's coda or the next syllable's onset according to one of the following four possibilities:

MidC41—1 coda consonants, 3 onset consonants,
MidC31—1 coda consonants, 2 onset consonants,
MidC32—2 coda consonants, 1 onset consonants,
MidC20—0 coda consonants, 2 onset consonants,
MidC21—1 coda consonants, 1 onset consonants.

This grammar in its current state is not fully deterministic. The fifth rule of MidC31 and the first rule of MidC32, for example, can result in ambiguous analyses for certain input sequences. For example, the phoneme sequence in *Andrew* can be parsed either by rule MidC31 (Nas Obs r) or by rule MidC32 (Nas Stp Lqd). How to deal with this problem is a practical issue. For parsing a large number of words automatically, our solution is to use this parser to first parse a pronunciation dictionary and then resolve the ambiguities through hand checking. The parsed pronunciation dictionary is then used to provide syllable structures of the words. We carried out this procedure on the TIMIT pronunciation dictionary. The results showed that the rules are a fairly precise model of English syllable and phonotactic structures: Out of 7905 pronunciations, only 135, or 1.7%, generated multiple parses. The ambiguities were hand-checked and the parsed dictionary was used for transferring phoneme sequences into syllable structures in our TIMIT-based experiments.

As an illustration, Fig. 7 shows the parse tree for word *display*, which denotes that the word it display consists of two syllables. The category ''CvCluster'' is used for dealing with multiple syllables recursively; ''MidC'' and ''MidC31'' are categories of intervocalic consonant clusters. The category ''Init-Onset'' denotes the word-initial syllable onset. The separation of syllable-internal consonants into coda and

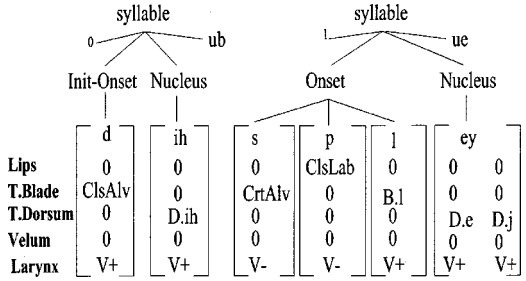

FIG. 8. Subsegmental feature structure for word *display*.

onset is based on the consonant types according to phonotactic principles.[11]

The parser output of an unambiguous tree is transformed into subsegmental feature vectors[3,10,12] with high-level linguistic information. This is illustrated in Fig. 8. Here, the word *display* is parsed as a single word utterance with **ub** standing for utterance beginning and **ue** for utterance end. Stress is denoted by 0 (unstressed syllable) and 1 (stressed syllable) at the syllable node. The subsegmental feature structure is viewed as an autosegmental structure[2,12] with skeletal and articulatory feature tiers and a prosodic structure placed on top of it. There is a resyllabification by which /s/ is moved to the second syllable. Currently, this is done in the lexicon on the word by word basis.

Feature overlapping is carried out by the phonological rules we have implemented computationally, incorporating high-level linguistic information. We have used a temporal feature logic[12] as the theoretical framework for imposing constraints and in the formulation of the phonological rules.

APPENDIX B: A TEMPORAL FEATURE LOGIC

A temporal feature logic for the constraint-based approach to feature overlapping is a language $\mathcal{L}(\mathcal{X},\mathcal{P},\mathcal{T},\mathcal{C})$, where

$\mathcal{X}$ is a set of variables: $a,b,c,\ldots x,y,z,\ldots$, etc.,
$\mathcal{P}$ is a prosodic structure: {*syl,sylconst,seg,boundary,stress*},
$\mathcal{T}$ is a tier structure: {*seg,articulator,feature*},
$\mathcal{C}$ is a set of logical connectors: $\{\delta,\prec,\circ,\bowtie,=,\neg,\vee,\wedge,\forall,\exists,\rightarrow,\equiv,(,),\top,\perp\}$, where δ, $\prec$, $\circ$, and $\bowtie$ are "dominance," "precedence," "overlap," and "mix," respectively.

1. The prosodic structure

(1) $\forall xy$, $syl(x)\wedge x\ \delta y\rightarrow sylconst(y)\vee boundary(y)$. Syllables can dominate syllable constituents and boundaries.
(2) $\forall xy$, $sylconst(x)\wedge x\ \delta y\rightarrow seg(y)\vee stress(y)$. Syllable constituents can dominate segments and stresses.
(3) $\forall x, boundary(x)\rightarrow x\in\{ub,ue,wb,we,mb,me\}$, where the boundary symbols stand for utterance beginning, utterance end, word beginning, word end, morpheme beginning, and morpheme end, respectively.
(4) $\forall x$, $sylconst(x)\rightarrow x\in\{onset,nucleus,coda\}$.
(5) $\forall x$, $stress(x)\rightarrow x\in\{0,1\}$.

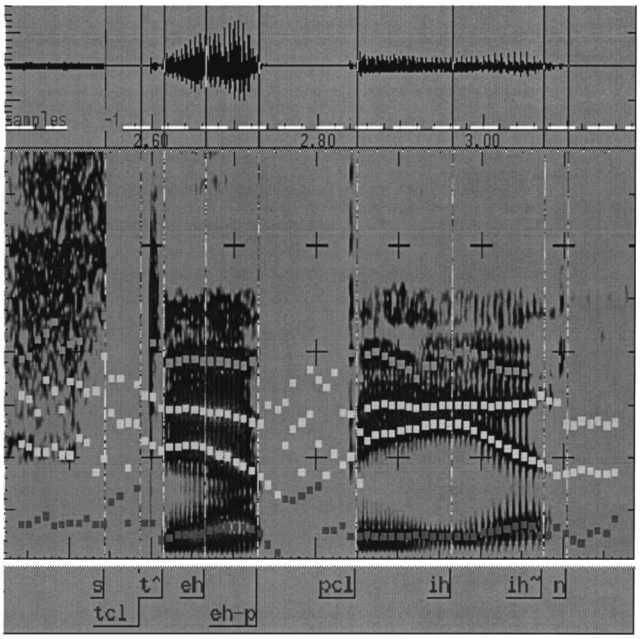

FIG. 9. An example spectrogram for *step in* illustrating acoustic properties associated with feature overlaps.

2. The tier structure

(1) $\forall x$, $seg(x)\rightarrow\exists y, x\ \delta y\wedge articulator(y)$. Every segment dominates one or more articulators.
(2) $\forall x$, $articulator(x)\rightarrow\exists y, x\ \delta y\wedge feature(y)$. Every articulator dominates one or more features.
(3) $\forall x$, $articulator(x)\rightarrow x\in\{lip,tbld,tdsm,vel,lyx\}$ where the articulator symbols stands for lip, tongue blade, tongue dorsum, velum, and larynx, respectively.
(4) $\forall x$, $feature(x)\rightarrow poa(x)\vee cdg(x)\vee shape(x)$, where poa stands for place of articulation; cdg stands for constriction degree, and *shape* stands for the shape of the lips. (Figure 8 shows how prosodic and tier structures are motivated by subsegmental *feature* structures.)

3. Dominance, precedence, overlap, and mix

The basic properties of δ, $\prec$, $\circ$ are described in Ref. 12. When some B is a component of some A, we say A dominates B, or A δ B. When two events A and B overlap in time, we denote this by A $\circ$ B; otherwise, either A precedes B or B precedes A: A $\prec$ B $\vee$ B $\prec$ A. In Bird's temporal feature logic, dominance implies overlap. This is called *the locality constraint*:

$$\forall xy,\ x\ \delta y\rightarrow x\circ y.$$

Precedence, on the other hand, implies no overlap and vice versa. This is described as *the mutual exclusion of L and* $\circ$

$$\forall xy,\ x\prec y\rightarrow\neg\, x\circ y,$$

and

$$\forall xy,\ x\circ y\rightarrow\neg\, x\prec y.$$

There is an important property related to the above two fundamental properties which is called *the transitivity of* $\prec$ *through* $\circ$: $\forall wxyz$, $w\prec x\wedge x\circ y\wedge y\prec z\rightarrow w\prec z$. Logically it

is hard to prove this. However, this property can be visualized in the following way. To see that $w \prec z$, we note that the left boundary of x is to the right of w and the right boundary of y is also to the right of w (since $x \circ y$) and the left boundary of z is to the right of the right boundary of y; therefore, the left boundary of z is also to the right of w. This situation can be illustrated by the following diagram:

```
   w       x
|-------|------|

  y       z
|----|-------|
```

Referring to Fig. 8, these operators can be illustrated in the following:

$$Syllable_1 \, \delta \, Nucleus_1 \, \delta \, /\text{ih}/ \, \delta \, Larynx \, \delta \, \text{V}+,$$

$$Syllable_1 \circ Nucleus_1 \circ /\text{ih}/ \circ Larynx \circ \text{V}+,$$

$$/\text{d}/ \prec /\text{ih}/ \prec /\text{s}/ \prec /\text{p}/ \prec /\text{l}/ \prec /\text{ey}/.$$

Feature overlapping in this temporal logic framework is defined as a process of dynamic realization of segmental tier structure synchrony (i.e., articulatory features are synchronous within segments). In dynamic realization, a feature on some articulator tier may spread temporally and may overlap with features of neighboring segments. If we use a predicate "*possib*" to denote possibility of realizing a planned segment sequence, this can be expressed as follows:

$$seg_a \circ articulator_p \circ feature_l \wedge seg_a \prec seg_b$$

$$\rightarrow possib(seg_b \circ feature_l).$$

When $feature_l$ overlaps with seg_b, it has a chance to overlap with the features dominated by seg_b.

We abandon the "linearity constraint" which requires that events of the same sort be in precedence relation only (i.e., features on the same articulator tier can only be in precedence relation). Instead, we allow features at the same tier (therefore, of the same sort) to overlap; we call this "feature mixing," denoted by $\bowtie$. This relation is expressed as

$$\forall xy, tier_i(x) \wedge tier_i(y) \wedge x \circ y \leftrightarrow x \bowtie y.$$

That is, if events on the same tier are in the same dominant group and overlap in time, they are said to mix with each other. As an overlap can be either partial or full, so is the mix relation. This mix relation is used to describe coarticulation involving the same tier in the articulatory feature space (i.e., *coproduction*). Articulatory mix is a very general phenomenon. Whenever consecutive phonemes involve the same articulator, there is often a feature mix in the transition phase.

The temporal feature logic described above is motivated by empirical observations of speech data including articulatory data and speech spectrograms. In particular, the subsegmental, articulatory features are components in forming a phoneme, and at the same time these features can spread beyond the conventional boundaries of phonemes, exerting influence on the articulatory or acoustic properties of neighboring phonemes up to some distance away. If we consider such spreading as independent events, these events can take the form of temporal overlap or temporal mix. Overlap refers to simultaneous events occurring at different tiers, while mix refers to simultaneous events occurring on the same tier. A combination of overlapping and mixing accounts for a great part of transitions between phonemes. In descriptive terms, these transitional phases in speech can be modeled by a set of feature bundles constructed from interactions between phonemes via the mechanisms of overlap and mix. These overlapped- and mixed feature bundles derived from the predefined, canonical, context-independent feature bundles are then taken as the basic units of speech to form the HMM state topology for speech recognition.

In Fig. 9, the spectrogram shows some acoustic properties of the utterance "step in," which can be described by feature overlapping in accounting for the transitional phases. The vowel /eh/ in the word *step* contains two transitional phases. One has a carry-over *tongue-tip* feature spread from the previous phoneme /t/; this overlapped feature from /t/ to /eh/ accounts for the initial formant transition in /eh/. The second transitional phase contains a look-ahead *lips* feature spread from the following phoneme /p/. The acoustic effect is a conspicuous formant transition over a major length of /eh/ with the formant transition targets towards those of /p/. The stop /p/, due to its coda position, has a very weak release phase. The spectral shape of the release burst in /p/ is affected by the look-ahead *tongue-dorsum* feature of the following vowel /ih/. The vowel /ih/ is partially nasalized due to the *velum* feature spread from the following phoneme /n/. At the same time, both the *lips* feature of /p/ and the *tongue-tip* feature of /n/ are overlapped into /ih/, creating the obvious formant transition throughout the entire vowel.

APPENDIX C: ABBREVIATIONS USED IN FIGURES

ASP	aspiration
B.e	tongue-blade of /e/
B.l	tongue-blade of /l/
C/V	consonant or vowel
ClsAlv.Br	(feature mix of) closure-alveolar and tongue blade of /r/
ClsAlv	closure-alveolar
ClsLab	closure-labial
CrtAlv	critical-alveolar
CvCluster	consonant vowel cluster
Fri	fricative (consonant)
Init-Onset	word initial onset
MidC	word-middle consonant
Nas	nasal (feature)
Rnd.o	lip-rounding of /o/
Rnd.r	lip-rounding of /r/
seg	segment
Stp	stop (consonant)
syl	syllable
T.Blade	tongue blade
T.Dorsum	tongue dorsum
ub	utterance begin
ue	utterance end
V−	unvoiced
V+	voiced

[1] C. Browman and L. Goldstein, ''Articulatory gestures as phonological units,'' Phonology **6**, 201–251 (1989).
[2] J. A. Goldsmith, *Autosegmental and Metrical Phonology* (Blackwell, Oxford, 1990).
[3] L. Deng and D. Sun, ''A statistical approach to automatic speech recognition using the atomic units constructed from overlapping articulatory features,'' J. Acoust. Soc. Am. **95**, 2702–2719 (1994).
[4] L. Deng, ''Autosegmental representation of phonological units of speech and its phonetic interface,'' Speech Commun. **23**, 211–222 (1997).
[5] *Automatic Speech and Speaker Recognition—Advanced Topics*, edited by C.-H. Lee, F. Soong, and K. Paliwal (Kluwer Academic, Dordrecht, 1996).
[6] L. Deng, ''Integrated-multilingual speech recognition using universal phonological features in a functional speech production model,'' in *Proceedings of the IEEE International Conference on Acoustics, Speech, and Signal Processing*, Munich, Germany, 1997 (IEEE, New York), Vol. 2, pp. 1007–1010.
[7] L. Deng and H. Sameti, ''Transitional speech units and their representation by the regressive Markov states: Applications to speech recognition,'' IEEE Trans. Speech Audio Process. **4**, 301–306 (1996).
[8] L. Deng, ''Finite-state automata derived from overlapping articulatory features: A novel phonological construct for speech recognition,'' in *Proceedings of the Workshop on Computational Phonology in Speech Technology* (Association for Computational Linguistics), Santa Cruz, CA, 28 June 1996, pp. 37–45.
[9] K. W. Church, *Phonological Parsing in Speech Recognition* (Kluwer Academic, Dordrecht, 1987).
[10] J. Coleman, *Phonological Representations* (Cambridge University Press, Cambridge, 1998).
[11] J. T. Jensen, *English Phonology* (Benjamin, New York, 1993).
[12] S. Bird, *Computational Phonology—A Constraint-Based Approach* (Cambridge University Press, Cambridge, 1995).
[13] L. Deng and J. Wu, ''Hierarchical partitioning of articulatory state space for articulatory-feature based speech recognition,'' in Proceedings of the International Conference on Spoken Language Processing, Philadelphia, PA, 3–6 October 1996, pp. 2266–2269.

Ultrasound-induced lung hemorrhage: Role of acoustic boundary conditions at the pleural surface

William D. O'Brien, Jr.
Bioacoustics Research Laboratory, Department of Electrical and Computer Engineering, University of Illinois, 405 North Mathews, Urbana, Illinois 61801

Jeffrey M. Kramer and Tony G. Waldrop
Department of Molecular and Integrative Physiology, University of Illinois, 407 South Goodwin, Urbana, Illinois 61801

Leon A. Frizzell and Rita J. Miller
Bioacoustics Research Laboratory, Department of Electrical and Computer Engineering, University of Illinois, 405 North Mathews, Urbana, Illinois 61801

James P. Blue and James F. Zachary
Department of Veterinary Pathobiology, University of Illinois, 2001 South Lincoln Avenue, Urbana, Illinois 61802

(Received 10 July 2001; accepted for publication 21 November 2001)

In a previous study [J. Acoust. Soc. Am. **108**, 1290 (2000)] the acoustic impedance difference between intercostal tissue and lung was evaluated as a possible explanation for the enhanced lung damage with increased hydrostatic pressure, but the hydrostatic-pressure-dependent impedance difference alone could not explain the enhanced occurrence of hemorrhage. In that study, it was hypothesized that the animal's breathing pattern might be altered as a function of hydrostatic pressure, which in turn might affect the volume of air inspired and expired. The acoustic impedance difference between intercostal tissue and lung would be affected with altered lung inflation, thus altering the acoustic boundary conditions. In this study, 12 rats were exposed to 3 volumes of lung inflation (*inflated*: approximately tidal volume; *half-deflated*: half-tidal volume; *deflated*: lung volume at functional residual capacity), 6 rats at 8.6-MPa *in situ* peak rarefactional pressure (MI of 3.1) and 6 rats at 16-MPa *in situ* peak rarefactional pressure (MI of 5.8). Respiration was chemically inhibited and a ventilator was used to control lung volume and respiratory frequency. Superthreshold ultrasound exposures of the lungs were used (3.1-MHz, 1000-Hz PRF, 1.3-μs pulse duration, 10-s exposure duration) to produce lesions. Deflated lungs were more easily damaged than half-deflated lungs, and half-deflated lungs were more easily damaged than inflated lungs. In fact, there were no lesions observed in inflated lungs in any of the rats. The acoustic impedance difference between intercostal tissue and lung is much less for the deflated lung condition, suggesting that the extent of lung damage is related to the amount of acoustic energy that is propagated across the pleural surface boundary. [DOI: 10.1121/1.1436068]

PACS numbers: 43.80.Cs, 43.80.Gx, 43.80.Jz [FD]

I. INTRODUCTION

A considerable amount of work has been published regarding lung hemorrhage caused by ultrasound.[1–21] There is agreement that gas in the lung plays a role in the ultrasound-induced damage mechanism, and that the mechanism is nonthermal. A distinction needs to be made between mechanisms involving large gas bodies, such as gas in the alveoli of the lung (38–49 μm),[22–24] and classical inertial cavitation that involves small microbubbles as nuclei (radii on the order of 1 μm or less).[25] Evidence has been slowly accumulating that suggests that the mechanism of damage in the lung may not be inertial cavitation. There seems to be no dependence on whether the positive or negative components of the ultrasonic pulse cause lithotripter-induced lung damage; however, inertial cavitation is associated with negative pressure.[26] The frequency dependence may not be the same as that associated with effects due to the presence of contrast agents that quite clearly nucleate inertial cavitation.[27] The hydrostatic pressure dependence of ultrasound-induced lung hemorrhage in mice is not the same as that associated with effects due to inertial cavitation.[17] Likewise, there is evidence that suggests the mechanism of damage in rat lung may be inertial cavitation.[9,28] However, the goal of this contribution is not to strengthen or weaken the arguments for or against inertial cavitation; the debate will probably continue for some time.[29–32] The goal is to inform the community of an interesting nonthermal observation that affects the degree of ultrasound-induced lung damage.

The study reported herein was motivated by an interesting finding that showed that the amount of lung damage was greater under increased hydrostatic pressure.[17] The acoustic impedance difference between intercostal tissue and lung was evaluated as a possible explanation for the enhanced lung damage with increased hydrostatic pressure, but hydrostatic-pressure-dependent impedance difference along could not explain the enhanced effects on hemorrhage. In

that study, it was hypothesized that the mouse's breathing pattern might be altered as a function of hydrostatic pressure, which in turn, might affect the volume of air inspired and expired by the mouse. With altered lung inflation, the acoustic impedance difference between intercostal tissue and lung would be affected thus affecting the acoustic boundary conditions. This brief report describes an experiment and some simple acoustic theory to provide insight into the mechanism of ultrasound-induced lung hemorrhage under *in vivo* conditions in which rats were subjected to three levels of lung inflation during ultrasound exposure.

II. ANIMAL EXPERIMENTS

A. Exposimetry

The exposimetry and calibration procedures have been described previously in detail[17,18] Ultrasonic exposures were conducted using one focused, 51-mm-diameter, lithium niobate ultrasonic transducer (Valpey Fisher, Hopkinton, MA). Water-based (distilled water, 22 °C) pulse-echo ultrasonic field distribution measurements were performed according to established procedures[33] and yielded a center frequency of 3.1 MHz, a fractional bandwidth of 15%, a focal length of 56 mm, a −6-dB focal beamwidth of 610 μm, and a −6-dB depth of focus of 5.9 mm.

An automated procedure described previously was used routinely to calibrate the ultrasound field.[17,18,34–36] The source transducer was mounted in a water tank (degassed water, 22 °C) and its drive voltage was supplied by a RAM5000 (Ritec, Inc., Warwich, RI). Calibrations were performed with a PVDF calibrated hydrophone (Marconi Model Y-34-6543, Chelmsford, UK). The *in situ* (at the pleural surface) pressure values were estimated using linear theory from procedures previously described.[18] They were estimated from measured *in vitro* peak rarefactional pressure of 10.1 and 18.9 MPa (s.d.'s=0.5 and 1.2 MPa, n=13), measured *in vitro* peak compressional pressure of 21.9 and 46.5 MPa (s.d.'s=1.9 and 1.6 MPa, n=13), an intercostal tissue attenuation coefficient of 1.1 dB/cm MHz,[37] and a mean chest wall thickness of 4.05 mm (s.d.=0.09 mm, n=12). The two *in situ* peak rarefactional pressures, $p_{r(in\ situ)}$, were 8.6 and 16 MPa and the respective *in situ* peak compressional pressures, $p_{c(in\ situ)}$, were 18 and 40 MPa. For comparison to a quantity that appears on the display of diagnostic ultrasound equipment,[35] the Mechanical Indices were 3.1 and 5.6, and were determined according to the procedures specified by the standard.[18,35] These exposure levels were known to be superthreshold values based on previous studies[18–20] where ultrasound exposures were conducted on normal-breathing animals.

B. Animals

The experimental protocol was approved by the campus Laboratory Animal Care Advisory Committee and satisfied all University of Illinois and NIH rules for the humane use of laboratory animals. Animals were housed in an AAALAC-approved animal facility, placed in groups of three or four in polycarbonate cages with beta-chip bedding and wire bar lids, and provided food and water *ad libitum*.

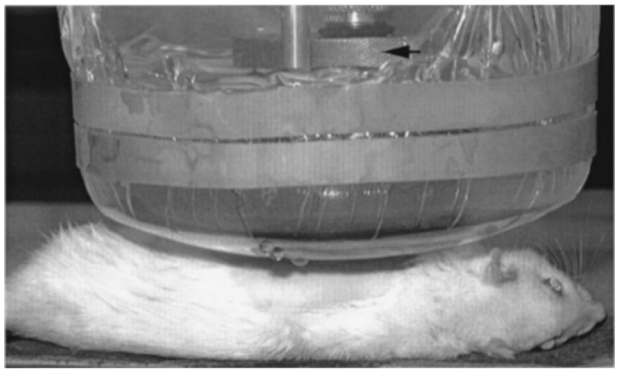

FIG. 1. Photograph showing the rat in right lateral recumbancy with the water-filled stand-off tank positioned in contact with the skin. The arrow points to the 3.1-MHz transducer.

Twelve 230-g (s.d.=10 g) 10-to-11 week-old Sprague-Dawley rats (Harlan, Indianapolis, IN) were initially anesthetized with an intraperitoneal injection of Ketamine (87 mg/kg) and Rompun (13 mg/kg). The rats were randomly assigned to one of three ultrasound exposure groups: sham (2 rats), $p_{r(in\ situ)}$=8.6 MPa (6 rats) and $p_{r(in\ situ)}$=16 MPa (6 rats). Additional doses of anesthetic were administered upon evidence of foot withdrawal to noxious paw pinch. The individuals involved in animal handling, exposure, necropsy, and lesion scoring were blinded to the exposure conditions.

The skin of the left thorax and ventral neck was shaved with an electric clipper. A cannula (PE-10, Clay Adams, Franklin Lakes, NJ) was placed into the right external jugular vein through a ventral midline incision in the neck for injection of supplemental anesthetic and paralytic agent, and a tracheotomy was also performed. Following the surgical preparation, the anesthetized rats rested for approximately 15 min during which time preparation for ultrasound exposure was completed. A depilatory agent (Nair,® Carter-Wallace, Inc., New York, NY) was used on the skin of the left thorax to maximize sound transmission. Three black dots were placed on the skin over the intercostal spaces between the fourth and fifth ribs, sixth and seventh ribs, and eighth and ninth ribs to guide the positioning of the ultrasonic beam. The center-to-center rib spacing of rats this size is about 5 mm,[37] and thus the distance between each black dot was 1 cm. The beamwidth at the pleural surface was 610 μm, thus preventing the overlapping of exposures. Respiration was suspended by paralyzing the animals with an intravenous injection of gallamine triethiodide (5–10 mg/kg, Sigma, St. Louis). Each rat was also placed on a ventilator (Model CTE-930 ventilator, CWE, Inc., Ardmore, PA) at a respiratory rate of 60 breaths/min and a tidal volume of approximately 4 mL with 100% oxygen. Total experimental time following paralysis was not longer than the effective dose of gallamine nor longer than the effective dose time of the anesthetic. Body temperature was maintained at 36.5–37.5 °C via a heating pad and radiant heat lamp.

Anesthetized rats were placed in right lateral recumbancy and a stand-off tank (degassed water; 30 °C) positioned in contact with the skin (Fig. 1). The circular transducer holder was visually centered above each black dot. The transducer was placed in the holder that was in the stand-off

tank. The low-power (*in vivo* peak rarefactional pressure of 0.4 MPa, *in vivo* peak compressional pressure of 0.5 MPa, pulse repetition frequency of 10 Hz, Mechanical Index of 0.13) pulse-echo capability of the exposure system (RAM5000, Ritec, Inc., Warwick, RI) displayed on an oscilloscope was used to adjust the axial center of the focal region to within 1 mm of the lung surface. Thus the ultrasonic beam was approximately perpendicular to the skin at the position of the black dot with the beam's focal region at the lateral surface of the lung, and approximately normal to the lung's pleural surface. This alignment procedure was repeated for each exposure.

For each rat, the same ultrasound exposure conditions were used at each exposure site. The volume of pulmonary inflation was varied for each rat. Three lung-inflation conditions were utilized in each rat. The second ultrasound exposure of the three was with the lung inflated. The first and third exposures were randomized either with the lung deflated or half-deflated. In a previous rat study[38] five adjacent lesions of equal size were created using the same superthreshold exposure conditions. Also, the same 3.1-MHz transducer used herein was used for this previous study. The exposure sites were located in the five adjacent intercostal spaces between the fourth and ninth ribs. This suggested that sensitivity across the lung surface does not change. Therefore, randomizing the location of the three exposure sites was not considered necessary.

Lung inflation was generated by attaching a 10-cc syringe to the tracheotomy tube after which air was pushed into the lungs. Two volumes of lung inflation (6 mL for the larger volume and 3 mL for the smaller volume) were generated to test for ultrasound-induced damage. Tidal volume for ventilation of rats was estimated from the allometric equation $\text{Tidal Volume}=7.69\text{M}^{1.04}$ (Ref. 39) where M equals the mass of the animal in grams and tidal volume is expressed in mL. Tidal volume for each rat was estimated prior to the experiment and the volume of inspired air was adjusted on the ventilator. In all cases, the maximal inspired volume (2 $\times$tidal volume) was well under vital capacity of the lungs[39] so as to prevent overinflation lung damage. The larger lung inflation volume was approximately 20% greater than tidal volume (TV) and the smaller lung inflation volume was 60% less than tidal volume (HTV). The lung inflation state was held constant for the duration of the ultrasound exposure (10 s). The smallest lung volume was achieved by detaching the ventilator from the tracheotomy tube and allowing the lungs to assume a volume at functional residual capacity (FRC). During all states of lung inflation a distinct apnea was associated with the ultrasound exposure period as determined by lack of chest wall movement.

Following the ultrasound exposure procedures, rats were euthanized under anesthesia by cervical dislocation. The thorax was opened and the thickness of each left thoracic wall (skin, rib cage, and parietal pleura) was measured at the point of exposure over the middle black dot using a digital micrometer (accuracy: 10 μm). These chest wall measurements were used for later calculation of the *in situ* ultrasonic pressures at the visceral pleural surface. Lungs were removed, rinsed in 0.9% sodium chloride, examined grossly for the presence or absence of lesion(s), and then photographed digitally. Each lung was placed in a sterile 50-mL clear polypropylene centrifuge tube and was fixed by immersion in 10% neural-buffered formalin for a minimum of 24 h. After total fixation, the elliptical dimensions of lung lesions at the visceral pleural surface were measured with a digital micrometer (accuracy: 10 μm), where "*a*" was the length of the semi-major axis and "*b*" was the length of the semi-minor axis. The lesions were then bisected and the depth "*d*" of the lesion within the lung was measured. In animals where the depth of the lesion was not visually discernible, the depth was determined from measurements made on histologic sections with a slide micrometer. The surface area (πab) and volume ($\pi abd/3$) of the lesion were calculated for each animal. Each half of the bisected lesion was embedded in paraffin, sectioned at 5 μm, stained with hematoxylin and eosin, and evaluated microscopically.

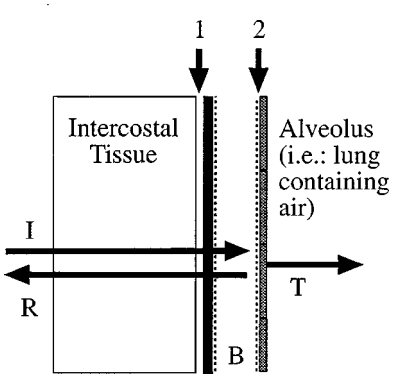

FIG. 2. Schematic diagram of the interface zone between intercostal tissue and lung (not to scale). The innermost layer of the intercostal tissue within the thoracic cavity is covered with parietal pleural. The lung is covered by visceral pleura (thick black line) and the two pleural layers glide over each other during the respiratory cycle. The space (thoracic cavity—arrow 1) between the two pleura layers is under negative pressure. The visceral pleura contains blood-filled capillaries (B) lined by a single layer of endothelial cells (open rectangles). The alveolus (air-filled) is separated from blood in the capillary by a single trilaminar membrane called the air–blood barrier (arrow 2). This barrier is formed by type 1 alveolar epithelial cells (filled rectangles), basement membrane, and capillary endothelial cells. It can measure as thin as 100 nm in some areas. Acoustic boundary conditions may exist and play a role in ultrasound-induced lung hemorrhage at the air-blood barrier (arrow 2). I=incident sound; R=reflected sound; T=transmitted sound.

III. APPLICATION ACOUSTIC THEORY

The acoustic impedance of the intercostal tissue and lung was evaluated to understand the acoustic propagation at and across the boundary. Figure 2 defines the boundary. In a previous study,[17] hydrostatic-pressure changes along could not explain the enhanced effects on lung hemorrhage. It was thus speculated that if the mouse's breathing pattern were altered as a function of hydrostatic pressure, and this alteration affected the volume of air inspired and expired, then an increase in the power transmitted into lung might occur. Therefore, for the study reported herein, the rat's inspiration was controlled, and thus the amount of air in the lung was the main experimental variable.

A planar boundary was assumed between intercostal tissue and lung with the incident ultrasonic field in the inter-

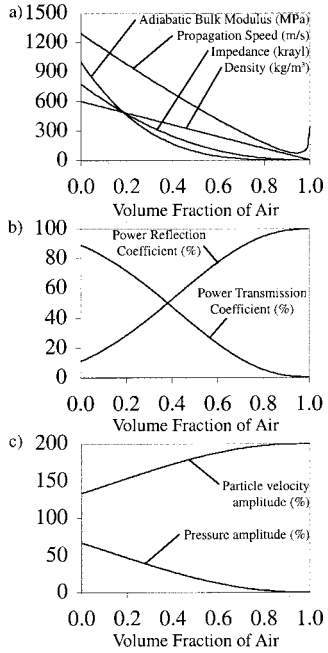

FIG. 3. (a) Adiabatic bulk modulus, propagation speed, characteristic acoustic impedance, and density of lung as a function of volume fraction of air in the lung. These curves were calculated from Eqs. (2), (3), (4), and (1), respectively. (b) Sound power reflection coefficient and sound power transmission coefficient as a function of volume fraction of air in the lung. These curves were calculated from Eqs. (5) and (6), respectively. (c) Particle velocity amplitude and acoustic pressure amplitude near the lung surface as a function of volume fraction of air in the lung. These curves were calculated from Eqs. (8) and (7), respectively.

costal tissue and the ultrasonic beam axis normal to the boundary. Lung was modeled as two components consisting of air and parenchyma where the lung's density is

$$\rho_{\text{lung}} = x_{\text{air}}\rho_{\text{air}} + x_{\text{parenchyma}}\rho_{\text{parenchyma}}, \tag{1}$$

the lung's adiabatic bulk modulus is

$$B_{\text{lung}} = x_{\text{air}}B_{\text{air}} + x_{\text{parenchyma}}^{3.5}B_{\text{parenchyma}}, \tag{2}$$

and the volume fractions of air and parenchyma sum to unity, that is, $x_{\text{air}} + x_{\text{parenchyma}} = 1$. This model was selected because it fit the experimental measurements of reflection coefficient versus lung inflation in the fixed lungs of dogs at 2.4 MHz,[40] and the experimental measurements of propagation speed at one lung inflation in fresh lungs of dogs at 2.25 MHz.[41] The fit to these published measurements yielded $\rho_{\text{air}} = 1.21$ kg/m^3, $\rho_{\text{parenchyma}} = 600$ kg/m^3, $B_{\text{air}} = 142$ kPa, and $B_{\text{parenchyma}} = 1$ GPa for $x_{\text{air}} = 0.31$, and, in turn, yielded $\rho_{\text{lung}} = 414$ kg/m^3 and $B_{\text{lung}} = 273$ MPa. Propagation speed is determined from

$$c_{\text{lung}} = \sqrt{B_{\text{lung}}\rho_{\text{lung}}}, \tag{3}$$

and acoustic impedance is determined from

$$z_{\text{lung}} = \sqrt{\rho_{\text{lung}}B_{\text{lung}}}. \tag{4}$$

These fit values agreed well with published results. The fit reflection coefficient value relative to 1.5 Mrayl was -7.7 dB; the published values were between -2 and -4 dB.[40] The fit and published[41] lung propagation speed values were 812 m/s.

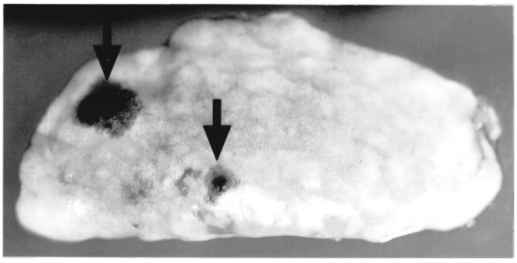

FIG. 4. Rat lung (R1694). Lung was exposed at superthreshold condition (*in situ* peak rarefactional pressure of 16 MPa) to ensure the formation of lesions. Arrows represent foci of lung hemorrhage caused by ultrasound exposure. The hemorrhage (depth=2.60 mm; area=2.54 mm^2; volume=2.20 mm^3) labeled by the right arrow (cranial most exposure) occurred when the lung was exposed under the "half-deflated" state. The hemorrhage (depth =2.92 mm; area=12.96 mm^2; volume=12.61 mm^3) labeled by the left arrow (caudal most exposure) occurred when the lung was exposed under the "deflated" state. The region of lung between the two areas of hemorrhage, which had no lesion, was exposed to ultrasound when the lung was under the "inflated" state.

The density and adiabatic bulk modulus of lung [from Eqs. (1) and (2)], along with their propagation speed and characteristic acoustic impedance [from Eqs. (3) and (4)] are graphed [Fig. 3(a)] as a function of the amount of air in lung. The four constant quantities used in Eqs. (1) and (2) were $\rho_{\text{air}} = 1.21$ kg/m^3, $\rho_{\text{parenchyma}} = 600$ kg/m^3, $B_{\text{air}} = 142$ kPa, and $B_{\text{parenchyma}} = 1$ GPa, and the one variable was $0 \leqslant x_{\text{air}} \leqslant 1$ where $x_{\text{parenchyma}} = 1 - x_{\text{air}}$.

The power reflection coefficient (R_π) and power transmission coefficient (T_π) were determined to assess the power transfer at the intercostal tissue-lung boundary. At normal incidence to the planar boundary, these quantities (which are the same as the intensity reflection and transmission coefficients at normal incidence) are given by

$$R_\pi = \left(\frac{z_{\text{lung}} - z_{\text{intercostal tissue}}}{z_{\text{lung}} + z_{\text{intercostal tissue}}}\right)^2, \tag{5}$$

$$T_\pi = \frac{4z_{\text{lung}}z_{\text{intercostal tissue}}}{(z_{\text{lung}} + z_{\text{intercostal tissue}})^2}, \tag{6}$$

where $z_{\text{intercostal tissue}}$ is 1.54 Mrayl. The power reflection and transmission coefficients are graphically shown as a function of the amount of air in lung in Fig. 3(b).

It had been previously hypothesized that because the lung boundary acts as an acoustic pressure-release surface, and if constructive interference occurred near to the lung surface, then there would be a significant increase in pressure *in situ*.[9,42] Though it is particle velocity that is a maximum right at the lung surface at a pressure-release surface, the pressure is significantly increased only one quarter of a wavelength into the intercostal tissue from that surface, so their idea has merit and is evaluated. The acoustic pressure (p_0) and particle velocity (u_0) amplitudes in the intercostal tissue and near the lung surface where constructive interference can be presumed are given by

$$p_0 = (1 + R)p_{in\ situ}, \tag{7}$$

$$u_0 = (1 - R)\frac{p_{in\ situ}}{z_{\text{intercostal tissue}}}, \tag{8}$$

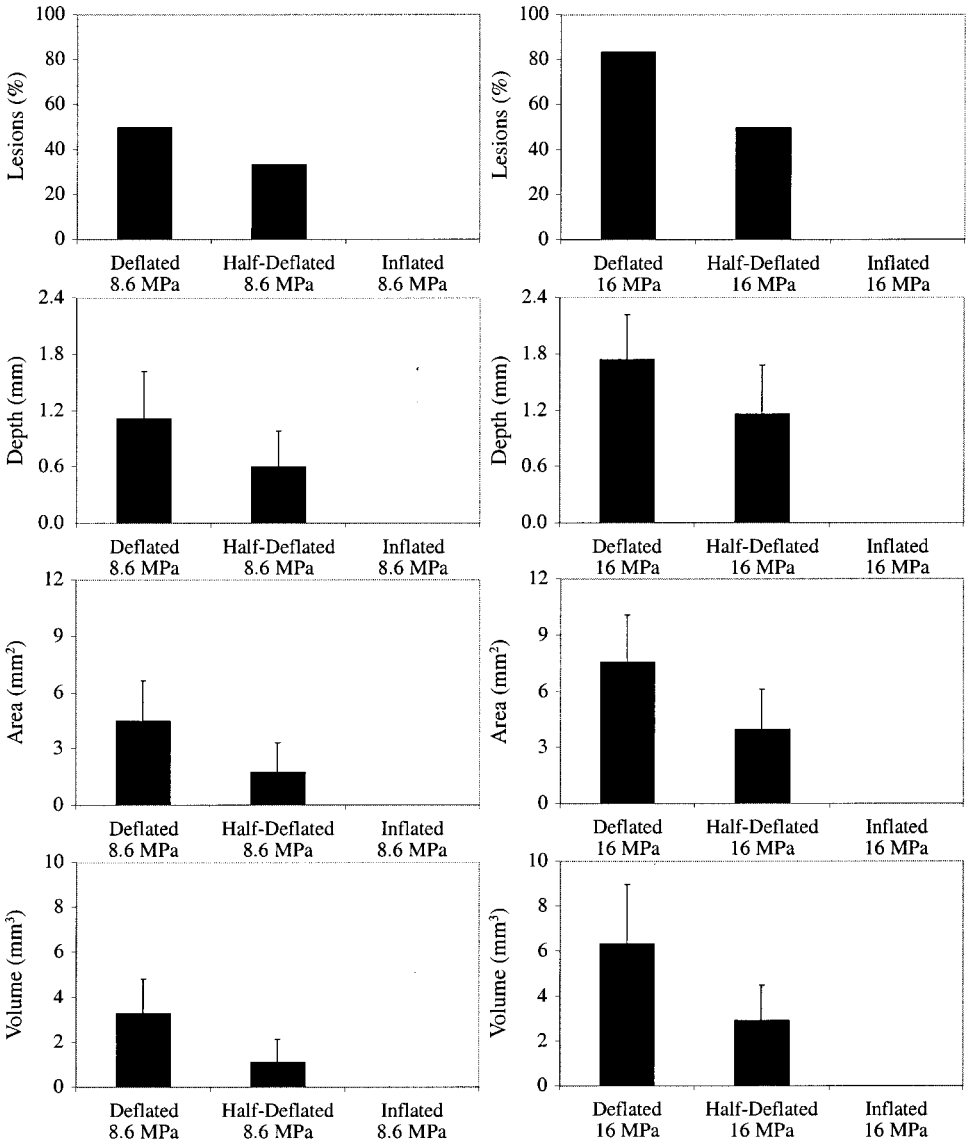

FIG. 5. Lesion occurrence, depth, surface area, and volume as a function of the three states of lung inflation (deflated, half-deflated, inflated). The four left-hand panels are for an *in situ* peak rarefactional pressure of 8.6 MPa. The four right-hand panels are for an *in situ* peak rarefactional pressure of 16 MPa.

where $p_{in\ situ}$ is the *in situ* (at the pleural surface) acoustic pressure amplitude, and R is the sound pressure reflection coefficient at normal incidence given by

$$R = \frac{z_{\text{lung}} - z_{\text{intercostal tissue}}}{z_{\text{lung}} + z_{\text{intercostal tissue}}}. \tag{9}$$

The acoustic pressure and particle velocity amplitudes relative to values for the incident wave [from Eqs. (7) and (8)] are shown graphically as a function of the amount of air in lung in Fig. 3(c).

IV. RESULTS

A. Gross and histological observations

A red-to-dark elliptical area of hemorrhage that formed along the pathway of the ultrasound beam was visible on the visceral pleural surface (Fig. 4). The hemorrhage assumed a conical shape whose base opposed the visceral pleural surface and whose apex extended into subjacent lung parenchyma to varied depths within the lung. Microscopically, the lesion was alveolar hemorrhage; alveolar septa did not appear injured. The principle tissue affected was the microvasculature.

B. Lesion occurrence and size

Lesion occurrence is related to the degree of inflation wherein there are a greater number of lesions for FRC volume (deflated lung state), fewer lesions for HTV (half-deflated lung state), and no lesions for the TV lung volume (inflated lung state). Lesion occurrence was also related to $p_{r(in\ situ}$ (Fig. 5) wherein there were a greater number of lesions at the higher $p_{r(in\ situ)}$ value compared to the lower $p_{r(in\ situ)}$ value.

Lesion size (depth, surface area, and volume) had a similar pattern as that for lesion occurrence (Fig. 5). Lesion size was larger for the higher $p_{r(in\ situ)}$ value (16 MPa) compared to the lower $p_{r(in\ situ)}$ value (8.6 MPa). Lesion size was also related to the degree of inflation wherein the lesions were largest for the deflated lung state [mean (SEM) depth: 1.11(0.50) and 1.74(0.48) mm for 8.6 and 16 MPa, respectively; mean area (SEM): 4.48(2.15) and 7.59(2.51)

mm^2 for 8.6 and 16 MPa, respectively], intermediate in size for the half-deflated lung state [mean (SEM) depth: 0.60(0.38) and 1.16(0.52) mm for 8.6 and 16 MPa, respectively; mean area(SEM): 1.72(1.60) and 3.97(2.15) mm^2 for 8.6 and 16 MPa, respectively], and were not initiated under the inflated lung state. A single-factor ANOVA yielded no statistically significant differences for lesion size at the lower $p_{r(in\ situ)}$ value (depth: $p=0.13$; area: $p=0.15$; volume: $p=0.12$). However, a single-factor ANOVA yielded marginally statistically significant differences for lesion size at the higher $p_{r(in\ situ)}$ value (depth: $p=0.03$; area: $p=0.04$; volume: $p=0.07$).

V. DISCUSSION

The magnitude of the acoustic pressure was selected for this study with the intent that it would be large enough to ensure that an ultrasound-induced lesion was produced every time. The *in situ* peak rarefactional pressures of 8.6 and 16 MPa (*in situ* peak compressional pressure of 18 and 40 MPa, respectively) were based on our previous findings.[18–20] These values bracket the peak *in situ* rarefactional pressure of 11 MPa at which the percentage of rats with lesions was 80% at an ultrasonic frequency of 2.8 MHz and 10-s exposure duration in normal breathing animals. We recognized that *in situ* peak rarefactional pressures of 8.6 and 16 MPa were considerably greater than those allowed under current regulations.[43] At these *in situ* peak rarefactional pressures, the equivalent Mechanical Indices were 3.1 and 5.6, whereas the regulatory limit is 1.9 for diagnostic ultrasound equipment that falls under FDA control. Our purpose was to evaluate the effect of lung inflation at superthreshold exposure conditions.

At the lower $p_{r(in\ situ)}$ value (8.6 MPa), the two measured lesion quantities, depth, and area, were not significantly different whereas, at the higher $p_{r(in\ situ)}$ value (16 MPa), these two quantities were significantly different. This demonstrated that as $p_{r(in\ situ)}$ increases, there was increased lesion size separation.

The 3.1-MHz results reported herein are directly compared to one of our previous studies in which we conducted an exposure-effect study at two frequencies (2.8 and 5.8 MHz) with normal breathing adult ICR mice and Sprague-Dawley rats (Fig. 6).[18] The 2.8- and 5.6-MHz exposure conditions for the previous study were similar to the 3.1-MHz exposure conditions used herein (1-kHz PRF, 10-s exposure duration). In that previous study, there were no differences in occurrence (percentage) of lesions with either species or ultrasound frequency. Also, there was no dependence on frequency for either lesion depth or area, although there was a small dependence on species for lesion area. Lesion occurrences for the FRC state (deflated lung state) were about the same as those for the previous study. Lesion occurrences for the HTV state (half-deflated lung state) were less than those for the previous study. Lesion size (depth, surface area, and volume) for the deflated and half-deflated lung states appeared to bracket the comparable results for the normal breathing mice and rats. These observations show that lung lesions are not caused when the lungs are inflated at just over

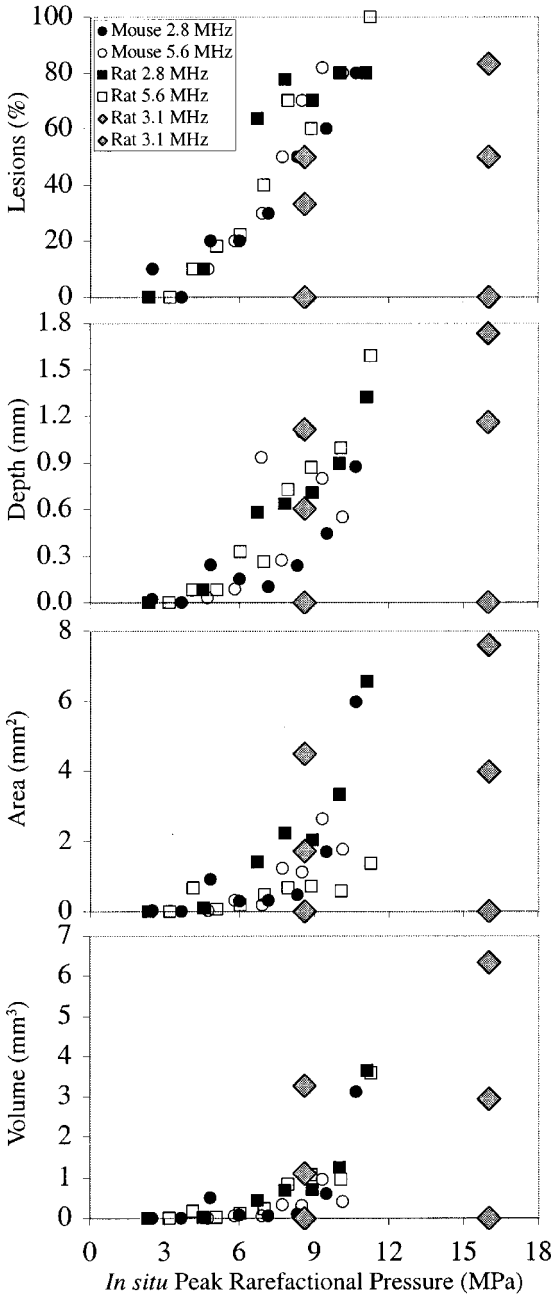

FIG. 6. Lesion occurrence, depth, surface area, and volume as a function of the *in situ* peak rarefactional pressure that compare the inflation-dependent data reported herein (large diamonds) to the previously published normal-breathing mice and rates data (Ref. 18).

tidal volume, but occur when the lung is less inflated. In fact, comparisons of the results reported herein to the normal breathing animal results suggest that the lesions occur and grow in normal breathing animals in a similar manner to lung inflation between FRC and HTC lung volumes.

Further, the extent to which lung lesions occur is inversely related to the acoustic impedance difference between intercostal tissue and lung. When the lung's acoustic impedance is more closely matched to the intercostal tissue, more lesions are produced and the sound power transmission coefficient is larger. And, a greater impedance difference produces fewer lesions and has a smaller sound power transmission coefficient. This finding suggests that the lesion cause

may be due to some kind of an energy-based mechanism within and near the lung's surface since the extent to which the lesions occur is directly related to the sound power transmission coefficient. Also, for all three lung inflation states, air is present in the lung, and yet, at tidal volume no lesions are produced.

The findings reported herein address the suggestion put forth earlier[6,42] that because the lung boundary acts as an acoustic pressure-release surface, a significant increase in particle velocity *in situ* near the lung surface might produce the lung hemorrhage. This suggestion is not plausible for the following reasons. A pressure-release surface would be approached when the lung is inflated (volume fraction of air in lung approaches unity). Under a more inflated lung state, where the lung's volume fraction of air is close to unity and the particle velocity in tissues adjacent the lung is greatest, no lung hemorrhage resulted. The lung hemorrhage increased as the lung's volume fraction of air decreased and was the greatest at the lowest volume fraction of air.

Finally, the relative geometry between the beam and the lung surface is considered for the three inflation states. The transducer alignment occurs while the ventilator is breathing for the animal. The distance between the transducer and the lung surface does not vary by more than 1–2 mm because the water filled stand-off tank is placed gently on the rat's lateral aspect, thus limiting chest expansion in that direction. The −6-dB depth of focus is 5.9 mm so the lung surface remains within the focal region for all three inflation states. Also, the orientation of the chest wall surface in contact with the water filled stand-off tank does not visually change as a function of breathing. Because the chest wall surface and the lung surface track each other, the orientation between the beam axis and the pleural surface does not change. Therefore, the observations and findings reported herein are not believed to be a function of lung surface orientation or position relative to the ultrasonic field.

ACKNOWLEDGMENTS

We thank our valued colleagues Joe Beatty, Ed Plowey, and Bill Zierfuss for technical contributions. This work was supported by NIH Grant No. HL58218 awarded to WDO and JFZ.

[1] S. Z. Child, C. L. Hartman, L. A. Schery, and E. L. Carstensen, "Lung damage from exposure to pulsed ultrasound," Ultrasound Med. Biol. **16**, 817–825 (1990).
[2] C. L. Hartman, S. Z. Child, R. Mayer, E. Schenk, and E. L. Cartensen, "Lung damage from exposure to the fields of an electron hydraulic lithotropter," Ultrasound Med. Biol. **16**, 675–683 (1990).
[3] C. H. Raeman, S. Z. Child, and E. L. Carstensen, "Timing of exposures in ultrasonic hemorrhage of murine lung," Ultrasound Med. Biol. **19**, 507–512 (1993).
[4] D. P. Penney, E. A. Schenk, K. Maltby, C. Hartman-Raeman, S. Z. Child, and E. L. Carstensen, "Morphologic effects of pulsed ultrasound in the lung," Ultrasound Med. Biol. **19**, 127–135 (1993).
[5] L. A. Frizzell, E. Chen, and C. Lee, "Effects of pulsed ultrasound on the mouse neonate: Hind limb paralysis and lung hemorrhage," Ultrasound Med. Biol. **20**, 53–63 (1994).
[6] A. F. Tarantal and D. R. Canfield, "Ultrasound-induced lung hemorrhage in the monkey," Ultrasound Med. Biol. **20**, 65–72 (1994).
[7] J. F. Zachary and W. D. O'Brien, Jr., "Lung hemorrhage induced by continuous and pulse wave ultrasound in mice, rabbits, and pigs," Vet. Pathol. **32**, 43–54 (1995).
[8] C. H. Harrison, H. A. Eddy, J.-P. Wang, and F. Z. Liberman, "Microscopic lung alterations and reduction of respiration rate in insonated anesthetized swing," Ultrasound Med. Biol. **21**, 981–983 (1995).
[9] C. K. Holland, C. X. Deng, R. E. Apfel, J. L. Alderman, L. A. Fernandez, and K. J. Taylor, "Direct evidence of cavitation in vivo from diagnostic ultrasound," Ultrasound Med. Biol. **22**, 917–925 (1996).
[10] R. Baggs, D. P. Penney, C. Cox, S. Z. Child, C. H. Raeman, D. Dalecki, and E. L. Carstensen, "Thresholds for ultrasonically induced lung hemorrhage in neonatal swine," Ultrasound Med. Biol. **22**, 119–128 (1996).
[11] C. H. Raeman, S. Z. Child, D. Dalecki, C. Cox, and E. L. Carstensen, "Exposure-time dependence of the threshold for ultrasonically induced murine lung hemorrhage," Ultrasound Med. Biol. **22**, 139–141 (1996).
[12] W. D. O'Brien, Jr. and J. F. Zachary, "Lung damage assessment from exposure to pulsed-wave ultrasound in rabbit, mouse, and pig," IEEE Trans. Ultrason. Ferroelectr. Freq. Control **44**, 473–485 (1997).
[13] D. Dalecki, S. Z. Child, C. H. Raeman, C. Cox, and E. L. Carstensen, "Ultrasonically induced lung hemorrhage in young swine," Ultrasound Med. Biol. **23**, 777–781 (1997).
[14] D. Dalecki, S. Z. Child, C. H. Raeman, C. Cox, D. P. Penney, and E. L. Carstensen, "Age dependence of ultrasonically-induced lung hemorrhage in mice," Ultrasound Med. Biol. **23**, 767–776 (1997).
[15] WFUMB Symposium on Safety of Ultrasound in Medicine: Issues and Recommendations Regarding Non-Thermal Mechanisms for Biological Effects of Ultrasound, Ultrasound Med. Biol. **24**, Supplement 1, S1–S55 (1998).
[16] *Mechanical Bioeffects from Diagnostic Ultrasound: AIUM Consensus Statements* (American Institute of Ultrasound in Medicine, Laurel, MD, 2000). Also, J. Ultrasound Med. **19**, 67–168 (2000).
[17] W. D. O'Brien, Jr., L. A. Frizzell, R. M. Weigel, and J. F. Zachary, "Ultrasound-induced lung hemorrhage is not caused by inertial cavitation," J. Acoust. Soc. Am. **108**, 1290–1297 (2000).
[18] J. F. Zachary, J. M. Sempsrott, L. A. Frizzell, D. G. Simpson, and W. D. O'Brien, Jr., "Superthreshold behavior and threshold estimation of ultrasound-induced lung hemorrhage in adult mice and rats," IEEE Trans. Ultrason. Ferroelectr. Freq. Control **48**, 581–592 (2001).
[19] W. D. O'Brien, Jr., L. A. Frizzell, D. J. Schaeffer, and J. F. Zachary, "Superthreshold behavior of ultrasound-induced lung hemorrhage in adult mice and rats: role of pulse repetition frequency and exposure duration," Ultrasound Med. Biol. **27**, 267–277 (2001).
[20] J. F. Zachary, K. S. Norrell , J. P. Blue, R. J. Miller, and W. D. O'Brien, Jr., "Temporal and spatial evaluation of lesion resolution following exposure of rat lung to pulsed ultrasound," Ultrasound Med. Biol. **27**, 829–839 (2001).
[21] W. D. O'Brien, Jr., D. G. Simpson, L. A. Frizzell, and J. F. Zachary, "Superthreshold behavior and threshold estimation of ultrasound-induced lung hemorrhage in adult rates: Role of beamwidth," IEEE Trans. Ultrason. Ferroelectr. Freq. Control **48**, 1695–1705 (2001).
[22] M. L. Crosfill and J. G. Widdicombe, "Physical characteristics of the chest and lungs and the work of breathing in different mammalian species," J. Physiol. (London) **158**, 1–14 (1961).
[23] S. M. Tenney and J. E. Remmers, "Comparative quantitative morphology of the mammalian lung: Diffusing area," Nature (London) **197**, 54–56 (1963).
[24] E. R. Weibel, "Dimensions of the tracheobronchial tree and alveoli," in *Biological Handbooks: Respiration and Circulation*, edited by P. L. Altman and D. S. Dittmer (Federation of American Societies for Experimental Biology, Bethesda, MD, 1971), pp. 930–939.
[25] H. G. Flynn and C. C. Church, "Transient pulsations of small gas bubbles in water," J. Acoust. Soc. Am. **84**, 985–998 (1988).
[26] M. R. Bailey, D. Dalecki, S. Z. Child, C. H. Raeman, D. P. Penney, D. T. Blackstock, and E. L. Carstensen, "Bioeffects of positive and negative acoustic pressures *in vivo*," J. Acoust. Soc. Am. **100**, 3941–3946 (1996).
[27] E. L. Carstensen, D. Dalecki, S. M. Gracewski, and T. Christopher, "Nonlinear propagation of the output indices," J. Ultrasound Med. **18**, 69–80 (1999).
[28] C. K. Holland, R. A. Roy, P. W. Biddinger, C. J. Disimile, and C. Cawood, "Cavitation mediated rat lung bioeffects from diagnostic ultrasound," J. Acoust. Soc. Am. **109**, 2433(A) (2000).
[29] R. E. Apfel, "Comments on 'Ultrasound-induced lung hemorrhage is not caused by inertial cavitation' [J. Acoust. Soc. Am. **108**, 1290–1297 (2000)]," J. Acoust. Soc. Am. **110**, 1737 (2001).
[30] L. A. Frizzell, J. M. Kramer, J. F. Zachary, and W. D. O'Brien, Jr.,

''Response to ''Comments on 'Ultrasonic lung hemorrhage is not caused by inertial cavitation' '' [J. Acoust. Soc. Am. **110**, 1737 (2001)],'' J. Acoust. Soc. Am. **110**, 1738–1739 (2001).
[31] R. E. Apfel, ''Reply to Frizzell *et al.*'s Comment to our comment,'' J. Acoust. Soc. Am. **110**, 1740–1741 (2001).
[32] L. A. Frizzell, J. M. Kramer, J. F. Zachary, and W. D. O'Brien, Jr., ''Comment on Apfel's second comment,'' J. Acoust. Soc. Am. **110**, 1742 (2001).
[33] K. Raum and W. D. O'Brien, Jr., ''Pulse-echo field distribution measurement technique of high-frequency ultrasound sources,'' IEEE Trans. Ultrason. Ferroelectr. Freq. Control **44**, 810–815 (1997).
[34] *AIUM/NEMA, Acoustic Output Measurement Standard for Diagnostic Ultrasound Equipment*, Laurel, MD, American Institute of Ultrasound in Medicine, and Rosslyn, VA, National Electrical Manufacturers Association, 1998.
[35] *Standard for Real-Time Display of Thermal and Mechanical Acoustic Output Indices on Diagnostic Ultrasound Equipment, Rev. 1*, Laurel, MD, American Institute of Ultrasound in Medicine, and Rosslyn, VA, National Electrical Manufacturers Association, 1998.
[36] J. M. Sempsrott and W. D. O'Brien, Jr., ''Experimental verification of acoustic saturation,'' Proceedings of the 1999 IEEE Ultrasonic Symposium, pp. 1287–1290 (1999).
[37] G. A. Teotico, R. J. Miller, L. A. Frizzell, J. F. Zachary, and W. D. O'Brien, Jr., ''Attenuation coefficient estimates of mouse and rate chest wall,'' IEEE Trans. Ultrason. Ferroelectr. Freq. Control **48**, 593–601 (2001).
[38] J. M. Kramer, T. G. Waldrop, L. A. Frizzell, J. F. Zachary, and W. D. O'Brien, Jr., ''Cardiopulmonary function in rats with lung hemorrhage induced by pulsed ultrasound exposure,'' J. Ultrasound Med. **20**, 1197–1206 (2001).
[39] W. R. Stahl, ''Scaling of respiratory variables in mammals,'' J. Appl. Physiol. **22**, 453–460 (1967).
[40] T. J. Bauld and H. P. Schwan, ''Attenuation and reflection of ultrasound in canine lung tissue,'' J. Acoust. Soc. Am. **56**, 1630–1637 (1974).
[41] F. Dunn, ''Attenuation and speed of ultrasound in lung,'' J. Acoust. Soc. Am. **56**, 1638–1639 (1974).
[42] C. K. Holland, K. Sandstrom, X. Zheng, J. Rodriguey, and R. A. Roy, ''The acoustic field if a pulsed Doppler diagnostic ultrasound system near a pressure-release surface,'' J. Acoust. Soc. Am. **95**, 2855(A) (1994).
[43] *Information for Manufacturers Seeking Marketing Clearance of Diagnostic Ultrasound Systems and Transducers*, Rockville, MD, Center for Devices and Radiological Health, US Food and Drug Administration, September 30, 1997.

Quantitative investigation of acoustic streaming in blood

Xuegong Shi[a)]
Department of Bioengineering, Box 357962, University of Washington, Seattle, Washington 98195

Roy W. Martin
Applied Physics Laboratory and Departments of Anesthesiology and Bioengineering, Box 355640, University of Washington, Seattle, Washington 98195

Shahram Vaezy
Applied Physics Laboratory and Department of Bioengineering, Box 355640, University of Washington, Seattle, Washington 98195

Lawrence A. Crum
Applied Physics Laboratory and Department of Bioengineering, Box 355640, University of Washington, Seattle, Washington 98195

(Received 5 October 2000; accepted for publication 17 October 2001)

Acoustic streaming may have practical utility in diagnostic medical ultrasound in distinguishing between stagnant blood and tissue as well as clotted and unclotted blood. This distinction can be difficult with conventional ultrasound but have high value in managing trauma patients with internal hemorrhage. Ultrasound energy applies a force to blood by momentum transfer, resulting in bulk streaming that is a function of the acoustic attenuation, sound speed, acoustic intensity, blood viscosity, and the boundary conditions posed by the geometry around the hematoma. A simple tubular model was studied analytically, by finite element simulation, and experimentally by *in vitro* measurement. The simulation agreed closely with measurements while the analytic solutions were found to be valid only for beam diameters approximating the diameter of the tubular channel. Experimentally, the acoustic streaming in blood decreased as the blood began to clot and the streaming flow was not detected in clotted blood. In contrast, the echogenicity of the same blood samples did not change appreciably from the unclotted to the clotted state for the stagnant blood studied. Streaming detection appears to offer a potential tool for improving hemorrhage diagnosis.
 [DOI: 10.1121/1.1428544]

PACS numbers: 43.80.Jz, 43.25.Nm [FD]

I. INTRODUCTION

There are a variety of medical situations where it is important to determine whether an ultrasound imaged region is composed of a liquid or a solid structure. Three important examples include distinguishing between a cyst from a solid mass, stagnant blood from tissue, and clotted from unclotted blood. These last two cases are of particular importance in hemorrhage assessment. Although the ultrasound scattering characteristics, the presence of motion in the liquid or other clues may suffice to make this distinction, generally it is difficult. This difficulty arises from the fact that once the blood has exited the vascular system, the ultrasound appearance of it varies with time and with the position in the body. For instance, although fresh moving blood normally appears anechoic, stagnant unclotted blood may appear echogenic due to the aggregation of red blood cells.[1–3] The echogenicity increases more significantly when blood starts to clot. After clot retraction and separation, the retracted region may appear hyperechoic and the separated plasma hypoechoic. The amount of echogenic change can also depend upon the frequency of imaging transducer.[4] The current method of ultrasound detection of hemorrhage in blunt abdominal trauma, for example, is based on the difference in the sonographic appearance between the blood and other adjacent soft tissue.

Hemorrhage will often result in the formation of a hematoma. Depending on where in the body this occurs and the status of the individual's coagulation system, clotting action may not be initiated for some time or not at all. Arterial bleeding into or in-and-out of a hematoma can often be detected with Doppler ultrasound.[5,6] In contrast, the low velocity of the blood in venous bleeding has not generally allowed the use of Doppler in detecting it. Similarly stagnant unclotted blood also has been undetectable by Doppler techniques. Nevertheless, we realize that unclotted blood would flow under a pressure gradient whereas other soft tissues and clots would not. If such a gradient can be posed on a region and its resulting flow can be detected, this method would offer a technique of making the distinction between liquid and solid structures. This is the possibility presented by the phenomena of acoustic streaming.

Acoustic streaming occurs, as an ultrasound wave passes through a liquid medium, because of momentum being transferred from the wave to the fluid due to energy loss from the wave caused by attenuation. The magnitude of streaming velocity that results, v, is determined by the property of the fluid (acoustic attenuation α, viscosity μ, and sound speed

[a)]Current address: ATL Ultrasound, Post Office Box 3003, Bothell, WA 98041-3003.

c), the applied acoustic intensity I, and a geometric factor G with dimensions of length squared, as shown in the following equation:[7]

$$v = \frac{\alpha I}{\mu c} G. \tag{1}$$

The phenomenon of acoustic streaming has been used to measure the absorption coefficient[8] and viscosity of fluid.[9] In recent years, the streaming detection technique also found clinical applications in differentiating breast cysts from solid mass[10,11] and measuring blood coagulation time.[12,13]

The effect of geometric factor and viscosity were studied in this investigation for the streaming detection in blood. The blood from a hemorrhaging site will collect in a variety of ways, resulting in various sizes and shapes of pooled blood and these sizes and shapes can markedly affect the streaming magnitude. This geometric effect is represented by a factor G in Eq. (1), which is a function of the local boundaries of the space where streaming is taking place. A simple geometric model of closed circular tubes of various diameters was chosen to study because it lends itself to analytic treatment. The analytical solutions of streaming velocity were compared with the results of the simulations conducted using finite element analysis (FEA). *In vitro* experimental measurements with blood were made for the same geometric considerations and were compared with the finite element solutions. Since blood viscosity increases when the blood starts to coagulate, this action causes a decrease of streaming flow. Therefore, during the onset of coagulation the streaming and the echogenicity of blood were experimentally investigated. We chose for this study a transducer beam pattern for investigation that resulted from a highly focused transducer because of our interest in high-intensity focused ultrasound (HIFU) and its potential use in stopping hemorrhage.[14–16] Furthermore, because the intensity at the focus of these devices can be easily three or four orders of magnitude higher than that of the diagnostic ultrasound they can generate significant streaming in fluid. Finally, we selected a commercial imaging system and imaging scanhead for color Doppler measurements of the streaming velocity.

II. MATHEMATICAL CONSIDERATIONS, MATERIALS AND METHODS

A. Analytical solutions

The analytical solution to the streaming generated by a uniform cylindrical ultrasound beam in a closed circular tube was first given by Eckart.[17] Figure 1 illustrates the geometry of the tube and the streaming flow inside it (dashed lines with arrows pointing the flow directions). Both ends are closed so that no flow enters or leaves the tube. The ultrasound is transmitted from the top. The acoustic intensity is uniform within the beam cylinder, as represented by the shaded area in Fig. 1. The bottom end of the tube is sealed with a perfect sound-absorbing material so that there is no reflection of the beam. It is also assumed that the tube is long enough that the flow around the middle region of the tube length (the region between the horizontal dashed–dotted lines in Fig. 1) is not affected by the flow near the ends.

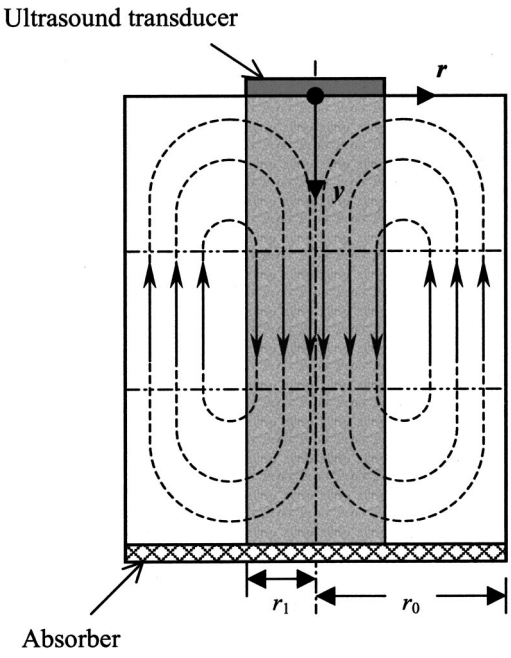

FIG. 1. Streaming in a closed cylindrical tube.

Assuming a nonslip wall boundary condition and parallel streamlines in the middle region of the tube, the radial distribution of velocity can be calculated by Eq. (1) with[17]

$$G = r_1^2 \cdot \left[\frac{1}{2}\left(1 - \frac{r^2}{r_1^2}\right) - \left(1 - \frac{1}{2}\frac{r_1^2}{r_0^2}\right)\left(1 - \frac{r^2}{r_0^2}\right) - \ln\frac{r_1}{r_0} \right] \tag{2a}$$

for $0 \leqslant r < r_1$, and

$$G = r_1^2 \cdot \left[-\left(1 - \frac{1}{2}\frac{r_1^2}{r_0^2}\right)\left(1 - \frac{r^2}{r_0^2}\right) - \ln\frac{r}{r_0} \right] \tag{2b}$$

for $r_1 \leqslant r \leqslant r_0$, where r_0 and r_1 are the radii of the tube and sound beam, respectively. r is the radial distance from the center of the tube, ranging from 0 to $+r_0$. Equations (2a) and (2b) only express one half of the symmetric velocity distribution across the central axis. The y axis in Fig. 1 is defined positive from top to bottom of the tube so that the forward streaming flow has positive velocities. The maximum streaming velocity occurs only on the central axis where $r = 0$. Substituting $r = 0$ into Eq. (2a) results in

$$G = r_1^2 \cdot \left[-\frac{1}{2} + \frac{1}{2}\frac{r_1^2}{r_0^2} - \ln\frac{r_1}{r_0} \right]. \tag{3}$$

Equation (2) is only valid when the ratio r_1/r_0 is not near the two extremes, i.e., 0 and 1. When the tube radius is very large comparing to the beam size ($r_1/r_0 \to 0$), the streaming becomes effectively unbounded (for a given value of r_0). An equation was found to describe the streaming generated by a focused beam in a large open space.[18] For a focused beam whose focal region is a uniform cylinder of radius a and length l, the peak streaming velocity can be estimated by Eq. (1) with (see Appendix for derivation)

$$G = a^2 \ln\left(\frac{l}{a}\right). \tag{4}$$

TABLE I. Values of the parameters used to calculate the geometric factor in Eqs. (2), (3), and (4) and the streaming velocity in Eq. (1). The sizes of the circular tubes are those used in the *in vitro* experiment. The focal size of the HIFU beam was measured with a needle hydrophone in water. The spatial peak intensity of the HIFU beam was measured using a radiation force balance under continuous excitation. Since the HIFU transducer was operated in the burst mode for real-time color Doppler measurement in the experiment, the temporal-averaged intensity was used to estimate the streaming velocity (Ref. 19). The spatial-peak temporal-average intensity was calculated by multiplying the spatial peak intensity with the duty factor of the HIFU burst, which was 1% in the experiment. The acoustic properties of blood were found in Ref. 20. Although blood is known to be non-Newtonian, its viscosity approaches an asymptotic value of about 3 cP at high shear rates ($>1000\ s^{-1}$) (Ref. 21). This constant viscosity was used for the calculation of streaming velocity.

Geometry of circular tubes	Diameter [$2r_0$ in Eq. (3)]	0.5, 0.8, 1.4, and 2.1 cm
	Length	2 cm for all
HIFU beam characteristics	Half-pressure-maximum focal diameter [$2r_1$ in Eq. (3) and $2a$ in Eq. (4)]	0.1 cm
	Half-pressure-maximum focal length [l in Eq. (4)]	1.4 cm
	Spatial-peak temporal-average (SPTA) intensity (I_{SPTA})	24 W/cm^2 [24×10^7 (egr/s)/cm^2]
Blood properties	Acoustic attenuation (α)	0.1 Np/cm at 5 MHz
	Sound speed (c)	1570×10^2 cm/s
	Viscosity (μ)	3 cP

Here the geometric factor is determined by the beam geometry alone, different from that in the closed tubes [Eq. (3)].

In order to experimentally quantify the theoretical solutions shown above, four circular tubes of selected diameters were made in an agar-based tissue-mimicking phantom to hold blood samples in the *in vitro* experiment. The streaming in a large open space was approximated by a 400 ml low form beaker (diameter of about 7.5 cm and length of about 9 cm) filled with blood. A HIFU transducer was used to generate streaming in blood in these tubes and the beaker. The characteristics of HIFU beam were fixed during the experiment. The HIFU beam near the focus was approximated as a cylinder of uniform intensity with the size of the half-pressure-maximum contour. Table I summarizes the tube geometry, ultrasound beam characteristics, and related blood properties. The factor G in Eqs. (2), (3), and (4) and the streaming velocity in Eq. (1) were determined using these parameter values and compared with the results of FEA simulation and experimental measurement.

B. FEA simulations

The finite element modeling was used to simulate the geometry and boundary conditions of the ultrasound beam and circular tube. The size of four circular tubes and the beaker, as listed in Table I, was used to create axisymmetric models in a computational fluid dynamics software (ANSYS/FLOTRAN™, ANSYS, Inc., Canonsburg, PA). The ultrasound intensity was first converted to body force using[7]

$$F=\frac{2\alpha I}{c}. \tag{5}$$

This force was then applied to the nodes of the mesh of the finite element model within the beam intensity field. In the first part of the simulation, the beam field was modeled as shown in Fig. 1; namely, the beam is a cylinder of uniform intensity (force) with the same length as the tube. The diameter of the beam cylinder was 1 mm. Using the attenuation, sound speed, and intensity values given in Table I, the body force applied to the nodes was calculated to be 3057 N/m^3. A constant viscosity of 3 cP was specified as the fluid property. The nonslip boundary wall condition was also applied. The simulation converged after about 200 iterations and a steady-state streaming flow was established. The maximum streaming velocity was recorded in each of the four circular tube models. A radial velocity distribution was also obtained at the center of each tube in order to compare with the analytical results calculated using Eq. (2).

In the second part of the simulation, the cylindrical beam pattern was replaced with the beam pattern of the HIFU transducer used in the experiment in order to provide more accurate simulation data. The pressure field of the HIFU transducer was measured with a needle hydrophone (NTR, Seattle, WA) in water. Figure 2(a) shows the five pressure contours at the focus of the HIFU transducer, corresponding to the intensity levels of -0.5, -1.5, -3, -5, and -10 dB, respectively, relative to the peak intensity at the center. With these contours, the continuously distributed intensity field was divided into five levels of uniform intensities. The shape of the intensity contours was simplified to four rectangles in the middle and two symmetric arcs at the outer boundary [Fig. 2(b)]. These intensities were then converted into body forces using Eq. (5).

The non-Newtonian viscosity of blood was also incorporated into this part of the simulation. The ANSYS/FLOTRAN™ provides a Carreau model[22] that describes the viscosity of non-Newtonian fluid, such as blood. The mathematical representation of the model is expressed as[23]

$$\mu=\mu_\infty+(\mu_0-\mu_\infty)[1+(\lambda D)^2]^{(n-1)/2}, \tag{6}$$

where μ_0 and μ_∞ are the viscosity values when the shear rate $D=0$ and ∞. λ is a time constant and n is the power factor. In order to use this model, the values of four parameters, μ_0, μ_∞, λ, and n, need to be determined. The experimental studies of blood viscosity suggested that the non-

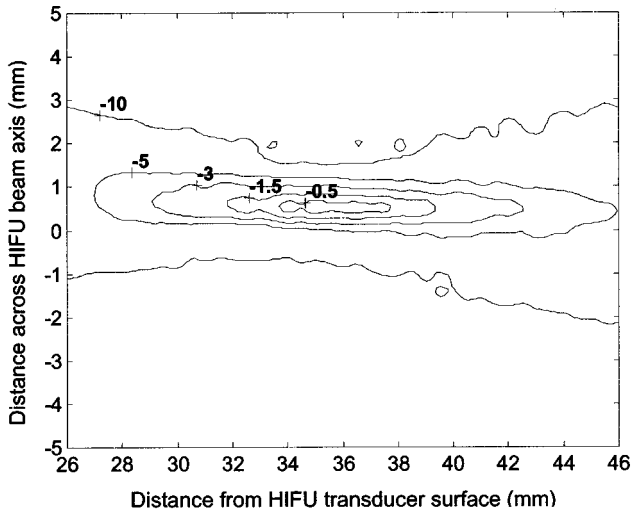

(a)

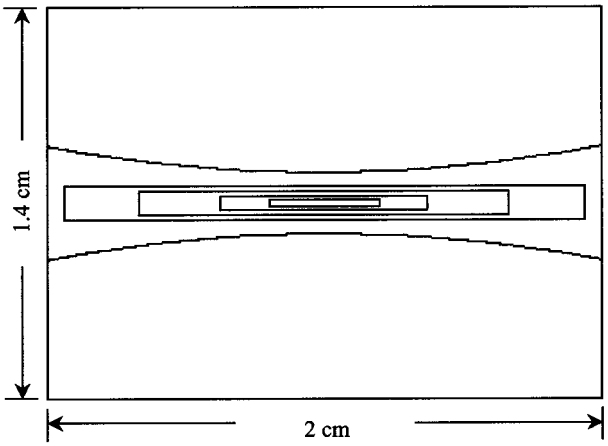

(b)

FIG. 2. (a) The acoustic pressure pattern of the HIFU transducer as measured and mapped with a hydrophone. The specified contours are pressure levels in dB relative to the peak pressure. (b) Simplified HIFU intensity field for analysis using five uniform intensity levels of −0.5, −1.5, −3, −5, and −10 dB. Note that the *y* axis is plotted to different scales in (a) and (b).

Newtonian behavior of blood could be approximated by Casson's equation,[24] whose least-squares fit to the experimental data gave the following equation:[21]

$$\mu = \frac{\tau}{D} = \left\{ 1.53\sqrt{\mu_p} + 2.0 \times \sqrt{\frac{\mu_p}{D}} \right\}^2, \tag{7}$$

where τ is the shear stress, D the shear rate and μ_p is the viscosity of plasma (1.2 cP). In order to fit Eq. (6) to Eq. (7), the blood viscosity was calculated using both equations at 21 logarithmically spaced shear rates from 1 to 1000 s^{-1}. The four parameters in Eq. (6) were adjusted by trial-and-error, until the viscosity difference between these two equations was smaller than 6% at these 21 shear rates. The following values of these four parameters were found to give such a fit: $\mu_0 = 80$ cP, $\mu_\infty = 3$ cP, $\lambda = 11$, and $n = 0.26$. The viscosity of the blood samples used in the experiment was also experimentally measured to further improve the accuracy of simulation using Eq. (6). The measurements were obtained using a double-gap, coaxial-cylinder viscometer at room temperature. The viscosity of four measured blood samples was 2.04 ± 0.11 cP for the shear rates >500 s^{-1}. Consequently, μ_∞ in Eq. (6) was adjusted from 3 cP to 2.04 cP, while other parameters remained unchanged. Figure 3 illustrates the three viscosity curves as calculated using Eq. (6) with $\mu_\infty = 3$ cP and 2.04 cP, and using Eq. (7). The viscosity curve with $\mu_\infty = 2.04$ cP was used in the simulation.

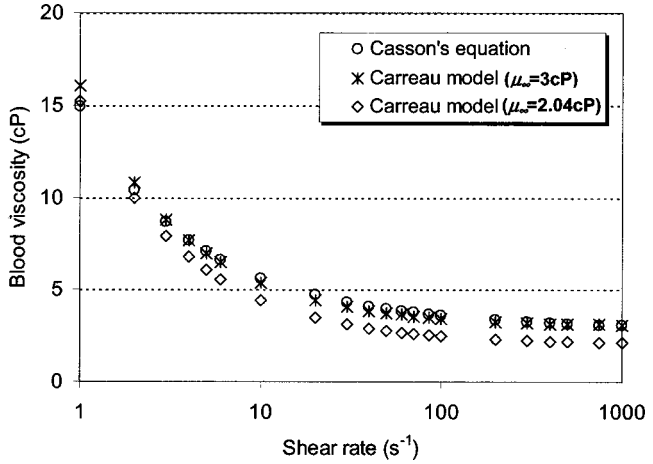

FIG. 3. Blood viscosity for finite element simulation. The *asterisks* are the model available in the simulation program fit to the *circular data* derived from blood rheology literature. The *diamonds* show further adjustment of the model to our measured viscosity data for blood shear rates greater than 500 s^{-1}. The *diamond curve* was used in the simulation.

The simulation was first run to obtain the steady-state streaming velocity after the body force and nonslip boundary wall condition were applied. However, experimentally the streaming was generated by bursts of HIFU followed a brief delay after each burst before the color Doppler determination of the streaming velocity could be made. Therefore, the velocity decrease due to this time delay was considered when the experimental measurements were compared with the simulation results. The transient-time analysis calculates the velocity decay after the body force is removed, which simulates the cessation of the HIFU burst. The time difference between the HIFU application and Doppler detection of streaming was measured with an oscilloscope to be 16 ms in this study. The transient analysis was then performed after the steady state solutions were obtained. The simulation was run after the body force was removed from the model and the transient results at 16 ms were obtained. These results were then available for comparison.

C. Experimental measurements

1. Integrated HIFU/imaging system

As mentioned earlier, the acoustic streaming in this study was investigated using a HIFU system. An integrated HIFU/imaging system was used to eliminate the normal interference of HIFU in the image so that ''simultaneous'' color Doppler imaging of the streaming in the fluid produced by the HIFU energy could be imaged in real time. The details of the design and implementation of the system have been published.[25] A brief description is included here (Fig. 4). A trigger signal which occurred in the middle of the image scan was obtained from the scanhead [(F) 5–10 MHz, curved lin-

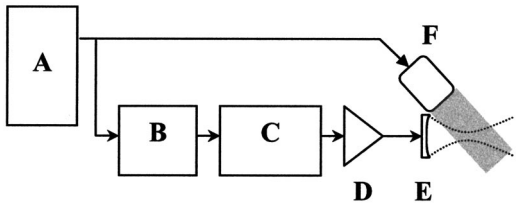

FIG. 4. Diagram of integrated HIFU/imaging system. (A) Advanced Technology Laboratory HDI-3000 ultrasound imaging system, (B) HIFU onset and duration control circuit, (C) HIFU excitation frequency generator, (D) power amplifier, (E) HIFU transducer, (F) 5–10 MHz curved-linear scanhead; the shaded area represents the imaging plane that passes through the HIFU beam axis. The connection between (A) and (B) is the synchronization pulse from the imaging scanhead (F).

ear probe] of the ultrasound imaging system [(A) HDI-3000, ATL Ultrasound, Bothell, WA]. This signal was used to initiate the HIFU onset-and-duration control circuitry (B), which let users control the time delay and duration of HIFU excitation burst relative to the trigger pulse. The output pulse from (B) turned on and off the frequency generator (C), thus producing a low amplitude sinusoidal burst which was then amplified by the power amplifier (D) and applied to the HIFU transducer (E). The HIFU transducer was a 5 MHz single element (Sonic Concept, Woodinville, WA) with a diameter of 16.1 mm and a radius of curvature of 35 mm. The synchronization stabilized the spatial position of the interference in the ultrasound image, and it could be adjusted to leave a clear window for normal visualization of the region of interest. The interference appeared as a bright band whose width was determined by the duration of the HIFU excitation burst. Both the HIFU transducer and the imaging probe were clamped on a lab stand. The longitudinal axis of the HIFU beam was aligned with the imaging plane (shaded area in Fig. 4) and the HIFU focus was placed near the center of the plane. This was achieved by visualizing the generation of acoustic streaming in a beaker of milk mixed with cornstarch as the scatterers. When HIFU was applied and streaming was generated, the position of the imaging probe was adjusted until the color Doppler display of the streaming showed that the imaging plane was aligned with the central axis of the streaming flow and the largest streaming velocities appeared near the center of the plane. The relative position of the HIFU transducer and the imaging probe was then secured on the lab stand and used in the following experiments.

2. Acoustic streaming in closed circular tubes and a large beaker

Four circular tubes, with diameters and lengths shown in Table I, were made in an agar phantom [Fig. 5(a)]. Pig blood was obtained under an institutional approved animal protocol and immediately heparinized to prevent clotting. Each of the circular tubes was filled with blood and a 200-micron thick polyeythelene membrane was placed over the top of the tubes. Water was added to the chamber above this membrane to provide an acoustic standoff as well as to seal the blood in the tubes [Fig. 5(b)]. The phantom was placed on a 3-mm thick rubber sheet to absorb the HIFU beams after they passed though the tube and phantom. The HIFU transducer was positioned as shown in Fig. 5(b) so that the HIFU focus

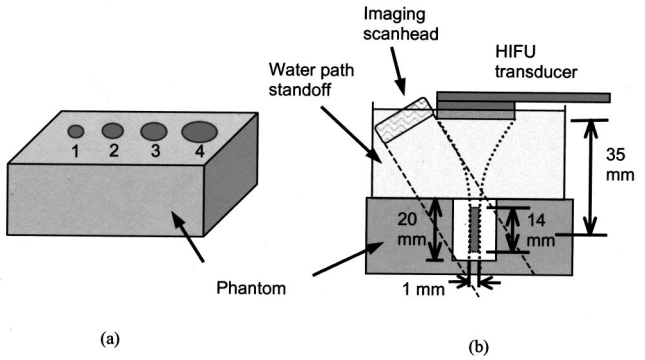

FIG. 5. Phantom setup for the streaming in closed circular tubes. (a) Agar phantom with four tubes of various diameters (Table I). (b) HIFU beam focus, approximated as a uniform cylinder, was positioned at the center of each tube. Water path standoff closed the top of the tube. Only one tube is shown in (b) for clarity.

would be at the center of each tube and the image scan would display the streaming flow in a plane crossing the tube central axis. The spatial-peak temporal-average (SPTA) intensity of 24 W/cm^2, with a duty factor of 1%, was used to test for streaming. Streaming measurements were performed on each tube by acquiring color Doppler images of streaming digitally. The digital images were analyzed offline using computer programs. The experiment was repeated for 10 sets of blood samples.

The streaming in a large open space was approximated by a 400 ml beaker filled with blood. After the beaker was filled, the HIFU and imaging transducers were submerged slightly below the blood surface. Therefore, unlike the earlier setup with a water standoff, the HIFU intensity at the focus was attenuated by the blood in the beaker between the transducer surface and the focus. A total of eight samples were measured and streaming was recorded and analyzed in the same way as mentioned above. All measurements were performed at room temperature.

Programs were written in C (Microsoft, Redmond, WA) and MATLAB™ (Math Works, Inc., Natick, MA) to aid in the offline analysis. The red (R), green (G), and blue (B) values of each color pixel of the streaming flow were compared with those of the velocity color map as displayed on the same image. The best match was found which had the minimum sum of the absolute differences of RGB between the streaming color pixel and the color map pixels. Since the velocity color map associated each color pixel with a velocity reading, the best match of color was converted into a velocity magnitude. The angle between the HIFU and imaging beams was measured from the ultrasound images and used to correct for the Doppler angle for the streaming velocities measured. The analyzed data allowed the production of a two-dimensional velocity distribution map. Four different velocity scales of color Doppler were used in the measurement. The scales were selected according to the magnitude of streaming velocity in each tube so that the color Doppler measurement would not be aliased. The largest velocity scale could measure streaming velocity up to 23.8 cm/s. The maximum velocity of streaming in the tube was obtained by averaging the 10 largest velocity pixels in each color image. The color Doppler measurement of the maxi-

mum streaming velocity was repeated three times and then averaged for each blood sample in each tube. The mean and standard deviation of the maximum velocity were calculated for 10 samples measured in each of the four tubes and for eight samples measured in the beaker.

3. Acoustic streaming in coagulating blood

The same integrated HIFU/imaging system with the 5MHz HIFU transducer was used. A single circular channel with a diameter of 9.5 mm was made in an agar phantom to hold blood samples. The HIFU and imaging transducers were placed at the side of the channel so that the top remained open for adding chemicals to induce coagulation in blood. Thus the streaming was generated transversally in the channel.

Blood samples were obtained from the first author, immediately citrated to prevent clotting and kept at room temperature before the experiment. For each experimental trial, 2 ml of blood was drawn from the vial and put into the channel in the phantom. The SPTA intensity of HIFU was 31 W/cm^2, with the duty factor of 1%. The HIFU was applied in blood for less than 2 seconds and the color Doppler images of the acoustic streaming were recorded on videotape. The coagulation was induced by adding calcium to the citrated blood in the channel. The HIFU was applied for approximately 2 seconds in every 2 to 3 minutes to monitor the change of streaming velocity due to coagulation. This brief exposure was used to minimize any effects HIFU might have on the natural coagulation process. When it was found that no streaming was being produced, indicating the blood had clotted, the contents in the channel were then removed and visually examined to confirm the formation of a clot. A total of four blood samples were studied.

The recorded color Doppler images were analyzed in the following way. The frames showing the streaming velocities were digitized using a frame grabber (Targa 2000 video capture card). Selected images were then analyzed using Adobe Photoshop® (Adobe Systems, Inc., San Jose, CA) software. First, the color bar in each image was divided into segments of 0.5 cm/s increment, according to the given velocity scale. The mean values of red (R), green (G), and blue (B) of each segment were measured using the histogram of each color channel. A lookup table was established to associate these RGB values with the velocity magnitudes. Second, the area of streaming in each still image was selected manually. The mean R, G, and B values of the streaming area were obtained using histograms. Third, these RGB values of the streaming flow were compared with the lookup table. The velocity of the streaming was then determined by finding the closest match of RGB values in the table. Linear interpolation was used when the RGB values fell between the table values. Finally, these streaming velocities were plotted against time as they were recorded during coagulation.

The echogenicity change of the clotting blood was also studied for the comparison with the change of streaming velocity. The same images were used as those in the streaming measurement. A fixed area in the clotting blood in the image was selected and the pixel density of the area was obtained by taking the mean gray-scale level of the area. Since the pixel density and the streaming velocity were measured in different units, they were both normalized according to their maximum dynamic range in order to compare with each other. The pixel density was normalized by 256 gray-scale levels. The streaming velocities were normalized according to the velocity scale of color Doppler, which was [0,7.2] cm/s in the experiment. The normalized echogenicity and velocity were then plotted together over time to compare their relative magnitude of change during coagulation.

III. RESULTS

Figure 6 shows the analytical solutions of the radial distribution of streaming velocity in four circular tubes, as calculated using Eqs. (1) and (2). The results of FEA simulation in the same four tubes, using the cylindrical ultrasound beam of uniform intensity field, are also plotted for comparison. Two vertical dashed lines in the middle of each plot represent the 1 mm ultrasound beam diameter. The results of FEA simulation agree very well with the analytical solution for the smallest tube [Fig. 6(a)], where the tube diameter is 5 times the beam diameter. However, when the tube diameter further increases, the analytical solution shows a larger increase of streaming velocity than the simulation [Figs. 6(b)–(d)]. In fact, the peak velocity in the simulation approaches a constant when the tube diameter becomes more than 10 times larger than the beam diameter. This constant velocity is approximately half of the magnitude of the analytical solution for the largest tube [Fig. 6(d)]. The area of forward flow (positive velocity) grows with the tube size in the analytical solution, whereas the simulation indicates a very limited increase of forward flow area. While the magnitude of the velocity of the reverse flow (negative velocity) remains similar in four tubes according to the analytical solution, it decreases significantly with the increasing tube size in the simulation. Such a decrease is expected since the cross-sectional area in which reverse flow occurs increases with tube diameter (i.e., velocity would thus decrease for the same total reverse flow in each tube). Both the analytical solution and FEA simulation has a zero flow rate through the tube cross-sectional area because the tubes are closed.

In the second part of the FEA simulation, the measured HIFU beam pattern was incorporated into the model to simulate the experimental setup. Figure 7 illustrates the velocity vectors (with overlaid HIFU beam contours) as obtained from the simulation of streaming in the tube of 1.4 cm diameter. The pattern of flow re-circulation is observed in the tube. The vectors are drawn with a uniform length because the reverse flow is so slow compared to the forward flow that it would not be displayed on a magnitude-based vector plot.

Figure 8 is the Doppler measured streaming in blood in the tube of 1.4 cm diameter. The picture has been rotated to upright from the original ultrasound image, as it was scanned tilted [Fig. 5(b)]. The color Doppler only acquired about 1.65 cm of the total tube length of 2 cm. HIFU was applied from the top of the tube with its focus positioned at the center of the tube. The color Doppler representation of velocity is shown in gray-scale here. It can be seen that the peak streaming velocity occurs at the center of the tube, where the HIFU focus is positioned. The peak velocity appears below the half

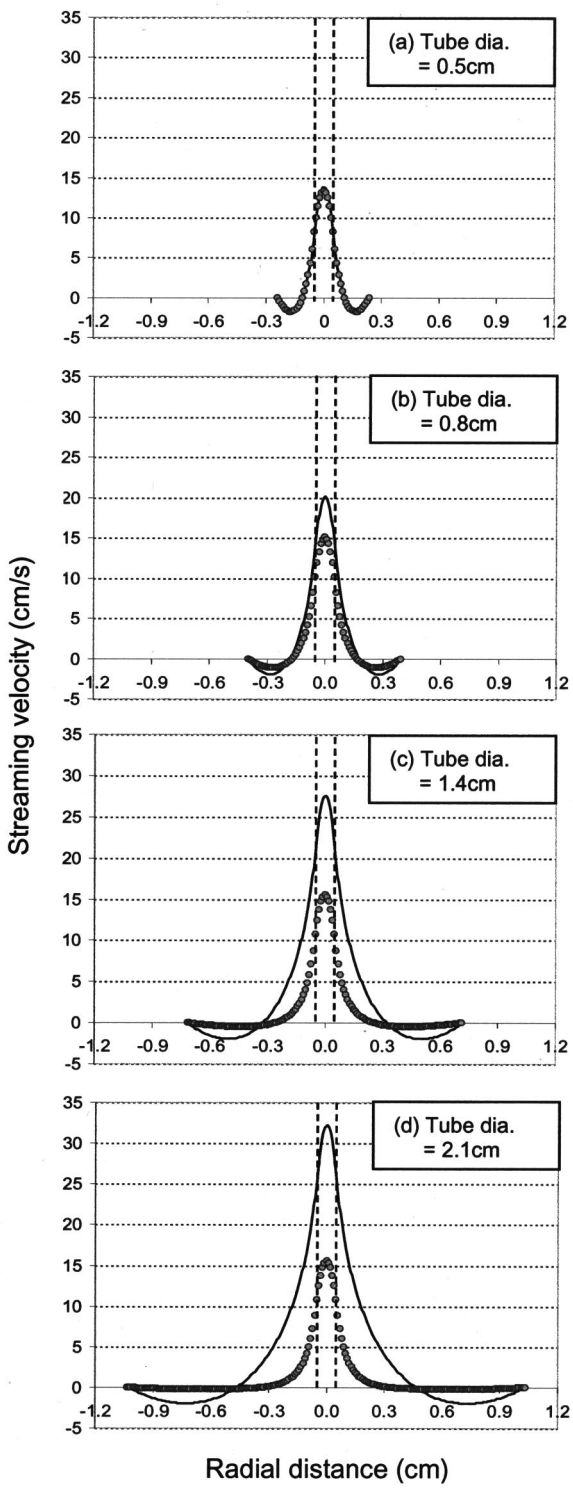

FIG. 6. The analytical solution (solid line) and FEA simulation (circles) of the radial distribution of streaming velocity in four closed circular tubes. The vertical dashed lines in the middle of each plot represent the diameter of the cylindrical ultrasound beam ($2r_1 = 0.1$ cm). The values of other parameters are given in Table I.

tube length (the 10 mm mark), indicating a velocity build-up along the beam. The similar velocity map was obtained for the other three tubes and for the beaker.

In all cases except the smallest tube, there is no reverse flow measured by color Doppler because the velocity is too small to pass the clutter filter of Doppler detection (the cutoff

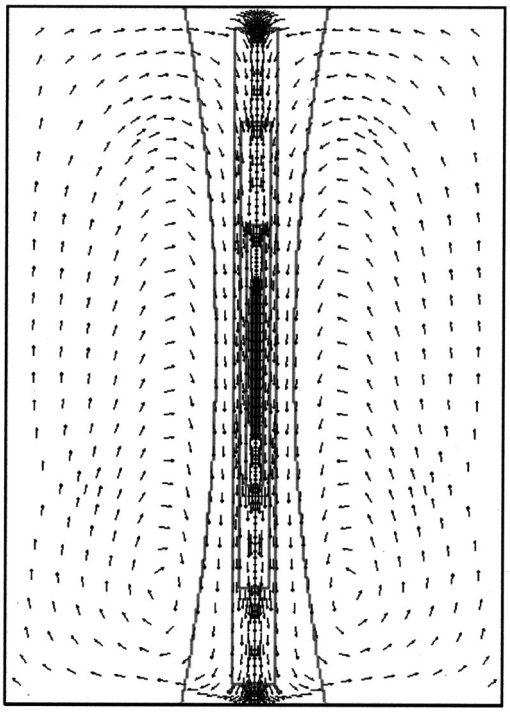

FIG. 7. Vector plot of HIFU-generated streaming using FEA simulation. The HIFU force field is overlaid to show the beam pattern. The HIFU beam is transmitted from the top of the tube. The HIFU focus is placed at the center of the tube. The tube diameter is 1.4 cm and length is 2 cm.

velocity was estimated from the velocity color map to be less than 1 cm/s). This observation agrees with the FEA simulation that the magnitude of the reverse flow decreases when the tube gets larger (Fig. 6).

The peak forward velocities measured by color Doppler in blood in four tubes are plotted in Fig. 9. The results of

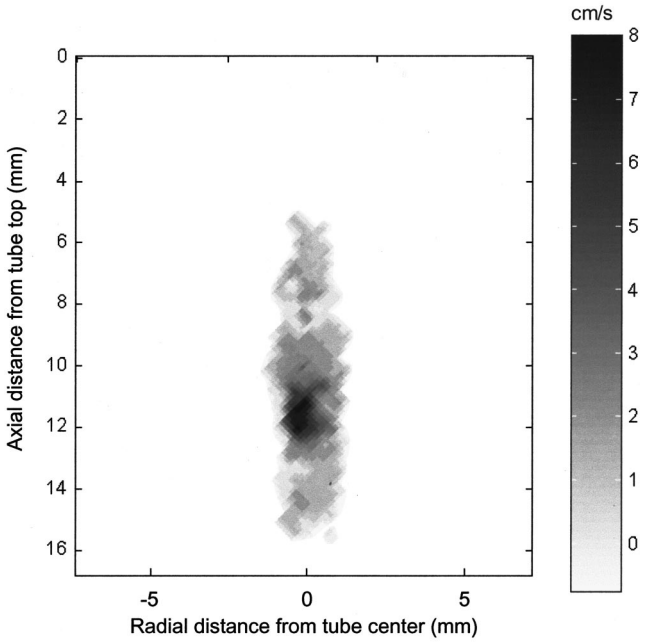

FIG. 8. *In vitro* Doppler measurement of HIFU-generated streaming in blood in a closed circular tube (diameter = 1.4 cm). The HIFU is applied from the top of the tube. The gray scale pixels represent the magnitude of the velocity component along the axial direction.

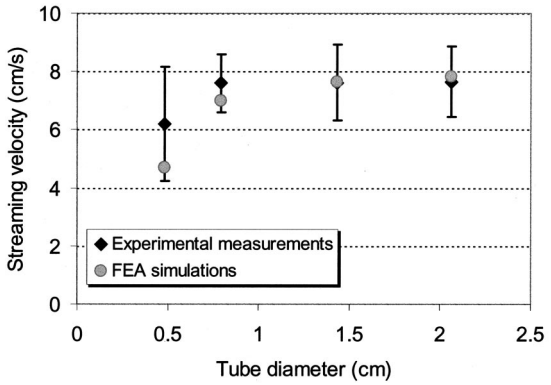

FIG. 9. Comparison of peak streaming velocities between experimental measurements and FEA simulations in four circular tubes. A total of 10 samples were measured in the experiment.

FEA simulation with transient analysis are also plotted for comparison. The transient analysis showed that the peak velocity decayed to an average of 80% in 16 ms after HIFU was stopped in these tubes. The simulation results of streaming agree well with the experimental measurements, especially in large tubes. Both experiment and simulation show that the peak velocity increases with the increasing tube diameter, but eventually reaches an asymptotic constant when the tube diameter is approximately 10 times larger than the beam diameter. The peak streaming velocity in the large beaker was measured by color Doppler to be 4.49 ± 1.42 cm/s. The FEA simulation showed that the peak streaming velocity was 4.51 cm/s in the beaker.

Table II gives the results of analytically calculated G on the axis in the closed circular tubes and open space, using Eqs. (3) and (4). For the FEA simulation and experimental measurement, G was derived from Eq. (1) using the simulated or Doppler-measured streaming velocity with the parameters given in Table I. The comparison demonstrates that the FEA simulation closely agrees with the experiment results, both indicating an asymptotic value of G when the tube diameter increases. However, the analytical solutions predict a monotonically increasing G when tube becomes bigger. The analytical solutions of G are approximately 2 to 4 times higher than the estimations based on the experimental measurement.

A significant decrease of streaming velocity was observed in the four samples of coagulating blood (Table III). Figure 10 illustrates the velocity change over time in sample #3 during its coagulation. The coagulation was induced at 19 min, after the baseline streaming velocity was obtained in blood at 0, 2, 10, and 15 min, respectively. The streaming velocity in blood was nearly constant around 3.7 cm/s (0.51 normalized). After the coagulation was induced by adding calcium, there was initially very little change in the streaming velocity (21 and 23 min). This was the time period necessary for calcium to activate the coagulation cascade. At about 6 minutes after calcium was added, streaming velocity started to decrease, indicating the formation of a fibrin network that restricted the blood motion. The velocity decreased gradually after this point. At approximately 30 minutes after calcium was added, the velocity was only about 30% of its initial value in the unclotted blood. At this point the sample was removed from the channel in the phantom. The clot formation was confirmed by visual inspection.

The change of normalized echogenicity of sample #3 is also shown in Fig. 10. It can be seen that the echogenicity varied very little in the unclotted blood. When the coagulation started, the echogenicity of the blood decreased initially, and then remained almost constant during the coagulation. The percentage change of the echogenicity was approximately 5% on 256 gray-scale levels. On the other hand, the change of streaming velocity was about 30% on a color Doppler scale of 0–7.2 cm/s. Similar plots were obtained for the other three samples. The echogenicity change exhibited no definitively increasing or decreasing trend in four channels. In contrast, the streaming velocity in all samples decreased gradually during the coagulation process. The average normalized change of streaming velocity during coagulation was about 26% in four samples.

TABLE II. Summary of G in closed circular tubes and large beaker. The analytical solution was calculated using the parameter values given in Table I. The Doppler and FEA estimations were derived using Eq. (1), with the measured or simulated streaming velocities as shown in Fig. 9.

	$G(\times 10^{-3}\ \text{cm}^2)$				
	Tube diameter (cm)				Large beaker
	0.5	0.8	1.4	2.1	
Analytical solution	2.71	3.95	5.40	6.32	8.33
Doppler estimation	1.52	1.86	1.87	1.88	2.22
FEA estimation	1.25	1.73	1.84	1.87	2.12

TABLE III. Streaming velocity in clotting blood. The velocity in blood was measured before calcium was added to the blood samples to induce coagulation. The velocity in clots was measured just before the color Doppler signal of streaming disappeared in clots.

	Streaming velocity (cm/s)	
Sample No.	in blood	in clots
1	3.6	2.1
2	3.2	2.0
3	3.7	1.2
4	4.7	2.5
Mean	3.8	2.0
Std. Dev.	0.6	0.5

IV. DISCUSSIONS AND CONCLUSIONS

The general expression of streaming velocity [Eq. (1)] has been used in many studies to investigate the change of streaming velocity when the intensity or viscosity is varied.[9,13,26,27] In those studies, the geometric setup of the flow chamber and the beam were fixed so that the geometric effect was eliminated for the comparison of velocity. However, in real clinical applications such as hemorrhage detection, the variation of hematoma shape and size may significantly affect the generation and detection of streaming. It is easy to appreciate the geometric effect on streaming, as it is just a special case of fluid dynamics. However, it is very difficult to theoretically quantify the geometric factor for

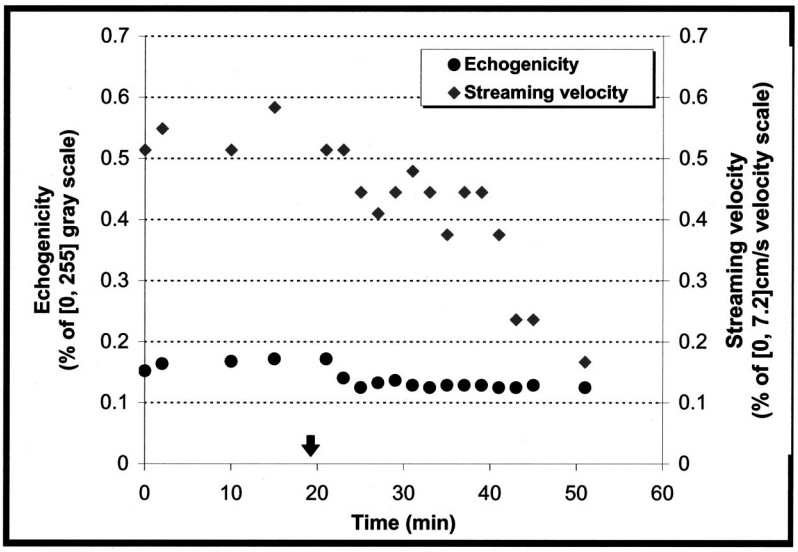

FIG. 10. Normalized change of echogenicity and streaming velocity in coagulating blood. The arrow represents the time point when calcium was added to initiate the coagulation. The echogenicity is normalized according to the gray scale of [0,255]. The streaming velocity is normalized according to the velocity scale of color Doppler, [0,7.2] cm/s.

complex structures. The experimental quantification has been lacking even for the simple geometry. This study quantifies the effect of geometry on streaming magnitude for a simple tubular model. The experimental results are compared with the analytical estimation and FEA simulation.

Equation (2) provides a simple solution to estimate streaming velocity in a closed cylindrical tube. However, some assumptions of this equation, such as an infinite long tube and a uniform cylindrical beam, may be impossible to be satisfied in practice. FEA simulation, on the other hand, offers a method to closely approximate the real geometry of both ultrasound beam and tube. The simulation in Fig. 6 models an ideal uniform cylindrical force field. The close agreement between the analytical solution and the simulation for the smallest tube [Fig. 6(a)] demonstrates that using Eq. (1) with Eq. (2) yields a good estimation of streaming in long narrow tubes. Eq. (2) predicts an ever-increasing G as the tube diameter increases, as long as the condition holds for $0<r_0/r_1<\infty$. However, when the tube diameter increases in the simulation the tube becomes relatively short, breaking one of the assumptions Eq. (2) is based on. The simulation results show the streaming velocity approaching a limit in large short tubes. Figure 6 suggests that Eq. (2) may overestimate the streaming velocity when the ratio r_0/r_1 is large and the tube length is limited. This agrees with other investigators' experimental measurement in similar cylindrical setups. Starritt *et al.* found in their experiment that the estimated streaming velocity using Eqs. (1) and (2) was 1.5 to 2 times higher than their measured velocity in a closed tube.[28] They also measured the cross-sectional velocity profile at the ultrasound focus and showed a similar plot as our simulation result for the tube diameter of 1.4 cm, which has a narrower forward flow and smaller reverse flow than the analytical solutions predicted.

The length of the circular tubes used in this experiment was slightly longer than the -6 dB focal length (2 cm vs 1.4 cm) in order to prevent the HIFU beam from damaging the phantom. However, the beam field in the middle region of the tube was considered a good approximation to that shown in Fig. 1. The experimental results show that the peak velocity of streaming generated by the HIFU beam appears slightly post focal, as demonstrated by Fig. 8. The peak velocity occurs at about 1.2 cm from the top of the tube although the HIFU focus was carefully positioned at the tube center, 1 cm from the top. This asymmetric distribution of streaming across the tube center was also documented by Liebermann,[29] who suggested that this phenomenon might be due to the omission of fluid inertia in the original derivation of Eq. (2) by Eckart. This buildup effect of streaming was also observed in other studies that used highly or weakly focused beams.[30,31]

The analytical solutions of G in Table II were calculated by approximating the real HIFU beam with a uniform cylinder. The calculation was independent from other parameters, namely the acoustic intensity, blood viscosity, attenuation, and sound speed. However, these parameters must be used in order to derive G from Eq. (1) with the FEA-simulated or Doppler-measured streaming velocities. By using the parameter values shown in Table I for acoustic intensity and blood properties, the assumptions were made that the HIFU field was approximated by a uniform cylinder and the blood viscosity was a constant. Therefore, the FEA or Doppler estimated G included both the geometric effects of varying the tube diameter and the nongeometric errors of these approximations. The significant discrepancies of G shown in Table II between the analytical solutions and experimental measurements suggest that the assumptions made on the beam geometry and fluid properties need to be carefully considered when estimating the streaming velocity using Eqs. (1), (2), and (4).

The FEA simulation is a valuable alternative for streaming estimation when the geometry of ultrasound beam or flow chamber is too complicated to obtain analytical solutions and the experiment is difficult to conduct. The FEA simulation method used in this investigation was similar to the approach used by Nightingale and colleagues in their study of streaming detection in the breast cyst.[26] The major differences are the use of non-Newtonian blood viscosity in our simulation model and the transient analysis because of the delay between the HIFU application and color Doppler

detection of streaming velocity. In this report, good agreements are found in Fig. 9 between the FEA simulation and experimental measurement. The simulated velocities in the small tubes appear smaller than the experimental measurements. This may be due to the approximation of HIFU beam with five uniform intensity levels. In the large tubes the errors of approximation are small because the beam is relatively narrow compared to the tube. However, these errors become significant when the beam geometry is comparable to that of the small tubes. Dividing the continuously distributed HIFU beam into more intensity levels may reduce these errors, but at the cost of a more complicated model. The simulation also incorporated the non-Newtonian property of blood. The literature report on the measurement of pig blood viscosity is rare and the results are contradicting.[32,33] We only measured the viscosity of pig blood at a high shear rate due to the limitation of the equipment. However, such a measurement is considered sufficient because only the peak streaming velocity was measured and compared with the simulation and the shear rate around the region of peak velocity is among the highest in the tube. The modification of Casson's equation with our measured viscosity at high shear rates improved the estimation using Carreau viscosity model. Further improvement can be made if the viscosity data are available for a wide range of shear rate.

The transient analysis of FEA simulation was used to study the decay of streaming after the HIFU force field was removed. We found that in 16 ms the streaming velocity decayed to 80% of the excitation value. Our finding compares favorably with the results of Hartley, who found in blood that the time constant of streaming decay (the point of decay to 37%) to be about 80 ms.[13] The decay of streaming velocity is affected only by the viscosity and tube geometry whereas the generation of streaming also is affected by the acoustic intensity. It is therefore possible to measure the attenuation coefficient and viscosity of the fluid by comparing the generation and decay of streaming flows if the acoustic intensity and sound speed are known.

It has been noted that Eqs. (1), (2), and (4) do not take into account the acoustic and hydrodynamic nonlinearity that may arise when the acoustic intensity is high and the streaming flow becomes turbulent. The results of incorporating these nonlinear terms into Eckart's analysis have been given.[28,31,34,35] However, the solution of those analyses can only be obtained numerically. The streaming in our study is not likely to be turbulent because the Reynolds number is estimated to be 50 (assuming the blood viscosity of 3 cP, blood density of 10^3 kg/m^3, streaming flow diameter of 1 mm, and streaming velocity of 15 cm/s). The acoustic nonlinear enhancement of streaming due to harmonic generation has been observed in water.[36] The biological acoustic nonlinearity terms B/A that have been measured[37] demonstrate the potential for such harmonic generation in blood if the acoustic pressures are high enough. However, Zauhar *et al*. found experimentally that, while increasing the acoustic pressure from 0.2 MPa to 1.4 MPa (while maintaining a constant temporal average intensity of 150 mW), the streaming velocity of water prominently increased nonlinearly at pressures greater than 0.6 MPa, whereas blood followed a consistent gradual incline.[27] This difference in behavior is most likely due to the higher viscosity of blood than water, even though the higher attenuation of blood would absorb the energy of higher harmonics more rapidly than in water. Overall, to a first approximation, the streaming in this study would appear to comply with the linear assumptions made for Eqs. (1), (2), and (4), and the use of Eq. (5) to convert intensity to force for the FEA simulation. This is confirmed by the agreement found between the simulation results and experimental measurements in large tubes (Fig. 9).

Acoustic streaming has been studied to quantify the coagulation time.[12] Our measurement in Fig. 10 also shows a significant decrease of streaming velocity in clotting blood. However, the challenge in hemorrhage detection is to identify a questionable area as unclotted blood, clots or other soft tissue. We have discussed the complex appearance of blood as imaged by regular ultrasound imaging. The use of streaming would be most valuable in helping to decide the nature of a sonographically indeterminate region. The echogenicity of blood was measured as the mean pixel density in the recorded ultrasound images in this investigation. Although commercial ultrasound systems usually use nonlinear transformation to transfer the original echo signals to gray scale displays, the pixel density is a measure of the perception of how bright or dark a region appears in the image as we see it. Figure 10 demonstrates the significant improvement of differentiation between blood and clots when streaming detection was used, comparing with the change of echogenicity during the same coagulation process. The reduction of streaming velocity in clotted blood is mostly due to the increase of viscosity. The attenuation coefficient and the speed of sound in blood also increase during coagulation.[38] Although the increased attenuation coefficient results in a higher radiation force [Eq. (1)], the viscosity increase is more dominant in clots. One study showed that the blood viscosity increased about seven times in value during coagulation,[39] compared to a 24% increase of the attenuation coefficient in clots.[38] The increase of sound speed further reduces the streaming velocity. By using real-time color Doppler detection of streaming, we also observed the change of streaming flow pattern as blood was coagulating, such as the diminishing of reverse flow in the clots. We also observed a ''checkerboard'' appearance of color Doppler image that did not appear as movements of bulk streaming. Comparing with spectral Doppler detection, color Doppler imaging of streaming not only measures the magnitude of streaming velocities but also displays the two-dimensional visualization of streaming flows. This is especially valuable in hemorrhage detection where the direct visualization of streaming is more important than the quantified measurement of velocity magnitude. Comparing with other detection methods such as laser Doppler, hot-film anemometer and MR, ultrasound detection of streaming has advantages of being portable, suitable for *in vivo* measurement and compatible with the HIFU application that has shown the potential for hemostasis application.

In summary, the results indicate that the size and coagulation state of hematomas will affect the detection of streaming in them. FEA simulation can be useful for estimating

streaming velocity in various hemorrhage situations where analytical solution is impractical. This estimation can help determine the optimal ultrasound intensity and beam characteristics to generate detectable streaming in blood. Further investigation with *in vivo* hemorrhage models is needed to demonstrate the efficacy of streaming detection technique for practical hemorrhage diagnosis.

ACKNOWLEDGMENTS

The authors thank Karen Powers for her help in collecting blood samples. We also thank Professor Fred Forster for assisting in the viscosity measurement. This work was supported by a grant from the Defense Advanced Research Programs Administration (DARPA) under its MURI program, No. N00014-96-0630 and a grant from the National Institutes of Health No. RO1 HL64208.

APPENDIX: DERIVATION OF THE VELOCITY OF STREAMING GENERATED BY A FOCUSED BEAM IN A LARGE OPEN SPACE

In Ref. 18 Nyborg studied the acoustic streaming generated by a focused ultrasound beam in a large open space. The focal region was approximated to be cylindrical, with a radius of a and a length of l. The following equation was given to estimate the streaming velocity, v, at the center of the focal cylinder on the axis of the ultrasound beam:[18]

$$v = \frac{\Delta W}{4\pi\mu a c}\Phi, \tag{A1}$$

where μ and c are the viscosity of the fluid and the speed of sound. ΔW is the total loss of acoustic power in the distance of the focal cylinder due to the attenuation; therefore, $\Delta W = 2\alpha l W$, where α is the attenuation coefficient of the fluid and W is the time-averaged transmitted acoustic power at the center of the focus. Φ is a nondimensional factor

$$\Phi = \frac{a}{l}\ln\left(\frac{\chi+1}{\chi-1}\right), \quad \chi = \sqrt{1+(2a/l)^2}. \tag{A2}$$

Since W is assumed to be uniform in the focal cylinder, the acoustic intensity, I, can be calculated by

$$I = \frac{W}{\pi a^2}.$$

Therefore, ΔW can be expressed by I,

$$\Delta W = 2\alpha l W = 2\alpha l \cdot \pi a^2 I. \tag{A3}$$

Furthermore, when $l \gg a$, as in this investigation where $l = 14\,\text{mm}$ and $a = 0.5\,\text{mm}$,

$$\Phi \approx \frac{2a}{l}\ln\left(\frac{l}{a}\right). \tag{A4}$$

Replacing ΔW and Φ in Eq. (A1) with Eqs. (A3) and (A4), we obtain

$$v = \frac{\alpha I a^2}{\mu c}\ln\left(\frac{l}{a}\right). \tag{A5}$$

Comparing Eq. (A5) with Eq. (1), the geometric factor, G, can be expressed as

$$G = a^2 \ln\left(\frac{l}{a}\right),$$

which is Eq. (4) in the main text.

[1] B. Sigel, J. C. Coelho, D. G. Spigos, D. P. Flanigan, J. J. Schuler, D. O. Kasprisin, L. M. Nyhus, and V. Capek, "Ultrasonography of blood during stasis and coagulation," Invest. Radiol. **16**, 71–76 (1981).

[2] K. O. Lillehei, W. F. Chandler, and J. E. Knake, "Real time ultrasound characteristics of the acute intracerebral hemorrhage as studied in the canine model," Neurosurgery **14**, 48–51 (1984).

[3] D. Recchia and S. A. Wickline, "Ultrasonic tissue characterization of blood during stasis and thrombosis with a real-time linear-array backscatter imaging system," Coron. Artery Dis. **4**, 987–994 (1993).

[4] J. C. Coelho, B. Sigel, J. C. Ryva, J. Machi, and S. A. Renigers, "B-mode sonography of blood clots," J. Clin. Ultrasound **10**, 323–327 (1982).

[5] M. Meissner, M. Paun, and K. Johansen, "Duplex scanning for arterial trauma," Am. J. Surg. **161**, 552–555 (1991).

[6] J. W. Edwards, J. M. Bergstein, D. L. Karp, R. F. Cato, and J. B. Towne, "Penetrating proximity injuries—the role of duplex scanning: a prospective study," J. Vasc. Technol. **17**, 257–261 (1993).

[7] W. L. Nyborg, "Acoustic streaming," in *Physical Acoustics*, edited by W. P. Mason (Academic, New York, 1965), pp. 265–331.

[8] J. E. Piercy and J. Lamb, "Acoustic streaming in liquids," Proc. R. Soc. London, Ser. A **226**, 43–50 (1954).

[9] S. O. Dymling, H. W. Persson, T. G. Hertz, and K. Lindstrom, "A new ultrasonic method for fluid property measurements," Ultrasound Med. Biol. **17**, 497–500 (1991).

[10] K. R. Nightingale, P. J. Kornguth, W. F. Walker, B. A. McDermott, and G. E. Trahey, "A novel ultrasonic technique for differentiating cysts from solid lesions: preliminary results in the breast," Ultrasound Med. Biol. **21**, 745–751 (1995).

[11] K. R. Nightingale, P. J. Kornguth, and G. E. Trahey, "The use of acoustic streaming in breast lesion diagnosis: A clinical study," Ultrasound Med. Biol. **25**, 75–87 (1999).

[12] J. C. Machado, A. Lenzi, W. G. Silva, and R. A. Sigelmann, "An ultrasonic method to measure human plasma coagulation time," J. Acoust. Soc. Am. **90**, 1749–1753 (1991).

[13] C. J. Hartley, "Characteristics of acoustic streaming created and measured by pulsed Doppler ultrasound," IEEE Trans. Ultrason. Ferroelectr. Freq. Control **44**, 1278–1285 (1997).

[14] S. Vaezy, R. Martin, U. Schmiedl, M. Caps, S. Taylor, K. Beach, S. Carter, P. Kaczkowski, G. Keilman, S. Helton, W. Chandler, P. Mourad, M. Rice, R. Roy, and L. Crum, "Liver hemostasis using high-intensity focused ultrasound," Ultrasound Med. Biol. **23**, 1413–1420 (1997).

[15] S. Vaezy, R. Martin, H. Yaziji, P. Kaczkowski, G. Keilman, S. Carter, M. Caps, E. Y. Chi, M. Bailey, and L. Crum, "Hemostasis of punctured blood vessels using high-intensity focused ultrasound," Ultrasound Med. Biol. **24**, 903–910 (1998).

[16] S. Vaezy, R. Martin, P. Mourad, and L. Crum, "Hemostasis using high intensity focused ultrasound," Eur. J. Ultrasound **9**, 79–87 (1999).

[17] C. Eckart, "Vortices and streams caused by sound waves," Phys. Rev. **73**, 68–76 (1948).

[18] W. L. Nyborg, "Acoustic streaming," in *Nonlinear Acoustics*, edited by M. F. Hamilton and D. T. Blackstock (Academic, San Diego, 1998), pp. 207–231.

[19] J. Wu, and G. Du, "Acoustic streaming generated by a focused Gaussian beam and finite amplitude tonebursts," Ultrasound Med. Biol. **19**, 167–176 (1993).

[20] M. C. Ziskin and P. A. Lewin, *Ultrasonic Exposimetry* (CRC, Boca Raton, FL, 1993).

[21] R. L. Whitmore, *Rheology of the Circulation* (Pergamon, Oxford, UK, 1968).

[22] P. J. Carreau, R. P. Chhabra, and D. C. R. De Kee, *Rheology of Polymeric Systems: Principles and Applications* (Hanser-Garner Publications, Cincinnati, OH, 1997).

[23] *ANSYS Theory References*, 8th ed. (ANSYS, Inc., Canonsburg, PA, 1997).

[24] N. Casson, "A flow equation for pigment-oil suspensions of the printing ink type," in *Rheology of Disperse Systems*, edited by C. C. Mill (Pergamon, London, UK, 1959), pp. 84–102.

[25] S. Vaezy, X. Shi, R. W. Martin, E. Chi, P. I. Nelson, M. R. Bailey, and L. A. Crum, ''Real-time visualization of focused ultrasound therapy,'' Ultrasound Med. Biol. (in press).
[26] K. R. Nightingale and G. E. Trahey, ''A finite element model for simulating acoustic streaming in cystic breast lesions with experimental validation,'' IEEE Trans. Ultrason. Ferroelectr. Freq. Control **47**, 201–214 (2000).
[27] G. Zauhar, H. C. Starritt, and F. A. Duck, ''Studies of acoustic streaming in biological fluids with an ultrasound Doppler technique,'' Br. J. Radiol. **71**, 297–302 (1998).
[28] H. C. Starritt, C. L. Hoad, F. A. Duck, and D. K. Nassiri, ''Measurement of acoustic streaming using magnetic resonance,'' Ultrasound Med. Biol. **26**, 321–333 (2000).
[29] L. N. Liebermann, ''The second viscosity of liquids,'' Phys. Rev. **75**, 1415–1422 (1949).
[30] K. Matsuda, T. Kamakura, and Y. Kumamoto, ''Buildup of acoustic streaming in focused beams,'' Ultrasonics **34**, 763–765 (1996).
[31] T. Kamakura, K. Matsuda, Y. Kumamoto, and M. A. Breazeale, ''Acoustic streaming induced in focused Gaussian beams,'' J. Acoust. Soc. Am. **97**, 2740–2746 (1995).
[32] A. Laurent, J. J. Durussel, J. Dufaux, L. Penhouet, A. L. Bailly, M. Bonneau, and J. J. Merland, ''Effects of contrast media on blood rheology: comparison in humans, pigs, and sheep,'' Cardiovasc. Intervent Radiol. **22**, 62–66 (1999).
[33] T. M. Amin and J. A. Sirs, ''The blood rheology of man and various animal species,'' Q. J. Exp. Physiol. (1981) **70**, 37–49 (1985).
[34] T. Kamakura, T. Sudo, K. Matsuda, and Y. Kumamoto, ''Time evolution of acoustic streaming from a planar ultrasound source,'' J. Acoust. Soc. Am. **100**, 132–138 (1996).
[35] O. V. Rudenko, A. P. Sarvazyan, and S. Y. Emelianov, ''Acoustic radiation force and streaming induced by focused nonlinear ultrasound in a dissipative medium,'' J. Acoust. Soc. Am. **99**, 2791–2798 (1996).
[36] H. C. Starritt, F. A. Duck, and V. F. Humphrey, ''An experimental investigation of streaming in pulsed diagnostic ultrasound beams,'' Ultrasound Med. Biol. **15**, 363–373 (1989).
[37] F. Dunn, W. K. Law, and L. A. Frizzell, ''Nonlinear ultrasonic propagation in biological media,'' Br. J. Cancer Suppl. **45**, 55–58 (1982).
[38] K. K. Shung, D.-Y. Fei, Y.-W. Yuan, and W. C. Reeves, ''Ultrasonic characterization of blood during coagulation,'' J. Clin. Ultrasound **12**, 147–153 (1984).
[39] N. M. Henderson and G. B. Thurston, ''A new method for the analysis of blood and plasma coagulation,'' Biomed. Sci. Instrum. **29**, 95–102 (1993).

Source levels of clicks from free-ranging white-beaked dolphins (*Lagenorhynchus albirostris* Gray 1846) recorded in Icelandic waters

Marianne H. Rasmussen and Lee A. Miller
Center for Sound Communication, Institute of Biology, Odense University, Campusvej 55, 5230 Odense M, Denmark

Whitlow W. L. Au
Marine Mammal Research Program, Hawaii Institute of Marine Biology, Kailua, Hawaii

(Received 21 April 2001; accepted for publication 7 November 2001)

This study reports the source levels of clicks recorded from free-ranging white-beaked dolphins (*Lagenorhynchus albirostris* Gray 1846). A four-hydrophone array was used to obtain sound recordings. The hydrophone signals were digitized on-line and stored in a portable computer. An underwater video camera was used to visualize dolphins to help identify on-axis recordings. The range to a dolphin was calculated from differences in arrival times of clicks at the four hydrophones, allowing for calculations of source levels. Source levels in a single click train varied from 194 to 211 dB peak-to-peak (p-p) re: 1 μPa. The source levels varied linearly with the log of range. The maximum source levels recorded were 219 dB (p-p) re: 1 μPa. © *2002 Acoustical Society of America.* [DOI: 10.1121/1.1433814]

PACS numbers: 43.80.Ka, 43.80.Lb, 43.80.Nd, 43.80.Pe [FD]

I. INTRODUCTION

The white-beaked dolphin has a black and white robust body with a short, thick, gray, white, or brown rostrum. The adult dolphins weigh between 220 and 350 kg and have lengths between 220 and 280 cm (Reeves *et al.*, 1999). They are endemic to the North Atlantic and can be found in groups along the coast of Iceland during summer. The dolphins are very curious and will often swim near boats and bow ride.

The presumed echolocation clicks from white-beaked dolphins resemble those recorded from the bottlenose dolphin (*Tursiops truncatus* Montagu 1821). Bottlenose dolphins emit short, broadband clicks with peak frequencies about 120 kHz (Au, 1980). White-beaked dolphins also emit broadband clicks 10 to 30 μs in duration with peak frequencies about 120 kHz, but some clicks from white-beaked dolphins have a secondary peak at about 250 kHz (Rasmussen and Miller, in press). In most acoustical studies, the orientation of the whale with respect to the hydrophones is unknown and source levels cannot be calculated. Thus, source levels, the sound pressure 1 m from the source recorded on the acoustic axis, are reported for only a few odontocetes in the wild. Source levels and other parameters of clicks from several odontocete species during different recording conditions are summarized in Table I.

The purpose of this study was to measure source levels of clicks from free-ranging white-beaked dolphins using a four-hydrophone array.

II. METHODS

Recordings were made in Icelandic waters not far from Keflavik (64°00.5′N, 22°33.4′W) between 22 and 26 August 1998. Water depth at the recording sites was about 35 m and the bottom was sandy.

We used a four-hydrophone array (Au *et al.*, 1998) with omnidirectional, calibrated ITC 1094 hydrophones having a flat frequency response up to 160 kHz. The same array was used to measure source levels from free-ranging spinner dolphins and spotted dolphins (Schotten *et al.*, in press; Schotten, 1997). The three hydrophones were arranged in a triangle with the fourth hydrophone in the center. The outer hydrophones were spaced 0.61 m from the center hydrophone. The angle between each pair of outer hydrophones was 120°. A small underwater video camera was attached and fixed 10 cm above the center hydrophone. The hydrophone array was mounted on a long pole that was lowered to a depth of about 2 m from the side of a 10-m motorboat. The propellers were stopped during recordings, but the engines idled. Hydrophone cables were connected to a multichannel amplifier and then to a portable computer on board. Analog-to-digital conversion (500 ksamples/s) was accomplished using two GAGE 1210 pc-boards. Dolphin signals were continuously digitized and stored in a temporary memory, but only signals where the amplitude on the center hydrophone exceeded a preset trigger Level were saved to disk. Up to 80 clicks could be stored in one data file. The clock time of the computer was synchronized with the video and a time stamp for each triggering was stored in a companion file. A computer program determined the click with the highest amplitude within the sample and used it to determine the received sound-pressure level (SPL). Clicks for calculating source level were only used if these clicks showed high-frequency components on all four hydrophones and had a click with the highest (or equally high) amplitude on the center hydrophone. Au (1993) has shown that on-axis clicks have high amplitude and low distortion, while off-axis signals are more variable. Cursors were manually set at the maximum positive peak of each click on the four channels and time of arrival

 0001-4966/2002/111(2)/1122/4/$19.00

TABLE I. Characteristics of some odontocete clicks and recording conditions. The table is compiled primarily from field recordings where source levels could be calculated. Characteristics of clicks from bottlenose dolphins are shown for comparison.

Species	Peak-frequency kHz	Click duration μs	Maximum source level (p-p) dB *re*: 1 μPa	Number of hydrophones	Recording condition
White-beaked dolphin, *Lagenorhynchus albirostris*	120[a]	10–30[a]	219[b]	4	Wild
Pacific white-sided dolphin, *Lagenorhynchus obliquidens*	59	34–52	170	1	Captive, tank[c]
Bottlenose dolphin, *Tursiops truncatus*	52	50–250	170	1	Captive, tank[d]
Bottlenose dolphin, *Tursiops truncatus*	117	40–70	220	1	Captive, open waters, Kaneohe Bay[e]
Long-snouted spinner dolphin, *Stenella longirostris*	70	31	222	4	Wild[f]
Pantropical spotted dolphin, *Stenella attenuata*	69	43	220	4	Wild[f]
Narwhal, *Monodon monoceros*	40	29–45[g]	227	5	Wild[h]
Sperm whale, *Physeter catodon*	20[i]	200–300	232	4–5	Wild[j]

[a]Rasmussen and Miller (in press).
[b]This study.
[c]Fahner *et al.* (in press).
[d]Evans, 1973.
[e]Au *et al.*, 1980.
[f]Schotten, 1997.
[g]Miller *et al.*, 1995.
[h]Møhl *et al.*, 1990.
[i]Wahlberg (personal communication, 2001).
[j]Møhl *et al.*, 2000.

differences were measured. These differences were then used to calculate the range to the dolphin from which source levels could be determined, taking into account the transmission loss due to spherical spreading but ignoring the frequency-dependent attenuation due to the short distances (Urick, 1983). The accuracy for calculating ranges extended up to 30 m when using this array (Schotten, 1997). Source levels are expressed in dB (p-p) *re*: 1 μPa and the trigger setting allowed for the calculation of source levels (SL) greater than about 180 dB.

III. RESULTS

Only files consisting of clicks on all four hydrophones were analyzed and in these cases we assume the dolphins were interrogating our array. A total of 1718 source levels was calculated. The maximum recorded source level was 219 dB measured at a range of 22 m and the minimum recorded source level was 189 dB measured at a distance of 1.5 m from the dolphin. Figure 1 shows that source levels increase with the log of range (R) ($\mathrm{SL}=16\log R+192$), giving a correlation coefficient (r^2) of 0.69, which is significant [$n=1648$, one-way Anova, $p<0.01$ (Zar, 1996)]. The $20\log(R)$ and $40\log(R)$ lines, which are the one-way transmission loss and two-way transmission loss, respectively, are included in Fig. 1.

Figure 2 shows an example where one dolphin pointed its rostrum straight at the video camera during one second. This example contained 14 clicks from a sequence with good video recordings and many clicks. Source levels remain fairly constant at 204 to 206 dB at ranges of 3.5 to 6.5 m, but the source levels decrease to less than 200 dB at about a range of 2.7 m. The results from this individual dolphin reflect the tendency that source level increases with range as shown in Fig. 1.

Because of the way we selected clicks for source level analysis and for other reasons, interclick intervals could not be correlated with range.

IV. DISCUSSION

Source levels from free-ranging white-beaked dolphins are similar to those reported from trained bottlenose dolphins in open waters (Au, 1993). Source levels for the bottlenose dolphin varied from 208 dB at a range of 6 m to a maximum

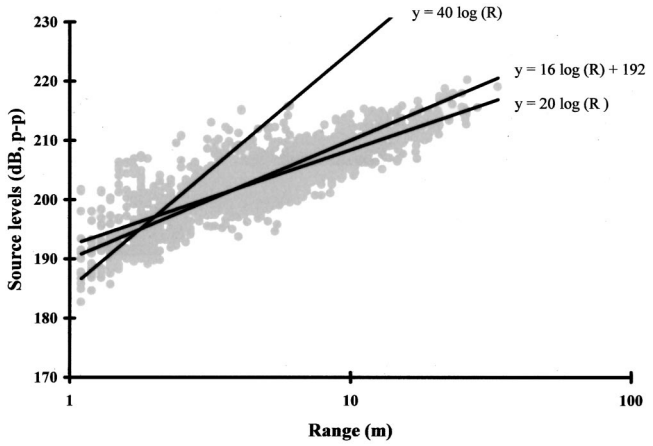

FIG. 1. Source levels in dB (p-p) *re*: 1 μPa as a function of range (m). The source levels ($n=1718$) increase with the log of range [$y=16\,\mathrm{Log}\,(R)+192$, $r^2=0.69$], which is close to the one-way transmission loss [$y=20\,\mathrm{Log}\,(R)$]. The two-way transmission loss line [$y=40\log(R)$] is also shown.

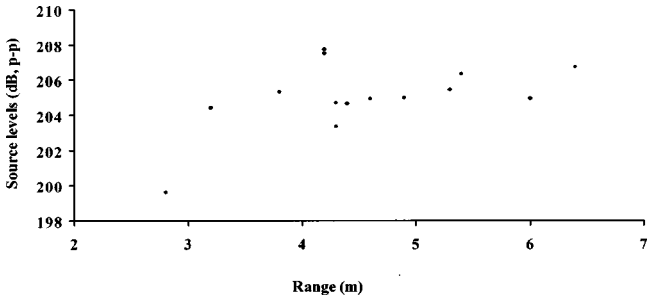

FIG. 2. An example from a file where one dolphin is looking straight towards the underwater video camera during one second. Source levels are in dB (p-p) *re*: 1 μPa.

of 230 dB at a range of 77.7 m (85 yards) to the target. The source level was 214 dB at a range of 20 m (Au, 1980). We calculated source levels of clicks from free-ranging white-beaked dolphins to 208 ± 2 dB ($n = 20$) at a range of 6 m and 214 ± 2 dB ($n = 20$) at a range of 20 m. Thus, source levels are essentially identical for these two species at the same target distance. We found a maximum source level of 219 dB when the dolphin was at a distance of 22 m. Our measuring system was limited at greater distances, so white-beaked dolphins can presumably produce clicks as loud as those from bottlenose dolphins. The maximum recorded source level from bottlenose dolphins (230 dB) was measured from one click in a sequence with an average source level of 220 dB (Au, 1980).

Calculated source levels from white-beaked dolphin clicks also resemble source levels from free-ranging spinner dolphins and spotted dolphins (Table I). Schotten (1997) reported source levels between 195 and 222 dB for spinner dolphins and between 197 to 220 dB for spotted dolphins. The minimum source levels in these recordings, as in our recordings, are dependent on the trigger level of the recording setup. Source levels of clicks from the Pacific white-sided dolphin (*Lagenorhynchus obliquidens* Gill 1865) measured in a tank were 170 dB (Evans, 1973); recently, Fahner (in press) measured source levels between 149 and 157 dB for the same species also in a tank. Bottlenose dolphins produce lower intensity clicks in tanks than in open waters (Au, 1993).

Our method of selecting clicks assured that these were directed toward the array and presumably on-axis, or nearly so. Assuming the array was the target, source levels increased linearly with the log of range for clicks from white-beaked dolphins (Fig. 1). Source levels also increase with range for a single dolphin looking straight towards the video camera (Fig. 2). This is the first documented case that shows a significant linear relationship between the source level and the log of range for a dolphin species. We expected the increase in click level to fall on the 40 log range line (Fig. 1), which would compensate for the two-way transmission loss for increasing distance. Had this been the case, the received echo level would be constant and independent of distance assuming no changes in target reflectivity. Surprisingly, the regression line [16 log (*R*) in Fig. 1] is closer to the one-way transmission loss with distance [20 log (*R*) in Fig. 1]. This implies that the sound level impinging on the target is nearly constant. Thus, as the dolphin closes on the target the received echo level increases by 6 dB for each halving of distance. In fact, this is exactly what bats do, except we know that contractions of the middle-ear muscles attenuate audition, thus compensating for the increased echo level, at least over some ranges (Henson, 1965; Hartley, 1992).

The white-beaked dolphin apparently controls the energy it puts in the outgoing signal. We found a variation in source levels of about 20 dB at any given range below 10 m (Fig. 1). At greater ranges the variation decreases. These variations are greater than we expected based on an assumed beam pattern similar to that of the bottlenosed dolphin, and on our method of selecting clicks for source level calculations. We therefore assume that the variation in source level is produced by the dolphin. Because of this, dolphins might compensate for the two-way transmission loss at ranges between 1 and about 3 m and for the one-way transmission loss at greater distances (up to about 14 m). Source levels for bottlenose dolphins can be quite variable in a click train. Au (1993) shows an example with 17-dB variation in source level in one click train produced by a dolphin during a sonar task, and variations as much as 20 to 25 dB were not uncommon.

The source levels of most odontocete echolocation signals are considerably higher than even the most intense bat signals. After converting source levels in dB (*re*: the reference Pa) to energy flux density (J/m^2) and assuming the signals are on the acoustic axis, the strongest bottlenose dolphin clicks are about 30 dB above the most intense signals recorded from a bat (*Eptesicus serotinus*, Jensen and Miller, 1999). The strongest white-beaked dolphin clicks are about 15 dB above the bat signals. However, harbor porpoise clicks (*Phocoena phocoena*, Au *et al.*, 1999) are about -26 dB relative to the strongest bat signals.

In conclusion, four dolphin species in three genera use clicks with high source levels when recorded in the wild or in open waters. Assuming our hydrophone array was the target, clicks from free-ranging white-beaked dolphins show a clear linear relationship between source level and log of range. This is the first documented case of decreasing source level with decreasing distance to target for free-ranging dolphins, but we predict this relationship will hold for other dolphin species as well.

ACKNOWLEDGMENTS

This study was supported by Danish National Research Foundation and Japetus Stenstrups Fond. We extend our thanks to the Marine Research Institute in Reykjavik and to Gisli Vikingsson for their cooperation. We thank Helga Ingimundardottir and Dolphin and Whale Spotting for their hospitality, as well as Jakob Tougaard, Magnus Wahlberg, and Bertel Møhl for their helpful suggestions. We also thank three anonymous reviewers for providing suggestions to improve the manuscript.

Au, W. W. L., Herzing, D. L., and Aubauer, R. (**1998**). ''Real-time measurement of the echolocation signals of wild dolphins using a 4-hydrophone array,'' in Proceedings of The World Marine Mammal Science Conference, Monaco, 20–24 January 1998.

Au, W. W. L., Kastelein, R. A., Rippe, T., and Schooneman, N. M. (**1999**). ''Transmission beam pattern and echolocation signals of a harbor porpoise (*Phocoena phocoena*),'' J. Acoust. Soc. Am. **106**, 3699–3705.

Au, W. W. L. (**1980**). ''Echolocation signals of the Atlantic bottlenose dolphin (*Tursiops truncatus*) in open waters,'' in *Animal Sonar Systems*, edited by R.-G. Busnel and J. F. Fish (Plenum, New York), pp. 251–282.

Au, W. W. L. (**1993**). *The Sonar of Dolphins* (Springer, New York).

Evans, W. E. (**1973**). ''Echolocation by marine delphinids and one species of fresh-water dolphin,'' J. Acoust. Soc. Am. **54**, 191–199.

Fahner, M., Thomas, J., Ramirez, K., and Boehm, J. (in press). ''Acoustic properties of echolocation signals by captive Pacific white-sided dolphins (*Lagenorhynchus obliquidens*),'' in *Echolocation in Bats and Dolphins*, edited by J. Thomas, C. Moss, and M. Vater (University of Chicago Press, Chicago).

Hartley, D. J. (**1992**). ''Stabilization of perceived echo amplitudes in echolocating bats. II. The acoustic behavior of the big brown bat, *Eptesicus fuscus*, when tracking moving prey,'' J. Acoust. Soc. Am. **91**, 1133–1149.

Henson, O. W. (**1965**). ''The activity and function of the middle-ear muscles in echo-locating bats,'' J. Physiol. **180**, 871–887.

Jensen, M. E., and Miller, L. A. (**1999**). ''Echolocation signals of the bat *Eptesicus serotinus* recorded using a vertical microphone array: Effect of flight altitude on searching signals,'' Behav. Ecol. Sociobiol. **47**, 60–69.

Miller, L. A., Pristed, J., Møhl, B., and Surlykke, A. (**1995**). ''The click-sounds of narwhals (*Monodon monoceros*) in Inglefield Bay, Northwest Greenland,'' Marine Mammal Sci. **11**, 491–502.

Møhl, B., Surlykke, A., and Miller, L. A. (**1990**). ''High intensity narwhal clicks,'' in *Sensory Abilities of Cetaceans*, edited by J. Thomas and R. Kastelein (Plenum, New York), pp. 295–303.

Møhl, B., Wahlberg, M., Madsen, P. T., Miller, L. A., and Surlykke, A. (**2000**). ''Sperm whale clicks: Directionality and source level revisited,'' J. Acoust. Soc. Am. **107**, 1–11.

Rasmussen, M. H., and Miller, L. A. (in press). ''Echolocation and social signals from white-beaked dolphins, *Lagenorhynchus albirostris*, recorded in Icelandic waters,'' in *Echolocation in Bats and Dolphins*, edited by J. Thomas, C. Moss, and M. Vater (University of Chicago Press, Chicago).

Reeves, R. R., Smeenk, C., Kinze, C. C., Brownell, R. L., and Lien, J. (**1999**). ''White-beaked dolphin, *Lagenorhynchus albirostris* Gray, 1846,'' in *Handbook of Marine Mammals*, edited by S. H. Ridgway and S. R. Harrison (Academic, San Diego), Vol. 6, pp. 1–30.

Schotten, M. (**1997**). ''Echolocation recordings and localizations of free-ranging spinner dolphins (*Stenella longirostris*) and Pantropical spotted dolphins (*Stenella attenuata*) using a four hydrophone array,'' in A Report to The Department of Marine Biology, University of Groningen, and to The University of Hawaii.

Schotten, M., Au, W. W. L., Lammers, M. O., and Aubauer R. (in press). ''Echolocation recordings and localizations of wild spinner dolphins (*Stenella longirostris*) and pantropical spotted dolphins (*Stenella attenuata*) using a four hydrophone array,'' in *Echolocation in Bats and Dolphins*, edited by J. Thomas, C. Moss, and M. Vater (University of Chicago Press, Chicago).

Urick, R. J. (**1983**). *Principles of Underwater Sound* (McGraw-Hill, New York).

Zar, J. H. (**1996**). *Biostatistical Analysis* (Prentice-Hall, Englewood Cliffs, NJ).

Erratum: "Attenuation and dispersion of sound in dilute suspensions of spherical particles" [J. Acoust. Soc. Am. 108, 126–146 (2000)]

S. Temkin
Department of Mechanical and Aerospace Engineering, Rutgers University, 98 Brett Road, Piscataway, New Jersey 08854-0858

(Received 2 October 2001; accepted for publication 24 October 2001)

[DOI: 10.1121/1.1427729]

PACS numbers: 43.35.Bf [ADP]

The appendix to the original paper[1] contains certain functions, obtained elsewhere,[2] that describe the temperature fluctuations of a pulsating bubble or droplet in a sound wave. Those functions contain an error[3] that invalidates the *explicit* results obtained in Ref. 1 for the attenuation and sound speed of gas bubbles and pulsating droplets at finite frequencies. The general theory developed in Ref. 1 is not affected by the error. Corrections for the temperature ratio, T, and for the related pressure ratio, Π, have been obtained[4] and are given below. To save space, the corrected results for these functions are given in complex form. In the notation of Ref. 1, they are given by

$$T=\left[\xi+3\frac{k_f}{k_p}\frac{1}{q_i^2F}(\xi-1)\right]\Pi, \tag{1}$$

where $q_i^2=2iz_p^2$ and where F now represents the complex function given by Eq. (3.40) of Ref. 2. This function is identical to Epstein and Carhart's function $F(b,b_i)$,[5] and to the inverse of Allegra and Hawley's function H,[6] that is,

$$F=\frac{1}{1+z-iz}+\frac{k_f}{k_p}G(q_i), \tag{2}$$

where $G(q_i)=j_0(q_i)/q_ij_0'(q_i)$. The corrected pressure ratio, Π, is given by

$$\Pi=\frac{1-i\hat{d}_{th}}{1-(\omega/\omega_0)^2-i\hat{d}}, \tag{3}$$

where $\hat{d}$ is the total nondimensional damping coefficient, which in this case is given by $\hat{d}=\hat{d}_{th}+\hat{d}_{ac}$ because viscosity is not included in the formulation, and ω_0 is the resonance frequency for the radial pulsations of bubbles or droplets, given by

$$\omega_0^2=\Omega_{T0}^2(1+b^2)\kappa_r/\zeta. \tag{4}$$

Here $\zeta=\rho_{p0}c_{sp}^2/\gamma_p p_0$, a quantity which reduces to unity for perfect gases, and κ_r is the real part of a complex polytropic index, $\kappa=\kappa_r+i\kappa_i$, given by

$$\kappa=\zeta\left(1-\frac{(\gamma_p-1)}{\gamma_p\xi}\frac{T}{\Pi}\right)^{-1}. \tag{5}$$

This is determined by using (1) for T/Π. This equation also shows that the polytropic index depends on the frequency. Thus, contrary to what was stated in the original paper, the resonance frequency varies as the frequency of the incident wave changes. In the case of gas bubbles, (4) is nearly equal to Prosperetti's value.[7] Finally, the thermal and acoustic damping coefficients appearing here are also obtained from the complex polytropic index, through $\hat{d}_{th}=|\kappa_i|/\kappa_r$ and $\hat{d}_{ac}=b(\omega/\omega_0)^2$, respectively.

The corrected values of T and Π should be used in the compressibility theory developed in Ref. 1 to obtain the attenuation and dispersion for bubbles and droplets. Below are some figures that show the effects of the corrections in the most important cases.

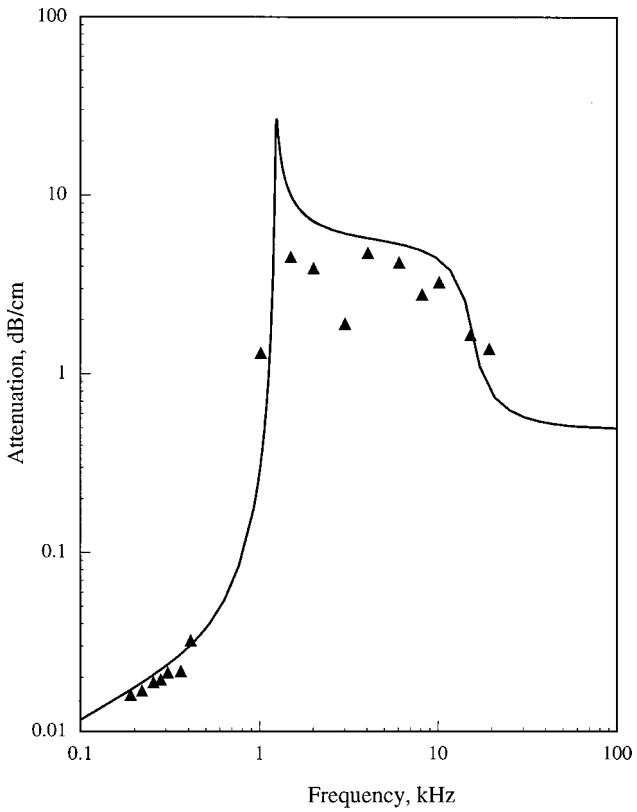

FIG. 1. Revised Fig. 13 of Ref. 1. Comparison between the attenuation predicted by the compressibility theory with Silberman's Fig. 5 data. $\phi_v=0.01$, $a=0.528$ cm.

 0001-4966/2002/111(2)/1126/3/$19.00

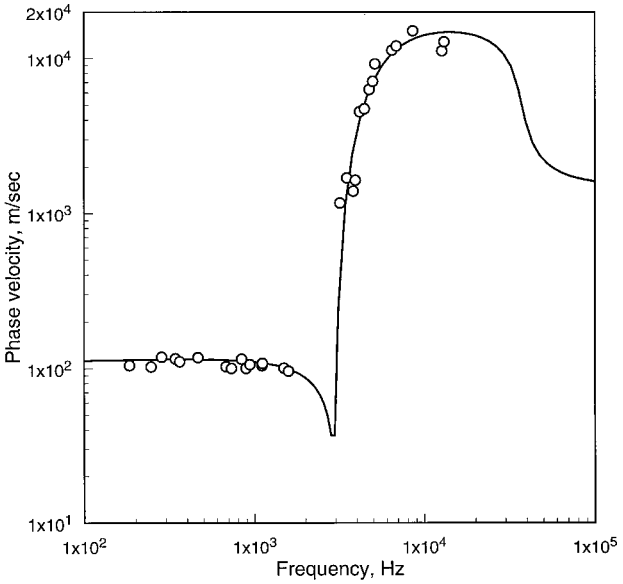

FIG. 2. Revised Fig. 14 of Ref. 1. Comparison between the phase velocity predicted by the compressibility theory with the experimental results of Cheyne *et al.*[10] $\phi = 0.01$.

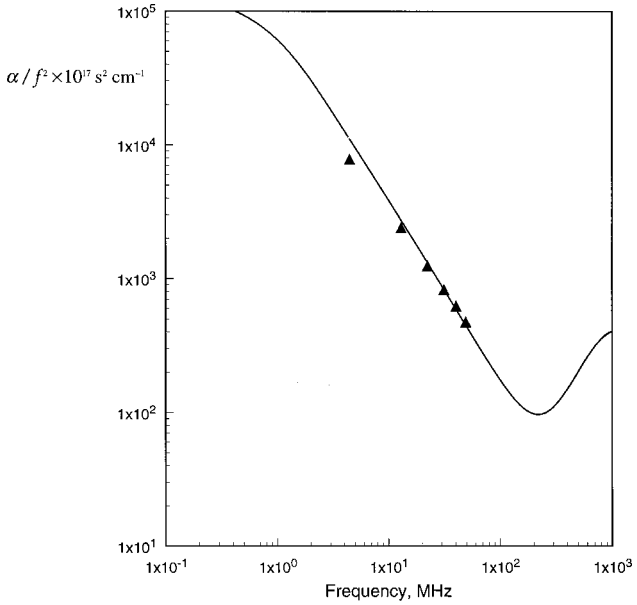

FIG. 4. Comparison between the attenuation predicted by the compressibility theory of Ref. 1 with Allegra and Hawley's data for toluene drops in water as shown in Fig. 4 of their paper. $\phi_v = 0.2$, $a = 0.3\ \mu$m.

We first consider bubbly liquids. Figure 1 shows the attenuation for gas bubbles as predicted by the corrected theory, together with the experimental results of Silberman.[8] This figure replaces Fig. 13 of Ref. 1. It is seen that the corrected theory departs from the initial one at lower frequencies, where it agrees well with Silberman's experiments. A similar agreement had been reported earlier by Commander and Prosperetti[9] who used a different theory. I had referred to that agreement as being fortuitous. That statement is clearly incorrect and is withdrawn. Figure 2 shows the phase velocity for gas bubbles as predicted by the corrected theory, together with the experimental results of Cheyne *et al.*[10] The corresponding original results are shown in Fig. 14. As in the attenuation case, the differences between the corrected theory and that of Commander and Prosperetti are small.

We now turn to emulsions. Figure 3, which replaces Fig. 5(a), shows the various attenuations in the case of an emulsion of toluene droplets in water. Figure 4 compares the corrected attenuation predictions to the experimental results of Allegra and Hawley.[6] The plot is shown in the manner used by those investigators to report their measurements. It should be added that the agreement between the compressibility theory and the experimental results displayed by this figure is closer than that reported earlier on the basis of dissipation alone (Fig. 2 of Ref. 4). Finally, Fig. 5 shows the corrected phase velocity ratios for an emulsion composed of toluene droplets in water. This figure replaces Fig. 9(b) of the original article.

To conclude, it should be stressed that the general compressibility theory developed in Ref. 1, whose results are expressed by Eqs. (2a), (33), and (34) of that article, remains unchanged.

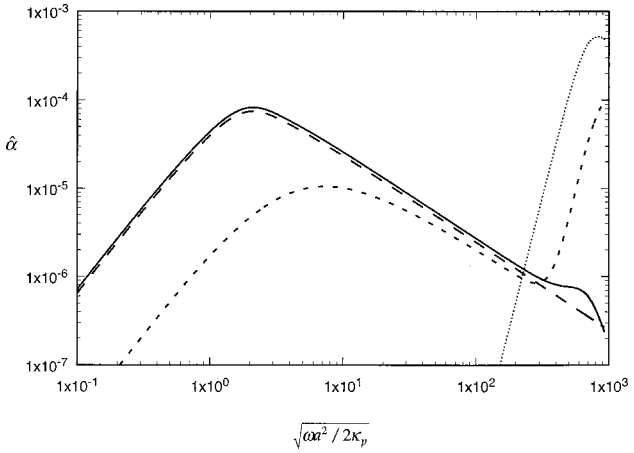

FIG. 3. Revised Fig. 5(a) of Ref. 1. Nondimensional attenuations for 100 μm toluene droplets in water. $\phi_v = 10^{-3}$. ——— Thermal; – – – thermal, Isakovich; --- translational; ⋯ acoustic.

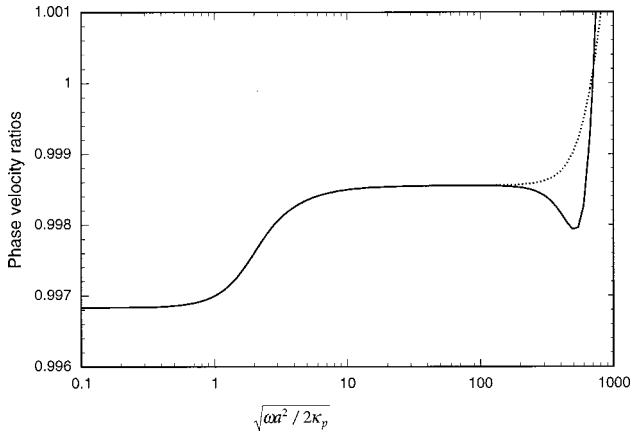

FIG. 5. Revised Fig. 9(b) of Ref. 1. Phase velocity ratios $c_s(\omega)/c_{sf}$ for an emulsion of 100-μm-diam toluene drops in water. $\phi_v = 10^{-2}$. ——— Reference 1, Eqs. (48) and (49); ⋯ Uniform pressure theory.

[1] S. Temkin, ''Attenuation and dispersion of sound in dilute suspensions of spherical particles,'' J. Acoust. Soc. Am. **108**, 126–147 (2000).
[2] S. Temkin, ''Radial pulsations of a fluid particle in a sound wave,'' J. Fluid Mech. **380**, 1–38 (1999).
[3] A. Prosperetti and M. Ren, ''Comments on 'Radial pulsations of a fluid sphere in a sound wave' by S. Temkin,'' J. Fluid Mech. **430**, 401–405 (2001).
[4] S. Temkin, ''CORRIGENDUM. Radial pulsations of a fluid particle in a sound wave,'' J. Fluid Mech. **430**, 407–410 (2001).
[5] P. S. Epstein and R. R. Carhart, ''The absorption of sound in suspensions and emulsions. I. Water fog in air,'' J. Acoust. Soc. Am. **25**, 553–565 (1953).
[6] J. R. Allegra and S. A. Hawley, ''Attenuation of sound in suspensions and emulsions: Theory and experiments,'' J. Acoust. Soc. Am. **51**, 1545–1564 (1971).
[7] A. Prosperetti, ''The thermal behavior of oscillating gas bubbles in liquids,'' J. Fluid Mech. **222**, 587–616 (1991).
[8] E. Silberman, ''Sound velocity and attenuation in bubbly mixtures measured in standing wave tubes,'' J. Acoust. Soc. Am. **29**, 925–933 (1957).
[9] K. W. Commander and A. Prosperetti, ''Linear pressure waves in bubbly liquids: Comparison between theory and experiments,'' J. Acoust. Soc. Am. **85**, 732–746 (1989).
[10] S. A. Cheyne, C. T. Stebbings, and R. Roy, ''Phase velocity measurements in bubbly liquids using a fiber optic laser interferometer,'' J. Acoust. Soc. Am. **97**, 1621–1624 (1995).